



Organizers

Shiraz University



Shiraz University of Technology



Regional Information Center for
Sciences and Technology



Iranian Chemical Society



Sponsors

Fars Organizers Office

Shiraz Petrochemical Co.

Fars Sciences and Technology Park

Islamic Azad University, Shiraz Branch

Islamic Azad University, Marvdashet Branch

Islamic Azad University, Firouzabad Branch

Fars Cultural Inheritance, Handicrafts, and Tourism Organization

Varech Shimi Bahar Co.

Mabnateyf Co.

Chemia Exir Co.

Perse Sanco



In the name of God, The compassionate, The merciful

Proceeding of The

13th Iranian Physical Chemistry Seminar

Shiraz-Iran

April 12-15, 2010

Vol. I





Dear Colleagues,

It is our great pleasure to welcome all participants in the 13th Iranian Physical Chemistry Conference that is held April 12-15, 2010 in Shiraz. The conference aim is to bring physical chemistry scientists and students together to discuss the latest and future developments in the rapidly advancing fields of various filed of physical chemistry. The conference covers nine topics in the field of physical chemistry. The scientific committee has received 435 extended abstracts, among them 88 were selected as oral presentation and 320 as posters. We also like to thank the team of referees for their collaboration in reviewing the submitted articles in each subject area. We also would like to appreciate Iranian Chemical Society to encourage the national physical chemistry community to consolidate this activity as annual event.

We hope that besides the interesting scientific contacts, you will find some time to enjoy the hospitality, historical richness and beauty of Shiraz.

Dr. A. Mohajeri

Scientific Chairman





Seminar Chairman: Dr. Ali Heydar Pakiari

Executive Chairman: Dr. Mohammad Mehdi Papari

Scientific Chairman: Dr. Afshan Mohajeri

Scientific Committee

Dr. A. H. Pakiari
Dr. A. Mohajeri
Dr. A. Maghari
Dr. G. A. Parsafar
Dr. H. Sabazyan
Dr. M. Tafazzoli
Dr. A. A. Rostami
Dr. H. Behnejad
Dr. J. Moghadasi

Organaizing Committee

Dr. A. H. Pakiari
Dr. J. Moghadasi
Dr. M.M. Papari
Dr. A. R. Nekoei
Dr. D. Mohamadaghaie
Dr. M. N. Soltani
Dr. R. Khalifeh
E. Shams

Sponsors

Shiraz University
Shiraz University of Technology
Iranian Chemical Society





List of Referees

Dr. Abbaspour, A.	Shiraz Univeristy
Dr. Azizian, S.	Bu-Ali Sina University
Dr. Azami, S. M.	Yasouj University
Dr. Bordbar, A.	University of Isfahan
Dr. Behnejad, H.	University of Tehran
Dr. Dehestani, M.	Shahid Bahonar University of Kerman
Dr. Ebrahimi, A.	University of Sisatan and Balouchestan
Dr. Eslami, H.	Persian Gulf Unviersity of Bushehr
Dr. Eskandari, K.	Damghan University of Basic Sciences
Dr. Ghatee, M. H	Shiraz University
Dr. Goharshadi, E.	Ferdowsi University of Mashhad
Dr. Gholami, M. R.	Sharif University of Technology
Dr. Habibi, M. H.	University of Isfahan
Dr. Habibi yangje, A.	University of Mohaghegh Ardebili
Dr. Hashemianzadeh, M.	Iran University of Science and Technology
Dr. Hormozinejad, M. R.	Sharif University of Technology
Dr. Hadipour, N.	Tarbiat Modares University
Dr. Habibi Khorasani, S. M.	University of Sisatan and Balouchestan
Dr. Hamadanian, M.	Kashan University
Dr. Jalili, S.	K. N. Toosi University of Technology
Dr. Jafarian, M.	K. N. Toosi University of Technology
Dr. Keshavari, E.	Isfahan University of Technology
Dr. Maghari, A.	University of Tehran
Dr. Mohajeri, A.	Shiraz University
Dr. Mahjani, M. G.	K. N. Toosi University of technology



Dr. Mosavipour, S. H.	Shiraz University
Dr. Nasehzadeh, A.	Shahid Bahonar University of Kerman
Dr. Namazian, M	Yazd University
Dr. Noorizadeh, S.	Shahid Chamran University of Ahwaz
Dr. Najafi, B.	Isfahan University of Technology
Dr. Pakiari, A. H.	Shiraz University
Dr. Papari, M. M.	Shiraz University of Technology
Dr. Parsafar, G. A.	Sharif University of Technology
Dr. Roohi, H.	University of Sisatan and Balouchestan
Dr. Rostami, A. A.	University of Mazandaran
Dr. Razavizadeh, S. A.	Payame Noor University of Shiraz
Dr. Rezai Sameti, M.	Malayer University
Dr. Rafati, A. A.	Bu-Ali Sina University
Dr. Sadeghi, R.	University of Kurdistan
Dr. Sabzyan, H.	University of Isfahan
Dr. Salabat, A.	Arak University
Dr. Shayesteh, A.	University of Tehran
Dr. Shafiee, A.	Sharif University of Technology
Dr. Solimannejad, M	Arak University
Dr. Tabrizchi, M.	Isfahan University of Technology
Dr. Tafazzoli, M	Sharif University of Technology
Dr. Yeganegi, S.	University of Mazandaran
Dr. Zafarni Moatar, M. T	University of Tabriz
Dr. Zeini Esfahani, A.	University of Isfahan



Table of Content

Classical Thermodynamics

	Page
1 Investigation on interaction of Ni(II)salen with Hen egg white lysozyme(HEWL): a Thermodynamic approach M. Reissi, N. Sohrabi, N. Rassoli	3
2 Study of self-diffusion of methane and carbon dioxide in BEA zeolite with MD simulation S.L. Fani, S. Alavi, B. Najafi, H. Mohammadimanesh	5
3 Liquid–liquid equilibria of water–cyclic hydrocarbon systems using asymmetric mixing rules P. Reshadi, Kh. Nasrifar	7
4 Thermodynamic study of adenine, adenosine and uracil at constant ionic strength E. Heiatian, S. Sharifi, A. Niazi, A. Bahadori	9
5 Surface tension determination of dense fluid methanol A. Siami, V. Moeini	11
6 Measurement and prediction of volumetric and transport properties of ternary aqueous solution of tri-potassium citrate + KCl at different temperatures M.T. Zafarani-Moattar, F. Izadi	13
7 Ionic strength dependence of formation constants, protonation and complexation of EDTA with dioxouranium(VI) M. Jabbari, A. Farajtabar and F. Gharib	15
8 Measurement and modelling of osmotic coefficients for three components systems at 298.15 K A. Ebrahimian Pirbazari, J. Jahanbin Sardroodi	17
9 Characterizing phase transition in liquid cesium with voronoi-tessellation method M. H. Ghatee, Kh. Shekoohi	19
10 Thermodynamics of interactions between Vanadium(V) and sulfonatocalix[4]arene K. Zare, F. Gharib, M. Hajmalek	21
11 DFT studies, NBO and NICS analysis of all chlorothiophenes and their cations as candidate monomers for new conductive polymers H. Shirani, S. Jameh-Bozorgi	23
12 Thermodynamic modeling of methane hydrate formation conditions in aqueous solutions of methanol and NaCl, KCl and CaCl₂ S. Babaee and J. Javanmardi	25
13 Volumetric study on the interactions of Schiff base ligand (salen) with 1-Pentyl–3-methylimidazolium bromide ([PnMIm]Br) in DMF (n,n-Dimethyl foramide) at T = (298.15 K and 308.15 K) H. Shekaari, A. Bezaatpour, A. Soltanpour	27
14 Vapor–Liquid equilibria, density and speed of sound of aqueous di-sodium hydrogen citrate solutions at different temperatures M.T. Zafarani-Moattar, N. Karimi	29



15	Isotherm, kinetic and thermodynamic study of methylene blue dye adsorption in aqueous solution by leaves of data palm	31
	F. Fakhari , N. Bahramifar, F. Ashrafi	
16	The competitive interaction studies between aspirin and tamoxifen with human serum albumin by nano-fluorescence spectroscopic	33
	S. Pourgonabadi, M.R. Saberi, J. Chamani	
17	Prediction of the activity coefficients for aqueous uni-univalent electrolytes by artificial neural network	35
	F. Nami , F. Deyhimi	
18	Excess molar volumes of (N,N-dimethylacetamide +N-methyl formamide) , (N,N-dimethylacetamide+ 1,2-propanediol) and (N-methyl formamide+ 1,2-propanediol) at different temperatures	37
	S. Akbary Golroudbari, H.A. Zarei	
19	Molecular dynamics simulation of ¹³C NMR power lineshapes of linear molecules in structure I clathrate hydrate	39
	H. Mohammadi-Manesh, S. Alavi and B. Najafi	
20	Adsorption thermodynamic and desorption studies of Cs-137 on manganese dioxide-polyacrylonitrile composite	41
	A. Nilchi , G. Aboulhasanlo, S. Rasouli Garmarodi	
21	Thermodynamics of binding copper ion to jack bean urease	43
	E. Poorakbar-Esfahani A. A. Saboury, and G. Rezaei-Behbehani	
22	Thermodynamics of aqueous solutions of L-serine+diammonium hydrogen citrate from the volumetric properties and the isopiestic determination of water activity	45
	R. Sadeghi, A. Gholamireza	
23	The second law of thermodynamics in an information-based language	47
	A. Shafiee, I. Khatam	
24	Liquid-Liquid equilibrium in mixture of Methanol + Cyclohexane and Ionic liquid N-R-4-(N,N-dimethylamino)pyridinium Bromide (R=C₄H₉, C₅H₁₁, C₆H₁₃) at 298.15 K	49
	J. Jahanbin , M. Ighaei, M. Dadfar	
25	Vapor-Liquid equilibria of binary disodium hydrogen citrate + water and ternary 1-octyl-3-methyl imidazolium bromide +disodium hydrogen citrate + water systems from isopiestic measurements	51
	R. Sadeghi , E. Parsi	
26	Isotherms and thermodynamic studies on biosorption of Pb(II) from waste waters using Syringa Vulgaris tree leaves	53
	S. Mahmoudzadeh, A. Niazi, V. Najafi	
27	Acid-base equilibria of salicylic acid in mixed water-DMSO solutions	55
	A. Farajtabar, F. Gharib, M. Jabbari	
28	A modified perturbed hard-sphere equation of state applied to room temperature ionic liquids	57
	S. M. Hosseini , M. M. Papari	
29	Selfdiffusion coefficient of liquid argon from generic van der Waals equation of state	59
	S. A. Razavizadeh	
30	Determination of thermodynamic properties of binary and ternary mixtures of {1-butanol (1) + cylohexylamine (2) + n-heptane (3)} at different temperatures: Experimental results and application of the Flory theory.	61
	H. Iloukhani , M. Rezaei-Sameti , M. Rakhshi	



31	Densities and volumetric properties of (<i>n</i>-butyl acetate + 1-butanol + 1,2-butanediol) binary and ternary mixtures from T = (298.15 to 308.15) K. theoretical and experimental study.	63
	H. Iloukhani , M. Rezaei-Sameti , M. Rakhshi	
32	Electrochemical determination of ionic products of 50% (v/v) water-methanol electrolyte solutions and ionic strength effect	65
	A. Farajtabar, F. Gharib	
33	Vapor–liquid equilibria, density and speed of sound of aqueous di-potassium oxalate solutions at different temperatures	67
	M.T. Zafarani-Moattar ,S. Davoodi	
34	Isotherm, kinetic and thermodynamic studies of eosin Y dye biosorption in aqueous solution by <i>Saccharomyces cerevisiae</i>	69
	M. Tavasolli , N. Bahramifar , F. Ashrafi	
35	Complex formation of cerium(IV) ion with glycyl-glycine at different ionic strength	71
	F. Kiani, A. A. Rostami, S. Sharifi, F. Gharib	
36	Equilibrium study of complexes of cadmium (II) with L-phenylalanylglycine and glycyl-L-phenylalanine	73
	A. Bahadori , S. Sharifi, D. Nori-shargh, F. Kiani	
37	Thermodynamic investigations on the interaction of vanadyl (IV) bis (acetylacetonate) with D-penicillamine, effective in several biological processes at different pHs	75
	R. Hakmelahi ,H. Aghaie , M.A. Seyed Sadjad	
38	Investigation of some dense system regularities for yukawa fluid	77
	N. Farzi, Se. Hosseini	
39	Effect of PEG, PVP and Triton X-100 on CMC of the aqueous solution of sodium dodecyl sulfate	79
	A. Salabat, M. Heydari, A. Barati	
40	Solute-solvent interactions in Co-Salen schiff base complex in organic solvents at 298.15 K	81
	H. Shekaari,A. Bezaatpour ,R. Elhami	
41	Solvent effects on protonation and guanine in different aqueous solutions of methanol	83
	M. Khoshbakht ,G. Geimachy, A. Shamel	
42	Application Of Surfactant based Aqueous Two Phase Systems in Amino acids Extraction	85
	A. Salabat, S. tiani,Moghadam, M. Rahmati Far	
43	Prediction of thermodynamic properties of pure and mixtures liquid alkali metals	87
	E. Faramarzi , M. H. Mousazadeh	
44	Study of dielectric behaviour of binary mixtures of butanediols in a non-polar solvent at 298.2 K	89
	A. Ghanadzadeh, H. Ghanadzadeh, Kh. Bahrpaima, R. Rostamiyan	
45	Effect of ionic liquid, [PrMIm]Br on the thermodynamic properties of aqueous solutions of L-Arginine at T= 298.15 K	91
	H. Shekaari, F. Jebali	
46	Kinetic and thermodynamic study of eosin Y dye biosorption by leaves of date palm (<i>Phoenix dactylifera</i> L.)	93
	N. Bahramifar, F. Ashrafi , A. Amini	
47	A DFT study of oxidative addition of hydrogen peroxide topPlatinum(II) complex	95
	F. Niroomand Hosseini , S. M. Nabavizadeh	



48	A charged particle source at atmospheric pressure	97
	E. Abedini, M. Tabrizchi	
49	Application of the group contribution method to long chain n-alkanes based on a new equation of state	99
	M. Moosavi	
50	Investigation of temperature dependencies of parameters of effective pair potential	101
	F. Namdari, G. A. Parsafar	
51	Equation of state for light solid molecules	103
	F. Safdari, G. A. Parsafar	
52	The pH effect on complexation of Alkali metal cation by p-sulfonatocalix(4)arene in aqueous solution	105
	N. Osouledini	
53	Salting-out effects in aqueous solutions of ionic liquid 1-Butyl-3-Methylimidazolium Iodide and sodium phosphate: cloud-point temperature shifts and volumetric properties	107
	R. Sadeghi, B. Mostafa	
54	Excess thermodynamic parameters of binary mixtures of {Methanol, Ethanol, 1-Propanol and 2-Butanol + Chloroform} at (288.15 to 323.15K) and comparison the Flory theory	109
	M. Rezaei Sameti , H. Iloukhani , M. Rakhshi	
55	The study of physico-chemical properties of binary systems (benzyl alcohol, cyclohexanol and 1,2-propanediol) at different temperatures	111
	E. Sokhanvary, H. A. Zarei	
56	Hetero-Diels-Alder reaction between Hexafluoro-2butyen and 1-Methyl-silene. A theoretical study	113
	S. Jameh-Bozorgi, H. R. Khalili ghaydar	
57	A comparison study between sodium dodecyl sulfonate and sodium dodecyl sulfate with respect to the interaction with poly(ethylene glycol) in aqueous solutions at several temperatures	115
	R. Sadeghi, S. Shahabi	
58	Spectrophotometric and thermodynamic studies on the protonation and nickel complexation equilibrium of hydroxynaphthol blue in aqueous solution	117
	M. Motiee , A. Niazi , S. Sharifi , B. Yasar	
59	Thermodynamic study of Zn (II)-G lycinamide complex formation by spectrophotometric method in various temperatures and pH=4, ionic strength=0.1 molL⁻¹	119
	N. Tajdini, S. Hosseini	
60	Interaction of dimethyltin(IV) dichloride with phenylalanine and tryptophan	121
	S. Babashpour , M. Moazzami , A. Shamel , F. Gharib	
61	p-v-T-properties of phosphonium-based ionic liquids using ISM equation of state	123
	S. M. Hosseini , F. Sabzi	
62	A modified perturbed hard-sphere equation of state compared with Peng-Robinson equation of state	125
	S. M. Hosseini , M. M. Papari , J. Moghadasi	
63	Interaction of dioxovanadium(V) with leucine and histidine	127
	S. Seifi , A. Shamel , F. Gharib	



64	Acoustical properties of the binary mixtures of <i>N,N</i>-dimethylacetamide and <i>N,N</i>-dimethylformamide + 1,2-Alkandiol (C2-C5) at 293.15 K – comparison with theories	129
	H. Iloukhani, K. Khanlarzadeh	
65	Phase diagrams for Liquid-Liquid and liquid-solid equilibrium of the ternary (Polyethylene glycol Dimethyl Ether 2000 + Potassium Phosphate + Water) system	131
	M. T. Zafarani-Moattar, E. Nemati Kande	
66	Conductometric study of NaF in different ROH+water mixed solvents (with R=1-Pr and 2-Pr) based on Fuoss-Hsia-Chen-Justice electrolytic model	133
	F. Deyhimi, E. Choobdari	
67	Densities, and excess molar volumes for binary mixtures of diethyl phthalate + bromocyclohexane at (298.15, 303.15 and 308.15) K.	135
	A. A. Rostami, s. yeganegi, A. Mossazade Rostamkolahi	
68	Phase equilibria of hydrocarbon-methanol systems from equation of state-excess gibbs energy (EoS-G^E)	137
	H. Hashemi, P. Reshadi, S. Babaei, F. Sabzi	
69	Temperature dependence of viscosity and relation with the surface tension of ionic liquids	139
	M. H. Ghatee, M. Zare	
70	Thermodynamic and kinetic studies for the adsorption system of Zinc (II) and ions from solution using functionalized mesoporous silica NH₂-MCM-41	141
	N. Jamshidi, F. Ashrafi, N. Bahramifar	
71	Liquid phase equilibria of (water + alcohols + 2-ethyl-1-hexanol) ternary systems at T=298.2 K	143
	A. Ghanadzadeh, H. Ghanadzadeh, S. Abbasnejad, S. Shekarsaraee	
72	A Cubic Equation of State Applicable to Ionic Liquids	145
	L. Maftoon-Azad	



Statistical Mechanics

	Page
1 Monte Carlo simulation of hard confined ellipses M. Moradi, S. Hashemi	149
2 Validity of some regularities of dense fluids for ionic liquids H. Azizi Toopkanlu, E. K. Goharshadi	151
3 Thermodynamic modeling of the solubility of carbon dioxide in aqueous monoethanolamine solution A. Gheisari, F. Rashidi, A. Maghari and S. Sadeghi	153
4 Calculation of entropy of cyclohexane V. Moeini, M. Deilam, H. Rahimi	155
5 Prediction of thermodynamic second derivatives and solubility of some gases in amines by statistical associating fluid theory A. Maghari, S. Sadeghi	157
6 An analytical perturbed equation of state for hard chain fluids: modeling P-V-T behavior of short n-alkanes and n-perfluoroalkanes M. Masoudi, H. Farrokhpour	159
7 The Expansion Coefficients Of Direct Correlation Function Of Spherocylinder Fluids M. Moradi, H. Mokhtari, M. M. Gharahbeigi	161
8 Attractive energy contribution to nano-confined fluids behavior: the normal pressure tensor E. Keshavarzi, F. Heidari, F. Sedaghat	163
9 The lateral pressure tensor of confined fluids in nanoslit pores E. Keshavarzi, F. Heidari	165
10 Structure of a confined hard sphere mixture in a nanoslit M. Kamalvand, E. Keshavarzi	167
11 Structure and phase transition of confined Lennard-Jones fluids in a nanotube M. Kamalvand, E. Keshavarzi	169
12 Transport properties of non-spherical gases A. Maghari, H. Diarmand, A. H. Jalili	171
13 Determination of critical concentration for polymer and surfactant mixture with lattice Monte Carlo simulation R. Behjatmanesh-Ardakani, F. Ghaderiyeh-Mahmood Abadi	173
14 Calculation of static structure factor, $s(k)$, for xenon fluid by using the hard sphere radial distribution function H. Nikoofard, Z. Kalantar, T. Rezayee	175
15 Calculation of isothermal compressibility and pressure of simple liquids using the hard sphere radial distribution function H. Nikoofard, Z. Kalantar, T. Rezayee	177
16 Investigation of molecular orientation at liquid-vapor interface by molecular dynamic simulation M. H. Ghatee, A. R. Zolghadr	179
17 Thermodynamic Behavior of Fluids: Crossover from Ising-like to Nonasymptotic Mean-Field Critical Behavior H. Behnejad, A. Bakhshandeha, J. V. Sengers	181
18 Second-order thermodynamic derivative properties of binary mixtures using the statistical associating fluid theory A. Maghari, M. Hamzehloo	183



19	Application of Tao-Mason equation of state to quantum systems	185
	M. M. Papari ,M. Kiani, J. Moghadasi, R. Behjat Manesh Ardekani	
20	Computation of some thermodynamic properties of nitrogen using a new intermolecular potential from molecular dynamics simulation	187
	E. K. Goharshadi M. Abbaspour , M. Namayandeh Jorabchi, M. Nahali	
21	The role of particulate-fluid and fluid-fluid interactions in surface tension and adsorption of a fluid in contact with a spherical particulate	189
	E. Keshavarzi, A. Taghizadeh	
22	Prediction of sound velocity of n-alkanols using the statistical associating fluid theory	191
	S. Hosseini , A. Maghari	
23	An analytical direct correlation function for hard core double Yukawa potential	193
	M. Khanpour, G. A. Parsafar	
24	Prediction of structure factor, $s(k)$, of simple fluids using the lir equation state in super critical region	195
	H. Nikoofard, Z. Kalantar, B. A. Esmaeili	
25	Prediction of the long-range correlation length for Ar fluid in the near critical point via LIR equation state	197
	H. Nikoofard, Z. Kalantar, B. A. Esmaeili	
26	Bulk and surface properties of formate esters by the application of SAFT-VR and molecular dynamics simulation	199
	M. H. Ghatee, F. Moosavi	



Quantum Chemistry

	Page
1 Investigation of gap energy in sensitized dye and some derivatives of N3 by DFT Method L. Tavakolizadeh, M. Oftadeh	203
2 Are resonance-assisted hydrogen bonds 'resonance assisted'? quantum chemical study M. Farrokhnia, A.H. Pakiari	205
3 Intramolecular hydrogen bond and tautomeric preference in thioaminoacrylaldehyde A. Nowroozi, M. Poorsargol, M. Shibaninia, P. Mohammadzadeh Jahani	207
4 DFT investigation of donor-acceptor in the charge transfer molecular complexes of C₃S₃H₆, with I₂, IBr, ICl, Br₂ and Cl₂ M. Moghadari, M. Oftadeh	209
5 NQR studies of the glycine radical addition to the carbon nanotubes N. Noorani, H. Rahemi	211
6 A detailed study of the electronic structure of the sub-nano-sized cluster of Fe₃ and associative adsorption of N₂ to this cluster A. H. Pakiari, M. Mousavi	213
7 A MP2 intermolecular potential energy surface for the CO-CO system M. Abbasinia, M. R. Noorbala, M. Namazian	215
9 Experimental and theoretical determination of the dipole polarizability of substituted thiophenols M. Oftadeh, S. Nasseh, M. Hamadianian	217
10 Gas-phase acidities of fulleropyrrolidynes, A AM1 study V. Nasr Isfahani, M. Oftadeh	219
11 Theoretical investigation of metallophilic bonding Z. Jamshidi	221
12 Density functional study of group 13-15 nanorods A. Mohajeri, M. Ebadi	223
13 Ab initio and DFT study of alkyle substituent effects on the electronic and structural properties of thiophene derivatives H. Nikoofard, Z. Kalantar, M. Khorrami	225
14 A theoretical investigation structure and electronic characteristics of the thiophene and 3-propyle thiophene oligomers H. Nikoofard, Z. Kalantar and M. Khorrami	227
15 Theoretical identification of local strain in cyclic molecules S. M. Azami	229
16 Electrostatic field gradient as a tool for aromaticity measurement A. H. Pakiari, N. Bagheri	231
17 Theoretical study of the interaction between uracil and parent nitrosamine H. Roohi, E. Anjomshoa	233
18 From information theories to electron correlation energy A. Mohajeri, M. Alipour	235
19 The corrosion inhibition of some substituted quinolones in water solvent by DFT method S. Rasti, M. Oftadeh	237
20 Coupled wave quantum scattering via separable potential model: Application to statistical mechanics A. Maghari, V. M. Maleki	239
21 Thermophysical properties of the dilute fluorine gas from a new ab initio potential energy surface M. H. Karimi Jafari, A. Maghari, M. Ashoori	241



22	Theoretical study of structural properties in alkali metal clusters	243
	A.Mohajeri, M. Mahmoodinia	
23	Relationship of dipole moment to hydrostatic pressure in hydrogen molecule	245
	M. Oftadeh, S. Saidi, M. Hamadani	
24	Quantitative structure-property relationship (QSPR) study of n-octanol-water partition coefficients (logP_{ow}) of fatty acids using multiple linear regression (MLR)	247
	S. A. Bavafa, R. Behjatmanesh-Ardakani	
25	Ab initio and DFT studies on proton transfer of nitrosamine in reaction of the nitrosamine isomers - H₂O₂	249
	S. A. Bavafa, H. Roohi	
26	Theoretical study of interaction between nitrosamine (NA)-(Formic acid (α1, α2) and Formamide (β)): Density functional theory study (DFT)	251
	S. A. bavafa, R. Behjatmanesh-Ardakani	
27	Investigation of the deflagration pathway for TNAZ and some of its derivatives as energetic materials by DFT method	253
	M. Radhoosh, M. Oftadeh, M. Hamadani	
28	Charge-density study of 5-Chloro-8-hydroxy-6-methylnaphthalene-1,4-dione: A hydroxynaphthoquinone derivative	255
	Z. Sharafi, R. Kia	
29	Quantum Monte Carlo methods	257
	S. Jalili, B. Kharazian	
	Ab initio study of single-wall boron nitride nanotube with various diameters under the static electric field	259
30	D. Farmanzadeh and S. Ghazanfary	
31	Theoretical study of few organic compounds on corrosion inhibition of stainless steel in acidic solution	261
	E. Jamalizadeh, S.M.A. Hosseini, M. Amiri	
32	Halogen bonding; L-hole versus σ-hole	263
	K. Eskandari, H. Zariny and M. Lesani	
33	An investigation of electronic excitation transfer between chlorophylls light harvesting complexes I and II, by using quantum computers	265
	M. Dehestani, S. Shojaei Baghini	
34	Implementation of quantum algorithms by NMR	267
	M. Dehestani, H. Heydari	
35	Ab initio potential energy surface for He-N₂ complex	269
	M. Dehestani, Z. Sharifzadeh	
36	Ab initio study of the effect of substitutional groups on the structure and torsional potential of conjugated diens	271
	Z. Zamani, H.R. Shamlouei	
37	Active C-H bond and rational of the anion-cation structural pattern in the ionic liquids 1-alkyl-3-methylimidazolium Chloride	273
	M. H. Ghatee, F. Moosavi, R. Jahromi	
38	Density functional theory study of the interaction between a nano bio switch as drug deliverer with procarbazine	275
	Z. H. Yazdi, M. A. Safarpour	
39	Comparison between Syn and Anti conformations in 8OG-C: AIM, NBO and NMR study	277
	A. Ebrahimi, A. Haghani, S. M. Habibi Khorassani, M. T. Maghsoodlou	



Molecular Spectroscopy

	Page
1 Aggregation behavior spectral studies of Copper (II) Tetrasulfonated phthalocyanine in aqueous salt solution and in the presence ct- DNA H. Dezhampanah, T. Darvishzad	281
2 Spectral studies of the interaction of rhodamine dyes with ct- DNA H. Dezhampanah, A. Ghanadzadeh, M. Aghazadeh.	283
3 Intramolecular hydrogen bonding and vibrational spectra of 2,2,6,6-tetramethyl-3,5-heptanedione M. Vakili, H. Miremad, S. Salemi, A-R. Nekoei	285
4 Study of Two Photon Time-Resolved Optogalvanic Signals of Neon in the 600-630 nm Region F. Abyar, F. Fathi, H. Farrokhpour, M. Tabrizchi, R. Omidyan	287
5 NO⁺ as Reactant Ion in Ion Mobility Spectrometry M. Darzi, M. Tabrizchi	289
6 The comparison between serum transferrin and HSA upon interaction with cyclophosphamide: A fluorescence spectroscopy investigation S. Hamed-Akbari Tousi, M.R. Saberi, J. Chamani	291
7 Dynamic ¹H NMR study around the heteroaryl-carbon and nitrogen-carbon single bonds (N⁺CH-N And N⁺C=CH) in a enaminoester involving a phenanthridine S. Nasiri, S. M. Habibi-Khorassani, M. T. Maghsoodlou, A. Ebrahimi, S. sam-salari	293
8 Secondary structure analysis of alpha-synuclein through the 3J-coupling constants and 1H, 13C, 15N chemical shifts measurements H. shaghaghi, M. F. Mulder, M. Tafazzoli	295
9 Theoretical and spectroscopic studies on Thiophenolato Mercury (ii) complexes S. Laleh, S. F. Tayyari, M. H. Habibi	297
10 The fluorescence spectroscopic studies of fluoxymestron and acetaminophen upon interaction with human serum albumin M. Sabaghian, M.R. Housaindokht, M.R. Saberi, J. Chamani	299
11 Observation of Space charge effects in ion mobility spectrometry V. Ilbeigi, M. Tabrizchi	301
12 Thermodynamic study of proton-bond dimer formation reaction in gas phase Z. Izadi, H. Farrokhpour, M. Tabrizchi	303
13 Fluorescence spectroscopic investigation of human serum albumin upon nano-interaction with Lomefloxacin at different pH R. Assaran Darban, H. Vahedian- Movahed, M. Saleh-Moghadam, J. Chamani	305
14 NMR studies of tautomerism in benzylacetoacetate F. Naghavi, S. F. Tayyari	307
15 A study on decolorization process of Malachite green and Crystal violet by 1-Aza 15-crown 5 A. Ghanadzadeh, S. Shekarsaraee	309
16 Prediction of ¹³C chemical shifts in solvents using PCM method and optimally selected wave function by factorial design M. Tafazzoli, F. Fathi, H. Shaghaghi	311
17 Thermodynamic characterization of Fe₂O₃ nanoparticles binding to human hemoglobin S. Zolghadri, A. A. Saboury	313
18 Local perturbations in the 001 (Σ_u⁺) vibrational state of BeD₂ A. Shayesteh	315



19	Protonated Benzene Dimer: An Experimental and Ab Initio Study	317
	Sh. Chakraborty, R. Omidyan, I. Alata, C. Dedonder, M. Broquier, and Ch. Jouvet	
20	Cis-enol conformational stability, Molecular structure, and intramolecular hydrogen bonding of 5,5-Dimethyl hexane-2,4 dione. A density functional theoretical study	319
	A. kanaani, M. Vakili, S.F. Tayyari, S. Salemi	
21	Synthesis, structure and vibrational assignment of bis(4-amino-3-penten-2-ono) nickel(II)	321
	M. Jamialahmadi, S. F. Tayyari, M. H. Habibi, M. yazdanbakhsh	
22	Calculation of absorption and resonance Raman cross sections of acetophenone in cyclohexane solution using displaced-distorted harmonic oscillator model	323
	M. Dehestani, Z. Rahmani	
23	Conformation, Structure, Intramolecular H-bonding, and Vibrational Assignment of 1-(2-thienyl)-4,4,4-trifluorobutane-1,3-dione	325
	A.-R. Nekoei, S. F. Tayyari, M. Vakili	
24	Nano-fluorescence spectroscopic studies of interaction between tamoxifen and human holo transferrin	327
	S. Sarzehi, M.R. Bozorgmehr and J. Chamani	
25	The comparison between Holo-transferrin and Holo-transferrin-Fe³⁺ upon interaction with Ropinirole hydrochloride: A nano-fluorescence spectroscopy approach.	329
	M. Kabiri, M.R. Bozorgmehr, and J. Chamani,	
26	A novel view of the comparison between transferrin and HSA upon nano-interaction with lomefloxacin	331
	H. Vahedian- Movahed, M.R. Saberi, J. Chamani	
27	Effect of Lomefloxacin on protein-protein interactions and origin of antibiotic's side effects: nano-molecular modeling and Spectroscopic investigations	333
	H. Vahedian- Movahed, M.R. Saberi, J. Chamani	



Chemical Kinetics

	Page
1 Degradation kinetics of carboxymethylcellulose under ultrasonic irradiation M. T. Taghizadeh, H. Rad	337
2 A kinetics study on the thermal degradation of starch/poly (vinyl alcohol) blend M. T. Taghizadeh, R. Abdollahi, Gh. Madani	339
3 Kinetic study of proton transfer reactions using ion mobility spectrometry E. Jazan, M. Tabrizchi	341
4 Competitive adsorption of auramine-o and methylene blue from solution using natural zeolite in single and binary systems A. Habibi-Yangjeh, F. Jafari-Zare	343
5 Effect of concentration on the ultrasonic degradation of poly (vinyl pyrrolidone) in aqueous solution M. T. Taghizadeh, E. Heydarpour, Serajeh Lou	345
6 Combustion characterization of modified double-based propellant containing nitroamines M. Norouzi Bakhsh and M. R. Nayeib Hosseini	347
7 The kinetics study of brilliant green fading in the presence of various surfactants M. Rafi Dargahi, B. Samiey, A. Rafi Dargahi	349
8 Investigation on mechanism and kinetic of decomposition on nitrate esters as main component of double base propellant in combustion process M. R. Nayeib Hosseini and M. Norouzi Bakhsh	351
9 Kinetic study of the reaction of catechol with cerium(IV) in aqueous sulphuric media M. Jabbari, F. Gharib	353
10 Synthesis of TiO₂ and Ni-Pd-Pt/TiO₂ nanoparticles for photocatalytic degradation of acid blue 92 Sh. Ghasemi, Z. Kaboli, M. R. Gholami	355
11 Enzymatic hydrolysis of carboxymethyl cellulose using ultrasound waves pretreatment M. T. Taghizadeh, Z. Nasrollahzadeh	357
12 Kinetics and mechanism of propene elimination from allyl methyl amine pyrolysis in the gas phase M. Izadyar, E. Esmaili	359
13 Effect of vitamin C addition on ultrasonic degradation of aqueous carboxymethylcellulose M. T. Taghizadeh, H. Rad	361
14 Sonolytic, sonocatalytic and sonophotocatalytic degradation of chitosan in the presence of TiO₂ nanoparticles M. T. Taghizadeh, R. Abdollahi	363
15 Solid-phase photodegradation of polystyrene-co-acrylonitrile (SAN) with TiO₂ as photocatalyst M. T. Taghizadeh, R. Abdollahi, C. Hasanifard	365
16 Sonocatalytic and sonophotocatalytic/H₂O₂ degradation of chitosan in the presence of Fe (III) as a catalyst M. T. Taghizadeh, R. Abdollahi	367
17 Effect of reaction volume on the extent of ultrasonic degradation of high-molecular weight chitosan M. T. Taghizadeh, R. Abdollahi	369



18	Ultrasonic degradation of amylose: effect of volume, concentration of amylose, power input and type of solvent on rate of degradation	371
	M. T. Taghizadeh, M. Dadashbeygi	
19	Kinetics of adsorption of methyl violet by pistachio/ CuFe₂O₄ nanocomposite	373
	S. Hashemian , M. Hassan Dad	
20	Quasi-classical trajectory study on the reaction of CH₃ + SiCl₃ radicals	375
	S. H. Mousavipour, E. Mazarei	
21	Interpolated potential energy surface and classical reaction dynamics for reaction of amidogen with hydroxyl radical	377
	S. H. Mousavipour, F. Pirhadi	
22	Direct-dynamics VTST study of the reactions of CH₃ with CH₄ and CD₄	379
	Sh. Ramazani	
23	Thermal behavior kinetic study of activated-carbon from pistachio shell	381
	N. Madadi Mahani, M.Oftade, Sh. Rafiei	
24	Kinetic study and mechanism investigation of the reactions between triphenylphosphine, dialkyl acetylenedicarboxylates and NH-acid such as Maleimide by UV spectrophotometry	383
	S. M. Habibi Khorassani, M. T. Maghsoodlou, A. Ebrahimi, E. Aghdae, M. Zakarianejad , M. Mohammadi	
25	Kinetic and mechanism investigation of the reactions between dialkyl acetylenedicarboxylates and 2-thiazoline 2-thiole in the presence of triphenyl phosphite by UV	385
	S. M. Habibi Khorassani, M. T. Maghsoodlou, A. Ebrahimi, M. Zakarianejad	
26	Effect of concentration on the ultrasonic degradation of poly (vinyl pyrrolidone) in aqueous solution	387
	M. T. Taghizadeh, E.I Heydarpour, S. Lou	
27	Kinetic and mechanism investigation of the reactions between dialkyl acetylenedicarboxylates and 2,4-dimethyl 2-mercapto pyrimidine the presence of triphenyl phosphite by UV	389
	M. T. Maghsoodlou, S. M. Habibi Khorassani, A. Ebrahimi and M. Zakarianejad	



Surface Chemistry

	Page
1 Photocatalytic degradation of nonionic surfactant using Zinc oxide nanoparticles M. Giahi, F. Ghanbari	393
2 Adsorption of phenol onto activated carbon cloth: effect of cosolvent Z. Afshari, S. Azizian	395
3 Effect of catalyst preparation parameters on the catalytic performance of Co/Ni catalyst used in FTS N. Karimpour, A. A. Mirzaei, S. Sharyari, M. Galavy, S. Vahid	397
4 On the investigation of adsorption of methyle violet onto titanium dioxide nanoparticles Sh. Jafari, B. Jaleh, S. Azizian	399
5 Effect of the Si/Al ratio of zeolite and metal loading on the catalytic activity of HY zeolite for methanol dehydration in a fixed bed reactor M. H. Peyrovi, V. Zarei, M. R. Toosi, T. Hamoule, B. Sabourb	401
6 Theoretical prediction of surface tension of binary liquid system (R290 + R600a) at various temperature and pressure A. A. Rafati, A. Bagheri	403
7 Surface Tension of Nonideal Ternary Liquid Mixtures at 298.15 K and Atmospheric Pressure A. A. Rafati, A. Bagheri	405
8 Preparation, characterization and photocatalytic activity of ZnO supported on clinoptilolite for decolorization of dye acid red 57 from aqueous solutions K. Mahanpoor, N. Niazi Hesar Sefeedi	407
9 Catalytic reforming of n-heptane over Al-containing mesoporous catalysts M. H. Peyrovi, T. Hamoule, B. Sabour, V. zarei	409
10 Liquid-phase adsorption of mordant yellow 10 on activated carbon prepared from almond shell: a kinetic and equilibrium study A. Soufi, K. Mahanpoor, H. Malekhoseani, N. Niazi Hesar Sefeedi	411
11 Effect of heat treatment on the corrosion resistance and hardness of Ni-P-TiO₂ electroless composite coatings S. Amjad Iranagh, H. Modarress	413
12 Adsorption of some phenolic compounds onto activated carbon cloth: kinetics and equilibrium A. Hajian, S. Azizian	415
13 Determination of impacted suspect bullet types on the suspect objects using splash phenomena A. Tarkashvand, J. Babaee	417
14 Effect of operating conditions on the catalytic performance of fused Co-Ce/SiO₂ catalyst used in FTS M. Galavy, A. A. Mirzaei, S. Vahid, N. Karimpour	419
15 Catalytic properties and characterization of Fe-Co catalyst at different operating conditions M. Galavy, A. A. Mirzaei, S. Vahid, N. Karimpour	421
16 Characterization of Fe/Mn catalysts using XRD, BET, TGA and DSC techniques S. Vahid, A. A. Mirzaei, M. Galavy, N. Karimpour	423
17 Study of adsorption of safranin on granulated active carbon (GAC) and evaluation of its thermodynamic and kinetic parameters Gh. Koutchakzadeh	425
18 The study of synergistic effects between cationic surfactant (Hyamine) and nonionic surfactant (Triton X-100) Z. Felegari, A. A. Rafati	427



19	Fe-Mn bimetallic catalyst prepared by sol/gel technique: operating conditions and characterization	429
	A. A. Mirzaei, N. Karimpoor	
20	Conformational analysis of vitamin P in solution by theoretical approaches and experimental validation	431
	M. Ghiasi, S. Taheri, M. Taffazoli	
21	Hydrogenolysis of n-hexane over Al₂O₃-Supported Ni-Co catalysts	433
	M. H. Peyrovi, B. Sabour, T. Hamoule, R. Sadeghi	
22	Adsorption of atomic hydrogen on V(110)	435
	B. Khezri ^a , H. Hoshyar ^b , S. Khanahmadzadeh ^c	
23	Composition and interaction of triton X-100 and dtmac surfactants at toluene/water interface at 25 °C	437
	J. Saien, S. AsadAbadi	
24	Equilibrium modeling of liquid-phase adsorption of azo dye acid red 57 on free and immobilized dead fungal biomass of aspergillus niger	439
	H. Malekhoseani, K. Mahanpoor, A. Soufi, N. Niazi Hesar Sefeedi	



Nanochemistry

		Page
1	Theoretical structural relationship and electrochemical properties study of [cp₂-fe]@c_n complexes A. Taherpour , R. Jalajardi	443
2	The effect of the calcined temperature on the TiO₂ nanoparticles size made with sol-gel process H. Milani Moghaddam, Sh. Nasirian	445
3	Phase transition of Nanocrystalline ZnS thin films to ZnO thin films: study by TGA-DTA, EDX, XRD and Uv-Vis. techniques A. Goudarzi, G. Motedayen Aval, R. Sahraei, Ch.-Sik Ha	447
4	The imbibition of liquids in microtubes S. Gharangian, Y. Ghayeb, E. Keshavarzi	449
5	Sonochemical method for synthesis of magnesium oxide nanoparticles R. Rezazadeh, S. Haghdad	451
6	Characterization of SnO₂ nanoparticles prepared in presence of a ionic liquid by solvothermal method A. Habibi-Yangjeh, V. Taghvaei, M. Behboudnia	453
7	Increasing the solubility of single wall carbon nanotube by adding four long functional groups M. Foroutan, M Moshari	455
8	Separation of He and Ne by adsorption in carbon nanotube: A molecular simulation study Z. B. Nojini, A. Abbas Rafati, S. Majid Hashemianzadeh, S. Samiee	457
9	Electrochemical supercapacitor electrodes based on nano magnetite/carbon black composite A. Zolfaghari, H. Sayahi, H. Mortaheb	459
10	Ion separation of electrolyte solutions using charged carbon nanotubes: A molecular dynamics study M. Froutan, A. Taghavi Nasrabadi	461
11	Cycloaddition reactions between c₂₄ and buta-1, 3-diene an ab initio study S. Abedini Khorrami, Sh. Moradi, H. Mohammadzadeh Bahar	463
12	Chemical deposition and optical characterization of nanocrystalline CDS thin films for application in solar cells as window materials R. Sahraei, A. Daneshfar, H. Kaviani, N. Shokri	465
13	Reverse nonequilibrium molecular dynamics simulation of the viscosity of nanoconfined polymers H. Eslami, F. Müller-Plathe	467
14	Investigation of photocatalytic activity for ZnO nanoparticles supported on natural zeolite prepared by microwave irradiation A. Habibi-Yangjeh, E. Sanatgar-Delshad, M. Khodadadi- Moghaddam ^c	469
15	Solubility of carbon nanotubes in ionic liquids: MD simulation approach M. Foroutan, M. Setareh, H. Akbari-Borhani	471
16	Study of the electronic properties of nitrogen doped graphene S. Jalili, R. Vaziri	473
17	Template-free preparation and characterization of various nanomaterials in aqueous solution of an ionic liquid and their photocatalytic activity A. Habibi-Yangjeh	475
18	Effect of nitrogen doping on the photocatalytic activity of nanotitania prepared by sol-gel method for photodecomposition of phenolic compounds in the presence of Visible light M. R. Toosi, V. Zarei, M. D. Ganji, F. Gholami	477
19	Synthesis and nonlinear optical properties of silver nanoparticles A. Daneshfar, R. Sahraei, H. Kaviani, M. H. Majles Ara	479



20	Fluorescence of Nanocrystalline Mn doped ZnS thin films Prepared by chemical deposition	481
	A.Goudarzi , R. Sahraei , Ch.-Sik Ha	
21	Synthesis of Nanostructured MnO₂/carbon black composites using sonochemistry method for electrochemical supercapacitors	483
	H. Naderi, A. Zolfaghari, H. Mortaheb , M. Rastgar, H. Sayahi	
22	Solubility Investigation of Nano Particles by Nonextensive Property and Fractal Dimension Approach	485
	A.Moradi, M. G. Mahjani	
23	Chemical bath deposition of Nanocrystalline SnS thin films from aqueous solution	487
	R. Sahraei, A. Daneshfar, A. Karimi, S. Sarfi	
24	Molecular dynamic simulation of CTAB surfactants on carbon nanotube	489
	M. Foroutan, F. Mirzaie Milani	
25	Preparation, characterization and photocatalytic activity of ZnO-coated activated carbon prepared by microwave method	491
	A. Habibi-Yangjeh, M.Sabri	
26	Oscillatory behavior of Fullerene inside carbon nanotube: effects of radius	493
	M. Foroutan, R. Hadidi, E.Masoumi	
27	New result about leakage current through the nano layer of silicon dioxide	495
	R. Rezazadeh , M. A. Rezazadeh	
28	Synthesis of thiol functionalized silica nano hollow sphere via templating method	497
	R. Rostamian, A.A. Rafati	
29	Study of the Structure and Electronic Properties of BN and B₃C₂N₃ Nanotubes	499
	S. Jalili, R. Vaziri	
30	Effect of Milling Time and Clay Content on the Thermal Stability of Polyethylene-Clay Nanocomposite	501
	M. Abareshi, S. M. Zebarjad, E. K. Goharshadi	
31	Micro-emulsion under ultrasound facilitates the fast synthesis of quantum dots of CdS at low temperature	503
	N. Ghows, M. H. Entezari	
32	Investigation of SiO₂ Nanoparticles for Encapsulating of Benzotriazole Corrosion Inhibitor	505
	S.M.A. Hosseini, E. Jamalizadeh, A.H. Jafari, , M. Shahidi	
33	Thermodynamic study of lead sorption on Nanostructure Titania-Silica mixed gel spheres	507
	A. Nilchi , S. Rasouli Garmarodi and G. Aboulhasanlo	
34	Preparation and characterization of CdS nanoparticles in presence of a ionic liquid, [EMIM][EtSO₄] using microwave irradiation and their photocatalytic activities	509
	A. Habibi-Yangjeh, M.Esmaili-Taramsari	
35	Molecular dynamics simulation of Ne adsorption on open-ended single-walled carbon nanotubes	511
	M. Foroutan, A. Taghavi Nasrabadi	
36	Electrochemical synthesis of copper nanoparticles in surfactant solution	513
	S. A. Seyed Sadjadi, M. H. Riazi, A. Banaei, A. Heidari	
37	Removal of dye pollutant by adsorption and photocatalysis of Clay-io₂ nanocomposite thin film prepared by electrophoretic deposition	515
	M. Rastegar, A. R. Zolfaghari, H. R. Mortaheb, H. Naderi	
38	The correlation of thermal conductivity of carbon nanotube suspension using artificial neural network	517
	F. Yousefi, M.M. Papari, J. Moghadasi, H. Karimi	
39	Theoretical Approach for Estimation of Nano Platinum and Palladium Particles Size Synthesized in the AOT Reverse Micelle System	519
	S. Salabat, H. Saydi	





Computational Chemistry

		Page
1	Investigation of explosive performance of substituted 1,1,3,5,5-pentanitro-1,5-bis(difluoramino)-3-azapentane by DFT methods M. Hamadani, F. Aghabozorgi	525
2	Novel C₂₀ carbon nanostructures: scanning tunneling microscopy (STM), electronic structure, vibrational and UV spectroscopic analysis H.A. Dabbagh, M. Zamani, H. Farrokhpour, A. Motahari	527
3	A computational study of dimers and trimers of nitrosyl hydride: Blue shift of NH bonds that are involved in H-bond and orthogonal interactions M. Solimannejad, Sh.Massahi, I. Alkorta	529
4	Aromaticity investigation of penta- and hepta-fulvene derivatives using shannon aromaticity index (SAI) S. Noorizadeh, E. Shakerzadeh	531
5	Theoretical studies of structural and electronic properties of nano-metric adamantane compounds containing alkali metals M. Hamadani, A. Vali pour	533
6	Effect of substitution on structure, stability and electronic properties of nanoscale polyhedral oligomeric silsesquioxane (T₁₂-POSS) M. Hamadani, R. Hosseinpour	535
7	Theoretical investigation of the intramolecular hydrogen bonding of 1-(2-methoxyphenyl)-o-carborane M. Hamadani, F. Mirzaei	537
8	A DFT study on Tetracycline and its derivatives for increasing affinity and decreasing environmental side effects S. Omid, S. Javadian, M. Noorinezhad	539
9	Stabilization of the Phenyl Salicylate in different conformers: Experimental and Theoretical analysis M. Emamia, M. Jabbaria, A. Teimourib, A. R. Najafic	541
10	The competition between the intramolecular hydrogen bond and amide resonance in N-formylformamide- a quantum chemical study A. Nowroozi, P. Mohammadzadeh Jahani, N. Asli, S. Dahmardeh, M. Poorsargol	543
11	Theoretical study of formation, stability and the interaction of Sm³⁺ complexes with bisphosphonates M. Arabieh, M. Ghannadi-Maragheh, M. Zahedi, M. H. Karimi-Jafari	545
12	The numerical study of the carbon impurity effect on electronic properties of BN nanotubes H. Milani Moghaddam, A. A. Nouroozi	547
13	Effect of CH₃CO functional group on the molecular and electronic properties of bn43zz nanotube H. Roohi, B. makiabadi	549
14	DFT studies, NBO and NICS analysis of all fluorothiophenes and their cations as candidate monomers for new conductive polymers H. Shirani, S. Jameh-Bozorgi	551
15	Interplay between the O-H...O intramolecular hydrogen bonding and pyrimidine ring in 5-formyl barbituric acid. A theoretical study A. Nowroozi, S. Dahmardeh, P. Mohammadzadeh Jahani, M. Poorsargol	553
16	Theoretical Study On ¹H, ¹³C NMR Shielding, Structure and vibrational assignment, And Physical Properties Of Diamantane Z. Bayat, S.J.Mehdzade, S. Bagheri, M. Fakoor	555



17	Conformational effect on ¹³C chemical shifts; analysis of 6-mono-substituted derivatives of 5,6,7,8-tetrahydrodibenzo[a,c]cyclo-octene by <i>ab initio</i> quantum mechanics method	557
	J. Najafpour, A. A. Salari, M. Porgham Daryasar	
18	First principles study of structure and electronic properties of Na-doped adamantane in disordered solid phase	559
	M. Hamadani, B. Khoshnevisan, F. Kalantary-fotooh	
19	Design of Anti-HIV Ligands by Means of Minimal Topological Difference (MTD) Method	561
	Z. Bayat, N. Abdossamadi, So. Norouzi, Sa. Norouzi	
20	DFT/B3LYP study on antioxidant activity of compounds based on vitamin E	563
	M. Najafi, E. Nazarpour, M. Zahedi	
21	Ab Initio Calculations of ¹⁷O NMR Chemical shielding tensors in benzyl ethers derivatives and comparison with experimental values	565
	M. Rezaei-Sameti	
22	Investigation of hydrogen bonding in methanol clusters and its electrical parameters by <i>ab initio</i> calculations	567
	I. Kazeman, M. Hasanzadeh, S. Mahmoodi Asl, R. Sherafati	
23	Theoretical study on physical properties, vibrational assignment and ¹H, ¹³C NMR shielding of Adamantane	569
	Z. Bayat, S.J. Mehdizade, S. Qanei nasab, M. Zanoosi	
24	Detonation performance of 1,4-bis(3,5-diamino-2,4,6-trinitrophenylamino)-1,2,4,5-terazine as a new thermally stable energetic compound	571
	M. A. Ghasemi, F. Seif and M. H. Keshavarz	
25	Cis-enol conformers and intramolecular hydrogen bond strength of 2,6-Dimethyl-3,5-heptanedione	573
	M. Vakili, S. H. Miremad, A-R. Nekoei	
26	Structures, stabilities and electronic properties analysis of substituted nano-scale polyhedral oligomeric silsesquioxane (T₈-POSS)	575
	M. Hamadani, M. Sharif	
27	Ab initio and DFT studies, NBO and NICS analysis of the decomposition ([2+2]elimination) mechanisms of 3-halo-2,3-dihydropyridine	577
	H. Nemat-Talab, H. Shirani, S. Jameh-Bozorgchi, A. Bodaghi, J. Hosseini	
28	Quantum mechanical study on all chloroanilines as candidate monomers for conducting polymers (as nano-wires)	579
	H. Shirani, S. Jameh-Bozorgchi	
29	Computational investigation on N₁₄, N₁₆, N₁₈ and N₂₀: A discrepancy between conjugated pentagons and stability	581
	J. Najafpour, F. R. Nikmaram, M. Kordi Peykani	
30	Investigation of the geometry optimization and spectroscopy of <i>N,N</i>-Dimethyl-<i>N,N'</i>-bis(4-methylphenyl)phosphoramidate and comparison experimental results with quantum mechanic calculations	583
	M.H. Akhbari shada, H. Hooshyara, B. Khezri	
31	Existence and characterization of HOO...HOOH radical-molecule complexes: A computational study	585
	M. Solimannejad, Sh. Massahi, S. Scheiner	
32	Surface study and adsorption mechanism of 2-butanol over the (100) surface of γ-alumina: a dft study	587
	H.A. Dabbagh, M. Zamani	
33	NICS-rate as a new measure of aromaticity	589
	S. Noorizadeh, M. Dardab	
34	Evaluation of ground-state correlation energies using an empirical model	591
	S. Noorizadeh, H. Parsa	



35	Ground state correlation energies and absolute hardness in atomic systems	593
	S. Noorizadeh, M. Mondanizadeh	
36	The study of structure and electron configuration of <i>closo</i>-B₅H₅⁻² and related isolobal compounds: Ab initio study and NBO analysis	595
	S. Jameh-Bozorgi, E. Jalali, H. R. Namdari, A. Ghaempanah	
37	Theoretical calculations of relative pK_a values for some of substituted amines in aqueous solution	597
	A. Ebady, R. Behjatmanesh-ardakani	
38	The investigation of hydrogen bonding effects on the calculated relative pK_a values for several compounds in aqueous solution	599
	R. Behjatmanesh-ardakani, A. Ebady	
39	Prediction of decomposition mechanism of compound 2-fluoropyridine; A Density Functional Study	601
	S. Jameh-Bozorgi, M. darvishpour, M. H. Fekri	
40	Effect of floating basis set on the electronic properties of adamantane	603
	H. Sabzyan, B. Saed	
41	DFT and ab initio study of metalotropic shift and prototropic shift mechanism of 5-terth-butylcyclopenta-1,3-diene and their analogs	605
	S. Rafatpanah, S. Jameh - Bozorgi, V. Daneshdoost	
42	Determination of the pK_a values of Glycine, Phenylalanine and glycylphenylalanine using DFT method	607
	F. Kiani, A. A. Rostami, S. Sharifi, A. Bahadori	
43	Host-guest inclusion complex formation of cucurbit [6]uril with some aliphatic alcohols: Ab initio calculations study	609
	Z. B. Nojini, A. A. Rafati, S. M. Hashemianzadeh	
44	The relation structure and detonation performance of explosives	611
	M. J. Gohar, H. R. Shamlouei	
45	A mathematical model for correlation rate constant of inorganic reactions with compositions in binary aqueous-organic systems	613
	A. Habibi-Yangjeh, M. Esmaili-Taramsari	
46	Intramolecular Hydrogen Bond in the Hydrazinoturns	615
	E. Rasti, H. A. Dabbagh	
47	Investigation of interaction host-guest chemistry of Cucurbit[6]uril-Ethylamine using DFT calculations of NQR parameters	617
	N. Ahmadian, A. Karamiyar	
48	Theoretical Study of the Antioxidant Properties of Trolox in the Gas Phase and Solvent Environment	619
	E. Nazarpour, M. D. Davari, M. Zahedi	
49	Study of the electric field effect on the electronic properties of Au/Cytosine/Au structure	621
	S. Azimi, H. Milani Moghaddam	
50	The complexation of tetracycline with Ca²⁺: A DFT study	623
	S. Omid, S. Javadian, M. Noorinezhad	
51	Ab initio thermodynamic evaluation of the DFTHP (the intermediate in TEX production)	625
	M. Mohammadi, H. R. Shamlouei, K. Asad Samani and R. Karimian	
52	Quantum mechanical study of electrophilic substitution reaction in diazole and their Analogs, NICS, and NBO analysis	627
	V. Daneshdoost, S. Jameh-Bozorgi, S. Rafatpanah	
53	Conformational study of (E,E,Z)1,3,5-cyclodeatriene using ab initio molecular orbital method	629
	R. Soleymani, S. Jameh-bozorgi	
54	Computational study on the stability of ternary (5, 7-dichloroquinoline-8-ol and 4- vinyl pyridine) Ln complexes (Ln: La, Ce, Nd, Sm)	631
	T. Hosseinejad, S. J. Ahmadi, S. Shirvani-arani, M. H. Karimi-Jafari	



55	An analytical potential energy surface for CO – N₂ dimer from ab initio calculations	633
	A. Farjamnia, A. Maghari, M. H. Karimi-Jafari	
56	Proton transfer reaction in variously substituted Aniline-OH/Anilide-(H₂O)_n complexes	635
	H. Roohi, B. Moghadam	
57	DFT study of gas-solid interaction in oxidative coupling of methane reactions: CH₄ + BaTiO₃ perovskite catalys	637
	M. Gharibi, M. Motalebipour	
58	Theoretical study for reaction between triphenylphosphine and activated acetylenic esters in the presence of SH heterocyclic compounds	639
	S. M. Habibi Khorassani, M. T. Maghsoodlou, A. Ebrahimi, H. Ghasempour, Z. Ghahghay	
59	Quantum chemical study of the interaction between O₃ and H₂O₂	641
	B. makiabadi, H. Roohi	
60	Study of the origin of rotational barrier in NH₂-X (X = NO, NS)	643
	H. Roohi, B. makiabadi, M. Hagealirezahi	
61	Substituent effect on local aromaticity in mono and di-substituted aza analogs of Indole	645
	A. Mohajeri, M. Shahamirian	
62	Conformational study for investigation of structure-function relationships in protein-based elastomeric materials	647
	B. Chahkandi, B. Seyed Hosseini	
63	The effect of hydrogen bond interactions on N-glycosidic bond in 3-methyl-2'-deoxyadenosine model	649
	A. Ebrahimi, M. Habibi-Khorassani, S. Bazzi	
64	Theoretical investigation on bailes-hillman reaction	651
	S. Z. Mohammadi, M. Zamani	
65	Study of the electric field effect on the electronic properties of the 6Au/S-Guanine-S/6Au structure	653
	F. Hashemi, H. Milani Moghaddam, M. Tayarani, F. Shariati	
66	Spin separation of deformation density in doublet state of Li@C₆₀	655
	S. Fakhraee	
67	Study of hydrogen bonding in Pyridine-2,6-dicarboxylic acid(dipic) using computational methods	657
	S. Jameh-Bozorgi, H. Esfandiari	
68	The theoretical study of ¹³C NMR chemical shielding tensors in 3- amino-2-nitrobenzo[b]thiophenes and comparison with experimental values	659
	M. Rezaei-Sameti	
69	Gas-Phase theoretical study on thermodynamic parameters (ΔG and ΔH) of binary mixtures ((CH₃OH)_m (H₂O)_n (m+n) 9-17) at various temperature	661
	M.vRezaei Sameti, S. Salehzadeh, M. Bayat	
70	Comparison between the experimental and theoretical vibrational frequencies of some halo-derivatives of aniline	663
	M. Rezaei-Sameti	
71	Ab initio and DFT study of dehydrogenation of 1,2-Dihydro-pyridine, ASE and NICS analysis	665
	S. Jameh-Bozorgi, V. daneshdoost, S. Rafatpanah, N. Zolfaghar	
72	Electric field effect on the HOMO-LUMO gap of the Au/S-Thymine-S/Au structure	667
	F.Shariatii, H. Milani Moghaddam, M.Tayarani, F.Hashemi	
73	Aromaticity variation in stacked nucleic acid base pairs	669
	A. Mohajeri, N. Davari	
74	Introduction a new high energetic compound to improve performance of solid propellants	671
	F. Seif, M. A. Ghasemi, M. H. Keshavarz	
75	Complexation of Glycine by Manganese (II) in the Gas Phase: A Theoretical Study	673
	M. H. Khodabandeh, M. D. Davari, K. Zare, M. Zahedi, G. Ohanessian	



76	AIM analysis for the ylide rotamers from the reaction between triphenylphosphine and dialkyl acetylenedicarboxylates in the presence of 2-mercapto-1-methylimidazole	675
	S. M. Habibi Khorassani, M. T. Maghsoodlou, A. Ebrahimi, Z. Ghahghayi, H. Ghasempour	
77	Vibrational analysis and theoretical study on NMR shielding and physical properties of triamantane	677
	Z. Bayat, S. J. Mehdizade, M. Emadian, M. Nejatpoor, S. Vahdani	
78	The one-dimensional model for anharmonic vibrations of a nano-sized oscillator using Rydberg potentials and Casimir force with fractional damping	679
	M. Dehestani, M. Mansoori Kermani	
79	The effect of the ring size and Benzene Ring Addition on Cyclic Ketones: FT-IR, FT-Raman, NMR spectra, and molecular structure investigation	681
	H. Hooshyar, K. Zare, S. Khanahmadzadeh, R. Sadeghi	
80	Ab initio and density functional studies on the structure and vibrational Spectra of 2-(4-methyl-2-biphenyl)-4-amino-1, 2, 4-triazole-3-thiol	683
	H. Hooshyar, R. Sadeghi, D. Setamdideh, H. gyan	
81	Direct derivation of Lennard-Jones parameters for CO using the DFT calculations	685
	J.r Jahanbin Sardroodi, Al. Rastkar Ebrahimpzadeh, M.Yaghoobie notash	
82	Aromaticity in terms of ring critical point properties	687
	A. Mohajeri, A. Ashrafi	
83	Hydrogen bonds in methylimidazolium-tetrafluoroborate ionic liquid	689
	H. Roohi, R. salehi	
84	Theoretical Study, Kinetics and Mechanism Investigation of the Reactions between Triphenylphosphine, Dialkylacetylenedicarboxylates and N-H Acid such as Benzhydrazide	691
	M. A. Kazemian, S. M. Habibi Khorassani, M. T. Maghsoodlou and A. Ebrahimi	
85	A computational study of molecular transport through carbon nanotubes	693
	Z. Tavangar, H. Sabzyan	
86	Thermodynamics of vapor-liquid equilibria of aqueous polymer solutions from the experimental vapor pressure osmometry and molecular thermodynamics modelling	695
	R. Sadeghi, Y. Shahebrahimi	
87	Determination of the melting point of the equimolar ionic liquid–benzene inclusion crystal by molecular simulation	697
	M. H. Kowsari, S. Alavi, M. Ashrafizaadeh, B. Najafi	
88	Effects of temperatures, pressures and pore size on the adsorption/separation of CO₂/N₂ gas mixture through carbon nanotube: canonical monte carlo simulation	699
	S. Razavi, S.M. Hashemianzadeh, S. Balilehvand	
89	Molecular dynamics studies on PolyG and PolyA in the presence of guanidine chloride	701
	Sh. Ghalehaghbababaei, D.Ajloo	
90	Interaction between amylin peptide and dioleoylphosphatidylcholine: a molecular dynamics study	703
	S. Jalili, B. Najafi, A. Maleki	
91	Molecular dynamics simulation of nanoconfined fluids in napt ensemble	705
	F Mozaffari, H. Eslami, J. Moghadasi	
92	Investigation of damaged DNA double strand using molecular dynamics simulation	707
	A. Arabbagheri, Gh.A. Parsafar	
93	Diffusion of different refrigerants in zeolite FAU: A molecular dynamics study	709
	R. Rabiei, M. Loghavi, F. Amirseifadini, S.Alavi, H. Mohamadimanesh, B. Najafi	
94	Study properties of imidazolium-based bromide ionic liquid's and effect of alkyl chain length by molecular dynamic simulation	711
	V. Sokhanvaran, S. Yeganegi, A. Soltanabadi	



95	Molecular dynamics simulation of hydrated nafion in sandwich model	713
	H. Abroshan , H. Akbarzadeh, G.A. Parsafar, E. Alizadeh , S.A. Mousavi	
96	Canonical Monte Carlo simulation of adsorption of pure and binary mixture of hydrogen and methane on silicon nanotube: temperature, pressure and bulk composition effects	715
	S. Balilehvand, S.M. Hashemianzadeh, S. Razavi	
97	Molecular dynamics simulation of the viscosity of ionic liquids	717
	N. Mehdipour, H. Eslami	
98	Study of the Solvent Effects on Hydrogen bonds of DNA base pairs using Molecular Dynamics Simulation	719
	S. Jalili, H. Fallah	
99	Molecular dynamics study of hydrogen adsorption on nitrogen doped graphene	721
	S.Jalili, A.Vahidi Ferdowsi	
100	Molecular dynamics simulation of hydrogen adsorption in double-walled carbon nanotubes	723
	S. Jalili, A. Gorji	
101	Comparison of the diffusion of CO and N₂ in ITQ-7 zeolite via Molecular dynamics simulation	725
	F. Amirseifadini, M. Loghavi, R. Rabiei, S. Alavi, and H. Mohammadimanesh, B. Najafi	
102	Investigation of surface free energy of platinum nanoparticles via molecular dynamics simulation	727
	H. Akbarzadeh, H. Abroshan, G. A. Parsafar	
103	Study of methane adsorption in single-walled carbon nanotube bundles	729
	S. Jalili, N. Alizadeh, and M. Vahedpour	
104	GCMC simulations of hydrogen adsorption in single-walled SiC nanotubes	731
	M. Rahimi Galugahi, S. Yeganegi, M. Shadman	
105	MD simulation of the dynamics of molecular motion in the equimolar mixture of [emim][NTf₂].C₆H₆	733
	M. H. Kowsari ,S. Alavi, M. Ashrafizaadeh, B. Najafi	
106	Molecular dynamics analysis of Proline-Rich Homeodomain (PRH) – DNA interaction	735
	S. Jalili, L. Karami	
107	Quantifying the anisotropy of potential energy surfaces with the aim of statistical central moments	737
	M. Ashouri, M. H. Karimi-Jafari	
108	Prediction of thermodynamic properties of ketones using artificial neural network	739
	Z. Kalantar, M. Arab Chamjangali, H. Nikoofard, M. Sabouri	
109	Molecular dynamics simulation study of self-diffusivity of carbon disulfide gas in ITQ-7 zeolite	741
	M. Loghavi, F. Amirseifadini, R. Rabiei, S. Alavi, H. Mohammadimanesh, B. Najafi	
110	The effect of using two different water models on the pressure-area isotherm of DPPC monolayer	743
	D. Mohammad-Aghaie, F. Bresme	
111	Molecular dynamic simulation of amorphous cellulos triacetate membrane	745
	M. Shadman, S. Yeganegi, F. Ziaie	
112	Molecular Dynamics Simulations of the Protein-Micelle Interaction	747
	S. Jalili, M. Akhavan	
113	New aldehyde as a new pre-material for synthesis of new liquid crystals, synthesis, Ab initio DFT study, characterization and structure	749
	O. Dadfar, R. Samimi, E. Alizadeh	
114	Simulation Studies on the Diffusion of Argon in Nanoporous PVB Membranes	751
	M. Shadman, S. Yeganegi, F. Ziaie	



Electrochemistry

		Page
1	Investigation of interaction ct-DNA with 10-molybdo 2- vanado phosphoric acid by UV/Vis spectroscopy and cyclic voltammetry N. Sohrabi, H. R. Zare, S. Shiralinasab	755
2	Corrosion and passivation of Ti-6Al-4V in acid -organic inhibitor S. M. A. Hosseini, M. Salari, M. M. Alizadeh	757
3	Dependence on ionic strength of phenylalanine protonation constants in NaClO₄ aqueous solution F. Gharib, F. Mofidi	759
4	The corrosion inhibition of austenitic chromium- nickel steel in H₂SO₄ + L-OH compound M. Amiri, S.M.A. Hosseini, R. Razavi	761
5	Inhibition action of some thiosemicabazones on the corrosion of mild steel in 1 M H₂SO₄ solution N. Soltani, A. Teimouri	763
6	Application of a new dioxime to potentiometric and its computational Studies M. H. Fekri, M. Darvishpour	765
7	Cr(III) ion selective electrode based on 2H-1,4-benzothioazine-2,3(4H)dione dioxime as a natural carrier M. H. Fekri, M. Darvishpour	767
8	Activity coefficients of NiCl₂ in (Glucose + water) mixtures at 298.15 K B. Ghalami –Chooobar, T. Nasiri	769
9	Investigation of stress corrosion cracking of sensitized stainless steel 304 in chloride media by using electrochemical impedance spectroscopy B. Adib, J. Neshati, A. Sardashti	771
10	Thermochemistry of natural hypersaline water systems using the urmia lake as a case S. Sakeni Alvanag, N. Heidari, M. Mokhtarpour	773
11	Physical chemistry of urmia lake, The carbonate system in hypersaline solutions: Alkalinity and CaCO₃ solubility of evaporated seawater M. Mokhtarpour, N. Heidary, S. Sakeni	775
12	Determination of thermodynamic properties of aqueous mixtures of MgCl₂ and Mg (NO₃)₂ by the EMF method at T=298.15 M. Giahi, M. Pournaghdy, H. Aghaie	777
13	Oxidation of Methanol at Nickel Chloride Modified Carbon Paste Electrode (NCMCPE) in Alkaline Medium J. Shabani shayeh, M. Jafarian, M.G. Mahjani, M. Rashvand avae	779
14	Modification of glassy carbon electrode by electrochemical reduction in situ generated diazonium salts N. Yazdizade, A.A. Rostami, A. Omrani	781
15	Ability of the potentiometric method on the thermodynamic modeling of the concentrated mixed electrolyte system F. Deyhimi, M. Abedi	783
16	Electrochemical impedance study on anomalous diffusion in poly pyrrole film A. Sharifi, M.G. Mahjani, A. Ehsani, M. Jafarian	785
17	Electropolymerization of PEDOT films on the glassy carbon electrode and study of ions transport during the redox process A.A. Rostami, A. Omrani, A. Moradi	787
18	Effect of nano-TiO₂ particles on the corrosion behaviour of epoxy polyaniline coatings on aluminium M. G. Hosseini, P. Zardari, R. Najjar	789



19	Electroless plating of Ni-Cu-B on Al and corrosion behaviours of the deposit	791
	S.Rahmani, S.A.Seyedsadjadi	
20	Investigation on Cathodic Disbonding of High Solid Thick Polyurethane Pipeline Using Electrochemical Impedance Spectroscopy (EIS)	793
	J. Neshati , J. Mofidi , F. Akvan	
21	Electrochemical study on supercapacitor properties of Poly ortho aminophenol conducting polymer	795
	M.G. Mahjani, M. Jafarian A. Ehsani	
22	Improvement of the electrosynthesis and properties of Poly (o-aminophenol) using a SDS Micellar Aqueous Medium	797
	M. Jafarian, M.G. Mahjani, A. Naeemy, A. Ehsani	
23	Electrochemical impedance spectroscopy study on intercalation and anomalous diffusion of aluminum ions into graphite in basic molten salt ($\text{AlCl}_3\text{-NaCl-KCl}$)	799
	M.G. Mahjani, M. Jafarian A. Ehsani	
24	Estimation of CMC of sodium dodecyl sulfate in different electrolyte solutions using conductimetry	801
	F. Farshchi Tabrizi, S. Naderi Mighan , H. Abedini, M. Bagherzadeh, N. Miri	
25	Effect of organic compounds on the electrochemicalBehavior of stainless steel in acid solution	803
	S. M. A. Hosseini, M. Salari	
26	Solvent effects on protonation and complexation of glutamic acids with molybdenum(VI) in different aqueous solutions of methanol	805
	M. Imanzadeh, A. Shamel, F. Gharib	



Miscellaneous

		Page
1	Density, dynamic viscosity, and derived properties of binary mixtures of 1,4 dioxane with 3-methyl 1-butanol at 298.15, 303.15 and 308.15 K A.A .Rostami, A Omrani, M.Mokhtari	809
2	Application of diffusion equation in experimental neutron diffusion parameters N.Mohammadtabar, R.Benvidi	811
3	A study of the interaction of calf thymus DNA with Co(III)-salen complex Z. Mashhadi khoshkhoo, M. R. Housaindokht, R. Jalal, H. Eshtiagh Hoseini, H. Mirtababaei, M. Mirzaei	813
4	Improved IMS Performance using an Inversed Mode of Operation for the Shutter Grid M. Tabrizchi, E. Jazan	815
5	Solvatochromic probe absorbance behavior in mixture of 2-hydroxy ethylammonium formate with methanol, ethylene glycol and glycerol H. Salari, A. R. Harifi-Mood, M. R. Gholami	817
6	The van der waals interaction between torus-shaped and spherical nanoparticles M. Moradi, M. Ebrahimzadeh, M. Noormohammadi	819
7	Development a dual-mode non-thermal plasma (NTP) ionization source for gas phase reactions study using ambient mass spectrometry M. Almassian , R. Zhang	821
8	Study on a zinc-manganese fischer-tropsch synthesis catalyst prepared from [Zn(H₂O)₆]₂[Mn(NCS)₆]/Al₂O₃ precursor M. Behzad Khoshgouei, A. R. Rezvani and A. R. Salehi Rad	823
9	CO hydrogenation to light olefins over K-Mn/Al₂O₃ catalyst A. R. Rezvani, M. Behzad Khoshgouei, A. R. Salehi Rad	825
10	Magnetic field effect in thermodynamic studies on binding of amlodipine to HSA: A spectroscopic approach Z. Rouhbakhsh Zaeri, M. R. Housaindokht , J. Chamani, M. Bahrololoom	827
11	Estimation of gibbs free energy of formation of haloalkanes by qspr modeling R. Behjatmanesh Ardakani, F. Mollaie Poli	829
12	Micellization of pantanediyl-1,5-bis(hydroxyethylmethylhexadecylammonium bromide) (GSP¹) cationic gemini surfactants. R. Zarganian, A.K. Bordbar, R.Amiri, A.R.Khosropour, I.Mohammadpour Baltork	831
13	QSPR study on logCMC of anionic surfactants using multiple linear regression (MLR) method R. Behjatmanesh-Ardakani, S. M. Mirhoseini-Abran Abadi, F. Ghaderiyeh-Mahmood Abadi	833
14	Kinetic investigation of photocatalytic degradation of azo dye by Ag/AgBr modified TiO₂ loaded on zeolite M. Padervand, M. Tasviri and M. R. Gholami	835
15	The effect of surfactants on asphaltene precipitation onset in presence of nano- tetra phenyl porphyrin M. NikAzar, M. A. Safarpour, S. Toufani, A. Heidari	837
16	Investigating the charge distribution in the semiconductor compound ZnTe H. Salehi, R. Mirzaei	839



- 17 **Solution properties of alkanediyl- α,ω -bis (hydroxy ethyl methyl hexadecyl ammonium bromide) as a Gemini cationic surfactant in aqueous media** 841
M. Tamannaeei, R. Amiri, A.K. Bordbar, A.R. Khosropour and I. Mohammad pour
- 18 **A novel view of the nano-spectroscopic investigation of human serum albumin upon interaction with paclitaxel and estradiol** 843
N. Amani, M.R. Saberi, J. Chamani
- 19 **Electrolyte effect on interfacial properties and the phase transition from Microstructures to Nanostructures in Ionic/Ionic Surfactants Mixture** 845
B. Sohrabi, S. Fazeli, M. Moallelemi
- 20 **A Non-Radioactive Electron Capture Detector for GC** 847
M. Tabrizchi, H. Bahrami
- 21 **The study of structural properties, aromatic stabilization energy and NBO analysis of indole and related analogs via quantum mechanics calculations** 849
A. Bodaghi, S. Jameh-Bozorgi, J. Hosseini, H. Shirani, R. Moradi- Bighashi

Classical Thermodynamics



Shiraz University

13th Iranian Physical Chemistry Seminar

Shiraz University of Technology



**Investigation on interaction of Ni(II)salen with Hen egg white lysozyme(HEWL): a Thermodynamic approach**M. Reissi^a, N. Sohrabi^{a,b,*}, N. Rassoli^a

a. Isfahan Payamenoor University, Nabavimanesh Avenue, Isfahan, Iran

b. department of chemistry, Yazd University, Yazd, Iran. Tel: 09133077033

(E-mail: nasrinsohrabi@yahoo.com)**Keywords:** Ligand binding, binding capacity, Hen Egg lysozyme (HEWL), Metallo salen**1. Introduction**

The ligand binding of small molecules to macromolecules is one of the most interaction fields of research. HEWL is a global protein, consists of 129 amino acids residues with a molecular weight of about 14400 and its have contain charge 129 amino acids then it can link to complex. Since lysozyme was recognized by Fleming in 1922 as a bacteriotoxic agent having an ability to hydrolyze bacterial cell walls Ni(II)salen complex a Schiff base salen ligand and have been employed in various areas such as analytical and bioinorganic chemistry, catalysis, material chemistry and pharmacological [1]. Metallo salens are structural models of naturally occurring metallo porphyrins[2]. In this work the interaction of Ni(II)salen with HEWL was studied using spectroscopic. Binding constants, binding sites, and the binding thermodynamic parameters was calculated.

2. Materials and methods

Lysozyme (HEWL) was obtained from sinajen and Ni(II)salen synthesized in laboratory[2,3] and other chemical materials were obtained from merck company. All solutions was prepared freshly. The differential UV/Vis was recorded by a Perkin Elmer spectrophotometer. The spectrophotometer was equipped with a cell thermost bath. In all experiments double distilled water was used.

3. Results and discussion

By analyzing the UV/Vis spectrums of binding of Ni(II)salen (N,N-bis salicylidene) with Hen egg white lysozyme(HEWL) in 5 mM phosphate buffer, pH=7 the binding degree was calculated using a simple derived model. The binding Isotherms of HEWL with Ni(II)salen at different temperature (figure 1) was present single binding site set. The Hill diagrams of interaction of HEWL with Ni(II)salen at different temperatures was plotted then the thermodynamic parameters of interaction of HEWL with Ni(II)salen in 5 mM phosphate buffer solution, pH=7 was plotted. The values of $\Delta G_{b,v}^0$ [3], the changes in intrinsic gibbs free energy according to following equation (1) was calculated and its curves was plotted (figure 2) and confirm the positive cooperativity.

$$\Delta G_{b,v} = -RTn_H \ln K + RT(1 - n_H) \ln[S_f] \quad (1)$$

Table 1: The Thermodynamic parameters of interaction of HEWL with Ni(II)salen in 5 mM phosphate buffer solution, pH=7

T	Log K	ΔG_b^0 (Kj/mol)	ΔH_b^0 (Kj/mol)	ΔS_b^0 (j/mol)
303	9.989	-25.1637	61.1819	284.9690
308	10.407	-26.6493	61.1819	285.1663
313	10.74	-27.9485	61.1819	284.7617
318	11.151	-29.4816	61.1819	285.1053

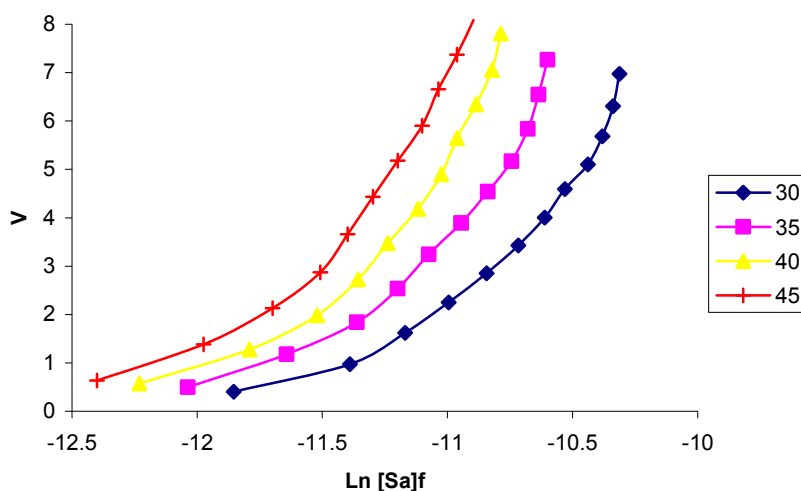


Fig. 1. The binding Isotherms of HEWL with Ni(II)salen in 5 mM phosphate buffer solution, pH=7 at different temperatures.

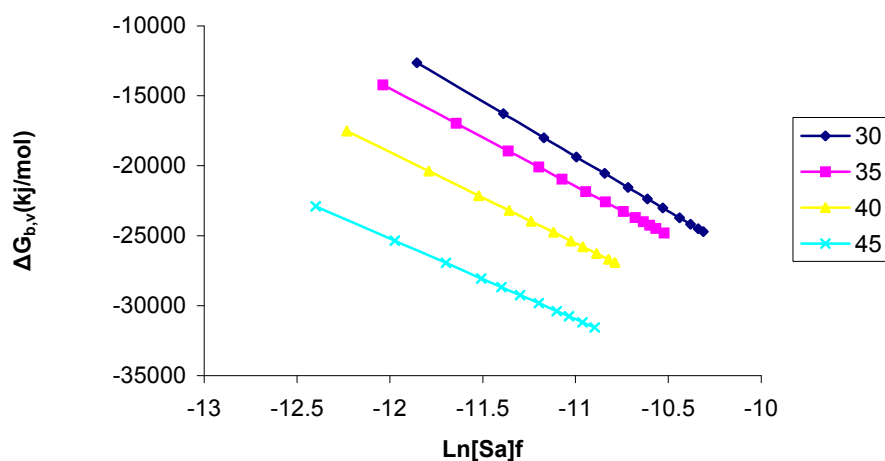


Fig. 2. The changes in the intrinsic Gibbs free energy, $\Delta G_{b,v}^0$, of interaction of HEWL with Ni(II)salen in 5 mM phosphate buffer solution, pH=7 at different temperatures.

4. Conclusions

The thermodynamic parameters such as binding constant (K_b), ΔG_b , ΔH_b , ΔS_b was calculated by analyzing the UV/Vis data with a simple binding model. The positive values of ΔH_b^0 and ΔS_b^0 represent that the binding is an endothermic process and the entropy has an essential role in this binding process. The binding isotherm, binding capacity and Scatchard plots were plotted. The positive values of n_H and Scatchard plots present that lysozyme (HEWL) has one set binding site and presents positive cooperativity.

References

- [1] N. Padama Priya, S. Arunachalam, A. Manimaran, D. Muthupriya, C. Jayabalakrishnan J. Spectrochimica Acta Part A 72(2009) 670-676
- [2] Gopa Barman Roy, , Inorganica Chimica Acta 362 (2009) 1709–1714
- [3] A. K. Bordbar, N. Sohrabi, E. Hojjati Colloids and Surfaces B: Biointerfaces 39(2004) 171-175.

**Study of self-diffusion of methane and carbon dioxide in BEA zeolite with MD simulation**S.L. Fani^a, S. Alavi^b, B. Najafi^a, H. Mohammadimanesh^a^aDepartment of chemistry, Isfahan University of Technology, Isfahan, IranE-mail: leilafani@gmail.com^bDepartment of chemistry, University of Ottawa, Ottawa, Canada**1. Introduction**

Understanding the diffusion of molecules absorbed in the pores of a zeolite is important for almost all applications of zeolites. Separation are often based on difference in diffusion coefficient of the components, and in catalytic application, diffusion of the molecules to the active site can be a rate limiting step. There has been significant progress in the development of novel computational techniques that can deal with these large ranges in diffusion coefficients. The most straightforward way is to compute a diffusion coefficient of an adsorbed molecule directly from a molecular dynamics simulation. In the present study, self-diffusion coefficient, binding energy, and activation energies of self-diffusion is investigated for CO₂ and CH₄ gases in BEA zeolite by molecular dynamics simulations. The aim of this study is to understand the effects of the temperature and kind of guest on the dynamics of the guest diffusion in BEA-type zeolites.

2. Computational and Methodology

Here, we report the results of molecular dynamics simulations of diffusion of CO₂ and CH₄ in BEA zeolite. The structure of BEA-zeolite consists of interesting 6.5×5.6 and 7.5×5.7 Å channels^[1]. The intermolecular van der waals potentials between atoms *i* and *j* on different molecules are considered to be the sum of Lennard-Jones (LJ) 12-6 and electrostatic point charge potentials centered on the atoms. To equilibrate the initial configurations, NVT molecular dynamics simulations with the Nosé-Hoover thermostat-barostat algorithm were performed on a periodic 3×3×3 (*a* = 12.6 Å, *c* = 26.2 Å) replica of the tetragonal unit cell with the DL_POLY molecular dynamics program version 2.18. The simulations we're done at a range of temperatures between 250 and 500 K, at ambient pressure and at a loading 4 of guest molecules per unit cell. The equations of motion were integrated with a time step of 1 fs using the Verlet leapfrog algorithm. Long-range electrostatic interactions were calculated using the Ewald summation method with a precision of 1×10⁻⁶ and all intermolecular interactions in the simulation box were calculated within a cutoff distance of *R*_{cutoff} = 13.0 Å. A total simulation time of 100 ps is used with an initial temperature scaled equilibration period of 30 ps. To obtain the mean-square displacement and diffusion coefficient, NVE simulations were performed for a minimum total simulation time of 500 ps, starting with configurations equilibrated by the previous NVT runs.

3. Results and discussion

The diffusion coefficient values of CH₄ and CO₂ in BEA zeolite are obtained from the slopes of the mean square displacement (MSD) versus time plots at different temperatures using the well-known Einstein relation,

$$D_{\alpha} = \frac{1}{6N_{\alpha}} \lim_{t \rightarrow \infty} \frac{d}{dt} \sum_{i=1}^{N_{\alpha}} \langle |r_i(t) - r_i(0)|^2 \rangle \quad (1)$$

where *N*_α is the number of diffusing molecules of type α, *r*_{*i*}(0) and *r*_{*i*}(*t*) are the location of the center of mass of molecule *i* at time zero and *t*. As can be seen from Table 1, the diffusion coefficients increase with temperature and the values are higher for CH₄. The binding energy for the BEA with *n* guest molecules per unit cell is defined as,

$$E_{\text{binding}} = E_{(\text{BEA}+\text{guests})} - E_{(\text{BEA})} - nE_{(\text{guests})} \quad (2)$$

The binding energy for CO₂ and CH₄ at different temperatures are given in Table 2. The binding energies increase with temperature and the values are higher for CO₂.

The activation energies (*E*_a) were calculated using the Arrhenius equation:

$$D = D_0 \exp\left(-\frac{E_a}{RT}\right) \quad (3)$$

The values of the activation energy for CO₂ and CH₄ at a loading 4 of guest molecules per unit cell are 5.76 and 3.38 kJ.mol⁻¹ respectively. The higher value for CO₂ is due to the high quadrupole moment of the CO₂^[2] which makes it bind more strongly to the zeolite framework.



T(K)	$D_{\text{CH}_4}(\text{m}^2\text{s}^{-1})$	$D_{\text{CO}_2}(\text{m}^2\text{s}^{-1})$
250	2.3077	0.61099
298	3.1537	1.0078
330	3.9887	1.2260
350	3.5335	1.1858
370	3.7270	1.3881
400	4.9558	1.6536
500	4.9696	1.9523

Table 1: Diffusion coefficient
BEA zeolite at loading 4 and

($10^{-8} \text{ m}^2\text{s}^{-1}$) calculated for CH_4 and CO_2 in
at different temperatures.

T(K)	$E_{\text{CH}_4}(\text{kJ mol}^{-1})$	$E_{\text{CO}_2}(\text{kJ mol}^{-1})$
250	-23.1257	-64.3229
298	-22.2728	-59.3099
330	-20.1654	-57.2025
350	-21.1631	-58.2001
370	-18.4571	-51.7904
400	-16.2499	-48.1254
500	-10.1272	43.4600

Table 2: The binding energies of CH_4 and CO_2 in BEA zeolite at loading 4 and at different temperatures.

References

- [1] J. M. Newsam, M. M. J. Treacy, W. T. Koetsier and C. B. de Gruyter, Proc. Roy. Soc. (London) A420 375–405 (1988).
- [2] P. Li, F. Handan Tezel, Microporous and Mesoporous Materials 98 (2007) 94-101

**Liquid–liquid equilibria of water–cyclic hydrocarbon systems using asymmetric mixing rules**

P. Reshadi, Kh. Nasrifar

Department of Chemical Engineering, Shiraz University of Technology, Shiraz ,Iran.

(E-mail: nasrifar@sutech.ac.ir)**Keywords:** Mixing rule; Water; 1-Methylnaphthalene; 1-Ethylnaphthalene; m-Diethylbenzene**1. Introduction**

Knowledge of the solubility of water in hydrocarbons is of importance in petroleum refining and petrochemical processes. On the other hand, according to environmental purposes, we must determine the amount of hydrocarbons that exist in wastewater. Despite the importance of these systems, it is quite difficult to describe their phase equilibria especially in aqueous phase since aqueous solutions of hydrocarbons have an extreme non-ideal behavior over a wide temperature range. In addition, the solubility of a hydrocarbon in water is several orders of magnitude lower than the corresponding solubility of water in the hydrocarbon. To predict the solubility of water in hydrocarbons we do not have such a problem. It is calculated accurately from cubic equations of state (EOS) with a temperature-independent binary interaction parameter [1].

Over the last three decades a number of approaches have been attempted to describe the mutual solubilities of hydrocarbons and water but majority of them were inefficient to correlate quite accurately the solubility of hydrocarbons in water (especially for a heavy and cyclic hydrocarbons). In this work by modifying the mixing rule proposed by Nasrifar-Moshfeghian [2], we try to present an asymmetric mixing rule and present mutual solubility of water with three aromatic hydrocarbons (including m-diethylbenzene, 1-methylnaphthalene and 1-ethylnaphthalene). Three cubic EOS are used for calculations, i.e. the Soave–Redlich–Kwong (SRK) EOS [3], the Peng–Robinson (PR) EOS [4] and the Nasrifar–Bolland (NB) EOS [5]. For each binary water–hydrocarbon system, four binary parameters are required to represent the liquid–liquid equilibria. The average absolute error for calculating water solubility or hydrocarbon solubility is within 7%.

2. Thermodynamic model

Kabadi and Danner (KD) [6] developed a non-quadratic mixing rule, considering the hydrophobic interactions between water and hydrocarbons in water-rich phase. The mixing rule is given by:

$$a = x_1^2 a_{11} f(x_2) + x_2^2 a_{22} + 2x_1 x_2 (a_{11} a_{22})^{1/2} (1 - k_{12}) \quad (1)$$

Latter, Michel et al. (MHP) [7] proposed:

$$f(x_2) = 1 + \beta_{12} x_2 \exp(-\alpha x_2) \quad (2)$$

With $\alpha = 10$ and

$$\beta_{12} = \tau T^n \quad (3)$$

Nasrifar and. Moshfeghian [2] defined a parameter Φ which corrects the water–water interaction in the presence of hydrocarbons.

by using this term according to Eq. (3) we have:

$$a = x_1^2 a_{11} \Phi + x_2^2 a_{22} + 2x_1 x_2 (a_{11} a_{22})^{1/2} (1 - k_{12}) \quad (4)$$

$$\Phi = 1 + \delta_{12} x_1^2 x_2 \quad (5)$$

$$\delta_{12} = (m_1 + \frac{m_2}{T}) \exp(-\frac{\Delta H^\circ}{RT}) \quad (6)$$

3. Results and discussion

Fig. 1 indicates that no matter which EOS is used with Eqs. (4-6) as mixing rule, the mutual solubility of water–1-methylnaphthalene system is predicted accurately. Fig. 2 illustrates the experimental and calculated data for the solubility of m-diethylbenzene, 1-methylnaphthalene and 1-ethylnaphthalene in water. The SRK EOS is used for the equilibrium calculations. As can be seen, Eqs. (4-6) as mixing rule fits the experimental liquid–liquid equilibrium data quite satisfactory, while the MHP mixing rule fails to correlate the solubility of cyclic hydrocarbons in water. Detailed comparisons of the new mixing rule and the



MHP mixing rule for calculating the mutual solubility of water + cycle hydrocarbons using the NB EOS, the SRK EOS and the PR EOS are given in Tables 1 and 2.

Table 1. Calculated solubility (%AAD^a) of water in hydrocarbons using different EOS (experimental data from [1])

Hydrocarbon	Temperature range (K)	NP	Eqs. (4-6) as mixing rule			MHP mixing rule		
			NB	PR	SRK	NB	PR	SRK
m-Diethylbenzene	293.9–553.6	19	6.88	3.23	5.68	6.9	3.18	6.39
1-Methylnaphthalene	340–553.8	13	4.21	3.92	4.04	4.37	3.89	4.09
1-Ethylnaphthalene	289.4–560.5	17	9.19	5.44	8.72	8.8	5.45	8.62
Overall		49	6.97	4.17	6.29	6.88	4.15	6.55

$$^a \%AAD = (100 / np) \sum_j^{np} |x_{cal,j} - x_{exp,j}| / x_{exp,j}$$

Table 2. Calculated solubility (%AAD^a) of hydrocarbons in water using different EOS (experimental data from [1])

Hydrocarbon	Temperature range (K)	NP	Eqs. (4-6) as mixing rule			MHP mixing rule		
			NB	PR	SRK	NB	PR	SRK
m-Diethylbenzene	293.9–553.6	19	0.71	1.3	0.74	26.42	19.74	26.08
1-Methylnaphthalene	340–553.8	13	2.01	1.21	1.88	18.75	13.32	18.11
1-Ethylnaphthalene	289.4–560.5	17	8.14	6.73	7.9	32.99	35.72	37.37
Overall		49	3.63	3.16	3.52	26.66	23.58	27.88

$$^a \%AAD = (100 / np) \sum_j^{np} |x_{cal,j} - x_{exp,j}| / x_{exp,j}$$

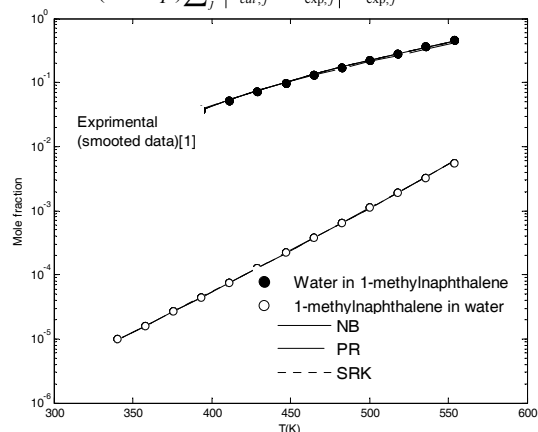


Fig. 1. Mutual solubility of water–1-methylnaphthalene system using Eqs. (4-6) as mixing rule.

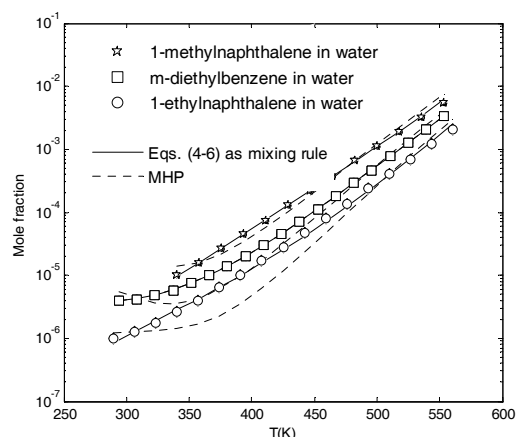


Fig. 2. Solubility of 1-methylnaphthalene, m-diethylbenzene and 1-ethylnaphthalene in water using the SRK EOS.

4. Conclusions

A modified form of Nasrifar-Moshfeghian mixing rule [2] which has been developed for the a -parameter of cubic EOS is able to quantitatively describe liquid–liquid equilibria of water–cyclic hydrocarbon systems for a wide range of temperature. The PR EOS shows a better agreement with the experimental data; while the NB EOS and the SRK EOS exhibit more or less the same quality.

References

- [1] I.G. Economou, J.L. Heidman, C. Tsonopoulos, *AIChE J.* 43 (1997) 535–564.
- [2] Kh. Nasrifar, M. Moshfeghian, *Fluid Phase Equilib* 193 (2002) 261–275.
- [3] G. Soave, *Chem. Eng. Sci.* 27 (1972) 1197–1203.
- [4] D.-Y. Peng, D.B. Robinson, *Ind. Eng. Chem. Fundam.* 15 (1976) 59–64.
- [5] Kh. Nasrifar, O. Bolland, *J. Petrol. Sci. Eng.* 51 (2006) 253–266.
- [6] V.N. Kabadi, R.P. Danner, *Ind. Eng. Chem. Process. Des. Dev.* 24 (1985) 537–541.
- [7] S. Michel, H.H. Hooper, J.M. Prausnitz, *Fluid Phase Equilib.* 45 (1989) 173–189.

**Thermodynamic study of adenine, adenosine and uracil at constant ionic strength**E. Heiatian^{a,*}, S. Sharifi^a, A. Niazi^a, A. Bahadori^a

a. Department of Chemistry, University of Islamic Azad, Arak, Iran

(E-mail: elham.heiatian@gmail.com)**Keywords:** Adenine, Adenosine, Uracil, Acidity Constant, Equispec Program**1. Introduction**

In the living cell, there are found nucleoproteins. Of all fields of chemistry, study of the nucleic acids is perhaps the most exciting, for these compounds control heredity on the molecular level. On the other hand, acid dissociation constants can be a key parameter for understanding and quantifying chemical phenomena such as biological activity, biological uptake, biological transport and environmental fate [1-2]. There have been several methods of the determination of acidity constants [1,3-6]. Spectroscopic methods are in general highly sensitive and are frequently used to analyze chemical equilibria in solution. If the components involved can be obtained in pure form, or if their spectral responses do not overlap, such analysis is trivial. For many systems, particularly those with similar components, this is not the case, and these have been difficult to analyze [5]. In 1971 Lawton and Sylvestre [7] introduced chemometric methods for spectral analysis. In general, such an analysis is made in two steps: first, the number of components is determined, and then the spectral responses and concentrations of the components are calculated [8]. In the present work, the protonation equilibria of Adenine, Adenosine and Uracil in aqueous solution were studied using a combination of potentiometric and spectrophotometric methods at different temperatures (10, 15, 20, 25, 30 and 35°C) and constant ionic strength (0.1 mol dm⁻³ sodium perchlorate). An accurate and sophisticated method based on chemometrical concepts was applied in order to determine acidity constants. For this purpose, spectral titration data were used and the spectra were recorded in the range (200-500 nm). The computer program equispec was used to extract the desired information from the spectral data. The effect of temperature on the protonation was studied and thermodynamic functions have been obtained for the heterocyclic bases from the acidity constants values and their temperature dependence.

2. Methods**2.1. Chemicals**

Adenine, Adenosine, Uracil and Sodium perchlorate were of analytical reagent grade commercial products from Merck. The aqueous stock solutions of the heterocyclic bases were freshly prepared daily. The NaOH solution was prepared from a titrisol solution (Merck), and its concentration was determined by several titrations with standard HCl. Perchloric acid was from Fluka and dilute perchloric acid solutions were standardized against standard NaOH solution. These chemicals were used without further purification. All solutions were prepared in deionized water with specific conductance equal to $(1.8 \pm 0.1) \mu\Omega^{-1} \text{ cm}^{-1}$.

2.2. Apparatus and software

A HORIBA M-12 pH-meter furnished with a combined glass-saturated calomel electrode was calibrated with at least two buffer solutions at pH 3.00 and 9.00. The calibration was repeated at each specific temperature ($t \pm 0.1$) °C by circulation of thermostated water through the jacket. A HP-8453 spectrophotometer controlled by a computer and equipped with a 1 cm path length quartz cell was used for UV-Vis spectra acquisition. Spectra were acquired between 200 and 500 nm. The data were transferred (in ASCII format) to a computer for subsequent analysis using MATLAB software, version 6.5 (The Mathworks) and for processing by using equispec program, version 3.1.

2.3. Measurements

All measurements were carried out at six different temperatures (10, 15, 20, 25, 30 and 35°C). The ionic strength was maintained to 0.1 mol dm⁻³ with sodium perchlorate. The pH meter was calibrated for the relevant H⁺ concentration with a solution of 0.01 mol dm⁻³ perchloric acid containing 0.09 mol dm⁻³ sodium perchlorate [4].

2.4. Procedure

Volumes of 10 cm³ acidic solution of the heterocyclic bases (5.6×10^{-5} to 2.8×10^{-4} mol dm⁻³) was titrated with an alkali solution (0.1 mol dm⁻³ NaOH), in ionic strength 0.1 mol dm⁻³ NaClO₄. The starting points of pH titrations were pH 1.0. The $-\log [H^+]$ and absorbance were measured after addition of a few drops of titrant, and this procedure was extended up to required $-\log [H^+]$.

3. Results and discussion .The protonation constants of the adenine, adenosine and uracil were determined using a potentiometric technique.

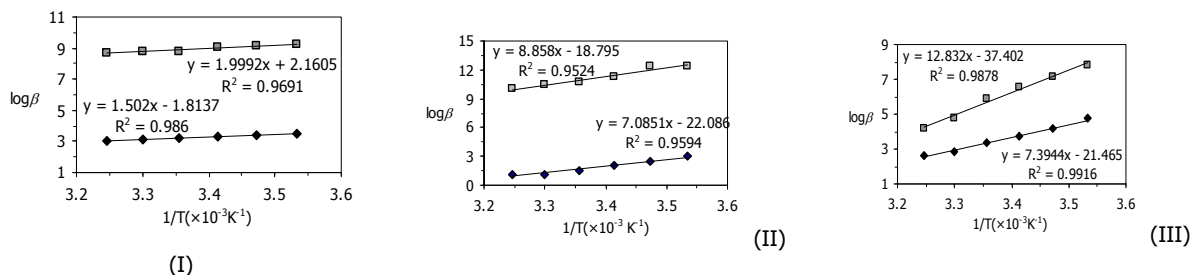


Fig. 1. Curve $\log \beta$ vs. $1/T$ for (I) Adenine, (II) Adenosine, (III) Uracil systems in ionic strength (0.1 mol dm⁻³ NaClO₄).

The electronic absorption spectra were recorded in different temperatures and at various pH values in the UV range (200 to 500) nm. Treatment of the spectrophotometric data (every 5 nm) obtained during the titrations, as a function of H⁺ concentration, was conducted with the computer program equispec. The stoichiometric protonation constants were computed from the data using the computer program. For determination of protonation constant, several protonated species were tested by the program. The protonation constants values for these species were calculated; but the species were not considered further because the estimated error in its protonation constants was unacceptable. The models finally chosen, formed by H₂L⁺, HL and L⁻ for the studied systems resulted in a satisfactory fitting. The calculated values of the protonation constants for different experiments are shown in Figure 1. In these heterocyclic bases, the possible sites are N and NH₂ groups for accepting a proton. The results for adenine led to conclude that N position are the most likely sites of protonation in adenine [9]. The thermodynamic functions for the heterocyclic bases have been obtained from the protonation constants values and their temperature dependence (Table 1). As shown by Figure 1, changes in temperatures have more or less observable effects on the spectral data of the heterocyclic bases. The results show apparent acidity constants are corresponding to thermodynamic constants. The investigation of influence temperature on the acid-base behavior of simple organic compounds may contribute to a better understanding of the properties of complex substances such as natural organic matters and the knowledge of the distribution of species with pH is a prerequisite for further kinetic studies [4].

4. Conclusions

The acid dissociation constants of adenine, adenosine and uracil were calculated with spectrophotometric titrations using a chemometric method. The striking advantage of the proposed method is using of the whole spectral information in the computation process which enable us to have more precise and accurate thermodynamic constants in comparison to the classical methods such as single wavelength approach. The reported values are comparable with those obtained in this work. However, the differences are mostly due to the different techniques, various ionic strengths with different background electrolytes, and different temperatures that were used.

Table 1. Values of the thermodynamic parameters at 25 °C

	$H_2L^+ + H_2O \rightleftharpoons HL + H_3O^+$					$HL + H_2O \rightleftharpoons L^- + H_3O^+$				
	ΔH (KJ/mol)	ΔS (J/mol)	ΔG (KJ/mol)	$\log \beta_{21}$	$\log \beta_{21}^a$	ΔH (KJ/mol)	ΔS (J/mol)	ΔG (KJ/mol)	$\log \beta_{11}$	$\log \beta_{11}^a$
Adenine	28.76	18.41	34.70	3.26±0.13	4.17	51.06	3.01	50.16	8.81±0.12	9.75
Adenosine	135.65	9.64	422.88	1.50±0.26	3.50	169.6	359.87	62.36	10.77±0.33	12.34
Uracil	3.49	3.49	3.49	3.40±0.17	-	248.33	724.77	32.34	6.60±0.34	-

^aThe values reported in the literature are also reported for comparison [9,10]

References

- [1] A. Niazi, M. Ghalie, A. Yazdanipour, J. Ghasemi, Spectrochim. Acta, Part A 64 (2006) 660.
- [2] J. Ghasemi, S. Ghobadi, B. Abbasi, M. J. Kubista, Korean Chem. Soc. 49 (2005) 269.
- [3] F. Kiani, A. A. Rostami, S. Sharifi, F. Gharib, J. Chem. Eng. Data 54 (2009) 3261.
- [4] S. Sharifi, D. Nori-shagh, A. Bahadory, J. Braz. Chem. Soc. 18 (2007) 1011.
- [5] A. Niazi, A. A. Rezaei, F. Shahhosseini, Ann. Chim. (Rome) 97 (2007) 199.
- [6] E. Fernández, L. García-Río, J. C. Mejuto, M. Parajó, Spectrochim. Acta, Part A 66 (2007) 1102.
- [7] W. Lawton, E. Sylvestre, Technometrics, 13 (1971) 617.
- [8] A. Elbergali, J. Nygren, M. Kubista, Anal. Chim. Acta 379 (1999) 143.
- [9] F. Gharib, M. Monajjemi, S. Ketabi, Main Group Met. Chem. 27 (2004) 71.
- [10] J. A. Dean, Lange's Handbook of Chemistry, 15th ed., McGraw-Hill, New York, 1999.

**Surface tension determination of dense fluid methanol**Atena Siami^a, Vahid Moeini^b

a. Payam Noor university, Sari Center

b. Payam Noor university, Behshahr Center

(E-mail: asiamei@yahoo.com)**Key words:** Surface tension, $g(\sigma, \rho, T)$, Radial distribution function (RDF), dense fluid, perturbation theory**1. Introduction**

A comparison of Helmholtz energy theory and perturbation theory for real molecules is presented. A new equation is derived. This new model has the exact surface tension behavior, converges to the correct mean-field behavior at high densities, and successfully interpolates between these two limits. This new equation is applied to molecules that interact via the Lennard-Jones potential. Comparison is made with experimental data results for the configurational energy, the compressibility factor, and the surface tension of Lennard-Jones molecules. One of the most striking demonstrations of the intermolecular forces is the tension at the surface of a liquid. At the molecular level, one may consider the boundary layer at the liquid-vapor interface to be a third phase with properties intermediate between those of a liquid and its vapor. The surface tension (γ), generally employed as a quantitative index of this tension, is defined as the force exerted in the plane of the surface per unit length (dynes cm⁻¹). Surface tension is one of the most important physicochemical properties for polymeric materials in various engineering processes, such as those involving foaming suspensions wetting and blending. In this communication, we propose a set of approximations for the higher-order terms in the perturbation expansion, which result in a very simple, closed-form expression for the configurational energy and other thermodynamic quantities. While we derive this equation for the Lennard-Jones fluid, we extend it to the Lennard-Jones fluid as well. Particular emphasis is given to the high-density behavior and the surface tension, since this region is extremely important for dense fluid calculations, especially calculations of liquid fluids.

2. Methods

Molecules possess repulsive forces (usually short-ranged for overlap forces and long-ranged for charge repulsion) and attractive forces (short-ranged for hydrogen bonds and longer ranged for dispersion and polar forces). The Lennard-Jones potential is a simple pair potential function that possesses both repulsive and attractive London forces' that has been studied extensively due to its simplicity. Lennard-Jones fluids exhibit vapor-liquid and fluid-solid transitions and a critical point. Characterization of the Lennard-Jones fluid represents a major advance in statistical mechanics and in understanding real fluid behavior.

Zwanzig, Rowlinson, and McQuarrie and Katz developed statistical mechanical perturbation theory by performing a perturbation expansion on the canonical partition function of the system and on the configurational integral in particular. The total potential is separated into two parts: the potential of the reference, or unperturbed, system and the perturbation potential. The Helmholtz free energy is obtained as a power series in inverse temperature with the coefficients being functions of density. Barker and Henderson developed the first generally successful perturbation theory for liquids. They derived expressions for the first-order term, which involves two-body interactions, and applied perturbation theory to Lennard-Jones molecules. They obtained good agreement of the second-order perturbation calculations with their molecular dynamics simulation results.

New method of statistical mechanical perturbation theory are use to calculate surface tension of dense fluid Methanol. An expression has been derived for radial distribution function (RDF) at constant temperature, $g(\sigma)$, for a real fluid by the use perturbation theory. This expression, which is related to intermolecular interaction, can be used to be describe temperature-density dependency of RDF at constant temperature, $g(\sigma, \rho, T)$.

We consider the second-order perturbation expansion for the residual Helmholtz function,

$$(A - A^*)/NkT = (A^0 - A^*)/NkT + A_1^0/NkT + A_2^0/NkT \quad (1)$$

The reference term $(A^0 - A^*)/NkT$ of the system of soft convex bodies follows from the equation of state of the representative hard convex bodies, in our case that of hard prolate spherocylinders of the same core (rod) as that ascribed to the studied molecule.



We drive an expression for surface tension of dense fluid Methanol using perturbation theory and $g(\sigma, \rho, T)$. To obtain a numerical estimate, Kirkwood and Buff assumed the gas phase to be infinitely dilute (as vacuum) and the liquid to be homogeneous up to the separation surface (Gibbs dividing surface). Their simplified expression for the surface tension is:

$$\gamma = \frac{\pi \rho^2}{8} \int_0^\infty R^4 \frac{d\phi(R)}{dR} g(R) dR \quad (2)$$

Where ρ is the average number density in the liquid, $\phi(R)$ is the intermolecular pair potential and $g(R)$ is the radial distribution function in the liquid. With additive pair interaction potentials, the statistical analysis gives the following virial expression for the surface tension γ :

$$\gamma = \frac{1}{4} \int_{-\infty}^{+\infty} dz_1 \int dr_{12} \left(r - 3 \frac{z^2}{r} \right) \frac{d\phi}{dr} \rho^{(2)}(r_1, r_2) \quad (3)$$

Where the z axis is perpendicular to the interface and directed from the liquid toward the gas, $r_{12} = r_2 - r_1$, $r = |r_{12}|$ is the two-particle distribution function.

$$\rho^{(2)}(r_1, r_2) = \rho(z_1) \rho(z_2) g(r_1, r_2) \quad (4)$$

Therefore:

$$\gamma = -\frac{1}{8} \pi \rho^2 \sigma^4 R T g(\sigma, \rho, T) \quad (5)$$

4. Conclusions

We drive an expression for surface tension of dense fluid Methanol using statistical mechanical perturbation theory and $g(\sigma, \rho, T)$, unlike previous models, it is shown in this work that, surface tension can be obtained without employing ΔH and ΔS , P - V - T experimental data have been used the calculation of surface tension. Comparison of the calculated values of surface tension by statistical mechanical perturbation theory with values obtained experimentally show this method is precise. The results shows the accurate of this method to be is general, quit good.

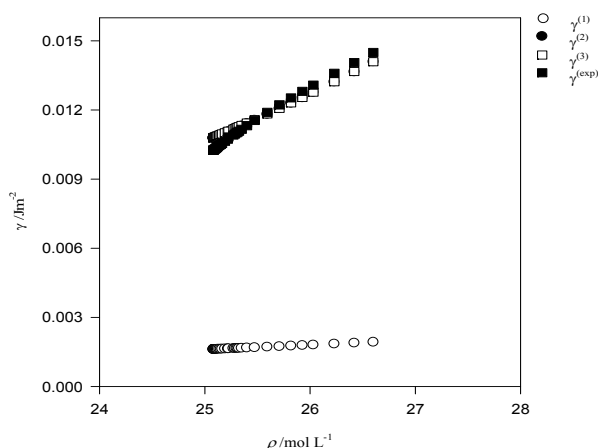


Fig. 1. plot of surface tension versus density for Methanol.

References

- [1] Parsafar.G and Mason.E.A, *Phys. Rev.B*,49 (1994) 3049.
- [2] Parsafar.G and Mason.E.A ,*J.Phys.Chem.*97 (1993) 9048.
- [3] Parsafar.G, Moeini.V and Najafi B, *Iran J.Chem.Eng.*20 (2001) 37.
- [4] Park. H, Thompson.R.B., N.Lanson, *J.phys. chem.* 111 (2007) 3859-3868.
- [5] Korochkova.E.A, Boltachev.G. Sh and Baidakov.V.G., *Russian Journal of physical chemistry* 80 (2006) 445-448.



Measurement and prediction of volumetric and transport properties of ternary aqueous solution of tri-potassium citrate + KCl at different temperatures

M.T. Zafarani-Moattar, F. Izadi^a

^aDepartment of Chemistry, University of Tabriz, Tabriz, Iran

(E-mail: farhad_izadi64@yahoo.com)

1. Introduction

Knowledge of volumetric and transport properties of electrolyte solutions have been proven to be a very useful tool in evaluating the structural interactions occurring in these solutions. Volumetric and transport properties of binary aqueous solutions of potassium chloride have been available in literature. Densities, speed of sound and viscosity values of binary aqueous solutions of tri-potassium citrate have been reported by Sadeghi, et al [1,2]; however, close examination indicated that densities, speed of sound and viscosity values of binary aqueous solutions of tri-potassium citrate have only been measured in the very dilute concentration range. Therefore, in this work, density and viscosity measurements of binary aqueous solutions of tri-potassium citrate were performed from dilute up to near saturated concentration range, from which apparent molar volumes have been calculated at different temperatures. Volumetric and transport properties of ternary aqueous solutions of tri-potassium citrate + KCl have also been measured at different temperatures. Density and viscosity values of binary aqueous solutions of tri-potassium citrate have been correlated with the empirical and semiempirical equations proposed by Laliberte et al [3,4] and Zafarani-Moattar et al [5]. From the obtained parameters the density and viscosity values of ternary solutions have been predicted on the basis of Arrhenius type mixing rule. The obtained results show the good predictions for density and viscosity values of ternary aqueous solutions of tri-potassium citrate + KCl system.

2. Methods

Density values were measured with a vibrating-tube densimeter (Antoine Parr DSA-500, Austria). By this apparatus, the working temperature can be controlled within ± 0.001 K. The apparatus was calibrated at each temperature with double-distilled-deionized water and dry air. The uncertainty in the measurement of density was estimated to be ± 0.003 kg \cdot m⁻³ for density. The viscosities of tri-potassium citrate solutions were determined with a suspended Ubbelohde-type viscometer (Julabo, MD-18V, Germany) at different temperatures in which the temperature was controlled with a precision of 0.01 K. The flow times were measured using a stopwatch. The precision of the used stopwatch was ± 0.01 s. The uncertainty for the dynamic viscosity determination was estimated to be ± 0.5 %. Each measurement was repeated five times.

3. Results and discussion

The apparent molar volumes V_{ϕ} of aqueous tri-potassium citrate solutions were calculated from the densities of the solutions d using the following equation:

$$V_{\phi} = \frac{M_1}{d} - \frac{(d - d_0)}{m d d_0} \quad (1)$$

where M_1 is the molar mass of tri-potassium salt. m and d_0 are the molality of solution and solvent density, respectively. The calculated apparent molar volume for binary aqueous tri-potassium citrate system has been plotted in Figure 1 at different temperatures. As can be seen from Figure 1 the apparent molar volume increase with increasing temperature and this indicate that with increasing temperature the interactions between solvent and solute were decreased. The apparent specific volumes V_{app} have been calculated with the following equation:

$$V_{app} = \frac{1 - \frac{d(1 - w_2)}{d_0}}{dw_2} \quad (2), \quad V_{app} = \frac{(1 - w_{H_2O}) + c_2 + c_3 t}{(c_0(1 - w_{H_2O}) + c_1) e^{(0.000001(t + c_4)^2)}} \quad (3)$$

where w_2 refers to mass fraction of salt. The apparent specific volumes of binary solutions have been correlated with the empirical equation proposed by Laliberte (eq 3) [3]. Solute viscosity values of tri-potassium citrate, η_{tr} , have been fitted with the empirical and semiempirical equations proposed by Laliberte[4] and Zafarani-Moattar et.al[5], eqs 4 and 5, respectively

$$\eta_e = \frac{\exp((c_0(1 - w_{H_2O})^{c_2} + c_2)/(c_3t + 1))}{c_4(1 - w_{H_2O})^{c_5} + 1} \quad (4)$$

$$\eta_e = c_0 \exp\left(\frac{c_1}{t - c_2}\right) \exp(c_3m + c_4m^2) \quad (5)$$

The obtained parameters along with the absolute average relative deviations (AARD) were reported in Table 1. With considering the method used by Laliberte[3] in the prediction of density of multicomponent systems and using the parameters collected in Table 1 and parameters of binary aqueous KCl system[3], we can predict the density values of aqueous ternary solution of tri-potassium citrate + KCl systems. The absolute average relative deviation between calculated and measurement density value is 0.173%. similarly the viscosity values of aqueous ternary solution have also been predicted with using the Arrhenius type mixing rule and parameters given in Table 1 and parameters of binary aqueous KCl solutions [4,5]. The estimated absolute average relative deviation with Laliberte equation is 0.035% and with the equation proposed by Zafarani et al is 0.023%. From the obtained results it is obvious that the performance of the equations proposed by Zafarani et al. in the prediction of viscosity values of tri-potassium citrate + KCl is better than of proposed by Laliberte.

Table 1. Parameters of eqs 3-5 along with the AARD values in the fitting of density and viscosity values of binary aqueous solutions of tri-potassium citrate

tri-potassium citrate	C ₀	C ₁	C ₂	C ₃	C ₄	C ₅	100.AARD
Density							
Equation 3	0.186	4993.000	1.641	1.549×10 ⁻³	0.064		0.042
Viscosity							
Equation 4	3.015	1766.	2.109	0.028	-1.57	0.982	0.0045
Equation 5	0.026	1109.000	-201.455	0.607	9.398×10 ⁻³		0.0047

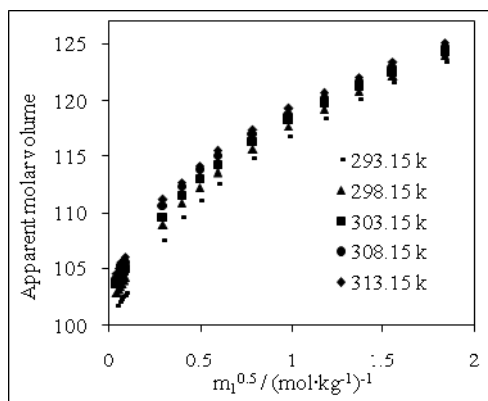


Fig. 1. Experimental apparent molar volume, plotted against rot of molality of salt, for the tri-potassium citrate +H₂O System.

4. Conclusions

The viscosity and density values of ternary aqueous tri-potassium citrate + KCl systems have been measured and predicted on the basis of Arrhenius type mixing rule and parameters obtained from binary aqueous solutions. The obtained results show that the performance of Laliberte and Zafarani et al equations in the prediction of viscosity and density values of aqueous organic salts is good and the results are same as that proposed by these authors for inorganic salts.

References

- [1] Sadeghi, R. Goodarzi, B. Karami, K. J. Chem. Eng. Data. 54 (2009) 791.
- [2] Sadeghi, R. Ziamajidi, f. J. Chem. Eng. Data. 52 (2007) 1753.
- [3] Laliberte', M. Edward Cooper, W. J. Chem. Eng. Data. 49 (2004) 1141.
- [4] Laliberte', M, J. Chem. Eng. Data. 52 (2007) 321.
- [5] Zafarani-Moattar, M, T. Majdan-Cegincara, R. Ind. Eng. Chem. Res. 48 (2009) 5833.



Ionic strength dependence of formation constants, protonation and complexation of EDTA with dioxouranium(VI)

Morteza Jabbari*, Ali Farajtabar and Farrokh Gharib

Department of Chemistry, Shahid Beheshti University, Tehran, Evin, Iran

(E-mail : m.jabari@sbu.ac.ir)

Keywords: Dioxouranium(VI), EDTA, Ionic strength, SIT model, Stability constant

1. Introduction

Polyaminocarboxylates form a group of organic compounds whose interaction with actinide cations could influence significantly the ecological and biological behavior of these cations. Uranium is a trace constituent in rock phosphate, which is extensively used as a source of phosphorous for fertilizers and livestock feed supplements. Calcium phosphate, for example, a source of calcium used as an animal feeding supplement, can present concentrations of uranium as high as 200 ppm [1]. Thus, the investigation of the pathway, uranium (from feeding) → animal → human, is particularly important, as far as the radiological protection of the general population is concerned.

The present work deals with the study of dioxouranium(VI) ion, UO_2^{2+} , with EDTA in aqueous solution and at different ionic strengths, 0.1 to 1.0 mol dm⁻³ sodium perchlorate as supporting electrolyte, using a combination of potentiometric and spectrophotometric techniques.

2. Experimental

All measurements were carried out at 25 ± 0.1 °C. The ionic strength electrolyte is much larger than ionic species formed in the protonation was maintained to 0.1-1.0 mol dm⁻³ with sodium perchlorate. pH-meter was calibrated for the relevant H^+ concentration with a solution of 0.01 mol dm⁻³ perchloric acid solution containing 0.09 mol dm⁻³ sodium perchlorate (for adjusting the ionic strength to 0.1 mol dm⁻³). The same procedure was performed for the other ionic strengths.

In this work a acidic solution of UO_2^{2+} (0.001 mol dm⁻³) was titrated with an alkali solution (0.1 mol dm⁻³ NaOH) of the ligand, both of the same ionic strength. The $-\log[\text{H}^+]$ and absorbance were measured after addition of few drops of titrant, and this procedure was extended up to the required $-\log[\text{H}^+]$. In all cases, the procedure was repeated at least three times.

3. Results and discussion

The complex $\text{M}_p\text{H}_q\text{L}_r^{(2p+q-4r)}$ formed, is characterized by its stoichiometry (p:q:r), where M and L represent the metal ion and the ligand, respectively. To determine the stability constant of complexation or protonation Eq. (2) is defined by β_{pqr} [2],



$$\beta_{pqr} = \frac{[\text{M}_p\text{H}_q\text{L}_r^{(2p+q-4r)}]}{([\text{M}^{2+}]^p [\text{H}^+]^q [\text{L}^{4-}]^r)} \quad (2)$$

The protonation constants of EDTA have been used for computation of the stability constant, β_{pqr} , of the metal-ligand. In this work, the protonation constants of EDTA were determined at different ionic strengths of sodium perchlorate using potentiometric technique and calculated using a computer program (Microsoft Excel Solver) which employs a nonlinear least-squares method.

The method of determination of the stability constant was based on the relation $A = f[\text{H}^+]$. The spectrophotometric data (255–290 nm) obtained during the titration as a function of the hydrogen ion concentration was conducted with the computer program. Different models including MH_4L^{2+} , MH_3L^+ , MH_2L and several polynuclear and protonated complex species were tested by the program. The program allows calculation of the stability constant for different stoichiometry models.

The values of protonation and stability constants of the studied system show the dependence on ionic strength for the different species in the supporting electrolyte. At low ionic strength (possibly less than 0.1 mol dm⁻³) the Coulomb interactions between ions screen by the ions of the atmosphere and are of primary importance. However, as the ionic strength increases, the ionic atmosphere becomes more compressed and screens the ionic charges more effectively. So, at higher



concentration of the supporting salt the intermolecular interactions (such as dipole–dipole or multipole–multipole) become more important and possibly have a primary role between the ions.

The dependence on ionic strength on formation constant was taken into account by using the specific ion interaction theory, SIT model [3]. In this work, SIT model was used to extrapolate the formation constants of all species found at infinite dilution and calculating the specific interaction coefficients.

References

- [1] J. Arruda-Neto, V. Likhachev, G. Nogueira, G. Araujo, S. Camargo, G. Cavalcante, A. Cestari and V. Vanin, *Appl. Radiat. Isotopes* 54 (2001) 947.
- [2] A. Gianguzza, A. Pettignano and S. Sammartano, *J. Chem. Eng. Data* 50 (2005) 1576.
- [3] F. Gharib and A. Farajtabar, *J. Mol. Chem.* 135 (2007) 27.

**Measurement and modelling of osmotic coefficients for three components systems at 298.15 K**

A. Ebrahimiyan Pirezabari*, J. Jahanbin Sardroodi

Department of Chemistry, Azarbaijan University of tarbiat moallem, Tabriz

(E-mail: Ebrahimiyan_ali2002@yahoo.com)**Keywords:** Modelling, Osmotic coefficients. Three components, Thermodynamic models**1. Introduction**

Phase equilibrium data for non-aqueous electrolyte solution are useful in the development of models for the description of electrolyte behaviour in non-aqueous solvent system. There is a growing interest in the study of non-aqueous electrolyte solutions in the two past decades [1]. there is no report on osmotic coefficient data for three component system including ethanol, LiNO_3 and 2-naphthol at 298.15K.

In this work, we report the osmotic coefficients and vapour pressures for aforementioned three components systems. The osmotic coefficients have been measured by an improved isopiestic apparatus. The osmotic coefficients data were successfully correlated with the thermodynamic models including, Clegg- Pitzer- Simonson (C.P.S) and Non-Random Two Liquid (NRTL).

2. Experimental

For this research, we used a special apparatus consisted of a five-leg manifold attached to round-bottom flasks. The five flasks were typically used as follows: two flasks contained the standard NaI solutions; two flasks contained LiNO_3 and 2-naphthol and the central flask was used as ethanol reservoir. The apparatus was held in a constant temperature bath for at least 120h for equilibration at 298.15 K.

3. Results and discussion**3.1 Experimental results**

Fig. 1 shows osmotic coefficients of the ethanol solutions at weight fractions 0.25, 0.5 and 0.75 obtained from the isopiestic experiments.

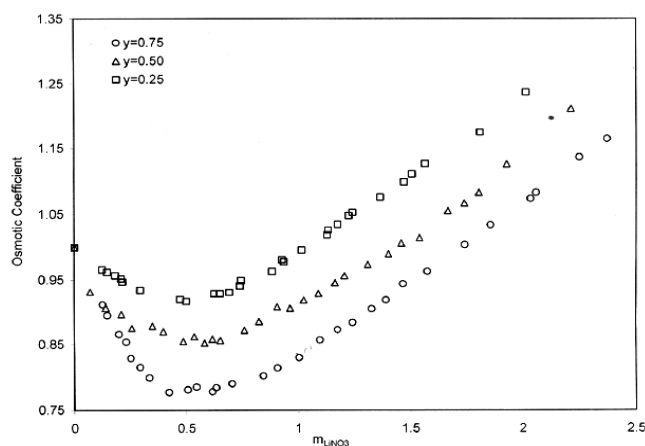


Fig. 1. Osmotic coefficients of the $[y \text{ LiNO}_3 + (1-y) \text{ 2-naphthol}]$ for all weight fractions

Fig. 2 shows of vapour pressure of the ethanol solutions at weight fractions 0.25, 0.5 and 0.75 obtained from the osmotic coefficient data.

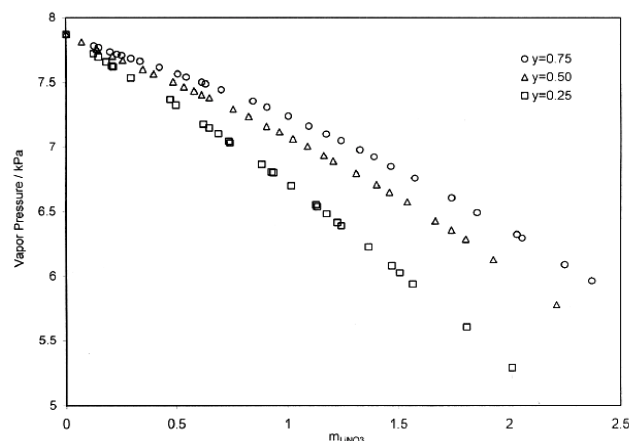


Fig. 2. Vapour pressure of the $[y \text{ LiNO}_3 + (1-y) \text{ 2-naphthol}]$ for all weight fractions

3.2. Correlation of data

Among these models, the NRTL model has been used for salt+alcohol system [2]. Also, the Clegg-Pitzer model has been used for representation of osmotic coefficients of some lithium salts in 2- propanol [3]. In the present work, we used the C.P.S and NRTL models for correlation of osmotic coefficients data.

Table. 1. Clegg-Pitzer-Simonson parameter for $[y \text{ LiNO}_3 + (1-y) \text{ 2-naphthol}]$ in the ethanol

weight fractions	0.25	0.5	0.75
$Y_{1,mx,n}$	0.14567	0.20468	0.32150
$\sigma(\phi)$	0.021	0.019	0.022

For the reliability of these two models, we calculated the standard deviation.

Table. 2. Standard deviation for osmotic coefficient on the basis of C.P.S and NRTL models for $[y \text{ LiNO}_3 + (1-y) \text{ 2-Naphthol}]$ system

Weight fractions	0.25	0.5	0.75
$\sigma(\phi)$ NRTL model	0.0195	0.019	0.018
$\sigma(\phi)$ Pitzer - Simonson- Clegg	0.021	0.019	0.022

4. Conclusions

Experimental osmotic coefficients data for the ethanol solutions of three components systems were obtained by isopiestic method at 298.15K. Experimental data are satisfactorily correlated using C.P.S and NRTL models. Model parameters are obtained by fitted to osmotic coefficients have been used to calculate the vapour pressure for the investigated systems

References

- [1] J. Barthel, H. Krienke, W. Kunz, in: H. Baumgartel, E.U. Franck, W. Grünbein (Eds.), Physical Chemistry of Electrolyte Solutions, Topics in Physical Chemistry, vol. 5, Springer, 1998.
- [2] M.T. Zafarani-Moattar, J. Jahanbin Sardroodi, Fluid Phase Equilib. 172 (2000) 221.
- [3] M.T. Zafarani-Moattar, M. Aria, J. Sol. Chem. 30 (2001) 351.

**Characterizing phase transition in liquid cesium with voronoi-tessellation method**

Mohammad Hadi Ghatee , Khadijeh Shekoohi

Department of Chemistry, Shiraz University, Shiraz 71454, Iran

(E-mail: ghatee@susc.ac.ir)(E-mail: shekoohi@shirazu.ac.ir)**Keywords:** phase transition, voronoi-tessellation, void, Gupta**1. Introduction**

This work investigates to identify phase transition in condensed liquid cesium metal by Voronoi–Tessellation method. The temperature dependence of the structure of liquid cesium metal is obtained with the analysis of Voronoi tessellation result.

2. Method

The Voronoi diagram of a set of atoms $i = 1, N$ is a decomposition of the space into N region (called Voronoi polyhedra (VP)) associated to each atom, such that every point of a Voronoi region (that is inside a VP) is closer to the associated atom to any other atom in the system. Then, the Voronoi region Π_i for each contains the points with coordinate X satisfying the following condition

$$\Pi_i = \{X \mid d(X, X_i) < d(X, X_j) \ \& \ \forall j \neq i\}$$

Where d denotes Euclidean distance between two atoms. By definition the Voronoi polyhedra turns out to be the equivalent of the Wigner-Seitz cell in a crystal solid [1-3]. The key to building of all VP is the *vertices*, the *edge*, and the *faces* of every VP.

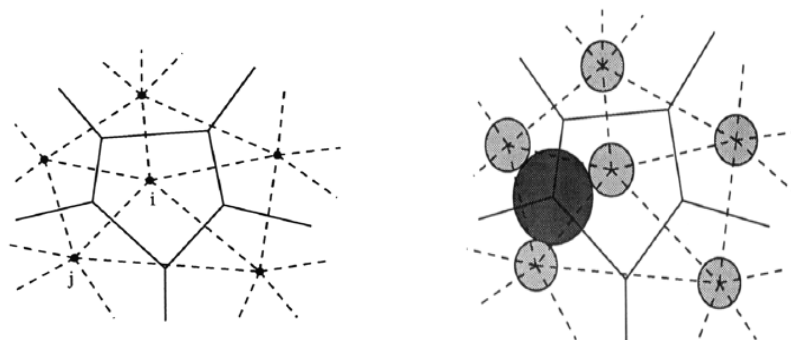


Fig.1. Two-dimensional illustration of the Voronoi Tessellation solid lines forms Voronoi polyhedron about atom i and the dashed line form Delaunay simplex.

In 3-D space a set of four atoms that have share face between their VP forms a tetrahedron which called *Delaunay simplex* or *Delaunay*, because every Voronoi vertex is a circumcenter of the Delaunay simplex. The volume inside the *Delaunay* simplex is always empty: by definition, there are no atomic centers insides. It is a main reason why the Voronoi -Method is used for the analysis of voids (Figure 1). There are several algorithms for construction Voronoi tessellation [4, 5].

3. Results and discussion

How quantifying the local environment around an atom is in the system?

After construction of Voronoi tessellation, the atom associated with that polyhedron can be quantified in many ways, (I) *polyhedral volume* representing the amount of space the atoms requires for itself. (II) Number of *faces* of the polyhedron, representing neighboring atoms around central atom (III) number of *vertices*, which correspond to the void surrounding the central atom (IV) volume of void.

This method has been used in many ways. For example change in structure characterize with number of vertices in each VP and Voronoi polyhedral volume. because they can naturally be used not only to inspect the free volume per particle, but even to



characterize the average local arrangement of particles in the liquid phase. A practical example can be phase transition in liquid alkali metals.

Liquid alkali metals have open shell electronic structure (ns^1), when the temperature is increases the valance electrons become more correlated with their parent's ions, leading to polarizable polyatomic clusters [6-8].

We have simulated the liquid cesium by the classical molecular dynamic using an NVT ensemble involving 432 atoms. For this simulation used force filed according to the n-body Gupta potential that is known to be suitable for metallic clusters. Simulation is performed in the temperature range 520K to 620K.

We chose the void volume to indicate phase transition of liquid cesium metal near 590 K, having system consist of liquid cesium close to the phase transition as a cluster. We consider the collapse of the void in the temperature range at which transition occurs and the volume of each polyhedron around atom deformed.

Figure 2 shows the variation of number of void with different size versus temperature. Figure 2 shows percent of void with different size versus temperature.

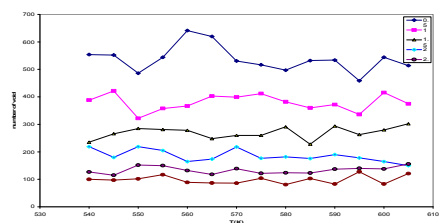


Fig.2. Number of void with different size verse Temperature

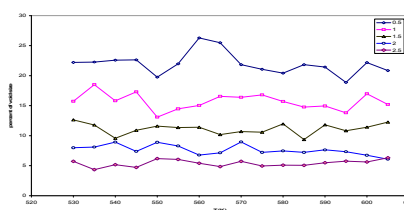


Fig.3. percent of void with different size verse Temperature

4. Conclusions

Circumsphere around each Voronoi vertices, which represent void between four atoms, can be used to characterize the behavior of the liquid cesium metal. In order structure like crystalline structure exit equal void when the temperature increases ,it becomes disorder and there is distribution of different void with different size. Therefore size of void can show change the structure and the phase transition.

References

- [1] N. N. Medvedev, Physica A 314 (2002) 678-685
- [2] G.L.Dirichlet, Z.Reine, Angew.Math.40 (1850).216
- [3] G.F.Voronoi, Z.Reine, Angew.Math. 134 (1908).198
- [4] A. Okabe, B. Boots, K. Sugihara, and S. N. Chiu, Spatial Tessellations: Concepts and Applications of Voronoi Diagrams _Wiley, Chichester,2000.
- [5] J.L.Finney, J.Wallace, J.Non-Cryst.Solids, 43(1981)165
- [6] F. Hensel H. Uchtmann Annu. Rev. Phys. Chem. 40 (1989) 61-68
- [7] F. Hensel Phil. Trans. Soc. Lond. A 356 (1998) 97-117.
- [8] M.H. Ghathe, M. bahadori, Fluid Phase Equilib. 233 (2005) 151-156.

**Thermodynamics of interactions between Vanadium(V) and sulfonatocalix[4]arene**

Karim Zare, Farrokh Gharib, Monire Hajmalek*

Department of Chemistry, Shahid Beheshti University, Tehran, Evin, Iran

(E-mail :monirehajmalek@yahoo.com)

Keywords: Parasulfonatocalix[4]arene, Dioxovanadium(V), formation constant**1. Introduction**

Calixarenes are a class of macrocycles, generally made up of phenol units linked via methylene bridges. During the last two decades, calixarenes have attracted much interest because of their unique molecular structure, and have been extensively investigated in various fields such as analytical, separation, and supramolecular chemistry [1]. A characteristic feature of the calixarenes is their insolubility in water and their low solubility in organic solvents. By introducing sulfonic acid groups at the *p*-position of the hydroxycalix[4]arenes, Shinkai *et al.* [2] first synthesized some water-soluble calix[4]-arenes.

In this work formation equilibrium constants and thermodynamic parameters (*i.e.*, ΔH and ΔS) for complexation Between dioxovanadium (VO_2^+) and *p*-sulfonatocalix[4]arenes in aqueous solution and in pH=2 have been determined by means of UV–VIS spectroscopy.

2. Experimental

Absorption spectra, 260–300 nm, were measured on Cecil UV-Vis scanning spectrophotometer with a Pentium IV computer using 10 mm quartz cells. 2.0 mL solution of the ligand, $0.0002 \text{ mol L}^{-1}$, were titrated with stepwise addition of an dioxovanadium solution. The UV-Vis spectra of the mixtures undergo small changes at 250–300 nm, but the measured absorbances were sufficient to allow the treatment of the data by the computer program.

3. Results and discussion

Assuming that the absorbance of each ligand would change upon complexation with a dioxovanadium(V) cation, we performed spectrophotometric measurements. The complex M_pL_q formed is characterized by its stoichiometry, *p* and *q*, where M and L represent a metal ion and a ligand, respectively. To determine the formation constant of complexation, K_s , Eq. 1 is defined,

$$pM + qL \rightleftharpoons M_pL_q \quad K_s = \frac{[M_pL_q]}{[M]^p [L]^q} \quad (1)$$

Absorbance, *A*, was measured by successive addition of a dioxovanadium ion solution to each ligand solution.

The absorption bands of the ligand increase upon addition of the metal ion solution in all cases.

Treatment of the spectrophotometric data (260–300 nm with an interval of 1 nm) obtained during the titrations was conducted with the computer program Squad [3,4]. Our results are consistent with the formation of 1:1 complexes.

Values of K_s were determined at least five different temperatures between 25 and 45 °C at pH = 2.00. From the linear plots of $\ln(K_s)$ vs. $1/T$, thermodynamic parameters (*i.e.*, enthalpy change, ΔH , and entropy change, ΔS) for the formation of complexes were calculated. The results show the inclusion complexations are driven by enthalpy ($\Delta H < 0$), accompanied by negative entropic changes ($\Delta S < 0$).

References

- [1] Ikeda and S. Shinkai, Chem. Rev., 1997, 97, 1713
- [2] S. Shinkai, K. Araki, H. Koreishi, T. Tsubaki and O. Manabe, Chem. Lett., 1986, 1351.
- [3] M. Meloun, M. Javůrek, J. Havel, Talanta 1986, 33, 513–524.
- [4] F. Gharib, M. Shakarami, S. Taghvaei-Ganjali. Acta Chim. Slov., 2008, 55, 570–574





DFT studies, NBO and NICS analysis of all chlorothiophenes and their cations as candidate monomers for new conductive polymers

H. Shirani^{a,b,*}, S. Jameh-Bozorgi^{a,b}

a. Chemistry Department, Faculty of science, Islamic Azad University, toyserkan branch, toyserkan, Iran

(E-mail: shiranihossein@gmail.com)

b. Chemistry Department, Faculty of science, Islamic Azad University, Arak Branch, Arak, Iran

Keywords: DFT-B3LYP, Dipole moment, Spin density, Chlorothiophenes, Conducting polymers

1. Introduction

Electrically conducting polymers as a new class of 'synthetic metals' reached a high interest in the last year[1]. Intrinsic conducting polymers with conjugated double bonds have attracted much attention as advanced materials. Conductive polymers have been used as biosensors, gas sensors, microactuators, data storage, polymer batteries, electronic devices, and functional membranes[3-7]. Furthermore, the electrochemical process parameters affecting the properties of polythiophenes (PTHs) coatings have also been investigated. PTH-based polymer blends can prevent the corrosion of metals[2]. The Several investigations have been performed to observe the effects of various parameters such as solvent, electrolyte, and monomer choices and polymerization temperature on the stability and conductivity of the synthesized PTH.

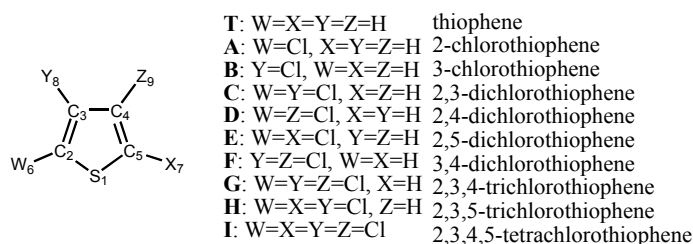


Fig.1. All possible mono-, di-, tri-, and tetrachlorothiophene isomers studied in this research

The aims of the present research are: (1) to study the electronic and structural properties of all chlorothiophene monomers (shown in Figure 1) and their singly ionized cations using ab initio and DFT-B3LYP methods and (2) to compare the calculated properties of these monomers and their cations.

2. Methods

Initially, structures of representative mono-, di-, tri-, and tetra-chlorothiophenes were fully optimized using Density Functional Theory (DFT) B3LYP method using the 6-311++G** basis set as implemented in the Gaussian 98 program package (G98W)[8]. The natures of the optimized stationary points were all characterized by frequency calculations at the same level of theory with the same basis set.

3. Results and discussion

To predict the bonding-characteristic behavior of the fluorothiophene rings in their corresponding polymer chains and to determine the extent of the π -conjugation character of these polymers, we have used the F_n coefficient for each thiophene ring in the isolated chlorothiophenes. The calculated values of the F_n coefficient for all chlorothiophenes and their cations shown that the molecule B have the smallest values of the F_n coefficient. Therefore, the quinoid character of monomer B is greater than that of other chlorothiophenes.

For all chlorothiophenes and their cations, the positive charge is distributed mainly on the C3 position in Figure1, whereas spin density is distributed mainly on the C5 position in Figure 1. In both series of molecules and their cation radicals, charge- and spin-density distributions have similar trends with the number and position of the substituted fluorine atoms. The analysis carried out on the calculated dipole moments shows that the size and direction of the dipole moment vector depend



mainly on the position (symmetry) of substituents rather than on the number of substituents. Furthermore, the orientation of the dipole moment vector is toward the sulfur atom for all chlorothiophenes. It can also be seen that the size of the dipole moment vector for monomer B is greater than all chlorothiophenes. It can be said that the electrochemical stability of monomer B is greater of all chlorothiophenes. The low-frequency values for all of the compounds are higher than for thiophene. Through mono-fluorine compounds, compound B has higher low-frequency values. This means that this compound has the largest force constants for their bending modes of vibration. Also HLG values for all of the chlorothiophenes is very good for transition band to conducting band. NICS results showed that compound B has the largest quantity of negative value therefore this compound has the largest electrical current and conductivity.

4. Conclusions

Chlorothiophenes have been designed as monomers for conductive polymers in the hope of having modified chemical and electrical properties. The primary advantage of the conductive polychlorothiophenes over their parent polymer, polythiophene, is their higher pyrolysis temperature, which decreases the risk of fire in the electronic/electrical devices made of these materials. Ab initio and density functional theory DFT-B3LYP/6-311++G** calculations have been carried out successfully to study the structural, electronic, electrochemical, and spectroscopic properties of all chlorothiophenes. Compared to thiophene, B monomer is more soluble in water and has a lower potential energy to form cations. These characteristics increase the efficiency of the electrochemical polymerization processes on this monomer.

References

- [1] A. J. Heeger, *J. Phys. Chem. B*, 105(36), (2001) 8475.
- [2] M. S. Ram, Srinivasan Palaniappan, *Journal of Molecular Catalysis A: Chemical* 201, (2003) 289.
- [3] Vidal, J. C.; Garcia, E.; Castillo, J. R. *Anal. Chim. Acta*, 385 (1999) 213.
- [4] Campbell, T. E.; Hodgson, A. J.; Wallace, G. G. *Electroanalysis*, 11, (1999) 215.
- [5] Kincal, D.; Kamer, A.; Chield, A. D.; Reynold, R. J. *Synth. Met.*, 92, (1998) 53.
- [6] Smela, E. J. *Micromech. Microeng.* 9, (1999) 1.
- [7] Skotheim, T. A., Elsenbaumer, R., Reynolds, J.; *Handbook of Conducting Polymers*; Marcel Dekker: New York, 1998.
- [8] Z. Chan, C. S. Wannere, C. Corminboeuf, R. Puchta, and P. V. R. Schlyere, *Chem. Rev.*, 105 (2005) 3842.



Thermodynamic modeling of methane hydrate formation conditions in aqueous solutions of methanol and NaCl, KCl and CaCl₂

S. Babaei and J. Javanmardi*

Department of Chemical Engineering, Shiraz University of Technology, Shiraz 7155713876, Iran

(E-mail: Javanmardi@sutech.ac.ir)

Keywords: Gas hydrates; Electrolyte solutions; Methanol; Binary interaction parameters

1. Introduction

Gas hydrates, are crystalline solids composed of water and some molecules of suitable size at appropriate conditions of temperature and pressure. These guest molecules are trapped in cavities of hydrogen-bonded water molecules. This crystalline compound may be found in oil and gas production, transportation and processing facilities and can cause serious economic, operational, and safety problems. Alcohols such as methanol and/or salt generally are used to inhibit formation of gas hydrates [1]. These inhibitors shift the three-phase equilibrium line to higher pressure and/or lower temperature conditions and used to reduce the risks associated with gas hydrate formation. There is, however, a need to develop a method to predict gas hydrate formation conditions in aqueous solutions containing electrolytes and methanol. Many researchers such as Javanmardi et al., 2001 [2], Nasrifar et al., 2001 [3], Masoudi et al. 2004 [4], Mohammadi et al., 2005 [5] represented different models to predict the hydrate formation conditions in the presence of electrolytes and alcohol.

The model of Masoudi et al. 2004 [4] can be is used for predicting the gas hydrate formation condition in the presence of ethylene glycol and salts. In this work, based on the model of Masoudi et al., 2004 [4], novel binary interaction parameters, BIPs, between NaCl-Methanol, KCl-Methanol and CaCl₂-Methanol have been estimated. In the original work, the BIPs of ethylene glycol and these salts have been reported. Finally, the predicted hydrate formation conditions in the presence of these inhibitors are compared with the available experimental data and a good agreement is observed.

2. Thermodynamic modeling

The hydrate formation conditions have been estimated using the solid solution theory of van der Waals and Platteeuw [6]. The potential functions of hydrate formers have been represented using the Kihara [7] model for spherical molecules. The Valderrama modification of the Patel and Teja equation of state, VPT EoS, [8] has been used to predict the fugacities of hydrate formers and inhibitors in liquid and vapor phases. For polar-nonpolar and polar-polar interaction, the classical mixing rules are not satisfactory and more complicated mixing rules are necessary. The non-density dependent mixing rules, NDD, developed by Avlonitis et al. (1994) [9], can be applied to describe the polar-non polar and polar-polar interaction in the attraction parameter, a . Masoudi et al., 2004 [4], considered each salt as a pseudo component. Based on this assumption, the values of T_c , P_c , Z_c and ω for each salt have been obtained from the literature, [4], [10]. The experimental data for the boiling point and the salt solubility of aqueous methanol-salt solutions, i.e. NaCl, KCl, and CaCl₂, have been used to obtain the parameters I_{pi}^0 , I_{pi}^1 and k_{ij} in the NDD mixing rules. Where, I_{pi}^0 , I_{pi}^1 are the BIPs between the polar component and other components, and k_{ij} is the classical BIP. To predict the solubility of salts in aqueous alcohol and electrolyte solutions, the model of Masoudi et al. 2004 [4] has been used. This model is based on equality of fugacity of salt in the liquid and solid phases.

3. Results and discussion

To obtain the optimized values of BIPs, I_{pi}^0 , I_{pi}^1 and k_{ij} the experimental boiling point and salt solubility data have been used Table 1 shows the optimized BIPs between methanol and NaCl, KCl and CaCl₂. Figures 1 through 3 show the experimental and predicted methane hydrate dissociation conditions for aqueous solutions of methanol and NaCl, KCl and CaCl₂, respectively. As shown in theses figures, a good agreement between model predictions and experimental data is observed.

Table 1. The BIPs between methanol and NaCl, KCl and CaCl₂.

System	k_{ij}	k_{ji}	I_{ij}^0	I_{ji}^0	I_{ij}^1	I_{ji}^1
Methanol(i)-NaCl(j)	-0.04271	-0.12059	0.03307	0.50925	-0.00118	0.00155
Methanol(i)-KCl(j)	-0.02979	0.03753	0.00479	-0.03453	0.00003	0.01894
Methanol(i)-CaCl ₂ (j)	-2.11168	-1.97546	-3.30900	-2.60311	-0.10198	-0.26949

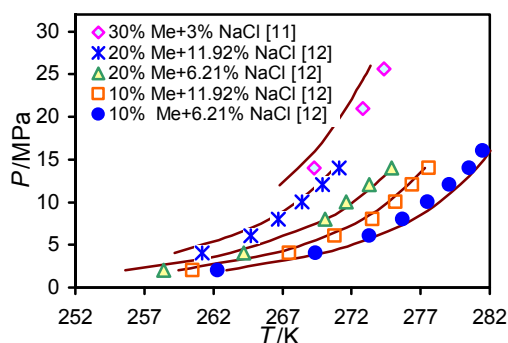


Fig. 1. Predicted and experimental methane hydrate dissociation conditions in the presence of methanol and NaCl, concentration in mass %, AAD%*=0.27.

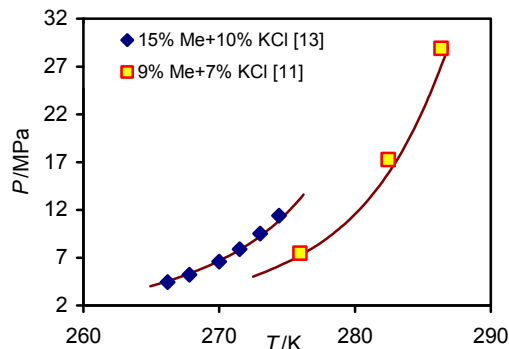


Fig. 2. Predicted and experimental methane hydrate dissociation conditions in the presence of methanol and KCl, concentration in mass %, AAD%*=0.05.

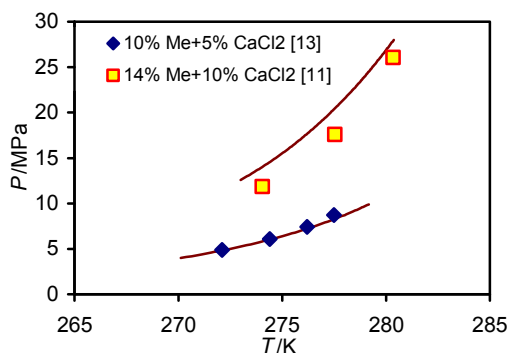


Fig. 3. Predicted and experimental methane hydrate dissociation conditions in the presence of methanol and

CaCl₂, concentration in mass %, AAD%*=0.24. * $AAD\% = \frac{1}{NP} \sum_{i=1}^{NP} \left| \frac{T_{exp} - T_{cal}}{T_{exp}} \right| \times 100$

4. Conclusions

The model of Masoudi et al., 2004 [4], have been extended for prediction of methane hydrate formation temperature in the presence of methanol and common salts, i.e., NaCl, KCl and CaCl₂. The vapor pressure and salt solubility experimental data for the aqueous solutions of methanol+salts have been used to optimize the BIPs between methanol and salts. The predicted hydrate formation conditions in the presence of these inhibitors are compared with the available experimental data and a good agreement is observed.

References

- [1] E.D. Sloan, Clathrate Hydrates of Natural Gases, Marcel Dekker, New York, 1998.
- [2] J. Javanmardi, M. Moshfeghian, R.N. Maddox, Can. J. Chem. Eng. 79 (2001) 367–373.
- [3] K. Nasrifar, M. Moshfeghian, J. Chem. Thermodyn. 33 (2001) 999–1014.
- [4] R. Masoudi, B. Tohidi, Ross Anderson, Rod W. Burgass and Jinhai Yang, Fluid Phase Equilibria 219 (2004) 157–163.
- [5] A. H. Mohammadi and B. Tohidi, Can. J. Chem. Eng. 83 (2005) 865–871.
- [6] J.H. Van der Waals, J.C. Platteeuw, Adv. Chem. Phys. 2 (1959) 1–57.
- [7] T. Kihara, Rev. Mod. Phys. 25 (4) (1953) 831–843.
- [8] J.O. Valderrama, J. Chem. Eng. Jpn. 23 (1) (1990) 87–91.
- [9] D. Avlonitis, A. Danesh, A.C. Todd, Fluid Phase Equilib. 94 (1994) 181–216.
- [10] R. Masoudi, B. Tohidi, A. Danesh, A.C. Todd, R. Anderson, R. W. Burgass, Chemical Engineering Science, 60 (2005) 4213.
- [11] H. Najibi, A. Chapoy, H. Haghighi, B. Tohidi, Fluid Phase Equilibria 275 (2009) 127.
- [12] M.D. Jager, C.J. Peters, E.D. Sloan, Fluid Phase Equilib. 193 (2002) 17–28.
- [13] A. H. Mohammadi, D. Richon, J. Chem. Thermodynamics 41 (2009) 1374–1377.



Volumetric study on the interactions of Schiff base ligand (salen) with 1-Penthyl-3-methylimidazolium bromide ([PnMIm]Br) in DMF (n,n-Dimethyl formide) at T = (298.15 K and 308.15 K)

H. Shekaari^a, A. Bezaatpour^b, A. Soltanpour^{c,*}

Department of Chemistry, University of Mohaghegh Ardabili, Ardabil, Iran

(E-mail: hemayatt@yahoo.com)

(E-mail: a_bezaatpour@yahoo.com)

(E-mail: Ayyob30Soltanpour@yahoo.com)

Keywords: ionic liquid, Schiff base ligand, limiting apparent molar volume, density.

1. Introduction

Schiff bases, or imines, which $R_2C=NR$ are the condensation products of aldehydes and ketones reacting with primary amines have been used extensively in the preparation of metal complexes [1-3]. Salen-type ligands are amongst the amongst oldest ligands in coordination chemistry and have received considerable interest Jacobsen and Katsuki first reported their significant success using chiral manganese (III) salen Schiff base catalysts in the asymmetric epoxidation of unfunctionalised olefins [4]. Room temperature ionic liquids (RTILs) are a class of organic salts that at or near room temperature in their pure state. They exhibit many interesting properties such as negligible vapor Pressure, low melting point ($T < 373$ K) a wide liquid range, suitable viscosity, stability up to high solubility for both polar and non-polar organic and inorganic substances [6]. Studies of volumetric properties of mixtures have a double objective. Firstly, they supply solution density data which are required in mass balance and mass transfer calculations. Secondly, they are a useful too to clearly separate the nature of interactions among RTILs, their ions and solvent molecules [5]. In this present study, experiments have been performed to measure the density, in (salen + 1-penthyl-3-methylimidazolium bromide ([PnMIm]Br) + DMF) systems. Apparent molar volume, V_ϕ , limiting apparent molar volume, V_ϕ^∞ , have been computed from the experimental density, ρ , data.

2. Methods

2.1. Synthesis of Schiff base ligand (salen) and ionic liquid

To a vigorously stirred ethanolic solution (70 mL) of 2-hydroxybenzaldehyde (200mmol) was added dropwise a solution of ethylene diamine (100mmol) in 70 mL of ethanol. After the addition was complete, the mixture was stirred and refluxed for 60 minutes. The mixture was then cooled and the yellow crystal of the ligand was collected by filtration, then washed with ethanol and dried in a dessicator. 19.56g (%73). Anal. Calcd for $C_{16}H_{16}N_2O_2$: 1H NMR (500MHz, $(CD_3)_2SO$): 12.8 (s, 2H, OH), 8.3 (s, 2H, Ar-CH=N), 6.7-7.3 (m, 8H, Ar), 3.9 (s, 4H, Alkane). The ionic liquids, 1-penthyl-3-methylimidazolium bromide was prepared and purified by using the procedure described in the literature [2].

2.2. Apparatus

The densities of the solutions were measured using a vibrating tube densimeter DMA, 4500 M (Anton Paar). The apparatus was calibrated with doubly distilled deionized and degassed water, and dry air at atmospheric pressure.

3. Results and discussion

The experimental density, ρ values as function of salen concentration, m , were measured. The apparent molar volumes V_ϕ were calculated from the densities of the (salen + [PnMIm]Br + DMF) solutions using the following expression:

$$V_\phi = \frac{M}{\rho - (\rho - \rho_0)} / m \rho \rho_0 \quad (1)$$

Where V_ϕ is the apparent molar volume, M is the molar mass of the salen, ρ and ρ_0 , respectively are the densities of the (salen + [PnMIm]Br) + DMF ternary systems and solvent, ([PnMIm]Br + DMF). Fig 1 shows the molal concentration dependence of V_ϕ values for salen in DMF and (0.000, 0.1005, 0.1508, and 0.1989) mol. kg^{-1} ([PnMIm]Br + DMF) solutions at 298.15 K and 308.15 K. The V_ϕ values data for the salen were found to be adequately presented by the linear equation:

$$V_\phi = V_\phi^\infty + S_s \cdot m \quad (2)$$

where V_ϕ^∞ is the apparent molar volume at infinite dilution and S_s is the experimental slope. in table 1 shows that V_ϕ^∞ and S_s values. V_ϕ^∞ indicates interaction of solvent-solute and S_s indicates interaction of solute-solute.



4. Conclusions

In this work, the effect of IL on the volumetric property of solute-solvent has been investigated. densities data for the (salen + ([PnMIm]Br) + DMF) and (salen + DMF), systems were determined at $T = 298.15$ K and 308.15 K. this table 1 shows that the V_{ϕ}^0 values of salen decrease with an increase in the concentration of non- aqueous ([PnMIm]Br), This is possible due to stronger polar- polar interactions between DMF and ([PnMIm]Br). but increase with increasing of temperatures.

Table 1. The V_{ϕ}^0 values of salen, in non-aqueous [PnMIm]Br solutions at $T = 298.15$ K and 308.18 K

$m_{\text{IL}} / (\text{mol} \cdot \text{kg}^{-1})$	$T = 298.15$ K		$T = 308.15$ K	
	$10^6 \cdot V_{\phi}^0 / \text{m}^3 \cdot \text{mol}$	$S_V / \text{m}^3 \cdot \text{mol}^{-2} \cdot \text{kg}$	$10^6 \cdot V_{\phi}^0 / \text{m}^3 \cdot \text{mol}$	$S_V / \text{m}^3 \cdot \text{mol}^{-2} \cdot \text{kg}$
0.0000	231.76 ± 0.11	-8.1314 ± 0.3115	232.43 ± 0.12	-5.0277 ± 0.3447
0.1005	231.52 ± 0.08	-6.6750 ± 0.2190	232.27 ± 0.07	-4.0720 ± 0.1810
0.1508	231.34 ± 0.10	-6.4780 ± 0.2860	231.92 ± 0.15	-2.8000 ± 0.4020
0.1989	231.05 ± 0.07	-5.9630 ± 0.2161	231.73 ± 0.07	-2.5780 ± 0.0620

m_{IL} shows that the molality of [PnMIm]Br

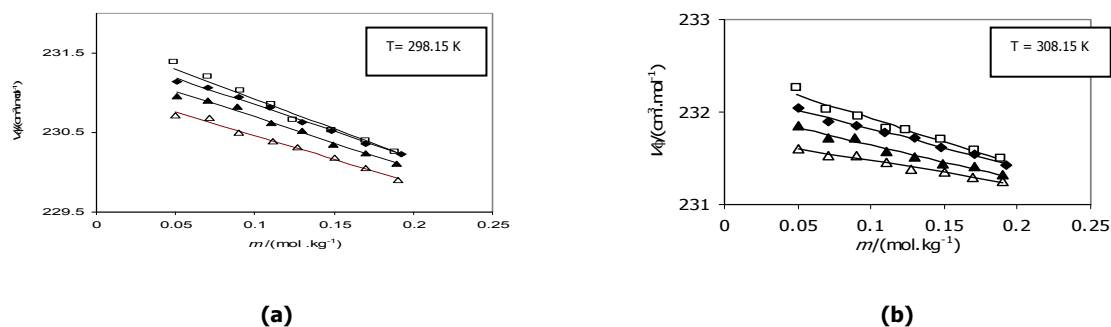


Fig. 1. Apparent molar volumes of salen in ([PnMIm]Br + DMF) system with different concentrations of ([PnMIm]Br): \square , 0.000; \diamond , 0.1005; \blacktriangle , 0.1508; \triangle , 0.1989 at (a) $T = 298.15$ K and (b) $T = 308.15$ K

References

- [1] Gakias, S. Rix, C. Fowlessa, A. Wills-Johnson, G. Latham, K. White, J. J. Mol. Struct. 737 (2005) 69–74
- [2] Yang, J. Z., Tong, J., Li, J.-B., J. Solution Chem, 36 (2007) 573 – 582.
- [3] Holm, R. H. Everett Jr, G. W. Chakravorty, A. Prog. Inorg. Chem. 7 (1966) 83.
- [4] Ambroziak, K. Szypa, M. Tetrahedron Lett 48 (2007) 3331-3335
- [5] A. Vicent Orchilles, V. Gonzalez-Alfaro, Pablo J. Migul, E. Vercher, A. Martinez- Andreu, J. chem. Thermodyn. 38 (2006) 1124-1129.
- [6] Zafarani-moattar, M. T. Shekaari, H. J. Chem. Thermodyn. 38 (2006) 624-633.



Vapor–Liquid equilibria, density and speed of sound of aqueous di-sodium hydrogen citrate solutions at different temperatures

M.T. Zafarani-Moattar, N. Karimi

a. Department of Chemistry, University of Tabriz, Tabriz, Iran

(E-mail: na_karimi88@yahoo.com)

Keywords: isopiestic, density, speed of sound, water activity

1. Introduction: The vapor–liquid equilibria, density, and speed of sound of aqueous di-sodium hydrogen citrate solution at different temperatures have been measured. From the measurements of water activity by isopiestic method, values of the vapor pressure of solutions were determined. The experimental vapor–liquid equilibria data were correlated with the Pitzer equation.

The experimental density and speed of sound data for di-sodium hydrogen citrate were used to obtain apparent molar volume values at different temperatures, and these data were satisfactorily fitted to the corresponding Pitzer equations.

Citrate ions in aqueous solutions are of considerable significance in many chemical processes. However, with respect to other thermodynamic or transport properties of citrate salts, little information can be found in the literature. In this work, vapor–liquid equilibria, density, and speed of sound measurements were performed from dilute up to near saturation, and to calculate accurate limiting apparent volumes and compressibilities, enough data were obtained in the dilute region (below 0.1 mol · kg⁻¹) at different temperatures. [1]

2. Methods

In this study, the isopiestic method is used to obtain the activity of water and the osmotic coefficient in an aqueous di-sodium hydrogen citrate system at $T = (298.15, 308.15, \text{ and } 318.15) \text{ K}$. The isopiestic apparatus used in this work was similar to the one used by Ochs et al [2]. This apparatus consisted of a five-leg manifold attached to round-bottom flasks. Two flasks contained the standard pure NaCl solutions; two flasks contained di-sodium hydrogen citrate solutions; and the central flask was used as a water reservoir. The apparatus was kept in a constant temperature bath for at least 120 h to achieve equilibrium. The temperature was controlled to within $\pm 0.005 \text{ K}$ by a Heto temperature controller (Heto PF, Heto Laboratory Equipment, Denmark). After equilibrium, the manifold assembly was removed from the bath, and each flask was weighed by an analytical balance (Shimadzu, 321-34553, Shimadzu Co., Japan) with an uncertainty of $\pm 1 \cdot 10^{-7} \text{ kg}$. From the weight of each flask and the initial weight of salt, the mass fraction of each solution was calculated. The water activity for the standard aqueous NaCl solutions at different concentrations and temperatures has been calculated from the correlation of Colin et al [3]. The uncertainty in the measurement of water activity was estimated to be ± 0.0002 . Densities and speed of sounds were measured with a vibrating-tube densimeter (Antoine Parr DSA-500, Austria). The apparatus was calibrated at each temperature with double-distilled–deionized water and dry air. The apparatus was also tested with the density of a known molality of aqueous NaCl using the data given by Pitzer et al [4].

3. Results and discussion

Isopiestic equilibrium molalities with reference standard solutions of NaCl in water enabled the calculation of the osmotic coefficient, Φ , of the solutions of di-sodiumhydrogen citrate in water from

$$\varphi = \frac{\nu^* \varphi^* m^*}{\nu m_1} \quad (1)$$

where ν^* and ν are the sum of stoichiometric numbers of the anion and cation in the reference solution and the solution of d, respectively; m_1 is the molality of the di-sodiumhydrogen citrate solution; m^* is the molality of the reference standard in isopiestic equilibrium with this solution; and φ^* is the osmotic coefficient of the isopiestic reference standard, calculated at m^* .

The necessary φ^* values at any m^* at different temperatures were calculated from the correlation given by Colin et al [3]. From the calculated

$$\varphi = - \frac{\ln a_2}{\nu m_1 M_2} \quad (2)$$



$$\ln a_s = \ln \left(\frac{p}{p^*} \right) + \frac{(B - V_s^*)(p - p^*)}{RT} \quad (3)$$

Where a_s is the activity of water; M_2 is the molar mass of the water; and B is the second virial coefficient of water vapor. V_s^* is the molar volume, and p^* is the vapor pressure of pure water. The second virial coefficients of water vapor at each working temperature were calculated using the equation provided by Rard and Platford [5]. Molar volumes of liquid water were calculated using the density of water at different temperatures [6]. The vapor pressures of pure water were calculated using the equation of state of Saul and Wagner[7]. After the establishment of isopiestic equilibrium, water activities were calculated using eq 2.

Volumetric and Isentropic Compressibility Results. The molar volumes V_ϕ of aqueous di-sodium hydrogen citrate solutions were calculated from the densities of the solutions d using the following equation

$$V_\phi = \frac{M_1}{d} - \frac{(d - d_0)}{m_1 d d_0} \quad (4)$$

where M_1 is the molar mass of di-sodium hydrogen citrate salt.

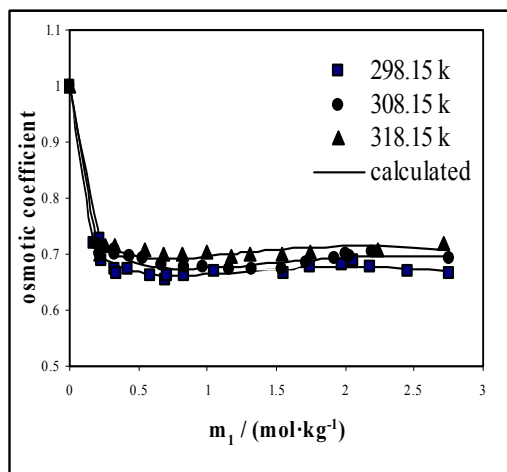


Figure 1. Experimental and calculated osmotic coefficient, plotted against molality of salt, m_1 , for the sodium citrate (1) + H₂O (2) system studied with the Pitzer model.

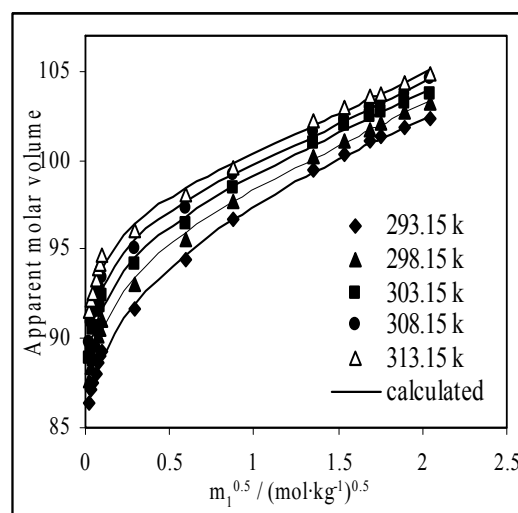


Figure 2. Experimental and calculated apparent molar volume, plotted against root of molality of salt, for the sodium citrate+H₂O (2) System studied with the Pitzer model.

4. Conclusions

The accurate osmotic coefficient data measured at $T = (298.15, 308.15,$ and $318.15)$ K for aqueous di-sodium hydrogen citrate solutions were fitted satisfactorily to The apparent molar volumes and apparent molar compressibilities were calculated from the measured density and speed of sound data at $T = (293.15, 298.15, 303.15, 308.15$ and $313.15)$ K, and these data were also fitted to the corresponding Pitzer equation with good accuracy.

References

- [1] Zafarani-Moattar, M.T. Asadzade, B. J.chem.Eng.Data 53(2008) 1000
- [2] Ochs, L. R. Kabiri-Badr, M. Cabezas, H. AIChE J. 36 (1990) 1908.
- [3] Colin, E. Clarke, W. Glew, D. N. J. Phys. Chem. Ref. Data. 14 (1985) 489.
- [4] Pitzer, K. S. Peiper, J. C. Busey, R. H. J. Phys. Chem. Ref. Data. 13 (1984) 1.
- [5] Rard, J. A. Platford, R. F. Pitzer, K. S. ActaVity coefficients in electrolyte solutions. (1991) 209.
- [6] Kell, G. S. J. Chem. Eng. Data. 20 (1975) 97.
- [7] Saul, A. Wagner, W. J. Phys. Chem. Ref. Data. 16 (1987) 893.



Isotherm, kinetic and thermodynamic study of methylene blue dye adsorption in aqueous solution by leaves of data palm

Farbod Fakhari , Nader Bahramifar, Ferydoon Ashrafi

Department of chemistry, Payame Noor university (PNU) of sari unit, Mazandaran, Iran

(E-mail: farbod.fakhari@yahoo.com)

Keywords: Adsorption, Basic dye, Isotherm, Kinetics, Methylene blue

1. Introduction

Several biological, physical and chemical methods have been used for the treatment of industrial textile wastewater including microbial biodegradation, membrane filtration, oxidation and ozonation [1]. However, many of these technologies are cost prohibitive, especially when applied for treating large waste streams. Consequently, adsorption techniques seem to have the most potential for future use in industrial wastewater treatment [2,3]. Because of their proven efficiency in the removal of organic and mineral pollutants and for economic considerations [4,6]. The most widely used adsorbent for this purpose is activated carbon, but its overlying cost has led to search for cheaper alternative materials such as orange and banana peels papaya seeds ulva lactuca and jackfruit peel. Methylene blue (MB, chemical formula: $C_{16}H_{18}N_3SCl$; FW: 319.86 g/mol, λ_{max} : 662 nm, class: thiazine) is the important basic dye . It is a dark green powder or crystalline solid. It is widely used as a stain and has number of biological uses. The adsorbate MB was chosen as a model dye because of its well- known adsorption characteristics. MB is not regarded as acutely toxic, but it can have various harmful effects. MB is a known teratogen that results in intestinal atresia when injected intra-amniotically. MB may also result in hemolytic anemia, hyperbilirubinemia, and acute renal failure [7]. The main focus of this study was to evaluate the adsorption capacity of the highly available, low cost and renewable for the removal of (MB) as a model compound for basic dyes. The effects of contact time, pH, initial dye concentration and sorbent amount on the sorption behavior were investigated. Also, we studied the efficacy of adsorption of water – soluble model basic dye, MB, by leaves of data palm and the chemophysical nature of adsorption to gather more information on the interaction of leaves of data palm and basic dye. In the present study a new adsorbent was investigated for its adsorption potential.

2. Materials and method

2.1. Preparation of adsorbent

The leaves of data palm that used in this study was ground and sieved to obtain a particle size range of 0.5-1.0 mm and repeatedly boiled with water until the filtered water was cleared. Then it was oven dried at 60°C for 24h. The dried sample stored in plastic bottle for further use. No other chemical or physical treatment was used prior to adsorption experiments.

2.2. Sorption experiment

Adsorption experiment was carried out by adding a fixed amount of sorbent (3g/l) into 250ml Erlenmeyers flask containing a definite volume (150ml) of initial concentration (100 mg/l) of dye solution at temperature of 22°C. The pH of dye solution adjusted to 7.0. The effect of pH on the absorption rate was investigated in the pH range of 4-12. The pH values were adjusted with diluted HCl and NaOH. The flask stirred with the aid of stirrer at 600 rpm for 180 min to ensure equilibrium was reached. Samples (5ml) were removed from experimental flask at times $t=0, 5, 10, 15, 30, 60, 90, 120$ and 180 min. Then the sorbent dosage was separated by filtration through 0.45 μ m microfilter. The concentration of dye in the filtered solution was determined using UV-Vis spectrophotometer (GBC- Cintra 20) at 663 nm and the amount of adsorbed material was calculated.

3. Results and discussion

In the present investigation it has been clearly shown that leaves of data palm could be effectively used as a low cost adsorbent for the removal of MB from aqueous effluents. The results showed that optimum initial pH for MB was determined at pH = 7.0. The minimum sorbent concentration experimentally found to be sufficient to reach the removal of the dye molecules from aqueous solution, was 3 g/l (95.5 %).

Equilibrium data commonly known as adsorption isotherms are basic requirements for the design of adsorption systems. Langmuir and Freundlich isotherms were used to describe the equilibrium. The results obtained show that the equilibrium data were best described by the Freundlich model (Fig.1). Kinetic data were tested using the pseudo – first – order and pseudo – second – order kinetic models. The kinetics of the adsorption process was found to follow the pseudo – second- order Kinetic model, suggesting that the adsorption process was controlled by chemisorptions (Fig.2). Thermodynamic parameters such as ΔH° , ΔG° and ΔS° estimated by using equilibrium constants changing with temperature (Fig.3). The positive value of ΔH° suggested the endothermic nature of adsorption. This is also supported by the increase in value of uptake capacity of sorbent with the rise of temperature. The positive value of ΔS° reflects the affinity of MB and shows the increasing randomness at solid/liquid interface during the sorption of MB on selected sorbent, and negative value of ΔG° confirms the feasibility of the process and spontaneous nature of adsorption.

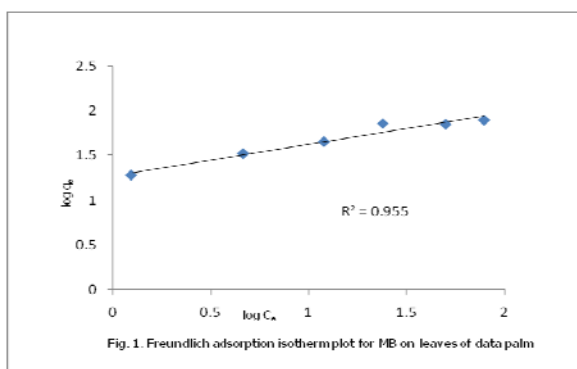


Fig. 1. Freundlich adsorption isotherm plot for MB on leaves of data palm

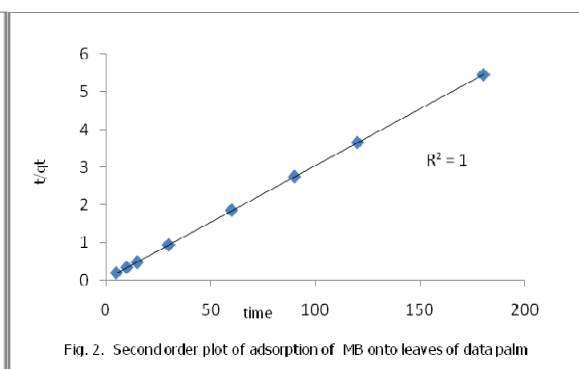


Fig. 2. Second order plot of adsorption of MB onto leaves of data palm

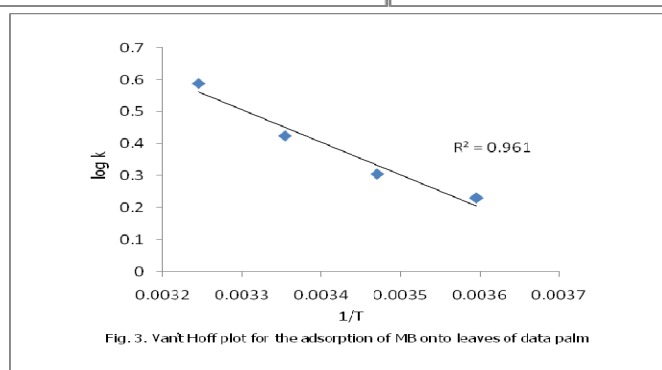


Fig. 3. Van't Hoff plot for the adsorption of MB onto leaves of data palm

4. Conclusions

In the present investigation it has been clearly shown that leaves of data palm powder could be effectively used as a low cost adsorbent for the removal dyes from aqueous effluents. The amount of dye adsorbed was found to vary with initial solution pH, initial dye concentration, contact time and adsorbent dose. The equilibrium data was very well-fitted in a Freundlich isotherm equation. The adsorption kinetic followed the pseudo-second order kinetic model. The process is endothermic and spontaneous in nature.

References

- [1] E. Forgacs, T. Cserhatia, G. Oros, *Environ. Int.* 30 (2004) 953–971.
- [2] M. Aliabadi, K. Morshedzadeh, H. Soheyli, *Int. J. Environ. Sci. Technol.* 3 (2006) 321–325.
- [3] S. Babel, M.E. Opiso, *Int. J. Environ. Sci.*
- [4] V.K. Garg, R. Gupta, A.B. Yadav, R. Kumar, *Bioresour. Technol.* 89 (2003) 121–124.
- [5] M. Taghi, M. Khosravi, R. Rakhshae, *Int. J. Environ. Sci. Technol.* 1 (2005) 265–271.
- [6] N.T. Abdel-Ghani, M. Hefny, G.A. El-Chaghaby, *Int. J. Environ. Sci. Technol.* 4 (2006) 67–73.
- [7] V. Ponnusami, S. Vikram, S.N. Srivastava, *J. Hazard. Mater.* 152 (1) (2008) 276–286.



The competitive interaction studies between aspirin and tamoxifen with human serum albumin by nano-fluorescence spectroscopic

S. Pourgonabadi^{1*}, M.R. Saberi², J. Chamani¹

¹Department of Biology, Faculty of Sciences, Islamic Azad University-Mashhad Branch, Mashhad, Iran,
sanaz.pourgonabadi@gmail.com, Tel: + 98511 8828447, +989155171554

²Medical Chemistry Division, School of Pharmacy, University Complex, Mashhad, Iran

Keywords: HSA, Tamoxifen, Aspirin, Ternary system, Nano-fluorescence spectroscopy

Introduction

Human serum albumin is a principal extra cellular protein with a high concentration in blood plasma. it is a globular protein. HSA contains 585 amino acids with 17 tyrosyl residues and one tryptophan [1]. ASA, also known as acetyl salicylic acid, is a salicylate drug, often used as an analgesic to relieve minor aches and pains [2]. Tamoxifen is a drug that interferes with the activity of estrogen, a female hormone. Tamoxifen has been used for more than 30 years to treat breast cancer in women and men [3].

Materials and methods

HSA, aspirin and tamoxifen were purchased from sigma. The solution HSA 0.03 % were prepared at room temperature and 50 mM phosphate buffer at pH 7.4. The final concentration of aspirin and tamoxifen was: 5×10^{-8} M and 5×10^{-7} M, respectively. Nano-fluorescence measurement was performed with a Hitachi spectrofluorometer model F-2500. The Nano-fluorescence emission spectra were recorded in the wavelength range of 300–600 nm with exciting wavelength at 280 nm.

Results and discussion

When a fixed concentration of HSA was titrated with different amounts of tamoxifen and aspirin, there was a slight blue shift at the maximum wavelength of HSA Nano-fluorescence emission when the solution of tamoxifen and aspirin were added. This suggests that the chromophore of protein was placed in a more hydrophobic environment after addition of TMX and ASA [4]. TMX–HSA and ASA–HSA interaction: study of the binary system. The original Stern-Volmer equation allows us to describe ligand movement within the fluorophore micro-environment when dynamic quenching occurs. $F_0/F = 1 + K_{sv}[Q]$ Where F and F_0 – fluorescence intensities of protein in the absence and presence of quencher, respectively. K_{sv} is the Stern-Volmer quenching constant (M^{-1}) and [Q] is the concentration of quencher Unmodified Stern-Volmer plot [Eq.(1)] is characteristic for the behavior of TMX and ASA molecules on interacting with HSA molecules on interacting with HSA fluorescence (see Fig. 2).

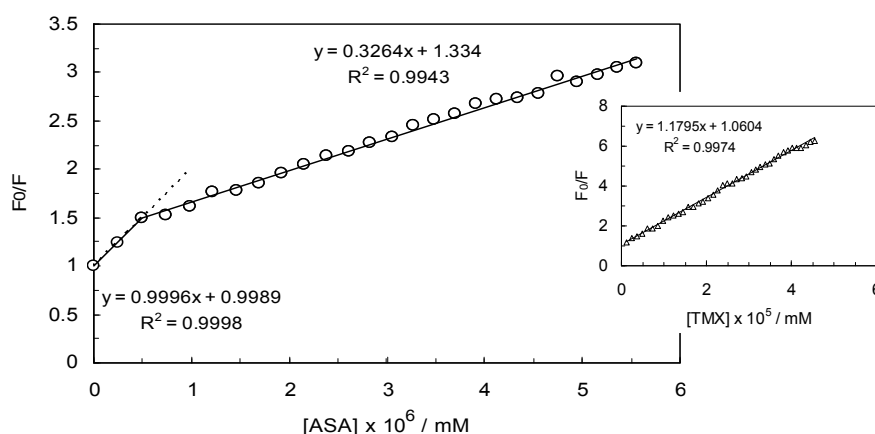


Fig.1: Stern-Volmer plot for the HSA-ASA, (pH 7.4, 50 mM phosphate buffer, $\lambda_{ex} = 280$ nm). Insret: Stern-Volmer plot for the HSA-TMX at the same condition.

Aspirin has two classes of binding sites in HSA, for the first class of binding sites K_{sv} values $0.99 \times 10^9 M^{-1}$ and for the second class of binding sites K_{sv} values $0.32 \times 10^9 M^{-1}$. The mean number of A.S.A molecules bound to one molecule of albumin in the given class of binding sites (n) is 1.06 for the first and 0.7 for the second binding site in HSA. For TMX in HSA $n = 1.04$ was found therefore TMX has one class of binding site in HSA and K_{sv} values $1.18 \times 10^8 M^{-1}$. The second class of ASA binding site is characterized by a much lower K_{sv} . In order to find out the changes in the nano-fluorescence of human serum albumin bound with a drug in the presence of another drug. The quenching of HSA fluorescence by ASA and TMX, in the presence of constant

concentration of TMX. This may suggest that in the presence of another ligand the structure of albumin changes. Therefore the analysis of the K_{SV} , n is necessary for the formulation of drugs. It was found that the presence of A.S.A changes the number of classes of TMX binding sites in the structure of HSA. TMX has one class of binding site in HSA while in the presence of ASA it has two classes binding sites. There are two classes of binding sites for A.S.A in HSA structure (Fig. 1) and the presence of TMX doesn't change this number (Fig. 2)

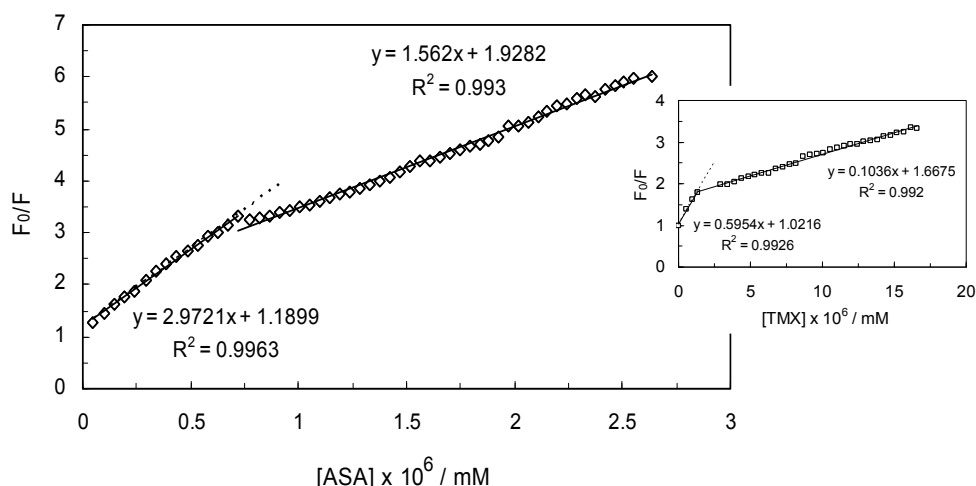


Fig.2. Stern-Volmer plot [HSA-TMX]-ASA. , (pH 7.4, 50 mM phosphate buffer, $\lambda_{exc} = 280$ nm). Inset: Stern-Volmer plot [HSA-ASA]- TMX at the same condition.

The values K_{sv} and the mean number of drug molecules bound to protein in the binding site "n" for TMX-HSA system in the presence of ASA and ASA-HSA in the presence of TMX are given in Table 1.

	K_{SV1}	n_1	K_{SV2}	n_2
[HSA-TMX]-A.S.A (TMX-constant)	$2.97 \times 10^9 \text{ M}^{-1}$	0.79	$1.56 \times 10^9 \text{ M}^{-1}$	0.79
[HSA-A.S.A]-TMX (A.S.A-constant)	$0.59 \times 10^9 \text{ M}^{-1}$	0.84	$0.10 \times 10^9 \text{ M}^{-1}$	0.54

Conclusion

Here we studied the comparison between binary and ternary systems in aspirin and tamoxifen upon interaction with HSA. We demonstrated that in the presence of aspirin, the binding affinity of tamoxifen to HSA decreased. On the other hand, in the presence of tamoxifen, the binding affinity of aspirin to HSA has not been changed, therefore there is not different between binary and ternary systems in the presence of tamoxifen. Meanwhile in the presence of aspirin, the interaction between HSA and tamoxifen has been shown two set of binding sites, however the tertiary structure of HSA change with interaction of aspirin.

References

- [1] M. Maciazek-Jurczyk, A. Sulkowska, B. Biojko, J. Rownicka, W.W. Sulkowski, J. Mol. Struct.,(2009).in press
- [2] U. Pflügers, Arch. Eur. J. Physiol., 84 (1991) 527-546
- [3] Fisher B, Costantino JP, Wickerham DL, et al. J. National Cancer Institute 90 (1998) 1371–1388.
- [4]Guowen Zhang , Qingmin Que, Junhui Pan, Jinbao Guo, J. Mol. Struct. 881 (2008)132-138



**Prediction of the activity coefficients for aqueous uni-univalent electrolytes
by artificial neural network**

Faezeh Nami , Farzad Deyhimi

Department of Chemistry, University of Shahid Beheshti, 19835-Tehran ,Iran

(E-mail: F_Nami@sbu.ac.ir)

Keywords: Electrolyte Solutions, Activity Coefficient, Uni-univalent Electrolytes, Artificial Neural Network

1. Introduction

Accurate prediction of the thermodynamic properties of aqueous electrolyte solutions is of interest in many industrial and natural processes [1,2]. In this context, mean activity coefficient, known as a key thermodynamic parameter, expresses the non-ideal behavior of electrolyte solutions and permit also the calculation of other thermodynamic properties. Besides, water is the most prevalent solvent in industrial, biological, geological and environmental electrolyte systems; therefore, the determination of mean activity coefficients in such concentrated aqueous electrolyte systems is of great interest. In the last few decades, various models such as Bromley, Pitzer, NRTL MSA, and SAFT models, etc, have been developed for describing the properties of electrolyte systems [3-4]. On the other hand, the statistical predictive models were found to be useful, economical and time saving tools for modeling many processes. In this context, ANN was successfully used to predict many thermodynamic properties [5-8]. In this work an ANN model is developed to predict the mean activity coefficient values for uni-univalent aqueous electrolyte solutions (up to 6 mol.kg⁻¹).

2. Artificial neural network model

Artificial neural network (ANN) is a powerful statistical tool for modeling highly complex and nonlinear processes. Briefly, an artificial neural network is defined based on a collection of neurons. The connections between neurons are realized by a set of connecting links, each characterized by a weight. Inputs multiplied by the connection weights are first summed (combined) and then passed through a transfer function to produce the output for that neuron [9], as described by the following relation

$$y = \phi(\sum_{j=1} w_{jk} x_j + b) \quad (1)$$

where ϕ is the transfer function, w the connection weights, b the bias, x and y are the input and output of artificial neuron, respectively. Sigmoid type function is the most widely used transfer function which squashes the output value of the neurons between 0 and 1 as given by Eq. (2)

$$\phi = \frac{1}{1 + \exp(-u)} \quad (2)$$

where u is a function (linear combiner) which computes the weighted sum of the inputs.

3. Results and discussion

The objective of this study is to develop an artificial neural network model to predict mean activity coefficients for concentrated uni-univalent aqueous electrolyte solutions. The first step in the design of a neural network is the selection of appropriate inputs. The selected inputs must theoretically have a relation to outputs. Electrolyte concentration, cation and anion radii are the influential parameters on estimation of activity coefficients of electrolyte solutions, so electrolyte molalities (m) and hydrated ionic radii (σ^+ , σ^-) were used as inputs in this work [5,8]. The relationship between the hydration number of ions and the activity coefficients have also been previously reported in literature [10-12]. Thus, hydration number (n) of the ions was also used as input. The values of ionic radii and hydration number were taken from Marcus model [13]. Some experimental value of activity coefficients have been collected from the literature [2,10,14]. The collected data set was divided into a training set and a testing set. Once the network was adequately trained, the test data were used to evaluate the performance of the resulting model. Approximately, 70% of the data of a total of 523 activity coefficients were randomly selected for training the network and 30% for validating (testing) the developed model. Different neural network topologies were first tested by a trial and error



procedure, using the related algorithms implemented in MATLAB programming language. Back-propagation method with Levenberg–Marquardt algorithm was used for training of all networks. A log-sigmoid transfer function (within the hidden layers) and a linear transfer function (within the output layer) were, as well, used. Among the neural network architectures, a multilayer perceptron neural network with two hidden layers (7, 6 neurons) was finally found to be an optimal ANN for our purpose. The estimated values for γ_{\pm} were in excellent agreement with the experimental data (see Fig. 1). RMSE and R^2 of the designed neural network were 0.031, 0.98 for the training data and 0.059, 0.97 for the testing data, respectively. The resulting model is valid for all aqueous uni-univalent electrolytes at 298.15K and in the concentration ranging from 0.001 to 6 mol.kg⁻¹.

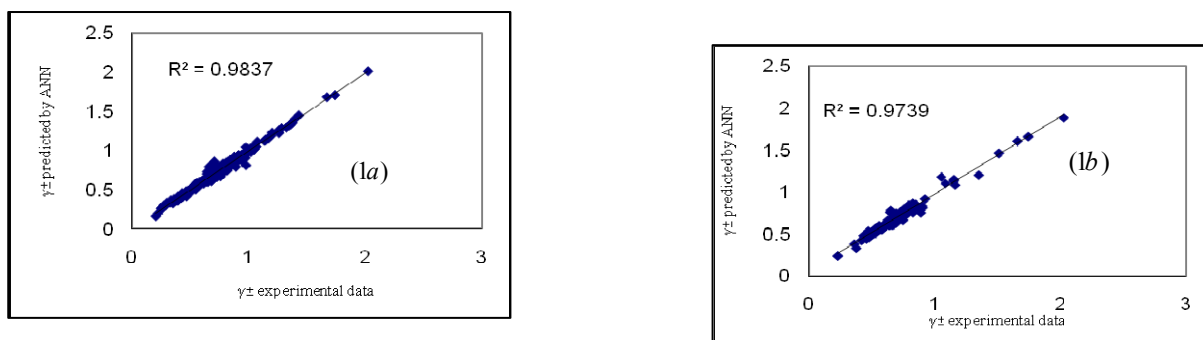


Fig.1. ANN activity coefficient prediction vs. experimental data: training data (1a) and testing data (1b).

4. Conclusions

An optimal neural network has been designed and tested for estimating mean activity coefficients of uni-univalent electrolytes in water. The results have indicated that artificial neural network is a powerful predictive tool for modeling of complex systems such as electrolytes. A noteworthy characteristic of the present model is that, any experimental data are not necessary for estimation of γ_{\pm} . A multi-layer feed forward network with two hidden layers of neurons can be trained better than other neural network types. RMSE and R^2 of the designed neural network were 0.031, 0.98 for training data and 0.059, 0.97 for testing data respectively.

References

- [1] K. S. Pitzer (Ed.), Activity Coefficients in Electrolyte Solutions, CRC Press, Boca Raton, Florida, 1991.
- [2] H. S. Harned, B. B. Owen, The Physical Chemistry of Electrolyte Solutions, third Edition, Reinhold, New York, 1958.
- [3] K. S. Pitzer, G. Mayorga, J. Phys.Chem. 77 (1973) 2300.
- [4] C. C. Chen, H. I. Britt, J.F. Boston and L.B. Evans, AIChE J. 28 (1982) 588.
- [5] V. D. Nguyen, R. R. Tan, Y. Brondial, T. Fuchino, Fluid Phase Equilibria. 254 (2007) 188.
- [6] L. Bernazzani, C. Duce, A. Micheli, V. Mollica, A. Sperduti, A. Starita, M. R. Tine, J. Chem. Inf. Model, 46 (2006) 2030.
- [7] J. Taskinen, J. Yliruusi, Advanced Drug Delivery Reviews, 55 (2003) 1163.
- [8] M. R. Dehghani, H. Modarress, A. Bakhshi, Fluid Phase Equilibria, 244 (2006) 153.
- [9] S. Agatonovic-Kustrin, R. Beresford, J. Pharm. Biomed. Anal, 22 (2000) 717.
- [10] R. H. Stokes and R. A. Robinson, J. Amer. Chem. Soc, 70 (1948) 1870.
- [11] A. A. Zavitsas, J. Phys. Chem. B, 105 (2001) 7805.
- [12] R. A. Robinson, H.S. Harned, Chem. Rev, 28 (1941) 419.
- [13] Y. Marcus, J. Chem. Soc. Faraday Trans, 87 (1991) 2995.
- [14] O. D. Bonner, J. Chem. Eng. Data, 24 (1979) 210.



**Excess molar volumes of (N,N-dimethylacetamide + N-methyl formamide)
, (N,N-dimethylacetamide+ 1,2-propanediol) and (N-methyl formamide+ 1,2-propanediol) at different
temperatures**

S. Akbary Golroudbari^{a,*}, H.A. Zarei^a

a. Department of Physical Chemistry, Faculty Of Chemistry, Bu-Ali Sina University, Hamedan, 65174 , Iran

(E-mail: sajadakbary@gmail.com)

Keywords: Excess molar volume, Densities, N,N-dimethylacetamide, N-methyl formamide, 1,2-Propanediol

1. Introduction

N-substituted amides have been attracting scientific attention for many years since this class of compounds can be regarded as a simple model of biological systems with the peptide groups. The number of studies on thermodynamic properties of ternary mixtures has increased in recent years due to industrial applications and the theoretical interest in studying the nature of molecular interaction and packing phenomena in ternary mixtures. Density of N,N-dimethylacetamide+N-methyl formamide, N,N-dimethylacetamide+1,2-propanediol, N-methyl formamide+1,2-propanediol binary mixtures have been measured using a vibrating tube densimeter in the temperature range of (293.15, 298.15, 303.15, 313.15, 323.15, 333.15) K for the whole composition range.

2. Methods

N,N-dimethylacetamide, N-methyl formamide and 1,2-propanediol were high purity grade reagents from Fluka and Merck. The purity of reagents was greater than 0.99 mass fraction. The densities of the pure N,N-dimethylacetamide, N-methyl formamide and 1,2-propanediol were measured at 298.15 K. It was checked by comparing the measured densities of the pure compounds with those reported in literature [1,2,3]. The densities of the pure compounds and mixtures were measured by means of Anton Paar DMA 4500 oscillating u-tube densimeter, provided with automatic viscosity correction. The temperature in the cell was regulated to ± 0.01 K with a solid state thermostat. The apparatus was calibrated once a day with dry air and bi-distilled fresh water. Air tight stopper bottles were used for the preparation of the mixtures. The mass of the dry bottle was first determined. The less volatile component of the mixtures was introduced in the bottle, and the mass of the bottle along with the two components was determined. All the weighing was performed on an electronic balance precise to ± 0.1 mg.

3. Results and discussion

The excess molar volumes (V_m^E) of the binary mixtures were calculated from the densities using the following equation:

$$V_m^E = \sum_{i=1}^n \frac{x_i M_i}{\rho} - \sum_{i=1}^n \frac{x_i M_i}{\rho_i}$$

Where ρ is the density of the mixture and x_i , ρ_i and M_i are the mole fraction, density and molecular weight of pure component i , respectively. The experimental excess molar volume of the binary mixture N-methyl formamide+1,2-propanediol at temperatures (293.15, 298.18, 30.15, 313.15, 323.15 and 333.15) K are graphically represented in figure 1. The results show that V_m^E are negative at high temperatures and become positive at some region with decreasing temperature (Fig. 1).

The volumes of V_m^E ($x=0.5$) at $T=298.15$ follow the order:

N,N-dimethylacetamide+ N-methyl formamide > N-methyl formamide+ 1,2-propanediol > N,N-dimethylacetamide+ 1,2-propanediol.

Each set of results was fitted using Redlich–Kister expression for the binary mixtures as follows:

$$V_m^E = x_i x_j \sum_{p=1}^4 \left(\sum_{q=1}^2 A_{pq} T^q \right) (x_i - x_j)$$

Where x_i and x_j are the mole fraction, A_{pq} are the temperature independent parameters for the binary mixtures, and T is the absolute temperature. These parameters were obtained by the unweighted least-squares method. The standard deviations were computed by applying the following equation :

$$\sigma(V_m^E) = \left(\frac{\sum_{i=1}^n \frac{(V_{m,exp,i}^E - V_{m,cal,i}^E)^2}{n-p}}{n-p} \right)^{\frac{1}{2}}$$

Where n is the number of experimental points and p is the number of adjustable parameter in the above equation.

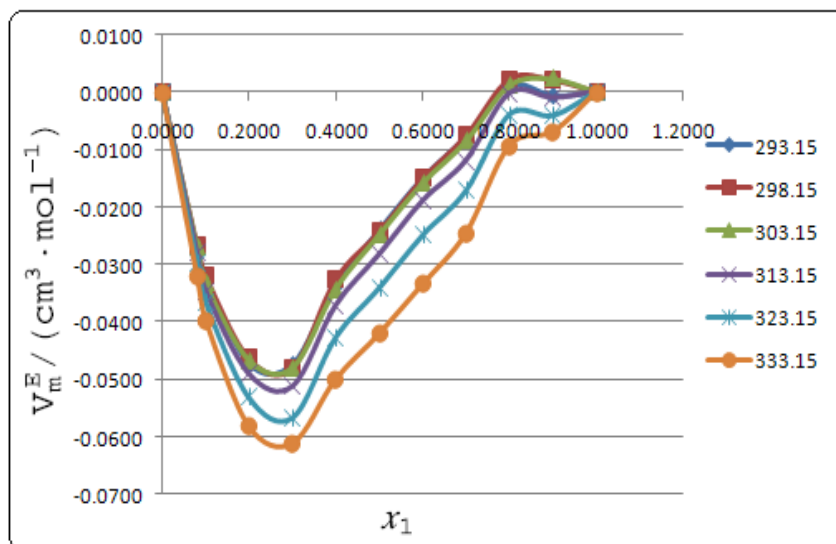


Fig .1. Excess molar volume, V_m^E , as a function of mole fraction for NMF(1). Experimental points for binary system (NMF+1,2-propanediol) at different temperatures.

4. Conclusions

The excess volume for binary mixtures consist of NMF and 1,2-propanediol were measured at (293.15, 298.15, 303.15, 313.15, 323.15, 333.15) K and ambient pressure for the whole composition range. The excess molar volumes for the binary systems (DMA+NMF and NMF+1,2-propanediol) are negative and become more negative with increasing temperature from (293.15 to 333.15) K but they become more positive for the system (DMA+1,2-propanediol).

References

- [1] H. Iloukhani, H.A. Zarei, M. Behrooz, J. Mol. Liq. 135 (2007) 141–145.
- [2] H. A. Zarei, F. Jalili, J. Chem. Thermodyn. 39 (2007) 55–66.
- [3] Jan Ziellkiewicz, J. Chem. Eng. Data , 43 (1998) 650-652.
- [4] O. J. Redlich, A. T. Kister, Ind. Eng. Chem. 40 (1948) 345-348.

**Molecular dynamics simulation of ¹³C NMR powder lineshapes of linear molecules in structure I clathrate hydrate**H. Mohammadi-Manesh^a, S. Alavi^b and B. Najafi^a

a. Department of chemistry, Isfahan University of Technology, Isfahan, Iran

(Email: hmmmanesh84@gmail.com)

b. Department of chemistry, University of Ottawa, Ottawa, Canada

1. Introduction

For the oblate shaped large structure I clathrate hydrate cages, the guest molecules rotate so that the plane which contains the long axis of the molecule is confined to the near to the equatorial plane of the cage rather than the axial regions. This non-uniform spatial distributions and motion can result in to anisotropic lineshapes in the solid-state NMR spectra of the guest species^[1]. In this work, molecular dynamics simulations are performed for a linear molecules include CS, CS₂, OCS, and HCCH in large cages of the structure I (sI) clathrate hydrate at three or four temperatures in the stability range of the linear molecules sI clathrate to determine the angular distribution of the guests in the large cages.

2. Computational Methodology

As a starting point for the calculation of the powder lineshapes, the chemical shielding tensor for the isolated linear guest molecules in the PA frame is calculated using the Gaussian 03 suite of programs with the gauge invariant atomic orbital (GIAO) method at the MP2 level of theory and 6-311++G(d,p) basis set. The calculated isotropic and anisotropies chemical shielding are in excellent agreement with the experimental value.^[2] Classical molecular dynamics simulations are performed to study the dynamics of the guest motions in the cages. The intermolecular van der waals potentials between atoms i and j on different molecules are considered to be the sum of Lennard-Jones (LJ) 12-6 and electrostatic point charge potentials centered on the atoms.

To equilibrate the initial configurations of each guest clathrate, isotropic NPT molecular dynamics simulations with the Nosé-Hoover thermostat-barostat algorithm were performed on a periodic 3×3×3 (35.8 Å per side initial dimensions) replica of the cubic sI clathrate hydrate cage with the DL_POLY molecular dynamics program version 2.18. The simulation cell contained a total of 162 large cages and 54 small cages with the corresponding guest molecules (one guest per cage). The simulations have done at four or three temperatures 70, 150, 200 and 250 K at ambient pressure. To obtain the angular distributions of the guest molecules in the large cages at different temperatures, NVE simulations were performed for a minimum total simulation time of 6 ns, starting with configurations equilibrated by the previous NPT runs. At each temperature, the ensemble averages of the eigenvalues of the chemical shielding tensor for each cage converged to within 2 ppm.

3. Results and discussion

The temperature-dependent polar angle distribution function, $P(\theta, T)$ for the linear molecules at 70 K is shown in Figure 1 and as expected, when the guest molecule length increases the angular width of $P(\theta, T)$ decreases. The orientational distributions extracted from molecular dynamics simulation were used to calculate the guest chemical shielding tensors and the NMR powder lineshape produced by each guest molecule. The total predicted lineshape anisotropy is calculated from the combination of the lineshapes of all guests and are shown in Figure 2. The calculated lineshapes agree well with the experimental ¹³C NMR powder patterns at each temperature. Temperature dependence the FWHM and the lineshape span decrease with increasing guest molecule length. At 70 K the skew of the lineshape of all the linear molecules in the sI large cages are similar to pure solid phases of these materials. At 200 K and 250 K, the skew of the lineshapes of molecules other than CS₂ is reversed with respect to the low temperature but the skew of CS₂ molecules which do not have free rotation at high temperature does not change with respect to solid state. In asymmetry molecules CS and COS the mobility S end is more than other end and it causes different distribution for two end atoms. The S atoms are mostly positioned toward the center of the cage. But in CO molecules where the mass difference C and O is small, the larger van der Waals interactions of O atoms compared to C to the clathrate cage bring about C atoms positioned toward the center of the cage^[3]. As a result, the O and C atoms of CO molecules are homogeneously distributed in the sI large cage while C and S atoms of CS molecules are not distributed homogeneously.

The MD simulations must be run long enough for sufficient sampling of the angular distributions to be obtained and the three eigenvalues of the chemical shielding tensor for each cage to converge. For the guest/clathrate system examined in this work,

several nanosecond MD simulations were required. An assumption of the method^[1], which was illustrated to be valid in the case of the guests in the clathrate structure, is that there are no strong dipolar couplings between guest and cage nuclei.

Fig. 1. The angular probability distribution function $P(\theta, T)$ of the guest molecules in the large cages at 1 bar and 70 K.

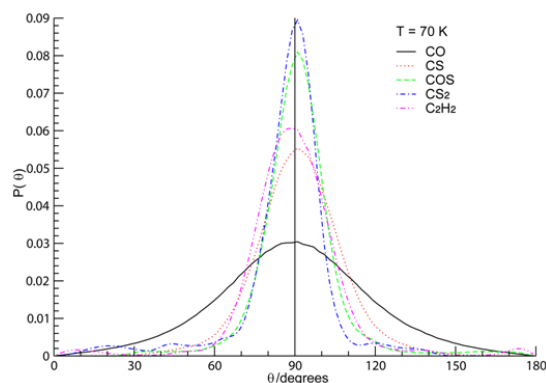
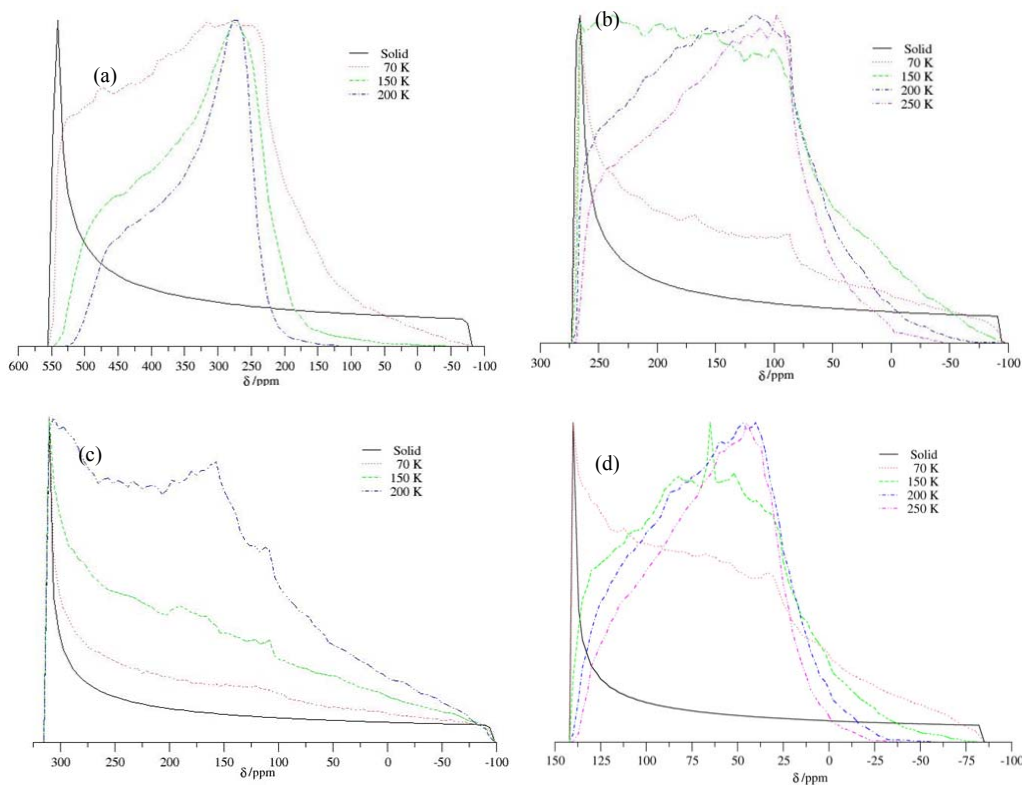


Fig. 2. The simulated ^{13}C NMR lineshapes at different temperatures and 1 bar for (a) CS, (b) COS, (c) CS₂, and (d) C₂H₂



References

- [1] S. Alavi, P. Dornan and T. K. Woo, *ChemPhysChem*, 2008, **9**, 911-919.
- [2] J. Jokisaari, P. Lazzeretti, P. Pyykko, *Chemical Physics*, **123**, 1988, 339-350
- [3] H. Mohammadi-Manesh, S. Alavi, K. Woo, M. Ashrafizaadeh and B. Najafia, *Phys. Chem. Chem. Phys.*, 2009, **11**, 8821–8828

**Adsorption thermodynamic and desorption studies of Cs-137 on manganese dioxide-polyacrylonitrile composite**

A. Nilchi *, G. Aboulhasanlo, S. Rasouli Garmarodi

Nuclear Science and Technology Research Institute, Nuclear Fuel Cycle School, Tehran, Iran,

(E-mail: anilchi@aeoi.org.ir)**Keywords:** Thermodynamic, manganese dioxide, polyacrylonitrile, adsorption, Cesium**1. Introduction**

Cesium and strontium are the most abundant radionuclides in nuclear fission products that are routinely or accidentally released. They have relatively long half-life of about 30 years and are considered as hazardous elements for the environment. Ion exchange technique has become one of the most commonly used treatment methods for such aqueous streams due to its simplicity, selectivity and efficiency [1, 2]. This paper presents the preparative conditions, adsorption thermodynamic and analytical applications of hydrous manganese dioxide-polyacrylonitrile polymeric-inorganic composite material used as a cation exchanger.

2. Experimental

Potassium permanganate, manganese sulfate, dimethylsulfoxide were purchased from Merck. Radioactive tracer ¹³⁷Cs was supplied by Nuclear Science and Technology Research Institute of Iran and subsequently used to label the Cs⁺ solutions of desired concentrations prepared by dilution of 0.1 mol/L Cs⁺ stock solution.

X-ray powder diffractometry was carried out using an 1800 PW Philips diffractometer, the radioactivity was counted using a high purity germanium detector gamma spectrometer Ortec model GMX-15185-5.

For hydrous manganese dioxide preparation, 250 mL of 1.5 mol/L KMnO₄ solution containing 1 mol/L H₂SO₄ was added to 500 mL of a mixed solution of 1 mol/L MnSO₄ and 1 mol/L H₂SO₄. Both solutions had a temperature of 60°C. The precipitate was left in the mother liquor for 48 hours, filtered, washed with 6 mol/L HNO₃ until it was free of sulphate ions, and then washed with distilled water until the washings were almost neutral, and dried at 60°C. Afterwards, the solid was soaked overnight in 300 mL of concentrated HNO₃. This soaking process was repeated over 5 times to remove K⁺ and SO₄²⁻ ions that may still have remained in the products. For composite beads preparation; the weighed amount of manganese dioxide powder was mixed with the solvent dimethylsulfoxide (DMSO) and a few drops of Tween-80 surfactant and stirred at 50°C for 1 hour. Then, 3.2 g of polyacrylonitrile powders were added to this solution with stirring at 50°C for 2 hours. The dissolved air in the dope was removed by vacuum pump, and the air-free composite dope was passed through inside the dual nozzle while the compressed air was ejected through the outside annulus of the dual nozzle to adjust the size of the composite beads. The ejected composite beads were then dropped in distilled water, which was used as a gelation agent. Finally, the beads were washed using demineralized water and dried at 50°C.

3. Results and discussion

The analysis of X-ray patterns of the synthesized materials and polyacrylonitrile revealed that the XRD data corresponding to synthetic MnO₂ agreed well with the powder diffraction files search manual (card no.12-716). It was also observed that the 2θ values at the peak points of MnO₂-PAN are the same as those in MnO₂, and hence their crystalline structure is similar.

Change in standard thermodynamic parameters during the adsorption process was evaluated using equations:

$$\Delta G^\circ = \Delta H^\circ - T\Delta S^\circ$$

$$\ln K_d = \frac{-\Delta H^\circ}{RT} + \frac{\Delta S^\circ}{R}$$

The values of ΔH° and ΔG° suggest that the sorption of cesium on synthesized composite is an endothermic and a spontaneous process (Fig. 1 and Table 1).

ΔH° (kJ/mol)	2.417
ΔS° (kJ/K mol)	0.065
$-\Delta G^\circ$ (kJ/mol)	
298K	16.953
308K	17.603
318K	18.253
328K	18.903
338K	19.553

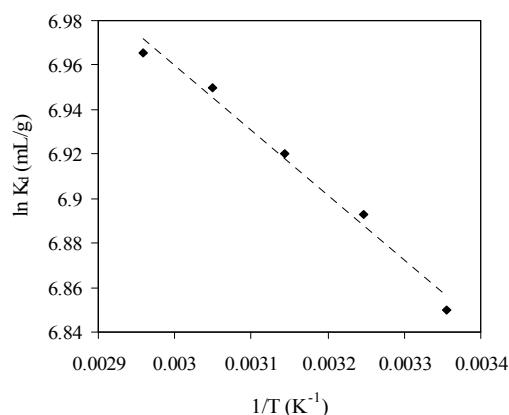

Table 1: Thermodynamic parameters for cesium adsorption

Fig. 1 Variation of $\ln K_d$ with $1/T$

The experimental data of adsorption were analyzed with the Freundlich and Langmuir models. The parameters calculated are summarized in Table 2. Higher correlation coefficients indicate that Langmuir model fits the data better than the Freundlich model.

Table2: Parameters of the Langmuir and Freundlich models

Langmuir constants			Freundlich constants		
Q° (mmol/g)	b (L/mmol)	R^2	K_F (mmol/g)(L/mmol) ^{1/n}	1/n	R^2
0.242	0.033	0.914	0.007	0.909	0.996

For elution studies, a glass column containing 0.2 g of the prepared composite on a glass wool support was loaded with a solution of 10–4 mol /L containing ¹³⁷Cs tracer. Desorption with 1 mol/L HCl solution was carried out at a flow rate of 0.5 mL/min at 25 °C. Fractions of 10 mL were analyzed for ¹³⁷Cs activity. Only 8.9% of the adsorbed Cs was eluted with 50 mL eluent.

4. Conclusion

The equilibrium data obtained in this study accorded excellently with the Freundlich adsorption isotherm over the entire concentration range investigated. The values of ΔG° , ΔH° and ΔS° prove that the sorption of cesium on MnO₂-PAN is an endothermic and a spontaneous process.

References

- [1] P. Rajec, L. Matel, J. Drechovska, J. Sacha, I. Navak, J. Radio. Nucl. Chem. Articles 208(1996) 477.
- [2] A.M.S. Oancea, A.R. Popescu, M. Radulescu, V. Weber, E. Pincovski, M. Cox, Solvent Extr. Ion Exch. 26 (2008) 217.



Thermodynamics of binding copper ion to jack bean urease

E. Poorakbar-Esfahani^{a,b,*}, A. A. Saboury^a, and G. Rezaei-Behbehani^c

a. Institute of Biochemistry and Biophysics, University of Tehran, Tehran, Islamic Republic of Iran

(E-mail: epoor2000@yahoo.com)

b. Biology Department, Payam Noor University, Tehran, Islamic Republic of Iran

c. Chemistry Department, Imam Khomeini International University, Qazvin, Islamic Republic of Iran

Keywords: Urease, Copper ion, Isothermal titration Calorimetry, Enthalpy of binding, Entropy of Binding.

1. Introduction

Ureases (urea amidohydrolases, EC 3.5.1.5) are a group of enzymes widespread in nature among plants, bacteria, fungi, algae and invertebrates; exercise a single catalytic function, which is the hydrolysis of urea. ^[1] Deceptively simple, this function is frequently looked at as a response of nature to the ubiquitous presence of urea. Jack bean urease (JBU) was the first enzyme obtained in the crystalline form. In 1926 James B. Sumner crystallized urease from jack bean (*Canavalia ensiformis*) and showed for the first time ever that enzymes are proteins. Equally importantly, ascertained by Dixon et al. in 1975, jack bean urease was the first enzyme shown to possess nickel ions in the active site, essential for activity. The best resolution obtained at 3.5 Å assigned the octahedral crystals of this enzyme. JBU has six identical subunits. Each subunit consists of a single kind of polypeptide chain containing 840 amino acid residue with relative molecular mass of 90770, excluding the two nickel ions per subunit. ^[1] Hence, a mass of the hexamer urease, including 12 nickel ions, being 545.340 kDa (590 kDa by a sedimentation method). The subunit of jack bean and microorganisms has difference in size and number.

Urease catalyzes the hydrolysis of urea to carbonic acid and two molecules of ammonia. The mechanisms of hydrolysis of urea by urease presently contemplated are those by Benini et al. and Karplus et al., a model for JBU catalysis in which one nickel coordinates the oxygen atom of urea, polarizing the carbonyl group, and a second nickel coordinates hydroxide ion, the catalytic nucleophile. Ureases are inhibited by a number of compounds. The study of urease inhibitors may have medical or agronomic significance, as well as providing insight into the urease catalytic mechanism. Inhibition of urease by heavy metal ions is important in view of heavy metal ion pollution, appropriate levels of urease activity in agricultural soils may be endangered, and this inhibition may be exploited in constructing urease inhibition-based sensing systems for in situ and real time determination of trace levels of the ions, e.g. in environmental monitoring, food control and biomedical analysis. Heavy metal ions inhibit both plant and bacterial ureases at the following order of effectiveness: $Hg^{2+} \approx Ag^+ > Cu^{2+} \gg Ni^{2+} > Cd^{2+} > Zn^{2+} > Co^{2+} > Fe^{3+} > Pb^{2+} > Mn^{2+}$.

Hg^{2+} , Ag^+ and Cu^{2+} ions nearly always listed as the strongest inhibitors. The inhibition has been habitually ascribed to the reaction of the metal ions with the thiol groups of the enzyme. However, both copper and silver ions coordinate to nitrogen- (histidine) and possibly oxygen- (aspartic and glutamic acids) containing functional groups in urease. Notwithstanding heavy metal ion binding to urease is important, there is not a comprehensive binding study in this case. Here, we applied isothermal titration Calorimetry (ITC) as a powerful tool for studying of copper ion binding to JBU, which all thermodynamic parameters for the binding process can be found.

2. Methods

JBU was obtained from Sigma Chemical Co. Copper nitrate was obtained from Merck. The buffer solution used in the experiments was 30 mM Tris using double-distilled water, pH=7.0, which was obtained from Merck. Experiments were carried out at two temperatures of 27 and 37 °C. The experiments were performed with the 4-channel commercial microcalorimetric system, Thermal Activity Monitor 2277 (Thermometric, Sweden). Copper ion solution (10 mM) was injected into the calorimetric titration vessel, which contained 1.8 ml JBU, 4 μM (2.2 mg/ml), using a Hamilton syringe. Injection of copper ion solution into the perfusion vessel was repeated 30 times and each injection included 20 μl copper ion solutions.

3. Results and discussion



The data obtained from ITC at two temperatures of 27 °C and 37 °C. For a set of identical and independent binding sites, we have before shown different methods of ITC data analysis.^[2-3] For a set of identical and independent binding sites; we have previously introduced the following equation:

$$(\Delta q/q_{\max})M_0 = ((\Delta q/q)L_0)(1/g) - K_d/g \quad (1)$$

where g is the number of binding sites, K_d is the dissociation equilibrium constant, M_0 and L_0 are total concentrations of biomacromolecule and metal ion, respectively, $\Delta q = q_{\max} - q$, q represents the heat value at a certain L_0 and q_{\max} represents the heat value upon saturation of all biomacromolecule. If q and q_{\max} are calculated per mole of biomacromolecule then the standard molar enthalpy of binding for each binding site (ΔH°) will be $\Delta H^\circ = q_{\max}/g$. According to the equation (1), a plot of $(\Delta q/q_{\max})M_0$ vs. $(\Delta q/q)L_0$ should be a linear plot by a slope of $1/g$ and the vertical-intercept of K_d/g , which g and K_d can be obtained. The value of g is 12 and values of K_d for a set of identical and independent binding sites are 285 μM and 346 μM at 27 °C and 37 °C, respectively. Dividing the q_{\max} amount of -182.4 kJ/mol and -175.1 kJ/mol by $g=12$, therefore, gives $\Delta H^\circ = -15.2$ kJ/mol and -14.6 kJ/mol at 27 °C and 37 °C, respectively.

The molar enthalpy of each binding site (ΔH°) and its dissociation equilibrium constant (K_d) in a set of binding sites can also be obtained via a simple graphical nonlinear fitting method using the following equation.^[2-3]

$$\Delta H^\circ = 1/A \{ (B + K_d) - [(B + K_d)^2 - C]^{1/2} \} \quad (2)$$

A , B and C are constants in each injection, which have been defined as follows:

$$A = V/2q \quad B = gM_0 + L_0 \quad C = 4gM_0L_0 \quad (3)$$

The intrinsic dissociation equilibrium constant and the molar enthalpy of binding were obtained 285 μM and -15.2 kJ/mol at 27 °C and 346 μM and -14.6 kJ/mol at 37 °C, respectively. These results are identical with results obtained by previous method described above.

To evaluate all thermodynamic parameters in metal binding process for JBU, the change in standard Gibbs free energy (ΔG°) should be calculated according to the equation (4), which its value can use in equation (5) for calculating the change in standard entropy (ΔS°) of binding process:

$$\Delta G^\circ = RT \ln K_a \quad (4)$$

$$\Delta G^\circ = \Delta H^\circ - T\Delta S^\circ \quad (5)$$

Where K_a is the association binding constant (the inverse of the dissociation binding constant, K_d). The K_a values are obtained 3509 and 2891 M^{-1} at 27 °C and 37 °C, respectively. Hence:

$$\Delta G^\circ = -20.4 \text{ kJ/mol} \quad \Delta S^\circ = +17.2 \text{ J/K mol} \quad (\text{at } 27^\circ\text{C})$$

$$\Delta G^\circ = -20.6 \text{ kJ/mol} \quad \Delta S^\circ = +19.1 \text{ J/K mol} \quad (\text{at } 37^\circ\text{C})$$

It means that the binding process is spontaneous resulted by not only enthalpic but also entropic driven.

4. Conclusions

All thermodynamic parameters for the interaction between JBU and copper ion at two temperatures of 27 and 37 °C have been obtained. There is a set of twelve identical and non-interacting binding sites for copper ions to JBU. The binding process is exothermic at both temperatures. The binding process is not only enthalpy driven but also it is entropy driven. The role of entropy driven in the binding process should be more effective by increasing the temperature. The molar entropy of binding means that there is difference between the entropy of Cu^{2+} -JBU complex ($S_{\text{Cu-JBU}}$) and the entropy of native JBU (S_{JBU}): $\Delta S = S_{\text{Cu-JBU}} - S_{\text{JBU}}$. Hence, the disorder of the protein structure has been increased due to the binding of copper ions.

References

- [1] Krajewska, B., J. Mol. Catalysis B: Enzymatic, 59(2009) 9.
- [2] Saboury, A. A. J. Iran. Chem. Soc., 3 (2006)1.
- [3] Saboury, A. A.; Atri, M. S.; Sanati, M. H.; Moosavi-Movahedi, A. A.; Hakimelahi, G. H.; Sadeghi, M., Biopolymers, 81(2006) 120.



Thermodynamics of aqueous solutions of L-serine+diammonium hydrogen citrate from the volumetric properties and the isopiestic determination of water activity

R. Sadeghi, A. Gholamireza

Department of Chemistry, University of Kurdistan, Sanandaj, Iran

(E-mail: rsadeghi@uok.ac.ir)

(E-mail: a_gholami281@yahoo.com)

Keywords: Thermodynamics, Aminoacid, Serine, Isopiestic, Volumetry

1. Introduction

Interactions of proteins with their surrounding environment play an important role in their conformational characteristics. These interactions are mainly between the protein molecules and the solvent, ions, and side chains of other protein molecules. The study of these interactions provides an important insight into the conformational stability and unfolding behaviour of globular proteins. However, proteins are complex molecules and their behaviour in solutions is governed by a combination of many more specific interactions. One approach that reduces the degree of complexity in the study of these interactions and requires less complex measurement techniques is to study the interactions in systems containing smaller biomolecules, such as amino acids (building blocks of the proteins). Salt solutions have large effects on the structure and properties of proteins including their solubility, denaturation, dissociation into subunits, and the activity of enzymes [1,2]. Although, there are many investigations about effect of inorganic salts on the thermodynamic properties of amino acids in aqueous solutions, but few studies have been done in the presence of organic salts [3]. In this work, we have measured the new density and sound velocity data of amino acid L-serine in aqueous solutions of diammonium hydrogen citrate at different temperatures. Furthermore, the improved isopiestic method [4] is used to obtain activities of water for the aqueous solutions of L-serine+diammonium hydrogen citrate at 298.15 K and a thermodynamic model is used for the correlation of the experimental water activity data.

2. Methods

Serine, diammonium hydrogen citrate and sodium chloride were obtained from Merck. All chemicals were used without further purification and double distilled, deionized water was used. All the solutions were prepared by mass on a Sartorius CP124S balance precise to within ± 0.0001 g. The density and sound velocity of the mixtures were measured at different temperatures with a digital vibrating-tube analyzer (Anton Paar DSA 5000, Austria) with proportional temperature control that kept the samples at working temperature within $\pm 10^{-3}$ K. In this work, the isopiestic method [4] has been used to obtain the activity of water in aqueous (serine +diammonium hydrogen citrate) mixtures. The used isopiestic apparatus consisted of eight-leg manifold attached to round-bottom flasks. Two flasks contained the standard pure NaCl solutions, one flask contained the pure serine, three flasks contained the (serine +diammonium hydrogen citrate) solutions, one flask contained the pure diammonium hydrogen citrate and the central flask was used as a water reservoir. The apparatus was held in a constant-temperature bath for at least 120 h for equilibrium. After equilibrium had been reached, the manifold assembly was removed from the bath, and each flask was weighed with an analytical balance with a precision of ± 0.0001 g. From the weight of each flask after equilibrium and the initial weigh of salt and amino acid, the mass fraction of each solution was calculated. The water activity for the standard aqueous NaCl solutions at different concentrations has been calculated from the correlation of Colin et al [5].

3. Results and discussion

The apparent molar volumes, V_ϕ , and apparent molar isentropic compressibility, K_ϕ , of alanine at different investigated solutions have been calculated from the density and sound velocity experimental data according to the following relations:

$$V_\phi = \frac{1000(d_0 - d)}{m_s d d_0} + \frac{M_s}{d} \quad (1)$$

$$K_\phi = \frac{1000(\beta - \beta_0)}{m_s d_0} + \beta V_\phi \quad (2)$$

$$\beta = d^{-1} u^{-2} \quad (3)$$



where subscript 0 denotes to solvent. d , u and β are density, sound velocity and isentropic compressibility, respectively M_s is the molar mass of solute and m_s is the molality of solute. The infinite dilution apparent molar volume and isentropic compressibility of serine in the investigated aqueous solutions have been obtained. The effects of temperature, salt concentration and charge of salt anion on the apparent molar volume, apparent molar isentropic compressibility and isentropic compressibility of serine in aqueous solutions have been studied and discussed on the basis of interactions exist in these solution. In the second part of this work, the isopiestic method was used to obtain activities of water for serine +diammonium hydrogen citrate + H₂O system at 298.15 K. The vapor pressures (P) of various aqueous solutions at each temperature were computed from the measured water activity data by using the following equation:

$$\ln a_w = \ln \left(\frac{P}{P_0} \right) + \frac{(B_w - V_w)(P - P_0)}{RT} \quad (4)$$

where B_w is the second virial coefficient of water vapor, V_w is the molar volume of liquid water, and P^0 is the vapor pressure of pure water.

References

- [1] P. H. Von Hippel, T. Schleich, *Acc. Chem. Res.* **2** (1969) 257.
- [2] W. P. Jencks, *Catalysis in Chemistry and enzymology*, McGraw-Hill, New York, 1969, p. 351.
- [3] R. Sadeghi, B. Goodarzi, *Biophysical Chemistry*, **135** (2008) 116.
- [4] L. R. Ochs, M. Kabiri-Badr, H. Cabezas, *AIChE J.*, **36** (1990) 1908.
- [5] E. Colin, W. Clarke, D. N. Glew, *J. Phys. Chem. Ref. Data* **14** (1985) 489.



The second law of thermodynamics in an information-based language

A. Shafiee^{a*}, I. Khatam^a

a. Department of Chemistry, Sharif University of Technology, Tehran, Iran

(Email: shafiee@sharif.edu)

Keywords: entropy, information measures, possibilities, energy and matter exchange.

1. Introduction

Applying Dretske's description of Shannon theory as a firm mathematical basis, we provide an information-based description for the second law of thermodynamics (using the familiar measures of information, i.e., $I(s)$, $I(r)$, N and E which are the information of source, information of receiver, noise and equivocation respectively, as well as that part of information available at receiver which is totally originated from the source, designated by $I_s(r)$). Defining the source and the receiver in terms of the initial and final thermodynamic states, we ascribe an amount of information to each state and show that the entropy change is a special case of the information difference between the states. In order to provide evidence for this assertion, we go on by describing some well known thermodynamic processes in the information-based language and compare it with the thermodynamic one. Incidentally, we show that $I_s(r)$ which is a different information measure from entropy change, is responsible for the dynamic aspect of thermodynamic processes. Subsequently, we introduce a genuine definition for the *isolated system* and thermodynamic *equilibrium* in an information context.

There are enormous attempts to provide an information based description for the second law of thermodynamics. We consider the flow of information as a fundamental entity in nature which is responsible for the entropy changes in thermodynamic processes. The proper approach to demonstrate the idea is first to introduce a coherent mathematical description for information; then model the physical processes based on this framework and see whether the information measures of the formulation have any significance in describing the physical phenomena. In this regard, we commence with the mathematical information theory in Dretske's description in the second section. In the third section of the paper we solve some thermodynamic problems in the information-based language and compare the results with what thermodynamics provide for us. In this section, the information measures introduced in the second section will be shown to have objective meaning in thermodynamics.

2. Results and discussion

As we show the relationship between information and entropy via the example A (i.e., Joule experiment), defining the source s and receiver r in terms of thermodynamic initial and final states, in the example B, (i.e., heat exchange between two systems) we find that through appearing of $I_s(r)$ due to noise and/or equivocation in form of heat, a dynamic character arises within the thermo-process indicating that the final state carries information about the initial state. Through the example C; the dissolution process of a crystal in liquid, we saw that the entropy change during the partial dissolution of a non-ionic solid in a solvent is composed of two parts; the transferring of the solid components to the liquid phase and the mixing process. The entropy change of the first process is usually ignored in thermodynamics while in the information description of the phenomena it could be easily computed.

3. Conclusions

In this work we elucidate the relationship between entropy and information. The information measures introduced by Dretske shown to have physical meaning in thermodynamics. The entropy change in corresponding to an information change during the thermo-process and another information measure, i.e., $I_s(r)$ determines a kind of dynamics due to energy exchange of thermodynamic systems. We also show that the entropy changes of some phenomena which cannot be computed in the thermodynamic notion, has a solution in this framework. In the dissolving process of a solid in liquid the entropy change of the mixing process is usually computed while the entropy change due to transferring of solid pieces to the liquid phase is usually ignored in thermodynamics. We show that in the information description of the phenomena the later entropy change can be easily computed.



References

- [1] F. Dretske, *Knowledge and the Flow of Information*, The MIT Press, 2000.
- [2] A. Shafiee, M. Karimi, On the Relationship between Entropy and Information, *Phys. Essays* **20**, 487, 2007.



Liquid-Liquid equilibrium in mixture of Methanol + Cyclohexane and Ionic liquid N-R-4-(N,N-dimethylamino) pyridinium Bromide (R=C₄H₉, C₅H₁₁, C₆H₁₃) at 298.15 K

J. Jahanbin^a, M. Ighaei^b, M. Dadfar

a. Molecular Simulations Lab. Faculty of Basic Sciences Azerbaijan University of Tarbiat Moallem, Tabriz, Iran

b. Molecular Simulations Lab. Faculty of Basic Sciences Azerbaijan University of Tarbiat Moallem, Tabriz, Iran

(Email: eighaie@yahoo.com)

Keywords: N-butyl-4-(N, N-dimethylamino) pyridinium Bromide (C₄-Br), N-pentyl-4-(N, N-dimethylamino) pyridine Bromide (C₅-Br), e- N-hexyl-4-(N,N-dimethylamino) pyridinium Bromide (C₆-Br), Methanol, Cyclohexane, Wilson model

1. Introduction

Ionic liquids are electrolytes with low melting temperatures. They have interesting physical and chemical properties which are giving them increasing attention in research and industry. In the recent years several works have been published about Ionic liquids and their application to liquid extractions. However, just a few of them report liquid-liquid equilibrium (LLE) data for ternary systems. Therefore in this work Liquid-Liquid equilibrium in mixture of Methanol + Cyclohexane and Ionic liquid N-R-4-(N,N-dimethylamino) pyridinium Bromide (R= C₄H₉, C₅H₁₁, C₆H₁₃) at 298.15 K investigated and the experimental correlated by Wilson model is studied.

2. Experimental

2.1. Materials

The Cyclohexane and methanol were used from Merck (Cyclohexane, min 99.5%, Methanol, min 99.5%) and Ionic liquid synthesized at organic chemistry lab. of our dept [1].

2.2. Experimental procedure

A glass vessel was used to carry out the phase equilibrium determinations. The glass vessel was provided with an external jacket in which water at Constance temperature was circulated using a thermostat. For determination of the tie line, feed samples (about 20 cm³) were prepared by mixing appropriately amounts of Cyclohexane, Methanol and Ionic liquid in the vessel. The thermostat was set in desired temperature and the sample was stirred for 4 hours. then the mixture was allowed to settle for 12 hours [2]. After separation of two phases, at first, for measuring the content of Ionic liquid, 3 cm³ samples were withdrawn from each phase using long-needle syringes, then Cyclohexane and methanol was separated from Ionic liquid by evaporation apparatus, and the mass of the dried Ionic liquid was determined.

The concentration of Cyclohexane in both phases was determined by refractive index measurement performed in 298.15 K using refractometer with precision of ± 0.0001 . For dilute methanol solution containing Cyclohexane and Ionic liquid, the relation between the refractive index and the mass fraction of Cyclohexane W_s , and Ionic liquid W_{IL} , is given by

$$n = a_0 + a_1 W_s + a_2 W_{IL} \quad (1)$$

The value of coefficient a_0 , a_1 , a_2 for the studied systems listed in table 1.

Table1. Coefficient of Equation1

system	a_0	$a_1 \cdot 10^2$	$a_2 \cdot 10^2$
C4Br+Methanol+Cyclohexane	1.3274	0.0840	0.2042
C5Br+Methanol+ Cyclohexane	1.3274	0.0840	0.2038
C6Br+Methanol+ Cyclohexane	1.3274	0.0840	0.2008

3. Results and discussion

3.1. Experimental LLE data.

The compositions of the experimental tie-lines for ternary systems at 298.15 K are reported in Tables 2- 4.

Table2. Tie Line data as mass fraction for the C4-Br (IL) + Methanol+Cyclohexane (s)

W_s^{bot}	W_{IL}^{bot}	W_s^{top}	W_{IL}^{top}
49.2983	8.4387	90.0193	0.0660
56.1745	11.9317	95.7775	0.0011
48.0872	8.0939	89.011	0.0009
51.7287	10.1524	94.4599	0.0010
49.714	8.6445	93.2998	0.0013

Table3. Tie Line data as mass fraction for the C5-Br (IL) + Methanol + Cyclohexane (s)



W_s^{bot}	W_{IL}^{bot}	W_s^{top}	W_{IL}^{top}
47.5674	11.7761	88.5423	0.1789
46.0789	11.3957	85.8769	0.3123
51.8201	13.1441	94.4381	0.1221
50.032	12.4143	92.9776	0.0001
56.4621	14.4651	94.6068	0.0019

Table4. Tie Line data as mass fraction for the C6-Br (IL) + Methanol + Cyclohexane (s)

W_s^{bot}	W_{IL}^{bot}	W_s^{top}	W_{IL}^{top}
69.2210	18.2681	97.8823	0.0011
65.7908	17.2789	95.3879	0.0008
64.8721	17.14121	95.0125	0.0014
61.8589	18.8032	94.542	0.0010
66.6917	18.2509	96.2488	0.0009

3.2. Correlation of LLE data.

The Wilson model [10] has been widely used to represent the non-idealities in mixtures of nonelectrolytes. Zhao et al. have extended the Wilson model for nonelectrolytes to electrolyte solutions containing several electrolyte. In this work we extended Wilson model for systems containing one electrolyte and multisolvent. Then this model was employed to correlate the experimental tie line data for the ternary systems investigated. The objective function, $F(P)$, was used to minimize the difference between the experimental and calculated mole fraction compositions defined as:

$$F(P) = \sum_i^n [x'_{1i} - x'_{1i}(\text{calc})]^2 + [x'_{2i} - x'_{2i}(\text{calc})]^2 + [x''_{1i} - x''_{1i}(\text{calc})]^2 + [x''_{2i} - x''_{2i}(\text{calc})]^2 \quad (2)$$

Where P is the set of parameters vector, n refers to the number of experimentally determined point x'_{1i}, x'_{2i} and $x'_{1i}(\text{calc}), x'_{2i}(\text{calc})$ are the experimental and calculated mole fractions of one phase and $x''_{1i}, x''_{2i}, x'_{1i}(\text{calc}), x'_{2i}(\text{calc})$ are the experimental and calculated mole fractions of the other phase. For the Wilson model, the C parameter, which represents the effective coordination number in the system was set at a values of C =4, 6, 8, 10. The accuracy of the calculated results is represented by the root mean square deviation (rmsd) values defined below as:

$$\text{rmsd} = \sqrt{\frac{\sum_i \sum_l \sum_m (x_{ilm}^{\text{calc}} - x_{ilm}^{\text{exp}})^2}{6K}} \times 100 \quad (3)$$

Where x is the mole fraction and the subscripts i, l and m provide a designation for the component, the phase and the tie line, respectively. The k value designates the number of interaction components. The rmsd values from table 5 provide a measure of the accuracy of the correlation. As can be inferred from the rmsd values, good correlation of the experimental values with the Wilson model was obtained.

Table5. The rmsd values for ternary mixture for different values of C

System	4	6	8	10
C4Br + Methanol + Cyclohexane	0.0622	1.2431	2.14	1.5322
C5Br + Methanol + Cyclohexane	$3.7492 \cdot 10^{-3}$	0.0988	0.7009	0.74
C6Br + Methanol + Cyclohexane	0.1389	0.1442	0.1011	0.0848

4. Conclusions

For N-butyl-4-(N,N-dimethylamino) pyridinium Bromid + Cyclohexane + Methanol or N-pentyl-4-(N,N-dimethylamino) pyridinium Bromid + Cyclohexane + Methanol and N-hexyl -4-(N,N-dimethylamino) pyridinium Bromid + Cyclohexane + Methanol systems, tie line data have been determined at 298.15 K. It was found that tie line data for these systems can be satisfactory described by electrolyte Wilson equations.

References

- [1] Ghale Asadi, m. in press
- [2] Zafarani-Moattar, M.T., Gasemi, J. j.Chem.Eng, Data 47(2002)525
- [3] Chen, C.C. Brit, H. Boston, J. F. and Evans, L. B. AIChE J 28(1982) 588
- [4] Chen, C.C., Evans, L. B. AIChE J. 32 (1986) 444



Vapor-Liquid equilibria of binary disodium hydrogen citrate + water and ternary 1-octyl-3-methyl imidazolium bromide + disodium hydrogen citrate + water systems from isopiestic measurements

R. Sadeghi^a, E. Parsi^b

a. Department of Chemistry, University of Kurdistan, Sanandaj, Iran

(E-mail: rsadeghi@uok.ac.ir)

b. Department of Chemistry, University of Kurdistan, Sanandaj, Iran

(E-mail: parsielham@gmail.com)

Keywords: Ionic Liquid, 1-Octyl-3-methylimidazolium bromide, Disodium hydrogen citrate, Water activity, Vapor pressure

1. Introduction

Ternary aqueous solutions of salts and ionic liquids separate into a salt-rich and a ionic liquid-rich phase over part of the composition space. Aqueous two-phase systems of this nature are useful for the separation and purification of biomaterials where the employment of a non-polar solvent/aqueous phase system would lead to degradation of biological activity [1,2]. Citrate is biodegradable and nontoxic and could be discharged into biological wastewater treatment plants and therefore the citrates can be considered as a substitute for inorganic salts, because the citrate forms aqueous two-phase system with ionic liquids which is suitable for protein extraction. Thermodynamic properties of aqueous ionic liquid-salt systems are necessary for a fundamental understanding of the phase-forming ability and also for the development of theoretical models for the prediction of the partitioning behavior of the two-phase system. In an ATPS, water constitutes the bulk component of the two phases and therefore water is a special and key component and closely related with the other two phase-forming components. Thus, the thermodynamic properties of water in these systems should be paid great attention. Also, the activity is an important and key thermodynamic property, because, it is closely related with the other thermodynamic properties and in thermodynamic modeling for separation methods, it is the essential variable. This work is devoted to obtaining the water activities of Binary Disodium Hydrogen Citrate (Na_2HCit) + Water and Ternary 1-Octyl-3-Methyl Imidazolium Bromide ($[\text{C}_8\text{mim}][\text{Br}]$) + Na_2HCit + water systems from isopiestic measurements at different temperatures.

2. Methods

The isopiestic apparatus used in this work was similar to the one used by Ochs et al. [3]. The apparatus used for determination of water activity of binary aqueous Na_2HCit solutions consisted of five-leg manifold attached to round-bottom flasks. Two flasks contained the standard pure NaCl solutions, two flasks contained the pure Na_2HCit solutions and the central flask was used as a water reservoir. The apparatus used for determination of water activity of ternary aqueous Na_2HCit + $[\text{C}_8\text{mim}][\text{Br}]$ solutions consisted of eight-leg manifold attached to round-bottom flasks. Two flasks contained the standard pure NaCl solutions, one flask contained the pure $[\text{C}_8\text{mim}][\text{Br}]$ solution, one flask contained the pure Na_2HCit solution, three flasks contained the $[\text{C}_8\text{mim}][\text{Br}]$ + Na_2HCit solutions and the central flask was used as a water reservoir. The apparatus was held in a constant-temperature bath at least 120 h for equilibrium. After equilibrium had been reached, the manifold assembly was removed from the bath, and each flask was weighed with an analytical balance with a precision of $\pm 1 \cdot 10^{-4}$ g. From the weight of each flask after equilibrium and the initial weight of salt and polymer, the mass fraction of each solution was calculated. The water activity for the standard aqueous NaCl solutions at different concentrations and temperatures has been calculated from the correlation of Colin et al. [4].

3. Results and discussion

Isopiestic measurements have been carried out on the aqueous solutions of both Na_2HCit and Na_2HCit + $[\text{C}_8\text{mim}][\text{Br}]$ over a range of temperatures at atmospheric pressure. Vapor-liquid equilibrium data such as water activity, vapor pressure, osmotic coefficient, activity coefficient and Gibbs free energies were obtained through the isopiestic method. The effect of temperature on the constant water activity lines of aqueous $[\text{C}_8\text{mim}][\text{Br}]$ + Na_2HCit systems has been studied. As an example, the lines of constant water activity or vapor pressure of $[\text{C}_8\text{mim}][\text{Br}]$ + Na_2HCit + H_2O system at 298.15 K is plotted in Fig. 1. An

interesting aspect of such ILs is that the $[C_n\text{mim}]^+$ cations possess inherent amphiphilic character when their alkyl group is a longer hydrocarbon chain. The results show that $[C_8\text{mim}]\text{Br}$ behaves as a surfactant in water and forms aggregates in water with the critical micelle concentration (cmc) about 0.18 mol.kg^{-1} . Micellization of this ionic liquid in water has also been discussed in this work.

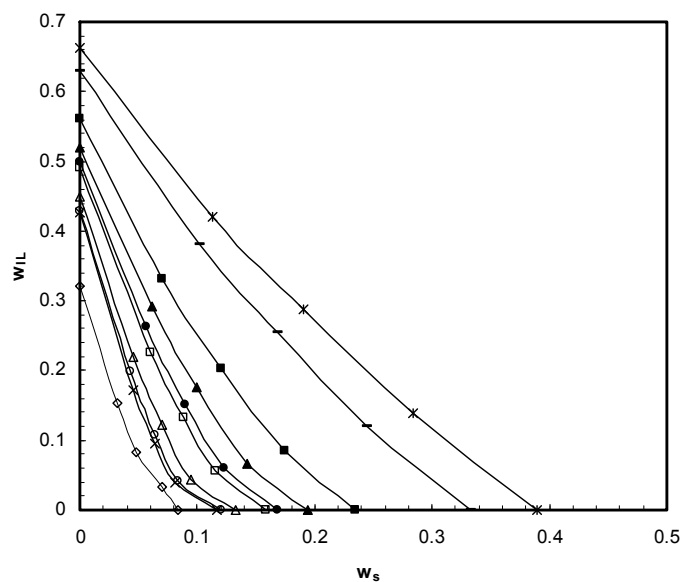


Fig. 1. Plot of weight fraction of $[C_8\text{mim}][\text{Br}]$, w_{IL} , against weight fraction of NaH_2Cit , w_s , for constant water activity curves of $[C_8\text{mim}][\text{Br}] + \text{Na}_2\text{HCit} + \text{H}_2\text{O}$ system at $T = 298.15 \text{ K}$

References

- [1] K. E. Gutowski, G. A. Broker, H. D. Willauer, J. G. Huddleston, R. P. Swatloski, J. D. Holbrey, R. D. Rogers, J. Am. Chem. Soc. 125 (2003) 6632.
- [2] R. Sadeghi, R. Golabiazar, H. Shekaari, J. Chem. Thermodyn. (2009), doi:10.1016/j.jct.2009.10.007
- [3] L. R. Ochs, M. Kabiri-Badr, H. Cabezas, AIChE J., 36 (1990) 1908.
- [4] E. Colin, W. Clarke, D. N. Glew, J. Phys. Chem. Ref. Data 14 (1985) 489.



Isotherms and thermodynamic studies on biosorption of Pb(II) from waste waters using *Syringa Vulgaris* tree leaves

S. Mahmoudzadeh^{a,b,*}, A. Niazi^{a,b}, V. Najafi^a

a. Department of Chemistry, Faculty of Sciences, Islamic Azad University, Arak Branch, Arak, Iran

b. Yong Researchers Club, Islamic Azad University, Arak Branch, Arak, Iran

Keywords: Heavy metal, Tree leaves, Isotherm, Thermodynamic parameters

1. Introduction

Heavy metal ions are nowadays among the most important pollutants in surface and ground water. They are often discharged by a number of industries, such as metal plating facilities, mining operations and tanneries, which can lead to the contamination of fresh water and marine environment. Heavy metal ions are extremely toxic and harmful even at low concentrations, which can seriously affect plants and animals and have been involved in causing a large number of afflictions. Therefore, the limination of these metals from water and waste waters is important to protect public health. The objective of this study was to investigate the biosorption potential of *Syringa Vulgaris* tree leaves to treat Waste waters contaminated with pb (II). The metal loading Capacity of yeast biomass was determined as a function of the initial metal ion concentration, contact time, temperature, biosorbent dose and pH. The biosorption data were analyzed by Freundlich, D-R isotherm, Temkin and Langmuir isotherm models. The effect of temperature and Thermodynamic parameters was studied too.

2. Methods

The *Syringa Vulgaris* tree leaves were gathered from twigs in to clean plastic bags, washed with ion-free distilled water and then dried at 80° C for 24 h. Dried biomass was powdered by using mortar and pestle. The powdered biomass was sieved to 40–50 mesh, then stored in plastic bags ready for use as a biosorbent in batch studies. Metal ion solution used in this study was prepared by dilution of 1000 mg l⁻¹ stock solution of Pb(II) obtained by dissolving Pb(NO₃)₂ in distilled and deionized water.

3. Results and discussion

The results show that the optimum uptake of metal ions was observable by *Syringa Vulgaris* tree leaves at pH 5–9. Increasing pH from 5 to 9 resulted in lower biosorption with sorbent for Pb(II). The metal ion biosorption capacities of *Syringa Vulgaris* tree leaves are presented as a function of equilibrium concentration (5–5000 mg/l) in aqueous solution in [1]. All other Parameters such as contact time (40 min), volume of solution (10 ml) and quantity of sorbents (10 g/l) and pH 6 were kept constant.

Sorbent exhibited very high metal loading capacities for this metal ion 290.98 and mg/g for Pb (II), for *Syringa Vulgaris* tree leaves respectively. The duration of the batch experiments was varied from 5 to 60 min.

Pb(II) show a rate of adsorption during the first 30 min. Fig.3, during which period the fraction removed were Pb(II) 91%, for the *Syringa Vulgaris* tree leaves. The percentage of metal ion adsorbed increased with increasing sorbent concentration.

The maximum metal ion uptake was observed at about 10 g/l for *Syringa Vulgaris* sorbents for Pb(II) ion. Adsorption isotherm models were used to characterize the interactions of metal ion with the sorbents.

In this study, Langmuir, Freundlich, Temkin and Dubini–Radushkevich (D–R) isotherms were applied to describe the equilibrium between adsorbed metal ions and metal ions in solution [2]. The experiments were carried out at 25, 30, 35, 40, 45 and 50 °C. The other parameters were kept constant [3]. Pb(II) solution was shaken with 0.1 *Syringa Vulgaris* at pH 5 for 40 min.

Adsorption enthalpy was measured using the method based on the Van't Hoff plot [4]. The values of ΔH° and ΔS° were calculated from the slopes and intercepts of the linear variation of ln K_c with reciprocal temperature, 1/T, Fig 1, using the relation:

$$\ln K_c = -\frac{\Delta H^\circ}{RT} + \frac{\Delta S^\circ}{R}$$

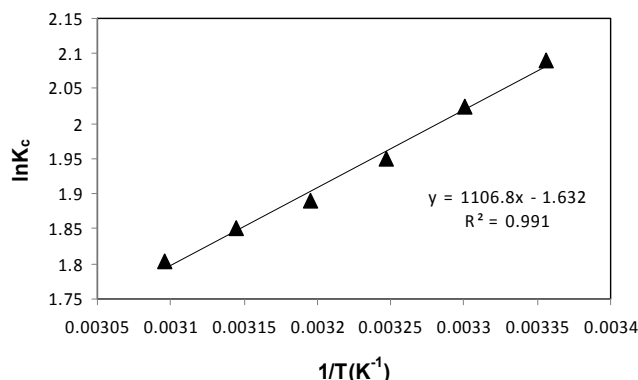


Fig. 1. K_c vs. $1/T$ for the Pb(II) adsorption

where H° and ΔS° are the standard enthalpy and entropy changes of adsorption, respectively. The free energy of specific adsorption ΔG° is calculated using the equation:

$$\Delta G^\circ = \Delta H^\circ - T\Delta S^\circ$$

The value of $\Delta H^\circ = -9.20$ kJ/mol and $\Delta G^\circ = -5.15$ kJ/mol for Pb(II) suggest that the sorption of Pb(II) on Syringa Vulgaris is an exothermic, favorable and spontaneous, Table 1, respectively.

Table 1. Thermodynamic parameters

Metal	Biosorbent	ΔG° (kJ/mol)	ΔH° (kJ/mol)	ΔS° (J/molK)
Pb	Syringa Vulgaris tree leaves	-5.156	-9.20	-13.574

4. Conclusions

The results obtained show that pH and initial Pb(II) concentration and time, highly affect the uptake of the biosorbent. The Langmuir adsorption model and Freundlich equation were used for mathematical descriptions of the biosorption of Pb(II) ions on to Syringa Vulgaris tree leaves. It was found that the adsorption equilibrium data fitted well to the Langmuir model. Thermodynamic parameters ΔH° , ΔS° and ΔG° were estimated and these parameters show that adsorption is exothermic, favorable and spontaneous, respectively. Another advantage of using this new sorbent is high capacity for removal of heavy metals from medium acidic aqueous solutions. Furthermore, the Syringa Vulgaris tree is grown widely in Iran, the leaves have no Commercial value and is a good, inexpensive source of readily available biomaterial.

References

- [1]. K. Vijayaraghavan, T.V.N. Padmesh, K. Palanivelu, M. Velan, J. Hazard. Mater., 304(2006).
- [2]. R. Han, J. Zhang, W. Zou, J. Shi, H. Liu, J. Hazard. Mater., 266 (2005) 125.
- [3]. J.U. Kennedy Oubagaranadin, N. Sathyamurthy, Z.V.P. Murthy, J. Hazard. Mater., 165 (2007) 142.
- [4]. J. Yu, M. Tong, X. Sun, Biochem. Eng. J., 126 (2007) 33.

**Acid-base equilibria of salicylic acid in mixed water-DMSO solutions**A. Farajtabar^{a*}, F. Gharib^b, M. Jabbari^b

a. Department of Chemistry, Islamic Azad University, Jouybar branch, Jouybar, Iran

b. Chemistry Department, Faculty of Sciences, Shahid Beheshti University, Tehran, Evin, Iran

(E-mail: a_farajtabar@yahoo.com)**Keywords:** Protonation constant, Salicylic acid, Water-DMSO, Yasuda-Shedlovsky method.**1. Introduction**

The acid ionization constants are important for the qualitative and quantitative treatment of systems involving acid–base equilibria in solution and the knowledge of these values are essential in a wide range of research area such as chemistry, biochemistry, pharmacology. For example, many compounds used as drug candidates have acidic or basic functionalities that the extent to which the drugs enter the blood stream is controlled by their pK_a values [1]. The systematic investigations of solvent effects on thermodynamic and kinetic functions are interesting both from experimental and theoretical perspective in chemical and biochemical analysis. The study of solvent effect on chemical and physical processes in binary mixtures is more complicated than in pure solvents because the solute–solvent and solvent–solvent interactions can create new solvent properties leading to preferential solvation. Preferential solvation occurs when the solutes interact more specially with one of solvent in binary mixtures and then this difference in interactions reflected in the composition of solute microenvironment [2, 3]. To continue of our previous works [4, 5] in this work the protonation constants of salicylic acid have been determined in various mixtures of water-DMSO solvents to examine the solvent dependence on its acid-base properties equilibria.

2. Methods

The electromotive force was measured using a Metrohm model 781 pH ion-meter. The combined glass-pH electrode (model 6.0258.000) was modified by replacing its aqueous KCl solution with 0.1 mol dm⁻³ with 0.01 mol dm⁻³ NaCl + 0.09 mol dm⁻³ NaClO₄ saturated with AgCl in appropriate solvent. The electrode was soaked for 15-20 minutes in water-organic solvent mixture before potentiometric measurements. All titrations were carried out in a 50 mL thermostated double-walled glass vessel. Spectrophotometric measurements were performed on a UV-Vis Shimadzu 2100 spectrophotometer with a Pentium 4 computer and using thermostated matched 10 mm quartz cells. The measurement cell was of flow type. A peristaltic pump allowed circulation of the solution under study from the potentiometric cell to the spectrophotometric cell, so the absorbance and the emf of the solution could be measured simultaneously. To exclude carbon dioxide from the system, a stream of purified nitrogen was passed through a sodium hydroxide solution and then bubbled slowly through the reaction solution.

3. Results and discussion

The spectrophotometric data (every 0.5 nm) obtained during the titration, as a function of H⁺ concentration, were conducted with the computer program STAR [6]. If we designate m absorption spectra that will be measured at n wavelengths, the individual absorbance readings thus can be arranged in a $m \times n$ matrix **R**; the m spectra form the rows of **R** and the columns consist of the n response curves gathered at the different wavelengths. According to Beer's law, for a system with N absorbing components, **R** can be decomposed into the product of a concentration matrix **C** ($m \times N$) and a matrix of the molar absorptivities **S** ($N \times n$). However, because of the inherent noise in the measured data, the decomposition does not represent **R** exactly. The matrix **T** of the residuals is given by the difference between **CS** and **R**

$$\mathbf{T} = \mathbf{CS} - \mathbf{R} \quad (1)$$

In the fitting procedure, those matrices **C** and **S** are determined which best represent the original matrix **R**. The task of the fitting procedure is to optimize the matrix **T** of the residuals. In eq 2, U is the sum of the squares of all elements of **T**. It is the task of the nonlinear least-squares fitting to find the set of parameters that result in a minimum of U .

$$U = \sum_{i=1}^m \sum_{j=1}^n \mathbf{T}(i, j)^2 = \text{minimize} \quad (2)$$



The program allows calculation of the different protonation constants which are determined in various water-organic solvents mixtures. To evaluate the accuracy of the pKa value in pure water, a comparison has been done between the experimental protonation constant value with those obtained by extrapolation of Yasuda-Shedlovsky approach in different aqueous solutions of DMSO mixtures [7, 8]. On the basis of Born electrostatic model and Bjerrum's theory of ion association, Yasuda [7] and Shedlovsky [8] derived an equation that the plot of $\log K + \log[H_2O]$ versus $1/\epsilon_r$ produces a straight line, where K represents the protonation constant of a weak acid or a weak base in different aqueous organic solvents mixtures, $[H_2O]$ is the molar concentration of water and ϵ_r shows the dielectric constant of the medium.

$$\log K + \log[H_2O] = a\epsilon_r^{-1} + b \quad (3)$$

a and b are two constants that should be determined in this work.

4. Conclusions

The protonation constant of some salicylic acid was successfully determined in water and water-DMSO mixtures of by spectrophotometric and potentiometric methods at 25 °C and in ionic strength of 0.1 M sodium perchlorate. Generally, it was observed that the pKa values of salicylic acid increase with the increase in the volume fraction of DMSO. The high correlation coefficients between the pKa values and physicochemical properties of binary mixtures demonstrate existence of a linear relationship between these magnitudes in these media.

References

1. M. Andrasi, P Buglyo, L. Zekany, A. Gaspar, J. Pharm. Biomed. Anal. 44 (2007) 1040.
2. A. Habibi-Yangjeh, Bull. Korean Chem. Soc. 25 (2004) 1165.
3. P. M. Mancini, L. R. Vottero, J. Phys. Org. Chem. 19 (2006) 34.
4. F. Gharib, M. Jabbari, A. Farajtabar, A. Shamel, J. Chem. Eng. Data 53 (2008) 1772.
5. F. Gharib, A. Farajtabar, Rev. Inorg. Chem. 29 (2009) 37.
6. J. L. Beltran, R. Codony, M. D. Prat, Anal. Chim. Acta 276 (1993) 441.
7. M. Yasuda, Bull. Chem. Soc. Jpn. 32 (1959) 429.
8. T. Shedlovsky, B. Peasce (Eds), Electrolytes, Pergamon, New York, 1962.

**A modified perturbed hard-sphere equation of state applied to room temperature ionic liquids**S. M. Hosseini ^{a,*}, M. M. Papari ^b

a. Department of Chemistry, College of Sciences, Shiraz University, Shiraz, Iran

(E-mail: Seied_Mostafa_Hosseini@Yahoo.com)

b. Department of Chemistry, Shiraz University of Technology, Shiraz, Iran

Keywords: Room Temperature Ionic Liquids, Equation of State**1. Introduction**

The room temperature ionic liquids (RTILs) consist of 1-alkyl-3-methylimidazolium, 1-alkylpyridinium and n-methyl-n-alkylpyrrolidinium ions. They have a low melting point below 100°C. The knowledge of volumetric behaviour of RTILs, or innovative organic solvents is important because of their distinctive properties. The technique of perturbation modeling was taken into account for this purpose.

The stated technique uses references values for systems that are similar enough to the system of interest that good estimates of desired values can be made with small corrections to the reference values. The reference model proposed here, is that of Carnahan-Starling(CS) [1]. In this work, a perturbed hard-sphere equation of state (EOS) has been employed to predict the volumetric properties of RTILs including, Imidazolium-, pyridinium- and pyrrolidinium-based in a broad range of temperatures and pressures. From about 900 data points examined for the aforementioned RTILs and the overall average absolute deviation compared with experimental data is 1.37%.

2. Theory

The hard-sphere fluid is taken into account as a reference system, and the influence of attractions and the softness of repulsions are considered as perturbations in statistical mechanical perturbation theory of fluids [2,3]. Many perturbed hard-sphere EOSs have been modified to improve the volumetric behaviour prediction of fluids from years ago. . Recent work by Roman et al. [4] led to a simple modification of equations of state for obtaining the main vapour-liquid properties of simple fluids. In this work we utilized the same modification proposed by Roman but, using acentric factor of pure RTILs. We applied the Carnahan-Starling equation for RTILs as the reference system and the modified van der Waals attraction proposed by Roman as perturbation part. The total formulation of modified equation of state considered in this study is:

$$Z_{\text{tot}} = Z_{\text{hard-sphere}} + Z_{\text{modified vdW-attraction}} \quad (1)$$

$$\frac{p}{\rho kT} = 1 + b\rho g(d^+) - \frac{a\rho}{kT(\beta+1)} \quad (2)$$

where p is the pressure, $\rho = N/V$ is the number density, kT is the thermal energy per molecule, $g(d^+)$ is the pair radial distribution function of hard spheres at contact, a reflects the strength of attractive forces between spheres, b is the van der Waals covolume and β represents an attraction optimizer exponent. In this work, we have developed an empirical formula for β by the use of acentric factors of pure RTILs:

$$\beta = a_1 + a_2\omega + a_3\omega^2 + a_4\omega^3,$$

Where:

$$a_1 = -1.7078$$

$$a_2 = 15.1522$$

$$a_3 = -42.1893.$$

$$a_4 = 40.4106$$

The coefficients a_1 - a_4 have been obtained using the experimental p - v - T data. In the present work, our purpose is determination of the parameters of intermolecular energy, a and the molecular size, b for RTILs, by applying the critical point constraints. This is clearly known that the critical parameters of RTILs are directly affected by intermolecular interactions.

3. Results and discussion

Our results showed that the calculated densities of ILs using the proposed equation of state were in a good agreement with experimental data from 40 to 600bar. In order to show how the modified perturbed hard-sphere EOS passes through the experimental points; typically, the deviation plots for the calculated high-pressure densities of RTILs including, 3-methyl-1-



propylpyridinium-bis(trifluoromethylsulfonyl)imide, [Prmpy][NTf₂], 1-butyl-1-methylpyrrolidinium-bis(trifluoromethylsulfonyl)imide, [Bmpyr][NTf₂] and 1-hexyl-3-methylimidazolium-bis(trifluoromethylsulfonyl)imide, [Hmim][NTf₂] are shown in Figures (1-2). This work showed that the modified equation of state previously used for ordinary fluids can be extended to mentioned-above RTILs.

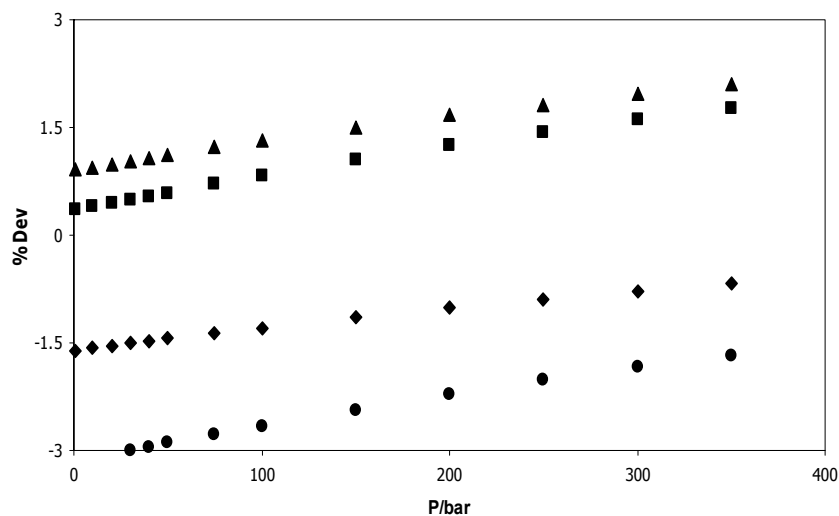


Fig. 1. Deviation plot for the predicted high-pressure densities of [Prmpy][NTf₂] using Eq. (2) at 353.15K (▲), 393.15K (■), [Bmpyr][NTf₂] at 293.15K (◆) and 393.15K (●) compared with the experiment [6].

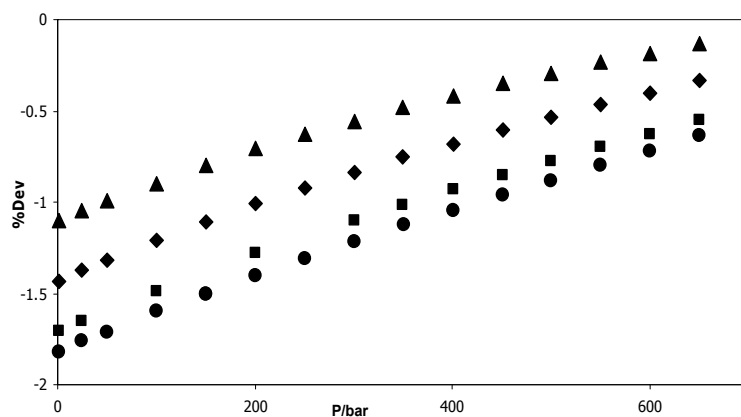


Fig. 2. Deviation plot for the predicted high-pressure densities of [Hmim][NTf₂] using Eq. (2) at 293.15 K (▲), 3313.15 K (◆), 328.15 K (■) and 338.15 K (●) compared with the experiment [7].

References

- [1] N.F. Carnahan, K.E. Starling, J. Chem. Phys. 51 (1969) 635.
- [2] A. Barker, D. Henderson, J. Chem. Phys. 47 (1967) 4714.
- [3] J. D. Weeks, D. Chandler, H. C. Andersen, J. Chem. Phys. 54 (1971) 5237.
- [4] F. L. Roman, A. Mulero, F. Cuadros, Phys. Chem.Chem Phys, 6 (2004) 5402.
- [5] H. Machida, Y. Sato, R. L. Smith Jr, Fluid Phase Equilibria. 264 (2008) 147.
- [6] R. L. Gardas, H. F. Costa, Mara. G. Freire, P. J. Carvalho, I. M. Marrucho, I. M. A. Fonseca, A. G. M. Ferreira, and J. A. P. Coutinho, J. Chem. Eng. Data. 53 (2008) 805.
- [7] R. Gomes de Azevedo, J. M. S. S. Esperanca, J. Szydlowski, Z.P. Visak a, P.F. Pires, H. J. R. Guedes, L.P.N. Rebelo, J. Chem. Thermodynamics. 37 (2005) 888.

**Selfdiffusion coefficient of liquid argon from generic van der Waals equation of state**

Seyed Ahmad Razavizadeh

Department of Chemistry, Payam Noor University, Jahrom Iran

(E-mail: razavi_zadeh@yahoo.com)**Keywords:** Equation of state, selfdiffusion, Generic van der Waals, Argon**1. Introduction**

Self-diffusion coefficients and mutual diffusion coefficients are basic transport coefficients, in terms of which other transport coefficients can be expressed. A typical example is the Stokes-Einstein [1] relation. Similar relations have been shown to hold for the bulk viscosities and thermal conductivities of monatomic and diatomic liquids [1]. Despite their importance in such phenomena the statistical mechanical theories of diffusion coefficients are not well developed at present and the only reliable alternative lies in molecular dynamics simulation methods [2]. Although free volume theories of diffusion have been around in literature[3-6] for a long time, the difficulty associated with defining the free volume in a rigorous and practical form and calculating it in a reliable accuracy by statistical mechanics has rendered them impractical to use for gaining molecular understanding of diffusion and relating them to experiment.

The Cohen-Turnbull (CT) theory [6] is a free volume theory that yields the self-diffusion coefficient D of a simple liquid in the form:

$$D = g\alpha(v)\bar{c} \exp[-\alpha v^* / v_f] \quad (1)$$

where v_f is the free volume per molecule, v^* is a critical volume just large enough to allow another molecule to move in, g denoting the geometric factor, $\alpha(v)$ a quantity that is roughly the diameter of the cage created in the liquid, and \bar{c} is the mean gas kinetic speed. The meaning of αv^* clearly must be that it is closely related to the minimum free volume into which a particle can make transition so as to accomplish diffusion.

2. Method

In the present work, we propose to take the hard sphere Chapman-Enskog selfdiffusion coefficient [7] D_{hs}^0 in place of the product $g\alpha(v)\bar{c}$. The Chapman-Enskog formula for D_{hs}^0 is given by

$$D_{hs}^0 = 1.019 \frac{3}{8\rho\sigma^2} \sqrt{\frac{k_B T}{\pi m}} \quad (2)$$

If the free volume of a fluid of N molecules contained in volume V is denoted by V_f , then the free volume per molecule is given by :

$$v_f = \frac{V_f}{N} \quad (3)$$

In the model of fluids represented by the generic van der Waals equation of state [8]

$$(p + A\rho^2)(1 - B\rho) = \rho\beta^{-1} \quad (4)$$

the excluded volume of N molecules is given by the generic van der Waals parameter NB , and thus

$$v_f = \frac{V_f}{N} = \frac{V - NB}{N} = v - B = v(1 - B\rho) \quad (5)$$

On substitution of the formula for B , it follows that

$$v_f(\eta, T) = v(1 - v_0 B_c^* [b_0(t) + b_1(y - z_s) + b_2(y - z_s)^2 + B_{na}(t, y - z_s)]) \quad (6)$$

where $b_0(t)$, $b_1(t)$ and $b_2(t)$ are temperature dependence parameters, B_{na} is nonanalytical part of equation of state and $v_0 = \pi\sigma^3/6$.

Then the free volume is reduced by $v^* = v_0$ in the present calculation. Therefore the self-diffusion coefficient is given by the formula



$$D = \frac{3}{8\sigma^2\rho} \sqrt{\frac{k_B T}{\pi m}} \exp\left(-\frac{\alpha v_0 \rho}{(1 - v_0 B_c^* [b_0(t) + b_1(y - z_s) + b_2(y - z_s)^2 + B_{na}(t, y - z_s)])}\right) \quad (7)$$

3. Results and discussion

The results are compared with the temperature and density dependency of argon that measured by Naghizadeh and Rice [9] in Figs. 1a and 1b, where the symbols (Δ) are experimental data and the symbols (\bullet) are the theoretical result computed with Eqs. (7). For this set of self-diffusion coefficients we choose $\alpha = 1.5$.

The temperature dependence of the calculated self-diffusion coefficient gives a good agreement with the available data.

4. Conclusions

In this work we have also presented a method of calculating self-diffusion coefficients of simple liquids that combines the Cohen–Turnbull theory of self-diffusion and the free volume expression provided by the generic van der Waals equation of state, which unambiguously suggests the free volume as a function of density and temperature that is required by the Cohen–Turnbull theory. Therefore the present method may be regarded as an example of applying the generic van der Waals equation of state to some practical problems. The free volume theory of self-diffusion, which, although simple in its basic physical concept, is difficult to apply in practice because the free volume is difficult to calculate unambiguously from the statistical mechanical viewpoint. Here we have overcome that difficulty with the help of the generic van der Waals equation of state. Since the generic van der Waals equation of state is valid for any state of matter consisting of spherical molecules, which includes the subcritical region of density and temperature, the method presented here, although containing an adjustable parameter, provides a useful and practical theoretical tool to calculate the transport coefficients of liquids, such as bulk and shear viscosity and thermal conductivity in such states, since such transport coefficients can be expressed in terms of the selfdiffusion coefficient of the liquids.

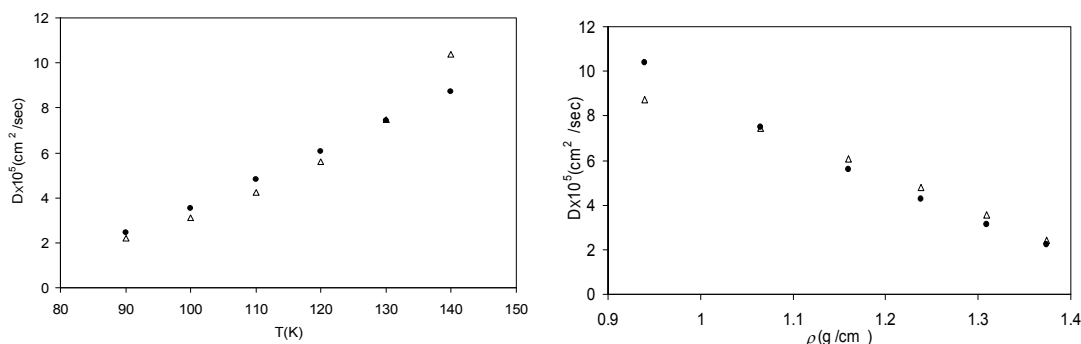


Fig.1. a) Temperature dependence b) Density dependence of the self-diffusion coefficient of liquid argon along the liquid curve ($\alpha = 1.5$). The symbols (\bullet) are the theoretical result of generic van der Waals equation and the symbols (Δ) are experimental data from Ref. 9.

References

1. K. Rah and B. C. Eu, Phys. Rev. Lett. 83 (1999) 4566.
2. M. P. Allen and D. J. Tildesley, Computer Simulation of Liquids, Clarendon, Oxford, 1987.
3. A. J. Batschinsky, Z. Phys. Chem. 84 (1913) 644.
4. H. Eyring, J. Chem. Phys. 4 (1936) 283.
5. A. K. Doolittle, J. Appl. Phys. 22 (1951) 1471.
6. M. H. Cohen and D. Turnbull, J. Chem. Phys. 31 (1959) 1164.
7. S. Chapman and T. G. Cowling, The Mathematical Theory of Nonuniform Gases, 3rd ed. Cambridge University Press, London, 1970.
8. B. C. Eu and K. Rah, Phys. Rev. E, 63, (2001) 031203.
9. J. Naghizadeh and S. A. Rice, J. Chem. Phys. 36 (1962) 2710.



Determination of thermodynamic properties of binary and ternary mixtures of {1-butanol (1) + cyclohexylamine (2) + *n*-heptane (3)} at different temperatures: Experimental results and application of the Flory theory.

Hossein Iloukhani^a, Mahdi Rezaei-Sameti^b, Mahdi Rakhshi^a

a. Faculty of Chemistry, University of Bu Ali Sina, Hamadan, Iran

b. Department of Chemistry, Faculty of Science, Malayer University, Malayer, Iran

(E-mail: mahdirakhshi.chem@gmail.com)

Keywords: Thermal expansion coefficients; Excess thermal expansion coefficients; Isothermal Coefficient of pressure excess molar enthalpy; Flory theory

1. Introduction

Thermal expansion coefficients α , and their excess values α^E , and isothermal coefficient of pressure excess molar enthalpy $(\partial H_m^E / \partial P)_{T,x}$, of the binary and ternary mixtures formed by 1-butanol + cyclohexylamine + *n*-heptane were measured at (288.15, 293.15, 298.15, 303.15, 308.15, 313.15, 318.15 and 323.15) K for the liquid region and at ambient pressure. The thermal expansion coefficients α , and their excess values α^E , and isothermal coefficient of pressure excess molar enthalpy $(\partial H_m^E / \partial P)_{T,x}$, were calculated from experimental densities. The excess thermal expansion coefficients and isothermal coefficient of pressure excess molar enthalpy were correlated as a function of the mole fraction by using the Redlich–Kister [1,2] equation for binary and, Cibulka [1,2], Jasinski and Malanowski [1-3], Singe *et al* [1-3], Pintos *et al* [1-3], Calvo *et al* [1-3], Kohler [1], and Jacob - Fitzner [1-3] for ternary mixture, respectively. The parameters a_i for the pure components are listed Table 1.

2. Methods

In this work for predicted the experimental and other thermodynamic parameters we used the flory model [4].

The Flory model has been commonly employed to analyse the molar volume of the mixture and the excess molar volume parting from the equation of the state in function of the reduced variables:

$$\frac{\tilde{P}\tilde{v}}{\tilde{T}} = \left[\frac{\tilde{v}^{\frac{1}{3}}}{\tilde{v}^{\frac{1}{3}} - 1} \right] - \left[\frac{1}{\tilde{v}\tilde{T}} \right] \quad (1) \quad \text{Where} \quad \tilde{v} = \frac{V}{V^*} = \left[\frac{1 + (\frac{4}{3})\alpha T}{(1 + \alpha T)} \right]^3 \quad (2)$$

$$\tilde{T} = \frac{T}{T^*} = \left[\frac{\tilde{v}^{\frac{1}{3}} - 1}{(\tilde{v}^{\frac{4}{3}})} \right] \quad (3)$$

Theoretical values of $\left[\frac{\partial V_m^E}{\partial T} \right]$ were calculated from the Flory theory using :

$$T \left[\frac{\partial V_m^E}{\partial T} \right] = \left[\sum_{i=1}^2 x_i V_i^* \left[\tilde{T} \left(\frac{\partial \tilde{v}}{\partial T} \right) \right] - \left[\sum_{i=1}^2 x_i V_i^* \left(\tilde{T} \left(\frac{\partial \tilde{v}}{\partial T} \right) \right) \right]_i \right] \quad (4) \quad \text{where} \quad \tilde{T} \left[\frac{\partial \tilde{v}}{\partial T} \right] = \left[\frac{\tilde{v}(1 - \tilde{v}^{\frac{1}{3}})}{[(\frac{4}{3})\tilde{v}^{\frac{1}{3}} - 1]} \right] \quad (5)$$

3. Results and discussion

In the present study the value of the reduced volume for the liquids and their mixtures \tilde{v} was determined for α values of the mixtures using the (5). The excess function $\left[\frac{\partial V_m^E}{\partial T} \right]$ was computed by analytical differentiation of (2) at (288.15 K to 323.15

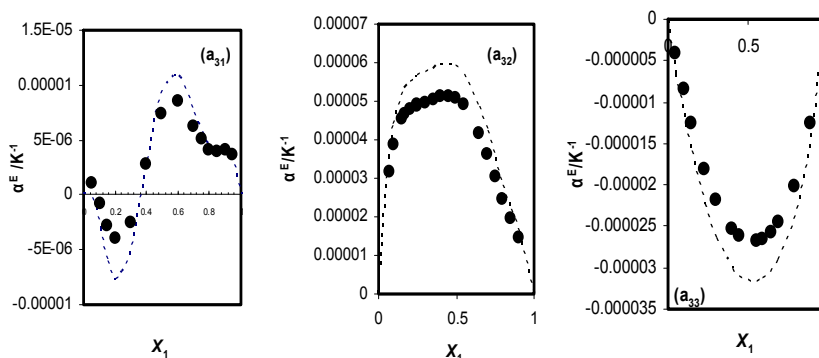
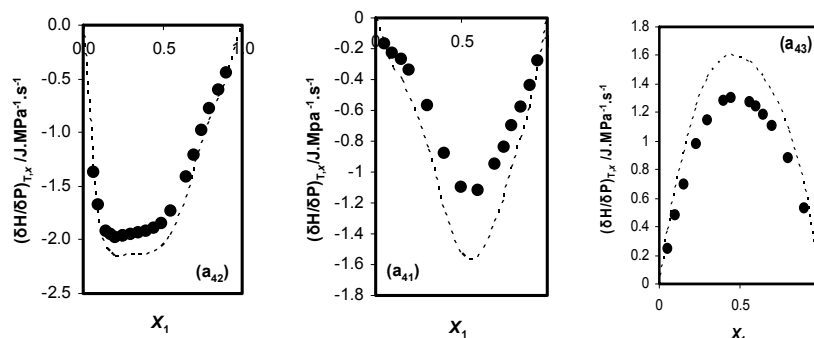
K) and V_m^E of this work we have also obtained isothermal coefficient of pressure excess molar enthalpy, $(\partial H_m^E / \partial P)_{T,x}$, and excess thermal expansions coefficient α^E . The comparison between experimental and theoretical values are graphically represented in Fig 1 (a_{31} to a_{33}) and Fig 2 (a_{41} to a_{43}). The obtained results show a good agreement between theory and experimental data. The flory parameters for pure components at different temperatures are given in Table 2.

Table 1. Coefficients a_i for the Fits of the Pure Components Densities in the Temperature Range (288.15K to 323.15K).

component	a_0	a_1	a_2	a_3	a_4
1-butanol	-0.390335999	0.0181684339410800	-0.0000948327669	$2.12121414 \times 10^{-7}$	$-1.78787878859 \times 10^{-7}$
cyclohexylamine	1.65606953592	-0.00768080896	0.0000328931141446	$-7.10385858 \times 10^{-8}$	$5.7575757591 \times 10^{-11}$
<i>n</i> -heptane	1.71227192743994	-0.011121198396131	0.000050275516654	$-1.0823464 \times 10^{-7}$	$8.63636363558 \times 10^{-11}$

Table 2. Flory and related parameters of pure components at different temperature

	T/K	$10^4 a/K^{-1}$	$\rho/g \cdot cm^{-3}$	$mol^{-1} / (cm^3 \cdot V^*)$	$/ K^{-1} T^*$	\tilde{v}	\tilde{T}
1-Butanol	288.15	9.298	0.813373	74.2960	5423.6663	1.2265	0.0531
	323.15	10.201	0.786238	74.2902	5424.4009	1.2690	0.0596
Cyclohexylamine	288.15	10.439	0.871290	91.0995	5080.0630	1.2495	0.0567
	323.15	10.782	0.839547	92.2011	5271.9498	1.2813	0.0613
<i>n</i> -Heptane	288.15	12.249	0.687954	113.4265	4670.3564	1.2842	0.0617
	323.15	13.349	0.657896	114.2979	4763.044	1.3326	0.0678


Fig.1. Plot of excess thermal expansion coefficients α^E , against mole fraction for $\{(a_{31}); 1\text{-butanol} + \text{cyclohexylamine}, (a_{32}); 1\text{-butanol} + n\text{-heptane}, (a_{33}); \text{cyclohexylamine} + n\text{-heptane}\}$ 323.15 K. (●) Experimental; (.....) calculated by using Flory theory.

Fig.2. Plot of isothermal coefficient of pressure excess molar enthalpy $(\partial H_m^E / \partial P)_{T,x}$, against mole fraction for $\{(a_{41}); 1\text{-butanol} + \text{cyclohexylamine}, (a_{42}); 1\text{-butanol} + n\text{-heptane}, (a_{43}); \text{cyclohexylamine} + n\text{-heptane}\}$ 323.15 K. (●) Experimental; (.....) calculated by using Flory theory.

References

- [1] M.Rezaei-Sameti, H.Iloukhani, M. Rakhshi, *J. Mol. Liq.* 149, (2009) 96.
- [2] H. Iloukhani, M. Rakhshi, *J. Mol. Liq.* 149, (2009) 86.
- [3] M. L. Kijevcanin *Thermochim. Acta* (2009) in press.
- [4] P.J. Flory, *J. Am. Chem. Soc.* 87 (1965) 1833.



Densities and volumetric properties of (*n*-butyl acetate + 1-butanol + 1,2-butanediol) binary and ternary mixtures from T = (298.15 to 308.15) K. theoretical and experimental study.

Hossein Iloukhani^a, Mahdi Rezaei-Sameti^b, Mahdi Rakhshi ^a

a. Faculty of Chemistry, University of Bu Ali Sina, Hamadan, Iran

b. Department of Chemistry, Faculty of Science, Malayer University, Malayer, Iran

(E-mail: mahdirakhshi.chem@gmail.com)

Keywords: Excess molar volume; *n*-butylacetate; 1-butanol ; 1,2-butanediol ; Molecular interactions

1. Introduction

This paper, as part of a continuing study in our laboratory [1–3], presents experimental densities for the ternary system formed by { *n*-butylacetate (1)+ 1-butanol (2) + 1,2-butanediol (3)}, and constituted binary mixtures. Experimental data for these properties allow us to test various fitting and predictive equations appearing in the literature. As computer design of chemical properties requires mathematical models to predict or describe transport properties of pure liquids and their mixtures over the entire range of composition engineering. The excess properties are analyzed because of their importance for inferring which type of interactions predominates in liquid mixtures.

2. Experimental

The density of the compounds and their binary and ternary mixtures were measured with Anton Paar DMA 4500 oscillating U-tube densitometer, operated in the static mode and the uncertainties were estimated to be within $\pm 1 \cdot 10^{-5} \text{ g} \cdot \text{cm}^{-3}$. The temperature in the cell was regulated to $\pm 0.01 \text{ K}$ with solid-state thermostat. The apparatus was calibrated once a day with dry air and double-distilled freshly degassed water. All the weightings were performed on an electronic balance (AB 204-N Mettler) accurate to 0.1 mg. The uncertainty in the mole fraction is estimated to be lower than $\pm 2 \cdot 10^{-4}$.

3. Results and discussion

Densities, and excess molar volume of the binary and ternary mixtures formed by *n*-butylacetate + 1-butanol + 1,2-butanediol were measured at (298.15, 303.15, and 308.15) K for the liquid region and at ambient pressure (81.5) k Pa, for the whole composition range.

The excess molar volumes, V_m^E , of the binary and ternary mixtures were calculated from the densities using the following equation:

$$V_m^E (\text{cm}^3 \cdot \text{mol}^{-1}) = \sum_{i=1}^n \frac{x_i M_i}{\rho} - \sum_{i=1}^n \frac{x_i M_i}{\rho_i} \quad (1)$$

where n is the number of components, x_i is the mole fraction of component i in the mixture, M_i its molecular weight, and ρ and ρ_i are the measured densities of the mixture, and the pure component, respectively.

The excess molar volumes are positive over the mole fraction range for binary mixtures of *n*-butylacetate (1) + 1-butanol (2) and *n*-butylacetate (2) + 1,2-butanediol (3) and increase with increasing temperatures from (298.15 to 308.15)K. The excess molar volumes of 1-butanol (1) + 1,2-butanediol (3) are negative and decrease with increasing temperatures from (298.15 to 308.15)K. The experimental data of constitute were correlated as a function of the mole fraction by using the Redlich–Kister equation for binary. The parameters M_{pq} for the binary mixture are listed in Table 1, along with the standard deviation σ .

Excess molar volumes of ternary mixture {*n*-butylacetate (1) + 1-butanol (2) + 1, 2-butanediol (3)} were calculated from experimental densities. Although prediction of the physical properties of multicomponent mixtures from those of their pure components is generally unreliable because of mixing effects, numerous schemes have been put forward for predictions based on the properties of the binary systems formed by pairs of components of the multicomponent system. In this work, we applied the following models: Cibulka, Jasinski and Malanowski, Singe *et al*, Pintos *et al*, Calvo *et al*.

In each case, the optimum number of coefficients was ascertained from an examination of the variation of standard deviation σ (Y) with

$$\sigma(Y) = \left[\frac{\sum (Y_{\text{mexp},i}^E - Y_{\text{mcal},i}^E)^2}{(n-p)} \right]^{1/2} \quad (2)$$

Where n and p are the number of experimental points and number of parameters retained in the respective equation.



Results show that the Jasiński model is suitable than other models.

The excess partial molar volumes ($\bar{V}_{m,i}^E$) for this system can be determined from excess molar volume data using:

$$V_i^E = V_m^E + (1 - x_i) \left(\frac{\partial V_m^E}{\partial x_i} \right)_{x_i, p, T} \quad (3)$$

The results graphically represented in Fig1.

Table1. Coefficients M_{pq} and standard deviations for the fits of the binary excess molar volumes in the temperatures range (298.15, 303.15, and 308.15) K.

	ρ					σ
q	0	1	2	3	4	
	{ <i>n</i> -butylacetate (1) + 1-butanol(2)}					
0	-130.056	0.84082	-0.0013	29.6942	-0.2009	0.001
1	0.00034	426.867	-2.8349	0.0047	21.4267	
2	-0.13791	0.0002	598.642	-3.9195	0.0064	
	{ <i>n</i> -butylacetate (1) + 1,2-butanediol (2) }					
0	-288.696	1.8665	-0.003	-265.684	1.7313	0.004
1	-0.0028	333.913	-2.195	0.00361101	902.753	
2	-5.9821	0.00991	972.418	-6.4119	0.0106	
	{ 1-butanol (1) + 1,2-butanediol(2) }					
0	77.0491	-0.5121	0.00084	-184.92	1.22026	0.0012
1	-0.00201	90.4656	-0.5992	0.00098	354.682	
2	-2.3414	0.0039	-35.6407	0.2355	-0.0004	

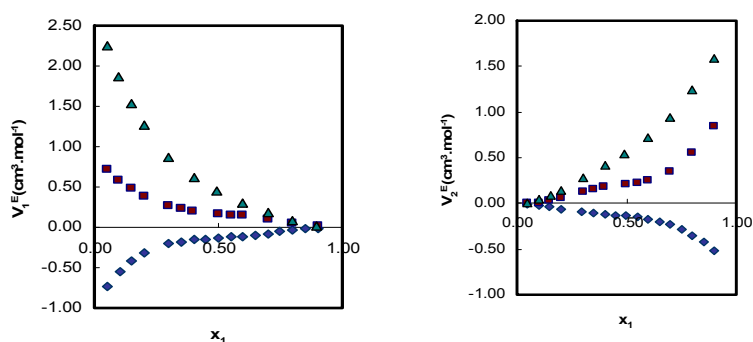


Fig.1. Plot of: Excess partial molar volumes against mole fraction for {(▲) *n*-butylacetate (1) + 1,2-butanediol (2), (■) *n*-butylacetate (1) + 1-butanol (2), (◆) 1-butanol (1) + 1,2-butanediol (2)} at $T = 303.15$ K.

References

- [1] M.Rezaei-Sameti, H.Iloukhani, *Monatsh Chem.*, **140**, (2009) 451.
- [2] M.Rezaei-Sameti, H.Iloukhani, M. Rakhshi, *J. Mol. Liq.* **149**, (2009) 96.
- [3] H. Iloukhani, M. Rakhshi, *J. Mol. Liq.* **149**, (2009) 86.



Electrochemical determination of ionic products of 50% (v/v) water-methanol electrolyte solutions and ionic strength effect

Ali Farajtabar^{a*} and Farrokh Gharib^b

a. Young Researchers Club, Islamic Azad University, Babol branch, Babol, Iran

b. Department of Chemistry, Shahid Beheshti University, Tehran, Evin, Iran

(E-mail: a_farajtabar@yahoo.com)

Keywords: Water-methanol mixture solvent, Ionic product constants, Ionic strength effect, SIT model

1. Introduction

The mixed aqueous organic solvents such as water-methanol mixtures are widely used in different area of chemistry such as evaluation of acidity constants of poor solubility and drug substances [1,2]. Some of nonaqueous and mixed aqueous organic solvents have a larger pH scale and a better ability to dissolve more compounds than water. Therefore, they are utilized as reaction media for a variety of organic and analytical processes such as synthesis, titrations or liquid chromatographic separations. The application of mixed aqueous organic solvents in physicochemical investigations needs an understanding of the ionic product constants that indicate the conditions for acids-base titrations to a great extent so that these constants determine the length of the pH scale of mixed solvent [3]. Potentiometry is a useful and reliable method to determine ionic product constants of different solvents. The influence of ionic strength on equilibrium constants such as ionic product constants has been intensively studied but Equilibrium constants measured in constant ionic media are conditional and valid only in the ionic strength in which they were determined. So it is necessary to have a model for correlation between equilibrium constant and ionic strength of media based on estimation of the activity coefficients of species including in equilibrium reaction. In the next step model extrapolated to zero ionic strength to calculation of thermodynamic equilibrium constant. The expression of activity coefficients can be obtained by the Debye-Huckel theory which takes into account long range electrostatic interactions and therefore dominates in dilute solutions. However a suitable model has to take into consideration short range and non electrostatic interactions in higher concentrated solution. The popular model is Specific Interaction Theory (SIT) [4, 5] which requires only one parameter to perform calculations of activity coefficients influence of macroscopic and microscopic solvent properties on it.

2. Methods

All mixtures were prepared by volume and concentrations of HCl and NaOH in these were 0.01 M and 0.1 M respectively. Potentiometric measurements carried out in a double-walled thermostated reaction vessel at 25 °C and ionic strength of mixtures was maintained with sodium perchlorate. A Jenway research potentiometer, model 3520, with a combined pH electrode was used for e.m.f measurement in potentiometric titrations of acidic solution mixtures. For each experiment, into double-walled reaction vessel, 2 ml of stock solution of hydrochloric acid, required amount of methanol and sodium perchlorate was diluted with double-distilled water to 20 ml. The vessel solution was titrated with small addition of the sodium hydroxide solution with same proportion of methanol and the same ionic strength. E.m.f readings of solution were taken after every addition of titrant when stabilization of solution potential was achieved. This stabilization criterion was 0.2 mV within at least 2 min. E.m.f data versus added volume of titrant in both acidic and basic region of titration were used for the determination of ionic product constants of water-methanol electrolyte mixtures.

3. Results and discussion

To obtain the thermodynamic ionic product constants, we applied the specific ion interaction theory model, SIT [4, 5]. According to SIT model, formation constants may be expressed as

$$\log \beta_m = \log \beta^\circ - Z^+ d + F(\epsilon, I_m) \quad (1)$$

where β_m is the molal formation constant, β° is the thermodynamic formation constant, d is the Debye-Huckel term, $[0.509 I_m^{1/2} / (1 + 1.5 I_m^{1/2})]$, I_m is ionic strength in molality, and $F(\epsilon, I_m)$ is a linear term dependent on ionic strength and



interaction coefficients, usually called SIT parameter. For the species involving in equilibrium reaction the SIT parameters in the supporting electrolyte, NaClO_4 , assumes the form [4, 5]

$$F(\varepsilon, I_m) = I_m[\varepsilon(\text{H}^+, \text{ClO}_4^-)] \quad (2)$$

$$F(\varepsilon, I_m) = I_m[\varepsilon(\text{OH}^-, \text{Na}^+)] \quad (3)$$

The concentrations of the ions of the ionic medium are usually very much larger than those of the reacting species. Hence, the ionic medium ions will make the main contribution to the value of ε for the reacting ions. The ion interaction coefficients assume to be zero for ions of the same charge sign and for uncharged species with the supporting electrolyte, but the activity coefficient can be obtained from the well-known relationship, $\log \gamma = \lambda I$, and therefore $\varepsilon(\text{uncharged species, supporting electrolyte}) \equiv \lambda$.

4. Conclusions

Main conclusions of this work are as follows

- (i) The use of the combined glass electrode for potentiometric determination of ionic product constants in 50% water-methanol cosolvents over the ionic strength of 0.1 to 2 M of NaClO_4 as electrolyte media.
- (ii) The dependence of ionic product constants on ionic strength can be investigated by SIT model and used in the ranges $0 < I < 2 \text{ M NaClO}_4$ as electrolyte salt.

References

- [1] L. Z. Benet, J. E. Goyan, J. Pharm. Soc. 56 (1967) 665.
- [2] A. Albert, E. P. Serjeant, The Determination of Ionization Constants, Chapman and Hall, London, 1984.
- [3] E. P. Serjeant, Potentiometry and Potentiometric Titrations, Wiley, New York, 1984.
- [4] I. Grenthe, J. Fuger, R. J. M. Konings, R. J. Lemire, A. B. Muller, C. Nguyen-Trung, H. Wanner, Chemical Thermodynamics of Uranium, North-Holland Elsevier Science Publishers, 1992.
- [5] F. Gharib, A. Farajtabar, J. Mol. Liquid. 135 (2007) 27.



Vapor–liquid equilibria, density and speed of sound of aqueous di-potassium oxalate solutions at different temperatures

M.T. Zafarani-Moattar^a, S. Davoodi^a

a. Department of Chemistry, University of Tabriz, Tabriz, Iran

(E-mail: nidavoodi2664@yahoo.com)

Keywords: density, water activity, speed of sound, isopiestic.

1. Introduction

The vapor–liquid equilibria, density, and speed of sound of aqueous dipotassium oxalate solution at different temperatures have been measured. From the measurements of water activity by isopiestic method, values of the vapor pressure of solutions were determined. The experimental vapor–liquid equilibria data were correlated with the Pitzer equation. The experimental density and speed of sound data for dipotassium oxalate were used to obtain apparent molar volume values at different temperatures, and these data were satisfactorily fitted to the corresponding Pitzer equations.

Oxalate ions in aqueous solutions are of considerable significance in many chemical processes. Viscosities of oxalic acid and its salts in water and binary aqueous mixtures of tetrahydrofuran at different temperatures have been measured [1]. However, with respect to other thermodynamic or transport properties of oxalate salts, little information can be found in the literature. In this work, vapor–liquid equilibria, density, and speed of sound measurements were performed from dilute up to near saturation, and to calculate accurate limiting apparent volumes and compressibilities, enough data were obtained in the dilute region (below 0.1 mol · kg⁻¹) at different temperatures.

2. Methods

In this study, the isopiestic method is used to obtain the activity of water and the osmotic coefficient in an aqueous dipotassium oxalate system at $T = (298.15, 308.15, \text{ and } 318.15) \text{ K}$. The isopiestic apparatus used in this work was similar to the one used by Ochs et al [2]. This apparatus consisted of a five-leg manifold attached to round-bottom flasks. Two flasks contained the standard pure NaCl solutions; two flasks contained dipotassium tartrate solutions; and the central flask was used as a water reservoir. The apparatus was kept in a constant temperature bath for at least 120 h to achieve equilibrium. The temperature was controlled to within $\pm 0.005 \text{ K}$ by a Heto temperature controller (Heto therm PF, Heto Laboratory Equipment, Denmark). After equilibrium, the manifold assembly was removed from the bath, and each flask was weighed by an analytical balance (Shimadzu, 321-34553, Shimadzu Co., Japan) with an uncertainty of $\pm 1 \cdot 10^{-7} \text{ kg}$. From the weight of each flask and the initial weight of salt, the mass fraction of each solution was calculated. The water activity for the standard aqueous NaCl solutions at different concentrations and temperatures has been calculated from the correlation of Colin et al [3]. The uncertainty in the measurement of water activity was estimated to be ± 0.0002 . Densities and speed of sounds were measured with a vibrating-tube densimeter (Antoine Parr DSA-500, Austria). The apparatus was calibrated at each temperature with double-distilled-deionized water and dry air. The apparatus was also tested with the density of a known molality of aqueous NaCl using the data given by Pitzer et al [4].

3. Results and discussion

Isopiestic equilibrium molalities with reference standard solutions of NaCl in water enabled the calculation of the osmotic coefficient, Φ , of the solutions of dipotassium oxalate in water from

$$\phi = \frac{\nu^* \phi^* m^*}{\nu m_i} \quad (1)$$

where ν^* and ν are the sum of stoichiometric numbers of the anion and cation in the reference solution and the solution of dipotassium oxalate, respectively; m_i is the molality of the dipotassium oxalate solution; m^* is the molality of the reference standard in isopiestic equilibrium with this solution; and ϕ^* is the osmotic coefficient of the isopiestic reference standard, calculated at m^* . The necessary ϕ^* values at any m^* at different temperatures were calculated from the correlation given by Colin et al [3]. From the calculated osmotic coefficient data, the activity of water in dipotassium solution and the vapor pressure of this solution were determined at isopiestic equilibrium molalities, with the help of the following relation



$$\varphi = -\frac{\ln a_s}{vm_1M_2} \quad (2)$$

$$\ln a_s = \ln\left(\frac{p}{p^*}\right) + \frac{(B - V_s^*)(p - p^*)}{RT} \quad (3)$$

Where a_s is the activity of water; M_2 is the molar mass of the water; and B is the second virial coefficient of water vapor. V_s^* is the molar volume, and p^* is the vapor pressure of pure water. The second virial coefficients of water vapor at each working temperature were calculated using the equation provided by Rard and Platford [5]. Molar volumes of liquid water were calculated using the density of water at different temperatures [6]. The vapor pressures of pure water were calculated using the equation of state of Saul and Wagner[7]. After the establishment of isopiestic equilibrium, water activities were calculated using eq 2.

Volumetric and Isentropic Compressibility Results. The molar volumes V_ϕ of aqueous dipotassium oxalate solutions were calculated from the densities of the solutions d using the following equation

$$V_\phi = \frac{M_1}{d} - \frac{(d - d_0)}{m_1 dd_0} \quad (4)$$

where M_1 is the molar mass of dipotassium salt.

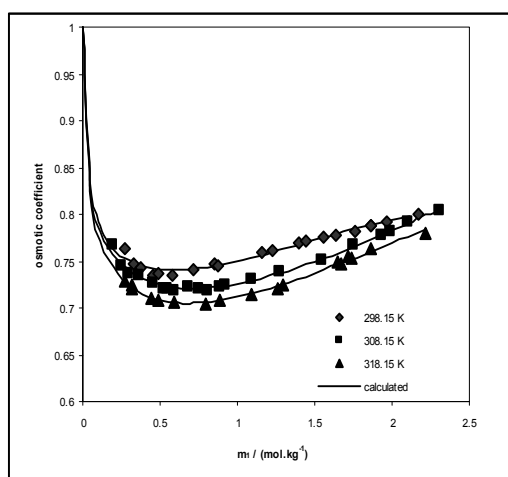


Fig.1. Experimental and calculated osmotic coefficient, plotted against molality of salt, m_1 , for the potassium oxalate (1) + H₂O (2) system studied with the Pitzer model.

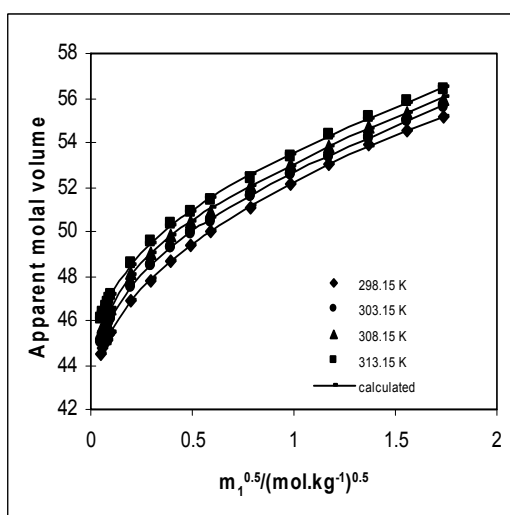


Fig.2. Experimental and calculated apparent molar volume, plotted against root of molality of salt, for the potassium oxalate+H₂O (2) System studied with the Pitzer model.

4. Conclusion

The accurate osmotic coefficient data measured at $T = (298.15, 308.15, \text{ and } 318.15) \text{ K}$ for aqueous dipotassium oxalate solutions were fitted satisfactorily to the Pitzer model. The apparent molar volumes and apparent molar compressibilities were calculated from the measured density and speed of sound data at $T = (298.15, 303.15, 308.15, \text{ and } 313.15) \text{ K}$, and these data were also fitted to the corresponding Pitzer equation with good accuracy.

References

- [1] Parmar, M. L. Guleria, M. K. Indian, J. Chem. Sci , 117 (2005) 351.
- [2] Ochs, L. R. Kabiri-Badr, M. Cabezas, H. AIChE J. 36 (1990) 1908.
- [3] Colin, E. Clarke, W. Glew, D. N. J. Phys. Chem. Ref. Data. 14 (1985) 489.
- [4] Pitzer, K. S. Peiper, J. C. Busey, R. H. J. Phys. Chem. Ref. Data. 13 (1984) 1.
- [5] Rard, J. A. Platford, R. F. Pitzer, K. S. ActaVity coefficients in electrolyte solutions. (1991) 209.
- [6] Kell, G. S. J. Chem. Eng. Data. 20 (1975) 97.
- [7] Saul, A. Wagner, W. J. Phys. Chem. Ref. Data. 16 (1987) 893.



Isotherm, kinetic and thermodynamic studies of eosin Y dye biosorption in aqueous solution by *Saccharomyces cerevisiae*

Maryam Tavasolli , Nader Bahramifar , Ferydoon Ashrafi

Department of chemistry, Payam Noor University (PNU) of sari unit, Mazandaran, Iran

(E-mail: maryam 5888@Yahoo. Com)

Keywords: Biosorption, Eosin Y, Isotherm, Kinetics, Thermodynamic, *Saccharomyces cerevisiae*

1. Introduction

Dyes are widely used in textile, paper and printing industries today, and the treatment of dye-containing wastewaters is one of the most difficult problems to be solved. Generally dyes are stable to light, heat and oxidizing agents, and are usually biologically non-degradable [1]. Eosin Y, coal tar xanthene dye, which used extensively in the perinting and dyeing industries was chosen as the model anionic dye to avoid environmental hazards during investigation, as this dye is not specifically listed as toxic by different health agencies [2]. Conventionally, chemical coagulation, ozonation and adsorption, etc. are all means used for the removal of dye stuffs. Although they can remove dyes partially, their initial investment and operational costs are so high that they can be widely used in dyeing and finishing industries, especially in developing countries [3]. Activated carbon has been extensively studied and might be the most widely used adsorbent for the treatment of color effluents in the past few years. However, due to its high price, activated carbon could not be used in developing countries [4]. Therefore biosorption, using biomaterials such as bacteria, fungi, yeast and algae, is regarded as a cost – effective biotechnology for treatment of wastewaters containing dyes. Among the promising biosorbents for heavy metal and dyes removal which have been researched during the past decades, *Saccharomyces cerevisiae* has received increasing attention due to the unique nature in spite of its mediocre capacity for metal and dye uptake. Compared with other fungi. *S. cerevisiae* is widely used in beverage production, is easily cultivated using cheap media, is also a by-product in large quantity as a waste of the fermentation industry, and is easily manipulated at molecular level [5]. In the present study, biosorption techniques are employed for removal of eosin Y by *S. Cerevisiae* yeast from aqueous solution. The effects of temperature, pH, initial dye concentration and sorbent dosage on biosorption investigated. Moreover, the biosorption isotherms, kinetics and thermodynamic were also explored. This work could provide useful information for the selection of cost- effective biosorbents as well as design and operation of biosorption systems for dye wastewater treatment.

2. Materials and method

S. cerevisiae was provided from Research and Technology Department of Ministry of Sciences (Persian Type Culture Collection) in the form of freeze dry, and then cultured in sterilized medium. The composition of growth medium was (grams per liter): glucose, 15; (NH₄)₂SO₄, 9; MgSO₄, 2.5; yeast extract, 1; KH₂PO₄, 1; K₂HPO₄, 0.2. The medium was sterilized by autoclaving at a pressure of 1.5 atm and temperature of 121°C for 20 min. The yeast cells were grown for 16 h and then filtered. Yeast biomass was deactivated by heating in an oven at 80°C for 24 h. The dried yeast was ground and screened through a sieve with 100 mesh. The pretreatment of the biosorbent was carried out with nonviable yeast cells in 700 g/l ethanol solution 20 min at room temperature. Then , it was centrifuged at 3600 rpm for 10 min and the ethanol solution was discarded. The ethanol washed biomass was rinsed several times with deionized water to remove excess ethanol and adsorbed nutrient ions. The rinsed yeast was again centrifuged and remaining biomass was dried at 70°C for 12 h. The dried cells were ground and screened as mentioned above. Adsorption experiments were conducted using 150 ml aqueous solution of eosin Y (100 mg/l) were taken in 250-ml Erlenmeyer flask. The pH of dye solution adjusted to 4.0. A fixed amount of *S. cerevisiae* (2.0 g/l) added to dye solution. The solution stirred with help of a stirrer at 600 rpm. All experiments were conducted at a fixed temperature (22 °C) , excluding the temperature experiment , where it was varied (15, 25, 35, 45 and 55 °C) . The sorbent dose was fixed at 2.0 g/l excluding the sorbent dosage experiment , where it was varied (0.5 , 0.75, 1.0 and 3.0 g/l). The initial dye concentration was fixed at 100 mg/l for all experiment excluding the initial concentration experiment, where it was varied (50 , 150, 200, 250, and 300) .The effect of pH on the biosorption rate was investigated in the pH rang of 2-9. Samples (5 ml) were removed from experimental flasks at times t=0, 5, 15, 25, 35, 60, 90, 120, 180, and 240 min. All samples were centrifuged at

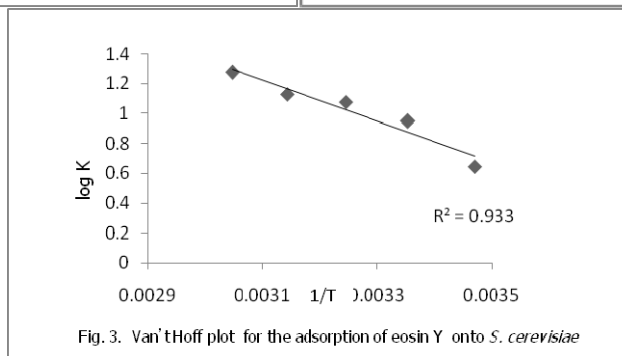
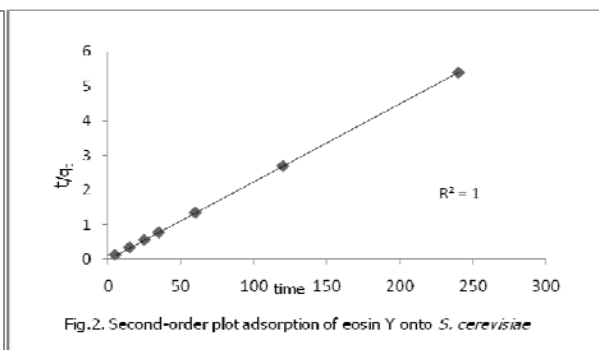
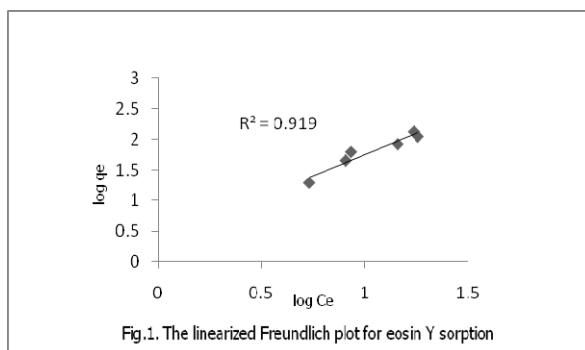


high speed (5000 rpm) for 5 min to remove particulates. The concentration of eosin Y was determined by GBC UV- Vis spectrophotometer (Cintra 20) at a wavelength of 510 nm.

3. Results and discussion

Adsorption of eosin Y on *S. cerevisiae* was studied in batch mode. The effects of various operating conditions, namely, pH, initial dye concentration, absorbent dose and temperature were investigated for the batch operation. The results showed that optimum initial pH for eosin Y was determined in pH=4.0. The minimum sorbent amount found to be sufficient to reach the total removal of the dye molecules from aqueous solution was 2.0 g/l.

Two well known models, namely the Langmuir and Freundlich models, are used analyze the experimental data. The Freundlich isotherm was found to be the most suitable for eosin Y adsorption on *S. cerevisiae*. The Freundlich isotherm indicates that the extent of heterogeneity of the surface of the adsorbent (Fig. 1). The kinetics of the adsorption of eosin Y on *S. cerevisiae* have been described by first and pseudo second-order models. The adsorption of eosin Y on *S. cerevisiae* is better represented by pseudo second – order kinetic model (Fig. 2). The biosorption capacity increased with an increase in temperature up to 55°C. The thermodynamic parameters ΔG° , ΔS° and ΔH° for this adsorption process have been determined (Fig. 3). The negative value of ΔG° and positive value of ΔH° were observed indicating the spontaneous and endothermic in nature, respectively. The positive value of ΔS° suggests increased randomness during adsorption.



4. Conclusions

The biosorption of *S. cerevisiae* were studied for eosin Y in this work. The results indicate that :

1. *S. cerevisiae* may be used as an inexpensive, effective and easily cultivable biosorbent for the removal of eosin Y from aqueous solutions.
2. Adsorption of the eosin Y on *S. cerevisiae* follows the Freundlich model.
3. The process is endothermic in nature. The highest efficiency of the adsorption process is observed at 55°C.
4. The sorption process is very fast initially, attains equilibrium within a few hours, and follow the second- order kinetic model.

References

- [1] Z. Aksu, Biochem. Eng. J. 7 (2001) 79–84.
- [2] M. K. Purkait, S. DasGupta, S. De, J. Environ.Manage. (2005) 135-142.
- [3] Z. Aksu, S. Tezer, Process Biochem. 36 (2000) 431–439.
- [4] M.S. El-Geundi, Water Res. 25 (1991) 271.
- [5] Jianlong Wang, Can Chen, Biotech Advanc. 24 (2006) 427-451.

**Complex formation of cerium(IV) ion with glycyl-glycine at different ionic strength**Farhoush Kiani, ^{a,*} Abbas Ali Rostami, ^b Sasan Sharifi, ^c and Farrokh Gharib ^d^a. Chemistry Department, Islamic Azad University, Ayatollah Amoli Branch, Amol, Iran^b. Physical and Inorganic Chemistry Department, Faculty of Chemistry, University of Mazandaran, Babolsar, Iran^c. Chemistry Department, Islamic Azad University, Arak Branch, Arak, Iran^d. Chemistry Department, Shahid Beheshti University, General Campus, Tehran, Evin, Iran**Keywords:** Stability Constants, Ionic Strength, Spectroscopy, Potentiometry**1. Introduction**

The interaction between amino acids, peptides, and proteins with metal ions plays an important role in biochemistry and biology and has been studied extensively during the last three decades. Complexes of amino acids and oligopeptides are involved in the exchange and transport mechanism of some trace metal ions in the human body. ¹ Oligopeptides have proved to be the most useful model compounds for such studies since they are able to mimic to a great extent the metal ion binding site of much more complicated protein molecules. ² The cerium(IV) ion readily reacts with in vivo amino acids, peptides, nucleic acids, proteins etc. to form stable complexes which are distributed in the body, primarily in the liver, bone, lung and kidneys. ³ Thus, the investigation of the pathway of cerium from agricultural products → animals → humans is particularly important as far as the radiological protection of the general population is concerned. In view of the above, the present work reports a study of cerium(IV) complexes by glycyl-glycine and as well as the protonation equilibria of the peptides at 25 °C and different ionic strength (from 0.02 to 0.15 mol dm⁻³ NaClO₄).

2. Experimental

Chemicals. All the chemicals used were of analytical reagent grade. Glycyl-glycine (C₄H₈N₂O₃), gly gly, was obtained from merck. The aqueous stock solution of the peptide was freshly prepared daily. The NaOH solution was prepared from a titrisol solution (Merck) and its concentration was determined by several titrations with standard HCl. Perchloric acid and ceric ammonium sulfate dihydrate were from Fluka and were used without further purification. Sodium perchlorate was purchased from Merck and was kept in a vacuum at least 72 hours before use. All dilute solutions were prepared from double-distilled water with specific conductance equal to (1.3 ± 0.1) μS cm⁻¹.

Apparatus. A Metrohm pH-meter, 665, was used for pH measurements. A combination Ag/AgCl pH electrode, 6.0228.010 Metrohm, was used for determination of protonation constants of the peptides. All titrations were carried out by a Metrohm automatic titrator unit equipped with a Dosimat automatic burette with 5 dispenser units, a syringe-burette and a pH electrode. Spectrophotometric titrations were performed on a UV-Vis Cecil 5000 spectrophotometer with a Pentium 4 computer and using thermostated matched 10 mm quartz cells. The measurement cell was of a flow type. A Masterflex pump allowed circulation of the solution under study from the potentiometer cell to the spectrophotometer cell, so the absorbance and the pH of the solution could be measured simultaneously.

3. Results and discussion

The species M_pH_qL_r^(4p+q-r) formed, is characterized by its stoichiometry (p:q:r), where M represents the metal ion. To determine the stability constant of complexation or protonation eq 2 is defined by β_{pqr} ⁴



$$\beta_{pqr} = [M_pH_qL_r^{(4p+q-r)}] / ([M^{+4}]^p[H^{+}]^q[L^{-}]^r) \quad (2)$$

The protonation constants of the peptide have been used for computation of the stability constant, β_{pqr} of the metal-ligand. The protonation constants of the ligand have been studied in different kind of background electrolytes and the results reported in the literature. ⁵ In this work, the protonation constants of the peptide were determined using a potentiometric technique and calculated using a computer program which employs a nonlinear least-squares method (Microsoft Excel Solver) at different ionic strength. These values are in good agreement with those reported earlier. ⁵

Determination of the formation constant was employed using the method mentioned before. Absorbance, A, and -log [H⁺] were measured by successive addition of an alkali solution of the ligand to the acidic metal ion solution in the UV range (250 to 320) nm; see Experimental Section. Treatment of the spectrophotometric data (every 0.5 nm) obtained during the titrations, as a

function of H^+ concentration, were conducted with the computer program Equispec (by using the matrix based in the Matlab environment).⁶ Considering eq 1, different models including ML and MHL and several polynuclear and protonated species were tested by the program at different ionic strength (0.02 to 0.15). As expected, polynuclear complexes were systematically rejected by the computer program, as also were MHL_3 , ML_3 , and MH_2L_3 (the charges are omitted for simplicity). The values for ML_2 and MHL_2 species were also calculated by the program at different ionic strength, but the species were not considered further, because the estimated error in their formation constants were unacceptable, and their inclusions do not improve the goodness of the fit. The models finally chosen, formed by ML and MHL for the studied system resulted in a satisfactory fitting at different ionic strength. The calculated average values of the stability constants for different experiments are listed in Table 1. In Fig. 1 the equilibrium distribution of various species of Ce(IV)-gly-gly systems are shown as a function of $-\log[H^+]$ at 0.1 mol dm^{-3} sodium perchlorate. The calculations are based on the stability constant values given in Table 1. The curves clearly demonstrate that an increase of the pH is accompanied by an increase in the formation of deprotonated complex species. The most stable complex species at different pH values are: $CeHL^{4+}$ at $pH \approx 2$ in all of cases, CeL^{3+} has the highest value around $pH \approx 4$ to 12 in all of cases.

Effect of Ionic Strength on Stability Constants. values of $\log \beta_{pqr}$ (see equation 3) were found to decrease with increasing ionic strength of the medium (Table 1) in agreement with the Debye-Huckel equation.⁷ The thermodynamic stability constants are obtained by extrapolating the straight line plot of $\log \beta_{pqr}$ versus $I^{1/2}$ to zero ionic strength. The $\log K^\circ$ (thermodynamic stability constant) values were (8.45, 3.32, 10.53 and 12.86) for H_2L^+ , HL, ML and MHL, respectively. The equation $\Delta G = -2.303 RT \log K^\circ$ gives the relationship between the thermodynamic stability constant and the free energy change according to complex formation. ΔG values were (-48.23, -18.95, -60.11 and -73.41) $kJ.mol^{-1}$ for H_2L^+ , HL, ML and MHL, respectively.

Table 1. Average values of the formation constants of Ce-gly-gly at 25 °C and different ionic strength (0.02 to 0.15 mol dm^{-3} $NaClO_4$) by spectrophotometric method, some examples of formation constant of cerium are also reported from the literature for comparison

species	Ionic strength / $mol\ dm^{-3}$	$\log \beta_{101}$	$\log \beta_{111}$
gly-gly	0.02 $NaClO_4$	10.18 ± 0.03	12.66 ± 0.05
gly-gly	0.05 $NaClO_4$	9.95 ± 0.04	12.57 ± 0.08
gly-gly	0.1 $NaClO_4$	9.74 ± 0.05	12.44 ± 0.04
gly-gly	0.15 $NaClO_4$	9.53 ± 0.04	12.32 ± 0.05

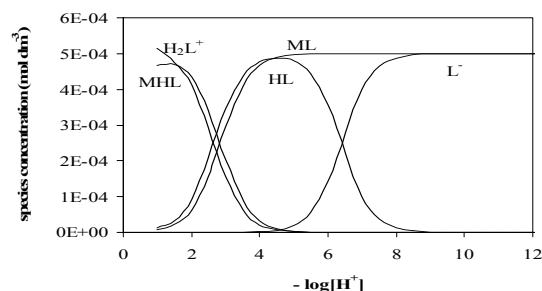


Fig. 1. Distribution curves for the system Ce-gly-gly at 25 °C and ionic strength, 0.1 mol dm^{-3} $NaClO_4$

References

- [1] Li, W. B. Wahl, W. Oeh, U. Holtriagl, V. Roth, P. Radiat. Prot. Dosim. 125 (2007) 500.
- [2] Sanna, D. Agoston, C. Micera, G. Sovago, I. Polyhedron 20 (2001) 3079.
- [3] Salonpää, P. Iscan, M. Pasanen, M. et al. Biochem. Pharmacol. 44 (1992) 1269.
- [4] Beck, M. T. Nagypal, I. Ellis Harwood: New York, 1990.
- [5] Gharib, F. Nasiri, R. Rev. Inorg. Chem. 25 (2005) 79.
- [6] Bevington, P. R. Data reduction and error analysis for the physical sciences; McGraw-Hill: New York, 1969.
- [7] Näsänen, R. Ekman, A. Acta Chem. Scand. 6 (1952) 1384.

**Equilibrium study of complexes of cadmium (II) with L-phenylalanylglycine and glycyl-L-phenylalanine**A. Bahadori^{a,*}, S. Sharifi^a, D. Nori-shargh^b, F. Kiani^c

a. Department of Chemistry, University of Islamic Azad, Arak, Iran

b. Department of Chemistry, University of Islamic Azad, Science and Research Branch, Tehran, Iran

c. Department of Physical and Inorganic Chemistry, University of Mazandaran, Mazandaran, Iran

(E-mail: bahadori.az@gmail.com)

Keywords: Cadmium (II) complexes, L-phenylalanylglycine, Glycyl-L-phenylalanine, Distribution Diagrams.**1. Introduction**

The recent increased use of peptides in biomedical therapy is a result of their large range of activity and specificity, usually with low toxicity and rapid metabolism. Thus, separation, analysis of peptides and peptide hormones and determination of stability constants of metal complexes with peptides has become increasingly important for an ever-widening range of research disciplines [1]. Research results have clearly demonstrated that certain transition metal ions play a basic role in directing a number of biochemical processes [2]. The increasing rate of the environment pollution has stimulated worldwide research concerning new materials capable to remove heavy metal of cadmium (II) from contaminated soils and wastes [3]. This revealed the need for comprehensive studies of metal ion-bioligand interactions, as model systems; within this, the investigation of the complex-forming properties of amino acids and peptides is of particular importance [2]. The protonation constants of the ligands have been used for computation of the stability constant of the metal-ligand. Potentiometry and UV-Vis spectrophotometry are the most widely used methods in the investigation of metal complexes [4-7]. Therefore has been decided to carry out an equilibrium study of the interaction of peptides with Cd(II) ion to determine stability of species formed. The stability constants of the complexes of cadmium(II) ions with dipeptides of glycyl-L-phenylalanine (gly-L-phe) and L-phenylalanylglycine (L-phe gly) were determined in aqueous solution at 25 °C and constant ionic strength 0.1 mol dm⁻³ NaClO₄, using a combination of potentiometric and spectrophotometric techniques.

2. Method**2.1. Chemicals**

Glyl-L-phe was obtained from Merck, while the L-phe gly was provided by Fluka. Both of the ligands were employed without further purification and the aqueous stock solutions of the ligands were freshly prepared daily. The NaOH solution was prepared from a titrisol solution (Merck) and its concentration was determined by several titrations with standard HCl. Perchloric acid, sodium perchlorate, cadmium (II) nitrate were from Merck as analytical reagent grade materials and were used without further purification. Dilute perchloric acid solutions were standardized against standard NaOH solution. All the standard solutions were prepared using deionized and twice-distilled water with specific conductance equal to $(1.8 \pm 0.1) \mu\Omega^{-1}\text{cm}^{-1}$.

2.2. Apparatus

A Horiba pH-meter, M-12 was used for pH measurements. The hydrogen ion concentration was measured with an Ingold UO 3234 glass electrode and Ingold UO 3236 calomel electrode. Spectrophotometric titrations were performed on a UV-Vis Lambda 25 double beam spectrophotometer from 200 to 350 nm and optical path 1.000 cm.

2.3. Measurements

All measurements were carried out at temperature $(25.0 \pm 0.1) ^\circ\text{C}$ and ionic strength 0.1 mol dm⁻³ NaClO₄. The pH-meter was calibrated for the relevant H⁺ concentration with solution of 0.01 mol dm⁻³ perchloric acid solution containing 0.09 mol dm⁻³ sodium perchlorate (for adjusting the ionic strength to 0.1 mol dm⁻³). For this standard solution, we set $-\log [H^+] = 2.0$ [8].

2.4. Procedure

Volumes of 25 cm³ acidic solution of Cd²⁺ in the concentration range 5×10^{-5} mol dm⁻³ was titrated with an alkali solution of each ligand containing a large excess of each ligand (the ratios of metal ion to ligand 1:100). Ionic strength was maintained at 0.1 mol dm⁻³, in the presence of NaClO₄. The $-\log [H^+]$ and absorbance were measured after addition of a few drops of titrant, and this procedure extended up to required $-\log [H^+]$.

3. Results and discussion

The complex $M_xH_yL_z^{(nx+y-z)+}$ formed is characterized by its stoichiometry (x:y:z), where M and L represent the metal ion and each ligand, respectively. To determine the stability constant of the complexation or the protonation, eq 2 is defined by β_{xyz} [8]

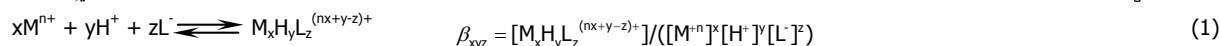


Table 1. **Average values of the protonation and formation constants of Cd (II) with L-phenylalanylglycine and Glycyl-L-phenylalanine at 25 °C and ionic strengths, I, 0.1 mol dm⁻³ NaClO₄**

Species	log β_{011}	log β_{021}	log β_{111}	log β_{101}	Ref.
L-phenylalanylglycine	3.7037 ± 0.0029	7.5236 ± 0.0032	12.06 ± 0.13	2.82 ± 0.08	This work
glycyl-L-phenylalanine	3.2314 ± 0.0020	8.1106 ± 0.0047	10.70 ± 0.04	1.70 ± 0.07	This work
glycyl-L-phenylalanine	3.11 ± 0.14	8.14 ± 0.17	-	-	9

The protonation constants of the peptides were determined using a potentiometric technique and calculated using a computer program which employs a nonlinear least-squares method (Microsoft Excel Solver) [5]. The method of determination of the stability constant is based on the relation $A = f(\text{pH})$ on account of the high stability of the complexes studied. Absorbance, A , and $-\log [H^+]$, were measured for a solution containing Cd^{2+} with a large excess of each ligand. Treatments of the spectrophotometric data (each 1 nm) obtained during the titrations were conducted on the computer program. The program allows calculation of stability constant for different models of stoichiometries. Different models including $ML_{2,}$, MH_2L , $M_2L...$ were tested and the stability constants for the species were calculated by the program, but some species were not further considered because the estimated error in their formation constants are unacceptable. The models finally chosen, formed by $Cd(HL)^{2+}$ and CdL^+ , for L-phe-gly and gly-L-phe. The composition of the formed complexes was determined and it was shown that cadmium(II) forms two mononuclear 1:1 species with the ligands, of the type $Cd(HL)^{2+}$ and CdL^+ in the pH range of study (1.5-10.5), where L represents a fully dissociated ligand. The values are listed in Table 1 together with the values reported in the literature, which are in good agreement with those reported. Figure 1 shows the equilibrium distribution of various species in Cd(II)-L-phe gly and gly-L-phe systems. Benzyl-containing ligands, L-phe gly and gly-L-phe, studied in this work may coordinate cadmium (II) via the $-COO^-$ and $-NH_2$ donor groups. In the Cd(II)-L-phe gly and gly-L-phe systems, the complexation of cadmium(II) by the ligands indicates influence benzyl group on the donor sites $-COO^-$ and $-NH_2$ in L-phe gly and gly-L-phe for complex formation, i.e. $-COO^-$ in the L-phe gly preference of cadmium(II) for the $-COO^-$ donor group in the gly-L-phe because benzyl group decreases Lewis basicity and nucleophilicity donor sites.

4. Conclusions

Many biological processes involve hydrolysis of proteins and peptides. Metal ions can promote the hydrolysis of peptides in both homogeneous and heterogeneous systems. In this work, the study of cadmium(II) with dipeptides of L-phe gly and gly-L-phe interaction was attempted in order to better understand the influence the presence of a benzyl group in the stability of dipeptides to bind cadmium(II). Table 1 shows the stability constant values of MHL and ML species formed by L-phe gly are much higher than the corresponding values of gly-L-phe.

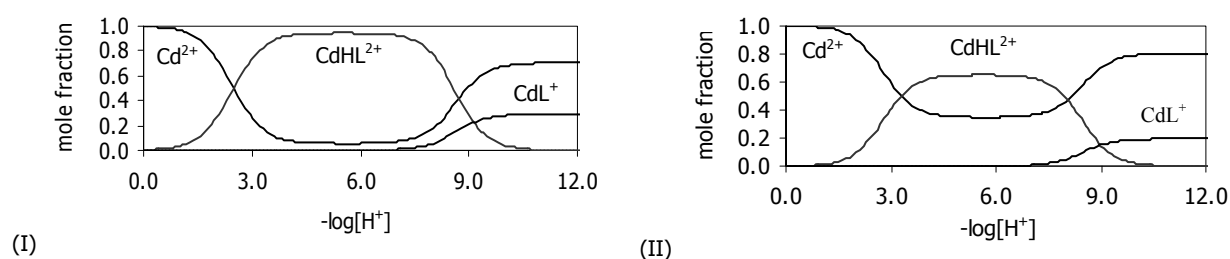


Fig. 1. The equilibrium distribution of (I) Cd(II)-phe gly and (II) Cd(II)-gly-L-phe systems at 25 °C and $\mu=0.1 \text{ mol dm}^{-3} \text{ NaClO}_4$

References

- [1] V. Sanz-Nebot, F. Benavente, I. Toro, J. Barbosa, J. Chromatogr., A 921 (2001) 69.
- [2] I. Sóvágó, G. Petocz, J. Chem. Soc. Dalton Trans. 7 (1987) 1717.
- [3] E. Mavropoulos, N. C. C. da Rocha, J. C. Moreira, L. C. Bertolino, A. M. Rossi, J. Braz. Chem. Soc. 16 (2005) 62.
- [4] F. Kiani, A. A. Rostami, S. Sharifi, F. Gharib, J. Chem. Eng. Data 54 (2009) 3261.
- [5] S. Sharifi, D. Nori-shagh, A. Bahadory, J. Braz. Chem. Soc. 18 (2007) 1011.
- [6] A. Niazi, M. Ghalie, A. Yazdanipour, J. Ghasemi, Spectrochim. Acta, Part A 64 (2006) 660.
- [7] M. T. Ramírez-Silva, M. Gómez-Hernández, M. L. Pacheco-Hernandez, A. Rojas-Hernández, L. Galicia Spectrochim. Acta, Part A 60 (2004) 781.
- [8] M. Monajjemi, F. Garib, H. Aghaei, G. Shafiee, A. Thghvamanesh, A. Shamel Main Group Met. Chem. 26 (2003) 39.
- [9] F. Gharib, R. Nasiri, Rev. Inorg. Chem. 25 (2005) 79.



Thermodynamic investigations on the interaction of vanadyl (IV) bis (acetylacetonate) with D-penicillamine, effective in several biological processes at different pHs

R. Hakimelahi ^{a,b}, H. Aghaie^b, M.A. Seyed Sadjad^b

a. Department of Chemistry, Islamic Azad university of Jahrom, Jahrom, Iran.

b. Department of Chemistry, Science and Research Campus Islamic Azad University, Tehran, Iran.

(E-mail: r.hakimelahi2002@gmail.com)

Keywords: Penicillamine, Bis(acetylacetonate)oxovanadium(IV), Schiff base, SQUAD, Thermodynamic parameters

1. Introduction

Vanadium coordination chemistry and biochemistry have attracted increasing interest during the last few years [1, 2]. Some vanadyl complexes were recently synthesized and characterized which are more effective as anti-cancer agent and as an inhibitor of synovial cell proliferation, compared to uncomplexed ligands or vanadyl ion alone [3]. Catalytic activities of Schiff base complexes of oxovanadium (IV) have been studied [4,5]. Besides the action of vanadium compounds are insulin-like or at least insulin enhancing and for vanadium to be useful as an orally available insulin mimetic agent (IMA) it should possess adequate thermodynamic stability [6]. In the present study we have investigated complexation of Bis(acetylacetonate)-oxovanadium(IV) with D-penicillamine by spectroscopic method.

2. Methods

The absorption spectra were recorded by Shimadzu 1650 spectrophotometer using 1 cm quartz cuvettes, with thermostated cell compartment. Titrations were carried out by adding 50 µl aliquots portions of a solution of D-penicillamine directly into the quartz cell containing VO(acac)₂. The titration experiments were continued until the absorbance of the VO(acac)₂ solution in the UV-Vis range remained constant. The spectra were recorded in the range of 500 to 900 nm at three different pHs (pH=7, 7.5 and 10) and 6 different temperatures (20, 25, 30, 35, 40, and 45 °C) with the ionic strength of 0.1 M (KCl). Our results showed that we had different products at different pHs.

3. Results and discussion

Reaction of D-H₂Pen (which is β and β-dimethyl cysteine) and VO(acac)₂ lead to the formation of different complexes at various pHs. At neutral pH the product is a Schiff base complex but in alkali pH, D-penicillamine is exchanged with acac⁻ due to the ability of coordinating of D-H₂Pen by hydroxide ion at the medium. Thermodynamic stabilities have been studied using UV/Vis Spectrophotometry and SQUAD program. This program is designed to calculate the best values for the stability constants of the proposed equilibrium model by employing a non-linear least square approach. The results show that the best fitting corresponds to 2: 1 complex model at all temperatures. Besides the Kettler method confirms that 1:1 complex model is rejected. The estimation of binding constant at various temperatures enables us to calculate all of the thermodynamic parameters of binding using van't Hoff equation. Thermodynamic studies of described reactions at pH=7, 7.5 and 10 shows exothermic, endothermic and exothermic modality, respectively.

The equilibrium of VO(acac)₂: D-H₂Pen can be conveniently characterized by three familiar thermodynamic parameters: standard Gibbs free energy, ΔG°, enthalpy, ΔH°, and entropy, ΔS°, changes. The ΔG° can be calculated from equilibrium constant, K, of the reaction using the familiar relationship, ΔG° = -RT ln K in which R and T referring to the gas constant and the absolute temperature, respectively. If the change of heat capacity of the reaction is negligible, the van't Hoff equation (eq. 1) gives a linear plot of ln K versus T⁻¹. The ΔH° can be calculated from the slope, ΔH°/R, and the ΔS° from the intercept, ΔS°/R from eq. 2.

$$\frac{d \ln K}{d(1/T)} = \frac{-\Delta H^\circ}{R} \quad (1)$$

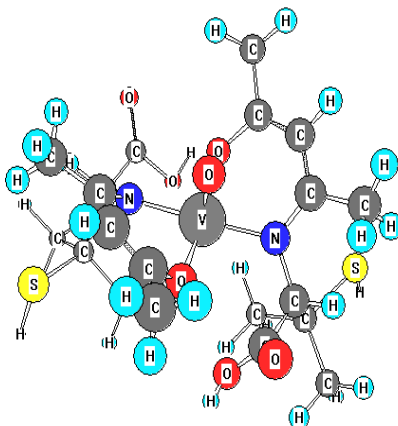
$$\Delta S^\circ = \frac{(\Delta H^\circ - \Delta G^\circ)}{T} \quad (2)$$

4. Conclusions

D-penicillamine is potentially tridentate ligand, but the pK_a for the -COOH, NH₃ and S-H groups are 1.99-2.00, 8.0 and 10.6 respectively, so S-H can't release H at pH=7.00 and the coordination of S is not possible [7]. [VO(acac)₂] is a coordination compound with four O-donor atoms (as β-diketonate), vanadium atom has square pyramidal coordination with

one terminal oxygen atom and four oxygen atoms from the ligand molecule. D-H₂Pen converts [VO(acac)₂] to a vanadyl schiff base (N-O) complex (Scheme 1), because imino nitrogen atoms are often suitable donor atoms for the coordination of transition metal ions and many schiff base ligands have been used for the synthesis of vanadium complexes. In spite of spectral techniques, two other points, are in good agreement with the schiff base complex formation :

1. There is no reaction between vanadyl sulphate(VOSO₄) and D-H₂Pen at pH=7.00 that confirms the participation of acac⁻ in the reaction.
2. the reaction of [VOL₂] formation is an exothermic process, due to decreasing of entropy through converting two molecules to one molecule (eq. 3) .



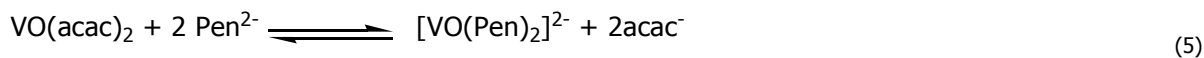
Scheme 1. Vanadyl Schiff Base Complex [VOL₂]

At pH=7.5, D-H₂ Pen is converted to HPen⁻ and the exchange of acac⁻ with HPen⁻ produces VO(HPen)₂, it is clear that the coordination has been formed via amine nitrogen and carboxylate oxygen (eq. 4) .



This reaction is an endothermic and entropy driven process. The hydration of HPen⁻ is more than acac⁻ because HPen⁻ is a hydrophilic anion.

At pH=10, the product of the reaction of VO(acac)₂ with D-H₂Pen is [VO(Pen)₂]²⁻, this reaction is an exothermic process and the changes of entropy is negative (eq. 5) .



In this condition vanadyl ion prefers thiolate ion to amine nitrogen for coordination.

References

- [1] N.D. Chasteen, vanadium in Biological systems, Kluwer Academic publishers, Dordrecht, The Netherlands, 1990.
- [2] A. Butler, C. Carano, J. coord. chem. Rev. 109 (1991) 61.
- [3] K.H. Thompson, K. Bořhmelerle, E. Polishchuk, C. Martins, P. Toleikis, J. Tse, V. Yuen, J.H. McNeill, C. Orvig, J. Inorg. Biochem. 98 (2004) 2063–2070.
- [4] D.M. Boghaei, S. Mohebi, J. Mol. Catal. A 179 (2002) 41–51.
- [5] G. Hoshina, M. Tsuchimoto, S. Ohba, K. Nakajima, H. Uekusa, Y. Ohashi, H. Ishina, M. Kojima, Inorg. Chem. 37 (1998) 142.
- [6] H. Katherine, Thompson and Chris Orvig, J. Chem. Soc. Dalton Trans. (2000) 2885–2892.
- [7] D.V. Derveer, Lyangs, S.Y. Qian., B. Sturgeon, polyhedron. 21 (2002) 2021.

**Investigation of some dense system regularities for yukawa fluid**

N. Farzi, Se. Hosseini

Department of Chemistry, Faculty of Science, University of Isfahan, I. R. Iran.

(E-mail:nfarzi@sci.ui.ac.ir)

(E-mail:se.hosseini@chem.ui.ac.ir)

Keywords: Regularity; Dense Fluids; Yukawa Potential**1. Introduction**

The development of simple models to describe the thermodynamic behavior of liquids is a difficult task, due to the diversity of molecular interactions that the liquid state presents. One of the major achievements has been the recognition of the quite roles played by the repulsive and attractive parts of the interatomic potential in determining the microscopic properties of simple fluids. In this case, Yukawa potential which have numerous applications in the different systems like as simple neutral fluids, chain molecules, emulsions, spherical proteins, liquid metals, colloids and etc, well present both the attraction and repulsion contributions of potentials. The hard core one Yukawa (HCOY) potential [1] is given by

$U_{HCOY}(r) = \begin{cases} \infty & r \leq \sigma \\ -\frac{\varepsilon\sigma}{r} \exp\left(z\left(\frac{r}{\sigma} - 1\right)\right) & r > \sigma \end{cases}$	1
---	---

Where z is the Yukawa parameter which is determine the attraction range, and the hard core double Yukawa (HCDY) potential [2] is given by

$U_{HCDY}(r) = \begin{cases} \infty & r \leq \sigma \\ -\frac{\varepsilon\sigma}{r} \left[\exp\left(-z_1\left(\frac{r}{\sigma} - 1\right)\right) + \exp\left(-z_2\left(\frac{r}{\sigma} - 1\right)\right) \right] & r > \sigma \end{cases}$	2
--	---

Where z1 and z2 determine the ranges of the attractive and the positive parts of the potential. At the present work, the Yukawa potential have been chosen in order to 1) investigation of the Yukawa ability in the prediction of some dense systems regularities, 2) recognition the effects of the attraction and repulsion forces in the some regularities of dense fluids, 3) determination of Yukawa parameters for some simple fluids using the regularity of dense fluids.

2. Method

The HCOY equation of state, which is driven using the perturbation method and mean spherical approximation, by Waisman [3] and the HCDY equation of state which is driven by Tang and Lu [4] have been used for prediction of some regularity. The common bulk modulus point, common compression point and the near linearity of the pressure with temperature regularities have been investigated by HCOY and HCDY [5] in the different ranges of temperature and density with the different z1 and z2. Fig. 1 typically shows the common bulk modulus point which is predicted by HCDY equation of state by z1=15, z2=2. The Yukawa parameters for N2, Kr, Ar have been determined by adjusting the calculated common intersection points with the experimental ones.

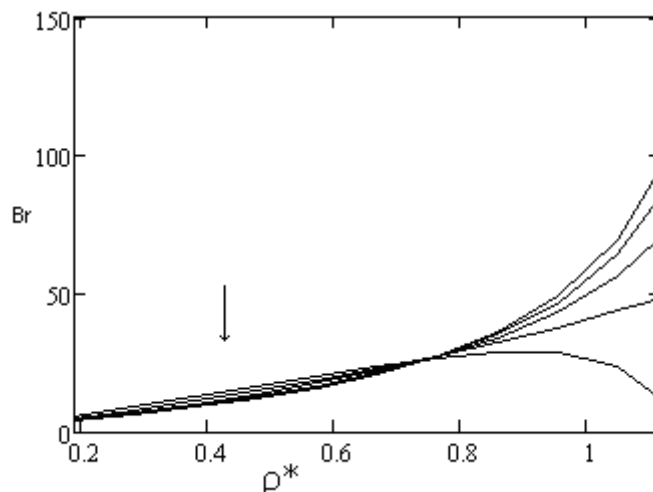


Fig.1. Plots $Br - \rho^*$ at the different reduced temperature (T^*): $T1^*=1$, $T2^*=1.2$, $T3^*=1.4$, $T4^*=1.6$, $T5^*=1.8$, $T6^*=2$, $z1=15$, $z2=2$ for HCDY, (\downarrow temperature increase)

3. Results and discussion

It is shown that the HCOY can just predict the common intersection point with $z=0.2$ and 0.3 in the reduce temperatures $T^*=1, 1.2, \dots, 3$ and when the reduced temperature increased, the intersection point is confined to $z=0.2$. It is interested to note that these common intersection points have not occurred in the liquid range of density while in the gas range. The common intersection points based on HCDY are found in the combination of $z1$ and $z2$ values which are related to each other. It is proved that the roles of both the soft repulsion potential and the attraction are affected to occurrence of such regularities. The HCDY, as a good means can be applied for the prediction of Yukawa parameters of the simple dense fluids.

4. Conclusions

In this work, It is found that, in spite of HCDY achievement in prediction of dense fluid regularity, the HCOY can not predict such regularities in the range of dense fluids. This behavior is related to the repulsion and attraction contributions which are existed in the HCDY potential but in HCOY potential only attraction contributions is existed.

References

- [1] D. Henderson, L. Blum, J. P. Noworyta. J. Chem. Phys. 102 (1995) 4973.
- [2] H. Guerin. Journal of Fluid Phase Equilibria.218 (2004) 47.
- [3] E. Waisman, Mol. Phys. 25 (1973) 45.
- [4] Y. Tang, B. C. Lu, J. Chem. Phys. 100 (1994) 3079.
- [5] S. Alavi, G. A. Parsafar, B. Najafi. J. Chem. Phys. 99 (1995) 9248.

**Effect of PEG, PVP and Triton X-100 on CMC of the aqueous solution of sodium dodecyl sulfate**A. Salabat^a, M. Heydari^b, A. Barati^b

a. Chemistry Department, Arak University, P.O. Box 38156-879, Arak, Iran

(E-mail: a-salabat@araku.ac.ir)

b. Chemical Engineering Department, Arak University, P.O. Box 38156-879, Arak, Iran

Keywords: Poly (ethylene glycol), Poly (vinylpyrrolidone), Viscosity, Apparent molal volume, Sodium dodecyl sulfate, Critical micelle concentration.

1. Introduction

The critical micelle concentration (CMC) is a key thermodynamic quantity of surfactant- water mixtures. Knowledge of this quantity is crucial for both scientific and practical understanding of how surfactants behave. A great deal of research has been devoted to determining the CMC experimentally [1] and through predictive [2] techniques. Surfactant-polymer systems in aqueous solution find extensive industrial applications in areas related to medicine, cosmetics, food, detergency, mineral processing, enhanced oil recovery, and so forth. The interaction between surfactants and polymers has been the subject of active research for the last three decades, and this subject has been the focus of some of the recent reviews [4]. Investigations into these systems are important also in relevance to many biological systems, such as biomembranes and vesicles, and also to biological processes, for example, lipid-protein interactions and so forth. The well explored systems till now are those containing nonionic water-soluble polymers and anionic surfactants, or polyelectrolytes and oppositely charged surfactants. There are plenty of references describing interactions between polymers and surfactants, but most of them are based upon equilibrium data, for example the effect of polymers on the critical micellar concentration (CMC) of the surfactant and the aggregation number of the micelles [3].

Addition of polymers could effectively reduce the critical micelle concentration (CMC) of surfactant and, thus, increase the detergency. Surfactant molecules interact with polymers at a critical aggregation concentration (CAC) forming micelle-like clusters along the polymer chains. Below CAC, there is no interaction between the surfactant and the polymer. CAC is used as a marker to measure the strength of the binding interaction between surfactant and polymer.

The purpose of this work is checking the influence of two water-soluble polymers and a nonionic surfactant on CMC of SDS by using viscosity and volumetric data at 298 K. Poly ethylene glycol (PEG) and Poly vinylpyrrolidone (PVP) as two water-soluble polymers and Triton X-100 as a nonionic surfactant are chosen for this study.

2. Methods

Methods. Different concentration of SDS from 0.001 up to 0.07 mol/L with 1.0% mass percent of PEG, PVP or Triton X-100 were prepared in triple distilled water. All solution densities were measured with a vibrating- tube densimeter (Mettler Toledo DE51) with proportional temperature control that kept the samples at working temperature with an accuracy of 0.01 K. The densimeter was calibrated at each temperature with distilled water and dry air. Precision of the instrument is reported to be $\pm 1.10^{-5}$ g.cm⁻³. Viscosities were measured with an Ubbelohde- type viscometer. The temperature of the water bath was controlled to within ± 0.1 K. For each solution the flow time was measured at least three times.

Materials. Sodium dodecyl sulfate (SDS) with purity 99.5% was purchased from Merck and used without purification. PVP (average molar mass of 40000), PEG (average molar mass of 35000) were obtained from Merck. Triton X-100 was obtained from Acros chemical company.

3. Results and discussion

From the density data apparent molar volume of the solutions were calculated by using the following equation:

$$V_a = \frac{1}{\rho} \left(\frac{1}{\phi} - \frac{1}{\rho^*} \right)$$

Where V_a is the percent weight, ρ is the density of solution, ρ^* is the density of pure water.

The calculated apparent molar volume against SDS concentration (mol/L) for SDS + H₂O and SDS + Triton X-100 + H₂O has been shown in Fig 1. As can be seen from this figure the CMC of the system is changed from 0.008 to 0.0025 mol/L. This point

is CAC of the SDS aqueous system with Triton X-100. The obtained CAC results for SDS system with PEG and PVP is about 0.006 mol/L. As a conclusion it is verified that the polymer type and molecular mass of the polymer has not significant effect on CMC. The viscosity of the systems against SDS concentration is also shown in Fig. 2. As can be seen this trend for reducing CMC with triton X-100 concentration is confirmed by the viscosity data.

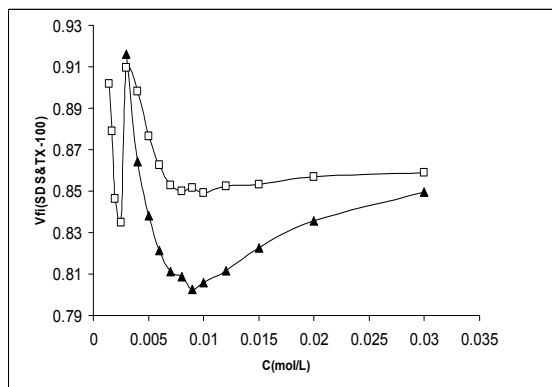


Fig.1. Apparent molar volume (\bar{V}_v) of sodium dodecyl sulfate (SDS) + H₂O (▲), and sodium dodecyl sulfate (SDS) + 1% mass fraction polyoxyethylene octyl phenyl ether (TX-100) (□) aqueous solution at 298 K.

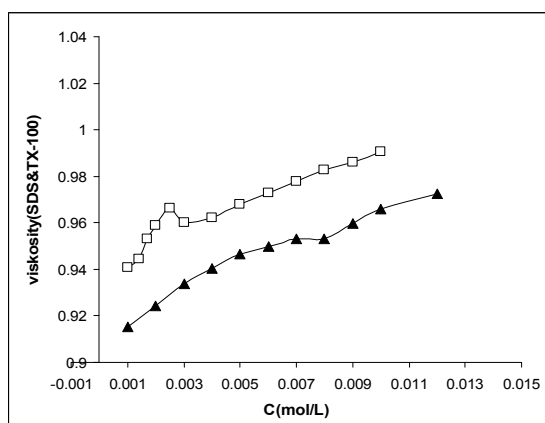


Fig.2. viscosity (η) of sodium dodecyl sulfate (SDS) + H₂O (▲), and sodium dodecyl sulfate (SDS) + 1% mass fraction polyoxyethylene octyl phenyl ether (TX-100) (□) aqueous solution at 298 K.

4. Conclusions

The interaction between ionic surfactant of SDS with polymers PEG and PVP and non-ionic surfactant TX-100 was investigated by viscosity and volumetric measurements. By using these data the CAC of these systems were calculated. From the calculated CAC of the systems the interaction of the polymers and surfactant with SDS can be concluded.

References

- [1]. T. Asakawa, K. Johten, S. Miyagishi, M. Nishida, Langmuir 4 (1988) 136.
- [2]. P.D.T. Huibers, V.S. Lobanov, A.R. Katritzky, D.O. Shah, M. Karelson, Langmuir 12 (1996) 1462.
- [3]. Dubin, P. L.; Gruber, J. H.; Xia, J.; Zhang, H. J. Colloid. Interface Sci. **1992**, 148, 92.
- [4]. Lindman, B.; Thalberg, K. In Interactions of Surfactants with Polymers and Proteins; Goddard, E. D., Ananthapadmanabhan, K. P., Eds.; CRC Press: Boca Raton, FL, 1993; p 203.

**Solute-solvent interactions in Co-Salen schiff base complex in organic solvents at 298.15 K**H. Shekaari^a, A. Bezaatpour^a, R. Elhami^{b*}

Department of Chemistry, University of Mohaghegh Ardabili, Ardabil, Iran.

^bEmail: rasoul.El2009@yahoo.com**Keywords:** Co-Salen schiff base complex, Salen, Density, Apparent molar volume, Solute - Solvent interactions.**Introduction**

Schiff-base complexes are considered to be among the most important stereochemical models in main group and transition metal coordination chemistry due to their preparative accessibility and structural variety [1] and [2]. They have played a key role in the development of coordination chemistry, resulting in an enormous number of publications, ranging from pure synthetic work to modern physicochemical and biochemically relevant studies of metal complexes [3]. Densities, d , of the solutions of Co-salen schiff base-complex (schiffbase complex) with non-aqueous solvents (DMA, DMF, DMSO, CH₃CN) were measured at $T = 298.15$ K. For the investigated systems, the limiting values for apparent molar volume, V_ϕ^0 , were obtained from the Redlich–Mayer equation.

Methods

Syntheses of salen : To a vigorously stirred ethanolic solution (70 mL) of 2-hydroxybenzaldehyde (200mmol) was added dropwise a solution of ethylenediamine (100mmol) in 70mL of ethanol. After the addition was complete, the mixture was stirred and refluxed for 60 minutes. The mixture was then cooled and the yellow crystal of the ligand was collected by filtration, then washed with ethanol and dried in a dessicator. Complexes of the Schiff bases were made by a modification of the Co(CH₃COO)₂ (5 mmol) was dissolved in 60 mL of methanol, and the Schiff base (5 mmol) was added to the stirring solution. Air was blown over or bubbled through the hot solution, and more methanol was added to replace losses due to evaporation. About after 6 or 7 h, the brown precipitate was filtered off. The precipitate was washed with ether.

Results and discussion

The experimental densities, d , as function of schiff base complex concentration, m , for (schiff-base complex + CH₃CN), (schiff-base complex + DMA), (schiff-base complex + DMF) and (schiff-base complex + DMSO) systems are reported in Table 1. The apparent molar volumes V_ϕ (in cm³.mol⁻¹) of schiff base complex in the organic solvents studied were calculated from the densities of the solutions using the following equation:

$$V_\phi = \frac{m}{d} - \frac{(d - d_0)}{md d_0} \quad (1)$$

where m (in mol.kg⁻¹) is molality of schiff base complex in organic solvents, d and d_0 are densities (in g.cm⁻³) of solution and pure solvent, respectively; M is molar mass of schiff base complex (in kg . mol⁻¹) The calculated apparent molar volume, V_ϕ , values for the solutions of schiff base complex in different organic solvents are also given in Table 1.

Determination of limiting apparent molar volumes

The concentration dependence of V_ϕ at fixed temperature and pressure can be described using the following Redlich–Mayer equation (equation (2)) [5] in the dilute region ($m < 0.2$):

$$V_\phi = V_\phi^0 + S_v m^{\frac{1}{2}} + b_v m \quad (2)$$

where V_ϕ^0 is the limiting apparent molar volume (equal to the partial molar volume at infinite dilution, V_ϕ^0), b_v is an empirical parameter and S_v is defined as

$$S_v = A_v \left[\frac{1}{2} \left(\sum_i v_i z_i^2 \right) \right]^{\frac{3}{2}} \quad (3)$$

where v_i and z_i are the stoichiometric number and absolute charge of ion i , respectively. The Debye–Hückel limiting slopes for apparent molar volume, A_v , is calculated with the help of the following equation [4]:



$$A_v = -4RT \left(\frac{\partial A_\phi}{\partial P} \right)_T = 6RTA_\phi \left[\left(\frac{\partial \ln \varepsilon}{\partial P} \right)_T - \frac{\kappa_T}{3} \right] \quad (4)$$

in which A_v , ε and κ_T are the Debye–Huckel constant for osmotic coefficient on the molal base and the dielectric constant respectively. The values for the pressure derivative of logarithm of ε respect to pressure, $(\partial \ln \varepsilon / \partial P)_T$, and the isothermal compressibility, κ_T , are available only for a few of these solvents

Table 1. The values of $V_\phi^0 / (\text{m}^3 \cdot \text{mol}^{-1})$, $S_v / (\text{m}^3 \cdot \text{mol}^{-2} \cdot \text{kg})$, r^2 (corr), S_d (stderr)

Solvent	$10^6 \cdot V_\phi^0$	D	$10^6 \cdot S_v$	$r^2 (V_\phi^0)$	$S_d (V_\phi^0)$
CH ₃ CN	264.67	36.04	12.72	0.9770	0.29
DMF	270.69	36.71	7.40	0.9764	0.1
DMA	271.81	39.63	7.70	0.9824	0.08
DMSO	280.62	46.50	4.83	0.9785	0.03

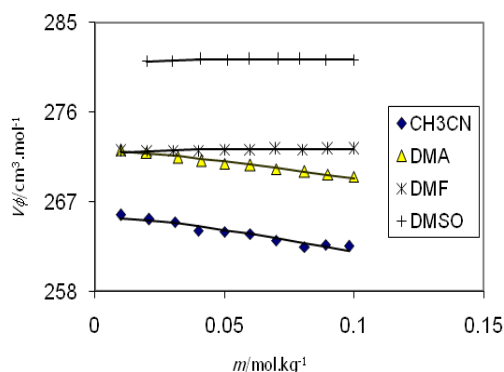


Fig1. Co-Salen schiff base complex apparent molar volumes at different organic solvents.

Conclusions

The results show that the apparent molar volume values decrease with increasing molality. This results arising from interactions between solute-solvent and packing the solution. It can be seen the limiting apparent molar volumes increasing with dielectric constants of organic solvents. Increasing the limiting apparent molar volumes show stronger solute-solvent interactions. Decreasing the S_v values show decreasing solute-solute interactions.

References

- [1] A.D. Granvoskii, A.L. Nivorozhkin and V.I. Minkin, *Coord. Chem. Rev.* 126 (1993), p. 1.
- [2] V. Alexander, *Chem. Rev.* 95 (1995), p.273.
- [3] M.A.V. Ribeiro Da Silva, M.D.S. Monte, j.M. Goncalves and E.M.R. Fernandes, *J. Chem. Soc., Dalton Trans.* (1997), p.1257.
- [4] M.T. Zafarani-moattar, H. Shekari, *J. Chem. Thermodynamics* 39 (2007) 1649-1660
- [5] O. Redlich, D.M. Mayer, *Chem. Rev.* 64 (1964) 221-227.
- [6] J. Anantaswamy, G. Atkinson, *J. Chem. Eng. Data* 29 (1984) 81-87.

**Solvent effects on protonation and guanin in different aqueous solutions of methanol**M. Khoshbakht^{a,*}, G. Geimachy^b, A. Shamel^c

a. Chemistry Department, I. Azad University, Sarab Branch, Iran

(E-mail: mahinkhoshbakht@yahoo.com)

b. Chemistry Department, I. Azad University, Ardabil Branch, Iran

c. Chemistry Department, I. Azad University, Ardabil Branch, Iran

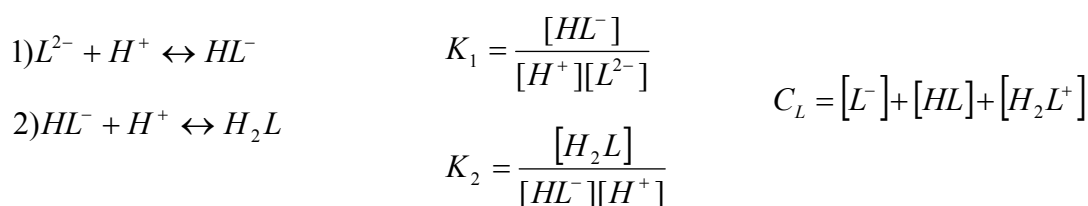
Keywords: Guanin; Kamlet-Taft ; thermodynamic**1. Introduction**

The use of solvents is ubiquitous in nearly every facet of chemical processing. In spite of the large amount of work on photoinduced electron transfer reactions the solvent effect on the rate constants and dielectric constants for intermolecular processes have received little consideration until recently. During the last years we have been involved in the study of the solvent effects on the rate constants and dielectric constants of several intermolecular protonation reactions.¹ The solvent effect on the charge separation efficiencies was also investigated in some of these systems. These studies were carried out in polar solvents of similar macroscopic dielectric properties with the goal of observing specific effects of the solvent structure on the kinetics of these reactions. In this sense protic (methanol) and aprotic (acetonitrile (MeCN), propionitrile (PrCN)) solvents were employed. In this paper, we report values for the Kamlet-Taft solvent parameters for guanin and their solutions in water obtained using solvatochromic probe compounds.²⁻³ In addition, the index of refraction was determined for each pure guanin and each aqueous solution. The three Kamlet-Taft solvent scale parameters measured are the solvent hydrogen-bond donor ability α , the solvent hydrogen-bond acceptor ability β , and the solvent dipolarity/polarizability Π^* .⁴⁻⁵

2. Experimental

2.1. Reagents: Methanol was obtained from Merck as an analytical reagent grade material and was used without further purification. The NaOH solution was prepared from titrisol solution (Merck), and its concentration was determined by several titrations with standard HCl. Guanin was either Merck chemicals and was used without further purification.

2.2. Measurements: Solutions of guanin were prepared gravimetrically using organic-free, distilled, deionized water prepared in-house. Within solubility limitations, solutions were prepared in guanin/water percentages (V/V) from 0 to 40%. All measurements were performed at $(25 \pm 0.1)^\circ\text{C}$. For each experiment, a 50 mL acidic solution guanin was titrated with an alkali solution, 0.1 mol \cdot dm⁻³ NaOH, both of the same ionic strength and mole fraction of methanol.

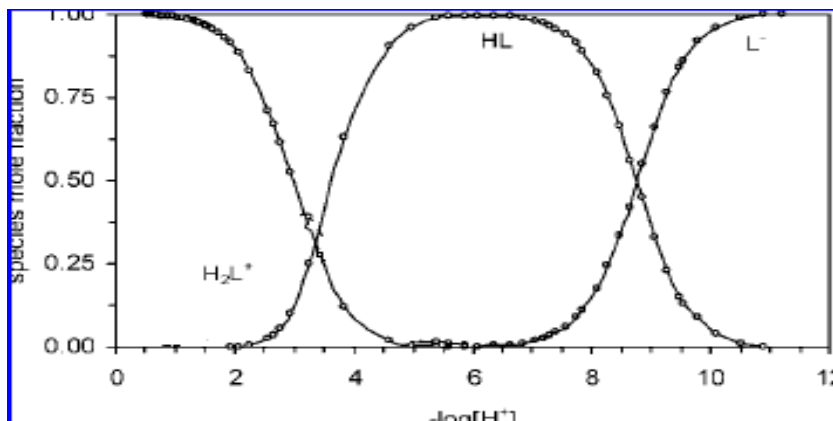
**3. Results and discussion**

The protonation constant values have been determined using the potentiometric technique under the same condition of temperature, ionic media, and mole fraction of methanol and calculated using the computer program (Microsoft Excel Solver) which employs a nonlinear least-squares method.⁶⁻⁷ The protonation constant values, expressed in log units, are collected in Table 1 together with the values reported in the literature for comparison.⁸⁻⁹

The solution L_z^{x+} that formed is characterized by its stoichiometry ($x:z$), respectively.¹⁰ To determine the formation constant of the solution, eq 1 is defined by β_{xz}

$$[H_2L] = \frac{C_L [H^+]^2}{[H^+]^2 + [H^+]K_1 + K_1K_2} \quad [HL] = C_L [H^+] K_1 / \beta$$

$$[L^-] = C_L K_1 K_2 / \beta$$



Distribution diagram of solution of guanin system at 25 °C, ionic strength 0.1 mol · dm⁻³ NaCl, and 20 % methanol.

4. Conclusions

The combined potentiometric and spectrophotometric measurements were used to characterize the different solution species of the guanin system in various aqueous methanol solutions. Our data reveal that solution species are formed at pH = 3, 6, and 11, respectively. The determined formation constants as well as the protonation constants of guanin are analyzed in terms of Kamlet, Abboud, and Taft parameters. Single-parameter correlations of the formation and the protonation constants are poor, but multiparameter correlation represents significant improvement with regard to the single-parameter models. The correlations between the protonation constant of the amino group of guanin in log units with the reciprocal of the dielectric constant of methanol-water mixtures are linear, but this is not true for the protonation of the carboxylic acid group of the amino acid. These findings are in agreement with the Born equation.

References

- (1) Lippard, S. S. J.; Barton, J. K. *Metal ions in biology*; Wiley: New York, 1980.
- (2) Oehme, F. W. *Toxicity of heavy metals in the environment*; Marcel Dekker Inc.: New York, 1978.
- (3) Prick, J. J. G.; Smitt, W. G. S.; Muller, L. *Thallium poisoning*; Elsevier: Amsterdam, 1955.
- (4) Lee, A. G. *The chemistry of thallium*; Elsevier: Amsterdam, 1971.
- (5) Garcia Bugarin, M.; Casas, J. S.; Sordo, J.; Filella, M. Thallium(I) interactions in biological fluids: A potentiometric investigation of thallium(I) complex equilibria with some sulfur-containing amino acids. *J. Inorg. Biochem.* **1989**, *35*, 95–105.
- (6) Sigel, S. Interactions of metal ions with nucleotides and nucleic acids and their constituents. *Chem. Soc. Rev.* **1993**, 255–267.
- (7) Blokzijl, W.; Engberts, B. F. N. Hydrophobic effects. Opinions and facts. *Angew. Chem., Int. Ed. Engl.* **1993**, *32*, 1545–1579.
- (8) Gharib, F.; Sadeghi, F. Solvent effects on complexation of thallium(I) with guanosine 5'-monophosphate in methanol-water mixtures. *Appl. Organomet. Chem.* **2007**, *21*, 218–225.
- (9) Gharib, F. Solvent effects on complexation of dioxovanadium(V) with penicillamine in methanol-water mixtures. *J. Chem. Eng. Data* **2005**, *50*, 196–200.
- (10) Gharib, F.; Zare, K.; Mohammadi, B. Solvent effects on complexation of molybdenum(VI) with nitrilotriacetic acid in different aqueous solutions of methanol. *J. Mol. Liq.* **2006**, *124*, 63–67.

**Application Of Surfactant based Aqueous Two Phase Systems in Amino acids Extraction**Alireza Salabat^a, Somayeh_tiani_Moghadam^{a,b,*}, Mina Rahmati Far^a

a. Department of Chemistry, University of Arak, Arak, Iran

(Email: A-Salabat@Araku.ac.ir)

b. Sama organization (offiliated with Islamic Azad *university*)-arak**1. Introduction**

Liquid-liquid equilibrium of aqueous two-phase systems (ATPS) has been used to separate and purify biological materials from the complex mixtures [1-3]. Purification of bioproducts is achieved by the different distribution between the two phases of the target compound and the contaminants. Four kinds of ATPS has been developed till today, they are polymer-polymer ATPS, polymer-salt ATPS, ionic liquid (IL)-based ATPS and surfactant-based ATPS. Due to the higher content of water in both phases and lower interface tension in comparison with others, surfactant-based ATPS has more advantages, such as lower cost, experimental conveniences, ease of waste disposal and consequently shorter time for phase separation. These systems are especially suggested for the separation of membrane proteins.

Triton X-100, which is considered a comparatively mild non-ionic surfactant, is often used in biochemical application to solubilize enzymes and proteins [4]. In continuation of our previous research works [5-8], in this paper for the first time the partitioning behavior of three amino acids with polar and non-polar side chains, L-phenylalanine, L-tryptophan and L-tyrosine, in the surfactant-based ATP systems composed of Triton X-100 and MgSO₄ or Na₃C₆H₅O₇ at 298.15 K has been studied. The effect of tie-line length (TLL) and salt type on the partitioning of amino acids has been discussed.

Keywords: Aqueous two-phase system, surfactant-based ATPS, partitioning coefficient, Triton X-100, amino acid.

2. Experimental

2.1. Chemicals: The non-ionic surfactant Triton X-100, magnesium sulfate and sodium citrate, amino acids L-phenylalanine, L-tryptophan and L-tyrosine.

2.2. Preparation of Phase System: The liquid-liquid equilibrium of Triton X-100 + MgSO₄ or Na₃C₆H₅O₇ + H₂O at 298.15 K has been investigated in details recently [8]. In order to determine partition coefficient of the amino acids in these ATP systems, two tie lines from each of the phase diagrams were selected. Preparation of the two-phase samples was performed in 20 mL graduated plastic bottles with tightly closed lids. The total weight of the components for each sample was about 15 g. The initial amounts of the amino acids added to the ATP systems were 1.0×10^{-2} g. The mixtures were shaken for about 30 min and then placed in a thermostatic water bath at 298.15 K for at least 24 h to ensure complete equilibration, as indicated by the absence of turbidity in each phase. After equilibration of the systems, samples of approximately 5 mL from the upper and lower phases were carefully removed for analysis using syringes.

2.3. Analysis of Samples: The liquid-liquid equilibrium data from our previous work [8] was used for the preparation of the samples. Therefore, the concentrations of the Triton X-100 and salts are known for two selected tie lines. The amino acid concentrations in the top and bottom phases were determined by HPLC.

3. Results and discussion

First, it has to be noted that the influence of the dissolved amino acids on the phase behavior of the aqueous two-phase systems can be neglected. Analysis of the surfactant and salt for the phase system of Triton X-100 + MgSO₄ (or Na₃C₆H₅O₇) + L-Phenylalanine + H₂O confirms this. Because of this, the compositions and tie line length of TX-100 + salt + H₂O two-phase systems at 298.15 K, were taken from our previous work [8].

The tie line lengths of the ATP systems are calculated by the following equation:

$$TLL = \sqrt{(w_{Salt}^{Top} - w_{Salt}^{Bottom})^2 + (w_{Surf}^{Top} - w_{Surf}^{Bottom})^2} \quad (1)$$

Where w_{salt} and w_{surf} are the weight percents of the salt and surfactant in the top or bottom phase. The partition coefficient (K) was defined as the ratio between amino acid equilibrium concentration in top phase and bottom phase. This coefficient is used to quantify the degree of separation reached in a one step extraction process. As can be seen the partitioning behavior of the amino acids in these two systems are significantly different, so that increasing of TLL in the system containing MgSO₄ lead to



decreasing of partition coefficient, but increasing of TLL in the system containing $\text{Na}_3\text{C}_6\text{H}_5\text{O}_7$ lead to increasing of partition coefficient. Effect of TLL on the partition coefficient of amino acids in Triton X-100 + MgSO_4 + H_2O and Triton X-100 + $\text{Na}_3\text{C}_6\text{H}_5\text{O}_7$ + H_2O systems has been shown in figures 1 and 2, respectively. Since hydrophobicity of the amino acids decreases as follows: L-tryptophan > L-phenylalanine > L-tyrosine, then as expected, more hydrophobic amino acids have greater affinity for the more hydrophobic surfactant-rich phase, and consequently, larger partition coefficient. As can be seen from figure 2, for Triton X-100 + $\text{Na}_3\text{C}_6\text{H}_5\text{O}_7$ + H_2O system, this trend is as usual and partition coefficient of amino acids increases with increasing hydrophobicity. For Triton X-100 + MgSO_4 + H_2O system, the partition coefficient has reverse trend with hydrophobicity, as can be seen from figure 1. This reverse trend may be because of complex formation between the amino acids and Mg^{2+} in the bottom phase, and then decreasing the partition coefficient. In our previous work [6], this reverse trend had been also seen for partitioning of these amino acids in PEG6000 + MgSO_4 + H_2O ATP system. Yield (Y%) of the amino acids in the top phase is calculated by the following equation:

$$y(\%) = \frac{100}{1 + (1/RK)} \quad (2)$$

Where R is V_T/V_B and V_T and V_B are the top and bottom phase volumes, respectively.

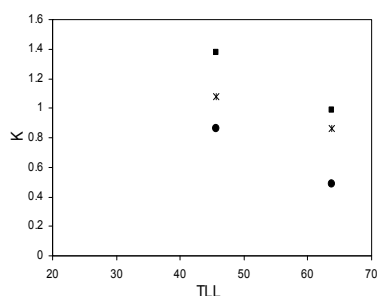


Fig.1. Effect of TLL on the partition coefficient of amino acids in Triton X-100 + MgSO_4 + H_2O system at 298.15 K; L-tryptophan (■), L-phenylalanine (*) and L-tyrosine (●).

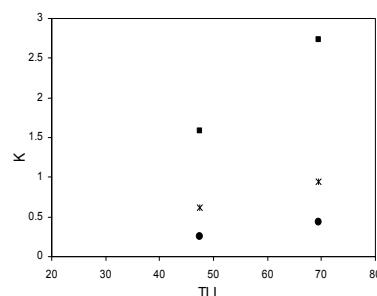


Fig.2. Effect of TLL on the partition coefficient of amino acids in Triton X-100 + $\text{Na}_3\text{C}_6\text{H}_5\text{O}_7$ + H_2O system at 298.15 K; L-tryptophan (■), L-phenylalanine (*) and L-tyrosine (●).

4. Conclusions

The partition coefficients of three amino acids L- phenylalanine, L- tryptophan and L- tyrosine were obtained in aqueous two-phase systems of TX-100 + salts + H_2O at 298.15 K. The effect of the two different organic and inorganic salts on partitioning of amino acids was determined. It was found that the effect of salts on the partition coefficients is quite different. It was verified that for Triton X-100 + $\text{Na}_3\text{C}_6\text{H}_5\text{O}_7$ + H_2O system, more hydrophobic amino acids had greater affinity for the more hydrophobic TX-100-rich phase and, consequently, larger partition coefficients. While, for Triton X-100 + MgSO_4 + H_2O system, the partition coefficient of amino acids has reverse trend with hydrophobicity This reverse trend may be because of complex formation between the amino acids and Mg^{2+} in the bottom phase, and then decreasing the partition coefficient.

References

- [1] P. A. Albertsson, Partition of Cell Particles and Macromolecules, 3rd ed., John Wiley, New York, 1986.
- [2] A. Greve, M.R. Kula, J. Chem. Technol. Biotechnol. 34 (1991) 27.
- [3] S. Klomklao, S. Benjakul, W. Visessanguan, B. K. Simpson, H. Kishimura, Process Biochem. 40 (2005) 3061.
- [4] J. H. Willam, W. H. Carmen, Talanta 39 (1992) 487.
- [5] A. Salabat, M. H. Abnosi, A. R. Bahar, J. Chromatogr. B 858 (2007) 234.
- [6] A. Salabat, M. H. Abnosi, A. Motahari, J. Chem. Eng. Data 53 (2008) 2018.
- [7] A. Salabat, M. Alinoori, CALPHAD 32 (2008) 611.
- [8] A. Salabat, S. M. Tiani, M. F. Rahmati, CALPHAD, in press.

**Prediction of thermodynamic properties of pure and mixtures liquid alkali metals**

E. Faramarzi , M. H. Mousazadeh

Department of Chemistry, Nuclear Science Research School, Nuclear Science & Technology Research Institute (NSTRI), 11365-3486, Tehran, Iran

(E-mail:faramarzi_ehsan@yahoo.com)

Keywords: Alkaline Metals, PC-SAFT Equation of State, Thermodynamic Properties**1. Introduction**

Liquid metals are complicated in structure. Alkali metals are typical metals. Hence, the study of their thermodynamic properties is of scientific significance. Technological applications of alkali metals [1] need the knowledge of high-temperature properties of them. In this condition, their ability to react with air and water leads to a poor accuracy in the experimental studies. These considerations also make the metals suitable candidates for theoretical investigation. In this study, the PC-SAFT equation of state [2] is extended to pure and mixtures of liquid alkali metals. This equation belongs to a class of theoretically based equations of state that are formulated based on continuum space (as opposed to lattice space) liquid state perturbation theories.

2. Methods

The PC-SAFT equation of state is applied to Alkali metals in a wide range of pressure and temperature. All metallic systems are considered as monatomic systems ($m=1$). Therefore, knowing two adjustable parameters σ and ε is sufficient to predict the equation of state for liquid metals. The parameters were identified for five alkali metals by correlating saturated liquid density. We have computed some selected thermodynamic properties of five alkali metals in liquid phase. The thermodynamic properties in question are the saturation and compressed liquid density for pure and mixtures, heat capacity at constant pressure and constant volume, and Isobaric expansion coefficient, for which accurate experimental data [3] exist in the literature.

3. Results and discussion

We have calculated the saturation liquid density of Li, Na, K, Rb, and Cs. The results show the deviation for alkali metals are within 1.90%. The ability of the present equation of state to predict PVT data is presented. The calculations cover the pressure range 10 MPa < P < 100 MPa and temperature range 600 K < T < 1600 K. We have calculated the densities of alkali metal alloys of Cs-K, Na-K, Na-K-Cs that we can acquire very good results. In the case of C_p , C_v and Isobaric expansion coefficient agreement between the calculated and corresponding experimental values is reasonably good. For heat capacities the electronic contributions were added to the calculated results the agreement would have been better.

4. Conclusions

There exist some similarities between fluid metals and ordinary fluids that lead us to check the present equation of state for them. Perturbation theory with hard sphere reference system is a good first approximation for the study of static properties of liquid alkali metals. The interesting point of this work is that this EOS is also suitable to employ to predict other thermodynamic properties as well as density within acceptable accuracies.

References

- [1] R. D. Kale, M. Rajan, *Curr. Sci.* 86 (2004) 668.
- [2] J. Gross, G. Sadowski, *Ind. Eng. Chem. Res.* 40 (2001) 1244.
- [3] N. B. Vargaftik, Y. K. Vinogradov, V. S. Yargin, *Handbook of Physical Properties of Liquids and Gases: Pure Substances and Mixtures*, Begell House, New York, 1996.



Shiraz University

13th Iranian Physical Chemistry Seminar

Shiraz University of Technology



**Study of dielectric behaviour of binary mixtures of butanediols in a non-polar solvent at 298.2 K**A. Ghanadzadeh^a, H. Ghanadzadeh^b, Kh. Bahrpaima^{a,c}, R. Rostamiyan^aa. Department of Chemistry, Guilan University, Rasht, Iran
(E-mail: Kh.bahrpaima@gmail.com)

b. Department of Chemical Engineering, University of Guilan, Rasht, Iran

c. Department of Chemistry, Islamic Azad University of Firoozabad, Firoozabad, Iran

Keywords: Butanediols, Permittivity, Dipole moment, Molecular association**1. Introduction**

Measurement of the dielectric constant (relative permittivity) is a useful technique for characterizing molecular structure, solute-solute and solvent-solute interactions, and molecular ordering in solutions. The value of the dielectric constant is strongly related to molecular structure and intermolecular interactions [1–3]. By using electric permittivity, density and refractive index measurements in solutions over a range of concentrations, it is possible to calculate the electric dipole moment with the aim of giving valuable information on the progressive association of the molecules.

In this work, experimental results of dielectric investigations for solutions of three butanediols (2,3-butanediol, 2,3-BD, 1,3-butanediol, 1,3-BD, and 1,4-butanediol, 1,4-BD) in 1,4-dioxane were reported for various mole fractions and at T=298.2 K. The molecular dipole moments were determined using Guggenheim method. The variations of effective dipole moment and correlation factor, g, with mole fraction in these materials were investigated using Kirkwood-Frohlich equation.

2. Methods

The densities of the solutions were measured at 298.2 K using DA-210 (Kyoto electronic) density meter. The refractive indices of the solutions were determined at a wavelength of 589 nm using an Abbe Refractometer (Model CETI). The density meter and the refractometer were initially calibrated before being used to perform measurements. The temperature was controlled by circulation of water through a jacket surrounding the sample and was measured to an accuracy of ± 0.1 K. The electrical capacitance of the dielectric cell was measured using a Wayne Kerr model 6425B Digibridge. Measurements of the capacitance required for calculating the static dielectric permittivity were performed at a frequency of 10 kHz.

3. Results and discussion

The dipole moments, μ , of the compounds (2,3-BD, 1,3-BD and 1,4-BD) dissolved in 1,4-dioxane were calculated using the Guggenheim-Debye equation [4]. The expression for the dipole moment is given by:

$$\mu^2 = \frac{27kT}{4\pi N_A (\epsilon_1 + 2)(n_1^2 + 2)} \left(\frac{\Delta}{C} \right)_{C \rightarrow 0} \quad (1)$$

where ϵ_1 is the static permittivity and n_1 is the refractive index of pure non-polar solvent, k is the Boltzmann constant and N_A is Avogadro's number. The dielectric increment given by:

$$\Delta = (\epsilon_{12} - n_{12}^2) - (\epsilon_1 - n_1^2) \quad (2)$$

where the subscript 12 denotes a property of the solution. C is the molar concentration (mol / cm^3), and $(\Delta / C)_0$ is the limiting gradient of the plot of versus concentration. The permittivity and the refractive index values of these liquids were measured at 298.2 K. Dielectric permittivity of solvent, 1,4-dioxane, was also measured at this temperature range. Dielectric permittivity increments of solutions of the compounds in the non-polar solvent were measured 298.2 K (Fig 1). The dipole moment of compounds in 1,4-dioxane solutions was calculated and is listed in Table 1.

The dipole moment data (dipole moment of the free molecule) measured for the solute in dilute solutions will be compared to the effective dipole moment (μ_{eff}) calculated using dielectric data obtained for high concentration solutions with aim of deducing information about molecular association. The concentration dependence of dipole correlation factor, $g = (\mu_{\text{eff}}/\mu)^2$, of obtained solutions, as a function of the mole fraction of solutes is shown in Fig 2.



Since, g is a measure of the molecular association between a reference molecule and its nearest neighbors, the departure of g from unity can be indicative of molecular association. For the solutions investigated here a positive deviations of g from unity, which is due to the parallel orientation of the dipoles of neighboring molecules were obtained. Also, it has been observed that

$$g_{2,3\text{-butanediol}} > g_{1,3\text{-butanediol}} > g_{1,4\text{-butanediol}}$$

It shows that 2,3-butanediol has the most self-association.

Table1. The molecular dipole moment of the investigated compounds obtained in 1,4-dioxane solutions at 298.2 K

Compound	μ (D) ± 0.05	μ_{eff} (D) Pure liquid	$g = (\mu_{\text{eff}}^2 / \mu^2)$
1,3-butanediol	2.54	3.83	2.27
2,3-butanediol	1.97	3.29	2.79
1,4-butanediol	2.67	3.98	2.22

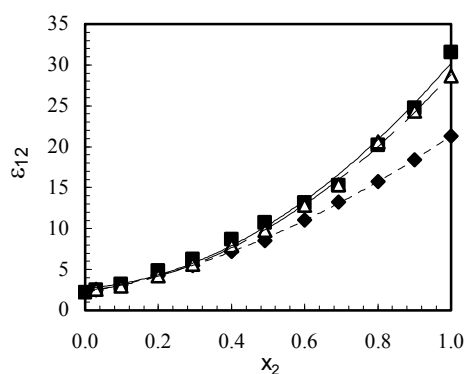


Fig 1

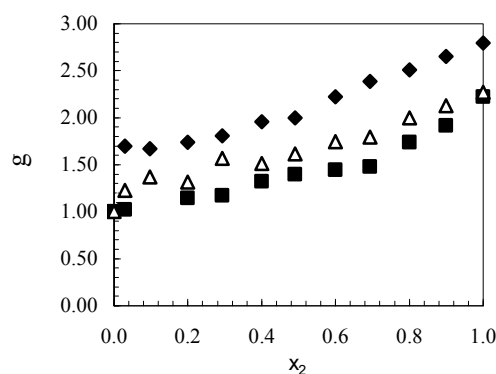


Fig 2

Fig.1. Dielectric permittivity of solutions of (♦) 2,3-BD, (■)1,4-BD and (Δ)1,3-BD in 1,4-dioxane as a function of the solute mole fraction at 298.2 K

Fig.2. Dipole correlation factor, g , of solutions of (♦) 2,3-BD, (■)1,4-BD and (Δ)1,3-BD in 1,4-dioxane as a function of the solute mole fraction at 298.2 K

4. Conclusions

At 298.2 K, values of the dipole moment and Kirkwood correlation factor for three butanediols (1,3-BD, 2,3-BD and 1,4-BD) were determined in 1,4-dioxane solutions at various concentrations. These results yield a Kirkwood factor $g > 1$, and indicate a high degree of parallel dipole self-associations.

References

- [1] J. W. Smith, Electric Dipole Moment, Butterworth, London, 1955.
- [2] W. Dannhauser, A. F. Flueckinger, J. Phys. Chem. 68 (1964) 1814.
- [3] G. M. Janini, A. H. Katrib, J. Chem. Educ. 60 (1983) 1087.
- [4] H. Frohlich, Theory of Dielectrics, Oxford University Press, London, 1949.

**Effect of ionic liquid, [PrMIm]Br on the thermodynamic properties of aqueous solutions of L-Arginine at** **$T = 298.15\text{ K}$** Hemayat Shekaari^a, Fatemeh Jebali^{b,*}

Department of Chemistry, University of Mohaghegh Ardabili, Ardabil, Iran.

(E-mail: Hemayat @yahoo.com)

(E-mail: Fatemeh. Jebali@yahoo.com)

Keywords: L-Arginine, Ionic liquid, density, Viscosity, electrical conductance**1. Introduction**

Thermodynamic properties of amino acids, as fundamental structural units of proteins in aqueous electrolyte solutions provide important information about solute–solvent and solute–solute interactions that can be of great help in understanding several processes, such as protein hydration, denaturation, and protein aggregation [1,2]. Ionic liquids stand for a class of organic electrolyte composed entirely of ions with very low melting points below $T = 373.15\text{ K}$. Because of their negligible vapor pressure at normal temperature, ionic liquids have been used as replacement for volatile organic solvents [3, 4]. In the present work, density, viscosity and electrical conductance of amino acid have been measured in different concentrations of aqueous [PrMIm]Br solutions at $T = 298.15\text{ K}$.

2. Methods

The ionic liquid, 1-propyl-3-methylimidazolium bromide was synthesized and purified according to literature methods [5]. The densities of the solutions were measured using a vibrating tube densimeter DMA, 4500M (Anton paar). The viscosities were measured using an Ubbelohde-type viscometer. The measurements of specific conductivity were performed using Metrohm conductometer (712).

3. Results and discussion

The values of apparent molar volume, V_{ϕ}^0 were calculated from the measured densities for the solutions of L-Arginine in different concentrations of aqueous [PrMIm]Br solutions at 298.15 K. The value of the V_{ϕ}^0 was obtained by least-squares fitting to the following equation:

$$V_{\phi} = V_{\phi}^0 + S_v \cdot m \quad (1)$$

Where, S_v is the volumetric virial pairwise interaction coefficient that characterizes interaction of solvated solute species in solution. The values of the V_{ϕ}^0 and S_v are given in Table 1. The values of S_v for L-Arginine containing solutions decrease with increasing the concentration of [PrMIm]Br. These results suggest that ionic liquid strongly with the zwitterionic end group of L-Arginine and ionic liquid has a strong dehydrations effect on the L-Arginine.

Table1. The V_{ϕ}^0 values of amino acid, L-Arginine in aqueous [PrMIm]Br solutions at 298.15 K

System	$m_L / \text{mol} \cdot \text{kg}^{-1}$	$V_{\phi}^0 / \text{cm}^3 \cdot \text{mol}$	$S_v / \text{m}^3 \cdot \text{mol}^{-2} \cdot \text{kg}$	r^2	$\delta(V_{\phi}^0)$
Arginine + water	0.0000	124.75	3.680	0.9989	0.027
[PrMIm]Br + L-Arg + water	0.0915	130.85	-8.531	0.9988	0.108
[PrMIm]Br + L-Arg + water	0.1850	133.007	-12.289	0.9897	0.227
[PrMIm]Br + L-Arg + water	0.2866	136.923	-21.244	0.9965	0.293

Most studies on viscosity are confined to the description of dilute solutions of electrolytes via determination of the A and B coefficients in the Jones-Dole equation. The values of A and B were calculated by the method of least squares by fitting the experimental data in the Jones–Dole equation and these values are given in Table 2. Generally, viscosity B -coefficients reflect the solute–solvent interactions, positive B -coefficients suggest kosmotropes since strongly hydrated solutes exhibit a larger change in viscosity with concentration.

**Table 2.** Value of A and B parameters of Jones-Dole equation for Arginine at 298.15 K

$m_L / \text{mol} \cdot \text{kg}^{-1}$	$A / \text{m}^3 \cdot \text{mol}^{-1}$	$B / \text{m}^3 \cdot \text{mol}^{-1}$
0.0000	-0.0170	0.662
0.0915	0.0006	0.592
0.1850	0.0011	0.573
0.2866	0.0267	0.500

Experimental conductivity data were correlated to low concentration Chemical Model (lcCM) equation. K_A is ion association constant As can be seen from Table 3 that the K_A values decrease with increasing concentration of amino acids. Increasing concentration of amino acids lead to form ion pairs that solute- solvent interactions decrease and Λ_0 and K_A values decrease. This results supports the conclusion obtained at by considering volumetric and viscometry results.

Table 3. The association constants K_A limiting molar conductance Λ_0 , distance parameter R , and standard deviation of ([RMIM]Br + H₂O + L-Arginine) system in low concentrations at 298.15 K

System	$c / \text{mol} \cdot \text{L}^{-1}$	$K_A / \text{dm}^3 \cdot \text{mol}^{-1}$	$\Lambda_0 / \text{S} \cdot \text{cm}^2 \cdot \text{mol}^{-1}$	$10^{10} R / \text{m}$	$\sigma(\Lambda)$
[PrMIm]Br + water	0.4399	13.36	146.76	10.85	0.25
[PrMIm]Br + L-Arg + water	0.9167	11.57	141.73	11.7996	0.36
[PrMIm]Br + L-Arg + water	1.7605	6.66	98.54	7.1722	0.13

4. Conclusions

We have shown the parameters of apparent molar volume, V_ϕ , limiting apparent molar volume, V_ϕ^ϕ , ion association constants, K_A , and viscosity B -coefficients interpreted in terms of solute-solute and solute-solvent interactions occurring between the various components of in these ternary mixtures.

References

- [1] Von Hippel, P. H. Schleich, T. Acc. Chem. Res, 2 (1969) 257 – 265.
- [2] Wang, J., Yan, Z., Zhao, K., J. Lu, Biophysic. Chem, 80 (1999) 179 – 188.
- [3] Welton, T., Chem. Rev. 99 (1999) 2071–2083.
- [4] Seddon, K.R., Stark, A., Torres, M.J., Pure Appl. Chem, (2000) 72 1391–1398.
- [5] Yang, J. Z., Tong, J., Li, J.-B., J. Solution Chem, 36 (2007) 573 – 582.

**Kinetic and thermodynamic study of eosin Y dye biosorption by leaves of date palm (*Phoenix dactylifera* L.)**

Nader Bahramifar, Fereydoon Ashrafi, Adel Amini*

Department of Chemistry, Payame Noor University (PNU), Sari Unit, Mazandaran, Iran.

(E-mail: k.oshtarga@gmail.com)**Keywords:** Eosin dye ; Adsorption ; Desorption ; Date palm ; Freundlich isotherm ; Biosorption .**1. Introduction**

Dyes and pigments to cater to the needs of not only the textile industries but also of other industries such as paper, rubber, plastics, paints, printing inks, art and craft, leather, food, drug and cosmetics. Eosin Y is as a model anionic dye that is used in wool and silk to give red colour with a yellow fluorescence[1]. Generally dyes are stable to light, heat and oxidizing agents, and are usually biologically non-degradable [2]. The dye-bearing effluent, when discharged into water bodies, affects photosynthesis, aquatic life, and also humans [3]. Many investigators have studied different techniques for removal of colored dye from wastewater, e.g. ozonations, nanofiltration, ultrafiltration, adsorption on to (i) agricultural solid waste (ii) calcined alunite (iii) various types of activated carbon[1]. The leaves of date palms, *Phoenix dactylifera* L. were used as biosorption of phosphates from aqueous solution, dyes (methylene blue dye) and were evaluated as biomonitors of heavy metal contamination in the cities. Since adsorption of eosin Y is used by chitosan hydrobeads [3] chitosan nanoparticles [4] the solar photo-fenton processes [5] activated carbon [1]. The present study deal with the adsorption of eosin Y from aqueous solution using the Leaves of date palm of *Phoenix dactylifera* L. The *Phoenix dactylifera* L. date palm is one of the most cultivated palms around the world. In this study, the effects of various parameters such as, contact time, pH of solution, adsorbent dosage, initial eosin Y concentration and effect of temperature were examined.

2. Methods

Eosin Y was obtained from Merck. The dye solutions were prepared by dissolving accurately weighed amounts of dye in distilled water at concentrations of 50, 100, 150, 200, 250 and 300 (mg/l). *Phoenix dactylifera* L. date palm turn obtained from Boshehr province (southern of Iran). *Phoenix dactylifera* L. date palm was washed with distilled water and the solution was placed in a constant temperature bath and stirred with the help of a stirrer at 700 rpm (Jenway hotplate and stirrer, model: 1203). Then dried at 100°C for 24 hour. (Ehret oven, model: BK3064)[6]. Five ml of solution was sampled for intervals between 0 and 180 minute of adsorption. At the end of the adsorption period, the solution was centrifuged with 5000 rpm for 5 minute. The concentration of dye was determined by a UV-visible spectrometer (GBC, Australia model: Cintra 20) at a wavelength (λ_{max}) of 517 nm[1]. The initial concentration C_i (mg/l) and left over eosin Y concentration at different time intervals, C_e (mg/g), were determined and the eosin Y uptake q_e (mg eosin Y adsorbed/g adsorbent) was calculated from mass balance equation as follows:

$$q_e = \left(\frac{C_i - C_e}{M} \times V \right) \quad (1)$$

The extent of sorption in percentage is found from the relation:

$$Sorption (\%) = \left(\frac{C_i - C_e}{C_i} \right) \times 100 \quad (2)$$

All statistical analysis was done using Microsoft Excel 2003 version office XP. [6]

3. Results and discussion

3.1. Effect of contact time: The results show that adsorption process is clearly time dependent. It is observed that most of the eosin Y specie uptake occurs within a time of 180 minute at 70% of the totally biosorbed for an initial eosin Y concentration of 100 mg/l. For periods greater than 90 minute, the uptake is further increased but with a much slower rate. Equilibrium began establishing itself after approximately a contact period of 180 minute.

3.2. Effect of pH on eosin Y adsorption: To achieve the maximum adsorption capacity of the adsorbent for eosin Y ions it was found pH = 4.0. The results show that the uptake of eosin Y specie adsorption onto *Phoenix dactylifera* L. date palm tends to decrease with the increase of pH. So with increasing acidity of the solution, the surface becomes more positively charged: consequently, higher removal is expected at low pH values.



3.3. Effect of adsorbent dosage : it was found that a dose of 8 (g/l) was sufficient for the maximum uptake of eosin Y ions under the reported experimental conditions. It is also seen that a further increase in adsorbent dose (greater than 8.0 (g/l)) affects the uptake of eosin Y adsorption greatly: the eosin Y uptake adsorption decreases .

3.4. Effect of initial eosinY concentration :Experiments were undertaken to study the effect of varying initial concentration 50 - 300 (mg/l) on eosinY specie removal onto *Phoenix dactylifera* L.date palm.It was found that a dose of 100 (mg/l) was sufficient.

3.5. Effect of temperature : Adsorption experiments were carried out for 100 (mg/l) , eosin Y at four different temperature (15.0 , 25.0 , 35.0 , 45.0) °C using 8.0 g of *Phoenix dactylifera* L date palm per liter of the solution in order to observe the effect of temprature on the adsorption capacity. It was observed that with an increase in temperature, adsorption capacity increased.The thermodynamic parameters ($\Delta G_{25}^0 = 2.77 \text{ kJmol}^{-1}$), ($\Delta S^0 = 76.73 \text{ Jmol}^{-1} \text{ K}^{-1}$) and ($\Delta H^0 = 25.636 \text{ kJ mol}^{-1}$)for this adsorption process have been determined.

3.5.1. Adsorption isotherms : Two well known models, namely the Langmuir and Freundlich models, are used to analyze the experimental data. The coefficients of these two-isotherm models for the Langmuir isotherm is ($R^2 = 0.8368$) and for Freundlich isotherm , is ($R^2 = 0.9283$). It was found that the adsorption isotherm for the eosin Y *Phoenix dactylifera* L date palm system is explained better by the Freundlich isotherm.

3.5.2. Adsorption kinetics : The kinetics of the adsorption of eosin Y on *Phoenix dactylifera* L date palm have been described by first and pseudo second-order models.

3.6. Desorption study : With the increase in pH , desorption increases. desorption of dye increases from about 18.11 % to 53.31% when pH increases from 11 to 13. These results indicate that the eosin Y adsorption onto *Phoenix dactylifera* L date palm is not completely reversible and the bonding between the sample particles and adsorbed eosin is likely strong.

4. Conclusions

Adsorption of eosin Y on *Phoenix dactylifera* L date palm was studied in this paper. The effect of various operating conditions, namely, pH , initial dye concentration and temperature were investigated for the operation. The equilibrium and kinetics of the process were investigated as well. The eosin Y uptake increased with the increase of initial eosin Y concentration and decreased with increasing pH value. . In nature and in normal treatment , the treated waters are usually at pH from 1.0 to 8.0 , so the adsorption capacity of eosin is about 7.8 mg P/g at pH 4 , for an adsorbent dosage of 8 (g/l) , initial eosin concentration of 100 (mg/l) , under a constant temperature of 15 - 45°C , and the equilibrium state was reached within 180 minute of exposure time. The Freundlich isotherm was found to be the most suitable for eosin Y adsorption on *Phoenix dactylifera* L date palm. A pseudo second-order kinetic model successfully explains the kinetic data.The positive values of ΔG^0 and ΔH^0 indicate that the adsorption process is unspontaneous and endothermic in nature. For desorption of the dye from the adsorbent, a number of pH values and different surfactants were used (pH = 11 – 13). It was observed that the desorption of the dye is favored at highly basic pH (desorption was 53.31% at a pH of 13). Desorptions were obtained after 120 minute of operation. The results of present investigation show that the relatively low cost and high capabilities of the *Phoenix dactylifera* L date palm make them potentially attractive adsorbents for the removal of eosin Y from aqueous solution.

References

- [1] M.K.Purkait , S.DasGupta , S.De , Adsorption of eosin dye on activated carbon and its surfactant based desorption , *Journal of Environmental Management*, 76 (2005) 135-142. [1]
- [2] Yi Wang , Yang Mu , Quan-Bao Zhao , Han-Qing Yu , Isotherms , kinetics and thermodynamics of dye biosorption by anaerobic sludge, *Separation and Purification Technology*, 50 (2006) 1-7. [1]
- [3] Sudipta Chatterjee , Sandipan Chatterjee , Bishnu P.Chatterjee , Akhil R.Das , Adsorption of a model anionic dye, eosin Y, from aqueous solution by chitosan hydrobaeds , *Journal of Colloid and Interface Scienc*, 288 (2005) 30-35. [1]
- [4] Wen Li Du , Zi Rong Xu , Xin Yan Han ,Ying Lei Xu , Zhi Guo Miao , Preparation , characterization and adsorption properties of chitosan nanoparticles for eosin Y as a model anionic dye, *Journal of Hazardous Material*, xxx (2007) xxx-xxx. [1]
- [5] Huaili Zheng , Yunxia Pan , Xiniyi Xiang , Oxidation of acidic dye Eosin Y by the solar photo-Fenton Processes , *Journal of Hazardous Material*, 141 (2007) 457-464. [1]
- [6] Khalifa Riahi , Bechir Ben Thayer , Abdallah Ben Mammou , Aouatef Ben Ammar , Mohamed Habib Jaafoura , Biosorption characteristics of phosphates from aqueous solution onto *Phoenix dactylifera* L. date palm fibers, *Journal of Hazardous Material*, xxx (2009) xxx-xxx. [1]



A DFT study of oxidative addition of hydrogen peroxide to Platinum(II) complex

Fatemeh Niroomand Hosseini^{a,*}, S. Masoud Nabavizadeh^b

(E-mail: niroomand55@hotmail.com)

a. Department of Chemistry, Islamic Azad University, Shiraz Branch, Shiraz, Iran

b. Department of Chemistry, College of Sciences, Shiraz University, Shiraz, 71454, Iran

Keywords: Density functional study; Platinum; Oxidative addition; Reaction mechanism

1. Introduction

There is a great interest in antitumor activity of platinum(II) complexes, *e.g.* iproplatin ($[\text{Pt}(\text{ipa})(\text{OH})_2\text{Cl}_2]$, ipa = isopropylamine) and cisplatin ($[\text{Pt}(\text{NH}_3)_2\text{Cl}_2]$).¹⁻⁵ One important route to dihydroxoplatinum(IV) complexes is by the oxidative addition of hydrogen peroxide to platinum(II) complexes. Thus, for example *trans* oxidative addition of an HO–OH bond to $[\text{PtMe}_2(\text{phen})]$ or $[\text{Pt}(\text{C}_6\text{F}_5)_2(\text{en})]$ gave $[\text{PtMe}_2(\text{OH})_2(\text{phen})]$ ⁶ or $[\text{Pt}(\text{C}_6\text{F}_5)_2(\text{OH})_2(\text{en})]$,⁷ respectively. Oxidation of square planar Pt(II) to octahedral Pt(IV) compounds has been utilized efficiently in the fields of the formation of mixed valence platinum compounds, the synthesis of oral antitumor (pro)drugs, and the elucidation of reaction mechanisms.¹⁻² The platinum(IV) chemistry has been largely based on hydroxo complexes *via* an oxidation of predesigned Pt(II) with hydrogen peroxide to axial dihydroxo Pt(IV) complexes. Although the oxidative addition of the electron-rich complexes $[\text{PtMe}_2(\text{NN})]$ (NN=bidentate nitrogen ligands) with a wide variety of reagents has been studied,^{8,9} however, despite the importance of hydrogen peroxide in chemistry, the literature contains no report of any theoretical study of the oxidative addition of this basic reagent, or any other O–O bond containing reagents, to platinum complexes. We have theoretically studied the reaction of H_2O_2 with the $[\text{PtMe}_2(\text{NN})]$ complex, where NN=2,2'-bipyridine to find the possible mechanism of oxidative addition reaction.

2. Method

In the present work, a density functional study has been used to investigate potential energy surface of the oxidative addition reaction of H_2O_2 to $[\text{PtMe}_2(\text{NN})]$ complex, where NN=2,2'-bipyridine. Density functional calculations were performed with the program suite Gaussian03 using the B3LYP. The basis sets used with B3LYP were constructed as follows. For platinum, we used LANL2DZ, while the 6-311++G** basis set was utilized for hydrogen, carbon, nitrogen and oxygen atoms. The geometries of all of intermediates as well as the corresponding transition states were optimized.

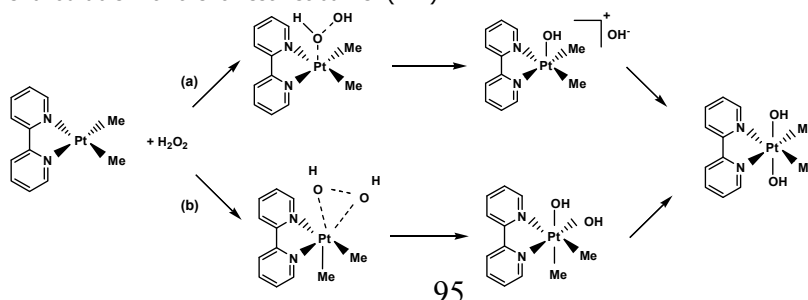
3. Results and discussion

The oxidation reaction of Pt(II) complexes with H_2O_2 has important mechanistic implications. The mechanism of the oxidative addition reaction of H_2O_2 and Pt(II) complexes has been the subject of some debate, and two reaction pathways have been proposed (See the Figure):

(a) Axial electrophilic attack by H_2O_2 at the square planar Pt(II) complex, followed by a heterolytic cleavage of the O–O bond and subsequent attack of the hydroxide anion.

(b) A concerted three-centered transition state and homolytic cleavage of the O–O bond to give a *cis*-dihydroxo complex as the initial kinetic product, which subsequently rapidly isomerises to the thermodynamically more stable *trans*-dihydroxo Pt(IV) complex.

In order to find the mechanism of this O–O oxidative addition, the two mechanisms have been elucidated using density functional theory (DFT). Our studies show among two possible reaction pathways to form dihydroxop Pt(IV) complex, the pathway b is more favourable with the lowest net barrier (ΔH^\ddagger).





References

- [1] G. K. Anderson, in, *Chemistry of the Platinum Group Metals*, ed. F. R. Hartley, Elsevier, Amsterdam, 1991, ch. 12.
- [2] H. E. Bryndza and W. Tam, *Chem. Rev.*, 1988, 88, 1163.
- [3] R. A. Taylor, D. J. Law, G. J. Sunley, A. J. P. White and G.J. P. Britovsek *Chem. Commun.*, 2008, 2800.
- [4] S. Choi, C. Filotto, M. Bisanzo, S. Delaney, D. Lagasee, J. L. Whitworth, A. Jusko, C. Li, N. A. Wood, J. Willingham, A. Schwenker and K. Spaulding, *Inorg. Chem.*, 1998, 37, 2500.
- [5] M. Rashidi, S. M. Nabavizadeh, R. Hakimelahi, S. Jamali, *J. Chem. Soc., Dalton Trans.*, 2001, 3430.
- [6] K. T. Aye, J. J. Vittal and R. J. Puddephatt, *J. Chem. Soc., Dalton Trans.*, 1993, 1835.
- [7] G. B. Deacon, E. T. Lawrenz, T. W. Hambley, S. Rainone and L. K. Webster, *J. Organomet. Chem.*, 1995, 493, 205.
- [8] L. M. Rendina and R. J. Puddephatt, *Chem. Rev.*, 1997, 97, 1735.
- [9] (a) S. M. Nabavizadeh, S. J. Hoseini, B. Z. Momeni, N. Shahabadi, M. Rashidi, A. H. Pakiari, K. Eskandari, *Dalton Trans.* 2008, 2414. (b) S. Jamali, S. M. Nabavizadeh, M. Rashidi, *Inorg. Chem.* 2005, 44, 8594. (c) S. Jamali, S. M. Nabavizadeh, M. Rashidi, *Inorg. Chem.* 2008, 47, 5441.

A charged particle source at atmospheric pressure

Ebrahim Abedini, Mahmoud Tabrizchi*

Department of Chemistry, Isfahan University of Technology, Isfahan 84156-83111 Iran

(E-Mail: m-tabriz@cc.iut.ac.ir)

Keyword: Particle Source, Charged Particle, Acceleration, Particle Detector

1. Introduction

Nano- and micro-particles play important roles in nature as in interstellar dust, atmospheric aerosols, viruses, and nanomaterials. Study of micro- and nanometer-sized particles is the subject of many fields of science and technology including physics, chemistry, biology, aerosol science and engineering. Most of the developed techniques for study of the physical and chemical properties of particles such as; differential mobility analyzer [1], particle beam mass spectrometry, and acceleration of particles to hyper velocities rely on the ability to produce charged particles. The conventional method of charging particles is based on diffusion charging, which employs radioactivity, electrical discharge, heat, or some other means of ionization. In this work we present a simple and effective method of charging particles at atmospheric pressure based on contact charging.[2]

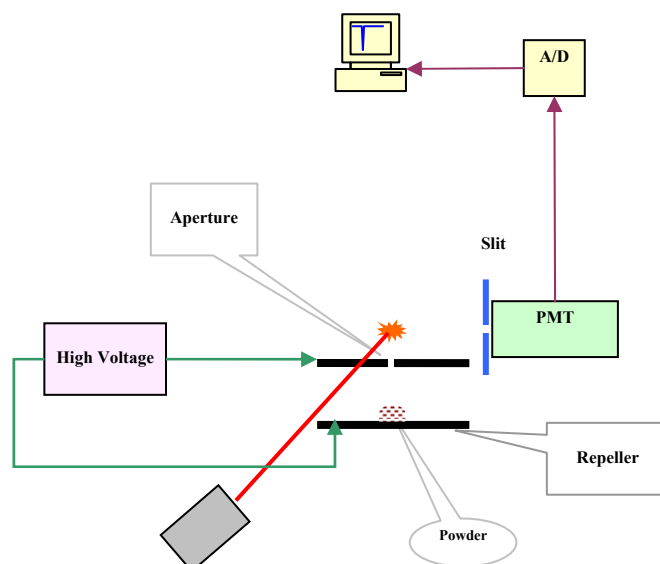


Fig.1 Experimental set up for the charged particle source.

2. The Design

The design consists of a parallel pair of stainless steel plates which are horizontally mounted. The lower plate (Repeller) holds the sample while the upper plate (Aperture plate) consists of a small orifice in its center. The two plates are separated by insulators. The two plates are connected to a high voltage to create an intense electric field between the gap. The powder sample is placed on the repeller where it feels the intense electric field. The electric field induces a charge on particles in contact with repeller and the resulting electrostatic force on each particle causes it to lift against gravity. Then the charged particles impact on the aperture plate which possesses an opposite charge. The particle discharges quickly and charges again oppositely upon contact with the aperture plate. As a result the particle falls down to the repeller and the discharging-charging cycle repeats. Consequently the particles oscillate in the gap between the two plates in touch with high voltage. The charged particle ultimately escaped through a small axial exit aperture in the top plate. The charged particles escaping from the opening of the charging region were detected by a particle detector. The detector was made up of a laser pointer emitting red light and a side window photomultiplier tube. Particles scattered the light when they crossed the laser beam. The resulting scattering was read by the PMT and appeared as a peak in time scale. The laser was mounted perpendicular to the movement direction of particles as well as the window of the PMT. Everything was housed by a thick black polyethylene rod.

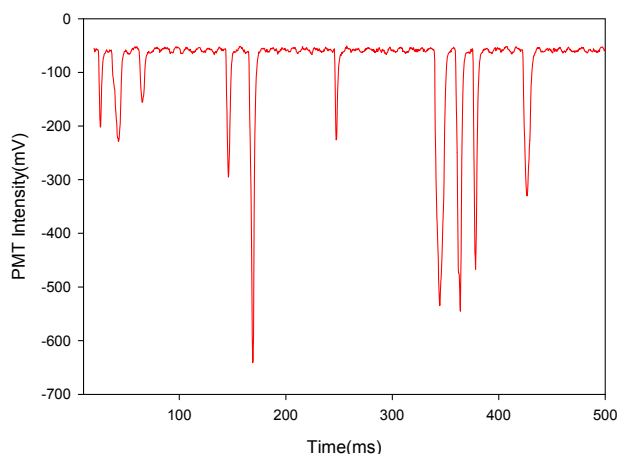


Fig.2. A typical response of the PMT for Al_2O_3 microparticles

3. Results and discussion

A typical response of the PMT for Al_2O_3 microparticles is shown in Fig.2. The S/N ratio is relatively high. The peak width varies from peak to peak as well as the intensities. This is due to differences in the size of the particles and their speed when exit from the charging region. The speed of the particle depends on its mass and charge. The acting force to lift the particle should be greater than its weight, thus

$$q \geq m \cdot g / E$$

where q is the charge of the particle and E is the electric field intensity between the two plates. A simple calculation for an Al_2O_3 particle of $100 \mu\text{m}$ in a 1500 V/cm electric field yields a charge of about 10^{-14} C which approximately corresponds to 10^5 e .

4. Conclusions

In this work, we proposed an efficient method of charging micro- and nano-particles. Unlike other designs, the proposed method easily works under atmospheric pressure. The particles are highly charged and may be used for electrostatic depositing. As no pumping, gas, or dispersing device is needed, the method is simple and inexpensive.

References

- [1] E. O. Knutson and K. T. Whitby, *J. Aerosol. Sci.* 6, 443 (1975).
- [2] P. J. Ziemann, *Trends in Analytical Chemistry*, 17, (1998) 322.

**Application of the group contribution method to long chain n-alkanes based on a new equation of state**

M. Moosavi

Dept. of Chemistry, Faculty of Sciences, University of Isfahan, Isfahan 81746-73441, Iran

(E-mail: m.mousavi@sci.ui.ac.ir)**Keywords:** Equation of state, Density, Group contribution method, Average effective pair potential**1. Introduction**

A general approach to the interpretation of the PVT properties of hydrocarbons is to use the theories that divide the molecule into segments. The group contribution method seems to be a powerful tool to describe the thermodynamic properties of real systems according to their chemical constructions. In this work, the group contribution method has been applied in combination with GMA equation of state (EoS) [1] to calculate the density of n-alkanes and their binary and ternary mixtures. Each normal alkane has been considered as a hypothetical mixture of methyl and methylene groups, in which the interaction potential between each pair is assumed to be the average effective pair potential (AEPP).

2. Theory

Each normal alkane has been considered as a hypothetical mixture of carbonyl groups. According to the one-fluid approximation, GMA EoS can be extended to mixtures [2,3], but the parameters of the EoS are dependent on composition as well as temperature. In the case of long chain hydrocarbons, this equation of state must be modified and the parameters of the new EoS must be depended on the length of chain. Since, the total density of a hypothetical mixture of methyl and methylene groups is $n\rho$, in which n and ρ are the number of carbonic groups and molar density of the n-alkane, respectively, the GMA EoS is modified to:

$$\frac{\left(\frac{2P}{\rho nRT} - 1\right)}{n^3 \rho^3} = A_m n^3 + B_m n^4 \rho = \left(\frac{2Z}{n} - 1\right) V_m^3 = A' + B' \rho \quad ; \quad A' = A_m n^3, \quad B' = B_m n^4 \quad (1)$$

where A_m and B_m are the new EoS parameters per each carbonic group. This new regularity is called GCM-GMA EoS hereafter.

Each normal alkane has been assumed as a hypothetical mixture of two methyl groups at the ends of the chain, two methylene groups each attached to the methyl groups, and $n-4$ middle methylene groups. Propane, n-butane and n-hexane have been used as basic compounds to investigate the contribution of each carbonic (methyl and methylene) groups in the new EoS parameters. The GCM-GMA EoS parameters for each n-alkanes can be predicted from the following expressions:

$$A_m = \left(x_1 \sqrt{A_{11}} + x_2 \sqrt{A_{22}} + x_3 \sqrt{A_{33}}\right)^2, \quad B_m = \left(x_1 \sqrt{B_{11}} + x_2 \sqrt{B_{22}} + x_3 \sqrt{B_{33}}\right)^2 \quad ; \quad x_1 = x_2 = \frac{2}{n}, \quad x_3 = \frac{n-4}{n} \quad (2)$$

where A_{11} - A_{33} and B_{11} - B_{33} parameters which are the contribution of three mentioned segments in A_m and B_m , must be calculated at a certain temperature. Temperature dependence of A_m and B_m are similar to the temperature dependence of the original GMA EoS. Thus, these parameters can be calculated at other temperatures easily. At 323.15 K, these contributions are as follows:

$$A_{11} = 2.19 \times 10^{-4} \text{ L}^3 \text{ mol}^{-3} ; A_{22} = 1.08 \times 10^{-4} \text{ L}^3 \text{ mol}^{-3} ; A_{33} = 1.11 \times 10^{-4} \text{ L}^3 \text{ mol}^{-3}$$

$$B_{11} = 7.18 \times 10^{-6} \text{ L}^4 \text{ mol}^{-4} ; B_{22} = 1.42 \times 10^{-6} \text{ L}^4 \text{ mol}^{-4} ; B_{33} = 1.63 \times 10^{-6} \text{ L}^4 \text{ mol}^{-4}$$

The calculated parameters along with GCM-GMA EoS have been used to calculate the density of n-alkanes and their binary and ternary mixtures at different temperatures, pressures and mole fractions. The results in prediction of density at different temperatures and pressures show good agreement with experimental data. For binary and ternary mixtures, one can use the Eq. (2) to calculate A_m and B_m for mixtures, but the mole fraction of carbonic groups in a mixture of n-alkanes may be calculated as follow:

$$x_1 = x_2 = \sum_i x_i \times \frac{2}{n_i} \quad ; \quad x_3 = \sum_i x_i \times \frac{n_i - 4}{n_i}$$

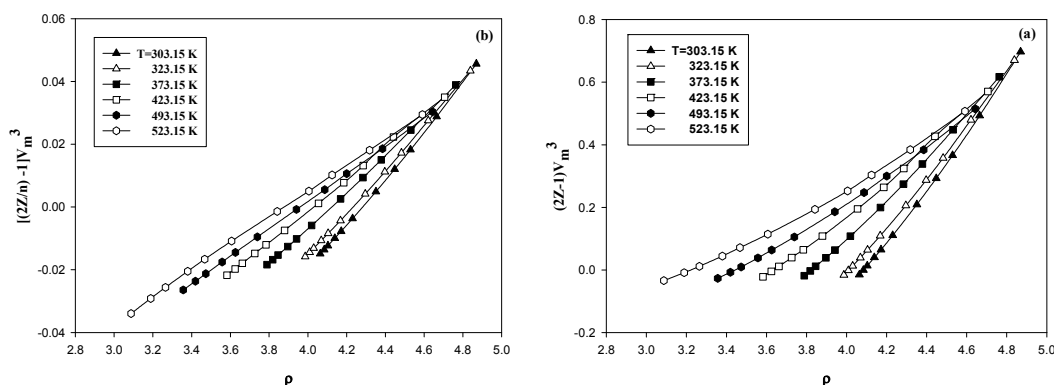


Fig. 1. Comparison between (a) nonlinearity in GMA EoS and (b) linearity in GCM-GMA EoS for n-tridecane at different temperatures.

3. Results and discussion

Figure 1 and the values of R^2 in Table 1 show that the $[(ZZ/n) - 1]V_m^3$ versus ρ is linear for each isotherm of all n-alkanes.

Table 2 shows the AAD values of the calculated density for some alkanes at 323.15 K. The results in prediction of density are in a good agreement with experimental data. To show the ability of this new equation of state in prediction of density of mixtures, the calculated densities of some liquid mixtures from GCM-GMA EoS have been compared with those of computed from original GMA EoS according to mixing and combining rules and also with Costald method. The results show that the GCM-GMA EoS gives better results than other methods (Tables (3) and (4)).

Table 1. Comparison of linear correlations (R^2) of the original GMA EoS and the GCM-GMA EoS for a given isotherm of some n-alkanes for given pressure range.

Alkane	T(K)	ΔP (Mpa)	R^2 for GMA	R^2 for GCM-GMA
C ₉ H ₂₀	423.15	20-800	0.9947	1.0000
C ₁₀ H ₂₂	373.11	0.1-416	0.9973	0.9996
C ₁₁ H ₂₄	473.15	5-500	0.9835	0.9999
C ₁₅ H ₃₂	383.15	0.1-149.55	0.9985	0.9998
C ₂₀ H ₄₂	473.15	5-500	0.9931	0.9997
C ₂₃ H ₄₈	393.15	0.1-149.55	0.9987	0.9998
C ₂₈ H ₅₈	403.15	0.1-149.55	0.9988	0.9998
C ₃₀ H ₆₂	473.15	5-500	0.9895	0.9997
C ₃₆ H ₇₄	393.15	0.1-151.30	0.9992	0.9998
C ₄₀ H ₈₂	473.15	5-500	0.9865	0.9997

Table 2. AAD values of the calculated density for some alkanes at 323.15 K for the given pressure range (ΔP), using the calculated values of A_m and B_m parameters along with Eq. (2).

Alkane	ΔP (Mpa)	A_m	B_m	AAD
C ₅ H ₁₂	5.21-251.6	-1.5394715	3.3804433	0.2311
C ₇ H ₁₆	0.1-240.98	-1.4847426	2.9853653	0.3021
C ₈ H ₁₈	0.1-460	-1.4678429	2.8669367	0.4481
C ₉ H ₂₀	20-800	-1.4547656	2.7764827	0.2413
C ₁₁ H ₂₄	5-500	-1.4358485	2.6475014	0.7861
C ₁₂ H ₂₆	0.1-441.9	-1.4287865	2.5999242	0.6550
C ₁₃ H ₂₈	5-500	-1.4228246	2.5600036	1.0924
C ₁₅ H ₃₂	0.1-149.55	-1.4133114	2.4967730	1.3903
C ₁₇ H ₃₆	0.1-149.55	-1.4060582	2.4489537	1.6188
C ₁₈ H ₃₈	0.1-149.55	-1.4030415	2.4291655	1.9365
C ₁₉ H ₄₀	0.1-149.55	-1.4003451	2.4115282	2.0784

Table 3. AAD between experimental and calculated densities for hexane (x_1)-heptane binary mixtures based on GCM-GMA, Costald method, and combining rules along with the original GMA EoS at 298.15 K and at different mole fractions.

T(K)	x_1	AAD _{combining}	AAD _{Costald}	AAD _{GCM-GMA}
298.15	0.125	0.308	0.443	0.467
	0.375	0.688	0.522	0.296
	0.750	0.636	0.684	0.170
	0.874	0.387	0.753	0.176

Table 4. AAD between experimental and calculated densities for ternary mixtures of pentane(x_1)-hexane(x_2)-heptane based on the original GMA EoS considering mixing and combining rules and GCM-GMA at 323.15 and different mole fractions.

x_1	x_2	AAD _{mixing}	AAD _{combining}	AAD _{GCM-GMA}
0.136	0.125	1.431	1.351	0.194
0.747	0.125	2.411	2.094	0.379
0.125	0.751	0.923	0.841	0.176
0.245	0.393	2.019	1.884	0.247

References

- [1] E.K. Goharshadi, A. Morsali and M. Abbaspour, Fluid Phase Equilib. 230 (2005) 170.
- [2] E.K. Goharshadi and M. Moosavi, Ind. Eng. Chem. Res. 44 (2005) 6973.

**Investigation of temperature dependencies of parameters of effective pair potential**F. Namdari^a, G. A. Parsafar^b

a,b. Department Of Chemistry, Sharif University Of Technology, Tehran, Iran

(E-mail: namdari@mehr.sharif.ir)

Keywords: Effective pair potential, equation of state, potential parameters, Extended Lennard-Jones (12, 6, 3).**1. Introduction**

Recently a new equation of state was introduced that gives an excellent representation of isotherms for widely differing materials, over wide ranges of density and temperature. It may be simply presented, as [1],

$$(Z-1)V^2 = e + f/\rho + g\rho^{-2} \quad (1)$$

where ρ is density and e , f , and g are nontrivial functions of temperature.

Equation (1) was derived on the basis of the extended Lennard-Jones (12, 6, 3) potential, from which the effective pair interaction potential can be given as,

$$U = k_3\rho + k_6\rho^2 + k_{12}\rho^{-4} \quad (2)$$

where k_i s are temperature-dependent parameters.

It is unlikely to find the Lennard-Jones (12, 6, 3) effective pair potential parameters in literature for any materials. The purpose of the present paper is to suggest a method to obtain the temperature dependencies of the potential parameters, via the new equation of state.

2. Method

We have used the experimental PVT data for several isotherms, to obtain the coefficients of equation of state (1) at different temperatures. we can fit e , f , and g parameters by a polynomial function as follows [2]:

$$e = e_0 + e_1/T + e_2/T^2 + e_3/T^3 \quad (6)$$

note that similar temperature dependencies can be used for f and g parameters.

Using some exact thermodynamic relations, we can provide relations between e , f , and g and the effective pair potential parameters, as follows:

$$RT^2 e' = -2k_6(T) \quad (3)$$

$$RT^2 g' = -4k_{12}(T) \quad (4)$$

$$RT^2 f' = -k_3(T) \quad (5)$$

where e' , f' , and g' are the temperature derivative of e , f , and g , respectively. R is universal gas constant

so we take temperature derivatives of e , f , and g parameters to calculate k_i s from equations (3), (4), and (5).

3. Results and discussion

As an example for N_2 the results are shown in below Figures and table:

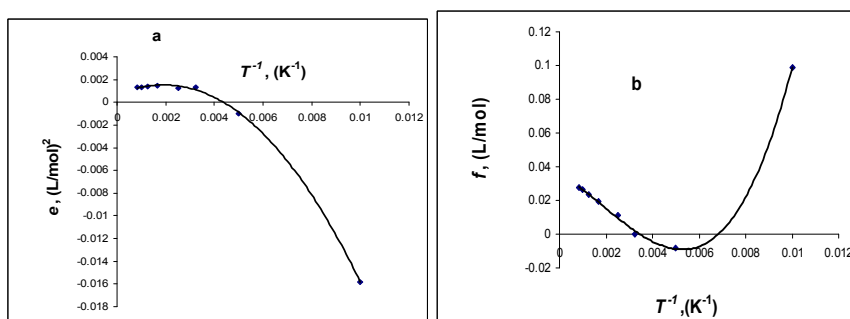


Fig.1: Temperature dependencies of e (a) and f (b) for N_2 [3]

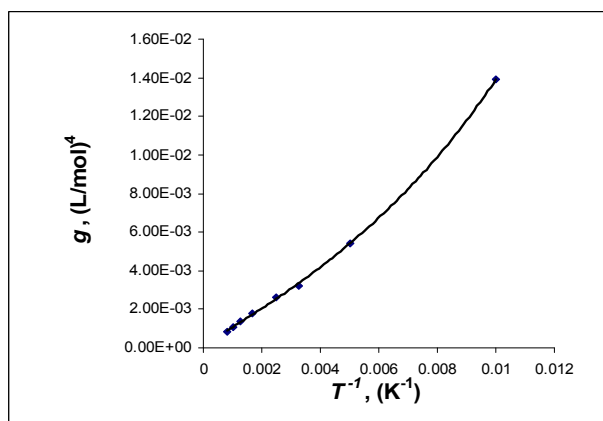


Fig.2. Temperature dependence of g for N_2 [3].

Table. Effective pair potential parameters for N_2 at three temperatures.

T(K)	K3(J.L/mol ²)	K6 (J.L ² /mol ³)	K12 (J.L ⁴ /mol ⁵)
100	-1.02029	-73.9724	1.9715
600	-1.09063	-21.2278	1.9057
1000	-1.10418	-13.3387	1.8397

4. Conclusions

We have derived temperature dependencies of effective pair potential parameters for N_2 , which were used to investigate temperature dependencies of the effective pair potential parameters. Such an approach may be used for others materials including ionic liquids, as well.

References

- [1] G. A. Parsafar; H. V. Spohr; G. N. Patey, J. Phys. Chem. B. 113 (2009) 11977.
- [2] G. A. Parsafar; N. Farzi; B. Najafi, Int. J. Thermophys. 18 (1997) 1197.
- [3] R. T. Jacobsen; R. B. Stewart; M. Jahangiri, J. Phys. Chem. Ref. Data 15 (1986) 735.

**Equation of state for light solid molecules**F. Safdari^a, G. A. Parsafar^b

a,b. Department Of Chemistry, Sharif University Of Technology, Tehran, Iran

(E-mail:F_Safdari@mehr.sharif.ir)

Keywords Equation Of State, Light Solid Molecules, Regularities, Lennard-Jones (12, 6, 3)**1. Introduction**

A general regularity has been found for dense fluids, both nonmetallic and nonionic fluids; namely, $(Z-1)V^2$ varies linearly with respect to ρ^2 , and the other equation of state (EOS) according to which the isotherms of $(Z-1)V^2$ are linear in terms of $1/\rho$, which gives a good Description for metallic and ionic fluids [1, 2]. Unexpectedly, Ne indicates a significant deviation from the linear isotherm regularity (LIR).

2. Method

The purpose of this research is to investigate the accuracy of LIR for the other dense systems, including light molecules such as He, H₂, and D₂, since we have noticed that these systems don't well obey the LIR EOS. First we have used experimental *PVT* data for solid He, H₂, D₂ and Ne at 4 K, to check the accuracy of the LIR [4, 5].

3. Results and discussion

Results for solid H₂ for the pressure range of 0-1.96 GPa is shown in Figure 1.

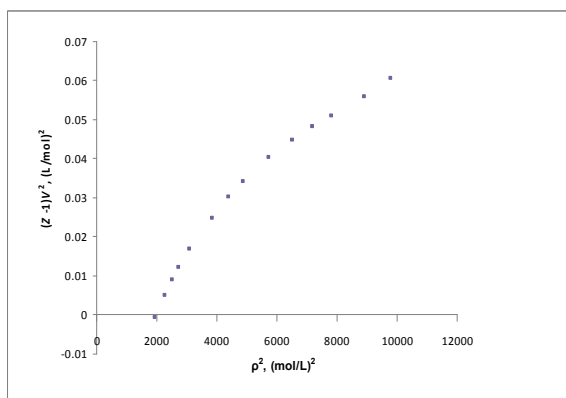


Fig.1. Typical isotherm of $(Z-1)V^2$ vs ρ^2 for solid H₂ at 4 K.

Similar investigation have been done for solid He and D₂, as well. The fitting results are summarized in Table 1.

Table 1. Examining LIR EOS for light solid molecules.

substance	<i>T</i> , K	$\Delta\rho$, mol/L	<i>R</i> ²
H ₂	4	44.15-99.00	0.956
He	4	58.48-156.78	0.933
D ₂	4	51.12-105.26	0.951

As shown in Figure 1 and Table 1, it is obvious that LIR cannot describe such light solids accurately.

Due to such significant deviation for LIR a general EOS based on an effective near-neighbor pair interaction of extended Lennard-Jones (12, 6, 3) type recently has been introduced, as,



$$(Z-1)V^2 = e + f/\rho + g\rho^2 \quad (1)$$

where e , f and g are nontrivial functions of temperature, and in general, one must expect all three functions to contain contributions from both the internal and thermal pressures [3]. we have used experimental data for the light solids to examine the accuracy of this EOS. The results of such examination are presented In Table 2.

Table 2. Examining EOS 1, for light solid molecules.

substance	T, K	$\Delta\rho, \text{mol/L}$	R^2
H ₂	4	44.15-99.00	0.999
He	4	58.48-156.78	0.997
D ₂	4	51.12-105.26	0.998

Equation 1, gives an excellent fit to the isotherm of the light solids, as shown in Table 2.

4. Conclusions

The linearity of $(Z-1)V^2$ vs ρ^2 has been checked with experimental data for dense light molecules. Despite LIR works well for many nonionic and nonmetallic solids, but light solids deviate significantly from the expected linearity. Equation 1, well presents the light solids, as well as many other systems.

References

- [1] G. A. Parsafar; E. A. Mason, J. Phys. Chem 97 (1993) 9048.
- [2] M. H. Ghatee; M. Bahadori, J. Phys. Chem. B. 105 (2001) 11256.
- [3] G. A. Parsafar; H. V. Spohr; G. N. Patey, J. Phys. Chem B. 113 (2009) 11977.
- [4] M. Shokouhi; G. A. Parsafar; M. H. Dinpajoo, Fluid Phase Equilibria 271 (2008) 94.
- [5] John w. Stewart, J. Phys. Chem. solids Pergamon press 1 (1956) 146 .

The pH effect on complexation of Alkali metal cation by p-sulfonatocalix(4)arene in aqueous solution

N. Osouleddini

Department of Chemistry, Islamic Azad University, Ardabil Branch, Ardabil, Iran

(E-mail: osouleddini.n@gmail.com)

Keywords: Formation constant, Spectrophotometric titration, Alkali metal cation, p-sulfonatocalix(4)arene

1. Introduction

The calixarenes constitute a class of macrocyclic receptors that is of great importance in supramolecular chemistry. These hosts, which are formed by phenolic units bridged by ortho-methylene group, are able to complex a variety of guests such as certain neutral and charged inorganic and organic species. The p-sulfonatocalix(4)arene is able to complex a variety of metal and organic cations in water. The binding of cations in water is a complicated phenomenon in which electrostatic forces, Vander-Waals forces and hydrophobic effects play a major role but other factors also have to be considered. For instance, the weak cation- π interactions between the positive charge of the cation and an electron rich aromatic ring or electrostatic attraction between host p-sulfonatocalix(4)arene and cations could be of special importance, particularly in biological recognition [1,2]. In this article, the complexation of alkali metal cations by p-sulfonatocalix(4)arene have studied at different pH. Further, the effect of pH on the formation constant has been discussed.

2. Spectrophotometric Measurements

All measurements were carried out at 25° C using a spectrophotometer scanning (UV-Vis 2101 Shimadzu) with a computer. The system was thermostated at 25° C by circulating water from an isothermal bath. 2 ml of the ligand solution (2×10^{-4} mol L⁻¹) was titrated with stepwise addition of an alkali metal cation solution (1.0×10^{-3} mol L⁻¹), all in water solvent. The measured absorbances were sufficient to allow the treatment of the data with the computer program. In all cases the procedure was repeated at least three times and the resulting average values and corresponding deviations from the average are shown in the text and Tables.

3. Results and discussion

The complex $M^+_pSC_{4q}$ formed is characterized by its stoichiometry, p and q , where M^+ and SC_4 represent each metal ion and p-sulfonato calix(4)arene, respectively. To determine the formation constant of complexation, K , Eq. 1 is defined,

$$pM^+ + qSC_4 \rightleftharpoons M^+_pSC_{4q} \quad K = [M^+_pSC_{4q}] / [M^+]^p [SC_4]^q \quad (1)$$

Absorbance, A , was measured by successive addition of an alkali metal cation solution to the ligand solution, see experimental section. Treatment of the spectrophotometric data (250-350 nm with an interval of 1 nm) obtained during the titrations were conducted with the computer program Squad [3].

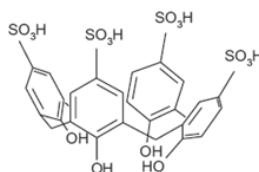


Fig.1. Structure of p-sulfonic acid calix(4)arene (25,26,27,28- tetrahydroxy-5,11,17,23- tetrasulfonic acid- calix(4)arene).

All proposed complex species existed in significant concentration were checked over a reasonable range of data. As expected, polynuclear complexes were systematically rejected by the computer program. Taking into account a binuclear complex alone or together with the mononuclear one does not improve the goodness of the fit and even leads to the rejection of the model. The model finally chosen, formed by M^+SC_4 , resulted in a satisfactory numerical and graphical fitting for all systems.

The formation constants values of complexation of alkali metal cations and p-sulfonic acid calix(4)arene in aqueous solution are given in Table 1. The study was carried out under different pH at 25° C. At pH 2.0 according to the pKa values [4], all sulfonic acid groups of the ligand are dissociated whereas all the phenolic hydroxyl groups are protonated. The recent investigations [1] have showed that the monovalent metal cations are included in to the calixarene cavity, Therefore they have π -cation interaction in addition of electrostatic interactions with the SO_3^- groups.

**Table1.** Formation constant values for the binding of metal ions by p-sulfonato calix(4)arene in water at different pH and 25°C

cations	log K					
	pH= 1.0	ref	pH= 1.5	ref	pH= 2.0	ref
Li ⁺	4.13± 0.06	this work	4.20±0.05	this work	4.51±0.02	[5]
Na ⁺	3.49± 0.04	this work	3.66± 0.07	this work	4.09± 0.05	[5]
K ⁺	3.48± 0.09	this work	3.52± 0.06	this work	3.96± 0.04	[5]
Rb ⁺	3.19± 0.08	this work	3.20± 0.04	this work	3.45± 0.02	[5]
Cs ⁺	2.96± 0.03	this work	3.01± 0.04	this work	3.16± 0.01	[5]

According the Table 1, at pH 2.0 [5] Li⁺ form strongly binding to the ligand by cation- π interactions with benzene rings and electrostatic interactions with SO₃⁻ groups whereas for Rb⁺ and Cs⁺ are weak because they have not significant cation- π interactions. At pH 1.5, the binding abilities of cations with to the ligand become weaker, when the pH value decrease, which is absolutely because of the competitive binding by H₃O⁺. The binding constants decrease again in more highly acidic solutions (pH =1.0) because of above reasons. That values indicate that electrostatic interaction between cations and SO₃⁻ groups become weaker.

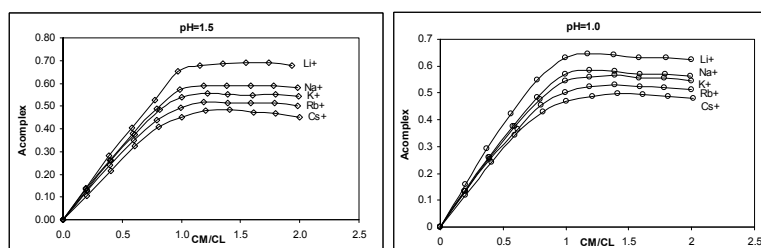
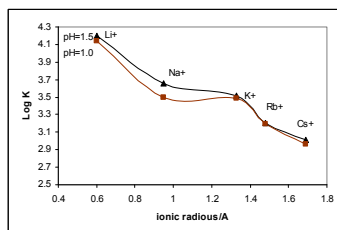
**Fig.2.** Spectrophotometric titration plots of p-sulfonato calix(4)arene by the metal ions, at pH 1.0, 1.5, 25 °C and 280 nm in water.

Figure 2 shows a sharp break point when the concentration of alkali metal cations to the ligand ratios reaches unity, indicating the formation of stable complexes for Li⁺, Na⁺ and K⁺ with the ligand for both pH. The same titration for Cs⁺-ligand system shows the absorbance increase within a very small and no significant break point in complexation curve, indicating low stability constant of formation. According fig. 3 the formation constant values of the complexes increase with decreasing the ionic radius of the cations.

**Fig.3.** The plots of log *K* versus the ionic radii of the alkali metal cations at pH 1.0, 1.5 and 25 °C.

According to the Table 1, Li⁺ forms strongly binding with the ligand by cation- π interactions with benzene rings and electrostatic interactions with the SO₃⁻ groups because of suitable size-fit on cavity, whereas for Rb⁺ and Cs⁺ those are weak because they have not significant cation- π interaction. As a total result, p-sulfonatocalixarene afford weaker binding abilities towards alkali metal cation guests at pH 1.0 and 1.5 than towards them at pH 2.0.

References

- [1] C.Bonal, Y.Israeli, J.P.Morel and N.M.Desrosiers, J.Chem.Soc.,Perkin Trans. 2(2001) 1075.
- [2] J.P.Morel and N.M.Desrosiers, Org.Boimol.Chem., 4(2006)462.
- [3] D.J.Leggett, computation Methods for the Determination of Formation Constants; Plenum Press: New York, 1985.
- [4] G.Arena, R.Cali, G.G.Lombardo, E. Rizzarelli, D. Sciotto, R.Ungaro and A.Casnati, Supramol. Chem., 1(1992)19.
- [5] N.Osouleddini, F.Gharib, K.Zare; J.Sci.I.A.U(JSIAU),19,72(2009)81.

**Salting-out effects in aqueous solutions of ionic liquid 1-Butyl-3-Methylimidazolium Iodide and sodium phosphate: cloud-point temperature shifts and volumetric properties**

R. Sadeghi, B. Mostafa

Department of Chemistry, University of Kurdistan, Sanandaj, Iran

(E-mail: rsadeghi@uok.ac.ir)(E-mail: m_bahar155@yahoo.com)**Keywords:** Ionic Liquid, 1-buthyl-3-methylimidazolium iodide, Sodium phosphate, Volumetric properties, Liquid-liquid equilibria**1. Introduction**

Typical aqueous two-phase systems (ATPS) are generated by mixing two different polymers [e.g. dextran and poly(ethylene glycol), PEG] or one polymer and one salt (e.g. PEG and sodium citrate) at certain concentrations in an aqueous solution. Liquid-liquid extraction utilizing these aqueous two-phase systems has been used to separate and purify biological products from the complex mixtures in which they are produced [1,2]. One of the very interesting properties of hydrophilic ionic liquids (ILs) is that they can be induced to form aqueous biphasic systems when contacted with concentrated solutions of water-structuring salts, forming an upper IL-rich phase and a lower salt-rich phase, both of which are aqueous. These aqueous biphasic systems can be utilized to recycle or concentrate hydrophilic ILs from aqueous solution, to carry out metathesis in the formation of new IL salts, and for separations, including reactive separations [3] and have been successfully used to separate testosterone, epitestosterone, opium alkaloids, and bovine serum albumin. In this work, we present our results on liquid-liquid equilibria and volumetric properties for the 1-buthyl-3-methylimidazolium iodide ($[C_4mim][I]$) + tri-sodium phosphate (Na_3PO_4) + H_2O system over a range of temperatures at atmospheric pressure.

2. Methods

The density and sound velocity of the mixtures were measured at different temperatures with a digital vibrating-tube analyzer (Anton Paar DSA 5000, Austria) with proportional temperature control that kept the samples at working temperature within $\pm 10^{-3}$ K. The experimental apparatus employed for determination of liquid-liquid equilibrium data is essentially similar to the one used previously [2]. A glass vessel was used to carry out the phase equilibrium determinations. The glass vessel was provided with an external jacket in which water at constant temperature was circulated using a thermostat. The temperature was controlled to within ± 0.05 K. The binodal curves were determined by a titration method. A salt solution of known concentration was titrated with the IL solution or vice versa, until the solution turned turbid. The composition of the mixture was determined by mass on a Sartorius CP124S analytical balance. For the determination of the tie-lines, feed samples (about 10 cm³) were prepared by mixing appropriate amounts of IL, salt and water in the vessel and brought into a thermostatic bath to maintain appropriate temperature. The systems were stirred and well mixed and allowed to settle, to ensure the proper phase separation at a desired temperature, as indicated by the absence of turbidity in each phase. Once the equilibrium was achieved, samples were collected from both equilibrium phases using glass syringes through the rubber septa that sealed the cells. The concentrations of the salts in the top and bottom phases were determined by flame photometry. The concentration of IL in both phases was determined by refractive index measurements performed at 298.15 K using a refractometer (QUARTZ RS-232, Ceti, Belgium).

3. Results and discussion

The aim of this work is to obtain further evidence about the salting-out effect produced by the addition of Na_3PO_4 to aqueous solutions of water miscible ionic liquid $[C_4mim][I]$ by evaluating the effect of Na_3PO_4 on the thermodynamic properties of aqueous solutions of this ionic liquid. Experimental measurements of density and sound velocity at different temperatures ranging from 288.15 to 308.15 K and the liquid-liquid phase diagram at different temperatures ranging from 288.15 to 338.15 K for aqueous solutions containing $[C_4mim][I]$ and Na_3PO_4 are taken. The apparent molar volume and isentropic compressibility of transfer of $[C_4mim][I]$ from water to aqueous solutions of Na_3PO_4 have positive values and increase by increasing salt molality. The effects of temperature, addition of Na_3PO_4 and $[C_4mim][I]$ on the liquid-liquid phase diagram of the investigated system have been studied. It was found that an increase in temperature caused the expansion of the one-phase region.



Na₃PO₄ triggers salting-out effect, leading to significant upward shifts of the liquid-liquid demixing temperatures of the system. The effect of temperature on the phase-forming ability in the investigated system has been studied based on a salting-out coefficient obtained from fitting the binodal data to a Setschenow-type equation for each temperature. Based on cloud point values, the energetics of the clouding process has been estimated.

References

- [1] B. Y. Zaslavsky, Aqueous Two-Phase Partitioning, Physical Chemistry and Bioanalytical Applications, Marcel Dekker, New York, 1995.
- [2] R. Sadeghi, R. Golabiazar, H. Shekaari, J. Chem. Thermodyn. (2009), doi:10.1016/j.jct.2009.10.007
- [3] K. E. Gutowski, G. A. Broker, H. D. Willauer, J. G. Huddleston, R. P. Swatloski, J. D. Holbrey, R. D. Rogers, J. Am. Chem. Soc. 125 (2003) 6632.



Excess thermodynamic parameters of binary mixtures of {Methanol, Ethanol, 1-Propanol and 2-Butanol + Chloroform} at (288.15 to 323.15K) and comparison the Flory theory

M. Rezaei Sameti ^{a*}, H. Iloukhani ^b, M. Rakhshi ^b

a. Department of applied chemistry, Faculty of Science, Malayer University, Malayer, Iran

b. Department of Physical Chemistry, Faculty of Chemistry, University of Bu-Ali Sina, Hamedan 65174, Iran

(E-mail : mrsameti@gmail.com)

Keywords: Thermal expansion coefficients; Excess thermal expansion coefficients; Isothermal Coefficient of pressure excess molar enthalpy; Flory theory

1. Introduction

Research activities of our laboratory comprise, among others, the systematic measurements of volumetric properties of different groups of organic compounds [1-2]. Excess thermodynamic properties of mixtures are useful in the study of molecular interactions and arrangements; they reflect the interactions that occur between solute-solute, solute-solvent and solvent-solvent species. In general, positive excess molar volumes may be due to the compensation between strong like interactions (such as those present in alcohols) and equally strong unlike H-bond interactions (such as those present between alcohols and ether). Negative excess molar volumes will occur when unlike interactions prevail over self-association, particularly when packing effects such as free molar volume and interstitial accommodation may be neglected [3-6].

2. Experimental

Densities of the pure liquids and their mixtures at different temperatures were measured with an Anton Paar digital densimeter (Model DMA 4500) operated in the static mode and capable of a precision of better than $\pm 10^{-2}$ kg.m⁻³ and automatically thermostated within ± 0.01 K.

3. Results and discussion

In this work thermal expansion coefficients α , and their excess values α^E , and isothermal coefficient of pressure excess molar enthalpy $(\partial H_m^E / \partial P)_{T,x}$, partial molar volumes $\bar{V}_{m,i}$, and excess partial molar volumes $\bar{V}_{m,i}^E$, for the binary mixtures {methanol, ethanol, 1-propanol and 2-butanol + chloroform} were measured at (288.15, 293.15, 298.15, 303.15, 308.15, 313.15, 318.15 and 323.15) K. The excess thermal expansion coefficients α^E and the isothermal coefficient of pressure excess molar enthalpy $(\partial H_m^E / \partial P)_{T,x}$ for binary mixtures of {methanol and ethanol + chloroform} are S-shaped and for binary mixtures of {1-propanol and 2-butanol + chloroform} are positive over the mole fraction. The isothermal coefficient of pressure excess molar enthalpy $(\partial H_m^E / \partial P)_{T,x}$, are negative over the mole fraction range for binary mixture of {1-propanol and 2-butanol + chloroform}. The obtained results were then compared with the calculated values by using the Flory theory of liquid mixtures. The results show a good agreement between the theory and experimental. The excess molar volumes, excess thermal expansion coefficients and isothermal coefficient of pressure excess molar enthalpy were correlated as a function of the mole fraction by using the Redlich-Kister equation. Figure 1-3 show the variation of α^E , $(\partial H_m^E / \partial P)_{T,x}$, $\bar{V}_{m,i}^E$ parameters vs mole fraction at different temperatures, Figure 4 show the comparison of experimental volumes with Flory theory. The results show that in this system the Flory theory is predicted experimental values.

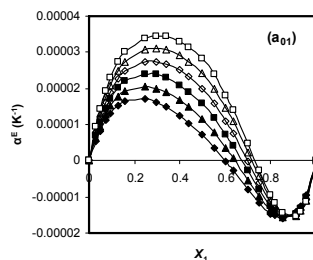


Fig. 1. Plot of excess thermal expansion coefficients α^E , against mole fraction for $\{(a_{01})$; methanol + chloroform, (a_{02}) ; ethanol + chloroform, (a_{03}) ; 1-propanol + chloroform, (a_{04}) ; 2-butanol + chloroform $\}$ at 288.15 K (\blacklozenge), 293.15 K (\blacktriangle), 298.15 K (\blacksquare), 303.15 K (\diamond), 308.15 K (Δ), 313.15 K (\square)

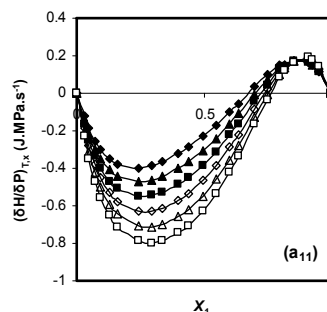


Fig.2. Plot of isothermal coefficient of pressure excess molar enthalpy $(\partial H^E / \partial P)_{T,x}$, against mole fraction for $\{(a_{11})$; methanol + chloroform, (a_{12}) ; ethanol + chloroform, (a_{13}) ; 1-propanol + chloroform, (a_{14}) ; 2-butanol + chloroform $\}$ at 288.15 K (\blacklozenge), 293.15 K (\blacktriangle), 298.15 K (\blacksquare), 303.15 K (\diamond), 308.15 K (Δ), 313.15 K (\square) .

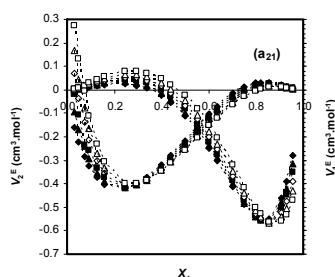


Fig.3. Plot of excess partial molar volume $\bar{V}_{m,i}^E$, against mole fraction for $\{(a_{21})$; methanol + chloroform, (a_{22}) ; ethanol + chloroform, (a_{23}) ; 1-propanol + chloroform, 2-butanol + chloroform $\}$ 293.15 K (\blacktriangle), 298.15 K (\blacksquare), 303.15 K (\diamond), 308.15 K (Δ), 313.15 K (\square) .

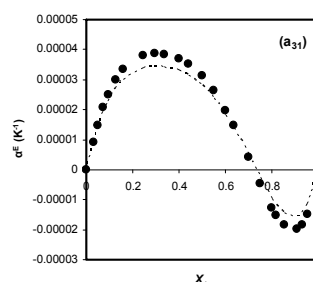


Fig.4. Plot of excess thermal expansion coefficients α^E , against mole fraction for $\{(a_{31})$; methanol + chloroform, (a_{32}) ; ethanol + chloroform, (a_{33}) ; 1-propanol + chloroform, (a_{34}) ; 2-butanol + chloroform $\}$ 313.15 K. (\bullet) Experimental; (.....) calculated by using Flory theory.

References

- [1] Rezaei-Sameti, M. Iloukhani, H. *Monatsh Chem.*, **140** (2009) 491 .
- [2] Rezaei-Sameti, M. Iloukhani, H. Rakhshi, M. *J. Mol. Liq.* **96** (2009) 140.
- [3] Iloukhani, H. Rakhshi, M. *J. Mol. Liq.* **149**(2009), 86 .
- [4] Iloukhani, H. Rezaei-Sameti, M. Basiri-Parsa, J. *J. Chem. Thermodyn.*, **38**, (2006) 975 .
- [5] Iloukhani, H. Rezaei-Sameti, M. Zarei, H.A. *Thermochim. Acta*, **438** (2005) , 9.
- [6] Iloukhani, H. Rezaei-Sameti, M. *J. Chem. Eng. Data* ., **50**,(2005) 1928 .



The study of physico-chemical properties of binary systems (benzyl alcohol, cyclohexanol and 1,2-propanediol) at different temperatures

Elham Sokhanvary^{*}, Hossein A. Zarei

Department of Chemistry, Faculty of Science, Bu-Ali Sina University, Hamedan, Iran

(E-mail: e.sokhanvary@gmail.com)

Keywords : Densities; Excess molar volume; benzyl alcohol; cyclohexanol ; 1,2-propanediol

1. Introduction

The excess properties of liquid mixtures are important to understand and interpret the nature of interactions between the molecules of the mixtures. Volumetric properties of binary liquid mixtures have been extensively studied, as they can contribute to clarification of the various intermolecular interactions existing between the different species found in solution. The aim of the present work is to analyse the volumetric behaviour of binary liquid mixtures of (benzyl alcohol, cyclohexanol and 1,2-propanediol) at different temperatures. We report densities ρ , excess molar volumes V_m^E for binary liquid mixtures of cyclohexanol (1)+ benzyl alcohol (2), benzylalcohol (1)+1,2-propanediol (2), cyclohexanol (1) +1,2-propanediol (2) at temperatures (303.15, 313.15, 323.15, and 333.15) K and ambient pressure.

2. Method

2.1. Materials

Chemicals of high purity obtained from Merck. The stated purities of the solvents by the manufacture were further ascertained by comparing their density with the corresponding literature values. They are in good agreement with the literature values [1].

2.2. Apparatus and procedure

The densities were measured with an Anton Paar digital vibrating u-tube densimeter (model DMA 4500) [2] with a certified precision of $\pm 5 \cdot 10^{-5} \text{ g} \cdot \text{cm}^{-3}$. The uncertainty in the density was $\pm 1 \cdot 10^{-5} \text{ g} \cdot \text{cm}^{-3}$. The binary mixtures were prepared just before use by mass, using a Mettler AB 204-N balance accurate to $\pm 0.1 \text{ mg}$. Conversion to molar quantities was based on the relative atomic mass table of 1995 issued by IUPAC [3]. Before measurements, chemicals were degassed by ultrasonic bath. Each mixture was used immediately after it was well mixed by shaking.

3. Results and discussion

The excess molar volumes, V_m^E of the binary mixtures were calculated from the densities according to the following equation:

$$V_m^E / \text{cm}^3 \cdot \text{mol}^{-1} = \sum_{i=1}^n x_i M_i (\rho^{-1} - \rho_i^{-1}), \quad (1)$$

where M_i and ρ_i are the molecular mass and density of pure component, respectively, and ρ is the density of a mixture and n is the number of components.

The excess molar volumes of binary liquid mixtures of (cyclohexanol (1) + benzylalcohol (2)) and (benzylalcohol (1) +1,2-propanediol (2)) and (cyclohexanol (1) +1,2-propanediol (2)) are positive and become more positive with increasing temperature. The calculated V_m^E for the binary mixtures at different temperatures are displayed in Figure 1.

The computed excess molar volumes of the binary mixtures were fitted using a temperature-dependent Redlich–Kister expression:

$$V_m^E / \text{cm}^3 \cdot \text{mol}^{-1} = x_i x_j \sum_{p=0}^4 \left(\sum_{q=0}^2 A_{pq} T^q \right) (x_i - x_j)^p, \quad (2)$$

where x_i and x_j are the mole fraction and A_{pq} are the temperature independent parameters for the binary mixtures, and T is the absolute temperature. These parameters were obtained by the un-weighted least-squared method. The standard deviations, σ calculated by using the following relation:

$$\sigma(V_m^E) = \left(\sum_{i=1}^n (V_{m,exp,i}^E - V_{m,cal,i}^E)^2 / n - k \right)^{1/2}, \quad (3)$$

where n is the number of experimental data points and k is the number of A_{pq} parameters.

The temperature dependence of density of pure components was fitted to the equation:

$$\rho(T) / \text{g} \cdot \text{cm}^{-3} = \sum_{i=0}^4 a_i T^i. \quad (4)$$

The thermal expansion coefficient, α as in the case of pure components was obtained by analytical differentiation of the density fitting equation:

$$\alpha = -\rho^{-1}(\partial\rho/\partial T)_P. \quad (5)$$

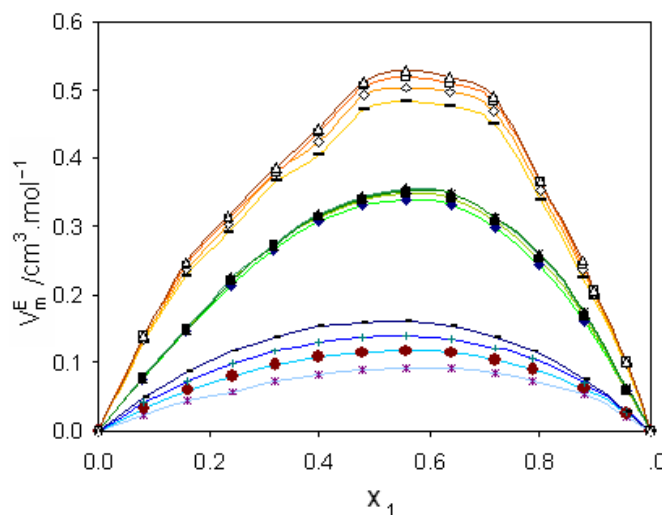


Fig.1. Plot of excess molar volume against mole fraction x_1 of { cyclohexanol (1) + benzylalcohol (2) } at temperatures 303.15 K (◆), 313.15 K (■), 323.15 K (▲), 333.15 K (×) and { benzylalcohol (1) + 1,2-propanediol (2)} at temperatures 303.15 K (*), 313.15 K (•), 323.15 K (+), 333.15 K (-) and { cyclohexanol (1) + 1,2-propanediol (2)} at temperatures 303.15 K (-), 313.15 K (◇), 323.15 K (□), 333.15 K (Δ) . Solid curves represent the values calculated from equation (2)

4. Conclusions

The densities for (cyclohexanol (1) + benzylalcohol (2) , benzylalcohol (1) + 1,2-propanediol (2) and cyclohexanol (1) + 1,2-propanediol (2)) binary mixtures have been measured at temperatures (303.15, 313.15, 323.15 and 333.15) K and the V_m^E over whole composition range were calculated. The V_m^E values for these binary mixtures are positive and become more positive with increasing temperature. The positive values of V_m^E over the entire range of composition may be attributed to the dominance of molecular dissociation over association.

References

- [1] Riddick, J. A.; Bunger, W. B. Organic Solvents, 3rd ed.; WileyInterscience: New York, 1970.
- [2] Anton Paar digital densimeter, Instruction Handbook, Graz, Austria, 2002.
- [3] T.B. Coplen, Pure Appl. Chem. 68 (1996) 2339–2359

**Hetero-Diels-Alder reaction between Hexafluoro-2butyen and 1-Methyl-silene. A theoretical study**S. Jameh-Bozorgi^{a,b,*}, H. R. Khalili ghaydar^a

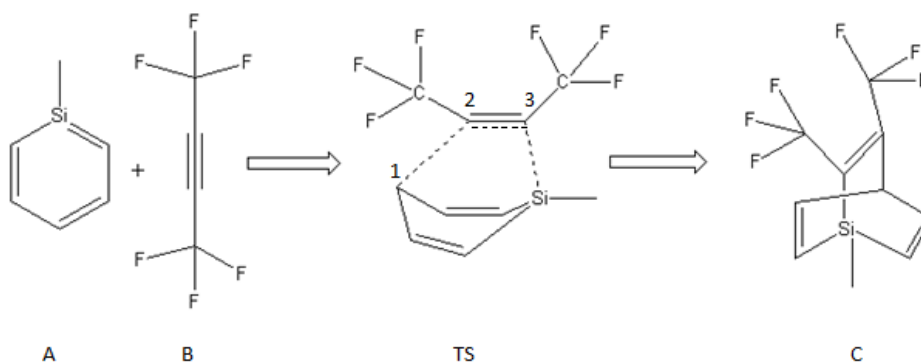
a. chemistry department, faculty of sciences, Islamic Azad University, Arak branch, Arak, Iran

b. Chemistry Department, Faculty of sciences, Islamic Azad University, Touyserkan branch, Touyserkan, Iran

(E-mail: sjamehbozorgi@gmail.com)

1. Introduction

Diels-Alder cycloaddition reaction is one of the best methods for synthesis cyclic molecule in organic and organometallic compounds. In this reaction two carbon-carbon bond formed in a single step[1]. Experimental study of Hetero Diels-Alder (HAD) reaction between 1-Methyl-silene(**A**) and 1,1,1,4,4,4-Hexafluoro-2-butyne(**B**) which causes product 1-Methyl-2,3-bis-trifluoromethyl-1-sila-bicyclo[2.2.2]octa-2,5,7-triene(**C**) was investigate[2]. The aim of this research is a theoretical study of above Hetero Diels-Alder (HAD) reaction for investigate energetic behavior, geometry optimization of reactants, transition state and product, natural Bond Orbital (NBO) analysis of reaction and so on.

**2. Method and Computational detail**

Ab initio calculations were carried out using B3LYP/6-311+G** level of theory with the GAUSSIAN 98 package of programs [3] implemented on a Pentium-PC computer with a 7300 MHz processor. Energy-minimum molecular geometries were located by minimizing energy, with respect to all geometrical coordinates without imposing any symmetrical constraints. The nature of the stationary points for compound A, B and C and transition state structures has been fixed by means of a number of imaginary frequencies. For minimum state structure, only real frequency values, and in the transition-state, only single imaginary frequency values, were accepted

3. Results and discussion

The compound (A) have a aromatic ring with n electron resonance. The result of NBO calculation in B3LYP/6-31+G** level of theory show that the π - π^* electron transitions inter ring are exist. In compound (B) $C \equiv C$ bond length is 1.187Å and electron density is 2.890409 Which shows that there is a triple bond between C-C. When compound (A) is coming close to compound (B), it makes TS (transition state) which after passing 0.006283 HARTREE (3.9 Kcal/mol) activation energy (B3LYP/6-31+G** method) this activation energy in HF and MP2 methods are 0.005676 and 3.56169 respectively. The NBO result about TS show that triple C-C bond with 1.2025 Å bond length and 2.534665 electron density is converting to double bond. In compound (C) length of C-C bond is 1.3275 Å and electron density of bond is 1.596425, length of C1-C2 bond is 1.5145 Å and electron density of bond is 0.364511 and finally, length of Si-C3 bond is 1.8925 Å and electron density of bond is 0.309175 electron.

4. Conclusions

B3LYP density functional-theory calculations provide a picture from structural, energetic, and natural charge distributions points of view for the cycloaddition mechanism. DFT- B3LYP/6-311+G** results revealed that the barrier height for reaction is 3.9 Kcal.mol⁻¹ and NBO analysis showed that pericyclic reaction performed.



References

1. J. McMurry, Organic chemistry, Thomson learning Inc. 2008
2. P. Powell, principles of organometallic chemistry, springer, 1998
3. 1. Gaussian 98, Revision A.5, M. J. Frisch, G. W. Trucks, H. B. Schlegel, G. E. Scuseria, M. A. Robb, J. R. Cheeseman, V. G. Zakrzewski, J. A. Montgomery, Jr., R. E. Stratmann, J. C. Burant, S. Dapprich, J. M. Millam, A. D. Daniels, K. N. Kudin, M. C. Strain, O. Farkas, J. Tomasi, V. Barone, M. Cossi, R. Cammi, B. Mennucci, C. Pomelli, C. Adamo, S. Clifford, J. Ochterski, G. A. Petersson, P. Y. Ayala, Q. Cui, K. Morokuma, D. K. Malick, A. D. Rabuck, K. Raghavachari, J. B. Foresman, J. Cioslowski, J. V. Ortiz, B. B. Stefanov, G. Liu, A. Liashenko, P. Piskorz, I. Komaromi, R. Gomperts, R. L. Martin, D. J. Fox, T. Keith, M. A. Al-Laham, C. Y. Peng, A. Nanayakkara, C. Gonzalez, M. Challacombe, P. M. W. Gill, B. Johnson, W. Chen, M. W. Wong, J. L. Andres, C. Gonzalez, M. Head-Gordon, E. S. Replogle, J. A. Pople, Gaussian, Inc., Pittsburgh PA, 1998. 2. D.
4. Margetic, M. R. Johnston and R. N. Warrener. *Molecules* 5 (2001) 1417



A comparison study between sodium dodecyl sulfonate and sodium dodecyl sulfate with respect to the interaction with poly(ethylene glycol) in aqueous solutions at several temperatures

R. Sadeghi and S. Shahabi
Department of Chemistry, University of Kurdistan, Sanandaj, Iran

(E-mail: rsadeghi@uok.ac.ir)

(E-mail: somayehshahabi@yahoo.com)

Keyword: Thermodynamics, Surfactant, Critical micelle concentration, Volumetry, Conductivity

1. Introduction

The polymer-surfactant interactions are interesting from a fundamental as well as from a practical point of view. These complex mixtures have important properties for a wide range of industrial application fields such as floatation processes, foaming control, detergency, and enhanced oil recovery [1,2]. Although interactions between ionic surfactants and nonionic water soluble polymers have been extensively studied during the last decades, but the subject is not clearly understood. Among all the mixed polymer-surfactant systems, sodium alkyl sulfates $[\text{CH}_3-(\text{CH}_2)_{n-1}-\text{SO}_4\text{Na}]$, especially sodium dodecyl sulfate ($\text{C}_{12}\text{SO}_4\text{Na}$), are the most used anionic surfactants. Sodium alkyl sulfonates $[\text{CH}_3-(\text{CH}_2)_{n-1}-\text{SO}_3\text{Na}]$ are one of the most important class of anionic surfactants which can form micelles in aqueous solution and also may interact with water soluble polymers such as poly(ethylene glycol) (PEG) or poly(vinyl pyrrolidone) (PVP) in aqueous solution [3]. It has been known that $\text{CH}_3-(\text{CH}_2)_{n-1}-\text{SO}_3\text{Na}$ is quite similar to $\text{CH}_3-(\text{CH}_2)_{n-1}-\text{SO}_4\text{Na}$ in many physicochemical properties. In this work, in order to study differences between sodium dodecyl sulfonate and sodium dodecyl sulfate with respect to the interaction with PEG, volumetric, compressibility and electrical conductivity properties of sodium dodecyl sulfonate and sodium dodecyl sulfate in pure water and in aqueous PEG solutions were determined at different temperatures below and above the micellar composition range.

2. Methods

PEG with a quoted molar mass 6000, sodium dodecyl sulfonate and sodium dodecyl sulfate were obtained from Merck. Conductance measurements were carried out on a digital conductivity meter (Metrohm model 712) with a sensitivity of 0.1% and a dipping-type conductivity cell with platinized electrodes with a cell constant of 0.824 cm^{-1} at a frequency of 1 MHz. The density and sound velocity of the mixtures were measured at different temperatures with a digital vibrating-tube analyzer (Anton Paar DSA 5000, Austria) with proportional temperature control that kept the samples at working temperature within $\pm 10^{-3} \text{ K}$.

3. Results and discussion

In this work, we observed that there are distinct differences between $\text{C}_{12}\text{SO}_3\text{Na}$ and $\text{C}_{12}\text{SO}_4\text{Na}$ with respect to the interaction with PEG, based on the measurements of volumetric, compressibility and electrical conductivity. The concentration dependence of the all investigated thermodynamic properties exhibit a change in slope at the concentration in which micelles are formed. The effect of temperature and concentration of PEG on the critical micelle concentration (CMC) of both $\text{C}_{12}\text{SO}_3\text{Na}$ and $\text{C}_{12}\text{SO}_4\text{Na}$ in aqueous solution has been investigated. The values of the Gibbs free energy of micelle formation (ΔG_{mic}) for both surfactant in pure water and in aqueous PEG solutions have been determined. The effects of temperature and concentration of PEG on the infinite dilution apparent molar volume and the infinite dilution apparent molar isentropic compressibility of monomer and micellar state of both investigated surfactants in this work have been studied.

References

- [1] E. D. Goddard, In Interactions of surfactants with polymers and proteins; CRC Press: Boca Raton, FL, 1993.
- [] E. D. Goddard, Colloids Surf., 19 (1986) 301.
- [3] R. sadeghi, R. Hosseini, Colloids and Surfaces A: Physicochemical and Engineering Aspects, 348 (2009) 177.





Spectrophotometric and thermodynamic studies on the protonation and nickel complexation equilibrium of hydroxynaphthol blue in aqueous solution

M. Motiee^{a,b,*}, A. Niazi^{a,b}, S. Sharifi^a, B. Yasar^a

a. Department of Chemistry, Faculty of Sciences, Islamic Azad University, Arak Branch, Arak, Iran

(E-mail: ali.niazi@gmail.com)

b. Young Researchers Club, Islamic Azad University, Arak Branch, Arak, Iran

Keywords: Thermodynamic, Hydroxynaphthol blue, Complex, Nickel, EQUISPEC

1. Introduction

In spectrophotometric titration, controlled displacement of a chemical equilibrium occurs through the addition of titrant. In most investigations in aqueous solution the titrant is a strong base or acid and the measurement produces absorbance data which is a collection of absorption spectra as a function of PH. It is most convenient to arrange the series of measured absorption spectra, as function wavelengths at different PH values as the rows of a matrix Y. According to the Beer- Lambert's law, Y can be the composed into the product of a concentration matrix C and a matrix A of molar absorptivities. The concentration profiles of the absorbing species from the columns of C; the molar absorption spectra from the corresponding rows of A. Due to instrumental and experimental errors, this the composition is not perfect, the difference being the matrix E of residuals. A matrix equation can be written as :

$$Y = CA + E \quad (1)$$

Data fitting consists of determining those unknown parameters for which the sum of the squares over all elements of the matrix E of residuals is minimal. Initially, the unknown parameters include the equilibrium constants, a vector p of non-linear parameters, overall formation constants, and all the molar absorptivities of all the component, i.e. the complete matrix A of linear parameters. C is defined by the model and the appropriate equilibrium constants and is calculated numerically using the law of mass action and the analytical (total) concentrations of each component in solution. If spectra are measured at many wavelengths, the total number of parameters can be very high and it is crucial to reduce this number by separation of the linear and non-linear parameters. For any set of non-linear parameters, p, which defines the concentration matrix C, the best set of linear parameters, the matrix \hat{A} is an explicit least-squares calculation:

$$\hat{A} = C^+ Y \quad (2)$$

C^+ is the pseudo-inverse which can be calculated as $C^+ = (C^t C)^{-1} C^t$ or preferably using a numerically more stable algorithm (i.e., an algorithm which guarantee to reach a physically meaningful final results), \hat{A} is now defined as a function of p, and consequently E and the sum of squares (ssq) are defined as a function of the non-linear parameters only:

$$ssq = \sum \sum E(i,j)^2 = f(Y, \text{model, parameters}) = f(p) \quad (3)$$

In equilibrium studies, the model is the collection of equilibria between the component species and the parameters are the equilibrium constants. The computation of the pseudo-inverse C^+ seems to be a trivial task. In C has, at least theoretically, full rank, i.e., the chemical and mathematical ranks are equal, and the concentration profiles for all species are linearly independent. C^+ can be computed and \hat{A} is determined by equation (2). This is, however, not always the case and near linear dependency (i.e., when the distribution diagram of some species can be expressed as linear combination of some other species) and/or species with only very low concentration, results in deficiencies in the equilibrium model. In this status, C then, does not have full rank and the pseudo-inverse, C^+ , is not or is only poorly defined, which can render its computation of C^+ difficult to impossible and thus corrupt the resulting \hat{A} as well as the residuals, E, and the sum of squares. there are powerful algorithms such as Neton-Gauss-Levenberg/Marquardt algorithm available for this task and interested reader may refer to the literature for detailed descriptions.

2. Experimental

Stock solution of nickel(II) were prepared from nickel nitrate (Merck). Standard of working solution were made by appropriate dilution daily as required. A stock 6×10^{-5} mol L⁻¹ solution of HNB (Merck) solution was prepared by dissolving reagent in triply distilled water. For the Ni/HNB titrations, absorption spectra were measured with an automatic titration set-up consisting of a computer interfaced to a HP8453 spectrophotometer, automatic stirrer. After each pH adjustment, solution is transferred into the cuvette and the absorption spectrum is recorded. Ionic strength was maintained at 0.1 mol L⁻¹ by adding appropriate



amounts of KNO_3 . The protonation were easily obtained in pH range 2-13 by the automatic titration apparatus at different temperature. The complexation of Ni^{2+} by HNB has been studied by titrating mixtures of Ni^{2+} and HNB at different temperature and $I=0.1 \text{ mol L}^{-1}$ (KNO_3) with standard solution of NaOH. The spectral measurements were carried out between 400 and 750 nm with 10 nm intervals. The concentrations of [HNB] and $[\text{Ni}^{2+} \text{ to HNB}]$ ratios in final solutions are 2:1, 1:1, 1:2, 1:3, 1:4, respectively. Then pH is adjusted in the range of 2-13 by adding hydrochloric acid and sodium hydroxide in titration vessel. All absorption spectra were digitized and transferred in ASCII format to an Athlon 2000 XP computer for analysis. Data treatment was done with MATLAB for windows (Mathworks, Version 6.5). The computer program EQUISPEC is written in MATLAB by M. Maeder et al.

3. Results and discussion

The absorption spectra of HNB at various pH values in 400-750 nm intervals were recorded. Singular value decomposition analysis performed on all absorption data matrices obtained at various pH values for HNB gives the number of components that best represent the system. Protonation and complexation constants of HNB in several temperatures (15, 20, 30, 35 °C) were evaluated with EQUISPEC program using the corresponding spectra absorption-pH data. By inspection of the experimental spectra, it is hard to guess even the number of protolytic species involved. The output of the program are pK_a , $\log\beta$ values and their standard deviations, the number of principal component, projection vectors (loadings), concentration distribution diagrams, and the spectrum of each assumed species. The enthalpy and entropy of the different reactions were determined from the dependence of the equilibrium constants on the temperature (van't Hoff equation). From the thermodynamic results the $T\Delta S - \Delta H^\circ$ plot was sketched. Despite the above-mentioned variations which have deterministic effect on the thermodynamics parameters of complexation, the $T\Delta S$ versus ΔH° plot shows a fairly good linear correlation indicating the existence of enthalpy-entropy compensation in the complexation reactions [4].

Table1. Values of thermodynamic parameters.

Equilibrium	$\Delta H(\text{KJ.mol}^{-1})$	$\Delta S(\text{J.mol}^{-1}.\text{K}^{-1})$	$\Delta G(\text{KJ.mol}^{-1})$
$\text{M} + 2\text{L} \rightleftharpoons \text{ML}_2$	438.13	1740.47	-37.27
$\text{M} + \text{H} + \text{L} \rightleftharpoons \text{MLH}$	104.41	690.82	-48.28
$\text{M} + \text{H} + 2\text{L} \rightleftharpoons \text{ML}_2\text{H}$	405.05	1587.15	-102.25
$\text{M} + 2\text{H} + 2\text{L} \rightleftharpoons \text{ML}_2\text{H}_2$	191.16	1302.38	-164.58

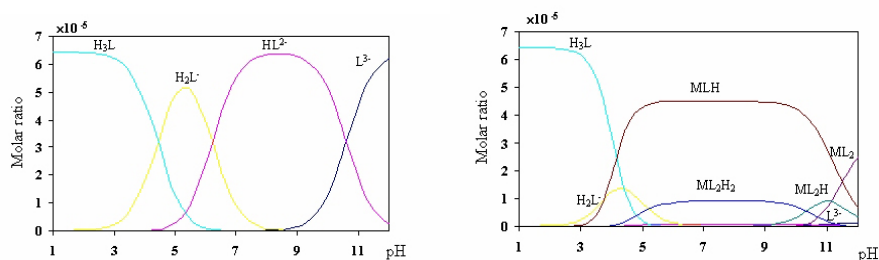


Fig.1. Distribution curve for L and ML

4. Conclusions

In this work, The behavior of protonation and Ni(II) complexation of Hydroxynaphthol blue in ionic strength $0.1 \text{ mol L}^{-1} \text{ KNO}_3$ at different temperature has been studied by multiwavelength spectrophotometric method. EQUISPEC is a computer program using the matrix based MATLAB environment for second order global analysis of spectrophotometric equilibrium data. According to the analysis, important complexes are as below: ML, MLH, ML_2 , ML_2H and ML_2H_2 , which results and obtained formation constants using global analysis are in accordance with reported results.

References

- [1] P. Bugnon, J.C. Chottard, J.L. Jestin, B. Bung, G. Laurency, M. Maeder, A.E. Merbach, A.D. Zuberbuhler, *Anal. Chim. Acta* 298 (1994) 193.
- [2] J. Ghasemi, A. Niazi, M. Maeder, *J. Braz. Chem. Soc.* 18 (2007) 267.
- [3] J. Ghasemi, A. Niazi, M. Kubista, A. Elbergali, *Anal. Chim. Acta* 455 (2002) 335.
- [4] Y. Inoue, T. Hakushi, *J. Chem. Soc. Perkin Trans. II* (1985) 935.



Thermodynamic study of Zn (II)-G lycinamide complex formation by spectrophotometric method in various temperatures and pH=4, ionic strength=0.1 molL⁻¹

N. Tajdini^{a*}, S. Hosseini^b

a. Department of Chemistry, Islamic Azad University, Vramin Pishva, Iran

(E-mail: nilofar_tajdini@yahoo.com)

b. Department of Chemistry, University of Emam Hossein ,Iran

Keywords: Glycinamide, SQUAD, Optical Absorption, Formation Constants, Thermodynamic Parameters.

1. Introduction

Zinc is a constituent of proteins, peptide and aminoacid complexes. The rich structural Information on zinc enzymes is unique[1-3]. It has long been known that certain naturally occurring substances(namely aminoacids, proteins and porphyrins) form stable complexes with the ions of heavy metals[4-6]. In most combinations, aminoacids have a behaviour such as bidentate ligands via NH₂ and COO⁻ ends[7-9]. This paper reports the interaction of Zn(NO₃)₂ with glycineamide(I=0.1molL⁻¹in NaClO₄)at various temperatures using Uv-Visible absorption technique. The binding constants were determined by analyzing optical absorption spectra of complexes at various glycineamide concentrations using SQUAD software [10]. In particular, we determined the standard free energy (ΔG⁰), enthalpy (ΔH⁰) and entropy (ΔS⁰) for the binding of mentioned complexes to glycineamide. Comparison of thermodynamic data leads us to understand the mechanism of interaction.

2. Methods

All experiments were carried out in double distilled water at pH=4.0 potassium hydrogen phthalate ,hydrochloric acid buffer and 0.1M NaClO₄ . In all exreriments, the complex solutions were freshly prepared before spectral analysis. In typical experiment, 2ml of Zn(NO₃)₂ solution 0.03M in 0.1M NaClO₄ (ionic strength) was titrated by glycineamide 0.24M solution.UV-Vis spectra of combinations were recorded in range of 200-800nm in 10 minutes after adding 50μl glycineamide solution.about 15 adds were taken place.about 50 wavelengths showing suitable variations by adding glycineamide solution were chosen and their absorbance rate was recorded.

3. Results and discussion

The figure 1 show typical titration spectra of Zn(NO₃)₂ upon increasing addition of glycineamide at 25.0 °C. The observed spectral changes were used for determining the combining constants due to by using SQUAD program which was developed to empower the evaluation of the best combining constants due to absorbance measurements by using a non-linear least-square method.The input data consist of (a) the absorbance values(b) the total glycineamide and Zn(NO₃)₂ concentrations. The Gauss-Newton non-linear least-squares algorithmis is used for making minimum total residual squares,calculating of eq.no.1.

$$U = \sum_{i=1}^I \sum_{k=1}^{NW} (A_{i,k}^{cal} - A_{i,k}^{obs})^2$$

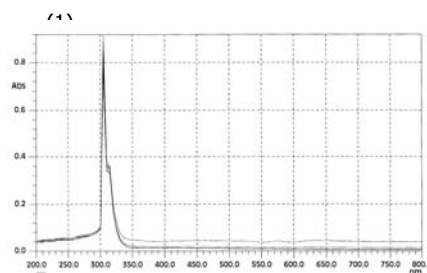


Fig.1. The titration absorption spectra of (ZnNO₃)₂ (0.03M) by Ga (0.24M) in NaClO₄ 0.1M at 25.0 °C

Where A_{i,k} is the absorbance value of ith solution at kth wavelength,give atotal of I solutions and a grand total of NW wavelength (in our experiments I=15 and NW=50). The output data are the logarithm of macroscopic binding constant (K_{i,j}) for formation of Zn_iGa_j, where Zn is Zn(NO₃)₂ and Ga is glycineamide corresponds to the following equilibrium



The values of U and percent of error represent uncertainty for logK_{i,j} calculating of program. The absorption data were analyzed by assuming 1:1 or 2:1 and/or simultaneous 1:1 and 2:1 molar ratios of Zn(NO₃)₂ to glycineamide. Fitting of the experimental data (15 points), to the propsed stoichiometric models was evaluated by the sum of squares of the calculated points by the

model. The results show that the most suitable case is corresponded to 1:1 and 2:1 combining models at range of studied temperatures with total residual squares, and range of U was between 10^{-3} and 10^{-4} . The combining constants are given in table (1). As it can be seen in this table, The combining constants are increased by increasing temperatures. It can be described as an increase of complex stability which results in higher values of combining constants.

A prerequisite for a deeper insight in to the molecular basis of $\text{Zn}(\text{NO}_3)_2$ -glycinamide interactions is thorough characterization of the energetic governing complex formation. The energetic of $\text{Zn}(\text{NO}_3)_2$ -glycinamide equilibrium can be conveniently characterized by thermodynamic parameters such as standard Gibbs energy, ΔG° , standard molar enthalpy change, (ΔH°) and standard molar entropy change, ΔS° . The standard Gibbs energy change is usually calculated due to equilibrium constant (K) of the reaction, by the following relationship.
$$\Delta G^\circ = -RT \ln K \quad (3)$$

Where R and T are the gas constant and the absolute temperature, respectively. Since the activity coefficients of the reactions are not known, the usual procedure is to assume them unity and to use the equilibrium concentrations instead of the activity

Therefore, it will be appropriate to adjust the terminology of apparent equilibrium constant K' , and Gibbs energy $\Delta G^{\circ'}$. Apparent standard enthalpies per mole in unique unit can be obtained due to depending on temperature of the apparent combining constant K' , by vant Hoff equation.
$$d \ln K' = - \left(\frac{\Delta H^{\circ'}}{R} \right) d(1/T) \quad (4)$$

This is the so-called vant Hoff enthalpy. The apparent standard entropy change, $\Delta S^{\circ'}$, can be derived from the Eq(5).

$$\Delta S^{\circ'} = \left(\Delta H^{\circ'} - \Delta G^{\circ'} \right) / T \quad (5)$$

The vant Hoff plots for interaction of $\text{Zn}(\text{NO}_3)_2$ complexes with glycinamide are shown in Fig. (2, 3) The calculated thermodynamic parameters for binding of $\text{Zn}(\text{NO}_3)_2$ to glycinamide are listed in table (1)

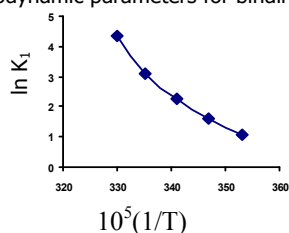


Fig.2. The vant't Hoff plot of Ga to $\text{Zn}(\text{NO}_3)_2$

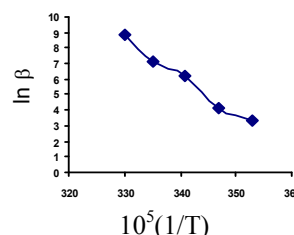


Fig.3. The vant't Hoff plot of Ga to $\text{Zn}(\text{NO}_3)_2$

Table 1. Thermodynamic parameters and binding constants for binding of $\text{Zn}(\text{NO}_3)_2$ to Glycinamide

T (K)	Log K_1 (M^{-1})	ΔG_1^0 (kJ mol^{-1})	ΔH_1^0 (kJ mol^{-1})	ΔS_1^0 ($\text{J mol}^{-1} \text{K}^{-1}$)
283	1.07 ± 0.25	-5.8	270.1	974.9
288	1.58 ± 0.21	-8.7	270.1	968.1
993	2.24 ± 0.40	-12.6	270.1	964.8
998	3.10 ± 0.38	-17.7	270.1	965.8
303	4.36 ± 0.00	-25.3	270.1	974.9

4. Conclusions

In respect to our results, the stoichiometry of glycinamide- $\text{Zn}(\text{NO}_3)_2$ combining are as 1:1 and 2:1. shaping these combinations in our results is increased entropy ($\Delta S^\circ > 0$). shaping constants are as magnitude in a satisfactory way concluding relative stability of studied complexes ($\Delta G^\circ < 0$).

References

- [1] D.W Christianson, Adv Protein. Chem.42(1991)281.
- [2] B.L.Vallee, D.S Auld, Acc. Chem. Res.26(1993)543.
- [3] T.G. Appelt, Coord. Chem. Rev.166(1997)313.
- [4] A.A.Shoukry, M.M. Shoukry, Spectrochim. Acta A.70(2008)686.
- [5] Y.Prashanthi, K. Kiranmai, N Sabhashini. J.P. Shivaraj, Spectrochim. Acta A.70(2008)30.
- [6] Abu-Melha. Khlood El-Metwally, S.M. Nashwa, Spectrochim.Acta A.70(2008)277.
- [7] A.M.Gaber, M. Hassanein, A.A. Lotfalla, J. Mol. Struct.875(2008)322.
- [8] B.B Tewari, J. Chromatogr. A.1103(2006)139.
- [9] M.Asadi, E.Safaei, B.Ranjbar, J. Mol. Struct.754(2005)116.
- [10] M.M.Ahmed Mohamed, M.M. Shoukry, Chem. Pharm. Bull.49(3)(2001)253.



Interaction of dimethyltin(IV) dichloride with phenylalanine and tryptophan

S. Babashpour ^{a,*}, M. Moazzami ^a, A. Shamel ^a, F. Gharib ^b

a. Department of Chemistry, Islamic Azad University, Ardabil, Iran

(E-mail: sbabashpour_ir@yahoo.com)

b. Department of Chemistry, Shahid Beheshti University, G. C., Tehran, Iran

Keywords: Dimethyltin(IV) dichloride, Tryptophan, Phenylalanine, Spectrophotometry, Stability constant

1. Introduction

Organotin(IV) compounds have long been characterized to exhibit relatively high antitumour activity. The structures adopted by di- and trialkyltin(IV) ions in aqueous solutions appear to have linear C-Sn-C and planar skeletons, respectively. Information pertaining to the structure and behavior of these ions in solution at different pH has been the subject of many recent papers.¹⁻³ These ions have rather unusual effects on the structure in water as solvent. There should be particularly pronounced ordering of water molecules in the equatorial plane of the dialkyltin(IV) ions because of the strong electrostatic field near the tin atom. In addition, the hydrophobic nature of the alkyl groups will tend to force more hydrogen bonding in the solvent around the axial positions.

2. Experimental

All measurements were carried out at 25 °C. The ionic strength was maintained to 0.1 mol dm⁻³ with sodium perchlorate. An Eyela pH-meter, PHM 2000, was used for pH measurements. The hydrogen ion concentration was measured with an Ingold UO 3234 glass electrode and an Ingold UO 3236 calomel electrode. The pH-meter was calibrated for the relevant H⁺ concentration with a solution of 0.01 mol dm⁻³ perchloric acid containing 0.09 mol dm⁻³ sodium perchlorate (for adjusting the ionic strength to 0.1 mol dm⁻³). For this standard solution, we set -log[H⁺] = 2.00. Junction potential corrections calculated from eq 1

$$-\log[H^+]_{\text{real}} = -\log[H^+]_{\text{measured}} + a + b[H^+]_{\text{measured}}$$

a and b were determined by measuring of hydrogen ion concentration for two different solution of HClO₄ with sufficient NaClO₄ to adjust the ionic media. 50 cm³ acidic solution of dimethyltin(IV) dichloride (2.0×10⁻³ mol dm⁻³) was titrated with an alkali solution, 0.1 mol dm⁻³ NaOH, of the ligands (1.91×10⁻³ - 1.97×10⁻³ mol dm⁻³ of tryptophan and 1.78 × 10⁻³ - 1.87×10⁻³ mol dm⁻³ of phenylalanine), both of the same ionic strength. The absorbance and -log[H⁺] were measured after addition of a few drops of titrant, and this procedure extended up to the required -log[H⁺]. To exclude carbon dioxide from the system, a stream of purified nitrogen was passed through a sodium chloride solution and then bubbled slowly through the reaction solution. In all cases, the procedure was repeated at least three times and the resulting average values and corresponding deviations from the average are shown in the text and Tables. Spectrophotometric measurements were performed on a UV-vis Shimadzu 2100 spectrophotometer with a Pentium 4 computer and using thermostated matched 10 mm quartz cells. The measurement cell was of flow type. A Masterflex pump allowed circulation of the solution under study from the potentiometric cell to the spectrophotometric cell, so the absorbance and -log[H⁺] of the solution could be measured simultaneously.

3. Results and discussion

Accepting the hypothesis that R₂Sn²⁺ and R₃Sn⁺ are the usual active species for antitumour action of organotins, a good antitumour agent should be easily dissociable following administration to animals. This requires weak bonds between tin and the donor atom of the coordinated ligands, which are readily hydrolysable. If the compound is hydrolytically unstable, the R₂Sn²⁺ and R₃Sn⁺ moieties will be released too soon, and if it is too stable, it may be released too slowly and consequently lower activity will be observed. Therefore, there is a relationship between the stability of the organotin compounds and their antitumour activity.

Using a combination of spectrophotometric and potentiometric methods different models including ML and MHL and several polynuclear and protonated species were tested by the computer program. As expected, polynuclear complexes were systematically rejected by the program, as also were MH₂L₂, MHL₂, and ML₂, (the charges were omitted for simplicity). A value for the MH₂L species (in both cases of the amino acids) was also calculated by the program, but the species was not considered further, because the estimated error in its formation constant was unacceptable, and its inclusion does not improve the



goodness of the fit. The models finally chosen, formed by MHL and ML for the ligands, besides the hydrolysis products of $\text{Me}_2\text{Sn(IV)}^{2+}$ resulted in a satisfactory of numerical and graphical fitting.

References

- [1] F. Gharib, E. Farzad, M. M. Amini, Can. J. Chem. 849 (2006) 1534.
- [2] F. Gharib, F. Jaber, M. Zandevakili, Appl. Organomet. Chem. 22 (2008) 215.
- [3] M. Jabbari, F. Gharib, M. M. Amini, A. Azadmehr, Can. J. Chem. 86 (2008) 751.

***p-v-T*-properties of phosphonium-based ionic liquids using ISM equation of state***S. M. Hosseini ^a, F. Sabzi ^b

a. Department of Chemistry, College of Sciences, Shiraz University, Shiraz, Iran
(E-mail: Seied_Mostafa_Hosseini@Yahoo.com)

b. Department of Chemistry, Shiraz University of Technology, Shiraz, Iran

Keywords: Ionic Liquids, ISM Equation of State

1. Introduction

Knowledge of the *p-v-T* properties of phosphonium-based ionic liquids (ILs) is important because of their superior properties as compared to imidazolium-based ILs [1]. The equation of state provides a basis for accurate thermophysical properties of these ILs. The purpose of this work is to explain how the equation of state (EOS) proposed by Ihm-Song-Mason (ISM) [2] can be applied with even less input information for phosphonium-based ILs. A knowing of only two critical constants (T_c and V_c) is sufficient to predict the volumetric properties of these ILs. From about 400 data points examined for the phosphonium-based ILs and the average absolute deviation compared with the experimental data is 1.04%.

2. Theory

Weeks–Chandler–Anderson (WCA)[3] perturbation theory of liquids have been developed based on the recognition that the structure of a liquid is determined primarily by repulsive forces, so that fluids of hard bodies can serve as useful reference states. In this work, we applied an analytical equation of state derived by Song and Mason[4], which is based on the WCA perturbation theory of liquids. The proposed equation of state has the following form;

$$\frac{p}{\rho kT} = 1 + \frac{(B_2 - \alpha) \rho}{1 + 0.22 \lambda b \rho} + a \rho G(b \rho) \quad (1)$$

where p is the pressure, ρ is the molar (number) density, B_2 is the second virial coefficient, α is the contribution of repulsive forces to the second virial coefficient, b is the van der Waals covolume, kT is the thermal energy and λ represents an adjustable parameter. Here, values of λ have been determined from experimental *p-v-T* data.

A new corresponding states principle has the form:

$$G(b \rho)^{-1} = \alpha \rho \left[Z - 1 - \frac{(B_2 - \alpha) \rho}{(1 + 0.22 \lambda b \rho)} \right]^{-1} = 1 - \lambda b \rho \quad (2)$$

where $Z = p/\rho kT$ is the compressibility factor and $G(b \rho)$ is the average pair distribution function at contact for equivalent hard sphere bodies that still have pairwise additivity of the intermolecular forces. The minimum input information needed for using Eq. (2) are the values of B_2 , α and b . If the intermolecular potential is not available, knowledge of experimental second virial coefficient data is sufficient to calculate values of the other two temperature-dependent parameters [2]. Boushehri and Mason [5] used the heat of vaporization and the liquid density at the triple point as two scaling constants for correlating B_2 . Our purpose here is the applying two critical parameters of pure phosphonium-based ILs, the temperature and volume at critical point (T_c and V_c) for a new correlation of B_2 .

3. Results and discussion

Our results showed that the calculated properties of phosphonium-based ILs using the ISM equation of state were in a good agreement with experimental data from zero to 650bar. In order to show how the proposed EOS passes through the experimental points; typically, the deviation plots for the calculated high-pressure densities of phosphonium-based ionic liquids including, trihexyl(tetradecyl)phosphonium chloride, $[(C_6H_{13})_3P(C_{14}H_{29})][Cl]$ and trihexyl-(tetradecyl) phosphonium-bis{(trifluoromethyl)sulfonyl}imide, $[C_6H_{13})_3P(C_{14}H_{29})][NTf_2]$ are shown in Figures (1-2).

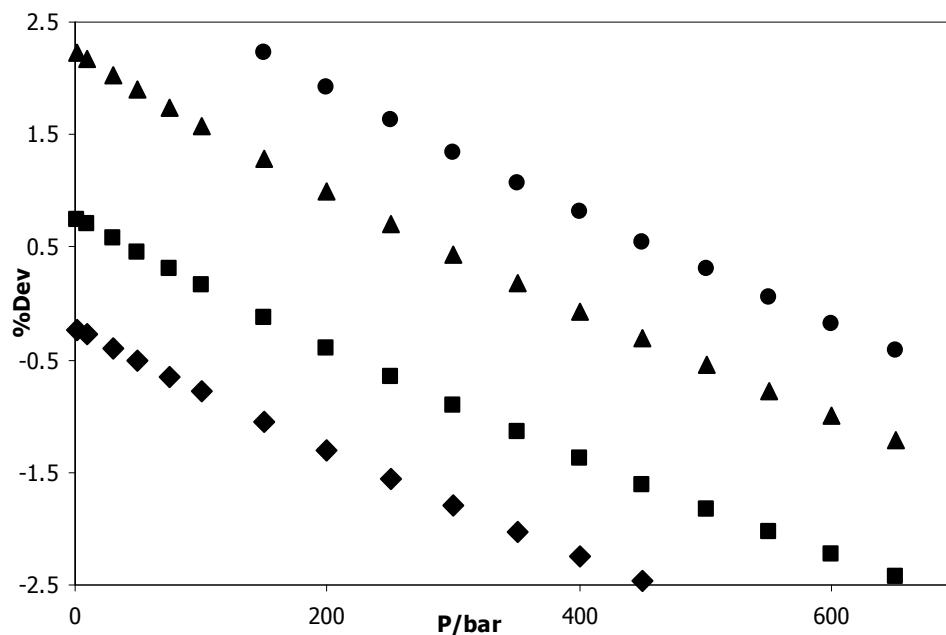


Fig.1. Deviation plot for the predicted high-pressure densities of $[(C_6H_{13})_3P(C_{14}H_{29})][Cl]$, by the use of ISM equation of state at 298.15 K (♦), 308.15 K (■), 323.15 K (▲) and 333.15 K (●) compared with the experiment [6].

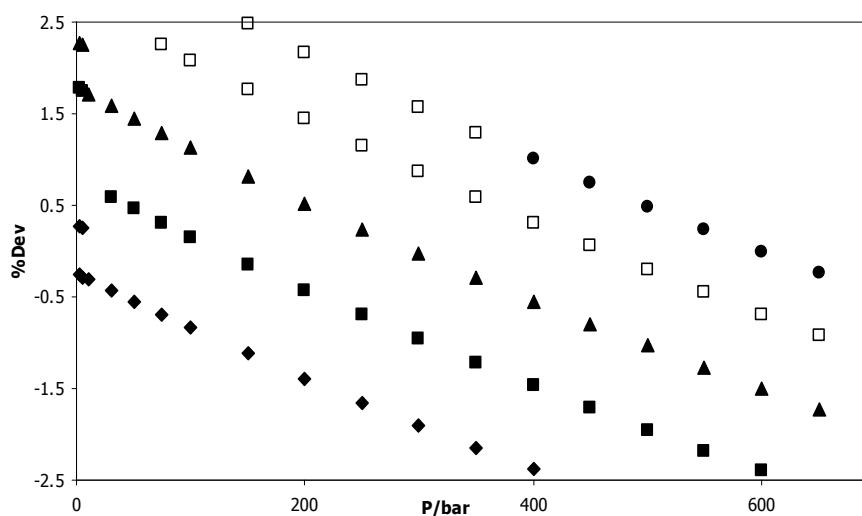


Fig.2. Deviation plot for the predicted high-pressure densities of $[(C_6H_{13})_3P(C_{14}H_{29})][NTf_2]$, by the use of ISM equation of state at 298.15 K (♦), 308.15 K (■), 318.27 K (▲), 328.39 K (□) and 343.43 K (●). compared with the experiment [6].

References

- [1] K. J. Fraser, D. R. MacFarlane, *Aust. J. Chem.* 62 (2009) 309.
- [2] G. Ihm, Y. Song, E. A. Mason, *J. Chem. Phys.* 94 (1991) 3839.
- [3] J. D. Weeks, D. Chandler, H. C. Andersen, *J. Chem. Phys.* 54 (1971) 5237.
- [4] Y. Song, E. A. Mason, *J. Chem. Phys.* 91 (1989) 7840.
- [5] A. Boushehri, E. A. Mason, *Int. J. Thermophys.* 14 (1993) 685.
- [6] J. M. S. S. Esperanca, H. J. R. Guedes, M. Blesic, L. P. N. Rebelo, *J. Chem. Eng. Data.* 51 (2006) 237.

**A modified perturbed hard-sphere equation of state compared with Peng-Robinson equation of state**S. M. Hosseini ^a, * M. M. Papari ^b, J. Moghadasi ^a

a. Department of Chemistry, College of Sciences, Shiraz University, Shiraz, Iran

b. Department of Chemistry, Shiraz University of Technology, Shiraz, Iran

(E-mail: Seied_Mostafa_Hosseini@yahoo.com)**Keywords:** Modified Equation of State, Perturbed Hard-Sphere**1. Introduction**

The technique of perturbation modeling uses references values for systems that are similar enough to the system of interest that good estimates of desired values can be made with small corrections to the reference values. The reference system proposed here is that of Carnahan and Starling (CS) [1]. In this work, a modified perturbed hard-sphere equation of state (EOS) has been employed to improve the volumetric properties prediction of several classes of fluids including, saturated hydrocarbons like C₃H₈, aromatic hydrocarbon like C₆H₆, inorganic polyatomic fluids like SO₂ and refrigerants like R22 in a broad range of pressures. Also the proposed modified EOS has been compared with the well-known Peng-Robinson (PR) EOS [2]. From about 200 data points examined and compared with the PR EOS. The average absolute deviations of derived compressed liquid densities from the modified EOS and those obtained by the use of PR EOS are 2.95% and 4.77% respectively

2. Theory

The hard-sphere fluid is taken into account as a reference system, and the influence of attractions and the softness of repulsions are considered as perturbations in statistical mechanical perturbation theory of fluids [3,4]. Many perturbed hard-sphere equations have been modified to improve the volumetric behaviour prediction of fluids from years ago. Recent work by Roman et al. [5] led to simple modification of equations of state for obtaining the main vapour-liquid properties of simple fluids. In this work we utilized the same modification proposed by Roman but, using acentric factor of pure fluids. We applied the Carnahan-Starling equation for the hard-sphere like fluids as the reference system and the modified van der Waals attraction proposed by Roman as perturbation part. The total formulation of modified equation of state considered in this study is:

$$Z_{\text{tot}} = Z_{\text{hard-sphere}} + Z_{\text{modified vdW-attraction}} \quad (1)$$

$$\frac{p}{\rho kT} = 1 + b\rho g(d^+) - \frac{a\rho}{kT^{(\beta+1)}} \quad (2)$$

where p is the pressure, $\rho = N/V$ is the number density, kT is the thermal energy per molecule, $g(d^+)$ is the pair radial distribution function of hard spheres at contact, a reflects the strength of attractive forces between spheres, b is the van der Waals covolume and β represents an attraction optimizer exponent. The first and second terms denote reference physical model such as hard-sphere, and the third term represents the attraction part. In this work, we have expressed a new empirical formula for β using the acentric factor of pure fluids:

$$\beta = a_1 + a_2\omega + a_3\omega^2,$$

where:

$$a_1 = 2.26971$$

$$a_2 = 7.70448$$

$$a_3 = 22.4046.$$

The coefficients a_1 - a_3 have been determined using the experimental p - v - T data for several classes of fluids.

In the present work, our purpose is determination of the parameters of intermolecular attractions, a and the molecular size, b by applying the critical point constraints. This is clearly known that the critical parameters of fluids are directly influenced by the intermolecular interactions.



3. Results and discussion

Typically, figure (1) shows the deviation percentage of the calculated compressed liquid densities using the modified equation of state in a wide range of temperatures/K(250-400) and pressures/bar(40-600) and those obtained by the use of Peng-Robinson EOS from the experimental ones [6].

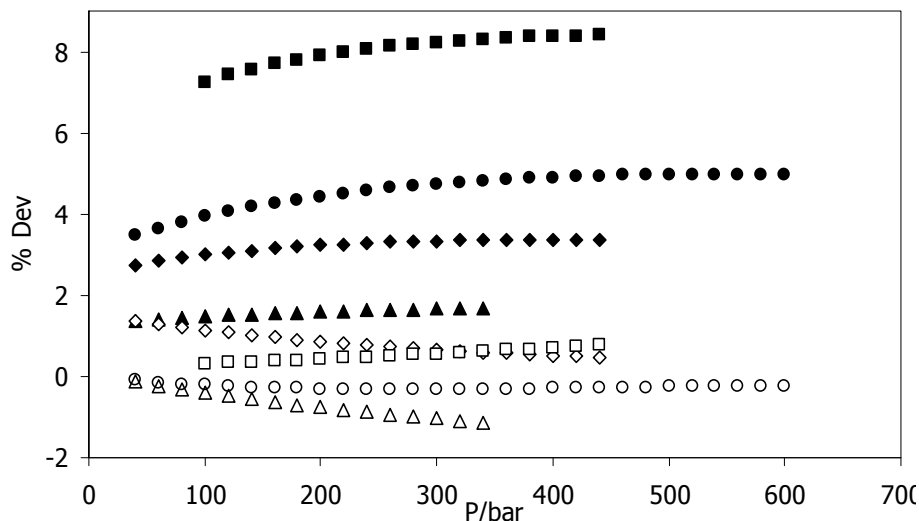


Fig.1. Deviation plot for the predicted compressed liquid density of R22 at 250K (◆), C₃H₈ at 270 K (■), SO₂ at 300K (▲) and C₆H₆ at 400K (●) compared with the experiment [6]. The open markers show the results of the modified EOS (Eq. 2) and the corresponding filled ones are from the Peng-Robinson EOS.

Our results showed that aforementioned calculated properties of liquid and vapor regions using the proposed modified EOS were in a good agreement with experimental data from 40 to 600bar. Since there is a difference in type of the interparticle attractions, we studied liquid and vapor phases separately. The comparison of the results of the calculations shows that, the modified EOS proposed here represents compressed liquid densities of the considered fluids with a better accuracy.

References

- [1] N.F. Carnahan, K.E. Starling, J. Chem. Phys. 51 (1969) 635.
- [2] D. Y. Peng, and D.B Robinson, Ind. Eng. Chem. Fundam. 15 (1976) 59.
- [3] F.L. Roman, A. Mulero, F. Cuadros, Phys. Chem.Chem Phys. 6 (2004) 5402.
- [4] A. Barker, D. Henderson, J. Chem. Phys. 47 (1967) 4714.
- [5] D. Weeks, D. Chandler, and H. C. Andersen, J. Chem. Phys. 54 (1971) 5237.
- [6] NIST Chemistry Webbook. NIST Standard Reference Data Base. National Institute of Standard and Technology. (<http://Webbook.nist.gov>).

**Interaction of dioxovanadium(V) with leucine and histidine**S. Seifi^{a,*}, A. Shamel^a, F. Gharib^b

a. Department of Chemistry, Islamic Azad University, Ardabil, Iran

(E-mail: sol_1364_nahid@yahoo.com)

b. Department of Chemistry, Shahid Beheshti University, G. C., Tehran, Iran

Keywords: Dioxovanadium(V), Leucine, Histidine, Spectrophotometry, Stability constant**1. Introduction**

Interaction between amino acids, peptides, and proteins with transition metal ions plays an important role in biochemistry and biology. Great attention has been paid to elucidating and interpreting the thermodynamic and structural characteristics of these biological ligands complexes. Vanadium complexes are particularly susceptible to external influences since the vanadium atom is small and readily accommodates several coordination geometries. The recent human clinical trials using vanadium compounds as oral insulin substitutes are encouraging, but the mechanism and the site of action are not yet known. It has been suggested that vanadate will spontaneously vanadylate a tyrosine residue in the insulin receptor leading to a vanadylated tyrosine protein or protein receptor, which will then mediate a response. So, it is important to understand how various factors affect the structure and properties of vanadium complexes.

2. Experimental

The present work deals with the study of dioxovanadium(V), VO_2^+ , complexes by leucine and histidine. The method of determination of the stability constant based on the relation $A = f([\text{H}^+])$ [1-2]. Using a combination of spectrophotometric and potentiometric methods, absorbance and pH were measured for a solution containing VO_2^+ with a large excess of each ligand. Treatments of the spectrophotometric data in the range 250-290 nm (in the interval of 5 nm) obtained during the titrations as a function of the H^+ concentration was conducted with the computer program. The program allows calculation of stability constants for different stoichiometric models.

3. Results and discussion

The complex $\text{M}_x\text{H}_y\text{L}_z^{(nx+y-z)+}$ formed, is characterized by its stoichiometry ($x:y:z$), where M and L represent the metal ion and each ligand, respectively. To determine the stability constant of the complexation or protonation of the ligands, equation (1) is defined by β_{xyz} [1].



$$\beta_{xyz} = [\text{M}_x\text{H}_y\text{L}_z^{(nx+y-z)+}] / ([\text{M}^{+n}]^x [\text{H}^+]^y [\text{L}^-]^z) \quad (2)$$

The method of determining ε_M was previously described [1] and its values at different wavelengths are used in this work. Using a suitable computer program, the data were fitted for estimating the formation constant of equation (2). We used the Gauss - Newton nonlinear least - squares method in computer program to refine the absorbance by minimizing the error squares sum from the following equation.

$$U = \sum (a_i - b_i)^2$$

where a_i is a quasi-experimental and b_i is a calculated one.

The protonation constant of the ligands have been used for computation of the stability constants, β_{xyz} , of the metal-ligand. In aqueous solution the ligands exist in its anionic form (L^-), zwitterionic species (HL), and cationic form (H_2L^+). In acidic pH, in this case, the predominant species for complexation is HL . The spectrophotometric titration data were analyzed as before [2]. For finding the proposed species, the spectrophotometric titration data were analyzed by offering the following species to the computer program: VO_2L , VO_2HL^+ , VO_2HL_2 , $\text{VO}_2\text{H}_3\text{L}_2^{+2}$, $\text{VO}_2\text{H}_3\text{L}_3^+$, $\text{VO}_2\text{H}_4\text{L}_4^+$. As expected, all the proposed species were systematically rejected by the computer program except VO_2HL^+ and $\text{VO}_2(\text{HL})_2^+$. A value for the formation constant of $\text{VO}_2\text{H}_2\text{L}^{+2}$ was calculated by the program, but the species was not considered further because the estimated error in its formation constant is unacceptable, and its inclusion does not improve the goodness of the fit. The model finally chosen, formed by VO_2HL^+ and $\text{VO}_2(\text{HL})_2^+$, resulted in a satisfactory numerical and graphical fitting.



References

- [1] F. Gharib, Phys. Chem. Liq. 45 (2007) 105.
- [2].F. Gharib, M. Sayadian, A. Shamel, M. M. Moghaddam, J. Mol. Liq. 138 (2008) 9.



Acoustical properties of the binary mixtures of N,N-dimethylacetamide and N,N-dimethylformamide + 1,2-alkandriols (C2-C5) at 293.15 K – comparison with theories

K. KHANLARZADEH, H. ILOUKHANI

Department of Physical Chemistry, Faculty of Chemistry, University of Bu-Ali Sina, Hamedan, Iran

E-mail: iloukhani@basu.ac.ir (H. Iloukhani) kh.khanlarzadeh@basu.ac.ir Tel: 08118282807

1. Introduction

This paper is a continuation of our earlier work¹⁻⁵. The number of studies on acoustical properties of binary mixtures has increased in recent years due to industrial applications and the theoretical interest in studying the nature of molecular interaction and packing phenomena in ternary mixtures. In this work, we measured densities and speeds of sound of the binary mixtures of N,N-dimethylacetamide and N,N-dimethylformamide + 1,2-alkandriols at 293.15 K were measured over the whole composition range. The data obtained are used to calculate isentropic compressibility, k_s deviation in isentropic compressibilities, Δk_s and acoustic impedance, Z of the binary mixtures. Theoretical models dealing with liquid state including Jacobson free length theory (FLT)⁶, Schaaff collision factor theory (CFT)⁷, have been proposed for the prediction of the speeds of sound of the binary mixtures.

2. Method

All chemical substances were purified with the standard methods described by Perrin and Armarego⁸. All mass measurements were performed on an electronic balance (AB 204-N Mettler) accurate to 0.1 mg. The estimated accuracy in the mole fractions was $\pm 1 \times 10^{-4}$. The densities of the pure compounds and their binary mixtures were measured with an Anton Paar DMA 4500 oscillating U-tube densimeter. The density measurements accuracy was $\pm 1 \times 10^{-2}$ kg m⁻³. The temperature in the cell was automatically regulated to ± 0.01 K with a solid state thermostat. The speed of sound in the pure compounds and their binary mixtures was measured with a multi-frequency ultrasonic interferometer supplied by Mittal Enterprise, New Delhi with an accuracy of 1 m s⁻¹. In this work, 1 MHz frequency was employed. Densities and refractive indices of the pure reagents were in good agreement with values found in the literature⁹.

3. Result and discussion

Isentropic compressibility κ_s , was calculated using Newton–Laplace equation

$$\kappa_s = 1 / \rho u^2 \quad (1)$$

Deviation in isentropic compressibilities $\Delta \kappa_s$, n-component were calculated using the following relation

$$\Delta k_s = k_s - \sum_i (k_{s,i}^*) x_i \quad (2)$$

The corresponding values for densities, ρ isentropic compressibility, k_s deviation in isentropic compressibilities, Δk_s and acoustic impedance, Z of the binary mixtures measured at 298.15 K. The isentropic compressibility values and deviations in isentropic compressibility were plotted against mole fraction of first component. Speeds of sound and isentropic compressibilities of the binary mixtures were fitted to the following polynomial equation:

$$Q = \sum_{i=0}^n A_i x^i \quad (3)$$

The speeds of sound were also calculated using Jacobson free length theory (FLT), and Schaaff collision factor theory (CFT) as following equations:

(i) Jacobson free length theory (FLT)

$$u = \frac{K}{L_f \rho^{1/2}} \quad (4)$$

(ii) Schaaff collision factor theory (CFT)



$$u = u_{\infty} \frac{\left(\sum_{i=1}^n x_i S_i \right) \left(\sum_{i=1}^n x_i B_i \right)}{V} = u_{\infty} S r_f \quad (5)$$

where $u_{\infty} = 1600 \text{ m s}^{-1}$, S = collision factor and $r_f = B/V$, space filling factor. B is the actual volume of the molecules per mole. Each set of results for deviation in isentropic compressibility, Δk_s were fitted using a Redlich–Kister polynomial¹⁰ which for binary mixtures is

$$\Delta k_s = x(1-x) \sum_{k=0}^N A_k (1-2x)^k \quad (6)$$

In each case, the optimum number of coefficients was ascertained from an examination of the variation of standard deviation σ with

$$\sigma = \left[\frac{\sum (Y_{\text{exp}} - Y_{\text{calc}})^2}{(n-p)} \right]^{1/2} \quad (7)$$

4. Conclusion

Speeds of sound (u) of the binary mixtures of N,N-dimethylacetamide and N,N-dimethylformamide + 1,2-alkandiol at 293.15 K were measured over the whole composition range. The results were analyzed in terms of the free length theory (FLT) due to Jacobson and collision factor theory due to Schaaffs. The data obtained are used to calculate the isentropic compressibilities (κ_s), and deviation in isentropic compressibilities ($\Delta \kappa_s$), of the binary mixtures. The data of the binary systems were fitted to the Redlich–Kister equation. The speeds of sound and isentropic compressibilities of the binary mixtures have been correlated by means of polynomial equation. The deviation in isentropic compressibilities showed negative values for systems consist of n,n-dimethylacformamide + 1,2-ethandiol and 1,2-propandiol and for n,n-dimethylformamide + 1,2-butandiol and 1,2-pentandiol showed positive values. All values for systems consist of n,n-dimethylacetamide + 1,2-alkanediols were positive except of 1,2-pentandiol. The obtained results are analyzed to discuss the nature and strength of intermolecular interactions in these mixtures.

Key Words: 1-Alkanols, Tetrahydrofuran, Speeds of Sound, Isentropic Compressibility

References

- [1]. Iloukhani, H. Samiey, B. and Moghaddasi, M. A. J. Chem. Thermodyn. 38, (2006) 190.
- [2]. Iloukhani, H and Zarei, H. A. J. Chem. Eng. Data 47, (2002) 195.
- [3]. Iloukhani, H and Samiey B., J. Chem. Eng. Data 50, (2005) 1911.
- [4]. Zarei, H. A. and Iloukhani, H. Thermochim. Acta 405, (2003) 123.
- [5]. Iloukhani, H and M. Rezaei-Sameti, J. Chem. Thermodyn. 37, 1151 (2005).
- [6]. Jacobson, B. Acta Chem. Scand. A 6, (1952) 1485.
- [7]. Schaaff, W. Molekularakustic, Springer, Berlin, 1963.
- [8]. Perrin, D.D. and Armarego, W.L.F. Purification of Laboratory Chemicals, Pergamon Press, New York, (1970).
- [9]. Riddick, J.A. Bunger, W. B and Sakano, T. K. Organic Solvent: Physical Properties and Methods of Purification, Wiley Interscience New York, (1986).



Phase diagrams for Liquid-Liquid and liquid-solid equilibrium of the ternary (Polyethylene glycol Dimethyl Ether 2000 + Potassium Phosphate + Water) system

Mohammed Taghi Zafarani-Moattar^a, Ebrahim Nemati Kande^{a,*}

a. Physical Chemistry Department, University of Tabriz, Tabriz, Iran

(E-mail: nemati.ebrahim@gmail.com)

Keywords: liquid-liquid equilibrium, Othmer-Tabias, Bancroft, Polyethylene glycol Dimethyl Ether(PEGDME), Potassium Phosphate.

1. Introduction

Liquid-Liquid extraction utilizing aqueous two-phase systems (ATPSs) has been used to separate and purify biological products from the complex mixtures in which they are produced. ATPSs can be formed by combining either two incompatible polymers or a polymer and a salt in water above a certain critical concentration [1]. The later systems are more attractive because of their greater selectivity, lower viscosity, lower cost, rapid phase disengagement, and availability of commercial separators, which allow a faster and continuous protein separation.

This work is devoted to study the phase diagram of the K_3PO_4 +PEGDME₂₀₀₀+H₂O system at $T=(298.15, 308.15$ and $318.15)$ K. Here, we report liquid-liquid equilibrium data for the aqueous K_3PO_4 +PEGDME₂₀₀₀+H₂O system that has not been previously published. The effect of temperature on the binodal curve was also studied. The obtained results are necessary for design and optimization of extraction processes.

2. Methods

A glass vessel, volume 50 cm³, was used to do the phase equilibrium determinations. The glass vessel was provided with an external jacket in which water at constant temperature was circulated using a thermostat. The temperature was controlled to within ± 0.05 K. The binodal curves were determined by a titration method. A salt solution of known concentration was titrated with the polymer solution or vice versa, until the solution turned turbid; which indicated the formation of two liquid phases. For the determination of the tie-lines, feed samples (about 20 cm³) were prepared by mixing appropriate amounts of polymer, salt and water in the vessel. The thermostat was set at a desired temperature, and the sample was stirred for 1 h. Then the mixture was allowed to settle for 48 h. After separation of the two phases, the concentrations of the salts in the top and bottom phases were determined by flame photometry. The concentration of PEGDME₂₀₀₀ in both phases was determined by refractive index measurements performed at 298.15 K using a refractometer (QUARTZ RS-232).

3. Results and discussion

The equilibrium compositions of the aqueous two-phase systems PEGDME+ K_3PO_4 +H₂O and the tie-line data determined at $T = (298.15, 308.15$ and $318.15)$ K. In the temperature range considered, the temperature has a little effect on the bi-nodal curves for the studied systems, so that as can be seen in Fig.1 the effect of temperature on the bi-nodal curve is only noticeable at lower concentration of polymer for the aqueous PEGDME+ K_3PO_4 +H₂O system. For the studied system the experimental bi-nodal data were fitted by least-squares regression method to the following empirical non-linear expression developed by Merchuk[3]

$$w_1 = a \cdot \exp(bw_2^{0.5} - cw_2^3) \quad (1)$$

where a , b , and c represent fit parameters and w_1 and w_2 are weigh fraction of polymer and salt, respectively. Using eq 1, the fitting parameters a , b , and c obtained from the correlation of experimental binodal data along with the corresponding standard deviations are given in Table 1. The binodals reproduced from eq.1 at different temperatures are also shown in Fig.1 on the basis of obtained standard deviations, we conclude that the eq 1 can be satisfactorily used to reproduce the binodal curves of the investigated system.

The correlation equations given by Othmer-Tabias (eq.2a) and Bancroft (eq.2b) have also been used to correlate the tie-line compositions.

$$\left(\frac{1-w_1^{\text{top}}}{w_1^{\text{top}}}\right) = k \left(\frac{1-w_2^{\text{bot}}}{w_2^{\text{bot}}}\right)^n \quad (2a)$$

$$\left(\frac{w_3^{\text{bot}}}{w_2^{\text{bot}}}\right) = k_1 \left(\frac{w_3^{\text{top}}}{w_1^{\text{top}}}\right)^r \quad (2b)$$

Here k , n , k_1 and r represent fit parameters and w_1 and w_2 are weigh fraction of polymer and salt, respectively. These equations have also been used to evaluate the reliability of LLE data. The corresponding correlation coefficient values, R and the values of the fitted parameters are given in Table 2. On the basis of theobtained standard deviations given in Table 2, we conclude that eqs 2a and 2b can also be acceptably used to correlate the tie-line data of the investigated systems.

The experimental and calculated tie-lines at 298.15 K are shown in figure 2, as an example.

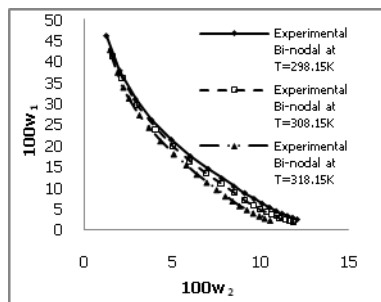


Fig.1. Effect of temperature on the bi-nodal Curves for the PEGDME+K₃PO₄+H₂O systems

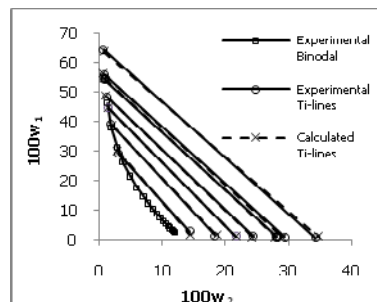


Fig. 2. Experimental and calculated tie-lines for PEGDME+K₃PO₄+H₂O system at 298.15K

Table1. Values of Parameters of eq for PEGDME+ K₃PO₄+H₂O at $T = (298.15, 308.15 \text{ and } 318.15) \text{ K}$

T/ K	a	b	c	sd
298.15	90.1378	0.6137	6.7027×10^4	0.15
308.15	75.2561	5.3302	1.0442×10^5	0.17
318.15	88.8505	0.6477	1.1071×10^5	0.15

$$sd = \left(\frac{\sum_{i=1}^N \left(\frac{w_1^{\text{cal}} - w_1^{\text{exp}}}{N} \right)^2}{N} \right)^{0.5}, \text{ here } N \text{ is the number of binodal data.}$$

Table2. Values of Parameters of eq.2a and eq.2b for PEGDME+K₃PO₄+H₂O at $T = (298.15) \text{ K}$

T / K	k	n	R ²	k ₁	r	R ²	Dev ^a
298.15	0.26715	1.21108	0.995	2.99703	0.83479	0.995	0.09

$$^a \text{Dev} = \left(\frac{\sum_p \sum_l \sum_j (w_{p,l,j}^{\text{cal}} - w_{p,l,j}^{\text{exp}})^2}{6N} \right)^{0.5},$$

here $w_{p,l,j}$ is the weight fraction of the component j (i. e. polymer, salt or water) in the phase p for l th tie-line and the superscripts "cal" and "exp" refer to the calculated and experimental values, respectively. N is the number of tielines data.

4. Conclusions

The phase behavior of the PEGDME+K₃PO₄+H₂O system is quit different that the previously studied Polymer+ Salt + H₂O systems [4]. In the PEGDME₂₀₀₀+K₃PO₄+H₂O system it can be observed that by adding the extra amount of salt solution into the two phase equilibrating solution, first the polymer is extracted in the solid form in the top phase, and then by adding extra amount of salt solution, the salt turns into solid form in the bottom phase. This observation is being reported for the first time and it is suggested here that this approach can be applied in the purification of polymers

References

- [1]. Zaslavsky, B. Y. Aqueous two-phase partitioning, physical chemistry and bioanalytical applications; Marcel Dekker, New York, 1995.
- [2]. Zafarani-Moattar, M. T.; Sadeghi, Fluid Phase Equilib. 2002 , 203, 1771.
- [3]. J. C. Merchuk, B. A. Andrews, J. A. Asenjo, J. Chromatogr B. 711 (1998) 285.
- [4]. M.T. Zafarani-moattar, D. Nikjoo J. Chem. Eng. Data. 53 (2008) 2666.



**Conductometric study of NaF in different ROH+water mixed solvents
(with R=1-Pr and 2-Pr) based on Fuoss-Hsia-Chen-Justice electrolytic model**

Farzad Deyhimi, Ebrahim Choobdari

Department of Chemistry, Shahid Beheshti University, Evin-Tehran 1983963113, Iran.

(E-mail: E.Choobdari@Gmail.com)

Keywords: Ionic Conductivity, Limiting Conductivity, Association Constant, Mixed solvent, NaF.

1. Introduction

Conductometry is known as one of the important tool for the determination of the physico-chemical properties of electrolyte systems. Ionic conductivity is a transport property extensively used in investigations on the control and design of industrial processes and development of high energy batteries. We report in this work, the molar electrolytic conductivities data of NaF solutions in 1-propanol + water and 2-propanol+water mixed solvents with alcohol/water mass fractions (%) = 10, 20, 30, 40, and 50 at 298.15 K. The maximum concentration of the used electrolyte was 0.36 mol.l⁻¹. The limiting molar conductivity (Λ°), association constant (K_A) and the Bjerrum closest approach distance (q) were calculated using the Fuoss-Hsia-Chen-Justice equation. The results were interpreted in terms of ion-ion and ion-solvent interactions in the mixed solvents systems.

2. Method

The experimental conductivity data were analyzed using Justice's modification of the Fuoss-Hsia and Chen equation as given by:

$$\Lambda = \Lambda^\circ - S(\alpha c)^{1/2} + E\alpha c \ln(\alpha c) + J_1(\alpha c) - J_2(\alpha c)^{3/2} - \Lambda\alpha c\gamma_{\pm}^2 K_A \quad (1)$$

$$K_A = \frac{1 - \alpha}{\alpha^2 c \gamma_{\pm}^2} \quad (2)$$

$$\log \gamma_{\pm} = \frac{-A\sqrt{\alpha C}}{1 + Bq\sqrt{\alpha C}} \quad (3)$$

$$\kappa^2 = \frac{16.10^3 N_A z^2 e^2 \alpha c}{\epsilon_0 \epsilon k_B T} \quad (4)$$

$$q = \frac{z^2 e^2}{8\pi \epsilon_0 \epsilon k_B T} \quad (5)$$

where Λ and Λ_0 are the molar conductivities at molarity, c and infinite dilution, α is degree of ionic dissociation, K_A , q and γ_{\pm} are the ion-pair association constant, distance parameter, and the corresponding mean activity coefficient of the free ions, respectively. S the coefficient of the Debye-Hückel-Onsager, and E depends only on the properties of the solvent and the charge on the ions, while J_1 and J_2 depend on the same parameters but also on the distance parameter. The rest quantities have their usual meaning. Three-parameter fits of molar conductivity data give the ion-pair association constant K_A , the limiting molar conductivity Λ_0 , and distance parameter q , by non-linear least-squares iteration. The calculation is made by finding the values Λ_0 , K_A , and q that minimized the root of mean square deviation $\sigma(\Lambda)$, of the experimental and calculated conductivities.

3. Results and discussion

Figure 1 shows the resulting typical trend of experimental molar conductivity as a function of concentration of NaF in 1-PrOH (40%) +water (60%) mixed solvent. The variation of the logarithm of the ion-pair association constant as a function of the alcohol mass fraction percent is presented in Fig. 2. The linear trend of the association constant versus the inverse of the



dielectric constant is also presented in Fig. 3, for different mixed solvents. The corresponding limiting conductivity at infinite dilution for NaF electrolyte in different mixed 1-PrOH +water solvent are given in Table 1. The logarithm of ionic association constant as a function of the inverse of dielectric constant for different mixed 1-PrOH +water solvent mass fractions (%) are reported in Table 2.

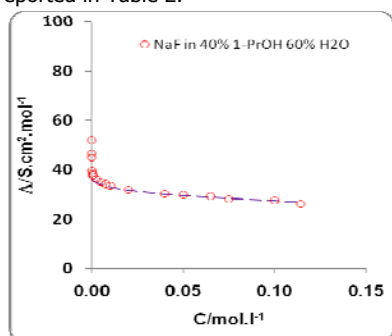


Fig.1. Molar conductivity versus concentration for NaF in 1-PrOH(40%) +water (60%) mixed solvent.

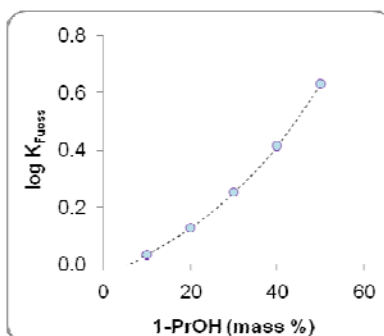


Fig.2. Variation of the logarithm of the ionic association constant for NaF in different 1-PrOH+water mixed solvent.

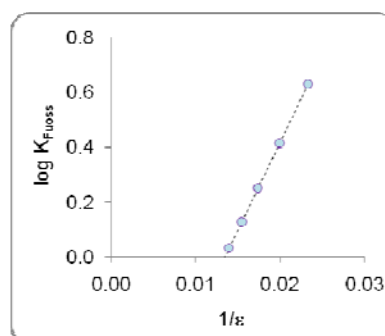


Fig.3. Linear trend of the log K_A as a function of the inverse of the dielectric constant for NaF in 1-PrOH+water mixed solvent.

Table 1. Limiting conductivity at infinite dilution and the inverse of dielectric constant for different 1-PrOH +water mixed solvent.

1-PrOH(x%)/H ₂ O(100-x)% x(mass %)	Λ_o S.cm ² .mol ⁻¹
10:90	79.10
20:80	64.96
30:70	46.87
40:60	36.98
50:50	34.31

Table 2. Value of logarithm of ion-pair association constant as a function of the inverse of dielectric constant for different 1-PrOH +water mixed solvent.

1-PrOH(x%)/H ₂ O(100-x)% x(mass %)	log K_A	1/ ϵ
10	0.03	0.0139
20	0.13	0.0154
30	0.25	0.0173
40	0.41	0.0199
50	0.63	0.0233

4. Conclusions

Based on the experimental conductivity data, modeling of the NaF electrolyte in different ROH+water mixed solvents (with R=1-Pr and 2-Pr, and alcohol/water mass fractions percent 10-50%) were performed based on the Fuoss-Hsia-Chen Justice theoretical model. The values of the parameters such as limiting conductivity, ion-pair association constant (K_A), and Bjerrum closest approach distances were determined for these electrolyte systems. The variation of these parameters shows the following trends in the investigated mixed solvent electrolyte systems:

- the limiting conductivity data decreases with the increase of the alcohol content,
- the ion-pair association constants show an increasing trend with the decrease of the dielectric constant of the mixed solvent, confirming the increasing tendency of the ion-pair association in solvent with lower dielectric constant,
- The Bjerrum closest approach parameters show also an increasing trend (from 3.9 to 6.52 Å) with the increase of the alcohol content (from alcohol/water mass fraction x%=10 to 50, respectively), confirming the more difficulty of the ion approach in solvent with lower dielectric constant.

References

- [1] R. M. Fuoss, J. Phys. Chem., 82 (1978) 2427.
- [2] R. M. Fuoss, Journal of Solution Chemistry, 15 (1986) 1572.
- [3] J. C. Justice, J. Solution Chem., 7 (1978) 859.
- [4] J. C. Justice, J. Solution Chem., 20 (1991) 1017.
- [5] K. Izuta, Electrochemistry in Non-aqueous Solutions. Wiley, New York, 2002.
- [6] J. Barthel, H. Krienke, W. Kunz, Physical Chemistry of Electrolyte Solutions: Modern Aspects, Science, 1998.



Densities, and excess molar volumes for binary mixtures of diethyl phthalate + bromocyclohexane at (298.15, 303.15 and 308.15) K.

A. A. Rostami, S. Yeganegi, A. Mossazade Rostamkolahi,
Faculty of chemistry, University of Mazandaran, P.O.BOX 453, Babolsar, Iran
(E-Mail: Abass_Mr86@yahoo.com)

Keywords: Density, Bromo cyclohexane, Binary mixture, Viscosity deviations

1. Introduction

Density (ρ) of liquid mixtures are required in most engineering calculation where fluid flow or mixing is an important factor. Moreover, knowledge of the dependence of densities of liquid mixture on composition is of great interest from a theoretical stand point since it may lead to better conition of the fundamental behavior of liquid systems. The studies of excess thermodynamic properties are of considerable interest in understanding the intermolecular interactions in binary liquid mixtures [1]. In the present study, density were measured for the binary mixture of diethyl phthalate (DEP) + bromocyclohexane at atmosphereic pressure at (298.15, 303.15 and 308.15) K. Although the physical property data of the pure components are available in the literature [2-4-6] no experimental data are available for these mixtures at the comparable conditions of this study.

2. Experimental

2.1. Materials, diethyl phthalate and bromocyclohexane were purchased from Fluka. The purities of these substances are more them 98mol%, all reagents were used without further purification. Binary mixtures were prepared by known masses of each liquid in airtight stoppered glass bottles.

2.2. Apparatus and Procedure. The mass measurements were made on a single pan Mettler balance with an accuracy of ± 0.0001 g. No buoyancy corrections were applied. The possible error in mole fraction is calculated to be less than $\pm 1 \times 10^{-4}$. Density (ρ) measurements of pure components and binary mixtures over the complete composition range were carried out using Anton Paar oscillating utube densitometer (DMA 58), with $\pm 10^{-5} \text{ g cm}^{-3}$ accuracy at 298.15, 303.15 and 303.15K. It was calibrated with doubledistilled water and air [6,5]. The temperatures were regulated using a circulating bath Heto DBT with a precision of ± 0.01 K. The kinematic viscosity was measured with Ubbelohde viscometers with a Schott-Geräte automatic measuring unitmodel AVS 400 provided with a transparent thermostat, which allows temperature stabilization with a tolerance of 0.01 K.

3. Results and discussion

Table 1 lists the measured density ρ and viscosity η , data at (298.15, 303.15 and 308.15) K with the corresponding excess molar volume V^E for the binary mixture of Diethyl Phthalate + bromocyclohexane the excess molare volumes V^E of binary mixtures were calculated from density data according to the following equation.

$$V_m^E = \frac{x_1 M_1 + x_2 M_2}{\rho} - \frac{x_1 M_1}{\rho_1} - \frac{x_2 M_2}{\rho_2}$$

Where ρ is the density of the mixture, ρ_1 and ρ_2 are the densities of the pure substances, M_1 , and M_2 are the molar mass, and x_1 and x_2 are the molar fractions. The V^E of the binary mixture were plotted against mole fraction and are shown in figure. Figure shows that excess molar volume are positive for binary mixture of Diethyl Phthalate + bromocyclohexane and the values of V^E increases with temperature rising. V^E values may be affected by two factors. The first factor is the physical intermolecular forces including electrostatic forces between charged particles and between permanent dipoles ect., induction forces between a permanent dipole and an induced dipole, and forces of attraction (dispersion forces) and repulsion between nonpolar molecules. Physical intermolecular forces are weak usually, and the sign of V^E values may be positive or negative .the second factor is the structural characteristics of the components, arising from geometrical fitting of one component into the other's structure due to the differences in shape and size of components and free volume.



4. Conclusions

Densities of the binary system of diethyl phthalate + bromo cyclohexane have been measured at several temperatures and for the whole composition range. The excess molar volume were computed fitted to the RedlichKister equation. The excess molar volume are positive. The excess molar volume show a systematic change with increasing temperature. The effect of interactions of components on excess molare volumes is discussed.

Table. Experimental Densities, ρ , and Excess molar Volume V^E for Bromocyclohexane(1) + DEP(2) at Different Temperature

X_1	$\frac{\rho}{\text{g.cm}^{-3}}$	$\frac{V^E}{\text{cm}^3.\text{mol}^{-1}}$	X_1	$\frac{\rho}{\text{g.cm}^{-3}}$	$\frac{V^E}{\text{cm}^3.\text{mol}^{-1}}$
298.15 K					
0.00000	1.1137	0.00000	0.68135	1.2293	0.43403
0.13152	1.1304	0.20398	0.76086	1.2491	0.41121
0.25415	1.1486	0.31254	0.84520	1.2720	0.34810
0.36874	1.1674	0.36525	0.92469	1.2972	0.21254
0.47611	1.1868	0.39854	1.00000	1.3232	0.00000
0.57687	1.2065	0.42540			
303.15 K					
0.00000	1.1098	0.00000	0.68135	1.2233	0.56034
0.13152	1.1260	0.26371	0.76086	1.2428	0.52092
0.25415	1.1434	0.39565	0.84520	1.2657	0.44697
0.36874	1.1616	0.48094	0.92469	1.2955	0.26032
0.47611	1.1807	0.51862	1.00000	1.3173	0.00000
0.57687	1.2005	0.54567			
308.15 K					
0.00000	1.1063	0.00000	0.68135	1.2188	0.65065
0.13152	1.1220	0.34291	0.76086	1.2381	0.62386
0.25415	1.1392	0.49540	0.84520	1.2611	0.52657
0.36874	1.1573	0.58305	0.92469	1.2858	0.34350
0.47611	1.1763	0.62202	1.00000	1.3133	0.00000
0.57687	1.1961	0.63650			

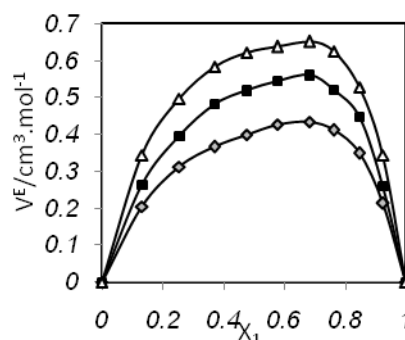


Fig. Deviation viscosities of mixture of Bromo cyclohexane(1) + DEP(2) at different temperatures; 298.15K; \diamond , 303.15 K; \blacklozenge , 308.15 K; Δ

References

- [1] Jose M. Resa, Cristina Gonzalez, Salome Ortize de Landaluze, and Juan Lanz, J. Chem. Eng. Data, 2002, 47, 1123.
- [2] Jyoti N. Nayak, and Tejjraj. J. Chem. Eng. Data, 2003, 48, 1489.
- [3] I-Chin Pan, Muoi Tang, and Yan-Ping Chen, J. Chem. Eng. Data, 2000, 45, 1012.
- [4] Chen-Chien Wang and Chein-Hsiun Tu*, J. Chem. Eng. Data, 2009, 54, 131.
- [5] Ching-Ta Yeh and Chein-Hsiun Tu*, J. Chem. Eng. Data, 2007, 52, 1760.
- [6] Hossein A. Zarei,* M. Zare Lavasani, and H. Iloukhani, J. Chem. Eng. Data, 2008, 53, 578.

**Phase Equilibria of Hydrocarbon-Methanol Systems from Equation of State-Excess Gibbs Energy (EoS- G^E)**

H. Hashemi, P. Reshadi, S. Babaei, F. Sabzi

Department of Chemical Engineering, Shiraz University of Technology, Shiraz 71555-313, Iran.

(E-mail: p.reshadi@sutech.ac.ir Tel.: +98-918-856-2990)**Introduction**

Liquid-Liquid Equilibrium (LLE) data are essential when considering separation processes. Recently, LLE data for wide pressure and temperature ranges have become necessary because of the diversification of separation processes. One of the common approaches for modeling of LLE is to use the equation of state-excess Gibbs energy (EoS- G^E) that combines the EoS with the excess Gibbs energy (G^E) model at a particular standard state. The attempt of this work is to use MHV1, MHV2 and Wong-Sandler (WS) mixing rules and modified Peng-Robinson (PR) EoS coupled with two excess Gibbs energy models: the modified Wilson equation (T-K-Wilson) proposed by Tsuboka and Katayama [1] and the UNIQUAC equations for calculating LLE at 0.1 MPa in cyclohexane + methanol and n-octane + methanol systems.

Keywords: EOS- G^E ; Mixing rule; LLE; Methanol; Cyclohexane; n-Octane.

Thermodynamic model

In this study, we have used the PR EoS model modified by Stryjek and Vera (PRSV) [2]. Three EoS- G^E models, the MHV1, MHV2 and WS with two excess Gibbs models (the Wilson equation modified by Tsuboka and Katayama (T-K-Wilson) and the UNIQUAC equation) were applied for calculating the mixture parameters a and b in which T-K-Wilson equation defined as following:

$$\frac{G^E}{RT} = \sum_i x_i \ln \frac{\sum_j (v_j^L / v_i^L) x_j}{\sum_k x_k \Lambda_{ik}} \quad (1)$$

$$\Lambda_{ij} = \frac{v_j^L}{v_i^L} \exp \left[-\frac{\lambda_{ij} - \lambda_{ii}}{RT} \right] \quad (2)$$

$$\lambda_{ij} - \lambda_{ii} = A_{ij} + B_{ij}T + \frac{C_{ij}}{T} \quad (3)$$

In UNIQUAC model G^E is split into the combinatorial and residual terms :

$$\frac{G^E(\text{combinatorial})}{RT} = x_1 \ln \frac{\phi_1}{x_1} + x_2 \ln \frac{\phi_2}{x_2} + \left(\frac{Z}{2} \right) (q_1 x_1 \ln \frac{\theta_1}{\phi_1} + q_2 x_2 \ln \frac{\theta_2}{\phi_2}) \quad (4)$$

$$\frac{G^E(\text{residual})}{RT} = -q_1 x_1 \ln [\theta_1 + \theta_2 \tau_{21}] - q_2 x_2 \ln [\theta_2 + \theta_1 \tau_{12}] \quad (5)$$

The average area fraction, θ , and the average segment fraction, ϕ , is given by [3].

Results and Discussion

In this study, we have obtained the parameters A_{ij} , B_{ij} and C_{ij} for two binary systems by using the T-K-Wilson and UNIQUAC G^E models. The parameters for MHV2 mixing rule are listed in Table 1. With MHV1, MHV2 and WS mixing rules, we have calculated LLE data for two binary systems that shown in Fig 1-2. In these figures the results are not satisfactory near the critical points. Thus in the calculations of the average errors in Table 2 these points have not been taken into account.

System	Parameters	T-K-Wilson		UNIQUAC		Ref.
		ij=12	ij=21	ij=12	ij=21	
Cyclohexane (1)-	$A_{ij}(\text{Jmol}^{-1})$	3.511403×10^4	-5.910371×10^4	1.195376×10^4	-1.250617×10^4	[4]
Methanol (2)	$B_{ij}(\text{Jmol}^{-1}\text{K}^{-1})$	-6.9812043×10	9.0511213×10	-2.4774876×10	1.8337865×10	
	$C_{ij}(\text{Jmol}^{-1}\text{K})$	-4.1876199×10^6	1.2016354×10^7	2.156704×10^5	2.118772×10^6	
n-Octane (1)-	$A_{ij}(\text{Jmol}^{-1})$	3.2260×10^4	-6.1636×10^4	3.4152×10^4	-1.8890×10^4	[5]
Methanol (2)	$B_{ij}(\text{Jmol}^{-1}\text{K}^{-1})$	-6.58695×10	9.20587×10	-6.09438×10	2.89935×10	
	$C_{ij}(\text{Jmol}^{-1}\text{K})$	-4.195×10^6	1.2642×10^7	-3.0475×10^6	3.0814×10^6	

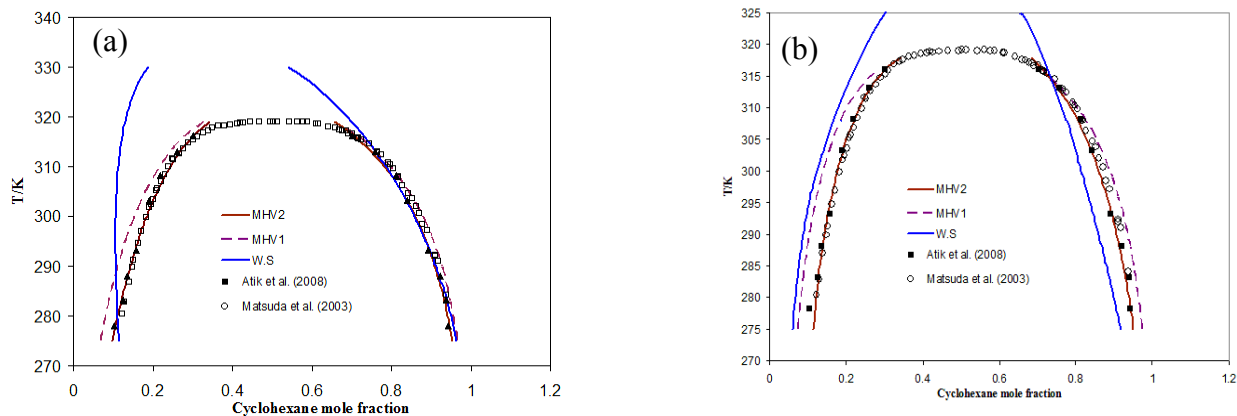
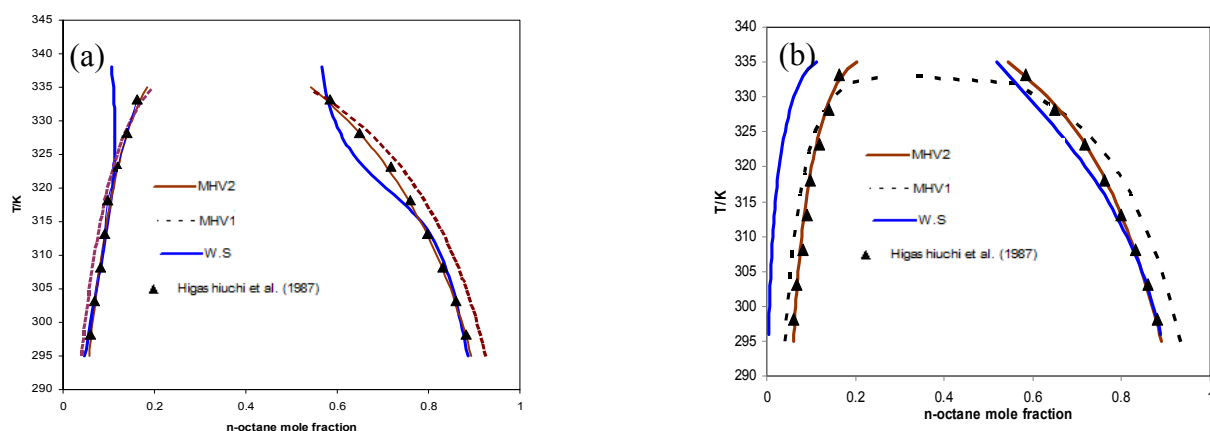
Table 1. Fitted T-K-Wilson and UNIQUAC parameters for two binary systems using MHV2 mixing rules.



Table 2. Predicted results of liquid–liquid equilibria at 0.1MPa using MHV1, MHV2, and Wong–Sandler model.

System	T-range/K	^a $ \Delta x_1 _{ave}$						NP
		UNIQUAC			T-K-Wilson			
		MHV1	MHV2	WS	MHV1	MHV2	WS	
Cyclohexane (1)-Methanol (2)	278.15-316.15	0.0194	0.0054	0.0420	0.0262	0.0053	0.0470	9
n-Octane (1) –Methanol (2)	298.15-333.15	0.0276	0.0038	0.0153	0.0629	0.00364	0.0459	8

$$^a |\Delta x_1|_{ave} = \frac{1}{2NDP} \sum_{k=1}^{NDP} (|x_{1,calc}^I - x_{1,exp}^I|_k + |x_{1,calc}^{II} - x_{1,exp}^{II}|_k)$$

Fig 1. Predicted results of liquid–liquid equilibria at 0.1 MPa by MHV1, MHV2 and WS mixing rule for Cyclohexane (1) + Methanol (2) using T–K–Wilson(a) and the UNIQUAC (b) equations, (\square , \circ) exp. from Ref. [6], (\blacktriangle , \blacksquare) exp. from Ref. [4].Fig 2. Predicted results of liquid–liquid equilibria at 0.1 MPa by MHV1, MHV2 and WS mixing rule for n-Octane (1) + Methanol (2) using T–K–Wilson (a) and the UNIQUAC (b) equations, (\blacktriangle) exp. from Ref. [5].

Conclusion

In comparing three EoS- G^E mixing rules, we found that MHV2 mixing rule with UNIQUAC G^E model shows better agreement with the LLE data than the other ones. The MHV1 and WS model is able to reproduce LLE data at 0.1 MPa; however, the accuracy of the predictions is not satisfactory.

References

- [1] T. Tsuboka and T. Katayama, J. Chem. Eng. Jpn. 8 (1975) 181.
- [2] R. Stryjek and J.H. Vera, Can. J. Chem. Eng. 64 (1986) 323.
- [3] D. S. Abrams and J.M.Prausnitz, AIChE J. 21 (1975) 116.
- [4] Z. Atik and W. Kerboub, J. Chem. Eng. Data 53 (2008) 1669.
- [5] H. Higashiuchi and Y. Sakuragi, Fluid Phase Equilibria 36 (1987) 35.
- [6] H. Matsuda, K. Ochi, and K.Kojima, J. Chem. Eng. Data 48 (2003) 184.

**Temperature dependence of viscosity and relation with the surface tension of ionic liquids**

M. H. Ghatee*, M. Zare

Department of Chemistry, Shiraz University, Shiraz, Iran

(E-mail: ghatee@susc.ac.ir)

(E-mail: zare.su@gmail.com)

Keywords: Correlation, Fluidity, Viscosity, Temperature dependence, Surface tension, Room temperature ionic liquids**1. Introduction**

Room temperature ionic liquids (RTILs) have attracted a significant and growing interest as green solvents because of their properties such as negligible vapor pressure, wide liquid range, high thermal stability and favorable solubility behavior [1]. Viscosity as a transport property has a great influence on the rate of mass transport and thus the solvent viscosity is an important factor in all chemical processes. The temperature dependence of transport properties of fluids is also essential for most industrial applications, and intensive research has been done for their measurement [2]. Liquid surface tension as an equilibrium thermodynamic property is also important as viscosity in design of industrial applications.

In this work, we propose two new regularities for ILs. The first one shows temperature dependence of viscosity of ILs and the second relates viscosity of ILs to their surface tension. We employ a variety of ILs to warrant generality of the proposed equations.

2. Results and discussion**2.1 Temperature dependence of viscosity**

An accurate linear correlation enables a reliable extrapolation, and importantly a better comparison, understanding, and characterization of different fluid classes. To achieve this for ionic liquids, we study the temperature dependence of fluidity. From the non-linear behavior of fluidity among different ILs, we conclude that the fluidity values can be represented by the following linear equation:

$$\left(\frac{1}{\eta}\right)^{\phi} = a + bT \quad (1)$$

where a , b and ϕ are substance dependent constants. The values of a , b and ϕ are obtained by fitting for 49 imidazolium-, pyridinium-, pyrrolidinium-, ammonium-, and nicotinium-based ILs. The value of the exponent ϕ is 0.300 (STDEV=0.004) for all ILs. Using the universal value of the exponent, the plots of the Eq. (1) are shown in Figures 1 and 2. LCC 's between 0.993 and 1.000 with the overall %AAD's of 1.833. Therefore, it can be concluded that Eq. (1) presents a new regularity for viscosity of ILs.

2.2 Relation between surface tension and viscosity

According to the fact that temperature dependence surface tension of fluids including ILs are perfectly linear and according to the successful applicability of the Eq. (1), we propose that the surface tension can be related to the fluidity as,

$$\ln \sigma = \ln C + D \left(\frac{1}{\eta}\right)^{\phi} \quad (2)$$

where $\ln C$ and D are substance dependent constants and ϕ is the universal exponent. The exponent $\phi=0.300$ is used in the Eq. (2) to fit the imidazolium-based ILs with simple anion content, which for them both experimental temperature dependent viscosity [3] and surface tension [4] data are available.

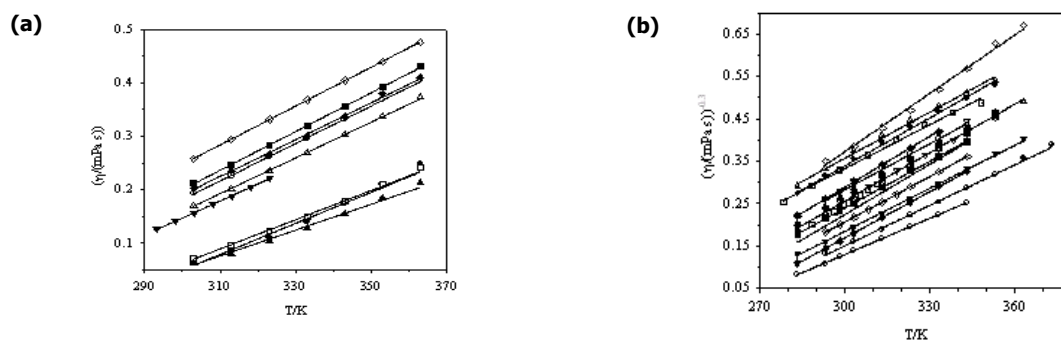


Fig. 1. Plots of $\eta^{-0.3}$ versus temperature **(a)**. For imidazolium-based ILs with simple anions. **(b)**. For imidazolium-based ILs with more complex anions.

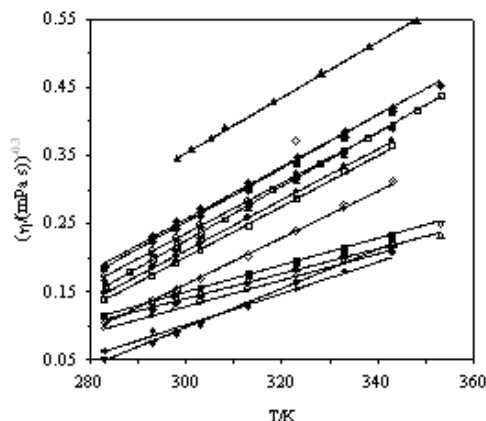


Fig. 2. Plots of $\eta^{-0.3}$ versus temperature for pyridinium-, pyrrolidinium-, nicotinium-, and ammonium-based ILs.

The characteristic exponent ϕ conveniently linearises the plots of $\ln\sigma$ versus fluidity of the ILs, as well as providing the best fit with high accuracy. From the plots shown in Figure 3, it can be seen that the viscosity of the ILs fits quite accurately in Eq. (2), with LCC's between 0.9955 and 0.9996 and %AAD's better than 0.240. This clearly demonstrates the usefulness of Eq. (2). Also we study the application of Eq. (2) to imidazolium-based ILs containing rather complex anions like TfSO_3^- , MeSO_4^- , EtSO_4^- , Tf_2N^- and OcsO_4^- . As shown in Figure 4, the Eq. (2) also fits these ILs quite accurately, with %AAD better than 0.164. Among other ILs, the application of Eq. (2) to $[\text{N}_{4111}]\text{Tf}_2\text{N}$, the quaternary ammonium-based IL, is also shown in the Figure 4. From the plots and LCC values, it can be seen that Eq. (2) fits $[\text{N}_{4111}]\text{Tf}_2\text{N}$ quite good with %AAD=0.092. For all ILs considered in Figures 3 and 4, the overall %AAD is 0.098, which clearly demonstrates that the new regularity Eq. (2) is quite accurate.

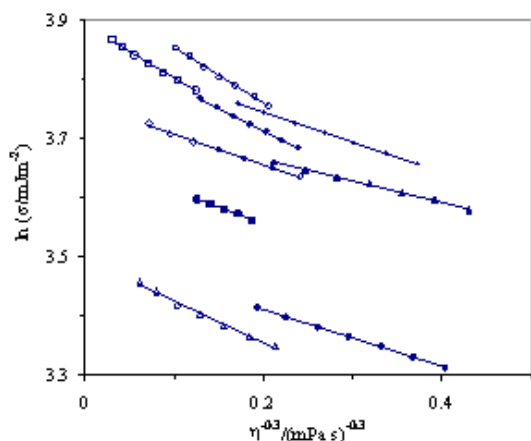


Fig.3. Plots of $\ln\sigma$ versus $\eta^{-0.3}$ for imidazolium-based ILs with simple anions.

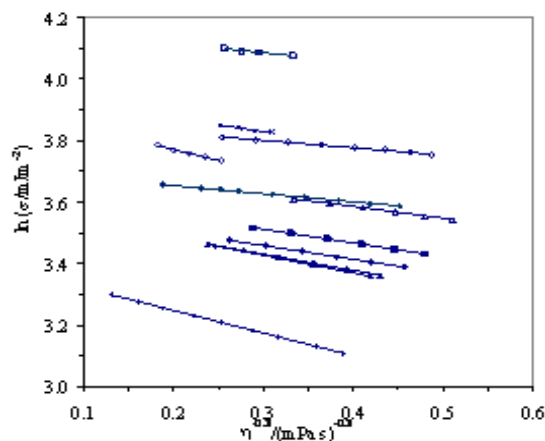


Fig.4. Plots of $\ln\sigma$ versus $\eta^{-0.3}$ for imidazolium-based ILs with simple anions and one ammonium-based IL.

3. Conclusions

We have found two linear correlations to characterize ILs. The first one (Eq. (1)) predicts temperature dependence of viscosity of ILs, and involves the exponent $\phi=0.300$. The accuracies are comparable with Litovitz and VFT equations. The second one (Eq. (2)) is a correlation of viscosity with surface tension involving the exponent ϕ and fits ionic liquids quite accurately.

References

- [1] J. Tong, M. Hong, W. Guan, J. -B. Li, J.-Z. Yang, J. Chem. Thermodyn. 38 (2006) 1416.
- [2] X. Meng, P. Zheng, J. Wu, Z. Liu, Fluid Phase Equilib. 271 (2008) 1.
- [3] K. R. Seddon, A. Stark, M. J. Torres, ACS Symp. Ser. 819 (2002) 35.
- [4] M. H. Ghatee, A. R. Zolghadr, Fluid Phase Equilib. 263 (2008) 168.



Thermodynamic and kinetic studies for the adsorption system of Zinc (II) and ions from solution using functionalized mesoporous silica NH₂-MCM-41

Nasim Jamshidi, Freydoon Ashrafi, Nader Bahramifar

Department of chemistry , Payam Noor University (PNU), sari unit , Mazandaran , Iran

(E-mail: nasim_5989@yahoo.com)

Keywords: Adsorption, Silver, Mesoporous silica NH₂-MCM -41, Kinetic , Thermodynamic

1. Introduction

Silver(I) is generally found in the combined state in nature, usually in copper(II) or lead(II) mineralization (1). Many techniques, such as ion exchange, precipitation, adsorption, membrane processes , revers osmosis, sedimentation, electro-dialysis, etc., have been employed for separation of heavy metals from wastewater. Some of materials such as zeolites, activated carbon, fly ash, biosorbents, resins (ion exchanger and chelating compounds) and others solvent extraction was used in the recovery of silver(I) from chemical solutions (2). The small but finite aqueous solubility of extractants, diluents and modifiers is a major disadvantage of solvent extraction. The loss of organics by evaporation and entrainment is also a potential problem. Adsorption has attracted attention because of new material types available for the recovery. With increase of environmental pollution, there is a growing demand to develop novel adsorbents of higher efficiency for heavy metal ions removal from aqueous media than those commercially available mesoporous silica have received considerable attention because of their unique large surface area, well- defined pore size and pore shape Mesoporous silica NH₂-MCM-41 has been functionalized and employed to eliminate traces of toxic heavy metal from wastewater. Mostly, the functionalizations of mesoporous silica have been studied. For example, Yoshitake *et al.*(3) investigated the amino-functionalized mesoporous silicas for removal of arsenate from a dilute aqueous solution. Lam *et al* (4) prepared gold-selective adsorbent from mesoporous silica MCM-41 by grafting organic amine groups. Algarra *et al.*(5) evaluated. the potential of removing nickel and copper from industrial electroplating wastewaters using aminopropyl groups functional mesoporous silica MCM-41 materials. Furthermore, the adsorption selectivity of NH₂-MCM-41 for Ni(II) and Cd(II) ions in binary component adsorption was recently examined by Lam *et al.*(4) recently. In this study, NH₂-MCM-41 mesoporous silica was prepared under basic condition by using hexadecyltrimethylammoniumbromide as template and fumed silica as the silica source by means of hydrothermal method. Then the effect of solution pH, contact time, silver ion concentration, adsorbent dosage and temperature on the adsorption capacity of NH₂-MCM-41 were studied in order to analyze the adsorption kinetics and thermodynamic and determine the equilibrium time.

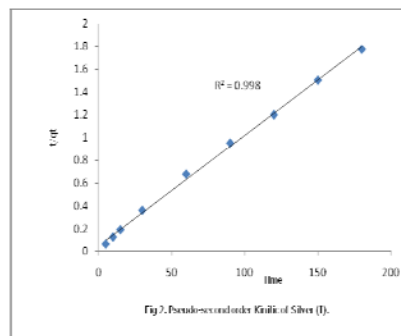
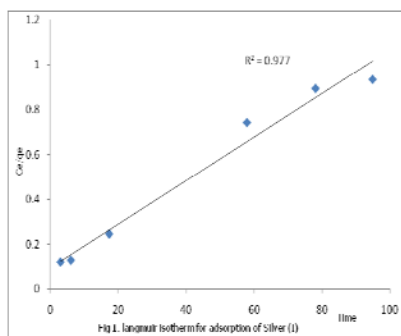
2. Materials and methods

Silver ion solution were obtained of nitrate salt of silver (MERCK) . NH₂-MCM-41 was prepared according to refluxed for 6 h. The mixture was filtered, washed with n-hexane (20 ml), dried at room temperature and stored in a desiccator. the method of Ho *et al.* In 50 ml of n-hexane, 2.5 g of calcined MCM-41 and 2.5 g of 3-aminopropyltrimethoxysilane were Atomic absorption spectrometry (Sens AA GBC) standard solution of 1000 mg/l were used for adsorption experiments. . The pH of the solutions was adjusted to desired values using either NaOH(1M) or HCl(1M) solutions. Adsorption experiments were conducted using 150 ml aqueous solution of mesoporous silica NH₂ – MCM- 41 were take in 250-ml Erlenmeyer flask. The pH of Silver solution adjusted to 7.0. one flask with dosage of metal solution but no adsorbent was used as control. A fixed amount of mesoporous silica NH₂ – MCM-41 (2.0g/L) added to metal solution. The solution stirred with help of a stirrer at 500 rpm. All experiments were conducted at a fixed temperature (22^o C), excluding the temperature experiment , where it was varied (5 ,15 ,25 and 35). The sorbent dose was fixed at 2.0 g/l excluding the sorbent dose experiment, where it was varied (0.5 , 0.75 , 1.0 , 1.5 , 2.0 and 3.0 g/l) The initial metal concentration was fixed at 100 g/l for experiment excluding the initial concentration experiment, where it was varied (50, 100, 150 , 200 , 250 and 300 mg/l). The effect of pH on the absorption rate was investigated in the pH rang of 3-8. Samples (5ml) were removed from experimental flask at 5 min intervals for the first 30 min of experiment, other samples take in 60, 90, 120 and 180 min of the experiment. Then the solid phase was separated by filtration through 0.2 μm microfilter. The concentration of Silver was determined by GBC flame atomic adsorption spectrometer(Sens AA) and the sorbed amount was calculated.



3. Results and discussion

pH is one of the most important environmental factors influencing not only site dissociation, but also the solution chemistry of the Silver. The obtained results shows that, the effects of initial pH on adsorption of Ag(I) ion onto NH₂-MCM-41 are investigated in a batch system. sorbent capacity, decreased with an increase in sorbent dose for an initial silver concentration of 100 mg/l. The equilibrium sorption capacity decrease from 59.3 to 29.053 mg/g when sorbent dose was increased from 0.5-3.0 g/l. This shows that increasing the sorbent dosage increased the surface area available, hence the number of sites available for sorption increased. The initial metal ions concentration was varied from 50 to 300 mg/L at temperature 22 °C. Therefore, the percentage of ions adsorbed at higher concentration level shows a decreasing trend, whereas uptake of ions displays opposite trend. The percent removal was increased as the initial Ag(I) concentration increased up to 50 mg/L but further increase in concentrations results in decrease in percent removal. Maximum percent removal of Ag(I) was observed 94.32 and with NH₂-MCM-41, respectively, at 50 mg/L. This may be due to the saturation of the sorption sites and increase in the number of ions competing for the available binding sites in the biomass for complexation of Ag(I) ions at higher concentration. The effect of temperature on uptake Ag(I) capacity of NH₂-MCM-41 was studied at 200 mg /l metal ion concentration. Maximum adsorption of Ag(I) were observed at pH 7.0 absorbent dose 2.0g/l, metal concentration 200 mg/l in 180 min of contact time. The adsorption equilibria data has been fitted very well to Langmuir as well as to freundlich adsorption model (Fig 1). The sorption kinetics followed the pseudo – second order rate equation Fig 2. It was shown that the removal of metal ions increased with increasing temperature up to 35 °C. 93.001% and 112.95 mg/l NH₂-MCM-41 was adsorbed at equilibrium at 35 °C. The adsorption of Ag(I) was endothermic, thus the extent of adsorption increased with increasing temperature. adsorbent rate constants increased with an increase in temperature. The thermodynamic parameters ΔG° , ΔS° and ΔH° for this adsorption process have been determined. The negative value of ΔG° and positive value of ΔH° were observed indication. Respectively, the spontaneous and endothermic in nature. The positive value of ΔS° suggests increased randomness during adsorption.



4. Conclusions

The present study showed that the NH₂-MCM-41 can be considered as a technology for removal Ag(I) in batch process. The obtained results showed that pH, sorbent dose, initial metal concentration uptake time and solution temperature highly affected the uptake Ag(I) capacity of the the NH₂-MCM-41 sorbent.

References

- [1] Buttermann, W.C., Hilliar, H.E., 2005. Silver—mineral commodity profiles. U.S. Geological survey, Reston, Virginia.
- [2] Wan, R.Y., Miller, J.D., 1986. Solvation extraction and electrodeposition of gold from cyanide solutions. J. Met. 38 (12), 35–40.
- [3] H. Yoshitake, T. Yokoi, T. Tatsumi, Chem. Mater. 15 (2003) 1713-1721.
- [4] K.F. Lam, K.L. Yeung, G. McKay, The journal of physical chemistry. B110 (2006) 2187-2194.
- [5] M. Algarra, M.V. Jiménez, E. Rodríguez-Castellón, A. Jiménez-López, J. Jiménez- Jiménez, Chemosphere 59 (2005) 779-786.
- [6] R. Kumar, N. R. Bishnoi *, G., K. Bishnoi Chemical Eng. J. 135 (2008) 202–208
- [7] V. Padmavathy * Bioresource Technology 99 (2008) 3100–3109
- [8] A. Heidari, H. Younesi, Z. Mehraban Chemical Eng. J. (2008) 2-6

**Liquid phase equilibria of (water + alcohols + 2-ethyl-1- hexanol) ternary systems at T=298.2 K**A.Ghanadzadeh ^a, H.Ghanadzadeh ^{a,b}, S. Abbasnejad^{a,*}, S. Shekarsaraee^a

a. Department of Chemistry, Faculty of Science, University of Guilan, Rasht, Iran

b. Department of Chemical Engineering, University of Guilan, Rasht, Iran

(E-mail: abbasnejad.s@gmail.com)**Keywords:** Extraction processes, UNIQUAC model**1. Introduction**

Liquid-phase equilibrium data of aqueous mixtures with organic solvents play an important role in the design and development of separation processes. In particular, liquid- liquid equilibria (LLE) investigations for ternary mixtures are important in the evaluation of industrial units for solvent extraction process. The accurate interpretation of phase equilibria and thermodynamic behavior for the different ternary mixtures is a fundamental and important key to improving solvent extraction techniques [1-4]. The separation of alcohols from aqueous solutions using the liquid-liquid extraction technique is industrially and scientifically important [5]. The aim of this study is to present the phase behavior and LLE data for the two ternary systems (water+ 1,3-butanediol+ 2-ethyl-1-hexanol), (water+1-butanol+2-ethyl-1-hexanol) [3] at 298.2K and atmospheric pressure. The experimental data ternary system of (water+ 1,3-butanediol+ 2-ethyl-1- hexanol) were compared with (water+1-butanol+ 2-ethyl-1-hexanol) [3] at 298.2 K. Phase diagrams were also obtained by solubility and tie-line data. Distribution coefficients and separation factors were determined from the tie-line data to establish the extracting capability of the solvent and the possibility of the use of this solvent for the separation of (water+ 1,3-butanediol or 1-butanol) mixtures. The experimental data were correlated using the UNIQUAC equation [6], and the values for the interaction parameter were obtained.

2. Experimental

2-Ethyl-1-hexanol and 1,3-butanediol were obtained from Merck with purities of 99.5% and 99.8%, respectively. The purity of these materials was checked by gas chromatography and used without further purification. Distilled water was used throughout all experiments.

The equilibrium data were determined using the experimental apparatus of a 300 ml glass cell. The equilibrium data were determined by preparing the ternary mixtures of known compositions. The prepared mixtures were introduced into the extraction cell and were stirred for 4h, and then left to settle for 4h for phase separation. After being allowed to reach equilibrium, samples were carefully taken from each phase and analyzed. Both the phase was analyzed using a Varian CP-3800 gas chromatography (GC) equipped with a thermal conductivity detector (TCD) and shimadzu C-R2AX integrator and the liquid-liquid Equilibrium data of (water+ 1-butanol + 2-ethyl-1-hexanol) data series at 298.2 K [3]. These systems are the source of experimental data.

3. Results and discussion

The LLE measurements for the ternary system of (water + 1,3-butanediol + 2-ethyl-1-hexanol) were made at atmospheric pressure in 298.2 K. Because (1,3-butanediol + water) and (1,3-butanediol + 2-ethyl-1-hexanol) are two liquid pairs that are completely miscible and the only liquid pair (water + 2-ethyl-1- hexanol) is partially miscible, this ternary system behave as type-1 LLE [7], and the ternary system of (water + 1-butanol + 2-ethyl-1-hexanol) [3] is the only liquid pair that is completely miscible and the two liquid pairs (water + 1-butanol) and (water + 2-ethyl-hexanol) are partially miscible, the ternary system behaves as type-2 LLE. The experimental data together with calculated tie lines for these ternary systems were listed in table 1 and plotted in figures 1 and 2.

4. Conclusions

The ternary system of (water + 1,3-butanediol + 2-ethyl-1-hexanol) exhibits type-1 behavior of LLE and the ternary system of (water + 1-butanol + 2-ethyl-1-hexanol) exhibits type-2 of LLE at 298.2 K. The UNIQUAC model was satisfactorily used to correlate the experimental LLE results and calculated the phase compositions of the studied mixtures. The corresponding optimized binary interaction parameters were also calculated. The results indicate to substitute branching -OH group located on

hydrogen atom of secondary, ternary carbons of butanol cause of that the solubility of water in 2-ethyl-1-hexanol increases with hydrogen bonding. The temperature in the range of the study has only a small effect on the solubility of water in 2-ethyl-1-hexanol. The average RMSD value between the observed and calculated mole fractions for (water + 1,3-butanediol + 2-ethyl-1-hexanol) and (water + 1-butanol + 2-ethyl-1-hexanol) 1.90% and 0.97%, respectively.

Table1. Experimental and calculated LLE for the ternary system {water (1) + 1,3-butanediol or 1-butanol (2) + 2-ethyl-1-hexanol (3)} at 298.2 K.

Aqueous phase				Organic phase			
X ₁		X ₂		X ₁		X ₂	
Exp.	UNIQU.	Exp.	UNIQU.	Exp.	UNIQU.	Exp.	UNIQU.
Water (1) + 1,3-butanediol (2) + 2-ethyl-1-hexanol (3)							
0.5603	0.5678	0.4370	0.4096	0.0174	0.0177	0.0568	0.0564
0.4928	0.5300	0.4998	0.4459	0.0232	0.0235	0.0844	0.0855
0.4747	0.5003	0.5155	0.4707	0.0255	0.0261	0.1000	0.1007
0.4498	0.4597	0.5337	0.5083	0.0281	0.0286	0.1159	0.1175
0.4293	0.4042	0.5520	0.5571	0.0404	0.0417	0.1650	0.1735
Water(1) + 1-butanol (2) + 2-ethyl-1-hexanol (3) [3]							
0.9948	0.9947	0.0047	0.0051	0.1351	0.1270	0.0990	0.1200
0.9921	0.9901	0.0072	0.0093	0.1610	0.1588	0.2292	0.2370
0.9907	0.9895	0.0086	0.0100	0.1909	0.1960	0.3019	0.3411
0.9869	0.9892	0.0124	0.0105	0.2240	0.2341	0.3740	0.4110
0.9832	0.9890	0.0159	0.0102	0.2660	0.2715	0.4401	0.4631
0.9816	0.9881	0.0175	0.0113	0.3161	0.3180	0.5080	0.5293
0.9807	0.9861	0.0181	0.0131	0.4101	0.4121	0.5896	0.5879

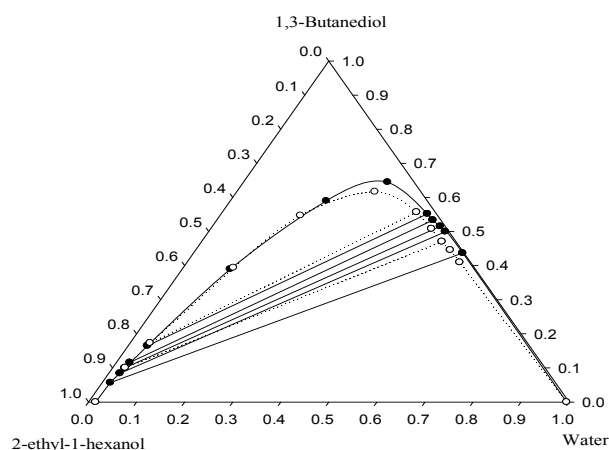


Fig. 1. Correlation of the experimental data for (water + 1,3-butanediol + 2-ethyl-1-hexanol) system at 298.2 K; (●), experimental points; (○), UNIQUAC calculated points.

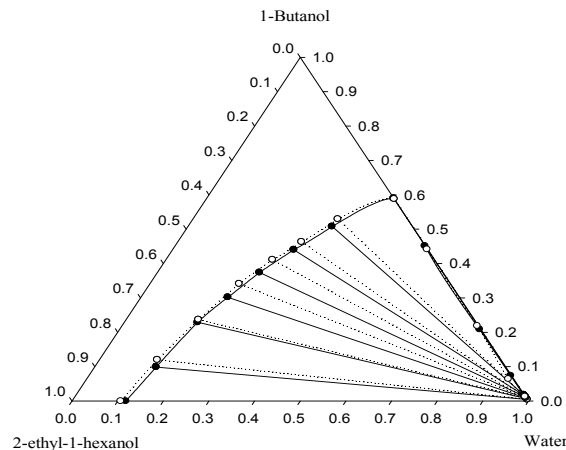


Fig. 2. Correlation of the experimental data for (water + 1-butanol + 2-ethyl-1-hexanol) system at 298.2 K; (●), experimental points; (○), UNIQUAC calculated points [3]

References

- [1] A. Arce, A. Blanco, Fluid Phase Equilibr. 109 (1995) 291-297.
- [2] A. Sensol, Fluid Phase Equilibr. 243 (2006) 51-56.
- [3] H. Ghanadzadeh, A. Ghanadzadeh, J. Chem. Eng. Data. 49 (2004) 783-786.
- [4] H. Ganadzadeh, A. Ghanadzadeh, R. Sariri, J. Chem. Thermodyn. 36 (2004) 1001-1006.
- [5] E. Ince, I. Kirbaslar, J. Chem. Thermodyn. 35 (2003) 1671-1679.
- [6] D.S. Abrams, J.M. Prausnitz, AIChE J. 21 (1975) 116-128.
- [7] S.I. Sandler, Chemical and engineering Thermodynamics; John Wiley and Sons: New york, 1998.

**A Cubic Equation of State Applicable to Ionic Liquids**

L. Maftoon-Azad

Chemistry Department, Persian Gulf University, Boushehr, Iran

(E-mail: maftoon@pgu.ac.ir)

Introduction

Room-temperature ionic liquids (organic salts that are liquid at conditions around room temperature) are being explored as potential environmentally benign solvents. A major reason for this interest in ionic liquids (ILs) is their negligible vapor pressure, which decreases the risk of worker exposure and the loss of solvent to the atmosphere. Accurate volumetric properties of any solvent are very important for thermodynamic calculations and process design. The design of equipment, material and energy balances involving liquids, vapor- liquid and liquid-liquid separations, all require accurate values of liquid density. Moreover, volume expansivities and isothermal compressibilities can provide information on fluid structure and molecular interactions. However, the data on volumetric properties of ionic liquids are rather limited [1].

There exist a great variety of analytical expressions that allow correlating and predicting the density of liquids. Such expressions are usually based on the use of adjustable parameters for each fluid correlations, on the concepts of corresponding state principle (semi-empirical and predictive), and on group contribution methods (semi-empirical and predictive). However, these types of generalized correlations and models were not developed for ionic liquids and have not yet been tested for appropriateness and accuracy with these special fluids. One of the main reasons could be the lack of some common basic data for ionic liquids, such as critical properties, normal boiling temperature and acentric factor [2,3]. As known, the critical properties of ionic liquids cannot be experimentally determined since most of these compounds start to decompose at low temperature and in many cases at temperatures approaching the normal boiling point [4].

Here we have proposed a cubic equation of state which is applicable to many ionic liquids with just one adjustable parameter. The basic data used for running the law of corresponding states are the properties at 298K which are readily available.

Methodology

The basic frame of the equation is similar to that proposed by Song and Mason [5].

$$\frac{P}{\rho kT} = 1 + B_2(T)\rho + \alpha \rho \left[\frac{1}{1 - \lambda b\rho} - 1 \right] \quad (1)$$

where $B_2(T)$, $b(T)$ and $\alpha(T)$ are temperature dependant parameters. λ is an adjustable parameter.

To determine $B_2(T)$, $b(T)$ and $\alpha(T)$ we tried to use the law of corresponding states. The following relations were used for the temperature dependant parameters and the whole equation fitted to the experimental data reported for BMIM PF₆ [6].

$$B_2(T)\rho_f = d_1 + d_2T^{*-1} + d_3T^{*-2} + d_4T^{*-3} + d_5T^{*-6} \quad (2)$$

$$\text{, and } T^* = [TT^{1/2}/T_{ref}T_f^{1/2}]^{3/4} \quad (3)$$

The term $\gamma_f \rho_f^{-2/3} N^{1/3} / RT$ is being referred to as T_{ref} . γ_f is the surface tension and ρ_f is the molar liquid density both at 298K and N is the Avogadro's number.

$$\rho_f \alpha = a_1 [\exp(-c_1 T^*)] + a_2 [1 - \exp(c_2 / T^{*1/4})] \quad (4)$$

$$\rho_f b = a_1 (1 - c_1 T^*) [\exp(-c_1 T^*)] + a_2 [1 - (1 + 0.25c_2 / T^{*1/4}) \exp(-c_2 / T^{*1/4})] \quad (5)$$

The following coefficients were found through out the fitting process:

$$\begin{array}{lllll} d1=0.986 & d2=-1.043 & d3=-1.123 & d4=-0.351 & d5=-0.030 \\ a1=-0.803 & a2=2.608 & c1=1.281 & c2=3.182 & \end{array}$$

The density at 298k (ρ_f), experimental densities in different temperature and pressures and the surface tension at 298k, were found in refs. [6-12]. Characteristic parameters of these ionic liquids are tabulated in Table I. The second step is to calculate the adjustable parameter λ for each element. The method is iterative and two matlab programs are used. Eq. (1) is



rearranged to a quadratic form in λ . All coefficients are calculable with data in tables I. The equation is solved for λ in a certain datum point. In another program, Eq. (1) which is rearranged to be a cubic equation in density, is solved for ρ . The coefficients are calculated by the evaluated value of λ at each temperature and pressure. Calculated densities are compared with experimental ones and the scattering of the points are considered. An iterative procedure to find the best value of λ is continued to the point of minimum scattering. Actually this is a simple manual fitting procedure.

Calculated λ 's for different liquids are reported in Table I.

Results and Discussion

The equation of state was applied to $BMIM PF_6$, $HMIM PF_6$, $OMIM PF_6$, $EMIM EtSO_4$, $EMIM N(CN)_2$, $EMIM NTf_2$, $[b_3mpy][N(CN)_2]$. The results are compared to the experimental data in refs. [7-12]. Temperature range (T range), number of data points investigated (N. P.) and the range of deviation percents (R. D. P.) at $p=1$ bar are reported in Table I. This shows a very good accuracy to predict the density.

Table I. Parameters and results for different ionic liquids.

Ionic liquid	T_f / K	$\rho_f / mol L^{-1}$	$\gamma_f / N \cdot m^{-1}$	λ	T range	N. P.	R. D. P.
$BMIM PF_6$	298.15	4.811	0.043	2.80×10^{-4}	298.15-328.15	14	-0.6- 0.8
$HMIM PF_6$	298.15	4.143	0.037	2.80×10^{-4}	292.79-391.29	9	-0.7- 0.2
$OMIM PF_6$	298.15	3.631	0.036	2.8×10^{-4}	273.15-363.15	14	-0.6- 1
$EMIM EtSO_4$	298.15	5.205	0.042	2.73×10^{-4}	292.8-391.27	9	-2- 2
$EMIM N(CN)_2$	298.15	6.094	0.043	2.66×10^{-4}	278.15-343.15	19	-1.5- 1.5
$EMIM NTf_2$	298.15	3.884	0.035	2.78×10^{-4}	278.15-318.15	9	-1.5- 1.5
$[b_3mpy][N(CN)_2]$	298.15	5.036	0.050	2.84×10^{-4}	298.15-343.15	7	-0.8- 0.6

Conclusion

As it is shown, the equation proposed in this work is capable of predicting the volumetric properties of ionic liquids in different cationic and anionic base structures. The properties at 298K are found to be fine reference points for this category of liquids. Later works will investigate the ability of this equation to predict the volumetric properties of other ionic liquids and to predict their thermodynamic properties.

References

- [1] Zh. Gu and J. F. Brennecke, J. Chem. Eng. Data 47 (2002) 339.
- [2] A. Mulero, I. Cachadiña, M.I. Parra, Ind. Eng. Chem. Res. 45 (2006) 1840.
- [2] R. A. Mantz, P. C. Trulove, in: P. Wasserscheid, T. Welton (Eds.), Ionic Liquids in Synthesis, Wiley-VCH Verlag GmbH & Co., Germany, 2002.
- [3] J.O. Valderrama, K. Zarricueta, Fluid Phase Equilibria 275 (2009) 145.
- [4] J. Jacquemin, P. Husson, A. A. H. Padua and V. Majer, Green Chem. 8 (2006) 172.
- [5] Y. Song, E.A. Mason, J. Chem. Phys. 91 (1989) 7840.
- [7] C. P. Fredlake, J. M. Crosthwaite, D. G. Hert, S. N. V. K. Aki, and J. F. Brennecke, J. Chem. Eng. Data 49 (2004) 954.
- [8] R. L. Gardas, M. G. Freire, P. J. Carvalho, I. M. Marrucho, I. M. A. Fonseca, A. G. M. Ferreira and A. P. Coutinho, J. Chem. Eng. Data 52 (2007) 80.
- [9] A. P. Froba, H. Kremer and A. Leipertz, J. Phys. Chem. B 112 (2008) 12420.
- [10] A. B. Pereiro a, J. L. Legido , A. Rodry' guez , J. Chem. Thermodynamics 39 (2007) 1168.
- [11] G. J. Kabo, A. V. Blokhin, Y. U. Paulechka, A. G. Kabo, and M. P. Shymanovich, J. Chem. Eng. Data 49 (2004) 453.
- [12] J. Troncoso, C. A. Cerdeirín, Y. A. Sanmamed, Y. Romaný and L. P. N. Rebelo, J. Chem. Eng. Data 51 (2006) 856.



Statistical Mechanics



**Monte Carlo simulation of hard confined ellipses**

M. Moradi* and S. Hashemi

Department of Physics, Shiraz University, Shiraz, Iran

(Email: moradi@susc.ac.ir)

(Email: sbhh_hashemi@yahoo.com)

Keywords: Molecular liquid, Ellipses, Confined fluid, Monte Carlo simulation.**1. Introduction**

In the last decades the thermodynamic [1-2] and structural [2-5] properties of molecular fluids and especially liquid crystal [6] become an important subject from the theoretical [1-6] and technological [7-8] point of view. Generally the structural properties are determined by the short range repulsive force acting between molecules. For two main reasons, the two dimensional molecular crystalline system are considered here. First, for many practical purposes we are interested in the behavior of thin films of liquid crystal. Second, it is interesting to know how the liquid crystalline behavior depends on the dimensionality and confinement [9-10]. Among the two-dimensional hard molecular system, the simplest one is the hard-ellipse model [11]. One of the efficient models in the Monte Carlo simulation study of molecular liquid is a system of hard ellipses. Because this model can be considered easily and fast and we can run the programs many times to check suggested theories and also find the optimum simulation parameters. In this article we study the structural and thermodynamic properties of hard ellipses between hard parallel walls using the Monte Carlo simulation. To our knowledge some researches have done on the properties of hard ellipses. For example Cuesta and Frenkel [9] reported constant-pressure Monte Carlo simulation of a system of hard ellipses. Buchalter and Bradley [12] examined the random packing of hard ellipses formed by pouring in to a two dimensional container by means of Monte Carlo simulation.

2. Methods

Moradi and Taghizadeh applied the density functional theory to study confined hard-ellipse molecules [4,10]. They obtained the angular and average density profiles of hard ellipses confined between two parallel hard walls. Here we obtain the average and angular density profile of hard ellipses confined between hard walls using the NVT Monte Carlo simulation, for different aspect ratios $k = \frac{2a}{2b}$, where a and b are semi major and semi minor of ellipses and separation of the walls. To perform the Monte Carlo simulation of hard ellipses between hard walls, we choose a two-dimensional simulation box such that one of the box sizes is exactly equal to the distance between walls and the other size is arbitrary. The images boxes are periodically repeated between and parallel to the walls. The number of particles in the box is chosen such that the average number density of particles in the box is being equal to the bulk number density of a given system of ellipses. To start the simulation, first we put the particles in the box systematically with an especial configuration for a given positions and directions such that no any overlap between the particles. Then we change the position and direction of ellipses to get a new configuration. To change the location and the direction of the particles we introduce maximum displacements in x and y directions as; dx_m and dy_m and also the maximum rotation $d\theta_m$, then we multiply dx_m , dy_m and $d\theta_m$ by three distinct random numbers ($R(n)-0.5$), where $R(n)$ is a random number between zero and one. Now we add these increments to the previous coordinates of particle to get new configuration. The maximum displacements and rotation are chosen such that, 50% of the configurations are accepted. To accept the new configuration the Metropolis algorithm is used. We change the position and direction of molecules and accept the configuration conditionally and repeat this for many times until we reach the system in equilibrium.

3. Results and discussion

Now we can obtain the required quantities such as angular number density, order parameter or the pressure of the system. We start with one hundred particles in the box and choosing $dx_m=0.6$, $dy_m=0.6$, $d\theta_m=10$ degree, and box sizes are $60b$ (parallel to the wall) and $41.6b$, the length of semi minor axis of ellipse is chosen a unit length. For the bulk number density, $\rho_b = 0.64$ ($\eta = 0.5$) the required number of configurations to reach the equilibrium is 9 million and we run the program for



another 30 million and we obtained the density profiles between the walls. The total angle in plane is (360°) is divided to 36 sectors and we define angular density profile, $\rho_\alpha(r)$, $\alpha = 0, \dots, 35$ for each sector. We also obtained the pressure of the fluid. The density profiles of ellipses parallel ($\rho_{\alpha=10}(r), \theta = 90^\circ$) and perpendicular ($\rho_{\alpha=0}(r), \theta = 0^\circ$) to the walls are shown in Fig.1. We also obtained the pressure of the hard ellipses between hard wall and in Fig.2 the pressure against the density is plotted.

4. Conclusions

As it is seen in the Fig.1 for the ellipses close to the wall the number of ellipses parallel to the wall is much bigger than the ellipses perpendicular to the wall and in the middle of the walls the angular density profiles are almost the same value and equal to 1/18 of the bulk density. There exists a peak for angular density profile at a distance 0.65 from the first layer of particles at the wall. As seen in Fig.2 the obtained pressure in a given density is equal to the total density of ellipses at the wall.

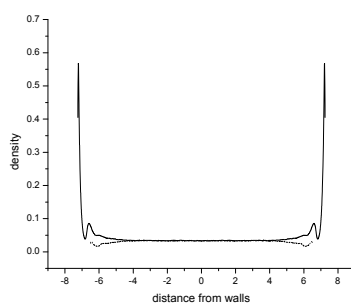


Fig. 1. Density profile of ellipses parallel (—) and perpendicular (.....) to the wall for $\eta = .5$ and $h=60b$ and $k=4$

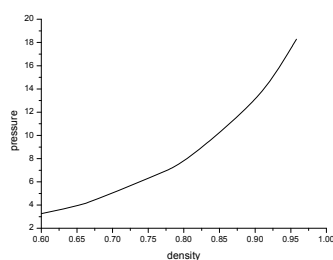


Fig. 2. Pressure versus density for $k=4.0$

References

- [1] B. Jerome, Rep. Prog. Phys. 54 (1991) 391.
- [2] J. P. Hansen and I. R. McDonald, Theory of simple liquids, Academic press, London, 1986.
- [3] Bruno Martinez – Haya, Juan M. Pastor and Jose A. Cuseta, Phys. Rev. E 59 (1999) 1957.
- [4] M. Moradi and F. Taghizadeh, Physica A 387 (2008) 6463.
- [5] M. Moradi, R. J. Wheatley and A. Avazpoor, J. Phys. Condens. Matter 17 (2005) 5625.
- [6] M. Moradi and R. Khordad, International Journal of Modern physics B to be published (2009).
- [7] S. Varga and I. Szalai, Mol. Phys. 95 (1998) 515.
- [8] A. Galindo et al., Journal chemical physics, 119 (2003) 5216.
- [9] J. A. Cuesta and D. Frenkel, Phys. Rev. A, 42 (1990) 2126.
- [10] M. Moradi and F. Taghizadeh, International Journal of Modern physics C (2009) 337.
- [11] D. Levesque, D. Schiff and J. Viillard-Baron, J. chem. Phys. 51 (1969) 3625.
- [12] B. J. Buchalter and R. Mark Bradley, Phys. Rev. A, 46 (1992) 2320.

**Validity of some regularities of dense fluids for ionic liquids**

H. Azizi Toopkanlu and E. K. Goharshadi*

Department of Chemistry, Ferdowsi University of Mashhad, Mashhad 91779, Iran

(Email: ho_azizi60@yahoo.com)

Keywords: Ionic liquids, Regularity, Bulk modulus, Isobaric expansion coefficient, Isothermal compressibility, Internal pressure.**1. Introduction**

Ionic liquids (ILs) are organic molten salts that have received special attention due to a negligible vapor pressure [1,2] a broad liquid range [3], thermal stability up to high temperatures, possess high solubility for both polar and nonpolar organic and inorganic substances, exhibit interesting solvation and coordination properties that depend on the nature of the cation and/or anion [4,5]. Ionic liquids usually consist of a large, asymmetric organic cation coupled with a generally smaller, weakly coordinating anion. Because a large number of cationic and anionic structure combinations are possible, their physicochemical properties can be easily tuned by changing the structure of the component ions. Among the many applications of ionic liquids that have been reported in the literature are the following: as media for clean liquid-liquid extraction processes, as solvents for electrochemical applications, for catalytic cracking of polyethylene, for radical polymerization, and in nanomaterial technologies. The design of industrial processes and new products based on ILs are only possible when their thermophysical properties are adequately known. Despite the fact that the description of dense fluids at the molecular level is very complicated, they obey some relatively simple regularity [6]. Five of the best known regularities, studied in this work, are the following:

- (1) Near linearity of the isothermal bulk modulus (reciprocal compressibility) of a liquid or supercritical fluid as a function of pressure.
- (2) Huang and O'Connell have found that isotherms of the bulk modulus as a function of density intersect at a common point [7].
- (3) It has been observed for many substances that isotherms of isobaric expansion coefficient versus pressure pass through a common intersection point.
- (4) There is a similar behavior for isothermal compressibility, namely isotherms of the isothermal compressibility of some liquids as a function of pressure intersect at a common point.
- (5) There exists a common intersection point for the isobars of internal pressure as a function of temperature.

2. Methods

In this work, two equations of states, Goharshadi-Morsali-Abbaspour (GMA) equation of state (EoS) and Tait EoS have been used to reproduce the regularities. The GMA EoS is based on the average potential energy and is given as [8]:

$$(2Z - 1)V_m^3 = A(T) + B(T)\rho \quad (1)$$

where Z , V_m , and ρ are compressibility factor, molar volume, and density, respectively. The intercept and slope of this equation depends on temperature via the equations:

$$A(T) = A_0 - \frac{2A_1}{RT} + \frac{2A_2 \ln T}{R} \quad (2)$$

$$B(T) = B_0 - \frac{2B_1}{RT} + \frac{2B_2 \ln T}{R} \quad (3)$$

where $A_0 - A_2$ and $B_0 - B_2$ are constants. To use the equation of state for a liquid, the A and B parameters must be known. To find these parameters, we may plot $(2Z-1)V_m^3$ versus ρ for different isotherms. The slope and intercept of the straight lines can be fitted to Eqs. (2) and (3) from which $A_0 - A_2$ and $B_0 - B_2$ can be found, respectively. The Tait EoS has the following form [9]:

$$\frac{1}{\rho(P, T)} = \frac{1}{\rho(P_o, T)} \left(1 - C \ln \left(1 + \frac{P}{B(T)} \right) \right) \quad (4)$$

$$\frac{1}{\rho(P_o, T)} = a_o + a_1 T + a_2 T^2 \quad (5)$$

$$B(T) = b_o \exp(-b_1 T) \quad (6)$$



where $p(P_0, T)$ is the density at ambient pressure P_0 . The $B(T)$ is dependent on temperature; C is a constant; and a_0, a_1, a_2, b_0 , and b_1 are the fitting parameters.

3. Results and discussion

In this paper different classes of ionic liquids, listed in Table 1 have been studied. The five regularities mentioned above have been checked using the existing experimental data. The results indicate that the some ionic liquids show these regularities.

Table 1. Formula, critical properties, and temperature and pressure ranges of ionic liquids of studied

Compound	Formula	T_c (K) ^a	P_c (MPa)	$10^6 V_c$ (m ³ /mol)	ΔP (MPa)	ΔT (K)
[C ₂ mim][CF ₃ SO ₃]	C ₇ H ₁₁ N ₂ F ₃ SO ₃	985.2	3.58	653.4	0.1-35	293.15-393.15
[C ₃ mpyr][NTf ₂]	C ₁₁ H ₁₄ N ₂ F ₆ S ₂ O ₄	1228.9	2.75	981.7	0.1-35	293.15-393.15
[C ₃ mpyr][NTf ₂]	C ₁₀ H ₁₈ N ₂ F ₆ S ₂ O ₄	1196.9	2.67	969.8	0.1-35	293.15-393.15
[C ₄ mpyr][NTf ₂]	C ₁₀ H ₁₇ N ₂ F ₆ S ₂ O ₄	1209.2	2.48	1026.9	0.1-35	293.15-393.15
[C ₄ mim][OS]	C ₁₆ H ₃₂ N ₂ O ₄ S	1189.8	2.02	1116.7	0.1-60	318.15-428.15
[C ₃ mim][NTf ₂]	C ₉ H ₁₃ N ₃ F ₆ S ₂ O ₄	1259.3	2.99	933.0	0.1-59.59	313.15-333.15
[C ₃ mim][NTf ₂]	C ₁₁ H ₁₇ N ₃ F ₆ S ₂ O ₄	1281.1	2.56	1047.2	0.1-59.59	313.15-333.15
[C ₄ mim][NTf ₂]	C ₁₀ H ₁₅ N ₃ F ₆ S ₂ O ₄	1265.0	2.76	1007.1	0.1-150	298.15-323.15
[C ₆ mim][NTf ₂]	C ₁₂ H ₁₉ N ₃ F ₆ S ₂ O ₄	1287.3	2.39	1121.3	0.1-150	298.15-323.15
[C ₄ mim][BF ₄]	C ₈ H ₁₅ N ₂ BF ₄	632.3	2.04	672.0	0.1-150	298.15-323.15
[C ₄ mim][PF ₆]	C ₈ H ₁₅ N ₂ PF ₆	708.9	1.73	779.5	0.1-40	298.15-323.15
[C ₆ mim][PF ₆]	C ₁₀ H ₁₉ N ₂ PF ₆	754.3	1.55	893.7	0.1-200	312.9-472.3
[C ₈ mim][PF ₆]	C ₁₂ H ₂₃ N ₂ PF ₆	800.1	1.40	1007.9	0.1-200	312.8- 472.3
[C ₆ mim][BF ₄]	C ₁₀ H ₁₉ N ₂ BF ₄	679.1	1.79	786.2	0.1-200	313.3-472.5
[C ₂ mim][PF ₆]	C ₆ H ₁₁ N ₂ PF ₆	663.5	1.95	665.3	0.1-200	312.8- 472.4

^aCritical properties taken from Ref 10 & 11.

GMA EoS is able to show the linearity of bulk modulus versus pressure. EoS can not predict the second, third, and fourth regularities for ILs. Tait EoS is not able to predict the second and fourth regularities for ILs, although the Tait EoS can predict these regularities for other compounds.

4. Conclusions

In summary, five of the best known regularities have been investigated experimentally and theoretically for different classes of ILs to develop solution theories for ionic liquids. All of this work points to the need for more experimental and theoretical research to extend our understanding of ILs so that researchers will have additional key information to help them systematically design IL systems to meet their specific target applications.

References

- [1] M. J. Earle, J. M. S. S. Esperancu^ˆa, M. A. Gilea, J. N. C. Lopes, L. P. N. Rebelo, J. W. Magee, K. R. Seddon, J. A. Widegren, *Nature* 439 (2006) 831.
- [2] D. H. Zaitsau, G. J. Kabo, A. A. Strechan, Y. U. Paulechka, A. Tschersich, S. P. Verevkin, A. Heintz, *J. Phys. Chem. A* 110 (2006) 7303.
- [3] K. J. Baranyai, G. B. Deacon, D. R. MacFarlane, J. M. Pringle, J. L. Scott, *Aust. J. Chem* 57 (2004) 145.
- [4] A. Heintz, *J. Chem. Thermodyn* 37 (2005) 525.
- [5] L. P. N. Rebelo, J. N. C. Lopes, J. M. S. S. Esperanca, E. Filipe, *J. Phys. Chem. B* 109 (2005) 6040.
- [6] G. Parsafar, N. Sohraby, *J. Phys. Chem* 100 (1996) 12644.
- [7] A. C. Colin, S. Cancho, R. G. Rubio, A. Copostizo, *J. Phys. Chem* 97 (1993) 10796.
- [8] E. K. Goharshadi, A. Morsali, M. Abbaspour, *Fluid Phase Equilib* 230 (2005) 170.
- [9] J. M. S. S. Esperancu^ˆa, H. J. R. Guedes, M. Blesic, L. P. N. Rebelo, *J. Chem. Eng. Data* 51 (2006) 237.
- [10] J. O. Valderrama, P. A. Robles, *Ind. Eng. Chem. Res* 46 (2007) 1338.
- [11] J. O. Valderrama, W. W. Sanga, J. A. Lazzs, *Ind. Eng. Chem. Res* 47 (2008) 1318.

**Thermodynamic modeling of the solubility of carbon dioxide in aqueous monoethanolamine solution**A. Gheisari^a, F. Rashidi^a, A. Maghari* and S. Sadeghi^b^a Department of chemical engineering, Amir Kabir university of technology, Tehran, Iran^b Department of Chemistry, University College of Science, University of Tehran, Tehran, Iran

(E-mail: abdolla.gh@aut.ac.ir)

(E-mail: sadegh.sd@gmail.com)

Keywords: vapor liquid equilibria, solubility, carbon dioxide, monoethanolamine,**1. Introduction**

Using aqueous solutions of alkanolamines for CO₂ capture from process streams is an established concept that has achieved wide industrial practice. Monoethanolamine (MEA) solutions are widely used for the removal of CO₂ from gas streams. Advantages of MEA solutions are the rapid reaction rate, low cost of the solvent, ease of reclamation, and the relatively low solubility of hydrocarbons in the solution [1]. To develop efficient processes for separation of CO₂ from flue gases, thermodynamic modeling of the vapor-liquid equilibrium (VLE) is the first step. A thermodynamic model is necessary to describe the partial pressure of CO₂ over an aqueous solution of alkanolamines, and it can quantify the energy required for regeneration of the alkanolamine. In this study for modeling purposes, activity coefficients are represented with the Pitzer equation [2] treating both long-range interactions between electrolytes and short-range forces. Both water and amine were considered as solvents. The equilibrium behavior of the vapor phase is explained using the Redlich-Kwong-Soave (SRK) equation of state. Accurate values for the partial pressure of CO₂ are obtained for a limited loading, temperature and pressure range that is useful in modeling CO₂ absorption plants.

At equilibrium, the fugacity of CO₂ in the vapor phase is equal to that of the liquid phase:

$$(\hat{f}_{CO_2})_V = (\hat{f}_{CO_2})_L \quad (1)$$

The CO₂ in the liquid phase reacts with other chemical components to produce ions. The following reactions were considered:



The thermodynamic equilibrium constants are function of temperature, and are represented by the following Eq.

$$\ln K = C_1 + C_2/T + C_3 \ln T + C_4 T \quad (5)$$

The coefficients required are listed in table 1[3]. Henry's constant is expressed in Pascal.

Table 1. Temperature dependent of the equilibrium constants and Henry's constant

Constant	C ₁	C ₂	C ₃	C ₄
K ₁	231.465	-12092.1	-36.7816	0
K ₂	2.1211	-8189.38	0	0
K ₃	2.8898	-3635.09	0	0
He	170.7126	-8477.711	-21.95743	.005781

The carbon dioxide liquid phase fugacity using Eq. 2, 3, and 4 can be expressed as

$$(f_{CO_2})_L = \frac{HK_2 x_N \gamma_N^* x_X \gamma_X^*}{K_1 x_1 \gamma_1 x_2 \gamma_2} \quad (6)$$

Where 1, 2, X, Y, and N denotes H₂O, MEA, HCO₃⁻, MEACOO⁻, MEAH⁺ respectively.

Where, activity coefficients (γ) were determined from the Pitzer equation. In this model, the excess Gibbs energy equation consists of two terms; short-range and long-range interactions.

$$g^E = g^S + g^L \quad (7)$$

$$\frac{g^E}{RT} = x_I \sum_n x_n \sum_{c,a} F_c F_a W_{nca} + \sum_{n,n'} x_n x_{n'} (A_{nn'} x_n + A_{nn'} x_{n'}) \quad (8)$$



$$\frac{g^L}{RT} = -\frac{4A_x I_x}{\rho} \ln(1 + \rho I_x / 2) + \sum_c \sum_a x_c x_a B_{ca} g(a I_x / 2) \quad (9)$$

$$F_c = \frac{2x_c}{x_I} \quad F_a = \frac{2x_a}{x_I} \quad (10)$$

$$x_I = 1 - \sum_n x_n \quad (11)$$

$$g(x) = 2[1 - (1 + x) \exp(-x)] / x^2 \quad (12)$$

$$\rho = 2150 \left(\frac{18.02 d_m \sum C_n}{1000 D_m T} \right)^2 \quad (13)$$

Where, d_m , D_m , C_n , c , a , and n are solution density, dielectric constant, concentration, cation, anion and neutral species. A , B and W are constant parameters.

$$\ln(\gamma_i) = \frac{\left(\frac{\partial g^E}{\partial n_i} \right)}{RT} \quad (14)$$

The fugacity of CO_2 in the vapor phase was calculated using the RKS equation of state.

$$(f_{\text{CO}_2})_V = y_i P \phi_i \quad (15)$$

$$P = \frac{RT}{v-b} - \frac{a(T, \omega)}{v(v+b)} \quad (16)$$

$$\ln \phi_i = -\frac{1}{RT} \int_0^P \left(\frac{RT}{P} - v_i \right) dP \quad (17)$$

Thereafter, the equilibrium partial pressure of CO_2 was computed by means of Eq. (1)

2. Results and discussion

The results obtained in this study were validated by experimental data [4]. Figure 1 shows a comparison between the model correlation and the experimental results for CO_2 partial pressure versus loading over 30 wt % aqueous MEA solution in different temperatures. Figure 2 shows the liquid phase concentration of a CO_2 -loaded 30 wt % MEA aqueous solution at 40°C. Results presented in these figures indicate that the present modeling can accurately predict the solubility data very well.

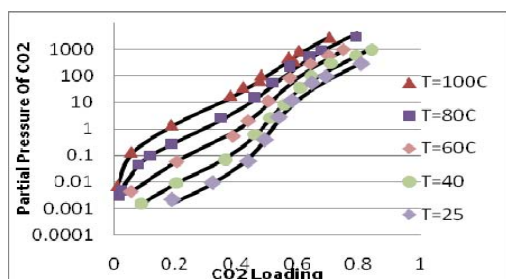


Fig. 1 solubility of CO_2 in a 30 mass % MEA solution

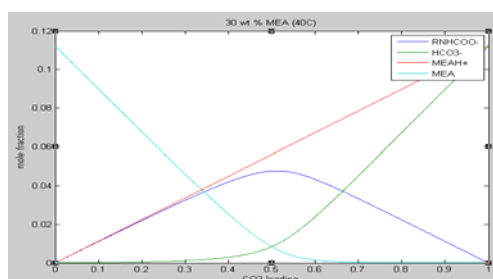


Fig. 2 liquid phase concentration of solution at 40°C

References

- [1] DuPart, M. S., Bacon, T. R. and Edwards, D. J. Hydrocarbon Process. 72 (1993) 89-94
- [2] Pitzer, K. S. Activity Coefficient In Electrolyte Solutions, Second Edition Chapter 3, Appendix I (1991)
- [3] Austgen, D. M., Rochelle, G. T., Peng, X., and Chen, C. C. Ind. Eng. Chem. Res. 28 (1989) 1060
- [4] Jou, F. Y., Mather, A. E., and Otto F. D. Canadian Journal Of Chemical Engineering, 73 (1995) 140

**Calculation of entropy of cyclohexane**

Vahid Moeini, Mehri Deilam and Hojatolaeh Rahimi

Department of Chemistry, Payame Noor University, Behshahr Center, Behshahr, Iran

(Email: mehrideilam@yahoo.com)

Keywords: Entropy, Helmholtz energy, Thermal pressure coefficient, Cyclohexane.**1. Introduction**

At present work, entropy for molecule cyclohexane, is studied in terms of the linear. For a suitable situation in initial states the entropies can calculate using Helmholtz energy for dense fluids and the linear entropy of each state is correlated to the negativities just for the dense states. The differences in the linear entropy between theory and experimental data are showed as well. Those are useful for molecular quantum computing and quantum information processing.

2. Methods

In this work, the entropy of cyclohexane, was calculated at the certain temperature and pressure using Helmholtz energy. The idea has been presented of a simple method using direct calculation of the entropy in place of using the equation of state to analyze the experimental $p-v-T$ data [1,2]. The equation of state described in papers is explicit in the Helmholtz energy A , with the two independent variables of density ρ and temperature T . At a given temperature, the thermal pressure coefficient can be determined from the Helmholtz energy [3]. At a given temperature, the pressure can be determined by Helmholtz energy.

$$p(T, \rho) = - \left(\frac{\partial A}{\partial V} \right)_T \quad (1)$$

Using the general expression of the relation to the reduced Helmholtz energy $\phi = A/(RT)$ and its derivatives gives

$$\frac{p(\delta, \tau)}{\rho RT} = 1 + \delta \phi_\delta^r \quad (2)$$

Where $\delta = \rho / \rho_C$ is the reduced density and $\tau = T_C / T$ is the inverse reduced temperature. Both the density ρ and the temperature T are reduced with their critical values ρ_C and T_C , respectively. Since the Helmholtz energy as a function of density and temperature is one of the four fundamental forms of an equation of state, all the thermodynamic properties of a pure substance can be obtained by combining derivatives of the reduced Helmholtz energy ϕ . Where ϕ_δ and ϕ_δ^r are defined as

$$\phi_\delta = \left(\frac{\partial \phi}{\partial \delta} \right)_\tau \quad (3)$$

and

$$\phi_\delta^r = \left(\frac{\partial \phi^r}{\partial \delta} \right)_\tau \quad (4)$$

Then, finally, to derive thermal pressure coefficient, we need only convert the $d\tau$ to dT

$$d\tau = - \frac{T_C}{T^2} dT \quad (5)$$

The above procedure leads to obtaining the thermal pressure coefficient from the reduced Helmholtz energy for real fluids:



$$\left(\frac{\partial p}{\partial T} \right)_{\delta} = \rho R \left[(1 + \delta \phi_{\delta}^r) - \delta \tau \left(\frac{\partial \phi_{\delta}^r}{\partial \tau} \right)_{\delta} \right] \quad (6)$$

In the present work, the Helmholtz energy has been used to calculate the entropy. The purpose of this paper is to point out an expression for the entropy of dense fluids using the Helmholtz energy [3].

In information theory and statistics, various generalized entropic quantities play a fundamental role. Some prototypical examples are the Shannon entropy, the Renyi entropy and the Tsallis entropy. A basic and important issue for these entropic quantities is their stability (or robustness) if a slight change of the underlying state (probability distribution) only causes a uniformly small deviation of the corresponding entropies, then the entropies are stable. To appreciate the subtlety and to gain and intuitive insight into this problem, let us first review briefly some related results.

Following Lesche, we will discuss the stability of a general state functional which is often a kind of entropic quantity. The framework is as follows: for any positive integer n , let P_n be the set of n -dimensional probability distributions (which is here interpreted as a state space), i.e.,

$$P_n = \left\{ p = (p_1, p_2, \dots, p_n), \sum_{i=1}^n p_i = 1, p_i \geq 0, \forall i = 1, 2, \dots, n \right\} \quad (7)$$

Let: $J : P_n \rightarrow R$ be a general state functional, and put

$$J^{\max}(n) = \max_{p \in P_n} J(p) \quad (8)$$

We will only consider probability distributions with finite support and assume that the number of supporting points equals n . Let X be a finite random variable supported on n points, with the probability distribution $\{P_X(i), i = 1, 2, \dots, n\}$. The generalized entropy we considered is [4]

$$S_f(P_X) = \sum_i P_X(i) f(P_X(i)) \quad (9)$$

3. Results and Discussion

Table 1 is shown that the helmholtz energy of the good method for calculation of the entropy of each state. In addition, for entropy in both molecules, liquid and supercritical state, it is found that the negativities are dominant in each state with Helmholtz energy.

Table1. Calculated values of entropy for cyclohexane fluid are compared with Experimental values of entropy calculated at 298K

P / MPa	$\rho / \text{mol.lit}^{-1}$	S_{cal}	S_{exp}
18.1000	9.3669	-45.4807	-30.9330
18.6000	9.3713	-41.5975	-30.9900
19.1000	9.3756	-37.6154	-31.0470
19.6000	9.3799	-33.5364	-30.1030

4. Conclusions

We have explored the theory properties of entropy correlation Hemholtz energy with various initial states, where the entropy and the entanglement are respectively measured by thermal pressure coefficient and the linear entropy. The initial states are taken to be the Boyle density of thermal states and squeezed states on each dense fluid. It is shown that negatively correlated behaviors of the linear entropies in each mode depend on initial states. Thus Hemholtz energy could be regarded as a measure of entanglement just for entropy.

References

- [1] Gholamabbas Parsafar, E. A. Mason. Linear Isotherms for Dense Fluids: A New Regularity. J. Phys. Chem, 97 (1993) 9048.
- [2] Vahid Moeini, Feridon Ashrafi, Mahnaz Karri, and Hojatolaeh Rahimi, Calculation of thermal pressure coefficient of dense fluid using the liner isotherm regularity. J. Phys. Condense matter, 20 (2008) 075102.
- [3] Vahid Moeini, A new regularity for internal pressure of dense fluid. J. Phys. Chem. B. 110 (2006) 3271-3275.
- [4] Xuelian Cao, Shunlong Luo, On the stability of generalized entropies, J. Phys. A: Math. Theor. 42 (2009) 075205 (9pp).



Prediction of thermodynamic second derivatives and solubility of some gases in amines by statistical associating fluid theory

Ali Maghari* and Sadegh Sadeghi

Department of Chemistry, University College of Science, University of Tehran, Tehran, Iran

(E-mail: maghari@khayam.ut.ac.ir)

(E-mail: sadegh.sd@gmail.com)

Keywords: Original SAFT, Equation of state, Speed of sound.

1. Introduction

Aqueous amine solutions are used for the removal of acidic gases, such as CO₂ and H₂S from industrial and natural gases. Calculation of solubility of the gases is very important for chemical engineers. In this study we have used the Statistical Associating Fluid Theory (SAFT) for calculating the solubility of gases in Dimethylamine as a solvent and obtained their second derivative thermodynamic properties, such as speed of sound and heat capacities. Perhaps the most successful of the molecular-based equation of state (EOS) is SAFT EOS, proposed by Huang and Radosz [1] on the basis of Wertheim's thermodynamic perturbation theory (TPT). Several versions of SAFT have been developed due to the different methods to calculate the free energy of monomers (segments) [1, 2]. We have applied SAFT EOS in its original version to study amines and their mixtures with acidic gases.

Within the statistical associating fluid theory framework, the residual Helmholtz free energy for a non-association chain fluid is written as a sum of the separate contributions to the energy

$$A^{\text{res}} \equiv A - A^{\text{ideal}} = A^{\text{seg}} + A^{\text{chain}} \quad (1)$$

Where A and A^{ideal} are the total Helmholtz energy and the ideal gas Helmholtz energy at the same temperature and density, A^{seg} is the contribution due to segment-segment interactions and A^{chain} is the contribution due to the formation of a chain of m segments.

In this work, we use the form of segments as hard sphere (hs) and a dispersion contribution that will account for the dispersive interactions between molecules, which have been written as:

$$A^{\text{seg}} = A^{\text{hs}} + A^{\text{dis}} \quad (2)$$

$$\frac{A^{\text{hs}}}{Nk_{\text{B}}T} = m \frac{4\eta - 3\eta^2}{(1 - \eta)^2} \quad (3)$$

Where η is the packing fraction. The dispersion contribution of Helmholtz energy A^{dis} appeared in Eq. (4), is expressed also with the results of Alder et al. [2] for square-well fluid as:

$$A^{\text{dis}} = m \sum_i \sum_j D_{ij} \left(\frac{u}{k_{\text{B}}T} \right)^i \left(\frac{\eta}{\tau} \right)^j \quad (4)$$

In which D_{ij} is universal constants and the interaction energy u is defined as

$$u = \frac{\sum_i \sum_j x_i x_j m_i m_j u_{ij}}{\sum_i \sum_j x_i x_j m_i m_j} \quad (5)$$

Where the binary interaction for unlike species u_{ij} is defined by the Lorentz-Berthelot combining rule using one adjustable interaction parameter k_{ij} to correct the dispersion energy as

$$u_{ij} = (1 - \kappa_{ij}) \sqrt{u_i u_j} \quad (6)$$

The chain contribution of Helmholtz energy is obtained as:

$$\frac{A^{\text{chain}}}{Nk_{\text{B}}T} = \sum_i x_i (1 - m_i) \ln g_{ii}^{\text{hs}}(d_{ii}) \quad (7)$$



Where $g_{ii}^{hcb}(d_{ii})$ is the radial distribution function.

The speed of sound is a mechanical property of a fluid and can be written as

$$v_s = \left[\left(\frac{\gamma}{M} \right) \left(\frac{\partial p}{\partial \rho} \right)_T \right]^{1/2} \quad (8)$$

Where M is the molecular mass and $\gamma \equiv C_p/C_V$, which is determined by calculating the ratio of the specific heats at constant pressure C_p and volume C_V , given by

$$C_V = C_V^{\text{ideal}} - T \left(\frac{\partial^2 A^{\text{res}}}{\partial T^2} \right); \quad C_p = C_V + \frac{T}{\rho^2} \frac{(\partial p / \partial T)_\rho^2}{(\partial p / \partial \rho)_T} \quad (9)$$

2. Results and discussion

Results obtained in this work in the modeling of the phase equilibrium with the original SAFT EOS have been compared to the ones obtained from the available correlations to experimental data from NIST [4]. Figure 1(a) compares the calculated pressure versus density for carbon dioxide at 250K with correlated data taken from NIST. Symbol represents correlation and solid line is the EOS prediction. As can be observed, result obtained from the original SAFT is in good agreement with the experimental data. Figure 1(b) is shown the calculated pressure versus density for dimethylamine at 250K. Afterwards, we have developed the model to determine the second-order thermodynamic derivative properties for carbon dioxide and dimethylamine in the wide density ranges. Figure 2 shows the calculated speed of sound for carbon dioxide and dimethylamine, and the agreement with available correlated data for CO₂, taken from NIST Chemistry WebBook, is generally satisfactory. In fact, the speed of sound is a derivative property most sensitive to deviations and generally represented as a severe consistency test for EOS, since it involves the temperature and density partial derivatives of pressure and to achieve this the EOS must describe with great accuracy the $p(\rho, T)$. For dimethylamine, we have not obtained any experimental data for comparisons yet.

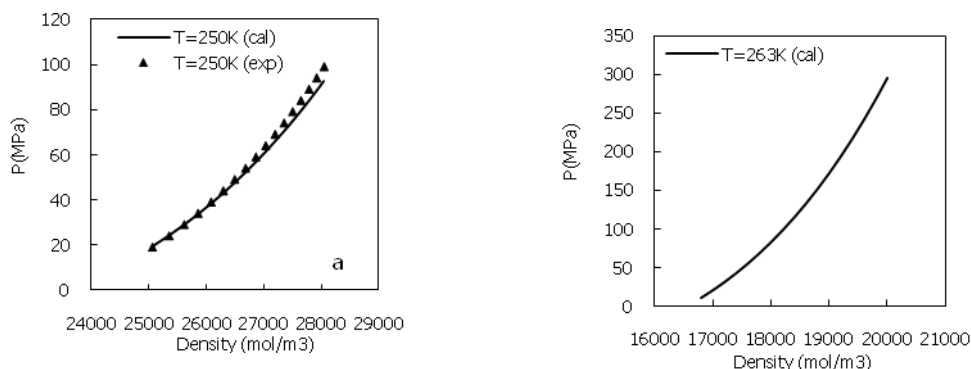


Fig. 1. Pressure vs. density for: (a) carbon dioxide (solid line), NIST (symbol); (b) dimethylamine

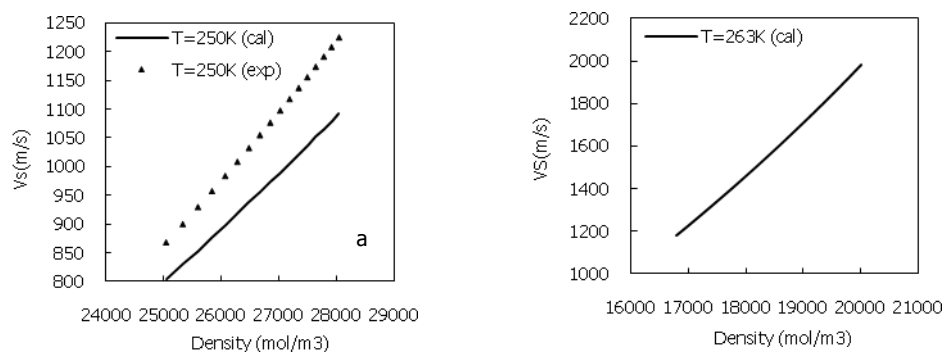


Fig. 2. Prediction of sound velocity for: (a) carbon dioxide (solid line), NIST (symbol); (b) dimethylamine

References

- [1] Huang, S. H. and Radosz, M. Ind. Eng. Chem. Res. 29 (1990) 2284.
- [2] Huang, S. H. and Radosz, M. Ind. Eng. Chem. Res. 30 (1991) 1994-2005.
- [3] Ali Maghari, Maryam S. Sadeghi, Fluid Phase Equilibria 252(2007) 152.
- [4] NIST Chemistry Webbook, NIST Standard Reference Database Number 69, National Institute of Standards and Technology.



An analytical perturbed equation of state for hard chain fluids: modeling P-V-T behavior of short n-alkanes and n-perfluoroalkanes

M. Masoudi^a and H. Farrokhpour^b

^aDepartment of Chemistry, University of Yazd, Yazd, Iran

(E-mail: ma.masoodi.420@gmail.com)

^bDepartment of Chemistry, Isfahan University of Technology, Isfahan, Iran, 84156-83111

1. Introduction

Equations of state play an important role in chemical engineering design. They have assumed an expanding role in the study of the thermodynamic properties of fluids. The derivation of an accurate and simple equation of state for large systems such as chain molecules is theoretically and experimentally important. Recently, a completely analytical equation of state for hard chain fluids has been derived [1,2] using a new extended square-well potential (ESW) [3]. The derived equation of state is able to describe the thermodynamic properties of many kinds of hard-chain fluids such as square-well and Yukawa chain fluids. In this work, we use this equation of state to predict the P-V-T behaviour of short n-alkanes and n-perfluoroalkanes above the critical temperature. The equation of state was fitted to the compressibility factor of n-alkanes, from methane to normal decane, and n-perfluoroalkanes including CF₄, C₂F₆, and C₃F₈ above the critical temperature. Then, the parameters of the ESW potential, obtained from the fitting, were used to predict the vapour-liquid equilibrium curve of each compound.

The Helmholtz free energy of the homonuclear hard chain fluid, within the framework of the perturbation theory, may be written as

$$\frac{A}{NkT} = \frac{A_{HSC}}{NkT} + \left(\frac{1}{kT}\right) \frac{A_1}{NkT} + \left(\frac{1}{kT}\right)^2 \frac{A_2}{NkT} \quad (1)$$

where, A_{HSC} represents contribution to the Helmholtz free energy from the reference hard sphere chain fluid, N is the total number of chain molecules in the system, k denotes Boltzmann constant, and T is absolute temperature. A_1 and A_2 are the first- and second-order perturbation terms and represent Helmholtz free energy from the attractive perturbation part of ESW potential based on the Gulati-Hall's perturbation theory [1,2] as

$$\frac{A_1}{NkT} = -2\pi^2 \rho \sigma^3 \varepsilon \left(I_1 + \alpha \frac{\lambda^3 - 27\lambda + 54}{54\lambda^3(3-\lambda)} \right) \quad (2)$$

$$\frac{A_2}{NkT} = -\pi^2 \rho \sigma^3 \varepsilon^2 kT \left(\frac{\partial \rho}{\partial p_{HSC}} \right)_T \frac{\partial (\eta I_2)}{\partial \eta} \quad (3)$$

where, n is the number of segments on the chain molecule, ρ is the number density of chain molecules, and η is the segment packing fraction of the hard chain fluid. I_1 and I_2 in Eqs. (2) and (3) are defined as

$$I_1 = \left(\frac{n}{24\eta} \right) \frac{1}{\eta \left(\frac{\partial Z_{HSC}}{\partial \eta} \right)_T + Z_{HSC}} + \left(\frac{8}{n} \right) \eta \lambda^3 - 1 \quad (4)$$

$$I_2 = I_1 + \frac{\alpha^2}{(3-\lambda)^2} \left(\frac{1}{551124} \right) \left(\frac{78732\lambda^2 - 413343\lambda + 551124 - \lambda^9}{\lambda^9} \right) \quad (5)$$

where Z_{HSC} is the compressibility factor of the reference system and defined as

$$Z_{HSC} = n \frac{1 + \eta + \eta^2 - \eta^3}{(1-\eta)^3} - (n-1) \frac{1 + \eta - \eta^2/2}{(1-\eta)(1-\eta/2)} \quad (6)$$

Finally, the compressibility factor of the hard chain fluid can be obtained from the Helmholtz free energy through the standard thermodynamic relations in classical thermodynamic.

2. Results and discussion

Five molecular parameters n , α , σ , ϵ/k and λ of ESW potential were optimized by fitting the calculated compressibility factor versus density to the experimental data from near the critical point to the highest temperature for each normal alkanes using a simplex algorithm written in Maple software. Figure 1 typically compares the calculated values for the compressibility factor (Z) with experimental results for pentane and heptane at different temperatures.

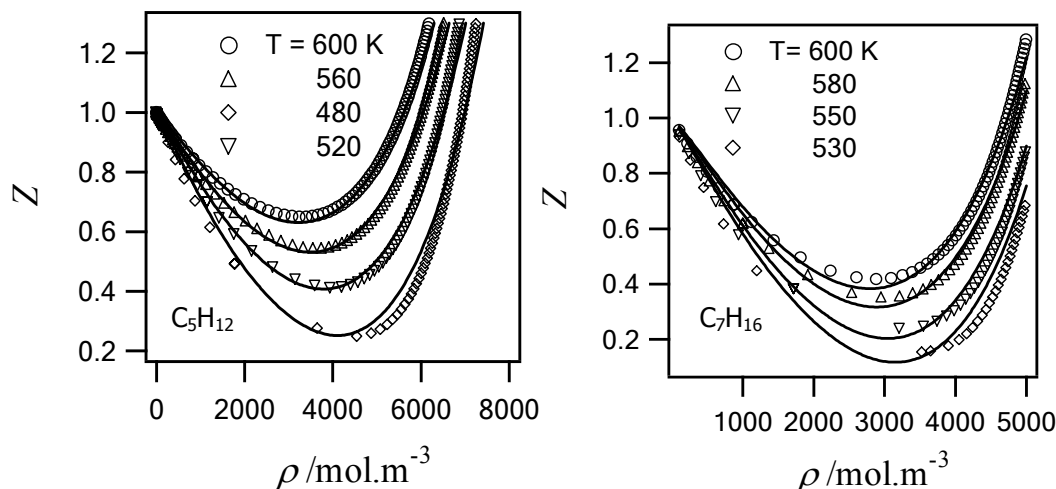


Fig. 1. Comparison of theoretical (line) and experimental (symbols) compressibility factor values for pentane and heptane at different temperatures.

The calculated coexistence density curves for propane, butane and pentane using the equation of state, have been compared with the experimental data and different equation of states in Figure 2.

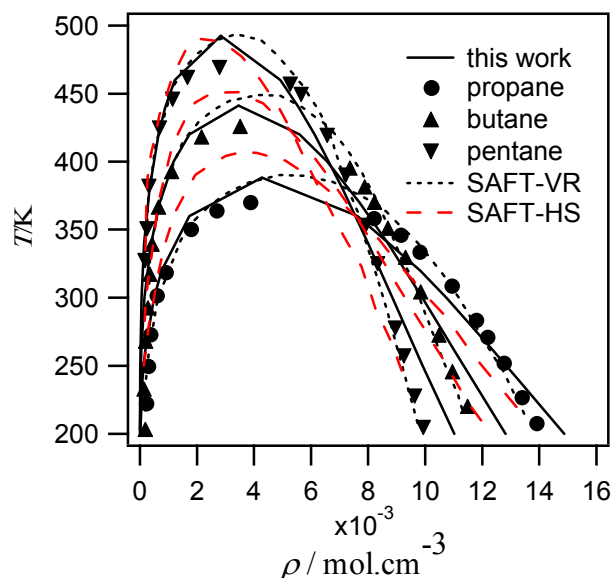


Fig. 2. Vapor-liquid coexistence curves for propane, butane, and pentane predicted in this work (solid line), compared with experimental data (symbols) and the predictions of SAFT-VR (dotted line) and SAFT-HS (dashed line) equation of states.

References

- [1] H. Farrokhpour and E. Satarinezhad, Chem. Phys. 348 (2008) 1-10.
- [2] H. Farrokhpour and E. Mojtabaie, Chem. Phys. 352 (2008) 157-166.
- [3] H. Farrokhpour and G. A. Parsafar, J. Phys. Soc. Jpn. 72 (2003) 2748.

**The Expansion Coefficients Of Direct Correlation Function Of Spherocylinder Fluids**M. Moradi^{a*}, H. Mokhtari^b and M. M. Gharahbeigi^b^a Department of Physics, University of Shiraz, Fars, Iran (Email: moradi@susc.ac.ir)^b Department of Physics, University of Yazd, Yazd, Iran (Email: hmaftab@yahoo.com)
(Email: mehdi.gharahbeigi@gmail.com)**Keywords:** Molecular liquid, Non-spherical molecule, Direct correlation function, Spherocylinder, Integral equation, Percus Yevich**1. Introduction**

In recent years, there have been many investigations of the structural properties of interface and confined molecular fluid using the liquid state theory such as integral equation, density functional theory and computer simulations [1]. Following the success of the density functional theory (DFT) in obtaining the structure and thermodynamics of homogeneous and inhomogeneous classical systems such as simple fluids [2], dipolar fluid [3,4], binary hard spheres [5] this theory was also applied to obtain the density profile of a molecular fluid in between hard planar walls by Kalpaxis and Rickayzen [6]. In the theory of molecular fluids, the DCF can be used to calculate the equation of state [4], free energy, phase transition, elastic constants [7], etc. It is well known that the hard core molecular models play an important role in understanding complex liquids such as liquid crystals [8]. We study a classical fluid of non-spherical molecules. The required homogeneous (DCF) is obtained by solving Ornstein-Zernike (OZ) integral equation numerically. Some of the molecules in the liquid crystals have a spherocylinder (SC) shape and we consider this kind of molecules here.

2. Methods

In the first step we need to obtain the DCF of the fluid using the Percus-Yevich (PY) integral equation theories by solving the OZ equation numerically. To solve OZ equation we first introduce the expansion of DCF. There are two common choices for this expansion. In one expansion, the molecular orientations are referred to an intermolecular reference frame in which the polar axis is along the intermolecular vector \mathbf{r}_{12} (body frame). In the other expansion, the molecular orientations are defined in a space-fixed or laboratory frame of reference. Here, we introduce the body frame expansion:

$$c(\vec{r}, \hat{\Omega}_1, \hat{\Omega}_2) = \sum_{l_1} \sum_{l_2} \sum_m c(l_1, l_2, m; r) Y_{l_1}^m(\hat{\Omega}_1) Y_{l_2}^{m*}(\hat{\Omega}_2) \quad (1)$$

where $c(l_1, l_2, m; r)$ are the expansion coefficients, Y_l^m the spherical harmonics, and * indicates the complex conjugate.

In the following, we calculate the DCF of the SC's fluids using a formalism which is proposed by Ram and Singh [9].

The interaction between two hard SC particles is given by [10]

$$u(\vec{r}, \hat{\Omega}_1, \hat{\Omega}_2) = \begin{cases} \infty & \sigma(\hat{r}, \hat{\Omega}_1, \hat{\Omega}_2) < D \\ 0 & \sigma(\hat{r}, \hat{\Omega}_1, \hat{\Omega}_2) > D \end{cases} \quad (2)$$

where $\Omega_i = (\theta_i, \varphi_i)$ is describing the orientation of particle i and $\hat{r} = \vec{r}/r$ is a unit vector along the line connecting the centers of the two particles and D is diameter of SC.

The DCF of fluid with non-spherical molecules can be defined through the OZ equation

$$h(r_1, \Omega_1, r_2, \Omega_2) = c(r_1, \Omega_1, r_2, \Omega_2) + \frac{\rho}{16\pi^2} \int d\Omega_3 \int dr_3 c(r_1, \Omega_1, r_3, \Omega_3) h(r_3, \Omega_3, r_2, \Omega_2) \quad (3)$$

where r_i is the position of the center of mass. To solve this equation we use the PY closure relation [11]:

$$c(r_1, \Omega_1, r_2, \Omega_2) = [h(r_1, \Omega_1, r_2, \Omega_2) - 1] \exp[-\beta u(r_1, \Omega_1, r_2, \Omega_2)] \quad (4)$$

Where $f(r_1, \Omega_1, r_2, \Omega_2)$ is the Mayer function and is defined by

$$f(r_1, \Omega_1, r_2, \Omega_2) = \exp[-\beta u(r_1, \Omega_1, r_2, \Omega_2)] - 1 \quad (5)$$

Here $u(r_1, \Omega_1, r_2, \Omega_2)$ is a pair potential energy of interaction and $h(r_1, \Omega_1, r_2, \Omega_2)$ is total correlation function.



3. Results and discussion

Here we are interested to study the thermodynamic and structural properties of molecular fluid containing spherocylindrical shape molecules. For calculating the DCF of the fluid it is required to calculate the closet approach between the molecules, therefore we calculate the closest approach of two spherocylinders by using two different methods. In the first method we use a fast algorithm proposed by Vega and Lago [12]. They actually applied their method for calculating the closest approach between two rods and we extend this method by introducing a new geometry to find the closest approach between two spherocylinders. In the second method for the first time we use the finite element procedure to find the closest approach. These methods are more general and can also be used for the mixtures. According to the results shown in the table 1, for the aspect ratio, $L/D=5.0$, these methods are in good agreement. Here L and D are the length and diameter of SC. To make calculation more accurate we use the average of these two methods.

Table 1. Calculated closest of spherocylinders with $L/D=5.0$, the angles are given in radian.

r	θ_1	φ_1	θ_2	φ_2	θ	φ	Closest approach (algorithm of Vega & Lago)	Closest approach (finite element)
2.8561	1.2419	2.6025	2.4872	5.1296	1.2419	5.1896	0	0
5.5697	0.6200	3.2049	0.6594	3.6442	3.0763	2.9350	2.5208	2.5141
4.2640	1.3601	1.5154	1.9937	2.3071	3.0763	1.8970	0.2196	0.2177
11.7971	0.6010	4.5526	3.0588	4.4264	2.5181	1.2959	6.5927	6.5851

With calculating the expansion coefficients, we can calculate DCF (by using Eq. (1)). In Fig. 1, the selected DCF expansion coefficients of SC are shown. The packing fraction $\eta = 0.2003$ of the fluid with aspect ratio $L/D=5$ are used.

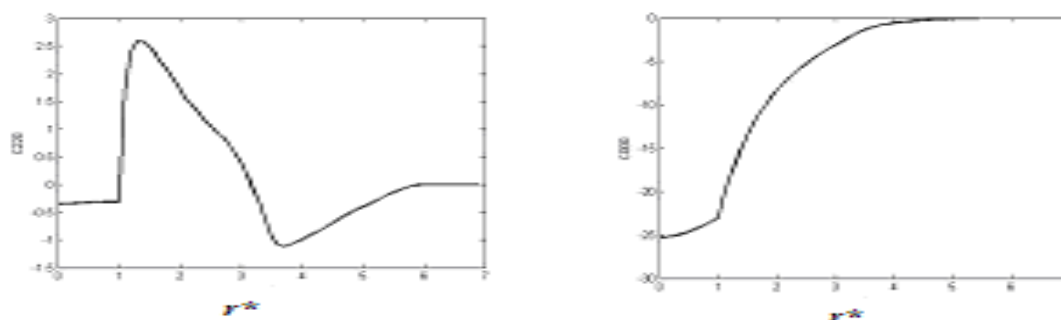


Fig 1. Selected expansion coefficients of the DCF as a function of the reduced distance $r^* = r/D$ for $\eta = 0.2003$

4. Conclusion

In this article we introduced the solution of OZ integral equation to obtain the DCF of non-spherical molecules and then we apply it to SC. We also obtained the closest approach for this geometrical shape using two new methods. As mentioned before now it is possible to obtain thermodynamic and structural properties of the fluid, such as equation of state, order parameters and elastic constants.

References

- [1] M. Moradi and A. Avazpour, *Modern Physics B*, 10 (2005) 1717.
- [2] M. Moradi and M. kavosh Tehrani, *Phys. Rev. E*, 63 (2001) 21202.
- [3] M. Moradi and G. Rickayzen, *Mol. Phys.* 68 (1989) 903.
- [4] M. Moradi and M. Kavosh Tehrani, *Iranian Journal of Science and Technology, Transaction A*, 25 (2001) 377.
- [5] M. Moradi and H. Shahri, *Iranian Journal of Science and Technology, Transaction A*, 27 (2003) 417.
- [6] P. Kalpaxis and G. Rickayzen, *Mol. Phys.* 80 (1993) 391.
- [7] A. ponievierski and J. Stecki, *Mol. Phys*, 38 (1979) 1931.
- [8] A. M. Somoza and P. Tarazona, *Phys. Rev. Lett*, 61 (1988) 2566.
- [9] J. Ram, R. C. Singh and Y. Singh, *Phys. Rev. E*, 49 (1994) 5117.
- [10] S. Lago and P. Sevilla, *J. Chem. Phys*, 7 (1988) 4349.
- [11] J. K. Percus and G. L. Yevick, *Phys. Rev*, 110 (1958) 1.
- [12] C. Vega and S. Lago, *Comp. Chem.*, 1 (1994) 55-59.

**Attractive energy contribution to nano-confined fluids behavior: the normal pressure tensor**

E. Keshavarzi, F. Heidari * and F. Sedaghat

Department of Chemistry, Isfahan University of Technology, Isfahan, Iran

(Email: keshavrz@cc.iut.ac.ir)

Keyword: Normal pressure tensor, Nanoconfined fluids, Van der Waals equation of state, Lennard-Jones fluid.**1. Introduction**

The molecular system confined with narrow pores with size of few molecular diameters in some direction exhibit physical properties which differ significantly from those the bulk. Consequently we can not use our knowledge of bulk fluids when we are dealing with fluids in confined geometries [1-4]. We know the molecules into nanopores show anisotropic behavior. Therefore the pressure has a tensorial character, also it should be noted that any component of the pressure tensor of confined fluid is not, in general, the same as is the pressure in macroscopic (bulk) fluid. The normal component of the pressure for inhomogeneous bulk systems was calculated by the well-known method of planes by Todd et al. Irving and Kirkwood proposed a method to obtain point function stress tensor based on the equation of hydro dynamics [5].

For weakly inhomogeneous fluids, the standard Irving Kirkwood procedure is well-studied but for strongly inhomogeneous flow (e.g fluid confined by walls in nano scale) it can not be used. We have already obtained a general expression for the normal pressure tensor of confined fluid in nanoslit pores with all kind of the fluid-fluid and fluid-wall interactions [6] via the statistical mechanics and solved it for the hard sphere confined fluid.

The aim of this research is to show that the vdW like equation of state is also valid for the normal pressure tensor of the LJ fluids in nanoslit pores. Since in the statistical mechanics the vdW EOS may be obtained from the perturbation theory we obtain the expression for the normal pressure tensor of the LJ fluid using the perturbation theory. It is so interesting that the obtained equation generates the exact van der Waals equation of state at macroscopic limit.

We consider a fluid confined in a nano slit pore consisting of two structureless and parallel walls in the xy plane located at $z=0$ and $z=H$, i.e. separated by length H in the z direction. We have derived a general equation for normal pressure tensor which it is applicable for all the confined fluids in nano slit with all kind of the wall-fluid and fluid- fluid interaction as [6]:

$$P_{zz} = kT\rho(r_{1z}) \left[1 + \frac{1}{kT} \frac{\partial \phi_{ext}}{\partial r_{1z}} dr_{1z} \right] - \frac{1}{2} \int_V \phi'(\vec{r}_{12}) \rho^{(2)}(\vec{r}_{12}, \vec{r}_1) \frac{(r_{12z})^2}{\vec{r}_{12}} d\vec{r}_{12} \quad (1)$$

Where $\vec{r}_{12} \equiv \vec{r}_1 - \vec{r}_2$ is the intermolecular position vector of molecule 2 with respect to molecule 1 and $r_{12z} = |\vec{r}_{12}|_z$ is the projection of distance of molecule 1 from molecule 2 in the z -direction, r_{1z} is the projection of the distance of molecule 1 from the wall on the z -coordinate, $\phi(\vec{r}_{12})$ is the intermolecular pair-potential energy function and ϕ_{ext} is the molecules-wall interaction potential function, for the nano slit pore we can write $\rho(r_{1z}) = \rho(z_1)$ which is the local density of the molecule 1 and $\rho^{(2)}(\vec{r}_{12}, \vec{r}_1)$ is the pair-probability density distribution. Now we want to use our previous approach to obtain such an equation for LJ fluid confined in nanoslit pores which it is more applicable than the previous equation because of its reality of the intermolecular potential.

Based on the statistical mechanical perturbation theory, the total potential energy may be separated in to two parts as $\varphi_N = \varphi_N^{(0)} + \varphi_N^{(1)}$. In perturbation theory with analogy to potential energy the other thermodynamic properties may be separated in to two parts. For example according to perturbation theory developed by Song and Mason for pressure of macroscopic systems we have $P_{zz} = P_{zz}^{ref} + P_{zz}^{perturb}$. Since the local density is a function of z and also the nanoslits is limited in this dimension therefore the spherical coordinate is not suitable for our calculation and we write equation (1) in the cylindrical coordinate in which the variable of z will be appeared explicitly. Also we use the definition of $\rho^{(2)}$ according to the local density approximation which it is valid for weakly inhomogeneous systems, so we have

$$P_{zz} = \rho(z_1)kT - \frac{1}{2} \int \int \int \phi'(\rho_{12}, z_{12}) \rho(z_1) \rho(z_2) g_{zH}(\rho_{12}, z_{12}) \frac{z_{12}^2}{(\rho_{12}^2 + z_{12}^2)^{\frac{3}{2}}} \rho_{12} d\rho_{12} dz_{12} d\theta \quad (2)$$



The upper limit of integral which it has been shown by star sign shows that the limits of the integral should be defined by considering the size of the confinement and its geometry. Now we separate the integral of Eq.(2) in to two parts including the reference and attraction terms according to the separation in the pair potential, by changing the limit of integral in cylindrical coordinate in such away that in spherical coordinate it generate $0 \rightarrow \sigma$ and $\sigma \rightarrow \infty$ while the dimension of the system in z is limited to H . Because our reference part is the hard-sphere potential, therefore $\phi'_{hs}(\rho_2, z_2)$ is zero everywhere except at $(\rho_2^2 + z_2^2)^{0.5} = \sigma$. Therefore we use from Dirac delta-function and the result will be simplified to the following equation.

$$P_{zz}^{ref} = \rho(z_1)kT + \pi kT \rho(z_1) \left[\int_{-\sigma}^{+\sigma} \rho(z_2) z_2^2 g_{hs}(\sigma) dz_2 \right] \quad (3)$$

To get the perturbation term the integral of eq. (2) should be solved using the perturbed pair potential.

$$P_{zz}^{perturb} = -\frac{1}{2} \int^* \int^* \int^{2\pi} \phi'^{(1)}(\rho_2, z_2) g_{zh}(\rho_2, z_2) \rho(z_1) \rho(z_2) \frac{z_2^2}{(\rho_2^2 + z_2^2)^{3/2}} \rho_2 d\rho_2 dz_2 d\theta \quad (4)$$

the normal pressure tensor for LJ confined fluid in nano slit pores is summation of Eq(3) and (4). The derived equation is a generalized van der Waals like equation for local normal pressure tensor of confined fluids in nano slit pores. It is so interesting that when the size of confinement, H , approaches to infinity, Eq. (3) becomes:

$$\frac{P}{\rho kT} = 1 + \frac{2\pi}{3} \rho \sigma^+{}^3 g(\sigma^+) \quad (5)$$

Which it is the hard-sphere pressure of equation of state of macroscopic systems. To obtain the macroscopic limit for the perturbed part we use $\phi'^{(1)}(r_{12}) = -kTf(r_{12})\exp(-\beta\phi'^{(1)}(r_{12}))$

where $f(r_{12})$ is the Mayer function of the potential. So we have $P_{zz}^{perturb} = \frac{2\pi}{3} \rho^2 \int_{\sigma}^{\infty} -kTf'(r) r^3 dr$

By integration by parts of integral we get:

$$P_{zz}^{perturb} = +2\pi \rho^2 \int_{\sigma}^{\infty} \phi^{(1)}(r) r^2 dr \Rightarrow P_{zz}^{perturb} = -\rho^2 a$$

In this way our derived equation in the macroscopic limit will be equal to $P = P_{HS} - a\rho^2$ where a is the Van der Waals constant and equal to: $a = -2\pi \int_{\sigma}^{\infty} \phi(r) r^2 dr$

In this way our derived equation in the macroscopic limit will be equal to $P = P_{HS} - a\rho^2$.

This is the vdW EOS for pressure of macroscopic system.

2. Conclusion

The normal pressure is an important thermodynamic property, when the fluid is anisotropic We have obtained an expression for the normal pressure tensor of the LJ confined fluid in nano slit pores using the perturbation theory and the effects of intermolecular attraction on that has been studied.

The important point is that the VdW like EOS is not only applicable for the average pressure in the nanoslit, but also it can be applied for the normal pressure tensor using the statistical mechanical perturbation theory. It is also remarkable because in the VdW like EOS all the contribution of the repulsive and attractive force in the normal pressure tensor has been separated completely. We have also shown that the behavior of attractive and repulsive interaction contribution in normal pressure tensor with temperature, density and size of confinement. The oscillations of normal pressure tensor become broad and smooth with H at constant T and density but they increase with density. We have also shown that by increasing the fluid-fluid interactions the oscillatory behavior of the normal pressure decreases.

References

- [1] I. Brovchenko, A. Geiger, A. Oleinikova, J. Chem. Phys. 120 (2004) 1958.
- [2] A. Fortini, M. Dijkstra, J. Phys. Cond. Matter. 18 (2006) 371-378.
- [3] D. Fu, Chinese J. Chem. 24 (2006) 1315-1320.
- [4] T. Keshavarzi, R. Sohrabi, G.A. Mansoori, J. Comput. Theor. Nanosci 3(1) (2006) 134-141.
- [5] J.H. Irving, J. Kirkwood, J. Chem. Phys. 18(6) (1950) 817-829.
- [6] T. Keshavarzi, F. Sedaghat, G.A. Mansoori, accepted in Microfluidics Nanofluidics (2009).

**The lateral pressure tensor of confined fluids in nanoslit pores**

E. Keshavarzi and F. Heidari*

Department of Chemistry, Isfahan University of Technology, Isfahan, Iran

(E-mail: keshavrz@cc.iut.ac.ir)

Keywords: Lateral pressure tensor, Confined fluids, Lennard- Jones fluid, Nanoslit.**1. Introduction**

One of the important thermodynamic properties as given by derivative of the partition function is the pressure which it determines the stability of system. In confined fluids or inhomogeneous fluids local pressures are important for calculation of interface tension and the analysis of mechanical response to strain and heat, photo excitation and phase transformations. In confined fluids the pressure is a tensor, with p_{ij} components where $i, j = x, y, z$ [1]. On the other hand the fluids confined between walls have a directional anisotropy and its pressure has form of a tensor that depends on spatial direction and position of the surface [2]. In nanoslits with immobility confined fluid, off diagonal components of pressure tensor is equal zero. So in this systems pressure is a diagonal tensor with p_{ii} ($i = x, y, z$) components. Its normal component, p_{zz} , exerted on a xy -plane parallel to the walls [3] and the transverse components (lateral pressure), p_{xx} , p_{yy} exerted on a zy and zx -plane of fluid perpendicular to the walls. The aim of this article is to generate a useful expression for the lateral pressure tensor, p_{yy} , of confined fluid in nanoslit pores with two hard walls in equilibrium with bulk fluid and solving it for hard-sphere and LJ fluids.

2. The Theory

We consider an equilibrium system of N particles with no velocity of the center of mass confined in a nano slit, consisting of two structureless and parallel walls in the xy plane separated by length H in the Z direction. We also assume the confined fluid in the nanoslit pore is in equilibrium with a bulk density and the same temperature and chemical potential. We imagine a small volume element somewhere within our system, ($d\vec{r}_1 = ds_y \times dy$), and want to know what the forces across the area s are. The forces on the area s changes from up to down the surface. The force on the closed surface of s in the direction of b is [4].

$$F_b = \oint_s \tau_{ab} n_b ds \quad (1)$$

where subscript b is referred to force component and subscript a is referred to normal to the surface s . The calculation for the total momentum, which is transferred in a unit time due to the entrance and exit of particles through the surface s perpendicular to the wall, consists of two parts: (i) the kinetic contribution, (ii) the fluid-fluid molecules interaction contribution. Since the fluid-walls potential is only a function of z -coordinate, the fluid-walls interactions contribution for lateral pressure tensor is zero.

The kinetic contribution

The momentum transfer in unit time, dt , through surface ds_y , by particles with momentum p_y passing through point \vec{r}_1 is $\frac{p_y \rho^{(1)}(\vec{r}_1) dw(p_y)}{dt} d\vec{r}_1$ where $dw(p_y)$ is the momentum distribution function in the y -direction and $\rho^{(1)}(\vec{r}_1)$, the probability density. After some mathematical calculation we have:

$$F_y = \frac{1}{m} \oint_s \rho^{(1)}(\vec{r}_1) ds_y \int p_y p_y dw(p_y) \quad (2)$$

The second integral in the above equation is equal to mkT . By comparing the result of Eq.(2) with Eq.(1), we obtain the following expression for the kinetic contribution part of the lateral pressure tensor as: $\tau_{yy} = -kT\rho(\vec{r}_1)$. However, since the lateral pressure tensor for all point of y -dimension has a same uniform value and it depends on the z -dimension, we use $\rho(\vec{r}_1) = \rho(z)$ for the nanoslit pore, and then we can write: $\rho_{yy}^k = \rho(z)kT$



The fluid-fluid molecules interactions contribution

To calculate this effect, we consider particle 1 at location range $\vec{r}_1 \rightarrow \vec{r}_1 + d\vec{r}_1$ in the small volume of $d\vec{r}_1$ and another particle, 2, at location range $\vec{r}_2 \rightarrow \vec{r}_2 + d\vec{r}_2$, outside volume $d\vec{r}_1$. The force acting on the particle 1 at \vec{r}_1 from particle 2 at \vec{r}_2 is:

$$F_{\vec{r}_1} = -\nabla_{\vec{r}_1} \phi(|\vec{r}_1, \vec{r}_2|) \quad (3)$$

where $\phi(|\vec{r}_1, \vec{r}_2|)$ is the pair-intermolecular potential energy between particles 1 and 2. We multiply this relation to the pair-probability density of finding particles 1 and 2 and then take the integral on \vec{r}_1 in the volume of v and \vec{r}_2 in volume of $V - v$.

The result will be the following double-integral

$$- \int_{V-v} \int_v \nabla_{\vec{r}_1} \phi(|\vec{r}_1 - \vec{r}_2|) \rho^{(2)}(\vec{r}_1, \vec{r}_2) d\vec{r}_1 d\vec{r}_2 \quad (4)$$

After some mathematical derivation the fluid-fluid interaction contribution of lateral pressure tensor is:

$$P_{yy}^{FF} = -\frac{1}{2} \int_v \phi'(\vec{r}_{12}) \rho^{(2)}(\vec{r}_{12}, \vec{r}_1) \frac{(r_{12y})^2}{|\vec{r}_{12}|} d\vec{r}_{12} \quad (5)$$

Therefore general equation of lateral pressure tensor for confined fluids in nanoslit pores is sum of kinetic and fluid-fluid interaction.

$$P_{yy} = P_{yy}^K + P_{yy}^{FF} = kT\rho(z) - \frac{1}{2} \int_v \phi'(\vec{r}_{12}) \rho^{(2)}(\vec{r}_{12}, \vec{r}_1) \frac{(r_{12y})^2}{|\vec{r}_{12}|} d\vec{r}_{12} \quad (6)$$

This equation has been calculated numerically for hard-sphere and LJ fluids confined in nanoslit pores. To calculate the fluid-fluid interaction contribution of the lateral pressure tensor of LJ fluids we have used the statistical mechanical perturbation theory. The lateral pressure tensor for LJ confined fluid in nano slit pores is equal to:

$$P_{yy}^{LJ} = kT\rho_d(z_1) \left[1 + \frac{\pi}{4} \int_{-\sigma}^{+\sigma} \rho_d(z_2) \right] (\sigma^2 - z^2) dz_2 - \frac{1}{2} \int \int \int^* \phi'(x_2, y_2, z_2) \rho(z_1) \rho(z_2) g_{zz}^{hs} \frac{y_2^2}{(x_2^2 + y_2^2 + z_2^2)^{0.5}} dx_2 dy_2 dz_2 \quad (7)$$

3. Conclusion

Our result shows that the both of the lateral pressure tensor indicate layering effects near the walls. When the bulk density decreases the layers become more diffuse and broad. Therefore the lateral pressure decreases but maintains its oscillatory behavior. When the pore width increases the layer of the molecules in the pore increase but the height of the layers decrease. The oscillations of lateral pressure tensor become broad and smooth with pore width at constant temperature and density but they increase with density. It is interesting that when the size of confinement, H , approaches to infinity the lateral pressure tensor of LJ fluid generate the van der Waals like EOS.

References

- [1] A. G. Meyra, G.J. Zaragoicoechea, V.A. Kuz, Fluid Phase Equi. 230 (2005) 9-14
- [2] D. Fu, J. Chem. Phys. 124 (2006) 164701
- [3] T. Keshavarzi, F. Sedaghat, G.A. Mansoori, Accepted in Microfluidics Nanofluidics. (2009)
- [4] Fisher IZ, Switz TM, Statistical Theory of Liquids, University of Chicago Press, Chicago, 1964

**Structure of a confined hard sphere mixture in a nanoslit**M. Kamalvand^{a,*} and E. Keshavarzi^b^a Department of Chemistry, Faculty of Science, Yazd University, Yazd, Iran^b Department of Chemistry, Isfahan University of Technology, Isfahan, Iran

(Email: m_kamalvand@ch.iut.ac.ir)

Keywords: Confined fluid, Density functional theory, Nanoslit, Mixture, Hard Sphere.**1. Introduction**

A property of central interest for theoretical study of confined fluids is the density distribution of the molecules. On the other hand, density-functional theory is a powerful approach to study the structure and the phase behavior of nano confined fluids [1]. The density profile of the hard-sphere mixture fluid confined within nanoslit pores is a key quantity for understanding the configurational behavior of real molecules, therefore, in this report we have produced the density profile of a hard-sphere mixture fluid, confined in nanoslit pores using the fundamental-measure density-functional theory. The results reveal a number of interesting features of colloidal mixtures in a nanoslit which are different from the bulk systems.

Fundamental Measure Density Functional Theory (FMDFT)

In a density functional theory for an inhomogeneous fluid, the grand potential functional energy is related to the Helmholtz free energy functional as follows [2]:

$$\Omega[\rho(\mathbf{r})] = F[\rho(\mathbf{r})] + \int d\mathbf{r} \rho(\mathbf{r})[V_{\text{ext}}(\mathbf{r}) - \mu] \quad (1)$$

Where μ is the chemical potential of the system and $V_{\text{ext}}(\mathbf{r})$ is the external field. According to the variational principle, the equilibrium density distribution function of the non-uniform fluid corresponds to the minimum of the grand potential [2],

$$\rho(\mathbf{r})\Lambda^3 = \exp \left(\beta\mu - \beta \frac{\partial F_{\text{ex}}[\rho(\mathbf{r})]}{\partial [\rho(\mathbf{r})]} - \beta V_{\text{ext}}(\mathbf{r}) \right) \quad (2)$$

In FMDFT the Helmholtz free energy exploits to an ideal and excess parts. The excess part can be obtained using 4 scalar and 2 vector weights. Finally, Eq. (2) can be solved using a standard Picard iterative method [3].

2. Results and Discussion

In Fig. 1 the density profiles of two components of a confined hard sphere mixture, $\rho(z)/\rho_{\text{bulk},i}$ have been Plotted, where i denotes the i th component. In this Figure, the ratio of the large to small sphere diameters, σ_b/σ_s , equals 2 and the mole fraction of the small spheres is 0.95, where b and s denote large and small spheres respectively. Also, the total packing fraction of the mixture, η , is 0.5. In this Figure, the distance between two hard and structureless walls is $6\sigma_s$. As is clear from this figure, the contact density for large spheres is greater than its value of small hard spheres which is due to stronger attractive depletion forces for large spheres. The position of the contact point of the large spheres has been appeared at $z=\sigma_s=0.5\sigma_b$ which is expectable. But, as a surprising result, the other maximums of the large sphere density profile can be finding at $z=2\sigma_s=\sigma_b$, $3\sigma_s=1.5\sigma_b$ and $4\sigma_s=2\sigma_b$; in other words, according to the results for a pure confined fluid, we should expect that the maximum number of parallel layers (large spheres) between two walls to be equal to 3 which is different with present case with 4 layers. As a reason for this observation, we should notice to the mole fraction of the large spheres in the mixture, X_b . The mole fraction of the large spheres in this figure is only 0.05 ($\rho_{\text{bulk},b}\sigma_b^3=0.0354$) that shows the mixture is very dilute. Therefore, large spheres can distribute in the slit without a clear layering order; in other words, a small number of large spheres (due to its very low density) aggregate near the walls and form the first layer. While this first layer is not very dense, cannot make a strong inhibition for forming of the second layer. Therefore, second layer will be formed at $z=2\sigma_s=\sigma_b$ instead of $z=3\sigma_s=1.5\sigma_b$. This must be pointed out that the small number of the large spheres inside the pore cannot affects the behavior of small spheres strongly and the structure of the small spheres in the mixture is very similar to a pure confined hard sphere fluid within a slit.

At a very high concentrated of large sphere in the mixture, a denser layer can be created near the walls and due to the inhibition of this dense layer, the second ordered layer cannot be formed in $z=2\sigma_s=\sigma_b$. This behavior can be observed in Fig. 2. In this figure, the mole fraction of the small spheres is 0.05 ($\rho_{\text{bulk},b}\sigma_b^3=0.1186$) and the total packing fraction of the mixture is

0.5. As is clear from this figure, only 3 layers of large spheres can be formed inside the slit with $H=6\sigma_s=3\sigma_b$ that is a conventional result. Therefore, large spheres create an ordered layer in centre of the slit which can affect the behavior of the small spheres strongly. As is showed in Fig. 2, probability of finding the small spheres in centre of the slit is very low, because this region has been occupied by large spheres. This should be pointed out that for a pure small hard sphere fluid inside this slit, 6 peaks can be observed that is different from the mixture case. According to Fig. 2, one can say that the central large sphere layer can act as a wall for small spheres and affects their arrangement inside the slit strongly.

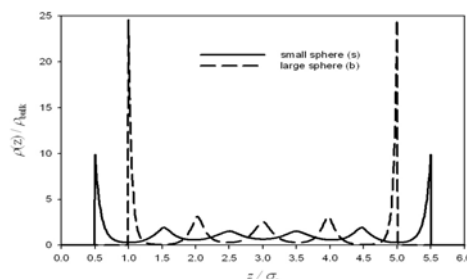


Fig.1. Reduced density profile of a confined two component hard sphere mixture with $X_s=0.95$, $\sigma_b/\sigma_s=2$, $\eta=0.5$, inside a slit with $H=6\sigma_s$.

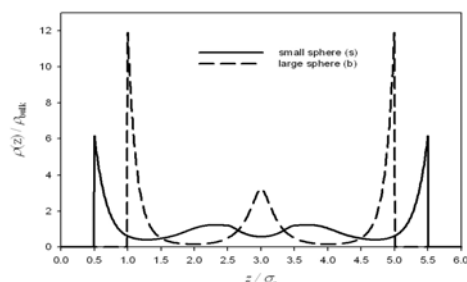


Fig. 2. The same as Fig. 1 but for $X_s=0.05$.

In intermediate mole fractions, for example $X_b=X_s=0.5$, the behavior of density profiles is different. In this case, while there are 3 clear layers of large spheres inside the pore, but residue of the layers in Fig. 1 (at 2σ and 3σ) is observable yet. Also, the structure of small spheres is dependent of the large spheres strongly and these spheres cannot form 6 independent layers inside the pore.

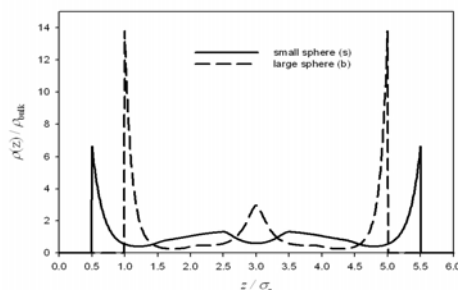


Fig. 3. The same as Fig. 1 but for $X_s=0.50$

3. Conclusions

In this work, the structure of a confined hard sphere mixture in a nanoslit is investigated by FMDFT method. Our results show that the structure of these fluids is strongly dependent of the mole fraction of the components as well as the size ratio of the confined molecules and the size of slit.

References

- [1] Keshavarzi, E., Kamalvand, M., J. Phys. Chem. B (2009) 113, 5493.
- [2] Roth, R., Evans, R., Lang, A., Kahl, G., J. Phys.: Condens. Matter (2002) 14, 12063.
- [3] Yu, Y.-X., Wu, J. Z., J. Chem. Phys., (2002), 117, 10156.

**Structure and phase transition of confined Lennard-Jones fluids in a nanotube**M. Kamalvand^{a*} and E. Keshavarzi^b^a Department of Chemistry, Faculty of Science, Yazd University, Yazd, Iran^b Department of Chemistry, Isfahan University of Technology, Isfahan, Iran

(Email: m_kamalvand@ch.iut.ac.ir)

Keywords: Confined fluid, Density functional theory, Nanotube, Phase transition.**1. Introduction**

When a fluid is confined in a microscopic pore, the introduction of wall forces and the competition between fluid–wall and fluid–fluid forces could lead to interesting phase transitions not observed in the macroscopic fluid systems; examples include layering and wetting transitions as well as shifts in regular bulk transitions.¹ Also, the molecular structure of confined fluids can differ dramatically from that of macroscopic fluid systems.¹ Molecular fluids like argon, hydrogen, water, etc which are confined in a carbon nanotubes are real examples of a confined system. Because of technological importance of these systems in nanotechnology, the main goal of this research work is study of the structure and phase transition of these confined fluids. In this work, structure and liquid-gas phase change of a Lennard-Jones fluid that is confined in a single wall carbon nanotube (CNT) are investigated using perturbative classical density functional theory.

Perturbative Density Functional Theory (P-DFT)

Density Functional Theory is one the powerful approaches for studying the confined fluids. In a density functional theory for an inhomogeneous fluid, the grand potential functional energy is related to the Helmholtz free energy functional as follows²:

$$\Omega[\rho(\mathbf{r})] = F[\rho(\mathbf{r})] + \int d\mathbf{r} \rho(\mathbf{r}) [V_{\text{ext}}(\mathbf{r}) - \mu] \quad (1)$$

Where μ is the chemical potential of the system and $V_{\text{ext}}(\mathbf{r})$ is the external field. According to the variational principle, the equilibrium density distribution function of the non-uniform fluid corresponds to the minimum of the grand potential²,

$$\rho(\mathbf{r})\Lambda^3 = \exp\left(\beta\mu - \beta\frac{\partial F_{\text{ex}}[\rho(\mathbf{r})]}{\partial[\rho(\mathbf{r})]} - \beta V_{\text{ext}}(\mathbf{r})\right) \quad (2)$$

In P-DFT the excess Helmholtz free energy exploits to a reference and perturbation part. The reference part can be obtained using Tarazona approach³ and the perturbation part may be obtained via the Rosenfeld method⁴. Finally, Eq. (2) can be solved using a standard Picard iterative method.

2. Results and Discussion

In this work, we studied the liquid-gas phase transition of a confined Lennard-Jones fluid in a CNT. The Lennard-Jones tail is approximated by a two-Yukawa potential with effective hard core diameter. Also, the Barker-Henderson method is used for obtaining the effective hard core diameter, d . For the CNT wall-fluid interaction potential (or external field in Eq. (4)), the following interaction potential is used

$$V_{\text{ext}}(r, R) = 3\pi\theta\epsilon_{\text{fs}}\sigma_{\text{fs}}^2 \left[\frac{21}{32} \left(\frac{\sigma_{\text{fs}}}{R} \right)^{10} M_{11}(x) - \left(\frac{\sigma_{\text{fs}}}{R} \right)^4 M_5(x) \right]; M_n(x) = \int_0^\pi d\varphi \frac{1}{(1+x^2-2x\cos(\varphi))^{n/2}}; x = r/R \quad (3)$$

where θ is a constant and R is the CNT radius.

In Fig. 1(a) the structure of a Hydrogen fluid obtained in this work is compared with simulation results. As is clear from this figure, our P-DFT result is in good agreement with simulation data. This should be noted that the deviation of the P-DFT results from simulation data will be diminished when integration of the density profile to obtain average properties like average density, which is a suitable property for study of phase transition. Therefore, our results for average density (and therefore predicting the phase transition) will be more accurate than the density profile. In Fig. 1(b) the structure of a confined Lennard-Jones fluid within some CNTs with different diameters is showed. In addition, in Fig. 1(c), the density profile is showed when the interatomic interactions changed. As is showed in this Fig. 1(b) and 1(c), the size of the CNT and also the interaction potential can affect the structure of the confined fluid dramatically. To study the phase behavior of this confined fluid, we examine the average density and its dependency to the size of the CNT, interatomic potential and also wall-fluid interactions. In Fig. 2(a),



the reduced average density of a confined Lennard-Jones fluid versus the size of the CNT is showed for various wall-fluid interactions. As is showed in this figure, increasing the CNT wall-fluid molecules attraction leads to an increase in the average density that show increasing tendency of the bulk fluid molecules to enter the CNT. In Fig. 2(b), the reduced average density of a confined Lennard-Jones fluid versus the size of the CNT is showed for various fluid-fluid interactions. According to this figure, increasing the interatomic attractions leads to decreasing the tendency of the bulk fluid molecules to enter the CNT. Therefore, when the interatomic attractions are low, the stable phase inside the pore is a liquid-like fluid and for high interatomic attractions, the stable phase is a gas-like fluid. For intermediate attractions, the stable phase is strongly dependent of the size of the CNT. A very interesting observation of this study is variations of the average density with increasing the size of the CNT. While the energy effect in these systems approximately is unchanged with increasing the CNT diameter, this behavior is due to entropy effects. In other words, entropy effect has the main role in determination of the structure and therefore phases transition in these systems. In fact, when the origin of the CNT will be occupied by an ordered chain of molecules, the stable phase is liquid and in the other side, when the center of the CNT is on-occupied, the stable phase will be a gas phase.

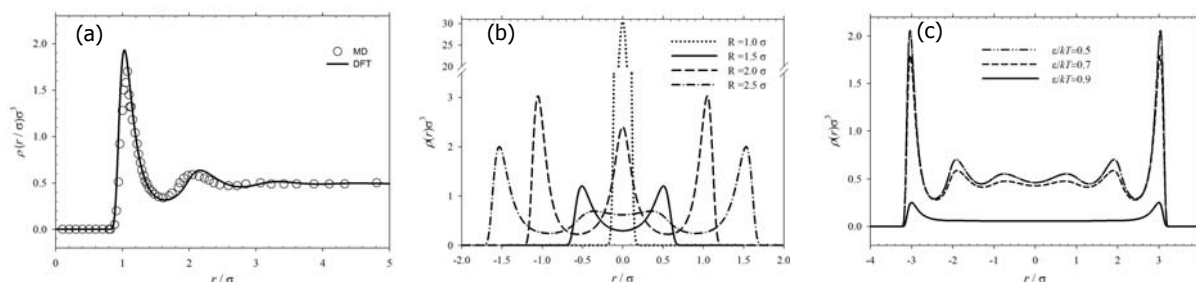


Fig. 1. a) Density profile of the Hydrogen fluid inside a single wall CNT at 300 K and $\rho\sigma^3=0.5$, obtained by molecular dynamic simulation (MD) and P-DFT (oure results); b) Density profile of a Lennard fluid with $\rho\sigma^3=0.6$, $\varepsilon/kT=1.0$ and $\varepsilon_w/kT=1.0$ within various CNTs with different diameters; c) Density profile of a Lennard fluid with $\rho\sigma^3=0.6$, $\varepsilon_w/kT=1.0$ and different ε/kT within a CNTs with $D=8\sigma$.

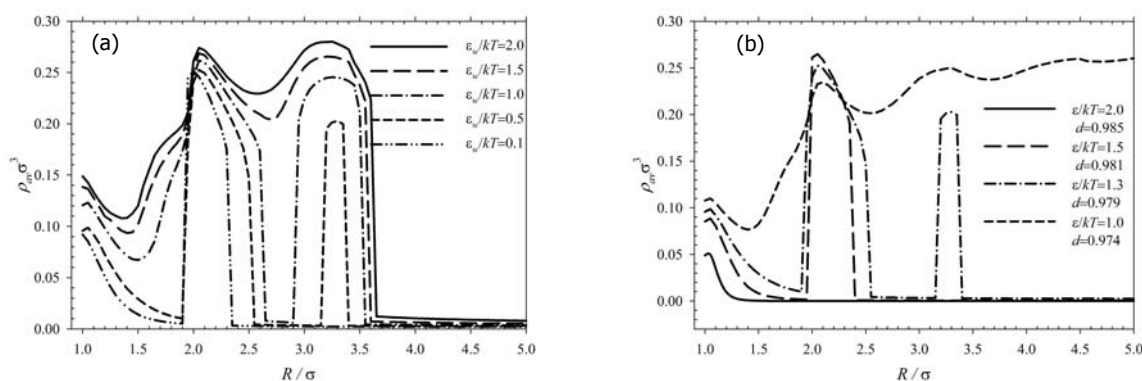


Fig. 2. a) Average density of a Lennard-Jones fluid and its dependency to the wall-fluid interactions. For all cases $\varepsilon/kT=1.3$ and $\rho\sigma^3=0.75$; b) Average density of a Lennard-Jones fluid and its dependency to the interatomic interactions. For all cases $\varepsilon_w/kT=0.5$ and $\rho\sigma^3=0.75$.

3. Conclusions

In this work, strong dependency of the structure and phase transition of a confined Lennard-Jones fluid in a CNT is investigated by an accurate perturbative DFT method. Our results show that the both energy and entropy effects can change the structure and phase diagram of this confined fluid. For these systems, the entropy effect has the main role in determination of the structure and phase diagram.

References

- [1] Koga, K., J. Chem. Phys. (2002) 116, 10882.
- [2] Yu, Y.-X., Wu, J. Z., J. Chem. Phys. (2002) 117, 10156.
- [3] Tarazona, P., Phys. Rev. A (1985) 31, 2672.
- [4] Keshavarzi, E., Kamalvand, M., J. Phys. Chem. B (2009) 113, 5493.

**Transport properties of non-spherical gases**

A. Maghari, H. Diarmand and A. H. Jalili

Department of Physical Chemistry, College of Science, University of Tehran, Tehran, Iran

(E-mail: maghari@khayam.ut.ac.ir) (E-mail: hdiarmand@gmail.com)

Keywords: Transport properties, Non-spherical contributions, Enskog-Chapman solution, Collision integrals.**1. Introduction**

The calculation of transport properties is based on the kinetic theory of gases and the knowledge of distribution function [1, 2]. When the system is not in the equilibrium, the distribution function satisfies the Boltzmann equation. Enskog and Chapman have introduced a solution to this equation [3]. Their method gives a satisfactory description only if the gas consists of atoms or molecules that can be treated as a sphere interacting centrally, but when the force fields in the molecules depend on relative orientations, it's impossible to use a spherical approximation, since their interaction potential depends on their mutual orientations. For non-spherical gases, the dependant part on the angular variables is separated and considered as a perturbation to the central intermolecular potential. Then investigation of the collision integrals makes it possible to gain information about the multipole moments of the molecules, since angular dependence of the potential energy arises primarily from electric multipoles in the molecule. The purpose of this work is introducing a general method for calculation of non-spherical contributions to the collision integrals. Expressions which are obtained from this method are valid for molecules of arbitrary symmetry and arbitrary electronic structure.

2. Theory

The transport coefficients of a dilute gas can be expressed in terms of collision integrals $\Omega^{(l,s)}(T)$, which are related to the intermolecular potential energy $u(r, \omega_a, \omega_b)$ as [4]:

$$\chi(b^*, E^*) = \pi - 2b^* \int_0^\infty \frac{r^{*-2} dr^*}{\left[1 - (b^{*2}/r^{*2}) - (u^*(r^*, \omega, \omega)/E^*)\right]^{1/2}} \quad (1)$$

$$Q^{(l)*}(E^*) = 2 \left[1 - \frac{1 + (-1)^l}{2(1+l)}\right]^{-1} \int_0^\infty (1 - \cos^l \chi) b^* db^* \quad (2)$$

$$\Omega^{(l,s)*}(T^*) = \left[(s+1)T^{*(s+2)}\right]^{-1} \int_0^\infty Q^{(l)*}(E^*) \exp(-E^*/T^*) E^{*(s+1)} dE^* \quad (3)$$

Where χ is the scattering angle, $Q^{(l)*}(E^*)$ is the reduced transport collision integral. Thus, three successive integrations can be performed once the intermolecular pair potential energy is known.

In this work, we used perturbation expansion to treat the directional component as a perturbation on the spherical field. We decomposed the potential to an unperturbed and a perturbed (directional part of intermolecular potential) by introducing a perturbation parameter ζ into the potential, so that:

$$u^*(r, \omega_1, \omega_2) = u_\theta^*(r) + \zeta u_{ns}^*(r, \omega_1, \omega_2) \quad (4)$$

The non-spherical contribution $u_{ns}^*(r, \omega_1, \omega_2)$ is normally divided into the interaction between permanent electrostatic distributions (dipoles and possibly higher- multipoles) as:

$$u_{12}^{el}(r_{ab}, \omega_a, \omega_b) = \sum_{n=0}^\infty \sum_{m=0}^\infty \frac{(-1)^{n+m} 2^{n+m} n! m!}{(2n)!(2m)!} \mathbf{M}_{a1}^{(n)} [n]^{(n)} \mathbf{T}_{ab}^{(m)} [m]^{(m)} \mathbf{M}_{b2} \quad (5)$$

And electric moments induced by the permanent moments of other molecules:

$$u_{12}^{ind}(r_{ab}, \omega_a, \omega_b) = -\frac{1}{2} \sum_{n=0}^\infty \sum_{m=0}^\infty \frac{(-1)^{n+m} 2^{n+m} n! m!}{(2n)!(2m)!} \left\{ \mathbf{M}_{a1}^{(n)} [n]^{(n)} \mathbf{T}_{ab}^{(l)} \cdot \alpha_{b2}^{(l)} \cdot \mathbf{T}_{ba}^{(m)} [m]^{(m)} \mathbf{M}_{a1} \right. \\ \left. + \mathbf{M}_{b2}^{(n)} [n]^{(n)} \mathbf{T}_{ba}^{(l)} \cdot \alpha_{a1}^{(l)} \cdot \mathbf{T}_{ab}^{(m)} [m]^{(m)} \mathbf{M}_{b2} \right\} \quad (6)$$

Where ${}^{(n)}\mathbf{T}_{ab}^{(m)} \equiv -\nabla^{n+m} (1/r_{ab})$ is a tensor of rank $n+m$ describing the $(2^n\text{-pole}) - (2^m\text{-pole})$ interactions between the molecules a and b , $\alpha_{\lambda i}$ is the electric dipole polarizability tensor of molecule $\lambda (\lambda=a,b)$ of species $i (i=1,2)$, α_i is the scalar dipole polarizability of species i , and $\mathbf{M}_{a1}^{(n)}$ is the n^{th} rank tensor of the electric multipole moment.



The scattering angle and cross section can be expanded as Taylor series in powers of ζ :

$$\chi(b^*, E^*, \zeta) = \chi_0(b^*, E^*) + \zeta \chi_1(b^*, E^*) + \zeta^2 \chi_2(b^*, E^*) + \dots \quad (7)$$

$$Q^{(l)*}(E^*, \zeta) = Q_0^{(l)*}(E^*) + \zeta Q_1^{(l)*}(E^*) + \zeta^2 Q_2^{(l)*}(E^*) + \dots \quad (8)$$

Substituting Eqs. (7) and (8) into Eqs. (1) and (2), collecting like powers of ζ and equating the coefficients of ζ^n terms,

$$\chi_0(b^*, E^*) = \pi - 2b^* \int_0^\infty \frac{r^{*-2} dr^*}{\left[1 - (b^{*2}/r^{*2}) - (u_0^*(r^*)/E^*)\right]^{1/2}} \quad (9)$$

$$\chi_1(b^*, E^*) = -\frac{b^*}{E^*} \iint d\omega_a d\omega_b \int_0^\infty \frac{u_{ns}^*(r^*, \omega_a, \omega_b) r^{*-2} dr^*}{\left[1 - (b^{*2}/r^{*2}) - (u_0^*(r^*)/E^*)\right]^{3/2}} \quad (10)$$

$$\chi_2(b^*, E^*) = -\frac{3}{2} \frac{b^*}{E^{*2}} \iint d\omega_a d\omega_b \int_0^\infty \frac{[u_{ns}^*(r^*, \omega_a, \omega_b)]^2 r^{*-2} dr^*}{\left[1 - (b^{*2}/r^{*2}) - (u_0^*(r^*)/E^*)\right]^{5/2}} \quad (11)$$

$$Q_0^{(l)*}(E^*) = 2 \left[1 - \frac{l+(-l)}{2(l+1)}\right]^{-1} \int_0^\infty (1 - \cos^l \chi_0) b^* db^* \quad (12)$$

$$Q_1^{(l)*}(E^*) = 2l \left[1 - \frac{l+(-l)}{2(l+1)}\right]^{-1} \int_0^\infty [\chi_1 \sin \chi_0 \cos^{l-1} \chi_0] b^* db^* \quad (13)$$

$$Q_2^{(l)*}(E^*) = 2 \left[1 - \frac{l+(-l)}{2(l+1)}\right]^{-1} \int_0^\infty [\chi_1^2 \cos^l \chi_0 + l \chi_2 \sin \chi_0 \cos^{l-1} \chi_0 + l(l-1) \chi_1^2 \sin^2 \chi_0 \cos^{l-2} \chi_0] b^* db^* \quad (14)$$

3. Results and Discussion

The integrals involved in computing $\Omega_{ns}^{(l,s)*}$ could be solved using numerical methods. The procedure for doing this calculation is introduced by Barker et al [5]. As can be seen from the results at articles [6], each term in the non-spherical part of the potential has a definite contribution to the collision integrals. In this work we have studied the effects of dipole and quadrupole moments and also the induce moments on the collision integrals at low, moderate and high temperatures. Figure 1 shows the dipole effect, as an example, on the collision integral at both low and high temperatures. As you can see, as more as the temperature rises, the effects of moments are more efficient and the procedure of changes is regularized. This happens because of this primarily assumption that the interactions are considered binary (in finding Boltzmann equation). Naturally the more temperature arises, the validity grows.

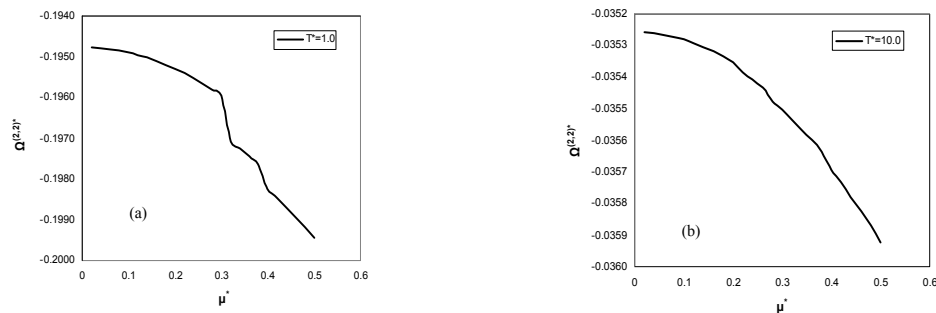


Fig. 1. Dipole effect on collision integral at low and high temperatures: (a) $T^* = 1$; (b) $T^* = 10$

References

- [1] F. R. McCourt, R. F. Snider, J. Chem. Phys. (1965) 43, 2276.
- [2] F. R. McCourt, J. J. M. Benakker, W. E. Kohler, I. Kuscer, Non- Equilibrium Phenomene in Polyatomic Gases, Clarendon Press, Oxford, (1990 and 1991) Vols. 1 and 2.
- [3] S. Chapman, T. G. Cowling, The Mathematical Theory of Non-Uniform Gases, 3rd ed., Cambridge University Press, London, (1970).
- [4] J. O. Hirschfelder, C. F. Curtiss, R. B. Bird, Molecular Theory of Gases and Liquids, John Wiley & Sons, New York, 1964.
- [5] J. A. Barker, W. Fock, F. Smith, Phys. Fluids. (1964) 7, 897.
- [6] A. Maghari, A. H. Jalili, Bull. Chem. Soc. Jpn. (2007) 80, 699.

**Determination of critical concentration for polymer and surfactant mixture with lattice Monte Carlo simulation**

R. Behjatmanesh-Ardakani, F. Ghaderiyeh-Mahmood Abadi*

Department of Chemistry, Payame-Noor University of Ardakan, Iran

(E-mail: ghaderiah@yahoo.com)

Keywords: Critical concentration, CAC, Lattice Monte Carlo simulation, Configurational bias Monte Carlo, Algorithm of Metropolis.

1. Introduction

Surfactants and polymers have a very broad range of applications. Their combined occurrence is found in such diverse products as cosmetics, paints, detergents, foods and enhanced oil recovery (EOR). Surfactant-polymer aggregation is described in terms of some characteristic concentrations, such as the CAC and CMC. CAC, is an indication of the beginning of the cooperative surfactant aggregation to the polymer [1]. The parameter critical concentration defined by Nagarajan is the one unique characteristic of aggregation of a micellar system. This critical concentration corresponds to a surfactant solution with no appreciable amount of aggregates, where as the CMC, defined in the literature, corresponds to systems with about 5-10% of amphiphiles in micellar form. Almost all of micellization studies consider the CMC, but ignore C_{crit} . In the present work, we investigate the C_{crit} for a lattice Monte Carlo simulation of a polymer-surfactant system.

In this lattice model, each segment occupies one lattice site in a simple cubic lattice of size $50 \times 50 \times 50$. Empty sites represent water as the solvent. Periodic boundary conditions and the excluded-volume condition are applied to mimic the box of the simulation to the bulk of solution. Interactions are repulsive between hydrophobic and hydrophilic segments. The total energy is calculated as follows:

$$\frac{E}{k_B T} = \frac{\varepsilon}{k_B T} (n_{T,s} - n_{T,H}) \quad (1)$$

where $n_{T,s}$ and $n_{T,H}$ are the numbers of tail-solvent and tail-head contacts, respectively, and k_B is Boltzmann constant. T is absolute temperature and $\frac{\varepsilon}{k_B T}$ is the interaction parameter. The interaction parameter has been set to be 0.7.

The Monte Carlo procedure based on the algorithm of Metropolis in the NVT ensemble involves one move for changing the position and configuration of the molecules, namely, reptation to randomly chosen lattice sites.

Also configuration bias Monte Carlo is used for changing the position and configuration of the molecules. Probability of the acceptance criteria for the configurational bias Monte Carlo move is as follows:

$$P_{acc} = \min \left\{ 1, \frac{W_{new}}{W_{old}} \exp(-\beta \Delta E) \right\} \quad (2)$$

Where, W is the Rosenbluth weight. ΔE is the total energy change due to the configuration change.

At the start of each simulation, all molecules are placed randomly in the simulation box. Equilibrium is assumed to be completed after a sequence of 1×10^9 Monte Carlo Steps. In this case, the total energy of the system fluctuates around a constant value.

2. Results and Discussion

At both CAC and CMC, a break in the slope of the curve of the monomer versus the total concentration of the surfactant occurs. So, it can be possible to determine CAC and CMC in the simulation from the monomer versus the total concentration. Figure 1 shows the determination of CAC and CMC by experimental approach. Nagarajan defined a critical concentration (C_{crit}) as the total surfactant concentration at which the micellar size distribution displays a horizontal inflection point. Below the C_{crit} , this function decreases monotonically with size indicating a small amount of aggregation. Above the C_{crit} , it exhibits both a minimum and a maximum, and the concentration of the aggregates becomes significant. One can take in to account the fact that near the CMC size distribution exhibits a minimum and a maximum. Figures 2 and 3 show the determination C_{crit} , CAC and CMC by Nagarajan's definition.



3. Conclusions

The values of the CMC when the various experimental techniques mentioned earlier are applied to the same surfactant species.

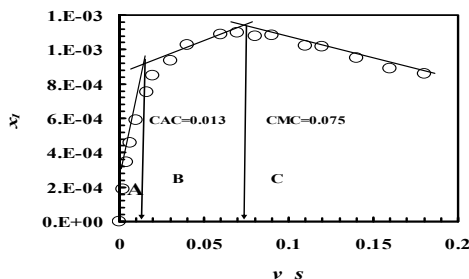


Fig. 1. Experimentalist CAC and CMC through slope variation of the monomer concentration versus volume fraction of surfactant for the system containing H_4T_4 as a surfactant and $(H_{10}T_{10})_2$ as a polymer. Volume fraction of polymer is constant at 0.01.

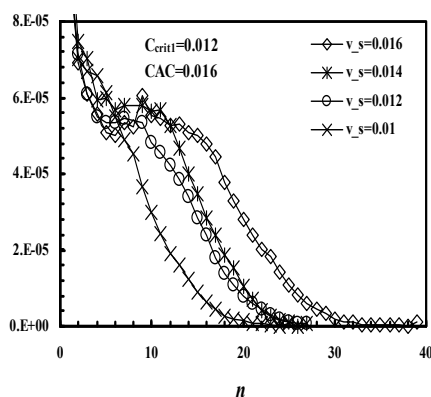


Fig. 2. CAC and C_{crit} determination by the definition of Nagarajan for the system containing H_4T_4 as a surfactant and $(H_{10}T_{10})_2$ as a polymer. Volume fraction of polymer is constant at 0.01.

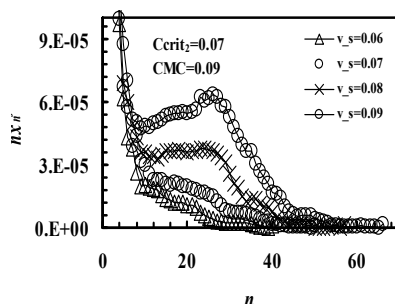


Fig. 3. CMC and C_{crit} determination by the definition of Nagarajan for the system containing H_4T_4 as a surfactant and $(H_{10}T_{10})_2$ as a polymer. Volume fraction of polymer is constant at 0.01.

differ from one another. But the parameter critical concentration (C_{crit}) as defined by Nagarajan C_{crit} is the one unique characteristic of aggregation of a micellar system. In the present work it is shown that a critical concentration is a close lower bound on the CMC values usually reported and C_{crit} is independent from micellar shape. Results show there are two critical concentration one before CAC and other before CMC.

References

- [1] B. Jonsson, B. Lindman, K. Holmberg, B. Kronberg, Surfactants and polymers in aqueous solution, John Wiley & Sons, 1999.
- [2] E. Ruckenstein, R. Nagarajan, J. Phys. Chem. 79 (1975) 2622.
- [3] D. Frenkel, B. Smit, Understanding Molecular Simulation from algorithms to applications, Academic, London, 2002.

**Calculation of static structure factor, $s(k)$, for xenon fluid by using the hard sphere radial distribution function**

H. Nikoofard, Z. Kalantar and T. Rezayee*

Faculty of Chemistry, Shahrood University of Technology, Shahrood, Iran

(Email: toktam_rezayee@yahoo.com)

Key words: Radial distribution function, Structural factor, Xenon fluid, Hard sphere fluid.**1. Introduction**

The radial distribution function (RDF) is the most informative feature of the structure of a substance. It represents the probability of finding a molecule at a specified distance from an arbitrary central molecule and is denoted $g(r)$, r being the distance between molecules [1]. By using RDF, it is possible to calculate structural factor. It is well known that the main feature of $S(k)$ in the large values of k are almost completely determined by the short-range repulsive part of the inter atomic forces that its range develops with density. But the behavior of $S(k)$ in low- k is correctly determined only by using long-range attractive forces. It is clear that $S(k)$ for monatomic liquids at very high density may be calculated quite well via the short-range repulsive forces [2]. In this work we use hard sphere radial distribution function to calculate the static structural factor, $S(k)$, for xenon fluid, and carry out the behavior of $S(k)$ in different thermodynamic states.

In order to calculate hard sphere radial distribution function we start from the expression given by Smith and Henderson [3] who give the following formula for spheres of uniform size, σ , with the scaled distance variable $x = r/\sigma$,

$$g(x) = \sum_{n=1}^{\infty} H(x-n) g_n(x) \quad (1)$$

Where $H(x-n)$ is the Heaviside step function

$$H(x-n) = \begin{cases} 0 & \text{for } x < n \\ 1 & \text{for } x \geq n \end{cases}$$

Which the final result as in the simplified formula for the g_n components of the hard sphere radial distribution function is

$$g_n(x) = \frac{(-12\eta)^{n-1}}{(n-1)!} \sum_{i=0}^{n-1} \frac{1}{(1-\eta)^{2i}} \frac{d^{n-1}}{dt^{n-1}} \left(\frac{t_i L(t_i)^n \exp\{t_i(x-n)\}}{(t_i - t_{i'})^n (t_i - t_{i''})^n} \right) \quad (2)$$

Where the equation (2) detailed in [3]. We display the hard sphere radial distribution function of xenon for different densities in Fig.1.

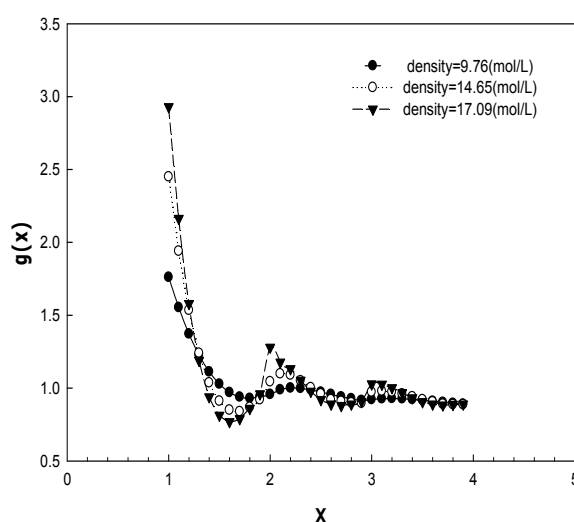


Fig.1. Hard sphere radial distribution function, $g(x)$, as a function of reduced distance, $x=r/\sigma$, in different densities for Xenon.



2. Methods

We used Maple 11 program package to obtain our values.

3. Results and Discussion

By having hard sphere radial distribution function we may calculate the structural factor of xenon fluid as

$$S(k) = 1 + 4\pi\rho \int_0^\infty (g(r) - 1) \frac{\sin kr}{kr} r^2 dr \quad (3)$$

We calculated structural factor for different densities of xenon and shown this result in Fig.2, In this way we investigate the behavior of $S(k_{\min})$ and k_{\min} for xenon in other thermodynamic states.

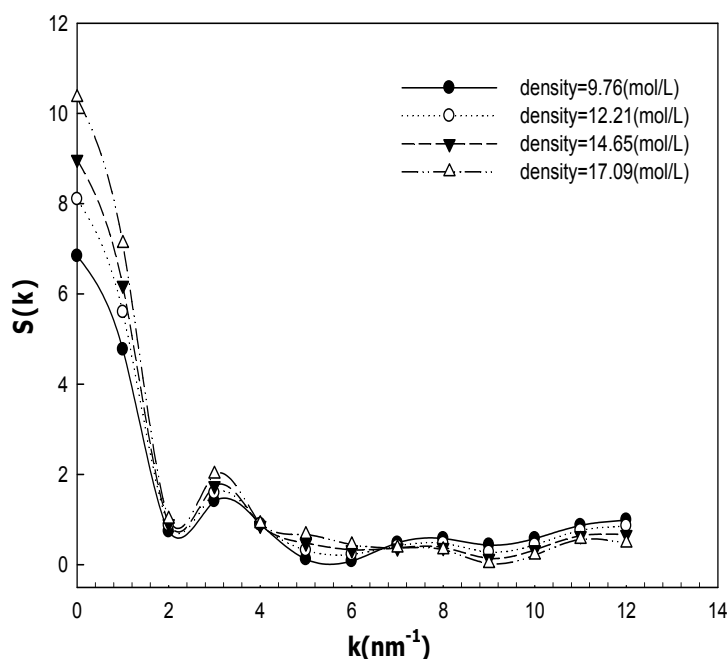


Fig.2. Structural factor, $S(k)$, versus wave vector, k , for xenon fluid in high densities.

4. Conclusions

By using the expression of the hard sphere radial distribution function, g_{HS} , an analytic solution for the calculation of structural factor, $S(k)$, for xenon fluid was obtained. The good behavior of structural factor, $S(k)$, observed in high densities. The approach here for structural factor, $S(k)$, of xenon can be used for showing the linear relation of k_{\min} and $S(k_{\min})$ with increase in density.

References

- [1] H. Toubia, G. A. Mansoori, Thermophysics. 18 (1997) 1217.
- [2] E. Keshavarzi, H. Nikoofard, A. A. Rostami, Phys. Soc. Jpn. 72 (2003) 1983.
- [3] S. P. Goodvin, J. D. Boughey, J. R. Heritage, Molecular Phys. 75 (1992) 917.



Calculation of isothermal compressibility and pressure of simple liquids using the hard sphere radial distribution function

H. Nikoofard, Z. Kalantar and T. Rezayee*

Faculty of Chemist, Shahrood University of Technology Shahrood ,Iran

(Email: toktam_rezayee@yahoo.com)

Key words: Isothermal compressibility, Pressure, Xenon, Hard sphere radial distribution function.

1. Introduction

The radial distribution function (RDF), $g(r)$, is the primary linkage between macroscopic thermodynamic properties and inter molecular interactions of fluids. In the present work we used hard sphere radial distribution function to predict the isothermal compressibility and pressure of xenon fluid.

2. Methods

We used Maple 11 program package to obtain our values.

3. Results and Discussion

The hard sphere radial distribution function, $g_{HS}(r)$, is frequently used to provide reference fluid properties in perturbation theories of simple liquids, we start from the expression given by Smith and Henderson[1] who give the following formula for spheres of uniform size σ , with the scaled distance variable $x=r/\sigma$,

$$g(x) = \sum_{n=1}^{\infty} H(x-n) g_n(x) \quad (1)$$

Where $H(x-n)$ is the Heaviside step function

$$H(x-n) = \begin{cases} 0 & \text{for } x < n \\ 1 & \text{for } x \geq n \end{cases}$$

Which the final result as simplified formula for the g_n components of the hard sphere radial distribution function is obtained,

$$g_n(x) = \frac{(-12\eta)^{n-1}}{(n-1)!} \sum_{i=0}^2 \frac{1}{(1-\eta)^{2n}} \frac{d^{n-1}}{dt_i^{n-1}} \left(\frac{t_i L(t_i)^n \exp\{t_i(x-n)\}}{(t_i - t_{i'})^n (t_i - t_{i''})^n} \right) \quad (2)$$

Where the equation (2) detailed in [1,2].

We demonstrated the hard sphere radial distribution function of xenon for different densities in Fig.1.

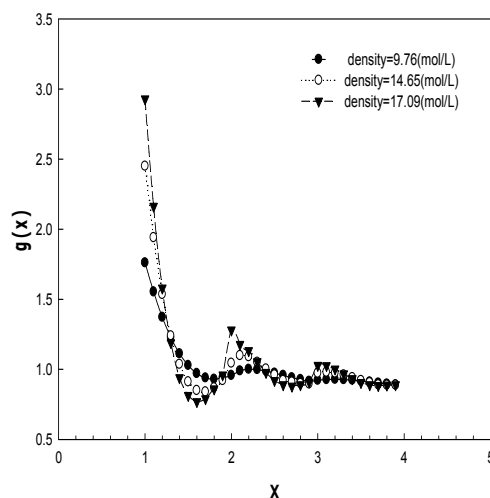


Fig.1. Hrad sphere radial distribution function, $g(x)$, as a function of reduced distance, $x=r/\sigma$, in different densities for Xenon.



In simple fluids the equilibrium properties such pressure and isothermal compressibility can be calculated in terms of $g(r)$ by the following expressions [3]:

$$\kappa_T = -\left(\frac{1}{V}\right)\left(\frac{\partial V}{\partial P}\right)_T = \left(\frac{1}{\rho}\right)\left(\frac{\partial \rho}{\partial P}\right)_T = \left(\frac{1}{\rho KT}\right) + \frac{4\pi}{KT} \int_0^\infty [g(r) - 1] r^2 dr \quad (3)$$

and reduced bulk modulus, B_r , is

$$B_r = \frac{1}{kT} \left(\frac{\partial P}{\partial \rho} \right)_T \quad (4)$$

We used to hard sphere radial distribution function to obtain the isothermal compressibility of xenon fluid.

Table1. values of κ_T for Xe fluid at density=12.21(mol/L).

T(k)	250	260	270	280
κ_T	0.32	0.30	0.29	0.28

Table2. values of κ_T for Xe fluid at density=17.09 (mol/L).

T(k)	250	260	270	280
κ_T	0.29	0.28	0.27	0.26

The values of Tables 1 and 2 determined that variation of isothermal compressibility, κ_T , with temperature is not remarkable. Also we use this approach to calculate pressure. We demonstrated the variation of pressure versus density and temperature in Figs.2 and 3. It is clear we observe the qualified behavior of pressure in which the increasing in temperature leads to increase the pressure too. Similarly we can see the behavior of pressure respect to density.

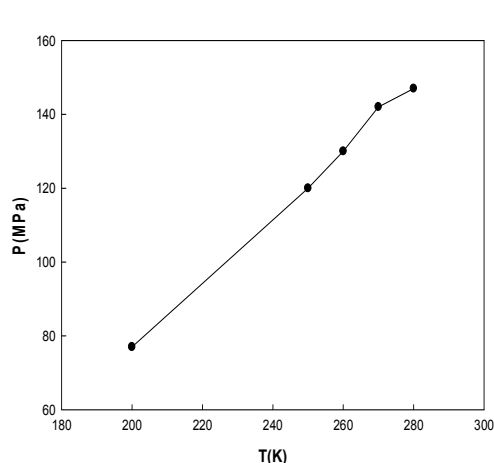


Fig.3. Pressure versus temperature for xenon at density=17.09(mol/L).

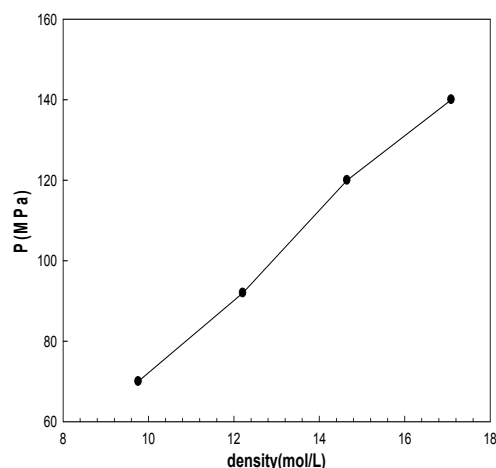


Fig.2. pressure versus density for xenon fluid at temperature=270K.

4. Conclusions

The main object of this work is carry out capability of presenting hard sphere radial distribution function for predicting thermodynamic properties for xenon fluid. The result shows this possible in high densities. We have shown using hard sphere radial distribution function as a starting point, how it is possible to calculate the equilibrium properties of simple fluids.

References

- [1] S. P. Goodvin, J. D. Boughey, J. R. Heritage, *Molecular Phys.* 75 (1992) 917.
- [2] W. R. Smith, D. Henderson, *Molec. Phys.* 19 (1970) 411.
- [3] H. Toubia, G. A. Mansoori, *Thermophysics.* 18 (1997) 1217.

**Investigation of molecular orientation at liquid-vapor interface by molecular dynamic simulation**

M. H. Ghatte and A. R. Zolghadr

Department of Chemistry, Shiraz University, Shiraz 71454, Iran

(E-mail: ghatte@susc.ac.ir, a.r.zolghadr@gmail.com)

Keywords: Molecular dynamics, Orientation, Density profile, Orientational parameter.**1. Introduction**

Microscopic surface structure of the liquid state has been one of the prime interests in surface science. Molecular dynamic (MD) simulation has been widely used to simulate the surface as well as the bulk properties of the liquids. MD provides useful information including time evolution of atomic coordinates of the simple as well as complex liquids, provided that accurate representation of the inter- and intra-molecular interaction is available. The outcome accurately describes properties of the system of interest [1, 2].

The purpose of present study is the simulation of liquid/vapor interface by classical molecular dynamics to demonstrate its ability as a method to derive the molecular orientation near surface layer.

2. Methods

The intramolecular force used for the simulation of model liquids, pyridine and its methyl and ethyl substituted, is in from of systematic all atom force field developed by Jorgensen et al. [3]. For each liquid system, the simulation ensemble consists of a slab of $10 \times 10 \times 14$ primitive cells. The equations of motion were solved using Verlet-Leapfrog integration algorithm. The simulations were performed in the NVT ensemble using Berendsen thermostat [4]. The state of a satisfactorily equilibrium is reached in about 4 ns.

The density profiles are calculated using the average density of constituting atoms at any point along the axis of the normal to the slab surface, the z-direction. The surface thickness is calculated by fitting the density profile to the hyperbolic tangent equation [5].

3. Results and discussions

The characteristics of the pyridine and its derivative molecules can be best defined by possession of hydrophilic part (the nitrogen) and the hydrophobic part (the ring body and alkyl tail). Certainly the differences in physical and chemical properties of these compounds arise from their structural details. Therefore, the simulation results indicate that as the hydrophobic part of the molecule is increased by one CH_2 group the liquid structure changes drastically. The density profiles of 4MPy atoms are shown in Figure 1. The molecular density in the bulk shows rather a uniform liquid state, while the density of each atom shows a characteristics periodic oscillation.

In particular the relative position of the molecule can be understood based on the understanding of methyl group position and the nitrogen atom, which are located at opposite sides of the ring. We sketch the interfacial region and the corresponding dividing surface as shown in the Figure 2. From the Figures 1 and 2, it can be seen that the profiles of methyl group in the dividing region are strictly unsymmetrical, while for nitrogen rather a perfect symmetry is held. In the vapor side of the Gibbs dividing surface the nitrogen bears a negative excess density. Conversely in the liquid side, the nitrogen distinctively is positive.

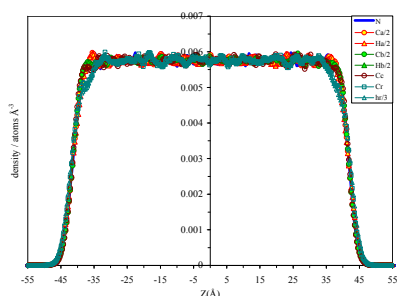


Fig. 1. Atomic densities for 4MPy molecules.

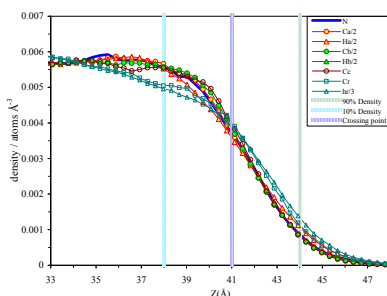


Fig. 2. Atomic densities in the interfacial region for 4MPy.

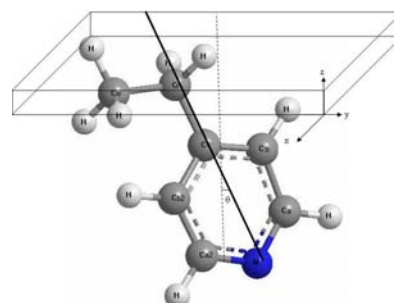


Fig. 3. Modeling the orientation of 4EPy molecules on the interface.



Figure 4 shows the atomic densities for the 4EPy system at 298 K as a typical example. Clearly, the non-polar group tends to be on the vapor side and the polar atom on the liquid side.

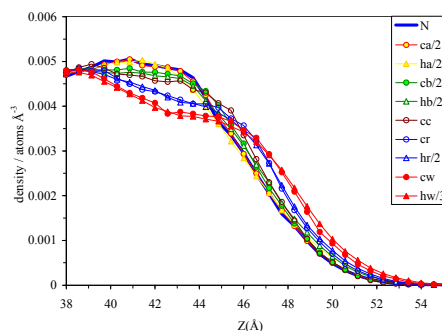


Figure 4: The atomic densities for the 4EPy molecules at 298 K.

In order to investigate the dependence of the average orientation of the Py, 4MPy and 4EPy molecules in the interface the angle, θ , between a given direction vector and z is averaged during the MD simulation. As shown in figure 3, θ is taken as the angle between specific direction vector in the molecule-fixed frame and the surface normal Z . The orientational parameters have been normalized in such a way that they give zero value in the bulk region. The obtained orientational profiles of the Py, 4MPy and 4EPy molecules are shown in Figure 5.

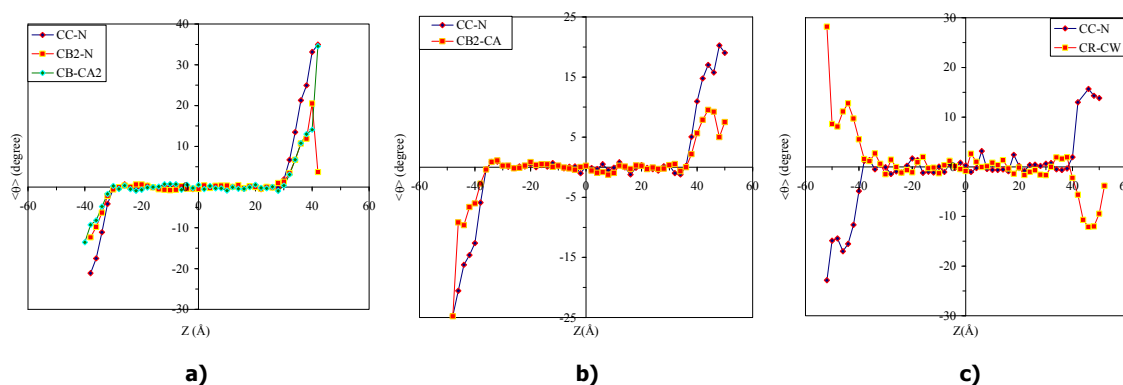


Figure 5: The angle between CC-N, CB₂-N and CB-CA₂ vectors with respect to vector Z normal of the ensemble. **a)** for pyridine **b)** for 4MPy **c)** for 4EPy molecules.

4. Conclusions

From these and more detailed considerations it can be concluded that in the vapor side, the methyl group is pointing to the surface and the plane of molecule tends parallel but angled beneath the surface such that nitrogen points away about 20 degree from the surface.

References

- [1] Bhargava, B. L. Balasubramanian, S. J. Am. Chem. Soc. 128 (2006) 10073.
- [2] Lynden-Bell, R. M. Po'polo, M. G. D. Phys. Chem. Chem. Phys. 8 (2006) 949.
- [3] Jorgensen, W. L. McDonald, N. A. J. Mol. Structure: THEOCHEM 424 (1998) 145
- [4] Berendsen, H. J. C. Postma, J. P. M. van Gunsteren, W. F. DiNola, A. Haak, J. R. J. Chem. Phys. 81 (1984) 3684.
- [5] Chapela, G. A. Saville, G. Thompson, S. M. Rowlinson, J. S. J. Chem. Soc. Faraday Trans. 2 (1977) 133.



Thermodynamic Behavior of Fluids: Crossover from Ising-like to Nonasymptotic Mean-Field Critical Behavior

H. Behnejad^{a*}, A. Bakhshandeha^a, J. V. Sengers^b

^aDepartment of Physical Chemistry, University College of Science, University of Tehran, Tehran, Iran

(Email: behnejad@gmail.com)

^bInstitute for Physical Science and Technology and Department of Chemical and Biomolecular Engineering, University of Maryland, College Park. MD 20742, U.S.A.

Keyword: Critical Behavior, Scaling Theory, Critical phenomena, Equation Of State, Crossover equation of state.

1. Introduction:

Critical phenomena in fluid and fluid mixtures have been the subject of many theoretical and experimental studies during the past decades as has been elucidated in various reviews. The microscopic structure of fluids becomes unimportant in vicinity of critical point, Universality of critical behavior results from the presence of large fluctuations in the order parameter associated with the critical phase transition the range of these fluctuations becomes much larger than any macroscopic scale[1]. As a consequence, the thermodynamic behavior can be characterized by scaling laws with universal critical exponents and universal scaling functions of three-dimensional Ising-like systems. That is, the three-dimensional Ising model, that can be reformulated as a lattice-gas model, is the prototype model for the critical behavior of fluids.[2]

2. Scaling Theory

Fluids and fluid mixtures belong to the universality class of Ising-like systems, whose critical behavior is characterized by two independent scaling fields, h_1 and h_2 , and one dependent scaling field, h_3 , which are analytic functions of the physical fields.

The theory of critical phenomena predicts that close to the critical point the dependent field h_3 becomes a generalized homogeneous function of the two independent scaling fields h_1 and h_2 of the form[2,3]

$$h_3(h_1, h_2) \approx |h_2|^{2-\alpha} f^{\pm} \left(\frac{h_1}{|h_2|^{2-\alpha-\beta}} \right), \quad (1)$$

where α and β are two universal critical exponents and where f^{\pm} is a scaling function with the superscript \pm referring to $h_2 > 0$ and $h_2 < 0$, respectively. In eq (1), h_1 is ordering field and h_2 is thermal field. Associated with these scaling fields are two conjugate scaling densities, a strongly fluctuating scaling density ϕ_1 (order parameter) and a weakly fluctuating scaling density ϕ_2 .

$$\phi_1 = \left(\frac{\partial \hat{P}}{\partial \hat{\mu}} \right)_T, \quad \phi_2 = \left(\frac{\partial \hat{P}}{\partial \hat{T}} \right)_\mu \quad (2)$$

3. Parametric Equation Of State

For two fields h_1 and h_2 an special representation is used that is called parametric equation by replacing the two independent scaling fields, h_1 and h_2 , with two parametric variables: a variable r which measures a "distance" from the critical point and an angular variable θ , which indicates the location on a contour of constant r : [2,4]

$$h_1 = r^{2-\alpha-\beta} H(\theta), \quad h_2 = rT(\theta). \quad (3)$$

4. Complete Scaling

To completely account for all asymmetric features of the critical phase transition one needs to relate the scaling fields to all the physical fields. For one-component fluids one thus should write the scaling fields in linear approximation as [2,4,5]

$$h_1 = a_1 \Delta \hat{\mu} + a_2 \Delta \hat{T} + a_3 \Delta \hat{P}, \quad h_2 = b_1 \Delta \hat{T} + b_2 \Delta \hat{\mu} + b_3 \Delta \hat{P}, \quad h_3 = c_1 \Delta \hat{P} + c_2 \Delta \hat{\mu} + c_3 \Delta \hat{T} \quad (4)$$

one obtains for the thermodynamic properties:

$$\hat{P} = \left(\frac{\partial \hat{P}}{\partial \hat{\mu}} \right)_T = \frac{1 + \phi_1 + b_2 \phi_2}{1 - a_3 \phi_1 - b_3 \phi_2} = 1 + (1 + a_3) \phi_1 + a_3 (1 + a_3) \phi_1^2 + (b_2 + b_3) \phi_2 + \dots, \quad (5)$$



$$\hat{\chi} = \left(\frac{\partial \hat{p}}{\partial \hat{\mu}} \right)_T = (1+a_3)^2 (1+3a_3\phi) \chi_1 + (b_2+b_3)^2 \chi_2 + 2(1+a_3)(b_2+b_3) \chi_{12} + \dots \quad (6)$$

Other thermodynamic properties can be obtained by using the aforementioned fields and the existing thermodynamic relations.

5. Crossover Equations

The equations presented in the preceding sections deal with the thermodynamic behavior of fluids in the near-critical region. For many applications one needs a global equation of state that not only incorporates the effects of critical fluctuations in the near-critical region, but also yields a representation of the thermodynamic properties of fluids over large ranges of temperatures and densities. To do this, one approach is inserting a parameter Y to parametric equation of state described by equation (3) as the following equations [4]

$$h_1 = r^{1/\nu} Y^{(1-\beta)/\nu} \tilde{h}_1(t) \quad , \quad \phi_1 = r^{1/\nu} Y^{(1-\beta)/\nu} \tilde{\phi}_1(t, Y_2) \quad (7)$$

Inserting eq. (7) in eqs. (5,6) and after some manipulation we obtained the crossover equation of state and the corresponding critical amplitudes as follow:

$$B_1 = \frac{2-2\beta}{\tau_0} Y_{20} \left(\frac{\tau_0}{\tau_0 - \tau_1} \right)^{2\beta} + m_{1,2}(0) Y_{20} \left(\frac{\tau_0}{\tau_0 - \tau_1} \right)^{2\beta}, \quad (8)$$

$$A_1^+ = \frac{2}{\tau_0} Y_{20} (\tau_0)^{2\beta} + q_{1,2}(0) Y_{20} (\tau_0)^{2\beta}, \quad (9)$$

$$\Gamma_1^+ = \frac{\tau_0 - 1}{\tau_0} Y_{20} (\tau_0)^{2\beta} + q_{1,2}(0) Y_{20} (\tau_0)^{2\beta}, \quad (10)$$

$$\Gamma_1^- = \frac{\tau_0 - 1}{\tau_0} Y_{20} \left(\frac{\tau_0}{\tau_0 - \tau_1} \right)^{2\beta} + q_{1,2}(1) Y_{20} \left(\frac{\tau_0}{\tau_0 - \tau_1} \right)^{2\beta}, \quad (11)$$

Where

$$\tau_0 = (1-b_2a_2) + p_1(b_3-a_3b_2) = (1-b_2a_2) + \frac{(c_2a_2-c_3)(b_3-a_3b_2)}{1-a_3c_2} \quad (12)$$

6. Conclusion:

Using crossover equations and complete scaling we have extended the validity of equation of state from Ising-like to Nonasymptotic Mean-Field, also we have obtained the corresponding critical amplitudes. The critical amplitudes are similar to those thatengers and coworkers derived [4] except in coefficient τ_0 .

References:

- [1] S.B.Kiselev, Fluid Phase Equilibria. **174** (2000) 93.
- [2] M.A. Ansimov , J.V Sengers, Equation of state and fluid mixtures, IUPAC Commission on Thermodynamics, Elsevier, Amsterdam (2000).
- [3] M. kardar, statistical physics of the fields ,Cambridge university press, New York(2007).
- [4] V.A. Agayan, Physical Review E **64** (2000) 026125.
- [5] M.E. Fisher, Phys, Rev, Lett. **85** (200) 696.



Second-order thermodynamic derivative properties of binary mixtures using the statistical associating fluid theory

Ali Maghari and Majid Hamzehloo

Department of Physical Chemistry, University of Tehran, Tehran, Iran

(Email: maghari@khayam.ut.ac.ir)

Keywords: SAFT, n-alkanes, Second derivatives, Sound velocity

1. Introduction

The equations of state (EOS) are used to estimate the thermodynamic properties of gases, liquids, and solids necessary for the design of processes and phase behavior calculations. Perhaps the most successful of the molecular-based EOS is the Statistical Association Fluid Theory (SAFT), proposed by Chapman *et al.* [1] on the basis of Wertheim's thermodynamic perturbation theory (TPT) [2-5]. A new version of SAFT (modified SAFT-BACK) has been recently developed by Maghari et al [6-8] to determine the thermodynamic derivative properties of pure fluids in the wide density and temperature ranges including critical temperature. Our previous works have been shown the accuracy of this equation for predicting the thermodynamic regularities as well as the second-order thermodynamic derivative properties, such as the speed of sound, heat capacities and Joule-Thomson coefficients of pure fluids. The goal of this work is to extend the modified SAFT-BACK EOS for the prediction of the second-order thermodynamic derivative properties as well as the vapor-liquid equilibria (VLE) of binary mixtures of *n*-alkanes.

Within the statistical associating fluid theory framework, the residual Helmholtz free energy for a non-association chain fluid is written as a sum of the separate contributions to the energy

$$A^{\text{res}} \equiv A - A^{\text{ideal}} = A^{\text{seg}} + A^{\text{chain}} \quad (1)$$

where A and A^{ideal} are the total Helmholtz energy and the ideal gas Helmholtz energy at the same temperature and density, A^{seg} is the contribution due to segment-segment interactions and A^{chain} is the contribution due to the formation of a chain as

$$A^{\text{seg}} = A^{\text{hcb}} + A^{\text{dis}}; \quad \frac{A^{\text{hcb}}}{Nk_B T} = m \left[\frac{\alpha^2}{(1-\eta)^2} - \frac{\alpha^2 - 3\alpha}{1-\eta} - (1-\alpha^2) \ln(1-\eta) - 3\alpha \right] \quad (2)$$

where the mixture-average segment number and shape parameter are $m = \sum_i x_i m_i$, $\alpha = \sum_i x_i \alpha_i$ and the packing fraction is defined as $\eta = \frac{\pi}{6} N_{\text{Av}} \rho m \sum_i x_i d_{ii}^3$. For determination of unlike size parameter, the Lorentz-Berthelot combining rule is employed as $\sigma_{ij} = \frac{1}{2}(\sigma_i + \sigma_j)$, $v_{ij}^0 = \left[0.5(v_i^0)^{1/3} + (v_j^0)^{1/3} \right]^3$. The dispersion contribution is expressed for square-well fluid as:

$$A^{\text{dis}} = m \sum_i \sum_j D_{ij} \left(\frac{u}{k_B T} \right)^i \left(\frac{\eta}{\tau} \right)^j \quad (3)$$

The binary interaction for unlike species u_{ij} is defined by the Lorentz-Berthelot combining rule using one adjustable interaction parameter k_{ij} to correct the dispersion energy as $u_{ij} = (1 - \kappa_{ij}) \sqrt{u_i u_j}$.

The chain contribution is obtained as a function of the chain length and the pair correlation function of the reference fluid:

$$A^{\text{chain}} = A^{\text{chain,hcb}} + A^{\text{chain,dis}}, \quad (4)$$

where $\frac{A^{\text{chain,hcb}}}{Nk_B T} = \sum_i x_i (1 - m_i) \ln g_{ii}^{\text{hcb}}(d_{ii})$ and $\frac{A^{\text{chain,dis}}}{Nk_B T} = \frac{\lambda A^{\text{chain,hcb}}}{A^{\text{hcb}}} A^{\text{dis}}$.

2. Results and discussion



In this work, we extend the pure fluid modified SAFT-BACK EOS to fluid binary mixtures of *n*-alkanes. The modified SAFT-BACK EOS, using one binary interaction parameter κ_{ij} can be used to describe the vapor-liquid equilibria of fluid mixtures and used to predict the second-order derivative properties of binary mixtures of *n*-alkanes in the wide density and temperature ranges. Conditions for binary mixtures require that the temperature, pressure and chemical potential of each component in each phase be equal. The binary interaction parameters are simultaneously fit to saturated liquid densities and vapor pressures by minimizing the following objecting function:

$$Of = \sum_{i=1}^{ndp} \left(\frac{\rho_{i,cal}^{liq} - \rho_{i,exp}^{liq}}{\rho_{i,exp}^{liq}} \right)^2 + \sum_{i=1}^{ndp} \left(\frac{p_{i,cal}^{sat} - p_{i,exp}^{sat}}{p_{i,exp}^{sat}} \right)^2 \quad (4)$$

These parameters together with the modified SAFT-BACK approach provide a description of the VLE and second derivative properties of the mixtures that is in excellent agreement with the experimental data. The results for some alkane mixtures (as examples) obtained from the modified SAFT-BACK EOS, which shown in Fig. 1, are in good agreement with the experimental data.

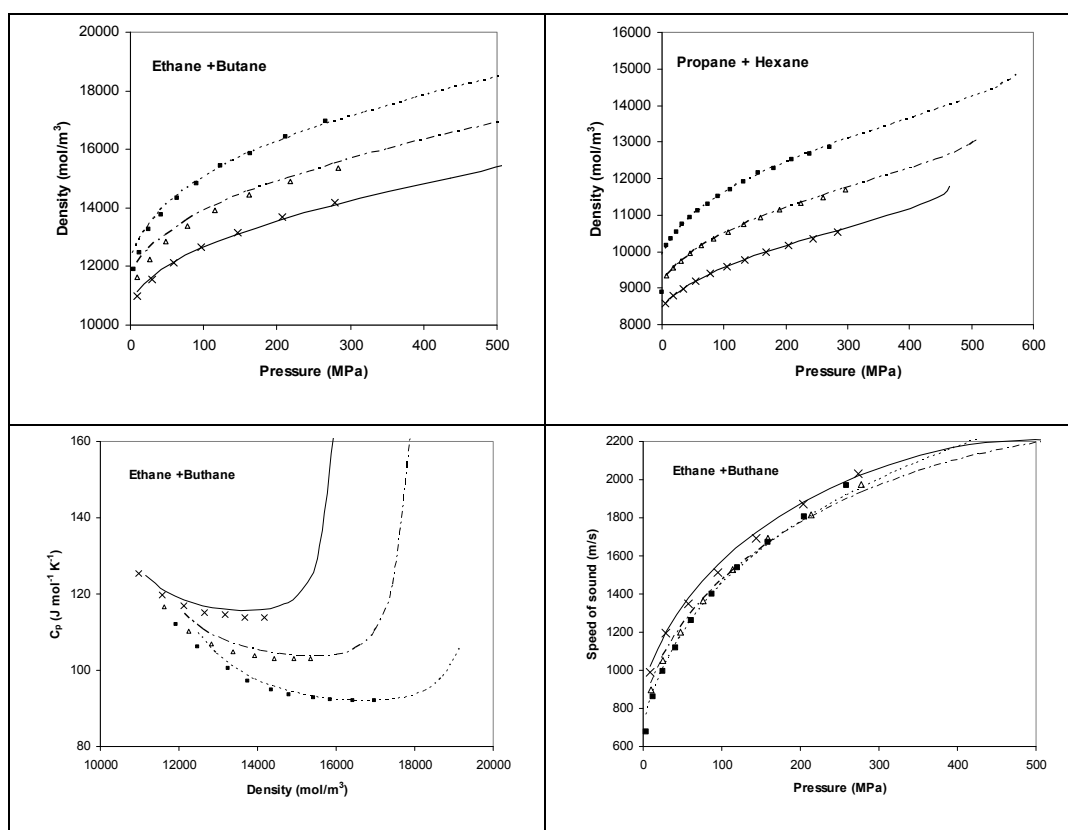


Fig. 1. VLE, heat capacity and speed of sound for some alkane mixtures.

Refereces

- [1] W.G. Chapman, K.E. Gubbins, G. Jackson, M. Radosz, Ind. Eng. Chem. Res. 29 (1990) 1709.
- [2] M.S. Wertheim, J. Stat. Phys. 35 (1984) 19.
- [3] M.S. Wertheim, J. Stat. Phys. 35 (1984) 35.
- [4] M.S. Wertheim, J. Stat. Phys. 42 (1986) 459.
- [5] M.S. Wertheim, J. Stat. Phys. 42 (1986) 477.
- [6] A. Maghari, M. S. Sadeghi, Fluid Phase Equilibria 252 (2007) 152.
- [7] A. Maghari, Z. Safaei, S. Sarhangian, Cryogenics 48 (2008) 48.
- [8] A. Maghari, Z. Safaei, J. Mol. Liquids 142 (2008) 95.
- [9] T. Boublik, J. Chem. Phys. 63 (1975) 4084.

**Application of Tao-Mason equation of state to quantum systems**M. M. Papari^a, M. Kiani^{a,b}, J. Moghadasi^c and R. Behjat Manesh Ardekani^b^aDepartment of Chemistry, Shiraz University of Technology, Shiraz, Iran

(Email: masoumehkiani@gmail.com)

^bDepartment of Chemistry, Payamenour University, Ardekan, Iran^cDepartment of Chemistry, Shiraz University, Shiraz, Iran**Keywords:** Hydrogen, Methane, Neon, Supercritical helium, Thermodynamics.**1. Introduction**

Quantum fluids have been studied experimentally for many years and have by now become a major focus of cryogenic physics. Applications of the subject are wide-ranging, from engineering (where, for instance, helium is used as a coolant for superconducting magnets and infrared detectors) to astrophysics (where it is invoked to explain glitches in the rotation of neutron stars). Tao and Mason presented a statistically-based equation of state [1]. In the present study we have applied this EOS to quantum systems including helium (⁴He), neon (Ne), methane (CH₄), and hydrogen (H₂) to predict densities of these systems at subcritical and supercritical regions.

2. Methods

In 1994, Tao and Mason [1] calculated a perturbation correction term for the effect of attractive forces and combined with Ihm-Song-Mason equation of state [2] to present an improved equation of state (hereafter we name it as TM EOS) [1]. The final form of the TM EOS is:

$$\frac{P}{\rho kT} = 1 + (B(T) - \bar{\alpha}(T))\rho + \frac{\bar{\alpha}(T)\rho}{1 - \rho b(T)\lambda} + A_1(\bar{\alpha}(T) - B(T))b(T)\rho^2 \frac{(e^{kT_c/T} - A_2)}{1 + 1.8(\rho b(T))^4} \quad (1)$$

Where P is the pressure, ρ is the density, kT is the molecular thermal energy, B_2 is the second virial coefficient, α is the second virial coefficient for the repulsive part of the intermolecular potential, b is the van der Waals covolume, and λ is an adjustable parameter. Other parameters in above equation are:

$$A_1 = 0.143$$

$$A_2 = 1.64 + 2.65[e^{(\kappa-1.093)} - 1] \quad (2)$$

$$\kappa = 1.093 + 0.26[(\omega + 0.002)^{1/2} + 4.50(\omega + 0.002)] \quad (3)$$

In Eqs. (2) and (3) ω is the Pitzer acentric factor.

The temperature-dependent parameters B , $\bar{\alpha}(T)$, and b relate to intermolecular potential energy according to the following expressions:

$$B = 2\pi \int_0^\infty \left(1 - e^{-u(r)/kT}\right) r^2 dr \quad (4)$$

$$\bar{\alpha}(T) = 2\pi \int_0^{r_m} \left(1 - e^{-u_0(r)/kT}\right) r^2 dr \quad (5)$$

$$b(T) = 2\pi \int_0^{r_m} \left(1 - \left[1 + \frac{u_0(r)}{kT}\right] e^{-u_0(r)/kT}\right) r^2 dr \quad (6)$$

Where the repulsive part, $u_0(r)$, is specified according to the Weeks-Chandler-Anderson [3].

For a spherical potential, $u(r)$, the Wigner-Kirkwood expansion [4] for the second virial coefficient yields:

$$B = B_{class} + \frac{\hbar^2}{m} B_1 + \frac{\hbar^4}{m^2} B_2 + \dots \quad (7)$$

Where B_{class} is given by eq. (2) and

$$B_1 = \frac{\pi}{6(k_B T)^3} \int_0^\infty e^{-u(r)/k_B T} (u')^2 r^2 dr, \quad (8)$$

$$B_2 = \frac{-\pi}{6(k_B T)^4} \int_0^\infty e^{-u(r)/k_B T} \times \left[\frac{(u'')^2}{10} + \frac{(u')^2}{5r^2} + \frac{(u')^3}{9k_B T r} - \frac{(u')^4}{72(k_B T)^2} \right] r^2 dr. \quad (9)$$



With $u' = du/dr$, $u'' = d^2u/dr^2$. In these expressions m is the molecular mass, $\hbar = h/2\pi$, and h is the Planck's constant.

3. Results and discussion

We have used the best available intermolecular potential energies for ^4He [5], Ne [6], H_2 [7], and CH_4 [8] to calculate the second virial coefficients. As mentioned before, for highly quantum systems, one must perform quantum corrections on the classical second virial coefficients. In the case of ^4He and H_2 , the eq. (8) converged after two quantum corrections on second virial coefficients for temperatures higher than 40K and 60K, respectively. The calculated second virial coefficients were in good agreement with experimental ones [9]. For heavier gases CH_4 and Ne at all temperatures the eq. (8) converged after first quantum correction. We founded that λ is a polynomial function of temperature according to the following equation:

$$\lambda = a_\lambda + b_\lambda T + c_\lambda T^2 + d_\lambda T^3 \quad (10)$$

The coefficients of eq. (11) have been tabulated in Table 1.

Table 1. Coefficients of eq. (11).

	a_λ	b_λ	c_λ	d_λ
CH_4	.44258	-0.00029315	8.2213e-7	-4.7109e-10
Ne	0.45524	0.00023438	2.614e-6	-6.2765e-9
H_2	0.73439	-0.0054698	2.7992e-5	-4.1046e-8
^4He	0.65796	0.0027059	-9.931e-6	9.1726e-9

the TM EOS was applied to calculate the densities for all aforesaid quantum systems in three different regions including gas, liquid, and supercritical. The results are shown in Table 2. It is clear that there is good harmony between the calculated and literature values [10] of the densities.

Table 2. Average absolute deviation (AAD) of the densities obtained using the TM EOS after and before performing quantum Corrections on the classical second virial coefficients from the literature data [10].

system	phase	T(K)	$\Delta P(\text{bar})$	after quantum correction	before quantum correction	NP
CH_4	gas	100-600	0.1-50	0.14267928	0.143673609	41
Ne	gas	30-300	0.1-30	0.056293946	0.29439	33
H_2	gas	60-400	5-15	0.027964009	0.766730938	12
He	gas	50-473.15	0.1	0.003769779	0.005765	5
CH_4	liquid	100-150	0.3-340	1.321611179	1.437842911	31
Ne	liquid	30	2.23-180	0.248218267	0.24981	16
CH_4	super critical	300-600	70-1000	0.753264019	0.885602605	30
Ne	super critical	100-300	30-1000	0.137389601	0.220728	62
H_2	super critical	60-400	20-200	0.385262893	2.081159095	32
He	super critical	50-473.15	0.1-200	0.086607	0.401524	37

Conclusions

The present work has successfully applied the TM EOS [1] to this class of fluids at temperatures ranging from 30K to 600K and pressures up to 1000 bar.

References

- [1] F. M. Tao, E. A. Mason, J. Chem. Phys. 100 (1994) 9075.
- [2] G. Ihm, Y. Song, E. A. Mason, J. Chem. Phys. 94 (1991) 3839.
- [3] J. D. Weeks, D. Chandler, H. C. Andersen, J. Chem. Phys. 54 (1971) 5237.
- [4] D. A. McQuarrie, Statistical Mechanics, Harper & Row, New York, 1976.
- [5] R. A. Aziz, R. Janzen, Phys. Rev. Lett. , 74 (1995) 1586.
- [6] R. A. Aziz, W. J. Meath, A. R. Allnatt, Chem. Phys., 78 (1983) 295.
- [7] R. Gengenbach, C. Hanh, W. Schrader, J. P. Toennies, Theoret. Chim. Acta (Berl.) 34 (1974) 199.
- [8] B. P. Reid, M. J. O'Loughlin, R. K. Sparks, J. Chem. Phys., 83 (1985) 5656.
- [9] J. H. Dymond, E. B. Smith, The Virial Coefficients of Pure Gases and Mixtures. A Critical Compilation, Oxford University, Oxford, 1980.
- [10] E. W. Lemmon, M. O. McLinden, D. G. Friend, Thermophysical properties of fluid systems in NIST chemistry webbook, NIST Standard Reference Database Number 69, eds. W. G. Mallard, P. J. Linstrom, November (2005), Nat. Inst. Stand. Tech. Gaithersburg, MD20899 <http://webbook.nist.gov>



Computation of some thermodynamic properties of nitrogen using a new intermolecular potential from molecular dynamics simulation

Elaheh K. Goharshadi^{a,*}, Mohsen Abbaspour^b, Majid Namayandeh Jorabchi^a and Masoud Nahali^c
(Email: gohari@ferdowsi.um.ac.ir)

^a Department of Chemistry, Ferdowsi University of Mashhad, Mashhad 91779, Iran

^b Department of Chemistry, Tarbiat Moallem University of Sabzevar, Sabzevar, Iran

^c Department of Chemistry, Sharif University of Technology, Tehran, Iran

Keywords: Potential energy function, Molecular dynamics simulation, Second virial coefficient, Self-diffusion coefficient, Viscosity, Thermal conductivity.

1. Introduction

It has been demonstrated that the excellent predictions of the thermodynamic data of pure fluids and mixtures can be obtained by molecular dynamics simulations. A crucial point in computer modeling of real substances is the determination of intermolecular interactions [1].

Since nitrogen is present in everyday life and many important technologies, the investigation of the nitrogen properties has been of great importance not only from basic scientific but also from technical point of view [2].

The purpose of the present paper is to determine an accurate nitrogen pair-potential energy function via the inversion of the reduced viscosity collision integrals. We have also computed the second virial coefficient of nitrogen using the obtained pair-potential at different temperatures and compared with experimental data. Some transport properties of nitrogen such as viscosity, thermal conductivity, self-diffusion coefficient, and thermal diffusion factor have been also calculated using the obtained pair-potential at the wide ranges of temperature and density.

Finally, we have performed molecular dynamics simulation to obtain pressure, internal energy, and self-diffusion coefficient of nitrogen at different temperatures and densities using our calculated pair-potential and some other potentials. The molecular dynamics simulation has been also used to determine the equation of state for nitrogen in low and high pressure ranges.

2. Method

The pair-potential energy function has been obtained using the inversion of the reduced viscosity collision integrals.

The aim of an inversion method is to obtain the potential by considering the experimental data as a functional instead of fitting the data to a constrained potential form having a few parameters [3].

3. Results and discussion

The reduced pair-potential energy function of nitrogen has been obtained using the inversion of the reduced viscosity collision integrals. A comparison between our calculated pair-potential with previously determined has been done. There is a good agreement between our calculated pair-potential and other literature potentials. The reason for a good accordance between our calculated potential and other potentials obtained using different methods such as the ab initio method and scattering experiment for nitrogen is based on the fact that our potential has been calculated using the inversion method. This method produces an isotropic pair potential energy that is a spherical averaged of the true potential multidimensional function over all possible relative orientations.

We have calculated the reduced second virial coefficient of nitrogen and compared with the corresponding literature data. The calculation of the second virial coefficient can be considered as a critical test for a potential [3]. The general agreement between the values of second virial coefficients calculated based on our resulting potential and the experimental and literature values confirm the validity of our potential.

We have calculated the viscosity, thermal conductivity, self diffusion coefficient, and thermal diffusion factor for nitrogen at different temperatures at atmospheric pressure. There are little deviations between our calculated properties and experimental data. It is plausible to say that this excellent accordance corresponds to the accuracy of our calculated potential for nitrogen.



We have performed MD simulation to obtain reduced pressure and internal energy of nitrogen using our calculated pair-potential and other potentials. At higher densities ($\rho^*=0.1$ and 1.0), the pressure values using our calculated potential show a better agreement with experimental data compared with other potentials.

We have also calculated the reduced heat capacity at constant volume, C_v^* , at different reduced temperatures using the simulated internal energies at constant reduced density. Our simulated values of C_v^* are nearly constant at different reduced temperatures which is expected for a classical MD simulation but at higher densities ($\rho^*=0.1$) our values decrease in spite of experimental data which increase at high temperatures which may be due to using the isotropic potential. Although our isotropic pair potential energy is a spherical averaged of the true potential multidimensional function but does not account explicitly for rotational motion which decreases degree of freedom and so decreases C_v^* in the simulation.

The MD calculations have been used to determine the equation of state for nitrogen which may be used as a reference for nitrogen especially at high pressures. We calculated the reduced pressure of nitrogen for the reduced temperatures from 1 to 21 and reduced density from 0.001 to 2.7.

We have compared our calculated reduced self-diffusion coefficient for nitrogen at different temperatures and densities with the experimental data. The temperature dependence of our simulated values using different potentials is much less than those of experimental values.

4. Conclusions

We have determined the pair-potential energy function and reduced collision integrals of nitrogen via the inversion of reduced viscosity collision integrals and fitted with a HFD-like potential. This potential can reproduce the second virial coefficient, viscosity, thermal conductivity, self-diffusion coefficient, and thermal diffusion factor of nitrogen in a good accordance with experiment.

References

- [1] C. Kriebel, A. Muller, M. Mecke, J. Winkelmann, J. Fischer, *Int. J. Therm.* 17 (1996) 1349.
- [2] S. Krukowski, P. Strak, *J. Chem. Phys.* 124 (2006) 134501.
- [3] G. C. Maitland, M. Rigby, E. B. Smith, W. A. Wakeham, *Intermolecular Forces, Their Origin and Determination*, Clarendon Press, Oxford, 1987.



The role of particulate-fluid and fluid-fluid interactions in surface tension and adsorption of a fluid in contact with a spherical particulate

E. Keshavarzi* and A. Taghizadeh

^aDepartment of Chemistry, Isfahan University of Technology, Isfahan, Iran

(Email: keshavrz@cc.iut.ac.ir)

Keywords: Density functional theory, Surface tension, adsorption, spherical particulate.

1. Introduction

Prediction of the properties of inhomogeneous fluids around curved surfaces has been the subject of many theoretical studies, because the substrate curvature influences processes such as wetting and adsorption, among others. The magnitude of surface tension may be affected by interfacial curvature. Surface tension greatly depends on particulate size for small particulates, but it does not vary with size for larger diameters. Despite the great number of studies on the surface tension of fluids in contact with a spherical particulate, no systematic study has yet been carried out on the effect of particulate-fluid and fluid-fluid interactions on the behavior of surface tension. In this paper we employ density functional theory to predict properties such as surface tension and excess adsorption of fluids in contact with spherical particulates.

Density Functional Theory

In our theory the excess Helmholtz free energy functional is formulated in terms of the MFMT¹ for short ranged repulsion and first-order mean spherical approximation theory² for a long ranged attraction.

$$F_{hs}[\rho(\mathbf{r})] = k_B T \int d\mathbf{r} \Phi_{hs}[n_\alpha(\mathbf{r})] \quad F_{att}[\rho(r)] = -\frac{kT}{2} \iint \rho(r) \rho(r') c_{att}(r-r') dr dr'$$

the equilibrium density distribution is obtained by minimizing the grand potential as:

$$\rho(r) = \rho_b \exp \left[\beta \mu_b^{ex} - \int dr' \sum_\alpha \frac{\partial \Phi}{\partial n_\alpha} w_\alpha(r-r') + \int dr' \rho(r') c_{att}(r-r') - \beta V_{ex}(r) \right]$$

Using density profiles, all the thermodynamic properties can be calculated. For example, the interfacial surface tension is obtained via³:

$$\gamma = \frac{\Omega[\rho(r)] - \Omega_b}{A}$$

2. Results and discussion

We have studied interfacial surface tension and excess adsorption of hard sphere and two-Yukawa fluids in contact with hard and attractive spherical particulates. We have also investigated the behavior of surface tension with spherical particulate sizes (R_s), fluid densities, and temperatures. The behavior of surface tension was explained using two contributions determining surface tension values. The first contribution arises from particulate-fluid interactions. It is zero for hard walls but is negative for attractive walls. The second contribution is due to uncontrolled changes in the structure of fluid molecules because of the existence of the spherical particulate. This factor always has a positive contribution for all kinds of fluid-fluid and particulate-fluid interactions. Our results show that particulate-fluid interactions play a more important role in the behavior of surface tension as compared to fluid-fluid interactions such that the sign and qualitative behavior of surface tension are determined by the kind of particulate-fluid interactions. Since the first contribution is absent in all kind of fluids near hard spherical particulates, with and without attractions, surface tension, therefore, is always positive, decrease with size, and increase with density as figure (1) shows. However, surface tension exhibits a different behavior for fluids near attractive spherical particulates. This means that in these cases, surface tension can take negative values for small sizes, increase with size, and gain positive values for larger sizes of the spherical particulate. Figure (2) shows the surface tension of hard sphere fluid in contact with attractive spherical particulates. In such cases, there may be a radius for each thermodynamic state in which surface tension is zero. This zero-surface tension value is the result of the competition between the first and second contributions which have opposite signs in surface tension. For radii smaller than R_{ZST} , the first contribution is the dominant factor and surface tension is negative. At R_{ZST} , the two contributions exactly cancel out each other and for radii larger than R_{ZST} , the second contribution gains the dominant role so that surface tension takes a positive value. It was shown that R_{ZST} decreases with density, but increases with



particulate-fluid attractions. Excess adsorption is negative for fluids in contact with hard spherical particulates (figure 3) but has both positive and negative values for fluids in contact with attractive spherical particulates (figure 4). In addition, changes in surface tension and adsorption with size work in opposite directions. It was also observed that for each thermodynamic state, there is a linear regularity between surface tensions and excess adsorptions for the whole range of sizes, and this regularity holds for all kinds of fluid-fluid and particulate-fluid interactions. As regards contact densities, we observed that for hard sphere fluids, contact density increases with particulate size. This behavior was explained by the entropy effect. But for fluids with long range attractions, variation of contact density with size is determined by competition between both energy and entropy effects. (In the figures below R is the radius of fluid particles and R_s is the particulate radius).

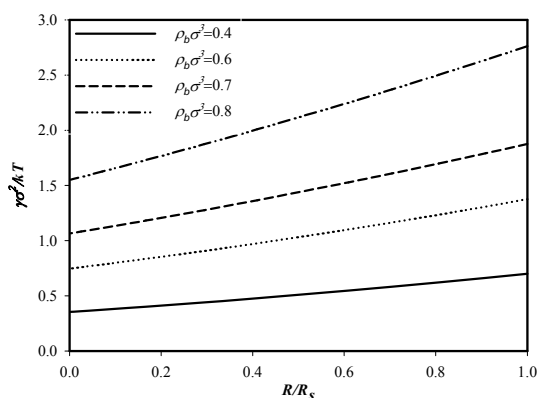


Fig. 1. Surface tensions of the hard sphere fluid in contact with hard spherical particulates as a function of particulate size for different fluid densities, $\rho_b \sigma^3 = 0.4, 0.6, 0.7, 0.8$.

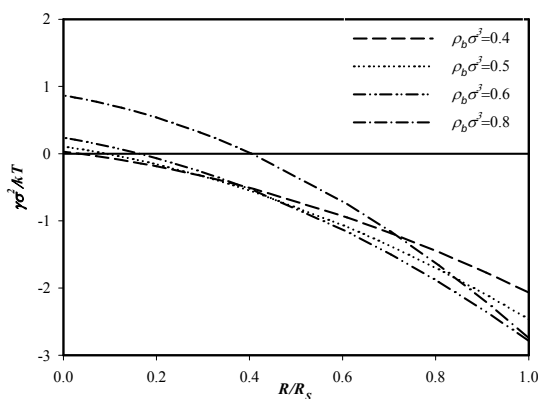


Fig. 2. Surface tensions of the hard sphere fluid in contact with attractive spherical particulates with $\varepsilon_W/kT=1$ as a function of particulate size for different fluid densities, $\rho_b \sigma^3 = 0.4, 0.5, 0.6, 0.8$.

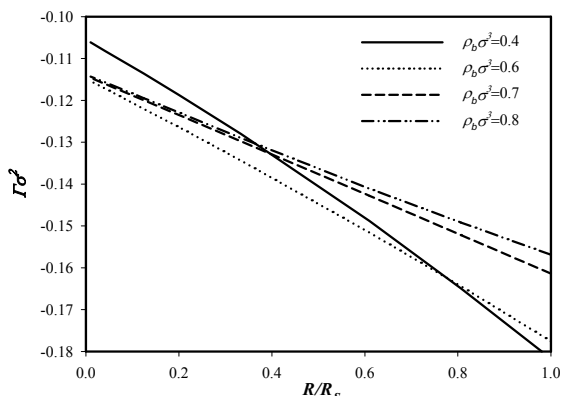


Fig. 3. Excess adsorptions of the hard-sphere fluid in contact with hard spherical nanoparticles as a function of nanoparticle size for different fluid densities, $\rho_b \sigma^3 = 0.4, 0.6, 0.7, 0.8$.

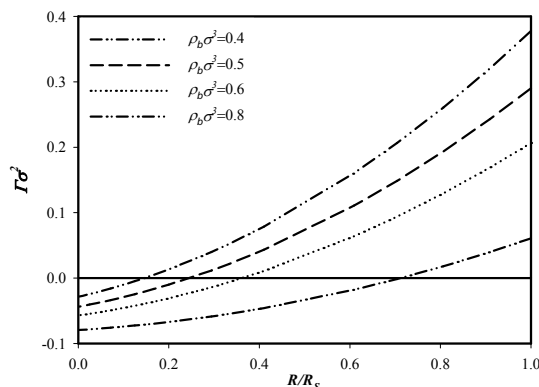


Fig. 4. Excess adsorptions of the hard-sphere fluid in contact with attractive spherical nanoparticles with $\varepsilon_W/kT=1$ as a function of nanoparticle size for different fluid densities, $\rho_b \sigma^3 = 0.4, 0.5, 0.6, 0.8$.

References

- [1] Yu, X.; Wu, J. Z. J. Chem. Phys. (2002) 117 (22), 10156.
- [21] Tang, Y. J. Chem. Phys. (2003) 118, 4140.
- [3] Bryk, P.; Roth, R.; Mecke, K. R.; Dietrich, S. Phys. Rev. E (2003) 68, 031602.

**Prediction of sound velocity of n-alkanols using the statistical associating fluid theory**S. Hosseini^{a*} and A. Maghari^b^aDepartment of chemistry, University of Payamnoor, Zahedan, Iran^bDepartment of chemistry, University of Tehran, Tehran, Iran

(Email: s.hosseini_60@yahoo.com)

Keywords: Simplified PC-SAFT, Equation of state, sound velocity, n-Alkanols**1. Introduction**

The thermodynamic properties of n-alkanols are a problem of great practical interest, since they are involved in a number of refinery processes. Moreover, the equations of state (EOS) are used to estimate the thermodynamic properties of gases, liquids, and solids necessary for the design of processes and phase behavior calculations. Among all of the EOSs proposed by different investigators, only a few are based on a fundamental theory, but the majority has been developed as a result of the mathematical processing of experimental data.

Two theoretical treatments commonly used in chemical engineering for n-alkanols are the simplified perturbed hard chain theory (SPHCT) and the statistical associating fluid theory (SAFT) [1]. For years, SAFT has been extensively used to calculate the phase behavior of associating and non-associating fluids.

In SAFT a molecule is composed of m segments correspond to atoms, functional groups or complete molecules. Each segment of this kind has the same volume and interaction energy parameters. Molecules are represented as covalently bonded chains of segments that may contain sites capable of forming associative complexes. By use of the SAFT, the contribution to Helmholtz free energy of bonding between segments can be calculated from the background correlation function for segments. Several versions of SAFT have been developed due to the different methods to calculate the free energy of monomers (segments).

SAFT EOS can be represented as a sum of Helmholtz energies:

$$A = A_{\text{ideal gas}} + A_{\text{hard sphere}} + A_{\text{dispersion}} + A_{\text{association}}$$

where A and A^{ideal} are the total Helmholtz energy and the ideal gas Helmholtz energy at the same temperature and density

Term of hard sphere:

The packing factor η is defined as

$$\eta \equiv \frac{1}{6} \pi N_{\text{AV}} m \rho d^3$$

$$\tilde{A}^{\text{hs}} = \frac{4\eta - 3\eta^2}{(1-\eta)^2}$$

in which, ρ is the molar density, m is the segment number and N_{AV} is the Avogadro's number.

Term of association:

$$A^{\text{assoc}} = (2 \log[X] - X + 1) N_{\text{AV}} k T$$

for determine X must refer to follow tables:

Table VIII. Types of Bonding in Real Associating Fluids ^a			
species	formula	rigorous type	assigned type
acid		1	1
alkanol		3B	2B
water		4C	3B

The mole fraction of molecules not bonded at site A can be determined as follow:

$$X = \frac{-1 + (1 + 4 \rho \Delta)^{1/2}}{2 \rho \Delta}$$

Term of dispersion:

The dispersion term is expressed also with the results of Alder et al.

$$\frac{A_{\text{dis}}}{NkT} = \frac{A_1}{NkT} + \frac{A_2}{NkT}$$

$$A_1 = -2 \pi \rho m^2 n_{\text{AV}} \sigma^3 \left(\frac{\epsilon}{kT} \right)_w$$

$$A_2 = -\pi\rho m \left(1 + m \frac{8\eta - 2\eta^2}{(1-\eta)^4} + (1-m) \frac{20\eta - 27\eta^2 + 12\eta^3 - 2\eta^4}{(1-\eta)^2(2-\eta)^2} \right)^{-1}$$

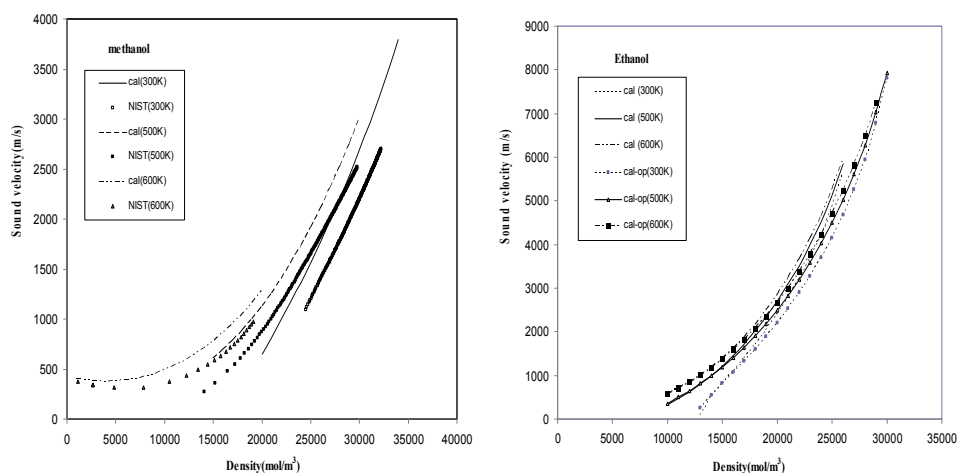
Speed of sound:

the Speed of sound calculations from:

$$V_s = \left[\left(\frac{\gamma}{M} \right) \left(\frac{\partial p}{\partial \rho} \right)_T \right]^{1/2}$$

2. Results and discussion

The results of Chen and Mi have shown that the Simplified PC – SAFT EOS predicts accurate phase envelope of chain fluids. In this work, the Speed of sound is calculated on the basis of the Simplified PC – SAFT EOS over the wide density and temperature ranges including critical temperature. In Figs. 1, 2 we compare correlated values of Speed of sound for methanol and ethanol with the values calculated with the Simplified PC – SAFT EOS. Very good predictions are obtained for the Speed of sound in both liquid and gas phases. Figs. 1,2 also display the calculated Speed of sound at three different temperatures, including liquid and supercritical regions. Finally, we have investigated the different microscopic contributions to the Speed of sound.



The dispersion contribution to the residual sound velocity decreases with increasing temperature, whereas the other contributions (segment, chain and chain-dispersion) increase with increasing temperature.

3. Conclusion

The Statistical Associated-Fluid Theory (SAFT) is based on the first – order perturbation theory of Wertheim (1987). The essences of this theory are that the Helmholtz energy is given by a sum of expressions to account not only for the effects of repulsion and dispersion forces but also for association and/or solvation.

The SAFT EOS has been applied successfully to describe thermodynamic properties and phase behavior of pure fluids and fluid mixtures containing small, large, non-associating and associating molecules, including supercritical and near-critical solutions of polymers.

References

- [1] Gross, G. Sadowski, Ind. Eng. Chem. Res. 40 (2001) 1244.
- [2] D. A. McQuarrie, Statistical Mechanics, Harper & Row (1976).
- [3] T. M. Reed and K. E. Gubbins, Applied Statistical Mechanics, McGraw-Hill, Inc (1973).

**An analytical direct correlation function for hard core double Yukawa potential**Mehrdad Khanpour^{*a}, and G. A. Parsafar^b^a Department of Chemistry, Islamic Azad University, Amol Branch, Amol, Iran^b Department of Chemistry, Sharif University of Technology, Tehran, Iran**Keywords:** Direct correlation function, Hard core double Yukawa potentials.**1. Introduction**

Direct correlation function (DCF) is of central importance in the theories of the liquid state both for homogenous and inhomogeneous fluids. The integral equation of homogenous fluids is based on the more generic equation by Ornstein-Zernike. In this work we intend to show by using a general expression for the second term in the density expansion of the correlation function of the hard core potential that has been found previously [2-3], one can propose an analytical expression for the DCF of hard core double Yukawa potential. Using the proposed DCF one can directly compute all thermodynamic properties of the fluid accurately. The proposed DCF can also be connected to the Ornstein-Zernike equation to yield the related RDF of the potential. Calculations based on the RDF give consistent results with those based on the DCF.

It has been proved in the statistical thermodynamics of fluids that the density expansion of DCF is [4]:

$$c(r) = (e^{-\beta u} - 1)(1 + G_1\rho + G_2\rho^2 + \dots) \quad (1)$$

$$\text{where } G_1(r) = \int (e^{-\beta u(r')} - 1)(e^{-\beta u(|r-r'|)} - 1) d^3\mathbf{r}'.$$

Here $\beta = 1/T^*$, and T^* and ρ are the reduced temperature and density, respectively. Obviously this integral can be analytically solved for hard core potentials [2,3]. Now if we assume the pair potential acting between particles has a long range attractive tail, at high densities or low temperatures where the average distance between particles ranges well below the value of the potential, $e^{-\beta u(r)}$ will nearly vanish, i.e., the fluid behavior is that of the hard sphere. In this way one may correctly assume that G_i for large values of i (which are important at high densities) should be those of hard spheres, whereas for the low densities G_i 's should be evaluated. On the other hand, at high densities or low temperatures where the fluid behaves like the hard spheres, one can approximate the DCF of hard spheres as the true $c(r)$ of the fluid in this limit.

$$c(r) = \begin{cases} c_{HS}(r) & \text{for } r \leq 1 \\ c_{HS}(r) + (e^{-\beta u} - 1)(1 + G_1\rho) & \text{for } r > 1 \end{cases} \quad (2)$$

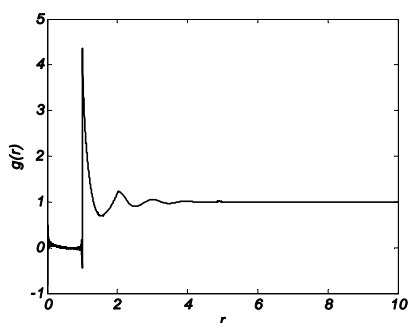
where $c_{HS}(r)$ represents the DCF of hard spheres and G_1 for hard core double Yukawa potential which can be analytically obtained. In order to assess the reliability of the proposed DCF we can apply this to compute the structure and thermodynamics of the hard core double Yukawa potential since by knowing DCF alone. We can also find the RDF originated from the proposed DCF through combining it to the Ornstein-Zernike equation. Some typical results of such calculations are summarized in Table 1 and Figure 1. As can be seen the results of thermodynamic properties by two methods are in close agreement with each other and with the Monte Carlo ones.



Table 1. Values of the compressibility factor $Z = \frac{PV}{NkT}$ and for the reduced excess internal energy U^{ex} for the hard core double Yukawa fluid. MC: Monte Carlo simulation data; S: analytical perturbation theory by Sun. All values other than the present work have been taken from [6].

		U^{ex}				Z			
T	ρ^*	MC	This work DCF & RDF		S	MC	This work DCF & RDF		S
0.3	0.3	0.221	0.2135	0.2218	0.223	1.23	1.2591	1.2787	1.23
	0.4	0.295	0.2817	0.2952	0.296	1.55	1.5868	1.6210	1.54
	0.5	0.367	0.3485	0.3679	0.369	2.07	2.1137	2.1672	2.07
	0.6	0.439	0.4138	0.4394	0.438	2.88	2.9230	3.0012	2.90
	0.7	0.509	0.4776	0.5094	0.507	4.13	4.1439	4.2521	4.16
	0.8	0.577	0.5400	0.5775	0.572	6.01	5.9830	6.1265	6.03
	0.9	0.644	0.6009	0.6435	0.636	8.85	8.7842	8.9684	8.72

Fig.1. Radial Distribution function $g(r)$ of the hard core Double Yukawa fluid with $\lambda_1 = 1.8$ and $\lambda_2 = 2$, at reduced density $\rho = 0.8$ and temperature $T = 1.5$.



One should notice that the core condition is fulfilled which is important for all hard core potentials.

Acknowledgement

We would like to thank the Islamic Azad University, Amol Branch for generous financial support of the research project.

References

- [1] P. Hansen and I. R. McDonald, Theory of Simple Liquids, third ed., Academic, London, 2006.
- [2] M. Khanpour, G.A.Parsafar, and B. Najafi, J. Phys. Soc. Jap, 73 (5) (2004), 1197-1204.
- [3] M. Khanpour, G.A.Parsafar, and B. Najafi, Fluid Phase Equilibria, 254 (2007) 138-143.
- [4] D. A. McQuarrie, Statistical Mechanics, Harper and Row, 1976.
- [5] V. I. Kalikmanov, Statistical Physics of Fluids, Springer, Berlin, 2001.
- [6] Sun Jiuxan, Phys. Rev. E, 68 (2003) 061503.

**Prediction of structure factor, $s(k)$, of simple fluids using the lir equation state in super critical region**

H. Nikoofard, Z. Kalantar and B. A. Esmaili *

Faculty of Chemistry, Shahrood University of Technology, Shahrood, Iran

(Email: asma.esmaili@yahoo.com)

Keywords: LIR, Structure factor, Supercritical fluid, DCF.**1. Introduction**

One of the important properties characterizing a fluid is its structure factor $S(k)$, which is a measure of inter particle correlations in the reciprocal space. An accurate knowledge of this quantity is crucial for studying numerous thermodynamic and transport properties of any fluid system. In this work, expressions for direct correlation function, $c(k)$ and structure factor $S(k)$, of simple dense fluids have been derived using the linear Isotherm regularity (LIR). We have predict the low-angle structure of factor $S(k)$ via LIR equation state for different temperature and densities.

2. Methods

We used Maple 11 program package to obtain our values.

3. Results and Discussion

As we know that the structure of a dense fluid is essentially a geometric packing problem. In fact the repulsive forces have important role in the determination of the fluid structure and the cohesive or attractive interactions in fluid just define the fluid volume. The consequent of these facts for the direct correlation function (DCF) is also clear via the compressibility equation.

$$B_r = \frac{1}{kT} \left(\frac{\partial p}{\partial \rho} \right) = 1 - 4\pi \left[\int_0^\sigma c(r)r^2 dr + \int_\sigma^\infty c(r)r^2 dr \right] \quad (1)$$

We used the LIR and obtained B_r as,

$$B_r = 1 + 3A''\rho^2 - 3\frac{A'}{RT}\rho^2 + 5\frac{B'}{RT}\rho^4 \quad (2)$$

Also, when temperature is very high, it may be present by,

$$B_r = 1 + 3A''\rho^2 \quad (3)$$

In this way, the expression of DCF can be consider as,

$$c(r) = \begin{cases} a + br & r < \sigma \\ \exp(-\beta u_{\text{eff}}) - 1 & r \geq \sigma \end{cases} \quad (4)$$

All above equations (1-4) detailed in [1].

We have used LJ(12,6) potential as the effective pair potential in the DCF, however, its well depth is expected to be state dependent and different from that of the isolated pair.

We have done the Fourier transformation on DCF calculated $S(k)$ via Ornstein-Zernik equation.

$$S(0) = \frac{1}{1 - \rho c(k)} \quad (5)$$

Fig.1, shows the structure factor of Ar fluid in different states. As it is clear, the qualitative behavior of the $S(k)$ is correctly generated and the number and heights of the bumping is increased with density which is expected.

In order to investigate our approach in super critical region, we also calculated the low- k behavior of $S(k)$ for Ar at the same thermodynamic which is shown in Fig.2, that our calculations in the super critical region can be presented qualifiedly the diverge behavior of $S(0)$ which is an important parameter related to critical fluctuation in the system.

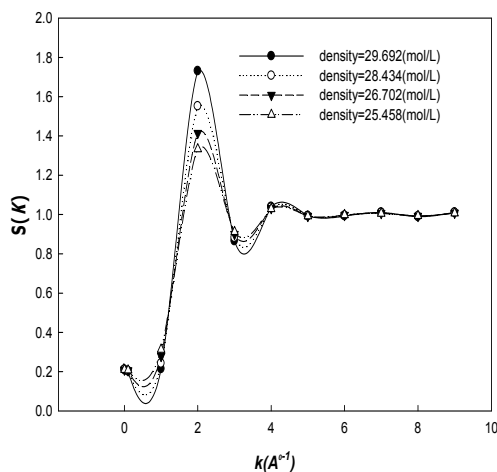


Fig.1. Behavior of structure factor with k for Ar in different densities.

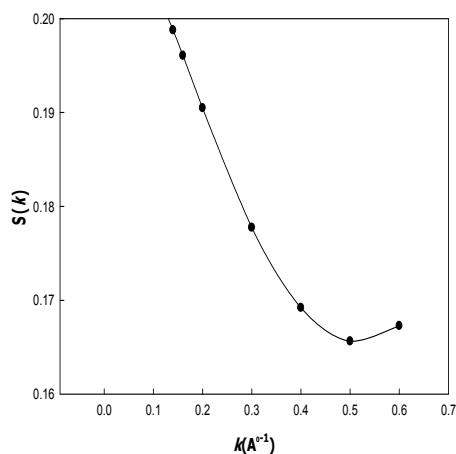


Fig.2. The structure factor for super critical dense Ar fluid, at Temperature=152K, density=28.435 (mol/L).

Since, $S(0)$ is related to thermodynamic properties of fluid via $S(0) = \rho k T \kappa_T$,

Where,

$$\kappa_T = \frac{1}{kT} \left(\frac{\partial p}{\partial \rho} \right)_T$$

One can be found the importance of this study.

4. Conclusions

We have shown, using an equation of state, LIR, as starting point it is possible to calculate the structure of factor $S(k)$ for simple fluids. The LIR can be successful in presentation of O-Z behavior of $S(k)$ in the small- k region. Also we shown that in the near critical point where the fluctuation phenomena increase the model is able to present the divergence behavior of $S(0)$.

References

- [1] E. Keshavarzi, G. A. Parsafar, Phys. Soc. Jpn. 70 (2001) 1979.
- [2] E. Keshavarzi, H. Nikoofard, A. A. Rostami, Phys. Soc. Jpn. 72 (2003) 1983.
- [3] N. Farzi, R. safari, Fluid Phase Equilibria 236 (2005) 212.
- [4] R. B. Stewart, R. T. Jacobsen, Phys. Chem. Ref. Data. 18 (1989) 641.

**Prediction of the long-range correlation length for Ar fluid in the near critical point via LIR equation state**

H. Nikoofard, Z. Kalantar and B. A. Esmaili*

Faculty of Chemistry, Shahrood University of Technology, Shahrood, Iran

(Email: asma.esmaili@yahoo.com)

Key word: Supercritical fluid, correlation length, LIR, Argon fluid.**1. Introduction**

Super critical fluids have attracted industrial interest as media for separation and chemical reactions because of their striking behavior near the critical point. Direct information on the fluctuation phenomena is obtained by small-angle scattering experiments. The static structure factor, $S(k)$, is the fundamental quantity characterizing correlations among particles in the fluid. In this work, we have used LIR equation state for the direct correlation function (DCF), which is related to $S(k)$ by Fourier transformation. We have used linear expression for the core of DCF and defined a non linear expression for its tail [2]. In this work we have obtained $S(k)$ in low-angle for some states near the critical point and then we have calculated the correlation length, ζ , for this region using the reduced bulk modulus data.

2. Methods

We used Maple 11 program package to obtain our values.

3. Results and Discussion

Since the DCF is always short-range at wide range of thermodynamic states, even near the critical point, we may use the small- k expansion of $c(k)$ for this region

$$c(k) = c(0) + c_2 k^2 + c_3 |k|^3 + c_4 k^4 + \dots \quad (1)$$

Where both c_2 and c_3 involves the two and three-body potentials and c_4 and higher terms will be neglected. Also, in simple liquid near the critical point, one can obtain ζ from the coefficient of c_2 by:

$$\zeta^2 = -\rho c_2 S(0) \quad (2)$$

Where $S(0)$ is the long-wave length limit of $S(k)$.

In order to obtain c_2 it is convenient to plot the quantity of $\lambda(k)$ defined as,

$$\lambda(k) = \frac{[c(k) - c(0)]}{k^2} = c_2 + c_3 |k| + \dots \quad (3)$$

Over the range of k where $\lambda(k)$ is linear versus k . By having ε_{eff} and σ we may obtain $c(r)$ then we calculate $c(k)$ and $S(k)$ at low- k from it and ζ may be predicted.

The OZ theory predicts $S(k)$ behavior for sufficiently small values of k and near the critical point the behavior of $S(k)$ should be given by,

$$\frac{1}{S(k)} = \frac{1 + \zeta^2 k^2}{S(0)} \quad (4)$$

According Fig.1, the behavior of $S(k)$ at low- k shows correctly the O-Z behavior, in which, $S(k)$ has a minimum at small k region.

According to Fig.2, we can see a good linear behavior for $\lambda(k)$ versus k , this linearity is depending on the thermodynamic states of system. Finally, by considering the values of c_2 and $S(0)$ for different states, we have calculated the correlation length Table 1.

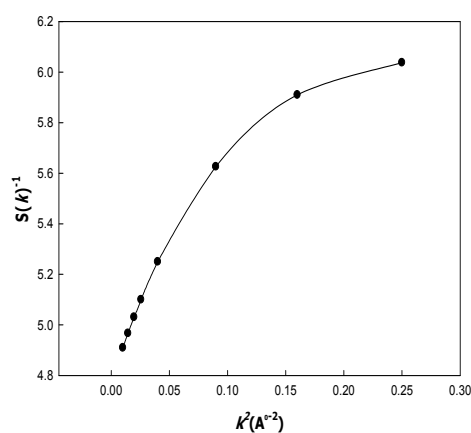


Fig.1. The Ornstein-Zernik plot for Ar fluid, at temperature=152K, density=28.435(mol/L).

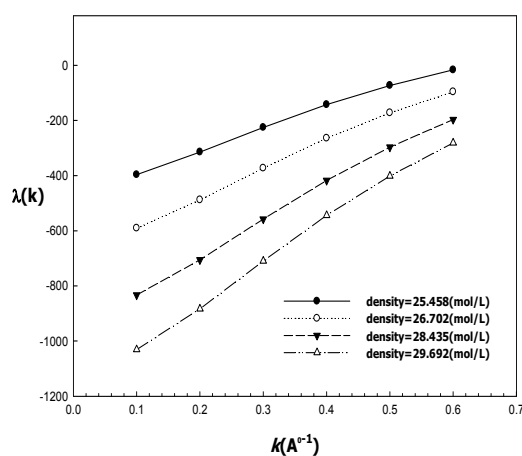


Fig.2. Theoretical results for $\lambda(k)$ versus k , for Ar fluid along Temperature=152K for different densities.

Table 1. The coefficients of small k -expansion of $c(k)$ for Ar fluid at Temperature=152K.

Density(mol/L)	c_2	c_3	ζ
25.458	-465.572	773.823	1.223
26.702	-683.399	1008.400	1.517
28.435	-955.980	1299.528	1.852
29.692	-1177.753	1530.888	2.136

4. Conclusions

In this work, we have presented a method for calculating of the correlation length in mono atomic fluids by using LIR equation state. We find that the coefficients of small- k expansion of $c(k)$ and show that plot of $\lambda(k)$ is linear *versus* k . It is found that this linear range is developed when the critical point approaches. For all thermodynamic states the value of c_2 is negative which verifies a minimum for $S(k)$ in small- k region.

References

- [1] E. Keshavarzi, H. Nikoofard, A. A. Rostami, Phys. Soc. Jpn. 73 (2004) 374.
- [2] E. Keshavarzi, G. A. Parsafar, Phys. Soc. Jpn. 70 (2001) 1979.
- [3] R. B. Stewart, R. T. Jacobsen, Phys. Chem. Ref. Data. 18 (1989) 641.

**Bulk and surface properties of formate esters by the application of SAFT-VR and molecular dynamics simulation**

Mohammad Hadi Ghatee and Fatemeh Moosavi

(Department of Chemistry, Shiraz University, Shiraz 71454, Iran)

(E-mail: ghatee@susc.ac.ir, fmoosavi_b@yahoo.com)

Keywords: Density functional theory, Vapor-liquid coexistence, Statistical associated fluid theory, Vapor pressure, Molecular simulation, Surface thickness.

1. Introduction

One statistical method to investigate the phase behavior of the complex fluids is statistical associated fluid theory (SAFT), which is based on the thermodynamic perturbation theory of Wertheim [1]. The molecular SAFT equation of state has been applied on many systems including non-polar, polar, and associating fluids [2] and the results are in the excellent agreement with the experiments.

The original SAFT equation has been developed by adding modifying dispersion term of the equation (simplified SAFT), treating the molecules as chains of hard sphere (HS) segments with van der Waals interaction (HS-SAFT), incorporating Lennard-Jones (LJ) interaction in the context of the thermodynamic perturbation theory to formulate the equation for the LJ fluids (LJ-SAFT), extending the equation of state to obtain an equation for chains of square well (SW) statistical associating fluid theory (SW-SAFT) molecules [3-5]. Originally, the validity of SW-SAFT equations was limited to a square well molecule. By providing an additional parameter, which characterized the range of the attractive part of the monomer-monomer potential, Gil-Villegas *et al.* [6] proposed a general version of SAFT for chain molecules formed from hard-core monomers with an arbitrary potential of variable range (VR). The adequacy of the SAFT-VR equation has been reported by different studies [7,8] that describe the phase equilibria of pure and mixtures containing the SW chain with a variable range potential.

We apply the advantageous SAFT-VR-DFT to long chain esters, butyl, pentyl, heptyl, and nonyl formate, for the understanding of their corresponding liquid-vapor behavior. In conjunction with the molecular dynamics simulation of the interface, the bulk and interfacial properties are studied.

2. Theory

The bulk Helmholtz free energy, A , of a square well associating chain molecule according to the SAFT-VR is obtained via the sum on the ideal contribution of the Helmholtz free energy and the residual contribution of A [9]:

$$\frac{A}{Nk_B T} = \frac{A_{\text{ideal}}}{Nk_B T} + \frac{A_{\text{mono}}}{Nk_B T} + \frac{A_{\text{chain}}}{Nk_B T} + \frac{A_{\text{assoc}}}{Nk_B T} \quad (1)$$

The corresponding contributions to the free energy are due to the ideal fluid, the monomer segments, chain formation, and intermolecular association, respectively. Terms of the Eq. (1) depend on the molecular parameters of the variable range potential. The variable range potential constitutes the simplest fluid model including both repulsive and short-range attraction,

$$\text{which is given by } \varphi(r) = \begin{cases} \infty & r \leq \sigma \\ -\varepsilon & \sigma < r < \lambda\sigma \\ 0 & r \geq \lambda\sigma \end{cases}, \text{ where its parameters } \varepsilon, \sigma, \lambda, \text{ and } m \text{ are well depth, diameter of segments, well}$$

width, and number of tangent spherical segments, respectively. A new developed method to calculate these parameters is group contribution method [10].

Using standard relationships, the thermodynamic properties including pressure, chemical potential, and grand potential can be obtained from the Helmholtz energy.

The phase equilibrium conditions for the coexisting liquid and vapor phase require the temperature, pressure, and chemical potential in each phase to be equal. Under the coexisting condition for liquid-vapor, it is possible to select the densities of liquid and vapor and thus to study the interfacial properties.



3. Results and discussion

By using SAFT and the square-well potential between m segments of every ester, the liquid/vapor coexistence densities are calculated. Predicted critical temperature, critical pressure, and critical density of the formates are reasonably in good agreement with the experiment.

The main factors of liquid/vapor equilibrium are temperature, pressure, and chemical potential, which are responsible for thermal, mechanical, and material equilibrium between the coexisting phases. These form the key factors for the calculation of liquid/vapor properties by DFT method, which must be maintained and evaluated accurately. By establishing mechanical and thermal equilibration, we can calculate the vaporization enthalpy by predicting saturated vapor pressure. The value of vapor pressures for the formates is in accord with the literature data [11] as the figures show.

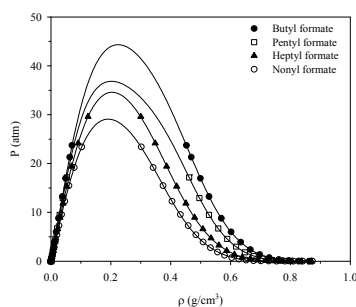


Figure 1. The vapor pressure versus density by SAFT-VR of vapor-liquid coexistence.

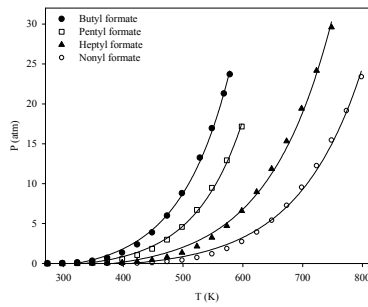


Figure 2. The predicted vapor pressure SAFT-VR of vapor-liquid coexistence.

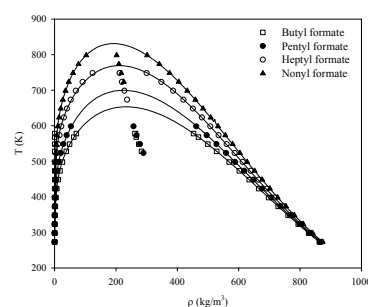


Figure 3. Theoretical predictions and SAFT-VR results of vapor-liquid coexistence.

The density profile of the interface is the main part of the calculations in the interface. In this small region, the surface thickness can be obtained from the known densities of the liquid and vapor bulks. Properties of the interface are calculated from the gradual changes of liquid properties to the vapor properties in the interfacial region. Alongside these studies, the interfacial properties were simulated by classical molecular dynamics simulation. From the simulation results and the tangent hyperbolic shape of the density profile, coexistence densities and surface thickness are calculated.

4. Conclusion

Using SAFT-VR EOS the properties of coexisting liquid/vapor of long chain formates have been predicted. The accuracy of this method depends highly on the elaborated molecular parameters. The same rectilinear diameter is applied almost symmetrically to all formates. The estimated densities at low temperature are in good agreement with the literature and molecular dynamics simulation. Estimated critical temperatures, pressures and densities are also in good agreement with literature and simulations. The estimated surface thickness from the simulation results can be used securely to predict the surface tension by SAFT-VR EOS reasonably well.

References

- [1] Wertheim, M. S. J. Chem. Phys. 87 (1987) 7323.
- [2] Tavares, F. W. Chang, J. Sandler, S. I. Fluid Phase Equilibria 140 (1997) 129.
- [3] Fu, Y-H. Sandler, S. I. Ind. Eng. Chem. Res. 34 (1995) 1897.
- [4] Chapman, W.G. Sauer, S. G. Ting, D. Ghosha, A. Fluid Phase Equilibria 217 (2004) 137.
- [5] Gross, J. Sadowski, G. Ind. Eng. Chem. Res. 40 (2001) 1244.
- [6] Gil-Villegas, A. Galindo, A. Whitehead, P. J. Mills, S. J. Jackson, G. Burgess, A. N. J. Chem. Phys. 106 (1997) 4168.
- [7] Li, J. He, H. Peng, C. Liu, H. Hu, Y. Fluid Phase Equilibria 276 (2009) 57.
- [8] McCabe, C. Jackson, G. Phys. Chem. Chem. Phys. 1 (1999) 2057.
- [9] Gloor, G. J. Jackson, G. Blas, F. J. del Rio, E.M. de Miguel, E. J. Chem. Phys. 121 (2004) 12740.
- [10] Vijande, J. Pineiro, M. M. Mosteiro, L. Legido, J. L. Fluid Phase Equilibria 212 (2003) 165.
- [11] NguyenHuynh, D. Falaix, A. Passarello, J.-P. Tobaly, P. de Hemptinne, J.-C. Fluid Phase Equilibria 264 (2008) 184.



Quantum Chemistry





Investigation of gap energy in sensitized dye and some derivatives of N3 by DFT Method

L. Tavakolizadeh and M. Oftadeh

Department of chemistry, Payame Noor University (PNU), Isfahan, Iran

(Email: ltavakolizadeh@gmail.com)

(Email: m_oftadeh@pnu.ac.ir)

Keywords: Gap energy, DFT, Sensitized dye, Optical properties.

1. Introduction

One of the subjects of the quantum chemistry is conversion of solar energy into electricity in dye-sensitized solar cells (DSSCs) [1]. It has been investigated for many years by using chromophore properties. Ruthenium polypyridyl complex is one of the conventional dyes which shows optical adsorption spectra [2] related to the size and conjugation of linkers to the surface at semiconductor TiO_2 . N3 dyes, $\text{Ru}(4,4'\text{-dicarboxy-2,2'-bipyridine})_2(\text{NCS})_2$, is probably one of the most well known of sensitized dye which transfers electron by adsorbing sunlight followed by injection electron to the conduction band of TiO_2 so that the gap energy will be increased. The electron transfer depends on different parameters, for example type of attaching such as bridge, chelating, mono dentate, etc [3, 4]. The present study investigates the role of acceptor and donor groups on N3 dyes and also the variation of gap bonds.

2. Method

The full geometry optimization and investigation electronic properties of N3 dyes and some derivatives are performed by using density function theory [1]. The results were obtained by DFT and support by HF calculations. The singlet ground state geometries were fully optimization at the B3LYP/3-21G** level of theory. All calculations performed with Gaussian 98/03 program. In the present research, the variation of gap energies were investigated by insertion of electron donor groups such as: CH_3 , C_2H_5 , NH_2 , $\text{N}(\text{CH}_3)_2$ or electron acceptor groups such as F and Cl on the α position related to carboxylat on N3 dye. All calculations were first done in gas phase then for comparison of the results they were done in solvent. In this work PCM model of ethanol ($\epsilon=25$) and acetonitrile ($\epsilon=37$) were used.

3. Results and discussion

The computational results of density functional theory by B3LYP method and 3-21G** basis set in gas and solvent phases are shown in Table 1. The Mulliken charges of the CO of carboxylat group which besides of X-substituted of the N3 dyes. $Q(\text{CO})$ and $Q(\text{Ru})$, are presented in Table 2. This table shows $Q(\text{CO})$ for N3 dyes is almost independent of the environment. The results show that the substituted groups do not have an important role in transferring of wavelength absorption from UV to visible region. In addition the groups have a few influences to decrease on gap energy of N3. In solvent environment the energy silently decreases as the difference between gas and solvent environment is about 0.5 eV for all groups. The solvent effect upon the gap energy variation occurs through interaction with dye and ethanol or acetonitrile molecules. This interaction has an effective on charge distribution upon carboxylat atoms. On the other hand, the carboxyl groups have an important role in dye adsorption on the TiO_2 surface. The calculated absorption thresholds are shown in Table 1. It indicates a significant influence by the environment on the optical properties of these complexes, notably the wavelength of N3 complexes are shifted by inclusion of solvent from 830 to 580 nm. The range of variation optoelectronic properties are taken as a model for complexes with along conjugated whether the theoretical modeling is capable of providing a physically realistic description of the complexes with extended conjugation.

4. Conclusions

In order to significant experimental efforts to develop DSSCs and related photo electrochemical devises [2], the quantum chemical calculations was performed to provide a better theoretical understanding of the basic physical and chemical processes at dye-sensitized semiconductors. The modified of N3 dyes is seen to have high effects on calculated electronic structure [3]. This gives rise to significant changes in the absorption spectra as compared to the N3 dyes. The optical absorption spectra are related to environment and probably are not related to the type of X-substituted groups.



Table 1. The calculated HOMO, LUMO, Gap Energy, and absorption threshold by DFT at B3LYP/3-21G** level of theory for N3-X dyes (X is the substituted groups by one of the hydrogen on pyridine beside of carboxylat group) in gas and ethanol and acetonitrile phases.

X	Gas Phase				Ethanol				Acetonitrile			
	HOMO	LUMO	GAP Eng. (ev)	λ (nm)	HOMO	LUMO	GAP Eng. (ev)	λ (nm)	HOMO	LUMO	GAP Eng. (ev)	λ (nm)
H	-0.106	0.108	1.494	830	-0.198	-0.120	2.105	620	-0.199	-0.120	2.1355	581
CH ₃	-0.173	-0.117	1.508	822	-0.194	-0.118	2.082	595	-0.196	-0.118	2.109	588
C ₂ H ₅	-0.163	-0.105	1.565	792	-0.187	-0.116	1.913	648	-0.191	-0.117	2.008	614
NH ₂	-0.170	-0.112	1.574	788	-0.187	-0.115	1.978	626	-0.188	-0.115	1.996	621
N(CH ₃) ₂	-0.161	-0.102	1.609	770	-	-	-	-	-0.159	-0.106	1.462	848
F	-0.174	-0.119	1.498	828	-0.194	-0.124	1.977	627	-0.198	-0.122	2.059	602
CL	-0.174	-0.120	1.479	838	-0.193	-0.123	1.894	654	-0.198	-0.124	2.008	618

Table 2. The Mullikan charge analysis of CO group and of Ru by DFT at B3LYP/3-21G** level of theory

X	Gas		Ethanol		Acetonitrile	
	Charge on CO	Charge on Ru	Charge on CO	Charge on Ru	Charge on CO	Charge on Ru
H	1.151	0.966	1.170	0.919	1.155	0.910
CH ₃ -	1.161	0.946	1.182	0.912	1.183	0.910
C ₂ H ₅ -	1.168	0.961	1.181	0.923	1.184	0.916
NH ₂ -	1.212	0.932	1.227	0.915	1.228	0.913
N(CH ₃) ₂ -	0.895	0.911	-	-	0.8972	0.893
F	1.145	0.967	1.168	0.923	1.171	0.916
CL	1.142	0.968	1.159	1.182	1.164	0.916

References

- [1] M.J. Lundqvist, Ph.D thesis, Uppsala University, Sweden, (2006).
- [2] A. Aghtar, M.S.C thesis, Payamnoor University, Shiraz, Iran, (2009).
- [3] M.J. Lundqvist, E. Galoppini, G.J. Meyer, T. Persson, J. Phys. Chem. A. 111 (2007) 1487.
- [4] M. F. Iozzi, Ph.D Thesis, Napoli University, Italy, (2006).

**Are resonance-assisted hydrogen bonds 'resonance assisted'? quantum chemical study**

M. Farrokhnia and A.H. Pakiari*

Chemistry Department, College of Sciences, Shiraz University, Shiraz, Iran 71454

(Email: pakari@shirazu.ac.ir)

(Email: farrokhnia.m@gmail.com)

Keywords: Resonance assisted hydrogen Bond, QTAIM, NBO.**1. Introduction**

As the result of importance of hydrogen bond in natural science, many researchers have devoted their attention to study different aspects of this interaction. Their attempts relate particularly to crucial roles of H-bond in biological systems, such as molecular recognition that could be a basis for the creation of life [1-3]. Very strong hydrogen bonds are the most interesting features of hydrogen bond's categories which have essential roles in biochemical reactions and enzyme catalysis as transition state [4, 5]. Very strong hydrogen bonds have been widely studied, both experimentally and theoretically [6, 7]. This type of H-bonds has been classified to three fundamental types by Gilli: negative charged assisted hydrogen bond $[(-) \text{CAHB}]$, positive charged assisted hydrogen bond $[(+)\text{CAHB}]$ and resonance assisted hydrogen bond $[\text{RAHB}]$ where the H-bond donor and acceptor are connected through π -conjugated double bonds [7]. Alkorta et al [8], have investigated some examples of resonance assisted hydrogen bonds by theoretical NMR study. Their computed results show that the stronger intramolecular hydrogen bonds in unsaturated compounds is directly associated with the σ -skeleton of the molecule that allows the two heteroatoms (the HB donor and the HB acceptor) to be in closer proximity than in the saturated ones and the NMR properties of these molecules do not receive significant contributions from resonance.

In the current research, the main purpose is to study the influence of π electron delocalization and hyperconjugation on the strength of H-bond in addition to study the nature of heteroatom RAHB in two different categories of compounds by means of Quantum Theory of Atoms in Molecules (QTAIM) [9] and Natural Bond Orbital (NBO) analysis [10].

2. Method

The calculation of molecular geometries and their electronic wave functions have been performed using Gaussian 2003 series of programs [11]. Geometry optimization was carried out at B3LYP/6-311++G**[12, 13] level of theory. Frequency analysis was also performed for the structures to make sure that they are minimum structures. QTAIM was applied to obtain electronic parameters of our interested systems. NBO program also was used for studying the details of the hyperconjugation mechanism of methyl substituents by mainly focused on charge transfer between donor and acceptor orbital participating in hyperconjugation. The stabilization energy $E(2)$ associated with charge transfer between donor (i) and acceptor (j) can be evaluated by second-order perturbation theory analysis of the Fock matrix.

The degree of conjugation has been measured by a generalized conjugation index ζ defined by the difference in length between the longest and shortest carbon-carbon (carbon-nitrogen) bonds namely $C_1=C_2$ ($C_1=N_2$) and C_2-C_3 (N_2-C_3) ones.

3. Results and Discussion

We have studied several systems which contain heteroatom RAHBs in both enol and keto forms. Our species can contain oxygen, nitrogen, sulfur and phosphor. In accordance with our computational results, the enol form of $\text{O}-\text{H}\cdots\text{N}$ is the strongest one and its stabilization energy is approximately 17.30 kcal/mol. Hence, we have restricted our study to two different categories of compounds which contain $\text{O}-\text{H}\cdots\text{N}$ RAHBs. Schematic figures of investigated systems are summarized in Fig 1. For inspecting the influence of electron delocalization on the strength of H-bond and its stabilization energy, distinguishable types of substituents have been selected.

The effect of hyperconjugation will be discussed here for species with CH_3 substituents in both positions Q and R (or S and T). The both cases of hyperconjugation can be detected in these molecules, though, the primary hyperconjugation has noticeable role in comparison with the secondary case, so that the $\sigma \rightarrow \pi^*$ donor-acceptor interaction has more than 67% portion in q_{CT} . These charge transfers can be divided into two categories. The first category is the charge transfer from C-H belonging to methyl connected to the core system in Q (or S) position. This type of charge transfers clearly cause to increase electron density in core system, which make stronger hydrogen bond. The second category of hyperconjugative charge transfers are from C-H belonging to methyl connected to the core system in R or (T). This type of charge transfer causes to

increase charge of N_4 , and therefore, make N_4 as better H^+ acceptor and finally it creates stronger hydrogen bond. Hence, hyperconjugative charge transfer can help to make stronger hydrogen bond in the species include methyl groups.

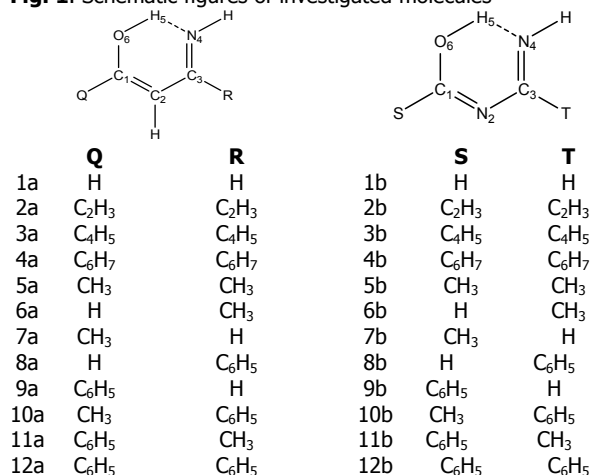
The stabilization energy related to intramolecular H-bonds has been estimated by using the local potential energy density proposed by Espinosa [14]. The nature of this hydrogen bond $N_4 \cdots H_5$ for all compounds is partially covalent and partially electrostatic from the results of QTAIM. As the value for H becomes more negative, the percentage of covalent character will increase, and the hydrogen bond is getting stronger.

There are three different ways to investigate if this stabilization is as the result of resonance-assisted processes or not. 1- Degree of conjugation (ζ), 2- electron delocalization index (EDI) and 3- ellipticity (ϵ). There is no good correlation between ζ and HB-strength in both categories and regression coefficient equal to 0.27 and 0.13 in *a* and *b*. Electron delocalization index (EDI) of two conjugated bonds decrease. Although the differences between $C_1=C_2$ ($C_1=N_2$) EDI and C_2-C_3 (N_2-C_3) EDI reduce too, it is expected that if substituents amplify the HB-strength by reinforcing the delocalized electron in core systems, C_2-C_3 (N_2-C_3) EDI should be increased. Finally, Ellipticities results fail badly and there is bad correlation between $\epsilon_1 - \epsilon_2$ and HB-strength. R^2 coefficients equal to 0.44 and 0.40 in categories *a* and *b*. From the results of these three parameters, it is evident that there is not very strong relation between amount of delocalized electrons in substituents and conjugation in core system. It seems that they affect HB stabilization in the other way rather than resonance-assisted ones.

4. Conclusions

Three different groups of substituents have affected the HB-strength and increased it. However, geometrical properties in addition to QTAIM analysis didn't show participation of conjugation with HB-strength increases and all the calculated parameters, which can reveal the degree of π -delocalized electron in core system, have no good correlation with HB-strength. It is evident from the results, the increase of HB-strength in this special category of compounds is more affected by structural factors rather than resonance assisted procedure. Geometrical results suggest that substituents allow the HB donor and acceptor to be in closer vicinity and this cause to have stronger HB.

Fig. 1. Schematic figures of investigated molecules



References

- [1]. J. M. Lehn, *Supramolecular Chemistry*; Verlag-Chemie: Wein-heim, Germany 1995.
- [2]. F. Teda, *Biorg. Chem.* 19 (1991) 157.
- [3]. R. Jr. Rebek, *Science*. 235 (1987) 1478.
- [4]. P. A. Frey, S. A. Whitt, J. B. Tobin, *Science* 264 (1994) 1927.
- [5]. S. Vishveshwara, M. S. Madhusudhan, J. V. Jr. Maizel, *Biophys. Chem.* 89 (2001) 105.
- [6]. P. Gilli, V. Bertolasi, L. Ferretti, L. Antonov, G. Gilli, *J. Am. Chem. Soc.* 127 (2005) 4943.
- [7]. M. G. Viloca, A. G. Lafont, J. M. Lluch, *J. Am. Chem. Soc.* 121 (1999) 9198.
- [8]. I. Alkorta, J. Elguero, O. Mo, M. Yañez, J. E. Del Bene, *Chemical Physics Letters* 411 (2005) 411–415.
- [9]. R. F. W. Bader, *Atoms in Molecules: a quantum theory*, Oxford, UK: Oxford university press, 1990.
- [10]. A. E. Reed, L. A. Curtiss and F. Weinhold, *Chem. Rev.* 88 (1988) 899.
- [11]. Frisch et al. *Gaussian 03, Revision B.04*; Gaussian, Inc., Pittsburgh PA, 2003.

**Intramolecular hydrogen bond and tautomeric preference in thioaminoacrylaldehyde**

A. Nowroozi*, M. Poorsargol, M. Shibaninia and P. Mohammadzadeh Jahani

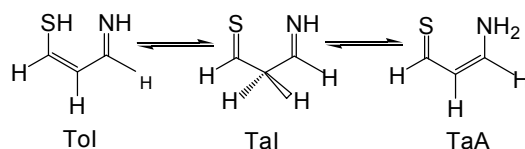
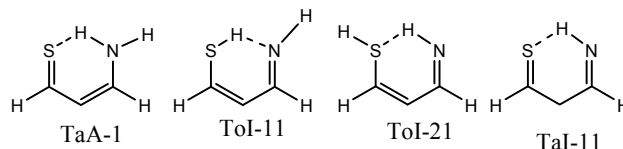
Department of Chemistry, Faculty of Science, University of Sistan and Baluchestan, P.O. Box 98135-674, Zahedan, Iran

(Email: Poorsargol.mahdiye@yahoo.com)

Keywords: Thioaminoacrolein, Intramolecular hydrogen bond, ab-initio, AIM and NBO.**1. Introduction**

Hydrogen bonding is one of the most important concepts in chemistry because it is decisive to understand many different interactions both in the gas phase and condensed media [1]. A particular subject is represented by resonance assisted hydrogen bond (RAHB), which frequently observed in biological systems. In RAHB systems, the intramolecular hydrogen bond and π -electron delocalization are coupled. Gilli et al. have proposed the resonance assisted hydrogen bond effect present in the chelated systems as well as in characterizing the strength of the hydrogen bond [2-3]. The consequences of the π -electron delocalization within the chelated forms are as follows: (I) the shortening of A...B distance, in A-H...B unit; (II) the strengthening of hydrogen bond; (III) the equalization of the corresponding bonds, such as C-C and C=C.

Thioaminoacrolein (TAMAC) is the simplest molecule, which involved in asymmetric NH...S and N...HS intramolecular hydrogen bonds and strongly coupled with π -electron delocalization. Theoretically, TAMAC has 28 different possible conformers. In view of functional groups, three classes of tautomers, Thial-Amine (TaA), Thiol-Imin (ToI) and Thial-Imine (TaI) which interconvert by tautomeric equilibriums (see Fig. 1) with 4, 16, 8 conformers, respectively. The existence of various intramolecular hydrogen bond (see Fig. 2) and variety of conformers are two important aspects which specify this molecule for more considerations.

**Fig.1.** Tautomeric equilibrium in TAMAC.**Fig.2.** Various of conformers contain Intramolecular hydrogen bond.**2. Methods**

Intramolecular hydrogen bonds existing for tautomers of Thioaminoacrolein have been studied with the use of B3LYP, MP2, G2MP2 and G3 methods and the most extended basis set, 6-311++G(d,p). The ab initio calculations of the present study were performed using the Gaussian 03 series of programs. The natural bond orbital (NBO) [4] and quantum theory of atoms in molecules (QTAIM) [5] were applied as a powerful approach for evaluation of the hydrogen bond strength in the chelated conformer (TaA-1, ToI-11, ToI-21 and TaI-11) of TAMAC.

3. Results and discussion

The hydrogen bond energy is the most important characteristics of the HB systems, which strongly depend on the choice of the reference state. The hydrogen bond energy in NH...S systems can be evaluated by the related rotamers method (RRM) [6]. The RRM hydrogen bond energy at various levels of theory for TaA-1 form is greater than ToI-11 and ToI-21. Our theoretical calculations reveal that the Thial-Amine (TaA) conformeric group is more stable than the Thiol-Imin (ToI) and Thial-Imine (TaI) ones. The results population analysis of TaA conformer for TAMAC show that the origin of tautomeric and conformational preference is mainly due to the π -electron delocalization, especially the charge transfer between the $\pi_{C=C}$ and $\pi_{C=S}^*$.



References

- [1] Grabowski, Hydrogen Bonding, New Insights, Springer, Berlin, 2006.
- [2] P. Gilli, F. Belluchi, V. Ferretti, V. Bertolasi, J. Am. Chem. Soc. 111 (1989) 1023.
- [3] V. Bertolasi, P. Gilli, V. Ferretti, G. Gilli, J. Am. Chem. Soc. 113 (1991) 4917.
- [4] A. E. Reed, L. A. Curtis, F. A. Weinhold. Chem. Rev. 88 (1988) 899.
- [5] R. F. W. Bader, Atoms in Molecules. A Quantum Theory, Clarendon, Oxford, U.K., 1990.
- [6] A. Nowroozi, H. Raissi, F. Farzad, J. Mol. Struct. (Theochem). 730 (2005) 161.

**DFT investigation of donor-acceptor in the charge transfer molecular complexes of****C₃S₃H₆, with I₂, IBr, ICl, Br₂ and Cl₂**

M. Moghadari and M. Oftadeh

Department of chemistry, Payame Noor University (PNU), Isfahan, Iran

(Email: m_moghadari@yahoo.com)

Keywords: Charge transfer, Complexation, Dihalogen, Donor-acceptor, DFT.**1. Introduction**

Among all the charge transfer complexes M-XY, where M is charge donor lewis base and XY is either a homo or a hetero-nuclear charge acceptor dihalogen, those having C₃S₃H₆, C₄S₄H₈, and C₆S₃H₁₂ as n-donor lewis base are important in the studying of interaction between the thianes and σ -acceptors in dichloromethane, trichloromethane and tetrachlormethane solutions [1]. The remarkable stability of these complexes, which still pose a challenging problem to theoreticians, had also to be taken into account [2]. To aid in the understanding of intermolecular charge-transfer complexation, numerous computational simulations have been attempted on I₂ with electron donor compounds, but there is not any publications on such interaction between I₂ and thrithiane compounds. Within this context, density functional theory (DFT) and MP2 offer an alternative treatment of electron correlation effects with respect to the more traditional molecular orbital theory, and it has recently been suggested to be a good choice for the study of difficult problems in general and charge-transfer complexes in particular. Consequently in this paper, we present a detailed calculation using DFT based methods of the charge-transfer complexes in particular [3-5].

In this paper, we calculate the properties of the charge-transfer complexes between C₃S₃H₆, as donor and I₂, Br₂, Cl₂, IBr and ICl as acceptor for ground and singly excited states in gas phase using DFT based method.

2. Method

The electronic molecular structure calculations performed at the restricted B3LYP hybrid method level of theory using the Gaussian 98. The B3LYP hybrid method was employed in combination with different basis sets for included various atoms. The 6-31G** basis set was used for Cl, Br, S, H and C, the 3-21G** basis set was used for I with GEN keyword. The full geometry optimizations of the s₁ state were carried out at the CIS/6-31G** level as well as CIS/GEN level. The excited state properties were also calculated in the gas phase by the optimized geometries.

3. Results and discussion

The thermochemical quantities and the natural charges based on Mulliken analysis on the atoms accompanying the S(1)-X band distances and S(1)-X-Y angles for the two electronic states of complexes between C₃S₃H₆, and I₂, Br₂, Cl₂, ICl and IBr are listed in Table 1. The complexation enthalpy and Gibbs free energy at 298 K represents the energy differences in the gas phase between the molecular adduct and separated fragments.

With increasing of electronegativity of outer halogen (Y in M-XY), the distances between internal halogene (X in M-XY) with sulfur atom (S1-X) decrease, the charge on S(1) atom (the nearest S atom from inner halogen) increases (more positive), the charge on inner halogen increase (more positive). All of three complexes are planner. On the other hand, the charge on S(1) is more positive than on X (inner halogen). So the charge transfer from I-Y to C₃S₃H₆ is occurred.

The analysis of HOMO-LUMO energy levels of these complexes showed that the HOMO level of I-Y is upper than of S(1) atom. So this charge transfer direction is confirmed. The data for Br₂ and Cl₂ complexes show such charge transfer phenomena from inner halogen to S(1) atom. This effect is more high than three I-Y complexes because of more negatively charge on inner halogen and more positively charge on S(1) atom.

The excited complexes are nonplanner and there is not any charge transfer. However in solvent or the other conditions such electron inner transfer will be happen.

The calculated enthalpies and Gibbs free energies of complexation will be more negative with decreasing of the S(1)-X distances form I₂ to ICl. Thus, the C₃S₃H₆-ICl is more stable than the others. The complex C₃S₃H₆-Br₂ is the most stable in comparison with the others. The formation Gibbs free energies of the complexes in ground state show the thermodynamic



stability of the complexes are as $I-Cl > I-Br > I-I$ and $Br_2 > Cl_2 > I_2$. The excited states of the complexes are unstable in gas phase.

Table 1. Calculated complexation enthalpies, Gibbs free energies (ΔH_f and ΔG_f), the natural charges on the atoms based on Mulliken analysis, S(1)-X and X-Y bonding distances (in Angstrom) and S(1)-X-Y angles of M -XY complexes compared with of $C_3S_3H_6$ by B3LYP/6-31G**

X2	ΔH_f (KJ/mol)	ΔG_f (KJ/mol)	Charge on C(2)	Charge on S(1)	Charge on X(inner)	S(1)-X	X-Y	S(1)-X-Y Angle
$C_3S_3H_6$			-0.1798	-0.0807				
Ground								
(I - I)	-4253.71	-4223.27	-0.4786	0.1513	0.0237	3.1425	2.7746	174
(I-Br)	-7178.39	-7128.83	-0.4803	0.1561	0.1302	3.0115	2.5899	175
(I-Cl)	-7185.54	-7149.81	-0.4817	0.1633	0.1134	2.8961	2.3879	174
(Br-Br)	-7178.39	-7169.87	-0.4857	0.1800	-0.003	2.8961	2.3879	182
(Cl-Cl)	-7189.62	-7158.76	-0.4851	0.1997	-0.038	2.8233	2.1234	181
Excited								
(I - I)	17737.75	17744.48	-0.5487	0.1789	0.0324	4.7654	3.0373	134
(I-Br)	12476.93	12653.17	-0.5477	0.1698	0.1899	4.6214	2.8764	136
(I-Cl)	9599.18	9634.32	-0.6024	0.2368	0.2989	4.8072	2.7806	
(Br-Br)	17527.01	10412.73	-0.5436	0.1689	0.0387	4.1229	2.6317	
(Cl-Cl)	4518.33	4576.65	-0.5434	0.1749	0.0207	4.3878	2.3964	135

4. Conclusions

The calculated electronic properties of ground and excited states of $C_3S_3H_6 \cdots I-X$ ($X=I, Br, Cl$) complexes were analyzed. The calculations show the I-X acts as electron donor and $C_3S_3H_6$ acts as electron acceptor. This is investigated by analyzing partial charges and complex geometries. The Mulliken charges on S at position 1 respect to molecule halide, I-X, show the intermolecular interactions, namely it is found that the I-X moiety transfer electronic charge to $C_3S_3H_6$. this conclusion is reached analyzing the $n_I \rightarrow \sigma^*C_3S_3H_6$ donor-acceptor interaction or charge transfer (CT) between the n_I lone pair and the antibonding $\sigma^*C_3S_3H_6$ natural orbitals. This phenomenon is unlike the publications about the other complexes accompanying CT.

References

- [1] A. Semnani, H. R. Pouretdal, M. H. Keshavarz, A. R. Firooz and M. Oftadeh, *Heterocyclic Communications*, 14 (2008) 205.
- [2] D. K. Payannis and A. M. Kosmas, *J. Molecular Structure (Theochem)* 851 (2008) 175.
- [3] A. Garcia, J. M. Elorza and J. M. Ugalde, *J. Molecular Structure (Theochem)* 501-502 (2000) 207.
- [4] H. Kusama and H. Sugihara, *J. Photochemistry and Photobiology A: Chemistry*, 187 (2007) 233.
- [5] M. Pavanello, A. F. Jalbout, B. Trzaskowski and L. Adamowicz, *Chem. Phys. Lett.*, 442 (2007) 339.

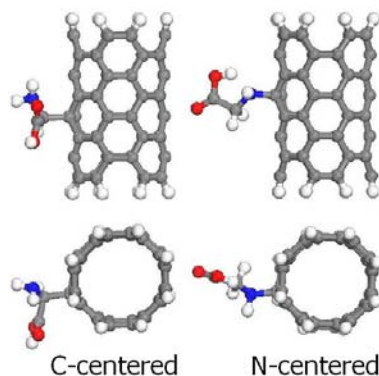
NQR studies of the glycine radical addition to the carbon nanotubesN. Noorani ^{a*}, H. Rahemi ^b^aDepartment of Chemistry, University of Payam - Noor, Urmia, Iran

(Email: nnorani1@yahoo.com)

^bDepartment of Chemistry, University of Urmia, 57159-165, Iran**Keywords:** DFT, NQR, Electric field gradient, Nuclear quadrupole resonance.**1. Introduction**

Carbon nanotubes (CNT) have attracted considerable interest in nanotechnology due to their unique shape. Their outstanding mechanical and electronic properties have made them promising materials for new applications such as nanoelectronic devices, fuel storage materials, and energy capacitors [1,2]. However, few applications have so far been reported in biology. The selective opening and closing [3] at the ends of nanotubes provide many opportunities of conducting experiments with biological macromolecules in nanoscale test tubes. One basic way to understand the interaction of nanotubes with biomolecules is by means of theoretical modeling. In this study, NQR tensors (EFG) were calculated at the sites of the oxygen, nitrogen and hydrogen nucleus in the Glycine and directly interacted Glycine radical on the walls of a (4,4) armchair carbon nanotube (CNT). The Glycine radical has two form isomers, among the possible isomers are the ones from which one hydrogen atom is abstracted either from (a or b carbon's atom) or the N-atom. The most stable geometries for complexes of the C- and N - radicals with (4,4) CNT are shown in Fig. 1. It is found that the N-centered Glycine radical binds strongly to the tube, having interaction energy of the 22 kcal/mol.

The electric field gradient (EFG) tensors arisen at the sites of quadrupole nuclei are important physical parameters to investigate the structural properties of molecules [4]. Those nuclei with spin angular momentum greater than one-half ($I > 1/2$) are quadrupole and have electric quadrupole moment, eQ , which can interact with the EFG tensors [5]. The strength of this interaction depends on the magnitude of eQ and the EFG eigenvalues.

**Fig. 1:** optimized structures of the clusters Glycine radicals – CNT.**2. Method**

Quantum chemical calculations were carried out at the level of density functional theory (DFT) using Gaussian 98 package of program [6]. B3LYP exchange-functional method and 6-311G* standard basis sets were employed in the EFG tensors calculations. NQR calculations on ¹⁷O, ¹⁴N and ²H nuclei EFG tensors were carried out on Glycine and the Glycine radical addition to carbon nanotube via density functional theory (see Table 1). However, to the best of our knowledge, there is no experimental NQR study on Glycine radicals – CNT in the literatures. The EFG tensors are calculated by equations 1 and 2.

$$C_Q \text{ (MHz)} = e^2 Q q_{zz} / h \quad (1)$$

$$\eta_Q = \left| \frac{q_{xx} - q_{yy}}{q_{zz}} \right| \quad (2)$$



3. Results and Discussion

The calculated EFG tensors at the sites of ^{17}O , ^{14}N and ^2H nuclei of the Glycine and the Glycine radical addition to carbon nanotube are shown in Fig. 1 and listed in Table 1. These positions were optimized at the theory level of DFT/BLYP/6-311G*. The magnitude of these changes for each nucleus depends on its contribution to the interactions. Therefore, more changes in each nucleus NQR parameter between the Glycine and the Glycine radical addition to carbon nanotube structures. Since both EFG tensors are originated by electronic environment at the sites of nuclei, it is expected that they undergo parallel changes in the clusters Glycine radicals – CNT. The most stable geometries for the complexes of the C- and N-radicals with the (4, 4) CNT are shown in Fig.1. It is found that the N-centered Glycine radical binds strongly to the tube, having interaction energy of the 22.1 kcal/mol. The $\text{C}_{\text{tube}} - \alpha\text{C}_{\text{glycine}}$ single bond is 1.61 Å, while the $\text{C}_{\text{tube}} - \text{N}_{\text{glycine}}$ is 1.50 Å. The calculated EFG tensors at the sites of ^{17}O , ^{14}N and ^2H nuclei in Glycine and the clusters Glycine radicals – CNT are discussed are given in Table 1. The C_Q values of ^{14}N reduce from the clusters glycine radicals – CNT to the Glycine while C_Q values of ^{17}O increase. η_Q values of ^{14}N and ^{17}O reduce from the clusters Glycine radicals – CNT to Glycine.

Table 1. The EFG tensors at the sites of ^{17}O , ^{14}N and ^2H nuclei for Glycine and Glycine radicals – CNT.

Nucleus	$C_Q(\text{MHz})$			η_Q			Experimental ^a	
	Glycine	$\text{C}_{\text{tube}} - \text{N}_{\text{glycine}}$	$\text{C}_{\text{tube}} - \alpha\text{C}_{\text{glycine}}$	Glycine	$\text{C}_{\text{tube}} - \text{N}_{\text{glycine}}$	$\text{C}_{\text{tube}} - \alpha\text{C}_{\text{glycine}}$	$C_Q(\text{MHz})$	η_Q
N	1.02	0.62	0.51	0.37	0.66	1.14	1.18	0.25
O	8.17	9.12	8.27	0.46	0.096	0.51	8.40	0.0
O-H	7.51	11.0	12.26	0.56	0.68	1.04	7.60	0.54

^a Experimental for Glycine [7,8]

4. Conclusions

The DFT/B3LYP/6–311G* optimizations of the Glycine radicals – CNT that the N -centered Glycine radical binds strongly to the tube is 22 kcal/mol. A systematic computational study on NQR of Glycine and Glycine radicals – CNT structure are presented by DFT calculations of EFG tensors at the sites of ^{14}N , ^{17}O and ^2H nuclei in Glycine and Glycine radicals – CNT. The C_Q values of ^{14}N reduce from the clusters Glycine radicals – CNT to the Glycine while C_Q values of ^{17}O increase and η_Q reduce.

References

- [1] M. Terrones, W. K. Hsu, H. W. Kroto, D.R.M.Walton, Topics in Current Chemistry 199 (1999) 189.
- [2] M.S Dresselhaus, G. Dresselhaus, P. C. Eklund, Science of Fullerenes and Carbon Nanotubes (Academic Press, 1996).
- [3] S. C. Tsang, Y. K. Chen, P. J. F. Harris, M. L. H. Green, Nature, 372 (1994) 159.
- [4] M.A. Rafiee, N.L. Hadipour, H. Naderi-mannesh, J. Comp. Aid. Molec. Des. 18 (2004) 215.
- [5] C.P. Slichter, Principles of Magnetic Resonance, Harper & Row, London,(1992) 15.
- [6] M.J. Frisch, *et al.*, GAUSSIAN 98 Revision A.7, Gaussian, Inc., Pittsburgh, PA, 1998.
- [7] K.J. Pike, V. Lemaitre, A. Kukol, T. Anupold, A. Samoson, A.P. Howes, A.Watts, M.E. Smith, R. Dupree, J. Phys. Chem. B 108 (2004) 9256.
- [8] R.A. Haberkorn, R.E. Stark, H.V.Willigen, R.G. Griffin, J. Am. Chem. Soc. 103 (1981) 2534.



A detailed study of the electronic structure of the sub-nano-sized cluster of Fe₃ and associative adsorption of N₂ to this cluster

A.H.Pakiari* and M.Mousavi

Chemistry Department, College of Science, Shiraz University, Shiraz 71545, Iran

(Email: fereshteh_mou@yahoo.ca)

1. Introduction

Clusters containing few up to a dozen or more metal centers can be considered as models mimicking metal surfaces with catalytically active centers. Definitive identification of the ground state of iron, in the gas-phase clusters containing few atoms, has been (and still is) the controversial topic for scientists. Nearly degenerate states and the corresponding small energy gaps make this ambiguity^{1,2}. It is not therefore too much of surprise that iron, in its various states of aggregation, has drawn considerable attention. we present a systematic DFT study of nitrogen adsorption on Fe₃ cluster at various converges (bridge-site, top-site and hollow-site). The aim is to develop a precise picture of the sub-nano-sized cluster structure of Fe₃ and energies of the N₂/Fe₃ systems, and further to elucidate the relative activity of adsorption sites on each of the N₂ site occupancy. Through NBO analysis of metal-ligand interaction, we derive the orbitals that participate actively in chemical interactions in this system and disclose basic features of the interaction between nitrogen molecule and iron cluster.

2. Method

Calculations been performed at the framework of DFT level being implemented with the Gaussian 03 program³. Exchange-correlation functional consists of BPW91, within the generalized gradient approximation (GGA)⁴. The basis sets for all atoms is 6-311+G*.The nature of metal-metal and metal-ligand bonds has been analyzed by means of NBO⁵ (natural bond orbital)and NRT⁶ (natural resonance theory) implemented in the program package GenNBO.

3. Results and Discussion

3.1. Fe₃ Cluster

As our preliminary effort, the equilibrium geometry of the iron trimer is investigated. In optimization processing, we consider the high multiplicity of iron cluster to find the lowest energy spin state. Our calculations show that the lowest energy state has the C_{2v} symmetry (isosceles triangle) for S=5 (where S is the net spin and 2S+1=11), and states with 2S+1=7, 9 and 13 are higher in total energy than the lowest energy state with multiplicity 11 by +0.89 eV, +0.26 eV and +0.33 eV, respectively.

To confirm the accuracy of our calculations to distinguish the lowest energy state of Fe₃ from several energy states which are found within a narrow energy range, we compare the performance of our method with experimental data that exists for electron affinity (EA) and ionization potential (IP) for the various Fe_n cores (n=2-6).

3.2. NBO Analysis for Fe₃ Cluster

NBO-based computational detects the presence of multiple bond (σ , π or δ) for this small cluster. It means that there are two triple bonds separately for Fe₍₁₎ – Fe₍₂₎ and Fe₍₁₎ – Fe₍₃₎, and one single bond for Fe₍₂₎ – Fe₍₃₎. Highly unsaturated structure of Fe₃ and a delocalization interactions of the parent reference structure (single NBO configuration) draw one's attention to the possible candidate structures to present the correct electronic structure of Fe₃. β -spin (minority spin) electrons are significantly more delocalized than α -spin (majority spin) electrons and the number of resonance structures are mainly due to the β -spin part. In β -spin part, the NRTSTR (natural resonance theory structure) specification gives three leading resonance structures. Our theoretical study of high-order bonds between Fe atoms in a triangle geometry can present a logical justification upon the interaction of some ligands such as N₂ with metal centers like Fe.

3.3. Adsorption patterns of N₂ on Fe₃ cluster

In this part of the study, the reaction of nitrogen with a bare Fe₃ cluster is investigated with special attention given to the most favored adsorption sites for nitrogen on the trinuclear of iron cluster. Different *probable* adsorption patterns on Fe₃ cluster, such as 1)bridge-site 2)hollow-site 3)top-site, are examined through optimization processes. In optimization processing, we also consider the high multiplicity which involves iron cluster and its probable reduction over the Fe₃N₂ complex formation to find the lowest energy state among all possible structures. Our calculations have revealed that among all nitrogen sites examined,



"bridge-site" is the most favorable site for N₂ adsorption on Fe₃ cluster. "Hollow-site" is not suited to chemically bind N₂ to Fe₃ cluster, and "top-site", through passing TS region, ends up the same optimized structure in "bridge-site". So, an effective chemical between Fe₃ cluster and N₂ can be generated only at the bridge, and that all of the other adsorption sites do not give chemical interactions of significance.

3.4. Interacting metal-ligand orbitals

In this part of the study, we examine N₂ adsorption on the metal centers and try to clarify the orbital interactions that underlie Fe₃N₂ complex. Polarization and charge transfer interactions, as consequences of the metal-ligand interactions, are reflected in slight shifts of geometry and charge distribution in both monomers of complex. The elongation of N-N bond length of this structure, 0.096 Å (relative to the isolated monomer), is of the removal of electron density from its bonding n-orbital and increase of electron density in its anti bonding π* orbital as a consequence of $n_{Fe(3)} \rightarrow \pi_{N-N}^*$ and $\pi_{N-N} \rightarrow n_{Fe(3)}^*$. The optimized complex of bridge site model (C_s symmetry), exhibits the characteristic N₂...Fe₃ tilted geometry over one edge of nitrogen ligand. The unequivalent intermolecular distances, d_{Fe(3)-N(4)} = 2.091 and d_{Fe(2)-N(5)} = 1.843 are indicative of the existence of distinct types of donor-acceptor interactions for two ends which are in consistent with the tilted geometrical structure for this complex.

Short-intermolecular distance: $n_{N(5)} \rightarrow n_{Fe(2)}^* (sp_x^{0.6} - sd_{xy}^{0.5})$

Long-intermolecular distance: a mutual interaction of $\pi_{N-N} \rightarrow n_{Fe(3)}^* (p_x - sd_{xy}^{1.92})$ and $n_{Fe(3)} \rightarrow \pi_{N-N}^* (d_{x^2-y^2} - p_x)$

Slopping path: $n_{N(5)} \rightarrow n_{Fe(2)}^* (sp_x^{0.6} - sd_{xy}^{0.5})$ and $n_{N(5)} \rightarrow n_{Fe(3)}^* (sp^{0.6} - sd_{xy}^{1.92})$

4. Conclusions

We have carried out a theoretical study on the nature of chemical bonding of Fe₃ cluster, as a building block of our study, and taking into account the delocalization character of the metal valence electrons, by NBO analysis. NBO-based computational detects the presence of multiple bond (σ, π or δ) for this small cluster. NRT analysis reveals that single NBO configuration can be considered as only one of the many alternative resonance structures contributing to the electronic distribution. In the second part, nitrogen adsorption on our small cluster of iron, at a set of coverage has been investigated. In bridge site of the adsorption pattern, N₂ has a significant bonding attraction while it has no significant contribution in the other adsorption patterns. Indeed, in this adsorption pattern, N₂ is completely activated, but not dissociated. In this geometrical structure (bridge-site) N₂ has a tendency to be tilted, in order to have the maximization of orbital amplitude in the direction of the bond to be formed. A detailed discussion of metal-ligand interaction show that the main factor governing in this interaction is the delocalized nature of the valence electrons. That is, in short intermolecular separation of Fe-N, the bonding situation is mainly due to the ligand→metal σ-donation of $n_{N(5)} \rightarrow n_{Fe(2)}^*$, whereas long intermolecular distance is involved with mutual interaction of metal→ligand and ligand→metal interactions. Nevertheless, back-donation property predominates over the donation and the net charge is from iron to nitrogen.

References

- [1] Chen, J. L.; Wang, C. S.; Jackson, K. A.; Pedeson, M. R. Phys. Rev. B (1991) 44, 6558.
- [2] Gutsev, G. L.; Khanna, S. N.; Jena, P. Phys. Rev. B (2000) 62, 1604.
- [3] Becke, A. D. Phys. Rev. A (1988) 38, 3098.
- [4] Glendening, E. D.; Weinhold, F. J. Comput. Chem., (1998) 19, 593. Glendening, E. D.; Weinhold, F. J. Comput. Chem., (1998) 19, 611. Glendening, E. D.; Badenhop, J. K., Weinhold, F. J. Comput. Chem., 1998, 19, 629.
- [5] Reed, A. E.; Curtiss, L. A.; Weinhold, F. Chem. Rev. (1988) 88, 899.

**A MP2 intermolecular potential energy surface for the CO-CO system**

M. Abbasinia*, M. R. Noorbala and M. Namazian

^aDepartment of Chemistry, Yazd University, Yazd, I. R. Iran

(Email: noorbala@yazduni.ac.ir)

Keywords: Intermolecular potential, CO-CO, Basis set superposition error, MP2.**1. Introduction**

Ab initio quantum mechanical calculations offer a way to obtain intermolecular potentials of the atomic and molecular systems of interest. This approach can be used to extract detailed information about the intermolecular potential energy surface (IPS), which is sometimes difficult or practically impossible by other methods [1]. In particular, in recent years, there have been extensive quantum computational studies on interactions of diatomic–diatomic systems [2–5].

2. Methods

Calculations of the IPS for CO–CO system were performed using MP2/aug-cc-pVTZ levels of theory based on the geometry presented in Fig. 1 for 7 values of each dihedral angle ϕ and θ_2 between 0 and 180° with a step size of 30°, and 64 values of separation (R) between the two CO monomers in the range of 1.7–8 Å. Because of similarity of the roles of the two orientation angles θ_1 and θ_2 in the interaction between the two CO molecules, θ_1 is kept fixed at 90° throughout this study. In these calculations, C–O bond length in the individual CO monomers was left relaxed and has been optimized at each point of the CO–CO geometry space. For all computations, GAUSSIAN 98 software package has been used.

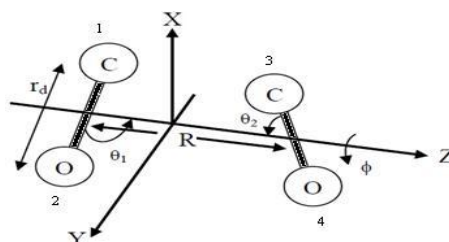


Fig.1. General representation of the CO–CO dimer geometry used in this study. C(1)–O(2) and C(3)–O(4) denote the two CO monomers 1 and 2. R is the distance between centers C(1) and O(3), that lies on the z-axis. θ_1 and θ_2 are the angles between monomers 1 and 2 bond axes and the z-axis, respectively. ϕ is the dihedral angle between the two monomers' bond axes.

The IPS of the CO-CO system has been calculated using supermolecular approach in which the interaction energy (E_{int}) between two CO monomers is calculated by $E_{\text{int}} = E(\text{CO-CO}) - 2 E(\text{CO})$.

The intermolecular interaction energy was corrected for BSSE using the counterpoise (CP) method of Boys and Bernardi [6].

$$E_{\text{Corr}} = \sum_{M=1,2} (E_M(\beta_D, r_D) - E_M(\beta_M, r_D)) \quad \text{B : Basis set , D: Dimmer, M: Monomer}$$

$$\Delta E = E_{\text{int}} - E_{\text{Corr}} \quad \text{and} \quad E_{\text{int}} = E_D(\beta_D, r_D) - \sum_{M=1,2} E_M(\beta_M, r_M)$$

3. Results and discussion

For brevity, only potential energy contour plots for $\theta_2 = 90^\circ$ with 6 value of ϕ between 30–180° have been demonstrated in Fig. 2 and the characteristics of potential energy curves such as: σ , the position of the potential minimum (R_e) and well-width $\Delta R_{1/2}$ of the potential curves and $\Delta R_{1/2}$ are reported in Table 1.

Table 1. Uncorrected and BSSE corrected well-depth D_e , position of the potential minimum R_e , well-width $\Delta R_{1/2}$ and hard sphere collision diameter σ calculated for the CO–CO system at MP2/aug-cc-pVTZ levels of theory for $\theta_2=90^\circ$ and 7 values of ϕ . Numbers in parentheses are corresponding values calculated based on the uncorrected IPS.

ϕ^*	D_e	R_e	$\Delta R_{1/2}$	σ
$\phi = 30^\circ$	37.57(67.89)	3.88(3.77)	0.93(1.06)	3.50(3.35)
$\phi = 60^\circ$	58.58(91.10)	3.81(3.71)	1.10(1.14)	3.39(3.27)
$\phi=90^\circ$	81.90(116.56)	3.74(3.66)	1.15(1.19)	2.31(3.21)
$\phi= 120^\circ$	95.14(130.01)	3.72(3.65)	1.18(1.23)	3.28(3.19)
$\phi= 150^\circ$	95.64(129.69)	3.73(3.67)	1.20(1.25)	3.29(3.20)
$\phi= 180^\circ$	93.53(127.01)	3.683.76(3.68)	1.21(1.26)	3.31(3.22)

* D_e and R_e , $\Delta R_{1/2}$, σ are given in cm^{-1} and \AA , respectively.

The calculated IPS's can further be compared based on the values of the position of the minimum point (R_e) and well-width $\Delta R_{1/2}$ of the potential curves. The calculated values of R_e and $\Delta R_{1/2}$ are reported in Table 2. As is evident from this table, both of these quantities are very sensitive to the variation of angle θ_2 and ϕ in the computations. The BSSE-corrected CO–CO IPS's and their contour plots are plotted in the left and right parts of Figs. 3, respectively.

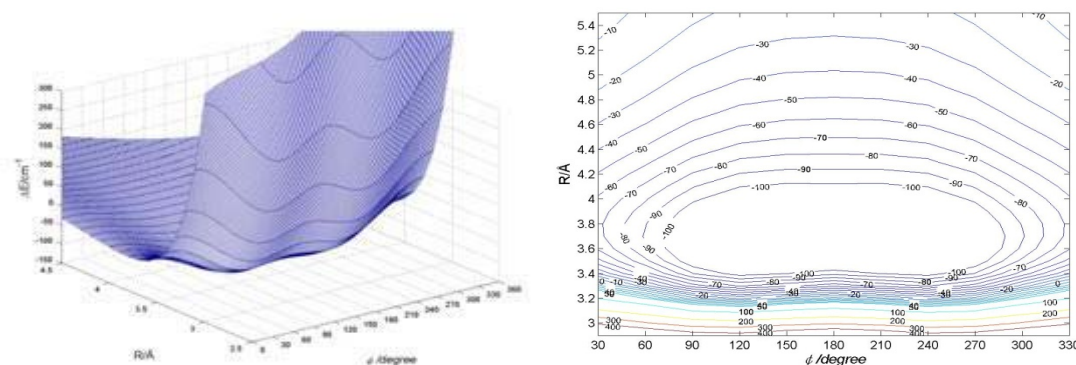


Fig. 3. The BSSE corrected IPS's (left part) and their contour plots (right part) for CO-CO system.

4. Conclusions

In this research, IPS of the CO–CO system has been studied using ab initio MP2/aug-cc-pVTZ levels of theory. The calculated potential energy curves are very sensitive to the intermolecular distance R and the relative orientation of the two CO monomers. The uncorrected potential energy curves show the typical form of an interaction potential consisting of attractive and repulsive parts that result in a potential well. Compared with the uncorrected potential characteristics (Table 2), D_e value for the BSSE-corrected MP2 potentials is decreased significantly, and R_e is shifted towards longer intermolecular distances. The values of $\Delta R_{1/2}$ for the BSSE-corrected MP2 potentials are also decreased compared to those of the corresponding uncorrected potentials. Analysis of the uncorrected and BSSE-corrected IPS's clearly demonstrates that Counterpoise (CP) correction is necessary in order to obtain physical characteristics of the CO–CO system for practical purposes. It can be concluded that use of CP correction is necessary for the derivation of realistic intermolecular interaction potential energy surfaces.

References

- [1] J. R. Maple, M.J. Hwang, T.P. Stockfish, U. Dinur, M. Waldman, C. Ewig, A. T. Hagler, J. Comput. Chem. 15 (1994) 162.
- [2] M. R. Noorbala, H. Sabzyan, J. Mol. Struct. (Theochem) 678 (2004) 67.
- [3] J. Fiser, R. Polak, Chem. Phys. Lett. 360 (2002) 565.
- [4] A. van der Pol, A. van der Avoird, P.E.S. Wormer, J. Chem. Phys. 92 (1990) 7498.
- [5] N. Tanaka, W. N. Sisk, J. Fluorine Chem. 126 (2005) 313.
- [6] S.F. Boys, F. Bernardi, Mol. Phys. 19 (1970) 553.

Experimental and theoretical determination of the dipole polarizability of substituted thiophenols

M. Oftadeh^a, S. Nasseh^a and M. Hamadani^b

^aDepartment of Chemistry, Payame Noor University (PNU), Isfahan, Iran

(Email: m_oftadeh@pnu.ac.ir)

(Email: sara_nasseh@yahoo.com)

^bDepartment of Chemistry, Kashan University, Isfahan, Iran

(Email: mhamadani@kashanu.ac.ir)

Keywords: Thiophenol, Dipol Polarizability, Refractometry, Energy Gap, Hardness, DFT.

1. Introduction

The importance of sulfur-containing compounds in biological systems as well as in atmospheric and environmental chemistry is now well established. Since the thiol group (R-SH) could easily be oxidized, especially in the presence of light, they have been used as efficient antioxidants of organic matter ranging from polymers to living cell systems [1]. In this regard, aromatic thiols (Ar-SH) that have the pK_a values ranging from 4 to 7 have been shown to be effectively more reactive than aliphatic thiols (R-SH) of similar pK_as [2]. The oxidation of thioanisole (Ph-S-Me) has also been found to be of potential use in the decontamination of toxic chemicals [3,4]. One of the important electronic properties is the electric dipole polarizability, which is a measure of the linear response of the electron density in the presence of an infinitesimal electric field, *F*, and represents a

second-order variation in the energy, viz.: $\alpha = -\left(\frac{\partial^2 E}{\partial F_a \partial F_b}\right)$ $a, b = x, y, z$ $\langle \alpha \rangle = \frac{1}{3}(\alpha_{xx} + \alpha_{yy} + \alpha_{zz})$ (1)

The Lorentz-Lorentz equation gives a molecular expression for the polarizability [5,6]: $\frac{n^2 - 1}{n^2 + 2} = \frac{N \langle \alpha \rangle}{3 \epsilon_0 V}$ (2)

In this work, some aromatic sulfur-containing compounds have been studied theoretically and experimentally.

2. Method

Theoretical calculations were performed at the B3LYP/6-31+G(3d,3p) level of theory. Molecules have been characterized using the Gaussian 98. Calculated characters are including energy, dipole moment, total charge on sulfur atom, energy gap, hardness and dipole polarizability. The studied molecules are listed in table 1.

Table 1. Number of molecule and substitution

NO.	X	NO.	X	NO.	X	NO.	X
1	-H	4	-Ph	7	CO-CL	10	CL
2	-CH ₃	5	CO-H	8	CO-Br	11	Br
3	-C ₂ H ₅	6	CO-F	9	F		

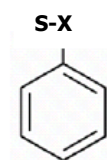


Fig.1. The Substituted thiophenol

Table 2. Calculated α_{ii} (*i*=x,y,z) and average of the dipole polarizability at B3LYP/6-31+G(3d,3p) level

NO.	α_{xx} (au)	α_{yy} (au)	α_{zz} (au)	α_{ave} (au)	α_{ave} (10 ⁻²³ esu)	NO.	α_{xx} (au)	α_{yy} (au)	α_{zz} (au)	α_{ave} (au)	α_{ave} (10 ⁻²³ esu)
1	94.217	127.719	58.443	93.459	1.3618	7	139.464	168.681	70.626	126.257	1.8397
2	139.428	116.043	66.543	107.338	1.5640	8	149.544	179.317	76.084	134.982	1.9668
3	136.417	152.244	75.973	121.545	1.7710	9	112.799	110.267	56.519	93.195	1.3579
4	268.480	165.235	91.045	174.92	2.5487	10	133.698	126.002	64.387	108.029	1.5741
5	128.995	141.23	62.055	110.760	1.6139	11	123.92	156.051	70.763	116.911	1.7035
6	123.821	145.447	62.077	110.448	1.6093						

**Table 3.** Total energy, dipole moment, charge on sulfur atom, energy gap and hardness for molecules at B3LYP/6-31+G(3d,3p)

NO.	E (Hartree)	μ (Debye)	q_s (esu)	E_{HOMO} (Hartree)	E_{LUMO} (Hartree)	Gap Energy (Hartree)	η
1	-630.47361	1.0591	-0.091806	-0.22639	-0.02537	0.20102	0.10051
2	-669.79147	1.3220	-0.133903	-0.21467	-0.02058	0.19409	0.09705
3	-709.11064	1.4628	0.216155	-0.21307	-0.01928	0.19379	0.96895
4	-861.53518	0.8512	-0.173793	-0.20981	-0.03366	0.17615	0.08808
5	-743.80423	4.0249	-0.174536	-0.24614	-0.06201	0.18413	0.09207
6	-843.06303	3.9509	-0.156389	-0.25414	-0.05328	0.20086	0.10043
7	-1203.40669	3.9176	-0.171953	-0.25351	-0.06420	0.18931	0.09466
8	-3314.96786	3.8595	-0.013703	-0.25356	-0.06584	0.18772	0.09386
9	-729.69058	1.8260	0.468097	-0.22943	-0.07299	0.15644	0.07822
10	-1090.06274	1.6984	0.024879	-0.22968	-0.08625	0.14343	0.07172
11	-320.63010	1.5497	0.137629	-0.22846	-0.09746	0.13100	0.06550

The average electronic polarizability was determined experimentally by using the refractometric technique, where the refractive index were measured with a DTM-1 refractometer at 20 °C on frequency range 50-60 Hz.

Table 4. Density, molecular mass, refractive index, experimental and theoretical polarizability (esu) of the molecules.

Molec.	ρ (Kg/Lit)	M (g/mol)	n	$\alpha_{EXP.}$ $\times 10^{-23}$	α_{B3LYP} $\times 10^{-23}$
1	1.08	110.18	1.5880	1.3615	1.3618
2	1.06	124.21	1.5842	1.5556	1.5640
4	1.11	186.28	1.6323	2.3748	2.5488

3. Conclusions

It is observed that the substitution of activating or deactivating groups causes decreasing energy and more stability compared with thiophenol (No. 1). Also molecules with electron-acceptor groups due to better charge distribution and increasing distance have higher dipole moment. CO-H substitution has the highest dipole moment, the lowest gap energy and hardness because of resonance. The highest polarizability and the most reactivity is related to phenyl-substitution molecules because of two ring delocalizing π electrons resonance. The electronegativity of halides effects on the polarizability and hardness. The CO-X and halide substituted molecules obey the maximum hardness and minimum polarizability principles. Agreement between theoretical and experimental polarizability showed that the theoretical method and selected basis set has been corrected.

References

- [1] Nam, Ph.-C., Flammang, R., Gerbaux, P., Nguyen, M. Th.. International J. of Mass Spectrometry. 228 (2003) 151-165.
- [2] T.V. DeCollo, W.J. Lees, J. Org. Chem. 66 (2001) 4244.
- [3] C.A. Bunton, N.D. Gillitt, J. Phys. Org. Chem. 15 (2002) 29.
- [4] S. Ozaki, S. Watanabe, S. Hayasaka, M. Konuma, Chem. Commun. (2001) 1654.
- [5] A. Hinchliffe, H. J. Soscun Machado, Int. J. Mol. Sci. 1 (2000) 8-16.
- [6] P.K. Chattaraj, J. Phys. Chem. A 105 (2001) 511.

**Gas-phase acidities of fulleropyrrolidynes, A AM1 study**

V. Nasr Isfahani and M. Oftadeh

Department of chemistry, Payame Noor University (PNU), Isfahan, Iran

(Email: m_oftadeh@pnu.ac.ir)

(Email: vvnasr@gmail.com)

Keywords: Fulleropyrrolidynes, AM1, Acidity.**1. Introduction**

Choice of a computational procedure for supermolecular systems depends on the level of needed accuracy, size of molecular system and the available computational facility. Often, semiempirical calculations at the AM1 or PM3 level provide the geometry and they may predict the electronic structure accurately. Good correlations have been obtained between experimental pKa values and their calculated gas phase deprotonation enthalpies for a series of nitrogen bases [1]. The ability to predict acidity using coherent, well defined theoretical approach, without external approximation or fitting to experimental data, would be very useful to chemists. The optimization process requires much experience and considerable computational time to confidently achieve an optimized structure at ab initio level. The acid base equilibria of 2-(N-alkyl)fulleropyrrolidines and N-methyl-2-(N-alkyl)fulleropyrrolidines in gas phase were modeled theoretically by using AM1 method. The calculations were performed on four conformations of the pyrrolidines substituents of the fulleropyrrolidine. The pKa values of these compounds were calculated. A correlation between the different energy types and the pKa values are investigated and compared with the experimental values [2]. The aim of this work is to extract a correlation model for determining the pKa values of nitrogen base equilibrium at 298.15 K by AM1 studying with a series of 18 (N-alkyl)fulleropyrrolidines (table 1).

1. Method

The quantities including Hf-SCF energy, thermal energy, enthalpy and Gibbs free energy of the protonated pyrrolidine nitrogen of the some fulleropyrrolidines in gas phase were calculated by AM1 method by using Gaussian 98 coding. The pKa for the protonated process is calculated and the variation of each of mentioned energy versus pKa is plotted and the linear variation is investigated. All geometry optimizations were carried out by using initial Z-matrix obtained by HyperChem 7 software and used as input file for Gaussian. The gas-phase Gibbs free energies change (ΔG_{gas}^0) of the reaction of scheme 1 were calculated. For $G_{\text{gas}}^0(\text{H}^+)$ the experimental value of -6.28 kcal/mol was used [3].

2. Results and discussion

The calculated gas-phase ΔG_{gas}^0 of the protonated compounds (table 1) and pKa values at 298.15 K are listed in table 2. Figure 1 shows the correlation of the ΔG_{gas}^0 values with the pKa values. A satisfactory linear equation is obtained. The results showed that ΔG_{gas}^0 of protonation generally increases when the acidity of these compounds were decreasing. The regression equation with SD and R^2 values are given as:

$$\Delta G_{\text{gas}}^0 = -1.3723 \times pKa + 19.2128 \quad (R^2 = 1.00, \quad SD = 0.949)$$

3. Conclusions

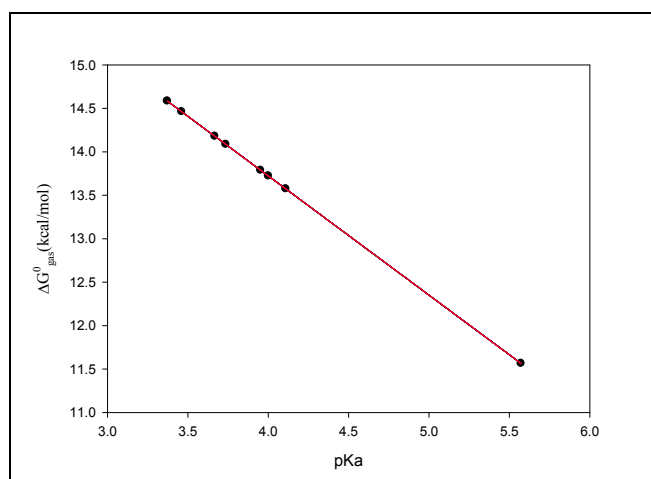
In the present work, we have estimated the pKa values of different series of fulleropyrrolidine derivatives using a semiempirical method. We have shown satisfactory linear equation between pKa values of a variety of some fulleropyrrolidine derivatives and theoretical gas protonation Gibbs free energy changes. This equation may be used to predict pKa values for the other derivatives of such supermolecules. These results can be interpreted through the inductive and resonance effect. We could rationalize this effects by calculating transfer energy between the nonbonding orbital localized on N-atom of the base and unoccupied antibonding orbital associated with the alkyl groups. Also we could try to correlate the pKa values with electrostatic potential on N atom for substituted fulleropyrrolidines using quantitative-structure activity or property relationships (QSAR or QSPR, respectively) [4].

Table 1. The considered (N-alkyl)fulleropyrrolidines compounds

$\Delta G_{\text{gas}}^0 = \Delta G_{\text{gas}}^0(\text{A}) + G_{\text{gas}}^0(\text{H}^+) - G_{\text{gas}}^0(\text{AH}^+)$ $pK_b = \Delta G_{\text{gas}}^0 / 2.313 RT \quad pK_a = 14 - pK_b$ <p style="text-align: center;">Scheme 1</p>					
NO	R1	R2	No	R1	R2
1	H	H	5	CH3	C12H25
2	H	CH3	6	CH3	C4H9
3	H	C4H9	7	CH3	C8H17
4	H	C8H17	8	CH3	C12H25

Table 2. The caculated ΔG_{gas}^0 and pKa for some (N-alkyl) fulleropyrrolidines

No	ΔG_{gas}^0 (kcal/mol)	pKa	No	ΔG_{gas}^0 (kcal/mol)	pKa
1	14.0856	3.74	5	11.5650	5.57
2	14.1782	3.67	6	13.5732	4.11
3	13.7879	3.95	7	13.7226	4.00
4	14.4620	3.46	8	14.5840	3.37


Fig. 1. the linear correlation of the ΔG_{gas}^0 values with the pKa values.

References

- [1] I. E. Charif, S. M. Mekelleche, D. Villemin and N. Mora-Diez, J. Mol. Struct. (THEOCHEM), 818 (2007) 1-6.
- [2] F. D'Souza, M. E. Zandler, G. R. Deviprasad and W. KutnerK. Phys. Chem. A 104 (2000) 6887.
- [3] M. D. Liptak, K. C. Grass, P. G. Seybold, S. Felgus and G. C. Shields, J. Am. Chem. Soc. 124 (2002) 6421.
- [4] E. Soriano, S. Cerdan and P. Ballesteros, J. Mol. Struct. (THEOCHEM), 684 (2004) 121.



Theoretical investigation of metallophilic bonding

Z. Jamshidi

Department of Chemistry, University of Tehran, Tehran, Iran

(Email: na.jamshidi@gmail.com)

1. Introduction

The formation of metallophilic interactions [1] between closed-shell metal atoms has become a topical area of research. From a fundamental standpoint, the forces responsible for these interactions continue to challenge existing chemical bonding paradigms. Recent theoretical advances [2,3] suggest that dispersion forces magnified by relativistic effects play a crucial role when these interactions involve heavy ions such as Au(I) or Hg(II). While much effort has been devoted to homometallic systems, the study of metallophilic bonds involving different atoms is attracting an increasing interest. Theoretical work in this area was pioneered by Pyykkö, that studied the aurophilicity (metallophilicity between gold atoms) in $(X-Au-L)_2$ dimers [4]. This is now commonly attributed to unusually strong $d^{10}-d^{10}$ interactions, although ligand interactions and packing effects may also play a role.

In this work we investigated theoretically the nature of M-M bonds by three quantum chemical methods which are widely used for analyzing the chemical bond in TM compounds: natural bond orbital (NBO) method, quantum theory of atoms-in-molecules (QTAIM), and energy decomposition analysis (EDA).

2. Methods

The geometries of $(Cl-M-PH_3)_2$ dimers were fully optimized by MP2, and DFT, Beck's three parameter hybrid functional incorporating the correlation functional of Lee, Yang, and Parr (B3LYP). These calculations were done using Gaussian 03 suit of programs. Recently developed pseudopotential-based augmented correlation-consistent basis sets, aug-cc-pVDZ-PP, based on the small core relativistic pseudopotential (PPs) of Figgen et al.,²⁷ were employed for metals, while, the aug-cc-pVDZ dunning basis set was used for lighter atoms (H, P, and Cl).

To reveal the nature of bonds, the NBO, QTAIM, and EDA analysis were carried out on optimized structure. The energy decomposition analysis (EDA) available through the program package ADF(2009.01) which is based on the methods suggested by Ziegler and Rauk, and Morokuma. The bonding analysis was carried out at the B3LYP/TZ2P level of theory. Scalar relativistic effects have been considered using the zero-order approximation (ZORA).

3. Results and Discussion

Closed shell neutral atoms such as He, Be, Pd or Xe form weak van der Waals bonded dimers. If the closed shell atoms carry positive charges such as Cs^+ , Cu^+ or Au^+ , then only excimers may exist, i. e., the ground states of M_2^{2+} possess repulsive potential curves only. However, when M^+ is attached to Lewis bases such as in $Cl-M-PH_3$, the reduced electrostatic repulsions may be overcome by the "metallophilic attraction", particularly if the ligands are soft and electron-rich.

Many theoretical calculations had investigated the dimer $(Cl-M-PH_3)_2$ by means of ab initio and DFT methods [5]. The M-M energy curves are quite flat so that the equilibrium distance becomes strongly dependent on small calculational errors such as the finite basis set, especially in the case of ab initio calculations. Both theory and experimental evidences show that the preferred structure of the free dimer with small ligands is the antiparallel eclipsed one, which results from the electrostatic attraction between the phosphine with positive partial charge and negative chlorine.

A breakdown of Au-Au binding energy at the B3LYP level is given in Table 1. At equilibrium Au-Au separation, the overlap of the two unmodified monomers is already large enough to result in quite strong Pauli repulsion. Without the B3LYP exchange-correlation correction, this repulsion would be even larger. The penetration of the electron density cloud of one monomer into the cloud of the other monomer, where the nuclear attraction is only incompletely shielded, results in significant electrostatic attraction. The energy lowering due orbital mixing is about -8.21 kcal/mol, therefore the total interaction energy are negative and about -10.44 kcal/mol.

**Table 1.** Breakdown of the Cl–Au–PH₃ ... Cl–Au–PH₃ interaction energy. ($R_{\text{Au–Au}} = 3.49 \text{ \AA}$)

Pauli repulsion energy ^a	16.16
Electrostatic attraction	-18.39
Orbital relaxation ^b	-8.21
Total interaction energy	-10.44

^a Including exchange-correlation, i.e., the simulated dispersion attraction.^b Hybridization, polarization, charge transfer, orbital interference.

References

- [1] Pyykkö, P. Straka, M. Phys. Chem. Chem. Phys. 2 (2000) 2489.
- [2] Pyykkö, P. Inorg. Chim. Acta 358 (2005) 4113.
- [3] Pyykkö, P. Angew. Chem., Int. Ed. 43 (2004) 4412.
- [4] Pyykkö, P. Adv. Quantum Chem. 11 (1978) 353.
- [5] Magnko, L. Schweizer, M. Rauhut, G. Schuz, M. Stoll, H. Werner, H. J. Phys. Chem. Chem. Phys. 2 (2002) 1006.



Density functional study of group 13-15 nanorods

A. Mohajeri* and M. Ebadi

Department of Chemistry, College of Science, Shiraz University, Shiraz 71454, Iran

(Email: ebadi.mahsa@gmail.com)

Keywords: Nanorod, Oligomer, HLG, Group 13-15.

1. Introduction

Group 13-15 binary compounds are prospective materials for optoelectronics and microelectronics. With modern technology moving steadily toward reducing the dimensions of operating devices, controlled synthesis of small nanosized structures with diameters in the range 1-20 nm becomes an essential task.

One of the possible approaches is gas-phase particle generation using chemical vapor deposition (CVD) process [1]. Chemical vapor deposition (CVD) is one of the leading methods for the production of 13-15 materials. In recent years, nanostructure 13-15 materials have become an extremely hot topic. Instead of manufacturing smooth films and coatings, the experimentalists now turn their attention into fabrication of one, two, and three dimensional 13-15 architectures. The simplest architectures of interest here are one-dimensional (1D) nanorods or whiskers [2].

Formation of the group 13-15 gas-phase stable oligomers may be a good starting point (initial step) for nanoparticle generation. It is widely thought that the oligomers compounds $[RMYR]_n$ (M-group 13, Y-group 15 element) should obey the isolated square rule found for the boron-nitrogen cages. In contrast to these expectations, the needle-shaped oligomers, which violate this rule, are more stable compared to the cage (fullerene-like) oligomers for all MY pairs (M) B, Al, Ga, In; Y) N, P, As). The stability of the needle-shaped clusters improves with increasing oligomerization degree. Thus, the isolated square rule, which is analogous to the isolated pentagon rule widely applied for fullerenes, should not serve as the basis for searches for the most stable structures of the inorganic oligomers. Generation of the needle-shaped oligomers from the group 13 and 15 hydrides is thermodynamically favorable [3]. In this work we report electronic properties of group 13-15 needle-shaped compounds $(HMYH)_n$ {M=B, Al, Ga-Y=N, P, As} $n=1-10$.

2. Computational details

All geometries are optimized at the Becke's three-parameter hybrid functional (B3) with the nonlocal correlation of Lee-Yang-Parr (LYP) level of theory and the 6-311+G* basis set using GAUSSIAN 03 suite of program [4]. The AIM2000 program was employed for calculating the bond critical points and visualizing the bond paths [5].

3. Results and discussion

The optimized structures for $(HMYH)_n$ {M=Al, Y=P} are presented in figure 1. It should be noted that in trimer compound among these oligomers, $(HBNH)_3$, $(HAINH)_3$, $(HGaNH)_3$ are planar and have D_{3h} symmetry and other structures are in C_{3v} or C_s symmetry.

By considering monomers $(HMYH)$, formation of corresponding oligomers are theoretically considered in reaction (1):



we first consider both singlet and triplet multiplicity for monomers by comparing corresponding energy, singlet species are found to be more stable and are chosen for calculating enthalpy of reactions. Oligomers with higher n become more stable since the enthalpy reaction are more exothermic. The results are collected in Table 1.

HOMO-LUMO gap energies (HLG) for $(HBNH)_n$, $(HAINH)_n$, $(HGaNH)_n$ are presented in Figure 2. Group 13 nitride have large homo-lumo gap ranges 6.32-7.73, 5.52-7.18 and 4.95-6.67 for $(HBNH)_n$, $(HAINH)_n$, $(HGaNH)_n$, respectively. Group 13 phosphides have HLG ranges 4.27-5.63, 3.4-5.07 and 3.17-5.12 for $(HBPH)_n$, $(HAIPH)_n$ and $(HGAPH)_n$, respectively. Arsenides lie better around semi conducting regime 3.98-5.23, 3.33-4.61 and 3.11-4.7 for $(HBAsH)_n$, $(HAIAsh)_n$ and $(HGAsH)_n$, respectively. In most compounds maximum charge density at BCP takes place for ($n=3$) since planar trimers have special stable structure.

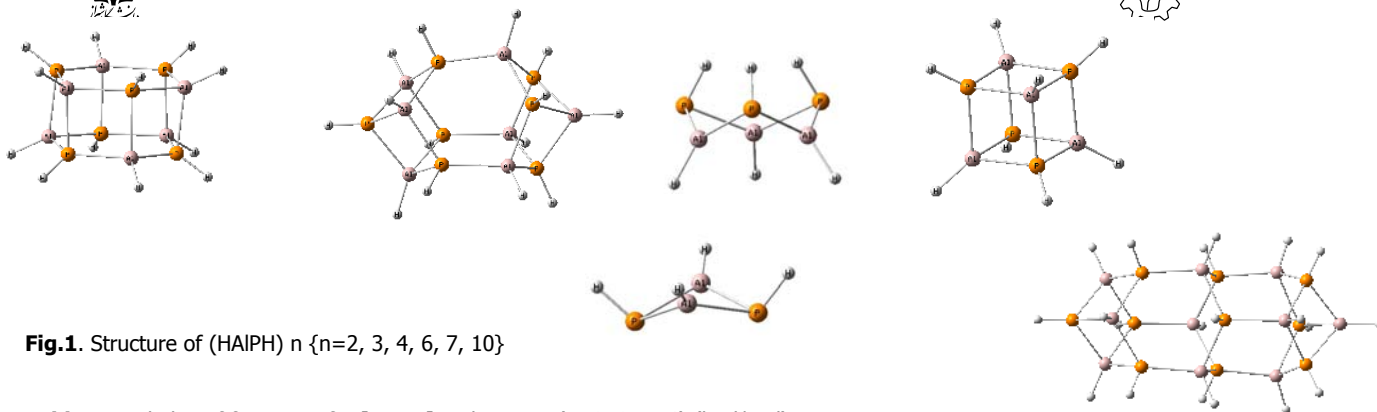


Fig.1. Structure of (HAIPH) n { $n=2, 3, 4, 6, 7, 10$ }

Table 1. Enthalpy of formation for [HMYH] n oligomers ($n=2, 3, 4, 6$) (kcal/mol)

molecules	$n=2$	$n=3$	$n=4$	$n=6$
(HBNH) n	-51.249	-147.028	-114.953	-223.950
(HBPH) n	-59.752	-120.529	-131.815	-250.522
(HBAsH) n	-49.125	-98.949	-103.876	-205.916
(HAINH) n	-132.501	-238.299	-369.366	-587.362
(HAIPH) n	-77.265	-126.338	-212.259	-348.960
(HAiAsH) n	-69.958	-117.284	-180.727	-301.079
(HGaNH) n	-95.711	-182.796	-276.489	-442.721
(HGaPH) n	-57.975	-98.634	-154.738	-261.901
(HGAsH) n	-53.715	-93.843	-132.459	-228.166

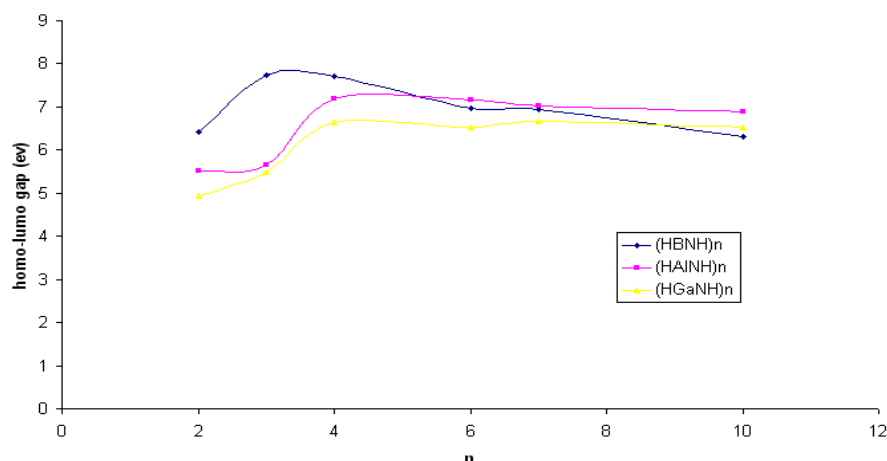


Fig. 2. HOMO-LUMO GAP for (HBNH) n , (HAINH) n , (HGaNH) n { $n=2, 3, 4, 6, 7, 10$ }

4. Conclusion

Enthalpy of reaction predict stability of these oligomers are more favorable for higher n . bond critical point analysis show (MY) bonds are strong covalent bonds except BP and BAs which are weaker. Electronegativity differences in Pauling units also show the same result and BP, BAs have less electronegativity differences while AlN, GaN have larger.

References

- [1] Timoshkin, A.Y.; Schaefer, H.F.J.AM.Chem.Soc.(2004) 126, 12141.
- [2] Timoshkin, A.Y.; Schaefer, H.F.J.Phys.Chem.c (2008) 112, 13816-13836.
- [3] Timoshkin, A.Y.; Schaefer, H.F.Inorg.chem.(2005) 44,843-845.
- [4] Frisch, M.J.et al.,Gaussian 03 ,revision B03,Gaussian Inc.,Pittsburgh PA,2003.
- [5] F.W.Bader, AIM Program, ver 2.0; Mc. Master University: Hamilton, Canada, 2000.



Ab initio and DFT study of alkyl substituent effects on the electronic and structural properties of thiophene derivatives

H. Nikoofard¹, Z. Kalantar and M. Khorrami*

Faculty of chemistry, Shahrood University of Technology, Shahrood, Iran

(Email: monire.khorami@yahoo.com)

Keywords: HOMO-LUMO gaps, Ionization Potential, Alkyl thiophenes, Transition state.

1. Introduction

The conducting polymers are known as new materials that have a lot of applications in industry. The advantage of these polymers is insensitivity to air and wet [1]. One of these substances is thiophene which substituting on the β -positions of monomer gives more application properties to poly thiophene. In this work we carried out the effect of different alkyl substituents in the β -position on electronic, electrical, structural properties of thiophenes. In this way, we consider our calculations for all neutral and radical cation of alkyl thiophene (ATHs).

2. Methods

All calculations were done with Gaussian 03 program. We calculated full optimization on two level of theory (HF, B3LYP) with the 6-31G** basis set. We used these methods to find optimized geometries and electrical and electronic properties of ATHs and their radical cations.

3. Results and discussion

It is known that electrical conductivity of polymer films depend on planarity, orientation and alignment of their monomers in the polymer chain back bone [2]. Thus, some related geometrical parameters having important role in polymerization mechanism calculated and presented in Table1. Obviously α (C_2), α' (C_3) carbon atoms are identical for thiophene, but they vary with insert a substituent group in ATHs. The results show entering alkyl groups on backbone monomer has a clear effect on geometrical parameters, but where increasing the length of substituent we were not considerable effect. The values of dihedral angles shows that torsion angles which confirm the planarity of these monomers. It is clear that the planarity of compounds is a necessary condition for conductivity of these materials.

Table1. Some of the optimized geometrical parameters of ATHs at B3LYP/6-31G** method (angles in degree and length in Angstrom).

ATH	R ₁₃	R ₁₂	R ₄₈	D ₆₂₄₈	IP
Th	1.7255	1.7255	1.0738	0	NC*
MTh	1.7249	1.7282	1.5041	0	8.2082
ETh	1.7247	1.7278	1.5082	-0.0743	8.1296
PrTh	1.7247	1.7277	1.5078	0.8942	8.1296
BTh	1.7247	1.7278	1.5079	0.8511	8.0328
PtTh	1.7247	1.7278	1.5079	0.8519	8.01
HzTh	1.7247	1.7278	1.5079	0.8545	7.9887

* NC: not calculated.

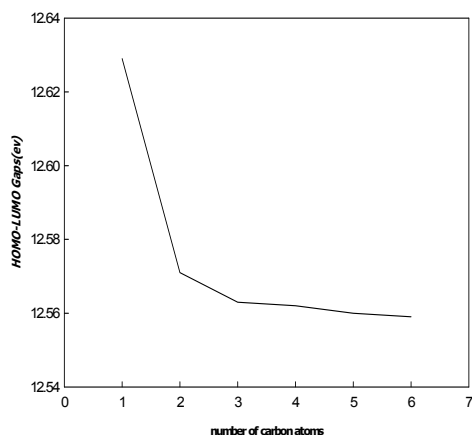
Since the polymerization mechanism of ATHs is based on the radical cationic process we carry out the charge and spin density distribution of α , α' positions for all monomers which presented in Table 2. The results show that equality of charge and spin density distribution of α , α' positions vanish where a substituent group inserted on ATHs molecules. The difference between α , α' positions in charge and spin density distribution related to inserting alkyl group in β -position of thiophene. The positive charge and spin density distribution decreases on both positions where the length of substituent groups increases.

**Table2.** Distribution of charge (spin) density at B3LYP/6-31G** level of theory.

ATHs	S ₁	C ₂	C ₃	C ₄	C ₅
Th ⁺	NC*	NC	NC	NC	NC
MTh ⁺	0.498(-0.024)	-0.235(0.447)	-0.215(0.475)	-0.028(-0.126)	0.146(0.236)
ETh ⁺	0.492(-0.032)	-0.238(0.44)	-0.218(0.484)	-0.034(-0.125)	0.158(0.224)
PrTh ⁺	0.487(-0.012)	-0.245(0.465)	-0.219(0.408)	-0.029(-0.13)	0.147(0.235)
BTh ⁺	0.483(-0.001)	-0.249(0.452)	-0.221(0.386)	-0.027(-0.131)	0.145(0.238)
PtTh ⁺	0.48(0.006)	-0.253(0.44)	-0.223(0.368)	-0.027(-0.129)	0.144(0.24)
HzTh ⁺	0.475(0.12)	-0.256(0.426)	-0.226(0.351)	-0.027(-0.126)	0.143(0.235)

* NC: not calculated.

In this way we calculated the HOMO-LUMO gaps, HLGs, for all ATHs and shown in Fig 1. As it can be seen, the values of HLGs decreases when the length substituent increases and this reducing behavior are converged for larger than propyle substituent. In following, we have calculated Ionization Potential (IPs) of ATHs (indicated in last column of Table 1) [3]. It was interesting that the values of IPs confirmed the other geometrical and electronic properties.

**Fig .1.** Variation of HLG (in eV) with the number of carbon atoms.

Conclusions

It is found that substituting alkyls group in the thiophene monomer have considerable effect on ATHs but this behavior converges when the length of substituent reaches to over 3 carbon atoms. The main of results indicate that ATHs are better candidate to produce conductive polymer with higher conductivity respect to thiophene monomers. The calculations for both methods confirm these results and are not presented for brief.

References

- [1] T. A. Skotheim, R. Elsenbaumer, J. Reynolds, Handbook of Conducting Polymers, Marcel Dekker, New York, 1998.
- [2] H. Sabzyan, H. Nikoofard, Chemical Physics 306(2004)105.
- [3] C. Alemán, E. Armelin, J. Ignacio Iribarren, F. Liesa, M. Laso, J. Casanovas, Synthetic Metals 149 (2005) 151.



A theoretical investigation structure and electronic characteristics of the thiophene and 3-propyle thiophene oligomers

H. Nikoofard, Z. Kalantar and M. Khorrami*

Faculty of chemistry, Shahrood University of Technology, Shahrood, Iran

(Email: monire.khorami@yahoo.com)

Keywords: HOMO-LUMO gaps, Thiophene oligomers, Stabilization energy, Transition state.

1. Introduction

In our previous work, we studied 3-alkyle thiophenes (ATHs) as candidates for conducting polymers. In that research, we found that propyle thiophene (PrTh) has the favorite conditions for this aim. In this work we report the results of a series of *ab initio* quantum mechanical calculations on the structure and the electronic properties of thiophene and 3-propyle thiophene oligomers. The calculations were performed on oligomers formed by n repeating units, where n ranges from 1 to 8.

2. Methods

All calculations were done with Gaussian 03 program package. The structures of neutral oligomers were fully optimized at HF level with 6-31G** basis set as studying geometry the all anti conformation.

3. Results and discussion

Geometry optimization of all oligomers at HF/6-31G** level symmetrically led to a planar all-anti conformation independently of the monomer rings in the oligomer. This conformation was predicted as the global minimum at both levels of theory including HF with different basis set which shown in Fig .1.

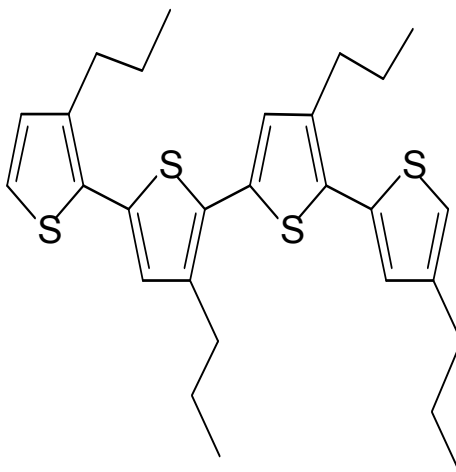


Fig.1. Optimized geometries of the all-anti conformations for tetra 3-propyle thiophene.

The values of energy gap between HOMO and LUMO (HLG) levels calculated for all thiophene oligomers ($n=1-8$) and presented in Table 1. As we know the lower HLG is an important parameter corresponding to higher conductivity [1, 2]. Table 1 shows the gradual variation with n of the HLG decreases when the length of oligomer chain increases. It is found that HLG have the lower value when $n=7$ (heptamer type) and we observed that HLG values converged to $n=7$. That is agreement with the Alemán *et al* report [3].



Table1. The HF/6-31G** calculated values for energy gaps between HOMO-LUMO in eV.

oligomers	HLG	oligomers	HLG
Th	12.675	PrTh	12.563
Di Th	10.151	DiPrTh	10.422
Tri Th	9.103	Tri PrTh	10.697
Tetra Th	8.563	Tetra PrTh	10.214
Penta Th	8.247	Penta PrTh	10.321
Hexa Th	8.048	Hexa PrTh	10.241
Hepta Th	7.914	Hepta PrTh	10.161

The importance of long-range interactions in the stabilization of oligomer chains was investigated by examining the stabilization energy (ΔE_{stab}), which was defined as the energy gain obtained upon the addition of the n th unit to the oligomer formed by $n-1$ units with respect to the energy gain of the formation of the oligomer with $n=3$ from that with $n=2$. Thus, for an oligomer formed by n units, ΔE_{stab} was computed as, $\Delta E_{stab} = (E_n - E_{n-1}) - (E_3 - E_2)$ where E_n , E_{n-1} , E_3 and E_2 units, respectively. It should be noted that the energy difference ($E_3 - E_2$) corresponds to the change of energy at the formation of the oligomer formed by three units, which is free from long range effects [3]. Our calculations demonstrated that ΔE_{stab} s for thiophene oligomers are zero but these values reduce for PrTh oligomers. Also it is found that the ΔE_{stab} decrease when the number monomers increased in back bone chain.

4. Conclusions

HF quantum mechanical calculations have been performed to examine and compare the structural and electronic properties of n -Th and n -PrTH oligomers. It is found that the planar anti conformation is stable and increases when n increases. Also, our consider on stabilization energy demonstrated that PrTh oligomers are more stable than similar oligomers for Th. In addition to, longer oligomers are more stable than shorter oligomers.

References

- [1] T. A. Skotheim, R. Elsenbaumer, J. Reynolds, Handbook of Conducting Polymers, Marcel Dekker, New York, 1998.
- [2] H. Nikoofard, H. Sabzyan, Journal of Fluorine Chemistry, 128 (2007) 668.
- [3] C. Alemán, E. Armelin, J. Ignacio Iribarren, F. Liesa, M. Laso, J. Casanovas, Synthetic Metals 149 (2005) 151.

**Theoretical identification of local strain in cyclic molecules**

S.M. Azami

Department of Chemistry, College of Sciences, Yasouj University, Yasouj, Iran.

(E-mail: azami@mail.yu.ac.ir)

Keywords: Localized orbital, Strain, NBO, Angular momentum.**1. Introduction**

Identification of molecular electronic structure is one of the important concerns of modern quantum chemistry and several theoretical tools are developed to inspect and analyze intra- and intermolecular interactions, such as Natural Bond Orbitals (NBO) [1].

Chemical bonding is a concept which all methods try to define via certain criteria. While a chemical bond in H_2^+ can be detected via a simple Molecular Orbital (MO) analysis, molecular orbitals of non-linear polyatomic systems are extremely complicated which avoids chemical interpretation of the molecular electronic wave function. In order to *translate* the electronic wave function into chemical concepts, localized orbitals can be helpful. In general, localization procedure consists of one or more (non-)unitary transformations on the molecular orbitals which results in orbitals localized on one or two centers. There exist several localization techniques, such as the localized orbitals by Boys [2], Edmiston and Rudenberg [3], and NBO by Weinhold et al [1].

The presence of *strain* in molecular systems, has been well known for cyclic molecules such as three-membered rings. Many researches in the literature are devoted to explain the strain according to some theoretical approach [4]. However, the strain in a chemical bond has not yet been quantified in terms of localized orbitals. In the present work, we wish to take advantage of orbital angular momentum to measure the degree of strain in a chemical bond.

2. Method

The molecular geometries and electronic wave functions are optimized at HF/6-311G level of theory utilizing Gaussian 03 suite of programs [5]. Frequency analysis is also performed to make sure that the resultant geometries are minimum structures. NBO orbitals are employed as localized orbitals, however, the procedure is general and any other localized orbital can be used.

The components of angular momentum operator around point **C** is defined as Eq. 1:

$$\hat{L}_\mu = \{(\mathbf{r} - \mathbf{C}) \times \nabla\}_\mu \quad (\mu = x, y, z) \quad (1)$$

The matrix representation of \mathbf{L}_μ in the basis of Gaussian type orbitals can be evaluated by recursive formula developed by Obara and Saika [6]. According to their work, the matrix element between two Gaussians **a** and **b**, centered at **A** and **B**, respectively, with arbitrary angular momentum is defined as:

$$\begin{aligned} \langle \mathbf{a} + \mathbf{1}_i | \hat{L}_\mu | \mathbf{b} \rangle &= (\mathbf{P}_i - \mathbf{A}_i) \langle \mathbf{a} | \hat{L}_\mu | \mathbf{b} \rangle + \frac{1}{2\zeta} \mathbf{N}_i(\mathbf{a}) \langle \mathbf{a} - \mathbf{1}_i | \hat{L}_\mu | \mathbf{b} \rangle + \frac{1}{2\zeta} \mathbf{N}_i(\mathbf{b}) \langle \mathbf{a} | \hat{L}_\mu | \mathbf{b} - \mathbf{1}_i \rangle + \frac{\zeta_b}{\zeta} \{ \mathbf{1}_i \times (\mathbf{B} - \mathbf{C}) \}_\mu \langle \mathbf{a} | \mathbf{b} \rangle \\ &+ \frac{1}{2\zeta} \sum_{k=x,y,z} \mathbf{N}_k(\mathbf{b}) \{ \mathbf{1}_i \times \mathbf{1}_k \}_\mu \langle \mathbf{a} | \mathbf{b} - \mathbf{1}_k \rangle \end{aligned} \quad (2)$$

where

$$\mathbf{a} = (x - \mathbf{A}_x)^{n_1} (y - \mathbf{A}_y)^{n_2} (x - \mathbf{A}_z)^{n_3} e^{-\zeta_a(\mathbf{r} - \mathbf{A})^2} \quad (3)$$

$$\mathbf{b} = (x - \mathbf{B}_x)^{n_1} (y - \mathbf{B}_y)^{n_2} (x - \mathbf{B}_z)^{n_3} e^{-\zeta_b(\mathbf{r} - \mathbf{B})^2} \quad (4)$$

$$\zeta = \zeta_a + \zeta_b \quad (5)$$

$$\mathbf{P} = \frac{1}{\zeta} (\zeta_a \mathbf{A} + \zeta_b \mathbf{B}) \quad (6)$$

$\mathbf{N}_i(\mathbf{a})$ is the i -th angular momentum components of the GTO and $\mathbf{1}_i$ is a Kronecker's delta row matrix whose elements are defined as $\mathbf{1}_i = (\delta_{ix}, \delta_{iy}, \delta_{iz})$.

The above formula can be started from matrix elements between the corresponding zero angular momentum orbitals i.e., s -type GTO as Eq. 7:

$$\langle \mathbf{0}_A | \hat{L}_\mu | \mathbf{0}_B \rangle = 2 \frac{\zeta_a + \zeta_b}{\zeta} \{ (\mathbf{A} - \mathbf{C}) \times (\mathbf{B} - \mathbf{C}) \}_\mu \langle \mathbf{0}_A | \mathbf{0}_B \rangle \quad (7)$$

3. Results and discussion

An ideal σ bond possesses cylindrical symmetry and consequently the corresponding $\langle \hat{L}_q^2 \rangle$ vanishes with regards to symmetry considerations, where \vec{q} is some vector joining the two nuclei. Fig. 1 represents a typical \vec{q} for cubane. In the cases of unfavorable hybridizations, i.e. bond strain, the σ bond appears to be bent and deviates from the cylindrical symmetry. Therefore, $\langle \hat{L}_q^2 \rangle$ can be used to measure how much strain has influenced the σ bond. As Fig. 1 shows, the C-C NBO σ bond is not strictly of Σ symmetry type which is a result of molecular strain.

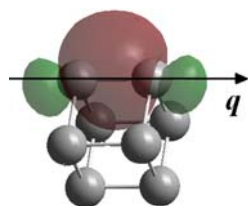


Fig. 1. \vec{q} vector for a C-C bond in cubane and the corresponding bent σ bond.

In order to obtain $\langle \hat{L}_q^2 \rangle$ for a typical NBO, \mathbf{L}_q matrix is required. Since the coordinate axes do not necessarily coincide with the C-C bond, the three components of \mathbf{L} matrices ($\mathbf{L}_x, \mathbf{L}_y, \mathbf{L}_z$) are first calculated. \mathbf{L}_q can then be obtained as a proper summation over the three matrices with respect to the normalized vector joining the two nuclei. \mathbf{L}_q is then transformed to NBO basis and squared. The diagonal element corresponding to the C-C σ bond in the squared matrix is reported as $\langle \hat{L}_q^2 \rangle$. Table 1 displays $\langle \hat{L}_q^2 \rangle$ for C-C bonds of six simple systems as examples to show how $\langle \hat{L}_q^2 \rangle$ can act as bond strain descriptor. As this table shows, the $\langle \hat{L}_q^2 \rangle$ values for normal alkanes do not exceed 0.03 while it is greater than 0.16 for strained systems. Also, these values reveal that tetraheadrane C-C bonds possess more strain than cubane which is in agreement with the carbon's hybridization and unfavorable structure of tetraheadrane.

Table 1. $\langle \hat{L}_q^2 \rangle$ values for some C-C bonds in atomic units.

System						
	Ethane	Propane	Butane	Tetraheadrane	Spirane	Cubane
(C-C) $\langle \hat{L}_q^2 \rangle$	0.00	0.02	0.02	0.28	0.23 , 0.20	0.17

4. Conclusions

The square of angular momentum along an internuclear axis can be employed as a criterion to estimate local strain in a molecular system. This method requires a localized orbital which describes the chemical bond. Although the presented examples discuss σ bonds, π bonds can be considered as well. In the case of a normal π bond, $\langle \hat{L}_q^2 \rangle$ is expected to be 1.

References

- [1] A.E. Reed, L.A. Curtiss, F. Weinhold, Chem. Rev. 88 (1988) 899.
- [2] J.M. Foster, S. F. Boys, Rev. Mod. Phys. 32 (1960) 300.
- [3] C. Edmiston, K. Ruedenberg, Rev. Mod. Phys. 34 (1963) 457.
- [4] H. Chevreau, A. Sevin, Chem. Phys. Lett. 322 (2000) 9.
- [5] M.J. Frisch et al., Gaussian 03, Pittsburgh, PA, 2003.
- [6] S. Obara, A. Saika, J. Chem. Phys. 84 (1986) 3963.

**Electrostatic field gradient as a tool for aromaticity measurement**A.H. Pakiari^{a*} and N. Bagheri^b^{a*} Chemistry Department, College of Sciences, Shiraz University, Shiraz 71454, Iran.

(Email: pakiariah@gmail.com, Mobile 0917-113-5735)

^b Chemistry Department, Islamic Azad University, Firuzabad Branch, Firuzabd, Iran**1. Introduction**

Aromaticity is the most widely used concept that plays an important role in chemistry. Conjugated planar cyclic hydrocarbon compounds that follow $4n + 2$ electrons rule are aromatic, and also contain π -delocalization electrons. The concept of aromaticity has been subject of debate and is still today attracting considerable interest. There are some issues of Chemical Reviews were dedicated to cover this topic [1-3]. Many descriptors of aromaticity have been introduced until now such as; Clars rule, (CGT) index, NKVS, ASE, SESE, HOMA, n-DI's, PDI, FLU, ATI, I_{NG} , I_{NB} indices, H-NMR and NICS. In this research, we have presented a new procedure for evaluation of aromaticity of cyclic compounds, which have conjugated (π delocalized bond) character.

2. Computational Details

All the compounds have been fully optimized at equilibrium geometries and energies by using DFT at B3LYP level with 6-311++G** basis set. Frequency test has been done to ensure all the optimized geometries in ground state. The calculations have been carried out by GAUSSIAN03 [4] package.

3. Results and discussion

The electric field gradient tensor is a symmetric second rank tensor with zero off diagonals elements $\partial^2 V / \partial z^2 + \partial^2 V / \partial y^2 + \partial^2 V / \partial x^2 = 0$ which can be expressed in an axis system. Thus, the quantity $q = \partial^2 V / \partial z^2$ is a component which can be assigned by "EFG" in this research. The computation of EFG can be evaluated at various points of molecule such as any points on/out of bond. EFG at zero point any points of A-B bond distance, which presented by $EFG^{(0)}$, means that EFG value of the same Cartesian coordinate of any point at inter-atomic bond distance. In order to demonstrate the changes EFG value at different positions of molecule, $EFG^{(0)}$ values have been calculated at any point at bond distance, then, distance from 0.0 to 2.0 Å (0.1 Å in each step) above the point on the perpendicular line to the molecular plane is gradually increased and perform EFG calculation at each point. The above procedure has been done for ethane, ethylene, acetylene and benzene as presented in Table 1. $EFG^{(0)}$ at the middle of bond distance is chosen for any molecular system, which is compared with points 0.0 in NICS index by Schleyer [5]. Table 1 have clearly shown the difference EFG of C-C bond in these molecules as follows. The $EFG^{(0)}$ values for C-C bond in ethane, ethylene and acetylene are 2.0548, 3.6325 and 5.1470, respectively. The differences between $EFG^{(0)}$ for ethylene and ethane for C-C bond distance is 1.5777, which can be attributed to "ethylenic π -bond". Similarly, the difference between $EFG^{(0)}$ of acetylene and ethane is about 3.0922 which is attributed for "acetylenic π -bond". Interestingly, $EFG^{(0)}$ for acetylenic is about twice of ethylenic as expected.

Let check the aromaticity for benzene from EFG view point. The EFG procedure for evaluation of aromaticity is in the following. Let us use $EFG^{(0)}$ for this analysis without losing the generality of concept. It is observed that $EFG^{(0)}$ of six C-C bonds is equal, and it is 1.1986 which is between single bond of ethane and double bond of ethylene ($2.0548 < 3.0064 < 3.6325$). It clearly confirms the existence of "delocalization" of π bonds in this molecule. The EFG value for benzene as localized form is three ethylenic bonds, (3×1.5777) = 4.7331. If benzene is considered as delocalized form, then π -delocalization contribution of EFG in benzene is;

$$\Sigma EFG^{(0)} = (6 \times EFG^{(0)}_{\text{of benzene}} - (6 \times EFG^{(0)}_{\text{of ethane}})) = (6 \times 3.0064) - (6 \times 2.0548) = 5.7096$$

Then, the aromaticity $\Delta EFG^{(0)}$ for benzene is,

$$\Delta EFG^{(0)} = 5.7096 - (3 \times 1.5777)_{\text{of ethylenic}} = 0.9765$$

In order to show EFG procedure can also show antiaromaticity, some known anti-aromatic compounds have been chosen to test. First, the aromaticity of cyclobutadiene has been evaluated by the same procedure as benzene. The results show that there are two single bonds with $EFG^{(0)}$ of 1.8460 and two double bonds with $EFG^{(0)}$ of 3.6231. Therefore,



$$\Sigma \text{EFG}^{(0)} = 2 (1.8460 + 3.6231)_{\text{of cyclobutadiene}} - (4 \times 2.0548)_{\text{of ethane}} = 2.7190$$

The $\text{EFG}^{(0)}$ value for cyclobutadiene as localized form is twice of ethylenic $(2 \times 1.5777)_{\text{of ethylenic}} = 3.1554$. Then, the aromaticity

$\Delta \text{EFG}^{(0)}$ for cyclobutadiene is,

$$\Delta \text{EFG}^{(0)} = 2.7190 - 3.1554 = -0.4364$$

Therefore, $\Delta \text{EFG}^{(0)}$ value is negative for antiaromatic compounds.

The aromaticity of many compounds has been evaluated by mentioned procedure. These tables clearly reveals that $\Delta \text{EFG}^{(0)}$ is positive for all aromatic systems. Some results are presented in Table 2.

4. Conclusions

Several series of various compounds have been optimized at B3LYP/6-311++G** level of theory with no imaginary frequencies. All the rings have been optimized to be planar. DFT-based calculations of electric field gradient on bond have been performed and presented a new criterion for aromaticity. $\Delta \text{EFG}^{(0)}$ is differences between sum of EFG at the above the middle of bond in delocalized system and localized one. Positive $\Delta \text{EFG}^{(0)}$ values indicate presence of aromaticity, while negative values denote antiaromaticity.

Table 1. EFG calculation of Ethane, Ethylene, Acetylene and Benzene at different middle of bond distances (in angstrom)

Distance	Ethane	Ethylene	Acetylene	Benzene
0.0	2.0548	3.6325	5.1470	3.0064
0.1	1.9810	3.2992	4.8985	2.7671
0.2	1.7797	2.9176	4.2574	2.4597
0.3	1.4998	2.4033	3.4257	2.0316
0.4	1.1969	1.8679	2.5950	1.6002
0.5	0.9140	1.3874	1.8810	1.1986
2.0	0.0063	0.0016	0.0034	0.0027

Table 2. NICS and $\Delta \text{EFG}^{(0)}$ Values for Substituted Benzenes.

Molecule	NICS(0)	$\Delta \text{EFG}^{(0)}$	Molecule	NICS(0)	$\Delta \text{EFG}^{(0)}$
Benzene	-8.03	0.9765	Pyridine	-6.82	0.8876
Benzene-F	-9.98	1.2120	2-Azapyridine	-5.33	0.7342
Benzene-Cl	-8.81	1.1212	3-Azapyridine	-5.51	0.8063
Benzene-Br	-8.52	1.0887	4-Azapyridine	-5.30	0.7805
Benzene-NO ₂	-9.97	1.5891	2,3-Diazpyridine	-4.32	0.8658
Benzene-CHO	-7.68	0.9016	2,4-Diazpyridine	-3.77	0.6364
Benzene-COOH	-7.95	0.9383	3,5-Diazpyridine	-4.04	0.7244
Benzene-OH	-9.06	1.0829	2,3,4-Triazapyridine	-2.67	0.7068
Benzene-CN	-9.44	0.9327	2,3,5-Triazapyridine	-2.37	0.7779
Naphthalene	-17.1	0.91	2,4,5-Triazapyridine	-1.80	0.7576
Anthracene	-26.47	0.57	2,3,4,5-Tetraazapyridine	-0.62	0.8505
Phenanthrene	22.75	0.87	Pentaazapyridine	+1.86	0.9566

References

- [1] Mitchell, R. H. Chem. Rev., 101 (2001) 1301.
- [2] Krygowski, T.M.; Cyranski, M.K. Chem. Rev. 101 (2005)1385.
- [3] Sobczyk, L.; Grabowski, S.J.; Krygowski, T. M. Chem. Rev. 105 (2001) 3513.
- [4] Frisch M.J. et al., Gaussian03, Inc., Pittsburgh, PA, 2003.
- [5] Schleyer, P. v. R. Chem. Rev. 105 (2005) 3433.

**Theoretical study of the interaction between uracil and parent nitrosamine**H. Roohi^{a,b,*} and E. Anjomshoa^a^aDepartment of Chemistry, Faculty of Science, University of Sistan & Baluchestan, P.O. Box 98135-674, Zahedan, Iran^bDepartment of Chemistry, Faculty of Science, University of Guilan, Rasht, Iran.

(danesh.anjomshoa@Gmail.com)

Keywords: Uracil, Nitrosamine, Hydrogen bond interaction, Binding energy.**1. Introduction**

The nucleic acid bases have tremendous versatility in the formation of hydrogen bond complexes because of the presence of numerous hydrogen bond donor and acceptor groups [1,2]. Uracil with acidic and basis sites is a pyrimidine nucleobase of RNA[3]. Hydrogen bonding between uracil and adenine in nucleic acids is a consequence of the acid/base character of these important biological compound [4]. Because of the simple structure of uracil, the theoretical analysis of its interaction with one or several water molecules has received a great deal of attention during the past years [5]. Most of nitrosamines are carcinogenic compounds and play an important role in the development of tumors and cancer in animals. N-nitrosamines are believed to require metabolic activation to exert their carcinogenic effects [6]. The main scope of this work is to systematically analyze the interaction between Uracil and parent nitrosamine (NA).

2. Computational methods

The structure of the Uracil-nitrosamine (UN) complexes were fully optimized at B3LYP/6-311++G(2d,2p) level. The harmonic frequencies were calculated at the same level of theory. All calculations were performed using the Gaussian 03 program. The UN binding energy was calculated as the difference of the energy of the complex and the sum of the energies of the separated monomers. The Zero-point vibrational energy correction (ZPE) has also been included. The counterpoise procedure (CP) was used to correct for basis set superposition error (BSSE) in the calculation of binding energies.

3. Results and discussion

As can be seen in Fig. 1, all optimized complexes have cyclic structures with two H-bonds involved in the interaction. In eight-membered cyclic complexes UN1, UN3, UN5 and UN8 the O atom of nitrosamine and one C=O group of uracil act as proton acceptors and N-H bond of nitrosamine and one N-H bond of uracil (with the exception of C-H bond in UN7 and UN8) as proton donors. In eight-membered structures UN2, UN4, UN6 and UN7, instead of O atom, the N atom of NO group acts as proton acceptor. The other interactions are the same as the interactions observed in the eight-membered structures. In all complexes the intermolecular N(C)H...O(N) distances are longer than the NH...OC ones. This reflects the stronger strength of the NH...OC H-bonding as compared with the N(C)H...ON one. Complex formation results in an elongation of the NH bonds of U and NA. The greater change in NH bond involved in H-bonding interaction is observed in UN1.

Binding energies (BE) of the UN complexes including the BSSE and ZPE corrections are given in Table 1. The binding energies range from -39.543 to -19.665 kJ mol⁻¹. The highest binding energy is for UN1 with shortest hydrogen bond distances and the lowest binding energy is for UN8. From the values presented in Table 1, it can be seen that the relative stability order of the eight complexes is UN1 > UN2 > UN3 > UN4 > UN5 > UN6 > UN7 > UN8.

Table1. Binding energies (kJ mol⁻¹) at B3LYP/6-311++G(2d,2p) level

	BE	BE ^{BSSE}	BE ₀ ^{BSSE}
UN 1	-39.543	-38.041	-30.374
UN 2	-33.738	-32.236	-25.089
UN 3	-28.116	-26.614	-19.880
UN 4	-25.050	-23.548	-17.089
UN 5	-23.971	-22.469	-16.110
UN 6	-21.169	-19.667	-13.547
UN 7	-20.038	-18.536	-12.655
UN 8	-19.665	-18.163	-12.106

$$BE = E_{UN} - (E_U + E_{NA}), BE^{BSSE} = BE + BSSE, BE_0^{BSSE} = BE^{BSSE} + \Delta ZPE.$$

4. Conclusions

The hydrogen-bond interaction of the complexes between nitrosamine and Uracil is analyzed using the B3LYP method at 6-311++G (2d,2p) basis set levels. Eight cyclic structures are considered with two hydrogen bonds involved in the interaction. All the structures are eight membered rings. Of these, the structure UN1 is the most stable and cyclic structure UN8 is the less stable.

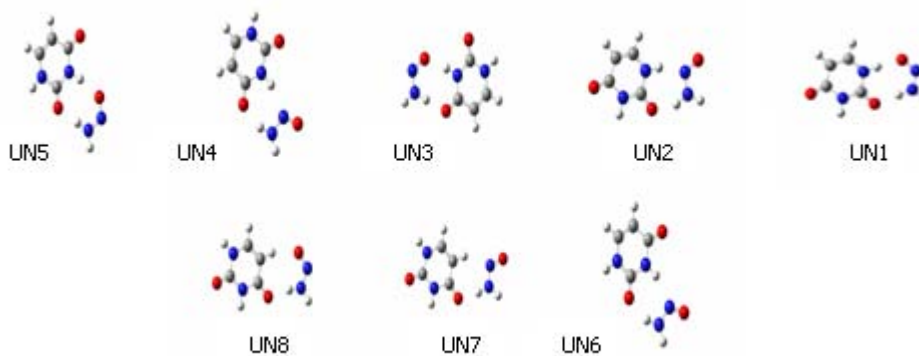


Fig. 1. Optimized structures for UN complexes

References

- [1] D. Chunsheng, W.U. Qunyan, M.A. Hongkun, Z.H. Xinming, Z.H. Zhengyu, *International Journal Of Quantum Chemistry*. 107 (2007) 1253.
- [2] M.H. Almatarneh, C.G. Flinn, R.A. Poirier, *J.Phys.Chem.A*. 110 (2006) 8227.
- [3] I. Dabkowska, J. Rak. M. Gutowski, *J.Phys.Chem.A*. 106 (2002) 7423.
- [4] T.M. Miller, S.T. Arnold, A.A. Viggiano, A.E. Stevens Miller, *J.Phys.Chem.A*. 108 (2004) 3439.
- [5] R. Wysokinski, D. Michalska, D.C.Bienko, *J.Phys.Chem.A*. 107 (2003) 8730.
- [6] M. Sulc, B.Kubickova,V. Maslova,P. Hodek, *Gen. Physiol. Biophys.* 23 (2004) 424.

**From information theories to electron correlation energy**

Afshan Mohajeri* and Mojtaba Alipour

Department of Chemistry, College of Sciences, Shiraz University, Shiraz, 71454, Iran

(E-mail: amohajeri@shirazu.ac.ir)

Keywords: Information theory, Correlation energy, Shannon entropy, Information energy, Natural atomic orbital.**1. Introduction**

The Hartree–Fock (HF) energy is not as low as the true energy of the system. The mathematical reason for this is that our requirement that wave function be a single determinant is restrictive and we can introduce additional mathematical flexibility by allowing wave function to contain many determinants. Also there is a corresponding physical reason for the HF energy being too high which is connected with the independence of the electrons in a single determinantal wave function. The energy difference between the HF and the exact (for a simplified nonrelativistic Hamiltonian) energy for a system is referred to as the correlation energy. Although a great deal of theoretical studies have been developed to estimate correlation energy [1-3], recovering the correlation energy for large systems still remains one of the most challenging problems in quantum chemistry. Also, recently, some information theoretic measures of the electron correlation in atomic systems have been proposed [4, 5]. Information theory is a branch of mathematics introduced by C. E. Shannon [6]. For a discrete probability distribution (p_1, p_2, \dots, p_k) Shannon entropy is defined as the quantity

$$H = - \sum_{i=1}^k p_i \ln p_i \quad (1)$$

with this constraint that the summation over all p_i is equal to one. Another measure of the information content of a quantum system in this theory is the concept of information energy, E , which is introduced by O. Onicescu [7]. For a discrete probability distribution (p_1, p_2, \dots, p_k) , E is defined as

$$E = \sum_{i=1}^k p_i^2 \quad (2)$$

Using the fact that the discrete functions of H and E varies between two extreme cases implies that these functions can be applied as an electron correlation measure in atomic and molecular systems.

2. Computational Details

Natural population analysis implemented in Guassian03 package has been employed to obtain occupation number of natural atomic orbitals. For the atomic species, natural population analysis has been carried out at HF/6-31G level of theory. In the case of molecular systems natural population analysis has been performed followed by the geometry optimization at HF/aug-cc-PVDZ level. The discrete probability distribution (p_1, p_2, \dots, p_k) can be calculated using

$$p_i = \frac{\gamma_i}{N} \quad (3)$$

where γ_i is the occupation number of the i -th natural atomic orbital which is divided by total number of electrons (N) in the atoms or molecules for normalization to one.

3. Results and Discussion

The probabilities of Eq. (3) was used for calculation of Shannon entropy and information energy according to the Eqs. (1) and (2), respectively. The computed values for atoms and their singly charged positive ions are given in Table 1. The results reveal that the calculated Shannon entropy using discrete probabilities is an increasing function while information energy is a decreasing function of the number of electrons and hence both can be used as possible measures of electron correlation. We propose an expression for correlation energy as a bilinear function of the form below,

$$E_{corr} = aF + bZ + c \quad (4)$$

where a , b and c are fitting parameters and F is either H or E in which the correlation energy dependence on the number of electrons is included. The exact correlation energies of neutral atoms and their singly charged positive ions are then used to



find the best fit for parameters a , b and c . The obtained correlation energies are added to the Hartree-Fock ground state energies of atoms and their cations to estimate their non-relativistic total energies and the first ionization potentials of the ground state of the main group elements from hydrogen through argon were computed. The calculated ionization potentials are in reasonably good agreement with their corresponding experimental values (Figure 1).

The applicability of the proposed method has been also checked for evaluation of molecular correlation energy. For developing and testing the proposed method we construct a set of 25 molecules composed of C, N, O, and H atoms. We consider each molecule consists of neutral atoms placed at their equilibrium position. The molecular Shannon entropy, $H(\text{molecule})$, and the molecular information energy, $E(\text{molecule})$, can be estimated using Eqs. (1) and (2), respectively. In this case summations run over natural atomic orbitals of all constituent atoms in the molecule and N is the total number of electrons in the molecule. The molecular correlation energy is expressed in terms of molecular Shannon entropy or molecular information energy and the number of electrons as follows

$$E_{\text{corr}}(\text{molecule}) = a'F(\text{molecule}) + b'N + c' \quad (5)$$

where $F(\text{molecule})$ is either $H(\text{molecule})$ or $E(\text{molecule})$. The parameters a' , b' and c' are determined for reproducing best the Gaussian-3 (G3) correlation energies in our molecular data set.

4. Conclusion

We found that it is possible to discretize the probability distribution in natural atomic orbitals to calculate Shannon entropy and information energy. The dependency of the correlation energy on the atomic number and number of electrons prompts us to propose an expression in terms of Shannon entropy and information energy for estimation of correlation energy in atoms and cations. The applicability of the proposed method has been also analyzed to calculate correlation energy for molecular systems.

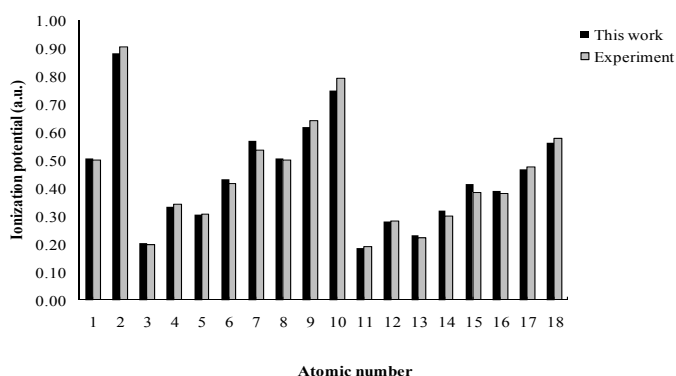


Figure 1. Experimental and computed values of first ionization potentials (a.u.) using information energy for atoms with $Z=1-18$

References

- [1] E. Clementi, G. Corongiu, Int. J. Quantum Chem. 62 (1997) 571.
- [2] S. Kristyan, G. I. Csonka, J. Comput. Chem. 22 (2001) 241.
- [3] J. A. Alonso, N. H. March, N. A. Cordero, A. Rubio, J. Phys. B: At. Mol. Opt. Phys. 36 (2003) 2695.
- [4] E. Romera, J. S. Dehesa, J. Chem. Phys. 120 (2004) 8906.
- [5] A. Grassi, Int. J. Quantum Chem. 108 (2008) 774.
- [6] C. E. Shannon, Bell Syst. Tech. 27 (1948) 379.
- [7] O. Onicescu, C. R. Acad. Sci. Paris A263 (1966) 25.

Table 1. The values of Shannon entropies and information energies for neutral atoms and singly charged positive ions.

Atom	H	E	Cation	H	E
H	0.000	1.000			
He	0.693	0.500	He ⁺	0.000	1.000
Li	1.099	0.333	Li ⁺	0.693	0.500
Be	1.386	0.250	Be ⁺	1.099	0.333
B	1.609	0.200	B ⁺	1.386	0.250
C	1.792	0.167	C ⁺	1.609	0.200
N	1.946	0.143	N ⁺	1.792	0.167
O	2.079	0.125	O ⁺	1.946	0.143
F	2.197	0.111	F ⁺	2.079	0.125
Ne	2.303	0.100	Ne ⁺	2.197	0.111
Na	2.398	0.091	Na ⁺	2.303	0.100
Mg	2.485	0.083	Mg ⁺	2.398	0.091
Al	2.565	0.077	Al ⁺	2.485	0.083
Si	2.639	0.071	Si ⁺	2.565	0.077
P	2.708	0.067	P ⁺	2.639	0.071
S	2.773	0.063	S ⁺	2.708	0.067
Cl	2.833	0.059	Cl ⁺	2.773	0.063
Ar	2.890	0.056	Ar ⁺	2.833	0.059

**The corrosion inhibition of some substituted quinolones in water solvent by DFT method**

S. Rasti and M. Oftadeh

¹Department of chemistry, Payame Noor University (PNU), Isfahan, Iran

(Email: m_oftadeh@pnu.ac.ir)

(Email: rasti_s66@yahoo.com)

Keywords: Corrosion inhibitor, DFT, Quinolone.**1. Introduction**

Today, one of the problems in the industry is corrosion problem. One of the most important methods to control corrosion is using inhibitor materials. These compounds are in fact a negative catalyst. Organic inhibitors have hetero atoms such as O, N, S, in the ring, including synthetic materials of quinolones. There is usually a correlation relation between physicochemical properties of corrosion inhibitor compounds and the percentage of inhibition in the solvent. By such correlation we can predict the lethal efficiency due to both electron donor and acceptor groups. Many researchers reported the inhibition effect mainly depends on some physicochemical properties such as: the highest occupied molecular orbital energy (HOMO), lowest unoccupied molecular orbital energy (LUMO), the energy gap between HOMO and LUMO, dipole moments (μ), charges on the C, O and N atoms and polarizabilities (α) [1]. Such data offer a unique opportunity for searching for correlation between inhabitation efficiency and molecular properties. Calculations based on calibration procedures employ an ordinary least squares methodology with a simple descriptors. The choice of descriptor set was based on several articles found in the literature, which indicate the most usual descriptors. We added several others base on common sense and evaluation ease of in order to explore new possibilities. In this paper such a relationship was obtained for some substituted fluoro quinolones (floxacin) compounds between the mentioned descriptors with efficiency inhabitation [2].

2. Method

The molecular structure calculations were performed with B3LYP hybrid method by using the Gaussian 98. The 6-31G** basis set was used for these molecules and full geometry optimization was carried out. The calculations were performed in the presence of a solvent, using an Onsager model (SCRF). The ordinary regression analysis (OLS) was performed by SigmaPlot11 coding.

3. Results and discussion

According to the results of previous works [1, 3], the best correlation between experimental efficiency inhibitors of the molecules (No. 2, 3, 6 and 8 [4]) and HOMOs, LUMOs, dipole moments (μ) and polarizabilities (α) obtained from the optimized structure of the compounds in water solvent listed in table 1 is carried out by ordinary regression analysis (OLS). All OLS calculations were carried out with centered on four descriptors for four molecules (No 2, 3, 6 and 8 in table 1) whose efficiency inhabitation (%EI) extracted from literature [4]. In order to identify the effect of the descriptors, we carried out an elimination algorithm by which the descriptor with the least contribution to the response function (%EI) is eliminated from the denominator of the proposed relation. Finally the following correlation relation is obtained:

$$\%EI = \frac{a \times E_{HOMO} + b \times E_{LUMO} + c \times \mu + d \times \alpha}{1 + a \times E_{HOMO} + c \times \mu + d \times \alpha}$$

where $a=-3.7765$, $b=-12.9910$, $c=0.1212$ and $d=0.0009$ with correlation coefficient, R^2 , and mean absolute deviation, MAD, are 1.00 and 0.827, respectively. It is a linear multiregression. We can predict the EI% for the other substituted quinolone compounds which listed in table 1. These compounds have near similar EI%. It means H and $NHCH_3$ as R1 group do not highly effect on calculated physicochemical properties compared with C_2H_5 and cyclopropyl groups. Maybe, E_{LUMO} does not effect as E_{HOMO} , μ and α because of trying the best fit for the parameters.

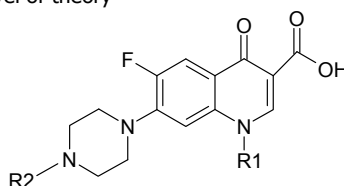
The corrosion inhibitor increases with increasing E_{HOMO} and decreasing E_{LUMO} . Also with increasing dipole moment(μ) and polarizability (α) the corrosion inhibitor efficiency increases too. The highest maximum μ has maximum efficiency when it is considered as a corrosion inhibitor.





4. Conclusions

The corrosion inhibition of mild steel in solution of sodium chloride solution containing norfloxacin (No. 2), ciprofloxacin (No. 3), perfloxacin (No. 6) and amifloxacin (No. 8) have been experimentally investigated [4]. These compounds have been found to act as good corrosion inhibitors for mild steel in this solution. We attempted to find theoretical parameters to characterize inhibition property of eight floxacin derivative compounds using an ab initio method employing the B3LYP/6-31G** basis set. No significance differences were found for the calculated and experimental results of these compounds. The effects of substituents on the inhibition efficiency can be due to HOMO and LUMO energies, dipole moments and polarizabilities, so they are introduced as good and simple descriptors for this purpose. Although the molecule No. 1 and 5 are simpler than the others, they have IE% a little higher than the others. In other words, we have reached the conclusion that the synthesis of better corrosion inhibitors can be achieved by controlling all electronic properties and parameters of a selected group of molecules.

Table 1 HOMOs, LUMOs, dipole moments (μ) and polarizabilities (α) obtained from the optimized structure of the compounds in water solvent based on B3LYP/6-31G** level of theory



NO	R ₁	R ₂	E _{HOMO}	E _{LUMO}	μ	α	IE%	IE% (exp)[4]
1	H	H	-0.2059	-0.0551	12.6925	183.2	91.84	
2	C ₂ H ₅	H	-0.2041	-0.0509	12.3986	190.4	90.17	90.17
3		H	-0.2009	-0.0517	12.7237	208.1	90.59	90.59
4	NHCH ₃	H	-0.2026	-0.0558	14.4733	139.9	92.45	
5	H	CH ₃	-0.2025	-0.0559	12.2601	142.1	91.90	
6	C ₂ H ₅	CH ₃	-0.1909	-0.0526	12.9373	206.4	90.89	90.89
7		CH ₃	-0.2059	-0.0512	12.7907	154.9	90.34	
8	NHCH ₃	CH ₃	-0.2018	-0.0552	13.4078	203.9	92.08	92.08

References

- [1] G. Gece, Corrosion Science 50 (2008) 2981.
- [2] S. P. Cardoso, J. A. C. P. Gomes, L. E. P. Borges, E. Hollauer, Brazilian Journal of Chemical Engineering, 24 (2007) 547.
- [3] M. Mirheydari and M. Oftadeh, Investigation of Functional Group Effect on Corrosion Inhibitor of Thiophen, BSC project, Payame Noor University, Isfahan, Iran (2009).
- [4] S. Acharya and S. N. Upadhyay, Trans Indian Inst. Met, Chemical Physics Letters 57 (2004) 297.

**Coupled wave quantum scattering via separable potential model: Application to statistical mechanics**

A. Maghari and V. M. Maleki

Department of Physical Chemistry, University of Tehran, Tehran, Iran

(Email: maghari@khayam.ut.ac.ir)

Keywords: Coupled wave, Separable potential, Second virial, Collision integral**1. Introduction**

The behavior of a certain kind of nonlocal separable potential has been studied by Mitra et al [1-3] in the complex angular momentum plane. In our two recent works, the scattering properties of a system with zero angular momentum $\ell = 0$ (s-wave) via a separable potential of rank two was calculated [4] and then applied to obtain the equilibrium statistical mechanical properties of fluids [5]. We then have generalized a formulation for partial-wave scattering wave function and its properties, subjected to the potential scattering in a given partial-wave form factor with arbitrary angular momentum, which applied to obtain the statistical mechanical properties [6,7]. In this work, we present a new formulation of the equilibrium and non-equilibrium statistical mechanical properties of a gas consisting of free particles and independent correlated pairs interacting via coupled wave scattering subjected to a non-local rank-two separable potential. Analytical expressions for some equilibrium thermodynamic properties, such as Helmholtz free energy and second virial coefficient as well as some non-equilibrium thermophysical properties, such as collision cross sections and transport collision integrals are described.

2. New formulation for statisticat mechanics via coupled-waves

A separable potential model for coupled-waves can be written as

$$\hat{V} = \sum_{i=1}^n \sum_{\ell, \ell'} (2\ell+1)(2\ell'+1) v_i |\chi_i; \ell\rangle \langle \ell'; \chi_i| \quad (1)$$

where n is the rank of the potential operator \hat{V} , v_i the coupling strength and $|\chi_i; \ell\rangle$ the state of the system with angular momentum quantum number ℓ . The corresponding partial-wave off-shell two-body transition matrix elements for coupled waves in the momentum representation can be written as

$$T_{pp'}^{(\ell\ell')}(z) = \langle p | \hat{T}_{12}^{(\ell\ell')} | p' \rangle = \langle p | \hat{V}_{12} (\hat{1} - \hat{Q}^{(\ell\ell')} \hat{V}_{12})^{-1} | p' \rangle \quad (2)$$

where $\hat{Q}^{(\ell\ell')} = (z - \hat{H}_0)^{-1}$ is the free motion resolvent, in which $\hat{H}_0 = \hat{p}^2/2\mu$ is free motion Hamiltonian, μ is reduced mass and $z \equiv E + i\varepsilon$ is the complex energy parameter, wherein the energy E is the eigenvalue of \hat{H}_0 , $\hat{H}_0 |E\rangle = E |E\rangle$.

The two-body transition matrix leads to the series in terms of partial-wave transition matrix $\hat{T}_{pp'}^{(\ell\ell')}(z)$

$$T_{12}(\mathbf{p}, \mathbf{p}'; z) = \sum_l \frac{(2\ell+1)(2\ell'+1)}{4\pi} T_{pp'}^{(\ell\ell')}(z) f_{\ell, \ell'}(\hat{\mathbf{p}}, \hat{\mathbf{p}}') \quad (3)$$

in which $\hat{\mathbf{p}}$ and $\hat{\mathbf{p}}'$ are unit vectors corresponding to the off-shell momentum.

Moreover, for the N -particle spinless system, the N -particle partition function can be written as $Z_N \equiv \text{Tr} e^{-\beta \hat{H}^{(N)}}$,

where the trace (Tr) is over all states in a complete set corresponding to the given $\beta \equiv 1/k_B T$. In our present work, we assumed that the system consists of free particles and independent correlated pairs. For this system, the N -particle partition function can be approximated by

$$Z_N \approx \frac{1}{N!} Z_1 \left(1 + 2 \frac{Z_{12}}{Z_1} \right)^N \quad (4)$$



where Z_1 is one-particle partition function and $Z_{12} = \frac{1}{2} \text{Tr} \hat{U}_{12}$ is the correlated pairs partition function. Defining the Green operators $\hat{G}_0(z) \equiv (z - \hat{H}_0)^{-1}$ and $\hat{G}_{12}(E, \varepsilon) \equiv (z - \hat{H}_{12})^{-1}$, the correlated pairs partition function is written as

$$Z_{12} = \frac{1}{4\pi i} \int_C d\tilde{q} e^{-\tilde{q}^2/2\tilde{T}} \tilde{q} \text{Tr} [\tilde{G}_0(\tilde{q}) \tilde{T}_{12}(\tilde{q}) \tilde{G}_0(\tilde{q})] \quad (5)$$

Moreover, the $\ell\ell'$ th partial-wave scattering amplitude can be written in terms of the partial-wave transition matrix

$$f_{\ell\ell'}(\tilde{E}) = -(2\pi)^2 \lim_{\tilde{\varepsilon} \rightarrow 0^+} \tilde{T}_{pp}^{(\ell\ell')}(\tilde{E} + i\tilde{\varepsilon}) \quad (6)$$

where $\tilde{T}_{pp}^{(\ell\ell')}(\tilde{E} + i\tilde{\varepsilon})$ can be obtained in terms of $\tilde{Q}_{ij}^{(\ell\ell')}(\tilde{q})$. We can show, however, that the formula for the correlated pairs partition function can be obtained by

$$Z_{12} = 2\sqrt{2} \sum_{\ell, \ell'} (2\ell + 1)(2\ell' + 1) \left[\sum_b \left(\exp(-\tilde{E}_b^{(\ell\ell')}/\tilde{T}) - 1 \right) + \frac{1}{\pi} \int_0^\infty w_{\ell\ell'}(\tilde{E}) \exp(-\tilde{E}/\tilde{T}) d\tilde{E} \right] \quad (7)$$

where $\tilde{E}_b^{(\ell\ell')}$ is the two-body bound state and the function $w_{\ell\ell'}(\tilde{E})$ is defined as $w_{\ell\ell'} \equiv \frac{u_\ell v_{\ell'}' - u_{\ell'}' v_\ell}{u_\ell u_{\ell'} + v_\ell v_{\ell'}}$.

3. Results and discussion

The method proposed in this paper applies to arbitrary angular momentum of coupled-waves and rank-two separable potential. The relation between the correlated pairs partition function Z_{12} and the Helmholtz function leads to the expression:

$$A(N, W, T) \approx -Nk_B T \ln(eV/\lambda^3) - Nk_B T (\lambda^3 Z_{12}/V) \quad (8)$$

where λ is the thermal de Broglie wavelength and V is the volume. The various equilibrium thermodynamic properties of the system can be derived from equation (7) that includes evaluation of the correlated pairs partition function Z_{12} . As an example, the quantum second virial coefficient requires knowledge of the bound-states and continuum spectra and can be written as

$$B(T) = \sum_{\ell, \ell'} (2\ell + 1)(2\ell' + 1) B^{(\ell\ell')}(T) \quad (9)$$

$$B^{(\ell\ell')} = -2\sqrt{2}\lambda^3 \left[\sum_b \left(\exp(-\tilde{E}_b^{(\ell\ell')}/\tilde{T}) - 1 \right) + \frac{1}{\pi} \int_0^\infty w_{\ell\ell'}(\tilde{E}) \exp(-\tilde{E}/\tilde{T}) d\tilde{E} \right] \quad (10)$$

Furthermore, the transport properties are described by the effective transport cross sections. These cross sections are related to the so-called transport collision integrals, which is determined from the partial-wave phase shift η_ℓ by

$$\tilde{Q}_n(\tilde{E}) = \frac{4\pi}{\tilde{E}} \sum_{v>0} \sum_{\ell=0}^n \sqrt{a_{nv}^\ell a_{nv}^{\ell'}} \sin(\eta_{\ell+v} - \eta_\ell) \sin(\eta_{\ell'+v} - \eta_{\ell'}) \quad (11)$$

and then the reduced collision integrals are obtained from an average over a Maxwell-Boltzmann distribution as

$$\tilde{\Omega}^{(n,s)}(\tilde{T}) = \frac{F(n,s)}{2\tilde{T}^{s+2}} \int_0^\infty e^{-\tilde{E}/\tilde{T}} \tilde{E}^{s+1} \tilde{Q}_n(\tilde{E}) d\tilde{E} \quad (12)$$

The superscripts n and s appearing in the collision integral denotes weighting factors that account for the mechanism of transport by molecular collision. The Chapman-Enskog kinetic theory of a dilute gas leads to the expressions for the coefficients of transport properties as a function of collision integrals.

References

- [1] Mitra A N, Phys. Rev. 123 (1961) 1892.
- [2] Mitra A. N., Anand J. D., Phys. Rev. 130 (1963) 2117.
- [3] Mitra A. N., Bhasin V. S., Phys. Rev. 131 (1963) 1265.
- [4] Maghari A., Tahmasbi N. J. Phys. A: Math. Gen. 38 (2005) 4469.
- [5] Maghari A., Dargahi M., J. Phys. A: Math. Theor. 41 (2008) 275306.
- [6] Maghari A., Dargahi M. J Stat Mech, (2008) P10007.

**Thermophysical properties of the dilute fluorine gas from a new *ab initio* potential energy surface**

M. H. Karimi Jafari, A. Maghari and M. Ashoori

Department of Physical Chemistry, University of Tehran, Tehran, Iran

(Email: maghari@khayam.ut.ac.ir)

Keywords: F₂-F₂, potential energy surface, collision integrals, second virial**1. Introduction**

Diatomic fluorine molecule F₂, is a highly chemically reactive material, and because of its corrosive nature, there are limited experimental measurements for its molecular and bulk properties [1-4]. Molecular fluorine is one of the weakest covalently bound species and the existence of an accurate knowledge of intermolecular pair potential will be helpful in both experimental and theoretical studies. Since the importance of the physical properties of fluorine, we have recently obtained the F₂-F₂ potential energy surface (PES) from *ab initio* calculations using a newly developed aug-cc-pVTZ basis set supplemented with bond functions at the MP4 level of theory, and this surface has been represented analytically [5]. In this work, the new F₂-F₂ intermolecular potential model has been applied in the framework of the quantum-statistical mechanics and of the corresponding kinetic theory to calculate the most important thermophysical properties of F₂ governed by two-body and three-body interactions. Among various macroscopic properties, second virial and transport coefficients usually are appropriate candidates. The Wigner-Kirkwood expansion in \hbar^2 is suitable for the computation of the second virial coefficient. To calculate the transport coefficients, the Mason-Monchick approximation (MMA) has been used for the calculation of collision integrals [6]. Since fluorine is a highly reactive material, and because of its corrosive nature, there are limited experimental measurements for its molecular and bulk properties.

2. Analytical *ab initio* F₂ - F₂ Potential Function

Details of the *ab initio* calculations leading to the F₂-F₂ potential energy function have been described in our previous work [5]. Potential energy landscape for molecular fluorine was calculated using counterpoise corrected interaction energy at the MP4/aug-cc-pVTZ level of theory. The interaction energies were fitted to the spherical expansion as

$$U(R, \theta_a, \theta_b, \varphi) = \sum_{L_a, L_b, L} V_{L_a, L_b, L}(R) A_{L_a, L_b, L}(\theta_a, \theta_b, \varphi) \quad (1)$$

$$A_{L_a, L_b, L}(\theta_a, \theta_b, \varphi) = \sum_{M=0}^{(L_a, L_b)} (-1)^M (2 - \delta_{M,0}) \langle L_a, M; L_b, -M | L, 0 \rangle \left[\frac{(L_a - M)!(L_b - M)!}{(L_a + M)!(L_b + M)!} \right]^{1/2} P_{L_a}^M(\cos \theta_a) P_{L_b}^M(\cos \theta_b) \cos(M\varphi) \quad (2)$$

and the expansion coefficients $V_{L_a, L_b, L}(R)$ have been evaluated using a weighted linear least-squares procedure. The long range and short range contributions of $V_{L_a, L_b, L}$ are represented as

$$V_{L_a, L_b, L}^{LR}(R) = \frac{C_{L_a, L_b, L}}{R^{V_{L_a, L_b, L}}} F(R; n, \alpha); \quad V_{L_a, L_b, L}^{SR}(R) = \exp(-\alpha_{L_a, L_b, L} R) \sum_{k=0}^{k_{\max}} d_{L_a, L_b, L} R^k;$$

$$F(R; n, \alpha) = 1 - \exp(-\alpha R) \sum_{k=0}^n \frac{(\alpha R)^k}{k!}.$$

3. Results and Discussion

The classical second virial coefficient at temperature T can be calculated for the F₂-F₂ dimer using the formula:

$$B(T) = -\frac{1}{2} \int_{\omega} \left\langle e^{-U(R, \omega)/k_B T} - 1 \right\rangle R^2 dR \quad (3)$$

The rotational contribution for quantum second virial coefficient can be obtained as:

$$B_{\text{rot}}^{(1)} = -\frac{N_A \hbar^2 \beta^2}{96} \sum_{L_a, L_b, L} \left(\frac{L_a(L_a+1)}{I_a} + \frac{L_b(L_b+1)}{I_b} \right) \iint e^{-\beta U} R^2 V_{L_a, L_b, L}(R) A_{L_a, L_b, L}(\omega) dR d\omega \quad (4)$$



The results for classical second virial coefficient is shown in Fig. 1, where we compare the calculated values with experimental results.

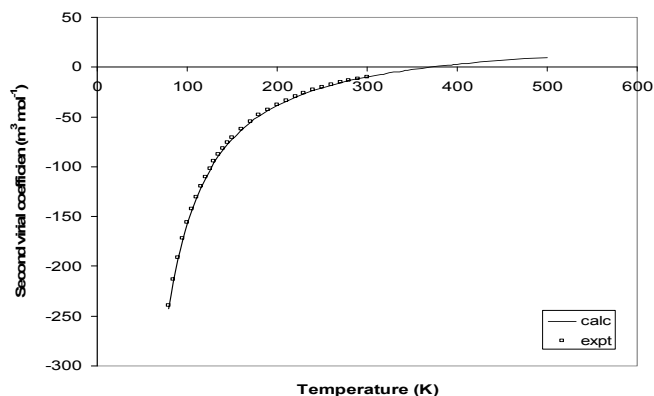


Fig. 1. Second virial coefficient of F₂ as a function of temperature

Moreover, according to the MMA procedure, the coefficients of viscosity η and self diffusion D can be written as

$$\eta = \frac{5}{16} \left(\frac{mk_B T}{\pi} \right)^{1/2} \frac{f_\eta}{R_m^2 \langle \Omega^{(2,2)*} \rangle} ; D = \frac{3}{8n} \left(\frac{k_B T}{m\pi} \right)^{1/2} \frac{f_D}{R_m^2 \langle \Omega^{(1,1)*} \rangle} \quad (5)$$

where R_m is a distance parameter of potential, $\langle \Omega^{(l,s)*} \rangle$ is a reduced collision integral averaged over all relative orientations, f_η and f_D are correction factors resulting from higher-order kinetic theory approximations. The results are given in Fig. 2, which show a good agreement between calculation and available experimental data.

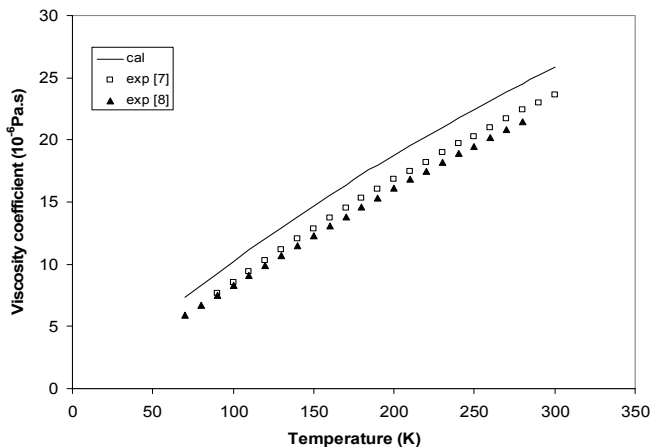


Fig. 2. Viscosity coefficient of F₂ as a function of temperature

References

- [1] Chan, K. W., Power, T. D. Jai-nhuknan, J. and Cybulski, S. M., J. Chem. Phys. 110 (1999) 860.
- [2] Karpfen, A. Chem. Phys. Lett. 299 (1999) 493.
- [3] Karpfen, A. Chem. Phys. Lett. 316 (2000) 483.
- [4] Lourderaj, U.; Sathyamurthy, N. Chem. Phys. 308 (2005) 277.
- [5] Karimi-Jafari, M. H. and Maghari, A. J. Phys. Chem. A 111 (2007) 6077.
- [6] Monchick, L. and Mason, E.A., J. Chem. Phys. 35 (1961) 1676.
- [7] Frank, E.U. and Stober, W., Z. Naturforsch. 7a (1951) 822.
- [8] Hanly, H.J.M. and Prydz, R., J. Phys. Chem. Ref. Data, 1 (1972) 1101.



Theoretical study of structural properties in alkali metal clusters

A. Mohajeri* and M. Mahmoodinia

Department of Chemistry, College of Sciences, Shiraz University, Shiraz 71454, Iran

(Email: mahmoodinia.mehdi@gmail.com)

Keywords: Magic number, DFT, Alkali metal cluster, Multiplicity.

1. Introduction

The study of the geometry, electronic structure, properties, and chemical reactivity of atomic clusters of small and medium size is an area of continuous interest because of their specific characteristics [1]. The properties of small atomic clusters, A_n , vary as a function of n . The addition of a single atom to cluster some-times has dramatic effects on its reactivity. Clusters of metallic elements have very interesting chemical and physical properties that are completely different from those of single atoms and bulk materials [2]. In this study we would like to explain cluster properties on the basis of electronic and geometric structures [3].

2. Computational method

Gaussian 03 program package [4] has been used to perform geometry optimizations and total energy calculations by DFT (bpw91, ubpw91) methods and 6-311+G* basis set for A_n ($A=Li, Na, K$ and $n=2-10$) clusters. The dissociation energies were calculated by using the following formula [5]:

$$D=E(N) - E(N-2) - E(2)$$

Here $E(N)$ is the ground-state energy of the cluster consisting of N atoms of the cluster which was obtained by energy minimization [6].

3. Result and discussion

In this work, we have studied the stability, geometry, HOMO-LOMO Gap and spin multiplicity of A_n ($A=Li, Na, K$ and $n=2, 10$) clusters by DFT method. The calculated dissociation energies $E(N) - E(N-2) - E(2)$ is considered as a measure of cluster stability. Stability of metallic clusters is studied by plotting the dissociation energy versus the number of atoms N in the Li clusters. It is clear from Fig. 1, that the maximums for dissociation energy take place at $N_A = 2$ and 8, which delineate the abundance of magic number clusters.

The geometries are optimized with several spin multiplicities, the result show that the structures with even number of atom have odd multiplicity and the singlet multiplicity is more stable than others, while the structures with odd number of atoms have even multiplicity and doublet multiplicity is more stable. As seen in Fig.2, the gap between of singlet and triplet multiplicity is rang from 0.4 to16 kcal/mol in clusters with $n=2-10$.

The computed HOMO-LOMO Gap (HLG), show that structures with $n = 2$ and 8 have maximum value of HLG (Fig.3).

4. Conclusion

In this work, we have studied the stability, geometry, HOMO-LOMO Gap and spin multiplicity of A_n ($A=Li, Na, K$ and $n=2-10$) clusters by DFT method. The result shows that dissociation energy is maximum for $N_A = 2$ and 8 which are delineate the abundance of magic number clusters. Also the geometries are optimized with several spin multiplicities which indicate that the structure with even number of atom corresponded with singlet multiplicity, while the structure with odd number of atom has doublet multiplicity.

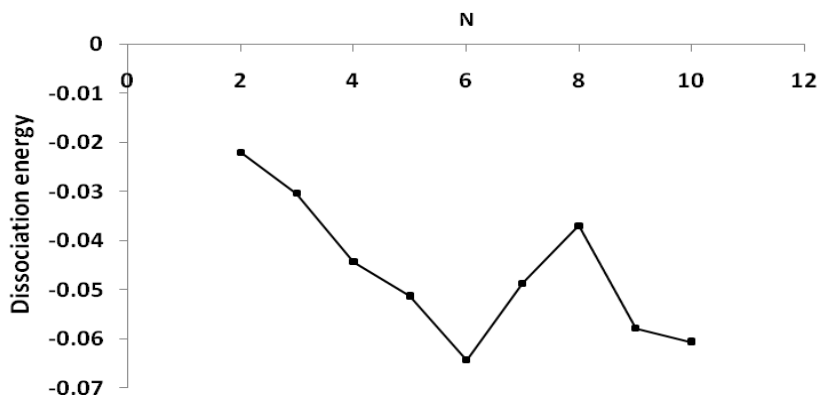


Fig.1. The dissociation energy (kcal/mol) versus the number of atom N in the Li clusters.

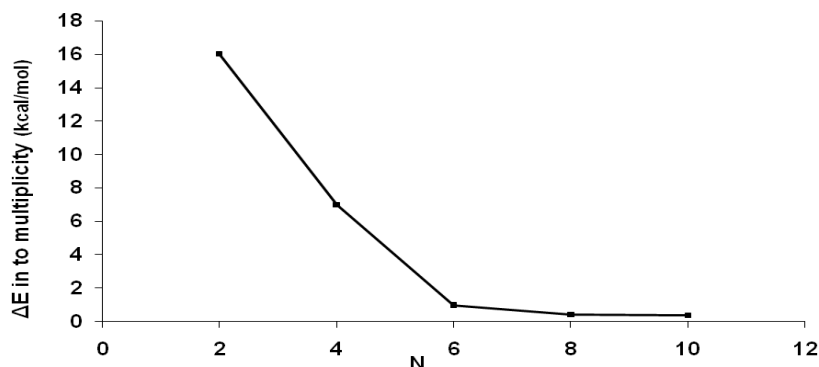


Fig. 2. The Gap between singlet and triplet multiplicity versus number of atom in Li cluster

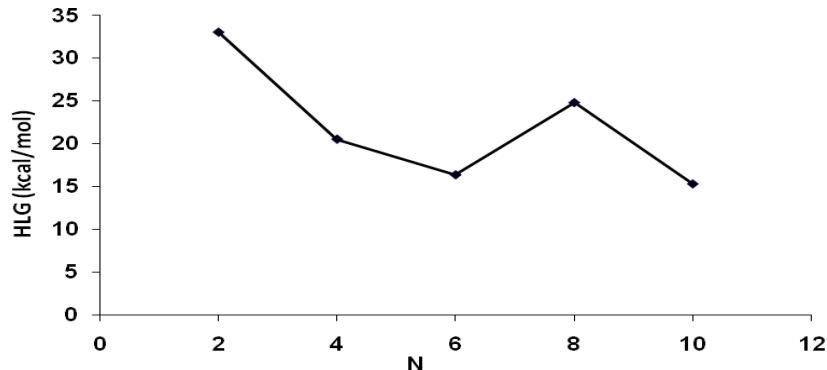


Fig. 3. The HOMO-LUMO GAP energy versus number of atom in Li cluster

References

- [1] E. Florez, P. Fuentealba, *Int. J. Quantum Chemistry*, Vol 109 (2009) 1080–1093.
- [2] F. Aguilera-Granja, J.M. Montejano-Carrizales J. Guevara, A.M. Llois. *Solid State Communications* 113 (2000) 147–151.
- [3] R. Fournier, J. B .Y. Cheng, A. Wong, *J. Chem. Phys.*, Vol 119 (2003) 9445-9445.
- [4] Frisch, M. J. et al., *Gaussian 03*, Revision B03, Gaussian Inc., Pittsburgh PA, 2003
- [5] M. K. Harbola, *Proc. Natl. Acad. Sci. USA*. Vol. 89 (1992) 1036-1039.
- [6] O. sugino, H. kamimura, *Materials Science and Engineering*, B3 (1989) 443-455

**Relationship of dipole moment to hydrostatic pressure in hydrogen molecule**M. Oftadeh^a, S. Saidi^a and M. Hamadani^b^aDepartment of Chemistry, Payame Noor University (PNU), Isfahan, Iran

(Email: m_oftadeh@pnu.ac.ir)

(Email: s.saeidi61@yahoo.com)

^bDepartment of Chemistry, Kashan University, Kashan, Iran

(Email: mhamadani@kashanu.ac.ir)

Keywords: Hydrostatic pressure, Dipole moment, H₂ Molecule, HF/3-21g***1. Introduction**

The diatomic molecules of Hydrogen gas in atmosphere pressure have intermolecular distance 3.3Å. Dipole moment for hydrogen molecules under normal conditions is zero but it is possible to distort the charge distribution of H₂ in two ways to create an induced dipole moment and the vibration lines can then be observed in absorption: (I) by the application of an external electric field or (II) by collision with other molecules [1]. The magnitude and number of collision of molecules change the magnitude of induced dipole moment. However variation of pressure changes the dipole moment and consequently forces, interactions of molecules and properties of system will be changed [2]. Application of hydrogen in production of many metallic hydride, Haber synthesis, catalytic reactions appears the effect of collision of molecules (pressure effect) on varying the hydrostatic pressure & the dipole moment [3].

2. Method

Hydrogen molecule system consider in normal and high hydrostatic pressures and 298°K temperature. The effort steps describe as follow:

- 1- Two hydrogen molecules consider in different configurations: linear with equilibrium and non equilibrium internuclear distances (A, B) planer perpendicular with equilibrium and non equilibrium internuclear distances (C, D and E), quadrilateral with equilibrium and non equilibrium internuclear distances (F, G), non planer perpendicular with equilibrium and non equilibrium internuclear distances (H, I) [4].
- 2- Each of configurations draw in Gaussview then they are optimized with HF/3-21g* level of theory in Gaussian 98.
- 3- In checkpoint of optimized files only intermolecular distance was changed from 2.5a₀ to 5.5a₀ & internuclear distances and dihedral angle were constant.
- 4- From output files dipole moment and energies were extracted.
- 5- Because energy and pressure is related to intermolecular distance as:

$$P = - \frac{1}{4\pi R^2} \frac{\partial E}{\partial R} \quad (1)$$

The intermolecular distance were defined as import predictor(X) and energy & pressure were defined as response(Y) data in MATLAB software.

- 6- Finally, by averaging of 9 equations evaluated in step 5; the electronic energies (HF energies) for any distances (R) and finally the total relationship between pressure and dipole moment was extracted.

3. Results and discussion

The equation of averaged E(R) versus based on data of table 1 is:

$$E(R) = \frac{-2.263R + 4.851}{R - 2.119} \quad (R^2=1, SD=9.288 \times 10^{-9}) \quad (2)$$

If we derivate of Eq. (2) and replace in Eq. (1), the equation of pressure and intermolecular distance is obtained:

$$P = \frac{0.00443495}{R^2(R - 2.119)^2} \quad (3)$$

This equation shows that when intermolecular distance decreases, the hydrostatic pressure increases.

In the point of symmetry view, x,y components of dipole moment are zero; only the z component may be nonzero. From table 1 and after averaging of 9 equations from evaluated for 9 configurations, the best fitted equation for μ(R) is:



$$\mu(R) = -1.403 \exp(-1.043R) \quad (R^2=0.9908 \quad SD=8.167 \times 10^{-5}) \quad (4)$$

This equation shows that by decreasing of the intermolecular distance, the dipole moment increases. This is adapted to the other works which had been shown the μ_z varies as $1/R^4$ [4]. After evaluating of R from (4) and substitute in (3); the total equation for $P(\mu)$ is obtained:

$$P = \frac{a}{(\ln(\mu'))^2 (\ln(\mu') + b)^2} \quad (5)$$

Where $\mu' = -\mu/1.403$, $a=0.003748$ and $b=2.210117$ and μ is average of μ_z s for all configurations with a definite R . The quality of variation of dipole moment with normal pressures and high pressures has been showed in figure 1.

Table 1. The HF energies (E) and dipole moment (μ_z) for some intermolecular distances (R)/pressure (P) for 9 configurations of H_2 molecules

Config.	$R(a_0)/P$ (atm)	$E(\text{au})$	$\mu_z(\text{au})$	$R(a_0)/P$ (atm)	$E(\text{au})$	$\mu_z(\text{au})$
A	2.5 / 1440	-2.048424	0	3.5 / 55	-2.2239783	0
B		-2.0398219	0.0370485		-2.2137938	0.0113786
C		-2.1350304	-0.0328751		-2.2223175	-0.1014945
D		-2.1340756	-0.3252321		-2.2214068	-0.1023607
E		-2.1330073	-0.367764		-2.2210277	-0.113273
F		-2.1416253	0		-2.2250247	0
G		-2.1400212	0.0059535		-2.2152304	0.0015612
H		-	-0.000008		-2.255023	-0.0000001
I		2.14650251	0.0056266		-2.224486	0.0015123
A	4.5 / 10	-2.2402984	0	5.5 / 4	-2.2448881	0
B		-2.2394233	0.0029567		-2.2441515	0.005483
C		-2.2418052	-0.0401448		-2.2453106	-0.0172408
D		-2.2410535	-0.040147		-2.244613	-0.0183495
E		-2.2409598	-0.0436318		-2.2445865	-0.0181835
F		-2.2421578	0		-2.2452825	0
G		-2.2413685	0.00017		-2.2445686	-0.0000741
H		-2.2422581	0		-2.2453146	0
I		-2.2414752	0.0001639		-2.2446028	-0.0000741

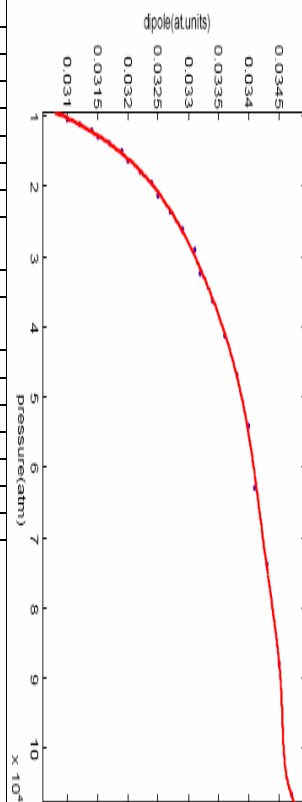


Figure 1

4. Conclusions

The hydrostatic pressure can be effect on the properties of molecular systems such as electronic configuration, electronic probability density and dipole moment, especially in the covalent fluid systems [5]. The obtained exponential relationship between the dipole moment with the pressure showed the dipole moment increases when the intermolecular distances was decreasing or pressure was increasing.

References

- [1] F.Toffolo, M.Tommasini, M.Del Zoppo, G.Zerbi, Chem. Phys. Lett., 405 (2005) 108-113.
- [2] E.Clifford, Abinitio Calculation of The Structures and Properties of Molecules, Elsevier Science Publishers B.V. 1988
- [3] v.Victor, V.Vasily, A.Roman, V.Aleksy, I.Anton, Chemistry for Sustainable Development, 10 (2002) 133-140
- [4] R.W.patch, Calculated Interaction Energy and Dipole Moment in Collision of Two Hydrogen Molecules. National aeronautics and space administration Washington, 1970.
- [5] M. Oftadeh, The Investigation of the High Pressures on the Displacement of the Radial Distribution of The Hydrogen Atom in Ground State, MSC Dissertation, Isfahan University, Isfahan, Iran (1993).



Quantitative structure-property relationship (QSPR) study of n-octanol-water partition coefficients ($\log P_{o/w}$) of fatty acids using multiple linear regression (MLR)

S. A. Bavafa* and R. Behjatmanesh-Ardakani

Department of Chemistry, Payame Noor University (PNU), Ardakan, Iran.

(E-mail: s.ali.bavafa@Gmail.com)

Keywords: QSPR, Partition coefficients ($\log P_{o/w}$), Fatty acids, Multiple linear regression (MLR)

1. Introduction

In this paper, we design a QSPR model for some fatty acids by using quantum chemical and structural descriptors. The logarithm of this coefficient, $\log P_{o/w}$, has been shown to be one of the key parameters in quantitative structure-activity/property relationship (QSAR/QSPR) studies. In chemistry, especially biochemistry, a fatty acid is a carboxylic acid often with a long unbranched aliphatic tail (chain), which is either saturated or unsaturated (ω -3 and ω -6). There is not $\log P_{o/w}$ information for some important saturated and unsaturated fatty acids in the literature. A model for these compounds have predicted.

2. Methods

Numerical data on the octanol/water partition coefficient ($\log P_{o/w}$) are taken from Ref [1]. Gaussian 2003 (GW03) program package has been used for calculation of quantum chemical descriptors. Results of calculation are from using two keywords FOPT and FREQ. FOPT, which is full optimization, was carried out by the level B3LYP that is a kind of Density Function Theory (DFT) method. 6-31G* basis set was used during all calculations. We have used NBO version 3.1 that is called by POP=NBO in the GW03 program. All statistical analyses were performed using SPSS version 16 program.

3. Results and discussion

The result shows that $\log P_{o/w}$ is highly dependent on the NSB and E_{LUMO} . Unstandard equation from stepwise MLR calculations is as follows:

$$\log P_{o/w} = -1.485 + 0.174NSB + 18.918E_{LUMO} \quad (1)$$

$$R^2 = 0.997, R^2_{cv} = 0.997, F = 2938, \text{Standard Error (SE)} = 0.148 \text{ and Durbin-Watson (DW)} = 2.606$$

Without standardization of above equation, it is not possible to discuss about importance of variables in the prediction model.

Following equation is obtained after standardization:

$$\log P_{o/w} = 1.012NSB + 0.116E_{LUMO} \text{ (standardized coefficient)} \quad (2)$$

In equation (1) the coefficient of E_{LUMO} is greater than the coefficient of NSB, but this is a wrong conclusion, if we say that E_{LUMO} variable is more important than NSB. Contrary to the equation (1), the corrected standardized coefficients show that NSB is much more important than E_{LUMO} . Fig. 1 shows relation between experimental and predicted $\log P_{o/w}$ values.

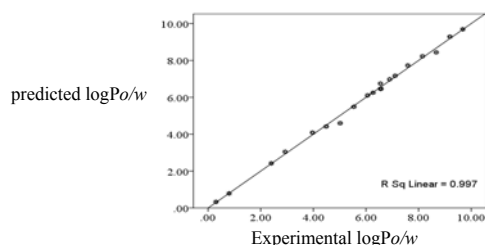


Fig 1. Experimental versus predicted values of $\log P_{o/w}$ with NSB and LUMO as descriptor.

Correlation coefficient (R^2) for this curve is equal to 0.997. The training set of 4 molecules (Table 1) with regularly distributed $\log P_{o/w}$ values is used to assess the predictive ability of the QSPR models produced in the regression.

**Table 1.** Experimental and Predicted values of logPo/w for fatty acids (training set).

training set						
NO.	common name	LogP. <i>Exp</i>	LogP. <i>Pred</i>	NSB	E _{LUMO} (eV)	Residual
1	Butanoic acid ^S	0.79	0.8	12	0.01039	-0.01
2	Heptanoic acid ^S	2.42	2.4	21	0.01243	0.02
3	Erucic acid ^U	9.69	9.68	63	0.01094	0.01
4	Palmitoleic acid ^U	6.75	6.55	45	0.01066	0.2

S: Saturated, U: Unsaturated, Exp: Experimental, Pred: Predicted

Table 2 shows the results of prediction of the model for five saturated and two unsaturated fatty acids as a test set. R² and residual value show that the model predictions are very good.

Table 2. Experimental and Predicted values of logPo/w for fatty acids (test set).

test set R _{cv} ² = 0.999						
NO.	common name	LogP. <i>Exp</i>	LogP. <i>Pred</i>	NSB	E _{LUMO} (eV)	Residual
1	Valeric acid ^S	1.39	1.32	15	0.0106	0.07
2	Hexanoic acid ^S	1.84	1.88	18	0.0123	-0.04
3	Docosanoic acid ^U	9.91	10.24	66	0.0126	-0.33
4	Linoleic acid ^U	7.05	7.1	48	0.0121	-0.05

The selfcorrelation coefficients of the independent variables in Eq. (1) are listed in Table 3. The table shows that the VIF values for Eq. (1) are all less than 2.0, and no intercorrelation exists for the selected variables.

Table 3. Self-correlation coefficient of independent variables in Eq. (1)

Equation	Variable	VIF
logPo/w = -1.485+0.174NSB+18.918LUMO	NSB	1.031
	E _{LUMO}	1.031

There is not logPo/w information for some important saturated and unsaturated fatty acids in the literature. Table 4 shows the predictions of the model for these compounds.

Table 4. Predicted logPo/w for some important saturated and unsaturated fatty acids.

NO.	common name	LogP. <i>Exp</i>	LogP. <i>Pred</i>	NSB	E _{LUMO} (eV)
1	lacceric acid ^S	No. Exp	15.46	96	0.0126
2	psyllic acid ^S	No. Exp	15.98	99	0.0126
3	Eicosatetraenoic acid ^U	No. Exp	5.38	48	-0.0786
4	adrenic acid ^U	No. Exp	8.14	54	0.0120

4. Conclusions

The success of any QSPR model depends on the selection of appropriate descriptors. Exploring the usefulness of descriptors, especially, conceptual DFT based descriptors along with other descriptors and analyzing their applicability could lead to drastic improvement in QSPR models. Traditional regression procedures along with cross-validation are carried out to evaluate the predicting power of the developed model. It has been shown that using the entire data set, the number of single bond index NSB and E_{LUMO} descriptors provides a reasonably good coefficient of determination (R²= 0.997) and cross-validated squared correlation coefficient R²_{cv} = 0.997 value indicating the significance of the developed model.

References

- [1] .<http://chem.sis.nlm.nih.gov/chemidplus>

**Ab initio and DFT studies on proton transfer of nitrosamine in reaction of the nitrosamine isomers - H₂O₂**S. A. Bavafa^{a*} and H. Roohi^b^aDepartment of Chemistry, Payame Noor University (PNU), Ardakan, Iran

(E-mail: s.ali.bavafa@Gmail.com)

^bDepartment of Chemistry, Faculty of Science, University of Sistan and Baluchestan, 98135–674 Zahedan, Iran**Keywords:** Proton transfer, H₂O₂, Nitrosamine**1. Introduction**

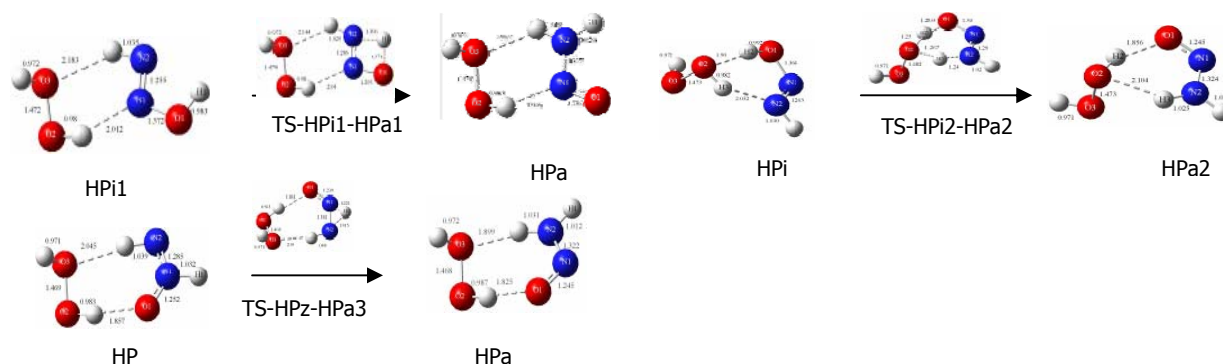
Hydrogen peroxide (H₂O₂) generating highly reactive radicals has been proven to play a role in the oxidation reactions[1]. Significant quantities of H₂O₂ can be detected as a byproduct of several metabolic pathways in human blood. The nitrosamines constitute a family of potent carcinogenic compounds, which are formed readily from various nitrogen compounds such as nitrite and their various derivatives. A chemical reaction, the main feature of which is the intermolecular or intramolecular transfer of a proton (hydron) from one binding site to another. proton transfer of nitrosamine study has not been when a H₂O₂ with NH₂NO do complex formation.

2. Methods

The geometries of the complexes and transition-states were optimized using B3LYP and MP2 methods with AUG-cc-pVDZ basis set by Gaussian-03 program package. The thermal and corresponding zero-point vibrational energies calculations were performed for all optimized species at aforementioned levels to evaluate. Vibrational frequencies (from the analytic Hessian) were calculated to ensure that each minimum is a true local minimum (containing only positive frequencies) and that each transition state has only a single imaginary frequency (one negative eigenvalue of the Hessian). The Mulliken electronegativity (χ), chemical hardness (η), and electronic chemical potential (μ) for all isomers of the nitrosamines were computed using orbital energies of the highest occupied molecular orbital (HOMO) and the lowest unoccupied molecular orbital (LUMO) at the MP2/AUG-cc-pVDZ level of theory.

3. Results and discussion

The HNNOH nitrosamine isomers can be classified into two types namely imino (type i) and zwitterionic (type z) isomers that reaction with H₂O₂. nitrosamine tautomers in trace interconversions (proton transfer) convert to amino (most stable species of the nitrosamine isomers). Supplementary Data, are categorized into three groups, Fig. 1 for group 1(imino- H₂O₂): HPi1, HPi2, and group 2 (zwitterionic- H₂O₂): HPz with transition-states: TS-HPi1-HPa1, TS-HPi2-HPa2, TS-HPz-HPa3: these structures computed at the MP2/AUG-cc-pVDZ level of theory. MP2/AUG-cc-pVDZ-optimized geometrical parameters are shown in Fig 1.

**Fig 1.** The structures all nitrosamine isomers -H₂O₂ (with transition-states)

The electronic binding energies with BSSE, thermal, and zero-point corrected energies for different complexes at several levels of theory are given in Table 1. From Table1, the relative stabilities of all isomers of the nitrosamine dimers based on their D_0^{BSSE} are in decreasing order: HPa3 > HPa1 > HPa2

**Table 1.** Binding energies (kcal/mol) for isomers of the nitrosamine-H₂O₂

complex	MP2			B3LYP		
	AUG-cc-pVDZ			AUG-cc-pVDZ		
	BSSE	D ₀	D ₀ ^{BSSE}	BSSE	D ₀	D ₀ ^{BSSE}
HPi1	1.66	-6.25	-4.59	0.29	-4.14	-3.85
HPi2	2.22	-5.28	-3.05	0.46	-3.85	-3.4
HPz	1.95	-7.23	-5.28	0.65	-5.6	-4.95

$$D_0 = D_e + \Delta ZPE, D_0^{BSSE} = D_0 + BSSE.$$

The relative thermodynamic properties (activation energies, activation free energies, reaction enthalpies, reaction free energies) of all transition-states of their interconversions, computed at the MP2/AUG-cc-pVDZ level of theory are shown in Table 2. The activation energies of the reactions are in the increasing order: HPi2→HPa2<HPi1→HPa1<HPz→HPa3.

Table 2. Thermodynamic quantities, transition-states of the nitrosamine- H₂O₂, computed at the MP2/AUG-cc-pVDZ levels of theory.

Reactions	ΔE^\ddagger	ΔG^\ddagger	ΔE^0	ΔG^0
TS-HPi1-HPa1	28.89	29.09	1.71	0.84
TS-HPi2-HPa2	9.55	12.16	2.41	1.49
TS-HPz-HPa3	50.52	50.43	1.68	0.58

Activation energy di-proton transfer less than monoproton transfer, in the middle of monoproton transfer H from O to N energy less than H from N1 to N2. This may be explained within the principle of the minimal proton affinity difference between donor and acceptor [2]. Based on the proton-transfer transition-states, the interconversions via transition state structures of the nitrosamine isomers - H₂O₂ are able to be classified into two types namely (i) monoproton transfer, MPT and (ii) di-proton transfer, which imaginary frequencies of TS-HPi1-HPa1 , TS-HPi2-HPa2 , TS-HPz-HPa3 corresponding transition-states are respectively , 1838.4i,1612.88i,2033.61i see Table 3.

Table 3.Types of transition-state structures computed at the MP2/AUG-cc-pVDZ level of theory

Types of transition-state (TS)			
Mono-proton transfer TS ^{a,b}		Di-proton transfer TS ^{a,c}	
TS-HPi1-HPa1	1838.4i	TS - HPi2- HPa2	1612.88i
TS-HPz-HPa3	2033.6i		

a Transition-state, imaginary frequency in cm⁻¹.

b Intermolecular proton transfer.

c Intermolecular proton transfer

4. Conclusions

Ab initio molecular orbital and DFT calculations have been carried out for proton transfer, 2 imino tautomers and 1 zwitterionic to amino (most stable species of the nitrosamine isomers) in reaction of HNNOH-H₂O₂.The structures and transition states were optimized using B3LYP and MP2 methods with AUG-cc-pVDZ basis set. The amines complexes are the more stable than imino and zwitterionic complexes. The activation energies of the reactions are in the increasing order: HPi2→HPa2<HPi1→HPa1<HPz→HPa3.

Activation energy di-proton transfer less than monoproton transfer, in the middle of monoproton transfer H from O to N energy less than H from N1 to N2. This may be explained within the principle of the minimal proton affinity difference between donor and acceptor. The effect of proton affinity difference between donor and acceptor on the proton transfer.

References

- [1] Glass W. A, Varma M. N, Eds. Physical and Chemical Mechanism in Molecular Radiation Biology, Plenum Press: New York, 1991.
- [2] Grabowski S.J, Hydrogen Bonding-New Insights, Springer: Netherlands, 2006



Theoretical study of interaction between nitrosamine (NA)-(Formic acid ($\alpha 1$, $\alpha 2$) and Formamide (β)): Density functional theory study (DFT)

S. A. bavafa* and R. Behjatmanesh-Ardakani

Department of Chemistry, Payame Noor University (PNU), Ardakan, Iran

(E-mail: s.ali.bavafa@Gmail.com)

Keywords: Nitrosamine, Formamide, Formic acid, DFT, H-bonding

1. Introduction

Formic acid (systematically called methanoic acid) is the simplest carboxylic acid. In hydrocarbons and in the vapor phase it consists of hydrogen-bonded dimers rather than individual molecules. Formamide is also used as an RNA stabilizer in gel electrophoresis by deionizing RNA. In capillary electrophoresis, it is used for stabilizing (single) strands of denatured DNA. The nitrosamines constitute a family of potent carcinogenic compounds, which are formed readily from various nitrogen compounds such as nitrite and their various derivatives. In this work, the hydrogen bonded complexes formed between nitrosamine and $\alpha 1$, $\alpha 2$, β have completely investigated at DFT study.

2. Methods

All the structures studied in this work were optimized by using B3LYP (DFT) method with AUG-cc-pVDZ basis set. It has been demonstrated that B3LYP and MP2 levels of theory give similar results in particular [1]. The B3LYP/ AUG-cc-pVDZ level to include the zero point- energy (ZPE) and BSSE correction. The NBO analysis was carried out with version 3.1 included in Gaussian-03 program at the B3LYP/AUG-cc-pVDZ level. AIM was calculated at the B3LYP/AUG-cc-pVDZ level of theory by the AIM2000 program package.

3. Results and discussion

3 minima structures were found for NA- $\alpha 1$ (formic acid1), NA- $\alpha 2$ (formic acid 2) and NA- β (formamide) complex. All complexes were identified for real minimum energy structures without imaginary frequency. The optimized structures of them are show in Figure 1.

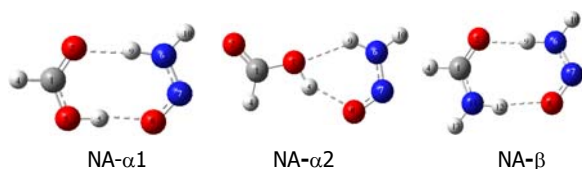


Fig 1. Complexes NA- $\alpha 1$, NA- $\alpha 2$, and NA- β .

As far as elongating or shortening the bond length due to hydrogen bonding, the different magnitudes for a certain bond are presented in Table 1, revealing the various strengths of the HBs. In particular, the eight-membered ring of complex NA- $\alpha 1$ exhibits the remarkable resonance-assisted hydrogen bonding (RAHB) mechanism. Namely, the bond C1=O2 and N7=O8 is elongated by 0.020 and 0.017 Å, while the bond N6-N7 and C1-O3 is shortened by 0.023 and 0.03 Å respectively, This mechanism is also found in complex NA- β and NA- $\alpha 2$. It is well known that the RAHB mechanism enhances the HB strength. Binding energy at the B3LYP/AUG-cc-pVDZ level are listed in Table 2. The D_0^{BSSE} (zero point- energy and BSSE correction) of complexes decreases in the order of NA- $\alpha 1$ > NA- β > NA- $\alpha 2$ at B3LYP/AUG-cc-pVDZ level. A strength sequence of the hydrogen bonds from the strongest to the weakest is found: O-H...O > N-H...O > N-H...N > C-H...O > C-H...N. The blue-and red-shifts in the local X-H (X= O, N, C) stretching frequencies are proportional to the bond elongations or shortening lengths.

**Table 1.** Optimized geometrical parameters for monomers and complexes at B3LYP/AUG-cc-pVDZ level.

parameter	$\alpha 1$	$\alpha 2$	β	NA	NA- $\alpha 1$	NA- $\alpha 2$	NA- β
C1=O2	1.198	1.205	1.218		1.222	1.201	1.234
C1-O3	1.356	1.349			1.32	1.349	
N7=O8				1.219	1.239	1.233	1.237
N6-N7				1.33	1.307	1.315	1.311
O2(3)...H9					1.827	2.153	1.812
H5(or 12)...O8					1.721	1.808	1.935

Table 2. Binding energies (kcal/mol) of NA-($\alpha 1$ (acid formic(1)), $\alpha 2$ (acid formic(2)), β (formamide) complexes.

B3LYP/AUG-cc-Pvdz			
compelex	D_0	BSSE	D_0^{BSSE}
NA- $\alpha 1$	-8.45	0.60	-7.85
NA- $\alpha 2$	-5.11	0.48	-4.64
NA- β	-7.60	0.64	-6.96

$D_0 = D_e(\text{Electronic binding energy}) + \Delta ZPE$, $D_0^{BSSE} = D_0 + BSSE$.

The topological features of electron densities of the complexes were predicted at the B3LYP/AUG-cc-pVDZ level of theory. The calculated topological properties have been summarized in Table 3.

Table 3. Topological Properties of the Bond Critical Points of the Intermolecular Hydrogen Bonds.

Bond	ρ	$\nabla \rho$	ρ	$\nabla \rho$
	NA- $\alpha 1$		NA- $\alpha 2$	
O8...H5	0.0421	0.1339	0.0363	0.115
O2(or 3)...H9	0.0337	0.1087	0.0153	0.0517
	NA- β			
O2...H9	0.0353	0.1116		
H12...O8	0.0267	0.0813		

Table 4. NBO data calculated at B3LYP/AUG-cc-pVDZ level.

E(2) (kcal/mol)	NA- $\alpha 1$	NA- $\alpha 2$	NA- β
LPN6 $\rightarrow\sigma^*$ N7=O8	98.67	88.78	94.19
LPO3 $\rightarrow\sigma^*$ C1=O2	71.09	48.92	
LPN11 $\rightarrow\sigma^*$ C1=O2			76.32

The strongest HB, O-H...O, has the largest densities, $\rho = (0.0363-0.0421 \text{ au})$, and the weak HBs, C-H...O have the smallest densities, $\rho = (0.0052-0.0124 \text{ au})$. The comparison between $\rho(r)$ of the O-H...O, N-H...O and C-H...O hydrogen bonds shows that the homonuclear O-H...O H-bonding in (NA- $\alpha 1$ and NA- $\alpha 2$) complexes is stronger than heteronuclear N-H...O and C-H...O. The results of NBO analysis including charge transfer energy of NBO at B3LYP/AUG-cc-pVDZ level of theory are given in Table 4. The NBO analyses show that the electronic charge is transferred from formic acids $\alpha 1$ and formamide to NH_2NO in these complexes except for $\alpha 2$. The NBO results show that the specific lp (N6) $\rightarrow\sigma^*$ (N7=O8), lp (O3) $\rightarrow\sigma^*$ (C1=O2) and lp (N11) $\rightarrow\sigma^*$ (C1=O2) interactions is the most important interaction in NH_2NO , formic acids ($\alpha 1$ and $\alpha 2$) and formamide (β) respectively. The value of this interaction energy increases upon complex formation.

4. Conclusions

All the structures studied in this work were optimized by using B3LYP (DFT) method with AUG-cc-pVDZ basis set. 3 minima structures were found for NA- $\alpha 1$ (formic acid1), NA- $\alpha 2$ (formic acid 2) and NA- β (formamide) complex. In particular, the eight-membered ring of complex NA- $\alpha 1$ exhibits the remarkable resonance-assisted hydrogen bonding (RAHB) mechanism. The D_0^{BSSE} (zero point- energy and BSSE correction) of complexes decreases in the order of NA- $\alpha 1 > \text{NA-}\beta > \text{NA-}\alpha 2$ at B3LYP/AUG-cc-pVDZ level. A strength sequence of the hydrogen bonds from the strongest to the weakest is found: O-H...O $>$ N-H...O $>$ N-H...N $>$ C-H...O $>$ C-H...N. The comparison between $\rho(r)$ of the O-H...O, N-H...O and C-H...O hydrogen bonds shows that the homonuclear O-H...O H-bonding in (NA- $\alpha 1$ and NA- $\alpha 2$) complexes is stronger than heteronuclear N-H...O and C-H...O.

Reference

[1] Simon. S, Sodupe. M, Bertain. J, J. Phys. Chem. A. 106 (2002) 5397.



Investigation of the deflagration pathway for TNAZ and some of its derivatives as energetic materials by DFT method

M. Radhoosh¹, M. Oftadeh¹, M. Hamadani²

¹Department of chemistry, Payame Noor University (PNU), Isfahan, Iran

(Email: m_oftadeh@pnu.ac.ir)

(Email: m.radhoosh@gmail.com)

²Department of chemistry, Kashan University, Kashan, Isfahan, Iran

Keywords: Deflagration pathway, DFT, Energetic materials, TNAZ

1. Introduction

It is difficult to establish structure–activity relationship from experimental data for explosives since the decomposition of these compounds is very fast and it is difficult to measure accurate energetic and kinetics data of these compounds. In this case, theoretical calculation, especially accurate quantum chemistry calculation, plays an important role. Thermal stability of nitramines is mainly related to the energy required for initial reaction of decomposition [1].

The thermal decomposition of energetic nitramines is a very complicated chemical process. It has been indicated that the elementary reactions involved in each system are often in the range of several dozens to well over a hundred [2]. We selected a new high energetic TNAZ [3] and some of its derivatives.

2. Computational method

The quantities including SCF energy, activation barrier energy and Gibbs free energies of first step of deflagration pathway of TNAZ and mono, di (Z & E), tri and tetra fluoridation, cyanidation and metoxidation derivatives that commonly used in explosives and propellants have been computed by means of density functional theory in quantum chemistry with B3LYP/6-31G** level of theory. The deflagration pathways including direct ring opening, N-NO₂ bond fission; C-NO₂ bond fission and HONO elimination are considered. All of activation energies are difference between the initial molecule SCF energy and the energy of molecule with increasing 2A⁰ in considered bond for each of the mentioned pathways.

3. Results and discussion

The smallest Gibbs free energy for TNAZ is 4.764411809 Kcal/mol belong to HONO elimination pathway; but the smallest activation barrier energy is 63.435 Kcal/mol belong to N-NO₂ bond fission. In 2005 Zhao [4] show that in gas phase in 250-2500 K, N-NO₂ bond fission have smallest rate constant rather than other considered pathways.

In fluoridation compounds the smallest Gibbs free energy is -0.010128 Kcal/mol for ring opening of 12. the smallest activation barrier energy is 63.435 Kcal/mol belongs of 13.

In derived compounds with cyanide the smallest amount of Gibbs free energy is -0.008811 Kcal/mol for ring opening of 25 but the smallest activation barrier energy is 46.1785 Kcal/mol for N-NO₂ bond fission of 23.

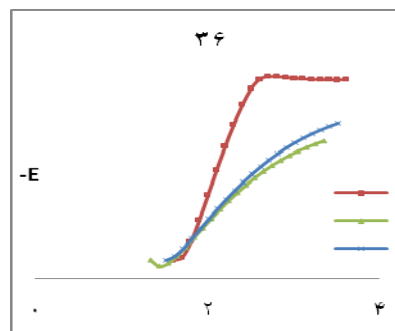
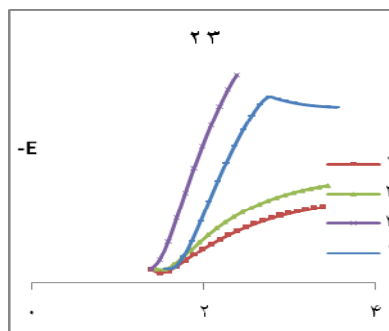
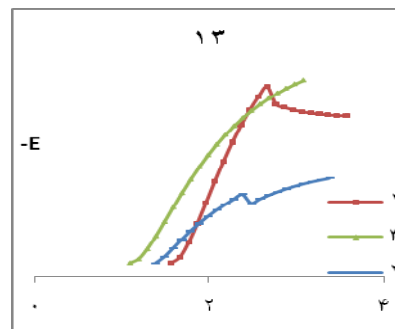
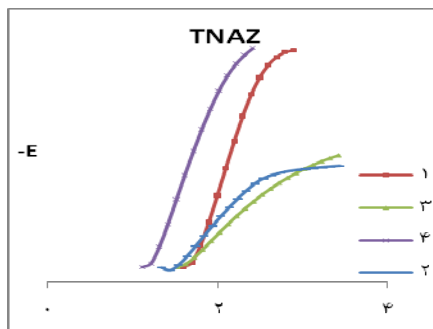
In metoxidation compounds Gibbs free energy difference of 36 is -0.023806 Kcal/mol that is smallest in this group but the activation barrier energy of 32 for C-NO₂ bond fission is 20.6012 Kcal/mol that is the least in all of the considered groups.

4. Conclusions

Results of 1, 2, 3, 4 groups show that, in kinetic aspect in 58% of reactions the N-NO₂ bond fission pathway is the most probability pathway. It means they have the least activation barrier energy. In 21% of reactions C-NO₂ bond fission and for remain 21% of these two pathways have contested together.

Thermodynamic calculations suggest direct ring opening pathway for 80% of reactions and 15% of reaction contend between ring opening and HONO elimination pathway. Remained 5% of reactions contend between ring opening and C-NO₂ bond fission pathways. Therefore, we suggest N-NO₂ bond fission pathway in kinetic aspect and ring opening in the aspect of thermodynamic. But it seems that in explosive materials kinetic properties is more important.

Some of considered compounds				
No	X	Y	Z	T
10	H	H	H	H
12	H	H	F	F
13	H	F	H	F
23	H	CN	H	CN
25	CN	CN	H	CN
32	H	H	OCH ₃	OCH ₃
36	OCH ₃	OCH ₃	OCH ₃	OCH ₃



No	Deflagration Pathway	-E (B3LYP/6-31G**) Hartree)	ΔE_{act} (kcal/mol)	ΔG (kcal/mol)
10	1	786.65225	148.860	63.17278
	2		69.302	24.76366
	3		76.625	26.54914
	4		139.347	4.76441
12	1	971.11063	151.531	-0.01013
	2		86.088	0.04590
	3		74.567	0.03866
	4			0.02017
13	1	971.05375	110.003	0.01214
	2		63.435	0.03813
	3			0.03527
	4			0.04165
23	1	984.82727	120.225	0.05153
	2		46.178	0.20525
	3		61.879	0.05153
	4		144.359	0.11885
25	1	1084.24578	120.614	-0.00881
	2		80.328	0.04664
	3		77.353	0.04350
	4			0.03336
32	1	1015.45675	110.310	0.01074
	2		50.584	0.04335
	3		20.601	0.04897
	4			0.04612
36	1	1244.75118	100.979	-0.02381
	2		66.973	0.02524
	3		76.920	0.03768

- 1: Ring Opening
- 2: N-NO₂ Fission
- 3: C-NO₂ Fission
- 4: HONO Elimination

References

- [1] Qinghua Zhao, Shaowen Zhang, Qian Shu L, Chemical Physics Letters 407 (2005) 105–109.
- [2] Qinghua Zhao, Shaowen Zhang, Qian Shu Li, Chemical Physics Letters 412 (2005) 317–321.
- [3] Wilcox, C.F., Zhang, Y.-X., Bauer, S.H., J. Molecular Structure (TheoChem), 528 (2000) 95–109.
- [4] Zhao, Q., Zhang, Sh., Li, Q. S., Chemical Physics Letters, 412 (2005) 317–321.



Charge-density study of 5-Chloro-8-hydroxy-6-methylnaphthalene-1,4-dione: A hydroxynaphthoquinone derivative

Zahra Sharafi^{a*} and Reza Kia^b

^a Chemistry Department, Islamic Azad University of Marvdasht, Marvdasht, Iran

(E-mail: zahra_sharafi@yahoo.com)

^b Chemistry Department, University of Bath, Claverton Down, BA2 7AY, Bath, UK

1. Introduction

The electron-density distribution of small molecules, peptides and amino acids carries information which is important in modeling their interactions. The molecular electrostatic potential and electric moments, which may be derived from the charge-density, help to determine the recognition properties such as reactivity in a desired molecule. The electron clouds around atoms in molecules are deformed primarily due to chemical bonding and secondarily by non-bonded interactions such as hydrogen bonds. In the routine crystal structure determination from X-ray diffraction data using least-squares refinement procedure, the continuous electron-density of molecule is subdivided into independent atomic charge densities, and the basic assumptions are that atoms are neutral and of spherical shape with a radial dependence equal to that of free atoms in the gas phase so-called Independent Atom Model (IAM). So, some corrections due to bonding and non-bonding effects must be considered which leads to multipolar atom model and allows mapping non-spherical electron-density map of the desired molecule. In this study, the title compound is a substituted 5-hydroxyl-1,4-naphthoquinone (Juglone). Juglone and its 5-acetoxy-2-bromo analogue are the essential dienophile in the highly convergent and regiospecific Dils-Alder synthesis of Ochromycinone, a type of natural anthraquinone which exhibits remarkable antibiotic and antitumor activities. Our aim is to obtain an insight of the nature of the chemical bonds by X-ray charge-density study of the title compound.

2. Methods

Indeed, accurate low-temperature high resolution X-ray data allow the non-spherical maps, and electron-density to be presented in deformation electron-density maps, and experimentally quantified by using a non-spherical model of the atomic electron-density and so charge-density is come of age. This model is described as a superposition of pseudo-atoms described by the multipolar Hansen-Coppens atom formalism [1] in program MOLLY [1] which is the most accurate model as follows:

$$\rho_{\text{atom}}(\mathbf{r}) = \rho_{\text{core}}(\mathbf{r}) + P_{\text{val}} \kappa^3 P_{\text{val}}(\kappa \mathbf{r}) + \sum_{l=0, l_{\text{max}}} \kappa'^3 R_{nl}(\kappa' \mathbf{r}) \sum_{|m| \leq l} P_{lm} y_{lm\pm}(\theta, \phi)$$

Where ρ_{core} and ρ_{val} represent the spherical core and valence unitary electron-density, respectively. P_{val} is the valence population parameter. $y_{lm\pm}$ represent multipolar spherical harmonic functions of the order l in real form, R_{nl} are Slater-type radial functions and P_{lm} are the multipolar populations. The coefficients κ and κ' describe the contraction-expansion for the spherical and multipolar valence densities, respectively. The low X-ray scattering power of H atoms is a well known problem in crystallography. However, as evident from structures based on neutron diffraction experiments (where the scattering length of H atom is comparable in magnitude with those of heavier elements such as carbon and oxygen), the use of an isotropic displacement parameter for hydrogen is a very crude approximation and should be corrected. So, the program SHADE [2] web server was used to model an estimation of hydrogen anisotropic displacement parameters which is based on the analysis of displacement parameters of the non-H frameworks as a rigid body in terms of a TLS (translation-liberation-screw) model by Schomaker and Trueblood method [3]. So, the procedure based on Simple Hydrogen Anisotropic Displacement Estimator (SHADE) calculated the anisotropic displacement parameters for the H atoms. The X-ray diffraction data were collected using a Bruker SMART APEXII CCD area-detector diffractometer. A series of ω scans were performed at a detector distance of 5 cm. Data integration and unit-cell refinement were performed with the program SAINT [4]. The structure was solved using SHELXTL [4]. A first crystal structure refinement was performed with SHELXTL based on the Independent Atom Model (IAM). Then the least-squares program MOLLY was then used to determine the charge-density of the title compound. The anisotropic displacement model of the H-atoms resulted from the SHADE program.



3. Results and Discussion

In charge-density results based on multipolar refinement, shared-shell interactions, such as covalent bonds, are characterized by positive values of the electron density and negative values of the Laplacian of the electron density at the bond critical points (bcps), while closed-shell interactions, such as ionic bonding, van der Waals and hydrogen bonding, tend to have small positive values for both of the electron density and its Laplacian at the bcps. The topological properties at the critical points identified for the title compound are listed in Table 1. The bond lengths and ellipticities (ϵ) are consistent with aromatic delocalized bonding as anticipated, and four ring critical points (rcps) were identified. Each of the carbon-carbon and carbon-oxygen bonds is a shared-shell covalent interaction. According to the experimental deformation density, polar interactions such as hydrogen bonds have a distorting effects on the electron cloud in the region of the oxygen lone pairs.

Table 1. Topological properties of the title compound at the bond critical points (b.c.p.s).

Bond		$R_{ij}(\text{\AA})$	$\rho(r)(\text{e.\AA}^{-3})$	$\rho(r)(\text{e.\AA}^{-3}) \nabla^2$	ϵ
Cl1	C10	1.7249	1.4330	-3.80	0.01
O1	C4	1.2235	2.7972	-15.14	0.05
O2	C1	1.2489	2.8145	-24.98	0.02
O3	C7	1.3411	2.3074	-21.58	0.04
O3	H1O3	0.9392	2.6231	-38.61	0.02
C1	C2	1.4621	1.8635	-14.01	0.10
C1	C6	1.4658	1.8855	-13.89	0.07
C2	H2A	1.0809	1.7766	-15.21	0.02
C2	C3	1.3472	2.4332	-22.36	0.13
C3	H3A	1.0604	1.8421	-16.61	0.01
C3	C4	1.4789	1.9429	-15.41	0.09
C4	C5	1.5014	1.8441	-13.38	0.09
C5	C6	1.4219	1.9912	-14.00	0.08
C5	C10	1.3947	2.1100	-16.63	0.13
C6	C7	1.4084	2.1325	-17.78	0.11
C7	C8	1.4010	2.1050	-16.10	0.11
C8	H8A	1.0338	1.8799	-15.42	0.03
C8	C9	1.3842	2.1502	-16.66	0.07
C9	C10	1.4202	2.0670	-16.33	0.09
C9	C11	1.4977	1.7281	-10.78	0.01
C11	H11A	1.0147	1.7433	-12.33	0.04
C11	H11B	1.0209	1.7093	-12.81	0.07
C11	H11C	1.0256	1.8300	-14.67	0.03
Cl1	O1	2.8197	0.1238	1.83	0.07
O2	O3	2.5475	0.2623	5.53	0.07

4. Conclusions

The experimental charge-density analysis for the title compound at 100 K afforded a good multi-polar refinement. The resulted shared- and closed-shell interactions are in good agreement with the model. According to the experimental deformation density, polar interactions such as hydrogen bonds have a distorting effects on the electron cloud in the region of the oxygen lone pairs.

References

- [1] Hansen, N. K., P. Coppens, *Acta Cryst.* A34, (1978) 909.
- [2] Madsen Østergaard A., *J. Appl. Cryst.* 39, (2006) 757.
- [3] Schomaker, V., Trueblood, K. N., *Acta Cryst.* B24, (1968) 63.
- [4] Sheldrick, G. M., *Acta Cryst.* A64, (2008) 112.

**Quantum Monte Carlo methods**S. Jalili^a and B. Kharazian*^aDepartment of Chemistry ,K. N. Toosi University of Technology, P.O.BOX 1587-4416,Tehran,Iran
(E-mail: b.kharazian@gmail.com)**Keywords :** Quantum Monte Carlo, Variation Monte Carlo, Hydrogen bond.**1. Introduction**

Quantum Monte Carlo (QMC) methods can yield highly accurate energies for atoms, molecules, and solids, offering an alternative to quantum chemistry approaches such as configuration interaction and coupled cluster. Although the cost of QMC calculations is large, the scaling with system size is much better than for accurate quantum chemistry approaches, and QMC method have been applied to systems of order 10^3 electrons.

The two most commonly used continuum QMC methods are variational quantum Monte Carlo (VMC) and diffusion quantum Monte Carlo (DMC) [1]. In the VMC method, expectation values are calculated as integrals over configuration space, which are evaluated using standard Monte Carlo techniques. In the more sophisticated (DMC) method imaginary time evolution of the Schrödinger equation is used to calculate very accurate expectation values. Importance sampling is included via a trial wave function and the fermion sign problem is evaded by using the fixed- node approximation [2].

2. Methods

The hydrogen bond in the water- methanol complex has been the subject of many electronic structure studies since it represents the prototype of all hydrogen- bonded system. In this work we studied variational Monte Carlo calculations of water and methanol monomers and water-methanol complex, using pseudopotential (PP) approach with CASINO code [3].

We used Slater- Jastrow (SJ) wave function. The standard SJ wave function can be written as:

$$\Psi_{SJ}(\mathbf{R}) = e^{J(\mathbf{R})} \Psi_S(\mathbf{R})$$

Where \mathbf{R} denotes the space-spin of electron, and $\exp[J(\mathbf{R})]$ is the Jastrow factor.

3. Results and Discussion

A plot of the local energy for 1000 Metropolis- sampled points in the configuration space of an approximate trial function for a water-methanol complex look like this:

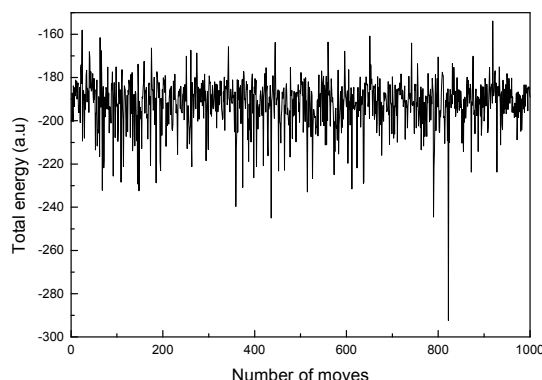


Fig . 1. Local energies of points in the random walk in a VMC run with an approximate wave Function

So having used the Metropolis algorithm to generate a sequence of configurations \mathbf{R} distributed according to $\Psi_T(\mathbf{R})$. We computed the desired expectation value by averaging the set of local energies:

$$\langle H \rangle = \frac{1}{M} \sum_{i=1}^M E_L(\mathbf{R}_i) = \frac{1}{M} \sum_{i=1}^M \frac{\hat{H} \Psi_T(\mathbf{R}_i)}{\Psi_T(\mathbf{R}_i)}$$



Our PP(SJ) result with TDHF type orbitals for water-methanol complex and water and methanol molecules are given in table 1.

Table 1. Total energy of the water-methanol calculation with different ab initio methods

Method	Total energy (a.u)
HF/6-31G*	-191/05
HF/aug-cc-PVDZ	-191/11
B ₃ LYP/6-31++G**	-192/18
VMC	-191/39

Figure 2 shows the local energies generated during VMC run for water-methanol complex. In figure 1(a) the trial wave function consists of product of up and down spin Slater determinants of molecular orbitals. Figure 2(b) show effect of adding a Jastrow factor which satisfies the electron-electron cusp conditions. The large positive spikes in the local energy are removed and the mean energy is lowered.

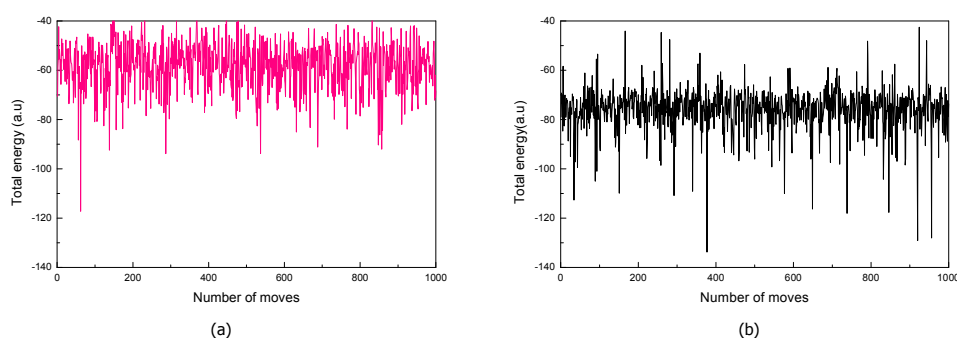


Fig. 2. Local energy of water-methanol complex from a VMC calculation (a) using a Slater- determinant trial wave function and (b) including a Jastrow factor.

4. Conclusions

We have performed pseudopotential QMC calculations of the total energy of the water and methanol and water-methanol complex using SJ wave functions with TDHF type orbitals. We have found that it is preferable to use orbitals which satisfy the electron-nucleus cusp condition and to require the Jastrow factor to be cusplless at nuclei rather than to enforce the electron-nucleus cusp condition through the Jastrow factor.

References

- [1] M. D. Brown, J. R. Trail, P. Lopez Rios, and R. J. Needs, J. Chem. Phys, 126 (2007) 224110.
- [2] Richard Needs, Mike Towler, Neil Drummond and Pablo Lopez Rios, CASINO; user's guide version 2.3.0 ,2008.
- [3] A. Ma, N. D. Drummond, M. D. Towler and R. J. Needs, Phys. Rev. E, 71 (2005) 066704.

**Ab initio study of single-wall boron nitride nanotube with various diameters under the static electric field**Davood Farmanzadeh^{a*} and Samereh Ghazanfary^a^aFaculty of Chemistry, University of Mazandaran, P. O. Box 453, Babolsar, I. R. Iran

(E-mail: d.farmanzad@umz.ac.ir)

Keywords: Boron nitride nanotube (BNNT), Electric field effect, DFT-B3LYP.**1. Introduction**

The existence of boron nitride nanotubes, BNNTs was predicted theoretically in 1994 and synthesized experimentally in 1995 [1]. In compared with other nanotubes, **BNNTs show interesting novel properties and can be used as a significant complement in nano-technology** [2]. It is well-known that any element in the electronic device must be subjected to a sizeable external electric field. Under this particular condition, a detailed study of the electric field (EF) effect on the electronic and geometric structures of BNNTs is highly preferred for understanding the nanotube properties. Our previous study shows that the geometric and electronic structure of BNNT can be modified by applying parallel and transverse external EFs [3]. On the other hand, we know that the geometric and electronic structure of BNNT dependent to its diameters, therefore it is interesting to see what will happen if we have both EF and BNNT with various diameter. Purpose of this study is investigation of the effect of an external uniform parallel EF on the molecular geometric and electronic structures of BNNTs with various diameters.

2. Computational methods

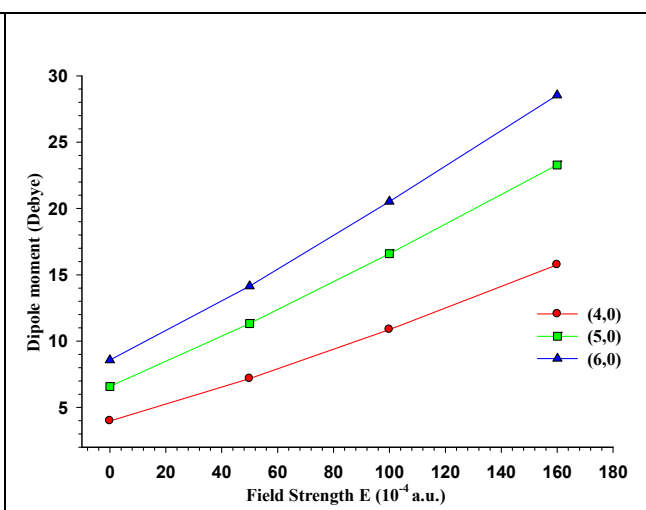
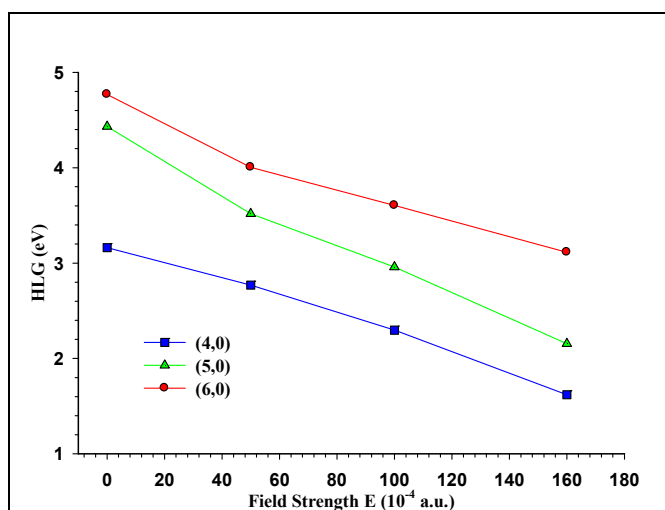
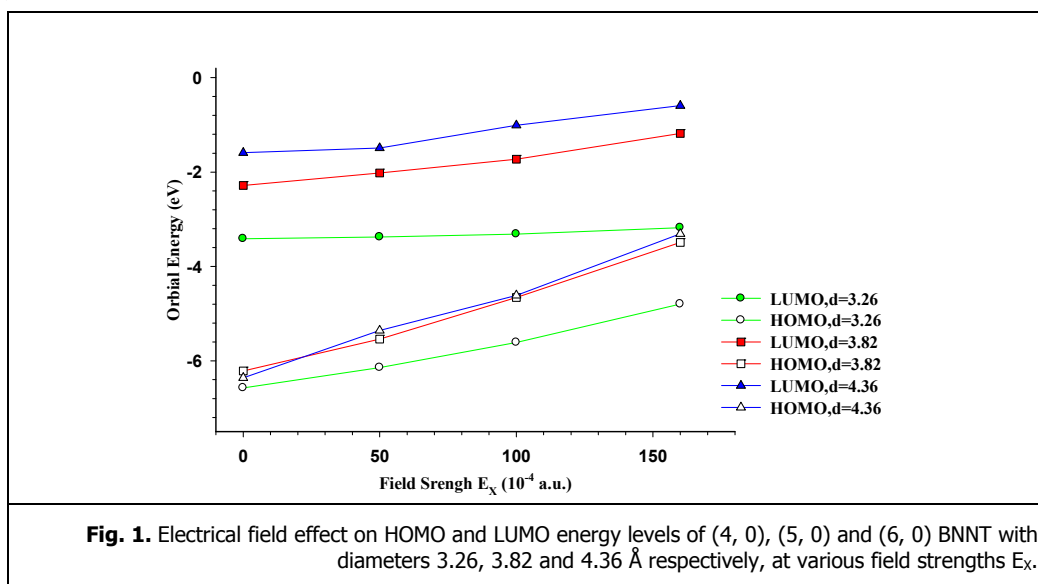
Geometry optimization and calculation of the structural and electronic properties of the zigzag BNNT (4, 0), (5, 0) and (6, 0) models with diameters 3.26, 3.82 and 4.36 Å respectively, at each value of the applied static electric field intensity have been carried out at the B3LYP level with the 6-31G* basis set by using the Gaussian 03 program. The numerical values of the applied static EF strengths on the BNNTs are 50×10^{-4} , 100×10^{-4} and 160×10^{-4} a.u. (1 a.u. = 5.14224×10^{11} V/m). Each applied field strength value (E) corresponds to a specific voltage V, applied over the the BNNT.

3. Results and discussion

3.1 Structural parameters, The obtain results show that the structural parameters (bond lengths, bond angles, and dihedral angels) of the BNNTs dose not change significantly with increasing the static electric field (EF) strengths.

3.2 Molecular orbital (MO), The energy of the frontier MO including highest occupied molecular orbital (HOMO) and the lowest unoccupied MO (LUMO) energy and the difference between the HOMO and LUMO, known as the energy (band) gap or simply HLG ($HLG = E_{LUMO} - E_{HOMO}$) are the excellent indicators of molecular electron transport properties. The calculated values of the HOMO and LUMO molecular orbital energies (in eV) for the (4, 0), (5, 0) and (6, 0) BNNT as function of the different applied parallel electric field strengths are plotted in Fig. 1. It can be seen from this Fig. that the trends of the HOMO and LUMO molecular orbital energy for series of BN molecules are increased gradually with increases of EF strength, these results show that application of the external EF results in more destabilization of HOMO and LUMO, also this Fig. show that the energy levels of the HOMO and LUMO depend on the diameter of the nanotube. In Fig. 2 the HLG values of the series of BNNT as function of the applied EF shows that when the electrical field increases from zero to 160×10^{-4} a.u., the HLG decreased by 1.55, 1.62 and 2.05 for BNNT with diameters 3.26, 3.82 and 4.36 Å respectively. This results show that HLG for grater diameter BNNT is easier to modulate by the external electric field and increases of diameter is an important factor in conductance of BNNT.

3.3 Electric dipole moment, The calculated values of the electric dipole moment, μ_{tot} (in Debye), are plotted in Fig. 3 as function of the applied electrical field strength for BNNTmolecules with different diameters. It can be seen from this Fig. that μ_{tot} increases considerably from $E = 0$ to $E = 160 \times 10^{-4}$ a.u. and also increases with increasing diameter of BNNT. Moreover, from this Fig. can be understood that an external electric field can be shifts the center of positive and negative charges, polarized BNNTmolecules and give it an induced electric dipole moment which it increases linearly with the external EF for BNNTs with various diameter. This results show that when the BNNT with greater diameter subjected to external electric field has a much stronger interaction with the poles (electrodes) of the nano-electronic circuit.



4. Conclusion

In summary, in this work, we have performed DFT calculation on the BNNT with diameters 3.26, 3.82 and 4.36 Å by applying static electric field. The results show that the HLG values of the BNNT gradually increase with increasing diameters, therefore, decreases the conductivity of BNNT. Also with increasing diameters of the BNNT the polarization and electronic stability of the BNNT are increased.

References

- [1] N.G. Chopra, et al., Science 269 (1995) 966.
- [2] M.Terrones, et al., Mater. Tody 10 (2007) 31.
- [3] D. Farmanzadeh, S. Ghazanfary, Struct. Chem. 20 (2009) 709.

**Theoretical study of few organic compounds on corrosion inhibition of stainless steel in acidic solution**

E. Jamalizadeh, S.M.A. Hosseini*, M. Amiri

Department of Chemistry, Shahid Bahonar University of Kerman, Kerman, 76169, Iran

(s.m.a.hosseini@mail.uk.ac.ir)

Keywords: **Corrosion, Organic inhibitor, Quantum chemical study, Semi-empirical.****1. Introduction**

The use of inhibitors is one of the most practical methods for protection against corrosion, especially in acidic media [1]. Various organic compounds decrease the corrosion of iron and steel in acidic solutions [2,3]. In the past few decades, theoretical investigations based on quantum chemical calculations have been suggested as a path for predicting molecular parameters which are directly related to the corrosion inhibiting properties of any chemical compound [4,5]. In this study semi-empirical quantum chemical methods have been used to study the structure of four inhibitors: [Benzotriazole (BTA), 2-Mercaptobenzoxazole (MBO), (3-Methoxy-4-{[5-oxo-2-pyrenyl-1,3-oxazol-4(5H)-yliden]methyl}phenyl acetate (MPA) and (4-[1-(5-nitro-2-furyl) methyldene]-2-phenyl-5(4H)-oxazolone (NFP)] for calculations of molecular parameters structure.

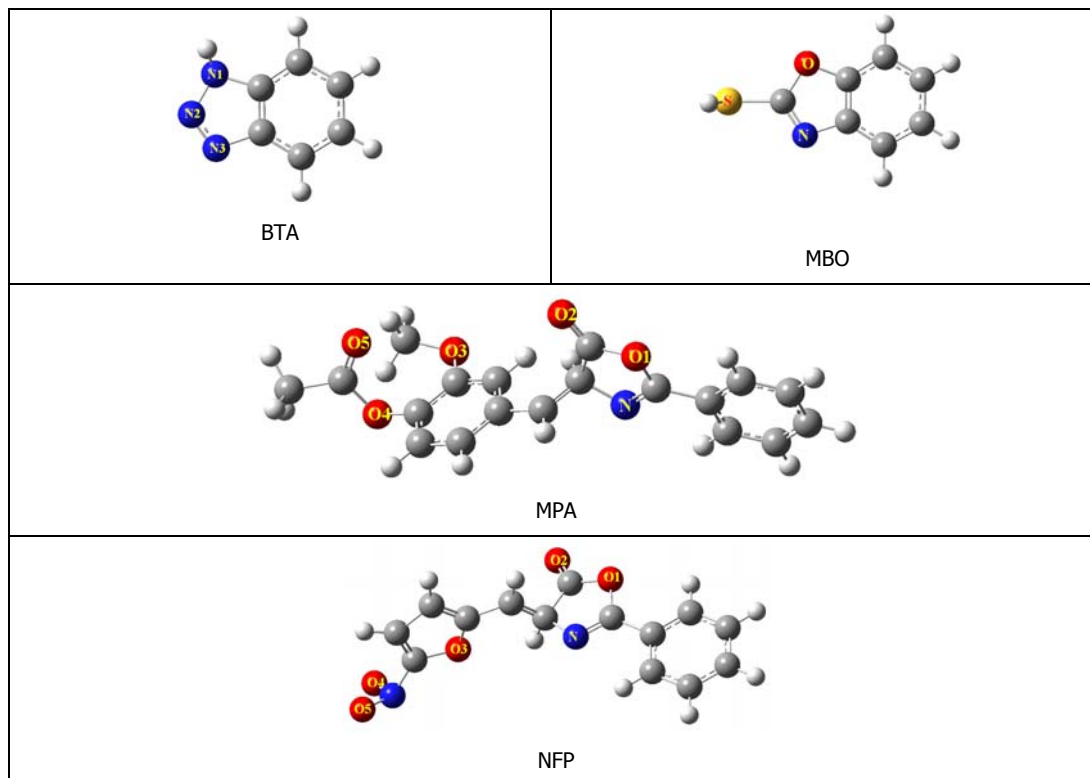
2. Methods

In this study Am1 semi-empirical method has been used to optimize the inhibitors structure and PM3 was employed as quantum chemical technique for calculations of molecular parameters structure. PM3 in between the other semi-empirical methods constantly gives better quality results for steel surfaces exposed to HCl and H₂S media [6].

3. Results and discussion

The optimized structures of the investigated compounds are given in Fig. 1.

Fig. 1. Optimized structure of studied inhibitor molecules.



Highest occupied molecular orbital energy level (HOMO), which is represented as E_H , as a measure of electron donating ability of a molecule explains the adsorption of inhibitor on metallic surfaces by way of de-localized pair of n electrons. A high E_H



value expresses intrinsic electron donating tendency to an appropriate acceptor, i.e. any molecule with lower HOMO energy and empty molecular orbital while, E_L , the energy of the lowest unoccupied molecular orbital signifies the electron receiving tendency of a molecule [5]. Accordingly, the difference between LUMO and HOMO energy levels (E_L-E_H), the dipole momentum (μ), the electron charge on nitrogen atoms (q_{N1} , q_{N2}) and (q_{N3}), the electron charge on oxygens (q_O), sulfur (q_S) and sum of electron charge of heteroatom were determined. The calculated difference (E_L-E_H) demonstrates inherent electron donating ability and measures the interaction of the inhibitor molecule with the metal surface. The above parameters and the measured inhibition efficiencies (IE %) for BTA, MBO, MPA and NFP are illustrated in Table 1. The results indicate that the differences of inhibition efficiencies may be expounded in terms of the value of electron charge of nitrogen atom (q_{N1}) with correlation coefficient 0.58. The data reveal the more negative value of q_{N1} for NFP amongst experimentally assessed compounds. Thus, NFP is expected to give better protection against corrosion in contrast to BTA which acquire more positive q_{N1} value spelling out its lower capability in protecting the surface. Calculated values of inhibition efficiency work out by regression analyses of IE% versus q_{N1} are given in Table 1. It is suggested that the electron pair on nitrogen able these compounds to make a complex with the d orbital of Fe hence it results reduction in corrosion rate.

Table 1. Quantum chemical indices of A, B and C compounds.

Quantum chemical parameters	BTA	MBTA	MPA	NFP	R2
Et (au)	0.151	0.062	-0.011	0.158	0.087
EH (au)	-0.357	-0.359	-0.341	-0.369	0.283
EL (au)	-0.030	-0.034	-0.024	-0.042	0.515
EL-EH (au)	0.327	0.325	0.317	0.327	0.024
μ (D)	3.772	2.169	3.001	4.093	0.241
q_{N1} (eV)	0.108	-0.024	-0.163	-0.166	0.576
q_{N2} (eV)	-0.083	-	-	0.506	-
q_{N3} (eV)	0.011	-	-	-	-
q_{O1} (eV)	-	-0.096	-0.177	-0.176	-
q_{O2} (eV)	-	-	-0.294	-0.291	-
q_{O3} (eV)	-	-	-0.171	-0.079	-
q_{O4} (eV)	-	-	-0.186	-0.203	-
q_{O5} (eV)	-	-	-0.341	-0.222	-
q_S (eV)	-	0.132	-	-	-
$q_{N(1-3)}+q_{O(1-5)}+q_S$ (eV)	0.036	0.012	-1.332	-0.631	0.153
Sum of negative charges	-0.083	-0.12	-0.1332	-0.137	0.541
IE (%) Exp.	40	47	52	78	-
IE (%) Cald.	38	50	64	65	-

4. Conclusions

In this study semi-empirical methods have been used to study the structure of BTA, MBO, MPA and NFP corrosion inhibitors of Stainless Steel for calculations of molecular parameters structure. The molecular structure parameters are directly related to the corrosion inhibiting properties of these compounds. Theoretical findings reveal that the differences in inhibition efficiencies can be explained in terms of value of the electron charge on nitrogen atom.

References

- [1] M. Almaj, J. Rawat, A. Quraishi, Bulletin of Electrochemistry. 14 (1998)199.
- [2] M.S. Morad, Mater. Chem .Phys. 60 (1999) 188.
- [3] S.M.A. Hosseini, M. Amiri, Journal of the Iranian Chemical Society, 4 (2007) 451.
- [4] K. F. Khaled, Electrochim. Acta, 48 (2003) 2493.
- [5] E. Jamalizadeh, S.M.A. Hosseini, A.H. Jafari, Corrosion science 51 (2009) 1428.
- [6] C. Ogertir, B. Mihci, G. Bereket, J. Mol. Struct. Theochem., 488 (1999) 223.



Halogen bonding; L-hole versus σ -hole

K. Eskandari*, H. Zariny and M. Lesani

School of Chemistry, Damghan University of Basic Science, Damghan 36715-364

(Email: eskandari@dubs.ac.ir)

Keywords: Halogen Bond, QTAIM, L-hole, σ -hole, Laplacian of Electron Density

1. Introduction

A halogen bond is a noncovalent interaction between a halogen atom and an electron donor species. These types of interactions play important roles in many areas of chemistry. But the strange nature of these bonds makes them more interesting for theoretical researchers. In fact, since bonded halogens are usually negatively charged, a negative-negative interaction between these atoms and a Lewis base is puzzling, however, Politzer et. al. [1,2] showed that the concept of σ -hole is very useful in rationalizing the formation of halogen bonds. They showed that the halogen atom in some RX molecule have regions of positive electrostatic potential, called σ -hole, on their outer surfaces. So in this point of view, a halogen bond could be explained as an electrostatic attraction between the positive potential of the halogen and a negative site on the other molecule.

Recently, on the other hand, we explained the problem by using topological aspects of the Laplacian of the electron density [3]. We showed that a halogen bond can describe as an interaction between a region of charge depletion on the halogen atom, a hole, with a region of charge concentration, a lump, on the other molecule. Furthermore, we showed that, as well as the chemical environment of halogen atom kept constant, a very good linear correlation exists between the halogen bond strength and the kinetic energy density at the hole of the halogen.

In this work we want to compare the abilities of these two models in predicting and describing the halogen bonds. Through this article we will use the term "L-hole" for the hole in the Laplacian of the electron density, to distinct it from the " σ -hole" which refers to a positive region in the electrostatic potential map of molecules.

2. Methods

The optimized geometries and their wave functions have been obtained with the Gaussian 03 program. The electron density and its Laplacian has been analyzed based on the Quantum Theory of Atoms in Molecules (QTAIM), with the Bader's AIM-PAC suite of programs and AIMAll package.

3. Results and Discussion

As mentioned in the introduction, both of the concepts, i.e. σ -hole and L-hole, can be used to predict the ability or disability of a halogen atom in forming a halogen bond. Although, in most of the cases, these models have similar predictions, there are some exceptions in which these concepts lead us to different conclusions. The chlorine atom in CH_3Cl and the fluorine atom in some molecules are examples of this problem.

3.1. Halogen bonding in CH_3Cl

First, let us take a look at the interpretations based on the σ -hole model. In the electrostatic potential map of CH_3Cl , Politzer and co-workers, found a completely negative surface around chlorine atom. This means that chlorine in CH_3Cl does not have a positive σ -hole and consequently, according to the σ -hole model, does not form a halogen bond with bases. But, when the distribution of the Laplacian of the electron density is considered, one can see that there is a L-hole in the Valence Shell Charge Concentration (VSCC) of chlorine atom. This means that the CH_3Cl is capable to form a halogen bond. It is clearly in contrast to the σ -hole model prediction.

But which model is right for this case? Does CH_3Cl is able to form a halogen bond? Unfortunately, there are no experimental results for this case, and we should find our answer in ab-initio calculations. Politzer et. al.[1] carried out a DFT calculation on $\text{CH}_3\text{Cl-NH}_3$ complex. Their results showed that this complex is not stable. On the other hand, MP2 calculation of Zou et. al. [4] indicated a small stabilization energy (about 0.5 kcal/mol) for this complex. It seems that the Zou et. al. calculation is in agreement with our L-hole model, however, we should mention and emphasize that their stabilization energy is very small and may be meaningless. So, to find a more trustworthy answer, we checked the complexation between CH_3Cl and pyridine, furan,



and oxirane. Our results show that CH_3Cl is able to form a halogen bond with these bases. Their stabilization energies (at MP2/6-311++G(d,p) level) are 1.12, 1.27 and 1.92 kcal/mol respectively. In addition, very accurate calculations of Riley and Hobza [5] (with CCSD(T) method and different basis sets including CBS) confirm the existence of halogen bond between CH_3Cl and OCH_2 . All of these results are in agreement with the L-hole model.

3.2. Does fluorine atom participate in halogen bonding?

The fluorine atom is usually deemed to not participate in halogen bonding interactions. This well-known behavior of fluorine is confirmed by both of the models; based on the electrostatic potentials, the fluorine atom does not have a positive σ -hole [1] and based on the Laplacian of the electron density, this atom does not have a L-hole [3]. But recently several theoretical studies raise doubts about this inability of fluorine atom. Politzer and co-workers [6] showed that some fluorine containing molecules, such as NCF and FCCF, are able to interact with Lewis bases. They also found a positive σ -hole in the electrostatic potential map of fluorine atom in these molecules.

On the other hand, our attempts to finding a L-hole in the VSCC of fluorine atom in FCCF and NCF has been failed. Again, σ -hole model and L-hole model come to different conclusions! But here, unlike the CH_3Cl , the computational evidences are in agreement with the σ -hole model. Do these systems reveal a weakness in the L-hole model? To answer this question, we need to know more about the nature of these new halogen bonds, because it seems that these bonds completely differ from traditional halogen bonds of chlorine and bromine. For example, QTAIM analysis of chlorine and bromine containing halogen bonds indicates that these halogens destabilize upon complexation, but this is not the case for fluorine in FCCF and NCF when these molecules interact with Lewis bases. The atomic energies are not the only cases which indicate that this fluorine bonds differ from traditional halogen bonds. So, we think that, first of all, we should answer this important question: *Are these fluorine bonds halogen bonds?*

4. Conclusions

Indeed, the local statement of virial theorem is behind of the L-hole model; this theorem relates the Laplacian of the electron density to the potential energy density, $V(r)$, and kinetic energy density, $G(r)$:

$$\frac{1}{4} \nabla^2 \rho(r) = 2G(r) + V(r)$$

the potential energy density involves the full quantum potential and contains the virial of Ehrenfest force. The electrostatic force, which is used in calculating electrostatic potentials, is only one component of this total force. This is the reason that the σ -hole model can not predict a halogen bond between CH_3Cl and Lewis bases. As indicated by Riley and Hobza [5], the dispersion forces are responsible for stabilizing complexes between CH_3Cl and bases, and the electrostatic forces are not important here.

References

- [1] P. Politzer, P. Lane, M. C. Concha, Y. G. Ma and J. S. Murray J. Mol. Model., 13 (2007), 305-311.
- [2] J. S. Murray, P. Lane and P. Politzer, J. Mol. Model., 15 (2009) 723-729.
- [3] K. Eskandari, H. Zariny, "Halogen bonding: a Lump-Hole Interaction" submitted.
- [4] Jian-Wei Zou, Yong-Jun Jiang, Ming Guo, Gui-Xiang Hu, Bing Zhang, Hai-Chun Liu and Q.-S. Yu, Chem. Eur. J, 11 (2005) 740.
- [5] K. E. Riley and P. J. Hobza J. Chem.Theor. Comput., 4 (2008) 232-242.
- [6] P. Politzer, J. S. Murray M. C. Concha, J. Mol. Model. 13 (2007) 643-650.



An investigation of electronic excitation transfer between chlorophylls light harvesting complexes I and II, by using quantum computers

M. Dehestani^a and S. Shojaei Baghini,^b

^aDepartment of Chemistry, Shahid Bahonar University, Kerman, Iran

(Email: dehestani2002@yahoo.com)

^bDepartment of Chemistry, Payameh Noor University, Kerman, Iran

(Email: somayeshojaei@yahoo.com)

Keywords: Electronic excitation transfer, Light harvesting complexes I and II, Quantum Fourier transform, Quantum gates

1. Introduction

Sunlight energy is absorbed and converted into chemical energy by pigments bound to photosystems I and II (PSI and PSII). Photosystems are composed of two sections: 1) a reaction center devoted to the conversion of light energy into chemical energy and 2) an antenna system that increases the capacity of light absorption. In green plants light harvesting complexes of PSII, consists of the major trimeric complex LHCII and three minor complexes, CP29, CP26 and CP24. In contrast to LHCII, the composition and structure of LHCI that associated with PSI is not well established, but it is thought to be composed of four types of LHC proteins, LHC type(I, II, III, I'), have been suggested to dimerize into LHCI-730 (type I and I') and LHCI -680 (type I and III) complexes [1]. The number of chlorophylls in each of the complexes in major and minor antenna systems of PSII and four light harvesting complexes of PSI are different. In this work we investigated excitation energy transfer between chlorophylls in these antenna complexes by using quantum fourier transforms. These transforms have an important role in more of the efficient quantum algorithms of quantum computers.

2. Computational Methods

1) Quantum Computers and Light Harvesting Antenna

Quantum computers process information in a way that preserves quantum coherence. Unlike a classical bit, a quantum bit, or qubit, can be in a superposition of 0 and 1 at once. This quantum mechanical feature allows quantum computers to perform some computations faster than classical computers. For example, quantum computers if built could factor large numbers, search data base and simulate quantum systems more rapidly and efficiently than corresponding classical algorithms. Physicists believe that all aspects of the world around us can ultimately be explained using quantum mechanics. In this sense a light harvesting antenna is a quantum mechanical many particle system composed of a large number of atoms. In the light of the quantum information and computation it is tempting to imagine LHCI, II of green plants as a quantum circuit that processes information (harvested photons) from the environment and funnels it to other complexes that surrounds the RC [2].

2) The quantum Fourier transform

One of the most useful ways of solving a problem in mathematics or computer science is to transform it into some other problem for which a solution is known. A great discovery of quantum computation has been that some such transformations can be computed much faster on a quantum computer than on a classical computer. One such transformation is the discrete Fourier transform. In the usual mathematical notation, the discrete Fourier transform takes as input a vector of complex numbers, x_0, \dots, x_{N-1} where the length N of the vector is a fixed parameter. It outputs the transformed data, a vector of complex numbers, y_0, \dots, y_{N-1} . The quantum Fourier transform is exactly the same transformation, although the notation is somewhat different. The quantum Fourier transform on an orthonormal basis $|0\rangle, \dots, |N-1\rangle$ is defined to be a linear operator.

In order to creating one relationship among excitation energy transfers with quantum fourier transform we used the equation $2^n = N$. In this equation n and N respectively represent the number of qubits requirement for simulation of transfers and the number of chlorophylls in the antenna complexes that often corresponding with the number of creating states [3].

3. Results and Discussion

We investigated excitation energy transfer between chlorophylls in the major and the minor antenna systems of LHCII and the antenna complexes of LHCI (four complexes) by quantum computers. Results indicated that we could simulate these transfers



in the antenna system by using quantum fourier transforms. In addition to we diagramed quantum circuits that performs these transforms by using Hadamard, Rotational and swap gates. Table 1 indicates our results briefly.

The number of swap gates	The number of R ₄ gates	The number of R ₃ gates	The number of R ₂ gates	The number of H gates	The number of qubit (n)	The number of chl (N)	Table 1. Representation the relationship among the number of qubits and chlorophylls with the number of gates				
0	0	0	0	1	n =1	N=2	Lumenial surface	LHCI I	Major antenna	PSII	
1	0	0	1	2	n =2	N=4					
1	0	1	2	3	n =3	N=8					Steromal surface
1	0	1	2	3	n =3	N=8	CP29		Minor antenna		
1	0	1	2	3	n ~3	N=9	CP26				
1	0	1	2	3	n ~3	N=10	CP24				
2	1	2	3	4	n ~4	N=14	Lhca1	LHCI	Major antenna	PSI	
2	1	2	3	4	n ~4	N=15	Lhca2				
2	1	2	3	4	n ~4	N=15	Lhca3				
2	1	2	3	4	n ~4	N=14	Lhca4				

4. Conclusion

In this work we simulated excitation energy transfer between chlorophylls in antenna systems of two PSII and PSI by using quantum fourier transforms . Quantum computers already exist in nature. Photosynthesis is one example in which a quantum computer component may play a role in the classical word of complex biological systems. These systems represent an untapped resource for thinking about the design and expanding our current concepatations of what defines a quantum computers in nature.

References

- [1] R. Tokutsu, H. Teramoto, Y. Takahashi, T. Ono and J. Minagawa, Plant. Cell. Physiol, 45 (2004) 138.
- [2] P. Dong, M. Yang, Z. Cao, Phys. Let A. 373 (2008) 30.
- [3] G. I. Karafyllidis, Quant. Inf. Proc. 2 (2004) 271.

**Implementation of quantum algorithms by NMR**¹Dehestani and M. ²Heydari, H¹Department of Chemistry, University of Kerman, Kerman, Iran

(Email: dehestani2002@yahoo.com)

(Email: heydarei@yahoo.com)

Keywords: Qubit, Quantum gates, Hadamard gate, Deutsch algorithm.**1. Introduction**

The classical information unit is the binary digit, or bit. One bit can assume the logical values "0" or "1". Analogously, the unit of information in Quantum Information and Quantum Computation is the quantum bit, or qubit. A qubit can assume the logical values 0 or 1 or linear combination of them. Physically, qubits can be represented by any quantum object with two well defined and distinct eigenstates. For example qubits are the photon polarization states, electrons in two-level atoms and nuclear spins under the influence of a magnetic field [3].

The eigenstates of a qubit are represented by $|0\rangle$ and $|1\rangle$. For the case of spin 1/2 particle, the logical state 0 can be represented by the spin up state ($|0\rangle = |\uparrow\rangle$), whereas the logical state 1 can be represented by the spin down state ($|1\rangle = |\downarrow\rangle$).

Quantum information processing requires unitary transformations operating on states of one and two qubits, called logic gates.

ONE-QUBIT GATES

Single-qubit gates that can be directly implemented by RF pulses are the X, Y and Hadamard gates. The action of RF pulse with arbitrary phase ϕ and duration t_p and frequency ω_1 is described by the following pulse propagator:

$$(\theta)_\phi^I = \exp(-i\omega_1 t_p I_\phi) = \exp(-i\theta I_\phi) \quad (1)$$

where $I_\phi = I_x \cos \phi + I_y \sin \phi$, $\omega_1 t_p = \theta$, I_x , I_y and I_z are Pauli matrices;

and consequence of this statement is that gates such X (equivalent to the NOT gate) and Y are obtained directly from the corresponding RF pulse, as shown in Equation $R_n(\theta) = \exp(-i\theta n.I)$ i.e.,

$$(\pi)_x^I = e^{-i\frac{\pi}{2}} \begin{pmatrix} 0 & 1 \\ 1 & 0 \end{pmatrix} = e^{-i\frac{\pi}{2}} \times NOT, \quad (\pi)_y^I = \begin{pmatrix} 0 & -1 \\ 1 & 0 \end{pmatrix} \quad (2)$$

and Hadamrd gate achieved by

$$|0\rangle \xrightarrow{H} \frac{|0\rangle + |1\rangle}{\sqrt{2}}, \quad |1\rangle \xrightarrow{H} \frac{|0\rangle - |1\rangle}{\sqrt{2}} \quad (3)$$

Where

$$H = \frac{1}{\sqrt{2}} \begin{pmatrix} 1 & 1 \\ 1 & -1 \end{pmatrix}, \quad H = (\pi)_x^I \left(\frac{\pi}{2}\right)_y^I \quad (4)$$

TWO-QUBIT GATES

Here we concentrate on the controlled- NOT gate, which plays a central role in the theory of quantum computation. It can be shown that the combination of a complete set of one-qubit gates. The fundamental two-qubit gate is the controlled- NOT gate, which applies a NOT gate to one qubit (the "target") if another qubit (the "control") is in state $|0\rangle$. It can be described as follows [2]:

$$C_{NOT} = \begin{pmatrix} 1 & 0 & 0 & 0 \\ 0 & 1 & 0 & 0 \\ 0 & 0 & 0 & 1 \\ 0 & 0 & 1 & 0 \end{pmatrix} \quad (5)$$

THE DEUTSCH ALGORITHM

The Deutsch algorithm is used to test whether a binary function of one qubit is constant ($f(0) = f(1)$) or balanced ($f(0) \neq f(1)$), without the need of computation the two possible values $f(0)$ and $f(1)$. However, knowing whether the function is constant or balanced corresponds to only one bit of information, and so it might be possible to answer this question using only one evaluation of the function f . Equivalently, it might be possible to determine the value of $(f(0) \oplus f(1))$ using only one



evaluation of f . (The symbol \oplus indicates addition modulo 2, and for two one bit numbers, a and b , $a \oplus b$ equals 0 if a and b are the same, and 1 if they are different.) In fact, this can be achieved as long as the calculation is performed using a quantum computer rather than a classical one. The quantum circuit that describes the Deutsch algorithm is illustrated in Figure 1;

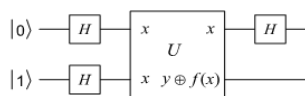


Figure 1: Quantum circuit that illustrates Deutsch algorithm

That U_f is the unitary transformation, which takes the two-qubit system from a generic state, $|x, y\rangle$ to the state $|x, y \oplus f(x)\rangle$.

2. Methods

In the NMR implementation that we will use, the four following steps are applied for this algorithm.

- (1) **Preparation:** perform the system in the quantum state $|\psi\rangle$ for example $|\psi_0\rangle = |0\rangle \otimes |1\rangle = |01\rangle$
- (2) **Excitation:** A Hadamard logic gate applied to all qubits. $|\psi_1\rangle = \frac{1}{2}(|0\rangle + |1\rangle)(|0\rangle - |1\rangle)$
- (3) **Evaluation:** This is done by implementing the unitary transformation. $|x, y\rangle \rightarrow |x, y \oplus f(x)\rangle$ and
- (4) **Observation**

3. Conclusions

This article seeks to give a short account of the-state-of-the-art in NMR quantum computing by quantum logic gates and quantum algorithms. We would like to reiterate that NMR is a promising technique to illustrate and explore ideas in quantum computations.

References

- [1] J. A. JONES, Fortschr. Phys. 48 (2000) 9-11, 909-924.
- [2] J. A. JONES, R. H. Hansen, and M. Mosca, J. Magn. Reson. 44, 409 (1981).
- [3] M. A. Nielsen, I. L. Chuang, Quantum Computation and Quantum Information (Cambridge press, 2001).



Ab initio potential energy surface for He–N₂ complex

M. Dehestani and Z. Sharifzadeh*

Department of Chemistry, University of shahid Bahonar of Kerman, Iran

(Email: Z_Sharifzadeh2009@yahoo.com)

Keywords: Potential energy surface, Nerve-fuzzy model, Symmetry-adapted perturbation theory, Nitrogen– Helium dimer.

1. Introduction

The He–N₂ interaction has been studied extensively over the past 25 years as a prototypical atom-molecule interaction. Of the four most accurate of the earlier potential energy surfaces proposed for this interaction, two are fully empirical and two semiempirical in nature. The two empirical surfaces are the exponential-spline-Morse-spline-van der Waals (ESMSV) potential surface of Beneventi *et al.* [1] and the Morse-Morse-Morse-spline-van der Waals (M3SV) potential surface of Gianturco *et al.* [2]. One of the two semiempirical surfaces is that of Bowers *et al.* [3], referred to herein as the BTT potential surface, and the other is a modification of the HFDI surface of Fuchs *et al.* [4] obtained by deleting the (ad hoc) anisotropy in the damping factor, and referred to herein as the HFD 1M potential surface.

2. Methods

There are two dominant methods for the *ab initio* calculation of a van der Waals Potential energy surface; symmetry adapted perturbation theory (SAPT) and the supermolecule method in which interaction energies are obtained simply as differences between the energies of the dimer and the monomers. Our calculations have been carried out using SAPT2008 software [5].

In all our calculations, the Nitrogen molecule was assumed to be rigid. The N–N bond length $r_{\text{N-N}} = 2.10$ bohr. The SAPT calculations were performed on a grid of points for which R equals from 3.78 to 11.33 bohr, θ equals from 0 to 90 degree. To obtain an analytic representation of the He–N₂ potential energy surface, the interaction energies calculated at grid points were fitted to an approach nerve-fuzzy model.

3. Results and discussion

The obtained potential energy surface from the present work for $\theta = 90^\circ$ have been compared with each of the empirical (ESMSV, M3SV) and semiempirical (BTT, HFD1M) potential energy surfaces and it is shown in the Figure 1.

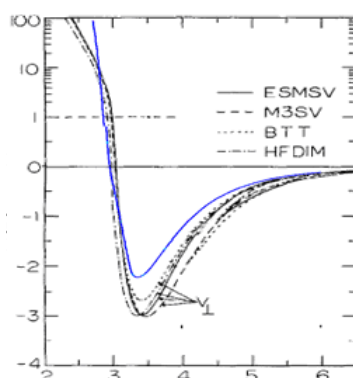


Fig. 1. Comparison between the potential surfaces of the ESMSV (continuous curve), M3SV (dashed curve), BTT (dotted curve), and HFDIM and this work (blue color curve) potential energy surfaces for the N₂–He system.

For the linear ($\theta = 0^\circ$) and T-shaped ($\theta = 90^\circ$) geometries, we have calculated the main characteristic parameters values of our potential energy surface which are the well depth (ϵ), distance at which the interaction potential vanishes (σ) and the position of the potential well (R_m). These parameters values have been listed in Table 1 and compared with values of the four potentials ESMSV, M3SV, BTT and HFD1M.

**Table1.** Characteristics of the (He-N₂) surfaces.

	BTT ^a	ESMSV ^b	HFDM1 ^c	M3SV ^d	Our model
$R_{m\perp}/\text{\AA}$	3.40	3.42	3.35	3.48	3.36
$\varepsilon_{\perp}/\text{meV}$	2.67	2.97	3.06	3.01	2.49
$\sigma_{\perp}/\text{\AA}$	3.03	3.04	2.96	3.03	3.10
$R_{m\parallel}/\text{\AA}$	3.93	4.11	4.09	4.03	4.00
$\varepsilon_{\parallel}/\text{\AA}$	2.01	1.32	1.31	1.48	2.65
$\sigma_{\parallel}/\text{\AA}$	3.56	3.65	3.70	3.62	3.62
$\Delta R_m/\text{\AA}$	0.53	0.69	0.74	0.55	0.64
$\Delta\varepsilon/\text{meV}$	0.66	1.65	1.75	1.53	0.16
$\Delta\sigma/\text{\AA}$	0.53	0.61	0.74	0.59	0.52

^a Ref. [3], ^b Ref. [1], ^c Ref. [4], ^d Ref. [2] Δ denotes a difference between linear and T-shaped geometries

4. Conclusions

A new potential energy surface has been obtained for the N₂-He complex using large basis sets (113 functions of spdf symmetry) and more grid points (347 total) in the present work. The method applied is symmetry-adapted perturbation theory. The computed points have been fitted by an approach nerve-fuzzy model containing 35 adjustable parameters. Our calculations also show that the T-shaped structure is the most stable one for our potential energy surface.

References

- [1] L. Beneventi, P. Casavecchia, and G. G. Volpi, J. Chem. Phys. 85, (1986) 7011.
- [2] A. Gianturco, M. Venanzi, R. Candori, F. Pirani, F. Vecchiocattivi, A. S. Dickinson, and M. S. Lee, Chem. Phys. 109, (1986) 417; 113, (1987) 166.
- [3] M. S. Bowers, K. T. Tang, and J. P. Toennies, J. Chem. Phys. 88, (1988) 5465.
- [4] L. Beneventi, P. Casavecchia, and G. G. Volpi, J. Chem. Phys. 95, (1991) 5827 .
- [5] R. Bukowski et al. SAPT2008: An AbInitio Program for Many – Body Symmetry - Adapted Perturbation Theory Calculations of Intermolecular Interaction Energies.

**Ab initio study of the effect of substitutional groups on the structure and torsional potential of conjugated diens**Z. Zamani^a, and H.R. Shamlouei^{b*}^{a,b} Faculty of Science, Islamic Azad University of Gachsaran, Gachsaran, Iran

(Email: shamluei@iaug.ac.ir)

Keywords: Conjugated dien, torsional potential.**1. Introduction**

The chemical reactivity and the distinguished electronic structure of many unsaturated molecular systems were of a great interest for many years. This prompted us to study the conformational stability and structural behavior of some conjugated aldehydes, isocyanates and ketenes. In such systems, the planar *s-cis* and *s-trans* conformations were predicted to be the stable forms due to π conjugation. When this conjugation is absent in other saturated analogues, it was found that the rotation around the C-C or the C-N single bond is less hindered with relatively lower energetic barriers as compared to unsaturated ones. Conjugated ketenes were of a particular interest in synthetic chemistry and were considered important reagents for many types of reactions.

Additionally, the torsional potential is considered a sensitive probe of the electronic structure of molecules leads to interesting conclusions on interactions between the double bond and the substituents, such as destabilizing steric perturbations and electronic conjugation.

In recent article, the structure and torsional potential of conjugated dien was calculated and the effect of some substitutional group in structure and torsional potential was studied.

2. Computational Details

The structure of some conjugated systems with substitutional group was calculated with the HF, DFT and MP2 methods. The names of the conjugated systems are listed in table1. After optimization of structure, the potential barrier for rotation about H-C-C-H, and C=C-C=C dihedral angle was calculated for each structure.

3. Results and Discussions

The structure of several substituted conjugated dien (C=C-C=C) systems were optimized by the HF, DFT and MP2 methods in *cis* and *trans* configurations. In table1, a list of the systems can be seen.

Table1. List of substituted diens

$\text{H}_2\text{C}=\text{CH}-\text{CH}=\text{CH}_2$	$\text{NH}_2\text{HC}=\text{CH}-\text{CH}=\text{CHNH}_2$
$(\text{NH}_2)_2\text{C}=\text{HC}-\text{CH}=\text{C}(\text{NH}_2)_2$	$(\text{NH}_2)_2\text{C}=\text{CH}-\text{CH}=\text{CF}_2$
$(\text{NH}_2)_2\text{C}=\text{CH}-\text{CH}=\text{C}(\text{NO}_2)_2$	$(\text{NO}_2)_2\text{C}=\text{CH}-\text{CH}=\text{C}(\text{NO}_2)_2$
$\text{F}_2\text{C}=\text{CH}-\text{CH}=\text{CF}_2$	

Table1. *cis* and *trans* configuration isomers for dien

System Name	<i>cis</i>	<i>trans</i>		<i>cis</i>	<i>trans</i>
$\text{H}_2\text{C}=\text{C}-\text{C}=\text{CH}_2$	-154.9571848	-154.9622612	$\text{F}_2\text{C}=\text{C}-\text{C}=\text{CF}_2$	-550.15615	-550.16523
$(\text{NH}_2)_2\text{C}=\text{C}-\text{C}=\text{C}(\text{NH}_2)_2$	-375.1713905	-375.168157	$(\text{NH}_2)_2\text{C}=\text{C}-\text{C}=\text{CF}_2$	-462.7238192	-462.822877
$(\text{NH}_2)_2\text{C}=\text{C}-\text{C}=\text{C}(\text{NO}_2)_2$	-671.61475	-672.1145917	$(\text{NO}_2)_2\text{C}=\text{C}-\text{C}=\text{C}(\text{NO}_2)_2$	-967.9895482	-968.1999482

As a predicted result, the *cis* configuration, due to space crowding, is less stable and its energy is higher than the *trans* configuration. In addition it was seen that because of the space effect, the planar structure of dien which is essential to maximize the conjugation, is removed to decrease the eclipsed repulsion in *cis* configuration. As a considerable result, the *cis* configuration of $(\text{NH}_2)_2\text{C}=\text{C}-\text{C}=\text{C}(\text{NO}_2)_2$ is located in a minima of potential surface. For understanding the effect of substitutional groups on dien properties, the dihedral of C=C-C=C is changed and surface potential for each systems were calculated. The results for $\text{H}_2\text{C}=\text{CH}-\text{HC}=\text{CH}_2$, In Fig 2.

The surface potential for $(\text{NH}_2)_2\text{C}=\text{CH}-\text{CH}=\text{C}(\text{NH}_2)_2$, $(\text{NH}_2)_2\text{C}=\text{CH}-\text{CH}=\text{C}(\text{NO}_2)_2$, $(\text{NH}_2)_2\text{C}=\text{CH}-\text{CH}=\text{CF}_2$ and $(\text{NH}_2)_2\text{C}=\text{CH}-\text{CH}=\text{CF}_2$ are compared in 3.

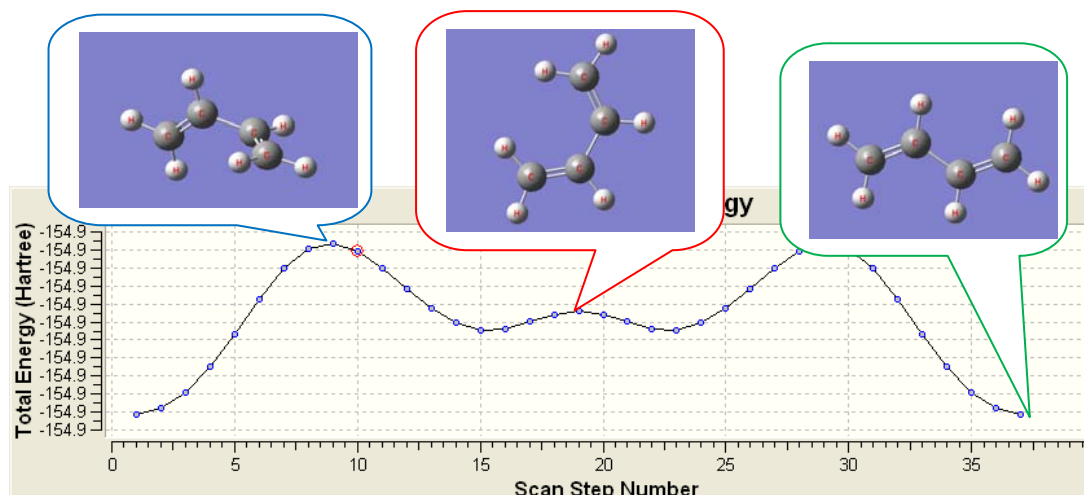


Fig2. Surface potential for the conjugated dien

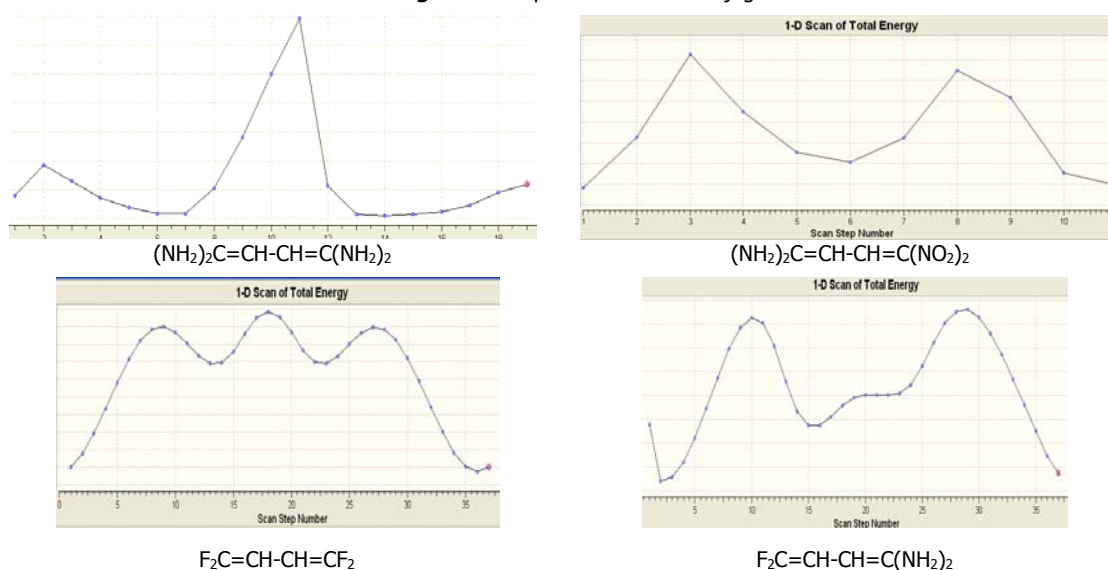


Fig4. Comparison of the potential surface of $(\text{NH}_2)_2\text{C}=\text{C}-\text{C}=\text{C}(\text{NH}_2)_2$ with $(\text{NH}_2)_2\text{C}=\text{C}-\text{C}=\text{C}(\text{NO}_2)_2$ and $\text{F}_2\text{C}=\text{C}-\text{C}=\text{CF}_2$ with $\text{F}_2\text{C}=\text{C}-\text{C}=\text{C}(\text{NH}_2)_2$

The results show that the potential barrier is considerably affected by the substitutional groups. The effect is substantially greater in $(\text{NH}_2)_2\text{C}=\text{CH}-\text{CH}=\text{C}(\text{NO}_2)_2$ and is the result of an intramolecular hydrogen bonding exist in molecule which stabilized the *cis* isomer. Fig5 represented the hydrogen bonding exist in *cis* isomer of it. The effect of hydrogen bonding in $\text{F}_2\text{C}=\text{CH}-\text{CH}=\text{C}(\text{NH}_2)_2$ is smaller than the previously discussed and has less effect on stabilization of *cis* form of it.

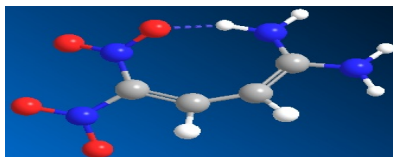


Fig5. The Hydrogen bonding between H and NO₂ Group in *cis* Isomer of the $(\text{NH}_2)_2\text{C}=\text{C}-\text{C}=\text{C}(\text{NO}_2)_2$

4. Conclusion

The results of this research are that the diens with higher degree of conjugation have higher stability. As the extra result of this paper, additional intramolecular interaction may be present to affect the structure and stability of systems.

References

- [1] H.M. Badawi, J. Mol. Struct. (Theochem) 343 (1995) 117.
- [2] H.M. Badawi, A. Al-Rayyes, J. Mol. Struct. (Theochem) 428 (1998) 247.
- [3] W. Forner, H.M. Badawi, Asian J. Spectrosc. 2 (1998) 72.
- [4] A. Al-saadi and H. M. Badawi, J. Mol. Model. Vol. 582, 153(2002).
- [5] H.M. Badawi, J. Mol. Struct. (Theochem) 336 (1995) 21.



Active C-H bond and rational of the anion-cation structural pattern in the ionic liquids 1-alkyl-3-methylimidazolium Chloride

Mohammad Hadi Ghatee, Fatemeh Moosavi, and Razyeh Jahromi
(Department of Chemistry, Shiraz University, Shiraz 71454, Iran)

E-mail: (ghatee@susc.ac.ir)

E-mail: (fatemeh.moosavi@gmail.com)

E-mail: (ra_ch_2007@yahoo.com)

I. Introduction

Interest in room temperature ionic liquids (ILs) provides highly active field of research [1]. These materials are making their marks as solvent for a variety of applications, including material synthesis, separation science, and battery applications. One of the attribute of these materials is the potential to generate a wide range of IL types by the combination of various organic cations with numerous organic and inorganic anions. Under most circumstances, the imidazole-derived ILs are considered to be inert solvents, but this is not always the case [2].

The most widely used methods for probing hydrogen bonding are IR and NMR spectroscopic techniques, in which the C-H stretching frequencies and chemical shifts of this hydrogen bonding have been examined [3].

This forms the objective of this study to characterize the hydrogen bond in 1-alkyl-3-methylimidazolium chloride by studying the structural properties including molecular parameters (bond distances, bond angles, dihedral angles) as well as atomic charges and the NMR chemical shifts. The effect of alkyl chain length is studied by incorporating alkyl group methyl to octyl. The final goal is to carry out a reaction relating to interionic reactivity of the target materials and explore how the theoretical calculations performed leads to an accurate insight into the interaction between anion and the cation.

II. Computational Details

An initial structure of the ILs was prepared and geometry optimized by classical method; subsequently, classical molecular dynamics simulation was performed to accelerate the final convergence in the next part of the computation. We believe that an initial dynamic optimization would provide a structure closely related to a true local minimum, which may adhere to global minimum. Then, further optimization for the final stable structure was performed by DFT quantum mechanical method at B3LYP/6-311G** level of theory, using the Gaussian 03 program [4]. The optimized structure of each IL was then improved by an extra optimization at the B3LYP/6-311++G** [5]; also fully characterized as minima by frequency analysis. This allows verifying the adequacy of B3LYP method using the basis set 6-311++G**. The results of B3LYP structural calculation were compared for accuracy with the more accurate MP2 method by the same basis set.

Two sets of reactions are proposed to estimate the extent and the consequent of interionic interactions in [C_nmim]Cl. Using DFT results, the variation of the Gibbs free energy (ΔG) with the alkyl chain length was investigated.

III. Results and Discussion

The study focuses on the interaction of the anion with the cation of ILs containing chloride anion and imidazolium cation with various alkyl groups, methyl to octyl. The simple monatomic chloride anion makes the study of the anion-cation interaction rather straightforward; however, the anion itself poses some complexity as compared to other halides.

The nature of particular C-H bond in many substances essentially determines their physical and thermodynamical properties. In this project, properties of the most active C-H bond of the imidazolium ring in 1-alkyl-3-methylimidazolium chloride are investigated by *ab initio* quantum mechanical methods. Gibbs free energy change of the reaction involving active C-H bond and anion in gas phase show the anion is very susceptible to interact strongly with C-H bond. The extent and pattern of this interaction depends on the systematic polarization induced on the C-H channel as the alkyl chain length increases.

A more detailed role played by alkyl chain on the structural behavior of the ILs can be obtained by studying H abstraction by Cl⁻. We study the gas phase free energy change, ΔG , of heterolytic cleavage of C-H bond, which leaves two electrons on positively charged C atom. Here it is assumed that the process passes through a transition state that may produce (**c**) in either singlet or triplet state (See Scheme 1). Notice that the structure of (**a**) used for the calculation of ΔG corresponds to the structural pattern discussed earlier. The values of ΔG as a function of chain length are plotted in Figure 1. From this Figure, it can be concluded that the compound (**a**) in [C_{1,6-8}mim]Cl ILs is more susceptible to release H atom than those compound in [C₂₋₅mim]Cl by about 6.081-7.449 kJmol⁻¹.

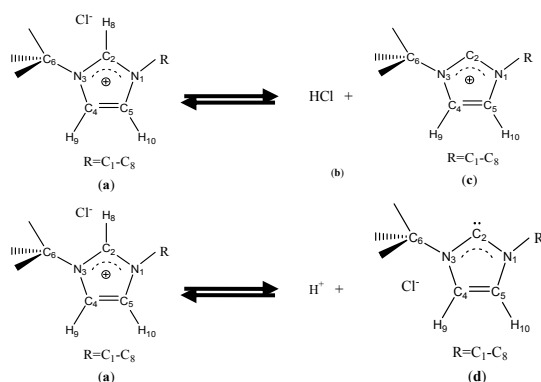
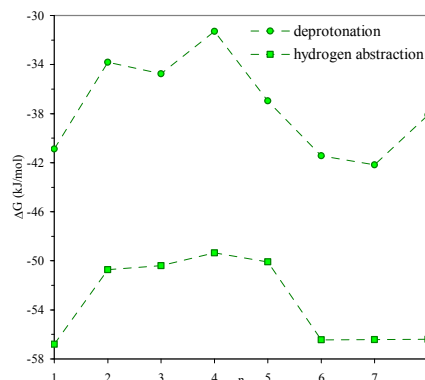


Figure 1. Gibbs free energy change of the considered reactions with alkyl chain length.

Scheme 1. The hydrogen abstraction reaction (above)

and the deprotonation reaction in the gas phase (below).



So far, we have considered the structure of the Cl^- anion in relation to the most reactive hydrogen (H_8) of the imidazolium ring. To see the reactivity towards H_9 and H_{10} , we consider the reaction shown in the Scheme 1. This reaction allows studying the interaction of Cl^- with other reactive centers in the absence of H_8 . The anion positioning near H_9 and H_{10} does not lead to a stable configuration because of the repulsion due to the excess π charge on the $\text{C}_4=\text{C}_5$ bond [6]. The role of alkyl group on the structure of anion with respect to the imidazolium ring can now be seen to affect the energetics of the Scheme 1 almost in the same way discussed earlier. As the plot of ΔG values indicates (Figure 1), the reaction energetics is more sensitive to the alkyl chain length than in the case that Cl^- interaction with the cation (**d**) is absence. These results might be used to conclude that the alteration in the properties of ILs with respect to the change in chain length is substantially due to specific interaction of the alkyl group with the imidazolium ring cation. From Figure 1, also it can be seen that the change in Gibbs free energy of first reaction is lower than for the reaction in the second as an indication of space charging due to presence of Cl^- that is made feasible by the cost of energy for instance 15 kJ mol^{-1} of $[\text{C}_1\text{mim}]\text{Cl}$.

IV. Concluding Remarks

The effect of alkyl chain length, methyl to octyl, on the strength of the interaction of anion with the cation in 1-alkyl-3-methylimidazolium chlorides has been studied by *ab initio* quantum mechanical calculation at B3LYP/6-311++G** level of theory and compared with the more accurate MP2 method. The results indicate that H_8 is more active than both H_9 and H_{10} . The alkyl chain length has a profound effect on the reactivity of these hydrogens.

Keywords

Structural Calculation, Hydrogen Abstraction, Ionic Liquids, Chemical Reactivity.

References

- [1] (a) Welton, T. Chem. Rev. 99 (1999) 2071. (b) Freemantle, M. C&E News 2000, 37. (c) Wasserscheid, P. Keim, W. Angew. Chem. Int. Ed. 39 (2000) 3772. (d) Dupont, J. de Souza, R. F. Suarez, P. A. Z. Chem. Rev. 102 (2002) 3667.
- [2] Dupont, J. Spencer, J. Angew. Chem. Int. Ed. 43 (2004) 5296.
- [3] (a) Jang, Y. H. Goddard III, W. A. Noyes, K. T. Sowers, L. C. Hwang, S. Chung, D. S. Chem. Res. Toxicol. 15 (2002) 1023. (b) Carda-Broch, S. Berthod, A. Armstrong, D. W. Anal. Bioanal. Chem. 375 (2003) 375, 191.
- [4] Frisch, M. J.; *et al.* Gaussian 03; Gaussian, Inc.: Pittsburgh, PA, 2003.
- [5] Becke, A. D. J. Chem. Phys. 98 (1993) 5648.
- [6] Ghatee, M. H. Zolghadr, A. R. Fluid Phase Equilib. 263 (2008) 168.



Density functional theory study of the interaction between a nano bio switch as drug deliverer with procarbazine

Z. H. Yazdi^{a,*}, M. A. Safarpour^a

^a Faculty of Chemistry, Department of Physical chemistry, Iran University of Science and Technology, Narmak, Tehran, Iran

*E-mail: z_yazdi@chem.iust.ac.i

r

Keywords: (4-Aminomethyl)-phenyl-azobenzoic acid; drug deliver; procarbazine; cAMPB(H₂O); DFT

1. Introduction

The activity of a biological system, such as an enzyme, can be modulated by incorporating a photobiological switch into its structure [1]. A photobiological switch is a biologically active compound with a built-in photochromic group that allows light triggered switching of its biological target [2]. In biological systems, the photoreversible isomerization of a molecule attached to a macromolecular system induces conformational changes that in turn lead to a physiological response of the protein [3]. Optical control of peptide/protein conformation can be a powerful biochemical tool for probing protein function in diverse systems [4]. Chromophores, such as azobenzene, that undergo reversible *cis-trans* photoisomerization, can, in principle, be used for reversible conformational control of proteins [5]. We are interested primarily in designs that can operate in water and that are simple enough to allow the mechanism of the photocontrol to be understood in structural terms.

We have applied our molecular modelling strategy in designing further versions of cross-linked peptides that significantly extends the versatility of this approach to the photocontrol of protein structure and properties of drug delivery. These molecules with increasing conformational constraints are studied for the *cis* to *trans* and the *trans* to *cis* photoreactions. The results indicate that the chromophore AMPB acts simultaneously as a fast molecular switch and as a sensor for initial conformational dynamics in the peptide. Suitable azobenzene-derivatives, such as (4-aminomethyl)- phenylazobenzoic acid (AMPB), has been incorporated into peptides and biopolymers to change their structure by photoisomerization[6]. AMPB peptides are a new class of molecules where the photoisomerizable dye azobenzene is linked to the peptide moiety via a flexible methylene spacer [7]. The short peptide chain Ala-Cys- Ala-Thr-Cys-Asp-Gly-Phe with the active site motif Cys-Ala- Thr-Cys described in a series of publications originates from the redox active enzyme thioredoxin reductase from the bacteria *Escherichiacoli*. A monocyclic (cAMPB) as well as a bicyclic (bcAMPB) form with a disulfide bridge between the two cysteines was synthesized[8]. These peptides could be dissolved in DMSO but not in water. It was shown that the replacement of three amino acids outside the active site motif by lysines leads to solubility in water. The monocyclic peptide, cAMPB(H₂O) (peptide motif Lys- Ser-Ala-Thr-Ser- Asp-Lys-Lys with the two cysteines replaced by serines to prevent formation of the disulfide bridge) was synthesized that could be dissolved in water [8]. By investigating the results of cAMPB (H₂O) conformers, we conclude that we have to have changes in these conformers in order to have better interaction between the drug and drug deliverer. Therefore, we designed a drug deliverer called bic- cAMPB(H₂O). Then we found that bic- cAMPB(H₂O) had an effective interaction with Procarbazine. Procarbazine is an antineoplastic chemotherapy drug for the treatment of Hodgkin's lymphoma and certain brain cancers. It is a member of a group of medicines called alkylating agents. The Procarbazine was chosen because of it is small size and high selectivity [9]. In this work we report the results of interaction between *trans*- and *cis*-cAMPB(H₂O) with Procarbazine, and of interaction between *trans*- and *cis*-bic- cAMPB(H₂O) with procarbazine to investigate if cAMPB(H₂O) and bic- cAMPB(H₂O) are potent drug deliverers for procarbazine or not.

2. Modelling

All calculations were carried out using the Gaussian 03 suite of programs [10]. The gas-phase structures were optimized at the B3LYP/6-31G (d) level and then single-point calculations were done at the B3PW91/6-31G (d) level of theory.

The gas-phase structure for drug was optimized at the B3LYP/6-31G (d) level.

3. Results and Discussion

At first we tried to optimized the geometries of *trans*- and *cis*-cAMPB(H₂O) and calculate potential energy surfaces. We found that *cis* conformer was not stable at all and *trans* conformer is very little stable compound. In this way, to have a more effective drug deliverer we made attempt to change the structure. The attempt resulted in a better drug deliverer called bic- cAMPB(H₂O). Eventually, in designing a drug deliverer we came to this conclusion that 8 amino acids groups should be divided into 2 groups

containing 4 amino acids. These 2 groups were joined to two azobenzene switches to increase the size of our peptide ring to locate the drug into the ring. The structures of cAMPB(H₂O), bic- cAMPB(H₂O) and procarbazine selected for this study are shown in figure 1. The ground-state geometries of these compounds were optimized at the B3LYP/6-31G* levels. The potential function scans for distances between the conformers of cAMPB(H₂O) and procarbazine and bic- cAMPB(H₂O) and procarbazine were obtained. Figure 2. Presents the trans isomer potential energy surfaces for both compounds. Upon calculations it was shown that trans isomers are stable host-guest combinations whereas cis conformers are unstable compounds. The calculated values of binding energy for trans bic- cAMPB(H₂O) and procarbazine is 15/313 kcal/mol. It is almost three times as many as normal hydrogen bound. In this way, the trans- bic- cAMPB(H₂O) conformer, loaded with procarbazine, might release the drug when one makes it change to cis conformer; in other words, bic- cAMPB(H₂O) is probably a successful drug deliver.

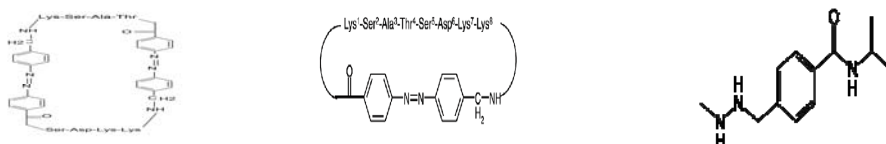


Fig. 1. (A) Structure of the monocyclic AMPB-peptide: bic-cAMPB(H₂O). (B) Structure of the monocyclic AMPB-peptide: cAMPB(H₂O). (C) Structure of the procarbazine.



Fig. 2. Potential energy surfaces for both compounds. (A) Diagram of trans-bic-cAMPB(H₂O)- procarbazine compound (B) Diagram of trans- cAMPB(H₂O)- procarbazine compound.

4. Conclusion

The interaction of bic- (cAMPB) as a host and procarbazine as a guest was studied by means of DFT method. The geometries of trans- and cis-bic- AMPB(H₂O) were optimized at B3LYP/6-31G* levels of theory. Then the potential energy surfaces of interaction of these host-guest combinations were investigated. Calculations present that trans- bic (cAMPB) and procarbazine consistently combine with each other whereas the combination of cis-bic (cAMPB) and procarbazine is not stable. The interaction between trans- and cis-AMPB (H₂O) with procarbazine is not stable. The discrepancy of the stability of these conformations suggests bic- (cAMPB) as a potent selective drug deliverer for procarbazine. After trans conformer transfers the drug to a favorite situation, under photoisomerization it might turn into cis conformer and release the drug.

References

- [1] H. Satzger, C. Root, C. Renner, R. Behrendt, L. Moroder, J. Wachtveitl, W. Zinth, Chem. Phys. Lett. 396 (2004) 191.
- [2] A.J. Harvey, A.D. Abell, Bioorg. Med. Chem. Lett. 11 (2001) 2441.
- [3] A.J. Harvey, A.D. Abell, Tetrahedron 56 (2000) 9763.
- [4] P.F. Loos, J. Preat, A.D. Laurent, C. Michaux, D. Jacquemin, X. Assfeld, J. Chem. Theory Comput. 4 (2008) 637.
- [5] A. Aemissegger, D. Hilvert, Nat. Protoc. 2 (2007) 161.
- [6] C. Renner, U. Kusebauch, M. Lweneck, A.G. Milbradt, L. Morder, J. Pept. Res. 65. (2005) 4.
- [7] J. Auernheimer, C. Dahmen, U. Hersel, A. Bausch, H. Kessler, J. Am. Chem. Soc. 127 (2005) 16107.
- [8] J. Wachtveitl, S. Sprlein, H. Satzger, B. Fonrobert, C. Renner, R. Behrendt, D. Oesterhelt, L. Moroder, W. Zinth, Biophys. J. 86 (2004) 2350.
- [9] <http://en.wikipedia.org/wiki/procarbazine>
- [10] M.J. Frisch, G.W. Trucks, H.B. Schlegel, G.E. Scuseria, J.A. Pople, GAUSSIAN03, Gaussian Inc., Pittsburgh, PA, 1998.

Comparison between Syn and Anti conformations in 8OG-C: AIM, NBO and NMR study

A. Ebrahimi, A. Haghani*, S. M. Habibi Khorassani, M. T. Maghsoodlou

Department of Chemistry, University of Sistan & Baluchestan, P.O. Box 98135-674, Zahedan, Iran

(E-mail: haghani14@yahoo.com)

Keywords: 8OG-C, Hydrogen bond, Base pairing energy, NMR study, NBO, AIM.

1. Introduction

Hydrogen bonding is the dominant interaction in the pairing of nucleic bases that determines the stability of the double-helical structure of DNA. 8-Oxoguanine (8OG), which is formed in the cell due to oxidation of free guanine in DNA and RNA, can forms both the syn and anti configurations (Fig. 1) with cytosine (8OG-C). Recent NMR studies on two-bond spin-spin coupling constants ($^2J_{X-Y}$) across $X-H\cdots Y$ hydrogen bonds have suggested that structural data and information about hydrogen bond type can be obtained from $^2J_{X-Y}$. In the present study, the relationship between calculated NMR data and the results of population analyses as well as the binding energies and optimized geometrical parameters have been studied in both syn and anti conformers.

2. Methods

All structures were optimized by Gaussian03 program package at B3LYP level with 6-311++G (d,p) basis set. Basis set superposition error (BSSE) has been calculated by the Boys-Bernardi counterpoise technique at mentioned level. The population analyses have been performed by atoms in molecules (AIM) and natural bond orbital (NBO) methods. In addition, $^2J_{X-Y}$, isotropic values of the proton shielding tensor, and isotropic chemical shift (δ_{iso}^H) have been calculated at mentioned level using SPINSPIN keyword.

3. Results and discussion

Three hydrogen bonds (**A**, **B**, **C**) in anti and two hydrogen bonds (**D**, **E**) in syn conformer (see Fig. 1) are formed between base pairs. **A**, **C**, and **E** are from $N-H\cdots O$ type, and **B** and **D** are from $N-H\cdots N$ type. The relationships between calculated properties have separately been investigated in two types. The optimized geometrical parameters are listed in Table 1. The orders of $N\cdots O$ and $N\cdots N$ bond lengths are **C** > **E** > **A**, and **D** > **B**, respectively. Also, the base pairing energy ΔE calculated at mentioned level with BSSE correction for syn and anti are equal to -10.26 and -25.83 kcal/mol, respectively.

Table 1. The most important geometrical parameters (in Å) and energy data (in kcal/mol) in syn and anti conformers.

anti		Syn	
O6 \cdots N4	(A) 2.814	N7 \cdots N3	(D) 3.144
N1 \cdots N3	(B) 2.927	O6 \cdots N4	(E) 2.827
N2 \cdots O2	(C) 2.931	N7-H7	(D) 1.02
N4-H4	(A) 1.03	N4-H4	(E) 1.02
N1-H1	(B) 1.03	$\Delta E(\text{kcal/mol})$	-11.00
N2-H2	(C) 1.02	$\Delta E(\text{BSSE})$	-10.26
$\Delta E(\text{kcal/mol})$	-6.81		
$\Delta E(\text{BSSE})$	-25.83		

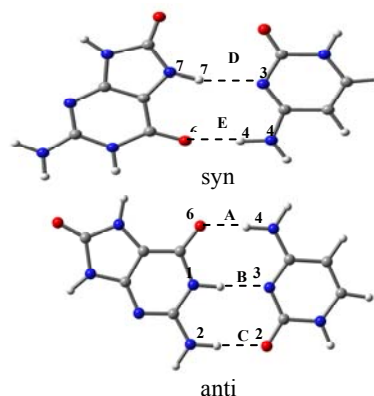


Fig 1. Anti and syn conformers.

The second-order perturbation energies $E^{(2)}$ of $n_X \rightarrow \sigma_{H-Y}^*$ interactions and the occupation numbers of antibonding orbitals $\sigma^*(H-X)$ and lone pairs (n_Y) obtained from NBO analysis are reported in Table 2. The maximum $E^{(2)}$ value (20.37 kcal/mol) corresponds to $n_N \rightarrow \sigma_{H-N}^*$ interaction in bond **B**. As can be seen in Table 2, the order of $E^{(2)}$ values in the $H\cdots O$ and $H\cdots N$ types are **A** > **E** > **C** and **B** > **D**, respectively. The strengths of donor-acceptor interactions are in agreement with the H-bond geometrical parameters. The trend in the occupation number (in e) of σ_{H-N}^* is **A** (0.052) > **E** (0.038) > **C** (0.032), which is in good agreement with the $E^{(2)}$ values and the $N\cdots O$ bond lengths. Also, the occupation number of σ_{H-N}^* in $H\cdots N$ bonds decreases by 0.0243 e from **B** to **D**, which is accompanied by the increase in H-bond length and the decrease in H-bond strength. The most important topological properties of electron charge density $\rho(r)$ calculated by AIM method at B3LYP/6-



311++G (d,p) level are gathered in Table 2. The maximum value of $\rho(r)$ calculated at H-bond critical point (HBCP) is equal to 0.0368 au that corresponds to bond **A**. The orders of $\rho(r)$ values calculated at HBCPs are **A** (0.037) > **E** (0.032) > **C** (0.027) and **B** (0.035) > **D** (0.02) for H \cdots O and H \cdots N types interactions, respectively. The trends are in accord with the H-bond strengths and the geometrical parameters. Also the values of laplacian of ρ ($\nabla^2\rho$) calculated at HBCPs is positive in all cases that is in agreement with closed-shell interactions. As can be seen in Table 2, the electronic energy density $H(r)$ calculated at HBCPs is in agreement with other characteristics of individual H-bonds.

The individual H-bonds have been characterized by NMR calculation at mentioned level. The total spin-spin coupling constant is the sum of four components (see Table 3): the paramagnetic spin-orbit (PSO), diamagnetic spin-orbit (DSO), Fermi-contact (FC), and spin-dipole (SD) terms. The isotropic chemical shifts (δ_{iso}^H), $^{2h}J_{X-Y}$, and isotropic value of the proton shielding tensor (protonic IS) decrease in the order **A** > **E** > **C** in H \cdots O type and **B** > **D** in H \cdots N type interactions. These trends are in accord with the result of AIM and NBO analyses, and geometrical parameters.

4. Conclusion

In Conclusion, different characteristics of individual H-bonds indicate that not only the number of H-bonds but also the strength of them make anti conformer more stable than syn.

Table 2. Most important result Obtained from AIM and NBO analysis

name	Bond	E ² kcal/mol	n/e	H(r)	$\nabla^2\rho(r)$	ρ_{BCP}
Anti	A	7.23 14.21	0.05154	0.0007	0.1190	0.0368
	C	4.09 8.54	0.03182	-0.0018	0.0947	0.0268
	B	20.37	0.06282	0.0015	0.0909	0.0346
Syn	E	7.36 9.08	0.03815	-0.0012	0.1196	0.0323
	D	9.16	-0.0385	-0.0018	0.0594	0.0197

Table 3. NMR data calculated at the B3LYP/6-311++G(d,p) levels of theory

Name	Bond	atoms	$^{2h}J_{X-H}$	FC	SD	PSO	DSO	δ_{iso}^H	protonic IS
Anti	A	O4 \cdots N6	7.55	7.57	0.09	-0.13	0.02	11.26	20.70
	B	N3 \cdots N1	5.56	5.53	0.06	-0.06	0.02	13.44	18.53
	C	O2 \cdots N2	4.95	4.99	0.07	-0.13	0.02	8.77	23.20
Syn	D	N3 \cdots N7	3.93	3.89	0.04	-0.02	0.02	10.53	21.44
	E	O6 \cdots N4	7.36	7.38	0.06	-0.10	0.02	9.66	22.30



Molecular Spectroscopy





Aggregation behavior spectral studies of Copper (II) Tetrasulfonated phthalocyanine in aqueous salt solution and in the presence ct- DNA

H. Dezhampanah^a and *T. Darvishzad^b

Department of Chemistry, Gilan University, Rasht, Iran.

Termeh_Darvishzad@yahoo.com

Keywords: Phthalocyanine, Aggregate, ionic strength, Ct-DNA, Absorption spectrum

1. Introduction

The aggregation of phthalocyanine (Pc), and related dye molecules, has been the subject of intensive study over many decades. Water-soluble phthalocyanines (Pcs) are used widely as textile dyes, and aggregation has significant effects on the light fastness and quality of the dye stuff. In recent years, interest in Pc aggregation has been stimulated by the adoption of Pcs as photosensitizers in photodynamic cancer therapy and the observation of that aggregates are much less active than monomers. Pcs are usually quite strongly aggregating because the planar molecular geometry admits significant $\pi - \pi$ interactions between molecules, hence stabilizing columnar aggregates. Spectroscopic techniques can often be employed to analyze the nature and degree of aggregation. In Pcs, the UV-vis absorption spectrum is dominated by the Q-band arising from $\pi - \pi^*$ transitions. Usually, one can assign individual peaks within the Q-band to either free molecules or molecules contained within aggregates, and hence the degree of aggregation within the solution can be inferred from the respective peak intensities. In general, the aggregate peak is blue-shifted with respect to the monomer peak because of the cooperative interaction between transition dipole moments on molecules within an aggregate. Quantitative predictions for the shift can be obtained using the molecular exciton approximation. In Pc aggregates, this approximation is compromised by the presence of the strong $\pi - \pi$ interactions, but the general trends remain valid. In this regard, we present in this article the results of study describing the aggregation of copper (II) 4, 4', 4'', 4'''- Tetrasulfonated phthalocyanine anion ($\text{Cu}(\text{tsPc})^{4-}$) (scheme1), in the presence of calf thymus DNA (Ct-DNA) at different concentrations and ionic strength effect using optical absorption spectroscopy and demonstrates the aggregation behavior of this phthalocyanine on basis of their molecular structure and intermolecular forces.

2. Methods

copper (II) 4, 4', 4'', 4'''- Tetrasulfonated phthalocyanine tetrasodium salt was purchased from Alderich. They were used without further purification. Calf thymus DNA was purchased from Sigma to prepare DNA stock solution, 2mg of DNA was dissolved in 1mL of phosphate buffer the day before the experiment and stored at 4 °C. The titration was made by addition of the DNA stock solution into a 1cm cuvette containing the phthalocyanine solution of appropriate concentration. The effect of ionic strength was investigated by titration of phthalocyanine solution of appropriate concentration in 1 cm cuvette by NaCl stock solution. The absorption spectra were recorded on Cary 100 model scan UV-vis spectrophotometer in the region from 200 to 800 nm.

3. Result and discussion

In Figure 1 we show absorption spectra in the range 500 nm $\leq \lambda \leq$ 800 nm for pure-water solutions of ($\text{Cu}(\text{tsPc})^{4-}$) with concentrations in the range 10^{-6} to 10^{-4} M. The maximum of the Soret band appears at 610 nm. The Soret band maximum of $\text{Cu}(\text{tsPc})^{4-}$ obeys Beer's law over an extended concentration range between 6×10^{-6} to 8.9×10^{-4} M in phosphate buffer 7.5 mM, pH 7.2. From this observation we can conclude that $\text{Cu}(\text{tsPc})^{4-}$ does not show concentration dependent aggregation in this concentration range. The effect of NaCl on absorption spectrum of $\text{Cu}(\text{tsPc})^{4-}$ (6.6×10^{-6} M) in water is shown in figure 2. As the concentration of NaCl increases, the absorbance at all of spectral regions has been decreased and the Soret band becomes very broad with a blue shift. Although, the absorption spectrum of $\text{Cu}(\text{tsPc})^{4-}$ shows a significant electrolyte effect, but no new band appears even in high salt concentration. This result means that $\text{Cu}(\text{tsPc})^{4-}$ does not form well-defined aggregates (i.e. H or J types) in the presence of a salt. Thus, these spectral changes can be attributed to the formation of extended ill- defined aggregates. Figure 3 shows a representative titration spectrum of $\text{Cu}(\text{tsPc})^{4-}$ upon increasing concentration of DNA. In both

cases, bathochromicity shift of $\Delta \lambda \leq 3$ nm and high hypochromism ($H \geq 30\%$) in the Soret band. The value for hypochromicity suggests that the interaction was via both the intercalative type of binding and external binding.

4. Conclusion

The Soret band maximum of $\text{Cu}(\text{tsPc})^{4+}$ obeys Beer's law over an extended concentration range between 6×10^{-6} to 8.9×10^{-4} M, which represents that this phthalocyanine does not show concentration dependent aggregation. The effect of salt on absorption spectrum of $\text{Cu}(\text{tsPc})^{4+}$ does not induce the formation of well-defined aggregation (i.e. H or J types). Binding studies of $\text{Cu}(\text{tsPc})^{4+}$ with DNA represent the formation $\text{Cu}(\text{tsPc})^{4+}$: DNA complex.

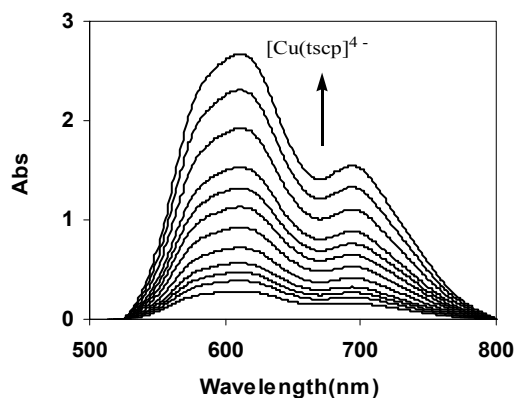
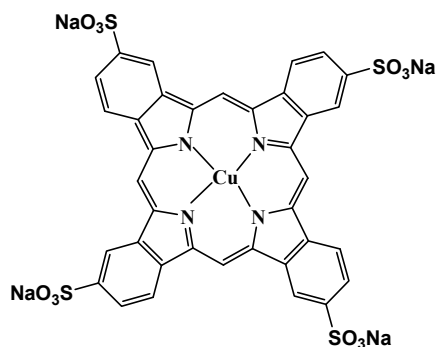


Fig.1. Absorption spectral changes of $\text{Cu}(\text{tsPc})^{4+}$ upon addition of concentration. The arrow shows the increasing of $\text{Cu}(\text{tsPc})^{4+}$ concentration.



Scheme 1: Chemical structure of phthalocyanine

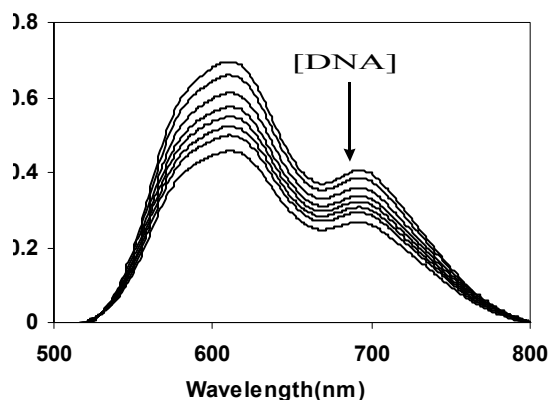


Fig.3. Absorption spectral changes of $\text{Cu}(\text{tsPc})^{4+}$ (6.9×10^{-5} M) upon addition of DNA (0 to 2.9×10^{-4} M). The arrow shows the increasing of DNA concentration.

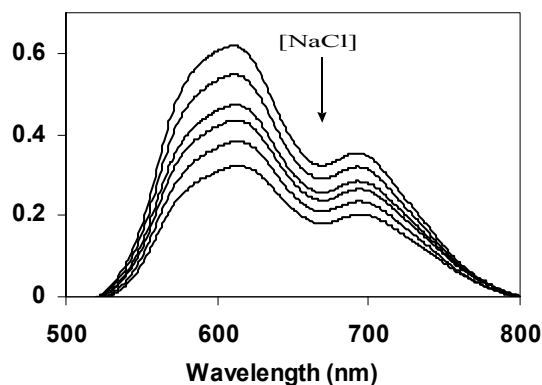


Fig.2. Absorption spectral changes of $\text{Cu}(\text{tsPc})^{4+}$ (6.9×10^{-5} M) upon addition of NaCl (0 to 2 M). The arrow shows the increasing of NaCl concentration.

References

- [1] G. D. Luca, A. Romeo, and L. M. Scolaro, J. Phys. Chem. B. 110, 7309-7315 (2006).
- [2] H. Abramczyk, I. Szymczyk, Journal of Molecular Liquids. 110, 51-56 (2004).
- [3] K. Kano, H. Minazono, T. Kitac and S. Negi, J. Phys. Chem. 101, 6118-6125 (1997)



Spectral studies of the interaction of rhodamine dyes with ct- DNA

H. Dezhampanah^a, A. Ghanadzadeh^b and *M. Aghazadeh.

Department of Chemistry, University of Guilan, Rasht, Iran.

Mehrnaz_Aghazadeh@yahoo.com

1. Introduction

The ability to understand the interaction of small molecules with specific DNA sequences is fundamental in any attempt to control gene expression. In designing novel chemotherapeutic agents, one of the major strategies is to develop novel DNA repair. Systematic modifications of clinically effective chemotherapeutic agents have the potential for positively influencing their activity and delivery. Fundamental to this approach is the rigorous description of the interactions of known DNA binding agents with their macromolecular target. Therefore, the detailed study of the selectivity of interaction between organic compounds and nucleic acids, along with the study of the selectivity of interaction between organic compounds and nucleic acids, along with the study of the influence of such interaction on the relaxation processes in chromophores, is important for modern molecular biology and biophysics. The effect of various chemical agents and radiations on nucleic acids has been studied for many years. Special attention has been paid to organic dyes that can bind to polyanions these substances belong to various chemical classes. On basis of this importance, in the present study, the interaction between rhodamine 6G (R6G) and rhodamine B (RB) (scheme1), with calf thymus DNA (Ct-DNA) at different concentrations and ionic strength effect using optical absorption spectroscopy and demonstrates the interaction behavior of these dyes on basis of their molecular structure and intermolecular forces.

2. Methods

Rhodamine dyes were obtained from Merck(pro-analysis) used without further purification. All experiments were run in phosphate buffer (consisted of 2.5 mM NaH₂PO₄ + 5 mM Na₂HPO₄ dissolved in Milli-Q quality water) at pH 7.2. Ct- DNA was purchased from Sigma, to prepare DNA stock solution; 2mg of DNA was dissolved in 1mL of phosphate buffer the day before the experiment and stored at 4 °C. The concentration of DNA from its optical absorption using molar absorption coefficient. The titration was made by addition of the DNA stock solution into a 1cm cuvette containing the rhodamine dyes solution of appropriate concentration. The effect of ionic strength was investigated by titration of rhodamine solution of appropriate concentration in 1 cm cuvette by NaCl stock solution. The absorption spectra were recorded on Cary 2100 model scan UV-vis spectrophotometer in the region from 200 to 800 nm.

3. Result and discussion

The optical absorption spectrum of both dyes shows a maximum band 525 nm for R6G and a maximum 552 nm for RB respectively. Beer's law experiments were carried out for both two dyes in homogeneous aqueous solutions at pH 7.2 and the molar absorptivity of these bands were calculated. The band maximum of both dye obeys Beer's law over an extended concentration range between 5 to 40 μ M for R6G and 4 to 20 μ M for RB in phosphate buffer 7.5 mM, pH 7.2. From this observation we can conclude that dyes do not show concentration dependent aggregation in this concentration range. The effect of NaCl on absorption spectrum of R6G (6.6×10^{-5} M) in water is shown in figure 1. As the concentration of NaCl increases, the absorbance at all of spectral regions has been decreased and the 525nm becomes very broad with a blue shift. Although, the absorption spectrum of R6G shows a significant electrolyte effect, but no new band appears even in high salt concentration. This result means that R6G does not form well-defined aggregates (i.e. H or J types) in the presence of a salt [2]. Thus, these spectral changes can be attributed to the formation of extended ill- defined aggregates. At the same result was obtained for the RB dye. A spectral change of R6G and RB with addition of DNA shown in figure 2 and 3. They exhibited the hypochromism on the incremental addition DNA with varying degrees of bathochromic shift, indicating interaction of dye with DNA. The percentage hypochromicity of maximum band of two dyes upon binding to DNA was found to be 30%. Red shift was 5 nm. From above mentioned changes (large hypochromicity and moderate red shift), we considered the interaction R6G and RB dyes with DNA were both out-binding modes.

Conclusion: The band maximum of R6G and RB obey Beer's law over an extended concentration range, which represents that these dyes do not show concentration dependent aggregation. The effect of salt on absorption spectrum of R6G and RB do not

induce the formation of well-defined aggregation (i.e. H or J types). Binding studies of R6G and RB with DNA suggest that the interaction were both out-binding modes.

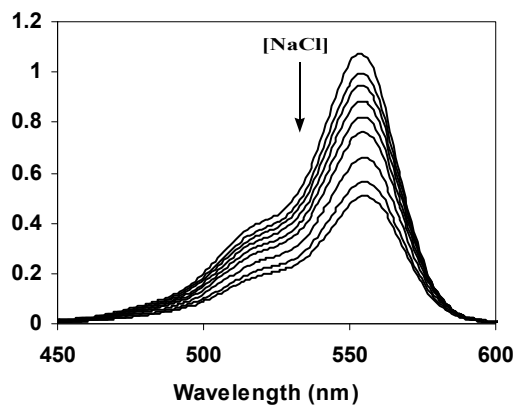
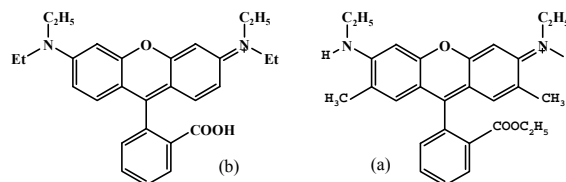


Fig. 1. Absorption spectral changes of R6G (1.9×10^{-5} M) upon addition of NaCl (0 to 1.5M). The arrow shows the increasing of NaCl concentration.



Scheme 1: Molecular structure of the (a) R6G and (b) RB

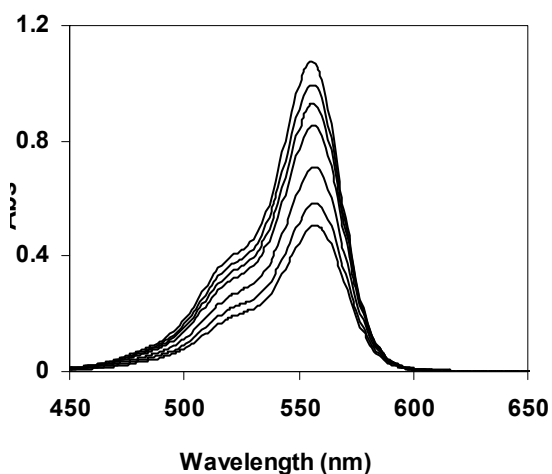


Fig. 3. Absorption spectral changes of RB (6.9×10^{-6} M) upon addition of DNA (0 to 2.9×10^{-4} M). The arrow shows the increasing of DNA concentration.

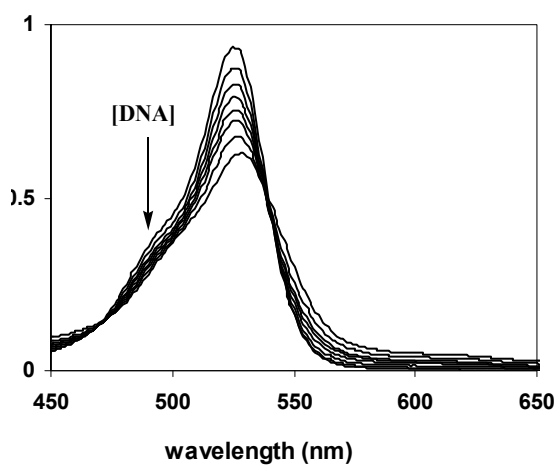


Fig. 2. Absorption spectral changes of R6G (1.9×10^{-5} M) upon addition of DNA (0 to 2.9×10^{-4} M). The arrow shows the increasing of DNA concentration.

References

- [1] J. Kang, H. Wu, X. Lu, Y. Wang and L. Zhou, *Spectrochimica Acta Part A* 61, 2041-2047 (2005).
- [2] K. Kano, H. Minanizono, T. Kitac and S. Negi, *J. Phys. Chem.* ; 101, 6118 - 6125 (1997).
- [3] G. D. Luca, A. Romeo, and L.M. Scolaro. *J. Phys. Chem. B* 109, 7149-7158 (2005).

**Intramolecular hydrogen bonding and vibrational spectra of 2,2,6,6-tetramethyl-3,5-heptanedione**M. Vakili ^{a,*}, H. Miremad ^b, S. Salemi ^a, A-R. Nekoei ^c^a Department of Chemistry, Sabzevar Tarbiat Moallem University, IranE-mail: ^{*} mvakili@yahoo.com^b School of Chemistry, Damghan University of Basic Sciences, Damghan, 36715-364, Iran^c Department of Chemistry, Shiraz University of Technology, Shiraz, 71555-313, Iran

Keywords: 2,2,6,6-tetramethyl-3,5-heptanedione; β -dicarbonyl; Conformational analysis, Vibrational assignment; Intramolecular hydrogen bond; Density Functional Theory.

1. Introduction

It is well known that the *cis*-enol form of a β -dicarbonyl is characterized by an intramolecular hydrogen bond. Any factor which affects on the electronic properties of the chelated ring can change Intramolecular hydrogen bond strength (IHB) and the tautomerization equilibrium [1-4]. To the best of our knowledge structure and vibrational spectra of 2,2,6,6-tetramethyl-3,5-heptanedione (TMHD), theoretically or experimentally, were not described earlier. The aim of the present paper is to predict intramolecular hydrogen bond strength and vibrational spectra of TMHD by means of density functional theory (DFT) levels.

2. Experimental and method of analysis

TMHD compound purchased from Aldrich chemical company. D₂-TMHD was prepared by mixing the TMHD with D₂O. The FT-IR, FT-Raman and Far-IR spectra were obtained on a Bomem MB-154 and Thermo Nicolet NEXUS 870 FT-IR spectrometers. All calculations were performed using Gaussian 03W package program, B3LYP/6-311++G** and MP2/6-31G** levels of theory for optimizing all possible *cis*-enol conformations and B3LYP/6-311G** level for calculating vibrational frequencies of the stable *cis*-enol forms.

3. Results and Discussion

Among 32 possible enol conformers of TMHD, only four conformers have the chelated structure. These four conformers and the atom numbering are shown in Fig.1. The B3LYP and MP2 calculations show that only two of these conformers are stable. The III and IV conformations are not stable, and under optimization turn to I and II. The energy difference between these stable chelated enol forms is 0.15-0.53 kcal/mol, calculated at B3LYP/6-311++G** and MP2/6-31G**. So, from the theoretical point of view, the coexisting of both *cis*-enol conformers (I and II), at least in the gas phase, is suggested. Molecular geometry, intramolecular hydrogen bond energy, E_{HB} (the energy difference between the chelated *cis*-enol and non-chelated *trans*-enol rotamers), and experimental vibrational frequencies related to IHB of TMHD are given in Tables 1 and 2. Comparing coordinates for TMHD and AA shows that upon substitution of *t*-But groups in the β positions and because of the more steric effects of these groups, the bond angles O1C2C8 and O5C4C21 in TMHD are smaller than those of acetylacetone (AA). This fact decreases the O...O distance and increases the IHB of TMHD in comparison with AA (Table 1).

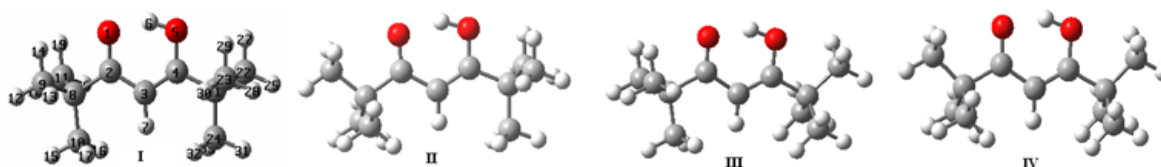


Fig.1. Numbering and Possible chelated *cis*-enol tautomers of TMHD.

The averaged values of RO...O and Θ HO for the chelated rings of Benzoylacetone (BA), AA and TMHD, E_{HB} and some spectroscopic properties, related to their IHB, are listed in Table 2. After comparing these data, the following trend in hydrogen bond strength is concluded: TMHD>BA>AA .

The IR and Raman spectra of TMHD and D₂-TMHD were also clearly assigned. Comparing the calculated and experimental band frequencies and intensities suggest coexisting of two stable *cis*-enol conformers in comparable proportions in the sample. The FT-IR spectrum of TMHD shows a very broad absorption that centered at about 2634 cm⁻¹, for ν_{OH} . By comparison of this

frequency with those of AA and BA, it is concluded that the trend of IHB strength for these molecules is same as above. The deconvoluted IR spectra of TMHD in 1600 cm^{-1} region indicates existing of three bands in this region with comparable intensities (Fig.2). Considering the calculated results, the first two bands which occur at 1614 and 1597 cm^{-1} , are attributed to

Table1. The geometrical parameters of TMHD and AA calculated at the B3LYP/6-311++G** level of theory.

Bond distances (Å)	TMHD (I)	TMHD (II)	AA (I)	AA (II)
O...O	2.497	2.518	2.529	2.540
C ₄ —O ₅	1.320	1.310	1.320	1.320
C ₂ —O ₁	1.250	1.240	1.240	1.240
O ₅ —H ₆	1.010	1.000	1.000	1.000
C ₃ —C ₄	1.370	1.370	1.370	1.370
C ₂ —C ₃	1.440	1.440	1.440	1.440
Bond angles (°)				
O ₁ H ₆ O ₅	150.40	150.30	149.19	148.52
O ₁ C ₂ C ₈	117.40	119.63	118.87	119.82
O ₅ C ₄ C ₂₁	113.45	113.22	113.98	113.78
E _{HB} ^a	17.8(18.1)	18(17.4)		

^a the calculated values at the MP2/6-31G** are given in parenthesis

Table2. Comparing several properties related to the hydrogen bond strength for AA, BA and TMHD.

	TMHD	AA ^b	BA
δOH	16.27	15.4	16.2
νOH	2634	2750	2650
γOH	964	952	957
R O...O ^a	2.508	2.544	2.516
θOHO^a	150.35	148.5	149.7
E _{HB} ^a	17.9	15.87	16.07

Bond lengths in Å and bond angle in degrees; δ , proton chemical shift in ppm; ν , and γ are stretching and out-of-plane bending frequencies in cm^{-1} .

^a calculated at the B3LYP/6-311++G**

^b Data from [3].

the $\nu_s\text{C}=\text{C}=\text{O}+\delta\text{OH}$ movement in I and II conformations, respectively. The third band at 1584 cm^{-1} with strong IR and Raman intensities, are assigned to the $\nu_s\text{C}=\text{C}=\text{O}+\delta\text{OH}$ for the both conformers. The relatively strong and broad IR bands at 1363 and 1345 cm^{-1} are attributed to the δOH modes in I and II conformers, respectively. This vibrational mode is strongly coupled to some other motions like $\nu_s\text{C}=\text{C}=\text{O}$ and $\delta_s\text{CH}_3$. The relatively weak and broad band at 964 cm^{-1} in the IR spectrum of TMHD is assigned to the, γOH , out-of-plane mode of OH bending. The corresponding bands of AA and BA appear at 952 and 957 cm^{-1} , which suggests that the intramolecular hydrogen bond in TMHD is considerably stronger than those in AA and BA.

4. Conclusion

The theoretical frequency calculations and the results of experimental IR and Raman studies suggest that both stable chelated conformers of TMHD coexist in the sample. Also, comparison of the calculated geometrical parameters, NMR results and some vibrational frequencies (like $\gamma\text{OH}/\text{OD}$ and $\nu\text{OH}/\text{OD}$) confirm that substitution of t-But and/or Ph groups with the CH_3 groups of AA increase the strength of the intramolecular hydrogen bond.

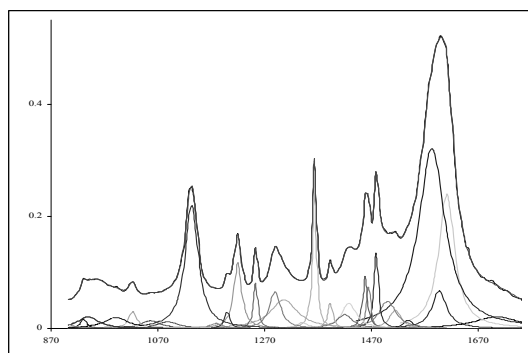


Fig.2. The deconvoluted IR spectra of CCl_4 solution of TMHD in the 1700-900 cm^{-1} region.

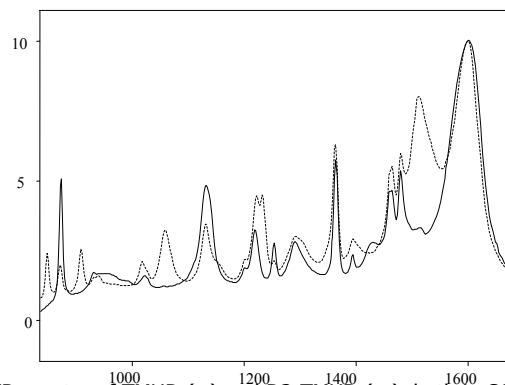


Fig.3. The IR spectra of TMHD (—) and D2-TMHD (···), both in CCl_4 .

References

- [1] S.F. Tayyari, F. Milani-Nejad, Spectrochim. Acta 56A (2000) 2679.
- [2] S.F. Tayyari, M. Vakili, A.R. Nekoei, H. Rahemi, Y.A. Wang, Spectrochim. Acta 66A (2007) 626.
- [3] S.F. Tayyari, J.S. Emampour, M. Vakili, A.R. Nekoei, H. Eshghi, S. Salemi, M. Hassanpour, J. Mol. Struct. 794 (2006) 204.
- [4] S.F. Tayyari, A.R. Nekoei, M. Vakili, Y.A. Wang, J. Theor. Comp. Chem. 5 (2006) 647.



Study of Two Photon Time-Resolved Optogalvanic Signals of Neon in the 600-630 nm Region

F. Abyar, F. Fathi, H. Farrokhpour, M. Tabrizchi and R. Omidyan

Isfahan University of Technology, Isfahan, Iran, 84156-83111

E-mail: f.abyarfirouzabady@ch.iut.ac.ir

Keywords: Neon, Two Photon Transition, Optogalvanic Spectroscopy, Dye Laser, Nd:YAG laser

1. Introduction

Laser optogalvanic spectroscopy is a very useful tool in the field of atomic and molecular spectroscopy. The optogalvanic effect occurs due to the variation of impedance in a discharge tube when illuminated by a laser resonant to an atomic or molecular transition of the element within the discharge [1]. The variation of impedance occurs because of the ionization perturbation in the plasma medium. Many theoretical and analytical models, based on the experimental observation, has been developed to understand the atomic and collisional processes in plasma [2,3]. Omidyan et al. have been recorded eleven two-photon transitions originating from the $2p^53s[3/2]_2$, $2p^53s'[1/2]_0$ and $2p^53s'[1/2]_1$ to $2p^54d$ configuration in the visible region 570-630 nm region [4]. Also, they have investigated the time behavior of the optogalvanic signal of four two photon transitions originating from $2p^53s[3/2]_2$ to $2p^54d'[3/2]_1$, $2p^54d'[3/2]_2$, $2p^54d'[3/2]_3$ and $2p^54d'[5/2]_2$ over a range of discharge current to obtain the collisional decay rates of the upper level [5].

In this work, we focus on the temporal evolution of the two-photon optogalvanic signals in the 600-630 nm region which have not been investigated in our previous work [5]. We used the theoretical model proposed by Ben-Amar et al [3] to obtain parameters influencing the decay rates of the upper states involved in the two photon transitions.

2. Experimental

The experimental arrangement consisted of a dye laser (Quatel TDL-90, France) pumped by a Nd:YAG laser (Quatel model YG-80 France), and a commercial Ag-Ne hollow cathode lamp. The dye laser produced a 100-200 $\mu\text{J}/\text{pulse}$ with a linewidth of 0.08 cm^{-1} which corresponds to 3 pm at 600 nm. An adjustable DC power supply (200-600 volt) were used to create the discharge in the hollow cathode lamp. The discharge current was controlled by a current limiting load resistor (50 k Ω). A ballast resistor (22k Ω) was used to read the discharge current. The laser beam illuminated the hollow plasma through the window on top of the lamp. The discharge current was adjusted between 1.8-9.8 mA. The laser was tuned to each selected resonant transition. Due to absorption of laser in the plasma channel, the voltage across the hollow cathode lamp varied. The voltage variation was coupled through a 0.01 μF capacitor and then fed to a digital oscilloscope (Pico scope ADC 212,UK) and recorded as a function of time.

3. Results and discussions

The time behavior of the optogalvanic signal of the ($2p^53s[3/2]_2 \rightarrow 2p^55s'[1/2]_0$) transition at 613.985 nm was recorded at different discharge currents from 1.8 to 9.8 mA. This is shown in Fig. 1, which is typically similar to those reported in our previous work [5]. The signal consists of a fast rising peak followed by decay to the base. The difference is a small negative overshoot in some cases depending on the discharge current.

As shown in Fig. 1a the decay rates of the signal increase with the current while the maximum of the signal shifts to the shorter time. This behavior is similar to that of one-photon transitions but it is completely different from the behavior reported in our previous work [5] for the transitions from $2p^53s[3/2]_2$ to $2p^54d$ configuration states in which the transition decay rate decreases with current and the maximum remains constant in time. The reason for this discrepancy is not clear.

For the range of 5.8 to 9.8 mA, the decay rate is not much influenced by the discharge current (Fig. 1b). This is due to saturation of the optogalvanic signal at high discharge current (5.8-9.8 mA).

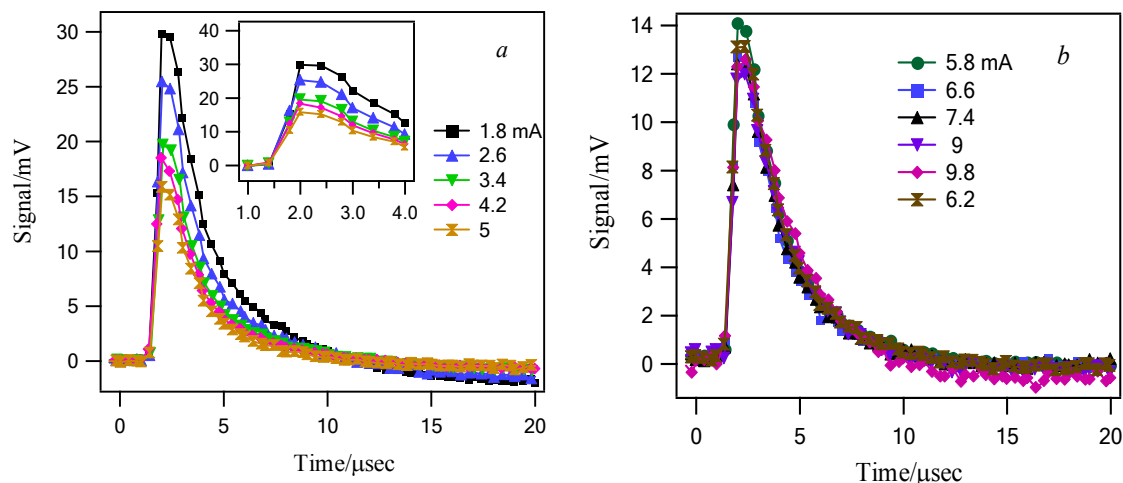


Fig.1. Two-photon time resolved optogalvanic signals of neon recorded at 613.985 nm, correspond to $2p^53s[3/2]_2 \rightarrow 2p^55s'[1/2]_0$ transition. The inset shows the expansion of the positive part of the optogalvanic signals in the range of 1-4 μsec .

The time resolved optogalvanic signals were fitted to the Ben-Amar theoretical model [3] to obtain the decay rates of the upper level at different discharge current. Figure 2 shows the decay rates, obtained from the fitting, versus the current for the ($2p^53s[3/2]_2 \rightarrow 2p^55s'[1/2]_0$) transition. As expected the decay rates increase linearly with current.

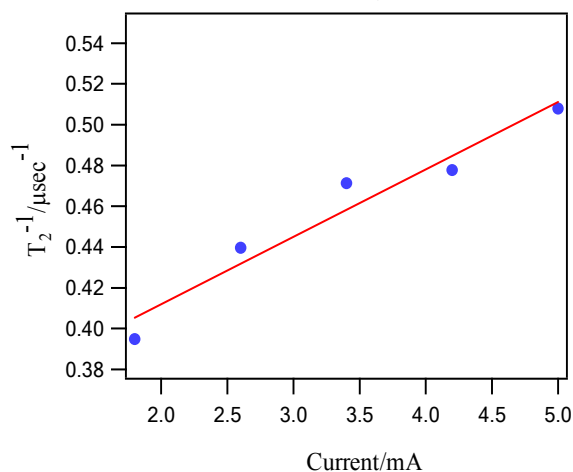


Fig.2. plot of the decay rates of $2p^55s'[1/2]_0$ versus discharge current for ($2p^53s[3/2]_2 \rightarrow 2p^55s'[1/2]_0$) transition. The solid line shows the linear fitting.

References

- [1] K. Alnama, J.H. Fillion and D. Gauyacq, J. Quant. Spectrosc. Radiat. Transfer 105 (2007) 39.
- [2] D.K. Doughly and J.E. Lawler, Phys. Rev. A. 28 (1983) 773.
- [3] A. Ben-Amar, G. Erz and R. Shuker, J. Appl. Phys. 54, 3688 (1983).
- [4] R. Omidyan, F. Fathi, H. Farrokhpour and M. Tabrizchi, Opt. Commun. 281 (2008) 5555.
- [5] R. Omidyan, H. Farrokhpour and M. Tabrizchi, Opt. Commun. 282 (2009) 4552.

NO⁺ as Reactant Ion in Ion Mobility Spectrometry

M. Darzi, M. Tabrizchi *

Department of Chemistry, Isfahan University of Technology, Isfahan, 84156-83111, Iran

Email: m-tabriz@cc.iut.ac.ir

Key words: NO⁺, Ion Mobility Spectrometry, Charge Transfer, Proton Affinity**1. Introduction**

In ion mobility spectrometry (IMS), an ion packet is moved in a gas by constantly applying an electric field to separate ions of different size. IMS is an analytical method that is used to investigate the composition of gas mixtures [1]. It is a powerful tool for the study of molecular conformations, the separation of mass isomers, and the analysis of complex mixtures [2]. IMS is similar to TOF mass spectrometry, except that it operates under atmospheric pressure. The sample is ionized using atmospheric pressure chemical ionization techniques such as corona discharge. The ions are then moved in an inert gas under a constant electric field.

The initial ions generated by the corona discharge are mostly the hydronium ions, H₃O⁺. In the presence of an analyte with proton affinity higher than that of water, protonated molecules (MH⁺) are formed via proton transfer reaction.



If the concentration of the molecule is high enough, the reaction proceeds further to produce proton-bound dimers (MHM⁺).



In this work we tried to produce NO⁺ instead of H₃O⁺ as reactant ion and compare the product ions with those produced via proton transfer reaction.

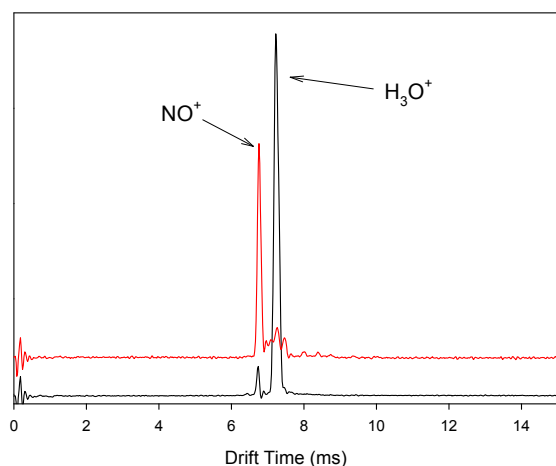


Fig.1. Production of NO⁺ ions when NO_x is introduced to the ionization region.

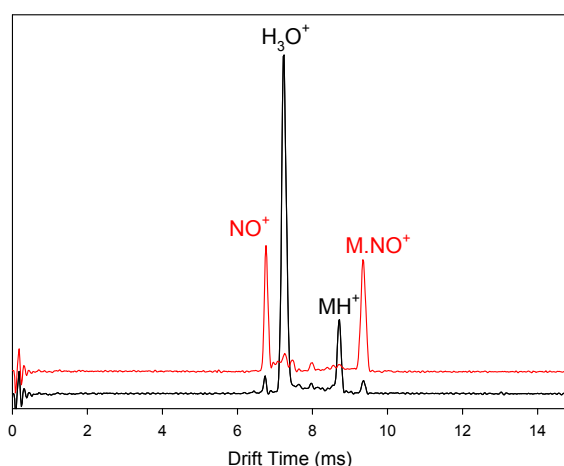
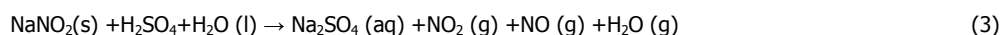


Fig.2. Ion mobility spectra of 1,2,4-trimethyl benzene With both H₃O⁺ and NO⁺ reactant ion

2. Experimental

The ion mobility spectrometer used in this study was constructed in our laboratory at Isfahan University of technology. A continuous corona discharge was used to produce reactant ions. In order to produce the NO⁺ ions, a mixture of NO and NO₂ was introduced into the discharge region. NO_x was produced via the following reaction.





3. Results and discussion

The production of NO^+ ion is presented in Fig.1. Upon introducing NO_x the H_3O^+ peak disappeared and the NO^+ peak raised. The reaction of NO^+ with some test compounds such 1,2,4,trimethyl benzene and propyl benzene was studied by introducing the sample into the reaction region. The ion mobility spectra of 1,2,4,trimethyl benzene both with H_3O^+ and NO^+ reactant ions are shown in Fig.2. As seen the product ions are different. This is well known that the product ion in the case of H_3O^+ is MH^+ . However, for the case of reaction with NO^+ , there are several possibilities, (a) charge transfer, (b) association reaction and (c) hydride transfer [3].



The product ion in the case of H_3O^+ is MH^+ . As the mass and mobility of M^+ and $(\text{M}-\text{H})^+$ is expected to be close to the MH^+ ion, if those ions are formed their corresponding peak would have appeared close to the MH^+ peak. However, comparing the drift times shows that the product ion produced by the NO^+ reactant is heavier than that produced by the H_3O^+ . Hence, the charge transfer and the hydride transfer reactions are rule out in this case and the product ion is most probably $\text{M} \cdot \text{NO}^+$. Similar results were observed for other compounds. For some compounds the M^+ peak was also observed.

The key parameter for determining the reactivity of H_3O^+ is the proton affinity (PA) of the compound. Having PA larger than H_2O ($=691 \text{ kJ mol}^{-1}$) exhibits a rapid proton transfer reaction. However, for low proton affinity the reaction is not easy. Hence compounds with low proton affinity are not ionized with H_3O^+ reactant ion. For NO^+ , the essential parameter is ionization energy (IE). If it is smaller than IE of NO ($=9.26 \text{ eV}$) then charge transfer occurs. Otherwise, $\text{M} \cdot \text{NO}^+$ or $(\text{M}-\text{H})^+$ may be produced. Hence the reactivity of NO^+ is higher than that of H_3O^+ . Therefore, those compounds with low proton affinity those are not ionized with H_3O^+ may be ionized and detected using NO^+ reactant ion.

4. Conclusions

It was shown that NO^+ reactant ion in IMS can be easily formed via introducing NO_x into the ionization region. Samples react rapidly with the NO^+ ion to produce either M^+ or $\text{M} \cdot \text{NO}^+$. Because of more reactivity, using NO^+ extends the application of IMS in detection of a wider range of compounds.

References

- [1] G.A.Eiceman; Z. Karpas; Ion Mobility Spectrometry, 2nd ed.; CRC Press: Boca Raton,(2005).
- [2] V.V. Laiko; J. Am. Soc. Mass Spectrom, 17, (2006) 500.
- [3] P. Spanel and D. smith, International Journal of Mass Spectroscopy, 181, (1998)

**The comparison between serum transferrin and HSA upon interaction with cyclophosphamide:****A fluorescence spectroscopy investigation**S. Hamed-Akbari Tousi^{1*}, M.R. Saberi² and J. Chamani¹

Department of Biology, Faculty of Science, Islamic Azad University Mashhad Branch, Mashhad, Iran,

E-mail: tusi1063@yahoo.com

Medical Chemistry Division, School of Pharmacy, University Complex, Mashhad, Iran

Keywords: HSA, Holo-transferrin, Cyclophosphamide, Fluorescence Spectroscopy**1.Introduction**

Human serum albumin (HSA) as a kind of main carrier protein that contains 585 amino acids with known sequences and a molecular weight of 66.5 kD [1,2]. HSA is most important and abundant constituent of blood plasma and serves as a protein storage component [3] and has a high affinity to an extra ordinarily diverse range of materials such as drugs and metal ions [4]. Human serum transferrin (hTf) is a single-chain glycoprotein containing 679 amino acids with molecular mass of 80 kD present in plasma of a concentration of about 35 mM [5] and transferring in human serum is only 30% iron-saturated [6]. Cyclophosphamide is a white crystalline powder with the molecular formula $C_7H_{15}Cl_2N_2O_2P \cdot H_2O$. Cyclophosphamide is soluble in water, saline or ethanol. Cyclophosphamide is used to treat cancer. It is a synthetic anti-neoplastic drug chemically related to the nitrogen mustards. We want to investigate the effect of cyclophosphamide on HSA and hTf and compare them with each other as a view point of binding affinity and number of binding site.

2.Materials and Methods

HSA, hTf and cyclophosphamide are obtained from sigma chemical company. All measurements were carried out at room temperature in phosphate buffer solution (pH 7.4) and value concentration of drugs was injected to 2 ml protein solution. All value measurement was done by F-2500 spectrophotometer (Hitachi, Japan)

3.Results and discussion

The fluorescence quenching of HSA and hTf induced by cyclophosphamide weekend regularly with increasing of cyclophosphamide concentration. It is noted that complex were formed between HSA and hTf with cyclophosphamide. In HSA the emission wavelength blue-shift was observed that indicate the fluorophor are exposed to hydrophobic region but in hTf the red-shift was observed that show the fluorophar are exposed to polar region [7].

Stern–Volmer plots of HSA and hTf with cyclophosphamide showed in Fig 1. A and B respectively. HSA and hTf have two different K_{sv} which are $K_{sv1} = 8.6 \times 10^8 \text{ M}^{-1}$, $K_{sv2} = 6.34 \times 10^8 \text{ M}^{-1}$ and $K_{sv1} = 6.08 \times 10^7 \text{ M}^{-1}$, $K_{sv2} = 4.7 \times 10^7 \text{ M}^{-1}$ respectively. These indicated the complex between HSA and cyclophosphamide was formed more than the other.

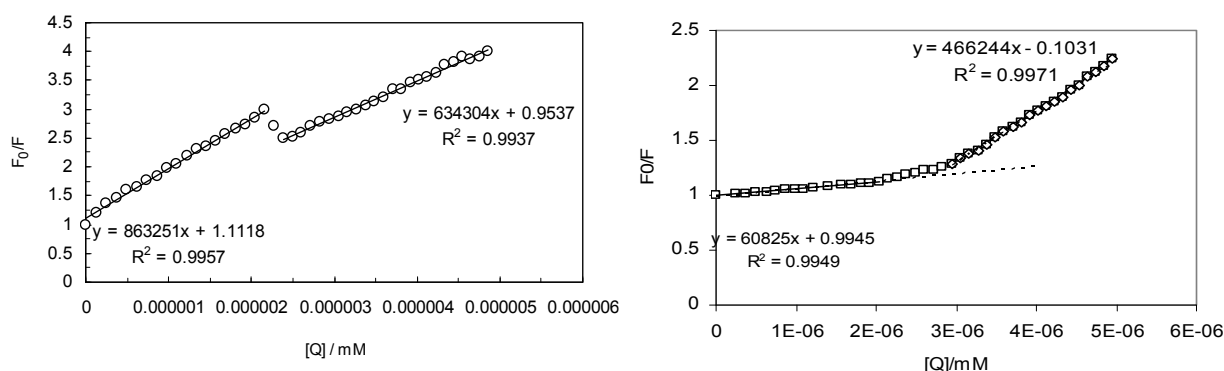


Fig.1. Stern – Volmer for the steady state Fluorescence quenching of HSA by cyclophosphamide. (B) Stern– Volmer for the steady state fluorescence quenching of hTf by cyclophosphamide. pH=7.4, 50 mM phosphate buffer.

Therefore, n values for HSA and hTf are 0.7, 0.8 and 0.4, 1.2 respectively. In Hill plots we obtained two series of binding sites for both of proteins. Fig .3 shows that below the 6.14×10^{-7} concentration of cyclophosphamide just tryptophan play an



important role in the cyclophosphamide-HSA interaction and upper this concentration, both of tryptophan and tyrosine are important in complex formation. This result was obtained for hTf as similarly.

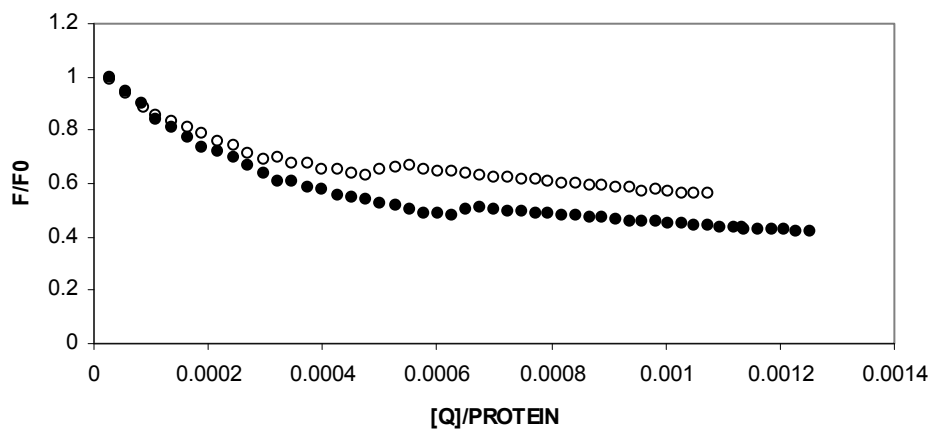


Fig. 2. Molar ratio plot of HSA in the presence of cyclophosphamide. pH 7.4, 50 mM phosphate buffer.

References

- [1] A. Dugiaczyk, S. W. Law, O.E. Dennison, *Proc. Nat. Acad. Sci. USA* **79** (1982) 71-75.
- [2] Y. Li, W.Y. He, Y. Dong, F. Sheng, Zh. Hu. *Bioorganic and Medical Chemistry* **14** (2006)1431-1436
- [3] Y.H. Pang, Li. Li. Yang, Sh.M. Shuang, Ch. Dong, M. Thompson. *Photochemistry and Photobiology A: Biology* **80** (2005)139-144
- [4] J. Yuan, Zh. Iv, Zh. Liu, Zh. Hu, G. Zoa. *Photochemistry and Photobiology* **191** (2007) 104-113.
- [5] J. Wally, P.J. Halbrooks, C. Vornrhein, M.A. Rould, S.J. Everse, A.B. Mason, S.K. Buchanan, *J. Biol. Chem.* **281** (2006) 24934-24944.
- [6] H. Du, J. Xiang, Y. Zhang, Y. Tang, G. Xu. *Inorganic Biochemistry* **102** (2008)146-149.
- [7] J.Q. Lu, F. Jing, T.Q. Sun, X.W. Zhou. *International Journal of Biological Macromolecule.* **40** (2007) 299-304.

Dynamic ¹H NMR study around the heteroaryl-carbon and nitrogen-carbon single bonds**(N[↔]CH-N And N[↔]C=CH) in a enaminoester involving a phenanthridine**

Shahin Nasiri, Sayyed Mostafa Habibi-Khorassani*, Malek Taher Maghsoodlou, Ali Ebrahimi and Sara sam-salari

Department of Chemistry, Faculty of Sciences, The University of Sistan and Baluchestan,

PO Box 98135-674, Zahedan, Iran

shahin_1980@ymail.com

Keywords: Enaminoesters, Restricted rotation, Dynamic ¹H NMR, Rotational energy barrier (ΔG^\ddagger).

1. Introduction

Enaminoesters, a class of versatile intermediates for the synthesis of the heterocycles, are common pharmacophores in a number of important medicinal agents. Many of their derivatives, including anticonvulsant, anti-inflammatory, and particularly the antibacterial fluorinated quinolone, possess a wide range of biological activities [1].

Molecules that contain a phenanthridine core have been found useful in many research areas [2] with applications as drugs [3], DNA targeting agents [4], dyes and molecular probes. Some of these compounds exhibited dynamic ¹H NMR effect that affords good information regarding the interchangeable process of rotational isomers that provide important kinetic data. We now describe this effect in reaction between dimethyl acetylenedicarboxylate **1** and 2-methyl indole **2** in the presence of phenanthridine **3** for generating a particular enaminoester **4**, synthesis of which has been reported previously

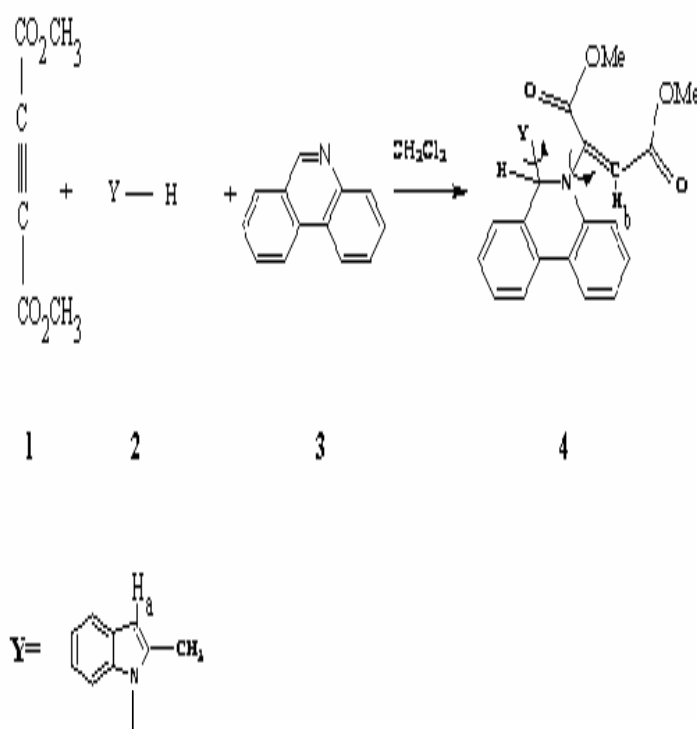


Fig.1. Synthesis of particular dimethyl-2-(6-(2-methylindol-1-yl)phenanthridine -5(6H)-yl) maleate **4** from reaction between **1** and **2** in the presence of phenanthridine involving two possible dynamic ¹H NMR effects around heteroaryl – carbon and nitrogen – carbon single bonds.

2. Result and discussion

The reaction of 2-methyl indole **2** with phenanthridine **3** in the presence of dimethyl acetylene dicarboxylate **1** proceeded at ambient temperature in dichloromethane and was completed after approximately 20 h. The structure of enaminoester **4** were deduced from elemental analysis, IR, ¹H NMR spectra. The ¹H NMR spectra of **4** exhibits signals for the methyl group of 2-methyl indol in heteroaryl – carbon single bond (N[↔]CH-N) at $\delta = 2.25$ ppm and a proton (H_a in enaminoester **4**, Fig. 1) and also a



proton (H_b in enaminester **4**, Fig. 1) in nitrogen – carbon single bond ($N \rightarrow C=CH$) at $\delta=6.30$ and $\delta=5.65$ ppm respectively. The presence of two separate signals for methyl group of 2-methyl indol in the 1H NMR spectra of **4** can be explained in term of restricted rotation around the heteroaryl – carbon single bond ($N \rightarrow CH-N$) in the enaminester. Effects of dynamic 1H NMR around the both heteroaryl – carbon and nitrogen – carbon single bonds will be followed according to the following discussion:

2.1. Dynamic effect for the enaminester **4** (Fig. 2, entry a and process I), as a result of restricted rotational process around the heteroaryl – Carbon single bond ($N \rightarrow CH-N$) at 246K

The 1H NMR spectrum for the enaminester **4** (Fig. 1) showed a resonance arising from methyl proton in heteroaryl – carbon single bond ($N \rightarrow CH-N$) that is appreciably broadened in comparison with a corresponding doublet that was measured at ambient temperature. This resonance coalescence occurred at approximately $-27^\circ C$ (246 K) which is relevant to restricted rotational process around the heteroaryl – carbon single bond ($N \rightarrow CH-N$). Investigation of 1H NMR spectrum of the enaminester **4** at variable temperature allowed us to calculate the rotational energy barrier (ΔG^\ddagger) for the restricted rotational process around heteroaryl – carbon (see Table 1). Using the expression $kc = n\Delta u/\sqrt{2}$, first – order rate constant was calculated for bond rotational process ($N \rightarrow CH-N$). Application of the absolute rate theory with a transmission coefficient (k) of one gave free Gibbs rotational energy barrier. These values are reported in Table 1. Effect of temperature on the rate constant was investigated on the basis of measurement of different chemical shifts in a series of other separate experiments. The results were too small so that the changes in first-order rate constant and Gibbs free energy barrier are negligible in comparison with the results obtained at $-27^\circ C$.

Table 1. Selected 1H chemical shifts (at 500/1) MHz , in ppm , Me_4Si) and activation parameters of enaminester **4** involving a 2-methyl indol, in $CDCl_3$, for rotation around the heteroaryl – carbon single bond in enaminester **4**, (a, I)

$T_{c \text{ methyl}}$ (K)	δ (ppm)	Δu (HZ)	ΔG^\ddagger (kJ/mol)	k_c (s ⁻¹)
246 k	2.86, 1.62	645.13	10.57 ± 1	1436.50

3. conclusions

For the first time, a series of separate dynamic 1H NMR effects are reported at different temperatures within a particular enaminester involving a phenanthridine namely dimethyl-2-(6-(2-methylindol-1-yl)phenanthridine -5(6H)-yl) maleate. These effects are attributed to restricted rotation around the heteroaryl – carbon and nitrogen – carbon single bonds ($N \rightarrow CH - N$ and $N \rightarrow C = CH$, respectively). Rotational energy barriers (ΔG^\ddagger) for their interconversion process of rotational isomers equals $(10.57, 10.56) \pm 1 kJ.mol^{-1}$, respectively.

References

- [1] Ke, Yi-Yin.; Li, Yu-Jin.; Jia, Jian-Hong.; Sheng, Wei-Jian.; Han, Liang.; Gao, Jian-Rong,. *Tetrahedron letters*. **2009**,1389-1391.
- [2] I, Juranovic.; Z, Meic.; I, Piantanida.; L. M Tumir. *Chem Commun (Camb)*. **2002**,13,1432-1433.
- [3] M. A, Lynch.; O, Duval.; A, Sukhanova.; J, Devy.; S. P, Mackay.; R. D, Waigh. *Bioorg Med Chem Lett*. **2001**,11,2643-2646.
- [4] J, Whittaker.; W. D, Mcfadyen.; B. C, Baguley.; W, Murray. *Anticancer Drug Des*. **2001**,16,81-89.



Secondary structure analysis of alpha-synuclein through the 3J-coupling constants and ¹H, ¹³C, ¹⁵N chemical shifts measurements

H. shaghaghi^a, M. F. Mulder^b, M. Tafazzoli^c

hoora.shaghaghi@gmail.com

^aPayame Noor University (PNU), Karaj, Iran

Groningen biomolecular sciences and biotechnology institute, Groningen, The Netherlands

^cDepartment of Chemistry, Sharif University of Technology, Tehran, Iran

Keywords: α-Synuclein, 3J-Coupling, Urea, TMAO, Secondary Structure.

1. Introduction

Purified α-synuclein (αS) structurally belongs to the family natively unfolded proteins [1] and a central role for αS fibrillization in Parkinson's disease is supported by the fact that fibrillar α-synuclein is a major component of Lewy bodies [2]. The secondary structure can be specified by backbone dihedral angles for consecutive residues and distances with the hydrogen bonding patterns. Magnitudes of scalar three-bond 3J_{HX} coupling constants [3] is related to dihedral angles subtended by the covalent bonds that connect the coupled nuclei H and X, where X denotes ¹H, ¹⁵N or ¹³C. For most amino acid residue types, six different J-couplings are available to characterize the backbone angle φ: 3J_{HNHα}, 3J_{HNCα}, 3J_{HNC'}, 3J_{C'H}, 3J_{C'CB}, and 3J_{C'C'}. Characterizing local structures of denatured proteins is crucial for understanding the protein folding and misfolding processes [4]. Osmolytes may fold unstructured proteins due to the osmophobic effect, a solvophobic thermodynamic force, arising from the unfavorable interaction between the osmolyte and the peptide backbone [5]. In this work, secondary structure of αS as a natively unfolded protein was studied. Three-bond J-couplings - 3J_{HNHα} and 3J_{C'C'} - for native, denatured, and folded by osmolytes α-synuclein were measured using heteronuclear 3D NMR spectra. HN, N and Co chemical shifts of three states of αS were also measured. Secondary structure of αS was studied by calculation J-couplings and chemical shifts differences in three states of αS.

2. Material and Methods

NMR sample of ¹⁵N&¹³C-labeled native αS with 200 μM αS concentration was prepared in 10mM Na₂HPO₄, 100mM NaCl, 0.02% NaN₃, and 7% D₂O at pH 7.4. To prepare a denatured sample of αS, urea was dissolved in the native sample of αS to have 6.8M solution and pH was also adjusted at 7.4. Trimethylamine-N-oxide (TMAO) with 1M concentration was selected as osmolyte. NMR data were collected on a Varian Inova 600 MHz at 10°C. Processing of NMR data were performed with NMRPipe software and also backbone resonance of 3D-HnCOco and HnHa were assigned with sparky software. 3J-couplings were calculated using ratio of cross peak to diagonal peak intensity as described in Ref. 6.

3. Results and discussion

To calculate 3J_{C'C'} and 3J_{HNHα} coupling constants, 15N-HSQC, 3D-HnCOco, and 3D-HNHA spectra were recorded and assigned for native, denatured, and folded by TMAO α-synuclein samples. All assignable cross and diagonal peaks were considered to extract the 3J_{C'C'} and 3J_{HNHα} except peaks that had overlap and peaks which belong to Aspartic acid (D) and Asparagine (N) residues and their neighbors. Figure 1 shows 15N-HSQC spectrum of native α-synuclein. As it can be observed, this spectrum belongs to unfolded proteins. Comparing 3J_{C'C'} and 3J_{HNHα} couplings constants values in three states of αS shows that N terminal of αS was mostly affected. So much so that, there was more than 0.15 Hz absolute deviation in 3J_{C'C'} coupling constants (denatured relative native αS) for M5,G7,S9,K10,A11 residues. C terminal residues illustrated some decrease in the 3J-coupling values. Except V77 and T92, it seems that the NAC section (61-95) was affected less. Comparison of NMR chemical shifts of three states of α-synuclein (denatured, native, native+TMAO) in carbonyl, amide proton, and amide nitrogen also demonstrated great changes in N terminal. As an example, the carbonyl chemical shifts changes in native and denatured α-synuclein are shown in figure 2. As it can be seen in this figure, there is an α-helix structure in the first of N terminal (4-31) and this confirms why there are large changes in 3J-couplings in N terminal of α-synuclein.

4. Conclusion

The secondary structure studies of α -synuclein was the main aim of present study. Although α S belongs to the family natively unfolded proteins, there is an α -helix structure in the first of N terminal (4-31). It seems that fibrillization of α S in Parkinson's disease may occur when this helical region converts to β -sheet structure. Therefore, not only 3J-couplings values of α S is basic data for molecular simulation investigations, but also understanding of folding and misfolding of α S is important in fibrillization in Parkinson's disease.

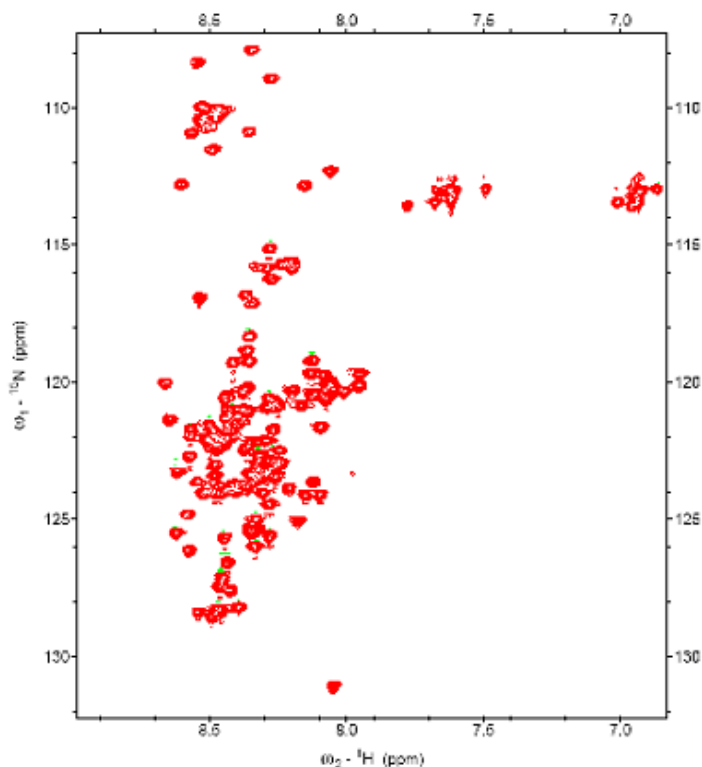


Fig.1. 15N-HSQC spectrum of native α -synuclein. 200 μ M α S 10mM Na_2HPO_4 , 100mM NaCl, 0.02% NaN₃, at pH 7.4.

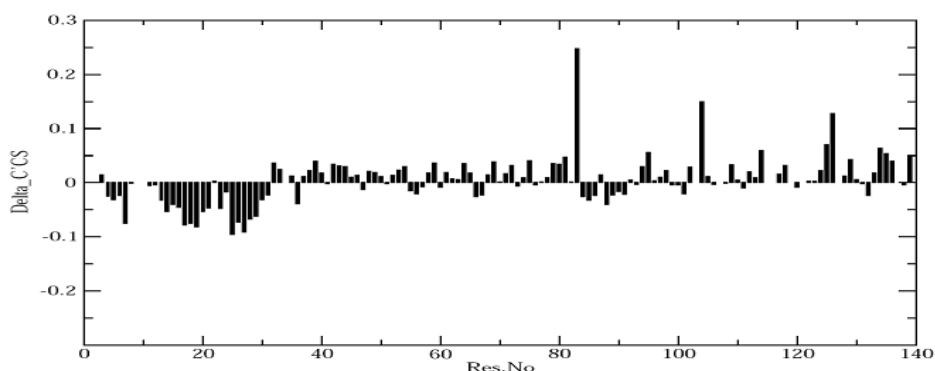


Fig.2. comparison of carbonyl chemical shifts (ppm) of two states of α -synuclein (denatured and native)

References

- [1] D. Eliezer, E. Kutluay, Jr. Bussell, G. Browne, J. Mol. Biol. 307 (2001) 1061.
- [2] M. G. Spillantini, et al. Nature 388 (1997) 839.
- [3] G. N. Ramachandran, et al. J. Mol. Biol. 7 (1963) 95 and M. Karplus, J. Chem. Phys. 30 (1959) 11.
- [4] K.A. Dill, D. Shortle, Annu. Rev. Biochem. 60 (1991) 795.
- [5] I. Baskakov, D. W. Bolen, J. Biol. Chem. 273 (1998) 4831.
- [6] G. W. Vuister, A. Bax, J. Am. Chem. Soc. 115 (1993) 7772.



Theoretical and spectroscopic studies on Thiophenolato Mercury (II) complexes

S. Laleh ^{a,*}, S. F. Tayyari ^a, M. H. Habibi ^b

^a Department of Chemistry, Ferdowsi University of Mashhad, Mashhad, Iran, 91775-1436

^b Department of Chemistry, University of Isfahan, Isfahan, Iran, 81745

*Email: Somayeh.Laleh@stu-mail.um.ac.ir

Keywords: Thiophenolato Mercury (II) Complexes, DFT Calculations, Vibrational Spectroscopy, Stability.

1. Introduction

Coordination chemistry of the Hg (II) ion has been in the focus of many investigations for many years due to the significant toxicological effects of mercury on living organisms. Due to the thermodynamically stable Hg-S bond a large number of data regarding thiolate complexes of mercury (II) are available [1]. Much attention has recently been focused on organo hetero bimetallic compounds from the catalytic and biochemical points of view. The transition metal can be stabilized by hetero ligands with multiple coordination modes and give mono- or di-nuclear complexes. An organo-metallic ligand can be an important starting material for preparing heterobimetallic complexes. There are a few reports on the use of mercury complexes for the construction of ion-selective electrodes [2,3].

The aim of the present work is the full assignment of the vibrational spectra, calculation of vibrational frequencies, relative intensities and optimization of geometry parameters for five Bis (para substitution-thiophenolato) mercury (II) complexes, where the substitutions are F, Cl, Br, CH₃, and SCH₃. Then obtained data will be compared with corresponding experimental quantities. Attempts will also be made to study the stability of Hg complexes. We also investigated the substitution effect on Hg-S bond strength in these compounds. According to our knowledge, there is no report on the IR and Raman spectra of these complexes in the literature.

2. Experimental

Mercury (II) complexes were prepared and purified according to the method described in [4]. The IR Spectra of mercury (II) complexes recorded by Bomem B-154 Fourier transform spectrophotometer in the 400- 4000 cm⁻¹ by averaging 20 scans with a resolution of 2 cm⁻¹. The spectra were measured as KBr pellets.

The FT-Raman spectra were recorded employing a 180° back-scattering geometry and a Bomem MB-154 Fourier transform Raman spectrometer. The instrument was equipped with a ZnSe beam splitter and a TE cooled InGaAs detector. Rayleigh filtration was afforded by two sets of two holographic technology filters. The spectra were accumulated for 500 scans with a resolution of 2 cm⁻¹. The laser power at the sample was 400 mW.

The Far-IR spectra in the region 50-400 cm⁻¹ were obtained using a Thermo Nicolet NEXUS 870 FT-IR spectrometer equipped with a DTGS/polyethylene detector and a solid state beam splitter. The spectrum of the polyethylene pellet was collected with a resolution of 2 cm⁻¹ by averaging the results of 64 scans.

3. Method of analysis

In this study, the equilibrium geometry and vibrational frequency of mercury (II) complexes were computed with the GAUSSIAN 03 software system [5] by using a selection of modern density functional, using B3LYP level at the LANL2DZ basis set. LANL2DZ is a useful basis set for heavier metal complexes.

The assignment of the experimental frequencies are based on the observed band frequencies and intensities in the infrared and Raman spectra confirmed by establishing one to one correlation between observed and theoretically calculated frequencies. The assignment of the calculated wavenumber is aided by the animation option of the Gauss View 3.0 [6] graphical interface for Gaussian programs, which gives a visual representation of the shape of the vibrational modes.

4. Results and discussion

The optimized geometry parameters of five mercury (II) complexes obtained at Density Functional Theory (B3LYP) level using LANL2DZ basis set. It was observed that the substitution of different functional groups at para position of thiophenol molecule does



not change the structural parameters widely. The minimum value of Hg-S bond length, 2.276 Å, obtained for thiomethyl substituted thiophenol molecule. The longest of Hg-S bond length, 2.549 Å, has been calculated for para-chlorothiophenolate ion.

The calculated frequencies are slightly higher than the experimental values. Two factors may be effective for the discrepancies between the observed and calculated spectra of these compounds. The first is caused by the environment. DFT calculations have been done at the gas phase and experimental frequencies are obtained from solid state. The second reason for this discrepancy is the fact that the experimental values are anharmonic frequencies while the computed data are harmonic frequencies. It was found that the stretching frequency of S-Hg-S in these complexes decreases by the substitution of electron withdrawing (EW) group.

5. Conclusion

The geometry of thiophenolato mercury (II) complexes with different functional groups has been optimized at B3LYP/LANL2DZ level of theory. It was found that the structural parameters of thiophenolato mercury (II) complexes are not much affected by the substitution of different functional groups. The calculated and experimental data showed that the substitutions of electron-withdrawing and -donating groups have negative and positive effect on the stability of these compounds respectively.

References

- [1] M. J. Stillman, F. C. Shaw, K. T. Suzuki, *Metallothioneins: Synthesis, Structure and Properties of Metallothioneins, phytochelatins, and metal-Thiolate Complexes*, VCH verlagsgesellschaft mbH, Weinheim, 1992.
- [2] S. Daunert, A. Florido, J. Bricker, W. Dunaway, L. G. Bachas, M. Valiente, *Electroanalysis* 5 (1993) 839-843.
- [3] Y. Q. Song, R. Yuan, M. Ying, Z. Q. Li, Y. Q. Chayi, H. Cui, G. L. Shen, R. Q. Yu, *Fresenius J. Anal. Cem* 360 (1998) 47-51.
- [4] M. K. Amini, M. Ghaedi, A. Rafi, M. H. Habibi, M. M. Zohory, *Sensors* 3 (2003) 309-325.
- [5] M. J. Frisch, G. W. Trucks, H. B. Schlegel, G. E. Scuseria, M. A. Robb, J. R. Cheeseman, J. A. Montgomery, T. Vreven, K. N. Kudin, J. C. Burant, J. M. Millam, S. S. Iyengar, J. Tomasi, V. Barone, B. Mennucci, M. Cossi, G. Scalmani, N. Rega, G. A. Petersson, H. Nakatsuji, M. Hada, M. Ehara, K. Toyota, R. Fukuda, J. Hasegawa, M. Ishida, T. Nakajima, Y. Honda, O. Kitao, H. Nakai, M. Klene, X. Li, J. E. Knox, H. P. Hratchian, J. B. Cross, C. Adamo, J. Jaramillo, R. Gomperts, R. E. Stratmann, O. Yazyev, A. J. Austin, R. Cammi, C. Pomelli, J. W. Ochterski, P. Y. Ayala, K. Morokuma, G. A. Voth, P. Salvador, J. J. Dannenberg, V. G. Zakrzewski, S. Dapprich, A. D. Daniels, M. C. Strain, O. Farkas, D. K. Malick, A. D. Rabuck, K. Raghavachari, J. B. Foresman, J. V. Ortiz, Q. Cui, A. G. Baboul, S. Clifford, J. Cioslowski, B. B. Stefanov, G. Liu, A. Liashenko, P. Piskorz, I. Komaromi, R. L. Martin, D. J. Fox, T. Keith, M. A. Al-Laham, C. Y. Peng, A. Nanayakkara, M. Challacombe, P. M. W. Gill, B. Johnson, W. Chen, M. W. Wong, C. Gonzalez, J. A. Pople, *Gaussian 03, Revision B.05*, Gaussian, Inc., Pittsburgh PA, 2003.
- [6] P. J. Hay, W. R. Wadt, *Gauss View 3.0*, Gaussian Inc., Carnegie Office, Park, Pittsburgh, PA 15106, USA, *J. Chem. Phys.* 82 (1985) 270.



The fluorescence spectroscopic studies of fluoxymestron and acetaminophen upon interaction with human serum albumin

M. Sabaghian^{1*}, M.R. Housaindokht², M.R. Saberi³ and J. Chamani¹

Department of Biology, Faculty of Science, Islamic Azad University-Mashhad Branch, Mashhad, Iran

Department of Chemistry, Faculty of Science, Ferdowsi University of Mashhad, Mashhad, Iran

Medical Chemistry Division, School of Pharmacy, University Complex, Mashhad, Iran

Keywords: Fluoxymestron; Acetaminophen; Human serum albumin (HSA); Physiological conditions; Fluorescence spectroscopy

1. Introduction

Human serum albumin (HSA) is the most abundant protein in the circulatory system (0.6 mmol dm^{-3}) and one of the most extensively studied proteins. It is used for the transportation and distribution of drug in the body and is very important to explain interaction mechanism, pharmaco-kinetics and toxicity of drug. Hence, the studies on binding of drug and serum albumin become an important research field in chemistry, life science and clinical medicine [1-3]. Here, the interaction of acetaminophen and fluoxymestron with HSA was investigated under physiological conditions by utilizing the fluorescence spectroscopy. The number of binding sites and affinity were determined according to the relevant fluorescence intensity.

2. Materials and methods

HSA, fluoxymestron and acetaminophen purchased from Sigma Chemical Company, was used without further purification. All HSA solutions were prepared in the pH 7.4 buffer solution. Buffer solution consists of phosphate buffer (0.05 M)). All reagents were used through out all the experiments. Fluorescence spectra were performed with a Hitachi F-2500. The emission spectra were recorded between 300 and 600 nm (excitation wavelength 280 and 295 nm).

3. Result and discussion

The fluorescence intensity of HSA was decreased regularly and the fluorescence maxima showed blue shift by increasing the fluoxymestron concentration, which validates the interaction of fluoxymestron with HSA leading to the quenching of the fluorescence of HSA and suggests that the chromophore of protein was placed in a more hydrophobic environment after addition of fluoxymestron [4]. It is well known that quenching occurs through the static or dynamic quenching process, both of which can result in a linear Stern-Volmer plot. To analyze the data from the quenching experiments, we used the Stern-Volmer equation (Eq. (1)) [4,5].

$$F_0/F = 1 + K_q \tau_0 [Q] = 1 + K_{SV} [Q] \quad (1)$$

Where F_0 and F are the fluorescence intensities of HSA in the absence and presence of the quencher, respectively. K_q is the quenching rate constant of the biomolecule. K_{SV} is the Stern-Volmer dynamic quenching constant, τ_0 is the average lifetime of the biomolecule without quencher, and $[Q]$ is the concentration of quencher.

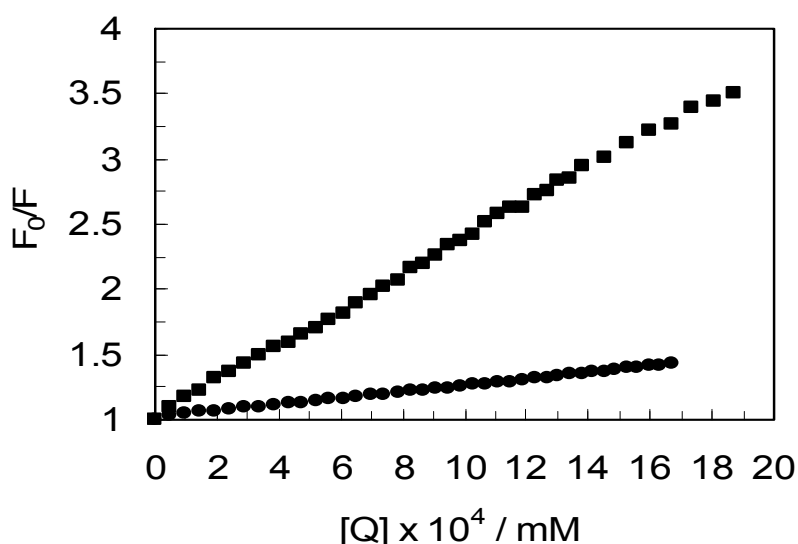


Fig.1. The Stern-Volmer curves for quenching of acetaminophen and fluoxymestrone with HSA at $\lambda = 295$ nm.

K_{SV} is the slope of linear regressions of Fig. 1. According to Eq. (1), Stern-Volmer constant be calculated and their values are for acetaminophen and fluoxymestrone 2.4×10^2 , 1.36×10^3 , respectively. The results indicated that acetaminophen has lower binding affinity than fluoxymestrone to HSA. Number of binding of sites (n) be calculated by the following equation:

$$\log [(F_0 - F)/F] = \log K_s + n \log [Q] \quad (2)$$

$$n_{\text{fluoxymestrone}} = 1.0066, \quad n_{\text{acetaminophen}} = 0.9583$$

The molar ratio curves (Fig. 2) represent 280 and 295 nm excitation wavelength does not overlap and in 280 nm wavelength the tryptophan residue in human serum albumin are excited, whereas the 295 nm wavelength excites tryptophan and tyrosine residues [6].

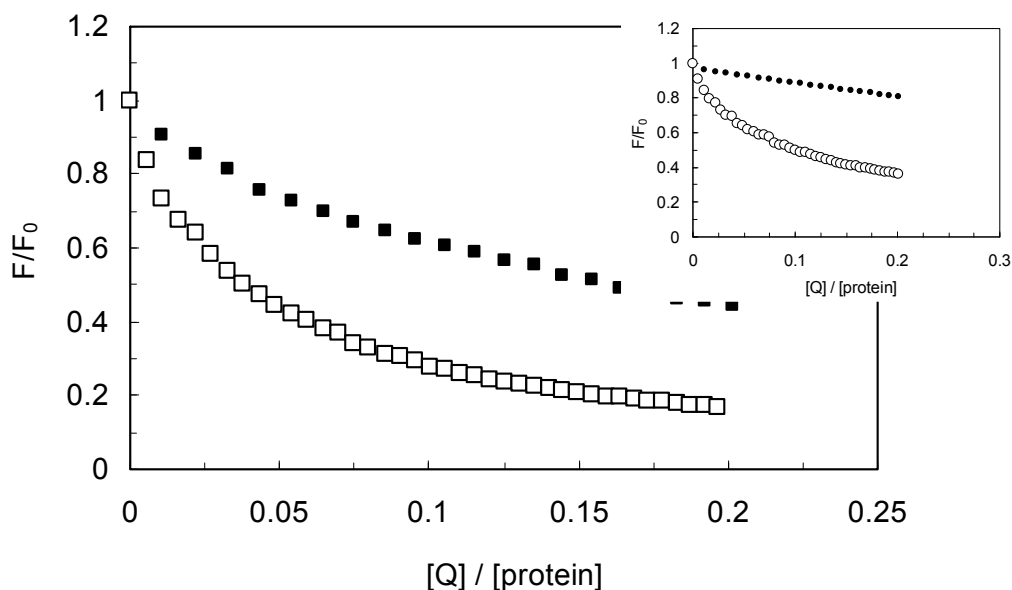


Fig.2. Quenching curves of HSA in the presence of fluoxymestrone. (Inset) Quenching curves of HSA in the presence of acetaminophen

4. Conclusion

The comparison between fluoxymestrone and acetaminophen upon interaction with HSA has been studied. For both drugs, the tryptophan and tyrosine residues participate in the interaction with HSA. On the other hand, fluoxymestrone and acetaminophen can be bound as 1:1 molar ratio with HSA. Our results show that acetaminophen has lower binding affinity than fluoxymestrone to HSA.

References

- [1] Xingguo Chen, Jianghong Tang, Feng Luan, *Bioorg. Med. Chem.*, 14 (2006), 3210-3217.
- [2] Fengling Cui, Junli Wang, Yanrui Cui, Jianping Li, Xiaojun Yao, Yan Lu, Jing Fan, *Luminescence*, 127 (2007), 409-415.
- [3] F.L. Cui, J. Fan, J.P. Li, Z.D. Hu, *Bioorg. Med. Chem.* 12 (2004) 151.
- [4] Guowen Zhang, Qingmin Que, Junhui Pan, Jinbao Guo, *J. Mol. Struct.*, 881 (2008) 132-138.
- [5] J.R. Lakowicz, "Principles of Fluorescence Spectroscopy", *Plenum Press*, New York, 1983 (pp. 257)
- [6] A. Sulkowska, M. Maciazek-Jurczyk, B. Bojko, J. Rownicka, I. Zubik-Skupien, E. Temba, D. Pentak, W.W. Sulkowski, *J. Mol. Struct.*, 881(2008) 97-106.

Observation of Space Charge Effects in Ion Mobility Spectrometry

Vahideh. Ilbeigi and Mahmoud. Tabrizchi*

Department of Chemistry, Isfahan University of Technology, Isfahan, Iran. 84156-83111

m-tabriz@cc.iut.ac.ir

Key words: Space Charge, Ion mobility spectrometry, Ion-ion repulsion.

1. Introduction

A cloud of charged particles can form a space charge region which is usually treated as a continuum of charge distributed over a region of space rather than point charges. This effect was first observed by Thomas Edison in light bulb filaments, where electrons emitted from the filament formed a space charge. The space charge effect is an important phenomenon in many instruments dealing with ions and charged particles such as mass spectrometry. Generally it is believed that the space charge effect is negligible in ion mobility spectrometry (IMS) [1]. Recently, Tolmachev et al. showed that the space charge is important in IMS when the number of ions is larger than 10^4 in an ion packet and it causes peak broadening [2]. They evaluated the effect of space charge within an ion packet and calculated the change in resolving power as a function of charged number density. We here report the first observation of space charge repulsion between two adjacent ion packets in IMS.

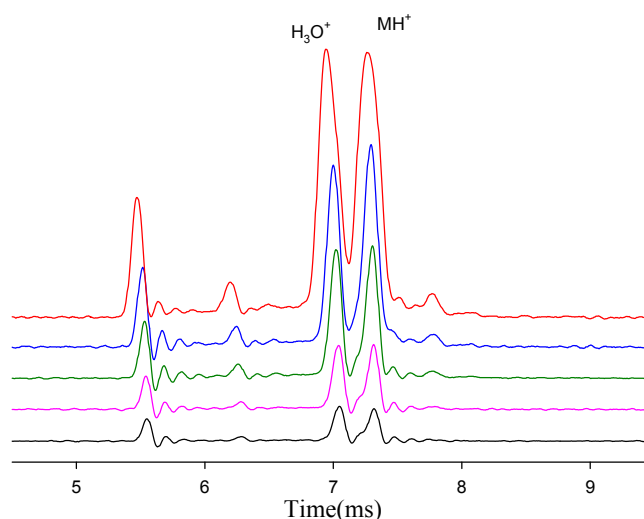


Fig.1. The two adjacent peaks (H_3O^+ and MH^+) push away each other. The H_3O^+ peak is the background peak and the MH^+ peak is protonated acetone.

2. Experimental

The ion mobility spectrometer used in this study was constructed in our laboratory at Isfahan University of Technology. In IMS ions are first produced by an ionization source and then injected as an ion packet into a drift region where they are separated according to their mass, size and charge. It is very similar to time-of-flight mass spectrometry but it operates under atmospheric pressure. A full description of the method is given in books and review articles [3,4]. A shutter grid was used to create the ion packets by chopping a continuous ion current coming from the source. The preferred width of the packet was chosen by adjusting the opening time of the shutter grid.

3. Results and Discussion

In order to observe the repulsion effect between two ion packets, an experiment was designed such that two closely peaks appear on the mobility spectrum. This was achieved by choosing acetone as sample which produces protonated acetone with a peak (MH^+) nearby to the background H_3O^+ peak. The concentration of acetone was adjusted so that the two peaks had similar intensities, as shown in Fig.1. The two adjacent peaks are well resolved because of the high resolution of our instrument. Then

the shutter grid pulse width was changed to record spectra at different intensities. The separation between the two peaks is in the order of 300 μs corresponding to 0.46 cm distance at the collector. It should be mentioned that the two ion packets are originally together but they separate as they travel in the drift region. Hence the distance between the two packets starts from zero and reach to its final separation. In the absence of space charge repulsion, the final separation should be independent of the intensity of the two peaks. However, close investigation of spectra shows that the separation between the two peaks grows as their intensity increases. This is demonstrated in Fig.2 where the separation is plotted versus the peak area. Clearly the increase in separation is the result of repulsion between the two ion packets.

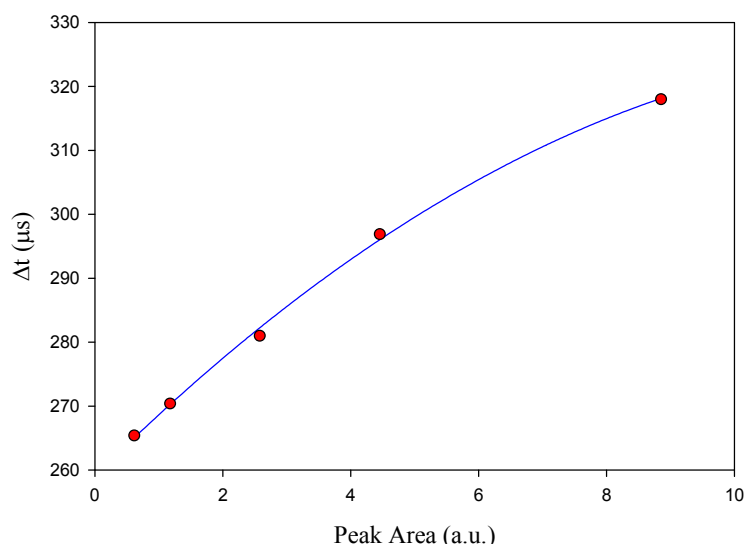


Fig.2. Separation between the two peaks (Δt) versus the peak area which is proportional to intensity

4. Conclusions

The repulsion between two ion packets in IMS was observed and reported for the first time. The reason to observe this phenomenon is the ability to create two very close and narrow peaks because of the high resolution of our instrument. This study shows that the space charge repulsion is not negligible in IMS and it should be considered in accurate studies. An example is the accurate determination of drift time of a small peak in neighborhood of a large peak. This work showed that the field of a large peak influences the drift time of its neighboring small peak.

References

- [1] R.H. St. Louis, H.H. Hill, Crit. Rev. Anal. Chem., 21(5), 321 – 355, 1990.
- [2] A.V. Tolmachev, B.H. Clowers, M.E. Belov, R.D. Smith, "Fundamentals of Coulombic Ion-Ion Repulsion Effects in Ion Mobility Spectrometry", ASMS 2009 (Philadelphia, PA).
- [3] G.A. Eiceman, Z. Karpas, "Ion Mobility Spectrometry", CRC Press, Boca Raton, FL, 2005.
- [4] C.S. Creaser, J.R. Griffiths, C.J. Bramwell, S. Noreen, C.A. Hill, C.L.P. Thomas, Analyst, 129 (2004) 984-994.

Thermodynamic study of proton-bond dimer formation reaction in gas phase

Z. Izadi, H. Farrokhpour and M. Tabrizchi

E-mail: z.izadinajafabadi@ch.iut.ac.ir

Chemistry Department, Isfahan University of Technology, Isfahan, 84156-83111, Iran

Keyword: Ion Mobility Spectrometry, Proton Bound Dimer, Vant's Hoff equation

1. Introduction

Proton bonding is responsible for many important phenomenon in physics, chemistry and biology [1]. Simple proton-bound dimers of the type AH^+A are often used as model systems to investigate the nature of intermolecular interaction such as proton bonding. The thermodynamic properties of proton bound dimers have been studied experimentally by various techniques such as; ion cyclotron resonance, pulsed electron beam, high pressure mass spectrometry and ion mobility spectrometry (IMS) [2]. In this work, we have used IMS to experimentally study the thermodynamic of proton bond dimer formation at atmospheric pressure for methyl-isobutyl-keton (MIBK) and 2,4-dimethyle pyridine (DMP).

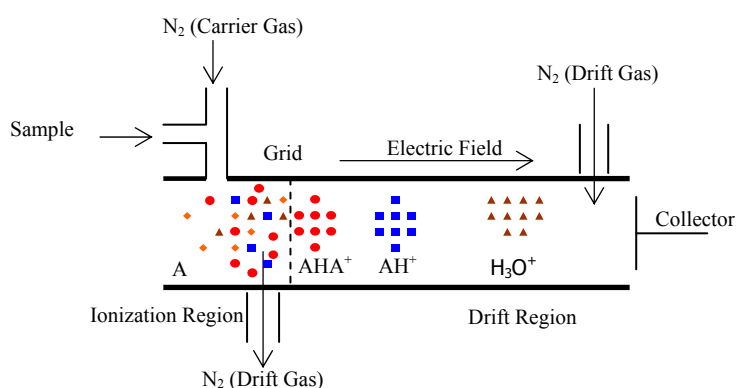


Fig. 1. Schematic diagram of the Ion mobility spectrometer and the sample introduction system.

2. Experimental and Method

The experiment was performed using an ion mobility spectrometer made in our laboratory. A detailed description of this instrument can be found elsewhere [3]. The IMS cell is in a thermostat oven where temperature could be adjusted from room temperature to 500 K. A continuous corona discharge ionization source was used as ionization source [3]. Nitrogen was used for the drift and carrier gas. Fig. 1 shows a simple schematic diagram of the instrument. The sample is injected into the carrier gas using a syringe pump at flow rates in the range of from 5-30 $\mu\text{L min}^{-1}$. The source continuously produces hydronium water clusters, $H_3O^+(H_2O)_n$ which then react with the sample A.



At adequately high concentrations of A, the proton-bond dimers may be formed in an exothermic displacement reaction, such as;



To establish Reaction 2 in the ionization region the sample flow rate was increased until equilibrium condition was achieved. To ensure the equilibrium condition, the reaction quotient (Q) of Reaction 2 was measured while the pump flow rate was increased. At equilibrium, Q was independent of the flow rate. Then the relative abundances of the monomer and dimer were obtained from the intensity of their corresponding peaks in the mobility spectrum.

3. Results

Typically ion mobility spectra of the MIBK at equilibrium condition are given in Fig. 2. As shown, by increasing temperature, the intensity of the dimer peak reduces, i.e. Reaction 2 is reversed. This means that Reaction 2 is exothermic. Also, all peaks shift towards shorter time as temperature increases. The equilibrium constant, K_{eq} , was calculated from the relative intensities at different temperatures. Then the $\ln(K_{eq})$ was plotted versus the reciprocal temperature for MIBK to obtain the enthalpy of

reaction 2 using Vant's Hoff equation. The value of the enthalpy for formation of proton bound dimer of MIBK was obtained to be about -13.2 ± 1 kJ.mol⁻¹. Similar method has been used to obtain the enthalpy for formation of proton bound dimer of DMP.

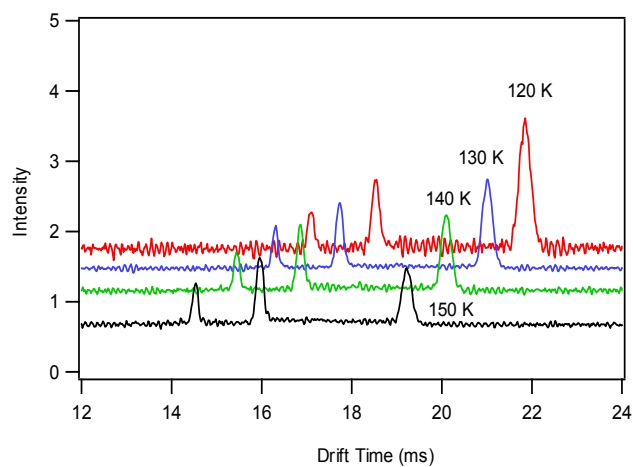


Fig. 2. Ion mobility spectra of IBMK at equilibrium condition for several temperatures. The spectra have been normalized to the intensity of the monomer peak. The drift field is 578 V/cm.

References

- [1] C. L. Perrin and J. B. Nielson, *Annu. Rev. Phys. Chem.* 48 (1997) 511.
- [2] R. G. Ewing, G. A. Eiceman and J. A. Stone, *Int. J. Mass. Spectros.* 193 (1999) 57.
- [3] H.R.Shamlouei and M.Tabrizchi, *Int. J. Mass. Spectros.* 273(2008) 78.



Fluorescence spectroscopic investigation of human serum albumin upon nano-interaction with Lomefloxacin at different pH

R.Assaran Darban^{1,2*}, H. Vahedian- Movahed², M. Saleh-Moghadam¹, J. Chamani²

1. Razavi Khorasan Payame Noor University, Mashhad, Iran

E-mail:mrassaran78@yahoo.com

2. Department of Biology, Faculty of Sciences, Islamic Azad University-Mashhad Branch, Mashhad, Iran

Keywords: Human serum albumin, Lomefloxacin, fluorescence spectroscopy

1.Introduction

Human serum albumin (HSA) is the most abundant plasma protein in the circulatory system. Has is a monomer protein composed of 585 amino acids, three homologous domains, a large number of disulfide bonds and a single tryptophan residue (Try214). The folding of such a multi-domain protein could be a complex process because each domain can fold independently and inter-domain interactions can regulate the overall folding process. The unfolding pathways of HSA have been examined in several studies (1-3). Lomefloxacin (LMF) is an antibiotic in a class of drugs called fluoroquinolones with wide spectrum of activity against various bacterial infection, such as bronchitis and urinary tract infections. It has been widely used in clinical practice. However, few reports on the binding of LMF to human serum albumin (HSA) are available in the literature, and to our knowledge there is not any report on the interaction of LMF with HAS at different pH, so a detailed study on the binding reaction of LMF will be of great interest to scientists in general and clinicians in particular (4).

2.Materials and methods

HSA, LMF phosphate buffer were purchased From Sigma Company (USA) and used without further purification. Deionized water was used throughout the experiments. Stock solution of HSA was prepared by dissolving the solid HSA in phosphate buffer and solution of LMFX was prepared by dissolving 0.0019 g LMFX in phosphate buffer, stored at 4 °C and protected from light. All the measurements were performed at room temperature. Fluorescence spectra were recorded with a F-2500 spectrofluorimeter (Hitachi, Japan) equipped. The pH measurements were made with a digital pH meter. HSA was titrated by successive additions of a 5 μmol aliquots of LMF. Titrations were done manually by using micro-injector.

3.Result and Discussion

The Stern-Volmer analysis which is the relative fluorescence intensity (F_0/F) as a function of quencher concentration $[Q]$ were employed to elucidate the quenching mechanism and binding affinity from Stern-Volmer constant. As seen in figure 1 there are two different binding sites for LMF on HSA at pH 7.4.

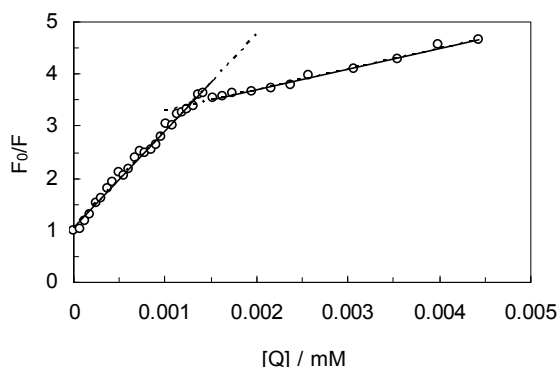


Fig. 1: Stern-Volmer plots for HSA titrated by LMF at pH=7.4 and 50 mM phosphate buffer.

The same trend was observed for other pH and the calculated Stern-Volmer constant were as $K_{SV1} = 7.84 \times 10^5 \text{ M}^{-1}$, $K_{SV2} = 19.12 \times 10^5 \text{ M}^{-1}$; at pH 5.4, $K_{SV1} = 19 \times 10^5 \text{ M}^{-1}$, $K_{SV2} = 6.86 \times 10^5 \text{ M}^{-1}$ at pH 6.4; $K_{SV1} = 18.6 \times 10^5 \text{ M}^{-1}$, $K_{SV2} = 4.03 \times 10^5 \text{ M}^{-1}$ at pH 7.4; $K_{SV} = 5.57 \times 10^5 \text{ M}^{-1}$, at pH 8.4 and $K_{SV} = 9.03 \times 10^5 \text{ M}^{-1}$ at pH 9.4. Also for further considerations we determine



the number of binding site as discussed below.

When small molecules binding independently to a set of equivalent sites on a macromolecule, the equilibrium between free and bound molecules is given by the equation:

$$\log \frac{F_0 - F}{F} = \log K_b + n \log [Q]$$

Where K_b and n are the binding constant and the number of binding sites, respectively, which could be got from the double logarithm regression curve of $\log (F_0 - F)/F$ versus $\log [Q]$ (5). As shown in figure 1, when the $[Q]$ was below 0.0015, there is only one binding site in HSA molecule, while after $[Q]$ increased above 0.0015 another binding site appear in HSA molecule. Similar results were obtained concerning the other pH (5.4 and 6.4). At pH 5.4 $n_1 = 0.75$, $n_2 = 0.55$, and pH 6.4 $n_1 = 0.99$, $n_2 = 0.5$. But there is only one binding site in HSA molecule at pH 8.4 ($n = 0.74$, $K_{sv} = 5.57 \times 10^5 \text{ M}^{-1}$) and pH 9.4 ($n = 0.7$, $K_{sv} = 9.03 \times 10^5 \text{ M}^{-1}$).

4. Conclusion

We studied the interaction of LMF with HSA by fluorescence spectroscopy at five different pH. At three pHs (5.4, 6.4 and 7.4) two set of binding sites in HSA molecule was revealed but at remaining pHs (8.4, 9.4) only one binding site was shown. We determined the net charge effect on the structure of HSA upon binding to LMF is very important to interaction HSA-LMF. Therefore the electrostatic interaction is the main force between HSA and LMF.

References

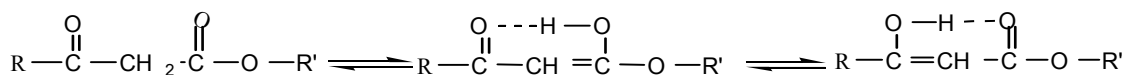
- 1- F. Jin, J.Q. Lu, X.W. Zhou, T.Q. Sun, Chinese Journal of Chemistry, 25 (2007) 1675-1680.
- 2- J. Gonzalez-Jimenez, M. Cortijo, J. Protein Chem. 21 (2002) 75-79.
- 3- S.S. Krishnakumar, D. Panda, Biochemistry, 41 (2002) 7443-7452.
- 4- J. Fan, X. Chen, Y. Wang, C.P. Fan, Z. Shang, Journal of Zhejiang University Science B, 7 (2006) 452-458.
- 5- L.W. Zhang, K. Wang, X. X. Zhang, Analytica Chimica Acta, 603 (2007) 101-110.
- 6- J. Wang, Z. Liu, J. Liu, S. Liu, W. Shen, Spectrochimica Acta Part A, 69 (2008) 956-963.

**NMR studies of tautomerism in benzylacetoacetate**Farnaz Naghavi ^{*a}, Sayyed Faramarz Tayyari ^b

E-mail: farnaz_naghavi@yahoo.com

^a Chemistry Department, Islamic Azad University, Shahroud Branch, Shahroud, Iran^b Chemistry Department, Ferdowsi university of Mashhad, Mashhad, Iran**Keywords:** NMR spectroscopy; Tautomerism; Hydrogen-bonding; DFT calculation.**1. Introduction**

β -ketoesters, such as β -diketones, are engaged in keto-enol tautomerization, as shown in scheme 1.



However, in spite of high investigation of β -diketones [1,2], tautomerization in β -ketoesters has not been much considered. This may be due to low enol content of most of these compounds. As in the β -diketones, the enol form of β -ketoesters is also stabilized by formation of an intramolecular hydrogen bond. Therefore, any parameter, such as conjugation, electron donating, and electro withdrawing, which affects the hydrogen bond strength, changes the enol content of the sample.

The aim of this project is study of the effects of benzyloxy substitution on the keto-enol equilibrium and hydrogen bond strength in benzylacetoacetate (BAA). For this propose, we study the NMR spectra of benzylacetoacetate by means of DFT method and comparing the results by the experimental data. The keto-enol tautomerization and hydrogen bond strength in BAA are compared with those in acetylacetone (AA) [3] and dimethyloxaloacetate (DMOA) [4].

2. Experimental

Benzylacetoacetate, $\text{C}_6\text{H}_5\text{-CH}_2\text{-O-CO-CH}_2\text{-CO-CH}_3$, has been purchased from Merck Co., and distilled under reduced pressure. ^1H NMR spectra on a JEOL Eclipse spectrometer at 400 MHz. ^1H chemical shifts are reported in ppm downfield from internal tetramethylsilane (TMS). The NMR spectra have been obtained in the CDCl_3 , d6-acetone, d6-benzene, and d4-methanol. The IR spectrum of BAA recorded by using Bomem B-154 Fourier Transform Spectrophotometer in region $1800\text{-}1000\text{ cm}^{-1}$. The spectrum was collected with resolution 2 cm^{-1} by coadding the results of 15 scans.

3. Method of calculation

It has been shown, theoretically [5], that there are 45 stable enol and 5 stable keto conformers. Two kind of enol forms may be considered for BAA (Fig.2), which in one of them, A, the enol group is near the CH_3 group and in another form, B, the enol group is attached the benzyloxy group. It has been shown that the A tautomers are more than 10 kcal/mol more stable than the B tautomers [5]. Therefore we only optimized the most stable conformers of enol and keto tautomers.

The geometries of the most stable tautomers are optimized at the B3LYP level using the 6-311++G** basis set. The absolute shielding for BAA and TMS have been obtained using the gauge-including atomic orbital (GIAO) method [5-6] at the B3LYP/6-311++G**//B3LYP/6-311++G** level. The predicted ^1H chemical shifts are derived from equation $\delta' = \rho - \rho_0$, where δ' is the chemical shift, ρ is the absolute shielding, and ρ_0 is the absolute shielding of TMS, and compared with the experimental results.

4. Results and discussion. The calculated and experimental ^1H NMR chemical shifts of BAA in the enol and keto forms in different solvents are given in Tables 1 and 2, respectively. As it is shown in these Tables, the experimental results of the NMR spectra are consistent with those of the most stable enol and keto conformers. However, the deconvoluted FTIR spectrum of BAA in the CCl_4 solution in the $1800\text{-}1000\text{ cm}^{-1}$ region, Fig. 3, indicates coexisting of two keto conformers in the sample (see the existing of 4 bands in the C=O stretching region). This discrepancy indicates that both keto conformers are in rapid equilibrium in the NMR time scale. The enol contents of the enol form in the different solution are shown in Table 3. According to this table, it is concluded that the enol content in the BAA samples in different samples is considerably reduced in compare with that in AA.

Table 1. Calculated and observed ¹H chemical shifts for the most stable enolated BAA.

	H5	H1	H3	H8	H-ph
Theory	12.340	1.772	4.881	5.170	7.389-7.999
Exp.(CDCl ₃)	12.053	1.898	5.045	5.125	7.31-7.33

Table 2. Calculated and observed ¹H chemical shifts for the most stable diketo BAA.

	H1	H3	H7	H-ph
Theory	2.263	3.207	5.185	7.46-7.78
Exp.(CDCl ₃)	2.162	3.437	5.125	7.31-7.33

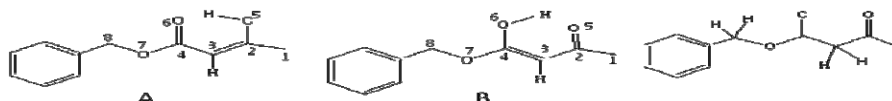

Fig 2. Structure and atom numbering of enol and keto BAA

Table 3. The effect of the solvent on the enol content in the BAA samples.

Solvent	C ₆ D ₆	CDCl ₃	CD ₃ OD	d6-acetone	d6-DMSO
%enol	17	9	3	>2	<2

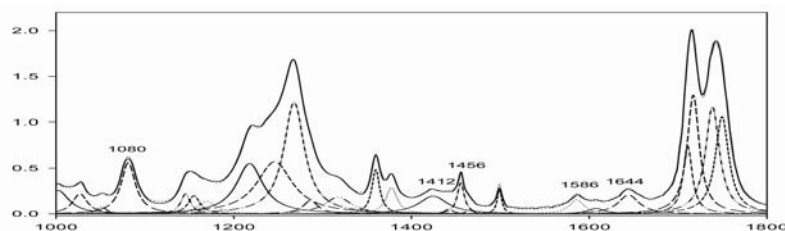
The hydrogen bond strength of the enolated BAA, AA, and DMOA are compared in Table 4 and. According to the Table 4, the O...O distance, O-H bond length, O-H stretching,

Table 4. Comparing of some important parameters reflecting of H-bond strength for BAA, DMOA, and AA. ^a

	O...O(Å)	O-H(Å)	ν O-H (cm ⁻¹)	ν O-D	γ O-H	γ O-D	δ' O-H
BAA	2.585	0.997	3100	2260	837	630	12.05
AA	2.544	1.003	2800	2027	957	907	15.45
DMOA	2.621	0.989	3120	2338	857	624	-

^a ν stretching; γ , out-of-plane bending; δ' , NMR chemical shift.

and OH/OD out-of-plane bending of BAA are between the corresponding values for AA and DMOA. The weakness of the hydrogen bond in DMOA is caused by the substitution of the CH₃ group by an electron withdrawing group, CH₃COO. However, substitution of the CH₃ group in AA by an electron donating group, C₆H₅CH₂, cause increasing of the keto content in the sample.


Fig. 3. The deconvoluted IR spectrum of BAA in the CCl₄ solution.

References

- [1] H. Ogoshi, K. Nakamoto, J. Chem. Phys. 45 (1966) 3113.
- [2] S.F. Tayyari, PhD thesis, London University, 1978.
- [3] S.F. Tayyari, F. Milani-Nejad, Spectrochim. Acta Part A, 56 (2000) 2679-2691.
- [4] S.F. Tayyari, S. Salemi, M. Zahedi Tabrizi, M. Behforouz, "Molecular structure and vibrational assignment of Dimethyl oxaloacetate" J. Mol. Struct. 694 (2004) 91-104.
- [5] Farnaz Naghavi, M.Sc. Thesis, Islamic Azad University, Shahroud Branch, Shahroud, 2009.



A study on decolorization process of Malachite green and Crystal violet by 1-Aza 15-crown 5

A. Ghanadzadeh and S. Shekarsaraee*

Department of Chemistry, Faculty of Science, Guilan University, Rasht, Iran

E-mail: Shekarsaraee@gmail.com

Keywords: Decolorization, Crown Ether, Triphenylmethane Dyes, Absorption Spectra

1. Introduction

Malachite Green (MG) and Crystal Violet (CV) are the one of the major constituents of the wastewater produced from many industries related to textile, paint and varnishes, ink, plastics, pulp and paper, cosmetics, tannery etc., and also to the industries, which produce dyes [1]. Colored dye effluents pose a major threat to the surrounding ecosystem. Therefore, the study on the interactions of the dyes with various media is very important and useful. MG and CV are triphenylmethane dyes (TPM+) [2]. In order to understand their interactions with crown ether, it is necessary to investigate the environmental effect on their spectral properties. Crystal violet and Malachite green have absorbance spectra with two overlapped bands, i.e. a maximum (λ_{max}) and a shoulder ($\lambda_{\text{shoulder}}$). The interaction between dyes and crown ether has not been investigated by a few researchers thus; the studies in this area are still important and interesting for the theory and technology of decolorizing and removing them from wastewater.

Experimental methods mostly used for studying interaction between dyes and other materials are uv/vis spectroscopy. In this work, the decolorizing process of triphenylmethane dyes by crown ether in water and micellar medium [3] was studied using optical spectroscopy, and a mechanism was suggested for dye-crown ether interaction.

2. Methods

Malachite green and Crystal violet were obtained from Merck (pro-analysis) and used without further purification as solute. Sodium dodecyl sulfate (SDS) was purchased from Merk as well. 1-aza 15-crown 5 (97%) was purchased from Sigma Aldrich. Distilled water was our isotropic host. The absorption spectra of the dyes in the solutions were scanned on a Cary UV-Vis double-beam spectrophotometer (Model UV-100). The dyes concentrations were fixed at 2×10^{-4} M. The surfactant concentration was chosen $\frac{1}{2}$ and 4 times of CMC point of SDS.

3. Results and discussion

Crown ether

Both MG and CV possess a central carbon atom in their structure that is partially positive because of resonance of conjugated bonds. Crown ethers are nucleophilic systems for non-bonding electrons on oxygen atoms. When crown ether is added to dye solution, an intermolecular bonding creates between crown ether and central carbon atom [4] that disturbs conjugation system and solution will be colorless [Fig.1].

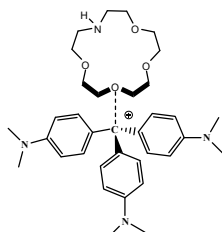


Fig. 1. crown ether effect on decolorizing the dyes

Micellar medium

Crown ether effect in micellar medium is also investigated. For comparison two surfactant solutions (below and above CMC point) were prepared. Above the CMC point, surfactants exert a solubility effect on many organic compounds [5] including the dyes we used in this paper. Absorption spectra were recorded for 80 minutes and results are reported in Fig.2.

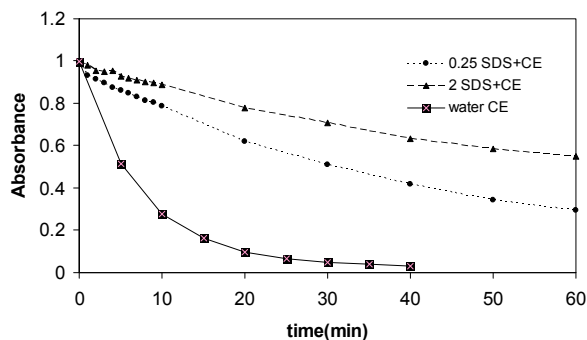


Fig.2. comparison of decolorizing process in water and micellar medium

As it can be seen in Fig.2, MG decolorized after 40 minutes but in surfactant solution, decolorizing process was reduced because of stronger interaction between dye and surfactant molecules. Above CMC point micellar system create a cavity to solve dye molecules and protect them to have interactions with crown ether.

4. Conclusions

Surfactant systems and decolorants are used to remove and decolorize dye molecules form textiles. These set of experiment shows that these two materials could have opposite effects on decolorizing process and may reduce performance of a detergent. Therefore, it should be noticed that use of a surfactant beside a decolorant needs more investigations.

References

- [1] Adak, A. Bandyopadhyay, M. Sep. Pur. Tech. 44 (2005) 139.
- [2] Jefferson, J. Ant. Age. Chemo. 12 (2003) 2323
- [3] Pourreza, N. and Elhami, S. J. Iran. Chem. Soc. 6 (2009) 784
- [4] Garcı, L. Godoy, A. Chem. Phys. Lett. 401 (2005) 302
- [5] Nasiruddin, M. Khan and Zareen U. J. Iran. Chem. Soc. 1 (2004) 152



Prediction of ^{13}C chemical shifts in solvents using PCM method and optimally selected wave function by factorial design

M. Tafazzoli^a, F. Fathi^a, H. Shaghghi^b

tafazzoli@sharif.edu

^aDepartment of Chemistry, Sharif University of Technology, Tehran, Iran

^bPayame Noor University (PNU), Karaj, Iran

Keywords: PCM, GIAO, ^{13}C Chemical Shifts, Factorial Design.

1. Introduction

In recent years, there has been a large number of theoretical studies of solvated systems, for either reactivity, structure, or properties. Although the best theoretical methods to study solvated compounds are molecular simulation ones, these approaches require a lot of time to predict different properties of only one molecule. Polarizable continuum model (PCM) has been used with the Hartree–Fock, density functional, and configuration interaction electronic structure methods for the inclusion of solvent effects [1]. PCM method allows nonspherical cavity using overlapping spheres. ^{13}C chemical shifts information plays an important role in the structure determination of complex compounds. Since the calculated ^{13}C chemical shifts are very sensitive to variations in methodology and basis sets, optimization of level of theory for the ^{13}C chemical shift calculations using multivariate techniques is necessary. In this work, ^{13}C chemical shifts of 11 different groups of compounds (89 molecules) were predicted using PCM method and optimally selected wave function by factorial design [2].

2. Methodology

To determine the optimum wave functions and calculation methods 2^4 factorial designs were considered. Based on preliminary experiences [3,4], electron correlation, triple- ξ valance shell, diffuse function, and polarization function were selected as A, B, C, and D factors in these designs respectively. Considering these four factors in two levels produces 16 levels of theory for the magnetic properties calculations. For each compound, magnetic properties were computed in solvent based on its optimized geometry with PCM method. GIAO method was applied to compute the shielding tensors, and tetramethylsilane (TMS) was considered as reference compound. The Gaussian 03 package was used to perform all the calculations. Experimental ^{13}C shielding constants were taken from the reference [5,6]. For each compound, the calculated values were compared with the experimental ones and the root mean squares deviation (rms) was determined. The normal plots were used to choose the main and interaction effects. Two typical normal plots for Propylamine and n-Pentane are illustrated in Fig. 1.

3. Results and discussion

The optimum level of theory for ^{13}C chemical shifts computation of 11 groups of compounds (alkane, alkene, alkyne, aldehyde, keton, alcohol, ether, acid, ester, aromatic, amine) are obtained from analysis of normal plots of four compound of each group. All calculations were done in CDCl_3 , a common solvent. Some samples of obtained optimum level of theory for calculation of ^{13}C chemical shifts are as follow: HF/6-31+G(d,p) for alkans, B3LYP/6-31G(d,p) for alcohols, HF/6-311+G(d,p) for amines. As an example, a few experimental and calculated ^{13}C chemical shifts for different molecules are presented in Table 1. It can be seen from this table that the calculated ^{13}C chemical shifts are in good agreement with the experimental ones. In order to assess further reliability of the wave functions and the methods, the ^{13}C chemical shifts of four other molecules of each group as a test set were predicted in CDCl_3 using the optimized level of theory obtained for the similar molecules. Correlation coefficient and RMS error values for the calculated ^{13}C chemical shifts related to the experimental values were 0.9998 and 1.65 respectively. These statistical data demonstrate that the method of calculation is reliable.

4. Conclusion

The main goal of the present study was to develop a theoretical method for predicting the ^{13}C chemical shifts in solvent for different groups of compounds. Among four factors (electron correlation, polarization function, triple- ξ valance shell, and diffuse function) that their effects and interactions were assessed using a 2^4 factorial design, polarization function was the most effective factor since all optimally selected basis sets of different groups contain polarization function. Inspection of the results



reveals the ability of the optimized GIAO method and PCM approach for calculating ^{13}C chemical shifts of different groups of compounds.

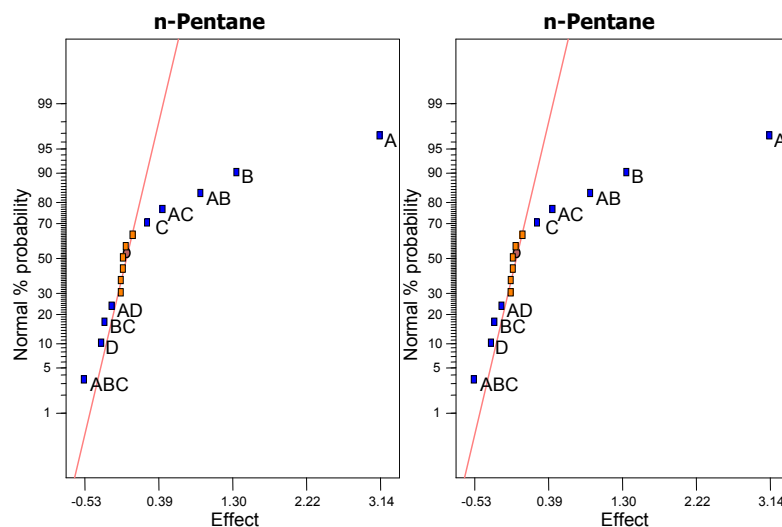


Fig 1. Normal plots for ^{13}C chemical shifts of methanol and methylamine using GIAO in CDCl_3

Table 1. Theoretical and experimental values of the ^{13}C chemical shifts (GIAO)

No.			Optimized basis set	This work	Exp. ^a
1	2-methylpropan-1-ol	CH_3	B3LYP/6-31G(d,p)	20.1	19.0
		CH_2		32.9	30.9
		$\text{CH}_2(\text{OH})$		69.8	69.5
2	acetaldehyde	CH_3	B3LYP/6-31+G(d,p)	32.5	30.9
		CO		198.5	199.9
3	n-Pentane	CH_3	HF/6-31+G(d,p)	16.1	14.1
		$\text{CH}_2(1)$		23.9	22.6
		$\text{CH}_2(2)$		32.9	34.4
4	cyclopentane		HF/6-31+G(d,p)	25.1	26.1
5	3-pentanone	CH_3	HF/6-31+G(d,p)	9.4	8.0
		CH_2		33.0	35.5
		CO		213.3	212.1
6	Methyl-propionate	CH_3	HF/6-31G(d,p)	10.4	9.2
		CH_2		26.6	27.5
		CO		175.9	174.9
		OCH_3		49.8	51.5

a: Ref. [5,6]

References

- [1] M. Kaoupp, M. Bühl, V. G. Malkin, Calculation of NMR and EPR Parameters: Theory and Applications, Wiley, New York, 2004.
- [2] D. C. Montgomery, Design and Analysis of Experiments, Wiley, New York, 2001.
- [3] Tafazzoli, M. Shaghghi, H. Jalali-Heravi M. Conc. Magn. Reson. 32A (2008) 449-460.
- [4] Tafazzoli, M. Shaghghi, H. Jalali-Heravi M. Conc. Magn. Reson. 32A (2008) 157-167.
- [5] H. E. Gottlieb, V. Kotlyar, A. Nudelman. J. Org.Chem. 62 (1997) 7512.
- [6] <http://riodb01.ibase.aist.go.jp/sdbs/> (National Institute of Advanced Industrial Science and Technology (AIST))

**Thermodynamic characterization of Fe₂O₃ nanoparticles binding to human hemoglobin**S. Zolghadri^{1,2}, A. A. Saboury²

E-mail: z.jahromi@ibb.ut.ac.ir

¹ Department of Biology, Islamic Azad University of Jahrom, Jahrom, Iran² Institute of Biochemistry and Biophysics, University of Tehran, Tehran, Iran**Keywords:** Hemoglobin, Thermodynamic, Fe₂O₃ nanoparticle, Binding**1. Introduction**

Due to their suitable surface chemistry, ferric oxide magneitc (Fe₂O₃) nanoparticles offer a great of interest for biomedical applications, such as drug delivery, cell engineering, magnetic carriers for bioseparation and for enzyme and protein immobilization, tissue repair, diagnostics, and as a contrast-enhancing medium. They are a promising group of imaging probes since MR signal intensity is manipulated, they have a favorable toxicity, and genuine potential for cellular uptake. When nanoparticles of Fe₂O₃ are injected into the blood for drug delivery and MRI imaging, the interaction of these particles with blood proteins must be avoided [1-5]. In this work we will address thermodynamic parameters of Fe₂O₃ nanoparticlebinding to hemoglobin.

2. Methods

The UV-Visible absorption spectra were measured with a Cary spectrophotometer, 100 Bio-model, with jacketed cell holders. Spectral changes of 3 μM hemoglobin were monitored after adding different concentration of iron oxide nanoparticles by recording the UV-Visible absorption (250-500 nm). All the experiments were run in phosphate buffer (0.1 M) at pH 7.0 in a conventional quartz cell thermostated to maintain the temperature at 20 ± 0.1 °C.

Intrinsic fluorescence intensity measurements were carried out using a Hitachi spectrofluorimeter, MPF-4 model, equipped with a thermostatically controlled cuvettecompartment. The working concentration of hemoglobin used was 3 μM so as to prevent quenching of Trp fluorescence by the neighboring heme group.

3. Results and discussion

According to the fluorescence results and thermodynamic parameters, the binding process of Fe₂O₃ nanoparticle to Hb is an enthalpy-driven and exothermic process. The possible number of binding sites (n) and binding constant (K) has been determined according to the following equation [6]:

$$\log\left[\frac{F_0 - F}{F}\right] = \log K + n \log[Q] \quad (1)$$

The binding constant and number of binding sites of Fe₂O₃ nanoparticle decrease by increasing the temperature, which indicates decreasing of the affinity of binding Fe₂O₃ nanoparticle to Hb by increasing temperature. The values of n approximately equal to 1 indicate the existence of just a single binding site on Hb for Fe₂O₃ nanoparticle. A quantitative description of the forces that govern molecular associations requires determination of changes of all thermodynamic parameters, including free energy of binding (ΔG°), enthalpy (ΔH°), and entropy (ΔS°) of binding. If the enthalpy change (ΔH°) does not vary significantly over the studied temperature range, then its value and that of ΔS° can be determined from the van't Hoff equation [6]:

$$\ln K = -\frac{\Delta H^\circ}{RT} + \frac{\Delta S^\circ}{R} \quad (2)$$

Where K is the binding constant at the corresponding temperature and R is the gas constant. The ΔH° and ΔS° are determined from the linear van't Hoff plots (Fig. 5). The Gibbs free energy (ΔG°) is estimated from the following equation:

$$\Delta G^\circ = \Delta H^\circ - T\Delta S^\circ \quad (3)$$

ΔG° reflects the possibility of reaction; ΔH° and ΔS° are the main parameters to determine molecular forces contributing to the ligand binding. The calculated thermodynamic parameters showed that the affinity of binding of Fe₂O₃ nanoparticle to Hb is decreased by increasing the temperature (from 25 to 42 °C), which shows a good consistence with exothermic process of binding. The negative sign for ΔG° indicates the spontaneity of the binding of Fe₂O₃ nanoparticle to Hb. Both ΔH° and ΔS° have



negative values. The negative values of ΔH° and ΔS° show that the binding process is an enthalpy-driven and exothermic process. Exothermic and enthalpy-driven binding events are associated with the hydrogen bonding and van der Waals interaction. The hydrogen bonding interaction of Fe_2O_3 -Hb may be occur between the monocoordinated surfaces -OH groups of Fe_2O_3 nanoparticles and the protonated amine groups in the protein at pH = 7.4.

Conclusion our thermodynamic results show that Fe_2O_3 nanoparticle binding to hemoglobin is an enthalpy driven process. Also it is concluded that Fe_2O_3 nanoparticle binds to hemoglobin, creating a local conformational change but does not alter the secondary structure of Hb.

References

- [1] A.S. Arbab, L.A. Bashaw, B.R. Miller, E.K. Jordan, B.K. Lewis, H. Kalish, J.A. Frank, *Radio*. 229 (2003) 838
- [2] U. Häfeli, W. Schütt, J. Teller, M. Zborowski, *Scientific and clinical applications of magnetic carriers*, Plenum Press, New York, 1997.
- [3] P. Reimer, R. Weissleder, *Radio*. 36(1996) 153.
- [4] E.X. Wu, H. Tang, K.K. Wong, J. Wang, *J. Magn. Reson. Imag.* 19 (2004) 50.
- [5] Y.-Q. Wanga, H.-M. Zhangb, G.-C. Zhanga, S.-X. Liub, Q.-H. Zhou, Z.-H. Feia, Z.-T. Liua, *Int. J. Biol. Macromol.* 41(2007) 243.
- [6] J.Q. Lu, F. Jin, T.Q. Sun, X.W. Zhou, *Int. J. Biol. Macromol.* 40 (2007) 299.

**Local Perturbations in the 001 (Σ_u^+) Vibrational State of BeD₂**

Alireza Shayesteh

School of Chemistry, College of Science, University of Tehran, Tehran, Iran

Email: shayesteh@khayam.ut.ac.ir

Keywords: Infrared Spectrum, BeD₂, Local Perturbations, Σ - Φ Interaction.**1. Introduction**

BeH₂ is a famous molecule. With only six electrons, BeH₂ is the smallest neutral polyatomic molecule, and it is a favorite target molecule for ab initio theoretical calculations. High quality experimental data on BeH₂ can serve as benchmarks for testing the accuracy of ab initio methods. The first observation of gaseous BeH₂ and BeD₂ was reported in 2002 by Bernath and coworkers [1], who recorded high resolution infrared emission spectra of BeH₂ and BeD₂ in the ν_3 (antisymmetric stretching) region. Analyses of the ν_3 fundamental band and several hot bands of BeH₂ and BeD₂ were carried out by the same research group and reported by Shayesteh et al. [2,3]. They also found small local perturbations in the 001 (Σ_u^+) rotational levels at high J values, caused by the nearby 030 (Σ_u , Σ_u) levels. Rotational analysis and deperturbation of the 001 (Σ_u^+) state of BeD₂ is reported here.

2. Methods

High rotational levels of the 001 (Σ_u^+) state of BeD₂ are perturbed locally by the nearby 030 vibrational level, which has 03¹0 (Σ_u) and 03³0 (Σ_u) states. Rotational levels of the 001 (Σ_u^+) state with $J \leq 30$ are shifted towards higher energies, whereas the $J \geq 31$ levels are shifted towards lower energies. Although the magnitudes of these perturbations are relatively small, i.e., the largest energy shifts being +0.24 cm⁻¹ at $J = 30$ and -0.11 cm⁻¹ at $J = 31$, they are definitely significant because the absolute accuracy of the observed spectral line positions is ± 0.002 cm⁻¹. The perturbation pattern observed in BeD₂ clearly indicates that the perturbing state has a larger effective B_{vJ} value and a smaller vibrational energy. The effective B_{vJ} values of the 03¹0 (Σ_u) and 03³0 (Σ_u) states can be estimated using the B_{vJ} values of the 000, 01¹0, 02⁰0 and 02²0 states [2,3]. The 03¹0 (Σ_u) and 03³0 (Σ_u) states have *e* and *f* parity components, but only the *e* parity levels can interact with the 001 (Σ_u^+) rotational levels. Due to the large rotational ℓ -type doubling in the 03¹0 (Σ_u) state [4], the effective B_{vJ} value of its *e* parity component becomes smaller than that of the 001 (Σ_u^+) state. In addition, because the vibrational g_{22} constant of BeD₂ is larger than the B_{vJ} values [3], the rotational levels of 03³0 (Σ_u) lie above those of the 03¹0 (Σ_u) state. Therefore, the 03³0 (Σ_u) state is responsible for the observed perturbations in the 001 (Σ_u^+) state. A 3×3 Hamiltonian matrix was constructed for the *e* parity levels of 001 (Σ_u^+), 03¹0 (Σ_u) and 03³0 (Σ_u) states. The 03¹0 (Σ_u) state was included in the matrix because it interacts with the 03³0 (Σ_u) state through rotational ℓ -type resonance [4], and thus has an indirect effect on the state of interest (001, Σ_u^+). The vibrational energy difference between the 03¹0 and 03³0 states is equal to $8g_{22}$ based on a quadratic expression for vibrational energy [2]. The Hamiltonian matrix for rotational ℓ -type resonance between Σ and Φ states was derived by Maki and Lide [4]. After parity transformation and including the Σ_u^+ (*e*) state, the following 3×3 Hamiltonian matrix [5] was obtained for the *e* levels:

$$\mathbf{H} = \begin{pmatrix} E_{\Sigma}^0(001) & -W_{03} & 0 \\ -W_{03} & E_{\Phi}^0 & W_{31} \\ 0 & W_{31} & E_{\Pi}^0 + W_{11} \end{pmatrix}. \quad (1)$$

The matrix element connecting the Σ_u^+ and Σ_u states was fixed to zero because the perturbations in the 001 (Σ_u^+) state are caused by the Σ_u state. The following expressions, in which $x = J(J+1)$, were used for the above matrix elements:

$$E_{\Sigma}^0(001) = G_{001} + B_{001}x - D_{001}x^2 + H_{001}x^3 \quad (2)$$

$$E_{\Phi}^0 = G_{\Phi} + B_{\Phi}(x-9) - D_{\Phi}(x-9)^2 \quad (3)$$

$$E_{\Pi}^0 = (G_{\Phi} - 8g_{22}) + B_{\Pi}(x-1) - D_{\Pi}(x-1)^2 \quad (4)$$

$$W_{11} = qx + q_Dx^2 \quad (5)$$



$$W_{31} = \frac{\sqrt{3}}{2} (q + q_D x) [(x-2)(x-6)]^{1/2} \quad (6)$$

$$W_{03} = K_{03} [x(x-2)(x-6)]^{1/2}. \quad (7)$$

The rotational energy expressions used for the \square_v ($\ell = 3$) and \square_v ($\ell = 1$) states in Eqs. (3)-(4) are power series in $[J(J+1) - \ell^2]$, in which ℓ is the vibrational angular momentum quantum number. The J -dependence of W_{03} , which connects the \square and \square states, was determined by applying the $(\hat{J}^+)^3$ operator (in the molecular frame) to the \square state basis function. The purpose of this perturbation analysis was to obtain the unperturbed constants for the 001 (\square_v^+) state, and to estimate the vibrational energy of the 03³0 (\square_v) state.

3. Results and Discussion

All rotational lines of the 001→000 and 002→001 bands of BeD₂ were fitted using the Hamiltonian matrix in Eq. (1) for the 001 levels, while the constants of the 000 and 002 states were fixed to the values reported in Ref. [2]. A few more rotational lines of the 001→000 band (up to $J' = 35$) were assigned and added to the data used in Ref. [2]. Rotational constants (B , D) and the ℓ -type doubling constants (q , q_D) of the 03¹0(\square_v) and 03³0(\square_v) states were fixed to the values estimated by extrapolating the 000, 01¹0, 02⁰0 and 02²0 constants. In order to estimate the $B_{[v]}$ and $D_{[v]}$ values as accurately as possible, a quadratic expression was used [5]. The ℓ -type doubling constants $q_{[v]}$ and $q_{D[v]}$ were estimated using the corresponding constants of the 010 and 020 levels, and by assuming a linear vibrational dependence. The vibrational constant g_{22} was also fixed to the value reported in Ref. [3] for BeD₂. The least-squares fitting resulted in determination of G_{\square} (vibrational energy of the 03³0 state), K_{03} (off-diagonal matrix element between \square and \square states), and the unperturbed constants of the 001 (\square_v^+) state of BeD₂ (Table 1). The constants of Table 1 differ slightly from those reported in Ref. [2] for the 001 (\square_v^+) state, but are more reliable because the effects of perturbations have been accounted for by the K_{03} constant. The constants of Table 1 can reproduce all the observed spectral line positions within their experimental uncertainties of ± 0.002 cm⁻¹.

Table 1. Unperturbed constants (in cm⁻¹) for the 001(\square_v^+) state of BeD₂; the numbers in parentheses are 1 \square uncertainties in the last quoted digits. The vibrational energies G_{001} and G_{\square} are relative to the ground state vibrational energy (G_{000}).

G_{001}	B_{001}	$10^5 D_{001}$	$10^{10} H$	$10^5 K_{03}$			
1689.6812(5)	2.330234(5)	2.5715(10)	3.14(6)	2.15(1)			
G_{\square}	B_{\square}	$10^5 D_{\square}$	g_{22}	B_{\square}	$10^5 D_{\square}$	$10^2 q$	10^6
1652.62(1)	2.38017	2.805	2.5276	2.38155	2.899	–	1.13

4. Conclusion

The vibrational energy of the 03³0 state (G_{\square}) and the \square - \square interaction constant (K_{03}) were determined to be 1652.62(1) and 2.15(1)×10⁻⁵ cm⁻¹, respectively. The off-diagonal matrix element W_{03} is zero for $J < 3$, and it increases rapidly with J . At the highest observed rotational level of BeD₂ ($J = 35$), W_{03} is about 0.95 cm⁻¹. Although the vibrational energy of the 03³0 state (G_{\square}) has a statistical uncertainty of about 0.01 cm⁻¹ in Table 1, an absolute accuracy of about ± 0.1 cm⁻¹ is estimated for this energy, because several constants in the fit were fixed to the extrapolated values.

References

- [1] P.F. Bernath, A. Shayesteh, K. Tereszchuk, R. Colin, Science 297 (2002) 1323.
- [2] A. Shayesteh, K. Tereszchuk, P.F. Bernath, R. Colin, J. Chem. Phys. 118 (2003) 3622.
- [3] A. Shayesteh, P.F. Bernath, J. Chem. Phys. 124 (2006) 156101.
- [4] A.G. Maki, Jr., D.R. Lide, Jr., J. Chem. Phys. 47 (1967) 3206.
- [5] A. Shayesteh, I.E. Gordon, D.R.T. Appadoo, P.F. Bernath, Phys. Chem. Chem. Phys. 7 (2005) 3132.



Protonated Benzene Dimer: An Experimental and Ab Initio Study

Shamik Chakraborty², Reza Omidyan^{1*}, Ivan Alata², Claude Dedonder², Michel Broquier², and Christophe Juvet²

1) Department of Chemistry, Isfahan University of Technology, Isfahan, Iran

(Email: omidyan@ch.iut.ac.ir)

2) Centre Laser de l'Université Paris Sud (EA. 4127), Bât. 106, Univ. Paris-Sud 11 - 91405 Orsay Cedex, France

1. Introduction

The characterization of structure, dynamics, and electronic properties of protonated molecules, mainly organic molecules, is of fundamental interest in physical organic chemistry. This transient species is important to study for understanding the dynamics and selectivity of chemical processes. As a first study we have investigated a simple system, the protonated benzene dimer, and we report the first observation of its excitation spectrum that is strongly perturbed as compared to the excitation spectrum of neutral benzene dimer. The neutral benzene dimer has been the subject of many investigations [1,2]. Indeed the formation of the dimer in the neutral system has the effect of breaking the D_{6h} symmetry, which allows the S_1 - S_0 origin transition to be observed. The spectral shift measured on the origin as well as on the vibronic transitions is very small as expected for a van der Waals interaction [3]. In this paper we report the S_1 - S_0 electronic excitation spectrum of protonated benzene dimer (BBH^+) compared with the benzene dimer radical cation (BB^+) spectrum in the wavelength range of 413-600 nm. Experimental results are supported by *ab-initio* quantum chemical computations.

2. Experimental details

Protonated benzene dimer and benzene dimer radical cation are produced in a pulsed high voltage electric discharge source. The gas mixture consists of 50% of He and 50% of H_2 seeded with benzene vapor (benzene from Sigma-Aldrich is used without any further purification). The buffer gas mixture is sent through the benzene kept in a container outside the chamber. Benzene has a very high vapor pressure and its concentration during the experiment is controlled by cooling the sample container with ice-water. The typical stagnation pressure is about 2 bars. The typical working pressure in the source chamber was 1×10^{-5} mbar, and in the TOFMS chamber it was 2×10^{-6} mbar.

The ions produced in the source chamber are pulsed extracted into a reflectron time of flight mass spectrometer. The mass spectrometer is in the perpendicular direction to the molecular beam axis. A reasonably good mass resolution is achieved with a field free time of flight distance of 157 cm before the channel plate detector. In this condition, two masses 156 au for benzene dimer radical cation (BB^+) and 157 for protonated benzene dimer cation (BBH^+) are well resolved. Mass selected Laser induced photo-fragmentation is carried out using a 10 Hz, nanosecond OPO laser (Euroscan). The third harmonic (355 nm) of the Nd^{+3} :YAG laser (Quintel YG981C) laser pumps the BBO crystal of the OPO laser delivering a tunable wavelength range of 413 to 670 nm with an output power in the range of 10 to 15 mJ.

3. Calculations

Ab initio calculations for protonated benzene dimer have been performed with the TURBOMOLE program package [4]. The equilibrium geometry of the protonated benzene dimer in its closed-shell singlet ground electronic state (S_0) has been determined with the MP2 method. Excitation energies and equilibrium geometry of the lowest excited singlet state have been determined at the CC2 level. All calculations were performed with the correlation-consistent polarized valence double- ζ (cc-pVDZ), with some comparison with the TZVP basis set. The basis set superposition error (BSSE) is obtained using the counterpoise method.

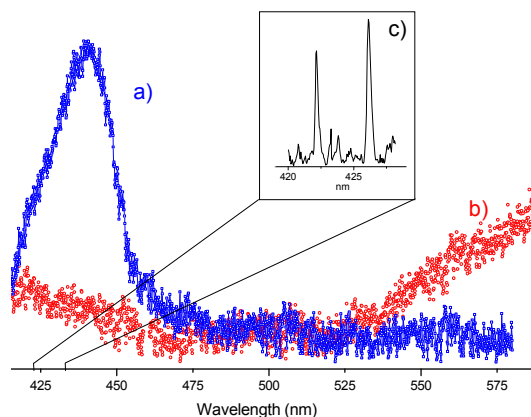
4. Results and discussion

The photo-dissociation spectrum of BBH^+ recorded in the same wavelength range using the OPO laser (Figure 1a) shows a marked difference compared to the BB^+ excitation spectrum. The excitation spectrum of BBH^+ displays only one broad absorption band in the 400-490 nm spectral range. We have scanned up to 670 nm in the lower energy side but could not observe any more absorption. As it can be seen in Figure 1a, no vibrational progression is observed. One reason could be the insufficient cooling of the sample. The possibility of a contribution from hot bands to the congestion of the spectrum was checked by repeating the experiment at different backing pressures (from 0.5 to 4 atm), gas composition (He/ H_2 50/50 or

(Ar/H₂ 50/50) and we could not see any structured band. In similar experimental conditions (1.5 atm, He/H₂, 50/50), protonated benzaldehyde and its complex with water have been observed with structured vibronic bands of widths smaller than 10 cm⁻¹ (Figure 1c).

It is however difficult to ascertain whether the spectral congestion is intrinsic of the system or is due to temperature. The simultaneous excitation of different ground state isomers of BBH⁺ could also be a reason for this structure less spectral behavior.

Figure 1: Photo-dissociation spectra recorded in the 415-600 nm wavelength range a) photo-fragmentation spectrum of protonated benzene dimer BBH⁺ b) photo-fragmentation spectrum of the radical cation BB⁺ presented for comparison. c) In the insert, part of the protonated benzaldehyde photo-fragmentation spectrum to show that in our experimental conditions structured spectra of cold cations can be observed.



The observed transition presents a broad absorption in the range of 415 to 500 nm, in between the calculated adiabatic and vertical transition, with a slow rising edge. Calculation shows that a large change in geometry occurs between the optimized ground state structure and the optimized excited state for both isomers. The 0-0 transition probably cannot be excited and the Franck Condon factors should be large enough only for high vibrational levels. This system being a cluster, low frequency modes are present and the density of levels should be quite large in the Franck Condon accessible region and thus the spectrum should probably be intrinsically congested. It should be noticed that the BBH⁺ absorption seems analogous to the visible absorption (in the 420- 550 nm range) of the excimer state of the benzene dimer evidenced by Saigusa [5] and assigned to transition from the excimer state to a charge transfer state. In the neutral benzene dimer, the visible absorption corresponds to a transition in the excited state manifold, while in BBH⁺ the visible absorption starts from the ground state.

5. Conclusion

The first transition in the protonated benzene dimer lies around 450 nm and is largely red shifted in comparison with the neutral dimer (isoelectronic) transition. This transition is also strongly red shifted with respect to the protonated benzene transition. This effect is due to the charge transfer character of the first excited state, where an electron of the π orbital localized on the neutral benzene moiety is transferred to a π^* orbital on the protonated benzene part [6].

References

- [1] G. Gregoire, C. Jouvét, C. Dedonder, A. L. Sobolewski. *Chem. Phys.* 2006, **324**, 398-404.
- [2] K. C. Janda, J. C. Hemminger, J. S. Winn, S. E., Novick, S. J. Harris, W. Klemperer. *Chem. Phys.* 1975, **63**, 1419-1421.
- [3] V. Spirko, O. Engvist, P. Soldan, H. L. Selzle, E. W. Schlag, P. Hobza. *J. Chem. Phys.* 1999, **111**, 572-582.
- [4] R. Ahlrichs, M. Bar, M. Haser, H. Horn, C. Kolmel. *Chem. Phys. Lett.* 1989, **162**, 165-169.
- [5] T. Hirata, H. Ikeda, H. Saigusa. *J. Phys. Chem. A* 1999, **103**, 1014-1024.
- [6] S. Chakraborty, R. Omidyan, I. Alata, I. B. Nielsen, C. Dedonder, M. Broquier and C. Jouvét, *J. Am. Chem. Soc.*, 2009, **131**, 11091.

Cis-enol conformational stability, Molecular structure, and intramolecular hydrogen bonding of 5,5-Dimethyl hexane-2,4 dione. A density functional theoretical study

a. kanaani^a, M. Vakili^b, S.F. Tayyari^c, S. Salemi^d

^a School of Chemistry, Damghan University of Basic Sciences, Iran

^b Department of Chemistry Sabzevar Tarbiat Moallem University, Iran

^c Department of Chemistry, University of Ferdowsi, Mashhad 91775-1436, Iran

^d Department of Chemistry, Sabzevar Tarbiat Moallem University, Iran

E-mail: a.kanaani@yahoo.com

Keywords: 5,5-Dimethyl hexane-2,4dione; β -Diketone; Conformational analysis; Intramolecular hydrogen bond; Density Functional Theory

1. Introduction

Over the years, the keto-enol tautomeric equilibrium, the structure of both keto and enol forms, and the nature of the strong intramolecular O-H...O hydrogen bond have been the subjects of intensive study [1-4]. The position of the keto-enol equilibrium in this class of compounds differs according to the electronic characteristics of the substituents at α and β positions, the temperature, and the nature of the solvents. The hydrogen bond formation, which stabilizes the chelated enol forms of β -diketones leads to an enhancement of the π -electron resonance conjugation that causes a marked tendency for the bond order equalization of the valence bonds in the resulting six-membered chelated ring. The aim of the present paper is a cis-enol conformational analysis of 5,5-Dimethyl hexane-2,4 dione (DIMHD) in order to obtain detailed information on the geometrical parameters, relative stabilities and intramolecular hydrogen bond strength (IHB).

2. Experimental and Method of Analysis

DIMHD compound purchased from Alfa Aesar chemical company. D₂-DIMHD was prepared by mixing the non-deuterated sample with D₂O. The FT-Infrared spectra were obtained in the range of 4000-500 cm⁻¹ on a Bomem MB-154 Spectrophotometer. All quantum calculations were carried out with the GAUSSIAN 03 software package. All possible cis-enol conformers of DIMHD were fully optimized at the B3LYP level of theory with the 6-31G** and 6-311++G** basis sets and at MP2, B3PW91 and G96LYP with 6-31G** basis set.

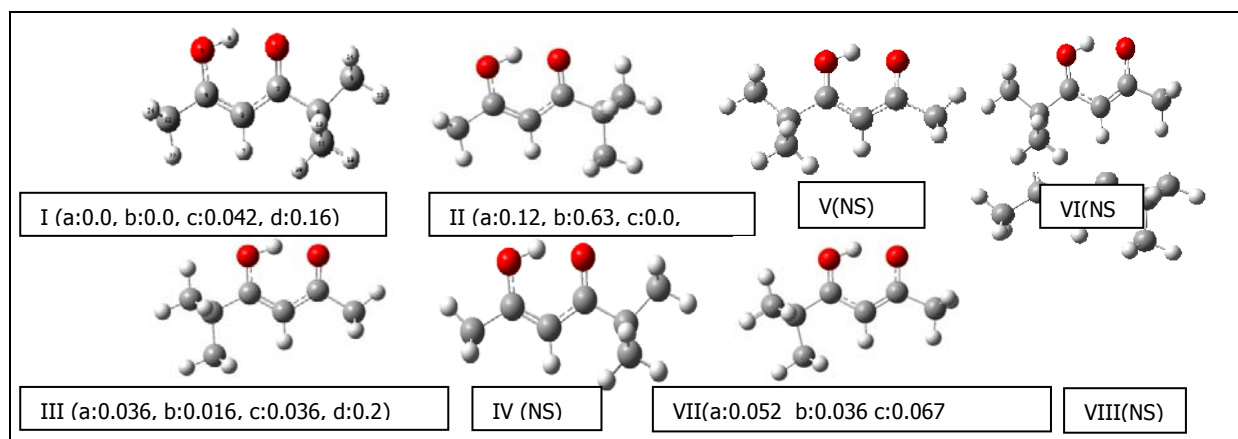


Figure 1: Numbering, relative stability and Possible chelated cis-enol tautomers of DIMHD (a: B3LYP/6-311++g**. b: MP2, c: B3PW91 and d: G96LYP at 6-31G** basis set).

3. Results and Discussion

From a theoretical point of view, 8-cis-enol forms can be drawn for DIMHD. These four conformers, the atom numbering of the system, and their relative stabilities (in kcal/mol) are shown in Fig 1. The DFT (B3LYP, B3PW91 and G96LYP) and MP2 calculations show that only 4 conformers of these are stable and there is a little difference between their energy and dipole moments.

Bond distance (Å)	DIMHD					AA
	I	II	III	IV	Aved	
C ₂ —O ₁	1.246	1.250	1.246	1.248	1.248	1.246
C ₂ —C ₃	1.447	1.441	1.444	1.442	1.443	1.444
C ₃ —C ₄	1.370	1.374	1.372	1.374	1.373	1.370
C ₄ —O ₅	1.326	1.322	1.328	1.326	1.325	1.326
O ₅ —H ₆	1.003	1.009	1.005	1.008	1.007	1.003
H ₆ —O ₁	1.623	1.591	1.611	1.595	1.601	1.633
O...O	2.534	2.512	2.529	2.519	2.522	2.544
Bond angles (°)						
C ₃ _C ₄ _O ₅	122.20	122.09	120.84	120.74	121.22	121.82
O ₁ _H ₆ _O ₅	148.58	149.26	149.63	149.92	149.54	149.19
O C C(Me) ₃	119.83	117.62	119.67	119.02	119.03	119.9
O ₅ _C ₄ _C ₂₁	113.70	113.94	113.33	113.43	113.55	113.8
Dihedral angles (°)						
Φ H ₇ C ₃ C ₂ C ₈	-0.005	-0.012	0.126	-1.48	-0.68	-0.305
Φ H ₇ C ₃ C ₄ C ₂₁	-0.015	-0.001	-0.035	0.15311	0.051	-0.015

Table 1: The geometrical parameters of the cis-enol forms of DIMHD and AA and E_{HB} calculated at the B3LYP/6-311++G**.

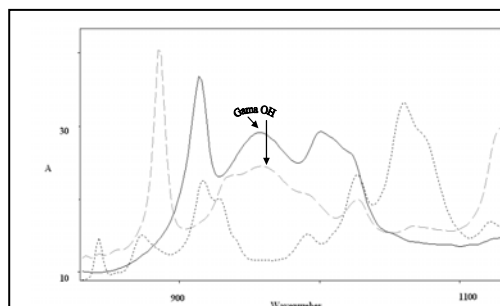


Fig. 2: The IR spectra of AA (—) DIMHD (---) and D₂-DIMHD (···) in neat liquid in the below 1000 cm⁻¹ region.

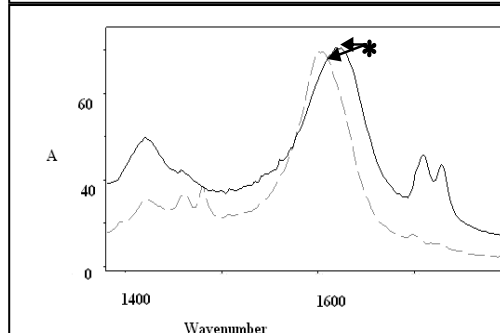


Fig. 3: The IR spectra of DIMHD (···) and AA (—) in neat liquid at the 1600 cm⁻¹ region (* are $\nu_a C=C-C=O$ region).

The structure of IV, V, VI and VIII is not stable, and under optimization turn to the conformers I, III, III, II respectively. Molecular geometry, the hydrogen bond energies, E_{HB} (the energy difference between the chelated cis-enol and non-chelated trans-enol rotamers) of DIMHD and AA are shown in Table 1. According to Table 1, Comparing coordinates for DIMHD and AA shows that upon substitution of t-But group in the β positions and because of higher steric effect of this group, the bond angles O1C2C8 and O5C4C21 in DIMHD are smaller than those of AA. This fact decreases the O...O, O...H distance and increases the E_{HB} strength, O-H bond length, and OHO bond angle of DIMHD in comparison with AA (Table 1), which suggests the intramolecular hydrogen bond in DIMHD, is considerably stronger than that in AA.

The IR spectrums of DIMHD and AA for ν_{OH} and $\nu_a C=C-C=O$ regions are shown in Fig. 2-3. According to IR spectrum, the ν_{OH} and ν_{OH} bands of DIMHD appear in 960 and 2607 cm⁻¹ and the corresponding bands for AA appear at about 952/2750 cm⁻¹.

These regions indicate that IHB -strength in DIMHD is considerably stronger than that AA.

4. Conclusion

The comparison of some vibrational frequencies like ν_{OH} , ν_{OH} and $\nu_a C=C-C=O$ mode and the calculated geometrical parameters confirm that substitution of t-But in β positions with the CH₃ group increase the IHB strength of the hydrogen bond.

References

- [1] S.F. Tayyari, T. Zeegers-Huyskens, J.L. Wood, Spectrochim. Acta A 35 (1979) 1266.
- [2] S.F. Tayyari, J.S. Emampour, M. Vakili, A.R. Nekoei, H. Eshghi, S. Salemi, M. Hassanpour, J. Mol. Struct. 794 (2006) 204.
- [3] S.F. Tayyari, A.R. Nekoei, M. Vakili, Y.A. Wang, J. Theor. Comp. Chem. 5 (2006) 647.
- [4] M. Vakili, H. Miremad, S. Salemi, A-R. Nekoei, paper submitted to 13th Iran Physical Chemistry Seminar.

Synthesis, structure and vibrational assignment of bis(4-amino-3-penten-2-ono) nickel(II)

M. Jamialahmadi^a, S. F. Tayyari^a, M. H. Habibi^b, M. yazdanbakhsh^a

^aChemistry Department, Ferdowsi University of Mashhad, Mashhad, 91775-1436, Iran

^bChemistry Department, Esfahan University, Esfahan

1. Introduction

The late transition metals can be stabilized by heterodonor ligands with multiple coordination modes and give mono- and di-nuclear complexes. In particular, the use of such ligands is of fundamental importance to the development of late transition metal complexes bearing N,O mixed ligands[1-3].

Ni is known to be an excellent catalyst for many processes. NiO films also have been extensively studied for applications of their optical, electrical, and magnetic properties. Bis-(4-amino-3-penten-2-ono) nickel(II) (hereafter $\text{Ni}(\text{APO})_2$) is used as a precursor for growing Ni[4] and NiO films.

According to Gurr's study[5] the unit cell of $\text{Ni}(\text{APO})_2$ is orthorhombic, space group $Ccca$, and the unit cell Dimensions are 16.7 X 15.1 X 13.5. In this research, the complex was prepared in high purity and experimental data were compared with theoretical calculation results.

2. Method of analysis

APO ligand was synthesized according to Lacey [6] . This ligand was added to an aqueous solution of nickel(II) acetate and then a precipitate of bis(4-aminopent-3-en-2-onato)nickel(II) was obtained.

The IR spectra were recorded on a Bomem B-154 Fourier transform spectrophotometer in the region 600-4000 cm^{-1} by averaging 20 scans with a resolution of 2 cm^{-1} . The spectra were measured as KBr pellets.

In this study, the molecular equilibrium geometry, harmonic force field, and vibrational transitions of $\text{Ni}(\text{APO})_2$ were computed with the GAUSSIAN 03 software system [7] by using a selection of modern density functionals, using 6-31G** and 6-311++G* basis sets.

3. Results and discussion

The optimized geometry parameters of trans $\text{Ni}(\text{APO})_2$ are summarized in Table 1 and its geometry is shown in Fig. 1. Fig. 2 shows the experimental IR spectrum of $\text{Ni}(\text{APO})_2$. Some of theoretical and experimental frequencies and relative intensities of IR and Raman are given in figure3.

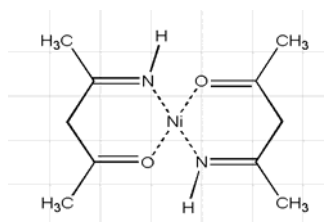


Fig. 1 Trans configuration of $\text{Ni}(\text{APO})_2$

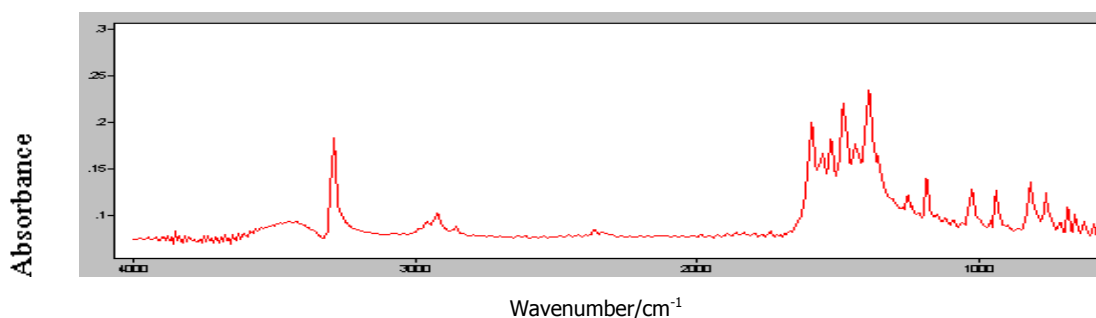


Fig. 2 IR spectrum of $\text{Ni}(\text{APO})_2$ (experimental)



4. Conclusion

According to the theoretical DFT calculations, trans configuration is more stable than cis (about 7.05Kcal/mol). The calculated bond lengths of C-O, C6-C7, and C6-C15 (table 1) are longer and C-N and C5-C11 are shorter than corresponding ones in APO[10]. This results show that resonance in Ni(APO)₂ has increased relative to APO. The Cu-O distance in Ni(APO)₂ is 1.955 Å that is longer and, therefore, weaker than the similar bond in Ni(acac)₂ [9].

The calculated frequencies are slightly higher than the observed values for the majority of the normal modes. Two factors may be responsible for the discrepancies between the experimental and computed spectra of Ni(APO)₂. The first is caused by the environment. DFT calculations have been done at the gas phase, and experimental data are obtained from solid complex. The second reason for this discrepancy is the fact that the experimental values are anharmonic frequencies while the calculated values are harmonic frequencies.

References

- [1] . Tjaden EB, Swenson DC, Jordan RF, Petersen JL. *Organometallics* 1995; 14: 371.
- [2] . Eric FC, Todd RY, Jason IH, Andrew WW, Grubbs RH. *Chem. Commun.* 2003; 18: 2272.
- [3] . Chang BS, Young HK, Bun YL, Yongkwan D, Hoseop Y. *Organometallics* 2003; 22: 4272.
- [4] . Becht, Gallus, Hunziker, Atamny, and Dahmen, *Journal de Physique IV*, 1995; 5: 465.
- [5] . G. E. GURR, *Inorganic Chemistry*, 1964; 3: 614.
- [6] . M. J. Lacey, *Aust. J. Chem.*, 1970; 23: 841.
- [7] Gaussian 03, Revision B.05, M. J. Frisch et al, Gaussian, Inc., Pittsburgh PA, 2003.



Calculation of absorption and resonance Raman cross sections of acetophenone in cyclohexane solution using displaced-distorted harmonic oscillator model

M. Dehestani¹, Z. Rahmani*¹

¹Department of Chemistry, University of shahid Bahonar of Kerman, Iran.

Correspondence to: zoha.rahmani@yahoo.com, phone

Keywords: density functional theory, resonance Raman cross sections, vector of dimensionless displacement, absorption spectrum

1. Introduction

Acetophenone (AP) is the simplest aromatic ketone. Its gas phase absorption spectrum exhibits three broad peaks centered at 325, 237 and 230 nm in the region of 210-380 nm (called A-, B-, and C-band), and are assigned, respectively as the $S_0 \rightarrow S_1$, $S_0 \rightarrow S_2$ and $S_0 \rightarrow S_3$ transitions. In this work we have performed the calculation of the absorption spectrum, and resonance Raman spectra for seven active vibrational modes of AP assuming displaced-distorted harmonic oscillator using the time-correlation function formalism.

2. Theoretical method

The multidimensional time domain integrals that arise in the calculation absorption and resonance Raman cross sections, where the potential-energy surfaces of the ground state and the excited state S_3 were assumed to be displaced, and distorted harmonic oscillators, were evaluated using the method developed by Islampour et al. [2]. The time-correlation function formalism have also been used to calculate absorption, resonance Raman cross sections and excitation profiles of trans-stilbene [3] and ClO_2 molecules [4].

The Vector of dimensionless displacement in the equilibrium positions of nuclei in the excited and the ground states (\mathbf{D}) were directly calculated from the expressions [5]

$$\mathbf{D} = 0.1723[\mathbf{M}\mathbf{P}'\mathbf{V}^{-1/2}]^{\dagger}\mathbf{R} \quad (1)$$

with

$$\mathbf{R} = \mathbf{Z} \mathbf{R}_{\text{eq}} - \mathbf{R}'_{\text{eq}} \quad (2)$$

where \mathbf{M} is the $3N \times 3N$ diagonal matrix with the atomic masses on the diagonal, \mathbf{P}' is the $3N \times 3N-6$ matrix of the GAUSSIAN program normal mode output the final state in the transition, respectively. \mathbf{V}' is a $3N-6 \times 3N-6$ diagonal matrix of the each mode reduced masses. \mathbf{Z} is a unit matrix for most molecules of C_{2v} or higher symmetry but for AP, \mathbf{Z} is the $3N \times 3N$ block diagonal matrix. \mathbf{R} is the N -dimensional vector of the change in equilibrium geometry between the lower (\mathbf{R}_{eq}) to the upper (\mathbf{R}'_{eq}) electronic state in Cartesian coordinate on the molecular center of mass.

3. Computational methods

Density functional theory (DFT) calculations were done in order to find the optimized geometry and vibrational frequencies as well as the electronic transition energies for AP. Complete geometry optimization and vibrational frequency computations were computed at the PBE/6-31+G(d, p) level, while the electronic transition energies were calculated by CIS/6-31+G(d, p) method. All of the density functional theory calculations were carried out in GAUSSIAN 03 program.

4. Results and discussion

The symmetry of AP molecule is C_s . It has 45 normal modes, in which, 30 and 15 modes are classified into a' and a'' , respectively. In terms of the C_s point group selection rules, the modes a' are Raman active, so the bands usually observed in the Raman spectra of AP are due to modes a' . In order to explore the effects of displaced and distorted of the potential surfaces, we consider the model of displaced-distorted harmonic potential surfaces for AP using its seven vibrational modes.

We have used the dimensionless displacements obtained from Eqs. (1) and (2), zero-zero transition frequencies Ω_{ba} , homogeneous width Γ_{ba} , and inhomogeneous width of the distribution (θ) to calculate the absorption and resonance Raman spectra. These parameters were readjusted several times to obtain the best simultaneous fit to the absorption spectrum and the Raman cross sections. The results are shown in Table 1.

Fig. 1 shows comparison of the computed absorption spectrum (dotted line) with the UV absorption spectrum of AP in cyclohexane solution (solid line) with excitation wavelengths for the resonance Raman experiments indicated above the spectrum. Fig. 2 shows comparison of the experimental resonance Raman spectra of AP in 228.7, 239.5, and 245.9 nm excitation wavelengths with calculated resonance Raman cross-sections [1].

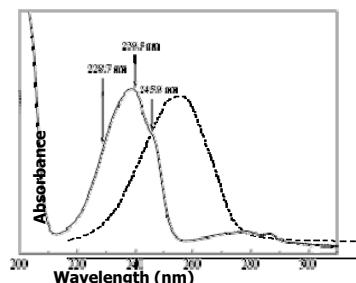


Fig. 1 comparison of the computed absorption spectrum AP in cyclohexane solution (dotted line) with the UV absorption spectrum of (solid line) with excitation wavelengths for the resonance Raman experiments indicated above the spectrum.

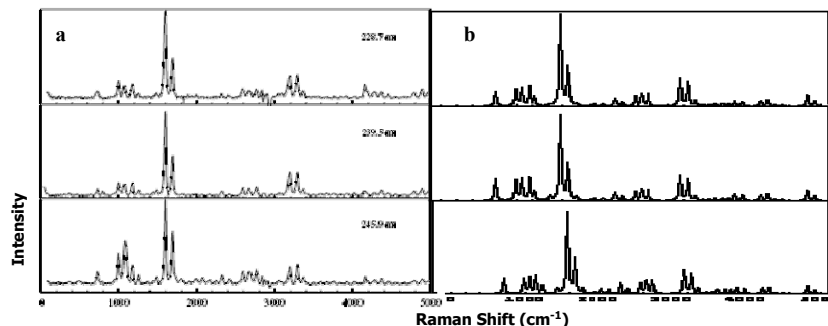


Fig. 2 calculated resonance Raman cross-sections of AP in cyclohexane solution (a) and experimental resonance Raman spectra of AP (b) in 228.7, 239.5, and 245.9 nm excitation wavelengths.

Table 1. The parameters used in calculating absorption and resonance Raman cross section for AP

mode	D
ν_8	0.019
ν_9	0.029
ν_{17}	0.012
ν_{18}	-0.021
ν_{21}	0.022
ν_{23}	-0.023
ν_{25}	-0.035
$\Omega_{ba}=40000 \text{ cm}^{-1}$, $\Gamma_{ba}= 370 \text{ cm}^{-1}$, $\theta=460 \text{ cm}^{-1}$	

5. Conclusion

In the present study, attempts have been made to calculate absorption spectrum, resonance Raman cross sections of the AP molecule in cyclohexane using a displaced-distorted harmonic model. We should mention that no changes in frequencies of ground and excited states have been considered to date in the previous calculations of electronic spectra for this molecule.

References

- [1] Y. Ma, K. M. Pei X. Zheng and H. Li, Chem. Phys. Lett. **2007**, 449, 107.
- [2] R. Islampour, M. Hayashi, S. H. Lin, J. Raman Spectrosc. **1997**, 28, 331.
- [3] M. Dehestani, R. Islampour, Int. J. Quantum Chem. **2005**, 103, 119.
- [4] M. Dehestani, J. Raman Spectrosc. **2009**, 40, 696.
- [5] D. W. Kohn, E. S. J. Robles, C. F. Logan, P. Chen, J. Phys. Chem. **1993**, 97, 4936.



**Conformation, Structure, Intramolecular H-bonding, and Vibrational Assignment of
1-(2-thienyl)-4,4,4-trifluorobutane-1,3-dione**

Abdo-Reza Nekoei ^a, Sayyed Faramarz Tayyari ^b and Mohammad vakili ^c

^a Department of Chemistry, Shiraz University of Technology, Shiraz, 71555-313, Iran (E-mail: nekoei@ymail.com)

^b Department of Chemistry, Ferdowsi University of Mashhad, Mashhad, 91775-1436, Iran

^c School of Chemistry, Damghan University of Basic Sciences, Damghan, P.O. Box 36715-364, Iran

Introduction

The Intramolecular hydrogen bond (IHB) strength of a β -dicarbonyl plays very important roles in stabilities of their different conformers and also in their chemical, physical and biological properties. Over the years, the keto-enol tautomeric equilibrium, the structure of both keto and enol forms, and the nature of the strong intramolecular O—H...O hydrogen bond in the enol forms of β -dicarbonyls, and also their spectra properties were the subjects of intensive studies using a large variety of different methods, including IR, Raman, microwave, and NMR spectroscopies, X-ray, electron and neutron diffraction measurements, and quantum-chemical calculations using variety of techniques [1,2].

In the present work, 1-(2-thienyl)-4,4,4-trifluorobutane-1,3-dione, known as thenoyltrifluoroacetone (TTFA, see Fig. 1) compound which has a wide range of applications in extracting lanthanides, actinides, and transition elements and also in medicine, has been studied as a β -dicarbonyl with two β -substituted groups having different electron-withdrawing, steric, and resonance effects. In this molecule, as other β -dicarbonyls, the electronic characteristics of the substituents, temperature, and the nature of the surrounding media have essential influences on IHB strength and the position of the keto-enol equilibrium [1]. Conformational stabilities in gaseous and different solution media, geometrical structure, rotational motion of the thienyl group, the barrier height for proton transfer and the IHB strength of TTFA have been theoretically investigated. The vibrational spectroscopy has been used as the empirical witness since it is a highly sensitive technique to experimentally examine the hydrogen bonding and interaction with solvents. Also a full and clear vibrational assignment of TTFA is presented by considering the theoretical calculations and IR and Raman spectra of the compound and its deuterated analogue.

Method of Analysis

All quantum calculations were carried out with the GAUSSIAN 03 software package, applying B3LYP method of the modern density functional theory (DFT) and MP2 method, using variety of basis sets. Besides, since the stable conformers in solution may differ from gaseous and solid states, the self-consistent Onsager reaction field model was used to study the solvent effects on the four most stable chelated cis-enol tautomers of TTFA at B3LYP/6-311++G** level of DFT theory. The rotational barrier of the thienyl ring and the frequencies calculations were performed at the B3LYP level using 6-311++G** and 6-311G** basis sets, respectively. The assignment of the calculated wavenumbers is aided by the animation option of GaussView 3.0 graphical interface for Gaussian programs.

Results and Discussion

Among the forty different tautomers of TTFA, only four cis-enol conformers have the six-member chelated ring of the IHB, which are illustrated in Fig. 1. The calculated relative energies clearly suggest that these chelated cis-enol conformers are so stable that the presence of other conformers (non-chelated enol and keto forms) in significant amounts is unlikely. Table 1 shows that all chelated A and B conformers of TTFA have nearly the same stabilities in the gaseous phase at B3LYP, but MP2 calculations indicate that the B2 conformer is at least 1.1 kcal/mol more stable than the other chelated conformations, which is consistent with the X-ray experiment [3]. However, these results are not reliable in solution states with the solvent of different polarities. Fig. 2 shows that the energy differences of the chelated forms, which are negligible in their gaseous states, become quite noticeable as the medium polarity increases. This causes the contents of the B conformers to be underestimated compare to the A conformers in the solution. For instant, the relative energies of A1, B2, and B1 chelated forms with respect to A2 in CH₃CN and DMSO are about 1.3, 2.5, and 3.3 kcal/mol, respectively.

The barrier of the thienyl group rotational was also estimated for A1 \leftrightarrow A2 interconversions. The barriers for internal rotation are calculated to be 7.396 kcal/mol for A1 \rightarrow A2 and 7.457 kcal/mol for A2 \rightarrow A1. The high potential energy barrier, regardless of steric effect, confirms the contribution of the thienyl ring's π -electrons in resonance conjugation with the chelated ring.

The barrier heights for proton transfers from A1 \rightarrow B1 and from A2 \rightarrow B2, calculated at B3LYP/6-31G**, are 2.01 and 1.89 kcal/mol, respectively. The corresponding barrier heights for AA and HFAA are 1.71 and 2.45 kcal/mol [4], respectively. These results confirm that the IHB strength in TTFA conformers is stronger than that in HFAA, but weaker than that in AA.

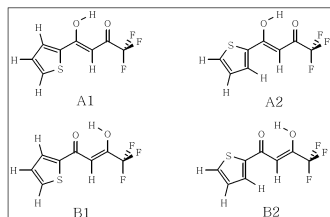


Fig. 1: Possible chelated cis-enol tautomers of TTFA.

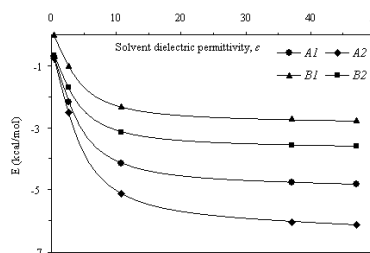


Fig. 2: The solvent influence on TTFA chelated forms stability.

To study the effects of the thienyl and trifluoromethyl groups on IHB, the main optimized geometrical parameters of the chelated rings of B2-TTFA, AA, TFAA (1,1,1-trifluoroacetylacetone), and HFAA as well as some of their experimental spectroscopic properties related to IHB strength are compared, and the following trend in IHB strength (S_{HB}) for the aforementioned molecules is concluded; $S_{HB}: AA > B2-TTFA > TFAA > HFAA$. This indicates the negative and positive effects of trifluoromethyl (as an electron-withdrawing group) and thienyl (as an electron-supplying group) in β position on the IHB strength of the β -dicarbonyls, respectively.

Deconvolutions (using Lorentzian functions) of the infrared spectrum of TTFA solutions in CCl_4 and CS_2 in the 3000-2400 cm^{-1} region display a broad band centered at 2850 cm^{-1} with a HWHM of about 300 cm^{-1} , which is assigned to the OH stretching frequency. Upon deuteration, this band shifts to a relatively narrower band centered at about 2080 cm^{-1} (see Fig. 3). These frequencies are considerably higher than those observed for AA/D₂-AA, 2750/2020 cm^{-1} , but lower than those of TFAA/D₂-TFAA, 2900/2120 cm^{-1} , which indicate a weaker IHB and a stronger IHB for TTFA in comparison with those of AA and TFAA, respectively. These results are in agreement with the ¹H-NMR of these compounds which reports the proton chemical shifts for AA, TTFA, and TFAA as 15.4, 14.9, and 14.2 ppm, respectively. In the 1650-1500 cm^{-1} region, we expect to observe three bands due to the asymmetric and symmetric C=C-C=O stretching and $\nu_a(C=C)$ of the thienyl group. The deconvoluted spectra of TTFA indicate existence of eight bands in this region with considerable intensities in either the Raman or IR spectra. The existence of these additional bands can be attributed to all four stable conformations of TTFA being present in comparable amounts in the sample, as this is well supported with the presence of other bands corresponding to these tautomers in the entire regions of both Raman and IR spectra of TTFA. The first five bands (1651, 1636, 1623, 1601 and 1583 cm^{-1}) are of special interest because in all IR and Raman spectra collected in the solid state, the intensities of the bands related to the B2 conformer dominate those of the other conformers. Contrarily, in the solutions, the intensities of bands for the A conformers are stronger than those of the B conformers (see Fig. 4). This means that in the solid state the major content of the sample is in the B2 form and in the solution states the A forms have more significant amounts. This result is in good agreement with the experimental X-ray results in the solid state and the theoretical calculations in solution.

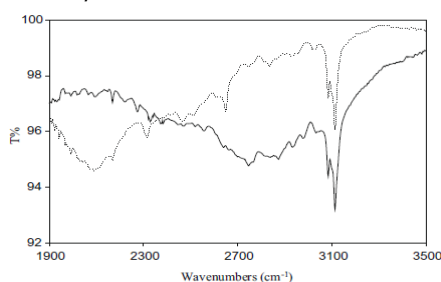


Fig. 3: The IR spectra of TTFA (—) and D₂-TTFA (···) in the OH/OD stretching region

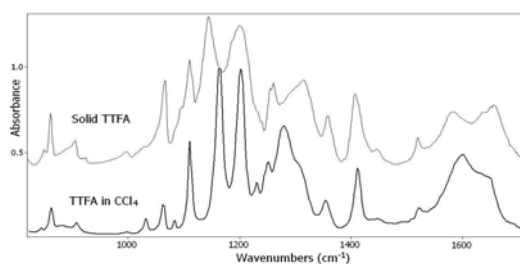


Fig. 4: The IR spectra of TTFA in solid state (—) and TTFA in CCl_4 (---).

Conclusion

All four chelated forms of TTFA coexist in the solid and solution states. The negative and positive effects for trifluoromethyl and thienyl groups, respectively, in β position on the IHB strength of the β -dicarbonyls are concluded. In agreement with the theoretical stability calculations and X-ray experimental investigation, the vibrational spectroscopy analysis specify a more ratio of A forms in the solution phases, and a more ratio of B forms in the solid state in the sample.

References

- [1] Z. Rappoport, The Chemistry of Enols, John and Wiley, New York, 1990.
- [2] J. Emsley, Struct. Bond. 57 (1984) 147.
- [3] R. D. G. Jones, Acta Cryst. B32 (1976) 1224.
- [4] S. F. Tayyari, F. Milani-Nejad, H. Rahemi, Spectrochim. Acta 58A (2002) 1669.

**Nano-fluorescence spectroscopic studies of interaction between tamoxifen and human holo transferrin**S. Sarzehi ^{a,*}, M.R. Bozorgmehr ^b and J. Chamani ^a^a Department of Biology, Faculty of Science, Islamic Azad University-Mashhad Branch, Mashhad, Iran.

(Email: Sareh_sarzehi@yahoo.com) Tel: +985116040642.

^b Department of Chemistry, Faculty of Science, Islamic Azad University-Mashhad Branch, Mashhad, Iran.**Keywords:** Human serum transferrin; Tamoxifen; pH-dependent; Conformational change; Fluorescence spectroscopy**Introduction**

Transferrin is a large non-hem iron-binding glycoprotein ($M_w = 80$ kDa) that done utilization, storage, transport and homeostasis of iron in vertebrates. It consists of a single polypeptide chain of about 679 amino acid residues, two metal binding sites that is only 30% iron-saturation, have two homologues lobes (N and C) [1]. One of the major factors that govern the binding and release of iron in transferrin is the pH. The binding of iron by the apo transferrin is very strong at the extracellular (pH 7.4), while the release inside the cell occurs of low endosomal (pH 5.5) and the binding of holo transferrin to its receptor [2]. Tamoxifen ($C_{26}H_{29}NO$) is an antagonist of estrogen receptor in breast tissue and used in the treatment of breast cancer.

It belongs to the chemical class of triphenylethylenes ($M_w = 371.5$). It exists as white, odorless crystals and slightly soluble in water and soluble in ethanol, methanol and acetone. Tamoxifen could bind to holo transferrin, transport and eliminated in body, which could be a useful guideline for further drug design [3].

Materials and method

Human serum transferrin and Tamoxifen were purchased from Sigma Chemical Co. all the solvations prepared in 50 mM phosphate buffer of pH= 7.4 and 6.4. All values concentration of drugs were inject to 2 ml protein solution and double distilled water was used throughout. Fluorescence measurements were performed on a spectrofluorometer Model F-2500 (Hitachi, Japan) equipped with a 150W Xenon lamp. The excitation wavelength was set at 280 nm and 295 nm, the emission wavelength was recorded between 300 and 600 nm. Wavelength of 280 nm excites the tryptophanyl and tyrosyl residues, while 295 nm excites only the tryptophanyl residues [4].

Results and discussion

The fluorescence intensity of holo transferrin gradually decrease upon increasing the concentration of Tamoxifen with accompanying bathochromic shift at two pH= 7.4 and 6.4, indicating the binding of Tamoxifen to holo transferrin and conformational changes induced by the interaction leading to a further exposure of tryptophan residue to the polar solvent and the binding site of Tamoxifen on holo transferrin was very close to tryptophan residue [5]. The occurrence of an isosabestic point at 375 nm indicated the existence of bound and free Tamoxifen in equilibrium and change λ_{max} , upon increasing concentration of Tamoxifen.

The Stern-Volmer plot of pH= 7.4 is shown in Fig. 1, the positive deviation from the straight line indicates that both static and dynamic quenching. The Stern-Volmer plot at pH=6.4, indicate a dynamic quenching in the subdomain where fluorophores, taking part in the interaction. The result shows that there are different type interactions of Tamoxifen to holo transferrin at two different pH. The number of binding sites, n and quenching constant values, K_q were noticed to be 2.683 and $(2.73 \times 10^2 M^{-1})$ for pH= 7.4 and 1.0941 and $(1.30 \times 10^2 M^{-1})$ for pH= 6.4 [6].

As can be seen from Fig. 2 the F/F_0 values excited at 280 and 295 nm decrease. The fluorescence quenching of protein excite at 280 nm is more expanded than that excited at 295 nm for two pH. This phenomenon shows that in the interaction of Tamoxifen with holo transferrin both tryptophanyl and tyrosyl groups take part [7].

Scatchard plot at two pH indicating that existence one set of binding site on interaction between Tamoxifen and holo transferrin [8].

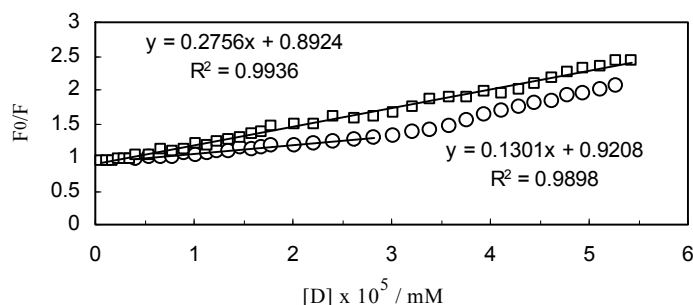


Fig. 1. Stern-Volmer plot for the Binding of Tamoxifen to holo transferrin at pH= 7.4 (○), 6.4 (□).

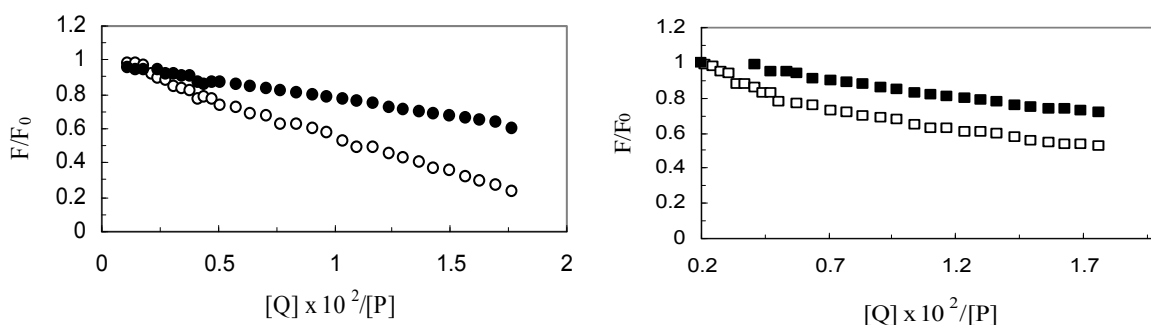


Fig.2. Quenching curve of holo transferrin in presence Tamoxifen at pH= 7.4: ○ $\lambda_{ex} = 280 \text{ nm}$, ● $\lambda_{ex} = 295 \text{ nm}$ and pH= 6.4: □ $\lambda_{ex} = 280 \text{ nm}$, ■ $\lambda_{ex} = 295 \text{ nm}$.

Conclusion

This paper is an example of rarely encountered study wherein the interaction of human holo transferrin and tamoxifen in pH= 7.4 and 6.4 that have been investigated by Nano-fluorescence spectroscopic techniques. The fluorescence data showed fluorescence quenching of holo transferrin by tamoxifen. On the basis of binding and quenching constants determined from Stern-Volmer and Scatchard equations it has been stated that a high affinity to holo transferrin for tamoxifen. Structural information obtained provides a richly detailed view of the binding site with which to interpret the biochemical and biophysical data already accumulated on drug interactions with the protein.

References

- [1] E.N. Baker, P.E. Lindley, *Inorg. Biochem.*, 47 (1992) 147-160.
- [2] R.D. Klausner, J.V. Ashwell, J.B. VanRenswoude, J. Harford, *Proc. Natl. Acad. Sci. USA*, 80 (1983) 2263-2267.
- [3] Cook, L. S., N. S. Weiss, S. M. Schwartz, E. White, B. McKnight, D. E. Moore, *J. Natl. Cancer Inst.*, 87(1995) 59-64.
- [4] D.C. Carter, J.X. Ho, *Adv. Protein Chem.*, 45 (1994) 153-203.
- [5] A.Gerbanowski, C. Malabate, C. Rabiller, J.Gueguen, *J. Agric. Food Chem.*, 47 (1999) 5218-526.
- [6] M.R. Eftink, C.A. Ghiron, *Anal. Biochem.*, 114 (1981) 199-227.
- [7] V. Maes, J. Hoebeke, A. Vercruysse, L. Kanarek, *Mol. Pharmacol.*, 16 (1979) 147-153.
- [8] G. Scatchard, *Ann. N. Y. Acad. Sci.*, 51 (1949) 660-673.



The comparison between Holo-transferrin and Holo-transferrin-Fe³⁺ upon interaction with Ropinirole hydrochloride: A nano-fluorescence spectroscopy approach.

M. Kabiri,^{1*}, M.R. Bozorgmehr², and J. Chamani,¹

1. Department of Biology, Faculty of Science, Islamic Azad University-Mashhad Branch, Mashhad, Iran.

Email: M_Kabiri@ymail.com, Tel: +985117285034, Mobile: 09155177176, Fax: +985117287513

2. Department of Chemistry, Faculty of Science, Islamic Azad University-Mashhad Branch, Mashhad, Iran.

Introduction

Transferrin comprises a class of monomeric glycoprotein found in all vertebrates, whose function is iron sequestration and transport [1]. Human serum transferrin (hTf) is a single chain glycoprotein containing 679 amino acids with molecular mass of ~ 80 kDa present in plasma at a concentration of about 35 µM. hTf is only 30% iron-saturated and the vacant sites can bind other metal ions [2]. Ropinirole hydrochloride (REQUIP) is an orally administered non-ergolin dopamine agonist and the molecular weight is 296.84 gr/mol. REQUIP as a treatment for Parkinson's disease and Rest legs syndrome (RLS).

Here, the interaction between Holo-transferrin and Holo-transferrin-Fe³⁺ with REQUIP studied under physiological conditions (pH=7.4) by nano-fluorescence spectroscopy for determining, the binding affinity and the number of binding sites for REQUIP.

Key words: Human serum transferrin, Holo-transferrin-Fe³⁺, Ropinirole hydrochloride, Nano- fluorescence spectroscopy.

Materials and Methods

Holo-transferrin and Ropinirole hydrochloride were purchased from Sigma chemical corporation, USA, and used without further purification. Potassium phosphate buffer in pH=7.4 was used for all experiments with concentration of 50 µM.

Nano-fluorescence spectra measurement of hTf and hTf-Fe³⁺ solution in the absence and presence of REQUIP were performed using a Hitachi F-2500 spectrofluorometer.

Results and discussion

It is reported in the literature that the binding of REQUIP to hTf and hTf-Fe³⁺ could induce the conformational changes in hTf, because the intermolecular forces involved maintaining the secondary structure could be altered and resulted in conformational changes of protein. Fluorescence quenching measurements have been widely used to study the interaction of drugs with proteins. The fluorescence intensity of hTf and hTf-Fe³⁺ decreased regularly and slight red shift were observed for the emission wavelength with increasing of REQUIP concentrations, suggesting that REQUIP could interact with hTf, hTf-Fe³⁺ and quench intrinsic fluorescence. The red shift in maximum wavelength and decreased in fluorescence intensity revealed the increased polarity of the solvent, changed the microenvironment of tryptophan and tyrosine residues and less hydrophobic of fluorophore microenvironment.

The fluorescence quenching was usually analyzed using the Stern-Volmer equation: $F_0/F = 1 + K_{SV} [Q]$, Where F_0 and F are the steady state fluorescence intensities in the absence and presence of quencher, respectively. K_{SV} is the Stern-Volmer quenching constant and $[Q]$ is the concentration of the quencher. Figure 1 was shown the plot of F_0/F versus quencher concentrations. The slop of the straight line the K_{SV} can be easily calculated. The Stern Volmer plots in absence of Fe³⁺ at 280 nm, 295 nm were linear, so the possible quenching mechanism between REQUIP and hTf suggested as dynamic quenching with one set of binding site. The Stern-Volmer plot in presence of Fe³⁺ at 280 nm was shown in Figure 1.

It demonstrated that there were two set of binding sites for hTf-Fe³⁺ upon interaction with REQUIP. The curvature with increase of the quencher concentration suggested the existence of additional binding sites for high REQUIP concentrations, therefore the quenching mechanism between REQUIP and hTf-Fe³⁺ was dynamic-static quenching with two set of binding sites.

In presence of Fe^{3+} at 295 nm, the Stern-Volmer plot was linear with one set of binding site, so the quenching mechanism was dynamic quenching, because in presence of Fe^{3+} , tryptophan and tyrosine residues were found and slight change conformation were shown, on the other hand, in the absence of Fe^{3+} tryptophan and tyrosine residues were found and lower change conformation was observed. The n value and K_{SV} of the hTf-REQUIP complex at 280 nm were determined 1.140 and 23.284×10^5 and at 295 nm the n value was 1.525 and the K_{SV} was 35.825×10^5 . The n value of REQUIP with hTf- Fe^{3+} at 280 nm were calculated 0.709 and 0.53 and the K_{SV} were 128.26×10^5 and 58.768×10^5 and at 295 nm the n and K_{SV} were 1.072 and 32.438×10^5 .

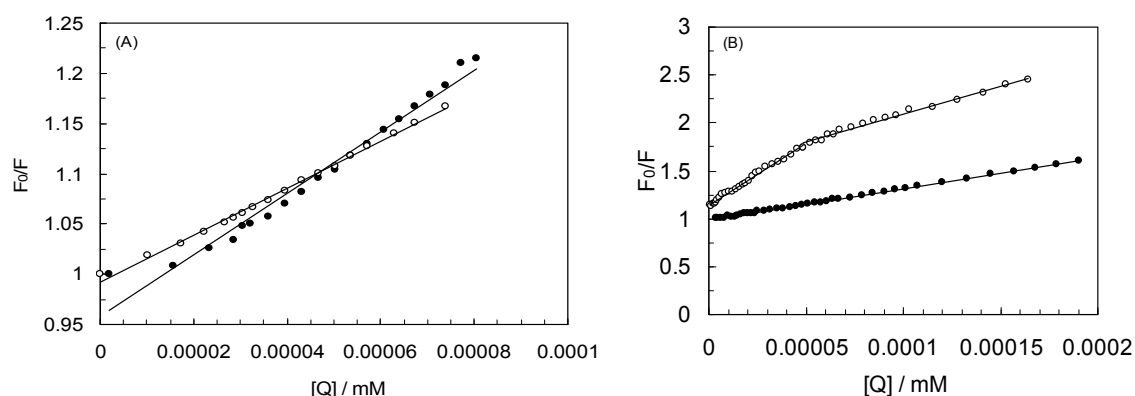


Figure 1: (A) Stern-Volmer plot for binding of REQUIP with hTf. (B) Stern-Volmer plot for binding for quenching of REQUIP to hTf- Fe^{3+} . ○ at 280 nm, ● at 295 nm.

Conclusion

The data of nano- fluorescence spectroscopy indicated the changes in microenvironment of hTf and hTf- Fe^{3+} induced by the binding of REQUIP and revealed a complex formation. The interaction between hTf and REQUIP in absence and presence of Fe^{3+} show that the tryptophan and tyrosine residues were changed and disturbed. This study is expected to provide important insight into the interaction of the physiologically important protein hTf with drug to use in various therapeutic projects.

References

- [1] M. Zhang, D.R. Gumerov, I.A. Kaltashov and A.B. Mason, *American Society for Mass Spectroscopy*, 15 (2004) 1658-1664
- [2] H. Du, J. Xiang, Y. Zhang, Y. Tang and G. Xe, *J. of Inorg. Biochem*, 102 (2008) 146-149
- [3] P.G. Thakurta, D. Choudhury, R. Dasgupta, J.K. Dattagupta, *Biochem. and Biophys. Research Communications*, 316 (2004) 1124-1131
- [4] L. Messori, P. Orioli, V. Banholzer, I. Pais, P. Zatta, *FEBS Letter*, 442 (1999) 157-161
- [5] S.N. Khan, B. Islam, R. Yennamalli, A. Sutan, N. Subbarao, A.U. Khan, *European J. of Pharmaceutical Science*, 35 (2008) 371-382

**A novel view of the comparison between transferrin and HSA upon nano-interaction with lomefloxacin**H. Vahedian- Movahed^{1*}, M.R. Saberi², J. Chamani¹

1. Department of Biology, Faculty of Sciences, Islamic Azad University-Mashhad Branch, Mashhad, Iran

(hanif_mbi@yahoo.com), Tel: +985116055624, +989151584001

2. Medical Chemistry Division, School of Pharmacy, University Complex, Vakilabad Boulevard, Mashhad, Iran

Keywords: Humsn serum albumin, Serum transferrin, Lomefloxacin, Nano-fluorescence spectroscopy,**Introduction**

It is of great importance to determine lomefloxacin's (LMF) content in biological fluids and actually there are some reports on the interaction of this antibiotic with proteins, however, a deep literature survey shows that the interaction of lomefloxacin with Serum Transferrin (ST) has never been taken so far. So this is of interest to study the interaction of this drug with Transferrin to evaluate the probability of the transport of lomefloxacin by transferrin and compare the result to that of HSA, which has been shown before to carry this drug in the blood [1-4].

Materials and methods

HSA, ST and LMF were all purchased from sigma and used without further purifications. All solution was prepared in potassium phosphate buffer at pH 7.4. Doubly distilled water was used throughout the experiments. All Nano-fluorescence spectra were recorded on F-2500 Fluorescence spectrophotometer (Hitachi, Japan) equipped with a quartz cell and 2 ml of protein solution was titrated with Nano-liters volumes of drug solution with fixed excitation at 280 nm or 295 nm.

Results and discussion

The fluorescence emission spectra of both HSA and ST were quenched which suggest a kind of interaction has occurred and the energy has been transferred. Also, the quenching processes were accompanied by a clear blue and red shift for HSA and ST, respectively. This means, that the microenvironment around Trp residue has changed upon interaction with LMF and the prtoeins's chromophore were placed in more hydrophobic and polar environment in the case of HSA and ST, respectively [5]. To further characterize this interaction the Stern-Volmer plot for both HSA and ST was analyzed which is illustrated in Figure 1. The Stern-Volmer equation is, $F_0/F = 1 + K_{SV}$, Where F_0 and F denote the Nano-fluorescence intensities in the absence and presence of quenchers, respectively. $[Q]$ is the concentration of quencher, K_{SV} is the Stern-Volmer quenching constant and exhibits the affinity of LMF to these proteins. This value was calculated as $2.35 \times 10^6 \text{ M}^{-1}$ and $0.32 \times 10^6 \text{ M}^{-1}$ for HSA and ST, respectively. From these data we can determine that the affinity of LMF to ST is less than HSA.

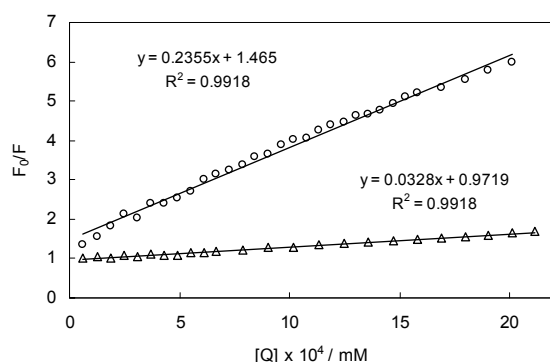


Fig. 1. Comparison between Stern-Volmer plots for HSA (○) and ST (Δ) at pH=7.4 and 50 mM phosphate buffer.

On the other hand, the binding capacities were calculated according to the hill plot. The binding capacities were calculated as 0.8 and 1.4 for HSA and ST, respectively as reference literature [6]. Moreover, in order to determine the involvement of individual residues of Trps and Tyrs in quenching effect of drug, the fluorescence of both HSA and ST at 280 nm and 295 nm were compared and are illustrated in Figure 2. At 280 nm wavelength both Trps and Tyrs are excited whereas at 295 nm wavelength excites only the Trps residues. As depicted in Fig. 2 by addition of drug, the quenching of two proteins at two



wavelengths do not overlap and this is truer for ST. So we can suggest that in these interactions both chromophores are involved and this is stronger in the case of ST [7].

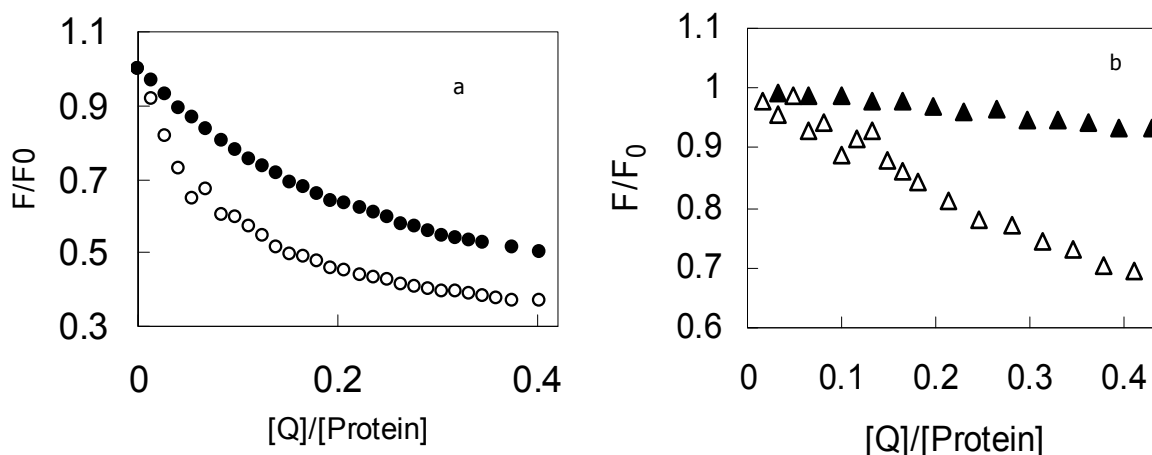


Fig.2. Comparison between quenching curves of HSA (a) and ST (b) in the presence of lomefloxacin at 280 nm (filled symbols) and 295 nm (open symbols)

Conclusion

Here, the interaction of LMF with HSA and ST was studied by fluorescence spectroscopy. We found that the binding capacity and binding affinity of LMF for HSA are lower and higher, respectively compared to those for ST. Also, we demonstrated for the first time that there is a probability of the transport of LMF with ST because, although, the affinity of LMF to ST is less than HSA, it is still enough to be carried by ST.

References:

- [1]. J.Flaraos, K.L. Morand, P. Vouros, *Anal. Chem.* 77 (2005) 1345-1353.
- [2]. D.Hongyan, Y.Tang, *Bioorganic & Medicinal Chemistry Letters* 17 (2007) 1701-1704.
- [3]. D.C. Hooper, J.S. Wolfson, *Quinolones Antimicrobial Agents*, American Society for Microbiology, Washington, 1993.
- [4]. F. Jin, *Chinese Journal of Chemistry*, 25, (2007) 1675-1680.
- [5]. T. Yang, A.M. Weljie, H.J. Vogel, *Biochemistry* 37 (1998) 3187-3195.
- [6]. J.R. Lakowicz, *Principles of Fluorescence Spectroscopy*, Plenum Press, New York, 1983 (pp. 257)
- [7]. D.C. Carter, J.X. Ho, *Adv. Protein Chem.* 45 (1994) 153-203.



Effect of Lomefloxacin on protein-protein interactions and origin of antibiotic's side effects: nano- molecular modeling and Spectroscopic investigations

H. Vahedian- Movahed^{1*}, M.R. Saberi², J. Chamani¹

1. Department of Biology, Faculty of Sciences, Islamic Azad University-Mashhad Branch, Mashhad, Iran

(Hanif_mbi@yahoo.com) ,Tel: +985116055624, +989151584001

2. Medical Chemistry Division, School of Pharmacy, University Complex, Vakilabad Boulevard, Mashhad, Iran

Keywords: Protein-protein interaction, Nano-molecular modeling, Nano-fluorescence spectroscopy

Introduction

Protein-protein interactions (PPIs) play a fundamental role in biological processes. Therefore, understanding the molecular principles and different factors governing these interactions are of great important. On the other hand, Human Serum Albumin (HSA) and Serum Transferrin (ST) are two function related protein which are responsible for transport of drugs and others ligands in the serum and as a consequence most of the researches are focused on the interactions of drugs with these proteins. However a deep literature survey reveals that there is not any report on the effect of drugs on the interaction of these proteins. Therefore, it is of interest to explore the effect of drugs on the protein-protein interactions, since it may shed some light on the mechanism that cause drug's side effects [1-5].

Materials and methods

HSA, ST and LMF were all purchased from sigma. All solution was prepared in potassium phosphate buffer at pH 7.4. Doubly distilled water was used throughout the experiments. All fluorescence spectra were recorded on F-2500 Fluorescence spectrophotometer (Hitachi, Japan) equipped with a quartz cell and 2 ml of protein solution was titrated with micro-liters volumes of drug solution.

Results and discussion

Intrinsic fluorescence is an elegant tool to study protein's complex formation, due to the dependency of its emission on the microenvironment of the fluorophores. Fig.1a. shows the variations in maximum emission wavelengths ($\lambda_{\max,em}$) for the mixture and algebraic average of HSA and serum transferrin (ST) in various concentrations of LMF.

On the whole, the variations in the $\lambda_{\max,em}$ are more blue- shifted for the mixture of HSA-ST compared to the computed average,

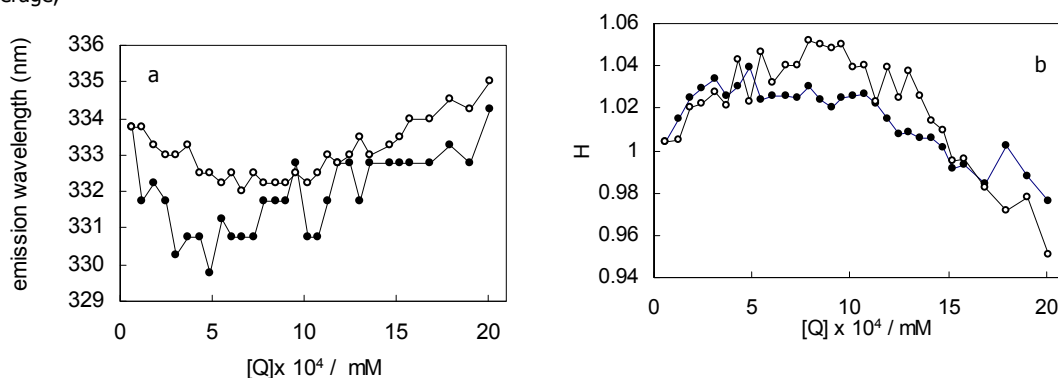


Fig.1. Variations in $\lambda_{\max,em}$ (a) and H factor (b) for the mixture (filled symbols) and algebraic average (open symbols) of HSA and ST in various concentrations of LMF at pH 7.4 and 50 mM phosphate buffer.

which indicate protein-protein interaction has occurred and the fluor residues of proteins are either located in the interface of the formed complex or are transferred to the core of the protein. For further considerations, we analyze the H factor of above mentioned groups (Fig. 1b.) interestingly; this is in good accordance to the previous results from Fig.1a.

Also, we are working on the nano-molecular dynamics studies on the interaction between these two drug carrier proteins in order to get a better understandings of the aforementioned interaction and to indicate whether the fluor residues are located within the interface of the formed complex or not, which will be presented in the conference.



Moreover, we measure the changes in surface hydrophobicity, since hydrophobic interactions play fundamental role in PPIs, and we found that at high drug concentrations there is a slight decrease in surface hydrophobicity for mixture of HSA-ST compared with their algebraic average, and this might be the result of protein-protein complex formation from hydrophobic regions [6, 7].

Conclusion

Here, the effect of a model drug, LMF, on the interaction between HSA and ST was evaluated by fluorescence spectroscopy and nano-molecular modeling studies. We found that this antibiotic is capable to induce protein-protein interaction between these two drug carrier proteins. Since, these complexes are not present in the normal body conditions, so, they may cause health problem because: 1) they may become immunogenic. 2) This complex formation may interfere with the natural function of these two proteins. Thus, if further studies establish this fact, this phenomenon might be consider as another mechanism for the emergence of antibiotic's side effects that pharmaceutical companies should pay attention to this fact.

References:

- [1]. C.O. Anderson, J.F.M. Niesen, H.W. Blanch, J.M. Prausnitz, *Biophysical Chemistry* 84 (2000) 177-188.
- [2]. B. Alberts, D. Bray, J. Lewis, K. Roberts, J. Watson, *Molecular Biology of the Cell*, Garland Publishing, New York, 1994.
- [3]. J.Flaraos, K.L. Morand, P. Vouros, *Anal. Chem.* 77 (2005) 1345-1353.
- [4]. D.Hongyan, Y.Tang, *Bioorganic & Medicinal Chemistry Letters* 17 (2007) 1701-1704.
- [5]. Y. Ofra, B. Rost, *FEBS Lett.*, 544 (2003) 236-239.
- [6]. L. Young, R.L. Jernigan, D.G. Covell, *Protein Science*, 3 (1994) 717-729.
- [7]. W. Kauzmann, *Adv. Protein Chem.*, 14 (1959) 1-63.



Chemical Kinetics



**Degradation kinetics of carboxymethylcellulose under ultrasonic irradiation**

Mohammad Taghi Taghizadeh* and Helen Rad

Department of physical chemistry, faculty of chemistry, university of Tabriz, Tabriz, Iran

(Email: mttaghizadeh@tabrizu.ac.ir)

1. Introduction

In the field of polymer chemistry, ultrasonication has been used as a conventional method to simply and efficiently obtain polymers of lower molecular weight by degradation of the original high molecular weight polymer [1]. A number of mechanisms have been suggested, however, it is now generally accepted that ultrasonic depolymerization proceeds by mechanical force [2]. In other hand, any waste stream containing carbohydrates has the potential for generation of useful chemicals. Substrates include sugar crops (sugar cane), starchy materials (corn, sweet potato) and cellulosic residues (wood and agricultural wastes). The most common form of carbohydrates encountered in biological systems is cellulose, with estimates of annual world biosynthesis of 10^{11} t [3]. The aim of the present work was to study the effects of polymer concentration and power of ultrasound as well as reaction temperature on the degradation of carboxymethylcellulose (CMC) polymers.

2. Experimental Method*Degradation experiments*

Carboxymethylcellulose (CMC) purchased from Fluka, with an initial Mw of 350000 kDa and polydispersity of 1.2 was degraded in a cylindrical 100ml Pyrex glass vessel. An ultrasound generator (Dr. Hielscher Ultrasonic Processor UP200 H) operating at a fix frequency of 24 kHz and a variable power output up to 100W nominal value, in aqueous media was used for sonication experiments.

Kinetic model

The kinetic model that was used is based on viscometry measurements results. Efflux times were measured for CMC solutions (t_s) and the solvent (t_0) and was converted to the ratio of t_s/t_0 , which is proportional to relative viscosity, η_r , of chitosan solution.

$$\eta_r = \frac{t}{t_0} \quad (1)$$

The final equation that can be applied to determine the rate constant of degradation reaction is,

$$\Delta \eta^{1-n} - \Delta \eta_0^{1-n} = (1-n) \left[\frac{\sqrt{2}}{(1+\alpha)\Gamma(1+\alpha)KC^{1+\alpha}} \right]^{(1-n)/\alpha} kt \quad (2)$$

The apparent rate constant, k' is:

$$k' = (1-n) \left[\frac{\sqrt{2}}{(1+\alpha)\Gamma(1+\alpha)KC^{1+\alpha}} \right]^{(1-n)/\alpha} k \quad (3)$$

3. Results and discussion*Effect of CMC solution concentration on the rate of degradation*

The relative viscosity (η_r) of CMC solution versus the sonication time for 0.5, 1.0, 1.5, 2.0 and 2.5 g/L concentrations are shown in Fig. 1. Based on these studies, it is clear that η_r decreases with sonication time and tends to have a constant value. It can be deduced that there is a limiting molecular weight that below which chain scission does not occur. Under the same conditions, the decrease in η_r of the sample with a high polymer concentration is lower than of the sample with a low polymer concentration [4]. Fig. 2. Are presented the plot of $\Delta \eta^{1.43} - \Delta \eta_0^{1.43}$ versus sonication time for different concentration of CMC solution that was indicated that the rate of reaction was increased with decreasing the concentration of solution.

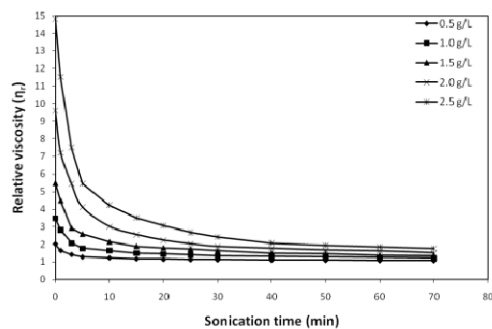


Fig.1. Variation of viscosity of CMC samples as a function of sonication time for 0.5, 1.0, 1.5, 2.0 and 2.5 g/L solution of CMC in aqueous medium at 25°C.

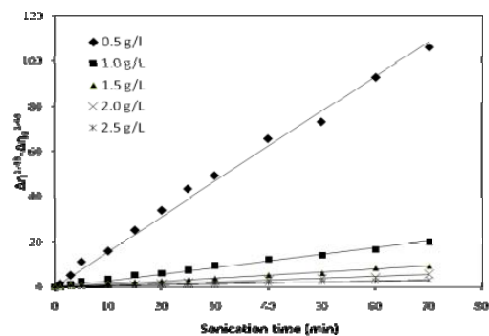


Fig. 2. The plot of $\Delta\eta^{1.43} - \Delta\eta_0^{1.43}$ versus sonication time for different concentration of CMC solutions at 25°C.

References

- [1] T. Miyazaki, C. Yomota, S. Okada, Polym. Degrad. Stabil. 74 (2001) 77.
- [2] A. M. Basedow, K. Ebert, Adv. Polym. Sci. 22 (1977) 83.
- [3] Goodger, Hydrocarbon Fuels, Production, Properties and Performance of Liquids and Gases, Macmillan, London, 1976.
- [4] M. T. Taghizadeh, A. Bahadori, J. Polym. Res. 16 (2009) 545.

**A kinetics study on the thermal degradation of starch/poly (vinyl alcohol) blend**

Mohammad Taghi Taghizadeh*, Reza Abdollahi and Ghods Madani

Department of Physical Chemistry, Faculty of Chemistry, University of Tabriz, Tabriz, Iran

(E- Mail: mttaghizadeh@tabrizu.ac.ir)**1. Introduction**

The thermal degradation of polymers refers to the case where polymers at elevated temperatures start to undergo chemical changes without the simultaneous involvement of another compound [1]. Starch is one of the main polymers present in nature and usually includes about 30% amylose and 70% amylopectin [2]. Structure and properties of starch have been investigated extensively in the past century. Starch has shown advantages and superior characteristics over other natural and synthetic biodegradable polymers, especially because of the low cost of the raw materials. Its applications have been extended from traditional food, paper and textile industries to packaging, controlled drug delivery and many other areas in either its native or modified forms [3].

2. Methods

The thermal degradation of starch/poly (vinyl alcohol) (PVA) blend was studied by using TG in air atmosphere. Thermoanalytic investigations on pure starch film and starch/PVA blend film were carried out to evaluate the thermal stability and the respective activation energy of the materials. Experiments in air atmosphere and under non-isothermal and isothermal condition carried out. The Kissinger and Flynn-Wall-Ozawa methods were used to calculate the activation energy of non-isothermal degradation of starch and starch/PVA blends. The results show that these two methods were suitable and effective to describe the thermal degradation of starch and starch/PVA blends. These results shown that starch/PVA blend was thermally less stable than pure starch and thermal stability of films decreased with increasing PVA content.

3. Results and discussion*Isothermal degradation*

Studies on the thermal degradation of starch reported that thermal reactions for starch start around 300 °C with thermal condensation between hydroxyl groups of starch chains to form ether segments and liberation of water molecules and other small molecular species. Dehydration of neighbouring hydroxyl groups in the glucose ring also occurred, resulting in the formation of C=C bonds or breakdown of the glucose ring [4]. Aldehyde groups were formed at the same time possibly as endgroups when the glucose ring was fractured. Increasing temperature generated aromatic rings, such as substituted benzene and furan structures with either -CH₂- or -CH₂-O-CH₂- as the main linkages between the aromatic groups. The starch structure disintegrated after heating to 400 °C, and above that temperature a highly crosslinked system was formed similar to thermally crosslinked phenol/benzene/furfuryl resins. Thereafter, the thermal reactions of the system followed similar reaction pathways as phenol-formaldehyde or furfuryl resins undergoing thermal crosslinking and decomposition at increased temperatures.

Non-isothermal degradation

Thermal degradation of polymeric materials is a consequence of the fact that the organic macromolecules inside the polymer matrix as well as low-molecular weight organic molecules are stable only up to a certain temperature range. The thermogravimetric TG/TGA curves for starch and starch/PVA blends at various heating rate are showed in Fig. 1 and 2. The pure starch and starch/PVA blend curves showed a three-step decomposition pattern.

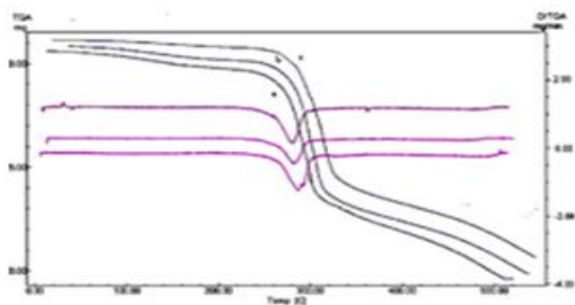


Fig.1. TGA/DTG curves of pure starch at various heating rate. Heating rate (a) 5 °C/min, (b) 10 °C/min, (c) 15 °C/min.

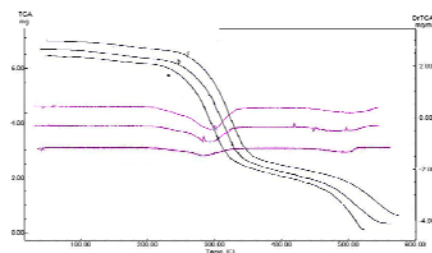


Fig.2. TGA/DTG curves of starch/PVA blend at various heating rate. Heating rate (a) 5 °C/min, (b) 10 °C/min, (c) 15 °C/min.

4. Conclusion

In this study we assessed the pure starch film and starch/PVA blend film were synthesized and their thermal stability studied by non-isothermal, isothermal thermogravimetric analysis. The results showed that starch/PVA blend was less thermally stable compared to pure starch and, thermal stability decreased with increasing the value of polyvinyl alcohol. The calculation of the activation energy of isothermal degradation of pure starch and starch/PVA blends were obtained by Kissinger and Ozawa methods. For pure starch film, the activation energy of degradation obtained by Kissinger and Flynn-Wall-Ozawa methods were 158 and 160 kJ/mol, respectively. For PVA/starch blend, the corresponding activation energies of degradation were 76 and 81 kJ/mol, respectively. Obviously, the activation energy obtained by Kissinger was close to that by Flynn-Wall-Ozawa, which means that these two methods were suitable to describe the thermal degradation of starch and Starch/PVA blends.

References

- [1] W. Schnabel, Polymer Degradation: Principles and Practical Applications, Akademie-Verlag, Berlin, 1981.
- [2] M. Zhai, F. Yoshii, T. Kume and K. Hashim, Carbohydr. Polym. 50 (2002) 295.
- [3] Z. Stojanovic, L. Katsikas, I. Popovic, S. Jovanovic and K. Jeremic, Polym. Degrad. Stab. 87 (2005) 177.
- [4] R. M. van der Eijnde, M. E. van der Veen, H. Bosman, A. J. van der Goot and R.M. Boom, J. Food Eng. 66 (2005) 147.

Kinetic study of proton transfer reactions using ion mobility spectrometry

E. Jazan and M. Tabrizchi*

Department of Chemistry, Isfahan University of Technology, Isfahan 84156-83111 Iran

(Email: m-tabriz@cc.iut.ac.ir)

Keywords: Ion mobility spectrometry, Kinetic, Proton transfer reaction

1. Introduction

Two important ion–molecule reaction occurring in ion mobility spectrometry (IMS) are the formation of protonated molecules (MH^+) and proton-bound dimers.



Any information about the kinetics and thermodynamics of those reactions are very useful in the interpretation of ion mobility spectra [1]. We have recently studied [2] the kinetics of proton-bound dimer formation (reaction 2). In the present work, we extend our proposed method to measure the rate constant for the formation reaction of protonated molecules (MH^+). The method was practically evaluated using DMP as test compound.

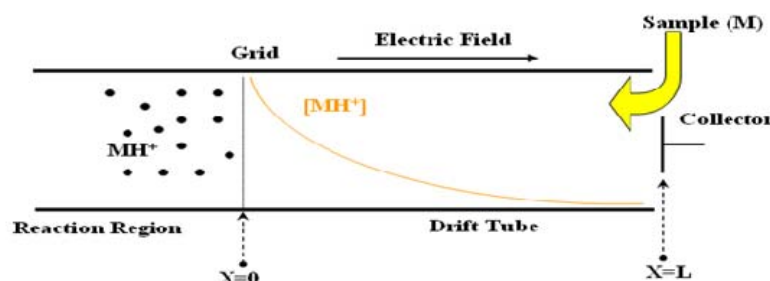


Fig.1 Sample is introduced into the drift region.

2. Experimental and Method

The ion mobility spectrometer used in this study was constructed in our laboratory at Isfahan University of Technology [3] The instrument and the method is fully described in ref 2. The sample was introduced into the drift gas to establish reaction (1) in the drift region (Fig.1). In this case, a package of reactant ions, H_3O^+ already formed in the ionization region, is released from the shutter grid to react with the neutral sample molecules present in the drift region. The monomer (MH^+) forms in the drift tube as the reactant ions travel towards the collector. As the traveling reactant ions are consumed, monomers are generated along the drift region. Therefore, the number density of reactant ions decreases with their distance from the shutter grid. Since, the production rate of monomers is proportional to the number density of the reactant ions, the number density of monomers also decreases with distance from the shutter grid. Therefore, a tail appears to the left of the monomer peak (Fig. 2). This tail contains information about the kinetics of the reactant–monomer reaction [2]. Also a tail is observed between the monomer and dimer peaks that is the result of reaction between MH^+ and M (formation of dimer) and gives information about the kinetics of MH^+ formation.

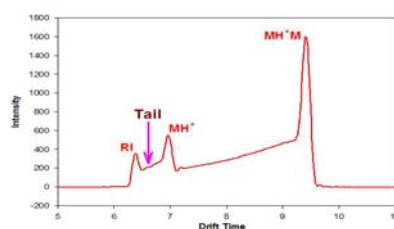


Fig. 2. Ion Mobility spectrum of formation of MH^+ from the reaction between M and reactant ion.



Similar to what described in ref 2, an expression can be written for the tail between the reactant and monomer peaks

$$[MH^+]_x = k_1[M][H_3O^+]_g t_g \exp\left(\frac{-k_1[M]x}{V_R}\right) \exp\left(\frac{-k_2[M]x}{V_M}\right). \quad (3)$$

where, $[MH^+]_x$ is the amount of monomer ion presents in the x distance from the shutter grid. This expression contains three terms. The first term denotes the monomer ions formed in the ionization region, which contributes to the background. The second term corresponds to the monomers forming in the drift region. It is an exponential term since the reactant ions exponentially decays as they attenuate in a bath of M molecules. The third term shows the consumption of the monomers to form dimers. This term is also exponential since the monomer itself is distributed exponentially in the drift region. The x coordinate may be converted to time coordinate using $x=vt$ and after taking Logarithm we have;

$$\ln[MH^+]_t = \ln(k_1[M][H_3O^+]_g t_g) - \frac{k_1[M]t_M}{\frac{t_M}{t_R} - 1} - \frac{k_2[M]t_M}{1 - \frac{t_R}{t_M}} + \frac{k_1[M]t}{\frac{t_M}{t_R} - 1} + \frac{k_2[M]t}{1 - \frac{t_R}{t_M}} \quad (4)$$

Thus, a plot of the logarithm of the ion current intensity versus drift time for the tail is expected to be a straight line with a slope proportional to the rate constant, k_1 and k_2 . If the sample concentration, the drift time for the RI and monomer ions, t_R and t_M , and the slope of the tail between monomer and dimer [2] are known, the rate constant, k_1 can then be easily determined.

3. Results and Discussion

DMP was used as test compound to evaluate the method. Fig. 2 shows the tails for DMP at 50 °C. The experiment was repeated in several drift fields. The average rate constant for the formation of monomer was obtained from the slopes to be, $2.3 \times 10^{-10} \text{ cm}^3 \cdot \text{s}^{-1}$.

4. Conclusions

A method was described to derive kinetic information for the protonated monomer ions MH^+ at ambient pressure from the tail between the reactant and monomer ions. In this method sample is continuously introduced into the drift region where it reacts with a swarm of reactant ions injected by the shutter grid. Protonated molecules are formed in the drift tube and a tail appears between the RI and Monomer ions. The proposed approach was examined for a test compound. The measured value for the rate constant is comparable with the rate constant for formation of protonated dimer.

References

- [1] Ewing, R.G. Eiceman, G.A. Harden, C.S. Stone, J.A. Int. J. Mass Spectrom. 255–256 (2006) 76.
- [2] Jazan, E. Tabrizchi, M. Chem. Phys. 355 (2009) 37.
- [3] Tabrizchi, M. Khayamian, T. Taj, N., Rev. Sci. Instrum. 71 (2000) 2321.



Competitive adsorption of auramine-o and methylene blue from solution using natural zeolite in single and binary systems

A. Habibi-Yangjeh and F. Jafari-Zare*

Department of Chemistry, University of Mohaghegh Ardabili, P.O. Box 179, Ardabil, Iran

(Email: farhadjafari59@yahoo.com)

Keywords: Competitive adsorption, Adsorption kinetics, Wastewater treatment, Adsorption isotherms, Methylene blue, Auramine-O.

1. Introduction

Waste effluent from the textile industry can be particularly problematic due to the presence of colour in the final effluent. Conventional treatment facilities are often unable to remove certain forms of colour, particularly arising from reactive dyes due to their high solubility and low biodegradability. Hence, adsorption is recommended as a important method for reactive dye removal [1,2].

2. Experimental

Natural zeolite was commercial (Afrand Tuska, Iran) from deposits in the region of Semnan. The XRD pattern of the natural zeolite used in this work indicated that it consisted of majorly from clinoptilolite [3]. The dyes were chosen for investigation are methylene blue (MB) and auramine-O (AO) and were obtained from Merck. The pH of the solutions was adjusted with HCl or NaOH (from Merck) solutions.

Adsorption kinetics and isotherm experiments for all samples were undertaken in a batch reactor with 200 ml capacity provided with water circulation arrangement to maintain the temperature at desired value. Adsorption of the dyes was performed by shaking 0.01g of the zeolite in 150 ml of the solutions with varying concentrations (10^{-6} – 10^{-5} M) at different temperatures (25 and 55 °C). Determination of the concentration for dyes was done spectrophotometrically.

3. Results and discussion

The adsorption of MB on the zeolite is faster to reach equilibrium approximately at 1000 minute while it will take a longer time for AO (1500 minute). For the dyes, the adsorptions at 55 °C are higher than those at 25 °C, suggesting the endothermic characteristic of the adsorption.

An adsorption isotherm shows how the adsorbate molecules partition between the liquid and solid phases when the adsorption process reaches equilibrium conditions. Several isotherm equations are available and two important isotherms are used in this study, the Langmuir and Freundlich isotherms. The parameters for two isotherms obtained from experimental data and the related correlation coefficients are presented in Table 1. One can see that regression coefficient obtained from the Langmuir isotherm is higher than the Freundlich isotherm. Then it can be concluded that adsorption of both dyes mainly obeys from Langmuir isotherm.

Table 1. Parameters for adsorption of MB and AO on the natural zeolite in single component systems.

Dyes	Temperature (°C)	Langmuir isotherm			Freundlich isotherm		
		q_{\max} (mol/g)	K_L (1/mol)	R^2	K_F (mol/g)	1/n	R^2
AO	25	6.46×10^{-5}	3.68×10^5	0.9192	3.84×10^{-3}	0.3676	0.9067
	55	1.47×10^{-4}	4.0×10^5	0.9031	5.68×10^{-2}	0.5175	0.9699
MB	25	6.40×10^{-5}	3.00×10^6	0.9933	2.34×10^{-4}	0.112	0.9184
	55	7.95×10^{-5}	3.40×10^6	0.9907	2.81×10^{-4}	0.109	0.9153

The adsorption of the basic dyes on the zeolite follows the pseudo-second-order kinetics. The adsorption occurs in two stages. The first one is attributed to external surface adsorption and the second one should be intraparticle diffusion process.

Table 2 compares the results obtained for fitting of the Langmuir and Freundlich isotherms for competitive adsorption of MB and AO. It is clear that similar to single component systems, the competitive adsorption data is mainly fitting in the Langmuir model.

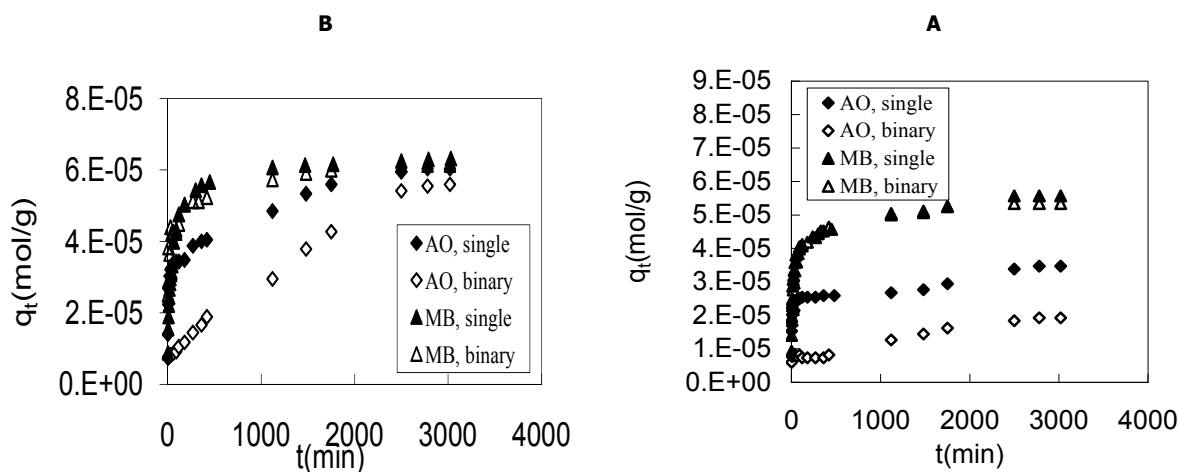


By comparing the results in Table 1 and 2, one can see that the Langmuir constant for adsorption of MB and AO in binary component system is lower than single component systems.

Table 2. Parameters for adsorption of MB and AO on the natural zeolite in binary component system.

Dyes	Temperature (°C)	Langmuir isotherm			Freundlich isotherm		
		q_{\max} (mol/g)	K_L (1/mol)	R^2	K_F (mol/g)	$1/n$	R^2
AO	25	3.73×10^{-5}	2.86×10^5	0.9147	1.84×10^{-3}	0.3637	0.8552
	55	1.26×10^{-4}	3.7×10^5	0.9011	3.99×10^{-2}	0.5051	0.9621
MB	25	6.20×10^{-5}	2.70×10^6	0.9967	0.0338	0.476	0.9950
	55	7.44×10^{-5}	3.02×10^6	0.9966	0.146	0.557	0.9941

Similar to single component systems, the adsorption of the basic dyes on the zeolite in binary component system follows the pseudo second-order kinetics. In single and binary component systems, the amount of adsorption of MB and AO on the zeolite increases with pH of solution. Fig. 1 demonstrates a comparison of MB and AO adsorption on natural zeolite in single and binary component systems at 25 (A) and 55 °C (B). It is clear that the adsorption of MB and AO is reduced in binary component system, which suggests a competitive adsorption.



4. Conclusions

A natural zeolite has been tested for single and binary component adsorption of two basic dyes, MB and AO. The maximal adsorption capacities for MB are 6.4×10^{-5} and 7.95×10^{-5} mol/g at 25 and 55 °C, respectively and those of AO are 6.46×10^{-5} and 1.47×10^{-4} mol/g at 25 and 55 °C, respectively. For single and binary component systems, the adsorption data could be fitted mainly by the Langmuir model. Also, the kinetics of adsorption is better described by the pseudo-second-order model with two step diffusion process.

References

- [1] M.İ. Özacar, I.A. Şengil, Adsorption of acid dyes from aqueous solutions by calcined alunite and granular activated carbon, Adsorption 8 (2002) 301.
- [2] M.İ. Özacar, I.A. Şengil, Adsorption of reactive dyes on calcined alunite from aqueous solutions, J. Hazard. Mater. B98 (2003) 211.
- [3] M. Nikazar, K. Gholivand, K. Mahanpoor, Photocatalytic degradation of azo dye Acid Red 114 in water with TiO₂ supported on clinoptilolite as a catalyst, Desalination 219 (2008) 293.

**Effect of concentration on the ultrasonic degradation of poly (vinyl pyrrolidone) in aqueous solution**

Mohammad Taghi Taghizadeh* and Esmail Heydarpour Serajeh Lou

University of Tabriz, Faculty of chemistry, Department of physical chemistry, Tabriz, Iran

(Email: mttaghizadeh@tabrizu.ac.ir)**1. Introduction**

Various methods like application of heat, light, chemical reagents, ultrasonic radiation can cause polymer degradation. Application of ultrasonic energy for polymer degradation date back to the 1930s when natural polymers were subjected to sonication, which resulted in a reduction of viscosity [1]. Schmid and Rommel [2] were the first to report the investigation of polymer degradation by ultrasonic energy.

2. Methods

A kinetic method based on viscometric data was used to determine the rate of degradation reactions for different concentration of PVP solutions. The rate of degradation is defined as the number of moles of scission that occur in 1 l in unit time. The chain scission yields the two pieces. The degradation rate equation is as follows:

$$\frac{dM}{dt} = kM^n \quad (1)$$

Where M is the total molar concentration of polymer, k is the rate constant and n is the order of reaction with respect to the total molar concentration of polymer. The solution of differential Eq. (1) is:

$$M^{1-n} - M_0^{1-n} = (1-n)kt \quad (2)$$

where M_0 is the initial total concentration of polymer. The total molar concentration is related to the number average molecular weight through:

$$M = \left[\frac{(1+\alpha)\Gamma(1+\alpha)KC^{1+\alpha}}{\sqrt{2}} \right]^{\frac{1}{\alpha}} \Delta\eta \quad (3)$$

Substitution of Eq. 3 to Eq.2 we have:

$$\Delta\eta^{1-n} - \Delta\eta_0^{1-n} = (1-n) \left[\frac{\sqrt{2}}{(1+\alpha)\Gamma(1+\alpha)KC^{1+\alpha}} \right]^{\frac{1-n}{\alpha}} kt \quad (4)$$

Finally, we obtain the following equation from Eq.4:

$$\Delta\eta^{1-n} - \Delta\eta_0^{1-n} = k't \quad (5)$$

3. Results and discussion

Fig. 1 shows the relative viscosity versus sonication time for different concentrations. As seen, when concentration of solution increased, reduce in relative viscosity decreased considerably. It can be deduced that there is a limiting molecular weight that below which chain scission does not occur. Under the same conditions, the decrease in η_r of the sample with a high polymer concentration is lower than of the sample with a low polymer concentration. At high concentration, entanglements influence the energy transfer processes between solvent and polymer and appears to reduce the probability of degradation accruing [3].

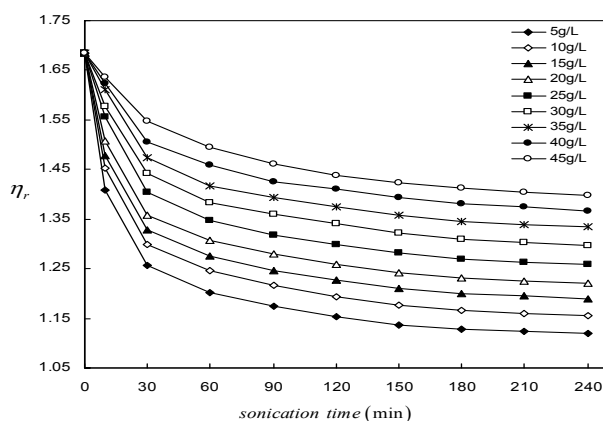


Fig. 1. The relationship between η_r and sonication time for different concentration of PVP solutions.

4. Conclusions

The aim of this research was to study the effect of concentration of polymer on the ultrasonic degradation of PVP in solution at 25°C. The experimental results indicated that the degradation rate reduced with increasing solution concentration. Relative viscosity decreases on sonication time and inclines to a limiting value, below which no further degradation occurs.

References

- [1] G.J. Price, P.J. West, P.F. Smith, *Ultrason. Sonochem.* 1 (1994) 51.
- [2] G. Schmid, O. Rommel, *J. Phys. Chem. A* 185 (1939) 97.
- [3] M. T. Taghizadeh, A. Bahadori, *J. Polym. Res.* 16 (2009) 545.

**Combustion characterization of modified double-based propellant containing nitroamines**

M. Norouzi Bakhsh and M. R. Nayeib Hosseini

Department of chemistry, Applied sciences complex, Malek-Ashtar University of Technology (Esfahan branch), Esfahan, Iran
(E-Mail: payamashu@gmail.com)

Keywords: double-based propellant, Combustion, heat transfer, mass transfer, Nitroamines

1. Introduction

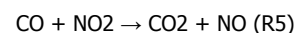
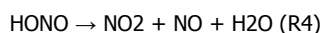
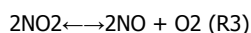
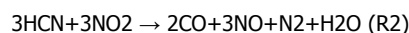
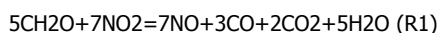
Double-base propellant is known as smokeless propellant, and is used for guns and rockets. The physicochemical properties of double-base propellants such as energy density, mechanical properties and chemical stability depend on the fractions of NC, NG, stabilizers, plasticizers, and catalysts [1,2]. In order to evaluate the actual pros and cons in the use of new nitroamines for solid rocket applications, the combustion properties of modified double-base propellants containing nitroamines such as cyclotrimethylenetrinitramine (RDX), trans-1,4,5,8-tetranitro-1,4,5,8-tetraazadecalin (TNAD), cyclotetramethylenetetranitramine (HMX) and 1,4-dinitropiperazine (DNP) are investigated in a large number of recent studies [3,4] so the present work is an effort to increase our knowledge in elucidating the combustion mechanism with the function of these nitroamines mentioned above, mean while, clarifying how the chemical reaction in different combustion zone which might control the burning characteristics of this kind of propellant.

2. Methods

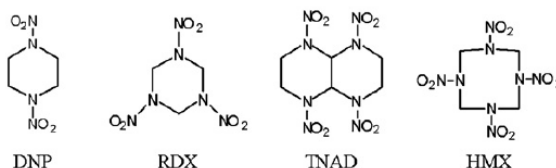
The Thermal Video Systems was introduced to test the temperature distribution of the flame zone and take a photo of the flame at different pressure. The uncoated sample (dimension, 5mm×5mm×15mm) was placed vertically on the ignition rack, and the rack was fixed in a combustion chamber with vitreous window. The chamber was filled with continuous flow of argon atmosphere from bottom to top achieving a definite pressure, which can ensure the flame transparency in the chamber. The nickel-chrome wire was used to ignite the propellant samples, in this way the flame pictures were obtained.

3. Results and Discussion

Typical flame structures of double-base propellant containing nitrogen heterocyclic nitroamines are shown in Fig. 1 as a function of pressure. A thin luminous flame zone stands some distance from the burning surface and a reddish flame is produced above this luminous flame zone. The flame zone approaches the burning surface as pressure increases [5]. When the pressure is less than 1MPa, the luminous flame will be blown away from the burning surface. The luminous flame gradually approaches the burning surface as the pressure increases, however, it becomes very unstable above the burning surface and forms a wave-shaped flame zone at the pressure of 3MPa. When the pressure was further increased above 5MPa, the luminous flame became stable and one-dimensional just above the burning surface. It was also indicated from the close-up view of the primary flame that there must be inherent factors such as temperature and oxidation reaction rate in both condensed phase and gas phase controlling the burning rate and the flame structure. According to Qi-Long Yan and co-workers results [6] and the reaction mechanisms presented in Table 1, the probable dominant reactions in the oxidation stage for gas phase reaction zone can be established as follows:



The entire oxidation reaction rate to reactions (R1)–(R5) is dependent on the pressure of the combustion chamber and temperature of the gas phase. In order to make it clearer that how the pressure controls the chemical reaction rate and affects the flame





structure of double-base propellants containing nitroamines, the flame photos of the RDX-CMDB propellant at the pressure of 3, 5 and 7 Mpa were selected to simulate the combustion process. When the pressure is relatively lower (e.g. 3 MPa), there might be fewer and larger inhomogeneous spill point for the gaseous products and the velocity of gaseous fuel flow is lower as a result of slow chemical reaction. Comparatively, when the pressure is higher (e.g. 7MPa), there might be replete and serried weeny spill point for the gaseous products and the velocity of the gaseous fuel flow is very fast as a result of quick uniform chemical reaction at the condensed phase. Actually only the RDX-CMDB and HMX-CMDB propellant under study have the pressure exponent in the burning law $0 < n < 1$ and their gas velocity increased with the pressure increased, whereas, the propellants which contain TNAD or DNP have the pressure exponent in the burning law n nearly equal to zero or even less than zero, thereafter, their gas velocity is independent on the pressure and they are more proper to applied to rocket motors.

Species	300 K	400 K	500 K	600 K	800 K	1000 K	1500 K	2000 K	2500 K	3000 K
NG	51.7	62.7	71.7	78.9	89.0	95.6	104.6	108.7	110.9	112.2
DNP	46.3	57.7	66.9	74.2	84.4	90.9	99.5	103.3	105.3	106.5
RDX	49.2	61.5	71.7	79.7	91.2	98.7	108.9	113.6	116.1	117.6
TNAD	72.7	91.8	107.8	120.5	138.7	150.6	167.0	174.6	178.6	181.0
HMX	66.9	83.0	96.5	107.2	122.6	132.7	146.4	152.8	156.2	158.1

Table1. Calculated C_p (cal mol⁻¹ K⁻¹) for some of the energetic components at the temperature range of 300–3000K [7]

4. Conclusions

In this study, the thermodynamic phase transition consisting of both evaporation and condensation of NG,HMX,TNAD, RDX and DNP, are considered to provide a complete description of the mass-transfer process in the combustion of double-base propellant containing nitroamines, and the combustion mechanisms of them are mainly involved with the oxidation mechanism of the NO₂, formaldehyde(CH₂O) and hydrogen cyanide(HCN). The entire oxidation reaction rate might be dependent on the pressure of the combustion chamber and temperature of the gasphase. The propagation mode of laminar flame is expected to govern many properties in the flames.

References

- [1] Merrill W. Beckstead, Karthik Puduppakkama, Piyush Thakreb, Vigor Yangb, Progress in Energy and Combustion Science 33 (2007) 497.
- [2] C.F. Melius, in: S.N.Bulusu(Ed.), Chemistry and Physics of Energetic Materials, KluwerAcademic Boston, 1990
- [3] N. Kubota, T.J. Ohlemiller, L.H. Caveny, et al., The Mechanism of Super-Rate Burning of Catalyzed Double Base Propellants, AMS Report No. 1087, Aerospace and Mechanical Sciences, Princeton University, Princeton, NJ, 1973
- [4] T.L.Boggs, in: K.K. Kuo, M. Summerfield (Eds.), Fundamentals of Solid Propellant Combustion, AIAA, NewYork, 1984
- [5] L.V.Moskaleva, M.C. Lin, The spin-conserved reaction CH+N→H+NCN: a major pathway to prompt NO studied by quantum/statistical theory calculations and kinetic modeling of rate constant, Proceedings of the Combustion Institute 28 (Part II 2) (2000) 393.
- [6] Qi-Long Yana, Zhen-Wei Songa, Xiao-Bing Shia, Zhi-Yuan Yangb, Xiao-Hong Zhanga, Combustion mechanism of double-base propellant containing nitrogen heterocyclic nitroamines(II): The temperature distribution of the flame and its chemical structure, Acta Astronautica 64 (2009) 602.
- [7] B.B.Goshgarian, The thermal decomposition of RDX and HMX, AFRPL-TR-78-76, October 1978.

**The kinetics study of brilliant green fading in the presence of various surfactants**Mohammad Rafi Dargahi^{a*}, Babak Samiey^a and Ali Rafi Dargahi^b^aDepartment of Chemistry, University of Lorestan, Lorestan, Iran

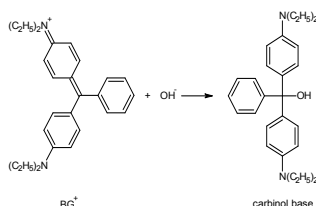
(Email: dargahi.m@gmail.com)

^bDepartment of Chemistry, University of Tehran, Tehran, Iran**Keywords:** Classical model, Brilliant Green, Kinetics, Fading, TX-100, DTAB, SDS.**1. Introduction**

The rates of chemical reactions are known to be changed by self-organized assemblies such as micelles. Effects of micelles on these reactions can be attributed to electrostatic and hydrophobic interactions. Brilliant green (BG⁺) is a triphenylmethane dye [1]. In this work, we have studied the BG⁺ alkaline fading in the presence of different concentrations of TX-100, DTAB and SDS at 283-303 K. The BG⁺ fading is a one-step reaction and kinetics of these kinds of reactions in the presence of surfactants can be studied using classical model [2].

2. Methods

The fading of BG⁺ was followed at its maximum wavelength (λ_{\max}) values in a thermostated cell compartment of a Shimadzu UV-1650PC spectrophotometer. The reaction of BG⁺ with hydroxide ion brings about fading the color of the BG⁺ and results to the formation of colorless carbinol base, Scheme 1. The experiments were conducted at 283, 293 and 303 K within ± 0.1 K. All the kinetic runs were carried out at least in triplicate. The reaction between BG⁺ and hydroxide ion has been found to be bimolecular but pseudo-first-order conditions (excess alkali) were used in all cases. We used the second-order reaction rate constants in our calculations.



Scheme 1

3. Results and Discussion

In classical model, it is assumed that in each range of surfactant concentration, the surfactant and substrate can bind together and there is an equilibrium relation between them. For each assumed equilibrium relation, following equation holds for:

$$\ln k' = c - \frac{E_s}{RT} [S]_t \quad (1)$$

where k' , c , $[S]_t$, R , T and E_s are the rate constant in the presence of surfactant, $\ln k$ (at first region) or $\ln k_{sc}$ (for other regions), total surfactant concentration, universal gas constant, absolute temperature and activation energy of reaction in constant temperature and various surfactant concentrations, respectively. k_{sc} is the k_{obs} in the starting of every region except region one. Eq. (1) is named Samiey equation and can determine the concentration range of each region.

Effect of TX-100 on the BG⁺ fading. As seen in Figs. 1 and 2, with increase in TX-100 concentration, the λ_{\max} value of BG⁺ shifts to red and the reaction rate of BG⁺ fading increases. kinetics of BG⁺ fading in the presence of TX-100 is three region. The first region is below its cmc point. In this region, interaction of BG⁺ with TX-100 is exothermic. In the second region, above cmc point of TX-100, the reaction rate and λ_{\max} value of BG⁺ fading keep approximately constant. In the third region, reaction rate increases with increase in TX-100 concentration, but there is no shift in the λ_{\max} value of BG⁺. This indicates that BG/TX-100 compound forms through hydrophobic association between bound TX-100 molecules. In this region, interaction is exothermic, interaction of BG⁺ with TX-100 molecules throughout concentration range of TX-100 is exothermic and its ΔS value is negative.

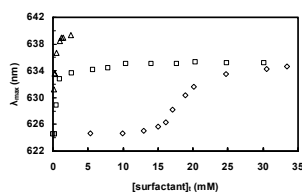


Fig. 1. λ_{\max} values of BG^+ vs. concentrations of Δ SDS, \square TX-100 and \diamond DTAB under alkaline conditions.

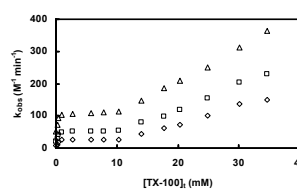


Fig. 2. k_{obs} values of BG^+ fading reaction vs. concentrations of TX-100 at \diamond 283, \square 293 and Δ 303 K under alkaline conditions.

Effect of DTAB on the BG^+ fading. As seen in Figs. 1 and 3, kinetics of BG^+ fading in the presence of DTAB is three-region. the first region is below the cmc value of DTAB. In this region, the rate constant of BG^+ fading and λ_{\max} value of BG^+ keep approximately constant and it seems that there is no interaction between BG^+ and DTAB molecules. Obviously, at the beginning of the second region ($\approx 13 \text{ mM} > \text{cmc value of DTAB}$), a weak electrostatic interaction occurs between $(\text{C}_2\text{H}_5)_2\text{N}^-$ group of BG^+ and positive head group of DTAB molecules and along with hydrophobic interaction of BG^+ with DTAB micelles results to the red shift in λ_{\max} value of BG^+ .

In the third region, the rate constant of BG^+ fading and λ_{\max} value of BG^+ keep approximately constant and it seems that there is no interaction between BG^+ and DTAB molecules [3].

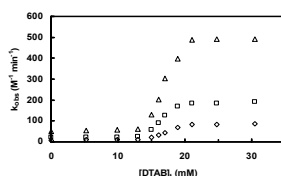


Fig 3. k_{obs} values of BG^+ fading reaction vs. concentrations of DTAB at \diamond 283, \square 293 and Δ 303 K under alkaline conditions.

Effect of SDS on the BG^+ fading. As seen in Figs. 1 and, kinetics of BG^+ fading in the presence of SDS is five-region. the used concentration range of SDS is below its cmc value. It is clear from Fig. 1 that the λ_{\max} value of BG^+ keeps constant at the end of region 3 (0.93 mM) where the rate constants of fading decrease. Interaction of BG^+ with SDS in regions 2, 3, 4 and 5 is endothermic.

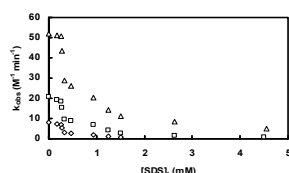


Fig4. k_{obs} values of BG^+ fading reaction vs. concentrations of SDS at \diamond 283, \square 293 and Δ 303 K under alkaline conditions.

4. Conclusions

The rate constants of alkaline fading of brilliant green (BG^+) were measured in various concentrations of TX-100, DTAB and SDS. It was observed that the reaction rate constants were increased in the presence of TX-100 and DTAB and decreased in the presence of SDS. Binding constants of surfactant molecules to BG^+ were obtained using classical models and the related thermodynamic parameters were calculated by classical model. The results show that binding of BG^+ to TX-100 is exothermic and binding of BG^+ to DTAB and SDS is endothermic.

References

- [1] C. Bravo-Diaz, M. J. Pastoriza-Gallego, S. Lasada-Barreiro, V. Sanchez-Paz, A. Fernandez-Alonso, Int J Chem Kinet 40 (2008) 301.
- [2] B. Samiey, K. Alizadeh, M. A. Moghaddasi, M. F. Mousavi, N. Alizadeh, Bul Korean Chem Soc 25 (2004) 726.
- [3] O. Olanrewaju, J. Ige, O. Soriyan, O. Grace, O. Segun Esan, O. Olanrewaju, Acta Chim Slov 54(2007) 370.



Investigation on mechanism and kinetic of decomposition on nitrate esters as main component of double base propellant in combustion process

Mohamad Reza Nayeab Hosseini* and Mehdi Norouzi Bakhsh

Department of Chemistry, Malek-ashtar University of Technology, Shahin shahr

(Email: rezamohamad54@yahoo.com)

Key word: Decomposition, Nitrate ester, Combustion process, Double base propellant, Kinetic of combustion dissociation.

1. Introduction

Nitrate esters are important class of energetic material they are high explosives and main ingredient of double base propellant. we want to investigate the mechanism and kinetic of combustion dissociation, combustion wave structure and explain the reaction and relation which related to each region of combustion wave structure.

By understanding combustion behavior of this kind of propellant we can better design the proper situation for having good performance on rocket motor.

2. Method

In this paper we use FT-IR spectra from burned surface and also study and compare Mulliken bond populations and bonding dissociation energy (BDE) which are proper methods for understanding combustion behavior.

3. Results and discussion

These energetic materials are used as explosives and propellant. For use as propellant they are desensitized for impact and thermal stress. We want these energetic compounds burning and produce hot gas with high velocities. Combustion wave structure are shown in figure 1

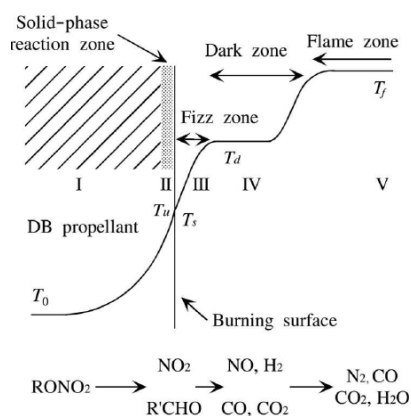


Fig.1 combustion wave structure of double base propellant

As shown in figure 1 there are five zones in combustion wave structure (I) Heat conduction zone: Though there is a thermal effect due to heat conduction from the burning surface, no chemical changes occur. The temperature increases from the initial propellant temperature, T_0 , to the onset temperature of the solid-phase reaction, T_u . (II) Solid-phase reaction zone: Nitrogen dioxide and aldehydes are produced in the thermal degradation process. This reaction process occurs endothermically in the solid phase and/or at the burning surface. The interface between the solid phase and the burning surface is composed of a solid/gas and/or solid/liquid/gas thin layer. The nitrogen dioxide fraction exothermically oxidizes the aldehydes at the interface layer. Thus, the overall reaction in the solid-phase reaction zone appears to be exothermic. (III) Fizz zone: The major fractions of nitrogen dioxide and the aldehydes and other C,H,O and HC species react to produce nitric oxide, carbon monoxide, water, hydrogen, and carbonaceous materials. This reaction process occurs very rapidly in the early stages of the gas-phase reaction zone, just above the burning surface. (IV) Dark zone: In this zone, oxidation reactions of the products formed in the fizz-zone reaction take place. Nitric oxide, carbon monoxide, hydrogen, and carbonaceous fragments react to produce nitrogen, carbon dioxide, water, etc. These exothermic reactions occur only very slowly unless the temperature and/or pressure is sufficiently high. (V) Flame zone: When the dark-zone reactions occur rapidly after an induction period, they produce a flame zone in which

the final combustion products are formed and attain a state of thermal equilibrium. When the pressure is low, below about 1 MPa, no flame zone is produced because the reduction of nitric oxide is too slow to produce nitrogen. [1-4] FT-IR spectra of burned surface of double base propellant are shown in figure.2 [5]

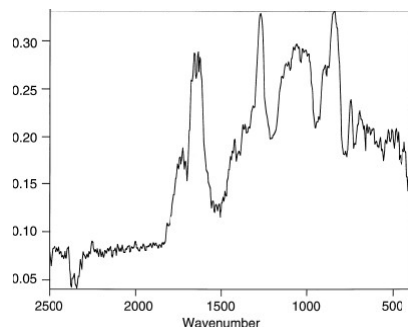


Fig.2 FT-IR spectra of burned surface of double base propellant

As shown in figure 2 appearance of band at 1730 cm^{-1} represent that one possible explanation for this change is that carbonyl especially aldehyde group are generated from loss of $-\text{NO}_2$

4. Conclusions

In condensed phase $\text{O}-\text{NO}_2$ bond are dissociated and cause aldehyde and Nitrogen dioxide are produced. Dark zone length is decreased by increasing in pressure because with supplying heat and pressure in dark zone the compound in dark zone obtain proper situation for reaction. Some catalysts cause increase decrease in dark zone and subsequent increasing in burning rate.

References

- [1] Crawford, B. L., Huggett, C., and McBrady, J. J., The Mechanism of the Double-Base Propellants, *Journal of Physical and Colloid Chemistry*, Vol. 54, No. 6, 1950, pp. 854–862.
- [2] Rice, O. K., and Ginell, R., Theory of Burning of Double-Base Rocket Propellants, *Journal of Physical and Colloid Chemistry*, Vol. 54, No. 6, 1950, pp. 885–917.
- [3] Parr, R. G., and Crawford, B. L., A Physical Theory of Burning of Double-Base Rocket Propellants, *Journal of Physical and Colloid Chemistry*, Vol. 54, No. 6, 1950, pp. 929–954.
- [4] Heller, C. A., and Gordon, A. S., Structure of the Gas-Phase Combustion Region of a Solid Double-Base Propellant, *Journal of Physical Chemistry*, Vol. 59, 1955, pp. 773–777.
- [5] M. A. SCHROEDER,* R. A. FIFER, M. S. MILLER, R. A. PESCE-RODRIGUEZ, C. J. S. MCNESBY, and G. SINGH U.S. Army Research Laboratory, Aberdeen Proving Ground, MD 21005-5066, USA

**Kinetic study of the reaction of catechol with cerium(IV) in aqueous sulphuric media**

Morteza Jabbari* and Farrokh Gharib

Department of Chemistry, Shahid Beheshti University, Tehran, Evin, Iran

(E-mail: m_jabari@sbu.ac.ir)**Keywords:** Kinetic and mechanism, Catechol, Cerium(IV), Aqueous sulphuric media**1. Introduction**

Cerium(IV) is one of a group of metal ion oxidants which react only via one electron steps and is of considerable importance and interest[1]. The oxidation of a variety of organic and inorganic compounds by Ce(IV) in acidic media has been the object of several studies.

Catechol (1, 2-dihydroxybenzene) is an important compound known for its antioxidant activity. The interaction of catechol with DNA is reported to increase the amount of a substance known as 8-oxod G which is believed to correlate with the incidence of cancer [2]. There are some evidences that the toxicity of catechol is increased by its oxidation [3]. This work reports a study of the reaction of catechol with Ce(IV) in sulphuric acid medium.

2. Experimental Method

The reaction of catechol with Ce(IV) was followed spectrophotometrically by monitoring the absorption band at the range of 361-374 nm. These wavelengths are the maximum absorption due to Ce(IV) in different concentrations of sulphuric acid, the absorption due to the other reaction species were negligible.

The reaction was arranged to be under pseudo first-order conditions by keeping a large excess of catechol over the cerium(IV). All kinetic measurements were performed at constant ionic strength ($2.0 \text{ mol dm}^{-3} \text{ Na}_2\text{SO}_4\text{-H}_2\text{SO}_4$).

The kinetic runs were followed for more than 80 % completion of the reactions and good first-order kinetics was observed. The pseudo first-order rate constants, k_{obs} , for different runs were calculated from the plots of $\log[a/(a-x)]$ versus time, where a is the initial concentration of Ce(IV) and $(a-x)$ is the concentration of Ce(IV) at different time intervals.

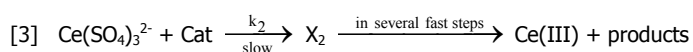
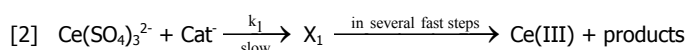
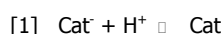
The stoichiometry of reaction will be given as



Product composition of the reaction was studied by mixing a known amount of cerium(IV) sulphate (0.1 mol dm^{-3}) with catechol (0.1 mol dm^{-3}) in the presence of 1.0 mol dm^{-3} sulphuric acid and ionic strength 2.0 mol dm^{-3} ($\text{Na}_2\text{SO}_4\text{-H}_2\text{SO}_4$). To evaluate the structural properties of final product, corresponding FT-IR spectrum was taken.

3. Results and Discussion

The kinetic measurements performed using different concentrations of sulphuric acid, as well various concentrations of ceric ion and catechol in 1.0 mol dm^{-3} sulphuric acid at constant ionic strength ($2.0 \text{ mol dm}^{-3} \text{ H}_2\text{SO}_4\text{-Na}_2\text{SO}_4$) and 25°C . Deviation from straight line of the plots $\log[a/(a-x)]$ versus time were prominent at higher Ce(IV) concentrations. However, the rate constant values calculated from the slope of the plots $\log[a/(a-x)]$ versus time are almost constant when the amount of complex X_1 formed between the oxidant and the substrate was negligible, eq. [2], which necessitate a low Ce(IV) concentration. Under the present experimental conditions of $[\text{H}^+]$, catechol exists in the full protonated ($> 99\%$), mono-protonated ($< 1\%$), and the diprotonated form is actually zero in the conditions used. Therefore, the full protonated and mono-protonated forms of catechol are presumed to be the reactive species and the following mechanism has been proposed:



The rate of reaction ($-d[\text{Ce(IV)}]/dt$) increase with increasing concentration of oxidant in the beginning but this is not prominent at higher concentration of the oxidant. Straight lines of plotting the reaction rate values versus Ce(IV) concentrations passing through the origin in the beginning but trend to become parallel to the x-axis at higher concentrations. This type of



trend indicates that one of the products, possibly Ce(III), is acting as an inhibitor. These considerations confirm that the reaction shows direct proportionality at low concentrations of Ce(IV), while order of the reaction trends to become zero at higher concentrations of the oxidant. Also, the rate of reaction increases proportionally with increasing the concentration of catechol in the beginning but this is not prominent at higher concentrations of the substrate. This trend in the rate values again indicate the reaction order is changing from unity at low concentrations to zero at higher concentrations of the substrate.

References

- [1] K.K. Adari, A. Nowduri, and V. Parvataneni. *Acta Chim. Slov.* 55 (2008) 425.
- [2] N. Aktas, and A. Tanyolac. *J. Mol. Catal. B* 22 (2003) 61.
- [3] A. Katafias. *Trans. Met. Chem.* 31 (2006) 907.



Synthesis of TiO₂ and Ni-Pd-Pt/TiO₂ nanoparticles for photocatalytic degradation of acid blue 92

Sh. Ghasemi, Z. Kaboli and M. R. Gholami

Department of Chemistry, Sharif University of Technology, Azadi Ave., Tehran, Iran

(Email: sh_ghasemi@mehr.sharif.ir)

Keywords: Nanocrystalline TiO₂, Sol-gel method, Transition metal, Acid Blue 92.

1. Introduction

Nowadays, the highly colored wastewater generated by the textile industry constitutes an important environmental problem. TiO₂ nanoparticles have attracted extensive attention due to its stability, biological and chemical inertness for organic pollutants in water and air. However, there are some limitations in usage: (i) its wide band gap (3.2 eV) that is activated by UV radiation, (ii) photoinduced electron-hole pair recombination that occurs within nanoseconds. It can be conquered these limitation by doping of metals and non-metals. Titania can be synthesized by the sol-gel method that is one of the most suitable ways to prepare various metal oxides. In this work we investigated the effect of transition metal on property and photocatalytic activity of TiO₂ nanoparticles [1-4].

2. Experimental

2.1. Catalyst preparation

Tetraisopropylorthotitanate (Tipt, Ti (OCH (CH₃)₂)₄) was added to the first part of ethanol. After 10 minutes stirring, After that, second part of ethanol with dissolving dopant was added. Finally the TiO₂ gel was obtained by standing sol for 24 h. The TiO₂ product was dried 1 h at 100 °C and calcined 4 h at 500 °C.

2.2. Photocatalytic experiments

Irradiation experiments were carried out in a pyrex UV reactor. Solutions with the desired dye concentration and TiO₂ loading were fed into the reactor and the pH was adjusted using phosphate buffer. Samples (Ca.2 ml) were withdrawn for UV-Visible analysis at regular time intervals and centrifuged. The concentration of dyes in each degraded sample was determined by a spectrophotometer (GBC Cintra 40) at $\lambda=574$ nm.

3. Result and discussion

3.1. XRD and SEM analysis

The powder X-ray diffraction patterns for TiO₂ and TiO₂/Pt-Pd-Ni are shown in Fig. 1. All peaks measured by XRD analysis could be assigned to those of TiO₂ crystal. The average crystallite size is calculated using Scherrer equation (Table 1). No peaks corresponding to the transition metal oxide is detected, suggesting that it exist as the amorphous phase without getting incorporated into the TiO₂ phase; that is, they are in a highly dispersed form on the surface. Fig. 2 showed SEM image of the samples.

3.2. BET surface area

BET surface area analysis was shown in Table 1. The samples showed a higher surface area compared to pure titania. Transition metals reduce the extent of surface area loss during high-temperature calcinations. This can be explained based on higher resistance to sintering as well as the delayed transformation from amorphous to crystalline state acquired by doping with transition metal ions [5].

Samples	Size(nm)	Surface area	Mean pore diameter
TiO ₂	46.16	39	10.2
0.5%Pt	37.5	44.77	14.078
1.5%Pd	22.58	64.352	7.9
1% Ni	24.1	40.499	9.84

Table 1. characterization of nanaoparticles.

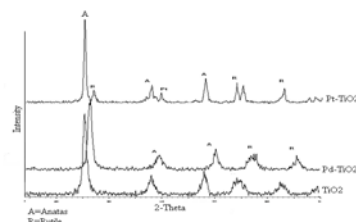


Fig 1. XRD patterns of the TiO₂ and TiO₂/Pt-Pd-Ni nanocomposites.

3.3. FT-IR and UV-VIS DRS spectral analysis

FT-IR spectra of the doped nanoparticles are shown in Fig. 3. The bands around 1636 and 3436 cm⁻¹ correspond to the bending and stretching modes of the –OH groups present in the catalysts. The FT- IR spectra of the modified samples do not show any band corresponding to the transition metal oxide, which confirms the XRD result. UV-VIS diffuse reflectance spectroscopy (Fig. 4) permits the detection of framework Ti in the samples.

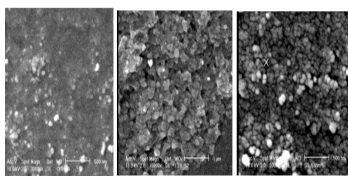


Fig. 2. The SEM images of doped TiO₂ nanoparticles

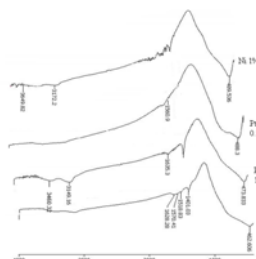


Fig.3. FTIR spectra of doped TiO₂ nanoparticles

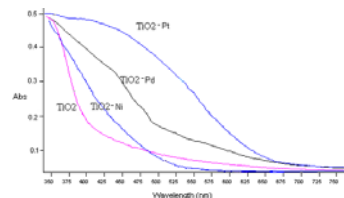


Fig.4. diffuse reflectance spectra of doped TiO₂ nanoparticles

3.4. Photocatalytic degradation of acid blue 92

The photocatalytic degradation of AB92 dye was observed to follow the first-order decay kinetics (by plotting $\ln(C/C_0)$ against irradiation time). In previous work, we found the optimum conditions for degradation of AB92 on prepared TiO₂ to be calcination temperature (500°C), dye concentration (10 ppm), and the amount of TiO₂ (60 ppm), pH (2). Here, we obtain photocatalytic degradation rate of AB92 dye in the optimum condition in present of doped TiO₂ and 25°C. The result was shown in

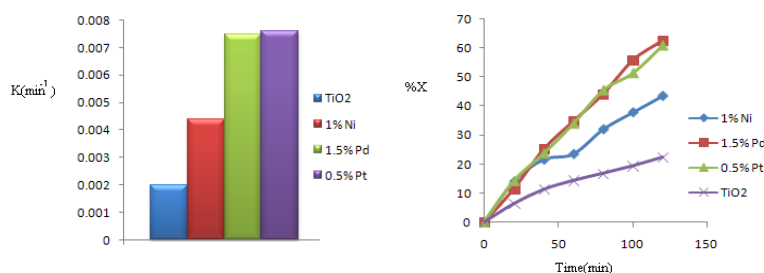


Fig5. photocatalytic degradation rate constant of AB92 on doped TiO₂ at 25°C. (pH = 2, [TiO₂] = 60 ppm, [AB92] = 20 ppm)

References

- [1] N. Venkatachalam, M. Palanichamy, V. Murugesan, Materials Chemistry and physics 104 (2007) 454.
- [2] K. S. Yoo, H. Choi, D. D. Dionysion, Catalysis Communications, 6 (2005) 259.
- [3] Ghasemi S, Rahimnejad S, Rahman Setayesh S, Hosseini M, Gholami M R., Prog. React. Kinetics. Mechan. 34(2009) 55.
- [4] Ghasemi S, Rahimnejad S, Rahman Setayesh S, Rohani S, Gholami M R., J. Hazard. Mat.; 172(2009) 1573.



Enzymatic hydrolysis of carboxymethyl cellulose using ultrasound waves pretreatment

M. T. Taghizadeh and Z. Nasrollahzadeh

Department of chemistry, university of Tabriz, Tabriz, Iran

(Email: lalehnasr25@gmail.com)

Keywords: Enzymatic hydrolysis, Ultrasonication, Carboxymethyl cellulose, Cellulases.

1. Introduction

Every wastes contain carbohydrates can use for producing useful materials such as biofuels, biomaterials and drugs. Current carbohydrate source in biological systems is cellulose. Cellulose is abundant renewable polymer in the world. Plants also produce cellulose by reduction of CO₂ in the atmosphere.

Cellulose is the polymer with anhydroglucose units that joined together with β (1-4) glucosidic bonds and its degradation to glucose is accomplished by addition of water molecules for each glucose molecules. Cellulose degrades in four major types (a) hydrolytic (b) oxidative (c) microbiological (d) mechanical [4].

Enzymatic hydrolysis is one of the most important microbiological degradation ways of cellulose to glucose. In plants cellulose forms complex with lignin. This complex is very resistant to attack from acid or enzyme molecules so the rate of enzymatic hydrolysis of lignocellulosic materials is low and very attempts are done to develop this reaction quality. Some of these efforts are consist of using pretreatments [5].

Pretreatments can be mechanical or chemical methods. One of the most important and frequently used methods that are on the base of structural modification is ultrasonic technique. Continues exposure of macromolecules with high energy ultrasound waves produces reduction in viscosity of polymer. The mechanism by which degradation occurs is still open to discussion but probably hydrodynamic forces between the ultrasonically accelerated faster moving solvent molecules and the larger, less mobile, macromolecules. Hydrodynamic forces may also be due to the high pressure associated with collapse of cavitation bubbles [3].

Cellulases are the enzymes that can hydrolyze β (1-4) glucosidic bond in CMC. This enzymes produces as a multicomponent enzyme system comprised usually of three enzymes that act synergistically in the hydrolysis of cellulose: endoglucanase, cellobiohydrolase, and cellobios [1].

In this study enzymatic hydrolysis of carboxymethyl cellulose to glucose by cellulases using ultrasound waves will perform. This reaction is very important process that can give back free carbon of cellulose to atmosphere for applying in other applications.

2. Materials and methods

In this reaction PH=4.8 and temperature is 323 K that temperature should be constant during the reaction. Different concentration of CMC is chosen for studying degradation phenomena. We determine produced glucose by using UV spectrophotometer. For this purpose we use glucose oxidase kit that oxidize glucose to quinoneimine then we measure this material absorbance that is equivalent with glucose concentration.

The enzymes are cellulases from *Aspergillus Niger* and *Trichoderma Viride*. This reaction is performed in usual condition and in the next step reaction performed by immersing a sonotrode in solution. With comparing of two states we can understand the effect of these waves on the rate of enzymatic hydrolysis.

3. Results and discussion

Little results are ready that you can see in figures 1 to 3. We hope ultrasound waves develop enzymatic hydrolysis by increasing rate of reaction. You can see that reaction was begun with high speed by using cellulose from *Aspergillus niger* but then it improve slow. By using *Trichoderma viride* it is begun slow but improves faster than the case of *Aspergillus niger*.

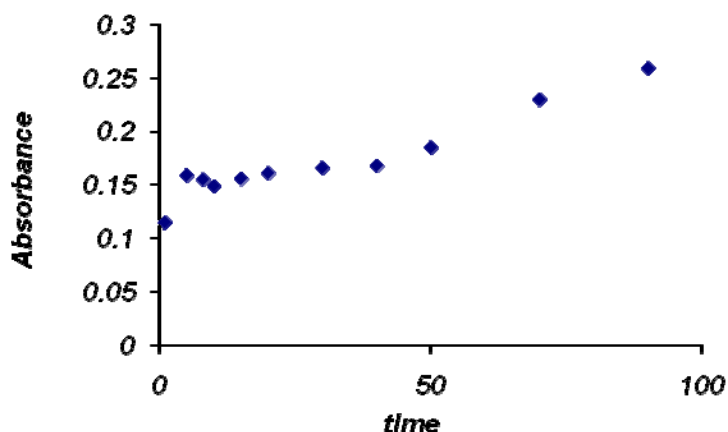


Fig 1. Variation of absorbance with time in degradation of CMC [10g/dm³] and E⁰_{Asp}[0.4g/dm]

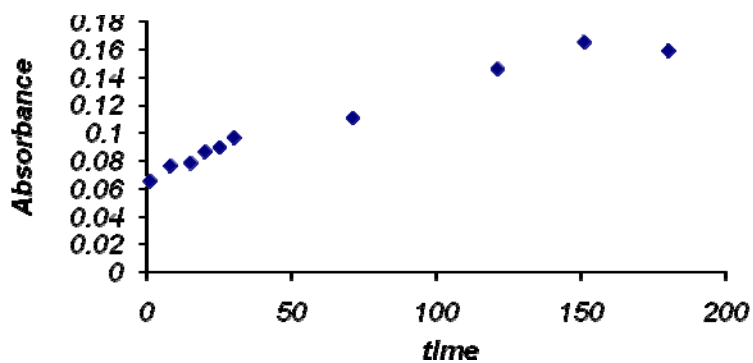


Fig 2. Variation of absorbance with time in degradation of CMC [10g/dm³] and E⁰_{Tri}[0.4g/dm]

4. Conclusions

Experiments aimed at developing a high performance hydrolysis of cellulose was carried out using CMC as a substrata model. In enzymatic hydrolysis of cellulose using mechanical pretreatment can help to increase rate of reaction.

References

- [1] Aliyu, M. Hepher, M.J. Ultrasonic Sonochemistry 7 (2000)265.
- [2] Cao, Y.Tan, H.Carbohydrate chemistry 337(2002) 1291.
- [3] Gronroos,A.Pirkonen,P.Ruppert,O.Ultrasonic Sonochemistry 11(2004) 9.
- [4] Imai,M. Ikar,K. Suzuki,I. J.Biochemical Engineering 17(2004) 79.
- [5] Kuo,H. Lee,K.G.Carbohydrate polymers 77(2009) 41.

Kinetics and mechanism of propene elimination from allyl methyl amine pyrolysis in the gas phase

M. Izadyar and E. Esmaili

Department of Chemistry, University of Payam-e-Noor, Gonabad, Khorasan-e-Razavi, Iran

(Email: Izadyar.m@gmail.com)

Keywords: Alkyl allyl Amine, Retro-ene reaction, Concerted mechanism, Gas-phase kinetics.

1. Introduction

The mechanism of the retro-ene reaction has been the subject of the interesting controversies [1-3]. Both experimental and theoretical studies indicate that this type of reaction proceeds through a concerted mechanism, although in some cases, stepwise mechanism involving diradical intermediate is less favorable [4-8]. The most important molecular mechanisms that are involved in the gas phase pyrolysis of these compounds include the radical and concerted mechanisms. Martin et. al. studied the gas phase thermolysis of alkyl allyl amine at 673-773 K [9]. The rate equation is accordance to Eq. 1.

$$K(\text{sec}^{-1}) = 10^{11.4} \text{Exp}(-181.6 \text{ kJ.mol}^{-1}(\text{RT})^{-1}) \quad (1)$$

Upon pyrolysis reaction, allyl methyl amine (AMN) eliminates propene and corresponding imine compounds via an intramolecular γ -hydrogen transfer (fig. 1).

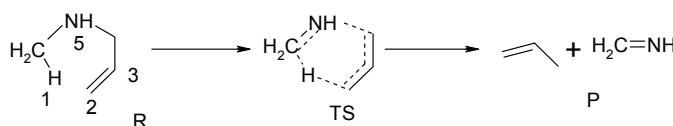


Fig 1. Atom numbering for the reactant, TS and products

The objective of this study is to provide a theoretical prediction of the kinetic and activation parameters. It is also important to elucidate the molecular mechanism associated with this retro-ene reaction in order to find out a precise idea of the reaction pathway.

2. Methods

The structures corresponding to the reactant, transition state and products for the studied reaction were optimized using the Gaussian 03 computational package. Optimized geometries of the stationary points on the potential energy surfaces (PES) were obtained using the Becke's-three parameter hybrid exchange functional with the correlation functional of Lee-Yang-Parr (B3LYP). In these calculations we used the 6-31G* basis set. The corresponding TSs were calculated using the STQN method.

Thermodynamic parameters (Enthalpy, Gibbs free energy and Entropy) for the stationary points along the pyrolysis reaction were calculated. In order to determine the atomic charges at the stationary points along the reaction paths, population analysis was applied.

3. Results and discussion

Propene elimination from the AMN may occur through the two probable mechanisms. The first one may be started by the cleavage of the C4-N5 bond followed by a step-wise mechanism. The second possibility is the intermolecular transfer of H-atom to an unsaturated center via six-centered cyclic TS, yielding propene and imine. This can proceed through the H1-C2 bond formation and C4-N5 bond cleavage.

The C4-N5 bond breaking is the rate-determining step in the former mechanism. Bond dissociation energy of the C4-N5 would be mainly the activation barrier of this process from the energy point of view. From the results it is obvious that the calculated activation energy is 288.55 kJ mol⁻¹ for the AMN pyrolysis. The calculated Activation energy is much greater than the experimental one; hence the radical mechanism is rejected. So, we should focus on the later one and consequently, the concerted mechanism was fully investigated.

Optimized structures for the reactants and the TSs are shown in figure 1 and geometrical parameters for the stationary points along the reaction are given in table 1 (See figure 1 for atom labeling).

**Table 1.** Main geometric parameters for the AMN (R) and the TS in the gas phase, using the B3LYP/6-31G(d) method (Distances in angstrom and dihedrals in degree).

Parameter	R	TS
H1-C2	2.89	1.38
C2-C3	1.33	1.41
C3-C4	1.51	1.39
C4-N5	1.45	2.01
N5-C6	1.46	1.36

During the pyrolysis reaction of alkyl allyl amine, H1-C2, C3-C4 and N5-C6 bond lengths are decreased, while H1-C6, C4-N5 and C2-C3 bond lengths are increased.

Calculated activation energies, free energies and entropies for the pyrolysis reactions are given in Table 2. From table 2 we can see that the calculated potential energy barriers for the reactions at the B3LYP/6-31G(d) is 186.4 kJmol⁻¹, the usual range for the experimental activation energies of alkyl allyl amines.

Table 2. Calculated kinetic and activation parameters for the pyrolysis of AMN at 626.65 K, using the B3LYP/6-31G(d) methods (E_a , ΔH^\ddagger in kJ mol⁻¹ and ΔS^\ddagger in J mol⁻¹K⁻¹).

E_a	ΔH^\ddagger	$\log A$	$-\Delta S^\ddagger$
186.35	181.15	12.80	14.31

Negative values for the activation entropy confirmed the concerted mechanism for the studied reactions (Table 2).

The reactivity of alkyl allyl amine can be explained in terms of the acidic character of the H1 atom. Charge distribution on the atoms for the reactants and the TSs was calculated using the NBO analysis at the B3LYP/6-31G(d) level. we can notice that the positive charge on C6 and H1 atoms increases. This positive character shows that acidic character for H1 atom increases. This makes the H1-C6 bond to break at the same time for C4-N5 bond. So the new bond formation of C6-N5 and C3-C4 is a synchronous phenomenon.

4. Conclusions

Kinetics and mechanism of alkyl allyl amine pyrolysis was studied theoretically in the gas phase and a valid reaction channel was established. The pyrolysis reaction is homogeneous, unimolecular and obeys the first-order rate law. Two probable mechanisms have been postulated, radical and concerted mechanisms, and the concerted one is preferred to other pathway.

An analysis of the atomic charges suggests that the initial migration of H1 atom with the extension of C4-N5 bond can be regarded as driving force for the pyrolysis reaction. Theoretical and experimental results are in good agreement, describing a synchronous six-center concerted mechanism. Experimental verification for some of these predictions is available.

References

- [1] Faragher, W.F., Morrel, J.C., Comay, S., Ind. Eng. Chem., 20 (1928) 527.
- [2] Gholami, M.R., Izadyar, M., J. Phys. Org. Chem., 16 (2003) 153.
- [3] Gholami, M.R., Izadyar, M., J. Mol. Struct. (THEOCHEM) (2003) 536, 53.
- [4] Izadyar, M., Jahangir, A.H., Gholami, M.R., J.Chem. Res. (2004) 585.
- [5] Izadyar, M., Gholami, M.R., J. Mol. Struct. (THEOCHEM), 686 (2004) 37.
- [6] Izadyar, M., Gholami, M.R., J. Mol. Struct. (THEOCHEM), 759 (2005) 11.
- [7] Izadyar, M., Gholami, J. Chem. Phys., 301 (2004) 45.
- [8] Martin, G., Roperio, M., Vila, R., Phosphorus and Sulfur, 13 (1982) 213.

Effect of vitamin C addition on ultrasonic degradation of aqueous carboxymethylcellulose

Mohammad Taghi Taghizadeh and Helen Rad

Department of physical chemistry, faculty of chemistry, university of Tabriz, Tabriz, Iran

(Email: mttaghizadeh@tabrizu.ac.ir)

1. Introduction

Cellulose is by far the most widespread and readily available of all solid organic materials. It comprises almost one-third of the weight of all trees, vines, grasses and straws. In addition, it is constantly replenishing itself by photosynthesis and growth. This represents a vast potential feedstock for a number of industries and has created a great deal of research interest [1]. Ultrasonic degradation of polymers is a suitable method to reduce the molecular weight of polymers and it has been proposed that the hydrodynamic forces associated with the implosion and cavitation processes of the bubbles formed develop sufficient shock wave energy and transient temperature increase for degradation of the polymer molecules to occur [2, 3].

2. Methods

The ultrasonic degradation of carboxymethylcellulose (CMC) was studied in the presence of different values of vitamin C content as a stabilizer for different CMC solution concentrations. The ultrasonic degradation rate, k , was calculated by means of a kinetical model that has defined based on this fact that the molar concentration of initial polymer solution was decreased within the ultrasonic degradation process time. Results demonstrated that, with an increase in vitamin C content added to CMC solutions with different concentrations, initial degradation rate decreased.

Carboxymethylcellulose (CMC) purchased from Fluka, with an initial Mw of 350000 kDa and polydispersity of 1.2 was degraded in a cylindrical 100ml Pyrex glass vessel. An ultrasound generator (Dr. Hielscher Ultrasonic Processor UP200 H) operating at a fix frequency of 24 kHz and a variable power output up to 100W nominal value, in aqueous media was used for sonication experiments. The kinetic model that was used is based on viscometry measurements results. Efflux times were measured for CMC solutions (t_s) and the solvent (t_0) and was converted to the ratio of t_s/t_0 , which is proportional to relative viscosity, η_r , of CMC solution. The apparent rate constant, k' , is:

$$\eta_r = \frac{t}{t_0} \quad (1)$$

The final equation that can be applied to determine the rate constant of degradation reaction is,

$$\Delta \eta^{1-n} - \Delta \eta_0^{1-n} = (1-n) \left[\frac{\sqrt{2}}{(1+\alpha)\Gamma(1+\alpha)KC^{1+\alpha}} \right]^{(1-n)/\alpha} k t \quad (2)$$

Or,

$$\Delta \eta^{1-n} - \Delta \eta_0^{1-n} = k' t \quad (3)$$

3. Results and discussion

The plots of $\Delta \eta^{1.43} - \Delta \eta_0^{1.43}$ versus sonication time for different CMC concentrations are presented in Figs. 1 and 2. The apparent degradation rate constants, k' , defined in Eq. (3), can be estimated from the slopes of the plots in Figs. 1 and 2 Based on these, degradation rate constants, k' , were calculated.

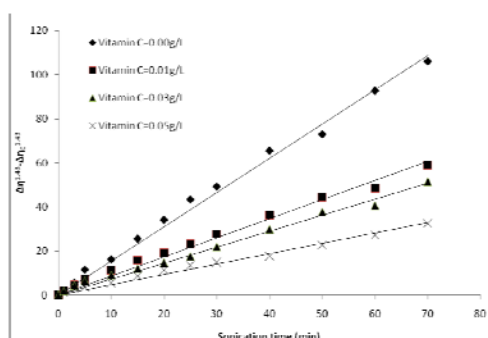


Fig.1. the plot of $\Delta \eta^{1.43} - \Delta \eta_0^{1.43}$ versus the sonication time for different content of vitamin C for 0.5g/L of CMC solution.

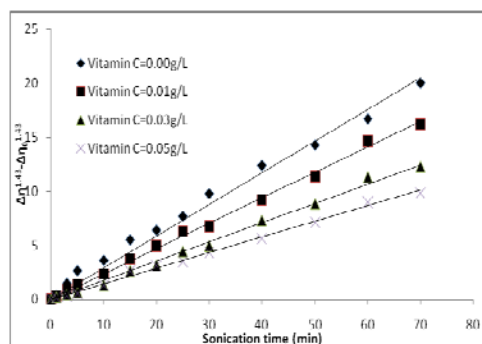


Fig.2. the plot of $\Delta\eta^{1.43} - \Delta\eta_0^{1.43}$ versus the sonication time for different content of vitamin C for 1.0 g/L of CMC solution.

4. Conclusion

The rate of degradation process decreased with increasing the content of vitamin C in reaction solution. Vitamin C act as a radical scavenger and inhibit the degradation reaction rate.

References

- [1] M. Aliyu, M. J. Hepher, Ultrason. Sonochem. 7 (2000) 265.
- [2] A. Weissler, J. Appl. Phys. 21 (1950) 171.
- [3] H. H. G. Jellinek, A. W. Brett, J. Polym. Sci. 13 (1954) 111.

Sonolytic, sonocatalytic and sonophotocatalytic degradation of chitosan in the presence of TiO₂ nanoparticles

Mohammad Taghi Taghizadeh* and Reza Abdollahi

University of Tabriz, Faculty of chemistry, Department of physical chemistry, Tabriz, Iran

(Email: mttaghizadeh@tabrizu.ac.ir)

1. Introduction

Chitosan, (1,4)-2-amino-2-deoxy- β -D-glucan, is a natural polymer generally obtained by extensive deacetylation of chitin isolated from crab shells. Due to its special biological, chemical and physical properties, chitosan and its derivatives have applications in many industrial and agriculture activities [1-3]. High-intensity ultrasonic treatment can be applied to degrade polymers and to facilitate emulsifying and cleaning processes. The ultrasonic energy is dissipated in solution, resulting in cavitations. Cavitation produces vibrational wave energy, shear stresses at the cavitation interphase, and local high pressure and temperature. These are the major factors causing the degradation of polymers [4-6].

2. Methods

Different treatments were tested, namely: TiO₂ sonolysis (US), photocatalysis (UV), combined sonolysis and photocatalysis (US+UV). For the experiments in the presence of TiO₂, a concentration range of 0.1-0.6 g/L of TiO₂ nanoparticles was used. Infrared spectrometry was used to determine the DD of the chitosans. Gel permeation chromatography (GPC) (HLC6A, Shimadzu) was used to compare molecular weight and molecular weight distribution (polydispersity) of the original chitosan and degraded samples. X-ray diffraction patterns of the degraded chitosan fractions were measured by a Siemens XRD-5000 diffractometer and used a CuK α =1.54 target at 40 kV and 50 mA at 25°C.

3. Results and discussion

3.1. Sonolytic (US) and sonocatalytic (US+TiO₂) degradation of chitosan

Fig. 1 shows the effect of increasing changing ultrasound power on relative viscosity (η_r) of chitosan solution as a function of the sonication time at 5g/L initial polysaccharide concentration under air. As seen, η_r decreases with increasing the nominal applied power from 30 to 90W. The plots of $\Delta\eta^{2.5} - \Delta\eta_0^{2.5}$ versus sonication time for different powers of ultrasound are presented in Fig.2. Effect of presence of catalyst TiO₂ and concentration of catalyst in constant power of ultrasound (30W) on the degradation rates has also been investigated. In principle, particles may enhance degradation providing additional nuclei for bubble formation. However, an imperfect effect may occur because of sound attenuation. As seen, the presence of TiO₂ particles in the reaction mixture increased partially the sonochemical degradation of chitosan. These results are shown in Table 1.

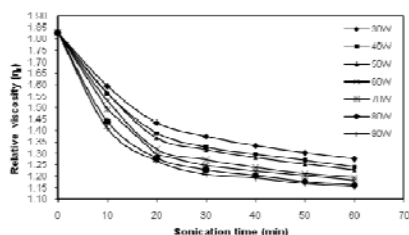


Fig.1. The relationship between η_r and sonication time in sonolytic process, for different power of ultrasound at 25°C.

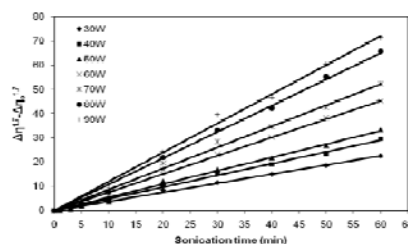


Fig.2. The plot of $\Delta\eta^{2.5} - \Delta\eta_0^{2.5}$ versus the sonication time in sonolytic process, for different power of ultrasound at 25°C.

Process	TiO ₂	$k \times 10^9$
	loading (g/L)	(mol ^{1.7} .L ^{-1.7} .min ⁻¹)
US	0.00	1.538
US	0.10	1.737
US	0.20	1.905
US	0.30	2.066
US	0.40	2.274
US	0.50	2.459
US	0.60	2.654
UV	0.10	0.354
UV	0.20	0.452
UV	0.30	0.578
UV	0.40	0.728
UV	0.50	1.004
UV	0.60	1.134
US+UV	0.00	1.873
US+UV	0.10	2.624
US+UV	0.20	3.071
US+UV	0.30	3.542
US+UV	0.40	4.801
US+UV	0.50	6.141
US+UV	0.60	8.102

4. Conclusion

It has been demonstrated on high-molecular weight chitosan that treatment with a variety of output ultrasound powers in aqueous solution is an efficient procedure for reduction of molecular weight of chitosan. Under sonolysis conditions, degradation is caused by OH radicals and mechanochemical effects. In other hand, the use of TiO₂ nanoparticles as catalyst in the presence of ultraviolet source in a constant threshold power of ultrasound (30W) retrieved the ultrasound power weakness and improved the applied degradation process.

References

- [1] X. Qu, A. Wirsén, A. C. Albertsson, *Polymer*, **41** (2000) 4841.
- [2] R. A. A. Muzzarelli, *Natural Chelating Polymers: Alginic acid, Chitin and Chitosan*, Pergamon Press, Oxford, 1973.
- [3] G. A. F. Roberts, *Chitin chemistry*, Houndmills, Macmillan, 1992.
- [4] A. Gronroos, P. Pirkonen, J. Heikkinen, J. Ihalainen, H. Mursunen, H. Sekki, *Ultrason. Sonochem.* **8** (2001) 259.
- [5] M. T. Taghizadeh, T. Asadpour, *Ultrason. Sonochem.* **16** (2009) 280.
- [6] M. T. Taghizadeh, A. Bahadori, *J. Polym. Res.* **16** (2009) 545.



Solid-phase photodegradation of polystyrene-co-acrylonitrile (SAN) with TiO₂ as photocatalyst

Mohammad Taghi Taghizadeh*, Reza Abdollahi and Cobra Hasanifard

Department of Physical Chemistry, Faculty of Chemistry, University of Tabriz, Tabriz, Iran.

(E- Mail: mttaghizadeh@tabrizu.ac.ir)

1. Introduction

As a conventional plastic materials, a large amount of polystyrene (PS) and its derivatives such as polystyrene-co-acrylonitrile (SAN) is used widely in our daily life. For example a large amount of polystyrene (PS) is used in food service and retail industry. Although SAN has higher heat distortion temperature (HDT), better chemical resistance, stiffness, fracture toughness and environmental stress corrosion resistance than PS [1]. It is interesting to note that the solid-phase photocatalytic degradation of polymer-TiO₂ composites has been known and studied for quite a long time in relation to the chalking phenomenon in the pigmented paint/polymer systems [2]. In this study, a new kind of SAN-TiO₂ composite film has been synthesized and its solid-phase photocatalytic degradation under the ambient air atmosphere was investigated. It demonstrates that the SAN-TiO₂ composite has a potential viability to be used as a photodegradable product. A possible mechanism for the photocatalytic oxidative degradation was also mentioned. A possible mechanism for the photocatalytic oxidative degradation was also mentioned.

2. Methods

SAN-TiO₂ Composite film was cast as follows: 10g SAN was dissolved in 60ml Tetrahydrofuran (THF) under vigorous stirring for 1h to obtain the SAN solution. At the same time 0.2g TiO₂ powder was dispersed uniformly into 10ml THF by ultrasonic vibration for 30min. Then the suspension was added to SAN solution to give 2.0 wt.% as the ratio of TiO₂ to SAN. The composite film were prepared by spreading the viscous solution on a slide glass surface (7×15 cm) and dried for 2 days at room temperature. The pure SAN film was also prepared in a similar procedure in order to compare the photocatalytic activity. The thickness of these films was measured to be 500μm by a micrometer. FT-IR spectrophotometer (Tensor 27) is used to characterize the spectral transmittance of the films before and after irradiation. The number-average molecular weight (M_n) and weight-average molecular weight (M_w) of SAN film were measured by gel permeation chromatography (GPC Agilent 110). Colorimetry results of SAN and SAN-TiO₂ films before and after photodegradation and also in different intervals was measured by colorimeter (Mini Scan XE plus). These results were used to determine the L^* and ΔE parameters that refer to brightness and change in color of samples, respectively.

3. Results and discussion

Fig.1. shows the FT-IR spectra of the pure SAN and SAN-TiO₂ films. The bands in the region of 1700-1740 cm⁻¹ are the characteristic absorption of carbonyl group ν (C=O) while the bands in 1450-1490 cm⁻¹ and sharp peak in 700 and 750 cm⁻¹ are related to phenil group. It can be seen that the intensities of carbonyl peak increase continually with increasing the illumination time in SAN-TiO₂ film as well as the intensities of phenilic peak was decreased (Fig. 1b). But the peak intensity does not change anymore when the irradiation time reached to 200h in pure SAN composite film (Fig. 1a). This phenomenon clearly proves that the presence of TiO₂ nanoparticles in polymer films promotes the photocatalytic oxidation of SAN composite film. In the composite, the adsorbed water on TiO₂ surface reacts with valance band (VB) holes to generate hydroxyl radicals or O₂ molecules that in their turn react with conduction band (CB) electrons to generate reactive oxygen species: this radicals and species are responsible for most of the oxidizing capability of TiO₂ photocatalyst. These hydroxyl radicals and active oxygen species the C—H bond in polymer chain to form the carbonyl group [3]. The photocatalytic degradation of pure SAN film is accompanied by the reducing of SAN molecular weight which was measured by GPC (as shown in Table 1). The M_w of these samples decreases from 134.26×10^3 to 117.45×10^3 g mol⁻¹ during a 300h photodegradation process time, which means that in pure sample decrease in molecular weight is not obviously considerable.

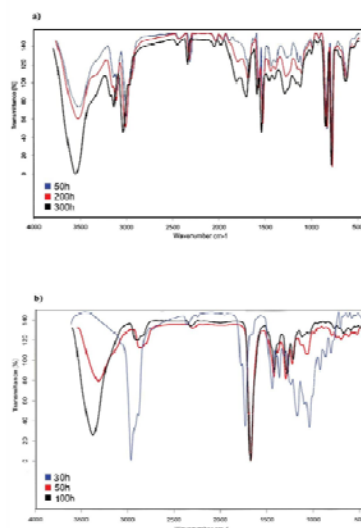


Fig. 1. FT-IR spectra of (a) pure SAN films and (b) SAN-TiO₂ (2 wt.%) films.

Table 1. The variation of molecular weight of pure polymer films with irradiation time by GPC.

Irradiation time/h	$M_n \times 10^{-3}$	$M_w \times 10^{-3}$	Polydispersity
100	92.28	134.26	1.45
200	86.62	131.00	1.51
300	84.01	117.45	1.40

4. Conclusions

In summary, the photocatalytic degradation process of SAN-TiO₂ composite film was much faster and more complete than the sample photolysis of pure SAN film under UV light irradiation. The development of this kind of composite polymer can lead to an eco-friendly disposal of polymer wastes.

References

- [1] T. Kirschnick, A. Gottschalk, H. Ott, V. Abetz, J. Puskas, V. Altstadt, *Polym.* 45 (2004) 5653.
- [2] S. P. Pappas, F. H. Winslow (Eds.), *Photodegradation and photostabilization in coatings*, ACS Symposium Series 151, American Chemical Society, Washington, DC, 1981.
- [3] L. Zhang, P. Liu, Z. Su, *Polym. Degrad. Stab.* 91 (2006) 2213.

**Sonocatalytic and sonophotocatalytic/H₂O₂ degradation of chitosan in the presence of Fe (III) as a catalyst**

Mohammad Taghi Taghizadeh* and Reza Abdollahi

University of Tabriz, Faculty of chemistry, Department of physical chemistry, Tabriz, Iran

(Email: mttaghizadeh@tabrizu.ac.ir)**1. Introduction**

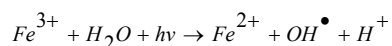
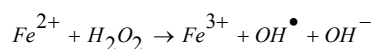
Chitosan is the deacetylated derivative of chitin. The presence of amino groups in chitosan causes the molecule to be polycationic and ultimately gives rise to its unique functional properties. There are many increasing evidences that a particular pharmaceutical and biological application and the effectiveness in exerting a specific action, such as fat-binding, antithrombotic activity, antitumor activity, antimicrobial activity or stimulating plant growth, depends on the molecular weight of chitosan [1]. When a polymer solution is exposed to ultrasound, micro-bubbles containing dissolved gas or vapor of volatile liquids are created and the bubbles grow and finally collapse in a short time as short as microsecond [2]. Radicals were detected by spin-trapping method when a polymer solution was exposed to ultrasonic irradiation [3]. A shear deformation during collapse of the bubbles in the vicinity of cavitation seems to be responsible for disintegration of polymers in organic solvents. Kanwal et al. [4] noted that both cavitation and viscoelastic response of a polymer molecule in solution are responsible for ultrasonic degradation.

2. Methods

Different treatments were tested, namely: Fe³⁺/H₂O₂ sonolysis (US), photocatalysis (UV), combined sonolysis and photocatalysis (US+UV). For the sonophotocatalytic experiments, a constant concentration of Fe(III) ions (2.5×10⁻⁴ mol/L) in the presence of a range of 0.0195-0.118 mol/L of hydrogen peroxide was used. Infrared spectrometry was used to determine the DD of the chitosans. Gel permeation chromatography (GPC) (HLC6A, Shimadzu) was used to compare molecular weight and molecular weight distribution (polydispersity) of the original chitosan and degraded samples. X-ray diffraction patterns of the degraded chitosan fractions were measured by a Siemens XRD-5000 diffractometer and used a CuKα=1.54 target at 40 kV and 50 mA at 25°C.

3. Results and discussion*Chitosan degradation by sonophoto-Fenton process*

In recent years, homogenous photocatalysis using iron as the photocatalyst has received considerable attention. This is due to the extremely low cost of the catalyst, the lack of mass transfer limitations that are typically encountered in heterogenous processes and the potential coupling with hydrogen peroxide to establish the so-called photo-Fenton process. Fig. 1 shows chitosan solution relative viscosity-time profiles during sonophoto-Fenton process at different contents of H₂O₂. The efficiency of the photo-Fenton system is closely related to iron participating in the following redox cycle generating two hydroxyl radicals per molecule of H₂O₂ decomposed:



An additional dark Fenton run was performed showing that degradation proceeds much slower than the respective runs under UV and/or ultrasound irradiation (Fig. 2).

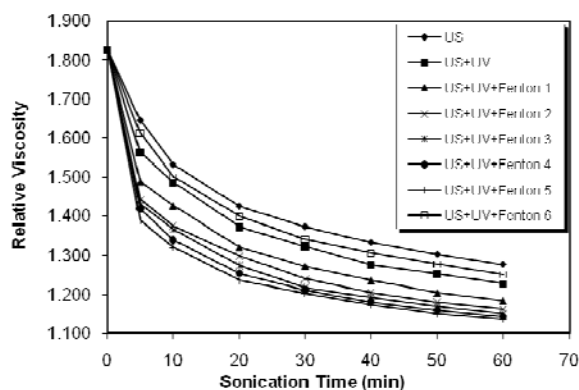


Fig.1. The relationship between η_r and sonication time in sonophoto-Fenton process, for different content of H_2O_2 at 25°C.

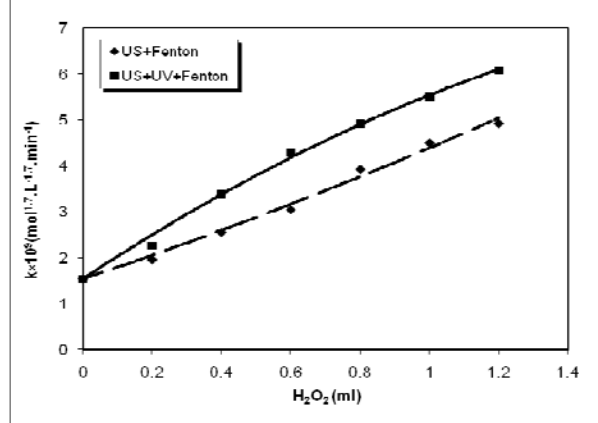


Fig. 2. Comparison of rate constant for sono-Fenton sonophoto-Fenton processes.

Conclusions

Efficiency of sonolytic and photocatalytic processes can be improved by coupling the two processes. The beneficial synergy of coupled system may be attributed to the increased production of reactive free radicals as well as enhanced catalytic activity.

References

- [1] J. Lee, J. Cai, L. Fan, J Appl Polym Sci, 109 (2008) 2417.
- [2] H. Kuttruff, Ultrasonics: Fundamentals and Applications, Elsevier Applied Science, London, 1991.
- [3] J. Sohma, Electron spin resonance studies of the mechanical degradation of polymers, in: N. Grassie (Ed.), Developments in Polymer Degradation, vol. 2, Elsevier, London, 1979.
- [4] F. Kanwal, J.J. Liggat, R.A. Pethrick, Polym. Deg. Stab. 68 (2000) 445.

Effect of reaction volume on the extent of ultrasonic degradation of high-molecular weight chitosan

Mohammad Taghi Taghizadeh* and Reza Abdollahi

University of Tabriz, Faculty of chemistry, Department of physical chemistry, Tabriz, Iran

(Email: mttaghizadeh@tabrizu.ac.ir)

1. Introduction

It is now well established that prolonged exposure of solutions of macromolecules to high-energy ultrasonic sound waves produces a permanent reduction in viscosity. Even when the irradiated polymers are isolated and redissolved their viscosity remains low in comparison with that of non-irradiated solutions [1]. Operating reaction volume plays a crucial role in deciding the extent of degradation, particularly where ultrasonic irradiation is achieved using horn-type reactor. Effect of reaction volume on the extent of degradation has been investigated at constant power dissipation of the ultrasonic reactor and constant concentration of the polymer species [2].

2. Methods

In the present work, the effect of operating reaction volume on the extent of ultrasonic degradation and the rate reaction was investigated. The effect of volume was investigated at three different concentrations (1.0 and 1.5%) and four different volume of reaction solution for each concentration. A kinetic model based on molar concentration change within sonication process was used to calculate the rate of reactions.

3. Results and discussion

The obtained results can be attributed to the fact that, increase in the reaction volume decreases the power density of the system (power dissipation per unit volume) resulting in a corresponding decrease in the cavitation activity. With a decrease in the operating power density, the number of cavitation events occurring in the system decreases lowering the effective cavitation intensity. Also in the case of cavitation horn, the active cavitation volume is restricted very near to the transducer surface, resulting in non-uniform distribution of the cavitation activity. With an increase in the operating volume, there exists enhanced number of dead zones where the cavitation activity is minimal resulting into detrimental effects. Fig 1 shows the change in relative viscosity of chitosan solution for the concentration of 15g/L. The plots of $\Delta\eta^{1.7} - \Delta\eta_0^{1.7}$ versus sonication time for different chitosan solution volume are presented in Figs.2.

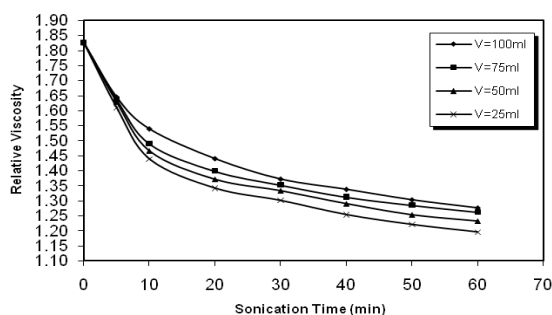


Fig.1. The relationship between η_r and sonication time for different volume of reaction solution.

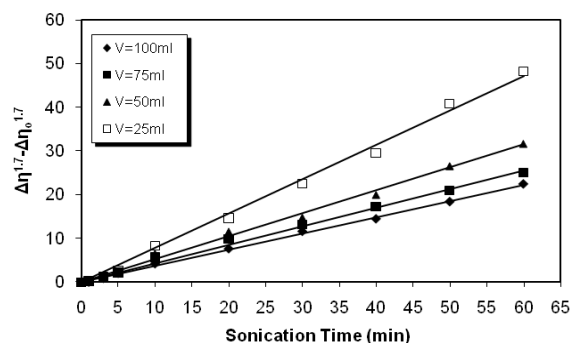


Fig. 2. The plot of $\Delta\eta^{1.7} - \Delta\eta_0^{1.7}$ versus the sonication time for different volume of reaction solution.

4. Conclusions

The effect of reaction volume, concentration on the ultrasonic degradation of polypropylene has been investigated. The results indicate that the percentage degradation reduced with increasing reaction volume and increasing concentration which affects the cavitation intensity in the system. The relative viscosity was also dependent on the solution concentration and the operating volume. The present work has clearly illustrated the suitability of ultrasound-induced cavitation phenomena as a technique for degradation of chitosan.

References

- [1] K.S. Suslick, *Ultrasound: Its Chemical, Physical & Biological Effects*, VCH, New York, 1990.
- [2] V. Desai, M. A. Shenoy, P. R. Gogate, *Chem. Eng. J.* 140 (2008) 483.

Ultrasonic degradation of amylose: effect of volume, concentration of amylose, power input and type of solvent on rate of degradation

Mohammad Taghi Taghizadeh* and Masoumeh Dadashbeygi

Department of physical chemistry, faculty of chemistry, university of Tabriz, Tabriz, Iran

(Email: mttaghizadeh@tabrizu.ac.ir)

1. Introduction

Starch is a polysaccharide, which consists of amylose and amylopectin as constituents. Amylose is known to be degradable in the colonic tract [1]. Starch is probably the most abundant and low-cost natural polymer commercially available. Moreover, it can be modified easily into a variety of useful polymeric products by chemical means [2]. Ultrasonic techniques are finding an increasing number of applications in the food industry for both the analysis and modification of foods [3]. Most of the experiments carried out use the effect of ultrasonic on the properties of starches [4].

2. Methods

The ultrasonic degradation of Amylose was conducted in a reactor described in Fig.1, included a cooling bath, an ultrasonic power supply with a generator/transducer/metallic probe and a glass reactor. To maintain the water temperature constant in the reactor a cooling loop circulated tap water through a chiller, and subsequently into a water bath where the reactor was set-up. Solutions of 10, 20 and 30 gLit⁻¹ of Amylose in aqueous solution of 0.33 M of KCl were prepared. For the degradation, 25 and 50 cm³ of Amylose solutions were placed in a cylindrical glass reactor with a diameter of 10 cm and a height of 20 cm, and its temperature was controlled to 25 ± 0.1 °C by circulating thermostated water (Grant model RC 1400 G England) through the cylindrical glass and sonicated for a long time. An ultrasonic generator (Dr. Hielscher UP 200 H ultrasonic processor) with an H3 sonotrode ($u = 3$ mm) was used in this experiment. The frequency of the ultrasound was 24 kHz, and output power was set at 100 W. The sonicator was a direct immersion probe system. A cylindrical metal probe, which intensified the mechanical vibrations to produce acoustic pressure, was connected to the transducer.

3. Results and discussion

Fig.1 shows the effect of the power of ultrasonic irradiation on the extent of degradation. Sonication was carried out for two different power of ultrasonic irradiation (200, 300 W) at 25°C. The results show that the extent of degradation of Amylose increased with power of ultrasonic irradiation at same concentration. The results in Fig.11 show the effect of power of ultrasonic irradiation on the rate during sonolysis. The higher power of ultrasonic irradiation resulted in higher reaction rate constants, whereas, lower-power ones had lower reaction rate constants [Table 1].

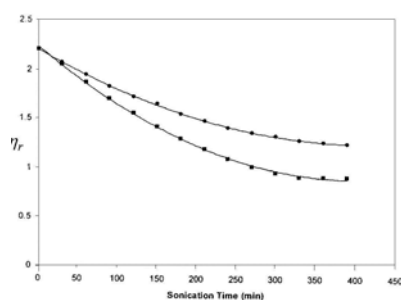


Fig.1. The effect of power of ultrasonic irradiation on the degradation rate with ○, 200, ■, 300 W at 25 °C.

**Table 1.** Calculated degradation rate constants at different power of ultrasonic irradiation

Power (W)	$k \times 10^6 (\frac{mol}{L \min})$
200	1.390
300	1.835

4. Conclusion

It has been demonstrated on Amylose that treatment with ultrasound is an efficient procedure for reduction of molecular weight of polysaccharides therefore, effect of concentration and volume of solution, type of solvent and the power of ultrasonic irradiation on the ultrasonic degradation of Amylose studied at 25°C with this procedure. The experimental results indicated that the degradation rate reduced with increasing solution concentration and volume of solution but on the other hand increased with increasing of power of ultrasonic irradiation and using DMSO as a solvent.

References

- [1] Milojevic S, Newton John M, Cummings John H, Gibson Glenn R, Botham R Louise. Journal of Controlled Release 38 (1996) 75.
- [2] Echeverria I, Silva I, Gorni I, Gurruchaga M. Journal of Applied Polymer Science 96 (2005) 523.
- [3] Knorr D, Zenker M, Heinz V, Lee D. Trends Foods Sci. Technol 15 (2004) 2616.
- [4] Czechowska-Biskup R, Rokita B, Lotfy S, Ulanski P, Rosiak J. Polym. 60 (2005) 175.

Kinetics of adsorption of methyl violet by pistachio/ CuFe_2O_4 nanocomposite

Saeedeh Hashemian and Mohammad Hassan Dad

Islamic Azad University, Yazd branch, Chemistry department, Iran, Yazd

(E-mail: Sa_hashemian@yahoo.com)

Keywords: Pistachio, methyl violet, Adsorption, Kinetic, Nanocomposite.

1. Introduction

Dyes are widely used in the textile industry to color products. One of the major problems concerning textile wastewaters is colored effluent. This wastewater contains a variety of organic compounds and toxic substances, which are harmful to fish and other aquatic organisms [1]. Methyl Violet is a triphenylmethane dye soluble in water, ethanol, methanol, diethylene glycol and dipropylene glycol, it has molecular formula $\text{C}_{24}\text{H}_{28}\text{ClN}_3$. It is used to obtain shades of deep colors that can be applied for dyeing of cotton, silk, paper, bamboo, weed, straw and leather[1]. The dye Methyl Violet is widely used in analytical chemistry laboratories as a pH indicator to test pH ranges from 0 to 1.6 [2]. From the chemical structure of the dye it is observed that there are three aromatic rings attached to a central carbon atom.

The toxic nature of the dye can be explained by considering the fact that on decomposition it gives out hazardous products. These products are toxic and may cause several health problems to mankind as well as animals, thus MV attracts noteworthy attention to innovate effective techniques for its removal. Adsorption has gained favor in recent years due to proven efficiency in the removal of pollutants from effluents to stable forms for the above conventional method [3-4].

2. Methods

Soft pistachio shells were used as starting materials. The pistachio shells were preheated in an oven at 100 °C for about 48 h to reduce the moisture content. They were then crushed with a high speed mill and sieved on a sieve mechanical shaker, and the size fraction of lower than 180 μm that has been passed through US standard sieve number 80, was used in this study. Analytical grade copper (II) chloride dehydrates and ferric chlorides were obtained from Merck. CuFe_2O_4 was prepared using a co-precipitation method. CuFe_2O_4 /pistachio composites were prepared using a co precipitation method. MV was purchased from Merck and used without further purification. The stock solution of MV was prepared with distilled water (100 mg l^{-1}). MV was analyzed by shimadzu 160A UV-Vis spectrophotometer.

3. Results and discussion

3. 1. Catalytic effect of CuFe_2O_4

The experiments were carried out with 50 ml of MV dye solutions on 0.1 g of pistachio, CuFe_2O_4 and CuFe_2O_4 /pistachio composite. Fig. 1 shows the effects of agitation time. The plots show that the adsorption of MV increases with an increase in agitation time and attains equilibrium earlier of adsorption (30 min) for CuFe_2O_4 /pistachio composite and more than 90%. In the equilibrium time of 60 min was needed for CuFe_2O_4 /pistachio and CuFe_2O_4 . The higher adsorption capacity of CuFe_2O_4 /pistachio composite than that pistachio attributed to the presence of CuFe_2O_4 catalyst.

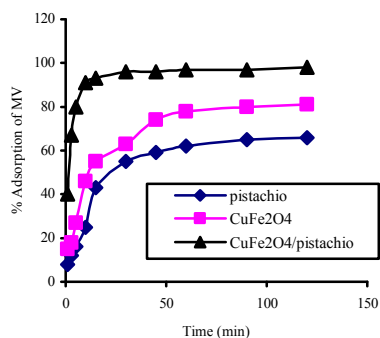


Fig. 1. Effect of time for adsorption of MV onto pistachio, CuFe_2O_4 and CuFe_2O_4 /pistachio composite.



3. 2. Effect of pH

The effect of pH on the adsorption of MV onto CuFe₂O₄/pistachio was investigated. The adsorption capacity increased with increasing pH of the solution. The maximum adsorption capacity of MV on CuFe₂O₄/pistachio was observed at pH 10. The effect of pH on MV removal from CuFe₂O₄ and pistachio were similar. This could be explained by the fact that at low pH, more protons will be available to protonate hydroxyl groups, reducing the number of binding sites for the adsorption of MV. The adsorption behavior showed that adsorption of MV onto nanoparticle composite is governed by electrostatic interactions. The influence of pH on the adsorption capacity showed decreasing affinity with increasing electrostatic repulsion between MV and the adsorbent with a maximum value at pH 10.

3. 3. Adsorption kinetics

The two adsorption kinetic modes used in this study are pseudo-first order and pseudo-second order equations. The pseudo-second order model is based on adsorption equilibrium capacity.

$$1/C_t = 1/C_i + k T$$

Where C_i is the initial concentration (mg/l), C_t the concentration at time t (mg/l) and k in the rate constant of the pseudo-second order equation ($l\text{ mg}^{-1}\text{ min}^{-1}$). The rate constant of the pseudo-second order at $25\pm 1^\circ\text{C}$ was $6.5\times 10^{-3}\text{ M}^{-1}\text{S}^{-1}$.

4. Conclusions

CuFe₂O₄/pistachio can be used as a cost effective adsorbent for removal of MV from water and wastewater. Alkaline pH is found to be better than acidic pH. The adsorption follows pseudo-second order kinetics.

References

- [1] Ramakrishna K. R., Viraraghavan T., Dye removal using low cost adsorbents, *water Sci. Technol.* 36 (2-3) (1997) 189.
- [3] Wu R, Qu J, He H, YU Y, Removal of azo-dye acid red B (ARB) by adsorption and catalytic combustion using magnetic CuFe₂O₄ powder, *Applied Catalysis B: Environmental* 48 (2004) 49.
- [4] Zhang G, Qu J, Liu H, Cooper A. T, Wu R, CuFe₂O₄/activated carbon composite: A novel magnetic adsorbent for the removal of acid orange II and catalytic regeneration, *Chemosphere* 68 (2007) 1058.

**Quasi-classical trajectory study on the reaction of CH₃ + SiCl₃ radicals**

S. H. Mousavipour* and Elham Mazarei

Chemistry Department, College Of Science, Shiraz University, Shiraz, Iran

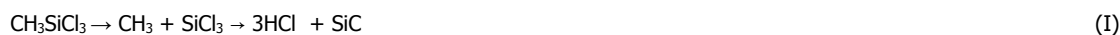
(Email: elhammazarei@yahoo.com)

Keyword: Ab initio, VENUS96, Collision theory, Quasi-Classical Trajectories.**1. Introduction**

SiC nanoparticles is an outstanding wide-gap semiconducting material for high temperature and high power electronic applications due to its excellent properties, such as high mechanical strength, high thermal stability, and high thermal conductivity [1]. CH₃SiCl₃ is one of the most important precursors for producing SiC nanoparticle, because of its equivalent ratio of Si to C.

2. Methods

Geometries and potential energy surface were optimized by means of Gaussian03 program. An analytical function was developed based on our ab initio data and also experimental data reported in the literature. Quasi-Classical Trajectories calculations were performed by using the VENUS96 program. The purpose of the present study was to investigate the mechanism of formation of SiC nanoparticle from Methyltrichlorosilane (MTS) and achievement rate constant of formation by molecular dynamics. Reaction (I) was the most probable path in this system:

**Analytical Potential Energy Surface:**

In our analytical potential energy function, bond stretches are represented by Morse function; bends are represented by harmonic function [2]. The total potential function might be written as:

$$\begin{aligned} V = & \sum_{i=1}^3 V(R_{C-H(i)}) + V(R_{C-Si}) + \sum_{i=1}^3 V(R_{Si-Cl(i)}) + \sum_{i=1}^3 V(R_{C-Cl(i)}) \\ & + \sum_{i=1}^3 V(R_{Si-H(i)}) + \sum_{i=1}^3 \sum_{j=i+1}^3 V(\theta_{Cl(i)-SiCl(j)}) + \sum_{i=1}^3 \sum_{j=i+1}^3 V(\theta_{H(i)-Cl(j)}) \\ & + \sum_{i=1}^3 V(\theta_{Si-CH(i)}) + \sum_{i=1}^3 V(\theta_{C-SiCl(i)}) \end{aligned}$$

where the subscripts i, j refer to the numbering of atoms. The stretching terms between two atoms i and j are expressed as:

$$V(R_{i-j}) = D_e' SW_i \{1 - \exp(-\alpha(R_{ij} - R_{ij(eq)}))\}^2 - D_e' SW_i$$

$$SW_1 = 1 - \exp[-C_{(i)}(R_{(i)} - R_{(i)eq})^2]$$

$$SW_3 = 1 - \tanh(C_7 \exp[-C_8(R_{C-H(j)} - R_{C-H(j)eq})])$$

Presence of the switching function in the stretching terms cause to turn on and off the reactants, products and the region between these extreme points and to optimize the force constant. Initial values for the force constant and potential well depths were taken from our ab initio results. VENUS96 classical trajectory code with some modifications was used in order to read our suggested analytical potential surface and its derivatives to generate the collisional cross sections and reaction probabilities.

3. Results and Discussion

The rate constant of formation of SiC nanoparticle were calculated from the calculated reactive cross section and reaction probability. Following expression based on the collision theory was used to calculate the rate constants [3]:

$$k \cong \left(\frac{8kT}{\pi\mu} \right)^{1/2} \pi b_{\max}^2 \frac{N_r}{N} g_e$$



The details of the results will be presented.

References

- [1] Guangcheng Xi; Yankuan Liu; Xiaoyan Liu, Xiaoqing Wang and Yitai Qian J. Phys. Chem. B. 110 (2006) 14172.
- [2] Lim K.F.J. Chem. Phys. 100 (1994) 738.
- [3] Liu.Y, Lohr. L. L, Barker J. R. J. Phys. Chem. A. 110 (2006)1267.

Interpolated potential energy surface and classical reaction dynamics for reaction of amidogen with hydroxyl radical

S. H. Mousavipour* and F. Pirhadi

Department of Chemistry, Shiraz University, Shiraz 71454, Iran

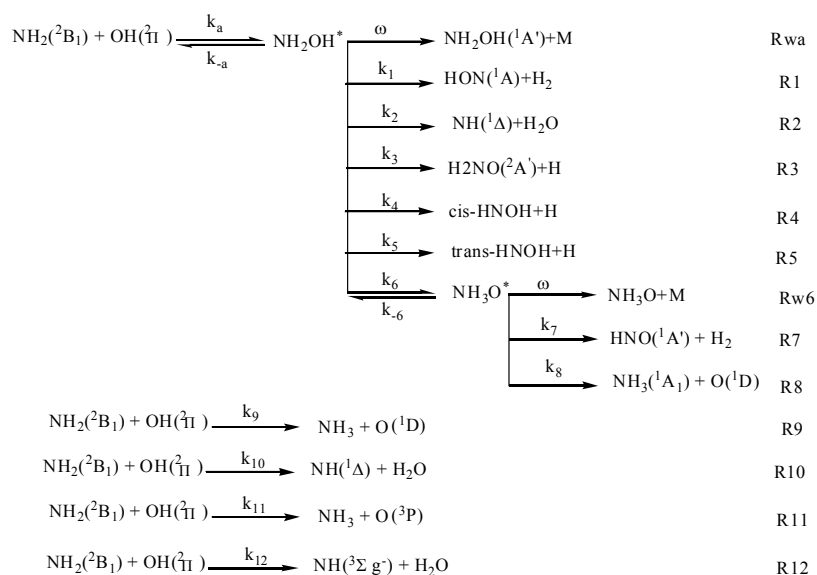
(Email: fpirhadi@yahoo.com)

1. Introduction

A fundamental goal of chemical dynamics is to obtain a microscopic picture of how energy flows and atoms move during the course of a chemical reaction [1,2].

Both theoretical and experimental approaches have focused on this goal and their use, in complementary ways, has often proven particularly effective [3]. Classical trajectory[4] and time-dependent quantum [5] calculations give a complete picture of the reaction event. In this regard, classical dynamics simulations have been investigated on an interpolated ab initio potential energy surface for studying the dynamics of reaction Amidogen and hydroxyl radicals that are two important reactive radicals in the atmosphere and combustion chemistry.

This system can take place on both singlet and triplet surfaces, and a possible mechanism for this reaction can be shown such as:



In this study, we report accurate PES for the dynamics of all processes, constructed by interpolation of ab initio ground-state energies, energy gradients and Hessians.

The molecular configurations which form the interpolation data set for the PES are scattered over the energetically accessible regions, including the minimum energy paths (MEP) for these reactions, NH_2OH and NH_3O minimums. Reaction cross sections and other observable quantities were calculated for the classical dynamics of all reactions. However, the classical simulations mostly serve to emphasize the need for accurate quantum dynamics. The provision of an accurate global PES for this system may facilitate such calculations.

2. Method of Calculations

The construction of the PES and the classical trajectory simulations were performed by means of Grow program suite [6].

The PES is calculated by an iterative interpolation method whose details have been presented elsewhere [7]. The general form of the PES is:

$$E(Z) = \sum_{g \in G} \sum_{i=1}^{N_{\text{data}}} w_{\text{goi}}(Z) T_{\text{goi}}(Z) \quad (1)$$



Where a number N_{data} of local Taylor expansions T_i of the energy, around certain molecular configurations, $Z(i)$, are combined as a weighted average. The N_{data} molecular configurations associated with the Taylor expansions are known as the "data set". The expansions are evaluated from ab initio calculation of the energies and up to energy second derivatives at each of the data set configurations. Each expansion is expressed in terms of a geometry-specific set of $3N-6$ independent coordinates which are linear combinations of the inverse inter-atomic distances, $Z=Z_1, \dots, Z_k, \dots, Z_{N(N-1)/2}$, where $Z_k = 1/R_k$. The sum over $g \in G$ in Eq. (1) represents a sum over the symmetry group of the molecule, the complete nuclear permutation (CNP) group: if $Z(i)$ is a data point, then a permuted configuration, $g \circ Z(i)$ (abbreviated to $g \circ i$) is also a data point. No additional ab initio calculations are required to evaluate the Taylor series coefficients at $g \circ Z(i)$, and by including all equivalent molecular configurations in Eq. (1), the PES has the correct invariance to permutation of indistinguishable nuclei $\{E(g \circ Z) = E(Z)\}$.

The weights w_i in Eq. (1) are functions of the distance coordinates Z with respect to the data point configuration $Z(i)$. They also depend on estimated "confidence lengths" for each data point [6,7]. The confidence lengths for this PES were evaluated using an energy tolerance, $E_{\text{tol}} = 0.53$ kJ/mol, and energy gradients at $M = 40$ data points (see Ref. [7] for definitions of E_{tol} and M).

So, in accordance with this method, we choose a set of molecular configurations on such a reaction path as an initial data set to describe the PES via Eq. (1).

From this initial data, points are added one by one to the data set following an iterative procedure. The interpolated PES was grown from the initial set of data points to 2000 data points.

At periodic intervals in this iteration, large scale classical trajectory simulations are performed to estimate reaction cross sections and other observable quantities, based on the current data set. The PES is taken to be converged when the calculated cross sections do not change with an increase in the number of data points.

3. Results and discussion

Interpolation data points were selected from samples of molecular configurations generated from classical trajectories.

Small batches of ten trajectories were run for each iteration of the PES construction procedure to simulate collisions for reactions. The trajectories were calculated with a velocity-Verlet integration algorithm, using a time step size of 1×10^{-17} s, starting with a fragment to fragment center of mass separation 12 Å. The reactant molecules were randomly oriented and given zero rotational angular momentum.

In this work we calculated total cross sections for all products as functions of the relative kinetic energy, ensuring the results were converged with respect to the size of the data set at which ab initio calculations had been performed. Also we report the probability of the reaction as a function of collision impact parameter (b). The details of the results will be reported.

References

- [1] Levine, R. D.; Bernstein, R. B. *Molecular Reaction Dynamics and Chemical Reactivity*; Oxford: New York, 1987.
- [2] Steinfeld, J. I.; Francisco, J. S.; Hase, W. L. *Chemical Kinetics and Dynamics*; Prentice Hall: Englewood Cliffs, NJ, 1989.
- [3] Hase, W. L. *Science* 266 (1994) 998.
- [4] Bunker, D. L. *Sci. Am.* 211 (1969) 100.
- [5] (a) Heller, E. J. *J. Chem. Phys.* 62 (1975) 1544. (b) Kosloff, R.; Kosloff, D. *J. Chem. Phys.* 79 (1983) 1823.
- [6] Collins, M. A. *Theor. Chem. Acc.* 2002, 108, 313.
- [7] Bettens, R.P.A, Collins, M. A. *J Chem Phys.* 1999 111, 816.

Direct-dynamics VTST study of the reactions of CH₃ with CH₄ and CD₄

Sh. Ramazani

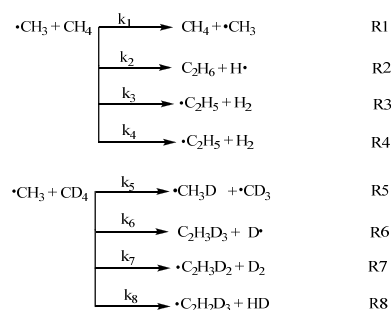
Department of Chemistry, College of sciences, Yasouj University, Yasouj, Iran

(Email: ramazani@mail.yu.ac.ir)

Keywords: VTST, Curvature, Tunneling effects, Isotope effects, Minimum energy path.

1. Introduction

The study of reactions of methane is very important because methane is the simplest alkane, and the principal component of natural gas. Methane is also a relatively potent greenhouse gas with a high global warming potential. On the other hand, methyl radical is an important reactive radical in the atmospheric processes and combustion chemistry. The kinetics and mechanism of the reactions between CH₃ and CH₄ and CD₄ have been theoretically investigated on adiabatic surfaces. There are hydrogen and deuterium abstraction from CH₄ and CD₄ to form reactant again (R1, R5). Reaction of these molecules apparently also leads to the formation of C₂H₆ (R2), C₂H₅ (R3 and R4), C₂H₃D₃ (R5), C₂H₃D₂ (R7) and C₂H₂D₃ (R8). R3 and R4 reactions result C₂H₅ in different procedures. In R3 reaction, two hydrogen atoms of CH₄ interact to form H₂, while in R4 reaction a hydrogen atom from CH₃ approaches to one from CH₄ to form H₂.



2. Computational Details

All the geometry optimizations have been performed at the MP2 [1] and MPWB1K [2] levels with the 6-311++G** basis set. It was used a method based on VTST [3] method to calculate the rate constants for reactions R1 to R8. Variational effects were incorporated by the canonical variational transition-state theory (CVT), in which the flux is minimized for a canonical ensemble. The CVT rate constant, $k^{CVT}(T)$, at temperature T , can be obtained as the minimum of the generalized transition-state theory rate constant, $k^{GT}(T, s)$, as a function of s , that is,

$$k^{CVT}(T) = \min_s k^{GT}(T, s) = \sigma \frac{1}{\beta h} \frac{Q^{GT}(T, s_*^{CVT})}{Q^R(T)} \exp\left[-\beta V_{MEP}(s_*^{CVT})\right]$$

where s is the arc along the MEP measured from the saddle point; s_*^{CVT} is the value of s at which $k^{GT}(T, s)$ has a minimum:

σ is the symmetry number, $V_{MEP}(s_*^{CVT})$ is the classical MEP potential at $s = s_*^{CVT}$; and $Q^{GT}(T, s_*^{CVT})$ and $Q^R(T)$ are the internal partition functions of the generalized transition state at $s = s_*^{CVT}$ and reactants, respectively. Tunneling effects were incorporated into the thermal CVT rate constants by a multiplicative ground-state (G) transmission coefficient, $\kappa^{CVT/G}(T)$:

$$\kappa = \left\{ \sum_{m=1}^{F-1} [B_{mF}(s)]^2 \right\}^{1/2} \quad \text{which } B_{mF}(s) \text{ is the curvature parameter.}$$

, so the final rate constant is given by

$$k^{CVT/G}(T) = \kappa^{CVT/G}(T) k^{CVT}(T) \quad \text{and} \quad \kappa^{CVT/G}(T) = \beta \exp\left\{ \beta V_a^G(s_*^{CVT}) \right\} \int_{E_0}^{\infty} P^G(E) e^{-\beta E} dE$$

where V_a^G is the vibrationally adiabatic potential, which is given by $V_a^G(s) = V_{MEP}(s) + \varepsilon_{int}^G(s)$

Where $\varepsilon_{\text{int}}^G(s)$ is the internal energy at s , which in the ground-state approximation equals the zero-point energy (ZPE) at s . The semiclassical ground-state probability $P^G(E)$ was calculated over the vibrational adiabatic potential by optimizing microcanonically the largest probability between the small curvature tunneling (SCT) probability, $P^{SCT}(E)$, and the large curvature tunneling (LCT) probability, $P^{LCT}(E)$, evaluated with the LCG4 version. The resulting probability is, therefore, given by $P^{\mu OMT}(E) = \max_E \left\{ P^{SCT}(E), P^{LCT}(E) \right\}$ Where μOMT stands for microcanonically optimized multidimensional tunnelling.

The primary kinetic isotope effect [4,5] (KIE) is consisted of the quantum mechanical part η_{tun} and classical part η_{cl} , $\eta = \eta_{\text{tun}} \eta_{\text{cl}}$ [6]. The quantum mechanical part is the ratio of the transmission coefficients for hydrogen transfer in reactions (R1-R4) to the transmission coefficients for deuterium transfer in reactions (R5-R8), $\eta_{\text{tun}} = \kappa_{\text{H}} / \kappa_{\text{D}}$.

And the classical part is the product of variational and internal (rotational and vibrational) contributions, $\eta_{\text{cl}} = \eta_{\text{int}} \eta_{\text{var}}$. The internal part η_{int} is the ratio of the partition functions as:

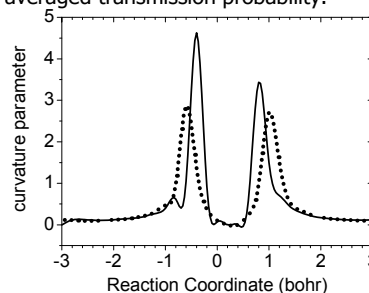
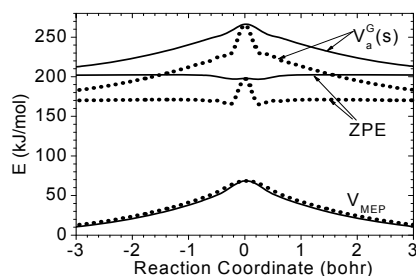
$$\eta_{\text{int}} = \frac{Q_H^{\#} / Q_H^R}{Q_D^{\#} / Q_D^R}$$

where Q 's represent the products of translational, rotational, and vibrational partition functions for the transition state ($Q^{\#}$) and reactants (Q^R). The variational part of KIE η_{var} is the ratio of TST rate constant k^{TST} to the canonical variational TST rate constant

$$k^{\text{CVT}} \text{ as } \eta_{\text{var}} = \frac{k_H^{\text{CVT}} k_D^{\text{TST}}}{k_H^{\text{TST}} k_D^{\text{CVT}}} \quad \text{for example in reactions (R1,R5): } \eta^{H/D} = \frac{k_1^{\text{CVT}} k_5^{\text{TST}}}{k_1^{\text{TST}} k_5^{\text{CVT}}} \times \frac{Q^{\#}(\text{R1}) / Q^R(\text{R1})}{Q^{\#}(\text{R5}) / Q^R(\text{R5})} \times \frac{\kappa(\text{R1})}{\kappa(\text{R5})}$$

3. Results and discussions

Variation of the vibrationally adiabatic ground state potential ($V_a^G(s)$), minimum energy path potential, V_{MEP} and Zero Point Energy (ZPE) for reactions R1 (solid line) and R5 (dot line), are shown in Fig. 1. We have also monitored variations of the normal mode vibrational frequencies along the MEPs for all channels. Fig. 2, shows the curvature parameter of the reaction paths $B_{\text{MF}}(s)$ for R1 and R5 channels. The most closely coupled modes to the reaction paths has shown in (-0.4, 0.8) and (-0.6, 1.0) for R1 and R5, respectively. All of the result will be reported in the conference, including rate constants, preliminary investigations of tunnelling effect, kinetic isotope effect, and thermally averaged transmission probability.



References

- [1] C. Møller, M.S. Plesset, Phys. Rev. 46 (1934) 618.
- [2] Y. Zhao, D.G. Truhlar, J. Phys. Chem. A. 108 (2004) 6908.
- [3] D.G. Truhlar, A. Kuppermann, J. Am. Chem. Soc. 93 (1971) 1840.
- [4] T.K.B. Wiberg, L.H. Slaugh, J. Am. Chem. Soc. 80 (1958) 3033
- [5] R.A. Lynch, S.P. Vincenti, Y.T. Lin, L.D. Smucker, S.C. Subba Rao, J. Am. Chem. Soc. 94 (1972) 8351.
- [6] S. H. Mousavipour, A. F. Ramos, R. M. Pan, E. M. Nuñez, S. A. Vázquez and M. A. Riós, J. Phys. Chem. A 111(2007) 719.

**Thermal behavior kinetic study of activated-carbon from pistachio shell***N. Madadi Mahani^a, M.Oftade^b and Sh. Rafiei^c^aPayam- Noor University, Sirjan, Iran

(Email: nmamadady@gmail.com)

^bPayam- Noor University , Esfahan, Iran^cEmam Khomeini International University ,Ghazvin, Iran**1. Introduction**

Activated carbon is a well known as porous material, with large specific surface area, which is useful in adsorption of both gases and solutes from aqueous solution. Therefore, it has been widely used for separation of gases, recovery of solvents, removal of organic pollutants from drinking water and a catalyst support.

As environmental pollution is becoming a more serious problem, the need for activated carbon is growing. It is a versatile adsorbent because of its good adsorption properties. Various materials are used to produce activated carbon and some of the most commonly used are agriculture wastes such as coconut shell, walnut shell, tropical wood, almond shell and pistachio shell [1]. Pistachio shell has high volatile and carbon contents, low ash content, and reasonable good hardness properties [2].

Thermal gravimetric analysis is a simple analytical technique that measures the weight loss (or weight gain) of a material as a function of temperature. As materials are heated, they can loose weight from a simple process such as drying, or from chemical reactions that liberate gasses. Thermo-analytical methods such as thermo gravimetric(TG), differential thermal analysis (DTA) and differential scanning calorimetric (DSC) have proved to play important role in the study of thermal decomposition of solid fuels and activated carbon[3,4].

Kinetic studies have become a crucial point in thermal analysis, in which the main purpose is to calculate the parameters of the Arrhenius equation. The knowledge of such parameters for energetic material and activated carbon is also meaningful in order to elucidate miscibility/ compatibility and its efforts on thermal stability [5].The purpose of this was to study the thermal behavior activated carbon of pistachio shell by thermo gravimetric (TG) method. the influence of heating rate on the this compound was investigated.

2. Experimental Methods

Raw pistachio shell was dried in oven at 110 °C for 12h to reduce the moisture content. They were crushed with a coffee grinder and sieved to a size 3-4 mm. The Experimental procedures for the chemical activation process using H₃PO₄ under N₂ atmosphere. Activated-Carbon from Pistachio Shell with a particle size of -200 m was used for the TG and DTG analyses. For experimental Parameters, 2.6 mg coal samples a nitrogen atmosphere (100 ml min⁻¹), and a linear heating rate of 20 C min⁻¹ were used. All experiments were performed over a temperature range of 25 to 800 C using platinum crucibles. Prior to the experiments, the TG apparatus was calibrated via the melting points of indium (156.6 °C), tin (231.9 °C), lead (327.5 °C), zinc (419.6 °C), aluminum (660.2 °C) and gold (1063°C) standards under the same conditions as for the samples. Alumina was used as reference material in all experiments. The weight loss (TG signal) and the rate of weight loss (DTG signal) as a function of time or temperature were recorded, while the coals were subjected to a computer-controlled temperature program. The TG and DTG curves were obtained by a Perkin Elmer model instrument.

3. Result and discussion:

For analyzing the kinetics of TG/DTG data, the model assumes that the rate of weight loss of the total sample is dependent only on the rate constant, the remaining weight of the sample and its temperature with a reaction order of unity. The shift in the DTG peak is a measure of reactivity value. The reactivity values were calculated according to the relationship

$$R_t = (1/W_0) * (dw/dt) \quad (1)$$

The kinetic parameters of the thermal decomposition reactions were calculated by using an Arrhenius-type kinetic model assuming, is based on the following equation:

$$\text{Log} [(dw_t/dt). (1/w_0)] = \text{Log} A - E/2.303RT \quad (2)$$

Where dw/dt is the rate of weight change of the reacting material in % min⁻¹. In the model, the plot of Log[(dW/dt).(1/W)] against 1/T is a straight line with a slope of E/2.303R.the activation energy(E_a) value for activated carbon of pistachio shell

were calculated. ($E_a=172.247\text{ kJ/mol}$) and maximum rate temperature ($R_t=670^\circ\text{C}$) that is approximately in ranges the E_a values from previous studies using types of activated carbon with values between 100 -300 kJ/mol. In the other hand the quality of activated carbon is sufficient and can be used in surface processes.

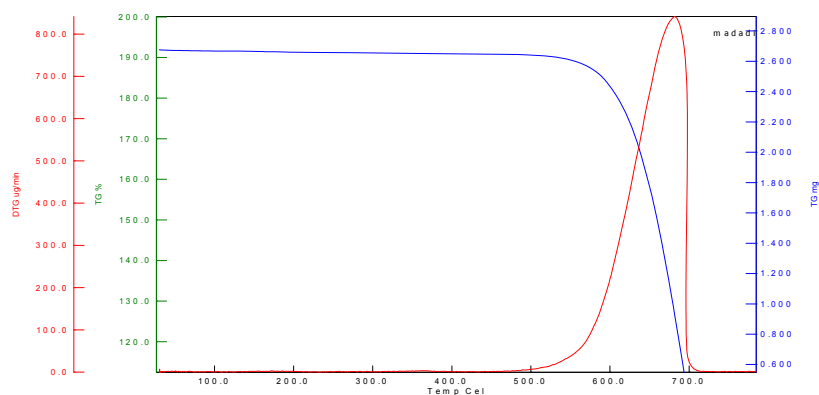


Fig1. TG and DTG curves

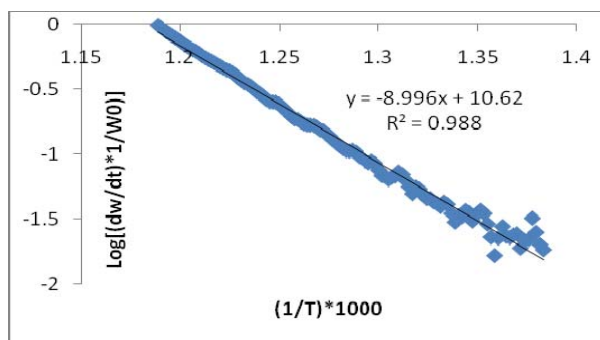


Fig.2 Log[(dW/dt).(1/W)] against 1/T

References

- [1] D. Adinata, W. M. Ashriwan, M. Kheireddine, Bioresource Technology 98(2007) 145-149.
- [2] I. I. El-Shakany, B. B. Saha, Sh. Koyana and K. Chonn Ng, International J. Heat and Mass Transfer, 49 (2006)3104-3110.
- [3] O. O. Sonibare, O. A. Ehinola, L.Kea Giap and R. Egashira, J. Appl. Sciences 5(1) 104-107(2005).
- [4] P Gabbott, Principles and application of thermal analysis (2008) Blackwell publishing LTD .
- [5] S .M. Pourmortazavi, J. Kohsari, M.B. Teimori, S. S. Hajimirsadeghi, Materials Letters, 61(2007) 4670-4773.

Kinetic study and mechanism investigation of the reactions between triphenylphosphine, dialkyl acetylenedicarboxylates and NH-acid such as Maleimide by UV spectrophotometry

S. M. Habibi Khorassani*, M. T. Maghsoodlou, A. Ebrahimi, E. Aghdaei and M. Zakarianejad, M. Mohammadi

Department of Chemistry, University of Sistan and Baluchestan, P.O. Box 98135-674, Zahedan, Iran

(Email: smhabibius@yahoo.com)

1. Introduction

The synthetic reactions between compounds **1**, **2** and CH, OH, SH or NH-acids have been reported earlier [1-4] but the kinetic studies of these reactions have not been investigated yet. Herein, we describe a kinetic investigation of a facile synthesis of the reactions between **1**, **2** and **3** (as NH-acid) (Figure 1). Numerous kinetic investigations over a large area of different reactions have been reported previously using UV analysis [5-8]. To gain further insight into the reaction mechanism, a kinetic study of the reactions was undertaken by UV spectrophotometric technique. First 1mL aliquot from the 3×10^{-3} M solutions of each compound of **1**, **2c** and **3** was pipetted into a quartz spectrophotometer cell and the reaction monitored by recording scans of the entire spectra every 12 min over the whole reaction time at ambient temperature. The ultra-violet spectra shown in Figure 2 are typical. From this, the appropriate wavelength was found to be 300 nm. Since at this wavelength, compounds **4**, **2c** and **3** have relatively no absorbance value, this provided the opportunity to fully investigate the kinetics of the reaction between **1**, **2c** and **3** at 300 nm in the presence of 1,2-dichloroethane as solvent. The reaction kinetics was followed by plotting UV absorbance against time. The original experimental absorbance curves (dotted line) accompanied by the second order fit curves (full line), which exactly fit experimental curves (dotted line), is shown in Figure 3 at 15.0°C and 300 nm. The results show that the rate of reaction in each case was increased at higher temperature. In addition, the rate of reaction was accelerated in a higher dielectric constant environment (1,2-dichloroethane) in comparison with a lower dielectric constant environment (Ethyl acetate) at all temperatures investigated.

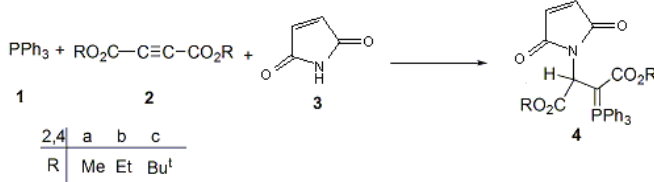


Fig. 1. The UV spectra of the reaction between **1**, **2c** and **3** with 10^{-3} M concentration of each compound as reaction proceeds in 1,2-dichloroethane.

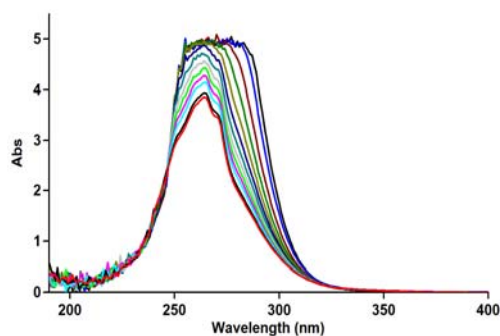


Fig. 2. The UV spectra of the reaction between **1**, **2c** and **3** with 10^{-3} M concentration of each compound as reaction proceeds in 1,2-dichloroethane.

To determine the reaction order with respect to **1** and **2** (**2c**), in the continuation of experiments, all kinetic studies were carried out in the presence of excess **3**. Under this condition, the rate equation may therefore be expressed as:

$$rate = k_{obs} [1]^{\alpha} [2]^{\beta} \quad k_{obs} = k_2 [3]^{\gamma} \quad \text{or} \quad \ln k_{obs} = \ln k_2 + \gamma \ln [3] \quad (\text{I})$$

In this case (3×10^{-2} M of **3** instead of 3×10^{-3} M), using the original experimental absorbance versus time data provides a second order fit curve (full line) against time at 300 nm which exactly fits the experimental curve. The value of the rate constant was the same as that of obtained from the previous experiment (3×10^{-3} M). In fact, the experimental data indicated that the observed pseudo-second-order rate constant (k_{obs}) is equal to the second-order rate constant (k_2), this is possible when γ is zero in equation (I). It is appeared, therefore, that the reaction is zero and second order with respect to **3** (NH-acid) and the sum of **1** and **2** (**2c**) ($\alpha + \beta = 2$), respectively. To determine the reaction order with respect to **1**, the continuation of experiment was performed in the presence of excess **2** (**2c**) ($rate = k'_{obs} [3]^{\gamma} [1]^{\alpha}$, $k'_{obs} = k_2 [2]^{\beta}$ (II)). The original experimental absorbance versus time data provides a pseudo-first-order fit curve at 300 nm, which exactly fits the experimental curve (dotted line) as shown in Figure 4. As a result, since $\gamma = 0$ (as determined previously), it is reasonable to accept that the reaction is first order with respect to compound **1** ($\alpha = 1$). Based on the above results, a simplified proposed reaction mechanism is shown in Figure 5.

A good kinetic description of the experimental result using a mechanistic scheme (Figure 5) based upon the steady-state approximation would allow that first step to be the rate-determining step. The rate formation of product **4** from the reaction mechanism (Figure 5) is given by: $rate = k_2[1][2]$ (III)

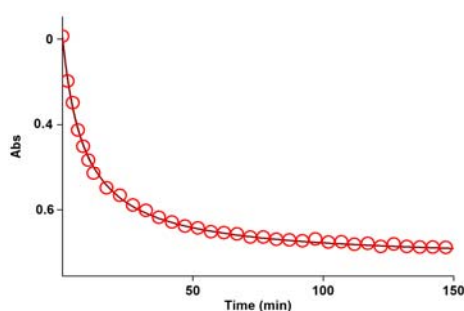


Fig. 3. Second order fit curve (full line) accompanied by the original experimental curve (dotted line) for the reaction between compounds **1**, **2c** and **3** at 300 nm and 15.0°C in 1,2-dichloroethane.

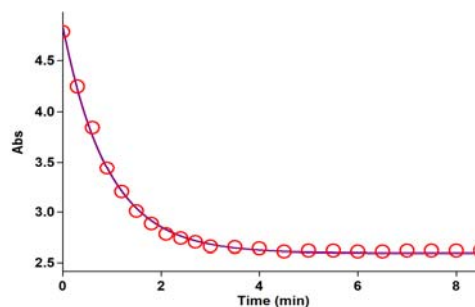


Fig. 4. Pseudo first order fit curve (full line) for the reaction between 1 and 3 in the presence of excess 2 (**2c**) (10^{-2} M) at 300 nm and 15.0°C in 1,2-dichloroethane

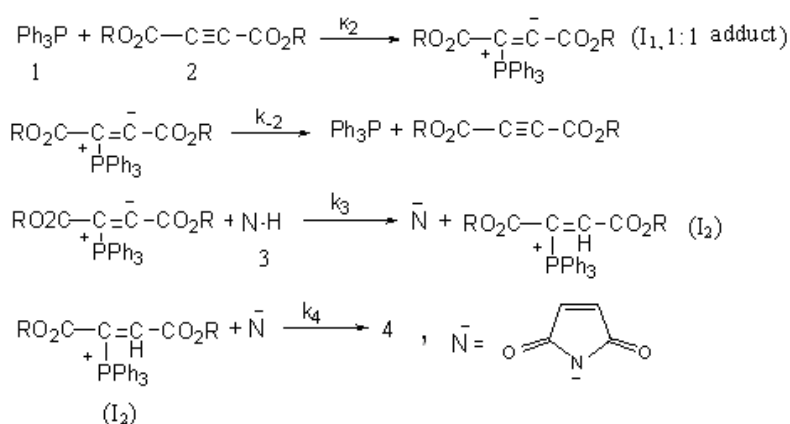


Fig. 5. Proposed mechanism for the reaction between **1**, **2** (**2a**, **2b**, **2c**) and **3** for generation of phosphorous ylides **4a-c**.

To confirm the above observations, further experiments were performed with compounds **2b** and **2a** instead of **2c**, under the same conditions used in the previous experiments. The behavior of **2b** and **2a** is the same as for **2c** with respect to the reaction with **1** and **3**. The rate of the former reactions was also accelerated in a higher dielectric constant environment and with higher temperatures; however, these rates under the same condition are approximately 5 to 8 times more than for the reaction with **2c**. It seems that both inductive and steric factors for the bulky alkyl groups in **2c** tend to reduce the overall reaction rate (equation III). In the case of **2a**, the lower steric and inductive effects of the dimethyl groups exert a powerful effect on the rate of reaction.

References

- [1] I. Yavari, L. Ahmadian-Razlighi, Phosphorus, Sulfur, and Silicon. 181 (2006) 771.
- [2] I. Yavari, M. Adip, L. Hojati, Tetrahedron. 58 (2002) 7213.
- [3] M. T. Maghsoodlou, N. Hazeri, G. Afshari, U Niroumand. Phosphorus, Sulphur, and Silicon. 181 (2006) 2681.
- [4] M. T. Maghsoodlou, N. Hazeri, S. M. Habibi-Khorassani, M. Nassiri, J. Sulfur Chem. 26 (2005) 261.
- [5] O. J. Nielsen, J. Sehested, S. Langer, E. Ljungstrom, I. Wangberg, Chem. Phys. Lett. 238 (1995) 359.
- [6] V.V. Ivanov, C. Decker, Polymer International 50 (2001) 113.
- [7] R. N. Carvalho, L.S. Moura, P.T.V. Rosa, M. Angela, Supercritical Fluids.35 (2005) 197.
- [8] F. Misiti, M. Castagnola, C. Zuppi, B. Giardina, I. Messina, Biochem. 356 (2001) 799.

Kinetic and mechanism investigation of the reactions between dialkyl acetylenedicarboxylates and 2-thiazoline 2-thiole in the presence of triphenyl phosphite by UV

S. M. Habibi Khorassani*, M. T. Maghsoodlou, A. Ebrahimi and M. Zakarianejad

Department of Chemistry, University of Sistan and Baluchestan, P.O. Box 98135-674, Zahedan, Iran

(Email: smhabibius@yahoo.com)

1. Introduction

The synthetic reactions between compounds **1**, **2** and SH or NH-acids have been reported earlier [1-4] but the kinetic studies of these reactions have not been investigated yet. Herein, we describe a kinetic investigation of a facile synthesis of the reactions between **1**, **2** and **3** (as NH-acid) (Figure 1). Numerous kinetic investigations over a large area of different reactions have been reported previously using UV analysis [5-8]. To gain further insight into the reaction mechanism, a kinetic study of the reactions was undertaken by UV spectrophotometric technique. First 1mL aliquot from the 3×10^{-3} M solutions of each compound of **1**, **2c** and **3** was pipetted into a quartz spectrophotometer cell and the reaction monitored by recording scans of the entire spectra every 50 min over the whole reaction time at ambient temperature. The ultra-violet spectra shown in Figure 2 are typical. From this, the appropriate wavelength was found to be 340 nm. Since at this wavelength, compounds **4**, **2c** and **3** have relatively no absorbance value, this provided the opportunity to fully investigate the kinetics of the reaction between **1**, **2c** and **3** at 340 nm in the presence of 1,2-dichloroethane as solvent. The reaction kinetics was followed by plotting UV absorbance against time. The original experimental absorbance curves (dotted line) accompanied by the second order fit curves (full line), which exactly fit experimental curves (dotted line), is shown in Figure 3 at 15.0°C and 340 nm (Figure 3). The results show that the rate of reaction in each case was increased at higher temperature. In addition, the rate of reaction was accelerated in a higher dielectric constant environment (1,2-dichloroethane) in comparison with a lower dielectric constant environment (Ethyl acetate) at all temperatures investigated.

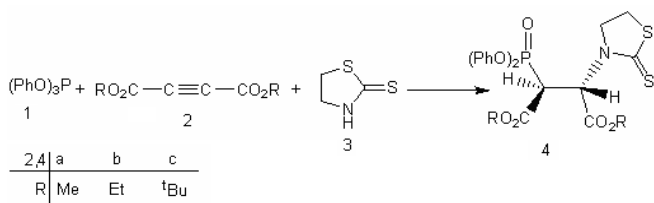


Fig.1. The UV spectra of the reaction between **1**, **2c** and **3** with 10^{-3} M concentration of each compound as reaction proceeds in 1, 2-dichloroethane with 10 mm light-path cell.

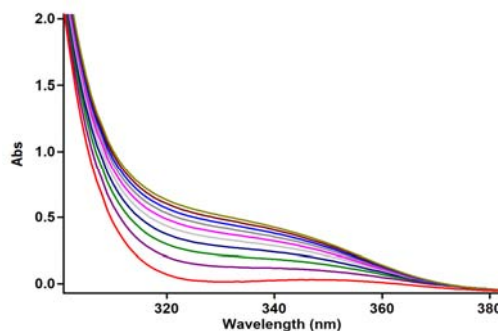


Fig.2. The UV spectra of the reaction between **1**, **2c** and **3** with 10^{-3} M concentration of each compound as reaction proceeds in 1,2-dichloroethane with 10 mm light-path cell.

To determine the reaction order with respect to compounds **2** (**2c**) and **3**, in the continuation of experiments, all kinetic studies were carried out in the presence of excess **1** (3×10^{-2} M of **3** instead of 3×10^{-3} M). Under this condition, the rate equation may therefore be expressed as: $rate = k_{obs} [2]^\beta [3]^\gamma$ and $k_{obs} = k_2 [1]^\alpha$ or $\ln k_{obs} = \ln k_2 + \alpha \ln [1]$ (I)

In this experiment obtained pseudo-second-order fit curve (full line) against time at 340 nm. This result indicates that α is zero in equation (I). Therefore, the reaction is zero and second order with respect to **1** and the sum of **2** (**2c**) and **3** ($\beta + \gamma = 2$), respectively. Experiment was performed in the presence of excess **2** (**2c**). Under this condition, the rate equation may therefore be expressed as: $rate = k'_{obs} [1]^\alpha [3]^\gamma$ and $k'_{obs} = k_2 [2]^\beta$ (II)

In this experiment pseudo-first-order fit curve obtained at 340 nm. As a result, since $\alpha = 0$ (as determined previously), it is reasonable to accept that the reaction is first order with respect to compound **3** ($\gamma = 1$). Because the overall order of reaction is **2** ($\alpha + \beta + \gamma = 2$), it is obvious that $\beta = 1$ and the order of compound **2** must be equal to 1. A good kinetic description of the experimental result using a mechanistic scheme (Figure 4) based upon the steady-state approximation would allow that first step to be the rate-determining step. The rate formation of product **4** from the reaction mechanism (Figure 3) is given by:

$$\text{rate} = k_2[2][3] \quad (\text{III})$$

Two reactants (**1** and **2**), have no charge and could not form powerful ion-dipole bonds to the 1,2-dichloroethane as a solvent with high dielectric constant in the reaction medium (see Figure 4). But the transition state carries a dispersed charge which here is divided between the attacking **1** and **2**. Bonding of solvent to this dispersed charge is much stronger than to the reactants with lack of charge. The solvent thus stabilizes the transition state more than it does the reactants, and therefore E_a is reduced which speed up the reaction instead of ethyl acetate as a solvent with lower dielectric constant. discussed effects altogether are compatible with first step (k_2) of proposed mechanism and would allow to be the rate determining step.

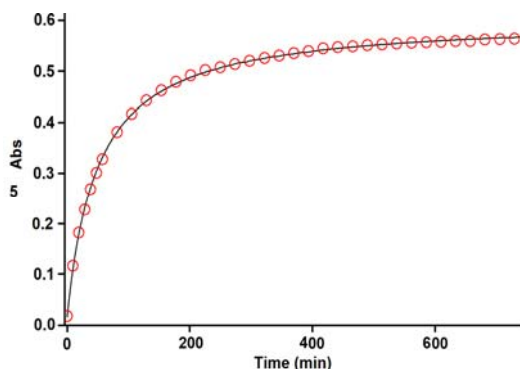


Fig. 3: Second order fit curve (full line) accompanied by the original experimental curve (dotted line) for the reaction between compounds **1**, **2c** and **3** at 340 nm and 15.0°C in 1,2-dichloroethane.

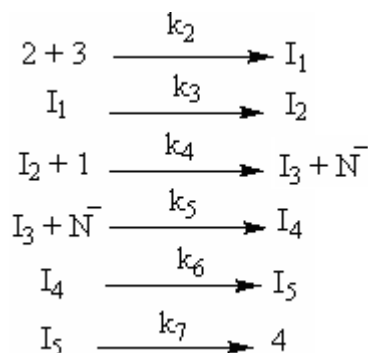


Fig. 4: Proposed mechanism for the reaction between **1**, **2** (**2a**, **2b** or **2c**) and **3** for generation of phosphorous ylides **4a-c**.

To confirm the above observations, further experiments were performed with compounds **2b** and **2a** instead of **2c**, under the same conditions used in the previous experiments. The behavior of **2b** and **2a** is the same as for **2c** with respect to the reaction with **1** and **3**. The rate of the former reactions was also accelerated in a higher dielectric constant environment and with higher temperatures; however, these rates under the same condition are approximately 5 to 7 times more than for the reaction with **2c**. It seems that both inductive and steric factors for the bulky alkyl groups in **2c** tend to reduce the overall reaction rate (equation III). In the case of **2a**, the lower steric and inductive effects of the dimethyl groups exert a powerful effect on the rate of reaction.

References

- [1] I. Yavari, L. Ahmadian-Razlighi, Phosphorus, Sulfur, and Silicon. 181 (2006) 771.
- [2] I. Yavari, M. Adip, L. Hojati, Tetrahedron. 58 (2002) 7213.
- [3] M. T. Maghsoodlou, N. Hazeri, G. Afshari, U Niroumand. Phosphorus, Sulphur, and Silicon. 181 (2006) 2681.
- [4] M. T. Maghsoodlou, N. Hazeri, S. M. Habibi-Khorassani, M. Nassiri, J. Sulfur Chem. 26 (2005) 261.
- [5] O. J. Nielsen, J. Sehested, S. Langer, E. Ljungstrom, I. Wangberg, Chem. Phys. Lett. 238 (1995) 359.
- [6] V.V. Ivanov, C. Decker, Polymer International 50 (2001) 113.
- [7] R. N. Carvalho, L.S. Moura, P.T.V. Rosa, M. Angela, Supercritical Fluids.35 (2005) 197.
- [8] F. Misiti, M. Castagnola, C. Zuppi, B. Giardina, I. Messina, Biochem. 356 (2001) 799.

Effect of concentration on the ultrasonic degradation of poly (vinyl pyrrolidone) in aqueous solution

Mohammad Taghi Taghizadeh*, Esmail Heydarpour Serajeh Lou

University of Tabriz, Faculty of chemistry, Department of physical chemistry, Tabriz, Iran

(Email: mttaghizadeh@tabrizu.ac.ir)

Introduction

Various methods like application of heat, light, chemical reagents, ultrasonic radiation can cause polymer degradation. Application of ultrasonic energy for polymer degradation date back to the 1930s when natural polymers were subjected to sonication, which resulted in a reduction of viscosity [1]. Schmid and Rommel [2] were the first to report the investigation of polymer degradation by ultrasonic energy.

Methods

A kinetic method based on viscometric data was used to determine the rate of degradation reactions for different concentration of PVP solutions. The rate of degradation is defined as the number of moles of scission that occur in 1 l in unit time. The chain scission yields the two pieces. The degradation rate equation is as follows:

$$\frac{dM}{dt} = kM^n \quad (1)$$

Where M is the total molar concentration of polymer, k is the rate constant and n is the order of reaction with respect to the total molar concentration of polymer. The solution of differential Eq. (1) is:

$$M^{1-n} - M_0^{1-n} = (1-n)kt \quad (2)$$

where M_0 is the initial total concentration of polymer. The total molar concentration is related to the number average molecular weight through:

$$M = \left[\frac{(1+\alpha)\Gamma(1+\alpha)KC^{1+\alpha}}{\sqrt{2}} \right]^{\frac{1}{\alpha}} \Delta\eta \quad (3)$$

Substitution of Eq. 3 to Eq.2 we have:

$$\Delta\eta^{1-n} - \Delta\eta_0^{1-n} = (1-n) \left[\frac{\sqrt{2}}{(1+\alpha)\Gamma(1+\alpha)KC^{1+\alpha}} \right]^{\frac{1-n}{\alpha}} kt \quad (4)$$

Finally, we obtain the following equation from Eq.4:

$$\Delta\eta^{1-n} - \Delta\eta_0^{1-n} = k't \quad (5)$$

Results and discussion

Fig. 1 shows the relative viscosity versus sonication time for different concentrations. As seen, when concentration of solution increased, reduce in relative viscosity decreased considerably. It can be deduced that there is a limiting molecular weight that below which chain scission does not occur. Under the same conditions, the decrease in η_r of the sample with a high polymer concentration is lower than of the sample with a low polymer concentration. At high concentration, entanglements influence the energy transfer processes between solvent and polymer and appears to reduce the probability of degradation accruing [3].

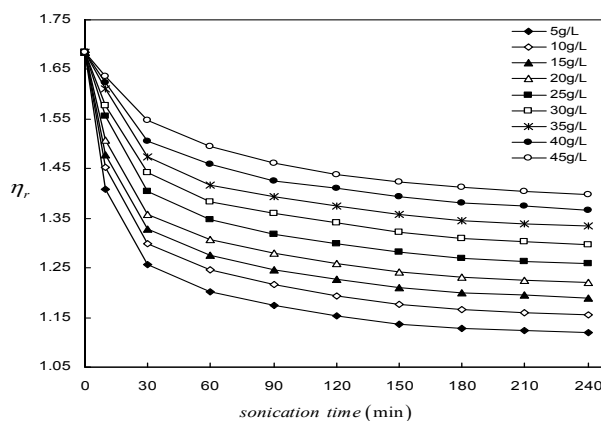


Fig. 1. The relationship between η_r and sonication time for different concentration of PVP solutions.

Conclusions

The aim of this research was to study the effect of concentration of polymer on the ultrasonic degradation of PVP in solution at 25°C. The experimental results indicated that the degradation rate reduced with increasing solution concentration. Relative viscosity decreases on sonication time and inclines to a limiting value, below which no further degradation occurs.

References

- [1] G.J. Price, P.J. West, P.F. Smith, *Ultrason. Sonochem.* 1 (1994) 51.
- [2] G. Schmid, O. Rommel, *J. Phys. Chem. A* 185 (1939) 97.
- [3] M. T. Taghizadeh, A. Bahadori, *J. Polym. Res.* 16 (2009) 545.

Kinetic and mechanism investigation of the reactions between dialkyl acetylenedicarboxylates and 2,4-dimethyl 2-mercapto pyrimidine the presence of triphenyl phosphite by UV

M. T. Maghsoodlou, S. M. Habibi Khorassani*, A. Ebrahimi and M. Zakarianejad

^aDepartment of Chemistry, University of Sistan and Baluchestan, P.O. Box 98135-674, Zahedan, Iran

(Email: smhabibius@yahoo.com)

Introduction

The synthetic reactions between compounds **1**, **2** and SH or NH-acids have been reported earlier [1-4] but the kinetic studies of these reactions have not been investigated yet. Herein, we describe a kinetic investigation of a facile synthesis of the reactions between **1**, **2** and **3** (as SH-acid) (Figure 1). Numerous kinetic investigations over a large area of different reactions have been reported previously using UV analysis [5-8]. To gain further insight into the reaction mechanism, a kinetic study of the reactions was undertaken by UV spectrophotometric technique. First 1mL aliquot from the 3×10^{-3} M solutions of each compound of **1**, **2c** and **3** was pipetted into a quartz spectrophotometer cell and the reaction monitored by recording scans of the entire spectra every 55 min over the whole reaction time at ambient temperature. The ultra-violet spectra shown in Figure 2 are typical. From this, the appropriate wavelength was found to be 410 nm. Since at this wavelength, compounds **4**, **2c** and **3** have relatively no absorbance value, this provided the opportunity to fully investigate the kinetics of the reaction between **1**, **2c** and **3** at 410 nm in the presence of 1,2-dichloroethane as solvent. The reaction kinetics was followed by plotting UV absorbance against time. The original experimental absorbance curves (dotted line) accompanied by the second order fit curves (full line), which exactly fit experimental curves (dotted line), is shown in Figure 3 at 17.0°C and 410 nm (Figure 3). The results show that the rate of reaction in each case was increased at higher temperature. In addition, the rate of reaction was accelerated in a higher dielectric constant environment (1,2-dichloroethane) in comparison with a lower dielectric constant environment (1,4-dioxan) at all temperatures investigated.

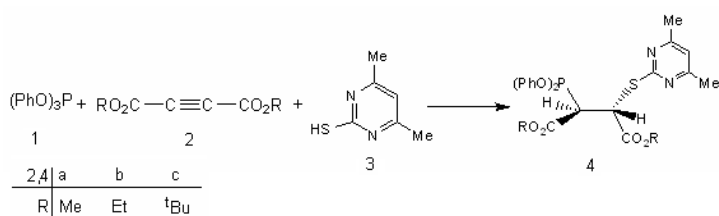


Figure 1: The UV spectra of the reaction between **1**, **2c** and **3** with 10^{-3} M concentration of each compound as reaction proceeds in 1, 2-dichloroethane with 10 mm light-path cell.

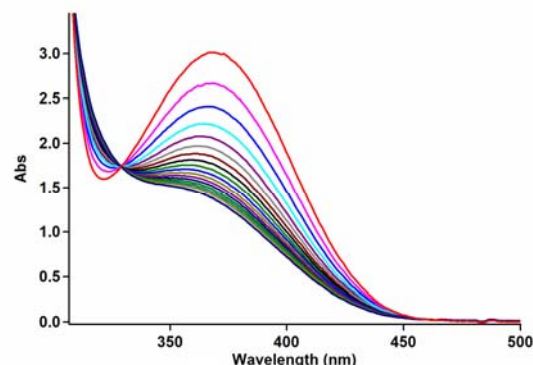


Figure2: The UV spectra of the reaction between **1**, **2c** and **3** with 10^{-3} M concentration of each compound as reaction proceeds in 1,2-dichloroethane with10 mm light-path cell.

To determine the reaction order with respect to compounds **2** (**2c**) and **3**, in the continuation of experiments, all kinetic studies were carried out in the presence of excess **1** (3×10^{-2} M of **3** instead of 3×10^{-3} M). Under this condition, the rate equation may therefore be expressed as: $rate = k_{obs} [2]^\beta [3]^\gamma$ and $k_{obs} = k_2 [1]^\alpha$ or $\ln k_{obs} = \ln k_2 + \alpha \ln [1]$ (I)

In this experiment obtained pseudo-second-order fit curve (full line) against time at 410 nm. This result indicates that α is zero in equation (I). Therefore, the reaction is zero and second order with respect to **1** and the sum of **2** (**2c**) and **3** ($\beta + \gamma = 2$), respectively. Experiment was performed in the presence of excess **2** (**2c**). Under this condition, the rate equation may therefore be expressed as: $rate = k'_{obs} [1]^\alpha [3]^\gamma$ and $k'_{obs} = k_2 [2]^\beta$ (II)

In this experiment pseudo-first-order fit curve obtained at 410 nm. As a result, since $\alpha = 0$ (as determined previously), it is reasonable to accept that the reaction is first order with respect to compound **3** ($\gamma = 1$). Because the overall order of reaction is **2** ($\alpha + \beta + \gamma = 2$), it is obvious that $\beta = 1$ and the order of compound **2** must be equal to 1. A good kinetic description of the

experimental result using a mechanistic scheme (Figure 4) based upon the steady-state approximation would allow that first step to be the rate-determining step. The rate formation of product **4** from the reaction mechanism (Figure 3) is given by:

$$\text{rate} = k_2[2][3] \quad (\text{III})$$

Two reactants (**1** and **2**), have no charge and could not form powerful ion-dipole bonds to the 1,2-dichloroethane as a solvent with high dielectric constant in the reaction medium (see Figure 4). But the transition state carries a dispersed charge which here is divided between the attacking **1** and **2**. Bonding of solvent to this dispersed charge is much stronger than to the reactants with lack of charge. The solvent thus stabilizes the transition state more than it does the reactants, and therefore E_a is reduced which speed up the reaction instead of 1,4-dioxan as a solvent with lower dielectric constant. discussed effects altogether are compatible with first step (k_2) of proposed mechanism and would allow to be the rate determining step.

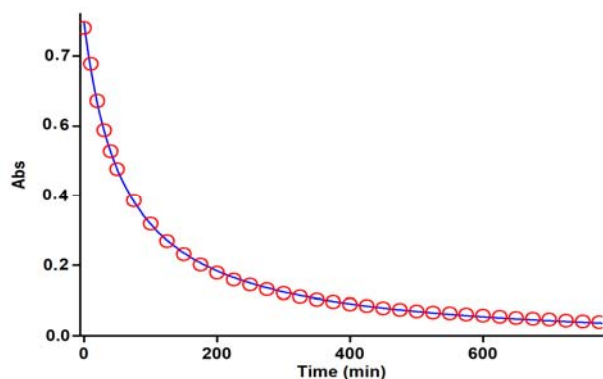


Figure 3: Second order fit curve (full line) accompanied by the original experimental curve (dotted line) for the reaction between compounds **1**, **2c** and **3** at 410 nm and 17.0°C in 1,2-dichloroethane.

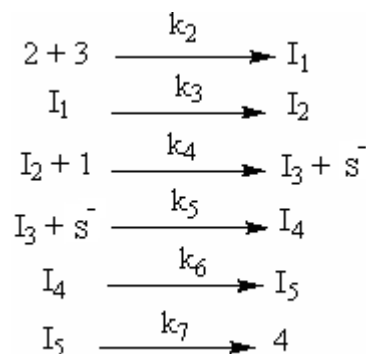


Figure 4: Proposed mechanism for the reaction between **1**, **2** (**2a**, **2b** or **2c**) and **3** for generation of phosphorous ylides **4a-c**.

To confirm the above observations, further experiments were performed with compounds **2b** and **2a** instead of **2c**, under the same conditions used in the previous experiments. The behavior of **2b** and **2a** is the same as for **2c** with respect to the reaction with **1** and **3**. The rate of the former reactions was also accelerated in a higher dielectric constant environment and with higher temperatures; however, these rates under the same condition are approximately 6 to 8 times more than for the reaction with **2c**. It seems that both inductive and steric factors for the bulky alkyl groups in **2c** tend to reduce the overall reaction rate (equation III). In the case of **2a**, the lower steric and inductive effects of the dimethyl groups exert a powerful effect on the rate of reaction.

References

- [1] I. Yavari, L. Ahmadian-Razlighi, Phosphorus, Sulfur, and Silicon. 181 (2006) 771.
- [2] I. Yavari, M. Adip, L. Hojati, Tetrahedron. 58 (2002) 7213.
- [3] M. T. Maghsoodlou, N. Hazeri, G. Afshari, U. Niroumand. Phosphorus, Sulphur, and Silicon. 181 (2006) 2681.
- [4] M. T. Maghsoodlou, N. Hazeri, S. M. Habibi-Khorassani, M. Nassiri, J. Sulfur Chem. 26 (2005) 261.
- [5] O. J. Nielsen, J. Sehested, S. Langer, E. Ljungstrom, I. Wangberg, Chem. Phys. Lett. 238 (1995) 359.
- [6] V.V. Ivanov, C. Decker, Polymer International 50 (2001) 113.
- [7] R. N. Carvalho, L.S. Moura, P.T.V. Rosa, M. Angela, Supercritical Fluids.35 (2005) 197.
- [8] F. Misiti, M. Castagnola, C. Zuppi, B. Giardina, I. Messina, Biochem. 356 (2001) 799.



Surface Chemistry



Photocatalytic degradation of nonionic surfactant using Zinc oxide nanoparticles

M. Giah^a, F. Ghanbari^b

^aDepartment of Chemistry, Faculty of Science, Islamic Azad University, Lahidjan Branch, Lahidjan, Iran.

^bDepartment of Chemistry, Faculty of Science, Semnan University, Semnan, Iran.

(Email: giah_m@yahoo.com)

Keywords: Zinc oxide nanoparticles, Photocatalytic, surfactant, degradation, pseudo-second-order model, K₂S₂O₈.

1. Introduction

Non-ionic surfactants in nd metallurgy. In contrast, ZnO, a kind of semiconductor with has the similar band gap as TiO₂, is not thoroughly investigated. However, the biggest advantage of ZnO in comparison with TiO₂ is that it absorbs over a larger fraction of UV spectrum[1-4] .In this paper, we selected a non-ionic surfactant as a model compound of organic pollutants and ZnO nanoparticles as a photocatalyst. The effects of various parameters on the photocatalytic degradation of NP10EO were studied.

2. Methods

The conditions used in the present study was a batch reactor(a cylindrical Pyrex vessel of 2 cm diameter with capacity of 50 mL), 20 cm distance between UV source (high pressure mercury vapour lamp 400 w) and solution with a stirring speed of 80 rpm and 30 min time for adsorption equilibrium. The quantitative estimation of the surfactant was carried out using a UV-Vis spectrophotometer (model Jenway 6405) at λ_{max}=223 nm.

Degradation kinetics -EO) versus irradiation time. As it is clear from Fig.1 that decreasing the surfactant concentrarion obeys a linear pattern towards the elapse of irradiation time. This means that the pseudo -second-order kinetics relative to surfactant is operative.

3. Results and discussion

Effect of UV, ZnO and S₂O₈²⁻

The effect of sulfate radical (SO₄^{•-}) as an oxidant on the degradation of NP10EO was investigated and compared with the ZnO (only), S₂O₈²⁻ (only), UV / S₂O₈²⁻,UV /ZnO and UV/ZnO/ S₂O₈²⁻ systems. as shown in Fig. 2 UV/ZnO system had more significant effect on the degradation of surfactant than the UV/ S₂O₈²⁻ system. When potassium peroxydisulfate was added to the UV/ ZnO system, surfactant concentration decreased from 30 mg/L to 3.21 mg/L after 120 min (Fig.2).

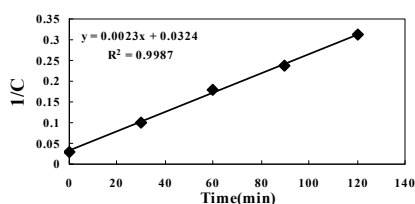


Fig. 1. Pseudo-second-order degradation rate of (NP10EO).

Fig.3 shows that degradation of NP10-EO was accelerated remarkably by adding peroxydisulfate:30 mg/L NP10-EO and in the presence of 0.2 g/L ZnO was completely disappeared under the irradiation of 8 to 2h respectively, in the absence and in the presence of 1 mM K₂S₂O₈.

Effect of pH

Figure 4 indicates the effect of pH on the degradation efficiency of NP10EO by UV/ZnO/S₂O₈²⁻ system is in the range of 4-10. The degradation of NP10EO was more enhanced in the range of pH 6-7 than in the other pH values.

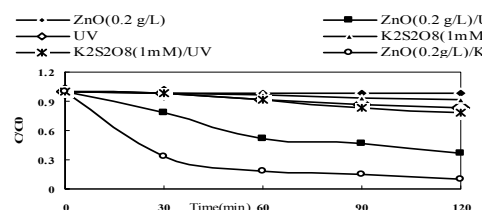


Fig. 2. Degradation of [NP10EO]₀=30 ppm

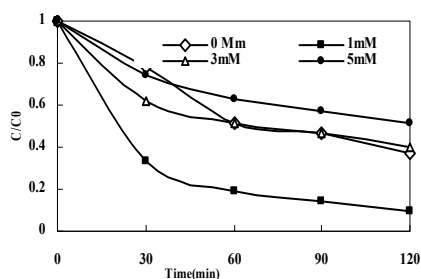


Fig. 3. Effect of $S_2O_8^{2-}$ concentration on the Degradation of NP10EO

Conditions: $[NP10EO]_0$: 30mg/L, ZnO: 0.2 g/L, pH=6, V_t : 25ml (C_0 : initial surfactant concentration, C: surfactant concentration at time t).

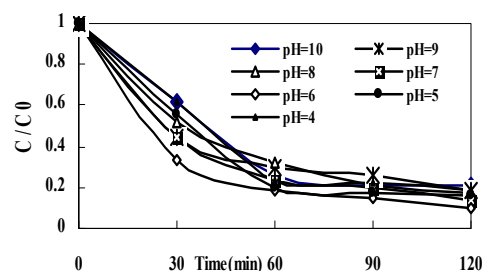


Fig. 4. Effect of pH Conditions: ZnO=0.2 g/L; $[NP10EO]_0$ =30mg/L; $[S_2O_8^{2-}]$ =1mM

Effect of nanocatalyst weight

The effect of photocatalyst weight on the photodegradation of the surfactant was studied in the range of 0.04-0.36 g/L. Fig. 5 showed that degradation rate was more enhanced in concentration of 0.2 g/L than the other concentrations.

Effect of surfactant the photocatalytic degradation

The photocatalytic degradation of the surfactant was carried out at different initial surfactant concentrations ranging from 30 to 120 mg/L. Fig.6 shows that rate of photodegradation of the surfactant decreased at higher concentrations.

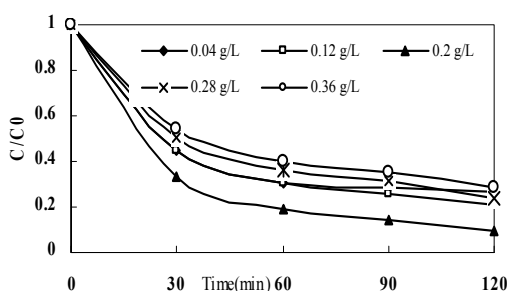


Fig. 5. Effect of catalyst weight on the photodegradation.

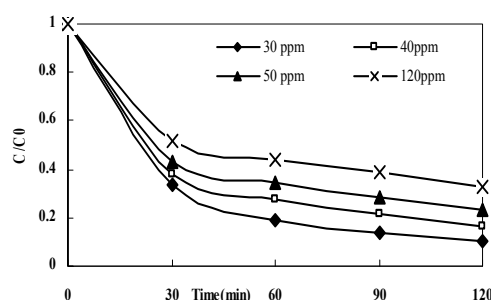


Fig. 6. Influence of initial surfactant concentration

4. Conclusions

The optimal degradation conditions of NP10EO obtained from the present research were: the dosage of catalyst 0.2 g/L, pH 6-7, the amount of $K_2S_2O_8$ 1mM. Undered by the 400w high pressure mercury -vapour lamp for 2h. Degradation of NP10EO was accelerated remarkably by adding peroxydisulfate. Therefore, when peroxydisulfate was added to the UV/ZnO system, surfactant degradation increased from 63.3 % to 89.3 % after 120 min. The kinetics of photocatalytic degradation for surfactant NP10EO follows a pseudo-second-order equation.

References

- [1] C. A. K. Gouvea, F. Wypych, S. G. Moraes, N. Duran, N. Nagata, P. Peralta Zamora, Chemosphere 40 (2000) 433-440.
- [2] C. Lizama, J. Freer, J. ee, G.J. Choi, Y.R. Do, J. Catal. 191 (2000) 192.
- [4] M.A. Behnajady, N. Modirshahla, R. Hamzavi, J. Hazard. Mater. B 133 (2006) 226

**Adsorption of phenol onto activated carbon cloth: effect of cosolvent**

Z. Afshari*, S. Azizian

Department of Physical Chemistry, Faculty Of Chemistry, Bu-Ali Sina University, Hamedan, 65174 , Iran

*(Email: zaafshari@gmail.com)

Keywords: Adsorption, Phenol, Activated carbon cloth, Cosolvent**1. Introduction**

Organic matter and micropollutants are readily removed in water treatment using granular or powdered activated carbon. Activated carbon fibers in the form of cloth or felt have received an increasing attention in recent years as an adsorbent for purifying water. Activated carbon cloths (ACCs) have received increasing interest in recent years due to several technological advantages in comparison with traditional forms, including faster pore diffusion and adsorption kinetics, higher efficiency, larger capacity for adsorption due to its high surface area, and low pressure drops in flow units [1]. Phenolic compounds are considered to be one of the major and most undesirable pollutants in wastewaters. Therefore, removal, destruction or modification to less noxious structures of phenolic compounds is essential for purification of wastewaters as well as raw water[2]. Recent discoveries have indicated that the presence of water- miscible organic solvents would lesson the adsorption reaction. In the present work, the adsorption of phenol onto activated carbon cloth in the presence of cosolvent, was studied.

2. Methods

Ethanol (technical grade , Merck), activated carbon cloth (CH 700-15) with the specific surface area >1300 m²/g were supplied by Kuraray Chemical Co., LTD, Japan. Phenol supplied by Merck Co. All aqueous solutions were made with distilled water. Adsorption from phenol solutions was performed at 298K and constant 150 rpm shaking rate (n-BioTEK, NB-304). Each sample contains 5 ml of phenol solution and 0.01 g of adsorbent. Initial and final concentration of phenol, were measured by a UV/Vis spectrometer (PG. Instrument Ltd Model T80) at 270 nm.

Determination of adsorption isotherm

The adsorption isotherms of phenol onto ACC were determined on the basis of batch analysis. ACC pieces of identical weights were allowed to equilibrate with phenol solutions of different initial concentration (30-700 mg/L) at 25 °C for 24 h. The equilibrium concentrations of phenol solutions were measured spectrophotometrically. The amount of phenol adsorbed per unit mass of carbon cloth, q_e was calculated by Eq. (1)

$$q_e = \frac{(c_0 - c_e)V}{m} \quad (1)$$

where V is the volume of phenol solution in L, c_0 and c_e are the initial and equilibrium concentrations of the phenol solutions in mg/L, respectively, and m is the mass of the carbon cloth in g. Eq. (1) gives q_e in mg phenol adsorbed per g carbon cloth. Furthermore, for investigating the cosolvent effect this experiment was carried out by 20% Ethanol solution. Results are shown in Fig. 1.

Adsorption kinetics of phenol

The identical initial concentrations of phenol (56 mg/L) in aqueous solutions were prepared. Absorbance data of phenol obtained in two minutes intervals during the course of adsorption were converted into concentration data using the corresponding calibration curves. For investigating the cosolvent effect, this experiment was carried out by 20% Ethanol solution with the same concentrations (56 mg/L). Results are shown in Fig. 2. q_t is obtained by Eq. (2).

$$q_t = \frac{(c_0 - c_t)V}{m} \quad (2)$$

q_t is the amount of adspecies at any time and c is the concentration of adsorbate at any time.

3. Results and discussion

The purpose of the present study is to investigate the cosolvent effect. The adsorption isotherms of phenol from water solutions and 20% ethanol solution are shown in Fig.1 .

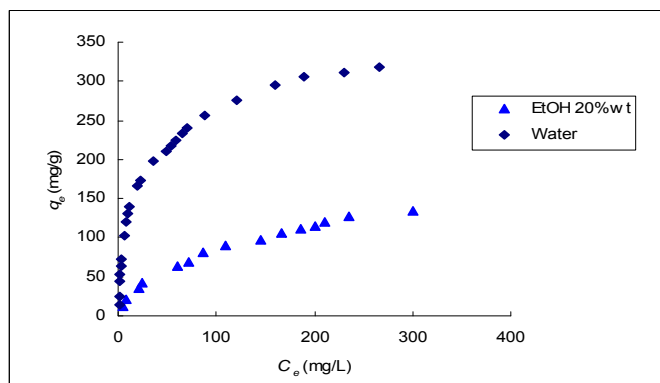


Fig. 1. Effect of cosolvent on the adsorption isotherms of phenol onto ACC at 298K.

Fig.1 shows in the presence of a cosolvent. The extent of phenol adsorption decreases because of specific chemical interactions, namely hydrogen bonding between ethanol and phenol.

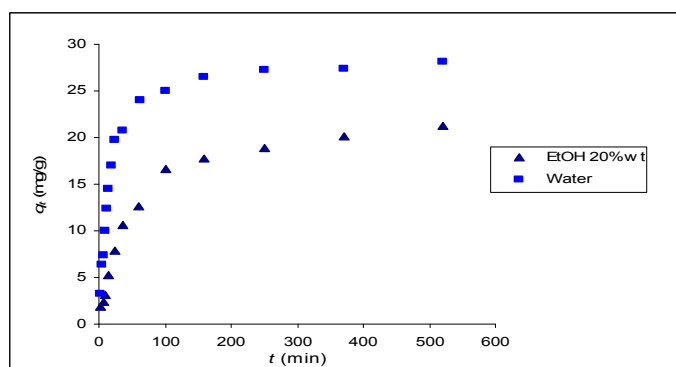


Fig. 2. Effect of cosolvent on kinetic adsorption of phenol onto ACC at 298K.

Fig.2 shows the adsorption of phenol from water solution and 20% ethanol solution as a function of time. This figure shows that the rate of phenol adsorption onto ACC in water solutions is faster than adsorption of phenol in the presence of cosolvent. This is due to the specific interactions (hydrogen bonding) between ethanol and phenol. The obtained equilibrium data were fitted to the different isotherm models including: Freundlich and Langmuir-Freundlich equations. Also the experimental kinetic data were fitted to the different kinetics models including pseudo-first order and pseudo-second order models [3].The results of these fitting will be discussed later.

Similar experiments were performed with water +ethylene glycol, too.

4. Conclusions

It was found that phenol could be removed to a certain extent from aqueous solutions by adsorption onto the ACC. But the adsorption process decrease in the presence of a cosolvent. Apparently adsorption of phenol onto ACC is determined by specific chemical interactions.

References

- [1] A.L. Cukierman, P.R. Bonelli, M.E. Ramos, Colloid Surf. A .324 (2008) 86-92 .
- [2] E. Ayranci, D. Osman, J. Hazard. Mater. B124 (2005) 125-132 .
- [3] S. Azizian, J. Colloid Interface Sci., 276 (2004) 47

**Effect of catalyst preparation parameters on the catalytic performance of Co/Ni catalyst used in FTS**

N. Karimpour, A. A. Mirzaei, S. Sharyari, M. Galavy, S. Vahid

Department of chemistry, Faculty of sciences, University of Sistan and Baluchestan, Zahedan, Iran.

(Email: neda_karimpour@yahoo.com)

Keywords: Co-precipitation, Fischer-Tropsch synthesis, Light olefins, Cobalt nickel catalyst, Characterization.**1. Introduction**

The Fischer-Tropsch synthesis leads to a wide variety of products, whose abundance depends on the catalysts employed, as well as operating conditions[1-3]. Although all VIII group metals[4] display some activity in C-C coupling reaction during CO hydrogenation, the most active metals for FTS are ruthenium, nickel, iron and cobalt[5,6].

2. Methods

All the tested catalysts in this study were prepared using a co-precipitation procedure and tested in a fixed bed stainless steel micro reactor.

3. Results and discussion**1) 1. Effect of solution [Co]/[Ce] ratio**

Cobalt nickel oxide catalysts were prepared by co-precipitation (70°C, pH=8.3±0.1, 2h ageing time) with a range of [Co]/[Ni] solution ratios varying from 100%Co to 100%Ni. After calcination of these materials (500°C, 6h), the catalytic performance of each catalyst for the Fischer-Tropsch synthesis, under the same molar feed ratio of H₂/CO 2:1 at 400°C, was investigated. It was found that molar ratio of 80%Co/20%Ni has shown the best catalytic performance.

2) Effect of precipitation temperature

Cobalt nickel catalysts were prepared by co-precipitation ([Co]/[Ni]=4/1, pH=8.3, 2h ageing time) with a range of solution temperature from 50 to 90°C. The catalytic performance of these series catalysts for the conversion of synthesis gas to light olefins was investigated for the materials following calcination (500°C, 6h). According to the obtained results, the temperature of 50°C was chosen as the optimum temperature for the catalyst preparation. Characterization of both precursors and calcined catalysts (before and after the test) with different precipitation temperature was carried out using BET surface area measurements and the results are listed in Table 1.

Table 2. BET results of the catalysts with different precipitation temperature.

T(°C)	Specific surface area (m ² /g)		
	Precursor	Calcined catalyst (before reaction)	Calcined catalyst (after reaction)
50	110.2	107.1	102.1
60	115.2	113.4	107.1
70	103.4	99.6	89.3
80	107.1	104.1	103.2
90	114.7	111.6	107.2

3) Effect of ageing time

In the present study, we examined the effect of catalyst ageing time on the performance of cobalt nickel oxide catalysts for the hydrogenation of CO. A series of mixed cobalt nickel oxide ([Co]/[Ni]=4/1) catalysts were prepared with a range of ageing time between 0min (unaged) to 180min for the precipitate. The obtained results show that there is considerable variation in the catalytic performance with respect to ageing time, with the sample aged for 150 min giving the optimal catalytic performance for FTS.

4) Effect of calcination temperature

In order to investigate the effect of calcination temperature on the catalyst performance, the calcination of catalyst precursor containing 80%Co/20%Ni was carried out at five different temperatures ranging from 400 to 600°C for 6h. The catalyst calcined at 550°C has higher selectivity toward light olefins and lower selectivity to methane; so that this temperature was chosen as the optimum calcination temperature.

5) Effect of calcination time

In order to investigate the effect of calcination time on the catalytic performance, the calcination process was carried out at four times including 6, 8, 10 and 12 hours. According to the obtained results the catalyst calcined at 550°C for 10h has shown the better catalytic performance. Characterization of this catalyst at different stages (precursor, calcined catalyst before and after the test) was carried out using SEM technique and the SEM images are shown in Fig.1 The electron micrograph obtained from catalyst precursor depicts larger agglomerations of particles (Fig. a) and show that this material has a high dense and homogeneous morphology and the particles of this precursor are near to spherical shape. After the calcination at 550°C, the morphological features were different to the precursor sample and showed that the particles and agglomerate size were greatly reduced compared with the precursor (Fig. b). However, after the test the morphological feature is completely transformed and this tested catalyst has an irregularly and woven structure and also has a less dense and disproportionate agglomerate (Fig. c).

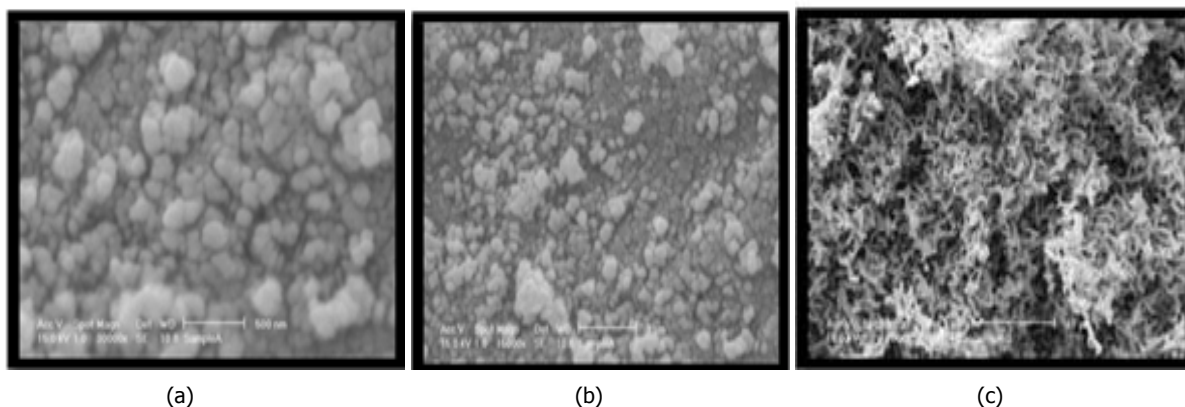


Fig. 1. SEM images of the catalyst containing 80%Co-20%Ni in (a) precursor (b) catalyst before the test and (c) catalyst after the test.

4. Conclusions

It was found that all the different preparation variables influenced the catalyst precursor structure and morphology of the precursors and calcined catalysts and consequently the catalytic performance of catalysts.

References

- [1] V. A. de la Pena O'Shea, M. C. Alvarez-Galvan, J. M. Campos-Martin, J. L. G. Fierro, *Appl. Catal. A: Gen.* 326 (2007) 65.
- [2] H. Schulz, *Appl. Catal. A: Gen.* 186 (1999) 3.
- [3] M. E. Dry, *Catal. Today.* 71 (2002) 227.
- [4] M. A. Vannice, *J. Catal.* 37 (1975) 449.
- [5] R. A. van Santen, *Catal. Rev-Sci: Eng.* 37 (1995) 557.
- [6] V. A. de la Pena O'Shea, M. C. Alvarez-Galvan, J. M. Campos-Martin, J. L. G. Fierro, *Catal. Lett.* 100 (2005) 105.

**On the investigation of adsorption of methyle violet onto titanium dioxide nanoparticles**Shila jafari^{1*}, Babak Jaleh², Saeid Azizian¹¹ Department of Physical chemistry, Faculty of chemistry, Bu-Ali Sina university, Hamedan, Iran² Department of physics, Faculty of science, Bu-Ali Sina university, Hamedan, Iran

*(Email: sheilajafari@ymail.com)

Keywords: Titanium dioxide, Adsorption, Methyle Violet**1. Introduction**

Titanium dioxide is known as an effective photocatalyst and has been used for wastewater treatment, extensively. Adsorption of pollutants on the surface of the photocatalyst can play an important role on the efficiency of catalyst. Among the large number of organic pollutants in wastewater, dye compounds are very important due to their toxicogenic. The purpose of the present work is to investigate the adsorption of a dye compound onto titanium dioxide nanoparticles.

2. Methods

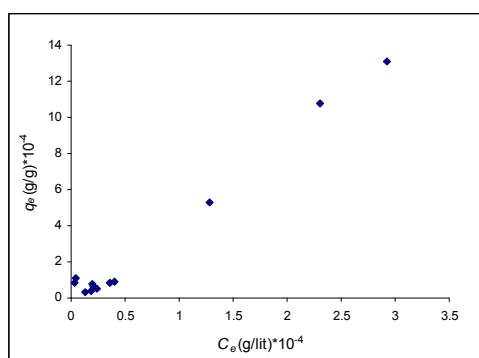
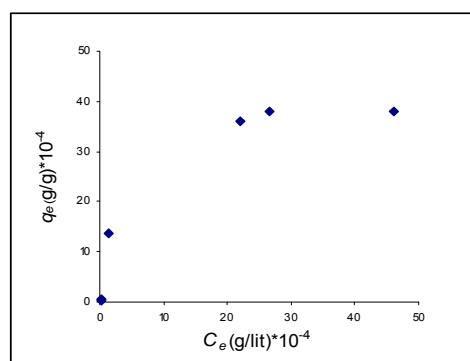
The equilibrium adsorption experiments have been carried out to assess the efficiency of TiO₂ to remove methyle violet (M.V.) from aqueous solution. Batch adsorption tests were performed to study the adsorptive removal of methyle violet from aqueous solution by TiO₂ or AgI-TiO₂ particles, where 5 ml of M.V. solution of known initial concentration (C₀) and a known amount of the adsorbent were taken in the 10 ml flasks. Then the mixture was put into a commercial ultrasonic bath (Parasonic mini-40±5% kHz) to disperse for 6 min. The flasks were placed in a water bath shaker (n-Bio TEK, NB-304) and shaken at 150 rpm for 24 h to ensure the adsorption process reaching equilibrium at dark condition. After that, the suspensions was centrifuged. The equilibrium concentration (C_e) of M.V. was determined using UV/Vis spectrometer (Instrument LTD Model T80).

3. Results and Discussion

The amount of solute adsorbed per mgr of titanium dioxide (q_e) was calculated by:

$$q_e = \frac{(C_0 - C_e)V}{m}$$

Where C₀, V and m are initial concentration, volume of solution and mass of adsorbent, respectively. Fig.1. shows the obtained equilibrium adsorption isotherm at 303. Fig.2. shows the obtained equilibrium adsorption onto AgI-TiO₂ at 303 K

**Fig.1.** Adsorption isotherm Of M.V. onto TiO₂ at 303 K**Fig. 2.** Adsorption isotherm of M.V. onto AgI-TiO₂ at 303K

These Figures show that M.V. can be adsorbed by TiO₂ and the amount of adsorbed M.V. increases with concentration. Fig.2. shows that the maximum amount of adsorbed M.V. onto AgI-TiO₂ is about 0.35 mg/g_(adsorbent)



The equilibrium data were fitted to and the Langmuir , Freandlich , Langmuir-Freandlich and Tempkin isotherms and the constants of isotherm models were derived. The best model which describes the equilibrium data was selected based on correlation coefficients. The analysis of equilibrium data with adsorption models will be discussed later.

4. Conclusions

The present study shows that the amount of adsorbed M.V. onto TiO₂ nanoparticles is low and therefore the role of adsorption for removal of M.V. in a photocatalytic reaction is negligible. Also the data show that at the same conditions the amount of M.V. adsorbed onto AgI-TiO₂ nanoparticles is more than TiO₂ nanoparticles.

References

- [1] M.E.Pena, G. P. Korfiatis, Water Research, 39(2005)2327-2337.
- [2] K. Vijayaraghavan, T.V. N. Padmesh, Journal of Hazardous Materials, B 133 (2006)304-308.



Effect of the Si/Al ratio of zeolite and metal loading on the catalytic activity of HY zeolite for methanol dehydration in a fixed bed reactor

M. H. Peyrovi^a, V. Zarei^{a*}, M. R. Toosi^b, T. Hamoule^b, B. Sabourb

Department of chemistry, Faculty of science, Shahid Beheshti University, Evin, Tehran, Iran

(Email: vahid_zarei181@yahoo.com)

Keywords: Dimethyl ether, Methanol, Zeolite Y, Catalytic activity, Si/Al ratio

1. Introduction

Dimethyl ether (DME) has recently been suggested as a clean alternative fuel for diesel engines instead of diesel, and as fuel additive and family cooking gas instead of liquefied petroleum gas (LPG) with much lower NO_x emission, near-zero smoke production, and less engine noise compared with traditional diesel fuels [1,2]. In view of DME's potential as a clean alternative diesel fuel, much consideration should be given to the production of DME in large quantities. At present, DME is produced by methanol dehydration over solid acid catalysts such as γ-alumina and zeolite HY:



It is known that the modified Y zeolite by various metals which has low acidic sites is the better catalyst than the pure HY [3]. In this study, we investigated the performance of catalytic activity of modified Y zeolites by different metals for production of the DME from methanol. Their catalytic activities were investigated at the several temperatures and two types compared for determination of the best condition for DME production.

2. Methods

Na-form of Y zeolite was prepared by hydrothermal synthesis by using mineral sources of aluminum (sodium aluminate) and silica (sodium silicate) in an autoclave. After it, the sample was ion-exchanged to NH₄⁺-form using NH₄NO₃ solution. After drying, H-form of zeolite was prepared by calcination of NH₄⁺-form samples at 500 °C by temperature rising of °C K/min from 100 to 500 °C while keeping the temperature at 500 °C for 5 h.

Table. Results of catalytic dehydration of methanol over HY and metal-modified HY at 400 °C (the best temperature for conversion).

Catalyst	Metal Oxide Content (%)	Si/Al Ratio	Conversion (%)	Selectivity (%)	
				DME	CO _x
HY	5	1.98	36.5	90.35	9.65
		2.5	33.2	72.5	27.5
Na-HY	5	1.98	57.2	96.5	3.5
		2.5	54.5	82.48	17.52
Ni-HY	5	1.98	63.5	98	2
		2.5	60.09	87.1	12.9
Al-HY	5	1.98	45.57	94	6
		2.5	43.48	78.1	21.9
Zn-HY	5	1.98	37.52	93.5	6.5
		2.5	35.25	75.6	24.4
Zr-HY	5	1.98	57	95.5	4.5
		2.5	53.81	80.41	19.59



HY modified by various metal oxides was prepared by wet impregnation with aqueous solutions of metal salts, followed by drying at 110 °C overnight and then calcined at 500 °C for 4 h in an air stream. By this method, 5 samples of modified zeolites: NaY, NiY, AlY, ZnY, and Zr-HY catalysts were prepared. Catalytic reactions were carried out at atmospheric pressure in a continuous fixed-bed glass microreactor packed with 1.0 g catalyst. The catalyst was pretreated in a N₂ flow (20 ml min⁻¹) and then, methanol was introduced into the reactor with a space velocity of 2 ml/ (gcat h). The effluent from the reactor was analyzed on-line with Shimadzu 8A gas chromatograph equipped with Porapak-Q column and the thermal conductive detector (TCD). The main products were DME and water. The reaction was carried in the temperature range of 250-450 °C to observe the effect of temperature on the conversion and various catalysts to determine the effect of the Si/Al ratio of zeolite and the type of impregnated metal on the catalytic activity.

3. Results and discussion

Table 1 shows the results of conversion and selectivity of different catalyst for methanol dehydration. Results indicate that the conversion and DME selectivity decreases with the increasing of Si/Al ratio in the all catalysts. Furthermore, adding of the metal in the surface of zeolite increases the catalytic activity of the methanol dehydration. Maximum activity is reached by using Ni-HY catalyst. For others, the activity is decrease by the respect of Na> Zr> Al> Zn.

It is well known that by increasing the Si/Al ratio, the strong acidic sites of zeolite convert into supper-acid sites. That this lead to increase of coke deposition and deactivation of the catalyst, ultimately with increasing the Si/Al ratio the conversion and DME selectivity are reduced [4].

References

- [1] Vishwanathan V, Jun KW, Kim JW, Roh HS., Appl Catal A 2004;276(1-2):251-5.
- [2] Arkharov AM, Glukhov SD, Grekhov LV, Zherdev AA, Ivashchenko NA, Kalinin N, Chem Petro Eng 2003; 39(5-6):330-6.
- [3] Dongsen Mao, Weimin Yang, Jianchao Xia, Bin Zhang, Qingying Song, Qingling Chen, Journal of Catalysis 230 (2005) 140-149.
- [4] M. Xu, D.W. Goodman, A. Bhattacharyya, Appl. Catal. A: Gen. 149 (1997) 303-309



Theoretical prediction of surface tension of binary liquid system (R290 + R600a) at various temperature and pressure

A. A. Rafati, A. Bagheri*

Faculty of Chemistry, Bu-Ali Sina University, Hamedan, Iran

(Email: abagheri79@gmail.com)

Keywords: Surface Tension, R290, R600a, Binary Mixture, Critical Constant

1. Introduction

Because of the low ozone-depletion potentials and low global-warming potentials, hydrocarbons and their mixture have been increasingly recognized as the working fluid in air-conditioning and heat-pump systems. Not only the pure substances of R290 (propane: C₃H₈) and R600a (isobutane: i-C₄H₁₀) but also their mixture have been expected as the alternative refrigerant of CFCs and HCFCs[1]. The surface tension of liquid mixtures is a thermophysical property of great importance for the heat transfer analyses with boiling and condensation states. Its experimental data are necessary to refine the model for evaluating refrigerant mixtures and for designing refrigeration cycles. However, there were very restricted data for this mixture. For the first time, Tanaka et al. [1] measured the surface tension of R290 + R600a mixture at various compositions at three isotherms of 278 K, 300 K and 320 K and the pressures up to 187 kPa. Pressure and temperature dependent measurements of the surface tension of multicomponent liquid mixture are not available in the literature. Most of the empirical and statistical methods developed so far cannot be applied to the present binary system due to the lack of experimental data on pure components (surface tension, density, thermal expansivity, and isothermal compressibility) under the desired physical conditions.

2. Methods

The application of corresponding states models extend for equilibrium properties such as vapor pressure, liquid density or surface tension. In spite of this versatility, and the small amount of experimental information required, corresponding states models can return very accurate estimates of thermophysical properties. The four corresponding states model for surface tension consist of:

1- For a liquid mixture, the Brock-Bird [2] relation for surface tension can be written as:

$$\sigma = P_c^{2/3} T_c^{1/3} Q (1 - T_r)^{11/9} \quad (1)$$

2- Pitzer[3] gives a series of relations for σ in terms of P_c , T_c and acentric factor (ω) that together lead to the following corresponding-states relation for surface tension:

$$\sigma = P_c^{2/3} T_c^{1/3} A (1 - T_r)^{11/9} \quad (2)$$

The parameter A is function of acentric factor.

3- In yet another corresponding-states method, Zuo and Stenby [4] have used a two-reference fluid corresponding-states approach patterned to estimate surface tension:

$$\sigma_r = \ln \left(1 + \frac{\sigma}{P_c^{2/3} T_c^{1/3}} \right) \quad (3)$$

To use this method, σ_r for the fluid of interest is related to two reference fluids, methane (1) and n-octane (2).

4- Sastri and Rao [5] present the following modification of the above equations

$$\sigma = KP_c^x T_c^y T_c^z \left[\frac{1 - T_r}{1 - T_{br}} \right]^m \quad (4)$$

k, x, y, m and z are constant values for different materials.

3. Results and discussion

In the present paper an effort is made to predict theoretically the surface tension of R290 + R600a mixture over the entire composition, temperature, and pressure range with using a minimum of parameters required, which is able to describe the

available data with a sufficient accuracy. Results clearly indicate the validity and success of modified expression of corresponding-states models for estimation of surface tension of liquid mixtures. Percent average absolute deviation (%AAD) presented by these models for 43 binary mixtures are compared in Table 1. The maximum deviations were observed in the Pitzer relation and the behavior of other methods is nearly identical.

Table 1. Comparison of %AAD values between various methods

Method	Brock–Bird	Pitzer	Zuo–Stenby	Sastri–Rao
%AAD	1.01	4.69	1.75	0.92

The influence of mixture composition and the effect of temperature upon surface tension value for this system can be observed in Fig. 1.

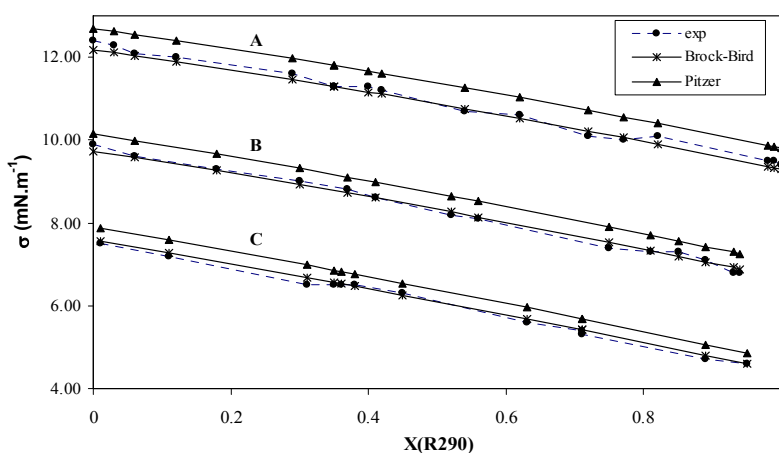


Fig. 1. Surface tension σ_{cal} (mNm⁻¹) and σ_{exp} (mNm⁻¹) plotted against mole fraction of the R290, at three isotherm: (A) 278.28 K ; (B) 300 K ; (C) 320 K

4. Conclusions

The corresponding states models were evaluated for the estimation of the measured data. It was shown that the use of simple mixing rules can return accurate surface tension values. These methods are expected to be useful in calculating the surface tension of a large number of such liquid systems. The results obtained from the proposed methods are found to be in excellent agreement with the experimental values.

References

- [1] K. Tanaka, Y. Higashi, Int. J. Refrigeration 30 (2007) 1368.
- [2] J. R. Brock, R. B. Bird, AIChE J. 1 (1955) 174.
- [3] M. Prausnitz, J. P. O'Connell, The Properties of Gases and Liquids, Fifth Edition, McGraw-Hill, 2004.
- [4] Y. X. Zuo, E. H. Stenby, Can. J. Chem. Eng. 75 (1997) 1130.
- [5] S. R. S. Sastri, K. K. Rao, Chem. Eng. J. 59 (1995) 181.

**Surface Tension of Nonideal Ternary Liquid Mixtures at 298.15 K and Atmospheric Pressure**

A. A. Rafati, A. Bagheri**

Faculty of Chemistry, Bu-Ali Sina University, Hamedan, Iran

(Email: abagheri79@gmail.com)

Keywords: Surface Tension, Correlation, Water, Acetonitrile, Alcohol**1. Introduction**

The surface tension of a liquid mixture is an important property in process design, because it plays an important role in affecting the mass and heat transfer at the interface [1]. Many investigations have been conducted to determine the effect of composition on surface tension at constant temperature. In the present paper we report surface tensions of the ternary system (water + acetonitrile + Ethanol or Ethandiol) and of the corresponding binary mixtures (water + acetonitrile), (water + Ethanol), (acetonitrile + Ethanol), (water + Ethandiol) and (acetonitrile + Ethandiol) at the temperature 298.15K and atmospheric pressure.

2. Methods

The surface tensions (σ) were measured using the Du-Noüy ring method on a KSV Sigma 70 automatic tensiometer. The deviations in the surface tension, $\Delta\sigma$, were calculated from the following equation:

$$\Delta\sigma = \sigma - \sum_{i=1}^N x_i \sigma_i \quad (1)$$

where σ is the surface tension of the mixture and σ_i is the surface tension of the i th component of mole fraction x_i . A few empirical and thermodynamic-based equations are available to correlate the surface tension; The surface-tension data of binary mixtures were correlated with the models of Redlich-Kister(RK); Santos et al(SFF); Li et al(LWW); Fu et al(FLW); Sonawane and Kumar(SK); Myers and Scott(MS) [2,3].

3. Result and discussion

The systems Water + Acetonitrile + Ethanol (or Ethandiol) measured at 298.15 K have similar behavior, showing negative surface tension deviations in the whole composition range. The ternary data was also well correlated using pair additivity and a ternary term which is a rational function of the composition leading to standard deviations of about 0.4 mNm⁻¹:

$$\Delta\sigma = \Delta\sigma_{12} + \Delta\sigma_{13} + \Delta\sigma_{23} + \Delta\sigma_T \quad (2)$$

$\Delta\sigma_{ij}$ represent the surface tension deviations for the binary mixtures and $\Delta\sigma_T$ is a ternary contribution. As an example, figure 1

show, the isolines of $\Delta\sigma$ for the ternary mixture (Water + Acetonitrile + Ethandiol) at 298.15 K. The surface tension deviation $\Delta\sigma$, all mixtures show negative values that increase with the increase in the difference of surface tension values of pure compounds. The asymmetry in the curves of {Water + Acetonitrile}, {Water + Ethanol} and {Water + Ethandiol} indicates that the components with the strongest molecular interactions in each binary mixture settle down in the bulk liquid phase instead of doing it in the surface phase between liquid and vapour phases, moving the curves to the rich region of these compounds.

4. Conclusions

The surface tension deviations of the ternary systems were correlated using the methods of Pando et al. and Ku et al. For the ternary mixtures, the correlations of the two models are similar. Results obtained with the MS and FLW models are very good, as can be seen from the low AAD values. In this work we observed some significantly different behavior when the LWW model was applied to the Water + Acetonitrile + Ethanol and Water + Acetonitrile + Ethandiol systems.

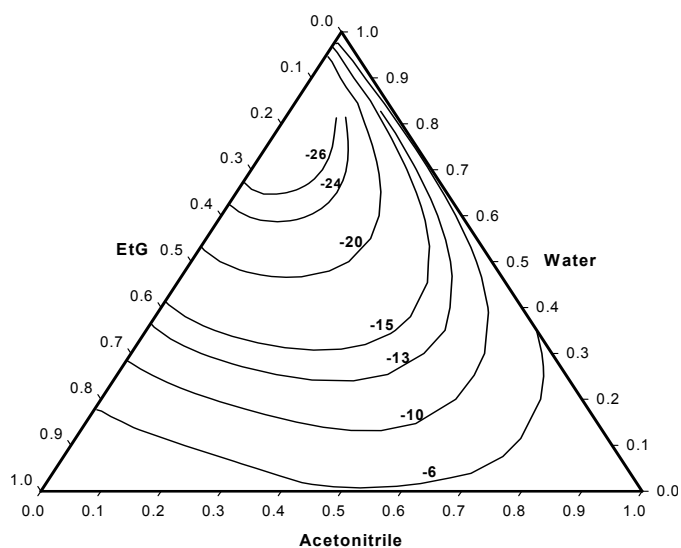


Fig. 1. Isolines of $\Delta\sigma$ for the ternary system Water + Acetonitrile + Ethandiol(EtG) at 298.15 K

References

- [1] A. A. Rafati, E. Ghasemian, Journal of Colloid and Interface Science. 328(2008) 385.
- [2] B.M.S. Santos, A.G.M. Ferreira, I.M.A. Fonseca, Fluid Phase Equilibria. 208 (2003) 1.
- [3] M. j. Kijevcanin, I.S.A. Ribeiro, A.G.M. Ferreira, I.M.A. Fonseca, Fluid Phase Equilibria. 218 (2004) 141.

Preparation, characterization and photocatalytic activity of ZnO supported on clinoptilolite for decolorization of dye acid red 57 from aqueous solutions

K. Mahanpoor, N. Niazi Hesar Sefeedi

Department of Chemistry, Faculty of Science, Islamic Azad University of Arak Arak, Iran

(Email: kazem_mahanpoor@yahoo.com)

Keywords: Photocatalytic, Acid Red 57, Clinoptilolite

1. Introduction

ZnO is a wide-bandgap semiconductor having many applications, such as being a photocatalyst, transducer, varistor, phosphor, and transparent conductor [1], and wide varieties of synthesis techniques have thus been developed to produce this material in different forms [2]. They are, for instance, sol-gel process [3], hydrothermal process [4], chemical vapor deposition [5], and solution deposition [6]. In this work we supported ZnO on Iranian natural zeolite (Clinoptilolite) and study photocatalytic efficiency for photocatalytic decolorization of azo dye Acid Yellow 23 from aqueous solutions by using Fenton reaction in a Batch Photoreactor and then study kinetic of this reaction.

2. Methods

Acid Red 57 (Aldrich Chem. Co., USA) shown in Fig. 1 as a target dye. Another material was purchased from Merck (Germany). Double distilled water was used for preparation of requisite solutions.

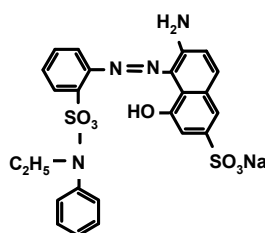


Fig. 1. **Structure of Acid Red 57**

For UV/photocatalyst process, irradiation was performed in a batch photoreactor of 2 liter in volume with six mercury lamp 6W (UV-C manufactured by Philips, Holland). UV-VIS Spectrophotometer, Perkin-Elmer lambda25 was employed for absorbance measurements using silica cells of path length 1 cm. For the photodegradation of AR57, a solution containing known concentration of dye and photocatalyst was prepared and it was allowed to equilibrate for 30 min in the darkness, then 50 ml of the prepared suspension was transferred to a 2 liter quartz reactor. The suspension pH values were adjusted at desired level using dilute NaOH and H₂SO₄ and then the pH values were measured with pH meter (HORIBA M12). During irradiation, agitation was maintained to keep the suspension homogeneous, and the suspension was sampled after an appropriate illumination time. The concentration of dye in each degraded sample was determined with a spectrophotometer (UV/VIS Spectrophotometer, Perkin-Elmer lambda25) at $\lambda_{\text{max}} = 537 \text{ nm}$ and a calibration curve. By this method decolorization percent of AR52 can be obtained in different intervals.

3. Results and discussion

Sem and XRD pattern of catalyst show in the below. The SEM show that ZnO supported on CP.

Kinetics of photocatalytic degradation of AR 57

Several experimental results indicated that the degradation rates of photocatalytic oxidation of various dyes over illuminated TiO₂ fitted by the first-order kinetic Model. [7-8].

Fig. 11. Shows the plot of $\ln ([\text{Dye}]_0 / [\text{Dye}])$ versus irradiation time for AR 57. The linearity of plot suggests that the photodegradation reaction approximately follows the pseudo-first order kinetics with rate coefficient $K = 0.0109 \text{ min}^{-1}$.

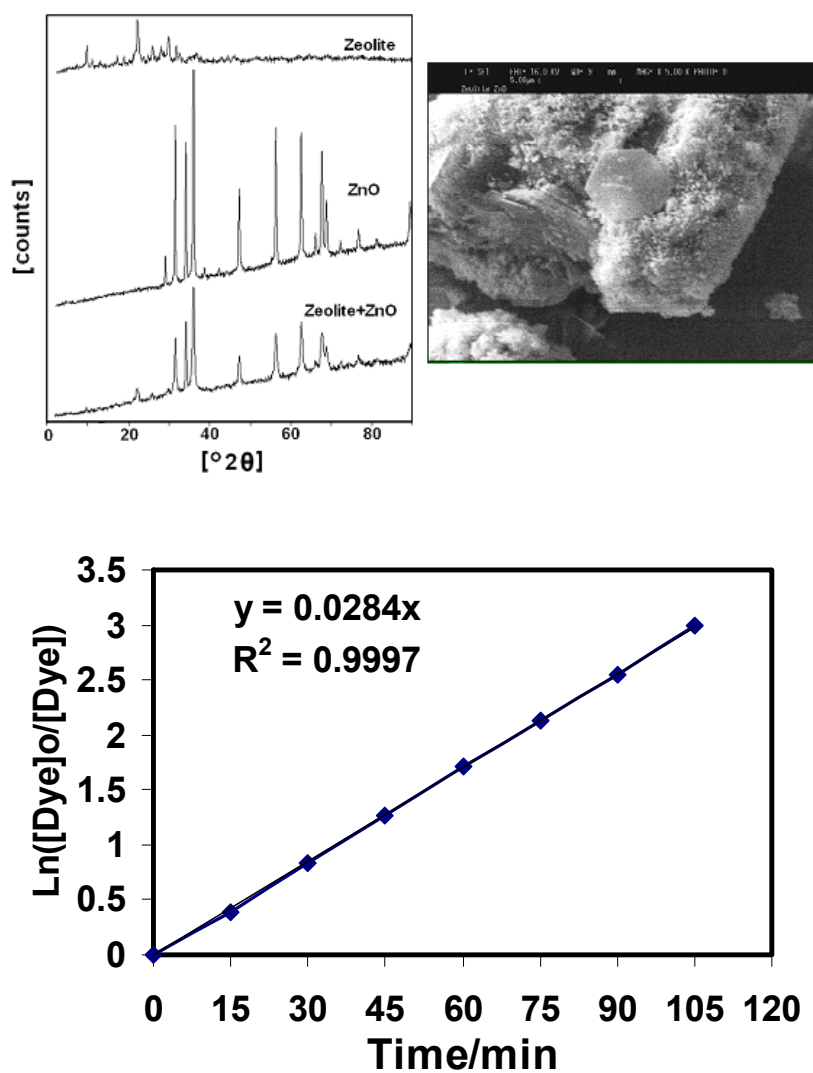


Fig. 6. Derivation of pseudo first order rate photocatalytic degradation of AY23. [Catalyst]=300mg l⁻¹, pH=7, [AR57]₀=50mg l⁻¹

4. Conclusions

References

- [1] D.C. Look, Mater. Sci. Eng. B80 (2001) 383–387.
- [2] Z.L. Wang, Mater. Today (2004) 26–33.
- [3] M.S. Tokumoto, S.H. Pulcinelli, C.V. Santilli, V. Briois, J. Phys. Chem. B 107 (2003) 568–574.
- [4] H. Xu, H. Wang, Y.C. Zhang, S. Wang, M.K. Zhu, H. Yan, Cryst. Res. Technol. 38 (2003) 429–432.
- [5] M.F. Ogawa, Y. Natsume, T. Hirayama, H. Sakata, J. Mater. Sci. Lett. 9 (1990) 1351–1353
- [6] S. Lindross, M. Leskela, Inter. J. Inorg. Mater. 2 (2000) 197–201.
- [7] M. Saquib, M. Muneer, Dyes Pigments 56 (2003) 37–49
- [8] A.L. Linsebigler, L. Guanguan, J.T. Yates, Chem. Rev. 95 (1995) 735.

Catalytic reforming of n-heptane over Al-containing mesoporous catalystsM. H. Peyrovi^a, T. Hamoule^{a*}, B. Sabour^b, V. Zarei^b

Department of Chemistry, Shahid Beheshti University, Tehran, Iran

(Email: m-peyrovi@cc.sbu.ac.ir)**Keywords:** Al-HMS, Pt-Re, catalytic reforming, n-Heptane.**1. Introduction**

Catalytic reforming is a chemical process used to convert petroleum refinery naphtha, typically having low octane ratings, into high-octane liquid products called reformates which are components of high-octane gasoline (also known as petrol). The overall process involves several reactions which are promoted by a bifunctional catalyst. The $\text{Pt}/\text{Al}_2\text{O}_3$ as a bifunctional reforming catalyst has been used since the 1950's in the oil industry. The noble metals (platinum and rhenium) are considered to be catalytic sites for the dehydrogenation reactions and the chlorinated alumina provides the acid sites needed for isomerization, cyclization and hydrocracking reaction [1,2]. It is well-known that Al substitution into silicate structure generates Bronsted acidity and these acid sites participate in many industrially important organic transformations [3]. In an attempt to evaluate of novel catalyst containing Al-HMS we decided to use catalyst containing Al-HMS as support in catalytic reforming.

2. Methods

The HMS and Al-HMS materials were synthesized following procedures similar to Pinnavaia and coworkers [4], Mokaya and Jones [5] via neutral templating pathway using hexadecylamine as the surfactant. The calcined mesoporous materials were characterized by XRD, XRF and adsorption-desorption unit for surface area and pore volume. Mono and bimetallic Pt-Re catalysts were prepared by impregnation of the support with appropriate concentration of H_2PtCl_6 and NH_4ReO_4 using HMS and Al-HMS (Si/Al=5, 10, 20, 35) materials as support. The catalytic reforming of n-heptane in the presence of hydrogen was carried out at atmospheric pressure in a continuous fixed-bed microreactor packed with 1.0 g catalyst. In order to observe the effect of temperature on the conversion, the reaction was carried out over different catalysts in various temperatures between 350 and 550 °C.

3. Results and Discussion

The XRD diagrams of the AlHMSx materials are shown in Fig. 1 and are similar to those reported by Mokaya and Jones [5]. All show a single broad reflection that can be assigned to a lattice with a short-range hexagonal symmetry. The increase in Al content results in a broadening of this peak, indicating that incorporation of Al is associated with an increasing lattice disorder. The contents of Al and Si were determined with X-ray fluorescence (Table 1).

The samples were examined by surface area distribution (Table 1). It can be seen that surface area decreases with increase of Al in to the structure. These results taken together with above discussed XRD data support the above suggestion that hexagonal order is decreasing with the decrease of Si/Al ratio.

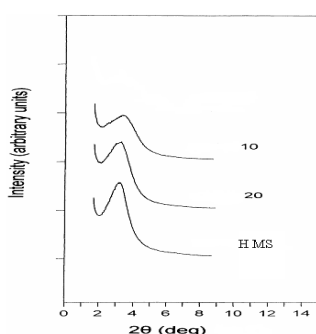
**Fig. 1.** XRD patterns of calcined AlHMSx samples



table 1. Physicochemical characteristics of mesoporous supports

Sample	Si/Al	surface area (m ² /g)	pore volume(cc/g)
HMS	∞	974	1.32
Al-HMS-20	18.7	1289	1.20
Al-HMS-10	9.6	1109	0.79

Catalytic activities of the samples were investigated in the reforming of n-heptane. Results show that activity and selectivity of catalysts are dependent on reaction parameters. For example catalytic functionalities vary in linear manner with the variation of Si/Al. the obtained data indicate that modification of catalysts by Re decreases the selectivity of catalysts especially for isomerization and aromatization. In table (2) is reported the conversion of n-heptane as a function of temperature in the presence of various catalysts.

Table 2. Overview of n-heptane conversion

T(°C)	350	400	450	500	550
catalyst					
Pt-HMS	37.6	23.6	30.2	30.9	38.1
Pt-Al-HMS-35	57.7	69.1	75.0	76.4	97.8
Pt-Al-HMS-20	59.6	85.3	94.6	94.5	97.7
Pt-Al-HMS-10	41.7	100	100	100	100
Pt-Al-HMS-5	56.2	96.6	86.7	95.6	89.1
Pt-Re-Al-HMS-35	45.5	81.0	80.5	97.6	98.7
Pt-Re-Al-HMS-20	54.0	78.1	99.3	80.0	91.7
Pt-Re-Al-HMS-10	63.3	93.3	98.3	100	100
Pt-Re-Al-HMS-5	76.1	89.6	100	100	100

4. Conclusions

Pt and Pt-Re-containing hexagonal mesoporous molecular sieves synthesized by impregnation of Pt and Pt-Re over Al-containing mesoporous materials. Catalytic activity of samples shows that the modification of support by Al and introduction of Re affected the activity and selectivity.

References

- [1] F. Epron, C. Carnevillier, P. Mare'cot Appl. Catal. A 295 (2005) 157–169.
- [2] F. G.D. Zakumbaeva, T.V. Van, A.I. Lyashenko, R.I. Egizbaeva Catal. Today 65 (2001) 191–194.
- [3] T. Chiranjeevi, G. Muthu Kumaran, J.K. Gupta, G. Murali Dhar Thermochimica Acta 443 (2006) 87–92.
- [4] T. Tanev, T.J. Pinnavaia, Science 267 (1995) 865.
- [5] R. Mokaya, W. Jones, J. Catal. 172 (1997) 211.

**Liquid-phase adsorption of mordant yellow 10 on activated carbon prepared from almond shell:
a kinetic and equilibrium study**

A. Soufi, K. Mahanpoor, H. Malekhoseani, N.Niazi Hesar Sefeedi

Department of Chemistry, Faculty of Science, Islamic Azad University of Arak, Iran P.O.Box:38135/567

(Email: aboalfazl.soufi@yahoo.com)

Keywords: Adsorption, Mordant yellow 10, Almond shell

1. Introduction

Adsorption by activated carbon has been used extensively in dye house wastewater treatment, either independently or coupled with biological degradation [1]. Though many lowcost materials have been tested for the removal of different dyes from their aqueous solutions, such as clay [2], sawdust [3], chitosan [4], and peat [5], adsorption by activated carbon remains one of the most efficient techniques in dye house wastewater treatment, especially as a final polishing step before discharging or recycling the treated wastewater.

In this paper, adsorption equilibrium and kinetics of Mordant Yellow 10 dye from their single-component aqueous solutions onto activated carbon were studied in a batch reactor. Effects of the initial concentration and adsorbent particle size on adsorption rate were investigated Adsorption equilibrium data were then correlated with several well-known equilibrium isotherm models. The kinetic data were fitted using the pseudo-first-order equation, the pseudo-second-order equation, and the intraparticle diffusion model. The respective characteristic rate constants were presented. A new adsorption rate model based on the pseudo-first-order equation has been proposed to describe the experimental data over the whole adsorption process. The results show that the modified pseudo-first-order kinetic model generates the best agreement with the experimental data for the three single-component adsorption systems.

2. Methods

Activated carbon prepared from almond shell as the adsorbent. dye provided by Rang Azar Company(Iran), namely Mordant yellow 10 were chosen as the adsorbate, due to their Extensive use in the textile industry. The structure of this dye is shown in Fig.1.

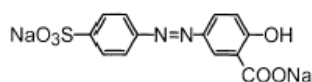


Fig. 1. structure of Mordant yellow 10

For determination of dye concentration used Perkin Elmar spectrophotometer (lambda-25).Experiment done in batch condition.

3. Results and discussion

Fig. 2 compares the experimentally determined adsorption equilibrium data with the model prediction by the Fritz– Schlünder isotherm. The excellent fitting of Fritz–Schlünder isotherm can be due to the fact that it contains more parameters than the other equilibrium isotherms do. This implies that it has more degree of freedom to fit the experimental data by changing another parameter if one parameter has ceased to generate good agreement between the model and the experiment.

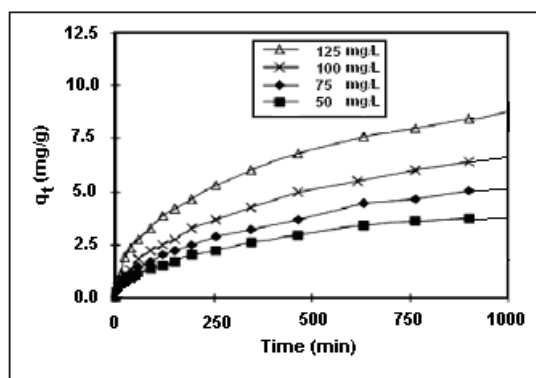


Fig. 2. Equilibrium isotherms for single-component adsorption systems at different initial concentrations of MY10.

The result of kinetic absorption in different initial dye concentration show in Fig. 3. The modified pseudo- first-order equation generates the best fit to the experimental data of the investigated adsorption systems.

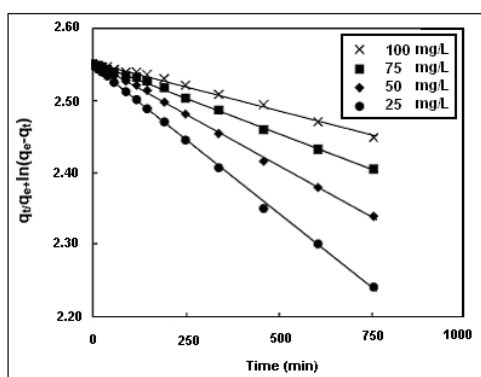


Fig. 3. The modified pseudo-first-order kinetic model for adsorption of MY10 at different initial concentrations

Reference

- [1] P. Cooper (Ed.), Colour in Dye House Effluent, Alden, Oxford, 1995.
- [2] G.S. Gupta, S.P. Shukla, G. Prasad, V.N. Singh, Environ. Technol. 13 (1992) 925.
- [3] R.Y. Yeh, R.L. Liu, H. Chiu, Y. Hung, Int. J. Environ. Studies 44 (1993) 259.
- [4] F.-C. Wu, R.-L. Tseng, R.-S. Juang, Water Res. 35 (2001) 613.
- [5] Y.S. Ho, G. McKay, Chem. Eng. J. 70 (1998) 115.

**Effect of heat treatment on the corrosion resistance and hardness of Ni-P-TiO₂ electroless composite coatings**S. Amjad Iranagh^{a,*} and H. Modarress^b^aDepartment of Chemistry, University of Amirkabi, Tehran, Iran^bDepartment of Chemical Engineering, University of Amirkabir, Tehran, Iran

(Email: amjad_i_s@aut.ac.ir)

Keywords: Electroless, Nano-composite, Heat treatment, corrosion, SEM, TiO₂.**1. Introduction**

Electroless Ni-P coating has been attracting extensive attention because it exhibits excellent wear and corrosion resistance[1]. Electroless nickel-phosphorus (ENP) coating is an autocatalytic deposition of Ni-P alloy from an aqueous solution without the application of an electrical current[2]. Composite coatings are produced by codeposition of fine inert particles into a metal matrix from an electrolytic or electroless bath. Currently, the research of the nano-composite Ni-P plating is focused on inorganic non-metal nanoparticles, such as Si, SiC, ZnO, PTFE, Si₃N₄ and Al₂O₃, etc.[3]. So far, nanometersized particles have drawn much interest in the electroless field because they can be dispersed and suspended well in the bath and show better properties than those of the micro-sized particles. The properties of coatings not only depend on the plating conditions such as pH, temperature and bath composition, but also depend on the type, concentration, size and distribution of the composite particles[4]. Considerable experiments to the electroless Ni-P composite coatings with nano-meter sized particles have been carried out. Recently, electroless nickel composite coatings have gained more attention in research community due to their ability to produce coatings that possess improved wear, abrasion and lubrication properties than Ni-P deposits[5]. Titanium dioxide is the one, which finds enormous applications due to its merits when applied as catalytic support, reinforcement and inert filler[6]. The aim of this study is to explore the effect of heat treatment on the corrosion resistance and hardness of Ni-P-TiO₂ electroless composite coatings. So we co-deposit TiO₂ nanoparticles with electroless nickel on low carbon steel and evaluate its properties. The physical properties of the coatings, including hardness, surface morphology and corrosion resistance were tested.

2. Methods

CK-45 steel is used as the substrate. Samples carbon steel substrates with a width of 10mm and height 20mm were used for composite electroless Ni-P-TiO₂ plating. Specimen was polished with emery paper, degreased with alkaline solution, activated in diluted HCl solution and rinsed with deionized water completely. Then the specimen was immersed in the nickel electroless plating solution. The bath composition and operation conditions used for preparing NiP-TiO₂ composite coatings are given in Table 1. The TiO₂ employed was of the anatase type oxide by Merck, with a mean diameter of 42-100 nm and concentrations in the bath equal to 5, 10, 15, 20, 25 and 30 g TiO₂/l. After this, Ni-P samples were heated for 1 hr at 200, 400, 600 and 700 °C and Ni-P-TiO₂ samples were heated at 400 °C.

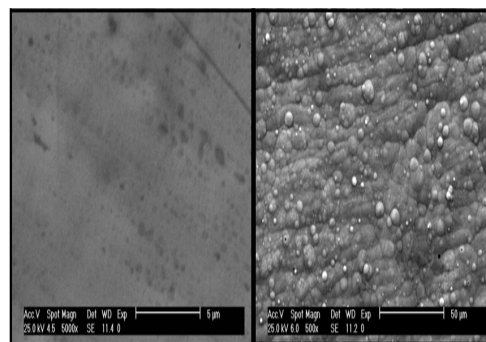
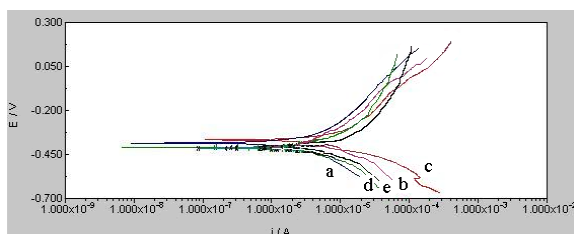
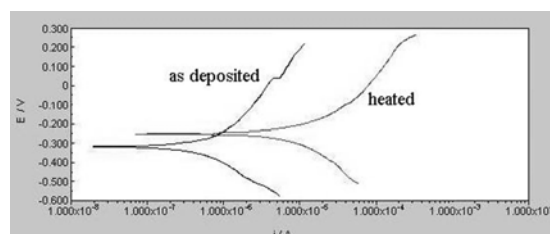
3. Results and discussion

Surface morphology was analyzed by Scanning Electron Microscope (SEM, Philips-XL/30). SEM images for plane (left) and composite coatings (right) are presented in Fig.1

The electrochemical Potentiostat/Galvanostat device (Auto-Lab 20A) was used to obtain polarization curves, where the working electrode was 1 cm² specimen immersed in 3.5% NaCl solution. Corrosion current density (i_{corr}) for as-deposited and annealed coatings at 200, 400, 600 and 700 °C was 5.4, 3.2, 2.1, 4.6 and 7.6 $\mu\text{A}\cdot\text{cm}^{-2}$ respectively. This is shown in Fig.2. Heating at 200 and 400 °C improves the corrosion resistance of plane coatings but high temperatures cause Ni/P coatings to lose their resistance in corrosive environment. The polarization curves for heated and as-deposited Ni/P/TiO₂ coatings are presented in Fig.3. The current density (i_{corr}) for as-deposited and heated composite coating was 2.4 and 0.61 $\mu\text{A}\cdot\text{cm}^{-2}$ respectively. The hardness was measured by a HV-1000 microscлерometer with a load of 50 g for 15s. Three readings were made on each specimen and the value was then averaged. The hardness values of electroless composite coatings before and after heating treatment were given 760 and 1310.1.

Table 1. Bath composition (pH:5.5, T(°C):88)

Bath composition and operating conditions	Concentration
NiSO ₄ .6H ₂ O	25 (gr.l ⁻¹)
NaH ₂ PO ₂ .XH ₂ O	18 (gr.l ⁻¹)
Na ₃ C ₆ H ₅ O ₇	18(gr.l ⁻¹)
CH ₃ COONa	20(gr.l ⁻¹)
TiO ₂ (nano-powder)	5/10/15/20/25/30(gr.l ⁻¹)
(NH ₂) ₂ CS	1 ppm


Fig. 1. SEM images of(left) plane and (right) composite coating Ni-P-TiO₂

Fig. 2. polarization curves for Ni/P coatings :(a) as deposite, (b), (c), (d) and (e) heated at 200, 400, 600 and 700 °C.

Fig. 3. polarization curves for heated and as- deposited Ni/P/ TiO₂ coatings

4. Conclusions

Ni/P and Ni/P/TiO₂ nano-composite coatings were obtained by electroless plating method. Presence of TiO₂ nano-particles enhanced the corrosion resistance of deposits. The high corrosion resistance (2.1 μA.cm⁻²) was obtained for composite coating annealed at 400 °C. Heating above 400 °C decreased the corrosion resistance of coatings due to oxidation of Ni/P matrix. The composite coating Ni-P/TiO₂ has the bigger hardness value after 400 °C heating treatment. The value is about 1310.1HV high. There are amorphous phases in as-deposited coatings. When the coating is heat-treated at 400 °C for 1 h, the hardening phase Ni₃P is formed.

Reference

- [1] S. Zhang, K. Han, L. Cheng, Surf. Coat. Technol. 202 (2008) 2807.
- [2] [2] Electroless Nickel Plating, Riedel W, UK, 1991.
- [3] A. Abdel Aal , Z.I. Zaki, Z. Abdel Hamid, Mater. Sci. and Eng. A 447 (2007) 87.
- [4] Y. Y. Lue, J. Yu, H. Huang, B. H. Xu, X. L. Liu, Y. Gao, X. L. Dong, Surf. & Coat. Tech. 201(2007)7246.
- [5] J. N. Balaraju, Kalavati, K. S. Rajam, Surf. & Coat. Tech. 200(2006)3933.
- [6] J. Novakovic, P. Vassiliou, Electrochimica Acta 54 (2009) 2499.

**Adsorption of some phenolic compounds onto activated carbon cloth: kinetics and equilibrium**A. Hajian¹, S. Azizian

Department of physical chemistry, Faculty of Chemistry, Bu-Ali Sina University, Hamedan, Iran

(Email: a.hajian@basu.ac.ir)

Keywords: Adsorption, Activated carbon cloth, Isotherm, Kinetic models**1. Introduction**

Phenolic compounds which are versatile raw materials in chemical industry constitute a major and important class of pollutants in industrial, agricultural and other wastewaters. These compounds are very toxic, non-biodegradable and therefore, pose environmental problems. There are some prevalent techniques to remove phenolic compounds from waste effluent such as chemical oxidation, coagulation, solvent extraction and adsorption. Among these techniques, adsorption is an effective method to remove organic compounds [1]. The focus of this work is to study of the adsorption of three phenolic compounds namely 3-methylcatechol, 3-methoxycatechol and 2,3-dihydroxybenzoic acid from aqueous solution onto activated carbon cloth.

2. Methods

Activated carbon cloth (ACC) used in this study supplied by Kuraray Chemical Co., LTD, Japan. The adsorbates were commercial products from Sigma or Merck Co. and were used without further purification. The concentrations of adsorbates in solutions were determined by a UV/Vis spectrometer (PG Instrument Ltd Model T80) at 273, 267 and 307 nm respectively.

Equilibrium experiments

The equilibrium adsorption experiments have been carried out to assess the efficiency of ACC to remove phenolic compounds from solutions. Batch adsorption tests were performed for this purpose, where 5 ml of solutions of known initial concentration (C_0) and a known amount of the adsorbent were taken in 10 ml flasks at 35.0 °C. The flasks were placed in a water bath shaker (n- BioTEK, NB-304) and shaken at 150 rpm for 24 h to ensure the adsorption process reaching equilibrium. The equilibrium concentrations (C_e) of phenolic compounds were determined using UV/Vis spectrometer. The equilibrium amount of solute adsorbed per gram of activated carbon (q_e) was calculated by use of C_0 and C_e .

Kinetic experiments

The kinetic experiments were carried out in the way similar to equilibrium experiments, except for that the initial concentration of each solution was constant. The amount of solute adsorbed per gram of activated carbon at time t (q_t) was calculated by use of C_0 and C_t (concentration of solution at time t).

3. Results and discussion

The equilibrium experimental data have been fitted to different models including Langmuir, Freundlich, Temkin, Langmuir-Freundlich and Redlich-Peterson isotherms by non-linear method and the values of the parameters of these isotherms were obtained [1,2]. The experimental data and results of the fitting to Langmuir-Freundlich and Redlich-Peterson isotherms (two-parameter isotherm models) have been shown in Fig.1 for 3-methylcatechol. This Figure shows the good fitting of the experimental data to these isotherms. Based on the obtained correlation coefficients it has been shown that the equilibrium data were fitted to the Temkin (except for 2,3-Dihydroxybenzoic acid), Langmuir-Freundlich (except for 3-Methoxycatechol) and Redlich-Peterson isotherms.

Since the kinetic modeling is very important for reactor design in adsorption process [3] the experimental kinetic data were fitted to pseudo-first-order (PFO) and pseudo-second-order (PSO) models (Fig.2) and rate constant of adsorption was obtained for different models. Based on the correlation coefficients, it was found that the pseudo-second-order model describes the kinetic of adsorption of these phenolic compounds on the surface of activated carbon cloth better than the other one.

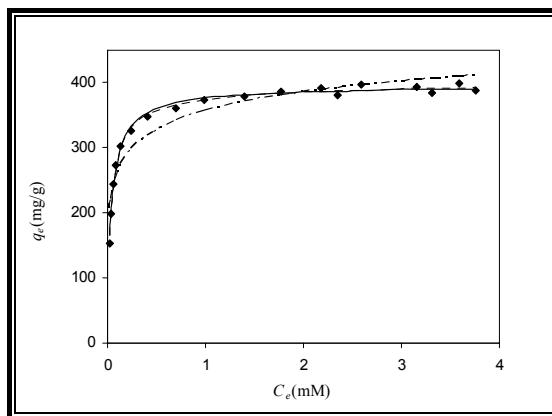


Fig. 1. The experimental equilibrium adsorption data for 3-methylcatechol (♦) and the predicted values based on Temkin (---), Langmuir-Freundlich (—) and Redlich-Peterson (----).

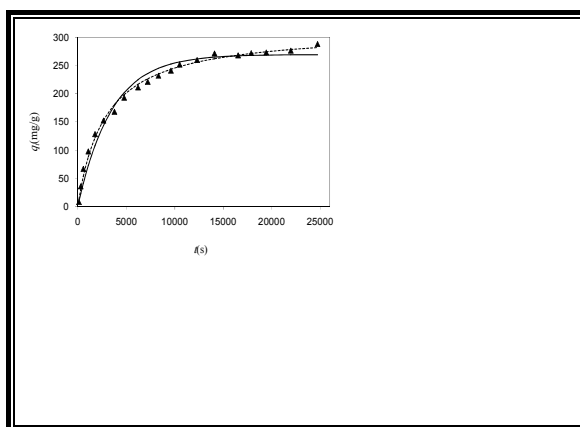


Fig. 2. The experimental kinetic data for 3-methylcatechol (♦) and the predicted values based on PFO (—) and PSO (----) rate models.

References

- [1] E. Bayram, N. Hoda, E. Ayranci, J. Hazard. Mater., 168 (2009) 1459.
- [2] S. Azizian, M. Haerifar, J. Basiri-Parsa, Chemosphere, 68 (2007) 2040.
- [3] S. Azizian, J. Colloid Interface Sci., 276 (2004) 47.

**Determination of impacted suspect bullet types on the suspect objects using splash phenomena**Azam Tarkashvand^a, Jamshid Babaee^b^aCriminal Scene Investigation Department, Tehran, Iran^bLabs of Criminal Investigation Department, Tehran, Iran

(Email: Tarkashvanda@gmail.com)

Keywords: Impact bullet residues, Gun shot, criminalistic manner, Splash Phenomena**1. Introduction**

One of common questions in the investigation of shooting scenes is that of determining whether a hole in or mark on some object was produced by a bullet. If it can be established as a bullet caused, additional questions may arise. For example, was it a lead bullet? Or it a copper jacketed bullet? Can directionality be determined [1]? A common method used to examine types of bullets is comparison of physical properties such as weight, dimensions, shape, and distinctive marking. [2] Determining the firing distance and bullet type is of great importance from the point of view of a criminal investigation. In close range shots, there may be deposits from smoke or unburnt powder particles either on the clothes which have been shot through or on the objects. The intensity and distribution of these deposits is related to ballistics [3]. The analysis of GSR is considered one of the most reliable methods for establishing the shooting distance [4]. GSR particles are produced from the primer, propellant, metals contained in the bullet, bullet jacket, cartridge case, and gun barrel when a gun is fired [5]. Detection and identification of GSR can be performed by several methods, which involve chemical tests; X-ray fluorescence analyses; and scanning electron microscopy (SEM) with energy-dispersive X-ray analysis, with wavelength-dispersive X-ray analysis, or with energy-dispersive Spectroscopy, Confocal laser scanning microscope [6, 7, 8]. Although these methods are all relatively sensitive and specific, some are costly and require highly specialized equipment [9]. In this study, we analyzed 100 samples of gunshot wounds, holes, and ricochet marks using a quantitative microscopic and macroscopic method based on the use of two chemical reagents to investigate the patterns of impacted bullet residues according to firing distance.

2. Methods

The materials in this study consist of criminal cases sent to criminal physics laboratory of Tehran, in 2008 – 2009. In all cases, FMJ projectiles and unjacketed lead bullets were fired by 0.22 inch, 7.65 mm, 9mm caliber pistols and 0.32 inch, 0.38 inch revolvers. A total of 100 samples were selected from cases in which the manner of death (accidental, suicide, and homicide) and the shooting distance was reliably determined on the basis of detailed scene report, examination of the clothes and impacted bullets, investigation of firing scenes, test all of suspect spots and report of post mortem findings. In addition to identifying and photographing the samples and examination stages. The samples consisted in 53 entrance holes (2 entrance holes had visible soot and powder tattooing), 10 ricochet marks, and 37 exit holes, were identified on basis of macroscopic appearance, physical parameters, and using two chemical reagents: dithionite for copper and Sodium rhodizonate for lead. FIG. 1. [10] Moreover, GSR – positive samples to verify results submitted to SEM department.

3. Results and discussion

Although sodium rhodizonate and DTO are capable of reacting with other metals, they were described to be relatively specific for demonstrating the presence of lead and copper bullet particles on the suspect surfaces [11]. In majority of the 100 samples taken from macroscopically identified entrance holes and ricochet marks DTO and rh reactions were positive and showing fig 3, 4.

4. Conclusions

Although test-firing the gun gives the best estimate of the range of fire, the pattern of soot and/or gunpowder deposited around the entrance holes or ricochet marks are frequently valuable tools in assessing the muzzle-to-target distance [12] in the study was investigated ballistics' suspect handguns, showing Splash Phenomena on the objects. The splash is the production and dispersal of vaporized and fine particles of metal (lead and copper) as a result of impact. FIG. 2. Metal splash is related to the bullet design and composition, the nature of the surface struck and the energy associated with the impact. The geometry of the deposition of metal splash can provide information on the direction of fire and position of shooter. The amount of metal splash is a function of impact velocity, angle. The microscopic evaluation of the entrance holes demonstrate different findings related to the range of fire. A pattern of sodium rhodizonate-positive residues centered very tightly on the entrance holes with

a contiguous distribution is characteristic of close-range shots. In these samples we observed the greater quantity (number) of GSBR and the dimensions of the single deposits were bigger than in the other specimens. When the firing distance increases, we could demonstrate a lower quantity of small, scattered DTO and sodium rhodizonate-positive bullet residues. As the shooting distance increased we observed dot-shaped, finely coarsely granulated, and noncontiguous sodium rhodizonate-positive. The combined utilization of morphometric analysis and leica microscopy using the DTO and rhodizonate staining technique for the analysis and the quantification of GSBR deposits present on surface sections is a simple and inexpensive method, which can be used in routine practice in forensic science laboratories. Moreover, this method has the potential to provide quantifiable, measurable, and comparable evidence for estimation of the shooting distances in the reconstruction of events in gunshot fatalities.

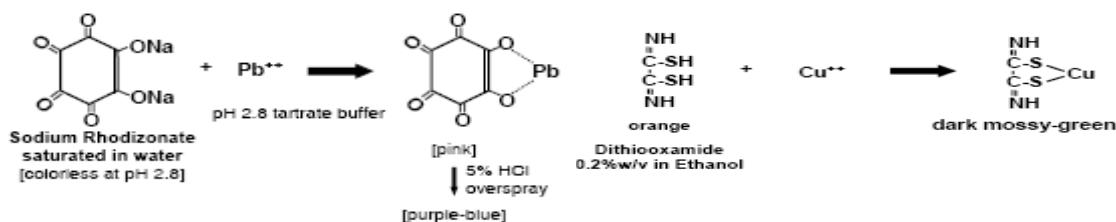


Fig. 1. Dithiooxamide and Sodium rhodizonate

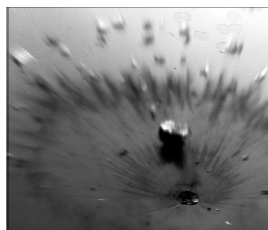


Fig. 2. An Example of Lead Splash

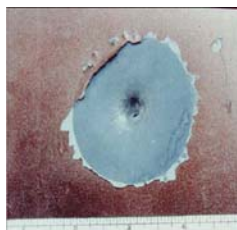


Fig. 3. A Suspected Bullet Impact Site in a Car Door



Fig. 4. Lead Splash as a Result of a Low Incident Angle Impact and Ricochet

References

- [1] Lucien C. Haag , Shooting Incident Reconstruction, Academic Press , 2005-12.
- [2] Andrea Ulrich .Christoph Moor · heinz Vonmont Hans-Rudolf Jordi . Martin Lory (2003) ICP-MS trace-element analysis as a forensic tool. Anal Bioanal Chem (2004) 378 : 1059–1068DOI 10.1007/s00216-003-2434-8.
- [3] K. M. Stein · M. L. Bahner · J. Merkel · S. Ain R. Mattern .Detection of gunshot residues in routine CTs. Int J Legal Med
- [4] Wallace JS (1990) Chemical aspects of firearms ammunition.Assoc Firearms Tool Mark Exam J 22:364–389.
- [5] Kage S, Kudo K, Kaizoji A, Ryumoto J, Ikeda H, Ikeda N (2001)A simple method for detection of gunshot residue particles from hands, hair, face, and clothing using scanning electron microscopy/wavelength dispersive X-ray (SEM/WDX). J Forensic Sci.
- [6] Karger B, Puskas Z, Ruwald B, Teige K, Schuirer G (1998)Morphological findings in the brain after experimental gunshots using radiology, pathology and histology. Int J Legal Med 111:314–319.
- [7] Romolo FS, Margot P (2001) Identification of gunshot residue: a critical review. Forensic Sci Int 119:195–211.
- [8] Lebedzik J, Johnson DL (2000) Rapid search and quantitative analysis of gunshot residue particles in the SEM. J Forensic Sci.
- [9] Margherita Neri & Emanuela Turillazzi & Irene Riezzo & Vittorio Fineschi (2007) The determination of firing distance applying a microscopic quantitative method and confocal laser scanning microscopy for detection of gunshot residue particles , Int J Legal.
- [10] Division of forensic science , FIREAREM/ TOOLMARK PROCEDURES MANUAL . (2007) 1-10.
- [11] Adeyi O, Duval JV, Dupre ME, Andrew TA , Role of chemical tests and scene investigation in determination of range of fire. (2005) Am J Forensic Med Pathol 26:166–169.
- [12] Karger B, Hoekstra A, Schmidt PF (2001) Trajectory reconstruction from trace evidence on spent bullets. I. Deposits from intermediate targets. Int J Legal Med 115:16–22.

**Effect of operating conditions on the catalytic performance of fused Co-Ce/SiO₂ catalyst used in FTS**

M. Galavy, A. A Mirzaei, S. Vahid, N. Karimpour

Department of chemistry, Faculty of sciences, University of Sistan & Baluchestan, Zahedan, Iran.

(Email: Maryam_galavy@yahoo.com)

Keywords: Co-Ce/SiO₂ catalyst, Fusion method, Characterization, Light olefins, Operating conditions.

1. Introduction

Typically, FTS catalysts include VIII group based metals (Co, Ru, Fe) with Co-based ones ensuring a superior long-chain hydrocarbon yield and longer life time [1-3]. Co-Ce catalysts have been investigated for its selectivity to lower molecular weight olefins [4-6].

2. Methods

In the present study, a catalyst with 80%Co/20%Ce/15wt%SiO₂ composition was prepared using fusion method. The required amounts of Co(NO₃)₂.6H₂O and Ce(NO₃)₃.6H₂O and SiO₂ were added to crucible and the mixed materials fused at high temperature. Solid chunks were obtained from the cooled mixture then ground. The catalyst was dried in an oven at 120°C for 12 h. The dried catalyst was calcined at 600 °C for 6 h.

3. Results and discussion

The operating conditions were investigated to identify and optimize the operation variables, such as H₂/CO molar feed ratios, reaction temperatures and reaction pressures that have a marked effect on the catalytic performance.

1) Effect of H₂/CO feed ratio

The influence of the reaction H₂/CO molar feed ratio on the steady state catalytic performance of the cobalt cerium oxide catalyst containing 80%Co/20%Ce/15wt%SiO₂ prepared using fusion method for the Fischer-Tropsch reaction at 450°C under atmospheric pressure was investigated and it was found that the catalyst has shown the best catalytic performance at H₂/CO=2/1. Characterization of this catalyst was carried out using XRD and the patterns of this catalyst in the different stages of precursor, fresh calcined catalyst (before the test)& used calcined catalyst (after the test) at H₂/CO=2/1 are shown in Fig. 1.

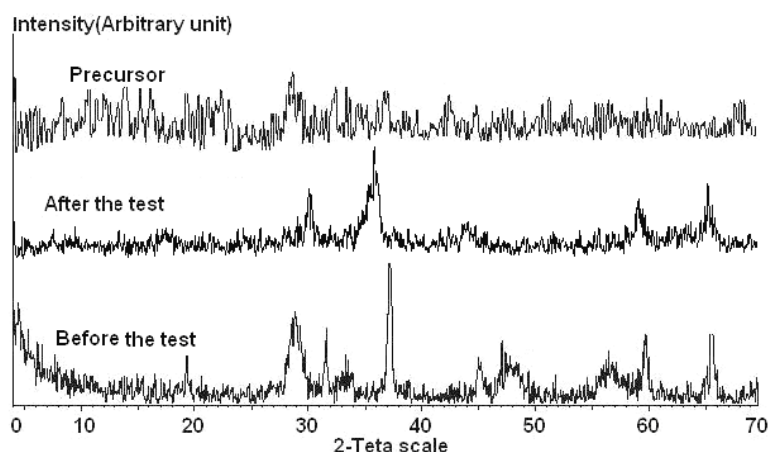


Fig. 1. XRD patterns of precursor and calcined catalysts (before and after the test) containing 80%Co/20%Ce/15wt% SiO₂.

2) Effect of reaction temperature

The effect of reaction temperature, ranging from 300-450°C on the catalytic performance of this catalyst was studied (P=1atm and H₂/CO=2/1). According to the obtained results (Fig. 2), the optimum reaction temperature was 350 °C, at which temperature the total selectivity of light olefins products was higher than those at the other reaction temperatures under the same operating conditions.

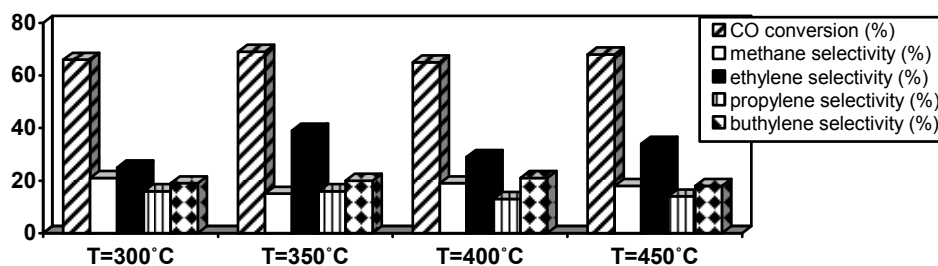


Fig. 2. Effect of different reaction temperatures on the catalytic performance.

3) Effect of total reaction pressure

The effect of reaction pressure, ranging from 1-10 bar on the catalytic performance of this catalyst was studied ($T=350^{\circ}\text{C}$ and $\text{H}_2/\text{CO}=2/1$). According to the obtained results, the optimum reaction pressure was 2 bar, at which pressure the total selectivity of light olefins products was higher than those at the other reaction pressure under the same operating conditions.

The BET surface area measurement was used in order to measure the specific surface area of catalyst. The specific surface area of the catalyst tested at pressure of 2 bar that compared with the precursor and calcined catalyst before the test are presented in Table 1. As shown, the calcined catalyst before the test has a higher specific surface area ($119\text{ m}^2/\text{g}$) than its precursor ($103\text{ m}^2/\text{g}$).

Table 1. BET results of the catalyst containing 80%Co-20%Ce/15wt%SiO₂.

fused Catalyst	Specific surface area (m^2/g)		
	Precursor	fresh catalyst	used catalyst
80%Co/20%Ce/15wt%SiO ₂	103	119	115

4. Conclusions

The obtained results showed that the catalyst is sensitive to the operating conditions. These operating parameters should be incorporated into achieve the highest selectivity toward light olefins from the catalyst containing 80%Co/20%Ce/15wt%SiO₂ prepared using fusion procedure.

References

- [1] P. J. Van Berge, R. C. Everson, *Stud. Surf. Sci. Catal.* 107 (1997) 207.
- [2] G. P. Van der Laan, A. A. C. M. Beenackers, *Catal. Rev. Sci. Eng.* 41 (1999) 255.
- [3] P. Chaumette, Ph. Coutry, A. Kiennemann, B. Ernst, *Top. Catal.* 2 (1995) 117.
- [4] L. A. Bruce, M. Hoong, A. E. Hughes, T. W. Turney, in: H. E. Curry-Hyde and R. F. Howe (Eds), *Natural Gas Conversion II*, Elsevier Science, 1994, pp 427-432
- [5] J. Barault, A. Guilleminot, J. C. Achard, V. Paul-Boneour, A. Percheron Guegan, *Appl. Catal. A: Gen.* 22 (1986) 273.
- [6] L. A. Bruce, M. Hoang, A. E. Hughes, T. W. Turney, *Appl. Catal. A: Gen.* 100 (1993) 51.

**Catalytic properties and characterization of Fe-Co catalyst at different operating conditions**

M. Galavy, A. A. Mirzaei, S. Vahid, N. Karimpour

Department of chemistry, University of Sistan & Baluchestan, Zahedan, Iran

(Email: Maryam_galavy@yahoo.com)

Keywords: Co-Fe bimetallic catalyst, Sol gel technique, Characterization, Operating conditions, Light olefins.**1. Introduction**

By Fischer-Tropsch (FT) reaction the synthesis gas is converted to a mixture of hydrocarbons. Then hydrocarbons undergo further treatment to yield distillates[1]. Fischer-Tropsch catalysts are mainly restricted to iron and cobalt and a lesser extent to nickel. The combination of Fe-Mn [2], Co-Mn [3,4] and Fe-Co catalyst [5,6] with or without promoters favors the formation of C₂-C₄ alkenes.

2. Methods

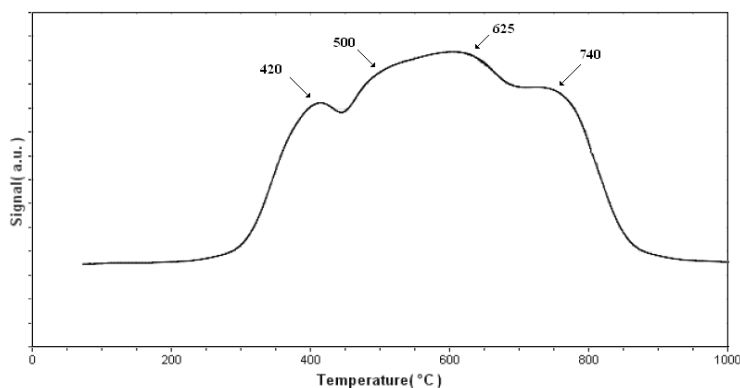
Co(NO₃)₂·6H₂O (8.73 g) and Fe(NO₃)₃·9H₂O (8.08 g) was dissolved in 3.8 g oxalic acid and 40 cm³ ethanol mixture at 80°C. After stirring for 10 min, tetraethyl orthosilane TEOS Si(OC₂H₅)₄ (9.2 cm³) and KNO₃ (0.252 g) was added to a homogeneous transparent solution. This mixture was slowly dried by evaporation during which the TEOS was hydrolyzed by adding a H₂O/C₂H₅OH(60/40 V/V) mixture to the transport solution; in order to hydrate water of the nitrates and the oxalic acid into Si(OH)₄ and condensed to form siloxane bonds. Then the sample was stirred at 110°C for 16h to give transparent monolithic gel. The gel was dried at 150°C in vacuum, powdered and calcined at 600°C for 6h in air.

3. Results and discussion**Effect of operation conditions**

The effect of a range of operation variables such as H₂/CO feed gas molar ratios, reaction temperatures and reactor pressures on the catalytic performance of 40%Fe/60%Co/15wt%SiO₂/1.5wt%K catalyst was investigated to identify and optimize the operation conditions for the Fischer-Tropsch synthesis.

1) Effect of H₂/CO feed ratio

The influence of the reaction H₂/CO molar feed ratio on the steady state catalytic performance of the cobalt iron oxide catalyst containing 40%Fe/60%Co/15wt%SiO₂/1.5wt%K prepared using sol-gel technique, at 400°C under atmospheric pressure was investigated. It was found that at a H₂/CO ratio of 2/1, the total selectivity toward C₂-C₄ olefins fraction was higher and the CH₄ selectivity was lower. In order to study the reduction behavior of catalyst, the calcined catalyst was characterized by using TPR and the H₂-TPR profiles are shown in Fig. 1. The TPR profiles of calcined catalyst revealed four distinct reduction peaks at 420, 500, 625 and 740°C, which can attributed to the reduction of Co³⁺ and Co²⁺ oxide species to metallic cobalt and also the reduction of Fe³⁺ and Fe²⁺ oxides to metallic iron.

**Fig. 1.** TPR profile of the calcined catalyst.**2) Effect of reaction temperature**

The effect of reaction temperature on the catalytic performance of this catalyst was studied at a range of temperatures between 300-450 °C under the same reaction conditions of H₂/CO=2/1 and P=1 bar. According to the obtained results (Fig. 2), the optimum reaction temperature was 350 °C, at which temperature the total selectivity of light olefins products was higher than those at the other reaction temperatures under the same operating conditions.

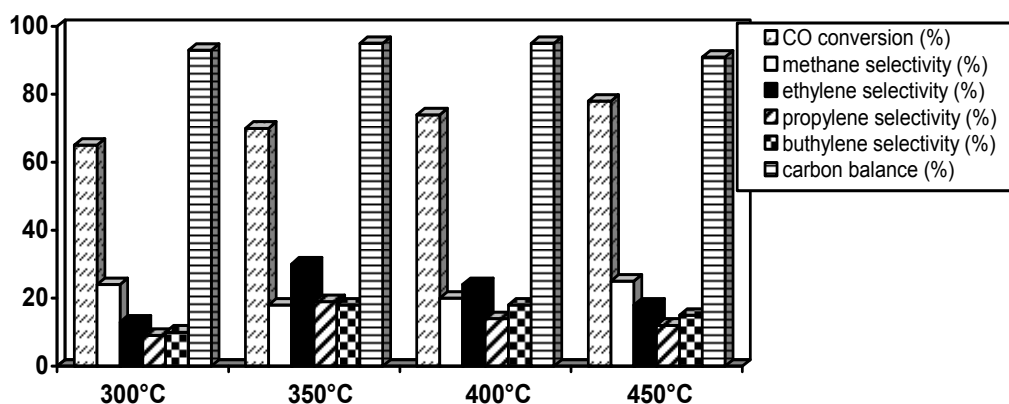


Fig. 2. Effect of different reaction temperatures on the catalytic performance.

3) Effect of total reaction pressure

The effect of reaction pressure, ranging from 1-10 bar on the catalytic performance of this catalyst was studied (T=350 °C and H₂/CO=2/1). According to the obtained results, the optimum reaction pressure was 3 bar, at which pressure the total selectivity of light olefins products was higher than those at the other reaction pressure under the same operating conditions. The BET surface area measurement was used in order to measure the specific surface area of the catalysts. The specific surface area of the catalyst tested at pressure of 3 bar that compared with the precursor and calcined catalysts before the test are presented in Table 1. As shown, the calcined catalyst before the test has a higher specific surface area (46 m²/g) than its precursor (33 m²/g).

Table 1. BET results of the catalyst containing 40%Fe/60%Co/15wt%SiO₂/1.5wt%K.

Catalyst	Specific surface area (m ² /g)		
	Precursor	Calcined catalyst (before the test)	Calcined catalyst (after the test at 3 bar)
Co/Fe(sol gel)	33	46	37

4. Conclusions

It was observed that all of the different operation variables influenced the structure, morphology and catalytic performance of the catalysts. The obtained results showed that the operating conditions have great effect on the catalytic performance of Fe-Co catalyst.

References

- [1] S. Jam, M. G. Ahangary, A. Tavasoli, K. Sadaghiani and A. Nakhaeipour, *React. Kinet. Catal. Lett.* 89(1) (2006) 71.
- [2] R. Malesa, M. Bearns, *Ind. Eng. Chem. Res.* 27 (1988) 279.
- [3] S. Colley, R. G. Coppertwaite, G. J. Hutchings, M. Vander Riet, *Ind. Eng. Chem. Res.* 27 (1998) 1339.
- [4] M. J. Keyser, R. C. Everson, R. L. Espinoza, *Appl. Catal. A: Gen.* 171 (1998) 99.
- [5] C. Cabet, A. C. Roger, A. Kiennemann, S. Lakamp. G. Pourroy, *J. Catal.* 173 (1998) 64.
- [6] F. Tihay, A. C. Roger, A. Kiennemann and G. Pourroy, *Catal. Today.* 58 (2000) 263.

Characterization of Fe/Mn catalysts using XRD, BET, TGA and DSC techniquesS. Vahid, A. A Mirzaei, M. Galavy, N. Karimpour

Department of chemistry, Faculty of sciences, University of Sistan & Baluchestan, Zahedan, Iran.

(Email: neda_karimpour@yahoo.com)

Keywords: Catalyst characterization, Precipitate ageing, Iron-manganese oxide, Fischer-Tropsch synthesis, Morphology.**1. Introduction**

Fischer-Tropsch (FT) synthesis is of great industrial importance due to the great variety of products obtained such as paraffins, olefins and alcohols. Existence of some of the advantages such as high selectivity to olefins, suitable price and to be available cause to iron has been widely used as one of the optimum catalysts for FTS reaction. Addition of manganese to iron produces stable catalysts with high selectivity for olefins and concurrent suppression of methane selectivity [1-6].

2. Methods

All the catalysts were prepared using the co-precipitation procedure and test of all of these catalysts were carried out in a fixed bed micro reactor.

3. Results and discussion**1. Effect of ageing time on the morphology of catalysts**

A series of mixed iron manganese oxide catalysts were prepared by co-precipitation method ($[\text{Fe}]/[\text{Mn}]=1/1$, 70°C , $\text{pH}=8.3$) with a range of ageing times between 0 min (unaged) and 300 min for the precipitate. there is considerable variation in the catalyst performance with respect to aging time and the sample aged for 3h gave the optimal catalytic performance for CO conversion in FTS. The catalyst precursors which were prepared using co-precipitation method in different aging times were characterized by thermal gravimetric analysis (TGA) and the TGA curves of these precursors are displayed in Fig. 1. For these precursors, the thermogravimetric curves seem to indicate three-stage decomposition. The first-stage is considered to be due to the removal of adsorbed water ($40\text{--}110^\circ\text{C}$) and the second stage is due to the decomposition of hydroxyl bimetallic or nitrate precursor ($230\text{--}420^\circ\text{C}$), respectively. The peak around $450\text{--}630^\circ\text{C}$ is due to the decomposition of MnCO_3 or $\text{Fe}_2\text{CO}_3(\text{OH})_2$ to oxides

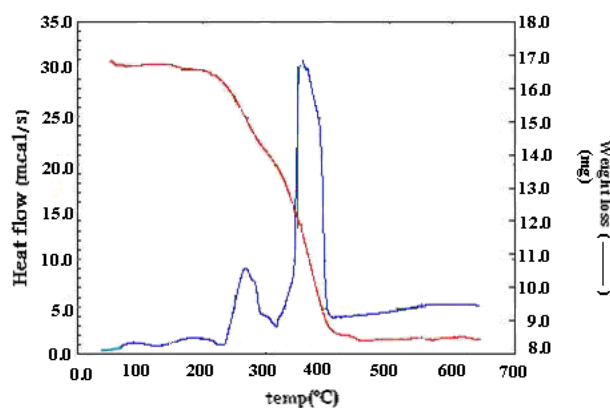


Fig. 1. TGA/DSC curves for the 50%Fe/50%Mn/5wt% Al_2O_3 catalyst precursor.

2. Effect of precipitation pH on the morphology of catalysts

A series of iron manganese oxide catalysts were prepared by co-precipitation method ($[\text{Fe}]/[\text{Mn}]=1/1$, 70°C and 3h ageing time) with a range of precipitation pH from 6.3 to 10.3. The catalyst was prepared at $\text{pH}=8.3$ gives the highest activity for FT synthesis in $T=400^\circ\text{C}$, $p=1$ atm and $\text{H}_2/\text{CO}=2/1$. The catalysts precursors prepared in different pH, were characterized by XRD and showed the MnCO_3 phase as rhombohedral structure. It is apparent that during precursor calcination, carbonate phase leads to the oxide phases. These calcined catalysts were characterized by XRD and their patterns are shown in Fig. 2. The actual phases identified in these catalysts were Mn_2O_3 (cubic) and Fe_2O_3 (rhombohedral). The calcined tested catalysts prepared at $\text{pH}=8.3$ also was characterized by XRD and different phases including MnO (cubic), FeO (cubic) and $\text{CFe}_{2.5}$ (monoclinic) were identified in this catalyst.

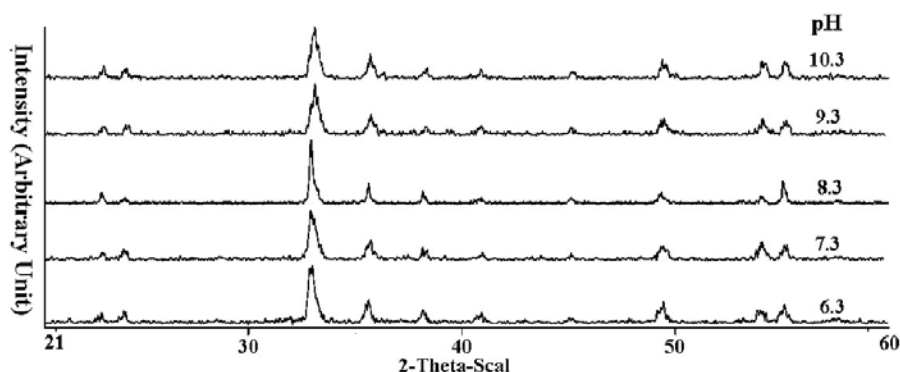


Fig. 2. XRD patterns of calcined catalysts with different precipitation pH.

3. Effect of solution [Fe]/[Mn] ratio on the morphology of catalysts

According to the obtained testing results, the catalyst containing 50%Fe/50%Mn was chosen as the optimum catalyst for the conversion of synthesis gas to ethylene and propylene. The BET results show that the calcined catalysts prepared with a range of [Fe]/[Mn] solution ratios varying from 100%Fe to 100%Mn have different specific surface areas. The catalyst with 1/1 [Fe]/[Mn] ratio has a higher specific surface area than the other catalysts (Table 1), which is one reason for the enhanced performance of this catalyst

Table 1. BET results for different molar ratios of Fe/Mn.

Fe/Mn		1/0	4/1	2/1	1/1	1/2	1/4	0/1
Specific surface area (m ² /g)	Precursor	65.1	71.2	98.1	107.9	109.8	111.3	110.8
	Calcined catalyst (before reaction)	62.7	68.2	96.7	98.6	104.7	108.9	107.9
	Calcined catalyst (after reaction)	59.3	66.4	84.3	95.6	102.1	106.1	105.6

4. Conclusions

Characterization of both precursors and calcined catalysts by powder X-ray diffraction, scanning electron microscopy (SEM), BET specific surface area and thermal analysis (TGA/DSC) methods, showed that the catalyst precursors are sensitive to the preparation conditions, so that these preparation parameters are important factors influencing the structure of the precursors and calcined catalysts and that these parameters should be incorporated into the design of experimental programs involving precipitation as the method of catalyst preparation.

References

- [1] Hiroyuki, Itoh, Shinichi Nagano, Kohtaro Takeda, Eiichi Kikuchi, Appl. Chem. Sci. Eng. (2001)
- [2] Hiroyuki, Itoh, Shinichi Nagano, Kohtaro Takeda, Eiichi Kikuchi, Appl. Catal. A: General. 96 (1993) 125.
- [3] J. Abbott, N.J. Clark, B.G. Barker, Appl. Catal. 26 (1986) 141.
- [4] T. Herranz, S. Rojas, F.J. Perez-Alonso, M. Ojeda, P. Terreros, J. L. G. Firro, Appl. Catal. A: General. 311 (2006) 66.
- [5] Nattaporn Iohitharn, James G. Goodwin Jr, Edgar Lotero, J. Catal. 255 (2008) 104.
- [6] G. C. Maiti, R. Malessa, M. baerns, Appl. Catal. A. Gen. 5 (1983) 151.



Study of adsorption of safranin on granulated active carbon (GAC) and evaluation of its thermodynamic and kinetic parameters

Ghazaleh Koutchakzadeh

Department of chemistry , Science Faculty , Islamic Azad University ,Khorramabad Branch , Khorramabad , Iran

(Email:gh_kouchakzadeh@yahoo.com)

Keywords : Adsorption , Safranin , Thermodynamic , Kinetic , Langmuire isotherm

1.Introduction

Dyes are widely used in various fields , and their discharge into water.

Causes environmental pollution effluents from many industries are rich in colour, acid and organic solvents . These effluents readily deteriorate the quality of receiving waters and soil ,which eventually are harmful to human . The removal of colour from waste water by adsorption method has these advantages , that is , simply designed , easy to handle and inexpensive[1].

In this study thermodynamic and kinetic parameters of surface adsorption of chrysoidin G on activated carbon granules in water solution at different temperatures were investigated.

Adsorption equilibrium data were correlated with the Langmuire and Freundlich isotherms. Thermodynamic parameters such as ΔS , ΔH and ΔG were calculated. The kinetic followed a pseudo first order reaction , and was fitted to the mass transfer model proposed by Lagergren.

2. Methods

Materials

GAC were of AR grade (Merck) , Safranin were of Merck , solution of Safranin were prepared in double distilled water.

Estimation of colour

The concentration of colouring matter in each sample was determined by calibration plots drawn by recording the absorbance of Safranin at different concentration , all measurement were made at λ_{max} (480).

Adsorption studies

Adsorption studies were performed by batch technique . A series of 100 ml flask employed , each having 25 ml of Safranin solution of varying concentration (20-40 ppm).

With a fixed amount is attained in 3 hours . sorption experiments were run at 298 and 303 K .

3. Results and discussion

Adsorption equilibrium data were correlated with the Langmuire and Freundlich isotherms . The isotherms fit the Langmuire equation (1) and to some extent Freundlich equation (2) .

$$1/(x/m) = 1/(kb) (1/c) + (1/b) \quad (1)$$

$$\log (x/m) = \log k + (1/n) \log c \quad (2)$$

Where x is the mass of adsorbate (mg) , m is mass of adsorbent (g) , c the equilibrium concentration of chrysoidin G (molL⁻¹) ,k and b are constants [2].

Thermodynamic parameters such as ΔS , ΔH and ΔG were calculated , it showed $\Delta S < 0$, $\Delta H < 0$ and $\Delta G > 0$. It indicates the reaction is exothermic.

The kinetic followed first-order kinetics , kinetics relation represented by the equation :

$$\ln c_0/c_t = -k'_1 t \quad (3)$$

Where c_0 is the initial Safranin solution concentration , c_t is the concentration at time t and constant k'_1 is pseudo specific reaction rate constant [3].

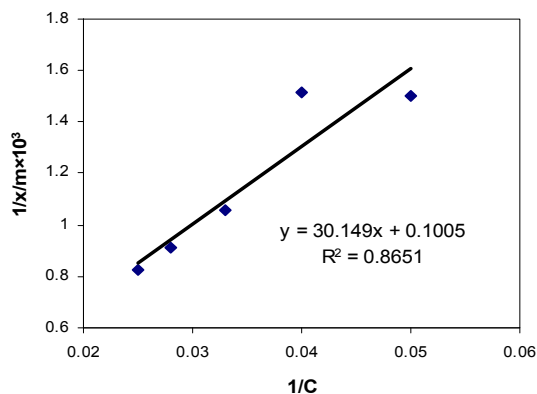


Fig. 1. Plot of $1/(x/m)$ vs $1/c$ in watery solution at 298 K

Table 1. The values of thermodynamic parameters .

ΔH KJ/mol	ΔS J/mol	ΔG / KJ/mol	
		298	303
-90.10	0.345-	12.64	14.37

Table 2 . pseudo first – order kinetics rate constant (control kinetics equation).

/ppm	C_0	T / K	Equation	R^2	/mink' $\times 10^3$
25		303	$y = 3.178 - 0.0016 t$	0.985	1.6
25		298	$y = 3.298 - 0.0017 t$	0.996	1.7

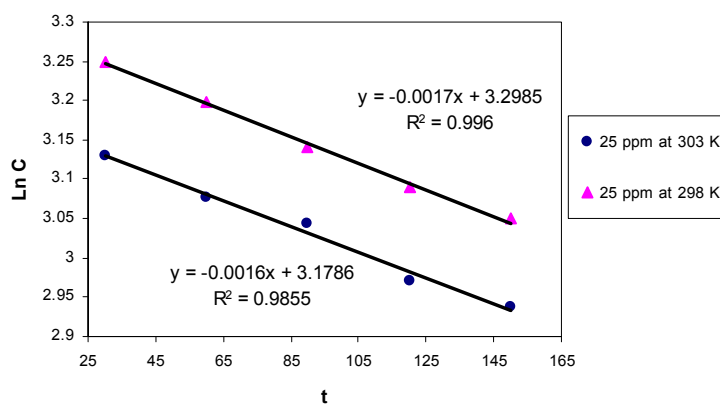


Fig.2. Plot of $\ln C$ vs t in watery solution at 25 ppm

References

- 1- Weber , W , J ; physico-chemical processes ; pp 199 , J . Wiley ed , (1972).
- 2- Potgiter , G . H ; Adsorption of methylen blue on activated carbon . J . Cheml . Edu ; 68 , 349 , (1991) .
- 3- Mondal , K . etal ; Modeling of mass transfer controlled adsorption . J . sci and technology ; 35 , 2583 , (2000) .



The study of synergistic effects between cationic surfactant (Hyamine) and nonionic surfactant (Triton X-100)

Z. Felegari^a, A. A. Rafati^b

^{a, b} Department of chemistry, University of Hamadan, Iran.

(Email: Zahra.felegari@gmail.com)

Keywords: Surfactant, Synergistic, Antagonism, Potentiometric method, Surface tension, Critical Micelle Concentration (CMC).

1. Introduction

Surfactants have natural polydispersity in length when they are produced with chain polymerization; therefore, obtaining a pure system requires additional processing and can be more expensive to produce [1-3]. In this research, we studied the synergistic effect between cationic surfactant (Hyamine) and non-ionic surfactant (Triton X-100) in water/ethanol and water/buthanol mixtures at different percentage of alcohol.

2. Methods

By using potentiometric and surface tension techniques, we study the effect of alcohol on synergism and mixed micellization. The obtained data from two techniques have been analyzed based on Regular Solution Theory, Maeda concept, ect [4].

3. Results and discussion

According to the experimental results, the synergism was observed in the alcohol as well as in pure water. Regular solution Theory approximation can be used for explanation of synergistic effect in these systems.

4. Conclusions

The results showed that β (the interaction parameter) is a composite dependent parameter. The additive (alcohol) behaves as co-surfactant at low concentrations and causes a decrease in CMC while behaves as co-solvent at higher concentrations and cause an increase in CMC by decreasing in hydrophobicity of solvent. The excess free energy of mixed micellization as a function of system composition shows a non-symmetric shape, which is contrary to Regular Solution Theory.

References

1. Georgui K. Bourov and Aniket Bhattacharya. Brownian Dynamics of Mixed Surfactant Micelles
2. Ciccarelli, D., Castantino, L., D' Errico, G., Paduano, L. and Viaglianilo, V ., 1998, "Mixed micellar aggregation of anionic and nonionic surfactant with short hydrophobic tails. A PQSE-NMR study", VOL. 14, PP. 7130-7139.
3. De Lisi, R ., Ingles, A., Milito, S. and Pellerito, A., 1997, "Demixing of Mixed Micells. Thermodynamic of sodium perfluoro octanate sodium dodecanoate mixtures in water", Langmurir, Vol. 13, pp. 192-202.
4. Gharibi, H., Javadian, A. S., Hashemianzadeh, A. M., 2004, "Investigation of interaction of cationic surfactant with HSA in the presence of alcohols using PFG-NMR and potentiometric technique Colloids and Surfaces A", Physicochem. Eng, Vol. 232, pp. 77-86.



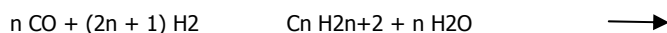
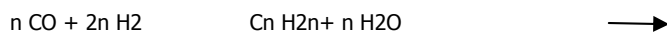
**Fe-Mn bimetallic catalyst prepared by sol/gel technique: operating conditions and characterization**A. A. Mirzaei^a, *N. Karimpoor^a^aDepartment of Chemistry, University of Sistan & Baluchestan, Zahedan, Iran

(Email: neda_karimpoor@yahoo.com)

Keywords: Fe/Mn bimetallic catalyst, Fischer-Tropsch synthesis, Sol gel technique, Fixed-bed micro reactor, Operating conditions, Characterization.

1. Introduction

Fischer-Tropsch (FT) synthesis produces hydrocarbons from syngas, which is a mixture of carbon monoxide and hydrogen.



Depending on catalyst, reactor and conditions, FT synthesis could produce a wide range of hydrocarbons: light hydrocarbons, gasoline, diesel fuel and wax [1]. All group VIII metals have noticeable activity in the hydrogenation of carbon monoxide to hydrocarbons. Ruthenium followed by iron, nickel, and cobalt are the most active metals for the hydrogenation of carbon monoxide. Vannice et al. showed that the molecular average weight of hydrocarbons produced by FT synthesis decreased in the following sequence: Ru > Fe > Co > Rh > Ni > Ir > Pt > Pd. Thus, only ruthenium, iron, cobalt, and nickel have catalytic characteristics which allow considering them for commercial production. Nickel catalysts under practical conditions produce too much methane. Ruthenium is too expensive; moreover, its worldwide reserves are insufficient for large-scale industry. Cobalt and iron are the metals which were proposed by Fischer and Tropsch as the first catalysts for syngas conversion. Both cobalt and iron catalysts have been used in the industry for hydrocarbon synthesis [2]. The Fe-Mn catalyst, as one of the most important catalyst systems, has received extensive attention in recent years because of the higher olefin and middle distillation cut selectivities which allow their products to be used as a feedstock for the chemical industry. Therefore, the Fe-Mn catalyst has a promising industrial application [3].

2. Methods**1. Catalyst preparation**

In our previous study [4] we were prepared Fe-Mn catalyst using co-precipitation method and we found that the catalyst containing 50%Fe/50%Mn/5wt%Al₂O₃ has shown the best catalytic performance for the production of light olefins. In the present work, we prepared a catalyst with the same composition using sol-gel technique in the following way to study its catalytic performance in the Fischer-Tropsch synthesis.

2. Preparation of 50%Fe/50%Mn/5wt%Al₂O₃ catalyst using sol-gel technique

Mn(NO₃)₂·4H₂O (4.56 g) and Fe(NO₃)₃·9H₂O (7.21 g) was dissolved in 3.8 g oxalic acid and 40 cm³ ethanol mixture at 80°C. After stirring for 10 min, tetraethyl orthosilane Si(OC₂H₅)₄ (9.2 cm³) and KNO₃ (0.252 g) was added to a homogeneous transparent solution. Then the sol was slowly hydrolyzed by adding H₂O/C₂H₅OH (60/40 V/V) mixture to the transparent solution and stirred at 110°C for 16h to give transparent monolithic gel. The gel was dried at 120°C in vacuum, powdered and calcined at 650°C for 6h in air. The activity and selectivity of prepared catalyst have been studied in a fixed-bed microreactor with reaction temperature of 240-440°C, pressure of 1-10 bar, H₂/CO molar feed ratio of 1-3 and space velocity of 3600 h⁻¹.

3. Results and discussion

The effect of a range of operation variables such as H₂/CO feed gas molar ratios, reaction temperatures and reactor pressures on the catalytic performance of 50%Fe/50%Mn/5wt%Al₂O₃ catalyst was investigated to identify and optimize the operation conditions for the Fischer-Tropsch synthesis. The typical reaction results are compared with respect to activity (CO conversion), product selectivity and the formation of methane. The results in terms of CO conversion, selectivity of products are given at each space velocity. The CO conversion (%) is calculated according to the normalization method:

$$\text{CO conversion (\%)} = \frac{(\text{Moles CO}_{\text{in}}) - (\text{Moles CO}_{\text{out}})}{\text{Moles CO}_{\text{in}}} \times 100$$



The selectivity (%) towards the individual components on carbon-basis is calculated according to the same principle:

$$\text{Selectivity of j product (\%)} = \frac{\text{Moles of j product}}{(\text{Moles CO}_{\text{in}}) - (\text{Moles CO}_{\text{out}})} \times 100$$

The results showed that with variation in H₂/CO feed ratio from 1/1 to 3/1, different selectivities with respect to C₂–C₄ hydrocarbons were obtained. However, in the case of the H₂/CO=3/2 the total selectivity of C₂–C₄ hydrocarbons products was favorite and the CH₄ selectivity was lower than the other H₂/CO feed ratios under the same temperature and pressure condition. It is also apparent that, for all of the H₂/CO feed molar ratios, the optimum catalyst shows a high selectivity toward ethylene. The optimum reaction temperature was 320°C, at which temperature the total selectivity of C₂–C₄ hydrocarbons products was higher than those at the other reaction temperatures under the same operating conditions. Also, at 320°C, the CO conversion and CH₄ selectivity were desirable. It was also shown that the reaction temperature should not be too low, since at the low reaction temperatures the total selectivity of C₂–C₄ hydrocarbons products is low, giving a high level of methane production. On the other hand, an increase in the reaction temperature (at 360°C) leads to the formation of large amounts of coke as an unwanted by-product, as we found in this work. A series of experiments were carried out to investigate the influence of the reaction pressure on the catalytic performance of Fe/Mn catalyst containing 50%Fe/50%Mn/5%wAl₂O₃ for production of C₂–C₄ hydrocarbons at the optimal reaction conditions of H₂/CO=3/2 and 320°C, during variation of total pressure in the range of 1-10 bar. The results indicate that, the optimum total pressure was 1 bar.

4. Conclusions

The result showed that the operating conditions have a great effect on the structure and catalytic performance of the catalyst. The effect of variable factors such as reaction temperatures, reaction pressures and H₂/CO molar feed ratios were examined on the catalytic performance of the catalyst containing 50%Fe/50%Mn/5wt%Al₂O₃. The optimal operating conditions for production of light hydrocarbons were found to be 320°C with molar feed ratio of H₂/CO=3/2 under the total pressure of 1 bar. The characterization of precursor and calcined catalysts (before and after the test) was performed by powder XRD, TGA/DSC and BET surface area measurement and it is concluded that the operating conditions has a marked effect on the morphology and texture of the catalysts. These operating parameters should be incorporated into achieve the highest selectivity toward light hydrocarbons from Fe/Mn catalyst prepared by sol gel technique on Al₂O₃ support.

References

- [1] Khodakov, A.Y. Catal. Today. 7 (2008) 5994.
- [2] Khodakov, A.Y. Chu, w. Fongarland, P. Rev. 2007, 107.
- [3] Liu, Y. Teng, B.T. Guo, X.H. Chang, J. Tian, L. Hao, X. Wang, Y. Xiang, H.W. Xu, Y.Y. Li, Y.W. J. Mol. Catal. A:Chem, 272 (2007) 182-190.
- [4] Mirzaei, A.A. Vahid, S. feyzi, M. Adv. Phy. Chem, Doi: 10.1155/2009/151489.

Conformational analysis of vitamin P in solution by theoretical approaches and experimental validation

Mina Ghiasi, Salman Taheri, Mohsen Taffazoli

Department of Chemistry, Faculty of Science, Alzzahra University, Vanak, Tehran 1234, Iran.

(Email:ghiasi@alzahra.ac.ir)

Keywords: **Rutin, Karplus equation, Coupling constants, 2D NMR.**

1. Introduction

Bioflavonoids are benzo-gamma-pyrone derivatives of plant origin with wide range of physiological activities such as antioxidant, antimicrobial, anti-inflammatory, antiallergenic, antiviral, and anti-tumor properties. Rutin, Figure 1. Rutin has more commonly been used in human medicine for the treatment of lymphoedema following axillary lymph node excision so it has less toxicity to human body and has the potential to be novel, environmentally friendly insecticides. Hence, it is necessary to develop methods for the structure determination of rutin in pharmaceutical preparations [1, 2]. So we study the structure of rutin in solution by advance technique of NMR spectroscopy and theoretical methods.

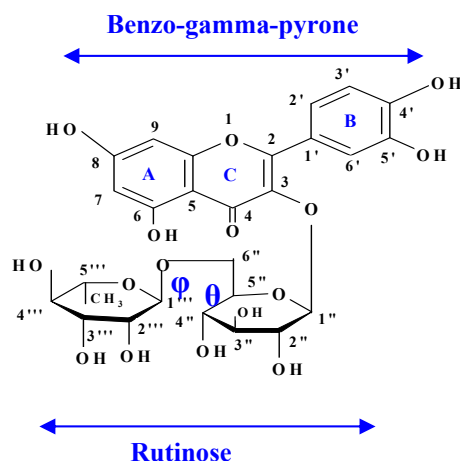


Fig. 1. Chemical structure of vitamin P.

2. Methods

NMR measurements:

¹H NMR, ¹³C NMR, ¹H-¹H COSY, HMQC and HMBC spectra of rutin were taken at 298 K in DMSO (99.99% D) on a Bruker DRX500 operating at 500.133 MHz for ¹H and 125.770 MHz for ¹³C, using 5mm broad band inverse probe with sufficient digital resolution to ensure errors ≤0.1 Hz in the measured J-couplings.

2D correlation spectroscopy (COSY) was used to confirm ¹H assignments. Heteronuclear multiple quantum correlation (HMQC) and heteronuclear multiple bond correlation (HMBC) were used for ¹³C assignments, Figure 2 shows the HMQC of this compound.

Calculation of chemical shifts and NMR spin-spin coupling constants :

NMR computations of absolute shieldings were performed using the GIAO method at the DFT optimized structure in present of solvent. ¹H-¹H and ¹³C-¹H spin coupling constants in rutinose, were obtained by finite field (Fermi contact) double perturbation theory calculations at the B3LYP/6-31G* level. Equation 1 to 3 that describe the dependencies of ²J_{H-H}, ³J_{H-H} on ω and θ were parameterized from the calculated couplings using a least-squares procedure.

$$^3J_{H5,H6R} = 5.07 + 0.49\cos(\omega) + 0.88\sin(\omega) - 0.15\cos(2\omega) + 4.65\sin(2\omega) \quad (\text{rms}=0.27 \text{ Hz}) \quad (1)$$

$$^3J_{H5,H6S} = 4.86 - 1.31\cos(\omega) + 0.07\sin(\omega) + 4.5\cos(2\omega) + 0.06\sin(2\omega) \quad (\text{rms}=0.18 \text{ Hz}) \quad (2)$$

$$^2J_{H6R-H6S} = -11.02 + 0.32\cos(\omega) - 2.22\cos(\theta) \quad (\text{rms}=0.22 \text{ Hz}) \quad (3)$$

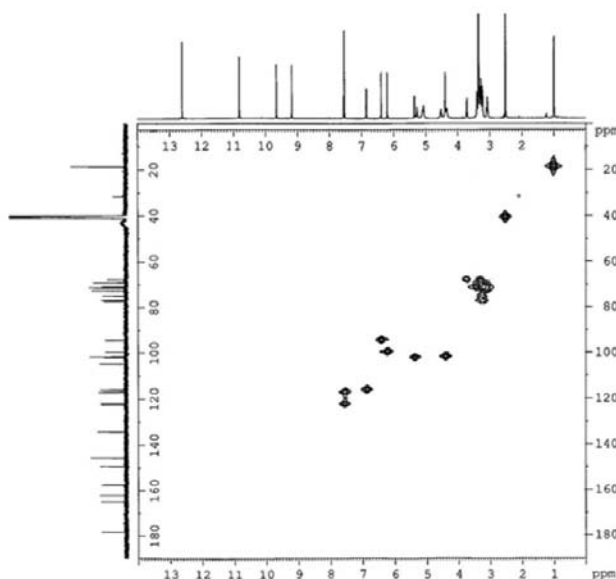


Fig. 2. HMQC spectrum of rutin in DMSO at 298 K.

3. Conclusions

Conformational studies of exocyclic hydroxymethyl group at disaccharide rutinose in rutin have relied heavily on the use of $^3J_{\text{HH}}$ values to estimate rotamer populations in solution. The strategy was first to obtain experimental data on chemical shifts, $^3J_{\text{HH}}$ and $^2J_{\text{HH}}$ from extracted rutin. These data were then used to test the ability of DFT methods to predict reliable chemical shifts and coupling constants. The good agreement between experimental and theoretical data confirms the accuracy of B3LYP/6-312G* method for this kind of molecules.

The results show $^3J_{\text{HH}}$ values in hydroxymethyl fragments are determined mainly by the C-C torsion angle (ω) and less so by the C-O torsion angle (θ). Importantly, in the absence of a hydroxyl proton on O₆, when the hydroxyl group is substituted for example in a (1→6)-glycosidic linkage, the $^2J_{\text{HH}}$ is determined mainly by the C-O torsion angle (θ).

Also this report generates new theoretical treatments in carbohydrates that make feasible their interpretation in oligosaccharide conformational analysis. The present findings have significant contribution not only for studies of oligosaccharides but also for related studies in oligonucleotides.

References

- [1] P. M. Aron and J. A. Kennedy, *Mol. Nutr. Food Res.*, 52 (2008) 79.
- [2] B. Halliwell, *Cardiovascular Research*, 73 (2007) 341.

**Hydrogenolysis of n-hexane over Al₂O₃-Supported Ni-Co catalysts**M. H. Peyrovi^a, B. Sabour^{a*}, T. Hamoule^a, R. Sadeghi^a^a Department of Chemistry, Shahid Beheshti University, Evin, Tehran, Iran(Email: m-peyrovi@cc.sbu.ac.ir)**Keywords:** hydrogenolysis, Ni- Co/ Al₂O₃, catalyst, n-Hexane**1. Introduction**

Hydrogenolysis of saturated hydrocarbons is a catalytic reaction, in which cleavage of C-C bond takes place in the presence of catalyst and hydrogen [1]. Conversion of heavier petroleum fractions to lighter one with higher value is one of the most important industrial applications of hydrogenolysis reactions. Hydrogenolysis reaction is also used as a model reaction in the investigations of catalysts designed for steam reforming of hydrocarbons [2]. Hydrogenolysis is a structure sensitive reaction, and takes place in metal active sites only [3]. Transition metals of Group VIII B have shown the highest activity and selectivity for these reactions [4].

2. Methods

The catalysts used for this study were prepared by co-impregnation of γ -Al₂O₃ (S_{BET} =200 m²/g, pore volume=0.7 m³/g) with aqueous solutions of Ni(NO₃)₂·6H₂O and Co(NO₃)₂·6H₂O at appropriate concentration; and atomic percentage of each metal in bimetallic samples varied from 0-20% (Table 1). After impregnation and drying in air oven at 100°C for 12 h, they were precalcined at 400 °C for 5h and then reduced at 500°C for 5h with a deoxidized and dried hydrogen flow of 30 cm³/min. A vertical fixed-bed quartz reactor with 9 cm length and internal diameter of 1.5 cm operating at atmospheric pressure was used for hydrogenolysis of n-hexane. Changes in activity and selectivity were obtained with respect to changes of percentage composition of Ni-Co catalyst and temperature (200-320°C) at constant ratio of H₂/HC=9.

3. Results and discussion

In this work the effect of composition, temperature and calcination on activity and selectivity of catalysts were studied. Catalysts showed high activity as temperature increased at first but activity decreased sharply during the first minutes and after almost 2h the activity of the catalysts was constant to time. Results have shown that uncalcined catalysts with high percent of Ni showed higher activity than calcined catalysts with the same composition, whereas uncalcined catalysts with high percent of Co showed lower activity than calcined catalysts with the same composition (Table 2). The results showed that by using catalyst with high percent of Ni the single hydrogenolysis occurs mostly; and the cobalt catalysts had more tendency to the multiple hydrogenolysis. Increasing the temperature leads to a strong increase in the selectivity for methane, a dramatic decrease in the selectivity for pentane, but no significant change in the selectivity for propane.

Table 1. Property of calcined catalysts

Catalyst	Composition (wt. %)			S_{BET} (m ² /g)	Pore volume (m ³ /g)
	Al ₂ O ₃	Co	Ni		
101-2	80	20	0	165	0.41
102-2	80	16	4	159	0.39
103-2	80	12	8	167	0.41
104-2	80	10	10	160	0.41
105-2	80	8	12	158	0.39
106-2	80	4	16	160	0.38
107-2	80	0	20	161	0.37

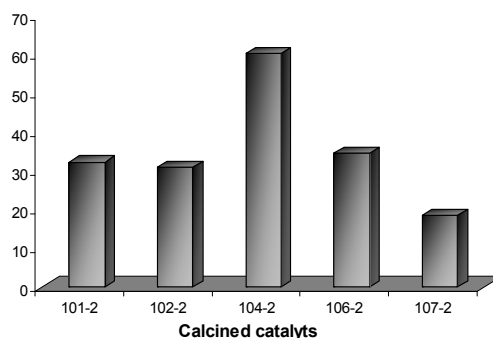


Fig. 1. Activity of calcined catalysts at 260°C

4. Conclusions

A series of bimetallic catalysts Ni-Co deposited on $\gamma\text{-Al}_2\text{O}_3$, with the same (Ni-Co) metal atom content (20 wt %) but various Ni/Co ratios, has been prepared and characterized by XRD, SEM, BET and atomic absorption spectroscopy. Results indicated that uncalcined catalyst 101-1 (16% Ni, 4% Co) and calcined catalyst 104-2 (10% Ni, 10% Co) have both high activity and selectivity for cleaving of terminal C-C bond, i.e. single hydrogenolysis. The effect of calcination on catalytic behavior was studied at mentioned conditions. The results showed that by using nickel catalyst the single hydrogenolysis occurs mostly; and the cobalt catalysts had more tendency to the multiple hydrogenolysis.

References

- [1] A. Majeste, S. Balcon, M. Guerin, C. Kappenstein, and Z. Paal; *Journal of Catalysis* 187 (1999) 486–492
- [2] T. Borowiecki, R. Dziembaj, M. Drozdek; *Applied Catalysis A: General* 247 (2003) 17–25
- [3] R.J. Chimentao, G.P. Valenc, a b, F. Medina; *Applied Surface Science* 253 (2007) 5888–5893
- [4] Francüois Locatelli, Jean-Pierre Candy, Blaise Didillon, Gerald P. Niccolai; *J. Am. Chem. Soc.* 123 (2001) 1658-1663



Adsorption of Atomic Hydrogen on V(110)

B. Khezri^a, H. Hooshyar^b, S. Khanahmadzadeh^c

^aDepartment of Chemistry, Islamic Azad University, Mahabad Branch, Mahabad, Iran

(Email: khezry55@yahoo.com)

^{b, c}Department of Chemistry, Islamic Azad University, Mahabad Branch, Mahabad, Iran

Keywords: VASP, V(110), Adsorption of Atomic Hydrogen, Surface calculation

1. Introduction

Both the clean surface as well as the C and O contaminated surface (i.e. C and O were coadsorbed to H) were considered in our models. In addition, we also studied the mechanism of absorption and diffusion of hydrogen into bulk V because of the well-known property of V of storing hydrogen.

2. Computational methods

All calculations presented in this paper were performed with the Vienna Abinitio Simulation Package (VASP). The surface calculations were done at the calculated bulk lattice parameter. Most calculations were done with a $p(2 \times 2)$ super cell with 7 layers within a repeated slab model relaxing the first and second layers of V(100). For modeling adsorption, the adatoms were placed on both surfaces of the slab.

A vacuum of about 11 Å (or 7 V layers) was chosen for all calculations. For the majority of calculations $4 \times 4 \times 1$ k-points were used after convergency tests with up to $16 \times 16 \times 1$ k-points. Tests with more layers (7, 9, 11, 13 layers respectively, $10 \times 10 \times 1$ k-points each) showed that a 7 layer model leads to well converged results for the atomic geometries and the energies. The convergence tests with more k-points and thicker layers indicate an average accuracy of 20 meV per adatom. The geometry was optimized until all forces were smaller than 0.02 eV/Å.

3. Results and Discussion

Clean V (110)

As described in our previous paper, the clean V(110) surface shows a strong contraction between first and second layer. The calculated value depends on the potential that was applied. In case of the ultra-soft pseudopotential used in this study, the interlayer distance between first and second layer is reduced by 0.235 Å (about 15%) as compared to the experimental 0.13 Å. The reason for this apparent discrepancy is also described in.

Comparison of the different adsorption sites for c (2×2) coverage

In our study, we considered fourfold coordinated hollow (H4), twofold coordinated bridge (B2) and finally one-fold coordinated top (T1) sites. To get a feeling for the relative stability of the different sites, we first calculated a $c(2 \times 2)$ type coverage of 0.5.

4. Conclusion

Our theoretical work tries to explain the experimental facts of, giving a study of H desorption from V(110). It can be shown that the surface quality (structure, chemical composition) plays an important role with respect to desorption energies. From several theoretical models we conclude that all surface H4 sites should be occupied, either by H or contaminants as C or O. Desorption from these sites will not take place as the adatoms are bound very strongly.

Desorption will rather occur from surface B2 sites and the B2-corresponding sites of the subsurface region and bulk. For a coverage higher than 1.65 ML H, no more surface B2 sites will be occupied and subsurface and bulk H can desorb directly through the free B2 sites. Also, in case of C or O contaminations we have shown that the B2 surface sites close to C or O in H4 sites, are empty and therefore give way for H desorbing from below.

Because there are some uncertainties in the assignment of the experimental desorption peaks, it is not clear if the atoms adsorb on the surface or diffuse (are absorbed) into the vanadium material. We therefore use the nomenclature "ad/bsorption" energy.



References:

- [1] G. Krenn, C. Eibl, W. Mauritsch, E.L.D. Hebenstreit, P. Varga, and A. Winkler. Surf. Sci., 445:343, 2000.
- [2] S. Crampin and P.J. Rous. Surf. Sci., 244:L137, 1991.
- [3] M. Beutl, J. Lesnik, E. Lundgren, C. Konvicka, P. Varga, and K.D. Rendulic. Surf. Sci., 447:245, 2000.
- [4] H.B. Nielsen V. Jensen, J.N. Andersen and D.L. Adams. Surf. Sci., 116:66, 1982.
- [5] W. Bergermayer, R. Koller, C. Konvicka, M. Schmid, G. Kresse, J. Redinger, P. Varga, and R. Podloucky. Surf. Sci., 497:294, 2002.

**Composition and interaction of triton X-100 and dtmac surfactants at toluene/water interface at 25 °C**

J. Saïen and S. AsadAbadi*

Department of Applied Chemistry, Faculty of Chemistry, University of Bu-Ali Sina, 65174, Hamedan, Iran

(Email: si.asadabadi@gmail.com)

Keywords: *Binary adsorption, Molecular interaction, Triton X-100, Dodecyltrimethylammonium Chloride, NIBM Theory***1. Introduction**

When two phase liquids are brought into contact, the interface thus formed possesses free surface energy. This surface energy is numerically equal to the interfacial tension [1]. The interfacial tension is an important property of organic-water-surfactant systems. It is a key parameter in inter-phase hydrodynamic and mass transfer operations. The presence of contaminants in most industrial grade chemicals is inevitable. The aim of this work is to investigate the simultaneous adsorption of two well-known surfactants, Triton X-100 and dodecyltrimethylammonium Chloride (DTMAC), at the interface of toluene/water, a recommended high interfacial tension system for liquid-liquid extraction [2]. In this regard Solutions of surfactant mixture are generally used for investigating the influence of contamination in operating conditions. The mole fraction of the adsorbed compounds in the mixed adsorbed monolayer for these systems is estimated by the Non Ideal Binary Mixtures (NIBM) theory and the molecular interactions between the two surfactants in the monolayer are obtained.

2. Methods

The interfacial tension of the samples was determined by the "drop-weight method" which is a reproducible method and has been used by other investigators. The aqueous phase was held in a narrow glass syringe conducted by an adjustable syringe pump and flowed through a rigid tube to the nozzle in the stagnant organic phase. A very low flow rate of aqueous phase was conducted to the nozzle and drops were formed very slowly at the tip of nozzle. Knowing the flow rate and number of drops per a measured time, drop volume can be calculated. The whole organic media and conducting tube was thermostated with a precision of ± 0.1 °C. Densities were measured at 25 °C using a density meter (Anton Parr DMA 4500).

The relationship between drop volume, V , and the nozzle radius, r , has been empirically determined in a careful experimental study by Harkins and Brown [3]. Thus:

$$\gamma = \frac{V \Delta \rho g}{r} \phi \quad (1)$$

where ϕ is a constant and should be obtained from the tables of Harkins and Brown [3], or it can be calculated from the appropriate empirical function [4]. The reliability of the method was examined by measurement of the interfacial tension of pure toluene/water at 25 °C which was in close agreement with the values reported in the literature [5].

3. Results and discussion

The interfacial tension data, for individual surfactants, are in excellent agreement with Szyskowski equation [6] as is shown by solid curve lines in Fig. 1:

$$\gamma = \gamma_0 - nRT\Gamma_m \ln(1 + K_L C) \quad (2)$$

where γ_0 is the interfacial tension for clean chemical system ($C = 0$) and Γ_m and K_L are the maximum interfacial concentration (saturated interface) of the adsorbed compound, and the Langmuir equilibrium adsorption constant respectively. The concentration is used in unit of molarity.

The variation of interfacial tension versus total concentration of surfactants is presented in Fig. 1. As it is shown it decreases significantly with surfactant concentration. Variation is non-linear, with higher changes in lower amount of surfactants within the range used. The mole fraction of the adsorbed compounds in the mixed adsorbed monolayer at interface can be estimated by the NIBM theory [7]:

$$\frac{X^2 \ln(\alpha C_{12} / C_1^0 X)}{(1 - X)^2 \ln[(1 - \alpha) C_{12} / C_2^0 (1 - X)]} = 1 \quad (3)$$

Where α is the molar fraction of compound 1 (Triton X-100) in the bulk solution, C_1^0 , C_2^0 and C_{12} are the total bulk molar concentration of compound 1, 2 and their mixture respectively, to give a specified equilibrium interfacial tension. The molecular interaction between the two compounds in the mixed adsorption monolayer, β , is obtained by [6]:

$$\beta = \frac{\ln(\alpha C_{12} / X C_1^0)}{(1 - X)^2} \quad (4)$$

The variation of X and β with the bulk mole fraction of Triton X-100 is shown in Figs. 2 and 3. Bulk mole fractions more than 0.2 exhibit no agreement with the adsorbed monolayer and NIBM theory, however, interface composition of Triton increases drastically at very low α values and then varies mildly. The interaction, on the other hand, shows strong dependency on the range of α showing a maximum absolute value at $0.05 < \alpha < 0.1$ and a minimum at $\alpha \cong 0.01$.

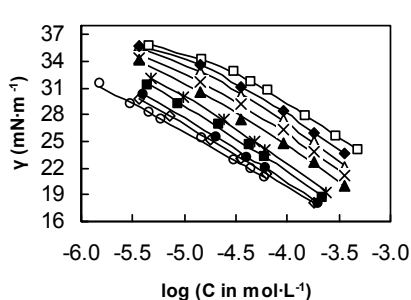


Fig. 1. Variation of interfacial tension with total Concentration at Triton mole fraction: (\square) 0, (\blacklozenge) 0.005, (\blacktriangle) 0.01, (\times) 0.05, (\blacktriangle) 0.1, ($*$) 0.2, (\blacksquare) 0.4, (\bullet) 0.6, (\diamond) 0.8 and (\circ) 1.

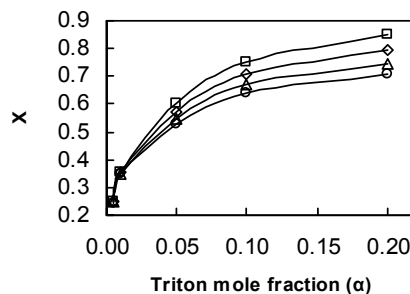


Fig. 2. Variation of X with Triton mole fraction at interfacial tension: (\square) 30, (\diamond) 28, (\blacktriangle) 26, (\circ) 24 mN/m.

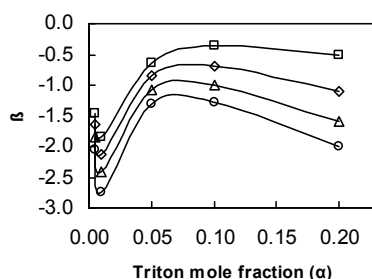


Fig. 3. Variation of β with Triton mole fraction at interfacial tension: (\square) 30, (\diamond) 28, (\blacktriangle) 26, (\circ) 24 mN/m.

4. Conclusions

The interfacial tension of toluene/water decreases with quite different trends when Triton X-100 or DTMAC are present. For binary mixtures, intermediate values are relevant. Interfacial mole fraction of surfactants varies regularly with interfacial tension and bulk mole fraction, α , however, strong dependency on the range of α is appropriate for the molecular interaction. The lowest attraction is achieved when Triton mole fraction is within (0.05 - 0.1).

References

- [1] G.W. Castellan, Physical Chemistry, 3rd ed, Addison-Wesley, Menro Park, CA, 1983.
- [2] T. Misek, Recommended Systems for Liquid Extraction Studies, Pub. Instn. Chem. Engs. for EFCE 1978.
- [3] F. Daniels, J.W. Williams, P. Bender, R.A. Alberty, C.D. Cornwell, J.F. Harriman, Experimental Physical Chemistry, 7th ed, McGraw-Hill Pub, USA, 1970.
- [4] J. Drelich, C. Fang, C.L. White in: Encyclopedia of Surface and Colloid Science, by: A.H.T. Hobbard, Marcel Dekker, Inc, New York, 2003.
- [5] J. Fu, B. Li, W. Zihao, Chem. Eng. Sci. 41 (1986) 2673.
- [6] D.K. Chattoraj, K.S. Birdi, Adsorption and Gibbs Surface Excess, Plenum, New York, 1984.
- [7] M.J. Rosen, Q. Zhou, Langmuir, 19 (2003) 4555.



Equilibrium modeling of liquid-phase adsorption of azo dye acid red 57 on free and immobilized dead fungal biomass of *aspergillus niger*

H. Malekhoseani, K. Mahanpoor, A Soufi, N.Niazi Hesar Sefeedi

Department of Applied Chemistry, Faculty of Science, Islamic Azad University of Arak, Arak, Iran

(Email: hhossein1@yahoo.com)

Keywords: Acid Red 57, Biomass, *Aspergillus niger*

1. Introduction:

Industrial effluents often contain residual dye which affects water quality and may become a threat to public health, since certain azo dyes or their metabolites (e.g. aromatic amines) may be highly toxic and potentially carcinogenic [1]. There are a few studies on dye removal using dead fungal biomass [2-6]. The study of adsorption equilibrium and kinetics is essential in supplying the fundamental information required for the design and operation of adsorption equipments for wastewater treatment. In this study, dead fungal biomass of *Aspergillus niger* (free and Immobilized on polyurethane foam) was used as a biosorbent to remove a dye, Acid Red57, from an aqueous solution. Equilibrium study provides fundamental information required to evaluate the affinity or capacity of an adsorbent, which is one of the most important criteria in selecting a suitable adsorbent [7].

2. methods

2.1. Dye solution preparation

The azo dye, Acid Red 57, was obtained from Rang Azar company (Iran) and used without further purification. The molecular structure of AR 57 is shown in Fig.1.

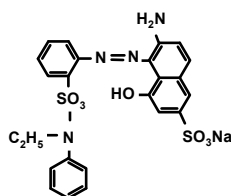


Fig. 1. Molecular Structure of Acid Red 57

Dye solution was concentration of 50 mg/l.. Dilute HCl or NaOH (0.01-1.0 M) was used for pH adjustment in order not to increase the volume of samples too much and keep the error created by pH adjustment in a reasonable range. Absorbance values were recorded at the corresponding maximum absorbance wavelength (λ_{max}) by a UV/VIS Spectrophotometer, (Shimadzu 160A). .

2-2. Microorganisms, medium and cultivation

The *A. niger* ATCC 5050, (prepared from center of Iranian industrial and science research, Iran), was used in this study. Spores from an established culture (6-7 days old) incubated on potato/glucose agar slants at 30 °C were used for the preparation of inoculate. The growth medium contained the following (per liter): 30 g starch, 1 g KH PO₄, 0.5 g MgSO₄·7H₂O and 1 g peptone. The pH was adjusted to 5.0 before sterilization. The polyether-polyurethane foam material (Iran foam Company, Tehran, Iran) used for the immobilization was purchased from the market. The foam, which had a porosity of 0.92-0.98, was cut into cubes of 2×2×2 mm in size. These were washed with distilled water and then submerged in 500-ml Erlenmeyer flasks containing 100 ml growth medium (previously autoclaved for 20 min at 120 °C). The biomass was washed with generous amounts of deionized water until the pH of the wash solution was close to that of deionized water(pH=6.5) . In order to confirm that all *A. niger* free biomass and immobilized on polyurthan foam biomass used in the study was dead, biomass was autoclaved for 30 min at 120°C and 18 psi, and then dried at 60-70 °C for 36 h in a drying oven. The powder with particles less than or equal to 150 μ m, which was defined by the sieve size, was used as biosorbent in the study.

3. Results and discussion

3.1. Adsorption equilibrium: The adsorption equilibrium data of the three adsorption systems were fitted with the Langmuir, the Freundlich, the Redlich–Peterson, and the Fritz–Schlunder equation. In order to get the best fitting, Newton optimization procedure was employed to minimize the root mean square (RMS) of the residuals between theoretical and experimental solid phase concentrations, denoted by $q_{e,cal}$ and $q_{e,exp}$ respectively. There are two kinds of RMS; the normalized RMS weights all points equally, while the nonnormalized RMS weights the actual error at all points,

$$Normalized\ RMS = \sqrt{\sum_{i=1}^N (1 - q_{e,cal}/q_{e,exp})^2 / N}$$

$$Nonnormalized\ RMS = \sqrt{\sum_{i=1}^N (q_{e,cal} - q_{e,exp})^2 / N}$$

Where N is the number of points on a fitted experimental curve. The results of the fitting procedure are presented in Table 1. Table 1 shows that, for free biomass and immobilized biomass systems, both the Redlich–Peterson isotherm and the Fritz–Schlunder isotherm could yield good fits over the whole concentration range.

Table1. Isotherms data for free biomass and immobilized biomass systems in T=298 K Initial concentration of Dye= 30 ppm and pH=3.5

Isotherm model	Free biomass		Immobilized biomass	
	Parameter values	Nonnormalized RMS	Parameter values	Nonnormalized RMS
Langmuir	$K_L=1.72$ $a_L=0.0247$ $K_L/a_L=95.4$	4.24	$K_L=1.88$ $a_L=0.0304$ $K_L/a_L=94.56$	5.68
Freundlich	$K_F=21.44$ $n_F=0.315$	8.84	$K_F=21.5$ $n_F=0.351$	7.32
Redlich-Peterson	$K_R=2.97$ $b_R=0.0845$ $=0.894\beta$ $K_R/b_R=47.9$	1.89	$K_R=3.64$ $b_R=0.0962$ $=0.925\beta$ $K_R/b_R=48.7$	2.81
Fritz-Schlunder	$k_s=6.44$ $a_s=0.014$ $b_1=0.753$ $b_2=0.685$	1.74	$k_s=9.23$ $a_s=0.241$ $b_1=0.784$ $b_2=0.693$	2.56

References

- [1] Styliadi, M., Kondarides, D.I., Verykios, X.E., Appl Catal B: Environmen., 2003, vol. 40, p. 271.
- [2] Benefield, L.D., Randall, C.W., Biological Process Design for Wastewater Treatment., Prentice-Hall, Englewood Cliffs, 1980.
- [3] Banat, I.M., Nigam, P., Singh, D., Marchant, R., Bioresour. Technol., 1996, vol. 58, p. 217.
- [4] Mou, D.G., Lim, K.K., Shen, H.P., Biotechnol. Adv., 1991. vol. 9, p. 613.
- [5] Zhou, J.L., Banks, C.J., Chemosphere., 1993. vol.127, p.607.
- [6] Gallagher, K.A., Healy, M.G., Allen, S.J., Biosorption of synthetic dye and metal ions from aqueous effluents using fungal biomass. In: Wise, D.L. Ed., Global Environmental Biotechnology. Elsevier, Amsterdam, 1997.
- [7] R.T. Yang., Gas Separation by Adsorption Processes., Butterworths, London, 1987.

Nanochemistry

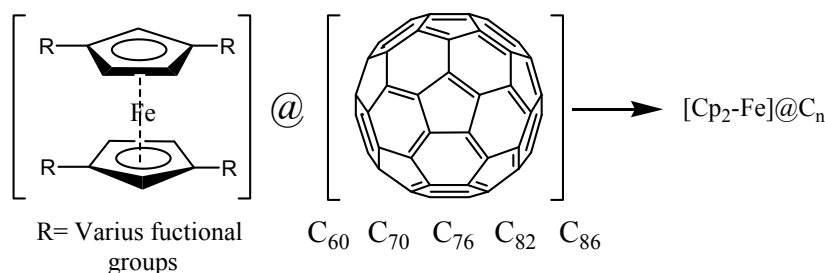


Theoretical structural relationship and electrochemical properties study of [Cp₂-Fe]@C_n complexes**Avat (Arman) Taherpour^{*a}, Rouhollah Jalajardi^b**^aChemistry Department, Faculty of Science, Islamic Azad University, P. O. Box 38135-567, Arak, Iran^bChemistry Department, Payamenoor University, Zanzan Branch, P. O. Box 45138-69987, Zanzan, Iran

E-mail: avatarman.taherpour@ gmail.com

1. Introduction

Ferrocene (Cp₂-Fe) and its derivatives are the broad-spectrum of organometal compounds which is commonly used in electronics and semiconductors. The electrochemical oxidation of the ferrocene and some of its derivatives were studied at various carbon electrodes. Since the discovery of fullerenes (C_n), one of the main classes of carbon compounds, the unusual structures and properties of these molecules and by the many potential applications and physicochemical properties have been discovered and were introduced. Up to now, various empty carbon fullerenes with a different number "n," such as C₆₀, C₇₀, C₇₆, C₈₂ and C₈₆ and so on, have been obtained. Topological indices are digital values which are assigned based on chemical composition. These values are purported to correlate chemical structures with various chemical and physical properties such as the free-energies of electron transfer ($\Delta G_{et(1)}$ to $\Delta G_{et(4)}$). They have been successfully used to construct effective and useful mathematical methods for establishing good relationships between structural data and the physical properties of these materials.

**2. Mathematical method**

The number of carbon atoms of these the fullerenes (C_n) was utilized as a structural index for compounds. All graphing operations were performed using *Microsoft Office Excel-2003*. The number of carbon atoms in these the fullerenes (C_n) seems to be a useful numerical and structural value for characterizing the empty fullerenes. For modeling, both linear (MLR: Multiple Linear Regressions) and nonlinear (ANN: Artificial Neural Network) models were examined in this study. Other indices were examined and the best results and equations for extending the physicochemical and electrochemical data were chosen.

3. Results and discussion

By using the equations which obtained in this modeling, it is possible to calculate the values of $\Delta G_{et(1)}$ to $\Delta G_{et(4)}$ of [Cp₂-Fe]@C_n supramolecular complexes. The $\Delta G_{et(n)}$ (n=1-4) for [Cp₂-Fe]@C_n supramolecular complexes (C_n=C₆₀, C₇₀, C₇₆, C₈₂, C₈₆, C₇₈, C₈₄, C₁₂₀, C₁₃₂, C₁₄₀, C₁₄₆, C₁₅₀, C₁₆₀, C₁₆₂, C₂₄₀, C₂₇₆, C₂₈₈ and C₃₀₀) are predicted by using the appropriate equations.

By utilizing these results, the electron transfer energies of $\Delta G_{et(n)}$ (n=1-4) of the complexes between selected ferrocene derivatives ([Cp₂-Fe]) with fullerenes (C₆₀, C₇₀, C₇₆, C₈₂, C₈₆, C₇₈, C₈₄, C₁₂₀, C₁₃₂, C₁₄₀, C₁₄₆, C₁₅₀, C₁₆₀, C₁₆₂, C₂₄₀, C₂₇₆, C₂₈₈ and C₃₀₀) were approximated. The calculated values of the free electron transfer energies of $\Delta G_{et(n)}$ (n=1-4) for selected [Cp₂-Fe]@C_n supramolecular complexes (n = 60, 70, 76, 82 and 86) in the equations were interpreted. There was good agreement between the calculated and the predicted values. In lieu of increasing the number of carbons atoms in the fullerene structure, the values of $\Delta G_{et(n)}$ (n=1-4) decreased. It seems that electron transfer increases as the electron population in the C_n structures increases. The results indicate that these results related to the HOMO and LUMO gap of the fullerenes. The obtained results also shows that some of the free electron transfer energies $\Delta G_{et(n)}$ (n=1-4) values of [Cp₂-Fe]@C_n supramolecular complexes are negative. The supramolecular complex structures which were discussed here and the calculated values of $\Delta G_{et(n)}$ (n=1-4) corresponding to these supramolecular complexes were neither synthesized nor reported before.



References

- [1] Molina P., Pastor A., M. Jesu ' s Vilaplana M., and Desamparados Velasco M., *Organometallics* 16 (1997) 5836-5843.
- [2] Taherpour A. A., Chem. Phys. Lett., 469 (2009) 135-139.
- [3] Taherpour A. A., J. Phys. Chem. C 113 (2009) 5402.
- [4] Taherpour A. A., Chem. Phys. Lett., 483 (2009) 233-240.

**The effect of the calcined temperature on the TiO₂ nanoparticles size made with sol-gel process**Hossain Milani Moghaddam^{a,b,c}, Shahrooz Nasirian^{a,b}^a Physics Department, University of Mazandaran, Babolsar, Mazandaran, Iran^b Molecular Electronics Lab, physics Department, University of Mazandaran, Babolsar, Mazandaran, Iran^c Nanophysic lab, Hariri Scientific Foundation, Babol, Mazandaran, IranEmail: shahruz_nasirian@yahoo.com**Keywords:** TiO₂, TiCl₄, sol-gel method**1. Introduction**

In the past two decades, study of synthesized nanoparticles titanium dioxide has been important [1-11]. TiO₂ is used in ceramics, motor and vehicles' external surfaces (as a cover and antirub material) and etc. Specially, the utilization of TiO₂ is of particular interest due to its ability in solar cells (as a good photocatalysis). When TiO₂ is irradiated with wavelength greater than 390 nm, electron-hole pairs is generated. Some success in enhancing the photocatalytic activities is obtained by the preparation of TiO₂ nanoparticles [8]. In the present work, we have prepared different TiO₂ nanoparticles using some form of chemical synthesis, called sol-gel. By changing in mixing time and calcined temperature, particles size can be improved by this method.

2. Experimental

3 ml TiCl₄ is slowly (Approximately 1 to 3 drop per minute) added drop wise into 30 ml ethanol in Argon gas at room temperature. After adding all TiCl₄, a light yellow solution is obtained. The product is ultrasonic for 30 min. Then our product in temperature 80 °C changes into a dry gel (slightly humid). Finally the product is calcined with initial heating rate $7\left(\frac{C^{\circ}}{\text{min}}\right)$ in temperature 120, 300, 400 and 500 °C for 1 hour.

3. Results and discussion

With taking XRD patterns of TiO₂ powder and SEM micrographs, crystallite size of TiO₂ powder can be obtained between 5 nm to 25 nm. Fig.1 shows the nanosize crystallites under different calcined temperature in mixing time 120 min. According to Fig.1, the nanosize crystallites are smaller in calcined temperature 120 °C however its XRD pattern (Fig.3) show that the product is not calcined favourably. In Fig.2, we see TiO₂ peak (Anatase) is intensified and sharpened in mixing time 120 min and calcined temperature 500 °C. This indicates that the nanosize crystallites are crystallized better and more complete. The crystallite size of the particles has been estimated from the Debye-Scherrer's equation using the XRD line broadening as follows: $S = \left(\frac{K \lambda}{\beta \cos(\theta)}\right)$ where S is the crystallite size, λ the wavelength of the X-ray radiation

($Cu_K\alpha = 0.15406 \text{ nm}$), K a constant taken as 0.94, θ the diffraction half-angle and β is the line width at half maximum height. The crystallite size is 22 nm by XRD pattern for the calcined temperature 500 °C. The SEM micrograph (Fig.4) shows a right homogeneity in the surface of TiO₂ powder sample and nanoparticles have dimension less than 100 nm.

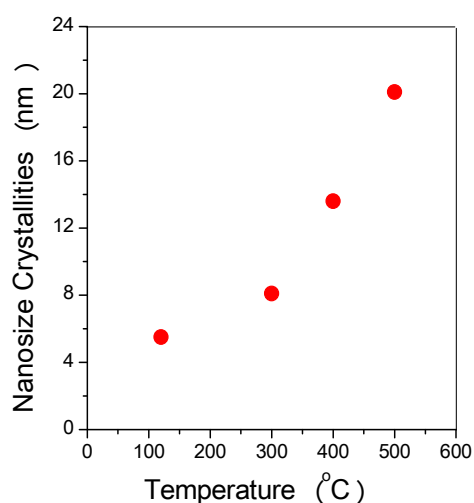


Fig. 1. Nanosize crystallinities, according to calcined temperature (mixing time is 120 min).

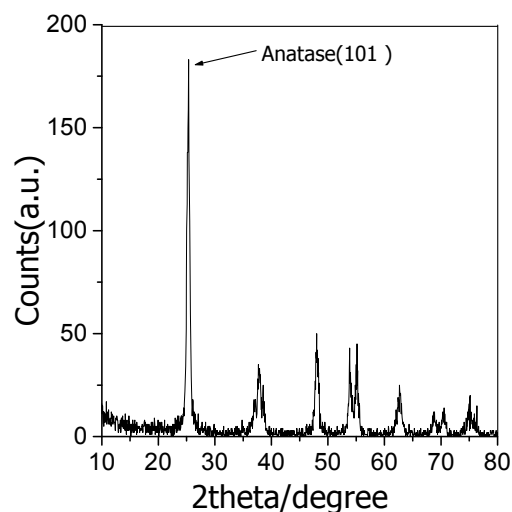
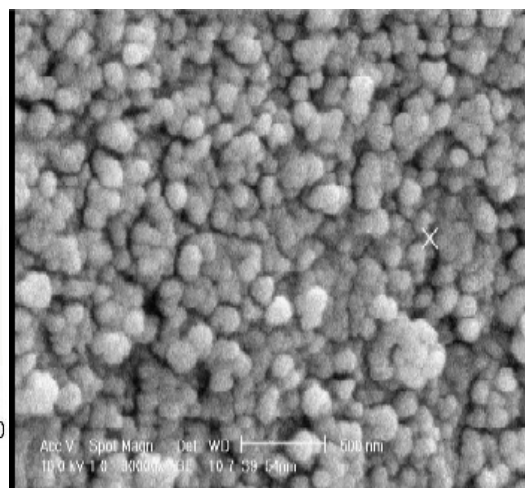
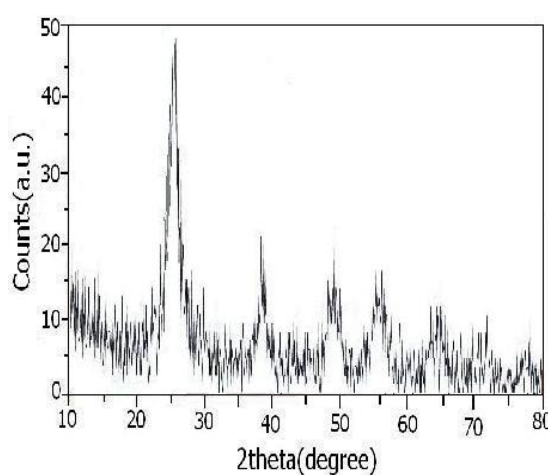


Fig. 2. XRD pattern of TiO_2 powder, calcined for 1 hour at 500°C (mixing time is 120 min).



References:

- [1] F.A.Deorsola, D. Vallauri, Powder Technology 190 (2009) 304–309.
- [2] Y.He, A.Tilocca, O.Dulub, A.Selloni³ and U.Diebold¹, Nature Material 8 (2009)585-587.
- [3] A.A.Ashkarran,M.R.Mohammadizadeh, Materials Research Bulletin 43 (2008) 522-530.
- [4] Ming-Zhou, Jian-Zhong Lie, Tat-Leung Chan, Chemical Engineering Science 63 (2008)2317-2329.
- [5] S.Mahshid , M.Askari , M.Sasani Ghamsari, Journal of Materials Processing Technology 189 (2007)296-300.
- [6] Y.Chen, An Lin, F.an, Power Technology 167 (2006)109-116.
- [7] J.Lee, Y.Yang, Journal of European Ceramic Society 25 (2005) 3573-3578.
- [8] O. Carp, C.L. Huisman, A. Reller, Progress in solid state chemistry 32 (2004)33-177.
- [9] Y.Bessekhouad, D.Robert, J.V.Weber, InterNational Journal of Photoenergy 05 (2003)153-158.
- [10] D.S.Lee, T.K.Liu, Journal of sol– gel Science and Technology 25 (2002) 121-136.
- [11] Y. Zho et al., Journal of materials science 35 (2000) 4049–4054.



Phase transition of Nanocrystalline ZnS thin films to ZnO thin films: study by TGA-DTA, EDX, XRD and Uv-Vis. techniques

Alireza Goudarzi^a, Gaffar Motedayen Aval^b, Reza sahraei^c, Chang-Sik Ha^{d,*}

^a Department of polymer Engineering, Golestan Univ., Gorgan, Iran

E-mail: goudarzi.alireza@gmail.com

^b Department of Chemistry, Tarbiat Moallem University, Tehran, Iran

^c Department of Chemistry, University of Ilam, Ilam, Iran

^d Department of Polymer Science and Engineering, Pusan National University, Busan 609-735, Republic of Korea

E-mail: csha@pusan.ac.kr

Keywords: Nanostructures, ZnO thin films, Phase transition, Optical properties

1. Introduction

Zinc oxide (ZnO) is a wide band gap semiconductor with hexagonal wurtzite structure [1] showing several outstanding physical properties for optical and electronic applications [2], ZnO has good photoconductivity and a high optical transparency in the visible and infrared spectral regions, and it has a large exciton binding energy that enables the use of ZnO thin films for organic light emitting diodes [3] and efficient UV lasers.

Thin films of ZnO can be used as a window layer as well as one of the electrodes in solar cells [4]. Along with these applications, ZnO films have also been used in gas sensors, and as the transducer of a biosensor, etc. In addition, ZnO films have interesting wetting properties, which are important for many industrial processes, such as cleaning, drying, painting, coating, adhesion, heat transfer, and pesticide applications.

In this work, we report the preparation of high quality (high transparency, high crystallinity and high adherence) nanocrystalline ZnO thin films via phase transition of nanocrystalline ZnS thin films by annealing at different temperatures.

2. Method

First, the nanocrystalline ZnS thin films on glass and quartz substrates were prepared by chemical bath deposition (CBD) method. The procedure of preparation of ZnS thin films has already been published by us [5]. The prepared ZnS thin films have been annealed in atmospheric air, at temperatures ranging from 200 to 700 °C, during 2 hours in furnace. The impact of the annealing temperature on the phase transition, nanostructure, and optical properties of ZnO films has been investigated by XRD, EDX, FE-SEM, UV- visible spectroscopy. The phenomena of phase transition of ZnS films to nanocrystalline ZnO films have been studied at temperatures ranging from 100- 900 °C by TGA- DTA.

3. Results and Discussion

The XRD patterns revealed that the peaks related to ZnO crystal lattice gradually appear with increasing of temperature. The XRD data also showed that the phase transition from cubic structure of ZnS to hexagonal-wurtzite of ZnO has been completed at 700 °C and their grain size increased with the increase of annealing temperature.

The TGA-DTA data shows that when temperatures arrive to 650 °C weight loss of sample will be 16%, which means in this temperature the ZnS changed to ZnO. The UV- Vis transmission spectroscopy showed that the obtained ZnO films were highly transparent (>90%) in the visible region. Besides, calculated band gap energy from UV- visible data of annealed films was 3.2 eV, which confirms the phase transition from ZnS ($E_g \sim 3.6$ eV) to ZnO ($E_g \sim 3.26$ eV). The EDX analysis during annealing also confirms the phase transition from ZnS to ZnO.

4. Conclusions

The ZnO thin films have been prepared on quartz substrates at temperatures ranging from 400 to 700 °C by annealing technique of ZnS thin films. The obtained ZnO thin films were highly transparent in visible range. The XRD and TGA-DTA measurements showed that the phase transition from the cubic structure of ZnS to hexagonal-wurtzite of ZnO has been



successfully happened at 700 °C. The results of XRD also showed that the crystallinity improves and grain size increases with the increase of annealing temperature.

References:

- [1] Malandrino, G., Blandino, M., Fragala, M., E., Maria Losurdo, M., Bruno, G., *J. Phys. Chem. C*, 112 (2008) 9595.
- [2] Özgür, Ü., Alivov, Y. I., Liu, C., Teke, A., Reshchikov, M. A., Doan, S., Avrutin, V., Cho, S.-J., Morkoç, H. *Appl. Phys. Rev.* 98(2005) 041301.
- [3] Kim, H., Horwitz, J. S., Kim, W. H., Qadri, S. B., Kafafi, Z. H., *Appl. Phys. Lett.* 83(2003), 3809.
- [4] Gao, Y., Nagai, M., *Langmuir* 22(2006), 3936.
- [5] Goudarzi, A., Motedayen Aval, G., Sahraei, R., Ahmadpoor, H., *Thin Solid Films*, 516 (2008) 4953.

The imbibition of liquids in microtubes

S. Gharangian, Y. Ghayeb, E. Keshavarzi*

Department of Chemistry, University of Technology, Isfahan, Iran

Email: keshavrz@cc.iut.ac.ir

Keywords: Imbibition, Microtube, Capillary action, Lucas-Washburn equation

1. Introduction

The transportation of liquids into the micro channel is important in many contexts: separation processes in zeolites; fluid transport in living organisms [1] and many other applications. The mobility of various liquids has been studied by in the last three decades.

The imbibitions of liquids in micro and nano channels are especially different from macro scale channels. This originates from the small dimension and their high surface-to-volume ratio. At such a small scale, surface-charging effect dominates the fluid behavior. Two major factors are involved in the diffusion of liquid in a micro/nano channel: ion diffusion and capillary action. The diffusion of ions into the channel covered by surface charges. Capillary action at air-liquid interface may also result in liquid filling. Such filling process strongly depends on liquid property, ion concentration, and the liquid-wall interface. [2]. On a macroscopic scale the rise of a fluid meniscus at height H over the entrance of a capillary is described by Laplace equation:

$$P_L = \frac{2\gamma \cos(\theta)}{R} \quad (1)$$

Where R is the channel radius, γ is the surface tension of the liquid, and θ the contact angles. In particular, for water with its surface tension σ of 72 mN/m, Eq.(1) yields that $P_L \sim 300$ bar for a pore with radius 5 nm. This corresponds to a hypothetical capillary rising height of 3 km. Which it is clear Eq.1 this can not be applied for micro and nano scales. In fact the time behavior of the imbibition of liquid into micro/nano channel follows from Lucas-Washburn law [4], which results from a competition of time invariant capillary forces driving the flow and an increasing viscous drag due to the increasing length of the paths advancing water front with the bulk reservoir [5], and the gravity force is much smaller than the surface tension and should be negligible. This equation predicts a \sqrt{t} law for the rise of the fluid meniscus $H(t)$ in the capillary with time t ,

$$H(t) = \left(\frac{\gamma_{LV} R \cos \theta}{2\eta} \right)^{1/2} \sqrt{t} \quad (2)$$

Where η is shear viscosity. The coefficient of \sqrt{t} is imbibition speed v_i , and it determines the dynamic of capillary rising.

Thus, we determine this ratio for different fluids in our experiment, to illustrate the relation between liquid imbibitions with ionic concentration and micro tube diameter.

2. Methods

In the present work, we have investigated the spontaneous imbibition of ionic-solution and nonionic-solution into microtubes glass with 42 μm and 35 μm mean diameter. We have demonstrated that velocity of liquid diffusion is controlled by liquids properties and the structure and dimension of microtube. In order to play with the complexity of the imbibing fluids we have chosen three different liquids; two of them are ionic-solution: zinc chloride (ZnCl_2) and sodium chlorate (NaClO_3), and one of them is nonionic-solution: n-heptanol.

To study of diffusion effect in microtubes, a droplet of each solution was gently released in the inlet chamber, then liquids spontaneously penetrating in the micro channel. The solution entered into channel path, which made the channels disappeared from the vision under an optical microscope. The filling was measured at 25°C by imaging the microflow along the capillary axis and the shape of the liquid-air interface.

The height uptake of zinc chloride and heptanol with different microtube diameter, versus t and \sqrt{t} are plotted in Fig.1 and Fig.2 respectively. For all investigated liquids we find distinct, monotonic increasing liquid uptake curves and in second curve in agreement with Washburn equation, the data point of our experiment, can be nicely fitted with straight lines. As these figure show, the imbibition speed decrease with diameter for all experiment liquid.



Fig.1 High uptake of $ZnCl_2$ as function of time (Fig.1.a) and \sqrt{t} (Fig.1.b) with different microtube diameter.



Fig.2 High uptake of heptanol as function of time (Fig.2.a) and \sqrt{t} (Fig.2.b) with different microtube diameter

3.Results

To interpret these curve we know that the solid in contact with a liquid bears a surface charge [5].The potential gradient exponentially decreases as the distance from the wall increases. This potential gradient can contribute to change of surface tension, thus influence liquid motion in the channels [4].In the other hand the contact angle can be changed by increasing the electric potential gradient thus electric field strength is changed at the interface. Surface charge density decrease when the diameter of microtube increase, so weak zeta potential gradient is generated across the channel, therefore the contact angle increase and according to that imbibitions speed is less than the situation that the diameter of microtube is shorter.



Fig.3 high uptake of $NaClO_3$ as function of time (Fig.3.a) and \sqrt{t} (Fig.3.b) with different concentration.

The height uptake of sodium chlorate with different concentration into microtube with 42 μm diameter, versus \sqrt{t} are plotted in Fig.3.As it is clear from these figures the imbibitions speed increase with concentration.When the ion concentration is high, a strong electric field is induced by surface charges close to the wall. This strong electric field induces the change of surface tension. The local field applied on the drop surface tends to pull the drop surface to the wall surface, which decreases the contact angle[2].SO according to that imbibitions speed is more than the situation that the concentration is low.

4.Conclusions

Electric field and surface tension induce the motion of liquids in micro/nano channels. As we have shown the imbibitions of fluids in microchannels is controlled by some properties of liquid such as, concentration, liquid-wall interaction, liquids surface tension and viscosity; and the structure and dimension of channel.

References

- [1] D. Dimitrov, A. Milchev, and K. Binder, Phys.Rev. Lett.99,054501 (2007)
- [2] Y. Liu, K. oh, J.G. bai, C-L. chang, W. Yeo, J-H. Chung, K-H. Lee, W.K. Liu, Comput. Methods Appl. Mech. Engrg 10.1016(2007)
- [4] R. Lucas, Kolloid-Z. 23, 15 (1918); E. W. Washburn, Phys.Rev. 17,273 (1921)
- [5] B. Schoch, *et al*,Rev. Mod. Phys., Vol. 80. No. 3 (2008)

Sonochemical method for synthesis of magnesium oxide nanoparticles

Robabeh Rezazadeh ^{a*}, Saeed Haghdar ^b

^a Department of Chemistry, Payam e Noor University of Sari, Sari, Iran

r_rezazadeh_kh@yahoo.com

^b Kara.Chem Company, Fax: +98 2144004396, Tehran, Iran

Keyword: Nanoparticles, Magnesium oxide, Ultrasonic Waves

1. Introduction

Magnesium oxide is obtained recently by the sol – gel process [1-4]. The oxide morphology and particle size depend on the preparation conditions (pH, gelling agent, calcinations rate and temperature). We report a new method for the preparation of MgO nanopowder. Preparation of the intermediate phase was obtained by the reaction of magnesium acetate with alkali solutions. The decomposition of intermediate has given highly monodispersed MgO particles. The morphology and particle size of products were examined using SEM.

2. Preparation of MgO nanoparticles

MgO nanoparticles were synthesized from magnesium acetate in water alcohol solution. In a typical reaction 10 g.L⁻¹ polyvinylpyrrolidone was dissolved in water ethanol solution (50:50 ratio) with intense stirring at room temperature. Subsequently, an aqueous solution containing 0.1 M of magnesium acetate was added at the same temperature and enough volume of tetra methyl ammonium hydroxide was slowly added into ultrasonicated solution of magnesium acetate and polyvinylpyrrolidone at 30 °C. Similar experiment was performed using 0.35 M of ammonia solution in place of tetramethylammonium hydroxide to study the effect of ammonia solution on the properties and morphology of nano size MgO powders produced. Suspension which has prepared in presence of ultrasonic wave was heated to obtain precipitation form. Finally, the obtained precipitation calcinated at 600 °C for 3h.

3. Results and discussion

3.1. Ultrasonication effect

In this method ultrasonic wave was one of the effective factors involved in synthesizing uniform nanostructured magnesium oxide. There are some other effective parameters in this suggested method including concentration of magnesium acetate, tetramethylammonium hydroxide, additive and synthesis temperature. The effect of all parameters was optimize by "one at a time" method [5]. In all optimized experiments the volume of 100 mL was used for magnesium acetate solution as a structure director additive and 50 mL for alkali solutions subsequently. The SEM images show that, the presence of ultrasonic waves makes magnesium oxide particles more uniform and smaller (Fig 1).

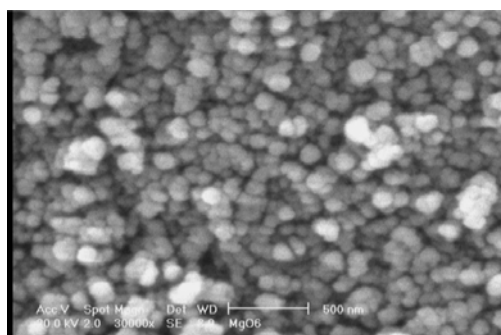


Fig 1. SEM image of sample which synthesized in the presence of ultrasonic waves.



3.2 Concentration optimization of reagents

SEM results showed that magnesium acetate concentration of 0.14 M produces more uniform and smaller particles . Therefore , the concentration of magnesium acetate 0.14 M was selected as optimizing concentration. At the optimum concentration of magnesium acetate hydroxide ions concentration was varied from 0.17 to 0.5 M . The SEM images of the synthesized samples showed that at hydroxide concentration of 0.34 M smaller and uniform particles of magnesium oxide can be produced.

3.3. Structure director

PVP concentration in synthesised solution was varied from 5 to 25 gl^{-1} to optimize the concentration of PVP and obtain the best structure for the final product of MgO . The SEM images show that at PVP concentration of about 10 gl^{-1} , magnesium oxide can be synthesized in excellent and more porous nanostructure .

4. Conclusions

Magnesium oxide can be synthesized in nanoscale in the presence of ultrasonic waves and PVPs as a structure director .

References

- [1] H.S. Choi, S.T. Hwang , J. Mater. Res. 15 (4) (2000) 842-845 .
- [2] T. Lopez, et al., J. Sol-Gel Sci. Technol. 13 (1-3) (1998) 1043-1047 .
- [3] M.A Aramendia, et al., J. Mater . Chem. 6 (12) (1996) 1943-1949.
- [4] B.Q. Xu, et al., Catal. Today 68 (1-3) (2001) 217-225.
- [5] J.C. Miller, J.N. Miller, Statistics for Analytical Chemistry, 2nd ed., Chichester, Horwood, 1988.

Characterization of SnO₂ nanoparticles prepared in presence of a ionic liquid by solvothermal methodA. Habibi-Yangjeh^a, V.Taghvaei^{b*}, M. Behboudnia^c^{a,b} Department of Chemistry, University of Mohaghegh Ardabili, Ardabil, Iran^c Department of Physics, Urmia University of Technology, Urmia, Iran.^b Email: vahidehtaghvaei@gmail.com**Keywords:** SnO₂, Nanoparticles, Ionic liquid**1.Introduction**

SnO₂ is an n-type semiconductor with a wide band gap (3.6 eV, at 300 K), and has been widely used as gas sensors, electrode materials, solar cells and catalysts [1]. Room-temperature ionic liquids (RTILs) have been widely studied as a new kind of reaction media owing to their unique physicochemical properties [2]. One of the largest barriers to the application of RTILs in various fields arises from their high-cost relative to conventional solvents. Solvothermal is one of the most efficient methods used to synthesize materials with different morphologies. It is simple, convenient and inexpensive [3].

2.Methods

The X-ray diffraction (XRD) pattern was recorded on Philips Xpert X-ray diffractometer. Diffuse reflectance spectra (DRS) recorded by a Scinco 4100 apparatus. Scanning electron microscope (SEM) image were obtained a LEO 1430VP apparatus.

The ionic liquid was [EMIM][EtSO₄] and synthesized according to the literature [4]. In order to examine adsorption capacity of the prepared nanoparticles, decolorization of methylene blue (MB) in dark was considered. The adsorption capacity, q_e (mol/g), of the prepared nanoparticles was calculated by a mass-balance relationship, which represents the amount of adsorbed dye per amount of the nanoparticles:

$$q_e = \frac{(C_0 - C_e)V}{W} \quad (1)$$

where C_0 and C_e are concentrations of the dye in solution (mol/dm³) at $t = 0$ and time of equilibrium. V is the volume of the solution (dm³), and W is the weight of dry adsorbent (g).

3.Results and discussion

The phase and purity of the samples were determined by XRD and the typical diffraction pattern is shown in Figure 1(a). It is clear from the figure that the peak broadening in the pattern indicates the SnO₂ nanoparticles formed are very small in size.

Fig. 1(b) exhibits diffuse reflectance spectra (DRS) of SnO₂ nanoparticles. Absorption maximum for the SnO₂ nanoparticles is in 310 nm. The band gap energy is increased compared to that of bulk SnO₂. The expansion of band gap (0.4 eV) or blue shift can be attributed to the quantum confinement effect of SnO₂ nanoparticles.

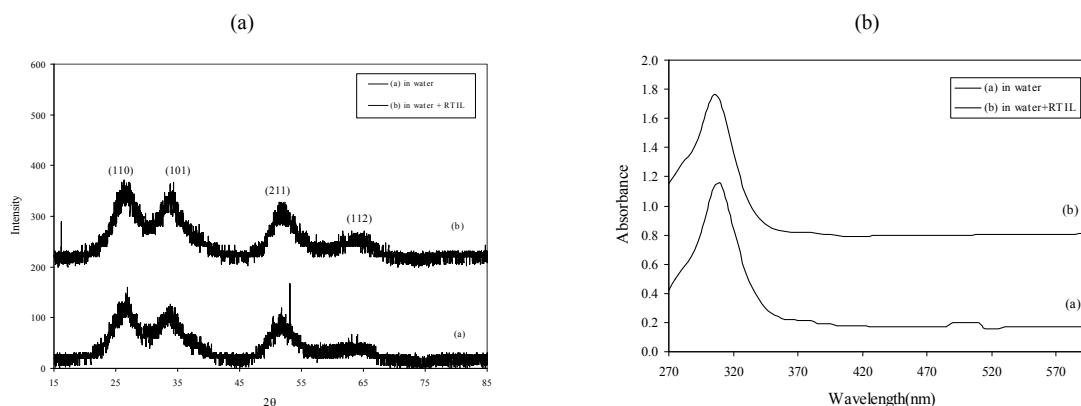


Fig.1 (a) The powder XRD pattern of SnO₂ nanoparticles and (b) the diffuse reflectance spectra (DRS) of SnO₂ nanoparticles.

Fig.2 exhibits morphology of the SnO₂ nanoparticles prepared in water and aqueous solution of the RTIL. It is evident that structure of the nanoparticles produced in presence of the RTIL have lower aggregation and the size of aggregated nanoparticles is small. Therefore the role of RTIL as a solvent is important in obtaining smaller nanoparticle size.

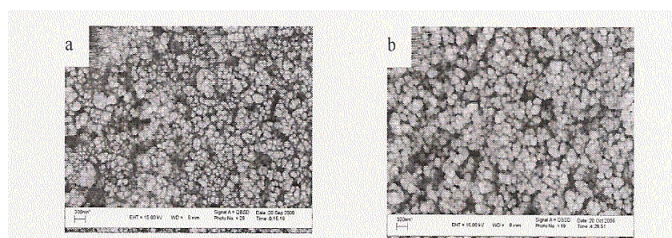


Fig. 2 The SEM images of SnO₂ nanoparticles prepared in (a) water and (b) aqueous solution of the RTIL.

Fig. 3 demonstrates the dynamic adsorption of MB on and SnO₂ nanoparticles prepared in (a) water, (b) aqueous solution of the RTIL and (c) bulk SnO₂. The values of q_e for MB adsorption on SnO₂ bulk, SnO₂ nanoparticles prepared in water and aqueous solution of the RTIL are 0.946×10^{-5} , 6.06×10^{-5} and 6.1×10^{-5} mol/g, respectively. It is clear that the adsorption ability of MB molecules on SnO₂ nanoparticles prepared is higher than that of bulk SnO₂.

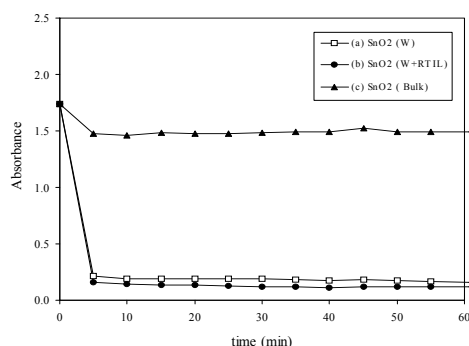


Fig. 3 Dynamic adsorption of MB at 25 °C on SnO₂ nanoparticles prepared in (a) water, (b) aqueous solution of the RTIL and (c) bulk SnO₂.

5. Conclusions

The method is simple and convenient route to obtain larger quantity of SnO₂ nanoparticles. The as-prepared SnO₂ nanoparticles show a blue shift of approximately 0.4 eV which can be attributed to quantum confinement effect of the SnO₂ nanoparticles. Investigation of adsorption capacity of the prepared nanoparticles reveals that the adsorption capacity of the prepared samples is considerably higher than the bulk SnO₂.

References:

- [1] Xi, L. Qian, D. Tang, X. Chen, C, Mater. Chem. Phys. 108 (2008) 232.
- [2] Welton, T. Coord, Chem. Rev. 248 (2004) 2459.
- [3] Thongtem, T. Phuruangrat, A. Thongtem, S, Ceramics International.
- [4] Gomez, E. Gonzalez, B. Calvar, N. Tojo, E. Dominguez, A, J. Chem. Eng. Data. 51 (2006) 2096.

Increasing the solubility of single wall carbon nanotube by adding four long functional groups

M. Foroutan, M Moshari*

Department of Physical Chemistry, School of Chemistry, College of Science, University of Tehran, Tehran, Iran.

Email: Mahshad.Moshari@khayam.ut.ac.ir

Keywords: MD Simulation, Solvation , Functionalized Nanotubes ,Water; RDF, Interaction Energ

1. Introduction

The insolubility of carbon nanotubes in water is generally considered as a significant barrier in both fundamental research and technological development toward the practical uses of SWCNTs. Thus, several chemical modification methods have been developed to functionalize and solubilize SWCNTs. In particular, the fictionalization of SWCNTs to introduce aqueous solubility has received much recent attention for investigations targeting potential biological applications of carbon nanotube [1].

2. Methods

Computer simulations of the structure of water-SWNT and water- FSWNT are carried out using a $2.8 \times 2.8 \times 3.3 \text{ nm}^3$ cubic computational cell with periodic boundary conditions applied in all three principal directions. The structure of glutamine which has been used as functional group in our study is $(\text{NHCH}_2(\text{CO})\text{C}_2\text{H}_4\text{C}(\text{CO})\text{NH}_2)$. 864 water molecules are placed in the cell to obtain the average density of water essentially equal to its experimental counterpart (1 kg/m^3). Figure1 shows the FSWCNT with four functional groups were have been used in our simulation. Molecular dynamic simulations at 300 K were carried out using tinker software package.

Non-bonded van-der-Waals' interactions are modeled by a Lennard-Jones potential with a cut-off distance of 0.9 nm. The values of $\sigma_{\text{C-C}}$ and $\epsilon_{\text{C-C}}$ used in the simulations are respectively 1.9080 \AA and 0.086 kcal/mol (from AMBER force field) [2]. In all simulations the SWCNTs are surrounded by a water bath in order to let the water spontaneously enter the nanotubes. All simulations are repeated using TIP3P of water model and nanotube flexibly, a time step of 1 fs is employed for simulation of flexible water and SWCNT or FSWCNT .The systems are initially equilibrated for 500ps ns then simulated for 3 ns.

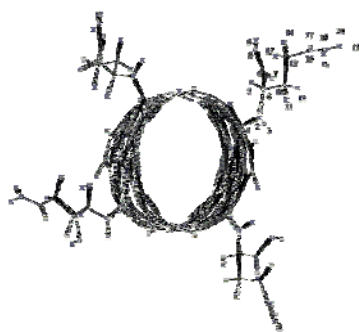
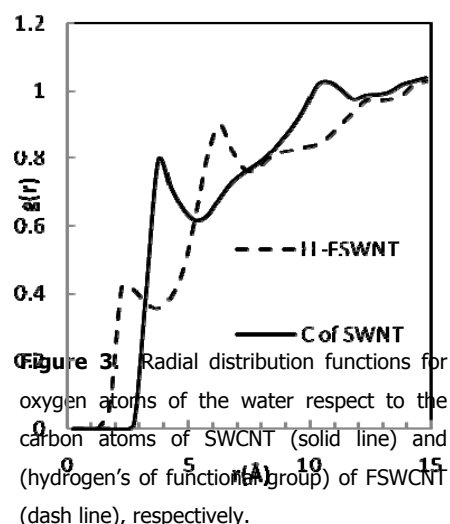
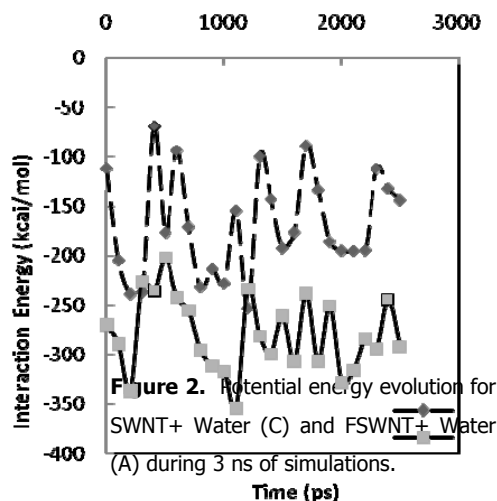


Figure1. Functionalized single wall carbon nanotubes with four functional groups

3. Result and discussion

Potential energy evolution for SWCNT- Water and FSWCNT -Water during 3 ns of simulations is shown in figure2. The interaction energy between water and a SWCNT and also between water and a FSWCNT has been calculated from the following equation. $E_{\text{interaction}} = E_{\text{total}} - (E_{\text{SWCNT}} \text{ or } E_{\text{FSWNT}} + E_{\text{Water}})$.

The lower values of interaction energies for FSWCNT-water respect to SWCNT-water emphasizes that stronger interactions have been established between FSWCNT and water.



The hydration structure of functionalized FSWNTs can be extracted from the MD simulation data in terms of atom-atom radial distribution function (RDF) analysis. In order to keep the text concise as possible as we present just one RDF.

The RDF plot for oxygen atoms of the water respect to the carbon atoms of SWCNT and hydrogen atoms of FSWCNT are shown in Figure 3. Two sharp peaks are appeared at 1.75 Å and 6.25 Å for FSWCNT and two peaks are appeared at 3.75 Å and 10.5 Å for SWCNT. These results indicate that water molecules prefer to localize at the FSWCNT closer than that of the SWCNT. The functional groups increase the interactions between the tube and water molecules. Therefore, the probability of finding water molecules surrounding the functionalized nanotube is higher than that of SWCNT.

4. Conclusions

Our MD simulation confirms increasing the solubility of CNT by adding the functional groups as it has been revealed in the experiment works.

References

- [1] H. Hu, Y. Ni, S. K. Mandal, J. Am. Chem. Soc. 109 (2005) 4285.
- [2] M. Gruzicic, G. Cao, J. Mater. Sci. Lett. 39 (2004) 2315.

**Separation of He and Ne by adsorption in carbon nanotube: A molecular simulation study**Zabiollah Bolboli Nojini^{a*}, A. Abbas Rafati^b, S. Majid Hashemianzadeh^c, S. Samiee^b^aDepartment of Chemistry, Faculty of Science, Shahid Chamran University, Ahwaz, Iran^bFaculty of Chemistry, Bu-Ali Sina University, Hamedan, Iran^c Department of Physical Chemistry, College of Chemistry, Iran University of Science and Technology, Tehran, Iran

E-mail: zb_nojini@scu.ac.ir and zb.nojini@gmail.com

[Keyword: Adsorption isotherms, Monte Carlo simulation, Carbon Nanotube, Separation Factor. Noble gas.**1. Introduction**

The study of gas adsorption on carbon nanotubes has been the subject of intense attention in recent years [1]. In the past two decades, the problem of clean energy storage in light nanoporous materials has received considerable attention due to the well-known "greenhouse effect" caused by the increase in the concentration of atmospheric gas pollutants (CO₂, SO₂, CH₄, CFCs, etc.). Note that the potential of the carbon nanotubes (CNTs) [2, 3] was understood.

2. Models and Simulation Method

In our previous works [4, 5] we studied adsorption of gases on the outer and inner surfaces of SWCNTs using DFT calculations. In those studies, we employed quantum mechanics to investigation gas adsorption on nanotubes. Also, we studied adsorption and separation of O₂ and N₂ mixture gases on nanotubes using Monte Carlo simulation [6]. In continue, here we present the results of an adsorption study of He and Ne gases mixture on SWCNT using Canonical Monte Carlo (CMC) simulation. The adsorption isotherms were considered for mixture of He and Ne gases on (15, 15) SWNT at both subcritical and supercritical temperatures. The intermolecular interaction was modeled by the isotropic pairwise additive site-site Lennard-Jones (LJ) potential

$$\phi_{fw} = 4\epsilon \sum_{i=1}^{N_f} \sum_{j=1}^{N_w} \left[\left(\frac{\sigma_{fw}}{r_{ij}} \right)^{12} - \left(\frac{\sigma_{fw}}{r_{ij}} \right)^6 \right] \quad (1)$$

To obtain adsorption isotherms, following commonly parameter is calculated:

Gravimetric storage capacity (absolute value adsorption per mass of adsorbent), ρ_w , was calculated as follow:

$$\rho_w = \frac{N_{gas} \cdot m_{gas}}{N_{gas} \cdot m_{gas} + N_c \cdot m_c} \quad (2)$$

In addition, to gain a better insight into the separation, we analyze the pressure and temperature dependence of the selectivity.

In mixture adsorption, the selectivity (or separation factor) of component i with respect to j is defined by S_{ij}

$$S_{ij} = \frac{x_i / y_i}{x_j / y_j} \quad (3)$$

Additionally, to obtain a visual picture of the physical adsorption of He and Ne molecules in SWCNT, we have selected some snapshots of prehensive configurations of the simulation boxes shown in Figure 1.

3. Results and discussion

The obtained adsorption isotherm of He and Ne at different temperatures are shown in Figure 2. Adsorption isotherms observed for He and Ne on (15, 15) SWCNT show that no capillary condensation occurred because the pore is not large enough to hold more than four layers of molecules. Also, we discussed the effect of temperatures (T=4 and 40 K) at constant pressure (P=0.2 MPa) on the selectivities of Ne to He (Figure 3). As can be seen in Figure 3 for higher temperature, the selectivity of Ne was increased with increasing gas bulk composition until reaching to a maximum at $y_{Ne} = 0.55$ (%55 of the gas bulk is Ne and; %45 is He). After this maximum, the selectivity decreased with increasing gas bulk composition. Figure. 4 show the isosteric enthalpy of adsorption of He and Ne mixture as function of amount adsorbed. Similar to the adsorption isotherms and

separation factors, Q_{st} of Ne is larger than that of He in identical conditions. The behavior of isosteric enthalpy of adsorption for He and Ne show gradually, nearly linear decrease in their values as function of the amounts of adsorbed.

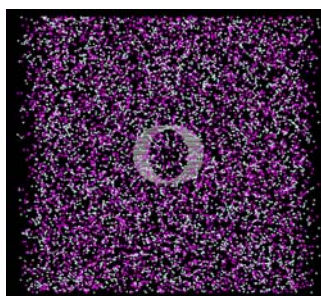


Fig. 1 Snapshots of the CMC simulation box of the SWCNT at 77 and under 10 MPa pressure.

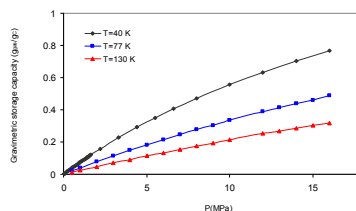


Fig. 2 He and Ne adsorption isotherms measured at 4, 77 and 130 K on (15, 15) nanotube.

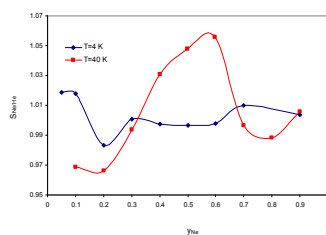


Fig. 3 Selectivity of Ne to He as function of the Ne bulk composition at (a) $T= 4$ and (b) $P=0.2$ MPa.

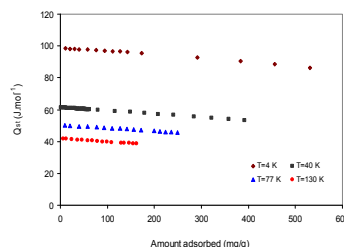


Fig. 4 Variation of isosteric enthalpy of adsorption ($Q_{st}/J.mol^{-1}$) with amount adsorbed (mg/g) for Ne adsorbed.

References

- [1] A. D., Migone, S. Talapatra, Encyclopedia of Nanoscience and Nanotechnology; Nalwa, H. S. Ed.; American Scientific Publishers: Los Angeles, 2004
- [2] S. Iijima, Nature, 354 (1991) 56.
- [3] P. George, Lithoxoos and J. S. Y. Carissan, J. Phys. Chem. C. 112 (2008) 16725.
- [4] A. Abbas Rafati, S. Majid Hashemianzadeh, Z. Bolboli Nojini, J. Phys. Chem. C. 112 (2008) 3597.
- [5] A. Abbas Rafati, S. Majid Hashemianzadeh, Z. Bolboli Nojini, J. Colloid and Interface Sci. 336 (2009) 1–12
- [6] A. Abbas Rafati, S. Majid Hashemianzadeh, Z. Bolboli Nojini, N. naghsheh, J. Comput. Chem. (Accepted).



Electrochemical supercapacitor electrodes based on nano magnetite/carbon black composite

A. Zolfaghari*, H. Sayahi, H. Mortaheb

Chemistry and Chemical Engineering Center of Iran

Email: zolfaghari@ccerci.ac.ir

Keywords: Electrochemical capacitor, Nano magnetite, Carbon black, Nanocomposite

1. Introduction

Electrochemical capacitors (supercapacitor) are electrical energy storage devices that utilize the double-layer formation at electrode-electrolyte interface (electric double layer capacitor, EDLC) or the reversible faradic reaction of metal oxide, carbon, polymer, etc, with current collector (pseudo-capacitor). High power and, long cycle life are advantages of supercapacitor devices relation to batteries, even though the relatively low energy density compared to batteries.

The first known pseudocapacitive oxide is hydrated amorphous ruthenium oxide, RuO_2 . Although it has high specific capacitance (720 F/g) and high power density, its high cost, toxic and requires the use of strong acidic aqueous electrolyte, has limited its large-scale application.

Magnetite (Fe_3O_4) is a new discovered inexpensive pseudocapacitive material that exhibiting pseudocapacitance in alkali sulfites electrolytes. Magnetite has very limited conductivity. It was necessary to combine Fe_3O_4 with conductive additives to obtain expressive capacitance. In the work reported here, the combination of oxide and conductive additive, carbon black, which referred as CB; were synthesized by new co precipitate method and the capacitive behavior of prepared electrodes was considered in alkali aqueous electrolyte.

2. Method

Reagents as ferric chloride hexa-hydrate ($\text{FeCl}_3 \cdot 6\text{H}_2\text{O}$ Merck 99%), ferrous tetra-hydrate ($\text{FeCl}_2 \cdot 4\text{H}_2\text{O}$ Merck 99%), Carbon black (Alfa Aesar) and sodium hydroxide (NaOH Merck) were used for synthesize magnetite/CB composite. Different amount of CB were dispersed in solution of iron salts. After that, NaOH solution was added at once and allowed the prepared solution to stir vigorously in argon ambient. The precipitated solution was filtered, washed with deionized water, and dried at room temperature in air.

The proportion of Fe_3O_4 and CB was confirmed by atomic absorption technic. The crystallographic structure of the powder was investigated using an X-ray diffraction. Surface morphology of the sample was examined with a scanning electron microscope (SEM).

The electrodes were prepared by mixing 95 wt% produced composite with 5 wt% of PTFE (polytetrafluoroethylene) dried powder (Merck). Before using the composite; it was mixed with few drops of ethanol. This resulting rubber-like paste was rolled into a film (100–200 μm thick) on a flat glass surface. A piece of film (1 cm^2) was cut and pressed onto stainless steel grid current collector.

An Autolab, Eco Chemie. B.V. potentiostat/galvanostat with a beaker type electrochemical cell equipped with a Fe_3O_4 based working electrode, an Ag/AgCl reference electrode and a 1 cm^2 Pt net counter electrode was used for all electrochemical measurements. Aqueous solution of 0.5M Na_2SO_3 with 9.45 pH values employed as electrolyte. It was degassed with purified N_2 before measurement.

3. Results and Discussion

The XRD patterns confirm the magnetite structure of the different synthesized powders (fig 1). Compared with the as-prepared samples, the patterns show the master CB peak ($2\theta \sim 25$) has increased as the CB weight increasing.

The morphology of the magnetite-carbon black nano composite (30% Fe_3O_4) and a pure magnetite powder were obtained by SEM as shown in fig 2.

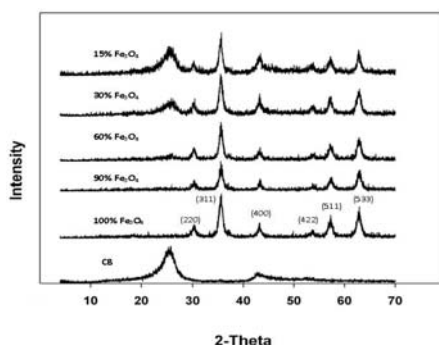


Fig 1. The XRD patterns of CB (carbon black), just magnetite (100% Fe_3O_4), and magnetite-CB with different percentage of Fe_3O_4 (90%, 60%, 30% and 15%).

The CV analysis has established that the oxides capacitor have an operating voltage rang of 0.6V (-1 ~ -0.4 V). The CV of the mixed electrodes by scan rate 2 mV/S in aqueous electrolyte (Na_2SO_3 0.5 M) are shown in fig 3. In all cases, the electrodes exhibit mirror image traces characteristic of a capacitor. The CV of 30% Fe_3O_4 sample is broader and shows greater capacitance than other samples.

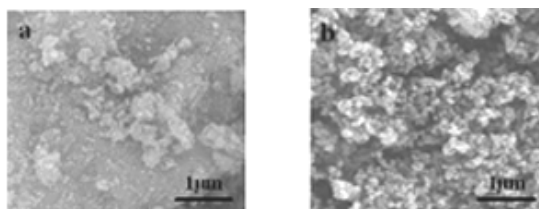


Fig 2. The SEM images of magnetite (a) and the composite of magnetite-CB(30% Fe_3O_4) (b).

Electrochemical capacitors that made of magnetite and carbon black composite have shown suitable capacitance in alkaline electrolyte. With increasing the weight percentage of CB, the specific capacitance has increased. The optimum sample (30% Fe_3O_4) exhibited high capacitance of 255 F/g.

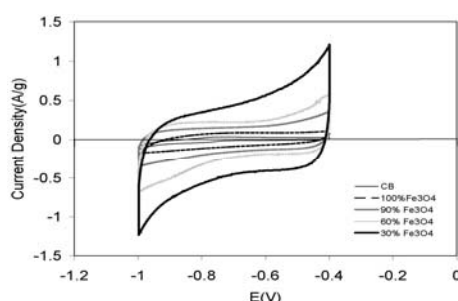


Fig 3. The CV of electrodes made with different amount of Fe_3O_4 (100%, 90%, 60% and 30%) by scan rate of 2mV/S

4. Conclusion

The different samples showed good stability of capacitance as the capacity was found to lose ~17% of the initial value after 1000 cycles for the best electrode (30% Fe_3O_4). The CV and the chrono-voltage plots of magnetite/ CB capacitors made with different amount of CB have shown that the charge storage capacity decreases with increasing the Fe_3O_4 weight percentage in composite.

References

- [1] John H. Jang, Kenji Machida, Yuri Kim, Katsuhiko Naoi, *Electrochimica Acta* 52(2006)1733.
- [2] Shin- Liang Kuo, Nae-Lih Wu, *Journal of Power Sources* 162 (2006) 1437.
- [3] M. Ghaemi, F. Ataterian , A. Zolfaghari , S.M. Jafari, *Electrochimica Acta* 53(2008) 4607.
- [4] Nae-Lih Wu, *Materials Chemistry and Physics* 75 (2002) 6.
- [5] Suh-Cem Pang, Marc A Anderson, Thomas W. Chapman, *Journal of the Electrochemical Society* 147 (2000) 444.
- [6] Mathieu Toupin, Thierry Brousse, Daniel Belanger, *Chem.Mater* (2002) 14.

**Ion separation of electrolyte solutions using charged carbon nanotubes: A molecular dynamics study**

Masumeh Foroutan and Amir Taghavi Nasrabadi*

Department of Physical Chemistry, Faculty of Chemistry, College of Science, University of Tehran, Tehran, Iran

Email: amirtaghavi@khayam.ut.ac.ir

Keywords: Ion separation, Charged carbon nanotube, Radial distribution function, External field**1. Introduction**

Ion separation is an essential process in chemical and biological analysis systems, which is conventionally performed by capillary electrophoresis [1] or by nanofiltration membranes [2]. Due to their desirable chemical stability and electrical conductivity, the nanoscale dimensions of carbon nanotubes (CNTs) produce a relatively large surface area-to-volume ratio, making their use attractive in ion separation devices [3]. Using molecular dynamics (MD) simulations, we demonstrated that charged carbon nanotubes can be used for separation of Na⁺ and Cl⁻ ions in a NaCl electrolyte. We analyzed this phenomenon from different aspects of view, using radial distribution functions (RDFs), normalized radial density function profiles and the other tools. Our findings are in a good agreement with each other.

2. Method

(10,10) single-walled armchair CNT with 13.56 Å diameter and 11.22 Å length is considered. In the simulation, the nanotubes are placed in a 27.5 × 27.5 × 33.66 Å³ box. The CNTs in the cuboid domain are initially surrounded by a uniform (13.66% by weight) aqueous sodium chloride solution. Periodic boundary conditions are used in all directions. A typical simulation considers 1300 molecules/atoms in a cyclically replicated parallelepiped, of which 400 atoms constitute the carbon nanotubes. There are 40 ions each of sodium and chloride with an additional 820 water molecules. The 13.66% solution has density of 1115.91 kg/m³. All site-site interactions in our study were thus modeled using this potential model,

$$u_{ij} = 4\epsilon_{ij} \left[\left(\frac{\sigma_{ij}}{r_{ij}} \right)^{12} - \left(\frac{\sigma_{ij}}{r_{ij}} \right)^6 \right] + \frac{q_i q_j}{r_{ij}}.$$

The potential parameters σ , ϵ , r , e , and charges q were obtained from the literature [4]. Lorentz–Berthelot mixing rules were used for cross interactions. The long-range electrostatic interactions were computed by using the Particle Mesh Ewald method and van der Waals forces were calculated within a cutoff distance of 10 Å. MD simulations were performed in a NVT ensemble with Tinker Molecular Modeling Package (version 5.0) [5]. For all simulated systems, the equations of motion were integrated by velocity Verlet algorithm method and the Nose-Hoover thermostat maintained the temperature at the constant value of 300 K. After the energy minimization and 1.0 ns MD run with integral step of 1.0 fs for equilibrium, another 2.0 ns MD run was carried out with integral step of 1.0 fs.

3. Results and Discussion

The magnitude of the charge placed on each atom of a CNT provides a finite overall surface charge density. We consider three different electrostatic charge densities on the nanotubes. Naturally, applying charges on the CNTs, results in the creation of an external electrical field spontaneously, that affects the solution. We defined 4 systems as cases 1 to 4, respectively, in which case 1 has uncharged (neutral) CNTs, while the other 3 cases have different surface charge densities of $\sigma = 0.84, 1.68$ and 3.36 C/m², respectively.

The ion pairs/clusters are formed easily and a successful breakup of these ion pairs/clusters is required for separation. In our cases, with increasing the charge density, we acquire the perfect separation gradually. The structural aspects of the simulated systems can be discussed well by the RDFs, which is a measure of the effective interaction among the particles. In order to keep the manuscript concise, as possible as, only the RDF profile for Na⁺-Cl⁻ is presented, while, carbon-Ion and Ion-water RDF profiles have been calculated for this work to show the separation process more clearly.

Fig. 1 shows the RDF profile of Na⁺-Cl⁻ for all cases. We observe that the height of peaks for cases 1, 2 and 3 decreases with increasing external field (showing separation of ion pairs); only for case 4 we observe perfect separation in which this peak completely wipes out. The break-up of an ion pair/cluster (ion separation) is observed when water molecules penetrate into the

ion pair/cluster. In the imperfect separation (cases 2 and 3); water molecules only surround the ion pair/cluster. As a result, the perfect separation occurs when the surface charge density is large enough (3.36 C/m^2 for our simulated systems). We can claim that in case 4 we have a perfect ion separation.

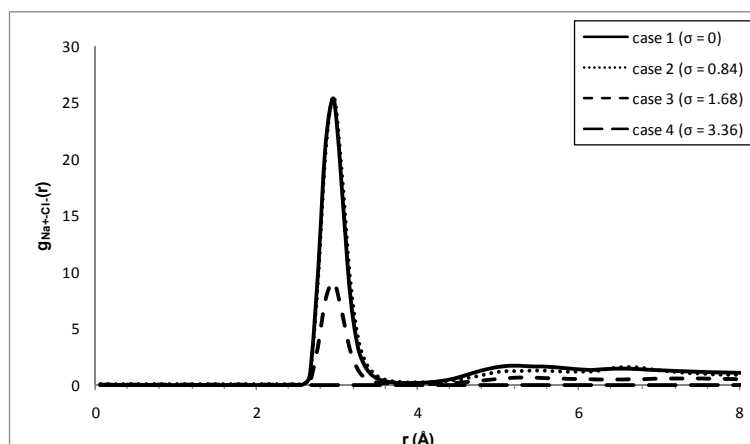


Fig. 1. Sodium-chloride RDF profile for all cases. Unit of σ is C/m^2 .

4. Conclusions

A NaCl electrolyte was separated into Na^+ and Cl^- ions by using charged CNTs, while on the other hand the water purification was being performed simultaneously. A perfect separation was observed when the surface charge density was 3.36 C/m^2 whereas an imperfect separation was observed for lower values of surface charge densities i.e. 0.84 and 1.68 C/m^2 .

References

- [1] C.A Monnig, R.T Kennedy, Anal. Chem. 66 (1994) 280.
- [2] A. M. Hollman, D. Bhattacharyya, Langmuir 20 (2004) 5418.
- [3] Q.L. Chen, K.H. Xue, W. Shen, F.F. Tao, S.Y. Yin, W. Xu, Electrochim. Acta. 49 (2004) 4157.
- [4] S. Banerjee, S. Murad, I. K. Puri, Chem. Phys. Lett. 434 (2007) 292.
- [5] J. W. Ponder, TINKER: Software Tools for Molecular Design, 5.0; Saint Louis, MO, 2009.

Cycloaddition reactions between C_{24} and buta-1, 3-diene an ab initio study

S. Abedini Khorrami, Sh. Moradi and H. Mohammadzadeh Bahar*

Faculty of Chemistry, Islamic Azad University, North Tehran Branch, Iran

Bahar.mohammadzadeh@gmail.com

Keywords: Nano structures of Fullerene; C_{24} ; AM1 calculations; cycloadditions

1. Introduction

Cycloaddition reaction between C_{24} and buta-1, 3-diene was studied within the framework of AM1 (RHF) level. The reaction involving the double bond between two hexagons and a hexagon and a pentagon, as well as the cycloaddition products followed by disrotatory $\sigma 2_s + \pi 4_s$ electrocyclic ring openings were considered. Thermodynamics parameters and stability energy are evaluated in different temperatures.

It is known that C_{60} undergoes various types of cycloaddition reactions, of these [4+2], [3+2], [2+2] and [2+1] are to be mentioned [1-9]. In addition, these chemical transformations also provide a very powerful tool for the fullerene functionalization. Almost any functional group can be covalently linked to C_{60} by the cycloaddition reactions of suitable addends with C_{60} . Some types of the cycloadducts were found to be remarkably stable even at high temperatures [10]. The double bonds between two hexagons in C_{60} structure are dienophilic, which enable the molecule to undergo a variety of Diels-Alder reactions ([4+2] cycloaddition) [10]. Fullerene and its derivatives are the most popular structural units in organic chemistry. Collision of fullerene under laser radiation or paralyse cause to preparation of some derivatives of fullerene such as C_{58} , C_{36} , C_{33} , C_{32} , C_{30} , C_{28} , C_{26} , C_{24} and C_{20} . The C_{24} is the interesting derivative molecules from C_{60} . The symmetrical structural of the C_{24} molecules and different position for cycloaddition cause choosing for these calculations. In this calculation cycloaddition reaction on some different position of double bond in C_{24} with butadiene (fig. 1) carried out and simulated by ab initio calculations. The stability of energy, reaction pathway, transition state and thermodynamics properties for these additions for all situations calculated.

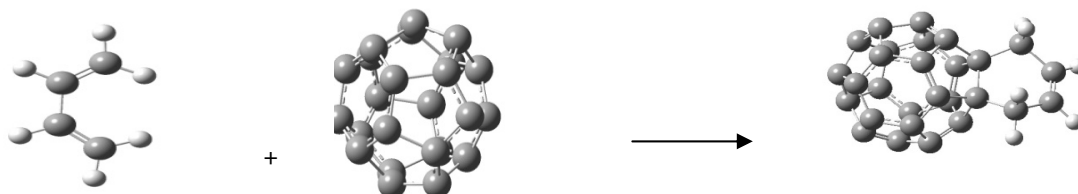


Fig.1 AM1 optimized geometry structures of p

2. Methods

In the present treatise, the geometry optimizations of all the structures leading to energy minima were achieved by using AM1 self-consistent fields molecular orbital (SCF MO) [11] method at the restricted Hartree-Fock (RHF) level [12]. The initial geometry of butadiene and C_{24} structures was excerpted from Gauss View. All these calculations were performed by using Gaussian 98.

C_{24} have three valence isomers that we calculated reaction pathway and transition state and intermediate structure in cycloaddition reaction for each different position of double bond in each three valence isomer reaction pathway scanned step by addredundant key words.



3.Results and Discussion

Somer thermodynamic geometry parameters of C₂₄ and butadiene for a position at different temperatures are listed in Table 1.

Table1. Some thermodynamic geometry parameters of the cycloadditions presently considered for a structure at different temperatures

$T(K)/\frac{KCal}{mol}$	298.15	303.15	308.15	313.15	318.15
$\Delta G/\frac{KCal}{mol}$	-148.103	-147.8	-147.59527	-147.34176	-147.0875
$\Delta H/\frac{KCal}{mol}$	-163.249	-163.24786	-163.24723	-163.24541	-163.24351
$\Delta E/\frac{KCal}{mol}$	9.223	9.234	9.245	9.257	9.269
$\Delta S/\frac{KCal}{mol}$	-0.05079	-0.050795	-0.05079	-0.050786	-0.050779
$C_v/\frac{KCal}{mol}$	0.00221	0.002254	0.002297	0.00234	0.002381
$ZPE/\frac{KCal}{mol}$	9.73835	9.73835	9.44409	9.73835	9.73835

Table 1 show that the ΔG increased with increasing the temperature and show that reaction between C₂₄ and C₄H₆ at high temperatures are more exothermic and unstable.

4.Conclusions

There are three status of double bond in structure of C₂₄ that are completely different from each other. Cycloaddition is selected as a main part of reaction and addition process for single stage is considered. Thermodynamics parameters and stability energy are evaluated in different temperatures. The new cycle that produced after cycloaddition reaction was opened and created a new cycle with large size. Three positions of double bond that lead to three products are strongly different. The structure that contain much resonance loop and the most double bond in resonance form was stable than that others, in the other hand these results completely Confirmed thermodynamics results that obtained from calculations.

When C₄H₆ is added to the C-C bond of C₂₄ structure, our investigation results show that the reaction mechanism is probably as below:

Reactants → Transition state 1 (Ts 1) → Closed Isomer → Transition state 2 (Ts 2) → products

References

- [1] L. Turker, J. Molecular Structure (Thochem) 165(2002)588.
- [2] V. M., Rotello, J. B., Howard, T. Ydeve, M. Conn, E.Viani, L. M. Giovane, A. L., Lafleur, Tetrahedr. Lett 34(1993)1561.
- [3] M .Maggini, G. Scorrano, M. Prato, Journal of American Chemical society 113(1993)9798
- [4] A. Hirsch, the Chemistry of Fullerenes, Verlag, Stuttgart, 1994.
- [5]M. Tsuda, T. Ishida, T. Nogami, S. Kurono, M. Ohashi, Journal of Chemical society. Chemical Commune.(1993)1296

Chemical deposition and optical characterization of nanocrystalline CDS thin films for application in solar cells as window materials

R. Sahraei^{a,*}, A. Daneshfar^a, H. Kaviani^a and N. Shokri^{a,b}

^aDepartment of Chemistry, University of Ilam, Ilam, Iran

^bDepartment of Chemistry, Payam-e Nour University, Urmia, Iran

* Email: reza_sahrai@yahoo.com

Keywords : Nanostructures, Thin films, Optical properties, Chemical deposition

1. Introduction

Cadmium sulfide thin films are widely used as a window material for thin films heterojunction solar cells such as the highly efficient CdTe and CuInSe₂ devices [1]. Although there are a number of ways in which thin films of CdS can be fabricated, deposition from weak acidic solution provides a simple, inexpensive, and a reliable method for large area device fabrication [2]. In this work nanocrystalline CdS thin films prepared by a new chemical solution deposition route [3]. These thin films have been studied as window and buffer materials which are an important part of the solar cell. The parameters studied include the transmittance/ reflectance spectra, energy band gap, absorption coefficient, refractive index, extinction coefficient, and thickness. In addition we have investigated the structural and morphological properties of CdS thin films.

2. Experimental

Glass slides were used as the substrates. The deposition solution was prepared by mixing 10 ml of Cd(OAc)₂, 0.02 M, 25 ml urea, 2 M, 50 ml thioacetamide (TAA), 0.2 M, and diluted to 100 ml by distilled water. Finally, the pH of deposition solution was adjusted to 4.0 by drop wise addition of 1 M HCl solution. This solution was poured into a glass tank being used as a reaction vessel for the film deposition. Glass substrates were immersed vertically in the reaction vessel, and the glass tank was placed in a thermostat bath set at 50 °C for 8 hours. Transmission, absorption and reflection spectra were obtained by means of a Varian Cary 300Bio UV-Visible Spectrophotometer. The thin films thickness was measured by a Dektak³ profilometer. The X-ray diffraction (XRD) analysis was used to determine the nanocrystalline structure of CdS thin films and scanning electron microscope (SEM) was used to observe the microstructure of the surface topology.

3. Results and discussion

Fig.1 (Left) show the transmittance and reflectance spectra of nanocrystalline CdS thin films deposited onto the glass substrates. The average transmittance of CdS films is calculated to be 85, 90, 95, and 97% respectively in the visible wavelength region.

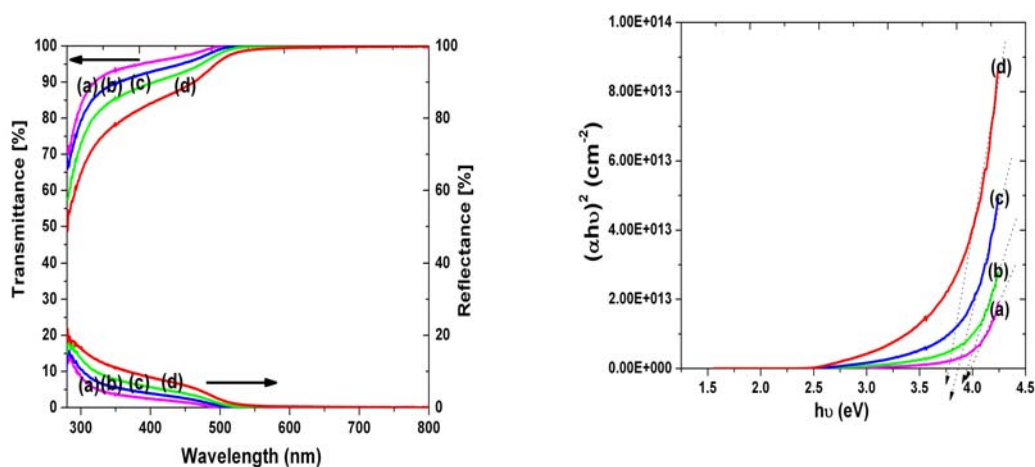


Fig.1: Optical transmittance and reflectance spectra (Left) and Plot of $(\alpha h\nu)^2$ (Right) for CdS thin films with different thicknesses: (a) 30, (b) 65, (c) 85, and (d) 130 nm.

Optical transmission spectra of the thin films are observed to be shifted towards the longer wavelength with increasing film thickness. It is strongly observed that the CdS thin films exhibit the least reflectance for almost at all the wavelengths. From the above studies, it is believed that the CdS thin films may be used as a window material for thin film solar cells. The values of the energy band gap, E_g , were calculated from the transmittance spectra by plotting $(\alpha h\nu)^2$ versus $h\nu$ (Fig. 1(Right)). α , h , and ν signify absorption coefficient, Planck constant, and frequency, respectively. CdS thin films grown here have the energy band gap in the range of 3.70 to 3.85 eV. These values are somewhat larger than the typical value of the bulk CdS (ca. 2.42 eV), probably due to the quantum size effect as expected from the nanocrystalline nature of the CdS thin films [4].

X-ray diffraction (XRD) data obtained by scanning 2θ in the range $20-80^\circ$, with a grazing angle equal to 1.5° for the deposited CdS film on the glass substrate. The thickness of the film was about 280 nm. The five broad peaks observed in the diffractogram at around 25.3° , 26.9° , 44.5° , 48.5° , and 55.2° reveal a hexagonal lattice structure of CdS. These peaks can be assigned to the planes (100), (002), (110), (103), and (004), respectively, of the hexagonal phase. In addition, we did not observe any diffracted peaks due to CdO or $\text{Cd}(\text{OH})_2$ in the XRD pattern.

SEM image of the film showed that the film consisted of small uniform grains free of pinholes (Fig. 2) and it reveals a hemispherical structure adherent to the substrate surface, which seems to be composed of aggregation of grains of around 150 nm in diameter. It is also interesting that no particles larger than about 200 nm are observed on the film surface.

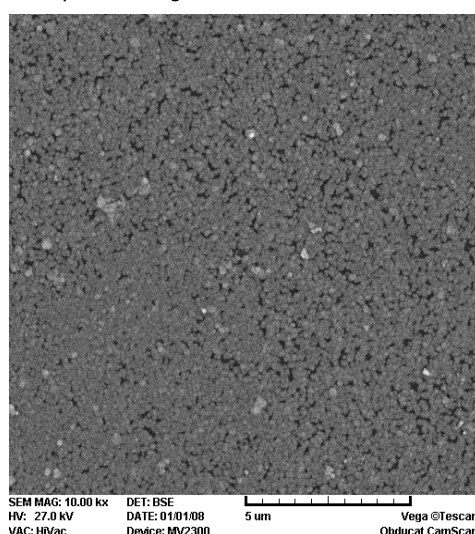


Fig.2 SEM images of the CdS thin film on glass substrate with thickness of about 65 nm.

4. Conclusions

Nanocrystalline cadmium sulfide (CdS) thin films of different thickness were deposited on glass substrate by a chemical solution deposition technique. Optical study is performed to calculate optical band gap (E_g) using transmission and reflection spectra in the wavelength range 300-800 nm. The band gap measured was found to be in the range of 3.70 - 3.85 eV. Our band gap values are somewhat larger than the typical value of the bulk CdS (2.42 eV), which could be attributed to quantum confinement effects due to the nanometer crystal size of the CdS thin films.

References

- [1] B. R. Sankapal, S. D. Sartale, C. D. Lokhande, A. Ennaoui, Sol. Energy Mater. Sol. Cells, 83 (2004) 447-458.
- [2] R. Sahraei, G. Motedayen Aval, A. Goudarzi, Journal of Alloys and Compounds, 466 (2008) 488-492.
- [3] I.O. Oladeji, L. Chow, Thin Solid Films, 474 (2005) 77-83.
- [4] K. Yamaguchi, T. Yoshida, D. Lincot, H. Minoura, J. Phys. Chem. B, 107 (2003) 387-397.



Reverse nonequilibrium molecular dynamics simulation of the viscosity of nanoconfined polymers

Hossein Eslami,^a and Florian Müller-Plathe^b

^aDepartment of Chemistry, College of Sciences, Persian Gulf University, Boushehr 75168, Iran

^bEduard-Zintl Institut für Anorganische und Physikalische Chemie, Technische Universität Darmstadt, Petersenstraße 20, D-64287, Germany

E-mail: heslami@pgu.ac.ir

1. Introduction

On confining a polymer in a nanometric pore, the density profiles show a strong layered structure [1]. Strong density fluctuations near the confining surfaces result in the deviation of transport properties from their corresponding bulk properties [2]. Molecular simulation methods, have provided most of the microscopic information on the molecular understanding of the confined fluids [1]. The molecular dynamics (MD) method has been used to investigate the behavior of simple fluids under shear [3]. There are, however, only a few reports in the literature on the MD simulation of confined chain molecules or polymers under flow. In this work, we employ our new molecular dynamics simulation method [4] in the isothermal-isobaric-isosurface (*NAPT*) ensemble to simulate the viscosity coefficient of polyamide-6,6 oligomers confined between graphite surfaces.

2. Method

Atomistic MD simulations were performed for ethyl- and butyl-terminated PA-6,6 trimers. The force field parameters for polyamide-6,6 as well as for the confining surfaces, graphene surfaces, are reported in our former publication [1]. In this work a number of systems with different intersurface separations, as well as the bulk fluid, are simulated. All MD simulations were carried out using our simulation package, YASP [5]. All nonbonded interactions were truncated at 0.95 nm with a reaction field correction for the Coulombic interactions. The time step for the leapfrog integration scheme was 1.0 fs. After an equilibration of 3 ns, in *NAPT* ensemble simulation, relaxed configurations were obtained for performing reverse nonequilibrium molecular dynamics (RNEMD) simulation. Here, the temperature is kept fixed (at 500 K) using a Berendsen thermostat, and the parallel component of pressure, is kept fixed (at 101.3 kPa) by coupling $P_{//}$ to a Berendsen barostat. In the RNEMD method, unphysical momentum transfer (flux) is performed by swapping the velocities of surface atoms and the resulting force is measured.

3. Results and Discussion

Linear Velocity Profiles and Shear Viscosity

The unphysical momentum transfer in the RNEMD method leads to the development of velocity gradient in the confined fluid. In this work the distance between surfaces is divided into a number of thin slabs, depending on the slit width, and the x -component of the velocities of all atoms of a slab are time-averaged during the simulation. Adjusting the proper exchange frequencies, MD simulations were performed for 5-10 ns, depending on the distance between the confining surfaces, to obtain a linear velocity profile within the polymer. After this initial time to achieve steady-state, simulations were performed for another 10 ns to calculate the shear rates and the viscosity coefficients. The results on the linear density profiles for a system with inter-surface separation of 3.2 nm are shown in Figure 1.

The viscosity coefficients are calculated as a function of shear rates and are shown in Figure 2. In Figure 2, a nonlinearity in the viscosity coefficient versus the shear rate is observable. The zero-shear rate viscosity coefficient is obtainable by extrapolating the results in Figure 2, using a suitable scheme. Our results show that the zero-shear rate viscosity increase for the confined films is due to the formation of structured layers near the surfaces. Furthermore, our results (not shown here) indicate that the increase in viscosity with decreasing the distance between surfaces shows an oscillatory behavior. This finding describes clearly that the origin of high viscosity in thin films is the formation of organized layers near the surfaces.

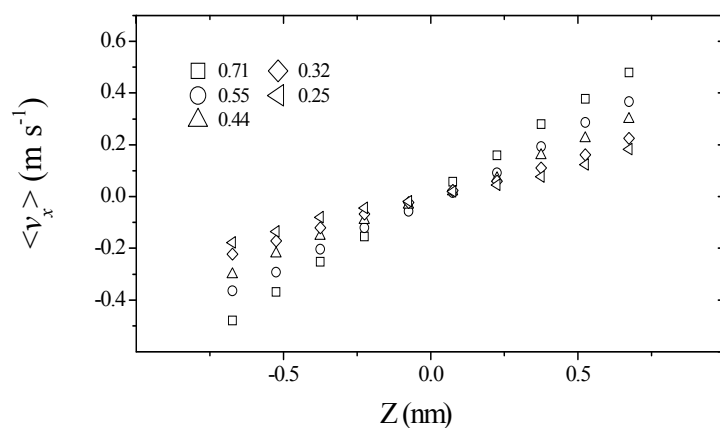


Fig.1 Velocity profiles for PA-6,6 confined between graphite surfaces. The distance between the surfaces is 3.2 nm and the shear rates are indicated in the figure, in 10^9 s^{-1} .

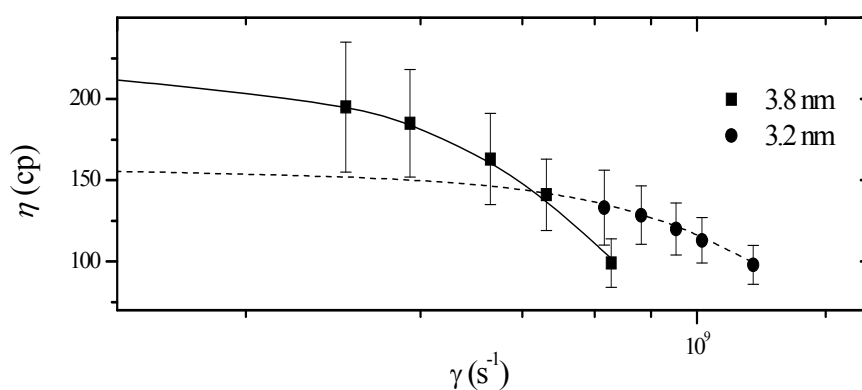


Fig.2 Shear viscosities as a function of shear rates. Solid lines represent the best fits to find the zero-shear rate viscosity coefficients. The distances between the surfaces are indicated in the figure.

References

- [1] H. Eslami, F. Müller-Plathe, J. Phys. Chem. B 113 (2009) 5568.
- [2] H. T. Davis, Chem. Eng. Commun. 58 (1987) 413.
- [3] J. Bitsanis, S. A. Somars, H. T. Davis, M. Tirrell, J. Chem. Phys. 93 (1990) 3427.
- [4] H. Eslami, F. Mozaffari, J. Moghadasi, F. Müller-Plathe, J. Chem. Phys. 129 (2008) 194702.
- [5] F. Müller-Plathe, Comput. Phys. Commun. 78 (1993) 77.

Investigation of photocatalytic activity for ZnO nanoparticles supported on natural zeolite prepared by microwave irradiation

A. Habibi-Yangjeh^a, E. Sanatgar-Delshad^{b*}, M. Khodadadi- Moghaddam^c.

^a Department of Chemistry, University of Mohaghegh Ardabili, Ardabil, Iran.

E-mail: ahabibi@uma.ac.ir

^b Department of Chemistry, University of Mohaghegh Ardabili, Ardabil, Iran.

E-mail: elham.sanatgar_63@yahoo.com

^c Department of Chemistry, Islamic Azad University, Ardabil, Iran.

Keywords: Supported ZnO, Photocatalysis, Natural zeolite, Methylene blue, Nanoparticle, Microwave.

1. Introduction

Photocatalysis, an advanced oxidation technology employing semiconductors as photocatalysts is a promising method for treatment of wastewater. This method is generally based on the generation of OH radicals. Despite the positive attributes of photocatalysts[1], poor adsorption properties of semiconductors lead to great limitation. Among various supporting materials, Natural zeolites seem attractive candidates [2]. For these reasons, in this paper preparation of ZnO nanoparticles supported on Iranian natural zeolite by microwave irradiation was considered. Microwave irradiation offers great advantages as the simplest and fastest procedure since selective dielectric heating [3]. The influence of various parameters such as catalyst composition, microwave irradiation time, weight of catalyst and calcination temperature and solution pH on the photodegradation rate constant has been studied to achieve maximum degradation efficiency.

2. Experimental

Natural zeolite was commercial clinoptilolite (Afrand Tuska, Iran). The catalyst supported on natural zeolite was prepared with different ZnO loading. In a typical synthesis procedure, zinc acetate dihydrate (5.38 g) was dissolved in 100 ml of double distilled water and then 2.0 g of the zeolite was added under stirring at room temperature. After 12 h stirring, aqueous solution of NaOH (5 M) was slowly added drop wise into the solution under magnetic stirring until pH of the solution was reached to 13. The formed white precipitate was irradiated using a domestic microwave oven for 5 min. The precipitate was centrifuged to get the precipitate out and washed with double distilled water and ethanol, respectively and dried in an oven at 50 °C. The XRD pattern and scanning electron microscope were studied. To examine the photocatalytic activity of the catalysts, photodegradation of methylene blue has been investigated.

3. Results and discussion

3.1. XRD analysis

The XRD patterns of the samples in various loading of ZnO are illustrated in Fig. 1.

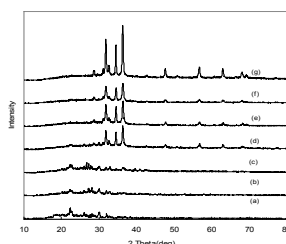


Fig.1 The powder XRD patterns for (a) natural zeolite, (b) 10 wt.% ZnO, (c) 20 wt.% ZnO, (d) 50 wt.% ZnO, (e) 80 wt.% ZnO, (f) 90 wt.% ZnO and (g) bare ZnO

For comparison, the XRD pattern of the pure natural zeolite is also shown which is similar to literature[4]. All diffraction peaks for bare ZnO are in agreement with the JCPDS file of ZnO, which can be indexed as a wurtzite hexagonal phase of ZnO. It can be seen from Fig. 1 that the gradual increase in the intensity of the peaks for ZnO and the corresponding decrease in the intensity of peaks for the zeolite clearly indicates the increase in loading of ZnO on the photocatalyst.

3.2. Scanning electron microscopy (SEM)

The morphology of the nanoparticles for as-prepared pure ZnO was investigated by scanning electron microscope. In Fig. 2a, 2b and 2c SEM of bare ZnO and the supported ZnO (50% ZnO) along with the natural zeolite have been shown, respectively.

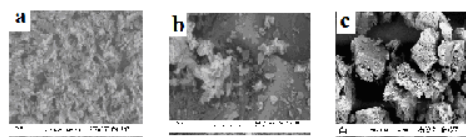


Fig. 2 The SEM image of the as-prepared nanoparticles for (a) ZnO, (b) 50% ZnO on zeolite and (c) natural zeolite

3.3. Effect of composition of the supported photocatalyst

In order to understand the effect of the catalyst composition on photocatalytic degradation of MB, the loading of ZnO on the catalyst was varied between 10 and 90 wt % and the results were shown as k_{obs} (observed first-order rate constant of the photodegradation reaction) in table 1. All the studies were carried out at 0.10 g of the catalyst and 1.70×10^{-5} M for MB.

Table 1. Values of k_{obs} for different compositions of the ZnO nanoparticles on natural zeolite

Compositions	10% ZnO	20% ZnO	50% ZnO	80% ZnO	90% ZnO	Bare ZnO
$k_{obs} \text{ (min}^{-1}\text{)}$	0.0074	0.0202	0.0258	0.0200	0.0193	0.0189

Rate of the photodegradation reaction is related to the formation of OH radical [5]. Then, the reaction rate constant will increase with ZnO loading in the photocatalyst. But, the produced OH radicals are transferred onto surface of the zeolite containing adsorbed MB (as organic pollutant), for this reason the reaction rate decreases after a maximum (at 50 wt.% ZnO) with increasing ZnO content[5].

Increase of microwave irradiation time from 5 to 10 min for preparation of samples initially rate of the photocatalytic degradation increased and then decreased. The reaction rate constant increases with calcinations temperature and reaches maxima and then decreases after 300°C. This decrease may be due to aggregation of the ZnO nanoparticles. With increasing catalyst weight initially degradation rate increase and then decrease. Increasing pH of solution increases the rate of photocatalytic activity, because in basic pH more adsorption of MB on the surface of photocatalyst can be occur.

4. Conclusions

Microwave method was proposed for preparation of ZnO nanoparticles on natural zeolite as a highly efficient photocatalyst. The reaction rate constant will increase with ZnO loading in the photocatalyst and decrease after a maximum. With increasing pH of solution will be increase the rate of photocatalytic degradation of MB.

References:

- [1] Rauf, M. A. Ashraf, S. S. Chem. Eng. J. 151 (2009) 10.
- [2] Yoon, S. J. Lee, Y. H. Cho, W. J. Koh, I. O. Yoon, M. Catal. Comm. 8 (2007) 1851.
- [3] Ponda, A.- B. Gelaspell, G. El-Shall, M. S. J. Am. Chem. Soc. 128 (2006) 2790.
- [4] Nikazar, M. Gholivand, K. Mahanpoor, K. Desalination. 219 (2008) 293.
- [5] Shankar, M. V. Neppolian, B. Sakthivel, S. Banumathi -Arabindoo, M. Palanichamy, V. Murugesan, Ind. J. Eng. Mater. Sci. 8 (2001) 104.

Solubility of carbon nanotubes in ionic liquids: MD simulation approach

M. Foroutan, M. Setareh^{*}, H. Akbari-Borhani

Department of Physical Chemistry, School of Chemistry, College of Science, University of Tehran, 14156-1514, Tehran, Iran
m.setareh@khayam.ut.ac.ir

Key words: Carbon Nanotube, Ionic Liquid, Solubility, Molecular Dynamic Simulation

1. Introduction

Carbon nanotubes (CNTs) due to extraordinary chemical, mechanical and electronic properties have attracted great attention and their suspension with water, organic solvents or polymer compounds are used greatly in electrochemistry. In water suspensions, CNTs are dissolved by help of different surfactants, polymers or proteins due to hydrophobicity of CNTs. Diverse investigations showed nonsolubility of CNTs in water [1] and toluene [2]. Many researches are concentrated on finding proper solvent with high efficiency.

Room Temperature Ionic Liquids (RTILs) which are called "green solvents" [3] possess new physicochemical properties such as good solvent ability toward a wide range of solutes [1]. Recently Shim *et al.* reported single walled carbon nanotubes can be solved in ionic liquid [4]. Such studies can be the origin of novel researches field of CNT and RTILs systems.

In the present work we study the solubility of armchair single-walled carbon nanotube (15,15) of 2.5nm length in bulk of 285 pairs of EMIM⁺ BF₄⁻ ionic liquid molecules with molecular dynamic (MD) simulation. Figure 1 shows the structure of ionic liquid which is used in this study.

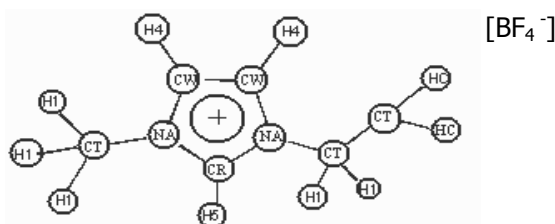


Fig.1 Schematic structure of [EMIM BF₄]

2. Simulation Method

Several force fields including AMBER, CHARMM and OPLS etc. have been developed and applied successfully in many systems. However limited researches have been done specifically for RTILs. The force field which is being used in this research is AMBER that is adopted with experimental

$$E = \sum_{bonds} K_r (r - r_0)^2 + \sum_{angles} K_\theta (\theta - \theta_0)^2 + \sum_{dihedrals} \frac{K_\phi}{2} [1 + \cos(n\phi - \gamma)] + \sum_{i < j} \left[\frac{A_{ij}}{r_{ij}^{12}} - \frac{B_{ij}}{r_{ij}^6} + \frac{q_i q_j}{r_{ij}} \right] \quad (1)$$

The first three terms represent the bonded interactions i.e. bonds, angles and torsions. The non-bonded interactions are described in the last term, including Van Der Waals in the Lenard-Jones (LJ) (6-12) form and columbic interactions of atom-centered point charges. Here the LJ 6-12 potential is written as (2)

$$U_{LJ} = 4\epsilon_{ij} \left[\left(\frac{\sigma_{ij}}{r_{ij}} \right)^{12} + \left(\frac{\sigma_{ij}}{r_{ij}} \right)^6 \right] = \epsilon_{ij} \left[\left(\frac{\sigma_{min,ij}}{r_{ij}} \right)^{12} - 2 \left(\frac{\sigma_{min,ij}}{r_{ij}} \right)^6 \right] \quad (2)$$

where ϵ_{ij} is the traditional well-depth. σ_{ij} and $\sigma_{min,ij}$ are the distance between atoms i and j at which the energy of the two atoms reaches zero and minimum, respectively. Obviously, $\sigma_{min,ij} = \sqrt[6]{2}\sigma_{ij}$

The LJ parameters for unlike atoms are obtained from the Lorentz-Berthelot (LB) combining rule

$$\epsilon_{ij} = \sqrt{\epsilon_i \epsilon_j}; \sigma_{ij} = \frac{\sigma_i + \sigma_j}{2} \quad (3)$$

The assignments of atom types of ionic liquid (EMIM⁺ BF₄⁻) exists in protonated histidine (HIS) in AMBER force field, also for carbon nanotube required parameters are available in literatures [6].

By adding proper parameters to key file of package and then running the program we can study the solubility of carbon nanotube (15, 15) inside ionic liquid and water molecules. Simulation with TINKER software of version 5 is performed for 2 ns, with time step of 1 fs in canonical ensemble (NVT) in 300 K and Nose-Hoover thermostat is applied.

3. Results

Equilibrium molecular simulation of similar system is done with water and results caused to completely different pattern of CNT movement in water and ionic liquid. It is such that in ionic liquid CNT movement is so small. It seems that this behavior can be related to solubility of CNT in ionic liquid more than water. This result is used for dispersing CNT bundles as CNTs are not available in single form and must be dispersed from aggregated nanotubes. As figure 3 shows the radial distribution function of all atoms of ionic liquid with carbon atoms CNT are approximately the same which indicates that CNT stays around ionic liquid molecules. Similarity of RDF plots for all atom types of EMIM BF₄⁻ shows that situations of all atom types of ionic liquid respect to CNT are the same. Complete results will be presented in full paper.

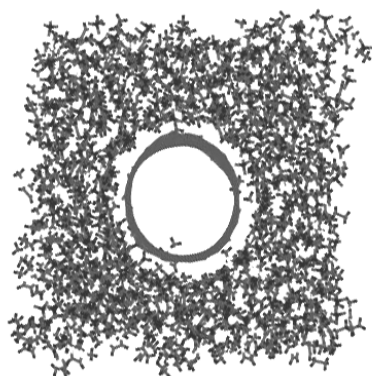


Fig. 2. Snapshot of dynamic run of solvation simulation of CNT (15, 15) in EMIM BF₄⁻ ionic liquid.

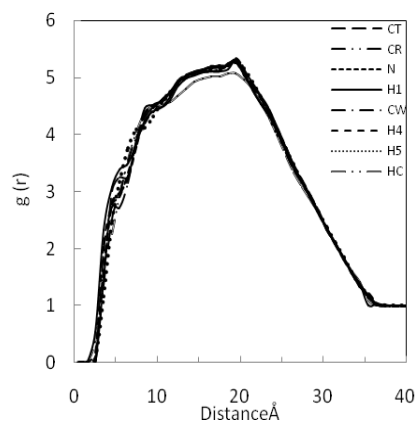


Fig. 3. Radial distribution of atoms of ionic liquid respect to C atoms of CNT.

4. Conclusion

With MD simulation, more solubility of CNT in RTIL bulk in comparison with water has been detected and obtained RDF plots confirmed this result.

References

- [1] J. Wang, H. Chu, Y. Li, *ACS NANO* 12 (2008) 2540.
- [2] M. Grujicic, G. Cao, *J. Mater. Sci.* 39 (2004) 2315.
- [3] C. Rey-Castro, L. F. Vega *J. Phys. Chem. B* 110 (2006) 14426.
- [4] Y. Shim, H. Kim, *ACS NANO* (2009)(in press).
- [5] Z. Liu, S. Huang, W. Wang, *J. Phys. Chem. B* 108 (2004) 12978.
- [6] A. Alexiadis, S. Kassinos, *Chem. Eng. Sci.* 63 (2008) 2793.

Study of the electronic properties of nitrogen doped graphene

S. Jalili^a and R. Vaziri^{a*}

^aDepartment of Chemistry, K. N. Toosi University of Technology, P.O. Box 15875-4416, Tehran, Iran

E-mails: sjalili@kntu.ac.ir, r_vaziri@dena.kntu.ac.ir

Keywords: Graphene, Electronic properties, Band gap, Density of states

1. Introduction

One possible candidate for the material for future electronics is graphene, the two-dimensional form of carbon with atoms arranged in a honeycomb lattice. Although it was only discovered very recently [1], it has received great interest since it could provide an excellent object for condensed physics and material science [2]. It combines high electron mobility with atomic thickness and promises widespread applications thus, it has been considered as one of the most promising materials candidate for future nanoelectronics [3]. To realize the graphene based circuits, various types of graphene are needed; thus, modulation of its electrical properties is of great technological importance. Doping it with other elements is a promising way to achieve this goal. Doping is a common approach to tailor the electronic properties of the semiconductor materials. For example, after doping with B or N atoms, carbon nanotubes become n-type or p-type, respectively [4]. The doped graphene promises many fascinating properties and widespread potential applications such as superconduction, ferromagnetism, etc. Theoretic studies show that the substitutional doping can modulate the band gap of graphene. In this work, we apply a first-principles method based on the spin polarized density functional theory (DFT) within the generalized gradient approximation to investigate the electronic and structural properties of graphene layer by doping with N atoms in the different bonding characters such as graphitic, pyridinic and pyrrolic.

2. Method

Our calculations have been performed with the Quantum espresso code [5], in which the spin polarized density functional theory method is implemented using the generalized gradient approximation (GGA) within the perdue and wang exchange correlation function. We employ a plane-wave basis set with periodic boundary conditions in conjunction with Vanderbilt ultrasoft pseudopotential. Kinetic energy cutoff is 60 Ry for the wave function and 245 Ry for the charge density. After geometric optimization, the forces on all atoms were less than 0.01 eV/Å. To investigate the doping effects of N impurities on graphene, we construct a 4×4 hexagonal supercell structure. The supercell parameters are set to be the same as $a = b = 9.84$ Å in the xy plane (a and b refer to the crystal lattice constants). The vacuum thickness along the z axis above and below graphene is represented with an empty space of 10 Å, avoiding any self-interaction of the slab. For calculation of electronic properties of graphene, the Brillouin zone was sampled by 6×6×1 k -point using the Monkhorst-pack scheme.

3. Results and discussion

According to the early studies in the N-doped graphene, indicating that N atoms are in the three different bonding characters inserted into the graphene network (Fig. 1). Note that the most of the C atoms in the N-doped graphene are arranged in a conjugated honeycomb lattice and the N atoms are substitutionally doped into the graphene lattice and mainly in the form of "graphitic" N.

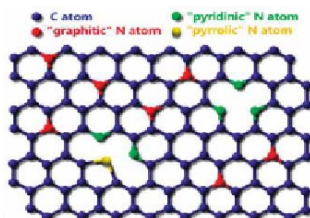


Fig.1 Schematic representation of the N-doped graphene. The blue, red, green and yellow spheres represent the C, graphitic N, pyridinic N and pyrrolic N atoms in the N-doped graphene, respectively.

First we studied the electronic properties of pristine graphene and then we investigated the electronic properties of graphitic, pyridinic and pyrrolic N-doped graphene. To investigate these structures, some electronic properties, such as Band structure,

the total density of states (DOS), projected density of states (PDOS) and charge density are calculated. As shown in Fig. 2, the DOS for spin up and down orientation are completely equal. The energy gap in graphene is zero therefore the electrons in valence band easily transit to conducting band. After doping with N the number of valence electrons is increased and some states of the conductance band are filled and consequently, the N impurity enhances electron carriers. It behaves like an n-type semiconductor, indicating the doping can modulate the electrical properties of graphene.

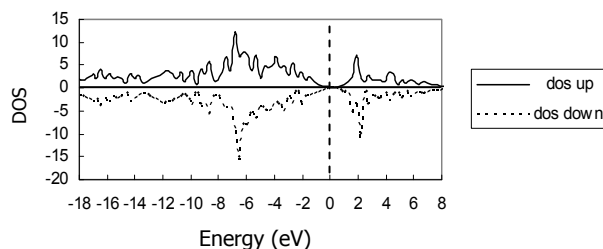


Fig. 2 DOS for pristine graphene. The Fermi level is plotted with dotted line and is at 0 eV.

References

- [1] K. S. Novoselov, A. K. Geim, S. V. Morozov, D. Jiang, Y. Zhang, S. V. Dubonos, I. V. Grigorieva, A. A. Firsov. *Science*. 306 (2004) 666.
- [2] A. K. Geim, K. S. Novoselov. *Nat. Mater.* 6 (2007) 183.
- [3] D. A. Areshkin, C. T. White. *Nano Lett.* 7 (2007) 3253.
- [4] R. Czerwl. *Nano Lett.* 1 (2001) 457.
- [5] S. Baroni, A. Dalcorso, S. D. Gironcoli, P. Giannozzi, C. Cavazzoni, G. Ballabio, S. Scandolo, G. Chiarotti, P. Focher, A. Pasquarello, K. Laasonen, A. Trave, R. Car, N. Marzari, A. Kokalj (2006).



Template-free preparation and characterization of various nanomaterials in aqueous solution of an ionic liquid and their photocatalytic activity

Aziz Habibi-Yangjeh

Department of Chemistry, University of Mohaghegh Ardabili, P.O. Box 179, Ardabil, Iran.

Email: ahabibi@uma.ac.ir

Keywords: Room-temperature ionic liquid, Photocatalysis, Nanomaterials, Kinetics

1. Introduction Morphological control of nanomaterials is of great significance for exploring new applications of them due to the interesting size and shape-dependent properties. High temperature or long reaction time was usually involved in preparation of nanomaterials. Also, most of the methods involved environmentally malignant chemicals and organic solvents, which are toxic and not easily degraded in the environment [1,2].

Room-temperature ionic liquids (RTILs) have shown tremendous promise as replacements for the toxic and volatile organic solvents used in many applications. These compounds readily dissolve many organic, inorganic and organometallic compounds and they have recently received a great deal of attention as potential new media for nanomaterials synthesis [3,4].

One of the largest barriers to the application of RTILs in various fields arises from their high cost relative to conventional solvents. Also, the most commonly used RTILs have PF_6^- and BF_4^- ions. RTILs with these ions are known to decompose in the presence of water and as a result toxic and corrosive species such as hydrofluoric and phosphoric acids are formed [5].

In continuing our investigations about nanomaterials and RTILs [6-10], simple methods were applied for preparation of ZnS, CdS and ZnO nanomaterials in presence of a RTIL. For above mentioned reasons, halide-free RTIL, 1-ethyl-3-methylimidazolium ethyl sulfate ([EMIM][EtSO₄]), was used in this work. Also, selection of the RTIL was mainly based on the fact that it can be obtained at a relatively low price and its synthesis method is simple. Therefore, a low temperature, cost effective, and simple route is proposed to obtain larger quantity of the nanomaterials with improved photocatalytic activity.

2. Experimental

The X-ray diffraction (XRD) pattern was recorded on Philips Xpert X-ray diffractometer with Cu K α radiation ($\lambda = 0.15406$ nm). Surface morphology and distribution of particles were studied *via* LEO 1430VP scanning electron microscope (SEM), using an accelerating voltage of 15 kV. The purity and elemental analysis of the products were obtained by energy dispersive analysis of X-rays (EDX) on the same LEO 1430VP instrument with the accelerating voltage of 20 kV. Diffuse reflectance spectra (DRS) recorded by a Scinco 4100 apparatus. To examine photocatalytic activity of the prepared samples, photodegradation of methyl orange (MO) and methylene blue (MB) have been investigated. A photochemical reactor provided with water circulation arrangement to maintain the temperature at 25 °C, was used in the experiments. The reaction kinetics was studied spectrophotometrically.

3. Results and discussion

The nanomaterials (ZnS, ZnO and CdS) were prepared by microwave and ultrasonic irradiations and solvothermal methods and they characterized using SEM, EDX, DRS and FT-IR instruments. To investigate the effect of solvent on properties of the nanomaterials, parallel experiments were carried out. The preparation procedures were similar to each other, except for changes in the solvent. Results demonstrate that mean size of the nanomaterials decreases as the amount of the RTIL increases in the reaction media. Moreover, aggregation of the nanomaterials decreases with increasing RTIL content of the media.

In order to investigate photocatalytic activity of the prepared samples, kinetics of photodegradation reaction for MB and MO on nanomaterials was studied. Observed first-order rate constant for photocatalytic degradation of MB and MO on the nanomaterials was calculated using plots of $\ln [\text{MB}]$ or $\ln A$ (logarithm of absorbance) *versus* irradiation time. The results demonstrate that photocatalytic activity of the nanomaterials prepared in presence of the RTIL is greater than the prepared samples in water. Significant improvement of photocatalytic activity for the nanomaterials prepared in presence of the RTIL should be related to the higher surface area of the nanomaterials due to lower aggregation. The small-sized nanocrystallines with high surface area are effective substrates for adsorption of the pollutant molecules and light [11]. Moreover, a limiting factor that controls the efficiency of photocatalysis is the rapid recombination of photogenerated electrons and holes in the

semiconductor particles [12]. Recombination of the electron-hole pair within the semiconductor particles is drastically reduced with decreasing particle size [13]. Hence, because of smaller size, recombination rate of electron and hole for the nanomaterials prepared in presence of the RTIL will be lower than the prepared sample in water. For these reasons, photocatalytic activity of the nanomaterials prepared in presence of the RTIL will be higher than the prepared sample in water.

A possible formation mechanism for the nanomaterials with small size and low aggregated forms in aqueous solution of the RTIL is presented. When aqueous solutions of the RTIL are used as a reaction medium, the solutes are solvated by ions, thus, the reactions proceeds in an environmentally different from that water or ordinary organic solvents are used. The imidazolium ring of the RTIL is an electron-withdrawing group and it can attract the electron pair shared by hydrogen and carbon of position 2 of imidazolium ring, thus the hydrogen-bonding between the RTIL and anion moieties of the nanomaterials are strong. Moreover, [EMIM]⁺ cations can combine with anion moieties of the nanomaterials through electrostatic attraction. As soon as the nanomaterials are formed, they get coated by the RTIL, thereby producing a control on the growth. Meanwhile, the activities of freshly generated the nanomaterials will be greatly inhibited by [EMIM]⁺ ions, so the growth of the nanomaterials will markedly be modified. Then, hydrogen-bonding and electrostatic interactions between the nanomaterials and the RTIL playing a crucial role in formation of small sized and low aggregated nanomaterials [14].

4. Conclusion

ZnS, CdS and ZnO nanomaterials were prepared in presence of 1-ethyl-3-methylimidazolium ethyl sulfate, [EMIM][EtSO₄], as a low-cost and halide-free RTIL. These environmentally benign green methods are fast and template-free which remarkably shortens preparation time and avoids the complicated synthetic procedures. The as-prepared ZnS, CdS and ZnO nanomaterials show blue shift which can be attributed to quantum confinement effect of the nanomaterials. Investigation of photocatalytic activity for the prepared nanomaterials reveals that photocatalytic activity of the prepared samples in presence of the RTIL is considerably higher than the prepared sample in water.

References:

- [1] X. Lu, H. Mao, W. Zhang, C. Wang, Mater. Lett. 31 (2007) 2288.
- [2] S. Shen, L. Gao, Mater. Res. Bull. 43 (2008) 437.
- [3] Y. Zhai, Y. Gao, F. Liu, Q. Zhang, G. Gao, Mater. Lett. 61 (2007) 5056.
- [4] H.K. Farag, F. Endres, J. Mater. Chem. 18 (2008) 442.
- [5] E. Gomez, B. Gonzalez, N. Calvar, E. Tojo, A. Dominguez, J. Chem. Eng. Data 51 (2006) 2096.
- [6] M. Behboudnia, A. Habibi-Yangjeh, Y. Jafari-Tarzanag, A. Khodayari, J. Crys. Growth 310(2008) 4544.
- [7] A.R. Harifi-Mood, A. Habibi-Yangjeh, M.R. Gholami, J. Phys. Chem. B 110 (2006) 7073.
- [8] A.R. Harifi-Mood, A. Habibi-Yangjeh, M.R. Gholami, Int. J. Chem. Kinet. 39 (2007) 681.
- [9] M. Khodadadi-Moghaddam, A. Habibi-Yangjeh, M.R. Gholami, App. Catal. A: Gen. 341 (2008) 58.
- [10] A.R. Harifi-Mood, A. Habibi-Yangjeh, M. R. Gholami, J. Phys. Org. Chem. 21 (2008) 783.
- [11] L. Wang, L. Chang, B. Zhao, Z. Yuan, G. Shao, W. Zheng, Inorg. Chem. 47 (2008) 1443.
- [12] D. Robert, Catal. Today, 122 (2007) 20.
- [13] A. L. Stroyuk, A. I. Kryukov, S. Ya. Kuchmii, V. D. Pokhodenko, Theor. Exper. Chem. 41 (2005) 207.
- [14] M. Esmaili, A. Habibi-Yangjeh, Physica Status Solidi (a) 206 (2009) 2529.

Effect of nitrogen doping on the photocatalytic activity of nanotitania prepared by sol-gel method for photodecomposition of phenolic compounds in the presence of Visible light

M. R. Toosi^a, V. Zarei^b, M. D. Ganji^a, F. Gholami^a, ,

^a Department of Chemistry, Islamic Azad University, Ghaemshahr Branch, Ghaemshahr, Iran

Email: mrtoosi@gmail.com

^b Department of Chemistry, Shahid Beheshti University, Tehran, Iran

Keywords : Photocatalyst, Nanotitania, Doping, Para-amino phenol.

1.Introduction

One of the new applications of nanotechnology is the preparation of nanomaterials for solution of the environmental problems associated with water contamination. Nanotitania, TiO₂, as a semiconductor with photocatalytic properties, has been widely used for removing water and air contamination [1]. It has shown high activity for degradation and mineralization of several organic contaminants [2]. However, conventional TiO₂ has a technological limitation for using in a large scale because it requires ultraviolet radiation ($\lambda < 400$ nm) to overcome its wide band gap energy (3.2 eV for anatase phase) for Photocatalytic activation [3] but UV radiation accounts only for 5% of the total solar spectrum compared to the visible region. Several methods have been obtained towards the development of modified TiO₂ with visible light response, such as dye sensitization [4], metal [5] and non-metal [6] doping of nanotitania to reduce the band gap energy. However, in some cases metal doping has decreased the visible light photocatalytic activity because of the increase of the carrier-recombination centers (electron-hole pairs) and low thermal stability of the modified material [7]. Moreover, metal doping of nanotitania can produce some new economical and environmental problems. Therefore, the non-metal doping of nanotitania has more safety and consists with the environmental considerations. This phenomenon can shift the optical absorption towards visible light and make possible the photocatalytic activity in the visible region. The aim of this study is to investigate the effect of nitrogen doping of TiO₂ nanoparticles in the photocatalytic decomposition of some phenolic compounds as the water contaminants under visible light irradiation. A novel sol-gel method was employed for preparation of N-doped TiO₂ nanoparticles.

2.Methods

A modified sol-gel method was used for preparation of N-doped nanotitania. tetrabutyl titanate (20 ml), as the titanium precursor dissolved in 10 ml ethanol and 5 ml acetic acid, was added dropwise to the ethylenediamine (10 ml), as the nitrogen source, dissolved in 20 cc of isopropanol. The solution was stirred rapidly for preventing the aggregation of the particles. The addition having been completed, slow stirring continued until the solution formed a transparent immobile gel. Afterwards, the gel was dried at 110 °C for 24 h and then calcined in a furnace where the temperature was increased up to 400 °C at a ramp rate of 2 °C/min. X-ray powder diffraction patterns were recorded for determination of the sample structure. The surface area of the samples was measured by N₂ adsorption and microporous volume was calculated using the t-plot method. UV-Vis absorption spectra of samples were obtained using a UV-Visible spectrophotometer (Perkin-Elmer). The photocatalytic activity of the synthesized TiO₂ nanoparticles was evaluated for the degradation of para-aminophenol as a commercial toxic contaminant. The photocatalytic reactions were performed in the aqueous solution by using a cylindrical glass vessel as photocatalytic reactor. A 15W fluorescent lamps in conjunction with a light filter (wavelength: 400-500 nm) were employed to irradiate visible light. Samples were analyzed by Shimadzu 8A gas chromatograph equipped with Porapak-Q column and the thermal conductive detector (TCD).

3.Results and discussion

The X-ray diffraction patterns indicated the anatase crystal phase (most active phase) without any indication of other crystalline phases, such as rutile or dopant related. It indicated good dispersion of nitrogen species since no other phase besides TiO₂ could be observed.

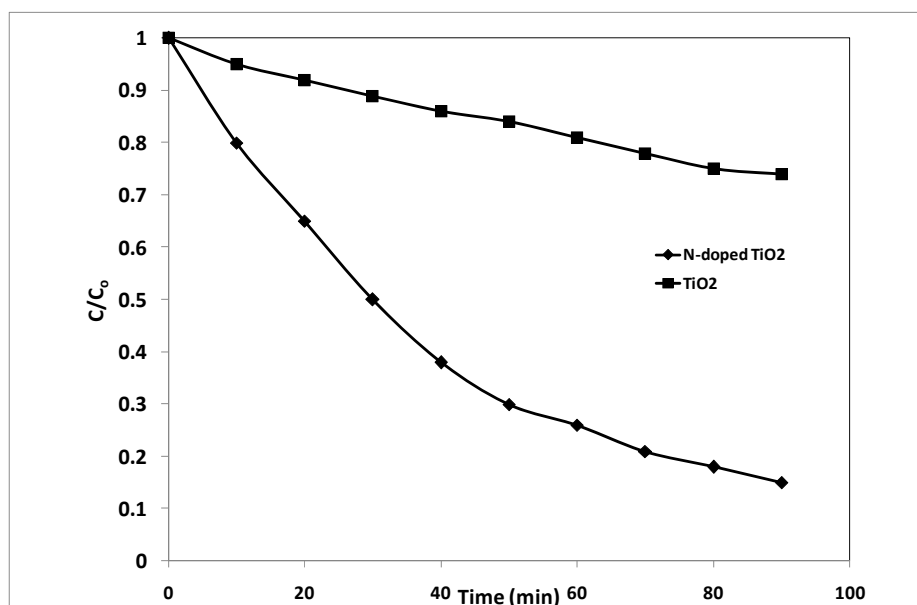


Fig.1 Photodegradation of para-amino phenol over N-doped TiO₂ and non-doped TiO₂.

The results of photodegradation of para-amino phenol over N-doped TiO₂ indicated kinetically as a first order reaction (Figure 1). Comparison of photocatalytic activity of N-doped nanotitania with the non-doped TiO₂ showed an increase in the photoactivity of N-doped TiO₂ in the presence of visible light. The results obtained from UV-Visible spectra was shown a new absorption band in the visible range of 400~550 nm in all N-TiO₂ powders, indicating the formation of N–Ti bonding in N-TiO₂ powder [7].

4. Conclusion

The nanoparticles exhibited enhanced structural properties such as active anatase phase, good dispersion of N atoms, and low degree of agglomeration, as well as photocatalytic properties under visible light irradiation compared to the reference TiO₂. Nitrogen doping led to a narrowing of the band gap by mixing the N2p and O2p states and consequently induced visible-light absorption.

References

- [1] H. Choi, E. Stathatos, D.D. Dionysiou, Appl. Catal., B 63 (2006) 60.
- [2] Y.Q. Wang, X.J. Yu, D.Z. Sun, J. Hazard. Mater. 144 (2007) 328.
- [3] W. Choi, A. Termin, M.R. Hoffmann, J. Phys. Chem. B 98 (1994) 13669.
- [4] A.E.J. Gonzalez, S.G. Santiago, Semicond. Sci. Technol. 22 (2007) 709.
- [5] S. Yin, K. Ihara, M. Komatsu, Q. Zhang, F. Saito, T. Kyotani, T. Sato, Solid State Commun. 137 (2006) 132.
- [6] H. Irie, Y. Watanabe, K. Hashimoto, J. Phys. Chem. B 107 (2003) 5483.
- [7] R. Asahi, T. Marikawa, T. Ohwaki, K. Aoki, Y. Taga, Science, 293 (2001) 269.

Synthesis and nonlinear optical properties of silver nanoparticles

A. Daneshfar^a, R. Sahraei^{a,*}, H. Kavian^a and M. H. Majles Ara^b

^aDepartment of Chemistry, University of Ilam, Ilam, Iran

^bDepartment of Physics, Tarbiat Moallem University, 49 Mofateh Ave., Tehran, Iran

* Email: reza_sahrai@yahoo.com

Keywords: Silver nanoparticles, Z-scan technique, Optical properties, Chemical deposition

1. Introduction

Silver nanoparticles certainly have the potential to be the building blocks of future photonic and plasmonic devices as the field of nanotechnology matures [1]. Additionally, silver nanoparticles have a surface plasmon resonance absorption in the UV-Vis region. The surface plasmon band arises from the coherent existence of free electrons in the conduction band due to the small particle size effect [2]. The band shift is dependent on the particle size, chemical surrounding and dielectric constant [3]. The aim of this work is to develop a simple method to modify the synthesis of long-time stable Ag nanoparticles and the study of the nonlinear optical properties of these nanoparticles under low power continuous wave (CW) He-Ne laser irradiation. Nonlinear refractive index, n_2 , for three input intensities, is easily measured by the z-scan method [4]. The obtained nanoparticles were also characterized by means of UV-Vis. absorption spectroscopy, X-ray diffraction (XRD), and transmission electron microscopy (TEM).

2. Experimental

Colloidal Ag nanoparticles were prepared in a 1.0 L Pyrex round-bottom three-neck flask equipped with a thermometer, a condenser, and a spout for drawing samples from the third neck. Each synthesis followed the same basic procedure: 160 mg AgNO_3 was dissolved in 200 ml of doubly distilled water and then mixed with 5 g of poly(vinyl pyrrolidone) denoted PVP dissolved in 200 ml hot pure water. The mixture was then poured into the flask for reduction by H_2 gas. The flask and its contents were then heated to 70 °C, and this temperature was maintained throughout the synthesis. As the reaction progresses, aliquots can be taken through the spout. Removing the aliquots from the reducing environment stops further growth of the particles. Likewise, the reaction can be stopped at any time simply by releasing the gas from the vessel.

The UV-Vis absorption data were collected on a Perkin Elmer Lambda 25 spectrophotometer using a quartz cell with an optical path of 1 cm. X-ray diffraction (XRD) pattern was recorded with an automated Philips X'Pert X-ray diffractometer with Cu K α radiation (40 kV and 30 mA) for 2θ values over 20-70°. The investigation of the nonlinear optical characteristics of silver nanoparticles suspensions was carried out using the CW He-Ne laser and the transmission z-scan technique.

3. Results and discussion

Silver nanoparticles absorb radiation in the 380-450 nm regions of the electromagnetic spectrum due to the excitation of surface plasmon vibrations and this is responsible for the striking yellow-brown color of silver nanoparticles in various media [9]. Absorption spectra measurements were extended to much longer times than the 3 h shown in Fig. 1 (Left). These show the surface plasma resonance absorption peaks are located in the 400 nm and as the reaction proceeds, no displacement occur in the position of the extinction maximum of peaks. In other words, as the time of reaction increases, the new nanoparticles are formed and no further growth of already existing nanoparticles occurs. The evolution of the maximum in the absorption spectra starts from the initial peak position around 400 nm representing the dipole component of the plasmon resonance of small silver nanoparticles. As the number of nanoparticles increases, the intensity of the resonance increases and its position remain at the same wavelength.

The laser radiation was focused by an 80 mm focal length lens. We calculated the linear absorption $\alpha = 3.71 \text{ cm}^{-1}$ by measuring output power for a sample as a function of the power without the sample in low powers. By experimental result of Optical limiting (OL) behaviour of the Ag nanoparticles suspension with different incident intensity one can find linear absorption from equation 1.

$$\alpha = -\frac{1}{L} \ln \left(\frac{P}{P_0} \right) \quad (1)$$

In order to observe the process of two photon absorption, by taking advantages of the z-scan technique, we applied a He-Ne laser beam with 632.8 nm wavelength. The effective nonlinear coefficient (n_2) of Ag nanoparticles was determined by the single beam z-scan technique. The normalized curves of close aperture z-scan have a pair of sharp peak and valley, which identifies itself as a self-defocusing material (Fig. 1 (Right)). Since the peak of the transmittance precedes the valley, the sign of the refractive nonlinearity of Ag nanoparticles is negative (negative lens effect). This suggests that the Ag nanoparticles could be considered as a promising candidate for optical limiting.

The XRD pattern of silver nanoparticles powder exhibits peaks at 2θ angles of 38.17, 44.21, 64.32, and 77.12 that correspond to the [111], [200], [220], and [311] crystal planes of a cubic lattice structure of silver nanoparticles, respectively [10]. From the full-width at half-maximum of diffraction peaks, the average size of the silver nanoparticles has been calculated using the Debye-Scherrer equation [5]. The calculated average size of Ag nanoparticles was around 22 nm.

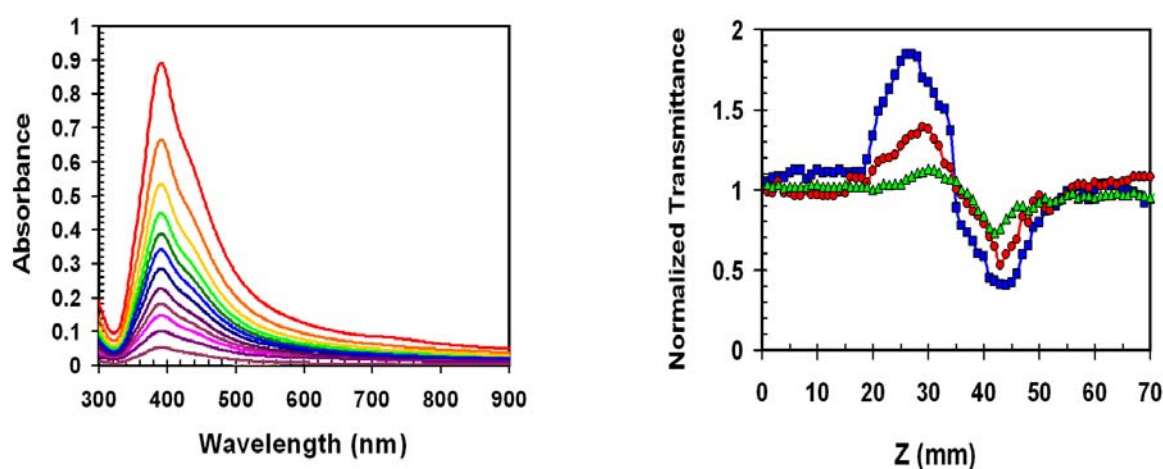


Fig. 1 Evolution of absorption spectra of the Ag nanoparticles taken at 15 min intervals following the initiation of the reaction for the first 3 h (Left) and Z-scan experimental curves of silver nanoparticles suspension under He-Ne laser beam with 632.8 nm wavelength at 3 input intensities (Right).

4. Conclusion

Silver nanoparticles in stable aqueous suspensions were prepared via reduction of silver nitrate (AgNO_3) by hydrogen gas. The nanoparticles were characterized by their UV-Vis absorption spectra, by X-ray diffraction, and by transmission electron microscopy. Average particle size obtained from TEM analysis is 20 ± 5 nm that agreed with XRD result fairly well. We also studied the nonlinear optical properties of the Ag nanoparticles by the z-scan technique. The nonlinear refraction was analyzed based on the two-photon absorption nonlinearity theory. The nonlinear refraction, n_2 , is obtained to be in the order of 10^{-7} and the values of the third-order nonlinearities of nanoparticles themselves are of interest from the application point of view.

References

- [1] J. A. Jacob, H. S. Mahal, N. Biswas, T. Mukherjee, S. Kapoor, *Langmuir*, 24 (2008) 528.
- [2] A. M. Smith, H. Duan, M. N. Rhyner, G. Ruan, S. A. Nie, *Phys. Chem. Chem. Phys.*, 8 (2006) 3895.
- [3] I. Lisiecki, *J. Phys. Chem. B*, 109 (2005) 12231.
- [4] M. H. Majles Are, E. Koushki, S. Salmani, S. H. Mousavi, *Opt. Commun.*, 278 (2007) 418.
- [5] A. Goudarzi, G.M. Aval, R. Sahraei, H. Ahmadpoor, *Thin Solid Films*, 516 (2008) 4953.



Fluorescence of Nanocrystalline Mn doped ZnS thin films Prepared by chemical deposition

Alireza Goudarzi^a, Reza sahraei^b, Chang-Sik Ha^{b,*}

^a Department of polymer Engineering, Golestan Univ., Gorgan, Iran

E-mail: Goudarzi.alireza@gmail.com

^b Department of Chemistry, University of Ilam, Ilam, Iran

^c Department of Polymer Science and Engineering, Pusan National University, Busan 609-735, Republic of Korea

E-mail: csha@pusan.ac.kr

1. Introduction

ZnS is a famous phosphor material with various luminescence properties, such as photoluminescence (PL), and electroluminescence (EL) and so generally used in the fields of displays, sensors, and lasers. ZnS has band-gap energy of 3.6 eV. Because of wide band gap energy of ZnS, we can have different radiation wavelengths by doping of transition or rare earth metal ions. The luminescence properties of ZnS doped with Mn have proven to be suitable for electroluminescence applications. It is well-known that Mn²⁺ can substitute for Zn²⁺ ions in the ZnS crystal lattice because of their close ionic radii (0.80 and 0.83, for Mn²⁺ and Zn²⁺, respectively).

There are only a few reports about preparation of ZnS:Mn thin films. In these reports ZnS: Mn films have been usually prepared by expensive and/or strict methods such as spray pyrolysis.[1,2] The present work reports a new and simple method for the preparation of nanocrystalline Mn doped ZnS thin films at different doping levels at 70°C, and studies surface morphology, structure, and effect of deposition times and doping level on photoluminescence properties of the films.

2. Method

Nanocrystalline ZnS: Mn thin films were deposited on quartz and (commercial microscope slide) glass substrates using EDTA solution as a complexing agent for zinc ions and Mn²⁺ ions as a dopant. Before the film deposition, the substrates were cleaned ultrasonically sequentially in acetone, 2-propanol, and deionized water. The substrates were then dried for one hour in an oven at 90 °C. Finally, the substrates were immersed in a dilute solution containing zinc, manganese and ammonium salts, EDTA and a source of sulfide at 70 °C. The chemical solution was not stirred during the film deposition. The coated substrates were removed at the end of the chosen duration of deposition, washed in de-ionized water, dried in air at room temperature, and subjected to further analyses.

The fluorescence (FL) emission and excitation spectra of the films were measured using a Hitachi F- 4500 fluorescence spectrophotometer. The crystallinity, phase and orientation of the films were determined by X-ray diffraction (XRD). The surface morphology of ZnS: Mn these films were observed by a field emission scanning electron microscopy (FE-SEM). The band gap energy values were determined from UV-visible spectroscopic data.

3. Results and Discussion

The steep absorption edge of the films and FE-SEM images demonstrated a dense and uniform surface that was free of pits or pinholes with a narrow grain size distribution. The fluorescence intensity of the films is strongly dependent on deposition time and doping level and shows Mn²⁺ concentration quenching effect at high deposition time and high doping level.

The FL spectra of the ZnS:Mn films showed an emission band at approximately 590 nm (yellowish orange) which is corresponded to characteristic emission of Mn²⁺ ions in ZnS crystal lattice [3],[4]. The XRD patterns revealed the films to be

polycrystalline. The nanocrystallite size was estimated to be ~ 3 nm. Debye-Scherrer equation was used to estimation of

nanocrystallite sizes. The XRD patterns also showed the films have a cubic zinc blend structure (JCPDS no. 05--0566). There were no obvious structural phase differences in XRD results of the Mn-doped ZnS films with different Mn concentrations.

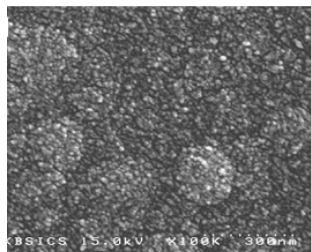


Fig.1 FE-SEM image of ZnS:Mn films prepared during 10 hours at 70 °C.

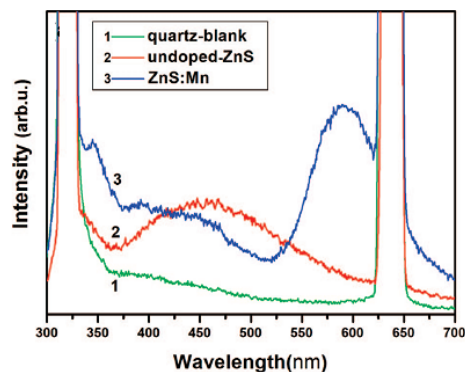


Fig.2 A typical Fluorescence spectrum of the uncoated quartz (blank), ZnS, and ZnS:Mn films deposited on quartz substrates .

4. Conclusions

The ZnS:Mn thin films have been deposited on glass and quartz substrates at 70 °C. The fluorescence emission spectra of the prepared ZnS:Mn thin films showed a strong emission peak at about 590 nm which is related to characteristic emission of Mn^{2+} ions in ZnS crystal lattice and means that the Mn^{2+} ions could successfully occupy defect sites which arises Zn vacancy in the ZnS lattice. In addition, the FL intensity of the films was strongly dependent on deposition time and doping level.

The FE-SEM image of the films showed that the film compactness was high, the surface's uniformity was good, the particle size was quite fine, and the particle size distribution was also narrow. By using XRD data, the nanocrystallite size of films was estimated to be ~ 3 nm .

References

- [1] Lo ´pez, M. C., Espinos, J. P., Mart ´n, F., Leinen, D., Ramos-Barrado, J. R. J. Cryst. Growth 285(2005), 66.
- [2] Hern ´andez-Fenollosa, M. A.; Lo ´pez, M. C.; Donderis, V.; Gonza ´lez, M.; Mari ´, B.; Ramos-Barrado, J. R. Thin Solid Films, 516(2008), 1622.
- [3] Goudarzi, A., Motedayen Aval, G., Sahraei, R., Habib Ullah, M., Park, S.S., Avanan, A., Choi, M.C., Ha C.S., Chem. Mater. 21(2009) 2375.
- [4] Angshuman, N., Sameer, S., Nagamani, A. S., Chem. Mater. 19(2007) 3252 .

Synthesis of Nanostructured MnO₂/carbon black composites using sonochemistry method for electrochemical supercapacitors

H. Naderi, A. Zolfaghari*, H. Mortaheb, M. Rastgar, H. Sayahi

Chemistry and Chemical Engineering Research Center of Iran, Tehran, Iran

Email: zolfaghari@ccerci.ac.ir

Keywords: Nanostructured Manganese dioxide, Supercapacitor, Sonochemistry, carbon black, Composite electrode

1. Introduction

Supercapacitors are energy storage devices, which exhibit acceptable capacity, high power density and long cycle life. On the basis of electrode materials used and the charge storage mechanisms, electrochemical supercapacitors are classified as: (a) electrochemical double-layer capacitors (EDLCs) which employ carbon or other similar materials as blocking electrodes and (b) redox supercapacitors in which electroactive materials such as insertion type compounds (e.g. RuO₂, MnO₂, etc.) or conducting polymers are employed as electrodes[1].

Electrochemical supercapacitors based on manganese dioxide as active electrode materials are currently attracting a lot of interest due to the relatively low cost of MnO₂ and the fact that it makes use of environmentally friendly aqueous electrolytes[2-3].

Sonochemistry methods have been successfully applied to the preparation of various nanostructured metal oxides [4-8] at room temperature, ambient pressure, and short reaction time. Some manganese oxides/carbon composites prepared by mechanical mixing, chemical and electrochemical deposition methods have been used as electrode materials in supercapacitors[9-11].

We report here a sonochemical method for synthesis of composite nanostructure manganese dioxide/carbon black by oxidation of Mn²⁺ and the characterization of the composites as an active material for supercapacitor electrodes.

2. Experimental

2.1. synthesis

Aqueous solutions of 0.5 M KBrO₃ (Merck, research grade) and 0.25 M MnSO₄ (Merck, research grade) and various amount acetylene black (Alfa Aesar, >99.9%, S.A. 80m²/g), by the total volume of 100 mL, were irradiated by ultrasonic radiation at constant temperature of 50-55 °C. A 24 kHz ultrasound horn transducer system (UP 200 H, Dr. Hielscher GmbH) with a 2mm microtip (titanium alloy) and a sonic power density of 480 W/cm² was employed.

2.2. Electrochemical measurement

Electrodes were prepared by mixing 66 wt% of MnO₂/carbon black powder as active material with 27 wt% of graphite (Alfa Aesar, conducting grade, -200 mesh), and 7 wt% of poly(tetrafluoroethylene) dried powder (Merck). The three first constituents were first mixed together to obtain a homogeneous black powder. The poly(tetrafluoroethylene) powder was then added with a few drops of ethanol. This resulted in a rubber-like paste that was rolled into a film (100–200 μm thick) on a flat glass surface. A piece of film (0.25 cm²) was cut and pressed onto stainless steel grid current collector.

An Autolab, Eco Chemie. B.V. potentiostat/galvanostat was used for all electrochemical measurements. A beaker type electrochemical cell equipped with a MnO₂ based working electrode, an Ag/AgCl electrode (Metrohm AG 9101 Herisau, 3M KCl, 0.207V versus SHE at 25 °C) reference electrode and a 1 cm² stainless steel grid counter electrode was used. The solution temperature was maintained at 25 °C by means of a water thermostat (RE 104 Ecoline, LAUDA).

The average specific capacitance was calculated by integrating either the oxidative or the reductive CV half-cycle over the potential window of the voltammogram. All the specific capacitances are reported per gram of active material.

3. results and discussion

Fig. 1 shows the cyclic voltammogram composites in aqueous 0.5M Na₂SO₄ electrolyte within a potential window of 0.0 to +1.0V versus Ag/AgCl. All the CVs show almost rectangular and symmetric current potential characteristics of a supercapacitor. The capacitance can be estimated on the basis of the following equation [1]:

$$C = \frac{q}{v \Delta x w} \quad (1)$$

q=voltammetric charge, v=scan rate of CV , w= oxide loading

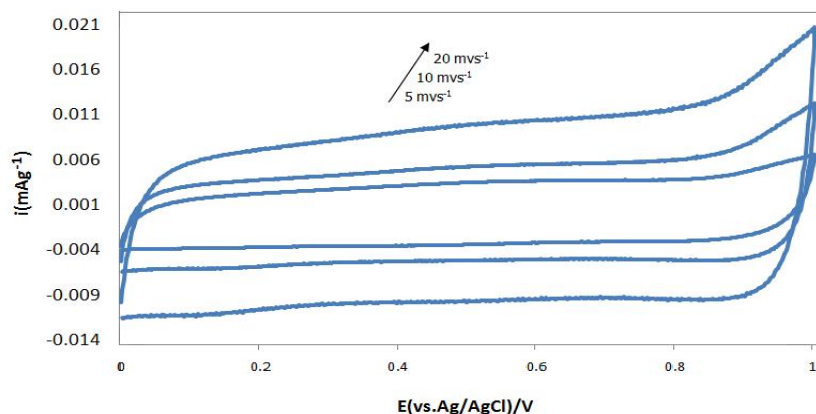


Fig.1 CV curves of MnO₂-20%carbon composite at different scan rates of 5, 10, 20.

4.conclusions

In this paper, Nanostructured MnO₂/carbon black composites and γ-MnO₂ have been synthesized using ultrasonic radiation. For MnO₂ the the specific capacitance is 204 and 100 F g⁻¹ at 2 and 200 mVs⁻¹, respectively. For MnO₂-carbon black composite of ratio 80-20, the specific capacitance based on MnO₂ is 245 and 118 F g⁻¹ at 2 and 200mVs⁻¹, respectively. In addition, the nanostructured samples demonstrate excellent reversibility and high power density.

References

- [1] B.E. Conway, Electrochemical Supercapacitors, Kluwer-Plenum, New York, 1999.
- [2] H. Y. Lee, J. B. Goodenough, J. Solid State Chem. 144 (1999), 220.
- [3] T.Brousse, M. Toupin, R. Dugas, L. Athouel, O.Crosnier, D. Be' langer, J. Electrochem. Soc. 153(2006), A2171.
- [4] A. Zolfaghari, F. Ataherian, M. Ghaemi, A. Gholami, Electrochim. Acta 52 (2007) 2806.
- [5] X. Cao, Yu. Koltypin, G. Katabi, I. Felner, A. Gedanken, J. Mater. Res. 12 (1997) 405.
- [6] N. Arul Dhas, A. Gedanken, J. Phys. Chem. B 101 (1997) 9495.
- [7] R. Vijaya Kumar, Y. Diamant, A. Gedanken, Chem. Mater. 12 (2000) 2301.
- [8] A. Patra, E. Sominska, S. Ramesh, Yu. Koltypin, Z. Zhong, H. Minti, R. Reisfeld, A. Gedanken, J. Phys. Chem. B 103 (1999) 3361.
- [9] R. K. Sharma, H. S. Oh, Y. G. Shul, H. Kim, Physica B. 403 (2008) 1763.
- [10] L. L. Zhang, T. Wei , W. Wang, X. S. Zhao, Microporous and Mesoporous Materials. 123 (2009) 260.
- [11] J. K. Chang, C. T. Lin, W. Ta. Tsai, Electrochem. Commun. 6 (2004) 666.

Solubility Investigation of Nano Particles by Nonextensive Property and Fractal Dimension Approach

A.Moradi*, M. G. Mahjani^a

^aDepartment of Chemistry ,Faculty of science, K. N. Toosi University of Technology, Tehran, Iran

*E-mail: Akrammoradi18@Yahoo.com

Keywords: solubility of nanoparticles, nonextensie thermodynamics, fractal surface

1.Introduction

The solubility of solid particles in liquids is of fundamental properties of materials with high application in industry. Solubility investigation is usually studied in classical thermodynamic for large solid particles. In recent years nano particles are vastly used in drug industry as well as chemical industry. The specific characters of nano paricles arises from nano scale (1-100 nanometer) . the classical thermodynamics could not explain the solubility of nano particles precisely. The nanoparticles solubility can be investigated by using nonextensive thermodynamics concepts or fractal dimension studies of particles surfaces. The aim of this work is the study of the relations between thermodynamic dimension and fractal dimensions [1].

2.Methods

Since the nanoparticles behaviours are extremely dependent on their sizes and shapes , $\tau d\chi$ parameter have an important role in internal energy calculations.

Our approach is based on a thermodynamic description involving the introduction in the internal energyexpression of an extensity (χ). χ is the mass particle Euler's function with a homogeneity degree (m). m is the thermodynamic dimation of the system [2].

3.Result and Discussion

To study the relation between thermodynamic and fractal dimensions [3] the Ostwald-freundlich relation is used as the principle relation

$$\ln \frac{C_i(p,m)}{C_i(p,\infty)} = \frac{V_i^* (2\gamma)^{1/m}}{RT} \quad (1)$$

$C_i(p,\infty)$ is the concentration of i at saturation when the solid i is in unlimited phase (no size effect), V_i^* is the molar volume of i , T the temperature, and R the perfect gas constant.

The relation which is derived to calculate the solubility is dependent on the system thermodynamic dimension (eq.2)

$$\ln \frac{C_i(p,m)}{C_i(p,\infty)} = \frac{V_i^*}{RT} \ln k m^m \quad (2)$$

where k is a characteristic constant of the nonextensive phase considered. In this work, by using the laplace's relationship for nonextensive systems the above-mentioned relation is correlated to fractal dimation. The achived results show that these two approaches can be related. The achived correlation make solubility calculations easily.

4.Conclusion

The nonextensive thermodynamics and fractal surface constitute a consistent set of relations which allow description of the physicochemical behaviours of nanoparticles.

Link fractal approaches and nonextensive thermodynamics led to power laws, and this show relation between thermodynamic dimensions and fractal dimensions.

References

- [1] W. L. Jorgensen and E. M. Duffy, Adv. Drug Deliv. Rev, 54 (2002) 355.
- [2] P. Letellier, A. Mayaffre, M. Turmine, J. Phys. Condens. Matter, 19 (2007) 436229.
- [3] A. Mhranyan, M. Strømme, Surface Scienncce, 601 (2007) 315-319.



Chemical bath deposition of Nanocrystalline SnS thin films from aqueous solution

R. Sahraei^{a,*}, A. Daneshfar^a, A. Karimi^b and S. Sarfi^c

^aDepartment of Chemistry, University of Ilam, Ilam, Iran

^bDepartment of Chemistry, Payam-e Nour University, Urmia, Iran

^cNuclear Fuel Cycle School, Nuclear Science & Technology Research Institute, Tehran, Iran

* (Email: reza_sahrai@yahoo.com)

Keywords : Nanostructures, SnS Thin films, Morphological properties

1. Introduction

The recent investigations in the field of photovoltaic are directed towards the development of cost effective and nontoxic materials that can be synthesized by a simple technology for solar cell fabrication [1]. Tin sulphide (SnS) has a near optimum energy band gap, additionally SnS has the advantage of its constituent elements being abundant in nature and not posing any health and environmental hazards. Therefore, SnS can be potentially used as a solar absorber in a thin film solar cell and near-infrared detector, as photovoltaic materials [2]. The deposition of SnS thin films have been made by various techniques. Chemical bath deposition (CBD) has been used widely to deposit the materials, because it is a cheap, simple and low temperature deposition method [3, 4]. In this paper we report the successful deposition of nanostructured SnS thin films at 25 and 50 °C and investigate the principal characteristics of these films.

2. Experimental

The deposition bath was prepared by transferring 10 ml of 0.1M Sn(II) to a 100 ml beaker, followed by the sequential addition of 15 ml 3.7 M triethanolamine, 16 ml 15 M ammonia, 10 ml 0.1 M thioacetamide and distilled water. The glass slides were immersed in bath solution. The deposition was carried out at 25 and 50 °C for 6 h and 2:30 h, respectively. Five consecutive deposits were made to achieve the nanostructured SnS thin films that these films had high thickness and absorbance. Optical absorbance (A) and transmittance (T) spectra of deposited SnS films were obtained by using Cary 300 Bio (Varian) double beam UV/VIS spectrophotometer in the wavelength range of 200-900 nm.

3. Results and discussion

Considering the fact that the CBD method is usually carried out at near ambient temperatures (~25-80 °C), so the two temperatures of 25 and 50 °C are chosen to investigate the effect of temperature on structure, thickness and absorbance of nanostructured SnS thin films. Fig.1 shows the transmittance and reflectance spectra for the films grew at 25 and 50 °C. The band gap energy of these films were calculated using the procedure given by plotting $(ah\nu)^2$ against $h\nu$. These results show that, with an increase in deposition temperature, the thickness of films increases but the band gap energy decreases.

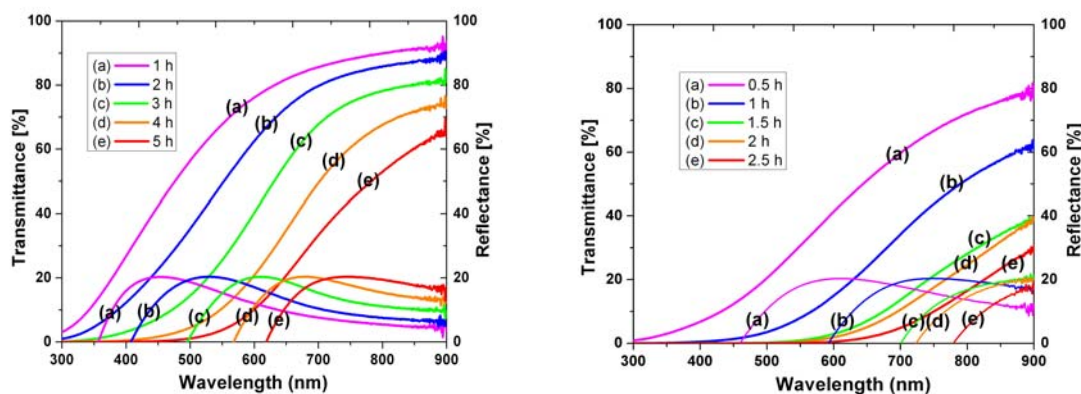


Fig.1 Optical transmittance and reflectance spectra of SnS thin films deposited at various temperatures: (Left) 25, and (Right) 50 °C as a function of the deposition times.

Despite the high thickness of nanostructured SnS thin films; these films had the band gap energy more than the previous works. The films grown at 25 and 50 °C had high transmittance about of 78% and 35%, respectively.

X-ray diffraction (XRD) data obtained by scanning 2θ in the range 20-80°, with a grazing angle equal to 1.5° for the deposited SnS film on the glass substrate. The thickness of the film was about 420 nm. The four broad peaks observed in the diffractogram at around 26.2°, 31.45°, 51.25°, and 64.4° reveal an orthorhombic lattice structure of SnS. These peaks can be assigned to the planes (120), (111), (151), and (251), respectively, of the orthorhombic phase.

Figs. 2 show SEM images of the SnS thin films on the glass substrate at two different temperatures of 25 (Left) and 50 °C (Right). From Fig. 2 for the thin films deposited at 25 and 50 °C the following points are observable: (i) The grains formed at 25 °C are small of about 50-150 nm in size and are uniform. (ii) The SnS grains at 50 °C reveal some size categories of 100, and 250 nm; larger clusters of about 350 nm in size are formed; the clusters themselves are aggregate of grains.

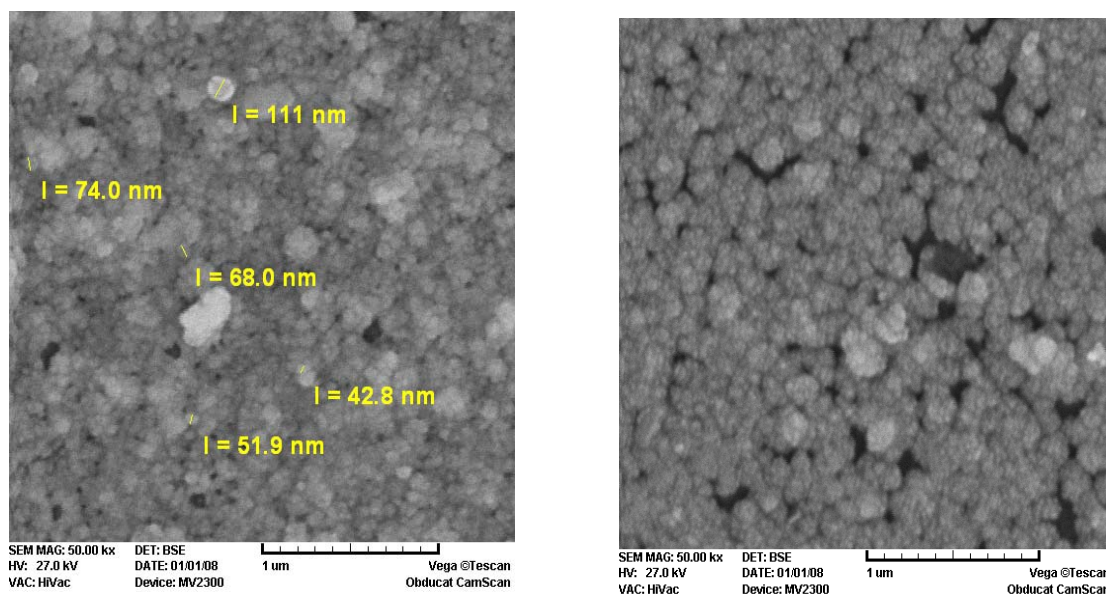


Fig.2 SEM images of SnS thin films deposited at 25 °C (Left) and at 50 °C (Right), respectively.

4. Conclusions

Nanocrystalline tin sulfide (SnS) thin films were deposited on glass substrate at two different temperatures of 25 and 50 °C by a chemical solution deposition technique. Optical study is performed to calculate optical band gap (E_g) using transmission and reflection spectra in the wavelength range 300-900 nm. The band gap measured was found to be in the range of 2.2 - 3.15 eV. These SnS thin films possess a nanocrystalline structure, exhibit quantum size effects due to the small crystal size and produce a blue shift in the optical spectra. This blue shift was attributed to a decrease in crystal size by using X-ray diffraction and scanning electron microscopy.

References

- [1] D. Avellaneda, G. Delgado, M. T. S. Nair, p. K. Nair, Thin Solid Films 515 (2007) 5771-5776..
- [2] G.i S. Paul, P. Gogoi, P. Agarwal, Journal of Non-crystalline solids 354 (2008) 2195-2199.
- [3] p.p. Hankare, A. V. Jadhav, P. A. Chate, K. C. Rathod, P. A. Chavan, S. A. Ingole, Journal of Alloys and Compounds 463 (2008) 581-584.
- [4] R. Sahraei, G. Motedayen Aval, A. Baghizadeh, M. Lamehi-Rachti, A. Goudarzi, M.H. Majles Ara, Materials Letters 62 (2008) 4345-4347.

Molecular dynamic simulation of CTAB surfactants on carbon nanotube

M. Foroutan, F. Mirzaie Milani*

Department of Physical Chemistry, School of Chemistry, College of Science, University of Tehran, Tehran, Iran,

E-mail: f.mirzaie.milani@khayam.ut.ac.ir

Key words: Molecular dynamic simulation; CTAB surfactant; Single wall carbon nanotube.

1. Introduction

Carbon nanotubes (CNT) have attracted widespread interest in research and increasing industrial attention. Unfortunately, nanotubes tend to bundle because of van der Waals interactions and in solution also because of hydrophobic interactions. Because tubes are very long, a relatively large amount of energy is required to separate a tube from a bundle, making it very difficult to suspend or disperse the tubes [1]. Surfactant molecules such as detergents consist of two chemically distinct functional groups, namely a hydrophilic head group and a hydrophobic tail group [2]. Regardless of the complexity of the assembly structures, it is well-known that the polar head groups of surfactants tend to be exposed to water whereas the nonpolar tail groups tend to be shielded from contacting water by the head groups. The final equilibrium morphology of the surfactant represents a delicate balance between forces involved in chemical interactions among the polar groups, nonpolar groups, and water molecules [2]. By considering the importance of two above systems, CNT and surfactant, in present work we study the behavior of aqueous solution containing surfactant and CNT.

2. method

Aqueous CTAB surfactants were simulated at contact with (5,5) single-walled CNTs. Computer simulations of this system were carried out using a 3.1 nm by 2.7 nm by 3.7 nm cubic computational cell with periodic boundary conditions applied in all three principal directions. Molecular dynamic simulations at 300 K were carried out using tinker software package. Non-bonded van-der-Waals' interactions are modeled by a Lennard-Jones (L-J) potential with a cut-off distance of 1.0 nm. Water molecules were modeled using the SPC/E model. The number of particles, the simulation box volume, and the temperature were maintained constant during our simulation. In our simulation the time step was 2 fs. simulation were conducted for 3ns. 598 water molecules are placed in the cell to obtain the average density of water essentially equal to its experimental counterpart (1 kg/m³) and 16 CTAB molecules are placed in the cell.

3. Result and discussion

Figure 1 shows two snapshots from the simulated system with 16 surfactant molecules and one single wall carbon nanotube.

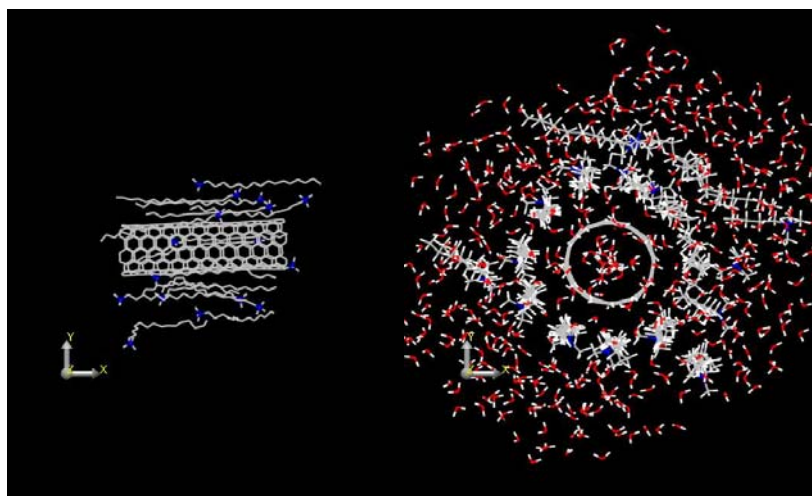


Fig. 1 side(left panels) and front views(right panels) of representative snapshots for (5,5)SWNT covered by CTAB surfactants. in left panel water molecules are not shown.

CTAB surfactants on (5,5) SWCNTs form rings in which the surfactants lie parallel to the nanotube axis.

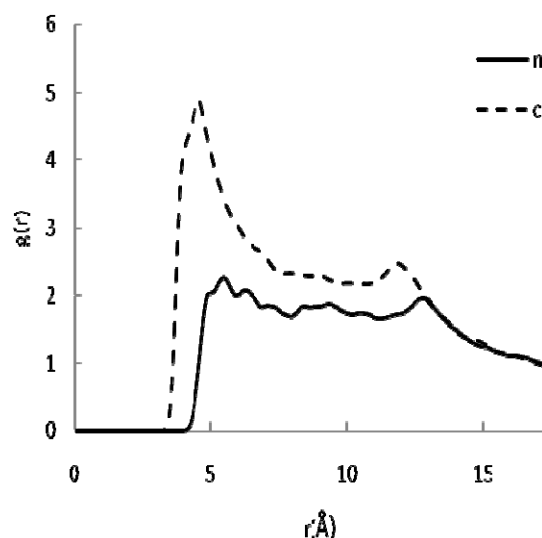


Fig. 2 CNT-nitrogen of surfactant (n) and CNT-carbon of surfactant (c) RDF.

Radial distribution function (RDF) analysis was a useful way to describe the structure of a system, particularly liquids in MD simulation. The association of CNT and CTAB could be analyzed using the RDF. Figure 2 shows the RDF of the carbon and nitrogen atoms of surfactant molecule respect to carbon atoms of CNT. Because of that the carbon peak appeared in smaller r , so that the carbon atoms are placed in smaller distance as compared with nitrogen atoms. The maximum height appeared in $r=5.25$ Å for carbon and in $r= 4.45$ Å for nitrogen atoms. The surfactant molecules approach the nanotube from their hydrocarbonic tail and this is predictable since the chemical nature of carbons of CNTs and carbons of surfactant chain are the same as each other. appearance of two peaks in RDF that refer to the double layer association of surfactant molecules near the nanotube wall, are also confirmed by snapshots.

4. conclusion

Molecular dynamic simulation was successfully used to simulate the aggregation behavior of CTAB surfactant in presence of CNT. The obtained RDF diagrams were used to describe the surfactant aggregating on the nanotube surface.

References

- [1] P. Angelikopoulos, H. Bock. *Langmuir* 2009 (in press).
- [2] N. Arai, K.Yasuoka, X.C.Zeng. *J. Am. Chem. Soc.*, 130 (2008)7916–7920.



Preparation, characterization and photocatalytic activity of ZnO-coated activated carbon prepared by microwave method

A. Habibi-Yangjeh^a, M. Sabri^{b,*}

Department of Chemistry, University of Mohaghegh Ardabili, Ardabil, Iran.

^aEmail: ahabibi@uma.ac.ir,

^bEmail: mina20sabri@yahoo.com,

Keywords: Photocatalytic degradation, Supported ZnO, Microwave irradiation, Activated carbon.

1. Introduction

The semiconductor mediated heterogeneous photocatalysis is an interesting and promising technique for environmental cleaning and remediation due to its potential to destroy a wide range of organic and inorganic pollutants at ambient temperatures and pressures [1]. This method is based on the generation of very reactive species such as hydroxy radicals ($\cdot\text{OH}$) that oxidize a broad range of pollutants quickly [2]. For practical applications, there are some difficulties such as fixation of catalyst particles and efficient utilization of UV/solar light. For these reasons many researchers have been working to increase the efficiencies of these process by using a variety of supporting materials. Among these materials, activated carbon is the most commonly used adsorbent for water treatment. Activated carbon has a large specific surface area and a well developed porous structure, resulting in an attractive force toward organic molecules [3]. For these reasons, in this paper, preparation of ZnO-supported activated carbon by using microwave method was considered. And the effect of various parameters such as catalyst composition, initial dye concentration, catalyst loading, calcination temperature, pH of the medium on the photocatalytic degradation of methyl orange using ZnO:AC were investigated.

2. Method

The catalysts were prepared by mixing appropriate proportions of zinc acetate dihydrate and AC in aqueous suspension and stirring continuously for 2 h. Then aqueous solution of NaOH (5 M) was slowly added drop wise into the solution under magnetic stirring. Addition of NaOH was continued until pH of the solution was reached to 13. The catalysts with the lower AC contents acquire a clear grey colour and when the AC concentration is increased they become darker. The formed precipitates was irradiated using a domestic microwave oven for 10 min. The precipitate was centrifuged to get the precipitate out and washed two times with double distilled water and ethanol, respectively and dried in an oven at 50 °C. The X-ray powder diffraction patterns were obtained using Philips Xpert X-ray diffractometer. Scanning electron microscopic (SEM) analyses were performed on a LEO 1430VP apparatus. The photocatalytic activity of the catalysts was studied by degradation of MO as a target pollutant.

3. Results and discussion

The X-ray powder diffraction pattern of the samples is shown in (Fig.1.) The identification of crystalline phase of ZnO was accomplished by comparison with JCPDS file of ZnO, which can be indexed as a wurtzite hexagonal phase of ZnO.

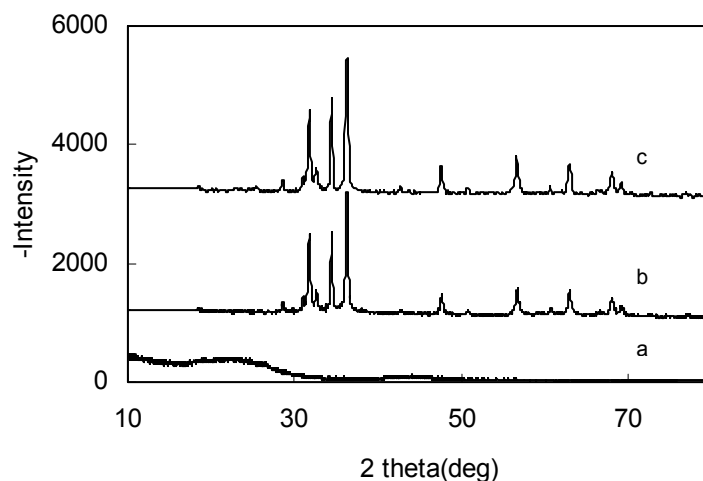


Fig.1 XRD patterns of (a) AC, (b) bare ZnO, (c) 15AC-ZnO.

The morphology of AC, ZnO and the AC-ZnO catalysts are parameters important in determining their photocatalytic behaviour and activity. It was investigated by SEM and can be observed in fig.2.

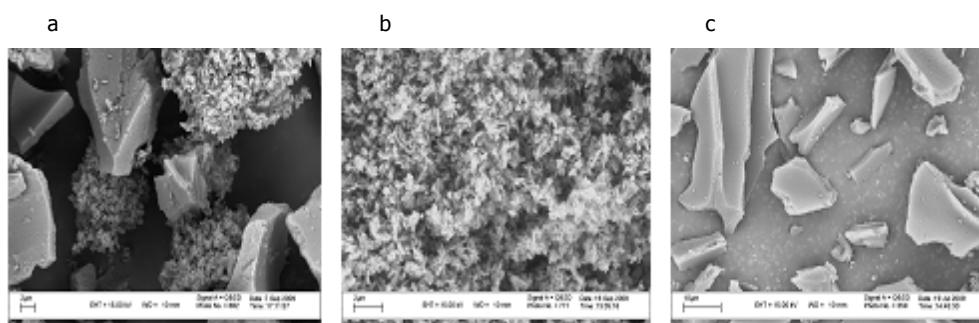


Fig. 2 SEM images of (a) 15AC-ZnO, (b) bare-ZnO and (c) AC.

For investigation effect of the catalyst composition on photocatalytic degradation of MO, weight percentage of initial carbon content was varied between 8 and 20 % and the results were compared by k_{app} (apparent first-order rate constants).

The results demonstrate the reaction rate decreases after a maximum (at 15AC-ZnO in 300 °C and pH=7) with increasing activated carbon content. Increasing of reaction rate at 20AC-ZnO seems to be due to the strong adsorption of the MO molecules on AC.

4. Conclusions

ZnO/activated carbon catalysts were prepared with various initial AC content. The results suggested that 15AC-ZnO at 300 °C have highest photocatalytic activity. Natural pH is found to be better than acidic and alkaline solutions.

References

- [1] Sobana, N. Muruganandam, M. Swaminathan, M. Catalysis Communications 9 (2008) 262.
- [2] Konstantinou, I. K. Albanis, T. A. Applied Catalysis B: Environmental 49 (2004) 1.
- [3] Sobana, N. Swaminathan, M. Solar Energy Materials & Solar Cells 91 (2007) 727.

Oscillatory behavior of Fullerene inside carbon nanotube: effects of radius

M. Foroutan, R. Hadidi *, E.Masoumi

Department of physical Chemistry, College of Science, University of Tehran, Tehran , Iran

E-mail: R.Hadidi@khayam.ut.ac.ir

Keywords: Molecular dynamics simulation; Carbon nanotube; Oscillator; Fullerene.

1. Introduction

Recent studies have proved that a fullerene oscillating inside a nano tube can create high frequencies, which are in gigahertz range. These gigahertz oscillators have drawn the attention of many researchers especially the electrical engineering for their useful applications [1-2]. Besides different studies concerning this interesting field, molecular dynamics simulations have revealed some new characteristics of these oscillating systems. In the present work the effect of radius of nanotube on the oscillator behavior of fullerene is studied.

2. Simulation method

In our simulation we have used armchair (n,n) nanotube in two vector (10,10) and (15,15) with 6.78 Å and 10.098 Å radiuses, respectively. The simulations were performed at the temperature of 300 K. Tinker software package were used for MD simulation.

SWNTs were represented by a flexible model based on AMBER force field. The SWNT-C₆₀ interactions were given by Lennard-Jones potentials. The ϵ parameter values for C₆₀ and carbon nanotube are equal to 0.1051 and 0.0860 Kcal/mole, respectively. Also the σ parameter values for C₆₀ and carbon nanotube are equal to 3.85 and 3.40 Å. After equilibration in 200 picoseconds, the system was run for 800 picoseconds with a time step of 1fs. Trajectories were stored every 1 picosecond for subsequent analyses.

Figure 1 shows a snapshot of the last configuration obtained for the fullerene oscillating in carbon nanotube.

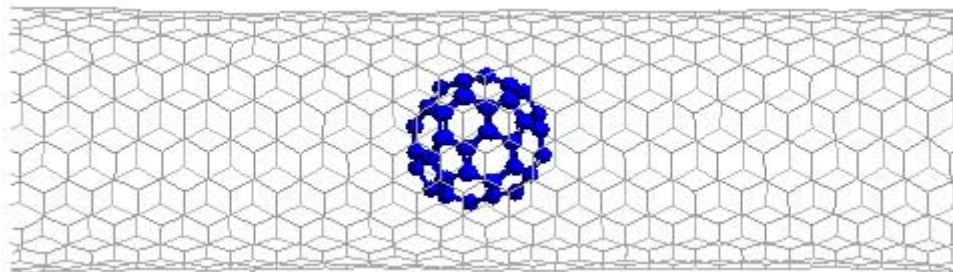


Fig.1 Snapshot of simulation C₆₀-nanotube oscillator

3. Results

The positions, kinetic energies and potential energies of the fullerene oscillating in single carbon nanotubes (10,10) and (15,15) with different lengths were obtained from the MD simulation. In order to keep the text concise as possible as just the diagrams of the changes of positions respect to simulation time is presented. As figure 2 shows the evolution of fullerene oscillating depends on the radius of the nanotube so that the values of the positions of the fullerene oscillating are very different for two nanotubes (10,10) and (15,15). Similar behavior can be observed for the evolution of kinetics and potential energies of fullerene oscillating in the nanotubes. Our results are in agreement with what has been reported for fullerene oscillating in zigzag (n,m) nanotubes with n=16, 17, 18 and 19 and m=0 [3]. The obtained time series for positions as well as potential and kinetics energies can be used for determining the chaotic dynamic behavior of fullerene oscillating in nanotubes [4].

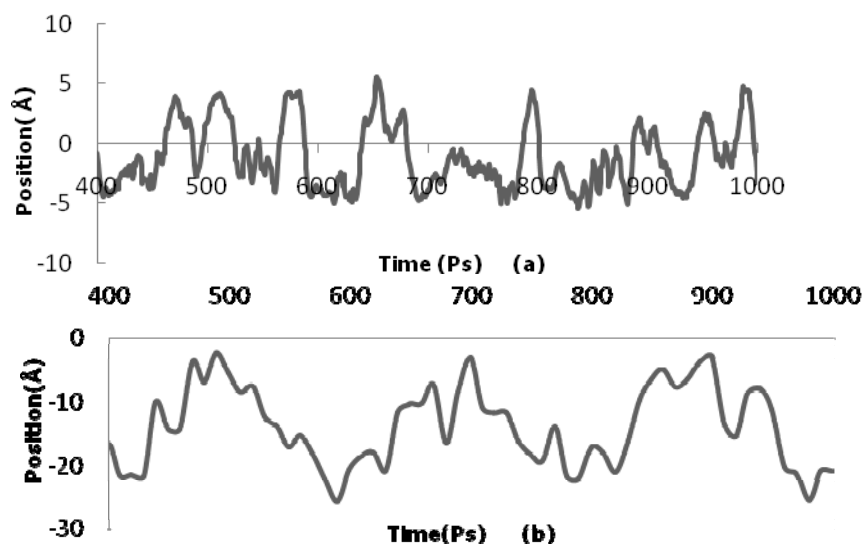


Fig.2 Variation of the position respect to time for fullerene inside carbon nanotube (a) nanotube (10,10) and (b) nanotube (15,15).

5. Conclusion

The obtained results for changes of positions respect to simulation time of the fullerene oscillating inside the nanotubes with difference radius show that radius of nanotube effect on the oscillator behavior of fullerene. Different patterns were observed for oscillator behavior of fullerene although regular oscillating for each case can be seen.

References

- [1] Q. Zheng and Q. Jiang, Phys. Rev. Lett. 88 (2002) 1–3.
- [2] F. N. Mayoof and M. A. Hawwa, Chaos solit. fract. 42 (2009) 1860-1867.
- [3] H. Y. Song and X. W. Zha, Phys. Rev. Lett. 373 (2009) 1058-1061.
- [4] M. Foroutan, A. H. Jalili and Z. Nikouei, J. Phys. Soc. Jpn. 78 (2009) 124003.

New result about leakage current through the nano layer of silicon dioxide

Robabeh Rezazadeh^{a *}, Mir Ali Rezazadeh^b

^a Department of Chemistry, Payam e Noor university of Sari, Sari, Iran

r_rezazadeh_kh@yahoo.com; 09379145129

^b Department of Computer, University of Science and Technology of Mazandaran; Babol, Iran

Keywords: Thin film, Nano transistor, CMOS, Gate oxide dielectric, Landaure-Buttiker method.

1.Introduction

Silicon oxide has received a tremendous attention in the last 40-50 years. It has been an excellent gate dielectric of CMOS devices. Due to its good structure and amorphous interface between it and Silicon substrate and the other properties quoted [1,2] numerous attempts to find a viable gate dielectric for CMOS have encountered two major difficulties: (1) increasing leakage current and (2) born penetration from poly silicon gate electrode through ultra thin silicon oxide. However, to date, no other gate dielectric could replace to Silicon oxide and fill this gap. To overcome this scaling limit of Silicon oxide as gate insulator. But, these materials can affect the carrier mobility through the channel of transistors. In this work, we have studied the quantized conductance of a ballistic quantum wire (QWR) from contact resistances and disturbing and disturbing the current flow. By using the direct transmission probability of each probe contact and Landaure-Buttiker formalism, a solution to overcome the scaling limit of Silicon oxide as gate dielectric is its substitution by double gate insulator.

2.Theory

In according to the current literature [3], the future of CMOS integration requires improvements of the gate dielectric materials. In this work, we used sample geometry in Fig.1, for four terminals resistance measurements on a QWR with Ohmic contact in interface between electrode and channel. With such geometries, the QWR in particularity quantum point contacts (QPCs) is produces by tuning the gate voltage to negative values, such that the electron gas underneath gets depleted.

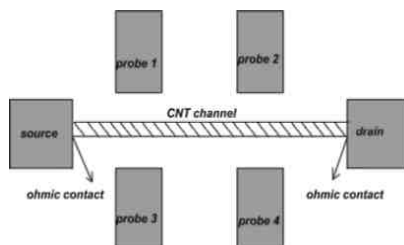


Fig.1 Sample geometry with 4 voltage probe.

In this regime a further reduction of the gate voltage, cause the lateral electric field and with it the lateral depletion zone around the gates increases, we can thus tune the electronic width and change the number (j) of occupied modes of the QPC. In a simple picture, we can imagine that at the absence of magnetic fields, the fraction of the electron trajectories close to the wire edge is minimized and the conductance of such QPCs can be quantized in units of $j2e^2/h$. In this picture, the QPCs is connected to source S and drain D via a transition region by ballistic, strictly one-dimensional QWRs and the QPC itself by a barrier with transmission probability T , as shown in Fig.2.

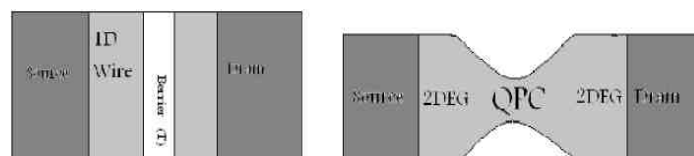


Fig.2 A QPC as a transition region between source and drain (left) and its idealized mode (right). This region is one-dimensional lead and the constriction is a barrier with transmission probability T .

3.Experimental details

The Silicon samples (n-type, 5 Ω -cm, 1cm×1cm) were cut out of wafers with 2mm thickness. These samples were introduced in quartz tube. The schematic of sample layout in Fig.3, clearly shows that one gate can be active gate (e.g.2), while two other gates grounded. In this case, the operation mode around gate 2, i.e. the left and right of gate 2 serve as source and drain. Now, let us show a top view of ballistic quantum wires circuit (see Fig.3). The gate is poly silicon and gate dielectric is the ultra thin Silicon oxide. We assume that each contact can absorb all incoming electrons and distribute the emitted electrons equally among all out going modes in which it can be filled up to the electrochemical potential (μ) at zero temperature. We define $T_{q \leftarrow p} = T_{qp} > 1(T_{q \leftarrow p} = T_{qp})$ as a direct transmission probability of contact p (q) into contact q (p). Therefore, from [9] and the current conservation law, we can apply the Landauer-Buttiker formula as follow:

$$I_p = \sum_{q \neq p} (T_{q \leftarrow p} \mu_p - T_{p \leftarrow q} \mu_q) \quad (1)$$

To the sample shown in Fig.3. And or

$$I_p = \sum_q G_{p \leftarrow q} (V_p - V_q) \quad (2)$$

Where

$$G_{p \leftarrow q} = \frac{2e}{h} T_{p \leftarrow q} \quad \text{and} \quad V_q = \frac{\mu_q}{e} \quad (3)$$

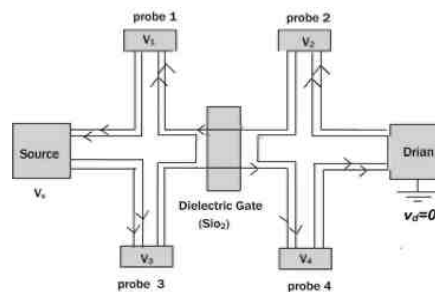


Fig.3. Edge states in system with 4 voltage probe.

4.Conclusion

In this work, the double gate oxide gate dielectric has been investigated in detail with the Landauer-Buttiker equation. Double oxide gate can reduce leakage current more than that single oxide gate. We thus suggest double gate oxide to replace single gate dielectric for the future of CMOS generations.

Acknowledgment

This work is supported with a grant from the university of Mazandaran, Denmark.

Reference

- [1] Baumvol, I. J. R.; Gusev, E.P.; Stedile, F.C.; Freire, F.L.; Green, M.L.; Brasen,D;"TE On the behavior of deuterium in ultrathin SiO2 films upon thermal annealing"Appl. Phys. Lett, vol. 36 , p.p. 450-452, 1998.
- [2] Bieniek, T.; Wojtkiewicz, A.; Lukasiak, L.; Beck, R.B.;"Silicon dioxide as passivating, ultrathin layer in MOSFET gatestacks", vol. p.p. 163 – 164, 2001.
- [3] Pourfath, M.; Ungersboeck, E.; Gehring, A.; Cheong, B. H.; Park,W.J.; Kosina, H.; Selberher, S.;" Optimization of schottky barrier of carbon nanotube field effect transistors", Micro. Eng., vol.81,p.p.428-433,2005.

Synthesis of thiol functionalized silica nano hollow sphere via templating method

R. Rostamian^{a,*}, A.A. Rafati^a

^a Department of Physical Chemistry, Faculty Of Chemistry, Bu-Ali Sina University, Hamedan, 65174 , Iran

Email: r.rostamian@gmail.com

Keywords: Nano hollow sphere, Functionalization, Template, Surfactant, Sonochemical method

1. Introduction

Over the past decade, much research has been undertaken concerning the synthesis of inorganic hollow spheres since these are known to have potential uses as low-density, mechanically and thermally stable materials in fields such as biomedicine (dental implant materials and controlled drug release agents) and engineering (thermal insulators, gas/chemical storage devices, and structural low-weight foams) [1–4]. For environmental applications, the development of functionalized nano materials is necessary, especially for the preparation of heavy metal adsorbents. Organically functionalized nano materials have generated considerable interest in their application in the fields of catalysis, adsorption and separation processes, because they combine in a single solid both the specific chemical reactivity of the organofunctional groups and attractive properties, including a mechanically stable structure ,high surface areas and large ordered pores with narrow size distributions, of an inorganic backbone [5–6] . This study presents the synthesis, characterization and functionalization of the silica nano hollow spheres (SNHSs). The SNHSs have been prepared using a template method at room temperature, in which the CTAB (cetyl trimethyl ammonium bromide) serve as core templates. The TEM and SEM have been employed to characterize morphologies and structures of the SNHSs. The experimental results indicate that the as-prepared sample has an average size about 80-120 nm. Then we provide a strategy to functionalize SNHSs with thiol group. FT-IR spectroscopy have been used to characterize the structure of nanoparticles before and after functionalization. This new synthesized nano particles were used to remove pollution from waste water.

2. Methods

Ethanol (technical grade , Merck), Tetraethyl ortho silicate (TEOS, 98%, Merck) as a silica source, ammonia solution (25%, Merck), the organosilan 3-mercaptopropyltrimethoxysilane were purchased from Merck and used as received. All aqueous solutions were made with double distilled water.

Preparation of SNHSs

In a typical synthesis procedure, 2 mL of aqueous ammonia and 0.1000 g CTAB were added into 75 mL water under ultrasonic. Simultaneously while ultrasonication the solution, 1 ml of TEOS was added into solution. The sample was centrifuged to remove surfactants from SNHSs. In order to remove the unreacted materials and surfactants, the precipitates were washed with ethanol and water. This procedure was repeated five times, after the hollow silica particles were collected. Then, particles were dried at 60 °C for 1 day. The obtained sediment was placed in furnace for 3 hours and 450 °C.

Characterization of nanoparticles

The different surface morphologies, shape and structure of particles were investigated through scanning electron microscopy (SEM) and TEM.

Surface modification of SNHSs with MPTMS

10 mmoles of 3-mercaptopropyltrimethoxysilane (MPTMS) was reacted with 2.000 grams of SNHSs in 100 mL of refluxing toluene for 150 minutes. Reactions were done in the presence of 50 µl of n-butylamine catalyst. The slurry was filtered and washed with toluene, then dried at 150°C for 3 hours. The thiol-modified SNHSs were resuspended in double distilled water, then once again dried at 100°C. Additionally, the sample was heated to remove water and thereby reducing the O-H peak in the FT-IR spectrum.

3. Result and discussion

Figure 1 shows the overall procedure used to synthesize the SNHSs. The morphologies of particles are shown in Figure 2. Size of nanoparticles was obtained about 80-120 nm.

Surface modification with MPTMS (was showed in Figure 3.a , 3.b) was verified by FT-IR spectroscopy as characteristic S-H functional group frequencies are readily detected.(Figure 4).

In the spectrum of thiol-functionalized SNHSs a weak, but clear S-H stretch band can be found around $\nu = 2500 \text{ cm}^{-1}$, which cannot be observed in the spectrum of the pure silica (Figure 4). Since the IR-spectra were made after thorough purification from free MPTMS, it can be concluded that the MPTMS is indeed bound to the silica particles.

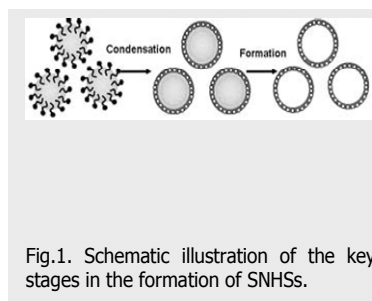


Fig.1. Schematic illustration of the key stages in the formation of SNHSs.

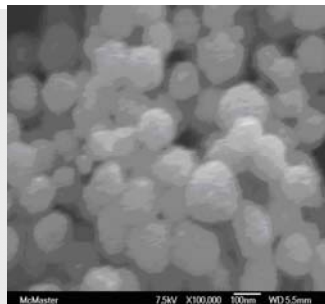


Fig. 2. a. SEM of SNHSs

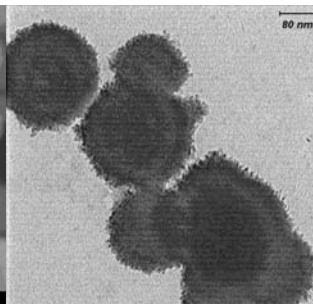


Fig. 2. b. TEM of SNHSs .

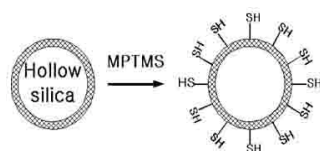


Fig. 3. b. Schematic illustration of the key stages in surface modification with MPTMS.

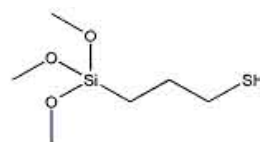


Fig. 3. a. Molecular structure of MPTMS

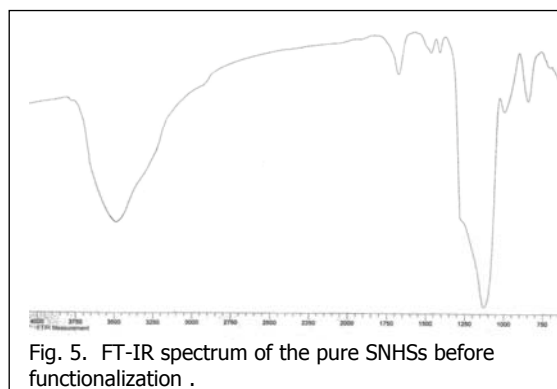


Fig. 5. FT-IR spectrum of the pure SNHSs before functionalization .

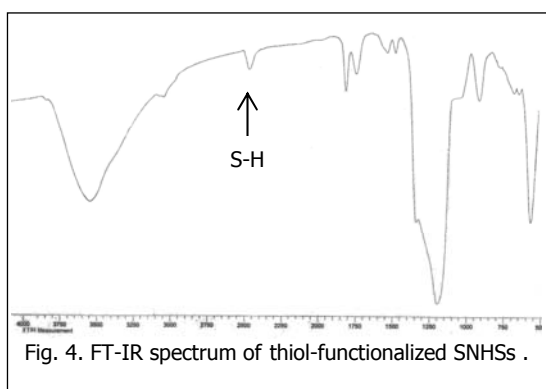


Fig. 4. FT-IR spectrum of thiol-functionalized SNHSs .

4. Conclusions

In conclusion, we have demonstrated that it is possible to synthesize the SNHSs by using surfactants as templates. The usage of CTAB as template provides a successful pathway for the fabrication of SNHSs. Then surface modification is done by thiol functionalization. This approach to synthesize the thiol functionalized silica hollow spheres nanostructures is attractive for the following reason: MPTMS-functionalized SNHSs have high metal loading capacity due to the densely immobilized thiol groups on the surface of them. The thiol functionalized SNHSs obtained here may be promising candidates for both fundamental research and applications. Hence, we expect that the strategy employed here can also be extended to templates particles of various shapes and functional groups. This method may also provide a novel approach to produce other functionalized SNHSs.

References

- [1] F. Caruso, Chem. Eur. J. 6 (2000) 413–419.
- [2] S. Kidambi, J. Dai, J. Li, M.L. Bruening, J. Am. Chem. Soc. 126 (2004) 2658–2659.
- [3] Y. Wang, L. Cai, Y. Xia, Adv. Mater. 17 (2005) 473–477.
- [4] Y. Wang, Y. Xia, Nano Lett. 4 (2004) 2047–2050.
- [5] M.E. Davis, Nature 417 (2002) 813.
- [6] A. Stein, Adv. Mater. 15 (2003) 763.

Study of the Structure and Electronic Properties of BN and B₃C₂N₃ Nanotubes

S. Jalili^a and R. Vaziri^{a*}

^aDepartment of Chemistry, K. N. Toosi University of Technology, P.O. Box 15875-4416, Tehran, Iran

Emails: sjalili@kntu.ac.ir, r_vaziri@dena.kntu.ac.ir

Keywords: BN nanotube, B₃C₂N₃ nanotube, Electronic properties, Band gap, Density of states

1. Introduction

BNNTs are semiconductors that characterized by wide band gap energy about 5.5 eV, almost independent of tube chirality's and morphology [1]. The wide band gap of BNNTs is a substantial obstruct for their applications in electronics. In numerous efforts to reduce the band gap, the doping of BNNTs, especially with carbon was proposed and implemented early on. On the other hand, an interesting possibility arises from the inclusion of substitutional carbon atoms in the BN structure, leading to the formation of ternary BCN compounds (B_xN_yC_z) with distinct stoichiometries. Theoretical calculations have predicted that the band structure of B_xN_yC_z nanotubes can be controlled by changing their atomic compositions and configurations. Therefore, it opens the possibility to produce materials with tunable electronic properties with potential applications in nanodevice engineering [2]. In spite of large number of previous studies about the electronic properties of B_xN_yC_z nanotubes with different atomic arrangement such as BC₂N, BCN,...[3], there has been no details report on the electronic properties of B₃C₂N₃ nanotubes based on first principles calculation. In this paper, we apply a first-principles method based on the density functional theory (DFT) within the generalized gradient approximation to investigate the electronic structure and properties of single-walled zigzag B₃C₂N₃ nanotubes (ZB₃C₂N₃NTs). These structures were obtained from the B₃C₂N₃ most stable sheet, according to previous results [4]. We calculated the energy gap of ZB₃C₂N₃NTs and these energy gaps compared to corresponding values for BNNTs.

2. Method

Our calculations have been performed with the Quantum espresso code [5], in which the spin polarized density functional theory method is implemented using the generalized gradient approximation (GGA) within the perdw and wang exchange correlation function. We employ a plane-wave basis set with periodic boundary conditions in conjunction with Vanderbilt ultrasoft pseudopotential. Kinetic energy cutoff is 40 Ry for the wave function and 165 Ry for the charge density. All the geometries are fully relaxed, with residual forces smaller than 0.01 eV/Å. One dimensional periodic boundary condition is applied along tube axis, that is periodically repeating tetragonal unit cell with lattice constants a, b and c were used. Both a and b were chosen to insure negligible interaction between the tube and its periodic images (vacuum space at least 10 Å), while c is relaxed during the optimization (c=8.46 Å). We studied the zigzag single-walled B₃C₂N₃ nanotubes (n, 0; n=4–10) and these structures were obtained from B₃C₂N₃ most stable sheet according to previous results of reference [2]. The unit cell of BN and B₃C₂N₃ nanotubes are shown in Fig. 1. Monkhorst-pack mesh of k-points (1×1×6) is used for sampling the one dimensional Brillouin zone during geometry optimization.

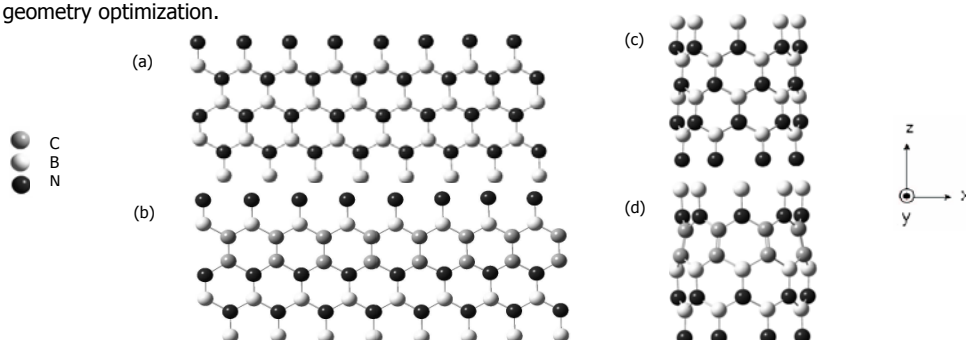


Fig. 1. Illustration of BN and B₃C₂N₃ nanostructure, where (a) and (b) are the BN and B₃C₂N₃ monolayer and (C) and (d) are the corresponding nanotube obtained using a similar procedure as described in reference [3]. The atoms are represented by different colors as shown in the inset.

3. Results and discussion

In this work, different possibility arises from the inclusion substitutional carbon atoms in the BN sheets and rolling them leading to the formation of ternary zigzag B₃C₂N₃ nanotubes (n, 0; n = 4–10) with distinct stoichiometries. For the BN and B₃C₂N₃ nanotubes (n, 0; n=4–10) the electronic band structures have been studied along the Γ Z direction. The Fermi energy (E_f) and

the band gaps (E_g) are listed in Table 1. In both types of nanotube (BNNTs and $B_3C_2N_3$ NTs) the band gap is increased by increasing the tube diameter, also all of these nanotubes are semiconductor with direct band gaps.

Table 1 Calculated Fermi energy (eV) and band gaps (eV) of BN and $B_3C_2N_3$ nanotubes. Direct band gap is denoted by 'D'.

BNNTs	(4,0)	(5,0)	(6,0)	(7,0)	(8,0)	(9,0)	(10,0)
E_f	-3.68	-3.47	-3/36	-3.24	-3.07	-3.17	-3.02
E_g	2.4 (D)	3.0 (D)	3.3 (D)	3.9 (D)	4.2 (D)	4.5 (D)	4.8 (D)
$B_3C_2N_3$ NTs	(4,0)	(5,0)	(6,0)	(7,0)	(8,0)	(9,0)	(10,0)
E_f	-3.57	-3.23	-2.78	-2.85	-2.61	-2.72	-2.58
E_g	0.9 (D)	1.3 (D)	1.8 (D)	2.1 (D)	2.4 (D)	2.7 (D)	3.0 (D)

In Fig. 2 we have given DOS of BNNTs {a; (4, 0), b; (7, 0), c; (10, 0)} and $B_3C_2N_3$ NTs {d; (4, 0), e; (7, 0), f; (10, 0)}. We observed that the DOS for spin up and down orientation are completely equal. In BNNTs DOS near Fermi level is very small, meaning that few of valence electrons occupy the highest level. The electrons in valence band can seldom transit to conducting band so that the conductivity of pure BNNTs is poor. For these doped nanotubes there is a peak near conducting band therefore energy gaps are reduced and the electrons are exited more easily from donor level to conducting level.

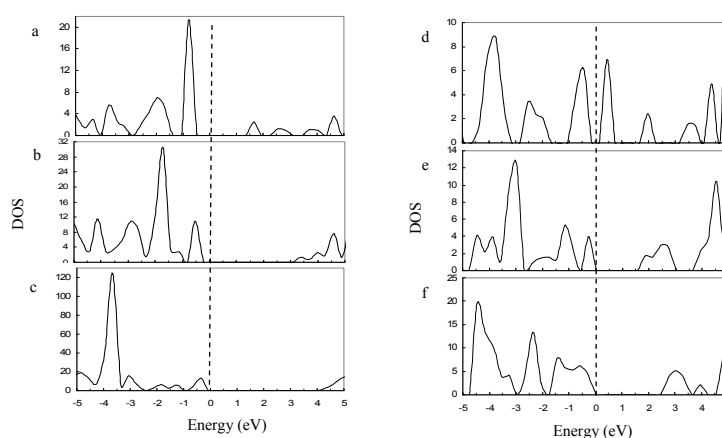


Fig. 2. DOS of BNNTs {a; (4, 0), b; (7, 0), c; (10, 0)} and $B_3C_2N_3$ NTs {d; (4, 0), e; (7, 0), f; (10, 0)}. The Fermi level is plotted with dotted line and is at 0 eV.

4. Conclusions

In summary, we investigated the structural and electronic properties of zigzag BN and $B_3C_2N_3$ nanotubes ($n, 0$; $n=4-10$) by first-principles spin polarized total energy calculations. We found that in both types of nanotube (BNNTs and $B_3C_2N_3$ NTs) the band gap is increased by increasing the tube diameter, also all of these nanotubes are semiconductor with direct band gaps. Although the band gap of the BN tubes are much larger than that of $B_3C_2N_3$ tubes (about 1.5–1.8 eV), they have similar dependence on the tube diameter and semiconducting character nevertheless remains. It means that the effect of the tube diameter on its electronic property is independent of carbon doping in BNNTs with these atomic arrangement. In $B_3C_2N_3$ NTs nanotubes there is a peak near conducting band therefore energy gaps are reduced and the electrons are exited more easily from donor level to conducting level. In fact, these kind of ternary BCN nanotubes ($B_3C_2N_3$) are N-type semiconductors. In $B_3C_2N_3$ NTs we see the significant contribution of C-2p in both occupied and unoccupied level because after doping carbon atoms the numbers of B and N atoms are still equal. The 2p orbital of C atoms near the boron atoms contributed to the top valence band, while the 2p orbital of C atoms near the nitrogen atoms contributed to the bottom conduction band.

References

- [1] X. Blasé, A. Rubio, S. G. Louie, M. L. Cohen, Europhys. Lett. 28 (1994) 335.
- [2] M. Matos, S. Azevedo, J. R. Kaschny, Solid State Communications, 149 (2009) 222.
- [3] H. Pan, Y. P. Feng, J. Lin, Phys. Rev. B. 74 (2006) 045409.
- [4] S. Azevedo, R de Pavia, Europhys.Lett. 75 (2006) 126.
- [5] S. Baroni, A. Dalcorso, S. D. Gironcoli, P. Giannozzi, C. Cavazzoni, G. Ballabio, S. Scandolo, G. Chiarotti, P. Focher, A. Pasquarello, K. Laasonen, A. Trave, R. Car, N. Marzari, A. Kokalj (2006).



Effect of Milling Time and Clay Content on the Thermal Stability of Polyethylene-Clay Nanocomposite

M. Abareshi^{a,*}, S. M. Zebarjad^b, and E. K. Goharshadi^a

^aDepartment of Chemistry, Ferdowsi University of Mashhad, Mashhad, Iran

Email:ma_ab60@stu-mail.um.ac.ir

^bDepartment of Materials Science and Engineering, Ferdowsi University of Mashhad, Mashhad, Iran

Keywords: PE-Clay Nanocomposite, Ball milling, Transmission electron microscopy, Thermal stability.

1. Introduction

Polymer/clay nanocomposites have a long history of development. The progress of development has been reported since the nineteen sixties and early seventies [1]. Polymer nanocomposites, in particular, nanoclay-reinforced polymers have attracted significant interest both in the industry and in academia during the past decade [2], owing to their potential for exceptional improvements in properties at lower filler concentrations compared to conventional micro- and macro-composites [3].

Nanocomposites are usually prepared by vacuum deposition or chemical methods. However, synthesis by mechanical methods offers unique advantages. Recently, it has been proved that High Energy Ball Milling (HEBM) can help to obtain novel nanocomposites with new characteristics which are difficult to obtain by other conventional techniques [4]. In our previous papers [5, 6], we proposed the HEBM as an alternative fabrication method for polyethylene-clay nanocomposite and indicate that although the milling time and the addition of clay have not affected on the crystal structure of MDPE matrix, the crystallinity of MDPE decreases with increasing milling time and clay content. In the present work, we try to investigate the thermal properties of polyethylene-clay nanocomposite fabricated using ball milling as a new method.

2. Methods

A medium-density polyethylene (MDPE, density: 0.937 g cm⁻³, MFI: 4.2, Vicat softening point: 117) was used as composite matrix resin and the used clay was china clay. These two commercial chemicals were used as received without further purification. High-energy ball milling was performed in a stainless steel container at the speed of 300 rpm. Total mass of the powder was 10 g. The weight ratio of ball to powder was kept 20:1. Medium density polyethylene and clay particles were mixed mechanical before ball milling, to achieve medium density polyethylene-clay nanocomposite with different clay contents i.e. (5, 10, 15 wt%). The process was done at different milling times (0-60 hours). The powder of neat polyethylene was also milled at the same times for comparison.

The microstructure of the nanocomposites was examined by transmission electron microscopy (TEM) and Fourier transform infrared spectroscopy (FTIR). Thermal stability of all milled samples including pure polyethylene and polyethylene-clay nanocomposites was measured by thermal gravimetric analysis (TGA).

3. Results and discussion

The results of TEM and FTIR show that the clay particles have been homogeneously dispersed in the polymer matrix without any aggregation of clay and there is not any detectable interaction between PE and clay.

The results of the TGA and derivative thermogravimetric (DTG) curves of pure PE, PECN10, and PECN15 after 40 and 60 hours of milling show that the clay layers play like a good barrier which can improve the thermal stability of polymer clay nanocomposites. On the other hand, clay itself can catalyze the degradation of polymer. At the initial stage of degradation, PECN10 and PECN15 show an earlier onset temperature in contrast to pure PE. This suggests that the addition of clay catalyzes the initial decomposition of PE. It has been reported [7] that the complex crystallographic structure and the habit of clay minerals can result in some catalytically active sites. Perhaps the initial decomposition of PE matrix is provoked by these catalytically active sites. Moreover, the addition of clay shifts the degradation of polyethylene to higher temperature after initial stage of the degradation. This is probably related to the lowering of the diffusion of oxygen molecules into the nanocomposites due to barrier property of clay and physicochemical adsorption of the volatile degradation products on the silicates [7]. All these effects increase the stability of PE-clay nanocomposites. The temperature corresponding to maximum decomposition rate obtained from the DTG curves are 415.62, 430.41, and 436.49 °C for pure PE, PECN10, and PECN15 after 40 hours of milling



and 421.36, 436.41, and 433.59 °C for pure PE, PECN10, and PECN15 after 60 hours of milling, respectively. These data also prove that the thermal stability of PE increases as clay content increases.

4. Conclusions

In a summary, thermal stability of PE increases with increasing milling time. Clay plays two opposed functions on the thermal stability of PE-clay nanocomposite, one as a barrier effect to improve the thermal stability and the other as a catalyst leading to decrease of the thermal stability.

References:

- [1] C. E. Powell, G. W. Beall, *Curr. Opin. Solid. State. Mater. Sci.* 10 (2006) 73.
- [2] M. Tanniru, Q. Yuan, R. D. K. Misra, *Polymer* 47 (2006) 2133.
- [3] R. K. Shah, D. R. Paul, *Polymer* 47 (2006) 4075.
- [4] Vertuccio, L. Gorrasi, G. Sorrentino, A. Vittoria, V. Carbonate. *Polymers* 75 (2009) 172.
- [5] M. Abareshi, S. M. Zebarjad, E. K. Goharshadi, *J. Vinyl. Addit. Technol.* (in press).
- [6] M. Abareshi, S. M. Zebarjad, E. K. Goharshadi, *J. Compos. Mater.* 43 (2009) 2821.
- [7] H. Qin, S. Zhang, C. Zhao, M. Feng, M. Yang, Z. Shu, S. Yang, *Polym. Degrad. Stab.* 85 (2004) 807.



Micro-emulsion under ultrasound facilitates the fast synthesis of quantum dots of CdS at low temperature

N. Ghows and *Mohamad H. Entezari

Department of Chemistry, Ferdowsi University of Mashhad, 91775, Mashhad, Iran *Corresponding author:

moh_entezari@yahoo.com

Keywords. ultrasound, semiconductor, crystallization, interface diffusion, intensity

1. Introduction

Semiconductor nano-crystals have been widely studied in recent years which are due to its unusual physical properties and the wide range of potential applications [1]. One of the important properties is the optoelectronic of the semiconductors which is often strongly dependent on the particle size, morphology and their crystal phases. In semiconductors with very small sizes, quantum confinement modulates the band structure of nano-particles and increases the band gap [1]. The control of nanoparticle's properties is significant for many technological applications such as light-emitting diodes, photocatalysts, biological labels, electrochemical cells, lasers, and microcavities.

Micro-emulsion processing has been proven to be an effective way for the controlled growth of inorganic nanoparticles with narrow size distribution and good mono-dispersity. The products of micro-emulsion process are particles with poor crystallinity. Therefore, to improve the crystal phase of product it is necessary to use a relatively high temperature and long reaction time (above 300-400 °C) [2]. Hence, it seems that the combination of ultrasound and micro-emulsion is very suitable for synthesis of CdS nano-particles. This combination could be useful for controlling of crystal phase, morphology, and the size of the nano-particles [3,4].

2. Experimental section

A quaternary oil-in-water micro-emulsion formed by CTAB/1-Butanol/p-Xylen /Water with a proper ratio in two separate. The part of contained sulfur in oil phase and the part of B contained cadmium chloride and ethylenediamine in aqueous phase. The mixed micro-emulsion was irradiated with ultrasound The precipitate was separated by centrifugation, washed with distilled water and ethanol.

Characterization of CdS nanoparticles has been studied by TEM, XRD, (EDAX), BET and UV-Vis spectroscopy.

3. Results and Discussion

In the present study, it is confirmed that ultrasonic irradiation would favor the formation of hexagonal phase CdS and facilitates the phase transition at relatively low temperature. The effect of important factors such as sonication time and other variables was studied on the CdS nano-particles.

The formation of cadmium sulfide nano-particles is based on the reaction between sulfur and ethylenediamine which present in two different phases. Ultrasound facilitates the approach of these two species by increasing the diffusion and promotes its reaction to produce H₂S. Then hydrogen sulfide quickly reacts with cadmium ion and leads to CdS

The XRD patterns indicate that the crystallites are nano-size and mostly in hexagonal phase at the presence of ultrasound On the other hand, the sharpness of the XRD peaks is higher for sonication than for classical method. Enhancing the crystal phase of the CdS in the presence of ultrasound should be explained according to the cavitation process.

The HRTEM of nano-particles shows that nano-particles have uniform spherical morphology and their sizes are very small. The results of EDAX measurement reveal that the prepared CdS nano-crystals has a high purity

In micro-emulsion, the control of particle size and composite depends on many parameters. One of the important factors is the amount of oil fraction in the solution. This parameter was investigated with changing the oil fraction. The particle size increased and the surface area of the particles decreased with increasing the oil fraction in the solution. This should be explained that with increasing the oil fraction in constant amount of sulfur, the concentration of sulfur reduced. Therefore, the rate of product formation reduced and leaded to the larger particles. In addition, the size of oil droplets in micro-emulsion can increase by increasing the oil fraction.

The UV-vis spectra of samples at different interval times and photoluminescence spectrum of CdS nano-particles are shown obvious blue shift which is due to quantum confinement



4. Conclusions

In conclusion, in the present work we have developed a new method to synthesize CdS nano-particles through combination of ultrasonic waves and o/w micro-emulsion. Nano-particles with a hexagonal phase were prepared at a relatively low temperature, short time, and fast transition phase. The advantageous of this combined method are due to its simplicity and efficient way for preparation of very fine nano-particles (quantum dot) with uniform shape. The study of optical properties also confirmed that there is a specific relationship between particle size and energy band gap.

Acknowledgment

The authors acknowledge the help given by Mrs. M. Hassanzadeh from Solid State Physics Research Center, Damghan University of Basic Sciences and Mrs. R. Pesyan from Central Research Laboratory of Ferdowsi University of Mashhad for analysis. This work has been supported by the "Iranian National Science Foundation: INSF" (No. 85103/31).

References

- [1] P. V. Kamat, J. Phys. Chem. C 112 (2008) 18737.
- [2] S. Q. Sun, T. Li, Crystal Growth & Design 7 (2007) 2367.
- [3] W. Huang, X. Tang, Y. Wang, Y. Koltypin, A. Gedanken, Chem. Commun. (2000) 1415–1416.
- [4] E. Ohayon, A. Gedanken, Ultrasonics Sonochemistry 17 (2010) 173-178.

Investigation of SiO₂ Nanoparticles for Encapsulating of Benzotriazole Corrosion Inhibitor

S.M.A. Hosseini^{a*}, E. Jamalizadeh^a, A.H. Jafari^b, M. Shahidi^a

^a Department of Chemistry, Faculty of Science, Shahid Bahonar University of Kerman, 22 Bahman, Kerman 76175, Iran

^b Materials Science and Engineering Department, Shahid Bahonar University of Kerman, Kerman 76188, Iran
s.m.a.hosseini@mail.uk.ac.ir,

Keywords: SiO₂ nanoparticle, Encapsulating, Corrosion inhibitor, Release

1. Introduction

Corrosion can be controlled by the addition of chemical compounds to the electrolyte, the compounds added are known as inhibitors which will reduce the rate of either anodic oxidation or cathodic reduction or both processes [1]. Benzotriazole (BTA) is one of organic compounds which is used as inhibitor for corrosion protection of metals and alloys [2].

Nanocontainers are used to develop the self-healing anticorrosion coatings, where the uses of micro and nanometer scale containers have been demonstrated as anticorrosion agents [3-7]. Encapsulation may also be employed as a means to fix main working components otherwise either inoperable on grounds of being noxious and harmful or prohibited when it stands alone form [8].

2. Experimental

The SiO₂ containers were used for keeping the benzotriazole corrosion inhibitor within the polyelectrolyte matrix. The effect of Polyelectrolyte shells i.e. outer skins for SiO₂ nanoparticles fabricated through layer-by-layer assembly of (PAH) / (PSS), (PAH) / (PMA) and (PAH) / (PMA+PSS) polyelectrolyte bilayers. The SiO₂ nanoparticles are negatively charged, therefore, the adsorption of positive (PAH) to them occurs during the first stage when 20 mL of 15 wt. % SiO₂ colloidal solution is mixed with 3 mL of 4 mg.mL⁻¹ (PAH) solution centrifuged following the adsorption step. As benzotriazole is only sparingly soluble in water of neutral pH hence the adsorption of the third layer containing the inhibitor happens from acidic conditions. Alternating adsorption layers was repeated until the final (PAH/PSS) / (BTA/PSS), (PAH/PMA) / (BTA/PMA) and (PAH/PSS+PMA) / (BTA/PSS+PMA) were assembled on the surface of the SiO₂ nanoparticles structures.

Size and charge of fabricated capsules was indicated by using Zetasizer Nano (Zs), model ZEN3600. The concentration of benzotriazole during release into the solutions was detected using a Varian CARY 50 Conc UV-vis spectrophotometer

3. Results and discussion

The results show the zeta potential of the initial SiO₂ nanoparticles is negative, which was confirmed electrophoretic mobility measurements on the nanoparticles coated with the adsorbed polyelectrolyte or inhibitor layer upon each added layer. Increase in the surface charge after deposition of the first (PAH) layer is followed by a drastic decrease after (PSS) next adsorption stage which is further augmented after benzotriazole deposition without complete recharging of the surface. The average diameter of the SiO₂ nanoreservoirs (PSN) obtained from zetasizer measurements increase with increasing the layer number and is around 60 nm for all monolayer increasing as about 20 nm steps per layer.

It is observed that the containers exhibit spontaneous release of the benzotriazole, the extent depending on the container type. The results depict that the quantity of corrosion inhibitor taking up and inhibitor releasing rate follows the sequence of (PAH) / (PSS+PMA) > (PAH) / (PSS) > (PAH) / (PMA), which reveals that the extent depending on polyelectrolyte shell components.



4. Conclusions

SiO₂ container is prepared by keeping benzotriazole corrosion inhibitor within the polyelectrolyte matrix and allowing release of BTA. The release properties of polyelectrolyte modified halloysite nanotubes (PHN), polyelectrolyte modified SiO₂ nanoparticles (PSN) and polyelectrolyte nanocontainers (PNC) investigated show that the quantity of corrosion inhibitor taking up follows the sequence: (PNC) > (PHN) > (PSN). Containers exhibit spontaneous release of the benzotriazole, the extent depending on the polyelectrolyte shell components.

References

- [1] P.A. Schweitzer, Encyclopedia of Corrosion Technology, CRC Press, 2004.
- [2] Y.N. Prasad, S. Ramanathan, Electrochim. Acta 52 (2007) 6353.
- [3] Y.M. Abu, K. Aoki, J. Electroanal. Chem. 583 (2005) 133.
- [4] M. Tomalino, G. Bianchini, Prog. Org. Coat. 32 (1997) 17.
- [5] M. Kendig, M. Hon, L. Warren, Prog. Org. Coat. 47 (2003) 183.
- [6] D.G. Shchukin, H. Mohwald, Adv. Mater. 18 (2006) 1672.
- [7] D. G. Shchukin, H. Mohwald, small 3 (2007) 926.
- [8] F. Kuang, T. Shi, J. Wang, F. Jia, J. Solid State Electrochem. 13 (2009) 1729.

**Thermodynamic study of lead sorption on Nanostructure Titania-Silica mixed gel spheres**

A. Nilchi *, S. Rasouli Garmarodi and G. Aboulhasanlo

Nuclear Science and Technology Research Institute, Nuclear Fuel Cycle School, Tehran, Iran

E-mail: anilchi@aeoi.org.ir**Keywords:** Thermodynamic, Lead, $\text{TiO}_2\text{-SiO}_2$, adsorption, Nano particle**1. Introduction**

The development of industries such as coating, electric battery manufacturing, paint, lead smelting, internal combustion engines, generates wastewaters containing large quantity of lead. Because of the toxic nature of lead, the removal of trace lead from drinking water systems or industrial effluents has been of increasing importance [1, 2]. The adsorption process is used exclusively in water treatment and many studies have been carried out to find inexpensive and chemico- physically feasible adsorbents. In The present study, the preparation of nanostructure $\text{TiO}_2\text{-SiO}_2$ mixed oxide and application of this highly efficient adsorbent in removal of Pb^{2+} ions diluted in a liquid phase is discussed.

2. Experimental

Titanium (IV) chloride (98% Fluka), tetraethylorthosilicate (98% Merck), ammonium hydroxide (25% Fluka) and Merck analytical grade nitrate salt of Pb^{2+} were used.

X-ray powder diffractometry was carried out using an 1800 PW Philips diffractometer, specific surface area and pore size distribution of the sample was determined through nitrogen adsorption isotherms using Quantachrome NOVA 2200e system; Pb^{2+} ions remaining in the solution were measured by ICP model 5500 Perkin-Elmer.

For $\text{TiO}_2\text{-SiO}_2$ preparation, TiCl_4 was added drop wise to deionised water under vigorous stirring in an ice water bath. The produced dispersion was treated with NH_4OH and pH was adjusted to 7. The resulting solid was collected by filtration and washed with distilled water in order to remove chlorine ions. The precipitate was dispersed in 200 mL of 0.3 mol/L HNO_3 . The mixture was refluxed under vigorous stirring at 70 °C for 16h as Titania sol was prepared. 25 mL of tetraethylorthosilicate was added drop wise to the above sol and stirred at 70 °C. The resulting powder was filtered and washed with deionised water and then dried at room temperature. The prepared mixed oxide was calcined in air, at 400 °C for 1h.

3. Results and discussion

XRD pattern of the sample reveals that nanosized $\text{TiO}_2\text{-SiO}_2$ has crystalline anatase phase beside brookite in amorphous silica matrix [3]. N_2 adsorption-desorption isotherm and pore size distribution analysis of synthesized oxide are illustrated that the prepared material had a BET surface area of up to 405.3 m^2g^{-1} and according to BJH plot the pore diameter of oxide was obtained around 4.65 nm.

The experimental data of lead adsorption were analyzed with the Freundlich and Langmuir models [4, 5]. The parameters calculated are summarized in Table 1. Higher correlation coefficients indicate that the Langmuir model fits the adsorption data better than the Freundlich model.

Table 1: Parameters of the Langmuir and Freundlich models at various temperatures

T(K)	Langmuir constants			Freundlich constants		
	Q^0 ($\mu\text{mol g}^{-1}$)	b ($\text{L } \mu\text{mol}^{-1}$)	R^2	K_F ($\mu\text{mol}^{1-1/n} \text{g}^{-1} \text{L}^{1/n}$)	$1/n$	R^2
298	97.46	0.04	0.99	1.17	0.87	0.98
308	169.77	0.10	0.99	2.45	0.89	0.98
325	203.25	0.77	0.96	0.13	0.59	0.96

The thermodynamic parameters, the values of standard free energy (ΔG°), enthalpy (ΔH°) and entropy (ΔS°) of the sorption are useful in defining whether the sorption reaction is endothermic or exothermic, and spontaneity of the adsorption process. The parameters can be calculated using the following equations [6]:



$$\Delta G^\circ = -RT \ln K_1 \quad (1)$$

$$\ln \frac{K_1}{K_2} = -\frac{\Delta H^\circ}{RT} + \left(\frac{1}{T_1} - \frac{1}{T_2}\right) \quad (2)$$

$$\Delta S^\circ = \frac{\Delta H^\circ - \Delta G^\circ}{T} \quad (3)$$

where R (8.3145 J /mol K) is the ideal gas constant, and T (K) is the temperature. K is the apparent equilibrium constant corresponding to the temperature which may be calculated from the product of the Langmuir equation parameters Q^0 and b. So, the values of the constants K_1 , K_2 , and K_3 corresponding to the temperatures of 298, 308, and 325 K, respectively, are given in Table 2. Also relevant data calculated from above equations are tabulated in Table 2.

Table 2: Thermodynamic parameters for Pb^{2+} adsorption onto TiO_2-SiO_2

T(K)	K (L g ⁻¹)	ΔG° (KJ mol ⁻¹)	ΔH° (KJ mol ⁻¹)	ΔS° (KJ mol ⁻¹ K ⁻¹)
298	$K_1 = 9.3670$	-5.5430	63.0511	0.2295
308	$K_2 = 17.5650$	-7.4580		
325	$K_3 = 75.6430$	-11.6170		

4. Conclusion

The study showed the ability of nanosized TiO_2-SiO_2 to sorbed lead from aqueous solution. As a result of the experimental conditions; it was shown that Pb^{2+} adsorption onto the prepared material is an endothermic and a spontaneous process. The fact that the Langmuir isotherm fits the experimental data better than the Freundlich model indicates the almost complete monolayer coverage of the adsorbent particles.

References

- [1] A. Oehmen, R. Viegas, S. Velizarov, M.A.M. Reis, J.G. Crespo, Desalination, 199 (2006) 405.
- [2] A.A. Inamuddin, Sensors Actuat. B 120 (2006) 10.
- [3] A. Paola, G. Cufalo, M. Addamo, M. Bellardita, R. Campostrini, M. Ischia, R. Ceccato, L. Palmisano, J. Colloid Interface Sci. A: Physicochem. Eng. Aspects 317 (2008) 366.
- [4] I. Langmuir, J. Am. Chem. Soc. 38 (1916) 2221.
- [5] H. Freundlich, Z. Phys. Chem. A 57 (1906) 385.
- [6] C. Chen, X. Li, D. Zhao, X. Tan, X. Wang, physicochem. Eng. Aspects 302(2007) 449.

Preparation and characterization of CdS nanoparticles in presence of a ionic liquid, [EMIM][EtSO₄] using microwave irradiation and their photocatalytic activities

A. Habibi-Yangjeh^a, M.Esmaili-Taramsari^{b*}

Department of Chemistry, University of Mohaghegh Ardabili, Ardabil, Iran

^aEmail: ahabibi@uma.ac.ir

^bEmail: esmaili_23@yahoo.com

Keywords: CdS, Photocatalysis, Nanoparticle, Ionic liquid.

1. Introduction

Being an important II-VI semiconductor ($E_g = 2.42$ eV), CdS has promising applications in multiple technical fields including mechanical, optoelectronic, solar cells and photodegradation of water pollutants [1].

Room-temperature ionic liquids (RTILs) have been widely studied as a new kind of reaction media owing to their unique physicochemical properties [2]. One of the largest barriers to the application of RTILs in various fields arises from their high-cost relative to conventional solvents.

Microwave irradiation has shown very rapid growth in its application to material science due to its unique reaction effects such as rapid volumetric heating and the consequent dramatic increase in reaction rates, etc.[3]. For these reasons, microwave-assisted room-temperature ionic liquid (MARTIL) method has been applied for synthesis of various nanomaterials [4].

2. Methods

The X-ray diffraction (XRD) pattern was recorded on Philips Xpert X-ray diffractometer. Diffuse reflectance spectra (DRS) recorded by a Scinco 4100 apparatus. Scanning electron microscope (SEM) image were obtained a LEO 1430VP apparatus.

The ionic liquid was [EMIM][EtSO₄] and synthesized according to the literature [5]. In order to examine photocatalytic activity of the prepared nanoparticles, photodegradation of methylene blue (MB) was considered. A UV Osram lamp of 125 W and a tungsten lamp of 200 W as visible source were used. The lamp was fitted on the top of the reactor.

3. Results and discussion

The phase and purity of the samples were determined by XRD and the typical diffraction pattern is shown in Figure 1. As can be seen, mean size of the nanoparticles decreases as the amount of the RTIL increases in the reaction media.

Fig. 1 exhibits diffuse reflectance spectra (DRS) of CdS nanoparticles, Absorption maximum for the CdS nanoparticles is in 330 nm. The band gap energy for the CdS nanoparticles (3.75 eV) increased compared to that of bulk CdS. The expansion of band gap (1.33 eV) or blue shift can be attributed to the quantum confinement effect of CdS nanoparticles. Also, the prepared samples have broad peaks around 400-550 nm. Hence, the samples have suitable absorption in UV and visible range of spectrum.

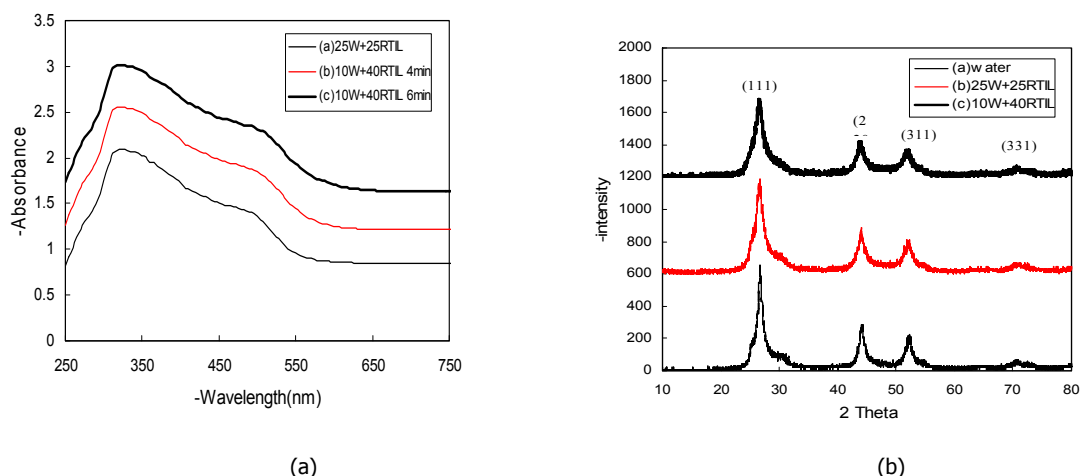


Fig. 1. The powder XRD pattern of CdS nanoparticles(a) and the diffuse and reflectance spectra (DRS) of CdS nanoparticles(b).

Fig. 2 exhibits morphology of the CdS nanoparticles prepared in aqueous solution of the RTIL with 1:1 composition using 4 minutes microwave irradiation and aqueous solution of the RTIL with 1:4 composition using 4 and 6 minutes microwave irradiations. It is evident that structure of the nanoparticles prepared in the all conditions is nanospheres with different sizes. It is clear that aggregation of the nanoparticles decreases with increasing microwave irradiation time and the RTIL content of the media.

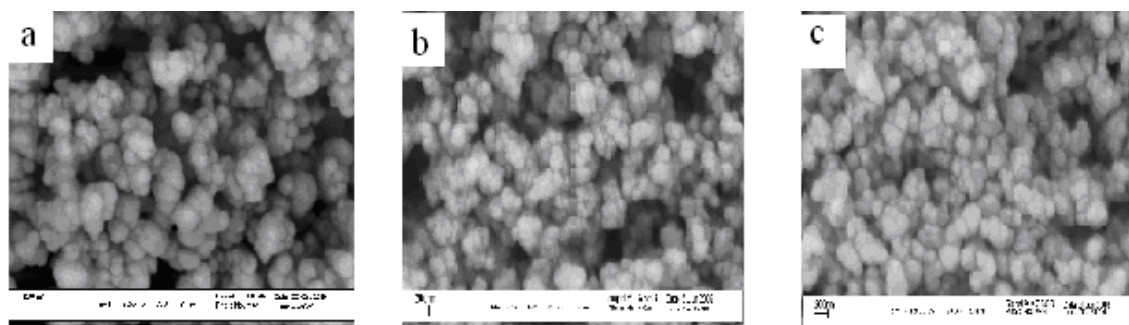


Fig. 2. The SEM images of CdS nanoparticles prepared in aqueous solution of the RTIL for (a) 1:1 position using 4 minutes microwave irradiation, and (b) and (c) 1:4 composition using 4 and 6 minutes microwave irradiations, respectively.

Observed first-order rate constant for the photocatalytic degradation of MB on the CdS nanoparticles prepared in various conditions was calculated using plots of $\ln [MB]$ or $\ln A$ (logarithm of absorbance) *versus* irradiation time and the results were tabulated in Table 1. As can be seen, rate constant of the reaction increases with the RTIL content of media and microwave irradiation time.

Table 1. Observed first-order rate constant for photocatalytic degradation of MB

Light	k_{obs}/min^{-1}			
	Water	25 Water + 25 RTIL	10 Water + 40 RTIL (4min)	10 Water + 40 RTIL (6 min)
Visible	22.9×10^{-4}	40.3×10^{-4}	74.9×10^{-4}	123×10^{-4}
UV	11.0×10^{-3}	15.9×10^{-3}	20.0×10^{-3}	27.4×10^{-3}

4. Conclusions

The method is simple and convenient route to obtain larger quantity of CdS nanoparticles. The as-prepared CdS nanoparticles show a blue shift of approximately 1.52 eV which can be attributed to quantum confinement effect of the CdS nanoparticles. Investigation of photocatalytic activity of the prepared nanoparticles using UV and visible lights reveals that the photocatalytic activity of the prepared samples in presence of the RTIL is considerably higher than the prepared sample in water.

References

- [1] Lakshmikumar, S. T. Rastogi, A. C, Sol. Energy Mater. Sol. Cells. 32 (1994) 7.
- [2] Welton, T. Coord, Chem. Rev. 248 (2004) 2459.
- [3] Liao, X.-H. Chen, N.-Y. Xu, S. S. Yang, B. J. Zhu, J, Cryst. Growth. 252 (2003) 593.
- [4] Xu, C. H. Luo, W. Liu, T. Ying, Ceramics Int. 35 (2009) 917.
- [5] Gomez, E. Gonzalez, B. Calvar, N. Tojo, E. Dominguez, A, Chem. Eng. Data. 51 (2006) 2096.

Molecular dynamics simulation of Ne adsorption on open-ended single-walled carbon nanotubes

Masumeh Foroutan and Amir Taghavi Nasrabadi*

Department of Physical Chemistry, Faculty of Chemistry, College of Science, University of Tehran, Tehran, Iran

Email: amirtaghavi@khayam.ut.ac.ir

Keywords: Carbon nanotube, Molecular dynamics simulation, Adsorption isotherms, Self-diffusion coefficient**1. Introduction**

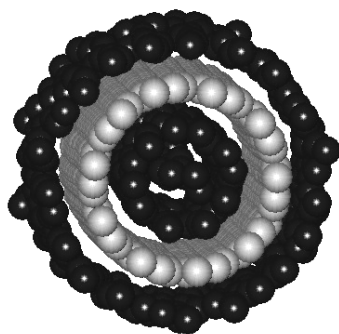
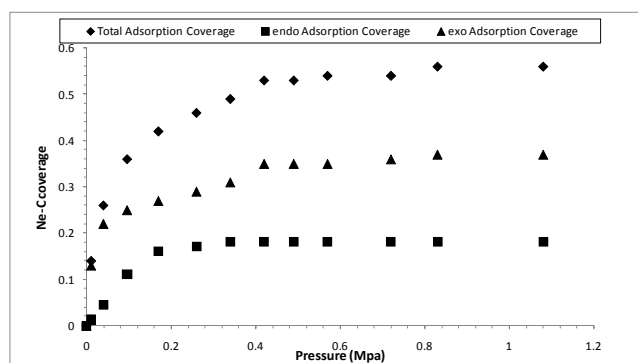
From the discovery of single-walled carbon nanotubes (SWCNTs) by Iijima [1] in 1993, numerous applications have been proposed for this type of nanomaterials, which one of the most important of them is to consider their adsorption characteristic for extensive range of gases, especially hydrogen, for industrial applications. Specifically, physisorption of noble gases on SWCNTs are currently investigated using both theoretical methods and experimental techniques extensively; because the inertness of the noble gases typically excludes the possibility of chemical and polar interactions with the surface [2]. In this paper, we investigate this process from different aspects of view, including calculation of adsorption energies, structural characteristics and transport properties.

2. Method

Molecular dynamics simulations were performed with Tinker 5 molecular modeling package in the NVT ensemble with volume box of $80 \times 80 \times 80 \text{ \AA}^3$. The unit cell of the (10,10) tube in the modeling contains 40 carbon atoms with radius and length of 6.78 and 2.46 \AA , respectively. Our (10,10) SWCNT contains 620 atoms, corresponding to 15 unit cells along the tube axis. The parameters of OPLS-AA [3] force field were used for description of the intramolecular and intermolecular interactions. The periodic boundary conditions were imposed in all three dimensions and Vander Waals cutoff was chosen 10 \AA . The initial configuration is randomly generated with the number of gas atoms, and the simulation boxes contain from 100 to 1200 Ne atoms. The system was equilibrated for 100 ps followed by a 200 ps production run. The equations of motion were integrated by the velocity Verlet algorithm method. A Nose-Hoover extended system thermostat was used for the temperature control.

3. Results and Discussion**1. Coverage of the isolated SWCNT**

Fig. 1 shows a typical snapshot of Ne adsorbed on the internal and external surfaces of SWCNT. A monolayer on the external surface of CNT is observed, and atoms filled the internal space of SWCNT. Adsorption coverage of Ne on the SWCNT has been expressed in terms of the atomic ratio of Ne to C as $N_{\text{Ne}}/N_{\text{C}}$. In the first simulation, Ne adsorption has been performed at 50 K. The Ne adsorption isotherms on (10,10) SWNT at 50 K is presented in Fig. 2. From the simulation results, the saturation coverage for the exohedral monolayer adsorption is about 0.37 Ne-C. Simulations at saturation conditions yield coverage of $N_{\text{Ne}}/N_{\text{C}} = 0.18 \text{ Ne-C}$ at 50 K inside the SWCNT. Adsorption isotherms for Ne at temperatures of $T = 70$ and 90 K were also considered in this work.

**Fig. 1.** A typical snapshot of endohedral**Fig. 2.** Adsorption isotherm for Ne at 50 K within (10,10) SWCNT. and exohedral adsorption of Ne at 50 K.

2. RDF and MSD plots

In analyzing the structural characteristics of the adsorption systems, the radial distribution function (RDF) provides a better understanding of the quality of the adsorption process. Fig. 3a shows the RDF plots of C–Ne, at 50, 70 and 90 K. The sharp rise after 2.8 Å represents the distance of closest approach of Ne to the SWCNT. This demonstrates a purely physisorption behavior. The RDF plots emphasize that the lower the temperature applied, the more is the Ne adsorbed. Fig. 3b represents the mean square displacement (MSD) plots of Ne atoms at different temperatures. The MSD of Ne atoms increases with increasing temperature that indicates the higher translation mobility of Ne atoms.

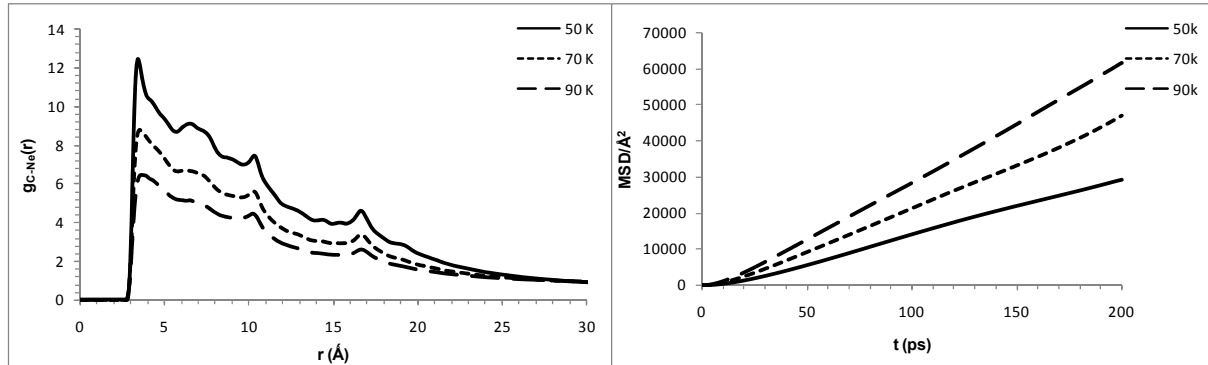


Fig. 3. (a) Carbon-Ne RDF and (b) MSD plots of Ne atoms at 50, 70 and 90 K.

3. Adsorption energy and self-diffusion coefficients

The time-averaged adsorption energies over the total simulation time (300 ps) were calculated using equation (1):

$$\Delta E_{ad} = [E_{tube+Ne} - E_{tube} - NE_{Ne}] / N \quad (1)$$

where N is the number of Ne atoms in the simulation box and E_{Ne} is the energy amount derived from running the system with one Ne alone. The self-diffusion coefficient has been calculated from the slope of the MSD using the Einstein relation (2):

$$D = \frac{1}{6} \lim_{t \rightarrow \infty} \frac{\langle |r(t + \Delta t) - r(t)|^2 \rangle}{\Delta t} \quad (2)$$

where $r(t)$ is the displacement at time t . The adsorption energies and self-diffusion coefficients of Ne fluid are listed in Table 1. Increasing the operating temperature decreases the adsorption energy and increases the self-diffusion coefficient. This is fundamentally consistent with the fact that higher temperatures give the adsorbates more kinetic energy and thus results in higher diffusion of Ne atoms and less chance of them to be adsorbed.

Table 1: Adsorption energies and self-diffusion coefficients of Ne in (10,10) SWCNT at various temperatures.

Temperature (K)	50	70	90
Adsorption energy (kcal/mol)	-0.948	-0.869	-0.825
self-diffusion coefficient ($\text{\AA}^2/\text{ps}$)	25.9	39.7	52.8

4. Conclusion

We have investigated the adsorption of Ne atoms on carbon nanotubes as a function of temperature. Analysis of the RDF plots demonstrates the pure physisorption behavior. The amount of adsorption was shown to be strongly influenced by the applied temperature, i.e. decreasing the temperature to 50 K results in higher adsorptions. It is also found that adsorption energy is higher for nanotubes at lower temperatures.

References

- [1] S. Iijima, T. Ichihashi, Nature 363 (1993) 603.
- [2] V. V. Simonyan, J. K. Johnson, A. Kuznetsova, J. T. Yates, J. Chem. Phys. 114 (2001) 4180.
- [3] G. A. Kaminsky, R. A. Friesner, J. Tirado-Rives, W. L. Jorgensen, J. Phys. Chem. B 105 (2001) 6474.



Electrochemical synthesis of copper nanoparticles in surfactant solution

S. A. Seyed Sadjadi^a, M. H. Riazi^{a,b,*}, A. Banaei^b, A. Heidari^c

^aDepartment of Chemistry, Iran University of Science and Technology, Tehran, Iran

^bResearch and Development, Padideh Shimi Nili Co., Tehran, Iran

^c Department of chemistry, Ferdowsi University of Mashhad, Mashhad, Iran

E-mail: naeemriazi@yahoo.com

1. Introduction

The synthesis of nanoparticles of controlled shapes has attracted much attention because their physical and chemical properties depend strongly on their size. Manipulating the morphology and the special nano-architectures of nanoparticles remain challenges for researchers who are interested in materials science. Hence, effectively controlling the shape and structure of synthesized nanoparticles is an emerging research topic. A variety of methods have been developed to prepare nanoparticles in all kinds of shapes [1]. For example cubic nanoparticles and mechanisms of their growth have been actively studied and attracted a great deal of attention [2]. Tetrahedral and cubic platinum nanoparticles were used as catalyst in the electron-transfer reaction between hexacyanoferrate (III) and thiosulfate ions in colloidal solution at room temperature [3]. The production of metal nanoparticles by an electrochemical method has been widely researched.

Recently, the electrochemical synthesis of gold nanorods provides yields fairly uniform gold nanorods with a controlled aspect ratio [4]. Huang et al. reported the synthesis of Monodispersed gold nanocubes of highly uniform size [2], gold nanodumbbells [5,6] and crooked gold nanorods [7] were fabricated by a simple electrochemical method. The shape of gold nanoparticles can be modified to form cube, dumbbell and rods structures by addition of solvents like acetone, cyclohexane, 2-propanol, etc. during the electrolysis. For the growth of these gold nanoparticles, generally, a template method with a dynamic surfactant micelle system serving as the soft template is employed and the addition of a small amount of organic solvent to the surfactant solution is necessary for enhancing the formation of the cubic-like, rod-like and dumbbell-like micelles.

Electrochemistry has not been employed as a means of preparing large numbers of metal nanoparticles yet, but some advantages of electrochemical methods over chemical ones in synthesis of small metal particles are the high purity of the particles and the possibility of a precise particle size controlled by adjusting current density or applied potential, surfactant concentration and growth temperature [8].

This study demonstrates a simple electrochemical method for synthesizing copper nanoparticles in the presence of acetone solvent with cationic surfactant solution. Transmission electron microscopy (TEM) and UV-Vis spectroscopy were used to elucidate the characteristic structures of copper nanoparticles.

2. Experimental

We have described elsewhere a method for synthesizing suspensions of Cu nanoparticles in aqueous solutions, wherein a mixed surfactant system was employed to define the size and shape of the nanocubes. Briefly, the synthesis is performed within a simple two-electrode electrochemical cell. Copper metal rod at the anode is oxidized to form a soluble complex, which then diffuses to the Pt cathode rod where it is reduced. The copper rod and the platinum rod, with 60mm length an 1mm diameter both 99.99% pure, were purchased from the conventional sources. These two electrodes were placed vertically, inside the cell, with 1mm distance between them. The electrolyte solution volume is typically 100 mL and contains 0.08 M of the cationic surfactant hexadecyltrimethylammonium bromide (CTAB, 99%, Merck), and 500 mg of the more hydrophobic co-surfactant tetradodecylammonium bromide (TDAB, 98%, Fluka). The CTAB-TDAB system serves as the supporting electrolyte and as the stabilizer for the Cu nanoparticles. The glass electrochemical cell containing the electrodes and mixed surfactant solution is then placed into an ultrasonic bath (Tecno-Gaz model Tecna 3, Italy) whose water solution is held at room temperature and sonicate for 20 min. The electrolysis is done under constant-current mode, with the typical setting being 60 mA. The electrolysis time is typically 5 min under constant sonication.

Following electrolysis, the solution is sonicated again for 20 min. Then result solution centrifuged (20 min at 12,000 rpm at 25°C) yields flocculent precipitates of Cu nanoparticles. The precipitates can be redispersed in deionised water to the desired concentration for further surface modification or transmission electron microscope (TEM) and UV-Vis spectroscopy analysis.

3. Results and discussion

Fig. 1 shows a typical TEM image of prepared copper nanoparticles synthesized by electrochemical method. The prepared nanoparticles obtained using the electrochemical method have a spherical shape and size distribution 17.4 ± 3.9 nm. This image shows that the shape and size of particles prepared by this method is very uniform. This method can be modified by add a solvent to the growth solution; adjust the surfactant concentration and current density to control the shape and size of copper nanoparticles.

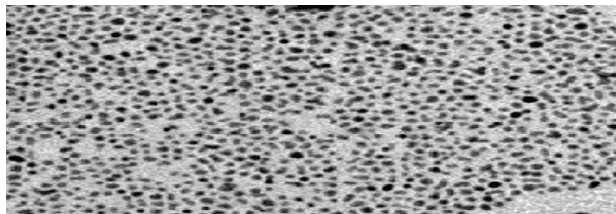


Fig. 1. A typical TEM image of copper nanoparticles synthesized by electrochemical method in surfactant solution.

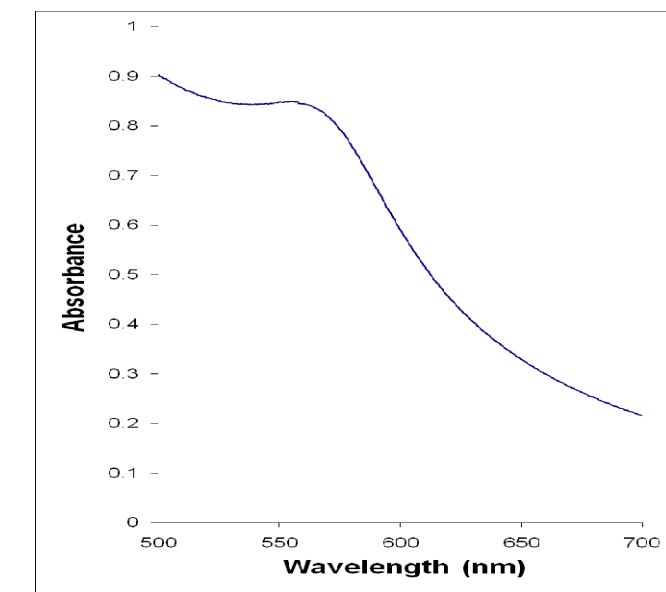


Fig. 2. UV-Vis spectrum of colloidal copper nanoparticle solution.

Fig. 2 shows the UV-Vis spectrum of dispersed copper nanoparticles in deionized water. There is an absorbance in 555nm that can be related to absorbance of copper nanoparticles in the solution.

4. Conclusion

In summary, single crystalline copper nanoparticles were fabricated. The size of the copper nanoparticles is 17.4 ± 3.9 nm. Well dispersed copper nanoparticles were reliably obtained by an electrochemical method with a cationic surfactant solution. This preparation of copper nanoparticles is proven to be a simple and effective synthetic method.

References

- [1] C. Burda, X. Chen, R. Narayanan, M. A. El-Sayed, *Chem. Rev.* 105 (2005) 1025.
- [2] C. J. Huang, Y. H. Wang, P. H. Chiu, M. C. Shih, T. H. Meend, *Materials Letters*, 60 (2006) 1896.
- [3] R. Narayanan, M. A. El-Sayed, *J. Phys. Chem.*, 108 (B2004) 5726.
- [4] C. W. Shih, W. C. Lai, C. C. Hwang, S. S. Chang, C. R. C. Wang, *Metal Nanoparticles: Synthesis, Characterization and Application*, 2002, Marcel Dekker, Inc., 163-182, New York, U. S. America.
- [5] C. J. Huang, P. H. Chiu, Y. H. Wang, W. R. Chen, T. H. Meen, C. F. Yang, *Nanotech.* 17 (2006) 5355.
- [6] C. J. Huang, P. H. Chiu, Y. H. Wang, C. F. Yang, *J. Colloid and Interface Sci.* 303 (2006) 430.
- [7] C. J. Huang, P. H. Chiu, Y. H. Wang, C. F. Yang, S. W. Feng, *J. Colloid and Interface Science*, 306 (2007) 56.
- [8] C. J. Huang, P. H. Chiu, Y. H. Wang, K. L. Chen, J. J. Linn, C. F. Yang, *J. Electrochem. Soc.* 153 (2006) 193.



Removal of dye pollutant by adsorption and photocatalysis of Clay- TiO_2 nanocomposite thin film prepared by electrophoretic deposition

M. Rastegar, A. R. Zolfaghari*, H. R. Mortaheb, H. Naderi

Chemistry and chemical engineering research center of Iran, Tehran, Iran

(Email: Zolfaghari@ccerci.ac.ir)

Keywords: Photocatalysis, Adsorption, Dye pollutant, Nanocomposite, Electrophoretic deposition

1. Introduction

Heterogeneous photocatalysis for water-treatment technologies has attracted the attention of many research groups around the world. The fixation of TiO_2 nanoparticles on the different substrates led to decreasing of difficulties due to separation of photocatalyst and treated phases. Therefore, the key to the problem of industrializing the technology seems to be immobilization of TiO_2 nano-particles, as the most successful photocatalyst reported [1–3]. But, deposition of photocatalyst nanostructure on the different surfaces redounded to reduction of photocatalysis efficiency in organic dye pollutant. Therefore, we needed to the support materials with high surface areas have been applied to immobilize photocatalysts. In this study, we prepared new type of montmorillonite (MMT) and TiO_2 composite by acidic treatment and investigated adsorption and photocatalysis responsibility of those in the removal of methylene blue (MB) at aqueous solution.

2. Methods

The composites of TiO_2 (Degussa P25) and MMT (K montmorillonite obtained from Fluka Co) were prepared by addition of TiO_2 –P25 to MMT (TiO_2 :MMT) with weight ratios of 1:1, 2:1, 5:1, 10:1 and 20:1 in 100 ml of hydrochloric acid (1 M). This suspension was mixed in the ultrasonic bath for 3 min. Then, those were stirred at 50 °C temperature for 4 h. The product was filtered and several times washed with deionized water. Five nanocomposites were prepared which named of TMMT11, TMMT21, TMMT51, TMMT101 and TMMT201 with the last two numbers representing the TiO_2 to MMT weight. For EPD experiments, 304 L stainless-steel plates as electrode with dimensions of 60 × 60 × 0.5 mm³, were used as-received except for a degreasing wash with water, followed by acetone. The sample suspension was prepared with 2 g.l⁻¹ concentration in the methanol solution, and sonicated in the ultrasonic bath for 3 min. A 15 V potential difference was applied by DC power source (EAST WYK-605) between two electrodes with distance of 15 mm for period of 5 min. After deposition, the specimens were carefully extracted from the solution and dried in ambient condition for several days. For adsorption and photocatalysis experiments, we selected 24 cm² (6 cm × 4 cm) which coated surface area, and other section was cleaned by acetone. Also, for comparison of adsorption and photocatalytic behaviors of samples, a film of only TiO_2 was obtained by identical procedure. Both dark adsorption and photocatalysis reactions were carried out in flow batch reactor. The 40 ml of MB dye (from Merck Co) solution was recycled by peristaltic pump (Cole-Parmer 7553-75) and transferred to flow cell of UV-Vis spectrophotometer (Agilent 8453). The declining procedure of MB concentration due to adsorption and photocatalysis process was recorded by UV-Vis spectrum changes in 5 min intervals at 662 nm as maximum wavelength. The initial concentration of MB and flow rate of recycling was 10 ppm and 75 ml. min⁻¹ respectively. Photocatalysis reactions, were conducted by illumination of a UV-C (11 W) light lamp.

3. Results and discussion

Fig. 1 demonstrates the effect of nanocomposite type in adsorption kinetic profile of MB on different substrates. It was observed, these nanocomposites exhibit different adsorption behaviors in the removal MB in dye solution. With increasing of MMT weight ratio to TiO_2 , the amount of adsorption was increased. All nanocomposites achieved the adsorption equilibrium after 120 min. The adsorbed MB appears to be dependent on the hydrophobic attraction of active sites. This adsorption behavior can be obtained by MMT layers with a high porosity and excellent surface area (200 m².g⁻¹). The photocatalytic studies of immobilized samples were conducted after adsorption equilibrium and under the same conditions, which show in Fig. 2. The degradation of organic pollutants by photocatalysis materials occurs primarily at or near the surface of the catalyst and thus adsorption is a critical factor in the efficiency of the process [4]. As it can be seen, approximately 24% of MB has been degraded under UV irradiation by direct photolysis. The removal efficiency of TiO_2 only coated surface has been received to 42%. Also, with

increment of MMT portion, the removal of MB has been increased by photocatalysis reaction. It can conclude, the using of supportive absorbent material in heterogeneous photocatalysis systems will be make improvement of removal efficiency.

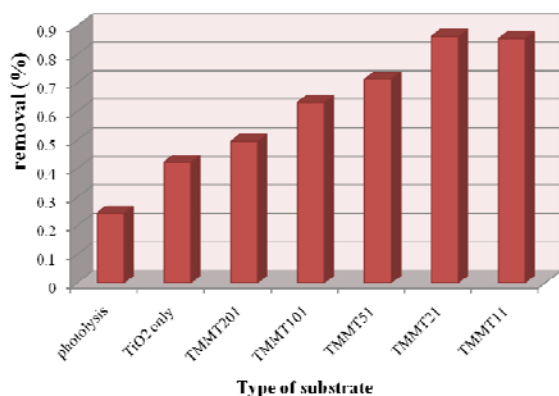


Fig. 1. The adsorption kinetic profile of MB on six prepared substrates.

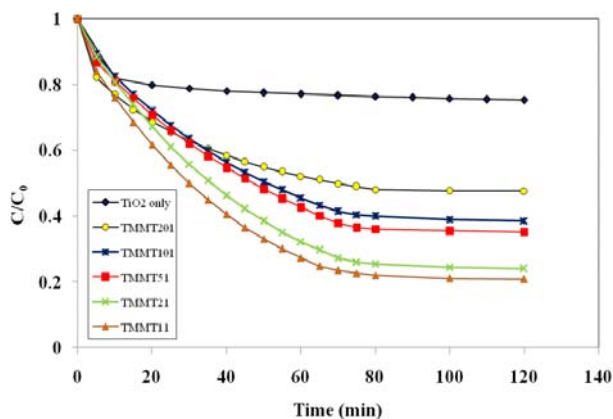


Fig. 2. The comparison removal of MB by photocatalysis process under UV irradiation.

4. Conclusions

The results of our study showed that combination of TiO₂ nanoparticles as photocatalysis material and MMT as absorbent agent led to enhancement removal efficiency of dye pollutant in aqueous solutions. The new catalyst which prepared in this work, exhibit very high adsorption and photocatalysis performance. With variation of TiO₂ to MMT weight ratios, we can obtain optimum catalyst for making of recyclable surfaces in Decolorization organic wastes.

References

- [1] N.R.C.F. Machado, V.S. Santana, Catal. Today 107 (2005) 595.
- [2] X. Hong, Z.Wang, W. Cai, F. Lu, J. Zhang, Y. Yang, N. Ma, Y. Liu, Chem. Mater. 17 (2005) 1548.
- [3] H. Liu, L. Gao, J. Am. Ceram. Soc. 87 (2004) 1582.
- [4] C. Minero, F. Catozzo, E. Pelizzetti, Langmuir 8 (1992) 481.



The correlation of thermal conductivity of carbon nanotube suspension using artificial neural network

Fakhri Yousefi^{*1}, Mohammad M. Papari², Jalil Moghadasi³, Hajir Karimi⁴

¹Department of Chemistry, Yasouj University, Yasouj, 75914-353, Iran
(mojyou54@yahoo.com)

²Department of Chemistry, Shiraz University of Technology, Shiraz 71555-313, Iran

³Department of Chemistry, Shiraz University, Shiraz 71454, Iran

⁴Department of Chemical Engineering, Yasouj University, Yasouj, 75914-353, Iran

Keywords: Carbon Nanotube, Thermal Conductivity, Neural network, Mega-Trend-Diffusion.

1. Introduction

Within the different classes of tubes made of organic or inorganic materials, carbon nanotubes (CNTs) are extremely promising for applications in materials and medicinal chemistry. Because of stiffness of the sp^2 bonding in CNTs, we expect that CNTs exhibit a very high thermal conductivity. Hence, it is interesting to study the increase of thermal conductivity of a nanofluid which is obtained by dispersing small amount of CNTs in traditional fluids. During the last years the study of the enhancement of the thermal conductivity of nanofluids has attained considerable interest. Assael et al [1] showed that by adding 0.6 vol% suspension of MWCNTs to water, the effective thermal conductivity of the resulting fluid experiences 38% enhancement compared to the thermal conductivity of pure water. Further, Choi et al. [2] found that 1 vol% of nanotubes in oil leads to 2.5 fold increase in thermal conductivity of the fluid.

2. Method

Several extended models [3- 6] capable of calculating the thermal conductivity of CNTs-based composites have been selected to be compared against our results. For example Xue [4] developed a new model for the effective thermal conductivity of CNTs-based composites relying on Maxwell theory considering the space distribution and axial effects of the CNTs. Considering the very large axial ratio and the space distribution of the CNTs, Xue built a new model for the effective thermal conductivity of CNTs-based composites. Based on Maxwell theory, two formulae of calculating the effective thermal conductivity of CNTs-based composites were generated. The model shows that the axial ratio and the space distribution of the CNTs can significantly affect the effective thermal conductivity of CNTs-based composites so that the dispersion of a very small amount of CNTs can result in a remarkable enhancement in the effective thermal conductivity of the composites.

Xue assumed that k_e is the effective thermal conductivity of the CNTs-based composites, k_c is the thermal conductivity of the CNTs and k_m is the thermal conductivity of the main media. By considering two kinds of distribution functions, the following relations for the effective thermal conductivities were developed:

$$k_e = k_m \frac{1 - f + (4f / \pi) \sqrt{k_c / k_m} \arctg(\pi / 4 \sqrt{k_c / k_m})}{1 - f + (4f / \pi) \sqrt{k_m / k_c} \arctg(\pi / 4 \sqrt{k_c / k_m})} \quad (1)$$

where f is the total volume fraction of the CNT and

$$k_e = k_m \frac{1 - f + 2f \frac{k_c}{k_c - k_m} \ln \frac{k_c + k_m}{2k_m}}{1 - f + 2f \frac{k_m}{k_c - k_m} \ln \frac{k_c + k_m}{2k_m}} \quad (2)$$

Xue concluded that the distribution state and large ratio of the CNTs play an important role in the thermal conductivity of nanofluids. However, the large discrepancy between the calculated values using Eqs. (1), (2) and the experimental measurements of the thermal conductivity of CNTs-oil composite was noticeable.

Also, the hybrid model that was employed in this work comprises both the mega-trend diffusion technique along with the neural network. This hybrid model comprises an input layer of four neurons corresponding to the thermal conductivity of the fluid (k_f), the volume fraction of CNTs (f) and their corresponding values of MF, plus a variable number of neurons in the hidden layer and a neuron in the output layer corresponding to the thermal conductivity ratio (k_e/k_f).

3. Result and Discussion

As already mentioned, in this study artificial neural network (ANN) scheme has been employed to compute the effective thermal conductivity of nanofluids. The selected nanofluids were suspended the multi-walled CNTs in oil (α -olefin), decene (DE), distilled water (DW), ethylene glycol (EG) and also single-walled CNTs in epoxy and poly methylmethacrylate (PMMA). Several improved models [3-6] capable of calculating the thermal conductivity of CNTs-based composites were selected to be compared against our results. In these models, the size of the particles and interface between CNTs and fluid (interface effect), and the concentration of CNTs are considered. It should be remembered that most of the old theoretical models depend only on the thermal conductivity of particles, the thermal conductivity of the base liquid and the particle volume fraction. In the present calculations, the thermal conductivity of CNTs is taken as 600-3000 W/m K, and the thermal conductivity of oil, decene, distilled water, ethylene glycol, epoxy and poly methylmethacrylate are taken as 0.1448, 0.14, 0.60, 0.25, 0.198 and 0.21 W/m K, respectively.

In order that the validity of the results obtained are checked further, the AAD of thermal conductivity ratios from the literature values in the entire range of volume fraction for whole of nanofluids has been tabulated in Table 1. As the numbers in Table 1 show, the thermal conductivity ratio computed from the Mega-Trend-Diffusion Neural network method stands over other models.

Table 1. The AAD of the effective thermal conductivity ratio using Xue, Yu and Choi models, and ANN method from the experimental data.

system	Q.Z. Xue2005	Q.Z. Xue2006	Yu and Choi 2004	Neural network
MWCNT/Oil	4.75	7.89	4.52	2.79
MWCNT/DE	0.38	0.62	0.81	2.50
MWCNT/DW	7.22	4.89	5.22	3.64
MWCNT/EG	1.24	1.15	1.79	1.86
SWCNT/Epoxy	15.86	5.47	3.32	2.48
SWCNT/PMMA	15.74	16.90	15.29	6.31
overall	7.53	6.15	5.16	3.26

4. Conclusion

From Table 1, it is immediately verifiable that the DNN-MLP model possesses a high ability to predict the thermal conductivity with an absolute average error of 3.26%. There is a good agreement between the predicted and the experimental values of the thermal conductivity ratio ($r = 0.991$). Herein, the standard deviation in the relative errors was 2.3%, meaning that the dispersion around the average was very small.

References

- [1] Assael, M. J.; Chen, C.-F.; Metaxa, I. and Wakeham, W. A. *Int. J. Thermophys.* 25(2004) 971.
- [2] Choi, S. U. S.; Zhang, Z. G.; Yu, W.; Lockwood, F. E.; and Grulke, E. A. *Appl. Phys. Lett.* 79(2001) 2252.
- [3] Xue, Q.-Z. *Phys Lett. A*, 307(2003)313.
- [4] Xue, Q.Z. *Physica B* 368 (2005) 302.
- [5] Xue, Q. Z. *Nanotechnology*, 17 (2006) 1655.
- [6] Yu, W. and Choi, S. U. S., *J. Nanoparticle Res.* 6(2004) 355.



Theoretical Approach for Estimation of Nano Platinum and Palladium Particles Size Synthesized in the AOT Reverse Micelle System

S. Salabat^a and H. Saydi^a

Department of Chemistry, University of Arak, Arak, Iran

saydih237@gmail.com

Keywords: Hamaker constant, Nanoparticle, Reverse micelle, Osmotic interaction, van der Waals interaction

1. Introduction

The factors controlling the ultimate size and shape of particles grown within the reverse micelles remains an area of significant interest. On opinion that the reverse micelles act as template for the production of particles has been suggested by nanoparticle synthesis in various geometries such as spheres and rods[1]. For material such as CdS, ZnS, and AgCl it has been observed that the particle size is controlled by the size of the micelle. However, time-resolved studies on the formation of Cu nanoparticles by Cason [2] have shown that, given adequate reaction time, the ultimate particle size obtained in the AOT/alkane reverse micelle system is independent of W ($W=[H_2O]/[AOT]$) and the bulk solvent type. This leads to an alternate theory that the particle sizes obtained are largely controlled by solvent stabilization of the particles where the surfactant acts as a stabilizing ligand.

2. Modeling

The total interaction energy is achieved by a simple summation of attractive and repulsive forces:

$$\Phi_{total} = \Phi_{vdW} + \Phi_{osm} + \Phi_{elas}$$

(1)

The repulsive energy contribution consist of an osmotic term, Φ_{osm} , and an elastic term, Φ_{elas} , which will be discussed later. The van der Waals attractive force, Φ_{vdW} , between two nanoparticles is a function of the particle radius R, the center to center separation d, and the Hamaker constant A.

$$\Phi_{vdW} = -\frac{A_{131}}{6} \left[\frac{2R^2}{d^2 - 4R^2} + \frac{2R^2}{d^2} + \ln \left(\frac{d^2 - 4R^2}{d^2} \right) \right] \quad (2)$$

$$\Phi_{osm} = \frac{4\pi R k_B T}{v_{solv}} \phi^2 \left(\frac{1}{2} - \chi \right) \left(1 - \frac{h}{2} \right)^2 \quad l < h < 2l \quad (3)$$

Here, R is the particle radius and d is the center-to-center separation, and h ($h = d - 2R$) is the separation distance from the particle surfaces. As will be seen from the interaction energy diagrams, this separation distance at a minimum energy will determine the dispersibility of the particles. It must also be noted that the repulsive forces are independent of the particle material and do not contribute to the total interaction energy until the separation distance is less than twice the ligand length l . To obtain the ligand volume fraction, ϕ , the AOT was modeled as a cylindrical structure extending from the particle surface with a headgroup cross-sectional area 75 \AA^2 and a length of 9.1 \AA with a 90% surface coverage by the following equation:

$$\phi = 0.90 \left(\frac{3R^2 l}{(R + l)^3 - R^3} \right) \quad (4)$$

This is a rough approximation due to the neglect of factors such as the actual surface coverage, the known cone-shaped structure of AOT, and the overlap of the surfactant tails, especially in the region of $h < 2l$ where repulsive forces come into play.

For the osmotic repulsion term v_{solv} is the molecular volume of the solvent, and χ is the Flory-Huggins interaction parameter which is function of the Hildebrand solubility parameters δ_i :

$$\chi = \frac{\bar{v}_3}{RT} (\delta_3 - \delta_2)^2 \quad (5)$$

Where R is the ideal gas constant and \bar{v}_3 is the molar volume of the solvent.

The Hamaker constant A_{131} is a proportionality factor that accounts for two nanoparticles of the same material (component 1) interacting through a solvent (component 3) and the TWA method [3] determines Hamaker constant as:

$$A_{131} = \frac{3\pi\hbar\nu_e (n_{vis0,1}^2 - n_{vis0,3}^2)^2}{4\sqrt{2} \left[(n_{vis0,1}^2 + n_{vis0,3}^2) \left(2(n_{vis0,1}^2 + n_{vis0,3}^2)^{1/2} \right) \right]} \quad (6)$$

Where $n_{vis,j}$ is the index of refraction for energy in the visible range. The vis0, j notation describes the limiting index for refraction in the visible range of material j. The characteristic absorption frequency, ν_e , is assumed to be equivalent for all tree materials.

3.Results and discussion

The contribution of each of the forces to the total interaction energy can be seen in Figure 1 and 2 as a function of separation distance of the particles. Along the total interaction energy curve a minimum value exists that corresponds to an optimum position of the particles with respect to each other. A threshold energy of $-3/2kT$ or greater is required to disperse the particles within the bulk solvent.

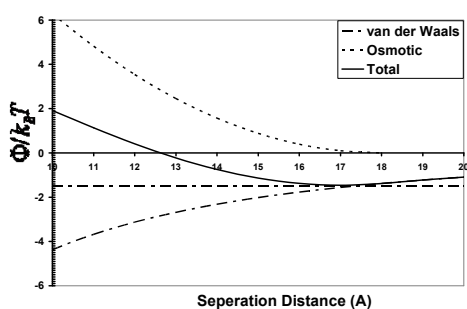


Fig.1 Contribution to Total Interaction Energy

Model for Platinum Nanoparticle coated with AOT.

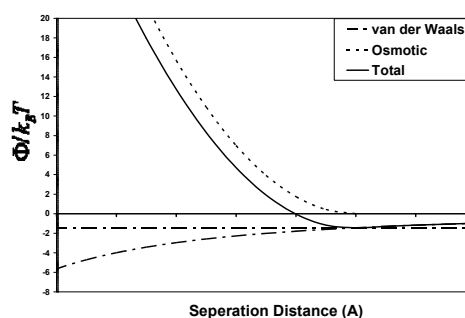


Fig.2 Contribution to Total Interaction Energy

Model for Palladium Nanoparticle coated with AOT.

Particle growth occurs through random exchange of micelle contents and will continue to grow until his threshold energy limit is reached. If particle growth occurs beyond on optimum size, the total interaction energy will drop below this threshold energy limit of $-3/2kT$ and particles will agglomerate and precipitate out of solution. In this case, the repulsive terms are insufficient to balance the attractive van der Waals forces, thereby resulting in an inability to disperse the particles.

In this research we found that this model is able to predict the ultimate size of some nanoparticles obtained experimentally. The calculated diameter of nanoparticles were obtained as $d=7.2$ nm for platinum nanoparticle and $d=10.8$ nm for palladium nanoparticle by using this model. These results were close to the experimental diameter for Pd and Pt nanoparticles as shown in figures 3 and 4[4, 5].

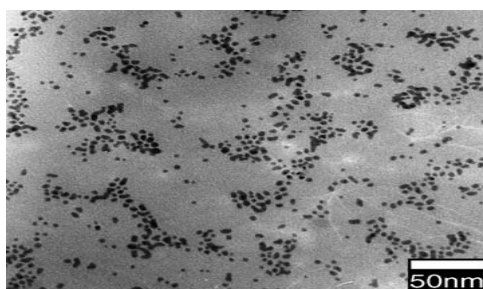


Fig. 3 TEM images and size distribution of palladium nanoparticles prepared in AOT-isooctane reverse micelles.

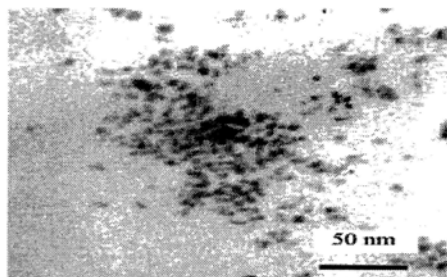


Fig.4 TEM image of the Pt nanoparticles prepared in AOT

References and Notes

- [1] C. L. Kitchens, M. C. McLeod, C. B. Roberts, J. Phys. Chem. 107 (B 2003) 11331.
- [2] J. P. Cason, M. E. Miller, J. B. Thompson, C. B. Roberts, J. Phys. Chem. 105 (B 2001) 2297.
- [3] D. Tabor, R. H. S. Winterton, Proc. Roy. Soc. A. 312 (1969) 435.
- [4] M. Chen, Y. Feng, L. Wang, L. Zhang, J. Zhang, Colloids and Surfaces A. 281 (2006) 119.
- [5] D. Chen, L. Zheng, Chinese J. Chem. 26 (2008) 276.



Sol-gel preparation of Cu,S-codoped TiO₂ nanoparticles and evaluation of phase transformation and photocatalytic activity

Adel Reisi-Vanani^a, Masood hamadani^{a,b}

^aDepartment of physical chemistry, Faculty of chemistry, University of Kashan, Kashan, Iran

^bInstitute of Nano Science and Nanotechnology, University of Kashan, Kashan, Iran

(E-mail: areisi@kashanu.ac.ir)

1. Introduction

Photocatalytic degradation and complete mineralization of toxic organic compounds in water, soil, and air in the presence of semiconductor powders have received much attention over the last two decades [1]. Titania has a large band gap (3.20 eV for anatase TiO₂) and therefore only a small fraction of solar light can be utilized. Many techniques have been examined to achieve the extend of the absorption wavelength range of TiO₂ in visible region, such as, dye sensitized, transition metals doping [2] and noble metal deposition. Recently, C, N, S, F, B anion-doped TiO₂ photocatalysts which show a relatively high level of activity under visible-light irradiation have been reported [3]. In order to further improve the photocatalytic activity, co-doped titania with double non-metal [4], metal-nonmetal [5], metal-metal ion and metal-semiconductor [6] has attracted more attention. Some studies demonstrated that the co-doping with transition metal and nonmetallic element could effectively modify the electronic structures of TiO₂ and shift its absorption edge to a lower energy [5]. The sol-gel technique has been adopted as one of the versatile methods for the preparation of metal and nonmetal doped nanocrystalline TiO₂. Preparation of TiO₂ nanocatalysts and modification of them that absorb visible irradiation instead of UV irradiation is a target in this study to degrade pollutants against sunlight and visible irradiation. Therefore, novel sulfur and copper co-doped TiO₂ photocatalysts with different amount of copper were synthesized by the sol-gel method and characterized and the photocatalytic activity of the samples was evaluated by using MO under UV and visible irradiation. Effect of the calcination temperature on photocatalytic activity and phase transformation was studied. The effect of copper, sulfur and copper-sulfur simultaneously were also compared on photocatalytic activity.

2. Material and methods

The typical synthesis procedure for TiO₂ nanoparticles has been described in our previous work [7]. Preparation of Cu,S-codoped TiO₂ nanoparticles was the same as that of TiO₂, except that the water used for the synthesis, 98.8 mL, contained the required amount of thiourea (corresponding to 0.05 mol % with respect to TiO₂) and CuCl₂·2H₂O (corresponding to 0.05, 0.1, 0.25, 0.5, 1.0 and 2.0 mol % with respect to TiO₂). The samples were characterized by XRD, DRS, SEM-EDX, TEM and FT-IR analysis. The photocatalytic activity of samples was tested using 100 mL aqueous MO solution (10 mgL⁻¹) containing 100 mg nanocatalyst. Aliquots of the mixture were taken at periodic intervals during the irradiation, and after centrifugation they were analyzed with the UV-Vis spectrometer.

3. Results and discussion

The XRD patterns of the samples were prepared and the nanocrystalline anatase structure was confirmed (Figure 1). The XRD pattern didn't show any copper or sulfur phase and may be concluded that Cu and S ions uniformly dispersed among the anatase crystallites. The average size of nanoparticles estimated from the Scherrer equation for TiO₂ and 0.1% Cu,S-codoped TiO₂ were around 13-15 nm and 10-16 nm, respectively. The XRD patterns of undoped TiO₂ and 0.1% Cu,S-codoped TiO₂ at different calcination temperatures indicate rutile phase appears around 650 and 700 °C for undoped and 0.1% Cu,S-codoped TiO₂, respectively. The amount of rutile in the samples was estimated using the Spurr equation. Results shows the phase transformation from anatase to rutile starts about 650 and 700 °C and completes about 800 and 850 °C for TiO₂ and 0.1% Cu,S-codoped TiO₂, respectively. SEM micrographs showed that nanoparticles are uniform, global and slightly agglomerated. The Existence of Cu and s in 1.0% Cu,S-codoped TiO₂ sample confirmed with EDX data. TEM images of the samples showed (Figure 2) the particle sizes of undoped and 0.1% Cu,S-codoped TiO₂ was found to be around 10-13 and 8-12 nm, respectively, which confirm XRD results. Addition of dopants to titania hinders the growth of nanoparticles. It seems that the Cu ions tend to form the complex with the surface oxygen of TiO₂, which it suppresses the growth of TiO₂ crystallite. UV-Vis diffuse reflectance spectra of samples showed a red shift in the absorption onset value in the case of copper and sulfur added titania that indicate dopant decreases band gap of the catalyst. FT-IR spectra of samples show peaks corresponding to stretching vibrations of the O-H and bending vibrations of the adsorbed water molecules about 3350–3450 cm⁻¹ and 1620–1635 cm⁻¹, respectively. In the

region below 1000 cm^{-1} , several peaks were ascribed to absorption bands of Ti-O ($653\text{-}550\text{ cm}^{-1}$) and O-Ti-O flexion vibration ($495\text{-}436\text{ cm}^{-1}$). Degradation of MO showed 0.05% Cu,S-codoped TiO_2 and 0.1% Cu,S-codoped TiO_2 under UV and visible irradiation are the best catalysts, respectively. Synergistic effect of sulfur and copper codoping showed Cu,S-codoped TiO_2 has higher activity than undoped or doped TiO_2 with Cu or S under UV and visible irradiation. Photocatalytic activity of the undoped TiO_2 calcinated at $500\text{--}700\text{ }^\circ\text{C}$ and 0.1% Cu,S-codoped TiO_2 calcinated at 500 and $700\text{-}850\text{ }^\circ\text{C}$ was done under UV and visible irradiation. Because of the sintering phenomenon, the size of nanoparticles increased while the calcination temperature was increased and surface area and photocatalytic activity decreased. It is also known that optimal photocatalytic efficiency is obtained with a mixture of anatase and a small percentage of rutile. Formation of rutile phase started at 650 and $700\text{ }^\circ\text{C}$ for undoped TiO_2 and 0.1% Cu,S-codoped TiO_2 , respectively. Therefore mentioned factors determine photocatalytic activity of samples. For undoped TiO_2 , calcinated samples at 500 and $650\text{ }^\circ\text{C}$ under UV and visible light are the best catalysts, respectively. For 0.1% Cu,S-codoped TiO_2 , calcinated sample at $500\text{ }^\circ\text{C}$ under UV and visible light is the best catalyst. At temperature higher than $750\text{ }^\circ\text{C}$, catalyst transforms to the rutile phase that its catalytic activity is very poor.

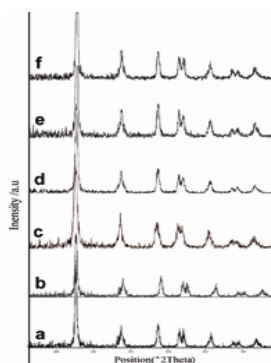


Fig. 1. XRD patterns of (a) undoped TiO_2 and 0.05% S TiO_2 nanoparticles codoped with different amount of Cu (b) 0.05% (c) 0.1% (d) 0.5% (e) 1.0% and (f) 2.0%

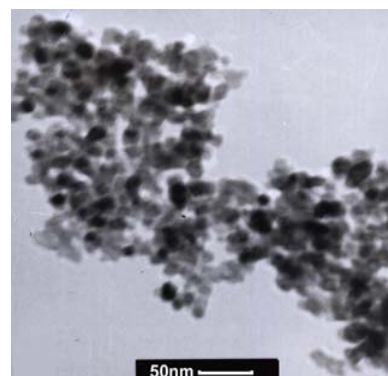


Fig. 2. TEM image of 0.1%Cu,0.05%S-codoped TiO_2 nanoparticles.

4. Conclusions

The sulfur and Copper codoped TiO_2 nanoparticles were successfully prepared by modified sol-gel method as a new catalyst to degrade the pollutants in water. The XRD results showed only anatase phase for undoped and Cu,S-codoped TiO_2 nanoparticles calcinated at $500\text{ }^\circ\text{C}$. The results showed codoping with Cu and S led to less grain size, red shift absorption and high photocatalytic activity. The results of photocatalytic activity of the samples for degradation of MO showed 0.1% and 0.05% Cu,S-codoped TiO_2 nanoparticles have higher photocatalytic activity than the other samples under visible and UV light, respectively. Because of synergetic effects of S and Cu, Cu,S-codoped TiO_2 catalyst has higher photocatalytic activity than undoped and Cu or S doped TiO_2 . Effect of calcination temperature showed the dopants have a significant role on the phase transformation.

Keywords: Codoped TiO_2 ; Sol-Gel Growth; Photocatalytic Activity; Phase Transformation.

References

- [1] A.L. Linsebigler, G. Lu, J.T. Yates Jr., *Chem. Rev.* 95 (1995) 735.
- [2] W. Zhao, C.C. Chen, X.Z. Li, J.C. Zhao, *J. Phys. Chem. B* 106 (2002) 5022.
- [3] D.M. Chen, D. Yang, Q. Wang, Z.Y. Jiang, *Ind. Eng. Chem. Res.* 45 (2006) 4110.
- [4] F. Wei, L. Ni, P. Cui, *J. Hazard. Mater.* 156 (2008) 135.
- [5] X. Yang, C. Cao, K. Hohn, L. Erickson, R. Maghrang, D. Hamal, K. Klabunde, *J. Catal.* 252 (2007) 296.
- [6] X. Yang, L. Xu, X. Yu, Y. Guo, *Catal. Commun.* 9 (2008) 913.
- [7] M. Hamadani, A. Reisi-Vanani, A. Majedi, *Mater. Chem. Phys.* 116 (2009) 376.



Computational Chemistry



Investigation of explosive performance of substituted 1,1,3,5,5-pentanitro-1,5-bis(difluoramino)-3-azapentane by DFT methods

M. Hamadani*, F. Aghabozorgi

Department of Physical Chemistry, Faculty of Chemistry, Kashan University, Kashan, Iran

(E-mail: hamadani@kashanu.ac.ir)

Keywords: DFT, 1,1,3,5,5-Pentanitro-1,5-Bis(difluoramino)-3-azapentane, Heat of formation, Isodesmic reaction.

1. Introduction

Compounds containing two fluorine atoms bonded to nitrogen, i.e., difluoroamino (NF₂), were known as energetic materials. The difluoroamino group strongly enhances the performance of formulation containing boron and aluminum as fuels [1]. We selected 1,1,3,5,5-pentanitro-1,5-bis(difluoramino)-3-azapentane (DFAP) [2] and changed substitutions on it. The shape of DFAP with different functional groups is brought in fig.1 and its corresponding table. In this paper, we compute the heat of formation and investigate the destruction paths of our compounds.

Compound	X ₁	X ₂	X ₃	X ₄	X ₅	X ₆	X ₇
1	NO ₂	NO ₂	NO ₂	NO ₂	NO ₂	NO ₂	NO ₂
2	NF ₂	NO ₂	NO ₂	NO ₂	NO ₂	NO ₂	NO ₂
3	NO ₂	NF ₂	NO ₂	NO ₂	NO ₂	NO ₂	NF ₂
4	NO ₂	NF ₂	NF ₂	NF ₂	NF ₂	NF ₂	NF ₂
5	NF ₂	NF ₂	NF ₂	NF ₂	NF ₂	NF ₂	NF ₂

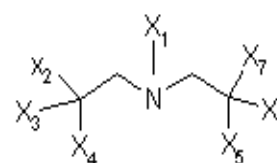
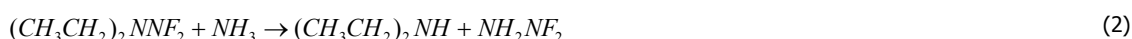


Fig. 1. The shape of

investigated Energetic materials.

2. Computational methods

Our computations were performed using Gaussian 03 package at B3LYP and B3P86 levels and 6-311G**, 6-311++G** basis sets. Moreover we investigated the path of destruction by scanning the interesting bond lengths at B3LYP/6-311G** level. Then, isodesmic reactions were adopted for prediction of heat of formation (HOF). Isodesmic reaction is a kind of process in which the number of each kind of formal bond is conserved. Calculation errors inherent in the individual reactant and product molecules in the reactions are reduced [3]. So, we designed the isodesmic reactions for our compounds [4].for example, for compound 2 isodesmic reaction can written as following:



For isodesmic reaction, heat of reaction ΔH_{298} at 298 K can be calculated from the following equation:

$$\Delta H_{298} = \sum \Delta H_{f,P} - \sum \Delta H_{f,R} \quad (3)$$

Where $\Delta H_{f,R}$ and $\Delta H_{f,P}$ are the HOFs of reactants and products at 298 K, respectively. Therefore, we should compute ΔH_{298} which can be calculated using the following expression:

$$\Delta H_{298} = \Delta E_{298} + \Delta(PV) = \Delta E_0 + \Delta ZPE + \Delta H_T + \Delta nRT \quad (4)$$

Where ΔE_0 is the change in total energy between the products and reactants at 0 K; ΔZPE is the difference between the zero-point energies (ZPE) of the products and the reactants; ΔH_T is thermal correction from 0 to 298 K. The ΔPV value in Eq. (2) is the PV work term which is equal to ΔnRT .

3. Results and discussion

The results of our calculations are shown in tables 1, 2. To predict the paths of destruction we plot the diagrams of the energy of each molecule versus corresponding bond lengths and calculate their Bond dissociations of energy. These results for first molecule are displayed in fig. 2 and table 3 respectively.



Table 1. Total energy (E_0), zero-point energy (ZPE), values of thermal correction (H_T), and heats of formation (HOF) of the title compounds. by using B3LYP and B3P86 methods with 6-311G** basis set.

B3LYP/6-311G**					B3P86/6-311G**			
Compound	E_0	ZPE	H_T	HOF	E_0	ZPE	H_T	HOF
1	-1645.6085	423.53	65.11	144.82	-1649.0863	430.01	64.35	138.14
2	-1694.82444	413.22	66.73	107.68	-1698.3304	419.401	66.06	99.57
3	-1744.04262	407.56	66.07	61.48	-1747.5783	413.77	65.35	55.799
4	-1940.90245	375.46	68.35	-82.61	-1944.5550	381.39	67.45	-89.63
5	-1990.11965	365.97	69.57	-	-1993.8008	371.60	68.74	-
				122.25				132.44

Table 2. Total energy(E_0), zero-point energy (ZPE), values of thermal correction (H_T) and heats of formation (HOF) of the title compounds by using B3LYP and B3P86 methods with 6-311++G** basis set.

B3LYP/6-311++G**					B3P86/6-311++G**			
Compound	E_0	ZPE	H_T	HOF	E_0	ZPE	H_T	HOF
1	-1645.6546	421.62	65.42	199.70	-1649.1267	428.36	64.62	177.11
2	-1694.8744	411.44	67.01	162.75	-1698.3739	417.90	66.26	138.14
3	-1744.0992	406.23	66.37	101.12	-1747.6295	412.95	65.43	77.23
4	-1940.9583	373.05	69.32	-18.52	-1944.6035	379.37	68.42	-41.33
5	-1990.1873	365.94	70.36	-77.18	-1993.8612	370.17	69.28	-107.21

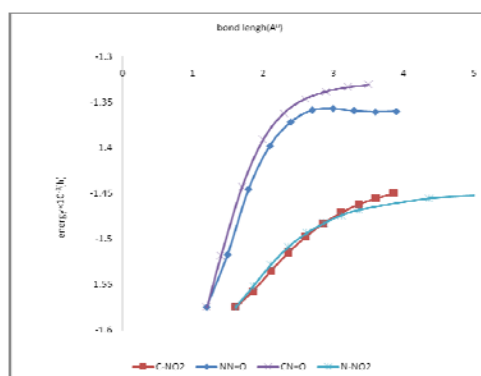


Fig. 2. Total energy of the Molecule number 1 versus Bond length calculated by using B3LYP method with 6-311G** basis set.

4. Conclusions

From the tables 1,2 we can see that, the HOFs decrease smoothly as $-\text{NO}_2$ groups being replaced by NF_2 . The calculated HOFs from B3P86/6-311G** are smaller than B3LYP/6-311G**. Using large basis set, 6-311++G**, shows an augment in HOFs than 6-311G** basis set. This shows that the basis set clearly affects on heats of formation. Moreover, by plotting energy versus bond lengths for all of our compounds, we observed that in 1,3,4 molecules, the Bond dissociation of energy of N-NO_2 and in 2,5 molecules, the Bond dissociation of energy of N-NF_2 are lower and these bonds break earlier.

References

- [1] X.W.Fane and X.H.Ju, J. Mol. Structure: THEOCHEM, 801 (2006) 55.
- [2] P. F. Pagoria and G. S. Lee, Thermochimica Acta, 384 (2002) 187.
- [3] Z. X. Chen and J. M. Xiao, J. Phys. Chem. A, 103 (1999) 8062.
- [4] X.W. Fane and X.H. Ju, J. Hazardous Mterials, 156 (2008) 342.

Novel C_{20} carbon nanostructures: scanning tunneling microscopy (STM), electronic structure, vibrational and UV spectroscopic analysis

H.A. Dabbagh*, M. Zamani, H. Farrokhpour, A. Motahari

Department of Chemistry, Isfahan University of Technology, Isfahan, Iran, 84156-83111

Keywords: C₂₀ Isomers, Fullerenes, IR, UV, STM.

1. Introduction

Carbon clusters are fascinating examples of the richness and variety of carbon chemistry. Calculation of the relative energies of the different C₂₀ isomers is a great theoretical challenge. For example, AM1 [1] SCF [2], GC-LDA [3], HF [4], BLYP [5], B3LYP [6,7] and HCTH [5] methods predict ring structures as optimal for C₂₀ whereas, MP2 [1], uncorrected LDA [5], LSD [8] and BP [8] methods predict the cage structure as having the lowest energy. Finally, high-level MP2 calculation [9], DMC [4] and CCSD [10] calculations predict the bowl is the most stable isomer. Furthermore, there are some papers in the literature dealing with the electronic, thermodynamic, vibrational, nuclear magnetic resonance (NMR) and aromatic properties as well as energetic studies for C₂₀ isomers. Unfortunately, these results restricted to famous C₂₀ isomers such as ring, bowl and cage. In this study we examined the STM, electronic structure, vibrational and UV spectra for a novel series of C₂₀ isomers (such as tadpole, bow-tie, dumb-bell, spiro, propellane as well as ring, bowl and cage) at different levels of calculations including B3LYP (6-31++G, 6-31++G**) and HF (6-31++G, 6-31++G**) and compared them with the results obtained using semi-empirical methods (AM1, PM3). Also, the calculated Nucleus Independent Chemical Shift (NICS) values used to determine the aromatic character of C₂₀ isomers considered.

2. Methods

All calculations were carried out using Gaussian-03 software package [11]. The eight isomers of C₂₀ (Fig. 1) optimized using the different theoretical methods including B3LYP (6-31++G, 6-31++G**) and HF (6-31++G, 6-31++G**). The relative energy of all isomers calculated using mentioned methods. Then, the IR and UV spectra, and electronic structure were calculated using these levels of theory. The NICS values for each isomer calculated based on NMR-GIAO-B3LYP/6-31G method. Simulated STM images at filled and the empty states were obtained using density functional theory at the local density approximation level.

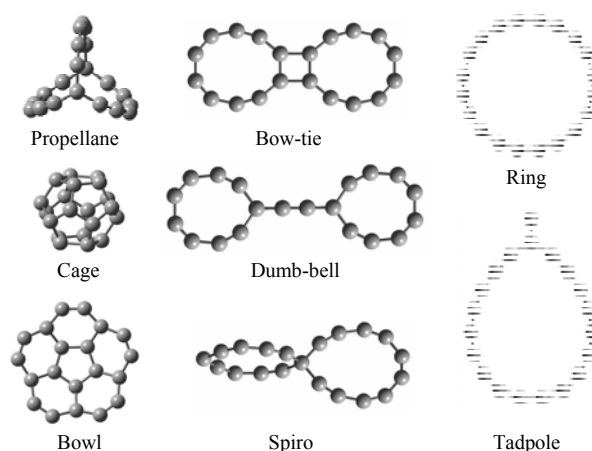


Fig. 1. Geometry optimized structures of C₂₀ isomers at B3LYP/6-31++G** level of calculation.

3. Results and discussion

The relative energy of these isomers indicated that stability sequence obtained at both B3LYP and HF levels of theory is ring > bowl > cage > propellane > bow-tie > tadpole > spiro > dumb-bell. The ring structure is the most stable isomer in this study and those reported in the literature at similar level of theory.

The calculated NICS values for ring, tadpole, propellane, bowl and cage are +28.27, -1.55, -15.94, +12.04 and -14.08, respectively. The value of NICS in the center of the four member-ring of bow-tie isomer is +42.80; while, for the big rings is -17.35. In the case of dumb-bell isomer this value for each of the ring is +15.55 and in the spiro isomer this is -10.35 and -4.64 for

the big and small rings, respectively. These results indicate that ring, bow-tie, dumb-bell, spiro and bowl isomers are anti-aromatic, the tadpole isomer is non-aromatic and the propellane and cage isomers are aromatic.

A broad range of IR spectrum, 400 to 2700 cm^{-1} , is covered by C-C bending vibrations (low frequency region) and C-C stretching vibrations (high frequency region) for all the isomers. For example, IR spectrum of ring isomer is very simple. Two scissoring vibrational modes are responsible for the appearance of base peak at 188 cm^{-1} by B3LYP method. The short appeared band at 551 cm^{-1} is assigned to the ring breathing vibration. The third band is assigned to in plane symmetric stretching vibration of ring carbon atoms and is observed above 2000 cm^{-1} by four levels of theory considered. These calculations are also performed for other C_{20} isomers.

The ring UV spectrum has two peaks with the same intensity at 376 nm. The number of UV peaks increase for tadpole isomer. The peaks are observed as two sets below and above 376 nm. The maximum of absorption (λ_{max}) for bowl, cage, tadpole, spiro, propellane, bow-tie and dumb-bell is observed at 266.53, 278.37, 329.88, 340.35, 343.71, 350.73 and 358.94 nm, respectively. These results reveal that the λ_{max} in UV spectra for bowl and cage isomers appears below 300 nm and for cyclic isomers above it.

Electronic structure of C_{20} ring isomer, for instance, is shown in Fig. 2. The band gap of this molecule is 1.99 eV which obtained by band structure and total density of state (DOS) diagrams, and value of the energy separation between the HOMO and LUMO. The simulated STM image for sample biases of +1 V, which corresponds to the empty state image is along with LUMO electronic contour is shown in Fig. 2.

4. Conclusions

These results show that STM, vibrational and UV spectroscopies are useful tools for identification of novel C_{20} geometrical isomers.

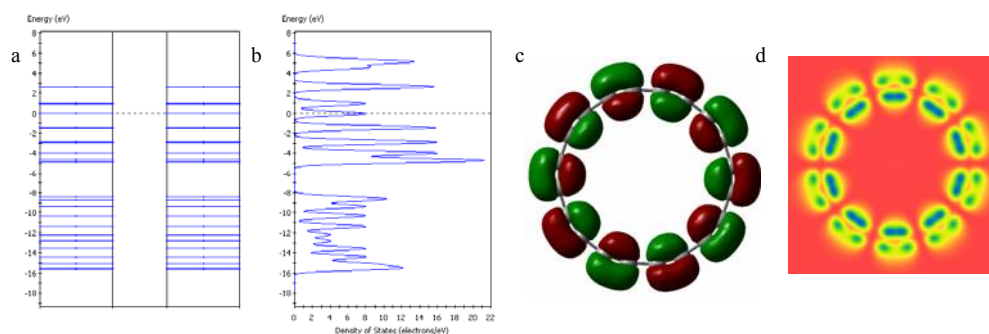


Fig. 2. Band structure (a), total density of state (DOS) (b), LUMO electronic contour (c) and simulated STM image of C_{20} ring isomer.

References

- [1] Z. Slanina, L. Adamowicz, *Fullerene Sci. Tech.* 1 (1993) 1.
- [2] G. von Helden, M.T. Hsu, N.G. Gotts, *Chem. Phys. Lett.* 204 (1993) 15.
- [3] P.R. Taylor, E.J. Bylaska, J.H. Weare, R. Kawai, *Chem. Phys. Lett.* 235 (1995) 558.
- [4] J.C. Grossman, L. Mitás, K. Raghavachari, *Phys. Rev. Lett.* 75 (1995) 3870.
- [5] A.H. Romero, D. Sebastiani, R. Ramirez, M. Kiwi, *Chem. Phys. Lett.* 366 (2002) 134.
- [6] C. Allison, K.A. Beran, *J. Mol. Struct. Theochem* 680 (2004) 59.
- [7] S. Xu, M. Zhang, Y. Zhao, B. Chen, J. Zhang, C. Sun, *J. Mol. Struct. Theochem* 760 (2006) 87.
- [8] R.O. Jones, *J. Chem. Phys.* 110 (1999) 5189.
- [9] Z. Wang, P. Day, R. Pachter, *Chem. Phys. Lett.* 248 (1996) 121.
- [10] E.J. Bylaska, P.R. Taylor, R. Kawai, J.H. Weare, *J. Phys. Chem.* 100 (1996) 6966.
- [11] M.J. Frisch et al., *Gaussian 03*, Revision B.02, Gaussian, Inc., Pittsburgh PA, 2003.



A computational study of dimers and trimers of nitrosyl hydride: Blue shift of NH bonds that are involved in H-bond and orthogonal interactions

Mohammad Solimannejad ^{*,a}, Shokofeh Massahi ^a, Ibon Alkorta ^b

^a Quantum Chemistry Group, Department of Chemistry, Arak University, Arak, Iran

(E-mail: m-solimannejad@araku.ac.ir)

^b Instituto de Química Médica (CSIC), Juan de la Cierva, Madrid, Spain

Keywords: Nitrosyl hydride clusters, Hydrogen bonding, Orthogonal interactions.

1. Introduction

Over the years, it had become accepted that the A–H covalent bond stretches, and its vibrational frequency shifts to the red and intensifies, when it participates in a A–H...B hydrogen bond [1,2]. Despite the greater electronegativity of nitrogen, and its participation in mostly red-shifting H-bonds, the HNO molecule is a principal example, forming a blue-shifting H-bond with such proton acceptors as HNO [3]. Continuing our recent studies [4,5] regarding theoretical evidence for the blueshifting hydrogen bond of NH bond, in this study electronic structure and stability of dimer and trimer of HNO molecules are reported. Thus the present work reports for the first time a detailed examination of the stabilities, electronic structure, and vibrational frequencies of HNO trimers along with locating three new structures (S2d, S3d, and S4d) on the potential energy surface of HNO dimer.

2. Computational details

The geometries of the isolated HNO molecule and its dimer and trimer complexes were fully optimized at the MP2/ aug-cc-pVTZ and M05-2x/aug-cc-pVTZ computational levels. The atom in molecules (AIMs) methodology has been used to analyze the electron density of the systems considered at the MP2/aug-cc-pVTZ computational level. The Natural Energy Decomposition Analysis (NEDA) within the Natural Bond Orbital methodology has been performed to obtain insight of the source of the interaction energy.

3. Results and discussion

Association of two HNO molecules leads to the formation of four minima (fig 1). The principal intermolecular interaction within the most stable minimum S1d corresponds to a cyclic structure with a pair of N–H...O interactions. S2d and S4d present a hydrogen bond interaction (N–H...N and N–H... O, respectively) and an interaction of the oxygen lone pair with the MEP positive region surrounding the nitrogen atom. This kind of interactions has been named as orthogonal interactions [6,7]. Finally, the S3d dimer presents a N...N interaction and is the conformation with the smallest uncorrected interaction energy. A total of nine minima structures have been found for the trimers (Fig. 1). S1t can be considered as the sum of the S1d and S2d complexes. S2t, S3t, S4t and S5t are formed through all the possible combination of N...H and O...H HB's. S6t presents two N...H interactions and a O...N orthogonal contact. All the interactions are confirmed with the presence of bcp between atoms of HNO molecules that obtained from Molecular graphs of HNO dimers and trimers from AIM studies. Using all intermolecular bcp found in the dimers and trimers, exponential relationships can be obtained for the H...N, H...O and N...O interactions as shown in

Fig. 2. The results of NEDA calculations for dimers and trimers show that in all the complexes the most important stabilizing component is the charge transfer followed by the electrostatic, then polarization and finally exchange correlation except in S4d. The integrated properties within the atomic basins in all the minima dimers and trimers based on the energetic variation per monomer indicates that all the molecules, stabilized upon complexation except molecule A in the S7t and molecule C in S7t, S8t, and S9t structures and molecule B in the S4d atoms, and a volume contraction is observed in all the monomers upon complexation when compared to the corresponding value of the non-interacted molecule. The results of vibrational analysis show that symmetric stretching frequency of all NH bonds that take part in N–H...N and N–H...O hydrogen bonds or N...O orthogonal interactions is shifted to blue except of N–H in molecule C of S8t complex.

4. Conclusions

A theoretical study of dimers and trimers of the HNO molecule has been carried out by means of ab initio (MP2/aug-cc-pVTZ) and DFT (M05-2x/aug-cc-pVTZ) calculations. Four and nine structures have been characterized for the dimers and

trimers, respectively. The most stable conformers of dimers and trimers are symmetric cyclic structures including a pair of NH...O interactions and three NH...N interactions, respectively. Blue shift of NH bonds that are involved in hydrogen bonding or uninvolved in hydrogen bonding but take part in orthogonal N...O interaction has been identified.

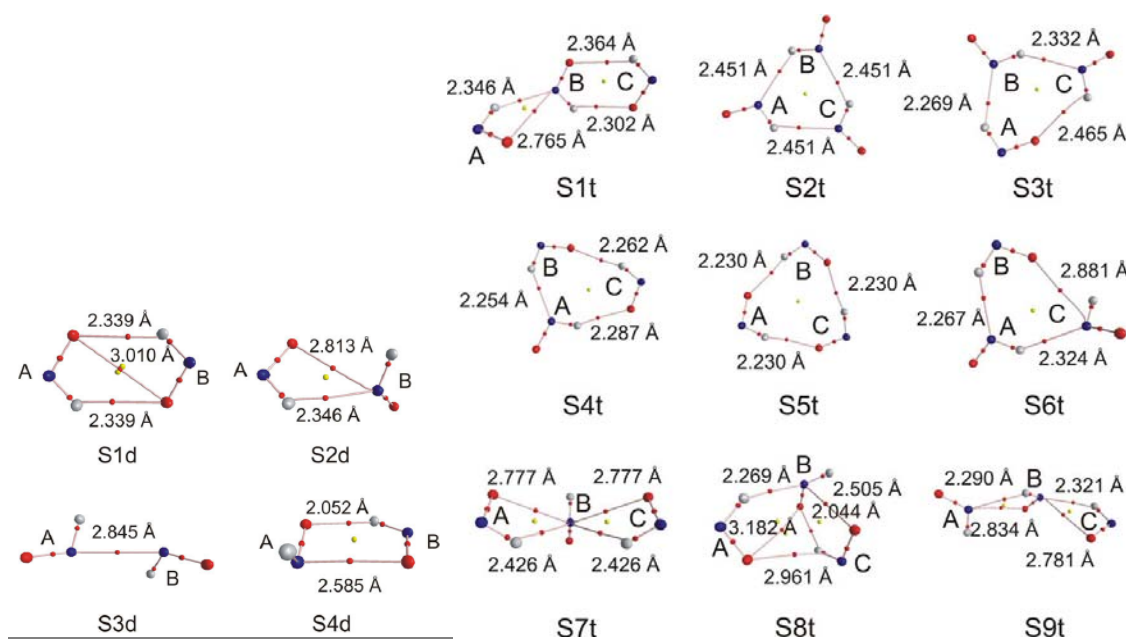


Fig 1. Molecular graph of the dimer and trimer minima obtained at the MP2/aug-cc-pVTZ computational level.

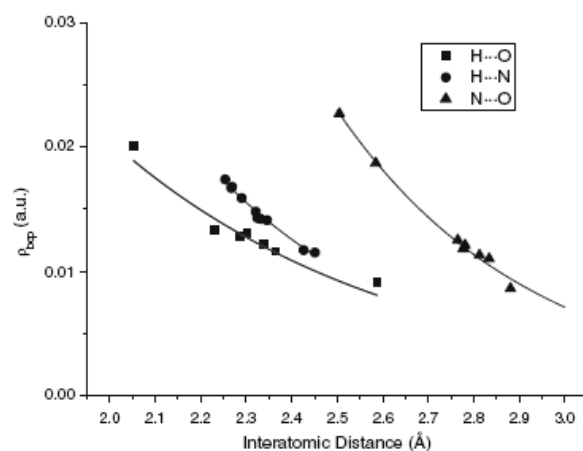


Fig 2. Electron density at the bcp vs. interatomic distance for the intermolecular interactions.

References

- [1] P. Schuster, G. Zundel, C. Sandorfy, *The Hydrogen Bond. Recent Developments in Theory and Experiments*, North-Holland Publishing Co., Amsterdam, 1976.
- [2] S. Scheiner, *Hydrogen Bonding – A Theoretical Perspective*, Oxford University Press, Oxford, 1997, and references therein.
- [3] Y. Liu, W. Liu, H. Li, J. Liu, Y. Yang, *J. Phys. Chem. A* 110 (2006) 11760.
- [4] M. Solimannejad, S. Scheiner, *J. Phys. Chem. A* 111 (2007) 4431.
- [5] M. Solimannejad, S. Scheiner, *J. Phys. Chem. A* 112 (2008) 4120.
- [6] R. Paulini, K. Muller, F. Diederich, *Angew. Chem. Int. Ed.* 44 (2005) 1788.
- [7] G.P.A. Yap, F.A. Jove, R.M. Claramunt, D. Sanz, I. Alkorta, J. Elguero, *Aus. J. Chem.* 58 (2005) 817.

**Aromaticity investigation of penta- and hepta-fulvene derivatives using shannon aromaticity index (SAI)**

S. Noorizadeh*, E. Shakerzadeh

Chemistry Department, College of Sciences, Shahid Chamran University, Ahvaz, Iran

(E-mail: ehsan_shakerzadeh@yahoo.com)

Keywords: Aromaticity, Fulvenes, HOMA, NICS, Shannon Aromaticity Index (SAI).**1. Introduction**

Aromaticity is a theoretical concept of great practical importance [1]. Since it is not an observable property, it should be studied from different features. In the basis of the molecular property the existent criteria can be divided into a few basic categories: energetic, such as Aromatic Stabilization Energy (ASE); geometrical, such as Harmonic Oscillator Model of Aromaticity (HOMA); magnetic, such as Nucleus-Independent Chemical Shift (NICS); and electronic, such as para-delocalization index (PDI). The exocyclically substituted fulvenes represent a very convenient sample to study the extent of changes of the cyclic n -electron delocalization as a result of substitution. This study represents an analysis of the aromatic character of some mono- and di-exocyclically substituted penta- and hepta-fulvenes using recently introduced Shannon Aromaticity Index (SAI). The reliability of this new index is also checked according to the obtained correlations of this index with the other prevalent aromaticity indices such as HOMA, NICS and ASE.

2. Theoretical section

Recently Shannon Aromaticity Index (SAI) is introduced based on the electronic feature of aromaticity [2]. By calculating the electron densities ($\rho_i(r_c)$) at the bond critical points (BCPs) it is possible to define the *Local Shannon Entropy* at the i th critical point as:

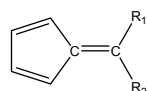
$$S_i(r_c) = -p_i(r_c) \ln p_i(r_c) \quad (1)$$

where the corresponding probability electron density $p_i(r_c)$ is given by $\frac{\rho_i(r_c)}{\sum \rho_i(r_c)}$ and N is the number of the considered critical points. The total Shannon Entropy ($S_t(r)$) of a given ring can now be defined as the sum of the *Local Shannon Entropies* of the constituted bonds in the ring. Since in an ideal full aromatic system, the electron densities at the BCPs must be exactly the same, thus $P_i = \frac{1}{N}$ and the expected total Shannon entropy for this hypothetical ring can be simply calculated ($S_{\max}(r_c) = \ln(N)$). $S_{\max}(r_c)$ is the maximum entropy which is expected for this full aromatic molecule. Hence the difference between the evaluated total Shannon entropy and the expected maximum entropy for a given ring is introduced as the Shannon Aromaticity index (SAI) for the proposed molecular system:

$$SAI = S_{\max} - S_t \quad (2)$$

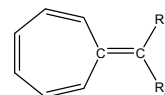
3. Result and discussion

The molecular geometries of all considered molecules, which are depicted in Scheme 1, are optimized at B3LYP/6-31+G** level of theory using *Gaussian 98W* program. The electron densities at BCPs are calculated using the electronic wave functions and AIM2000 software.



Penta

a) $R_1 = \text{H, CH}_3, \text{OCH}_3, \text{NH}_2, \text{CMe}_3, \text{NMe}_2, \text{F, CN, CONH}_2, \text{NO}_2, \text{OH, CF}_3, \text{CCH, COCH}_3, \text{B(OH)}_2, \text{SiMe}_3, \text{CC-}, \text{CH}_2^-, \text{NH}^+, \text{O}^-, \text{COO}^-$ and $R_2 = \text{H}$ or b) $R_1 = R_2 = \text{CH}_3, \text{OCH}_3, \text{NH}_2, \text{NMe}_2, \text{F, CN, NO}_2, \text{OH, CF}_3, \text{COCH}_3, \text{B(OH)}_2, \text{SiMe}_3, \text{CONH}_2, \text{CCH}$.



Hepta

a) $R_1 = \text{H, CH}_3, \text{OCH}_3, \text{NH}_2, \text{F, CN, NO, NO}_2, \text{N}_2^+$ and $R_2 = \text{H}$ or b) $R_1 = R_2 = \text{CH}_3, \text{OCH}_3, \text{NMe}_2, \text{F, CN, NO}_2$.

Scheme 1. Structures of the considered penta- and hepta-fulvene derivatives.

The reported ASE, NICS and the calculated HOMA index using the optimized geometries for mono derivatives of penta-fulvenes are summarized in Table 1 together with the SAI values calculated from Eq. 2. It must be mentioned that the range of $0.003 < \text{SAI} < 0.005$ is the boundary of aromaticity/antiaromaticity. The results in Table 1 show that electron-donating substituents increase the cyclic π -electron delocalization such as CH_2^- and NH^+ with $\text{SAI} = 0.00020$ and 0.00041 , respectively, which are in consistence with the Hückel $4n+2$ rule and *vice versa* for electron-accepting substituents; for instance in NO_2 substituent $\text{SAI} = 0.00584$ indicates the anti-aromatic character of this compound. The range of SAIs in this table is more than 0.5 units, which indicates dramatic substitution effects in mono-exocyclicly penta-fulvenes. Again according to the calculated HOMA and reported NICS and ASE values in Table 1, the same results are concluded. For these penta-fulvenes the calculated SAI values

exhibit very significant correlation with HOMA and NICS with regression coefficients $R^2=0.990$ and $R^2=0.986$, respectively (see Figures 1 and 2). The correlation of SAI with ASE is also considerable ($R^2=0.976$). The calculated SAI values for mono-derivatives hepta-fulvene are collected in Table 2. In the case of mono-exocyclic hepta-fulvenes, electron-donating substituents decrease the cyclic π -electron delocalization following the Hückel $4n+2$ rule and *vice versa* for electron-accepting substituents. It is obvious from the results of this table that the substituents also affected on the aromatic character of hepta-fulvenes dramatically; like penta-fulvenes. For hepta-fulvene $SAI=0.003317$ whereas for the NN^+ derivative it decreases to 0.00049; this indicates transition from non-aromatic character to highly aromatic character. The same trend can also be observed with HOMA and NICS indices. The SAI values show significant correlation with HOMA ($R^2=0.971$ see Figure 3). The correlation of SAI with NICS is also significant ($R^2=0.963$). This procedure is performed for di-exocyclic penta- and hepta-fulvenes and satisfactory results are obtained.

Table 1. The reported ASE and NICS values together with the calculated HOMA and SAI values for penta-fulvene and its mono-substituted derivatives.

R_1	ASE	NICS	HOMA	$SAI \times 10^2$
CH_2^-	22.72	-12.32	0.7042	0.0231
NH^-	21.90	-12.02	0.6934	0.0401
O^-	18.74	-11.92	0.6304	0.0679
CC^-	9.60	-6.99	0.3472	0.2061
NMe_2	7.42	-7.48	0.2365	0.2169
NH_2	7.62	-6.00	0.2327	0.2495
COO^-	2.13	-4.50	0.0771	0.3169
OCH_3	3.40	-3.96	0.0570	0.3369
OH	2.75	-3.72	0.0287	0.3479
F	0.02	-2.53	-0.1224	0.4119
CH_3	-0.11	-1.77	-0.1817	0.4197
CMe_3	-0.51	-1.71	-0.2226	0.4231
CCH	-3.64	0.46	-0.1957	0.4708
$SiMe_3$	-3.22	0.01	-0.325	0.4768
H	-2.9	-0.68	-0.2868	0.4818
$COCH_3$	-5.56	1.16	-0.3834	0.5084
$B(OH)_2$	-5.57	1.48	-0.3946	0.5229
CF_3	-5.76	1.24	-0.4349	0.5355
CN	-6.80	2.28	-0.3334	0.5404
$CONH_2$	-4.24	0.33	-0.4211	0.5497
NO_2	-8.90	3.77	-0.4865	0.5841

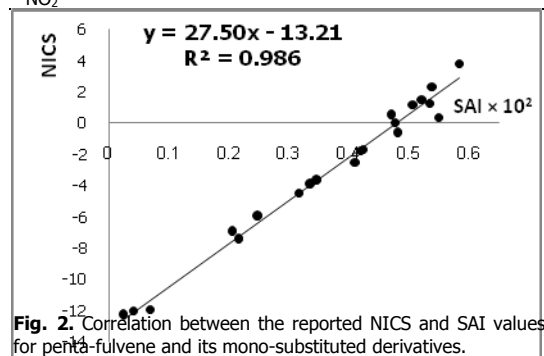
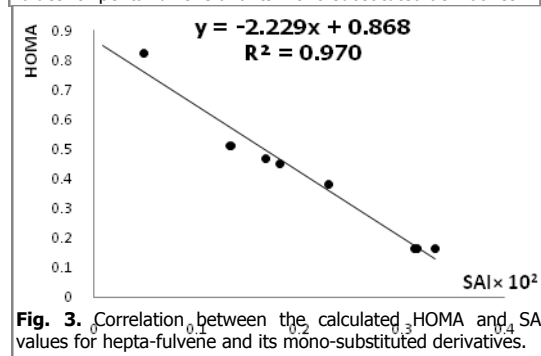
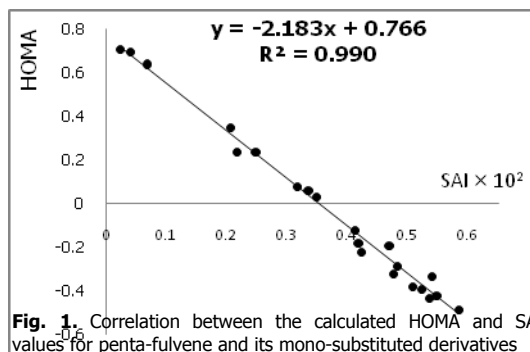


Table 2. The reported HOMA and NICS values together with the calculated SAI values for hepta-fulvene and its mono-substituted derivatives.

R_1	HOMA	NICS	$SAI \times 10^2$
NH_2	0.095	9.62	0.36464
OCH_3	0.146	10.73	0.3510
F	0.164	8.68	0.3317
H	0.164	8.47	0.3121
CH_3	0.165	8.87	0.3147
CN	0.381	4.71	0.2283
NH_3^+	0.449	2.29	0.1809
NO_2	0.467	2.06	0.1677
NO	0.509	2.70	0.1329
NN^+	0.822	-3.83	0.0490



The SAI is successfully applied in investigation of substitution effects on aromatic character of penta- and hepta-fulvene derivatives. It can be concluded that the substituents are affected considerably on the aromatic character of fulvenes. The obtained SAIs exhibit significant correlation with some other prevalent aromaticity indices such as ASE, HOMA and NICS.

References:

- [1] Schleyer, P.v.R. Chem Rev. 101 (2001) 1115.
- [2] Noorizadeh, S. Shakerzadeh, E. Phys. Chem. Chem. Phys (Submitted for publication).



Theoretical studies of structural and electronic properties of nano-metric adamantane compounds containing alkali metals

M. Hamadani^{a,b}, A. Vali pour^a

^aFaculty of Chemistry, University of Kashan, Kashan, I.R. Iran.

^bInstitute of Nano-Science and Nanotechnology, University of Kashan, Kashan, Iran.

(E-mail: hamadani@kashanu.ac.ir)

Key words: Adamantane, Conductance, nano electro-mechanical systems, Diamondoid.

1. Introduction

Diamondoids were first discovered and isolated from petroleum in 1933. They have diamond-like fused-ring structures. The rigidity, strength and assortment of their three-dimensional shape make them valuable molecular building block for nanotechnology. Adamantane (C₁₀H₁₆) is the simplest of these polycyclic diamondoids. The unique structure of adamantane is reflected in its highly unique physical and chemical properties, which can have many applications in nanotechnology [1,2]. Diamondoids have also been used as templates for crystallization of zeolite catalysts [3], the synthesis of high-temperature polymers [4] and in pharmacology.

In pharmacology, adamantane derivatives, for example, Amantadine and Rimantadine have been well-known because of their antiviral activity [3]. The main indication of these drugs is prophylaxis and treatment of influenza A viral infections. They are also used in the treatment of Parkinsonism and inhibition of hepatitis C virus (HCV) [5]. Memantine is used in slowing the progression of Alzheimer's disease [5,6]. Some derivatives of adamantane possess an antitumor and antibacterial activity [7].

Recently, theoretical simulations of quantum conductance of C₁₀H₁₆ have shown that it is electronically an insulator. However, its derivatives have interesting electronic properties, which make them useful for building nano electro-mechanical systems (NEMS) and other nano scale logic units [1,2]. In this paper, DFT studies of structural and electronic properties of nanometric adamantane compounds containing alkali metals were carried out.

2. Computational details

Adamantane (ADM) and its derivatives (ADM.X and ADM.X₂(X=Li, Na)) which are constructed by substituting one and two hydrogen atom in adamantane with one and two X ions (X=Li, Na) are chosen compounds. Therefore, two and twelve different structures have been selected for ADM.X ADM.X₂, respectively. Optimized geometry and thermo-chemistry parameters of each structure have been calculated. All calculations were performed using GAUSSIAN03 programs and Density functional calculations (DFT) at B3LYP level in the gas phase. In order to analyze the effect of basis sets on the calculated band gap of molecules, 6-31G** and 6-311++G** basis sets have been employed. Also, all of thermodynamic functions such as ΔE , ΔS , ΔH and ΔG reaction for preparation of ADM.X and ADM.X₂(X=Li,Na) are calculated.

3. Results and Discussion

The results show that the band gap of adamantane molecule is equal to 9.3161 eV. By adding one sodium atom to adamantane in two different positions, band gap of compounds reduce to 2.1115 and 2.3821 eV, respectively. These decrease in band gap displays that the conductance of ADM.Na becomes generally higher than adamantane molecule. Unlike the adamantane that is electronically an insulator; these derivatives have interesting electronic properties, which make them useful for building nano electro-mechanical systems (NEMS) and other nano scale logic units. According to available results, band gaps of ADM.Li molecules, are equal to 2.3903, 2.7624 eV respectively which show the higher conductivity compare with adamantane molecule.

By adding two conjunct sodium atoms, calculated band gaps using 6-31G** basis set are 2.4965, 2.5747 eV, respectively for two different structure. Also, these values for adding two conjunct lithium atoms are 2.7716 and 2.7407 eV respectively. These results show a little different compare with ADM.Na and ADM.Li molecules.

When two sodium atoms locate on separate carbons, band gap decrease more. For example, band gap of three of these compounds are equal to 1.2390, 1.2316 and 1.2443 eV which have the highest conductance in their group. The same trend have been observed for substituting two separated Li atoms to adamantane. The same calculation have been also performed using 6-311++G** basis set which did not change the results considerably.



For example some results of thermodynamic energy changes for ADM.Na and ADM.Na₂ using B3LYP with 6-31G** and 6-311++G** basis sets are shown in table 1 and 2.

Table 1. Thermodynamic energy changes for ADM.Na artificial molecule using B3LYP hybrid functionals and different basis sets.

Basis set structure	6-31G**		6-311++G**	
	I	j	i	j
$\Delta E(\text{kJ/mol})$	-25.615	-25.744	-25.548	-25.560
$\Delta S(\text{kJ/mol.K})$	0.0035	0.0046	0.0041	0.0045
$\Delta H(\text{kJ/mol})$	-28.092	-28.222	-28.025	-28.038
$\Delta G(\text{kJ/mol})$	-29.135	-29.592	-29.247	-29.379

Table 2. Thermodynamic energy changes for ADM.Na₂ artificial molecule using B3LYP hybrid functionals and 6-311++G** basis set.

Structure	1	2	3	4	5	6	7	8	9	10	11	12
$\Delta E(\text{kJ/mol})$	-14.178	-35.036	-	-	-	-	-	-	-37.013	-	-	-36.123
			35.492	35.496	35.952	36.035	14.675	32.440		34.752	36.123	
$\Delta S(\text{kJ/mol.K})$	-0.0297	-0.0033	-	-	-	-	-	-	-0.0049	-	-	-0.0061
			0.0024	0.0023	0.0061	0.0058	0.0327	0.0062		0.0036	0.0061	
$\Delta H(\text{kJ/mol})$	-15.417	-35.036	-	-	-	-	-	-	-37.0139	-	-	-36.123
			35.492	35.496	35.952	36.035	15.914	32.440		34.752	36.123	
$\Delta G(\text{kJ/mol})$	-6.566	-34.053	-	-	-	-	-6.170	-	-35.553	-	-	-34.305
			34.777	34.811	34.134	34.307		30.593		33.679	34.305	

4. Conclusion

According to our studies about ADM, ADM.X and ADM.X₂(X=Li,Na), We could that conclude when one and two Na&Li atoms are added to adamantane molecule, the electronic properties of adamantane can change such as the HOMO-LUMO gap of molecules, the conductance, etc. The conductance of ADM.X and ADM.X₂(X=Li,Na) is higher than adamantane molecule and the conductance of ADM.X₂ is higher than ADM.X. In ADM.X₂ artificial molecule, the conductance can be a function of two atoms position on carbons. In other words, When two atoms locate on separate carbons, the conductance is higher than when two atoms are conjuncted. Moreover, the conductance of adamantane compounds containing Na is higher than adamantane compounds containing Li.

References

- [1] Mansoori, G. A. and Xue, Y., Int J Nanosci., 7 (2008) 63.
- [2] Marsusi, F. Mirabbaszadeh, K. and Mansoori, G. A., Physica E, 41 (2009) 1151.
- [3] Mansoori, G. A., "Principles of Nanotechnology: Molecular- Based Study of Condensed Matter in Small Systems", World Sci. Pub. Co., Hackensack, NJ, 2005.
- [4] Meador, M. A., Annu. Rev. Mater. Sci., 28 (1998) 599.
- [5] Hardman, J. G. Limbird, L. E. and Gilman, A. G., " Goodman & Gilman's: The pharmacological basis of therapeutics", 10th Ed., McGraw-Hill Pub. Co., New York, NY, (2001).
- [6] Nazem, A. and Mansoori, G. A., journal of Alzheimer's Disease., 13 (2008) 199.
- [7] Kazimierzczuk, Z. Gorska, A. Switaj T. and W. Lasek, Bioorg. & Medici. Chem. Lett., 11 (2001) 1197.

Effect of substitution on structure, stability and electronic properties of nanoscale polyhedral oligomeric silsesquioxane (T_{12} -POSS)

M. Hamadani^{a,b}, R. Hosseinpour^a

^aFaculty of Chemistry, University of Kashan, Kashan, Iran

^bInstitute of Nano-Science and Nanotechnology, University of Kashan, Kashan, Iran

(E-mail: hamadani@kashanu.ac.ir)

Keywords: Polyhedral oligomeric silsesquioxane (POSS), Cage Shape, DFT, Hybrid nanofiller, Polymeric nanocomposite.

1. Introduction

The polyhedral oligomeric silsesquioxanes (POSS_n) are important nanostructure hybrid inorganic-organic chemical compounds. They are an important class of nanocompounds with cage-shaped structures; therefore POSS systems have been widely investigated in hybrid polymers and nanocomposites [1]. The building block of the H-silsesquioxanes is the trifunctional monomer unit ((HSiO_{1.5}) and the letter T is used to describe this unit [2,3]. Depending on the number of ((HSiO_{1.5}) units in the POSS cage, the POSS cage can be designated as T_n-POSS, where n=8, 10, 12, etc. The synthesis, applications and theoretical studies of POSS derivatives have been reviewed by Li et al [3].

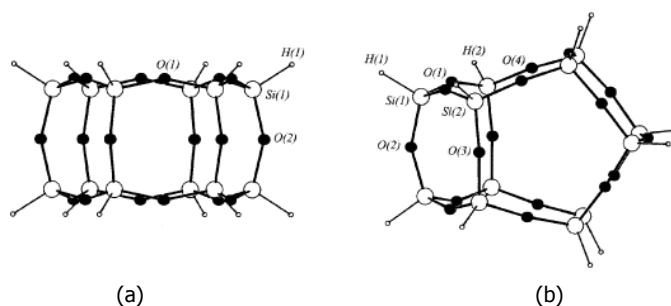


Fig. 1. Structures of the two most stable T₁₂-POSS, a) D_{6h}- {4⁶6²}, and b) D_{2d} - {4⁴5⁴}

The structures of substituted POSS compounds are based on replacing one or more H-Si bonds with R-SiDodecasisilsesquioxane, (HSiO_{1.5})₁₂, (denoted as T₁₂-POSS) consists of 12 silicon atoms that are connected to each other through intermediate oxygen atoms and a hydrogen atoms are attached to each silicon and pointed outside the cage [4]. They consist of a rigid, cubic silica core with a 0.53 nm side length, where each of the twelve corners carries one organic group. The corner groups can be reactive or unreactive groups. POSS molecules are much more variable in their properties compared with other inorganic components, such as clays or carbon nanotubes. POSS molecules can be incorporated into almost all kinds of the polymer matrices by blending, grafting, cross - linking or copolymerization, to produce POSS-containing organic-inorganic hybrids with many promising properties such as enhanced mechanical and thermal properties, oxidation resistance, and reduced flammability [5]. POSS derivatives incorporated to organic polymers, dendrimers and zeolites have a variety of applications in materials science and catalysis [6]. POSS compounds have also emerged as viable fillers in high -performance nanocomposites [7]. POSS are being used for synthesis of polymer-derived ceramics because of their nanosized structure and ceramic-like composition [8]. In this article, we report the results of our investigations of T₁₂-POSS compound with different substitutions.

2. Computational methods

All calculations were performed using the Gaussian 03 program package. Density functional theory (DFT/B3LYP) with 6-311G** basis set were used to optimize the geometry. Electronic-structure calculations have been performed to obtain structures for the bare T₁₂-POSS cage and different substituted POSS molecules. Information on the equilibrium bond lengths, bond angles, dihedral angles and the partial charge distributions for these systems have been also calculated.

In next step, the grafting of the transition metal atom (Sc) supported on isolated organic molecules such as cyclopentadiene on silsesquioxanes have been studied. Since T₁₂-POSS with R=-CH₂NH₂ has a shortest gap bond between



derivatives, this molecule was selected and its ability in hydrogen storage capacity was calculated. We used Gaussian 03 and AIM2000 program to compute hydrogen storage.

3. Results and discussion

The geometries of the polyhedral oligomeric silsesquioxane (T_{12} -POSS) cage molecule, $(HSiO_{1.5})_{12}$ with different substitutions have been optimized at the B3LYP/6-311G** level of theory. The density functional theory (DFT) calculations predict the effect of different substitutions on this type of nanoparticles. These calculations also predict the energies, electronic properties, and HOMO-LUMO gaps of these T_{12} -POSS compounds.

Table 1. Total energy, HOMO, LUMO Energies, HOMO-LUMO gap and Dipole moment of $(RSiO_{1.5})_{12}$ calculated in level of B3LYP/6-311G(d,p).

R	E(HF)	E _{HOMO} (ev)	E _{LUMO} (ev)	E _{LUMO} -E _{HOMO}	Dipole moment
-H	-4837.711	-0.318	0.015	0.333	0.0024
-CH ₃	-5309.840	-0.293	0.013	0.306	0.0192
-CH ₂ CH ₃	-5781.679	-0.291	0.010	0.301	0.0912
-OH	-5741.338	-0.319	-0.015	0.304	1.5244
-OCH ₃	-6213.023	-0.290	0.001	0.291	4.0020
-OCH ₂ CH ₃	-6684.987	-0.288	0.003	0.291	2.4114
-NH ₂	-5502.652	-0.246	0.016	0.262	0.8828
-CH ₂ NH ₂	-5971.628	-0.121	-0.067	0.054	4.1179
-CH ₂ CH ₂ F	-6972.800	-0.337	-0.022	0.315	0.3858
-CH ₂ CH ₂ CL	-11297.148	-0.315	-0.039	0.276	0.6730

For more detailed information about hydrogen bonding in $(Sc-C_5H_4)(CH_2NH_2)_{11}Si_{12}O_{18}$ complex, we have investigated successive adsorption of one, two, three, and more hydrogen molecules using AIM2000 program. When a single H₂ molecule is introduced to $(Sc-C_5H_4)(CH_2NH_2)_{11}Si_{12}O_{18}$ complex, Sc is able to donate just enough charge to the σ^* antibonding state of H₂ molecule, causing dihydrogen to be unstable which prefer the dihydride ligand. However, when the second hydrogen molecule is added to the system, the charge transferred to the second H₂ molecule is not enough to destabilize the dihydrogen state, and therefore the adsorption belongs to dihydrogen ligand.

4. Conclusion

These density functional theory (DFT) calculations predict that HOMO-LUMO gaps of the T_{12} -POSS compounds with different substitutions are smaller than that of pure cage, this gap about POSS-CH₂NH₂ is smaller than others so that is more stable of them which uses at next work. Therefore electron donor groups have smaller gaps.

Considering Hydrogen storage we have shown that can determine the maximum number of hydrogen atoms that can be stored in a metal-organic complex using the 18-electron rule. To maximize hydrogen storage, the transition metal atom should have nearly empty d shells and the organic frame should have fewer n electrons.

References

- [1] Delwar Hossain, Charles U. Pittman, Jr., and Svein Saebo, J.Phys. Chem. C.111 (2007) 6199.
- [2] Maitra, P.;Wunder, S. L. Electrochem. Solid-state Lett. 7 (2004) A8.
- [3] Li, G.; Wang, L.; Ni, H.; Pittman, C. U., Jr. J. Inorg. Organomet. Polym. 11 (2002) 123.
- [4] Delwar Hossain, Steven R. Gwaltney, Charles U. Pittman Jr., Svein Saebo, Chemical Physics. 467 (2009) 348.
- [5] Mabry, J. M.; Vij, A.; Iacono, S. T.; Viers, B. D. Angew. Chem.; Int. Ed. 47 (2008) 4137.
- [6] Lamm, M. H.; Chen, T.; Glotzer, S. C. Nano Lett. 3 (2003) 989.
- [7] Fu, B. X.; Hsiao, B. S.; Pagola, S.; Stephens, P.; White, J. Polymer, 42 (2001) 599.
- [8] Raj, R.; Riedel, R.; Soraru, G. D. J. Am. Ceram. Soc. 84 (2001) 2158.

Theoretical investigation of the intramolecular hydrogen bonding of 1-(2-methoxyphenyl)-o-carborane

M. Hamadani*, F. Mirzaei

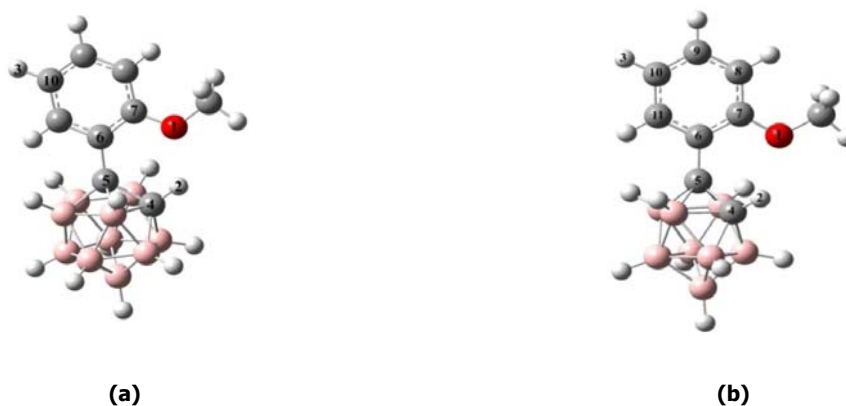
Faculty of Chemistry, University of Kashan, Kashan, I.R. Iran

(E-mail: hamadani@kashanu.ac.ir)

Keywords: 1-aryl-1,2-dicarba-closo-decaboranes; Intramolecular hydrogen bond; DFT, NBO; AIM**1. Introduction**

The potential application of 1,2-dicarba-closo-dodecaborane, o-carborane, as a building block for bioactive compounds, supramolecular assemblies, and macrocyclic molecules containing carboranes (carboracycles) has been the subject of many reports [1]. The C–H hydrogens of o-carborane are highly acidic ($pK_a=22.0$), owing to the electron deficiency of the carborane cage, and consequently have the potential for hydrogen-bond (H-bond) formation [2]. These contrasting features, i.e., high hydrophobicity and H-bonding ability, favor strong intramolecular or intermolecular interactions. Thus, supramolecular assemblies utilizing o-carborane are expected to be mainly generated through hydrophobic interaction and H bonding via the acidic o-carborane C–H vertices [3].

Formation of intramolecular hydrogen bonds is an important factor in the relative stability of structure of 1-aryl-1,2-dicarba-closo-dodecaboranes and 1-aryl-1,2-dicarba-closo-decaboranes (figure 1.). There are a number of geometrical criteria for the existence and stability of hydrogen bonds [4], but they are not so reliable, especially in the case of weaker intramolecular hydrogen bonds. In 1995, Popelier [5] showed in a study of C–H...O hydrogen bonds that the AIM theory of Bader can be used to characterize hydrogen bonds using a number of concerted effects in the electron density. In this paper, Hydrogen atom (H_3) in both structure are substituted by groups such as $-OCH_3$, $-NO_2$, $-F$, $-COOH$, $-NH_2$ and the effect of these substitutions on an intramolecular C–H...O interaction between the C–H hydrogen and the oxygen atom of the methoxyl group has been obtained and strength of this intermolecular hydrogen bond has been compared.

**Fig. 1.** Optimized structures of a) 1-aryl-1,2-dicarba-closo-dodecaboranes and b) 1-aryl-1,2-dicarba-closo-decaboranes.**2. Computational details**

All the calculations on These molecules and their substitutions were performed using *GAUSSIAN 03*. Optimized Geometries and frequency for all of the investigated molecules in this work were carried out using the B3LYP method with 6-311G** basis set. The topological parameters (i.e. bond critical points electron densities (ρ) and their Laplacians) were obtained using Bader theory of atoms in molecules (AIM) by means of *AIM2000*. Software. Finally, for an improved understanding of the nature of intramolecular interactions, the natural bond orbital (NBO) analysis was carried out.

3. Results and discussion

Some results of the NBO occupation numbers for the $\sigma^*(C-H)$ anti bonds, the Oxygen lone pairs, n_O , and their respective orbital energies, ϵ are reported in Table 1. Furthermore, some of significant donor–acceptor interactions and their second order perturbation stabilization energies $E^{(2)}$ were calculated at the B3LYP/6-311G** level for 1-aryl-1,2-dicarba-closo-dodecaboranes.

Also, the scheme of critical point properties for various covalent and hydrogen bonds from 1-aryl-1,2-dicarba-closo-dodecaboranes and 1-aryl-1,2-dicarba-closo-decaboranes and their substitution are shown in Figure2.

Table 1. Donor-acceptor natural bond orbital interactions and their second-order perturbation stabilization energies, ΔE^2 (Kcal mol⁻¹), calculated for structure of 1-aryl-1,2-dicarba-closo-dodecaboranes with various substitutions.

	O.N.(σ^*_{CH})	E(σ^*_{CH})	O.N.(n_1O)	E(n_1O)	$n_1O-\sigma^*_{CH}$
H	0.02317	0.45382	1.95864	-0.57180	1.67
OCH ₃	0.02336	0.45408	1.95819	-0.56838	1.81
NH ₂	0.02347	0.45562	1.95816	-0.56490	1.63
NO ₂	0.02232	0.42948	1.96460	-0.63283	0.74
COOH	0.02294	0.44592	1.95904	-0.58011	1.37
F	0.02233	0.43832	1.96432	-0.61686	0.75

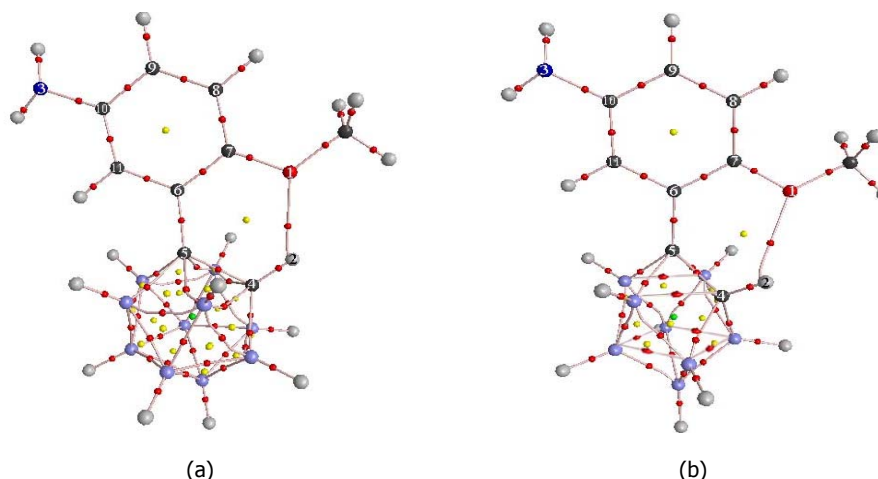


Fig. 2. Molecular graphs of structures of a) 1-aryl-1,2-dicarba-closo-dodecaboranes and b) 1-aryl-1,2-dicarba-closo-decaboranes with substitution OCH₃ showing all BCP and RCP and CCP.

4. Conclusions

The results obtained from the DFT calculations and the topological parameters derived from the Bader theory, suggest that the intramolecular hydrogen bond existing in 1-aryl-1,2-dicarba-closo-dodecaboranes is more stronger than 1-aryl-1,2-dicarba-closo-decaboranes. Also, frequencies and geometrical data, *AIM* analysis and *NBO* results show that electron-withdrawing group at the para position effect more on electron density of the oxygen atom than the electron-donating group. Since the electron density of the two unshared electron pairs on the oxygen atom of the methoxy group is decreased by introducing an electron-donating group, hydrogen bonding between o-carborane C-H hydrogen and oxygen atom of the methoxyl group become weaker.

References

- [1] Songkram, C.; Yamasaki, R.; Tanatani, A.; Takaishi, K.; Yamaguchi, K.; Kagechika, H. and Endo, Y., *Tetrahedron Lett.*, 42 (2001) 5913.
- [2] Leites, L. A., *Chem. Rev.*, 92 (1992) 279.
- [3] Frixa, C.; Scobie, M.; Black, S. J.; Thompson, A. S. and Threadgill, M. D., *Chem. Commun.* (2002), 2876.
- [4] Torshin, I.Y. Weber, I.T. and Harrison, R.W., *Protein Eng.*, 15 (2002) 359.
- [5] Koch, U. and Popelier, P.L.A., *J. Phys. Chem.*, 99 (1995) 9747.

A DFT study on Tetracycline and its derivatives for increasing affinity and decreasing environmental side effectsS. Omid¹, S. Javadian², M. Noorinezhad³^{1,3} *Department of Ecology, Shrimp Research Center, Boushehr, Iran*

(E-mail: smomidi@gmail.com)

² *Department of Chemistry, University of Tarbiat Modarres, Tehran, Iran***Key words:** Tetracycline, Oxytetracycline, NQR, NMR, Environmental impact, Biological activity (IC_{50}).**1. Introduction**

Tetracyclines are major group of antibiotics, with a broad spectrum of activity, which is widely used in medicine and veterinary science to treat bacterial infectious [1]. Despite of widespread using they can be created some problems such as increasing resistant bacteria and negative environmental impacts, especially when they consume for aquatic specimens [2], [3]. For increasing affinity and decreasing side effects of these compounds and suggesting suitable derivatives of tetracycline for environment, study of tetracyclines by use of theoretical methods was chosen.

2. Computational method

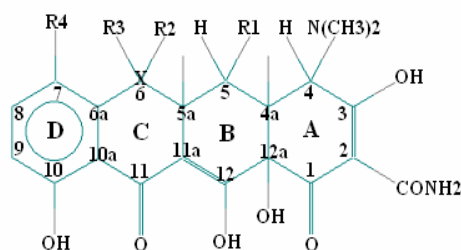
Density functional theory (DFT) at B3LYP/6-31G* level has been used to investigate on the structural properties of tetracycline and its derivatives. The spectroscopic properties; NQR (nuclear quadrupole resonance) and NMR (nuclear magnetic resonance), of these molecules using B3LYP and PW91P86 levels and 6-311++G** basis set have been calculated. All calculation was performed by use of Gaussian 98. In addition, regard to correlation between biological activity and the quadrupole coupling constants, in this work correlation between electron density of O, N and H atoms in interest molecules and their biological activity (IC_{50})¹ [4, 5] was studied.

3. Results and discussion

The results indicate that oxygen and nitrogen EFG and chemical shielding tensors are sensitive to substituent changes at the C₄, C₅, C₆ and C₇ positions and intermolecular hydrogen bonding in tetracyclines (Figure 1). Furthermore, it was found that EFG and chemical shielding tensors are more sensitive to electron density distribution in tetracyclines. Biological activities of tetracyclines were found to depend upon the electron density distribution at the O₁₂ region.

The results show that a possible correlation between NQCC (O₁₂) and Biological activities (IC_{50}) (Figure 2).

The results show that the 9-position of oxytetracycline can be altered with propyl, isopropyl and isobutyl and increase activity and lipophilicity of tetracycline (Table 1).

**Fig. 1.** Molecular structure of Tetracyclines.

¹ The half maximal inhibitory concentration

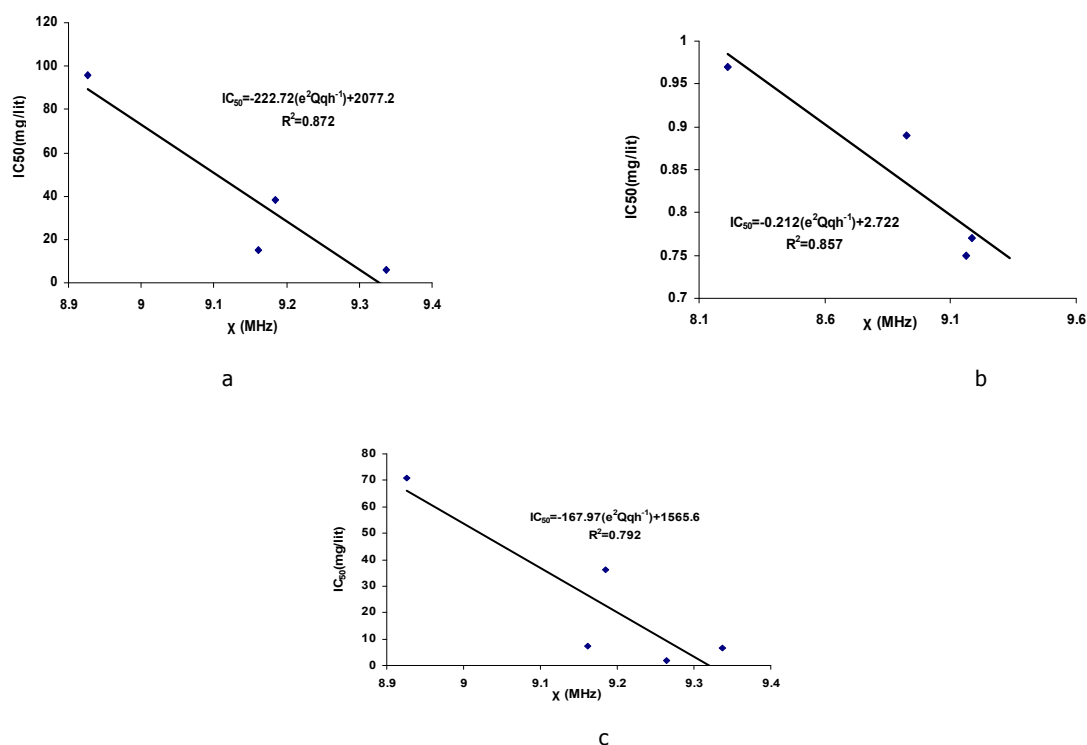


Fig. 2. Correlation between NQCC (O_{12}) and IC_{50} (**a**: *E. coli* R IP7 tet A, **b**: *E. coli* K-12 J5 nal, **c**: *Giardia lamblia*).

Table 1. O_{12} Nuclear Quadrupole Coupling Constant (χ) and biological activity (IC_{50}) in Oxytetracycline (OTC) and new compounds.

Compound	χ (MHz)	IC_{50}		
		<i>E. Coli</i> * <i>K-12 J5 nal</i>	<i>E. Coli</i> <i>R IP7 tet A</i>	<i>Giardia</i> <i>Lamblia</i>
OTC	8.926	0.89	96	71
OTC+ Propyl	9.452	0.72	----	----
OTC+ Isopropyl	9.138	0.79	41	30.69
OTC+ Isobuthyl	9.414	0.73	----	----

* *Escherichia coli*

4. Conclusions

On the basis of this research it seems that: Biological activities of tetracyclines have good correlation with electron density distribution at the O_{12} region as well as for increasing activity and lipophilicity of tetracyclines, the 9-position have suitable condition that can be useful for aquaculture industry and impressive for decreasing environmental side effects of tetracyclines.

References

- [1] B. G. Katzung, Basic and Clinical Pharmacology, Forth Edition, Prentice Hall, Englewood Cliffs, New Jersey, 1989.
- [2] R. W. Fedeniuk, Ph. D. Thesis, University of Saskatchewan, Saskatoon, Saskatchewan, 1998.
- [3] D. P. Weston, Proceedings of the Meeting on the Use of Chemicals in Aquaculture in Asia, University of California, 1996.
- [4] T. D. Edlind, *Antimicrob. Agents Chemother.* 33 (1989) 2144.
- [5] Y. A. Chabbert and M. R. Scavizzi, *Am. Soc. Microbiol.* (1976) 36.

Stabilization of the Phenyl Salicylate in different conformers: Experimental and Theoretical analysis

Mohammad Emamia,* Morteza Jabbaria, Abbas Teimourib, Ali Reza Najafic

^aDepartment of Chemistry, Shahid Beheshti University, Tehran, Iran

(E-mail: masterchem43@yahoo.com)

^bPayame Noor University, Isfahan, Iran^cDepartment of Chemistry, Yasouj University, Yasouj, Iran**Keywords:** Stabilization, Phenyl Salicylate, Salol, Different conformers.**1. Introduction**

Salicylates are the class of compounds that are widely valued for their pain killing, antipyretic and anti-inflammatory properties [1]. Recently, salicylic acid has been used primarily as an intermediate in the production of agrochemicals, dyes and colorants products [2].

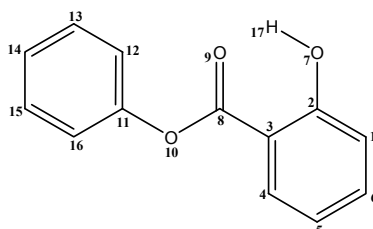
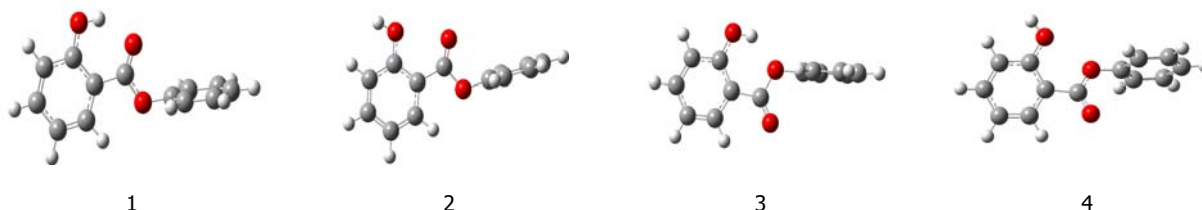
Salicylic acid and its derivatives have recently become attractive to theoreticians as well as experimentalists since their structures are of some biological significance particularly in medicinal and enzyme chemistry [3].

Benzoic acid 2-hydroxyphenylester (salol) is an organic material with the formula $C_{13}H_{10}O_3$ that undergoes a liquid-glass transition and for that reason it has been the subject of several experimental studies and theoretical considerations.

Salol (Fig. 1) has been well known as a pharmaceutical medium. It is sometimes used for coating tablets because it undergoes hydrolysis into phenol and salicylic acid in the stomach and in the small intestine [4].

2. Theoretical section

The structures and labeling of four conformers of Salol (**1-4**) presented in the figures 1 and 2. In the conformer **1** and **3** there are two hydrogen bondings between phenolic hydrogen and carbonyl and alcoholic oxygen's respectively. In salol an intramolecular hydrogen bond between hydroxyl group and C=O or C-O groups supposed to make a six membered ring, which causes the O...H interaction onto the resonance of the benzene ring. Gilli et al suggested that the formation of this intramolecular hydrogen bond was aided by a sort of such resonance.

**Fig. 1.** Chemical structure of Salol.**Fig. 2.** Four conformers of Salol

Molecular geometry, spectroscopic properties, hydrogen bonding and thermodynamic properties of phenyl salicylate (salol). HF and density functional theory (DFT) calculations have been carried out for four conformers of the title compound using the standard 6-311+G(d,p) basis set. In the gas phase the order of stability was found as **1** > **3** > **4** > **2**. The ^{13}C NMR and ^1H NMR of compounds 1-4 have been calculated by means of B3LYP/6-311+G(d,p) basis set. Comparison between the experimental and the theoretical results showed good correlation.



3. Results and discussion

The HF/6-311+G(d,p), B3LYP/6-311+G(d,p) calculations were performed for four conformers of Salol. The calculated results show that the predicted geometry can well reproduce the structural parameters. In the gas phase the order of stability was found as **1** > **3** > **4** > **2**. ¹³C, ¹H NMR of conformers have been calculated by means of B3LYP density functional method with 6-311+G(d,p) basis set. Comparison between the experimental and the theoretical results indicates that conformer **1** is able to provide satisfactory results for predicting NMR properties.

References

- [1] (a) S. Moncada, J. R. Vane, *Adv. Inter. Med.* 24 (1979) 1; (b) P. A. Insel, A. G. Goodman, A. G. Gilman, *The Pharmacological Basis of Therapeutics*, 9th ed., Pergamon Press, Oxford, 1991.
- [2] (a) R. J. Cremllyn, *Agrochemicals: Preparation and Mode of action*, John Wiley and Sons, 1991. (b) I. Raskin, *Plants. Mol. Biol.* 43 (1992) 439.
- [3] (a) B. Humbert, M. Alnot, F. Quiles, *Spectrochimica Acta Part A.* 54 (1998) 465.
(b) Y. Kwon, *Journal of Molecular Structure (Theochem)*. 532 (2000) 227.
(c) P. J. G. Goulet, R. F. Aroca, *Can. J. Chem.* 82 (2004) 987.
- [4] J. Hanuza, W. Sasiadek, J. Michalski, J. Lorenc, M. Maczka, A. A. Kaminskii, A. V. Butashin, H. Klapper, J. Hulliger, A. F. A. Mohamed, *Vibrational Spectroscopy* 34 (2004) 253.

The competition between the intramolecular hydrogen bond and amide resonance in N-formylformamide- a quantum chemical study

A. Nowroozi, *P. Mohammadzadeh Jahani, N. Asli, S. Dahmardeh, M. Poorsargol,

^a Department of Chemistry, Faculty of Science, University of Sistan and Baluchestan, P.O. Box 98135-674, Zahedan, Iran
(E-mail: mjpeyman@yahoo.com)

Keywords: N-formylformamide, Intramolecular hydrogen bond, Amide resonance, AIM and NBO.

1. Introduction

Resonance assisted hydrogen bond (RAHB) is a particular subject of hydrogen bond which frequently observed in various complex biological systems. Gilli and coworkers have been proposed the RAHB model as linking the strength of the hydrogen bond to the resonance in chelated systems [1-3]. The chelated enol form of β -dicarbonyl compounds is one of the most significant RAHB structures with O-H...O hydrogen bond which most widely studied, theoretically and experimentally [4-7].

The amide functional group is the fundamental unit of proteins, peptides, and other biologically important molecules and has been traditionally characterized by a restricted C-N bond rotation, coplanarity of the attached atoms, short C-N bond lengths, red-shifted carbonyl stretching frequencies, relative stability toward nucleophilic attack and protonation at oxygen rather than nitrogen [8]. By substitution an acyl group on the nitrogen atom of amide compounds, the new class of compounds which called β -diamides, was introduced. N-formylformamid (NFF) as the simplest member of β -diamide compounds can participate in the amide \leftrightarrow imidic acid equilibrium (Fig.1).

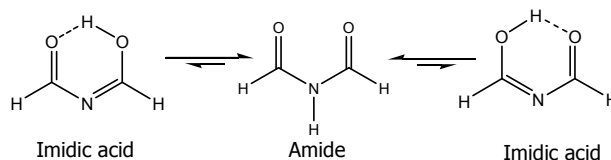


Fig 1. Amid \leftrightarrow Imidic acid tautomeric equilibriums in NFF.

2. Computational methods

Conformational study of N-formylformamide were carried out at HF, B3LYP and MP2 levels with the most popular basis set, 6-311++G(d,p), and the equilibrium conformations were determined. Furthermore to have more reliable results, the total energies of all the equilibrium conformers were recomputed at the high level ab-initio methods such as G2MP2, G2, G3 and CBS-QB3. The natural bond orbital (NBO) [9] and quantum theory of atoms in molecules (QTAIM) [10] were applied as a powerful approach for evaluation of the hydrogen bond strength in the chelated conformer.

3. Results and discussion

Theoretically, NFF has about 11 different conformers, which systematically arranged in two tautomeric classes, DA and AI with 3 and 8 members, respectively (Fig.2). The computational results reveal that the amide resonance and intramolecular hydrogen bonding are two superior factors in determining the most stable conformation of diamide (DA) and amide-imidic acid (AI) tautomers, respectively. The evaluation of hydrogen bond energy by Schuster and related rotamers methods at all of the computational levels, except HF/6-311++G(d,p), clearly predict that the hydrogen bond strength in N-formylformamid is lower than the malonaldehyde. But the results of quantum theory of atoms in molecules, the natural bond orbital analyses and geometrical parameters are given an opposite result, $E_{\text{HB}}(\text{NFF}) > E_{\text{HB}}(\text{MA})$. Although the bond average energies of tautomerization process emphasized on more stability of AI tautomer, but our theoretical calculations reveal that the DA conformers are more stable than the AI ones. The population analyses of equilibrium conformations by the natural bond orbitals method also predict that the origin of tautomeric preference is mainly due to the electron delocalization of amide functional group, especially $\text{LP}(\text{N}) \rightarrow \pi^*_{\text{C=O}}$ charge transfer.

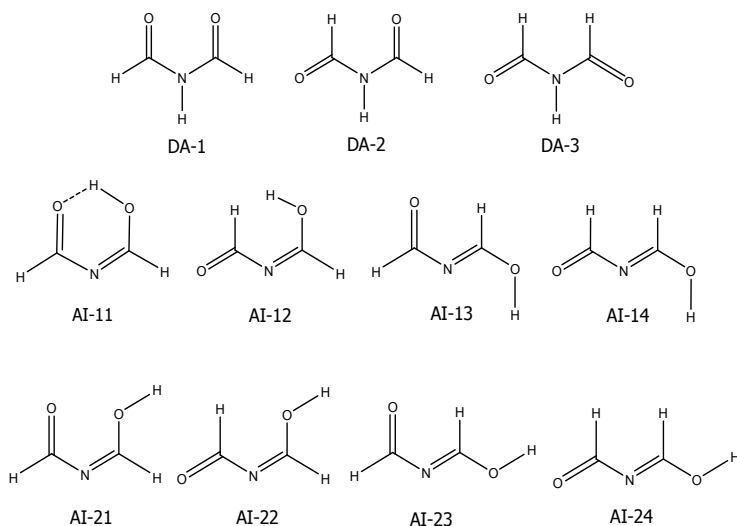


Fig 2. All of the plausible theoretical conformers of NFF.

References

- [1] P. Gilli, F. Belluchi, V. Ferretti, V. Bertolasi, *J. Am. Chem. Soc.* 111(1989)1023.
- [2] V. Bertolasi, P. Gilli, V. Ferretti, G. Gilli, *J. Am. Chem. Soc.* 113(1991)4917.
- [3] P. Gilli, V. Bertolasi, V. Ferretti, G. Gilli, *J. Am. Chem. Soc.* 116(1994) 909.
- [4] A. Nowroozi, A. F. Jalbout, H. Roohi, H. Raissi, *Int. J. Quantum Chem.* 109(2009)1505.
- [5] A. Nowroozi, H. Roohi, M. S. Sadeghi, M. Sheibaninia, *Int. J. Quantum Chem.* Under Publication.
- [6] A. Nowroozi, H. Raissi, *J. Mol. Struct. (Theochem)*, 759(2006)93.
- [7] A. Nowroozi, S. F. Tayyari, H. Rahemi, *Spectrochim. Acta*, 59A(2003)1757
- [8] C. R. Kemnitz, J. M. Loeven, *J. Am. Chem. Soc.* 129(2007) 2521
- [9] A. E. Reed, L. A. Curtis, F. A. Weinhold, *Chem. Rev.* 88(1988) 899
- [10] R. F. W. Bader, *Atoms in Molecules. A Quantum Theory*, Clarendon, Oxford, U.K. 1990.

**Theoretical study of formation, stability and the interaction of Sm³⁺ complexes with bisphosphonates**M. Arabieh^{a,b}, M. Ghannadi-Maragheh^a, M. Zahedi^b, M. H. Karimi-Jafari^{a*}^a Computational Chemistry Laboratory, NSTRI, Tehran, Iran^b Department of Chemistry, Faculty of Sciences, Shahid Beheshti University, Tehran, Iran

(E-mail: mhkarimijafari@gmail.com)

Keywords: Samarium, Bisphosphonates, Interaction energy, Complex formation, Complex sStability.**1. Introduction**

Radiopharmaceuticals are compounds containing a radionuclide and ligand(s) which are used routinely in nuclear medicine for diagnosis and therapy of various diseases [1]. The bisphosphonates which are synthetic analogues of pyrophosphate are widely used ligands in radiopharmaceuticals [2]. The classical pharmacological effects of bisphosphonates appear to be the result of two key properties: their affinity for bone mineral and their inhibitory effects on osteoclasts. Bisphosphonates inhibit bone resorption by being selectively taken up and adsorbed to mineral surfaces in bone, where they interfere with the action of the bone-resorbing osteoclasts.

Despite the individual modeling of several bisphosphonate ligands, or modeling their interaction with hydroxyapatite, the complexation of these compounds with radionuclides such as Samarium which is regularly used for attacking the bone tumor has not been studied theoretically to date. In this work we focus on the interaction of pamidronate with samarium trivalent cation in gas phase and solution.

2. Computational details

Initially the SPARKLE method which is an extension of available semiempirical models (AM1, PM3, PM6) to the lanthanide and actinide compounds are used to predict stable structures of complex. Lanthanide Complexes Sparkle Model calculations are hundreds of times faster than *ab-initio* ones, leading to geometries of comparable accuracy, especially for ligands with directly coordinating nitrogen or oxygen atoms. Accordingly, semi empirically derived conformations are used as initial structures for *ab initio* investigations. This initial set is augmented with a conformational search at the HF/STO-3G level of molecular orbital theory. Molecular orbital calculations are performed at Hartree Fock and DFT levels of theory with 6-31G** basis set for all atoms except Sm. For Sm the effective core potential of Dolg et al [3] and its corresponding basis set is used which implicitly accounts for relativistic effects.

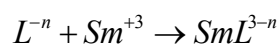
The total interaction energy of complex is calculated as

$$\Delta E = E[SmL^{3-n}] - E[Sm^{+3}] - E[L^{-n}]$$

Where different *n* values represent different protonation states of the ligand. The basis set super position error (BSSE) is computed and corrected using the counterpoise method. The effect of ligand relaxation effects is also investigated. To simulate the effect of solvent on the structure and stability of complex and ligands the polarized continuum model (PCM) calculations are performed. The PCM model calculates the molecular free energy in solution as the sum over three terms. These components represent the electrostatic (es) and the dispersion-repulsion (dr) contributions to the free energy, and the cavitation energy (cav). All three terms are calculated using a cavity defined through interlocking van der Waals-spheres centered at atomic positions.

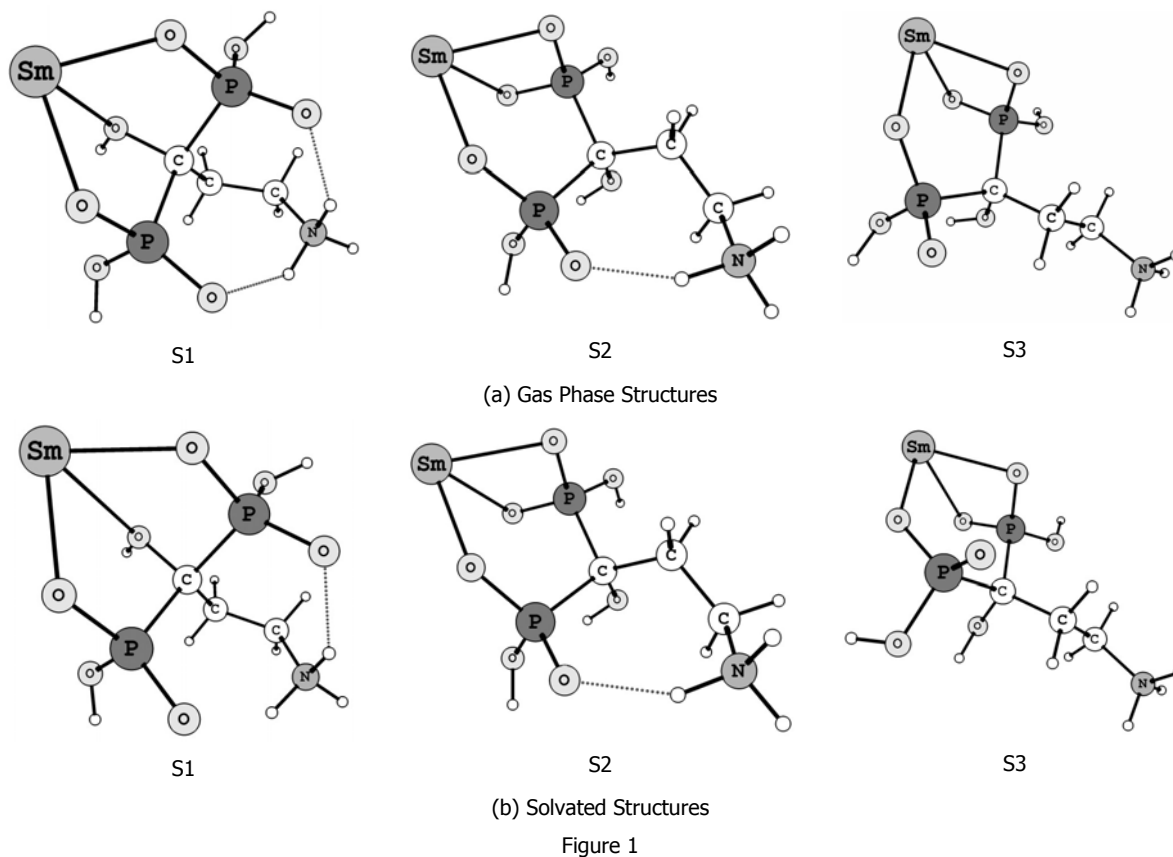
In Figure 1 three structures (S1, S2 and S3) of complex are represented as appeared in gas phase (a) and solution (b). As can be seen the complexed form of ligand has a zwitterion form with an R-NH₃⁺ tail, instead of R-NH₂. These three structures are characterized by the number of intermolecular hydrogen bonds formed between -NH₃⁺ tail and phosphonate anionic oxygen. The gas phase BSSE corrected interaction energies of these structures at the HF/STO-3G level of theory are 665.5, 701.9 and 720.2 Kcal/Mol for S1, S2 and S3 respectively.

We also investigate the complex formation reaction defined as



Zero point energy and thermal corrections to the Enthalpy and Gibbs free energy are calculated from a normal mode analysis at the stationary structures of ligands and complexes. To investigate the effect of ligand reorganization on the complex formation

reaction, the structures of ligands as appeared in the complex are isolated and relaxed to the nearest local minimum on the potential energy surface. These minima are also compared with the estimated global minimum of the ligand.



References

- [1] S. Liu, D. S. Edwards, *Chem. Rev.* 99 (1999) 2235.
- [2] J. Robinson, I. Cukrowski, H. Marques, *J. Mol. Structure* 825 (2006) 134.
- [3] M. Dolg, H. Stoll, A. Savin, H. Preuss, *Theor. Chim. Acta.* 75 (1989) 173.

**The numerical study of the carbon impurity effect on electronic properties of BN nanotubes**

Hossain Milani Moghaddam*, Ali Akbar Nouroozi

Physics department, Mazandaran University, Babolsar, Mazandaran, Iran

(E-mail: aliakbarnouroozi@yahoo.com)

Keywords: BN nanotube, Landauer formalism, Green's function, Density of states, Electronic conductance.**1. Introduction**

BNNTs have very remarkable properties where are expected to play an important role in nanoscale devices [1], so it is not surprising that BNNTs have been attracting increasing interest in the past several years. The possibility of BNNTs was first predicted by theoretical calculations [2], and afterwards BNNTs were first produced using arc discharge by Chopra et al. [3]. BNNTs are chemically and thermally stable and their band gaps are independent of diameter and chirality [4,5]. Electronic band structure calculations show that BNNTs are wide gap semiconductors with a gap value ~ 5 eV [6]. We investigate numerically the conductance properties, density of states of the BNNT doped with carbon atoms(C). Our numerical methods are based on Green's function theory, a tight-binding Hamiltonian and Landauer formalism.

2. Methodology

We Use a tight-binding Hamiltonian and methods based on Green's function theory and Landauer formalism. Our methodology is done according to reference [7].

3. Results and discussion

We have investigated the electronic properties of BNNTs where B atoms are replaced by C atoms in the middle unit cell of the BNNT. The BNNT length is considered ten unit cells. The onsite energy at B, N and C atoms and the hopping integrals has been taken from reference [7]. Figure 1 and 2 show the DOS of the BNNTs in the absence and the presence of the C impurity, respectively. In figure 3 and 4, we demonstrate the electronic conductance of the BNNTs in the absence and the presence of the C impurity. The peaks in figures show the resonance energy. g is the electronic conductance and g_0 is equal to $2e^2/h$ in figures 3 and 4.

Our calculations show that the energy gap is reduced by adding C atoms and some electronic states induce within that. The BNNTs with C impurity show a semiconductor behavior; therefore the BNNTs with C impurity can be candidate for electronic devices.

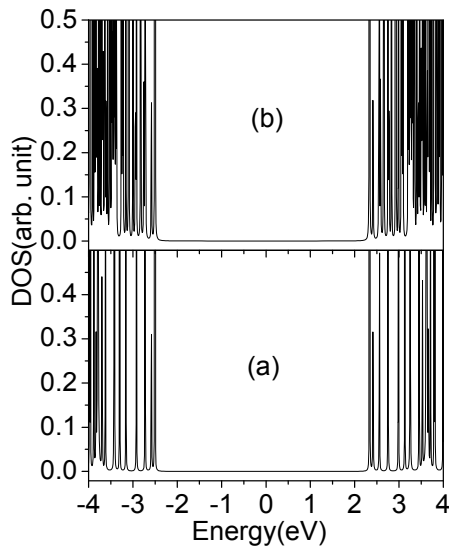


Fig. 1. (a) and (b) panels show the DOS for $n=6$ and 15 in the $(n,0)$ BNNT without impurity, respectively.

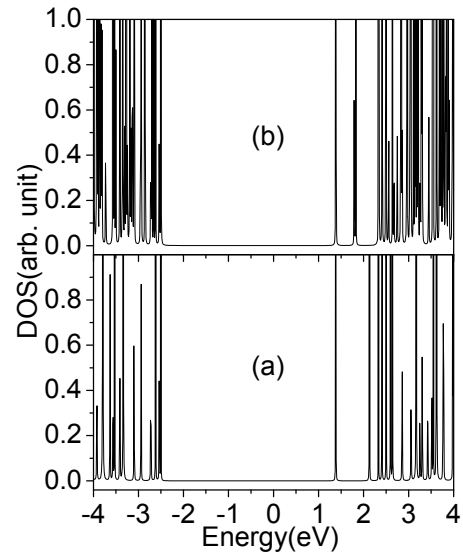


Fig. 2. (a) and (b) panels show the DOS for $n=6$ and 15 in the $(n,0)$ BNNT with C impurity, respectively.

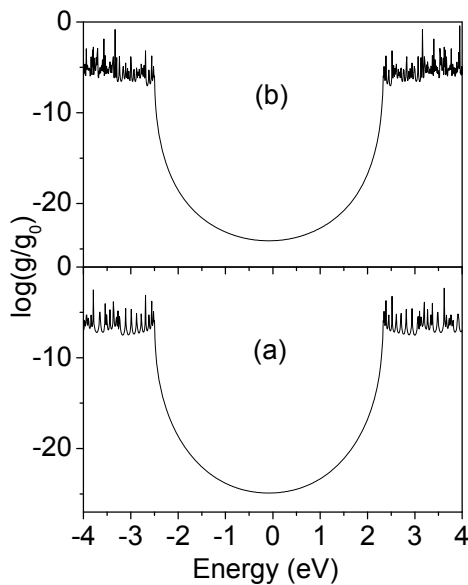


Fig. 3. (a) and (b) panels show the electronic Conductance for $n=6$ and 15 in the $(n,0)$ BNNT without impurity, respectively.

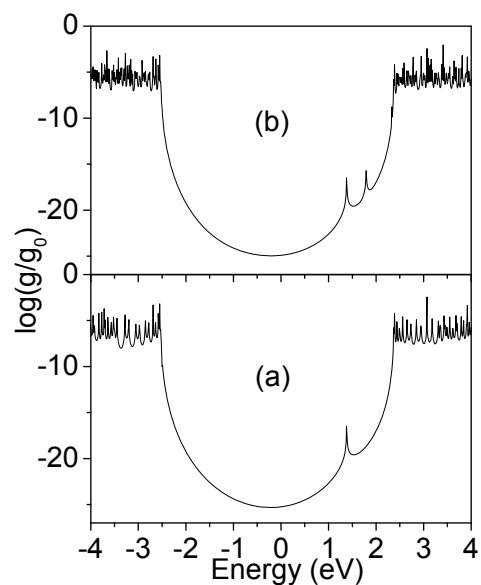


Fig. 4. (a) and (b) panels show the electronic Conductance for $n=6$ and 15 in the $(n,0)$ BNNT with C impurity, respectively.

References

- [1] Bi .Jian-Qiang, et al., Mater. Lett. 63 (2009) 1299.
- [2] X.Blase, A.Rubio, S.G.Louie, M.L.Cohen, Europhys. Lett. 28 (1994) 335.
- [3] N.G.Chopra, et al., Science. 269 (1995) 966.
- [4] D. Golberg, Y. Bando, CC .Tang, CY. Zhi. Adv. Mater.19 (2007) 2413.
- [5] X. Blasé, A .Rubio, SG .Lohen, Euro .Phys .Lett. 28 (1994) 335.
- [6] Alex Zettl,Adv.Matter. 8 (1996) 443.
- [7] H. Milani Moghaddam, Physics. E. 42 (2009) 167.

**Effect of CH₃CO functional group on the molecular and electronic properties of bn43zz nanotube**H. Roohi^{a,b}, B. makiabadi^{a,c*}

(bmakiabadi@yahoo.com)

^aDepartment of Chemistry, Faculty of Science, University of Sistan & Baluchestan, P.O. Box 98135-674, Zahedan, Iran^bDepartment of Chemistry, Faculty of Science, University of Guilan, Rasht, Iran.^cSirjan Engineering College, Shahid Bahonar University, P.O. Box 78185439, Sirjan, Iran**Keywords:** Functionalized BNNTs, NBO, AIM.**1. Introduction**

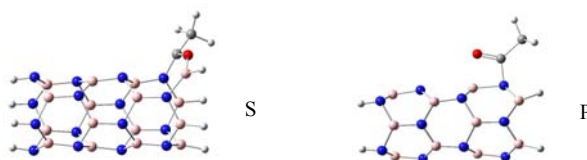
Chemical functionalization on the sidewall of CNTs has been a subject of intensive study [1-4]. The covalent sidewall functionalization can modify the structural and electronic properties of CNTs. As structural analogs of CNTs, boron nitride nanotubes (BNNTs), however, exhibit electronic properties of B–N bonds. For example, BNNTs are semiconductors with a wide band gap (5.5 eV), weakly depending on the diameter, the helicity, and the number of tube walls [5]. The unusual geometric structures and unique electronic properties offer promising BNNTs applications in nanotechnology. Recently, some experimental efforts have been made toward making soluble BNNTs through sidewall functionalization [6-8]. The functionalized BNNTs are shown to be soluble in many organic solvents. In this paper, we study structural and electronic properties of BN43zz nanotubes functionalized with CH₃CO by DFT method. Furthermore, we have investigated atomic charge distribution and characterization of B–O and N–C bonds in nanotubes by NBO and AIM analysis, respectively.

2. Methods

For the study of interactions between CH₃CO group and BN43zz nanotubes, DFT computations were carried out using B3LYP hybrid density functional method and the 6-31G (d) basis set on a Pentium 4 computer. The NBO and AIM analyses were carried out for all complexes at the B3LYP/6-31G(d) level of theory.

3. Results and discussion

First of all, we considered all sites for interaction between CH₃CO and sidewall of BN43zz nanotube. We found seven minima structures. Because of the curvature effect, there are two kinds of B–N bonds (r1 and r2) where the functionalization can undertake in BNNTs. In the BN43zz nanotube, r1 and r2, respectively, represent the B–N bond along and around the tube axis. As shown in Fig. 1, when CH₃CO is attached to the sidewall of BN43zz nanotube, the slanted B–N bond (r2) is more favorable than r1 for adsorption. For the structure **S**, CH₃CO is located on the r2 bond of BN43zz nanotube. The chemical bonds formed between C and O atoms of CH₃CO and N and B atoms of tube, which induce a radial deformation. The r2 bond attached to CH₃CO in complex **S** increases upon complex formation which causes the breaking of the B–N bond and the formation of open structures on the sidewall of BN43zz nanotube. For the structure **P**, CH₃CO is placed on the B–N bond parallel to the tube axis (r1). Similar to the complex **S**, two new B–O and N–C bonds are formed in complex **P** but B–N bond is not broken in it.

**Fig. 1.** Optimized structures for complexes **S** and **P**.

The calculated binding energies (kJ/mol) for complexes **S** and **P** at B3LYP/6-31G(D) level of theory have been summarized in Table 1. As can be seen from Table 1, all complexes are more stable than the separated reactants CH₃CO and BN43zz nanotube. It is evident from electronic binding energy BE in Table 1, that **S** complexes are more stable than **P** complexes. The order of stability of complexes dose not change by employing BSSE correction. The greater stability of **S** complexes with respect to **P** complexes can be attributed to the formation of stronger bond in **S** complexes. The negative binding energy means exothermic addition reaction on BNNT sidewalls. In the **S** complexes, the stability of complexes decreases in the order of **S1** >



S4 > S2 > S3. The order of the stability of **P** complexes is **P1 > P2 > P3**. According to NBO analysis, there is a transfer of electron charge between functional group and BN43zz nanotube. In the complexes **P** the charge is transferred from CH₃CO group to BN43zz nanotube whereas in the complexes **S** the charge is transferred from BN43zz nanotube to CH₃CO group. The most important interaction in the **S** complexes is $\text{lp}(\text{O}) \rightarrow \sigma^*(\text{B-N})$ donor acceptor interaction. The NBO results predict that $\text{lp}(\text{O}) \rightarrow \text{RY}^*(\text{B})$ donor acceptor interaction is the most important interaction in the **P** complexes. The theory of atoms in molecules (AIM) was also applied for characterization of B–O and N–C bonds in these nanotubes. The value of $\nabla^2\rho(r)$ and $H(r)$ at B–O and B–N BCP of all complexes show that B–O interaction has partially covalent nature. Whereas N–C bonds in these complexes are covalent in nature.

Table 1. Binding energies (kJ/mol) obtained at B3LYP/6-31G (D) level of theory.

	Bsse	BE	BE^{Bsse}
S1	31.34	-205.1	-173.7
S2	33.88	-159.9	-126.1
S3	34.11	-139.5	-105.4
S4	33.52	-195.5	-162
P1	25.33	-82.9	-57.57
P2	27.75	-79.14	-51.38
P3	24.84	-70.22	-45.38

BE = Electronic binding energy

$\text{BE}^{\text{Bsse}} = \text{BE} + \text{BSSE}$

4. Conclusions

In summary, we have investigated, on the basis of density functional theory calculations, the structural and electronic properties of chemically modified BN43zz nanotube with CH₃CO functional group. When one CH₃CO is added to the sidewall of 43zz BNNT, the addend prefers the B–N bonds with higher curvature, i.e., the slanted B–N bonds. A CH₃CO addition to the **S** complexes leads to the breaking of B–N bonds and the formation of open structures in the sidewall of BN43zz. The NBO results predict that $\text{lp}(\text{O}) \rightarrow \text{RY}^*(\text{B})$ donor acceptor interaction is the most important interaction in the **P** structures whereas the most important interaction in the **S** complexes is $\text{lp}(\text{O}) \rightarrow \sigma^*(\text{B-N})$ donor acceptor interaction. The theory of atoms in molecules (AIM) was also applied to characterize the B–O and N–C bonds in these nanotubes. The value of $\nabla^2\rho(r)$ and $H(r)$ at B–O and B–N BCP of all complexes show that B–O interaction has partially covalent nature. Whereas N–C bonds in these complexes are covalent in nature.

References

- [1] D. Tasis, N. Tagmatarchis, A. Bianco, M. Parto, Chem. Rev. 106 (2006) 1105.
- [2] S. Niyogi, M.A. Hamon, H. Hu, B. Zhao, P. Bhowmik, R. Sen, M.E. Itkis, R.C. Haddon, Acc. Chem. Res. 35 (2002) 1105.
- [3] A. Hirsch, O. Vostrowsky, Top. Curr. Chem. 245 (2005) 193.
- [4] X. Lu, Z.F. Chen, Chem. Rev. 105 (2005) 3643.
- [5] A. Rubio, J.L. Corkill, M.L. Cohen, Phys. Rev. B49 (1994) 5081.
- [6] S.Y. Xie, W. Wang, K.A. Shiral Fernando, X. Wang, Y. Lin, Y.P. Sun, Chem. Commun. (2005) 3670.
- [7] C.Y. Zhi, Y. Bando, C.C. Tang, S. Honda, K. Sato, H. Huwahara, D. Golberg, Angew. Chem., Int. Ed. 44 (2005) 7932.
- [8] M.D. Su, J. Phys. Chem. B 109 (2005) 21647.

DFT studies, NBO and NICS analysis of all fluorothiophenes and their cations as candidate monomers for new conductive polymers

H. Shirani^{a,b,*}, S. Jameh-Bozorgchi^{a,b}

^aChemistry Department, Faculty of science, Islamic Azad University, toyserkan branch, toyserkan, Iran

*(E-mail: shiranihossein@gmail.com)

^bChemistry Department, Faculty of science, Islamic Azad University, Arak Branch, Arak, Iran

Keywords: DFT-B3LYP, Dipole moment, Polarizability, Spin density, Fluorothiophene, Conducting polymer

1. Introduction

Electrically conducting polymers as a new class of 'synthetic metals' reached a high interest in the last year[1]. Intrinsic conducting polymers with conjugated double bonds have attracted much attention as advanced materials. Conductive polymers have been used as biosensors, gas sensors, microactuators, data storage, polymer batteries, electronic devices, and functional membranes [3-7]. Furthermore, the electrochemical process parameters affecting the properties of polythiophenes (PTH_s) coatings have also been investigated. PTH-based polymer blends can prevent the corrosion of metals [2]. The Several investigations have been performed to observe the effects of various parameters such as solvent, electrolyte, and monomer choices and polymerization temperature on the stability and conductivity of the synthesized PTH.

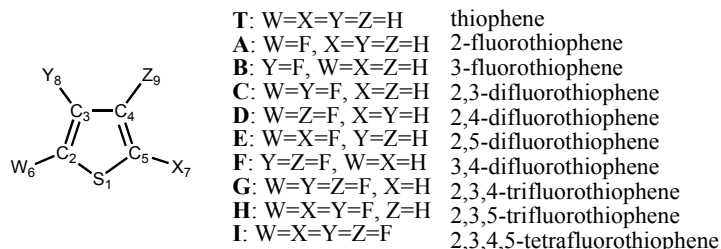


Fig. 1. All possible mono-, di-, tri-, and tetrafluorothiophene isomers studied in this research.

The aims of the present research are: (1) to study the electronic and structural properties of all fluorothiophene monomers (shown in Figure 1) and their singly ionized cations using ab initio and DFT-B3LYP methods and (2) to compare the calculated properties of these monomers and their cations.

2. Calculations

Initially, structures of representative mono-, di-, tri-, and tetra-fluorothiophenes were fully optimized using Density Functional Theory (DFT) B3LYP method using the 6-311++G** basis set as implemented in the Gaussian 98 program package (G98W)[8]. The natures of the optimized stationary points were all characterized by frequency calculations at the same level of theory with the same basis set.

3. Results and discussion

To predict the bonding-characteristic behavior of the fluorothiophene rings in their corresponding polymer chains and to determine the extent of the π -conjugation character of these polymers, we have used the F_n coefficient for each thiophene ring in the isolated fluorothiophenes. The calculated values of the F_n coefficient for all fluorothiophenes and their cations shown that the molecule B have the smallest values of the F_n coefficient. Therefore, the quinoid character of monomer B is greater than that of other fluorothiophenes.

For all fluorothiophenes and their cations, the positive charge is distributed mainly on the C₃ position in Figure1, whereas spin density is distributed mainly on the C₅ position in Figure 1. In both series of molecules and their cation radicals, charge- and spin-density distributions have similar trends with the number and position of the substituted fluorine atoms. The analysis carried out on the calculated dipole moments shows that the size and direction of the dipole moment vector depend mainly on the position (symmetry) of substituents rather than on the number of substituents. Furthermore, the orientation of the dipole moment vector is toward the nitrogen atom for all fluorothiophenes. It can also be seen that the size of the dipole moment



vector for monomer **B** is greater than all fluorothiophenes. it can be said that the electrochemical stability of monomer **B** is greater of all fluorothiophenes. The low-frequency values for all of the compounds are higher than for thiophene. Thru mono-fluorine compounds, compound **B** has higher low-frequency values. This means that this compound have the largest force constants for their bending modes of vibration. Also HLG values for all of the fluorothiophenes is very good for transit than valance band to conducting band. NICS results showed that compound **B** has the largest quantity of negative value (-14.3 for center than polymer rings), therefore this compound has the largest electrical current and conductivity.

4. Conclusions

Fluorothiophenes have been designed as monomers for conductive polymers in the hope of having modified chemical and electrical properties. The primary advantage of the conductive polyfluorothiophenes over their parent polymer, polythiophene, is their higher pyrolysis temperature, which decreases the risk of fire in the electronic/electrical devices made of these materials.

Ab initio and density functional theory DFT-B3LYP/6-311++G** calculations have been carried out successfully to study the structural, electronic, electrochemical, and spectroscopic properties of all fluorothiophenes. Compared to thiophene, **B** monomer is more soluble in water and has a lower potential energy to form cations. These characteristics increase the efficiency of the electrochemical polymerization processes on this monomer. Furthermore, it has been shown how the prediction of polymer characteristics from the molecular properties of the constituting monomers is possible via quantum mechanical computations.

References

- [1] A. J. Heeger, J. Phys. Chem. B, 105(36), (2001) 8475.
- [2] M. S. Ram, Srinivasan Palaniappan, Journal of Molecular Catalysis A: Chemical 201, (2003) 289.
- [3] Vidal, J. C.; Garcia, E.; Castillo, J. R. Anal. Chim. Acta , 385 (1999) 213.
- [4] Campbel, T. E.; Hodgson, A. J.; Wallace, G. G. Electroanalysis, 11, (1999) 215.
- [5] Kincal, D.; Kamer, A.; Chield, A. D.; Reynold, R. J. Synth. Met., 92, (1998) 53.
- [6] Smela, E. J. Micromech. Microeng. 9, (1999) 1.
- [7] Skotheim, T. A., Elsenbaumer, R., Reynolds, J.; Handbook of Conducting Polymers; Marcel Dekker: New York, 1998.
- [8] Z. Chan, C. S. Wannere, C. corminboeuf, R. Puchta, and P. V. R. Schlyere, Chem. Rev, 105 (2005), 3842.

Interplay between the O-H...O intramolecular hydrogen bonding and pyrimidine ring in 5-formyl barbituric acid. A theoretical study

*A. Nowroozi, S. Dahmardeh, P. Mohammadzadeh Jahani, M. Poorsargol

Department of chemistry, Faculty of Science, University of Sistan & Baluchestan, P.O. Box 98135-674, Zahedan, Iran

(E-mail: dahmardeh_s@yahoo.com)

Keywords: 5-formyl barbituric acid, Intramolecular hydrogen bond, AIM and NBO

1. Introduction

Hydrogen bonding (H-bonding) is an intensively studied interaction in physics, chemistry and biology, and its significance is conspicuous in various real life examples [1]. The intramolecular hydrogen bond (IHB) as a specific case, exist in numerous organic compounds and biomolecules, such as hormones, enzymes and proteins. Several of intramolecular hydrogen bond observed in the biological system, such as OHO, NHO and NHN. Although one of the most significant structures capable of bearing hydrogen bonds is the OHO unit, which is the most widely studied[2-6] Pyrimidine is a heterocyclic ring similar to benzene and pyridine, containing two nitrogen atoms at 1 and 3 positions. The most famous nucleobases, cytosine, thymine and uracil are pyrimidine derivatives. In DNA and RNA, these bases are involved in hydrogen bond with their complementary purines. Barbituric acid or malonylurea or 6-hydroxyuracil is an organic compound based on a pyrimidine heterocyclic skeleton. By substitution an acyl group on the methylene group of barbituric acid, the new class of compounds, was introduced. 5-formylbarbituric acid (FBA) as the simplest member of these compounds can participate in the keto \leftrightarrow enol equilibrium as a β -dicarbonyl (Fig. 1). Furthermore, the simultaneously existence of a chelated and pyrimidine rings is caused that the competition between the intramolecular hydrogen bond and amide resonance is occurred and interest this molecule for more considerations.

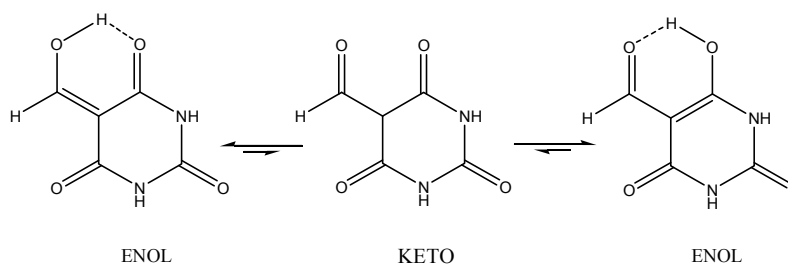


Fig 1. Keto \leftrightarrow Enol tautomeric equilibriums in FBA

2. Computational details

All of the computations in the present study were performed by Gaussian 03 series of programs [7]. The geometry optimizations were carried out by HF, B3LYP and MP2 methods with the most popular basis set, 6-311++G(d, p). The optimized structures at MP2/6-311++G (d, p) level of theory were used to obtained the appropriate wave function files for AIM [8] and NBO [9] analyses.

3. Results and discussion

Theoretically, the FBA has about 100 different conformers which classified to KETO, MH, DH, and TH. Our theoretical results show that the RAHB systems with endo and exo C=C, have extra stability respect to the other forms. The evaluation of hydrogen bond energy by Schuster method at all of the computational levels, clearly predict that the HB strength in exo- FBA is lower than the endo- FBA. For example at MP2/6-311++G** the HB energy for endo and exo FBA is about 78.24 and 49.20 kJmol⁻¹ respectively. In addition, the results of quantum theory of atoms in molecules, the natural bond orbital analyses and geometrical parameters are given a similar result. Although the HB energy is emphasized on more stability of endo- FBA, but our theoretical calculations reveal that the exo- FBA conformers is global minimum. The population analyses of these forms by



the NBO method also predict that the origin of this preference is mainly due to the electron delocalization of amide functional group (Amide resonance) in exo-FBA, especially $LP(N) \rightarrow n^*_{C=O}$ charge transfer.

References

- [1] G. A. Jeffrey and W. Saenger, *Hydrogen Bonding in Biology and Chemistry* (Springer-Verlag, Berlin, 1991).
- [2] J. Emsley, *Struct. Bonding* (Berlin) 57 (1984) 147.
- [3] J.J. Dannenberg, R. Rios, *J. Phys. Chem.* 98 (1994) 6714.
- [4] G. Gilli, F. Bellucci, V. Ferretti, V. Bertolasi, *J. Am. Chem. Soc.* 111(1989) 1023.
- [5] A. Nowroozi, S.F. Tayyari, H. Rahemi, *Spectrochim. Acta* 59A (2003) 1757.
- [6] S.F. Tayyari, H. Raissi, F. Milani-nejad, I.S. Butler, *Vib. Spectrosc.* 26 (2001) 187.
- [7] M. J. Frisch, G. W. Trucks, H. B. Schlegel, G. E. Scuseria, M. A. Robb, J. R. Cheeseman, J. A. Montgomery, Jr., T. Vreven, K. N. Kudin, J. C. Burant, J. M. Millam, S. S. Iyengar, J. Tomasi, V. Barone, B. Mennucci, M. Cossi, G. Scalmani, N. Rega, G. A. Petersson, H. Nakatsuji, M. Hada, M. Ehara, K. Toyota, R. Fukuda, J. Hasegawa, M. Ishida, T. Nakajima, Y. Honda, O. Kitao, H. Nakai, M. Klene, X. Li, J. E. Knox, H. P. Hratchian, J. B. Cross, C. Adamo, J. Jaramillo, R. Gomperts, R. E. Stratmann, O. Yazyev, A. J. Austin, R. Cammi, C. Pomelli, J. W. Ochterski, P. Y. Ayala, K. Morokuma, G. A. Voth, P. Salvador, J. J. Dannenberg, V. G. Zakrzewski, S. Dapprich, A. D. Daniels, M. C. Strain, O. Farkas, D. K. Malick, A. D. Rabuck, K. Raghavachari, J. B. Foresman, J. V. Ortiz, Q. Cui, A. G. Baboul, S. Clifford, J. Cioslowski, B. B. Stefanov, G. Liu, A. Liashenko, P. Piskorz, I. Komaromi, R. L. Martin, D. J. Fox, T. Keith, M. A. Al-Laham, C. Y. Peng, A. Nanayakkara, M. Challacombe, P. M. W. Gill, B. Johnson, W. Chen, M. W. Wong, C. Gonzalez, and J. A. Pople, *Gaussian 03, Revision C.01*, Gaussian, Inc., Wallingford CT, 2004.
- [8] R.F.W. Bader, *Atoms in Molecules. A Quantum Theory*, Oxford University Press, New York, 1990.
- [9] A. E. Reed, L. A. Curtis, F. A. Weinhold. *Chem. Rev.* 88 (1988) 899.



Theoretical Study On ^1H , ^{13}C NMR Shielding, Structure and vibrational assignment, And Physical Properties Of Diamantane

Z. Bayat^{a,*}, S.J.Mehdizade^b, S. Bagheriⁱ, M. Fakoor^d

^{a,c,d}Department of Chemistry, Islamic Azad University Quchan Branch, Iran

^bDepartment of Chemistry, Ferdowsi University, Meshad, Iran

(E-mail: z.bayat@ymail.com)

1. Introduction

Diamondoid molecules consist of a diamond-like carbon cage, where all carbon atoms are sp^3 hybridised, and dangling bonds at the edges of the systems are terminated with hydrogen atoms. The smallest member of the family, Adamantane ($\text{C}_{10}\text{H}_{16}$) is made up of the central cage of a single diamond unit cell and was first synthesized by carbonation equilibration in 1957 by von Rague Schleyer [4]. The next members of the family are Diamantane possessing two diamond cages (see Fig.1). There has been substantial interest in the spectroscopic properties of this class of molecules from an astrophysical view-point. Not only have nano meter sized 'diamond-like' molecules been found in meteorites [5], the occurrence of these compounds as isolated gas phase molecules in the interstellar medium, has also been suggested, based on the observation of infrared absorption [6] and emission [7,8] bands around $3.5\text{ }\mu\text{m}$ (2880 cm^{-1}) in the spectra of protostars as well as the post-AGB object HR 4049 [9]. This band has been assigned to the tertiary sp^3 carbon (i.e., carbon bound to three carbon atoms) C-H stretching mode [10], but other explanations have also been put forward [11].

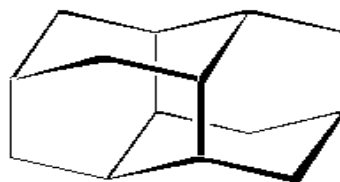


Fig.1. Structure of Diamantane.

2. Method

The assignments were made on the basis of relatively low-level calculations carried out using the Gaussian 03. The experimental Raman spectra were then matched to the overall patterns of the *ab initio* calculations and then modified in the light of the polarization information. In general the calculated frequencies were over-estimated. The small unassigned peak in the Diamantane spectrum between $2250\text{--}2800\text{ cm}^{-1}$ is most probably combination bands. The animations of Diamantane have been produced using the optimized geometry and maximum displacements from the *ab initio* calculations. The individual frames have been calculated using a simple sinusoidal interpolation, and the amplitudes of the vibrations have been exaggerated in order to make them visible on the screen.

3. Results

The third type carbon bending (γ) was calculated at 688 and 668 cm^{-1} (scaled frequencies are reported) in B3LYP/6-311+G** and HF/6-311+G** respectively. These vibrations don't appear in experimental IR and Raman spectra. CH_2 scissoring motions was calculated at 1469 and 1453 cm^{-1} in B3LYP/6-311+G** and HF/6-311+G** respectively and analogous experimental signal was appeared at 1433 cm^{-1} . A strong Raman band at 1233 cm^{-1} was assigned as CH_2 twisting (coupled with CH bending) motion and was calculated at 1240 and 1233 cm^{-1} in B3LYP/6-311+G** and HF/6-311+G** respectively. The isotropic chemical shifts δ with respect to TMS are 34.5746 , 24.8165 , 1.3016 , 1.1307 (HF) and 44.0266 , 33.1114 , 1.7816 , 1.7100 (B3LYP) of C(2), C(3), H(2) and H(3) respectively. The ΔG_{solv} of Diamantane is -1.39 kcal/mol at b3lyp/6-311+g**.

4. Conclusions

The structural parameters of Diamantane were calculated at the DFT level using B3LYP functional with 6-311+G** basis set. For comparison, these calculations were also performed at the HF/6-311+G** level of theory. The results obtained at the B3LYP/6-311+G** and HF/6-311+G** levels are in excellent agreement with the Raman experimental data.

**References**

- [1] <http://www.chm.bris.ac.uk/pt/diamond/diamondoids.htm>
- [2] May, P. W. Ashworth, S. H. Pickard, C. D. O. Ashfold, M. N. R. Peakman, T and Steeds, J. W, *Phys. Chem. Comm* (1998) 4.
- [3] Bayat, Z. Monajjemi, M, *Journal of physical and theoretical chemistry* , 5(2) (2008) 85.
- [4] Schleyer, P.V.R. *J. Am. Chem. Soc.* 79 (1957) 3292.
- [5] Anders, E. Zinner, E. *Meteorites* 28 (1993) 490.
- [6] Allamandola, L.J. Sandford, S.A. Tielens, A.G.G.M. Herbst, T.M. *Astrophys. J.* 399 (1992) 134.
- [7] Guillois, O. Ledoux, G. Renaud, C. *Astrophys. J.* 521 (1999) L133.
- [8] van Kerckhoven, C. Tielens, A.G.G.M. Waelkens, C. *Astron. Astrophys.* 384 (2002) 568–584.
- [9] Chang, H.C. Lin, J.C. Wu, J.Y. Chen, K.H. *J. Phys. Chem.* 99 (1995) 11081–11088.
- [10] Blades, J.C. Whittet, D.C.B. *Mon. Not. R. Astron. Soc.* 191 (1980) 701.
- [11] Schutte, W.A. Tielens, A.G.G.M. Allamandola, J.L. Cohen, M. Wooden, D.H. *Astrophys. J.* 360 (1990) 577.

Conformational effect on ^{13}C chemical shifts; analysis of 6-mono-substituted derivatives of 5,6,7,8-tetrahydrodibenzo[a,c]cyclo-octene by *ab initio* quantum mechanics method

Jamshid Najafpour*, Ali Akbar Salari, Mohammad Porgham Daryasari

Department of Chemistry, Faculty of science, Islamic Azad University Shahr-e-Ray Branch, Tehran, Po. Box: 18155/144, Iran

(E-mail: j.najafpour@gmail.com)

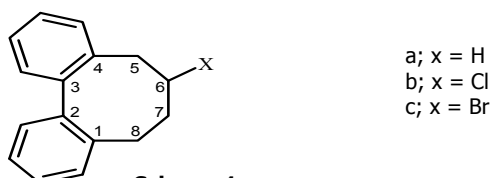
Keywords: ^{13}C chemical shift, Conformational effect, NMR, GIAO method.

1. Introduction

Nuclear magnetic resonance has become powerful tool in chemistry as well as molecular biology. It is one of the best methods for elucidation of the complex structures. Among the structural parameters available by NMR, chemical shift is the most important one, both ^1H and ^{13}C chemical shifts provide chemist with a wealth of structural information. Many *ab initio* methods have been developed to predict the chemical shifts in terms of the chemical properties of the environment of the atoms, so called the shielding tensor [1-6]. Since 1974, nuclear magnetic resonance (NMR) spectroscopy has been significant development in the *ab initio* theory of NMR shielding constant. In that year Ditchfield [2] used London's gauge invariant atomic orbitals (GIAO) to devise a method for calculating chemical shielding constant that has proven to be quite popular and accurate especially when applied in the context of highly correlated *ab initio* method. Traditionally, these calculations are carried out in the gas phase and the lack of consideration for solvent effect is one of the more obvious sources of discrepancy between experimental reality and theoretical models [7].

^{13}C chemical shifts are normally used for theoretical calculations as both the diamagnetic and paramagnetic shielding constant contribute to its chemical shift. There is a very few calculation on conformational dependence of ^{13}C chemical shifts, due to insufficient experimental data, so the important structural parameters which affects the ^{13}C chemical shifts by conformational changes have not been formulated yet.

Cyclo-octa-1,3-diene and its dibenzo analogue 5,6,7,8-tetrahydrodibenzo[a,c]cyclo-octene and their 6-mono-substituted derivatives (Scheme 1) have been studied by ^1H and ^{13}C NMR spectroscopy and by force field calculation [8-11]. Two types of minimum energy conformations are possible: twist boat chair (TBC) and twist boat (TB), the lower one being described as TBC. The 6-mono-substituted derivatives of 5,6,7,8-tetrahydrodibenzo[a,c]cyclo-octene with chlorine and bromine substitution (Scheme 1, b, c) are used as the model compounds, which show conformational equilibrium in solution at room temperature [9, 11]. They are used to study the conformational effect of axial and equatorial substitution on ^{13}C chemical shifts.



Scheme 1.

2. Computational details

The molecular geometry optimization of TBC conformational forms of 1a, 1b and 1c in gaseous phase have been done using RHF level of theory, implementing 6-311G(d,p) atomic basis set. Geometry optimization have been performed using WinGAMESS [12], GAUSSIAN03 [13] and Spartan'08 [14] computational packages. Vibrational frequencies were calculated at the same level for characterization of stationary point (no imaginary frequencies was observed). ^{13}C chemical shift studies have been carried out on the basis of GIAO method at RHF/6-311G(d,p) level of theory using GAUSSIAN03 [13] and Spartan'08 [14] computational packages. Tetra methyl silane: TMS is assumed as a standard substance in specifying of chemical shift from shielding value.

3. Results and discussion

Isotropic (σ_{el}) and anisotropic (σ_{A}) terms of shielding tensor of 1b and 1c with axial [a] and equatorial [e] forms are presented in Table 1. The relation between shielding and chemical shift δ is given by $\delta = \sigma - \sigma_{\text{TMS}}$. The calculated isotropic and anisotropic shielding values of carbon atoms in TMS at RHF/6-311G(d,p) are $\sigma_{\text{el}} = 196.0898$ and $\sigma_{\text{A}} = 5.7645$ respectively. We used Isotropic value to calculate chemical shift. The experimental chemical shifts in CDCl_3 environment [10] have been used to compare with this computational investigation in gaseous phase.

Table 1. Experimental and calculated ¹³C chemical shift of 6-mono substituted derivatives of 5,6,7,8-tetrahydrodibenzo[a,c]cyclo-octene

1b[a]	C5	C6	C7	C8
σ_{el}^*	159.5839	136.7297	157.9782	170.0577
σ_A^*	10.7173	50.0904	24.0046	24.0140
δ (calc)*	36.51	59.36	38.11	26.03
δ (calc)**	36.93	59.85	39.43	26.45
δ (exp)	39.65	58.43	38.73	27.07
1b[e]	C5	C6	C7	C8
σ_{el}^*	147.8021	134.2171	159.9158	166.3288
σ_A^*	41.3651	53.3970	26.5573	19.5245
δ (calc)*	48.29	61.87	36.17	29.76
δ (calc)**	41.03	63.40	39.26	29.84
δ (exp)	43.54	61.86	39.99	30.93
1c[a]	C5	C6	C7	C8
σ_{el}^*	158.8457	136.6100	157.2239	169.5634
σ_A^*	7.9453	54.5654	26.2171	23.5097
δ (calc)*	37.24	59.48	38.87	26.53
δ (calc)**	37.77	60.33	40.39	26.76
δ (exp)	40.50	53.39	39.44	28.04
1c[e]	C5	C6	C7	C8
σ_{el}^*	147.6217	133.3710	156.8861	165.7485
σ_A^*	43.6159	57.4356	29.9551	17.2383
δ (calc)*	48.47	62.72	39.20	30.34
δ (calc)**	41.79	62.60	40.27	30.81
δ (exp)	44.26	53.85	41.12	32.52

* Calculated with GAUSSIAN03 package, ** Calculated with Spartan'08

However, it's a well known fact that the change in environment is one of the most crucial factors in determining the chemical shift. In a molecule, shielding of a atom like carbon is greatly affected by neighboring bonded atoms and similar bonded atoms give different shielding values.

Our computed results have been shown good agreement with experimental results. Therefore, there is a suitable correlation between the experimental and calculated values and affect of neighboring atom as axial and equatorial substituted on ¹³C chemical shift.

References

- [1] H. Fukui, *Magn. Reson. Rev.* 11 (1987) 205.
- [2] R. Ditchfield, *Mol. Phys.* 27 (1974) 789.
- [3] H. Fukui, K. Miura, H. Yamazaki, T. Nosaka, *J. Chem. Phys.* 82 (1985) 1410.
- [4] H. Fukui, K. Miura, H. Shinbori, *J. Chem. Phys.* 83 (1985) 907.
- [5] J.D. Baker, M.C. Zerner, *Int. J. Quantum Chem.* 43 (1992) 327.
- [6] D.B. Chesnut, *Annu. Rep. NMR Spectrosc.* 21 (1989) 51.
- [7] M.A. Freitag, B. Hillman, A. Agrawal, M.S. Gordon, *J. Chem. Phys.* 120 (2004) 1197.

**First principles study of structure and electronic properties of Na-doped adamantane in disordered solid phase**M. Hamadiani^a, B. Khoshnevisan^b, F. Kalantary-fotooh^a^aDepartment of Physical Chemistry, Faculty of Chemistry, University of Kashan, Kashan, Iran

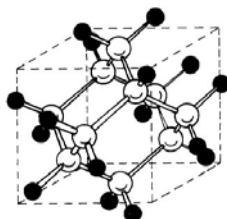
(E-mail: hamadani@kashanu.ac.ir)

^bDepartment of Physics, Faculty of Science, University of Kashan, Kashan, Iran**Keywords:** Adamantane, Electronic property, First principles calculations, Band structure**1. Introduction**

The smallest possible diamondoid is adamantane tricyclo [3,3,1,1] decane, consisting of 10 carbon atoms arranged as a single diamond cage, surrounded by 16 hydrogen atoms, as shown in figure 1. High temperature structure of adamantane was found to have the plastic properties and crystallized in Fm3m space group [1]. The origin of the plastic properties lies in compact, symmetrical, cage like molecule. Investigations for ordered structure at low temperature (under 208.62K) showed that it crystallize with P4₂C space group [2]. Theoretical investigations have been performed on structure and electronic properties of adamantane molecule and its derivatives in gas phase. These studies show that this molecule has a wide HOMO-LUMO gap about 7.6 eV [3,4]. Substituting H or C-H groups with different atoms and functional groups in adamantane was of interest [3]. These doping has changed the electronic properties such as HOMO-LUMO gap, conductance and binding energy of adamantane. In this paper we substitute one to four tertiary H-atom in plastic adamantane with Na and compare the structure and electronic properties with unsubstituted adamantane in both gas and solid phase.

2. Computational methods

These calculations have been based on the ab initio density functional theory (DFT). In bulk phase we considered adamantane in FCC lattice. Geometry optimization and electronic properties were calculated using first principles methods, as provided in the QUATUM- ESPRESSO package [5]. The exchange-correlation energy was accounted for through local density approximations (LDA). Core valence interaction was described by norm-conserving pseudo potentials for H, C and Na [6]. The plane-wave cut-off energy was taken as 160 Ry and a 5*5*5 Monkhorst-pack k-point sampling is used for integration of the Brillouin Zone (BZ), electronic structure and total energy calculations. The equilibrium lattice parameter was determined by minimizing the crystal total energy calculated for different values of lattice parameter. The best lattice constant considered to be 18.1616 bohr for all structures. DFT calculations were performed using GAUSSIAN 03 package and B3LYP for GGA approximations and 6-31+G(d, p) basis set.

**Fig. 1.** The structure of a adamantane molecule.**3. Results and discussion****3.1 bulk phase adamantane**

The Na-doped derivatives of adamantane have been considered which n Na-atoms (n= 1 to 4) are doped instead of tertiary Hydrogen atoms in adamantane. These compounds are crystallized in FCC lattice in adamantane's plastic form. All the structures were optimized. The corresponding Na-Na distances in n= 2, 3, 4 Na-doped adamantane are 3.611Å⁰, 4.079Å⁰, 4.862Å⁰, respectively. The total energies and the band gaps of these five derivatives are provided in table 1. The band gaps of these structures which are derived from their band structures display that the isolated adamantane is an insulator which coincides with the previous calculations [7]. By substituting the tertiary hydrogen atoms with odd numbers of Na (n=1,3) in adamantane, the metallic property can be observed (fig.3). Substituting them with even numbers of Na show the semi metallic (n=2) and semiconductor (n=4) properties with the band gaps about 1.64816 and 0.34379 eV, respectively. These observations can be described by the symmetry of the molecule in FCC lattice.

3.1- gas phase adamantane

Adamantane and its derivatives were optimized completely in gas phase. The corresponding Na-Na distances in $n=2$ to 4 Na-doped adamantane are 6.414 Å, 6.450 Å, 5.770 Å, respectively. Comparing the bond lengths in gas phase with the bond lengths in solid phase shows that the C-Na and tertiary C-H bond lengths in bulk phase change more rapidly by substituting the H with Na. The total energy and band gap of these five configurations are provided in table 1. The results display that the band gap decreases by substituting tertiary H with Na in gas phase which shows the semiconductor behavior.

Table1. Total energy and band gap of adamantane and its derivatives in bulk and gas phase (ev)

Compound		ADAM	1-Na-ADAM	2-Na-ADAM	3-Na-ADAM	4-Na-ADAM
Bulk phase	Total energy	-1794.46886	-1794.24181	-1777.65256	-1754.67697	-1735.47068
	Band gap	2.985473	-	1.64816	-	0.34379
Gas phase	Total energy	-390.7543	-552.396	-714.0384	-875.682	-1037.34
	Band gap	7.48694	2.171196	1.478939	1.357576	0.8226

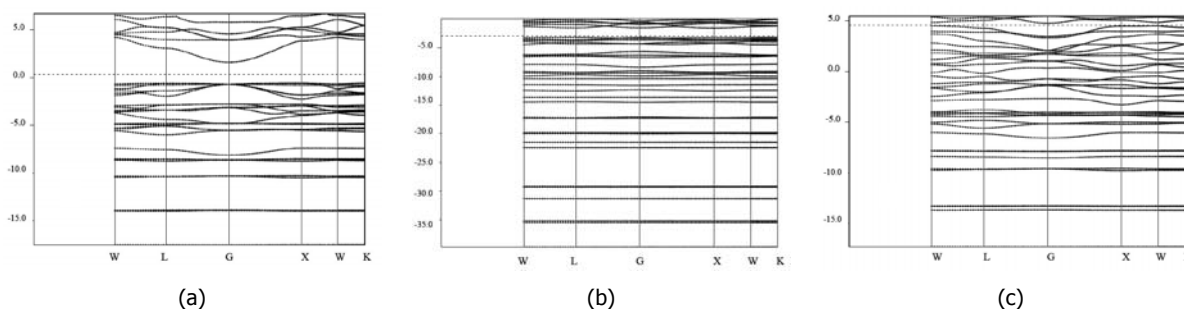


Fig. 2. Band structure of a) adamantine b) 2-Na doped adamantane c) 4-Na doped adamantane

4. Conclusion

The structure and electronic properties of adamantane and its derivatives have been investigated in FCC lattice and gas phase using density functional theory. Adamantane in both phase show the insulator property. In gas phase the band gap will reduce by substituting tertiary H-atoms by Na to get semiconductors. In solid phase the number of Na-atoms affects the metallic, semi metallic and semi conductivity of the substituted adamantane.

References

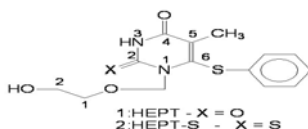
- [1] J. P. Amoureux, M. Bee, J. C. Damein, Acta Cryst. B 36 (1980) 2633.
- [2] J. P. Amoureux, M. Foulon, Acta Cryst. A 43 (1987) 470.
- [3] Y. Xue, G. A. Mansoori, J. Nanoscience. 7 (2008) 63.
- [4] F. Marsusi, K. Mirabbaszadeh, G. A. Mansoori, Physica E. 41 (2009) 1151.
- [5] S. Baroni, A. Dal Corso, S. de Gironcoli, P. Giannozzi, <http://www.quantum espresso.org>.
- [6] The "C.pz-vbc.UPF", "H.pz-vbc.UPF" and "Na.pz-n-vbc.UPF" from the PWscf table (<http://www.pwscf.org/pseudo.htm>) were used for carbon, hydrogen and sodium, respectively.
- [7] L. Nio, J. Zhu, X. Han. Phy. Let. A. 373 (2009) 2492.

**Design of Anti-HIV Ligands by Means of Minimal Topological Difference (MTD) Method**Z.Bayat*^a, N. Abdossamadi^b, So. Norouzi^c, Sa.Norouzi^aDepartment of Chemistry, Islamic Azad University Quchan Branch, Iran^bDepartment of physics, Sharif University of Technology, Iran^cDepartment of Chemistry, University of Kurdistan, Iran^dFaculty of chemistry, Mazandaran University, Babolsar, Iran

z.bayat@gmail.com

Keyword: Anti-HIV, HEPT, IC₅₀, QSAR, HF, GA-MLR.**1. Introduction**

Although new anti-HIV agents get better and better blocking the virus, novel inhibitors are still sought after [1,2]. HEPT (see Fig.1) form the non-nucleoside RT(Reverse transcriptase) inhibitors(NNRTIs)[3] series that does not target an active site of polymerase but rather the enzyme allosteric site.

**Fig. 1.** The structure of HEPT: 1-[(2-hydroxyethoxy)-methyl]-6-(phenylthio) thymine.

A major step in constructing the QSAR models is finding one or more molecular descriptors that represent variation in the structural property of the molecules by a number. the latest development of the computer technology and software of electronic structure theory allows calculating quantum chemical descriptors at first-principles levels, such as Density Functional Theory (DFT) and HF, with higher accuracy including some effective consideration of electron correlation effects.

2. Methods**2.1 Activity Data**

The biological data used in this study are the inhibitor concentration (IC₅₀) of the set of 51 HEPT derivatives. The biological activity data (IC₅₀) were converted to logarithmic scale (p IC₅₀) and then used for subsequent QSAR analysis as dependent variables.

2.2 Quantum Chemical Calculations

The molecular structures of all the HEPT derivatives were built with Hyperchem (Version 7, Hyper Cube Inc.). Gasphase full geometry optimization for the investigated molecules was carried out with the Gaussian 98 series of programs [4].

2.3 Data Processing and Modeling

The MLR analysis was employed to derive the QSAR models for different HEPT derivatives. MLR and correlation analyses were carried out by the statistics software SPSS 13.0 version. The better regression models were selected on the basis of the higher R, F value (a statistic of assessing the overall significance) and the lower SEE.

2.4 MLR Analysis

MLR analysis with the stepwise selection and elimination of variables was employed to model the structure – activity relationships with different set of descriptors. The third QSAR model was derived by using the chemical and quantum chemical descriptors calculated at the level of the HF theory using 6-31G (d) basis set the following equation was obtained:

$$\log IC_{50} = -560.901(\pm 155.284) + 0.102 HE(\pm 0.021) + 0.174 \delta_5(\pm 0.024) - 46.122 LC_6(\pm 13.220) + 0.339 \log P(\pm 0.102) + 49.719 NPA_5(\pm 121.679) + 41.427 NPA_6(\pm 16.019)$$

$$N=31 \quad R=0.972 \quad R^2=0.945 \quad F=68.097$$

2.5 GA-MLR



In order to select the most relevant descriptors, the evolution of the population was simulated. Each individual of the population defined by a chromosome of binary values represented a subset of descriptors. The GA was run many times with different parameters and initial populations. The most relevant equations for different set of descriptors are similar to MLR analysis.

3. Results obtained by GA-MLR

$$\log IC_{50} = -6.38(\pm 2.596) + 0.173 \delta_5(\pm 0.002) + 0.101 \log P(\pm 0.086) - 120.808 LC_6(\pm 14.664) - 0.017M(\pm 0.002) - 40.825 LC_5(\pm 7.703) + 6.23U(\pm 2.399)$$

N=31 R= 0.972 R²=0.95 F= 78.824

4. Conclusions

A quantitative structure – activity relationship study was employed to study the antiepileptic activity of 51 HEPT derivatives. In the MLR procedure, those of individual atoms in the molecule (LC at atom numbers 5 and 6), and the chemical descriptors, including log P, were found to have the same importance in controlling behavior of the molecules. In the GA-MLR procedure, the obtained results were better than to the MLR procedure.

References

- [1] Makhija, M. Kasliwal, R. Kulkarni, V. Neamati, N. Bioorg. Med. Chem, 12 (2004) 2317.
- [2] Pontikis, R. Benhida, R. Aubertin, A.-M. Grierson, D. S. Mohnert, C. J. Med. Chem. 40 (1997) 1845.
- [3] De Clerq, E. Med. Res. Rev. 13 (1993) 229.
- [4] Araujo, M. C. U. Saldanha, T. C. B. Galvao, R. K. H. Yoneyama, T. Chame, H. C. Visani, V. Chemomet. Intell. Lab. Syst. 57 (2001) 65.

DFT/B3LYP study on antioxidant activity of compounds based on vitamin E

M. Najafi*, E. Nazarpour, M. Zahedi

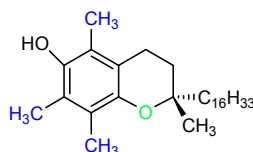
Department of Chemistry, Faculty of Sciences, Shahid Beheshti University, G.C., Evin, 19839-6313, Tehran, Iran

(E-mail-najafimm@yahoo.com)

Keywords: Vitamin E, DFT method, Antioxidant, Free radical, Bond dissociation enthalpy (BDE), Ionization potential (IP).

1. Introduction

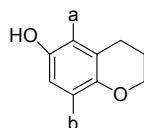
Vitamin E is a well-known lipid-soluble antioxidant in biological systems. It acts as the chain-breaking antioxidant in the chain propagation step thus protecting cell membranes from oxidative degradation. The term vitamin E represents a series of structurally similar compounds, which consist of a phenolic section with methyl substitutes in ortho and meta positions and a fused Heterocyclic ring with a side carbonic chain (C₁₆H₃₃).



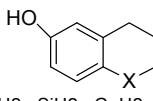
The side chain has no effect on its antioxidant activity, but serves to hold the chemically reactive 'head' in biomembranes.

The antioxidant activities of vitamin E come from heterocyclic ring, heteroatom and phenolic section substitutes [3]. In order to develop novel antioxidants better than vitamin E, several efforts have been made to synthesize vitamin E analogues, generally there are three ways:

- Replacing phenolic section methyl groups with various substituents (Figure 1),
- Replacing heteroatom with other atoms such as Selenium (Se), phosphor (P), selenium (Si) (Figure 2),
- Reducing the atom number of heterocyclic ring (Figure 3),



a and b= various substituent
Figure 1. replacing phenolic section methyl groups with various substituent



X= CH₂, SiH₂, GeH₂, NH, PH, AsH, O, S, Se
Figure 2. replacing heteroatom with other atoms

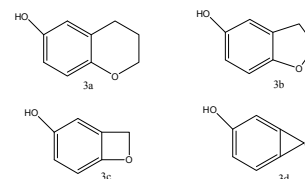
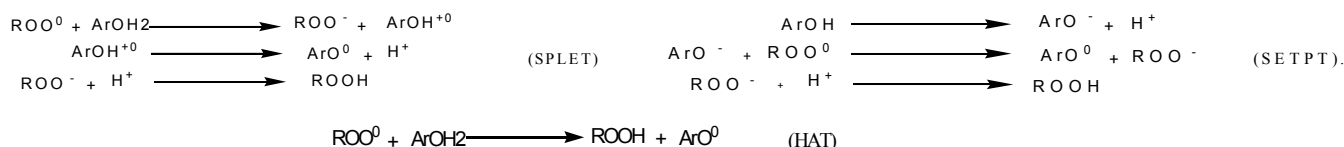


Figure 3. reducing the atom number of heterocyclic ring

2. Method and Computational details

In this paper, the effects of the heterocyclic ring, heteroatom and various substituent groups on the antioxidant properties of vitamin E are investigated by density functional method. The aforementioned method has been justified to be a useful and economical to investigate antioxidant mechanism. It is also possible to search various ways to develop vitamin E analogues with a better antioxidant activity.[4]

There are two generally accepted mechanisms of vitamin E, namely hydrogen atom transfer (HAT) and single-electron transfer followed by proton transfer (SETPT). Recently, another mechanism has been discovered. This was named sequential proton loss electron transfer (SPLET). [1]



The main aim of this study is to calculate reaction enthalpies related to the three antioxidant action mechanisms using DFT/B3LYP method. These enthalpies will be denoted as follows:

$$\begin{array}{lll}
 \text{BDE} = H(\text{ArO}^\bullet) + H(\text{H}^\bullet) - H(\text{ArOH}) & \text{IP} = H(\text{ArOH}^{+0}) + H(e^-) - H(\text{ArOH}) & \text{PDE} = H(\text{ArO}^\bullet) + H(\text{H}^+) - H(\text{ArOH}^{+0}) \\
 \text{PA} = H(\text{ArO}^-) + H(\text{H}^+) - H(\text{ArOH}) & \text{ETE} = H(\text{ArO}^\bullet) + H(e^-) - H(\text{ArO}^-) &
 \end{array}$$



The calculated enthalpy of proton, H (H⁺), is 6.197 kJ /mol; the enthalpy of electron, H (e⁻), is 3.145 kJ/ mol. [2] all calculations were performed using Gaussian 98 program package.[5] The geometry of each compound, radical, radical cation and anion was optimized using DFT (density functional theory) method with RB3LYP functional without any constraints. The calculations were performed in 6-31G* basis set .Optimized structures were confirmed to be real minima by frequency calculation (no imaginary frequency).The conformer with the lowest electronic energy was used in this work.

3. Results and Discussion

Heteroatom (O atom) plays a more important role than the heterocyclic ring in improving the antioxidant activity of vitamin E. The O atom in vitamin E has been regarded to delocalize the unpaired electron by its p-type orbitals and improve the stability of the phenoxyl radical. As for IP, the heterocyclic ring has a large reducing effect than the heteroatom (O atom). When the heteroatom (O atom) in vitamin E is replaced by other atoms, such as S and Se, the BDE is decreased slightly (Table 1).

When the heteroatom O is replaced by NH (1e), both the BDE and IP Are sharply reduced because the nitrogen is less Electronegative Than oxygen and tends to stabilize the radical formed by conjugative Delocalization of its lone pair of electrons. In

fact, this situation has been Found by Wright. Some functional groups should be adopted to improve the IPs of these kinds of molecules because a lower IP will cause reaction with oxygen easily. Result of Various substituent effects on antioxidant

Table 2. Calculated BDE, IP, PDE, PA, ETE of Figure 1.								
Substituent	ORTHO Substituent					META Substituent		
	BDE kcal/mol	IP kcal/mol	PDE kcal/mol	PA kcal/mol	ETE Kcal/mol	BDE kcal/mol	IP kcal/mol	PDE kcal/mol
Br	80.366	164.22	230.06	355.43	38.85	396.71	163.95	232.75
C2H5	79.46	157.08	236.30	363.07	30.32	395.70	156.82	238.88
CC(2)	76.79	157.32	233.39	357.34	33.37	396.69	157.21	239.48
CC(3)	80.33	160.64	233.62	357.00	37.25	396.95	160.05	236.89
Cl	80.32	164.94	229.31	356.15	38.10	396.64	164.72	231.91
CN	82.24	172.90	223.26	346.92	49.24	398.43	173.06	225.30
COH	80.73	168.70	225.95	347.10	47.55	399.49	169.25	230.26
COOH	81.72	164.93	230.72	352.77	42.88	397.62	165.35	232.27
F	79.90	164.13	229.69	361.05	32.77	396.07	163.63	232.44
NHCH3	71.46	146.45	238.92	359.90	25.47	395.03	143.23	251.80
OCH3	74.81	155.48	233.26	360.42	28.32	393.67	151.37	242.29
OCOH	80.0	163.63	230.29	356.28	37.64	395.55	161.06	234.49
OH	71.25	158.08	227.10	354.21	30.96	393.99	154.67	239.35
OSO2CH3	77.74	162.83	228.84	346.49	45.27	397.78	161.31	236.46
SO2CH3	79.83	169.85	223.89	341.90	51.84	395.96	168.71	227.25

Table1. Calculated BDE,IP of Figure 2 and3		
Compound	BDE(Kcal/mole)	IP(Kcal/mole)
3.a	80.75	166.40
3.b	79.83	168.57
3.c	80.18	176.18
3.d	76.62	181.45
2.CH2	85.16	177.55
2.NH	76.24	153.03
2.Se	81.06	162.78
2.O	80.75	167.38
2.S	80.91	163.91

activities of vitamin E reported in (Table 2).the less BDE and IP values lead to a more stable radical which result in more antioxidant activity.

4. Conclusions

The enhancing effects of heterocyclic ring and heteroatom on the antioxidant properties of vitamin E have been investigated by using density functional theory. The calculated results show that it is possible to synthesize the novel antioxidants by replacing O atom with S or Se. However, when the O atom is replaced by NH, the BDE and IP of molecule are decreased dramatically.

In addition, the results also reveal that reducing the atom number of heterocyclic ring is a better way to synthesize novel antioxidants which are better than that of vitamin E.

Reference

- [1] E. Klein ,V. Luke .*J. Phys. Chem. A*, 14 (2006) 110.
- [2] E. Klein, V. Lukas, M. Ilcin. *Chem. Phys.* 336 (2007) 51.
- [3] W. Chen, J. Song, P. Guo, W. Cao, J. Bian . *Bioorg. & Med. Chem. Lett.* 16 (2006) 5874.
- [4] N. Singh, P. J. O'Malley, P. A. Popelier. *J. Mol. Struct.* 811 (2007) 249.
- [5] M. J. Frisch et al., *Gaussian 98*, revision A.9; Gaussian, Inc.: Pittsburgh, PA, 1998.



Ab Initio Calculations of ¹⁷O NMR Chemical shielding tensors in benzyl ethers derivatives and comparison with experimental values

Mahdi Rezaei-Sameti

Department of Chemistry, Faculty of Science, Malayer University, Malayer, Iran

(E-mail: mrsameti@gmail.com)

Keywords: Ab initio, NMR, ¹⁷O, Shielding Tensor, CSGT, GIAO, *Density* functional theory, Benzyl ethers.

1. Introduction

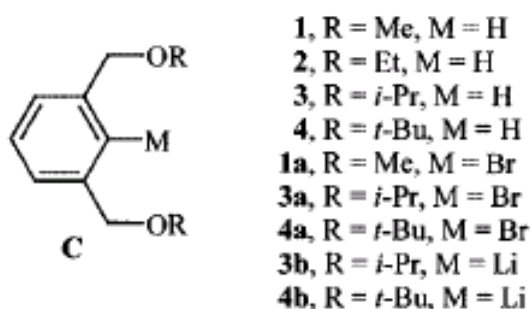
Nuclear magnetic resonance (NMR) spectroscopy is an important experimental tool to probe the local geometric and electronic structure of molecules. To analyze and understand such spectroscopic information, quantum chemical calculations of NMR chemical shifts are very helpful. Wave function based chemical shift calculations have meanwhile reached a high level of accuracy[1], but calculations beyond the MP2 approximation are still limited to small molecules. For quantum chemical calculations on large molecules, density functional theory (DFT) has become a popular and powerful tool [2]. However if one applies DFT to compute magnetic properties such as NMR chemical shifts, one faces the problem that the Hohenberg–Kohn theorem[3] assumes that there are only scalar potentials and is thus not valid in the presence of magnetic fields. In this case, the exchange–correlation energy should be calculated using not only the electron density, but also the current density induced by the magnetic field. Although the theory has been laid out for a current-density functional theory [4,5].

2. Computational Methods

Calculations were performed on a Pentium–PC computer with a 3000 MHz processor. The ¹⁷O NMR shielding results presented were obtained using density functional theory. All geometry optimizations employed B3lyp method using a 6–31++G (2d, 2p) basis set and using the GAUSSIAN 98 program. The ¹⁷O NMR shielding results presented were obtained using B3LYP methods and the 6–311++G (2d,2p), 6-31++G(2d,2p), 6-31G(2d,2p) basis set and the calculations of NMR shielding tensors were done using two of the most common procedures, namely GIAO and CSGT.

3. Results and discussion

This paper will focus on predicting NMR shielding tensors using two of these procedures, namely GIAO and CSGT at density functional theory level of theory, which achieve gauge invariance in different ways. We are interested in utilizing *ab initio* computational techniques to look at how variations in the molecular structure impact on the resulting ¹⁷O NMR calculated data. Ab initio calculations of ¹⁷O nuclear shielding were performed for following derivatives:



The isotropic value, the anisotropy ($\Delta\sigma$) of the tensor and the shielding tensor asymmetry parameter are calculated by following ways:

a) The isotropic value (or trace), σ_{iso} , of the shielding tensor which is defined as:

$$\sigma_{iso} = \frac{1}{3}(\sigma_{11} + \sigma_{22} + \sigma_{33}) \quad (1)$$

b) The anisotropy ($\Delta\sigma$) of the tensor,

$$\Delta\sigma = \sigma_{33} - \frac{1}{2}(\sigma_{22} + \sigma_{11}) \quad (2)$$

c) The shielding tensor asymmetry parameter (η) given by

$$\eta = \frac{(\sigma_{22} - \sigma_{11})}{(\sigma_{33} - \sigma_{iso})} \quad (3)$$

The assignment or ordering of the principal components in the ^{17}O CSA tensor depends on the convention used, but for this manuscript the principal components are defined using:

$$|\sigma_{33} - \sigma_{iso}| \geq |\sigma_{22} - \sigma_{iso}| \geq |\sigma_{11} - \sigma_{iso}| \quad (4)$$

The chemical shift of a substance (S) with respect to a reference compound is then given as:

$$\delta(s) = \sigma(ref) - \sigma(iso) \quad (5)$$

The absolute isotropic chemical shielding values (σ_{iso}) can be converted to chemical shifts (δ) relative absolute shielding reference 287.5, Comparison the experimental and theoretical data shows a good agreement. Figure 1 show the optimized structure of benzyl ether conformer (1). Figure 2 show the correlation between theoretical and experimental chemical shift, the results show that this method is useful for predicting experimental ^{17}O NMR.



Fig. 1. Optimized structures of benzyl ether conformer (1) with B3lyp/6-31++G(2d,2p) basis set

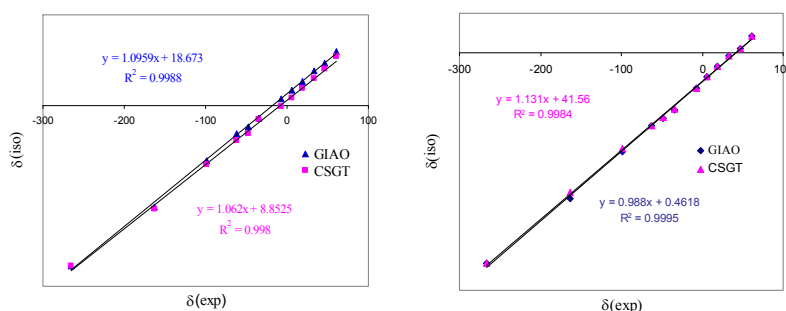


Fig. 2. Correlation diagrams between Isotropic shielding and experimental chemical shift for these series of benzyl ether with B3lyp/6-311++G(2d,2p) basis set

References

- [1] Wu^{thrich}, K. Nat. Struct. Biol. 5(1998) 492.
- [2] Klemperer, W. G. Angew. Chem., Int. Ed. Engl. 17(1978) 246.
- [3] Wu, G.; Dong, S. J. Am. Chem. Soc. 123(2001) 9119.
- [4] Wong, A. et all. J. Phys. Chem. A , 110(2006) 1824.
- [5] A. M. Lee, N. C. Handy, S. M. Colwell, J. Chem. Phys. 103 (1995) 10095.
- [6] Sarah K. McIntyre and Todd M. Alam. Magn. Reson. Chem. 45(2007) 1022.

**Investigation of hydrogen bonding in methanol clusters and its electrical parameters by ab initio calculations**I. Kazeman^{a,*}, M. Hasanzadeh^{a,b}, S. Mahmoodi Asl^c, R. Sherafati^d^aDepartment of Physical Chemistry, K. N. Toosi University of Technology, Tehran, Iran

(E-mail: j_kazeman@yahoo.com)

^bDepartment of Chemistry, Payame Noor University, Khoy, Iran^cDepartment of Chemistry, Payame Noor University, Asalouyeh, Iran^dDepartment of Chemistry, University of Urmia, Urmia, Iran**Keywords:** Methanol Clusters, Ab initio Calculations, Electrical property, Stabilization energy**1. Introduction**

Methanol clusters, groups of methanol held together by hydrogen bonds, have been the subject of a number of intense experimental and theoretical investigations because of their importance in understanding solution chemistry [1] and a large number of chemical and biochemical processes[2-3]. A number of ab initio calculations have also been carried out to investigate the strength of the hydrogen bonds and their cooperatively but all of them have not been arrived in details of these bonds and its clusters [4-6].

2. Methods

We have carried out a systematic study of methanol clusters, from isolated molecule to six molecules in the gas phase. This work reports all the stable geometry, all charts in geometrical parameters, O-H stretching frequencies in clusters and denotes to distinguished molecules with intensities at any molecules, oxygen and hydrogen charge in clusters and its effects in vibrational frequencies and hydrogen bond strength performed with the restricted HF and density functional theory (DFT) methods using the 6-31G(d) basis set. This allowed us to compare the data provided by the DFT method with those of an uncorrelated method (HF).

3. Results and discussion

Calculations of the structures, primary and secondary hydrogen bond properties, stabilization energy, vibrational frequencies and its intensities of 18 low-energy conformations of methanol clusters have been presented. Cyclic, chain and branched-cyclic are structural types that methanol clusters have been shown in these frameworks.

In all of conformers with equal methanol molecule number, the cyclic structure has the most stabilization energy and DFT calculations have the more SE than HF calculations. There is not marked relation between dipole moment and stabilization energy of conformers. Although, on the basis of dipole moments, Boat conformer is the best structures that it would appear the bulk liquid behavior. The C-O and O-H length in all of conformers are constant approximately, however, the O-H length very slow enhanced with growth clusters and the primary hydrogen bond length (O...H) decreased. There is a noticeable increase in the mean strength of the primary hydrogen bonds as n goes from 3 to 4 in HF calculations indicating increased stability of the cyclic trimer, tetramer. For n = 5 and 6, there is a very slight increase in the mean primary hydrogen bond strength. According to this work, the odd n-mers have a slightly greater stability than the even n-mers and the average number of primary hydrogen bonds per methanol molecule increases up to n = 3 but then levels off around one as n approaches 6. All of the secondary hydrogen bond (SHB) that is bonding between oxygen atoms and methyl's hydrogen are listed in tables.

4. Conclusions

The SHB roles prevailing forces opposite steric hindrance in structure of clusters and so caused more stability of them. The cyclic clusters in order to arrangement of methanol molecules have not any SHB instead of some of clusters (containing 1,3MCBu₁, 1,3MCBu₂ and 1,4MCBu) have three SHB.

According to tables secondary hydrogen bonds lead to decreasing of intensities for inclusive oxygen atoms vibration which this effect have been seen in 1M₂CPr, 1,3MCBu₁, 1M₂CBu, 1MCPe visibly and have been seen in 1MCPr, 1,3MCBu₁, 1,4MCBu very clearly.



References

- [1] M. S. Islam, R. A. Pethrick, D. Pugh, J. Phys. Chem. A 102 (1998) 1089.
- [2] D. Kim, E. A. Cho, S. A. Hong, I. H. Oh, H. Y. Ha, Journal of Power Sources, 130, (2004) 172.
- [3] H. C. Cha, C. Y. Chen, J. Y. Shiu, Journal of Power Sources, 192 (2009) 451.
- [4] A. K. Sum, S. I. Sandler, J. Phys. Chem. A 104 (2000) 1121.
- [5] S. L. Boyd, R. J. Boyd, J. Chem. Theory Comput. 3 (2007) 54.
- [6] W.L. Jorgensen, J. Am. Chem. Soc. 103 (1981) 341.

**Theoretical study on physical properties, vibrational assignment and ^1H , ^{13}C NMR shielding of Adamantane**Z. Bayat^{a*}, S.J. Mehdizade^b, S. Qanei nasab^c, M.Zanoozi^d^{a,c,d}Department of Chemistry, Islamic Azad University Quchan Branch, Iran^bDepartment of Chemistry, Ferdowsi University, Meshad, Iran

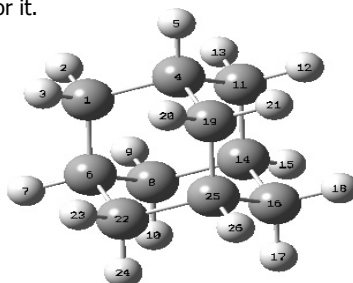
z.bayat@ymail.com

1. Introduction

Adamantane belongs to the most interesting structures produced by nature. It possesses a cage-like skeleton which is a unique, rigid, but strain-free ring system composed of three fused chair cyclohexane rings. The carbon skeleton with its T_d symmetry also represents a fragment of the diamond network. The vibrational spectra of Adamantane have been recorded in the literature numerous times under various conditions [5,6]. In this study, the infrared and Raman spectra of Adamantane were examined using the Gaussian 03 quantum chemistry package [7,8]. A detailed quantum chemical study will aid in making definitive assignments to the fundamental normal modes of Adamantane and in clarifying the considerable amount of experimental data available for this important molecule.

2. Method

For small molecules in the gas phase and in solution, Ab initio quantum chemical calculations can provide results approaching benchmark accuracy and they are used routinely to complement experimental studies. The vibrational frequencies of Adamantane were calculated at the Hartree–Fock and DFT (B3LYP) levels of theory using the 6-311+G** basis set. The calculations utilized the T_d symmetry of the Adamantane molecule (see Fig. 1). The computations were performed using the Gaussian 03 Program Package. Each of the vibrational modes was assigned to one of eight types of motion (C–C stretch, C–H stretch, C–C–C bend, CH bend, CH₂ scissors, CH₂ twist, CH₂ wag, and CH₂ rock) by means of visual inspection using the Gaussview program. Also the isotropic ^1H and ^{13}C chemical shifts for Adamantane have been considered. Adamantane is almost ideal model system for a study of both the ^1H and ^{13}C chemical shifts. In this study we have optimized geometries of Adamantane and calculated NMR parameter for it.

**Fig. 1.** Structure of adamantane**3. Results and discussion**

The third type carbon bending (γ) was calculated at 1030 and 1091 cm^{-1} (scaled frequencies are reported) in B3LYP/6-311+G** and HF/6-311+G** respectively. These vibrations have zero intensity in both IR and Raman spectra. CH₂ scissoring motions were calculated at 1444 and 1453 cm^{-1} in B3LYP/6-311+G** and HF/6-311+G** respectively and analogous experimental signal was appeared at 1435 cm^{-1} . A strong Raman band at 1220 cm^{-1} was assigned as CH₂ twisting (coupled with CH bending) motion and was calculated at 1208 and 1210 cm^{-1} in B3LYP/6-311+G** and HF/6-311+G** respectively. Another pretty strong Raman band at 1096 cm^{-1} was assigned as CH₂ Rocking motion (coupled with CH bending) and was calculated at 1088 and 1091 cm^{-1} in B3LYP/6-311+G** and HF/6-311+G** respectively. The isotropic chemical shifts δ with respect to TMS are 34.6845, 26.4291, 1.3525, 1.2954 (HF) and 42.8466, 35.7069, 1.8520, 1.7936 (B3LYP) of C(2), C (3), H(2) and H (3) respectively. The ΔG_{solv} of Adamantane is -0.65 kcal/mol at B3LYP.

4. Conclusions

In this paper, we report for the first time the experimental Raman spectra for Adamantane. These spectra have been nearly completely assigned, by comparison with computed vibrational frequencies and Raman intensities derived from density



functional and Hartree Fock theory computations. Calculated and experimental frequencies are generally in good agreement with each other. Also some of the properties for Adamantane were calculated.

References

- [1] Filik, J. Harvey, J. N. Allan, N.L. May, P.W. Dahl, J. E.P. Liu, S. Carlson, R.M.K, *Spectrochimica Acta Part A* 64 (2006) 681.
- [2] May, P. W. Ashworth, S. H. Pickard, C. D. O. Ashfold, M. N. R. Peakman, T and Steeds, J. W, *Phys. Chem. Comm.* 4 (1998).
- [3] <http://www.chm.bris.ac.uk/pt/diamond/diamondoids.htm>
- [4] Bayat, Z. Monajjemi, M, *Journal of physical and theoretical chemistry*, 5(2) (2008) 85.
- [5] Gough, K.M. Dwyer, J.R. R. Dawes, *Can. J. Chem.* 78 (2000) 1035.
- [6] Rao, R. Sakuntala, T. Deb, S.K. Roy, A.P. Vijaykumar, V. Godwal, B.K. Sikka, S.K. *J. Chem. Phys.* 112 (2000) 112.
- [7] Fort, R.C. Schleyer, P.V.R. *Chem. Rev.* 64 (1964) 277.
- [8] Landa, S. Hala, S. *Collect. Czech. Chem. Commun.* 24 (1959) 93.

Detonation performance of 1,4-bis(3,5-diamino-2,4,6-trinitrophenylamino)- 1,2,4,5-terazine as a new thermally stable energetic compound

M. A. Ghasemi^a, F. Seif^a and M. H. Keshavarz^a

^aDepartment of Chemistry, Malek-ashtar University of Technology, Shahin-shahr, Isfahan, Iran

(E-mail: gomesesh_a@yahoo.com)

Keywords: Energetic material, Detonation performance, Crystal density, Heat of formation, Stable explosive.

1. Introduction

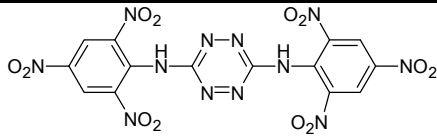
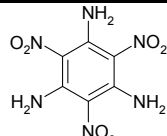
Energetic materials including explosives, propellants and pyrotechnics are used extensively for civil applications. There are strong requirements for explosives having good thermal stability, impact and shock sensitivity as well as better performance. The development of thermally stable explosives is a new line of research for space programmers, the drilling of deep oil wells etc., which is being actively pursued world-wide. The purpose of this work is to study 1,4-bis(3,5-diamino-2,4,6-trinitrophenylamino)- 1,2,4,5-terazine as a new thermally stable energetic compound. Various aspects of detonation performance containing detonation temperature (T_{det}), velocity (D_{det}) and pressure (P_{det}) have been computed by a new computer code [1]. Two new methods are used to calculate crystal density (ρ) [2] and solid phase heat of formation ($\Delta H_f(s)$) [3] as two inputs of computer code.

2. Results and discussion

The foremost objective for a new energetic compound consists of finding the molecule having both a good energy capability and optimal safety (reduced vulnerability, shock and impact sensitivity) to those in current use. Explosives with improved high temperature properties are usually termed as thermally stable explosives. Introduction of amino group into an aromatic ring is one of the simplest methods to improve the thermal stability of explosives [4]. A tetrazine based energetic compound 1,4-bis(3,5-diamino-2,4,6-trinitrophenylamino)- 1,2,4,5-terazine is a new explosive, which has considerably low hydrogen and high nitrogen content. There are several amino groups in this compound that can introduce it as a good heat resistance.

To evaluate detonation performance of 1,4-bis(3,5-diamino-2,4,6-trinitrophenylamino)- 1,2,4,5-terazine, it would be need to have its crystal density and solid phase heat of formation. Two new and reliable theoretical methods were used to calculate crystal density [2] and solid phase heat of formation [3]. 1,3,5-Triamino-2,4,6-trinitrobenzene (TATB) is an important insensitive and heat resistance explosive, which places it first on the list of thermally stable and safe explosives [4]. Detonation performance of 1,4-bis(3,5-diamino-2,4,6-trinitrophenylamino)- 1,2,4,5-terazine can be calculated by a new computer code [1]. Molecular structures and different detonation parameters of 1,4-bis(3,5-diamino-2,4,6-trinitrophenylamino)- 1,2,4,5-terazine and TATB are given in Table 1.

Table 1. Comparison of detonation properties of 1,4-bis(3,5-diamino-2,4,6-trinitrophenylamino)-1,2,4,5-tetrazine and TATB

	
$\rho = 1.913 \text{ g/cm}^3$	$\rho = 1.85 \text{ g/cm}^3$ [5]
$\Delta H_f(s) = 67.8 \text{ kcal/mol}$	$\Delta H_f(s) = -36.9 \text{ kcal/mol}$ [5]
$T_{det} = 3404 \text{ K}$	$T_{det} = 3238 \text{ K}$
$P_{det} = 286.1 \text{ kbar}$	$P_{det} = 259 \text{ kbar}$ [5]
$D_{det} = 8.04 \text{ km/s}$	$D_{det} = 7.66 \text{ km/s}$ [5]

3. Conclusions

As indicated, detonation parameters of 1,4-bis(3,5-diamino-2,4,6-trinitrophenylamino)- 1,2,4,5-terazine is higher than TATB. Thus, the overall comprehensive properties of 1,4-bis(3,5-diamino-2,4,6-trinitrophenylamino)- 1,2,4,5-terazine is better than TATB, which confirms the new energetic compound is a good candidate as a thermally stable energetic compound with high performance.



References

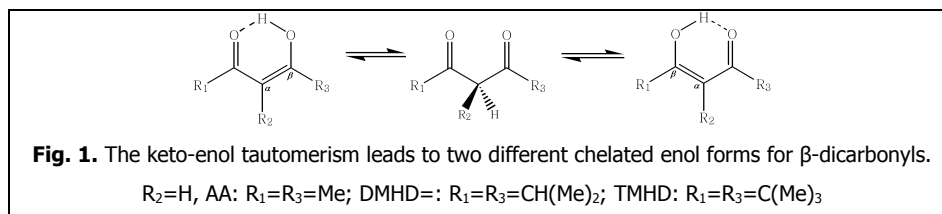
- [1] M. H. Keshavarz, H. Motamedoshariati, R. Moghayadnia, H. R. Nazari, J. Azarniamehraban, J. Hazard. Mater. "in press".
- [2] M. H. Keshavarz, J. Hazard. Mater. 165 (2009) 579.
- [3] M. H. Keshavarz, J. Hazard. Mater. 169 (2009) 890.
- [4] J. P. Agrawal, Prog. Energ. Combust. 24 (1998) 1.
- [5] M. L. Hobbs and M. R. Baer, Calibrating the BKW-EOS with a Large Product Species database and Measured C-J Properties, Tenth Symposium (International) on Detonation, Boston, MA, 1993.

Cis-enol conformers and intramolecular hydrogen bond strength of 2,6-Dimethyl-3,5-heptanedioneM. Vakili^{a,*}, S. H. Miremad^b, A-R. Nekoei^c^a Department of Chemistry, Sabzevar Tarbiat Moallem University, Iran^b School of Chemistry, Damghan University of Basic Sciences, Damghan, P.O. Box 36715-364, Iran

(E-mail: h_miramad2010@yahoo.com)

^c Department of Chemistry, Shiraz University of Technology, Shiraz, 71555-313, Iran**Keywords:** 2,6-Dimethyl-3,5-heptanedione, β -Dicarbonyl, Intramolecular hydrogen bond, Density functional theory.**1. Introduction**

Tautomerism equilibrium given in Fig. 1 shows that two keto-enol tautomerisms are possible for β -Dicarbonyls. The position of the keto-enol equilibrium for this class of compounds differs according to electronic characteristics of the substitution and the nature of the solvents. The cis-enol forms of β -dicarbonyl compounds are stabilized by a strong intramolecular hydrogen bond (IHB) with a double minimum character. The IHB of these compounds have been the subject of numerous investigations, which support the existence of a strong intramolecular hydrogen bond of chelating nature in the enol forms of β -dicarbonyl compounds [1–6]. The aim of the present paper is to predict IHB strength of 2,6-Dimethyl-3,5-heptanedione (DMHD) by means of density functional theory (DFT) levels and vibrational spectra.

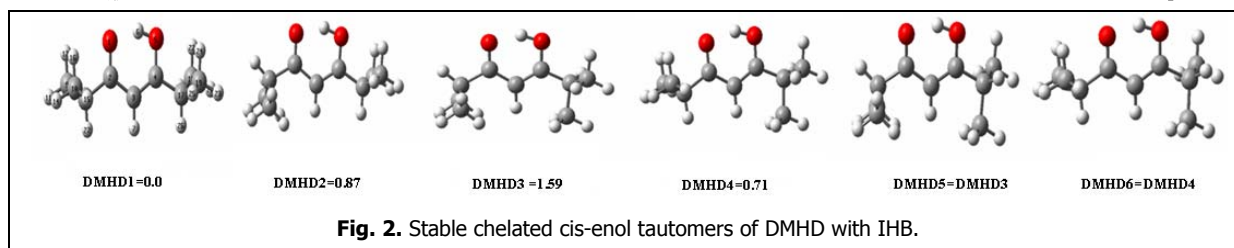
**2. Experimental and method of analysis**

DMHD compound purchased from Alfa Aesar chemical company. D₂-DMHD was prepared by mixing the DMHD with D₂O. The FT-IR, FT-Raman and Far-IR spectra were obtained on a Bomem MB-154 and Thermo Nicolet NEXUS 870 FT-IR spectrometers.

All calculations were performed using Gaussian 03W package program, B3LYP/6-311++G** for optimization all possible cis-enol conformations and B3LYP/6-311G** for calculation vibrational frequencies of the stable cis-enol forms.

3. Results and Discussion

The results were compared with those of acetylacetone (AA) and 2,2,6,6-tetramethyl-3,5-heptanedione (TMHD), the parent molecules. From the theoretical point of view, 23 cis-enol conformations can be drawn for DMHD molecule. Calculation shows that only 6 of these conformers are stable and the others do not show any stability and turn back to stable conformers by full optimization. The energy differences between these 6 stable chelated enol forms of DMHD, calculated at B3LYP/6-311++G**, are in the range of 0.7-1.6 kcal/mol which are shown besides their structures in Fig.2. The calculated IHB energies, EHB (the energy difference between the chelated cis-enol and non-chelated trans-enol conformers) and the averaged values for some geometrical and spectroscopic properties related to the IHB strength for DMHD, TMHD and AA are listed in Table 1. Comparing of these coordinates shows steric effects for t-Butyl and isopropyl groups in β positions which decrease O...O distance and increase IHB strength of TMHD and DMHD in comparison with that of AA (The average calculated O...O distance in DMHD conformers is about 0.024 Å shorter than that in AA). This increase in the hydrogen bond strength is also consistent with the experimental results (1H-NMR spectroscopy). According to the theoretical calculations, DMHD conformers have a hydrogen bond strength of about 16.4-16.5 kcal/mol (calculated at B3LYP/6-311++G** level of theory), which are about 0.6 kcal/mol stronger than the hydrogen bond of AA.



The IR spectra of DMHD and TMHD in the regions of γOH and $\nu_{\text{C}=\text{C}=\text{O}}$ are shown in Figs. 3-4. These regions indicate that the IHB in TMHD is considerably stronger than that in AA.

4. Conclusion

The comparison of some vibrational frequencies such as νOH , γOH and $\nu_{\text{C}=\text{C}=\text{O}}$ modes, observed NMR results and the calculated geometrical parameters confirm that substitutions of methyl groups with t-But and isopropyl groups in β positions of AA increase the strength of existing intramolecular hydrogen bond.

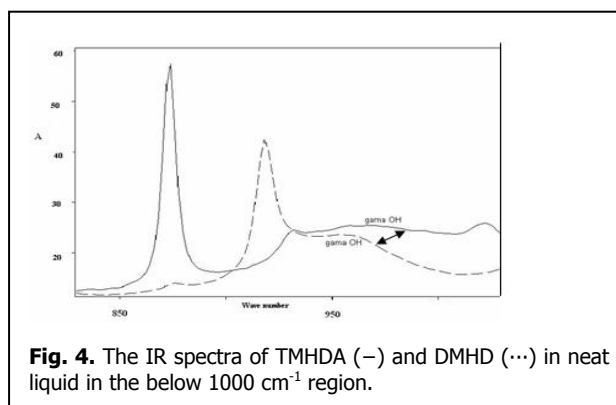
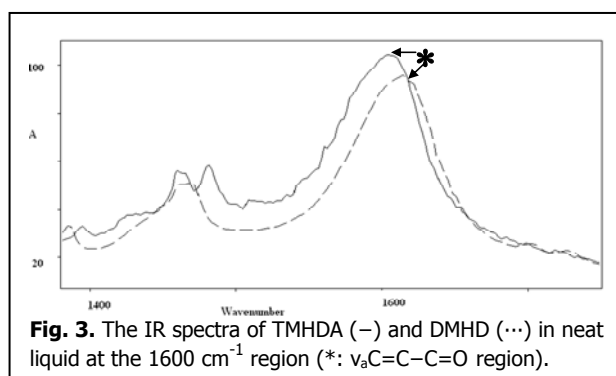
Table 1. Comparing several properties related to the hydrogen bond strength for TMHD, DMHD and AA.^a

Parameter	TMHD ^b	DMHD	AA ^b
δOH	16.27	15.65	15.40
νOH	2634	2720	2750
γOH	964	955	952
R O...O	2.508	2.520	2.544
R O-H	1.005	1.000	1.000
RH...O	1.575	1.598	1.620
$\angle\text{OHO}^\circ$	150.3	149.7	148.9
$E_{\text{HB}}(\text{kcal/mol})$	17.90	16.46	15.87

bond lengths in Å; δ , proton chemical shift in ppm; ν , and γ are stretching and out-of-plane bending frequencies in cm^{-1} , respectively.

^a calculated at the B3LYP/6-311++G** level.

^b Data from [6].



References

- [1] S.F. Tayyari, F. Milani-Nejad, Spectrochim. Acta 56A (2000) 2679.
- [2] S.F. Tayyari, M. Vakili, A.R. Nekoei, H. Rahemi, Y.A. Wang, Spectrochim. Acta 66A (2007) 626.
- [3] S.F. Tayyari, J.S. Emampour, M. Vakili, A.R. Nekoei, H. Eshghi, S. Salemi, M. Hassanpour, J. Mol. Struct. 794 (2006) 204.
- [4] S.F. Tayyari, A.R. Nekoei, M. Vakili, Y.A. Wang, J. Theor. Comp. Chem. 5 (2006) 647.
- [5] A-R Nekoei, S. F Tayyari, M. Vakili, S. Holakoei, A-H Hamidian, R-E Sammelson, J. Mol. Struct. 932 (2009) 112.
- [6] M. Vakili, H. Miremad, S. Salemi, A-R. Nekoei, paper submitted to 13th Iran Physical Chemistry Seminar.



Structures, stabilities and electronic properties analysis of substituted nano-scale polyhedral oligomeric silsesquioxane (T₈-POSS)

M. Hamadani^{a,b,*}, M. Sharif^a

^aFaculty of Chemistry, University of Kashan, Kashan, Iran

^bInstitute of Nano-Science and Nanotechnology, University of Kashan, Kashan, Iran

(E-mail: hamadani@kashanu.ac.ir)

Keywords: Silsesquioxane, Nanostructure, Nanocomposite, Hydrogen storage, DFT.

1. Introduction

Polyhedral oligomeric silsesquioxane (POSS) is a new class of lightweight, high- performance hybrid materials. It is called hybrid as the POSS molecules contain both inorganic (silica) and organic (carbon) molecules. This new generation material is supposed to combine the most beneficial molecular properties of both organic and inorganic systems.

POSS, essentially is a hybrid material (organic-inorganic) and falls in the category of nanostructured materials. This molecule has the potential to be used for preparation of nanocomposites. It is known that large-scale consumption of fossil fuels has been resulted in the gradual depletion of resources and used serious pollution to the global environment. Therefore, it is very important to look for alternatives for fossil fuels. Hydrogen is considered to be one of ideal energy resources to substitute the fossil fuels in the future.

Recently, some transition metal (TM)-doping- organic frame of this molecule has been reported that they have high reversible hydrogen storage capacity. The binding energies of such TM-H₂ metal complexes are intermediate between physisorption and chemisorption energies. Functionalized silsesquioxane complexes can be an effective and practical material for hydrogen storage.

2. Computational methods

Electronic-structure calculations have been performed to obtain structures, Stabilities and Electronic properties for the POSS (HSiO_{1.5})₈ cage and different octasubstituted POSS molecules (Figure 1: R=-H, -CH₃, -CH₂CH₃, -CH=CH₂, -CH₂NH₂, -CH₂CH₂NH₂, -CH₂CH₂F, -CH₂CH₂Cl -CH₂CH₂Br, -OH, -OCH₃, -OCH₂CH₃, -NH₂, -NH(CH₃)₂ and ...). All calculations were performed by using density functional theory (DFT), Becke-3 Lee-Yang-Parr (B3LYP) hybrid functional as implemented in GAUSSIAN03 code. Geometry optimizations were carried out using the 6-311G(d,p) basis sets.

In next step we have demonstrated computationally that substituting silsesquioxane with transition metal atom (Sc) supported on isolated organic molecules such as cyclopentadiene can bind up to some hydrogen atoms in nearly molecular form. The origin of this bonding is due to the open d-shell nature of the transition metal atoms and has been discussed by Kubas and other authors more than a decade ago. Since, POSS with R=-CH₂NH₂ has a shortest gap bond between derivatives, this molecule was selected and its ability in hydrogen storage capacity was calculated. All the hydrogen storage theoretical calculations were performed by GAUSSIAN03 and AIM2000 programs.

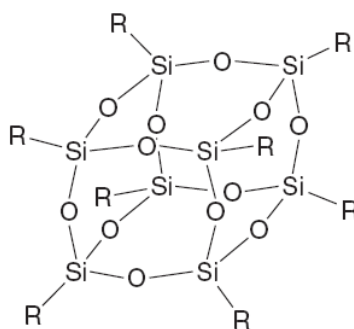


Fig. 1. Molecular structure of (RSiO_{1.5})₈

3. Results and discussion

In Table 1, the total energy, highest occupied molecular orbital (HOMO), lowest unoccupied molecular orbital energy (LUMO) and Dipole moment of different substituted POSS have been reported.

Table 1. Total energy, HOMO, LUMO Energies, HOMO-LUMO gap and Dipole moment of (RSiO_{1.5})₈ calculated in level of B3LYP/6-311G(d,p)

R	E(HF)	E _{HOMO} (ev)	E _{LUMO} (ev)	E _{LUMO} -E _{HOMO}	Dipole moment
-H	-3225.138	-0.343	0.040	0.383	0.0048
-CH ₃	-3539.893	-0.317	0.056	0.373	0.0021
-CH ₂ CH ₃	-3854.454	-0.300	0.042	0.342	0.0535
-CH=CH ₂	-3844.545	-0.282	-0.017	0.265	1.0195
-CH ₂ NH ₂	-3982.707	-0.238	0.018	0.256	0.1990
-CH ₂ CH ₂ NH ₂	-4297.341	-0.237	0.039	0.276	2.8569
-CH ₂ CH ₂ F	-4648.535	-0.340	0.018	0.358	0.3728
-CH ₂ CH ₂ Cl	-7531.435	-0.313	-0.017	0.296	0.7994
-OH	-3827.546	-0.317	-0.031	0.286	1.2850
-OCH ₃	-4142.001	-0.297	-0.037	0.260	6.3311
-OCH ₂ CH ₃	-4456.644	-0.294	-0.040	0.334	6.3036

For more detailed information about hydrogen bonding in (Sc-C₅H₄)(CH₂NH₂)₇Si₈O₁₂ complex, we have investigated successive adsorption of one, two, three, and more hydrogen molecules using AIM2000 program.

When one H₂ is introduced, it dissociates and binds atomically to Sc. The distance between these two H atoms is 3.07 Å, and they are 1.831 Å away from Sc. However, when two, three and more H₂ molecules are successively introduced, they bind nearly molecularly.

As we know, the gap between the HOMO and LUMO can indicate the kinetic stability of a system. The results show that as the by adding the H₂ molecules the HOMO-LUMO gaps increase.

4. Conclusion

Density Functional Theory calculations have been carried out to determine the structural and Electronic properties for substituted polyhedral oligomeric silsesquioxane macromolecules.

In this work, we carried out a systematic study on the hydrogen binding properties of (Sc-C₅H₄)(CH₂NH₂)₇Si₈O₁₂ complex. Since Sc atom's valence shells are fewer than half-filled, no more than four or five hydrogen molecules can be bound to organometallic compound. Furthermore, the HOMO-LUMO gap of (Sc-C₅H₄)(CH₂NH₂)₇Si₈O₁₂ increases by adding the H₂ molecule, which displays the kinetic stability. It is also found that the 18-electron rule is applicable to ScC₅H₅, for the maximum number of hydrogen molecules which can be added.

References

- [1] M. Joshi, B. S. Butola, Polymer Reviews 44 (2004) 389.
- [2] H. Ch. Li, Ch. Y. Lee, C. McCabe, A. Striolo, M. Neurock, J. Phys. Chem. A 111 (2007) 3577.
- [3] B. Kiran, A. K. Kandalam, P. Jena, J. Chem. Phys. 124 (2006) 224703.
- [4] Q. Sun, Q. Wang, P. Jena, B. V. Reddy, M. Marquez, Chem. Mater. 19 (2007) 3074.



Ab initio and DFT studies, NBO and NICS analysis of the decomposition ([2+2]elimination) mechanisms of 3-halo-2,3-dihydropyridine

H. Nemat-Talab^a, H. Shirani^{a,b,c,*}, S. Jameh-Bozorgi^{a,b}, A. Bodaghi^a, J. Hosseini^a

^aChemistry Department, Faculty of science, Islamic Azad University, toyserkan branch, toyserkan, Iran

*(E-mail: shiranihossein@gmail.com)

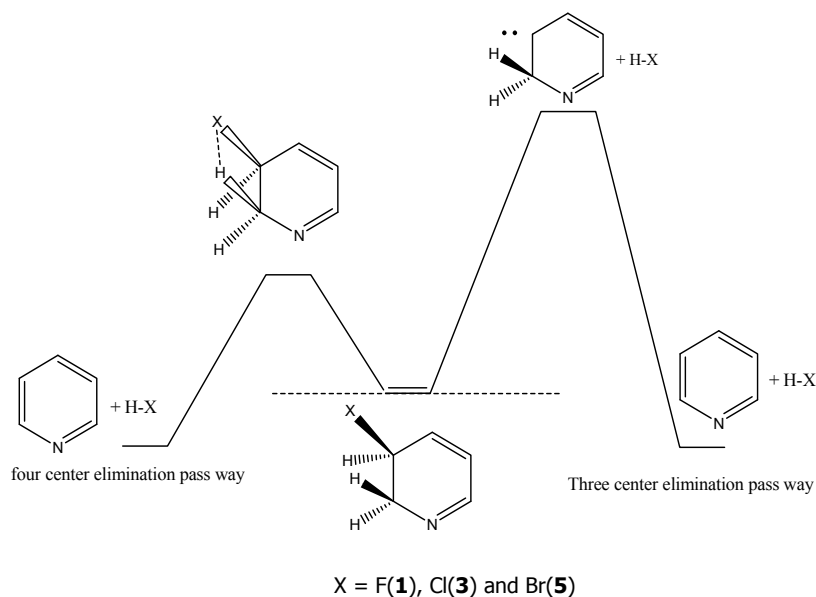
^bChemistry Department, Faculty of science, Islamic Azad University, Arak Branch, Arak, Iran

^cYoung researchers Club, Islamic Azad University, Toyserkan Branch, Toyserkan, Iran

Keywords: Ab initio, NBO, NICS, Elimination, 3-halo-2,3dihydropyridine

1. Introduction

The decomposition mechanism of 3-halo-2,3-dihydropyridines to pyridine and HX(X=F, Cl, Br) was investigated using ab initio Molecular Orbital (MO) and Density Functional Theory (DFT) [1]. The experimental study of the kinetic of dissociation process of 3-halo-2,3-dihydropyridinies, investigated by Liu [2], showed that the decomposition reaction is a unimolecular process and the occurred from two pass ways, three centered and four centered transition state. (See scheme 1).



Scheme 1.

2. Computational method

Ab initio calculations were carried out using B3LYP/6-311+G**, HF/6-311+G**// B3LYP /6-311+G**, and MP2/6-311+G**// B3LYP /6-311+G** levels of theory with the GAUSSIAN 98 package of programs [3] implemented. Initial estimation of the structural geometry of the compound **1**, **3** and **5** were obtained by a molecular mechanic program PCMODEL (88.0) [4] and for further optimization of geometry, we used the PM3 method of the MOPAC 7.0 computer program [5]. The GAUSSIAN 98 package of programs were finally used to perform ab initio calculations at the B3LYP/6-311+G** level [6]. These geometry structures were reoptimized by the QST2 subroutine.

3. Results and discussion

Zero point (ZPE) and total electronic (E_e) energies ($E_0 = ZPE + E_e$) for the energy minimum and energy maximum geometries of the decomposition of compound **1**, **3** and **5** to pyridine as calculated. Value of dihedral angles in transition state showed the planar structure for transition state. This form is the best structure for H-X dissociation. Internal dihedral angles in the heterocycle structures of reactants and products revealed that reactants are non-planar (non-aromatic) but products are planar and aromatic. The NBO analysis of donor-acceptor interactions showed that the C-C bond in reactant is a single bond. NICS values in ring center, 0.5 and 1 angstrom upper than ring center and magnetic susceptibilities are present at table1.

**Table 1.** Calculated NICS values at GIAO/B3LYP/6-311+G** and Magnetic susceptibilities at CSGT/B3LYP/6-311+G** level of theory for the energy minima structures.

compounds	X=F			X=Cl			X=Br		
	1	T.S	product	3	T.S	product	5	T.S	product
NICS(0)	2.626	0.2204	-6.75	2.851	5.265	-7.316	3.173	7.887	-7.880
NICS(0.5)	-	-0.931	-9.227	-	4.358	-9.620	-	7.338	-10.017
NICS(1)	-	-2.476	-10.151	-	2.654	-10.318	-	5.685	-10.288
χ	-44.058	-42.10	-54.836	-57.137	-34.03	-74.898	-66.547	-29.39	-88.255

4. Conclusion

NBO analysis revealed that resonance energies in products are greater than reactants. therefore, number of conjugated π bond increased in products. Also, NICS results showed that reactants are non-aromatic but products are aromatic compounds. This results showed that the four-membered transition state for this elimination ractione is a planar structure.

Acknowledgment

We thank the Islamic Azad University, toyserkan branch for financial support and research facilities.

References

- [1] Z. Chan, C. S. Wannere, C. corminboeuf, R. Puchta, and P. V. R. Schlyere, Chem. Rev. 105 (2005) 3842.
- [2] M. J. Frisch, G. W. Trucks, H. B. Schlegel, G. E. Scuseria, M. A. Robb, J. R. Cheeseman, et al.,GAUSSIAN 98 (Revision A.3) Gaussian Inc. Pittsburgh, PA, USA, (1998).
- [3] N. H. Martin, J. E. Rowe, E. L. Pittman, J. Mol. Graphics and Modeling, 27 (2009) 853.
- [4] Serena Software, Box 3076, Bloomington IN, USA.
- [5] J. J. P. Stewart, J. Comput.-Aided Mol. Des., 4 (1990) 1.
- [6] S. Kuns_agi-M_at_e, E. V_egh, G. Nagy, L. Koll_ar, J. Phys. Chem. A 106 (2002) 6319.

Quantum mechanical study on all chloroanilines as candidate monomers for conducting polymers (as nano-wires)

H. Shirani^{a,b,c,*}, S. Jameh-Bozorgi^{a,b}

^aChemistry Department, Faculty of science, Islamic Azad University, toyserkan branch, toyserkan, Iran

*(E-mail: shiranihossein@gmail.com)

^bChemistry Department, Faculty of science, Islamic Azad University, Arak Branch, Arak, Iran

^cChemistry Department, Faculty of science, UniVersity of Isfahan, Isfahan, Iran

Keywords: DFT-B3LYP, NBO-charge, chloroanilines, Conducting polymers, Nano-Wires.

1. Introduction

Conducting polymers because of change in their optical and electrical properties in nanometeric dimension are most probable systems for nanoelectrical applications [1]. Polyanilines can produce one-dimension morphologies, such as polymer nanostructures (nano-tube, -wire, -fiber, -filament –rod, -composite and –particle) the most researches is done about that [2]. Nanomaterials paid attentions more scientists to itself because of the high applications of nanotechnology in different sciences such as: medicine, petrochemical, materials, electronic, quantumic computers, etc [3]. Conductive polymers are typical of materials that play important roles in nanomaterial field [4].

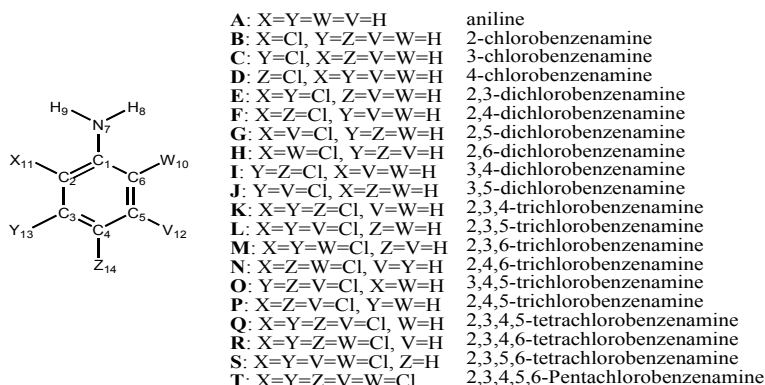


Fig. 1. All possible mono-, di-, tri-, and tetrachlorothiophene isomers studied in this research.

2. Methods

Initially, structures of representative mono-, di-, tri-, and tetra-chlorothiophenes were fully optimized using Density Functional Theory (DFT) B3LYP method using the 6-311++G** basis set as implemented in the Gaussian 98 program package (G98W) [5]. The natures of the optimized stationary points were all characterized by frequency calculations at the same level of theory with the same basis set.

3. Results and Discussion

To predict the bonding-characteristic behavior of the chloroaniline rings in their corresponding polymer chains and to determine the extent of the π -conjugation character of these polymers, we have used the F_n coefficient for each thiophene ring in the isolated chloroanilines. The calculated values of the F_n coefficient for all chloroanilines and their cations shown that the molecule B have the smallest values of the F_n coefficient. Therefore, the quinoid character of monomer B is greater than that of other chloroanilines.

For all chloroanilines and their cations, the positive charge is distributed mainly on the C3 position in Figure1, whereas spin density is distributed mainly on the C4 position in Figure 1. In both series of molecules and their cation radicals, charge- and spin-density distributions have similar trends with the number and position of the substituted fluorine atoms. The analysis carried out on the calculated dipole moments shows that the size and direction of the dipole moment vector depend mainly on the position (symmetry) of substituents rather than on the number of substituents. Furthermore, the orientation of the dipole moment vector is toward the nitrogen atom for all fluorothiophenes. It can also be seen that the size of the dipole moment



vector for monomer B is greater than all chloroanilines. It can be said that the electrochemical stability of monomer B is greater of all fluorothiophenes. The low-frequency values for all of the compounds are higher than for aniline. Thru mono-fluorine compounds, compound B has higher low-frequency values. This means that this compound have the largest force constants for their bending modes of vibration. Also HLG values for all of the chloroanilines is very good for transit than valance band to conducting band. NICS results showed that compound B has the largest quantity of negative value; therefore, this compound has the largest electrical current and conductivity.

4. Conclusion

Chloroanilines have been designed as monomers for conductive polymers in the hope of having modified chemical and electrical properties.

Ab initio and density functional theory DFT-B3LYP/6-311++G** calculations have been carried out successfully to study the structural, electronic, electrochemical, and spectroscopic properties of all chloroanilines. Compared to aniline, B monomer is more soluble in water and has a lower potential energy to form cations. These characteristics increase the efficiency of the electrochemical polymerization processes on this monomer.

References

- [1] M. S. Ram, Srinivasan Palaniappan, J. Molecular Catalysis 201, (2003) 289.
- [2] In Encyclopedia of Nanoscience and Nanotechnology, Vol. 2, H. S. Nalwa (Ed.), pp. 105–131, American Scientific Publishers, Los Angeles (2004).
- [3] X. Zhang, W. J. Goux, S. K. Manohar. J. Am. Chem. Soc., 126, (2004) 4502.
- [4] Gordon G. Wallace, Geoffrey M. Spinks, Leon A. P. Kane-Maguire, Peter R Teasda, Conductive electro active
- [5] Z. Chan, C. S. Wannere, C. corminboeuf, R. Puchta, and P. V. R. Schlyere, Chem. Rew, 105 (2005) 3842.

**Computational investigation on N₁₄, N₁₆, N₁₈ and N₂₀: A discrepancy between conjugated pentagons and stability**

Jamshid Najafpour*, Farrokh Roya Nikmaram, Maryam Kordi Peykani

Department of Chemistry, Faculty of science, Islamic Azad University Shahr-e-Ray Branch, Tehran, Po. Box: 18155/144, Iran

(E-mail: j.najafpour@gmail.com)

Keywords: Nitrogen cluster, Conjugated pentagon, Stability, Nano cluster, DFT method**1. Introduction**

Among the high-energy density materials (HEDMs), nitrogen clusters have been the subject of intense interest in the past 25 years. In these investigations, the studies of stability and bonding have received great attentions.

When nitrogen atoms are forming a three dimensional cluster, three equivalent single bonds are required for each atom. These three bonds are usually formed with the polarized sp³ type or delocalized sp³ type of structure. The favored bond angles of these bonds in each atom are usually more or less near to the tetrahedral angle (109°). The self-consistent field type optimized rings in the cluster of molecular orbital (MO) calculation are usually in favor of planar or near to the planar local ring structure due to the delocalization effect. In the planar regular polygonal rings, the inside bond angles of a triangle is 60°, of a square is 90°, of a five-membered ring is 108°, of a six-membered is 120°, of a seven-membered is 129° and of a eight-membered is 135°. If one compares these angles with the sp³ type of angle as shown above, it is not difficult to find out that 108° of five-membered ring is the most suitable local structure for the nitrogen clusters. Consequently, for the planar or nearly planar rings, small rings with a size of 3 or 4 get the prominent negative bond angular deviation from the sp³ angle ($\Delta\theta = 60^\circ - 109^\circ = -49^\circ$ for the size 3 and $\Delta\theta = 90^\circ - 109^\circ = -19^\circ$ for the size of 4); large rings with sizes of 7 or 8 get the prominent positive bond angular deviation from the sp³ angle ($\Delta\theta = 135^\circ - 109^\circ = 26^\circ$ for the size of 8 and $\Delta\theta = 129^\circ - 109^\circ = 20^\circ$ for the size of 7). Both of these negative and positive deviations from sp³ angle will cause the large angular strain for the single-bond-based nitrogen clusters [1].

The energy difference between the dodecahedral N₂₀ and octaazacubane N₈ for each nitrogen atom is $\Delta E(E_{SCF}(N_{20})/20 - E_{SCF}(N_8)/8) = -8.35 \text{ kcal mol}^{-1}$ at the MP2/DZP level [2,3]. The N-N bond lengths in N₂₀ (I_h) are 1.503 Å, 0.026 Å shorter than the N-N bond lengths in octaazacubane N₈. As a comparison, the averaged value of single and double N-N bond length in N₄ (D_{2h}) is 1.413 Å at the same theoretical level [4]. A reasonable explanation for these phenomena is that the aromaticity caused by delocalized interaction of the lone pairs of nitrogen atoms in the conjugated pentagons stabilizes N₂₀ and shortens the N-N bond lengths. The quantum chemistry calculation on the cage-like structure of N₁₈ (C_{2v}) at B3LYP/6-31G* level has also shown the similarity with N₂₀. The energy difference between the cage-like N₁₈ which has eight conjugated pentagons, and octaazacubane N₈ for each nitrogen atom at the B3LYP/6-31G* level is $\Delta E(E_{SCF}(N_{18})/18 - E_{SCF}(N_8)/8) = -9.285 \text{ kcal mol}^{-1}$ [5], 0.762 kcal mol⁻¹ less than the difference between the fully conjugated pentagon formed dodecahedral N₂₀ and N₈ (O_h). The energy difference between N₂₀ and N₈ is $\Delta E(E_{SCF}(N_{20})/20 - E_{SCF}(N_8)/8) = -10.047 \text{ kcal mol}^{-1}$ at the same level [5]. The averaged N-N bond length in N₁₈ (C_{2v}) is 1.4911 Å, 0.030 Å shorter than the N-N bond length in octaazacubane [5]. Based on the aromaticity assumption, the cage-like polynitrogen cluster N₁₈, which contains fewer conjugated pentagons than dodecahedral N₂₀, should be less stable than N₂₀.

2. Computational details

In the present study, we report new quantum chemical calculations for nano N_n clusters (n=14, 16, 18 and 20) by the density functional theory (DFT) with the exchange-correlation potential that constructed from Becke's three parameter formula for exchange (B3) [6] along with the Lee-Yang-Parr parameterization for correlation (LYP) [7]. These calculations were performed within a valence double-z basis set augmented with both diffuse and polarization functions (aug-cc-pVDZ). This basis set was contracted as: (10s5p2d/4s3p2d) and used pure spherical harmonic (i.e. 5 d-type), one-particle Gaussian functions. Ab initio calculations have been performed using Spartan'08 [8] and WinGAMESS.08 [9].

For comparing the stability of the atomic energy for each cluster, we calculated the average atomic energies (AE) with energy of atomization, i.e., sum of value of total electronic energy and zero point energy divided by the number of atoms (n) in the molecule as:

$$\overline{AE} = \frac{(E_t + ZPE)_{N_n}}{n}$$

3. Results and discussion

The geometric optimized structures of the N-N single bonded N_{14} , N_{16} , N_{18} and N_{20} clusters with D_{3h} , D_{4d} , C_{2v} and I_h symmetry (respectively) is shown qualitatively in Figure 1.

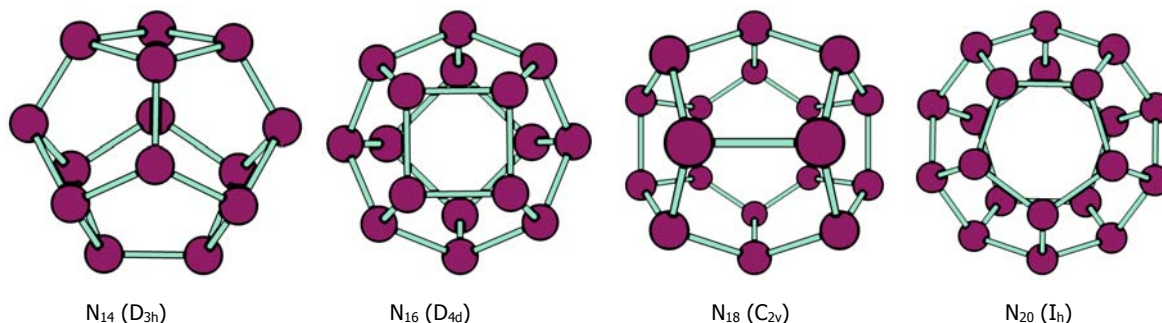


Fig. 1. The geometric optimized structures of cage-like single bonded polynitrogen N_n ($n=14, 16, 18$ and 20) clusters

At the B3LYP/aug-cc-pVDZ level of theory, the calculated energy difference between N_{14} (D_{3h}) and octaazacubane N_8 (O_h) is $\Delta E(\overline{AE}(N_{14})/14 - \overline{AE}(N_8)/8) = -10.097 \text{ kcal mol}^{-1}$, $0.357 \text{ kcal mol}^{-1}$ less than the difference between N_{16} (D_{4d}) and $N_8(O_h)$. The energy difference between N_{16} and N_8 is $\Delta E(\overline{AE}(N_{16})/16 - \overline{AE}(N_8)/8) = -10.454 \text{ kcal mol}^{-1}$ at the same level. This result confirms the conclusion that N_{16} is more stable than N_{14} in energy. At the B3LYP/aug-cc-pVDZ level of theory, the calculated energy difference between N_{18} (C_{2v}) and octaazacubane N_8 (O_h) is $\Delta E(\overline{AE}(N_{18})/18 - \overline{AE}(N_8)/8) = -9.044 \text{ kcal mol}^{-1}$, $0.357 \text{ kcal mol}^{-1}$ less than the difference between the fully conjugated pentagon-formed dodecahedral N_{20} (I_h) and $N_8(O_h)$. The energy difference between N_{20} and N_8 is $\Delta E(\overline{AE}(N_{20})/20 - \overline{AE}(N_8)/8) = -9.882 \text{ kcal mol}^{-1}$ at the same level. This result confirms the conclusion that N_{20} is more stable than N_{18} in energy.

The cage-like N_{18} , N_{16} and N_{14} have eight, eight and six conjugated pentagons respectively. It seems the dodecahedral N_{20} must be more stable than the others but we have obtained the cage-like N_{16} with the most stability. The thermodynamic stability order of average atomic energy the four cage-like (N_{14} , N_{16} , N_{18} and N_{20}) clusters toward to octaazacubane is $N_{16} > N_{14} > N_{20} > N_{18}$. These results are in discrepant with the relevance of number of conjugated pentagons in cage-like nitrogen clusters and stability of average atomic energy toward octaazacubane N_8 that reported previously [5].

References

- [1] C. Chen, K.C. Sun, Int. J. Qunt. Chem. Qunt. Chem. Symp. 30 (1996) 1709.
- [2] M.L. Leininger, CD. Sherrill, H.F. Schaefer III, J. Phys. Chem. 99 (1995) 2324.
- [3] A.A. Bliznyuk, M. Shen, H.F. Schaefer III, Chem. Phys. Lett. 198 (1992) 249.
- [4] W.J. Lauderdale, J.F. Stanton, R.J. Bartlett, J. Phys. Chem. 96 (1992) 1173.
- [5] J.-D. Gu K.-X. Chen H.-L. Jiang, J.-Z. Chen, R.-Y. Jia, Y. Renb, A.-M. Tian, J. Mol. Struct. (Theochem) 428 (1998) 183.
- [6] A.D. Becke, J. Chem. Phys., 98 (1993) 5648.
- [7] Lee, W. Yang, R.G. Parr, Phys. Rev., B37 (1988) 785.
- [8] Spartan '08, Version 1.0.0, B.J. Deppmeier, A.J. Driessen, T.S. Hehre, W.J. Hehre, J.A. Johnson, P.E. Klunzinger, J.M. Leonard, I.N. Pham, W.J. Pietro, Jianguo Yu, Wavefunction, Inc., Irvine, CA 2008
- [9] M.W. Schmidt, K.K. Baldridge, J.A. Boatz, S.T. Elbert, M.S. Gordon, J.H. Jensen, S. Koseki, N. Matsunaga, K.A.Nguyen, S.J. Su, T.L. Windus together with M. Dupuis, J.A. Montgomery, J. Comput. Chem., 14 (1993) 1347.

Investigation of the geometry optimization and spectroscopy of *N,N*-Dimethyl-*N,N'*-bis(4-methylphenyl)phosphoramidate and comparison experimental results with quantum mechanic calculations

M.H. Akhbari shada, H. Hooshyara, B. Khezri a

(E-mail: akhbari.muhammadhossein@gmail.com)

aDepartment of Chemistry, Islamic Azad University Mahabad Branch, Islamic Azad University Mahabad, Iran

Key words: Organophosphorus compounds, X-ray crystal, Hartree-Fock, Hydrogen bonding, Chemical shifts

1. Introduction

Organophosphorus compounds are chemical compounds containing carbon-phosphorus bonds, primarily used in pest control and are often persistent organic pollutants [1]. The title compound belongs to a class of amides of arylphosphonic acid that is expected to have antibacterial properties. An earlier study of bis(4-nitrophenyl)-*N,N* dimethylphosphoramidate confirmed the double-bond character of the P-N bond to the dimethylamino group. This molecule was chosen as the model for the present study, because the synthesis and X-ray crystal structure analysis have been reported [2].

2. Calculations Details

All the calculations have been carried out with Gaussian view 3.01, Gaussian 03 by using the Hartree-Fock (HF) [3], density functional using Becke's three-parameter hybrid method [4] with the Lee, Yang, and Parr correlation functional methods[5](B3LYP) with the standard 6-31G and 6-31G* [6] basis sets. The vibrational frequencies were also calculated with these methods. ¹H- and ¹³C- chemical shifts were calculated with GIAO method using corresponding TMS shielding calculated at the HF /6-31G (d) level.

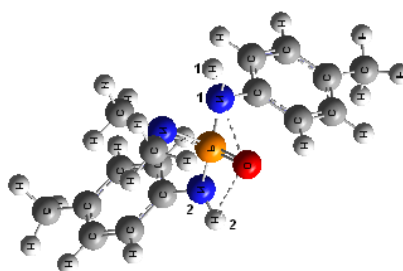


Fig. 1. The optimized molecular structure

3. Results and discussion

The compound was synthesized from the reaction of 4-toluidine and *N,N* dimethylaminophosphoryl dichloride in toluene at 268 K. Crystals were obtained by recrystallization of the product from chloroform/ethanol (1:1). In this work, we performed full geometry optimization of the title compound. **Figure 1** show the optimized structure of the title compound. The agreement for bond angles is not as good as that for the bond distances (**figure 2**).

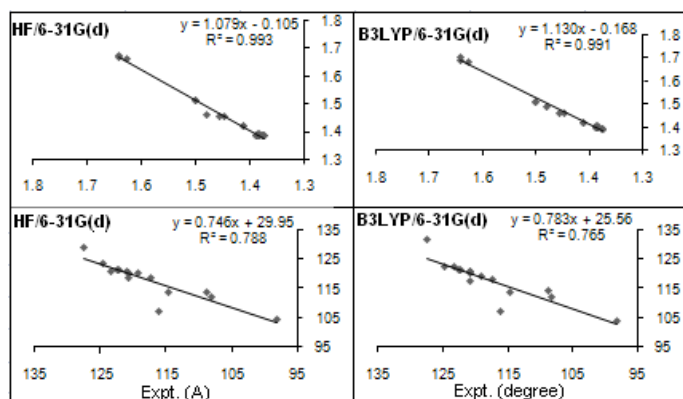


Fig. 2. Calculated bond lengths and bond angles in comparison with experimental data.



However, owing to our calculations, Hf/6-31G (d) method and basis set correlates well for the bond length and angle in comparison to the DFT method. Intermolecular hydrogen bonding geometry of the title compound computed at the HF/6-31G (d) method and basis set, and the major structural parameters are summarized in **Table 1**.

Table1. Intermolecular Hydrogen-bonding geometry (Å, °), using HF/6-31G (d) level

D-H...A	D-H	H...A	D...A	D-H...A
N1-H1...O	0.9988	3.1654	2.6998	53.86
N2-H2...O	0.9989	2.5108	2.5280	79.53

Calculated interaction energies including zero-point vibrational energy, SCF and thermal energy of the title compound at HF, B3LYP method and 6-31G, 6-31G (d) basis sets and selected properties are listed in **Table 2**.

Table2. Calculated zero-point vibrational energy, SCF and thermal energy for *N,N*-Dimethyl-*N'*,*N''*-bis(4 methylphenyl)phosphoramidate

Parameter	HF		B ₃ LYP	
	6-31G	6-31G(d)	6-31G	6-31G(d)
E _{SCF}	-1197.2442	-1197.7008	-1203.5176	-1203.8460
ZPE	0.386965	0.385603	0.361679	0.360253
thermal energy	-1196.8572	-1197.3152	-1203.1559	-1203.4858

We have calculated the theoretical vibrational spectra of title compound by using HF and B3LYP, methods with 6-31G, 6-31G (d) basis set. The vibrational bands assignments have been made by using both the animation option of GaussView 3.0 graphical interface for gaussian programs. Frequency changes well reflect the geometry changes. The ¹H and ¹³C NMR chemical shifts were referenced to TMS: δ ¹H and ¹³C (CH₃)₄Si=0.00 ppm. **Table 3** give the calculated NMR chemical shifts at HF /6-31G(d) levels of *N,N*-Dimethyl-*N'*,*N''*-bis(4 methylphenyl)phosphoramidate after subtraction of the value of tetramethylsilane calculated at the same level of theory.

Table3. ¹³C NMR and ¹H-NMR chemical shift, ppm from TMS, δTMS = 0.00, of *N,N*-Dimethyl-*N'*,*N''*-bis(4 methylphenyl)phosphoramidate

Atomic specific	¹³ C NMR	Atomic specific	¹ H-NMR
C1 : C8,9	141.92 -131.79	H1 : H35,36,37,38	6.718 -7.852
C2 : C14,15,16,17	122.90- 134.68	H2 : H31,32,33,34	6.343 -8.316
C3 : C18,19	123.75 - 140.17	H3 : H23,24,25,26,27,28	1.552 -3.989
C4 : C10,11,12,13	135.09 - 110.88	H4 : H39,40,41,22,42,43	2.707 - 1.701
C5 : C3,4	38.27931.455 -		
C6 : C20,21	20.182 - 21.803		

References

- [1] Quin, L. D. A Guide to Organophosphorus Chemistry; John Wiley & Sons, 2000.
- [2] K. Gholivand, A. Tadjarodi, A. Taeb , G. Garivani, Acta Cryst. 57 (2001) 472.
- [3] M. Begtrup, G. Boyer, P. Cabildo, C. Cativiela, R.M. Claramunt, J. Elguero, J.I. Toiron, P. Vedsø, Magn, Reson. Chem. 31 (1993) 107.
- [4] A.D. Becke, J. Chem. Phys. 98 (1993)5648.
- [5] C.T. Lee, W.E. Yang, R.G. Parr, Development of the Colle–Salvetti Correlation–Energy Formula into a Functional of the Electron–Density Phys Rev. 37 (1988) 785.
- [6] P.C. Hariharan, J.A. Pople, Theor Chim Acta. 28 (1973) 213.

**Existence and characterization of HOO...HOOOH radical-molecule complexes: A computational study**Mohammad Solimannejad ^{a,*}, Shokofeh Massahi ^a, Steve Scheiner ^b^a Quantum Chemistry Group, Department of Chemistry, Arak University, Arak, Iran

(E-mail: m-solimannejad@araku.ac.ir)

^b Department of Chemistry and Biochemistry, Utah State University, Logan, Utah, USA**Keywords:** Hydroperoxyl Radical, Dihydrogen Trioxide, Cooperativity**1. Introduction**

In recent years there has been increased interest in the study of radical-molecule hydrogen-bonded complexes, because of their importance in the chemistry of the atmosphere [1–3] and in biological [4,5] systems as well. The hydroperoxyl OOH radical participates in numerous oxidation reactions [6]. The existence of dihydrogen trioxide (HOOOH) has been confirmed in recent years [7,8]. Despite the potential importance of hydroperoxyl radical and dihydrogen trioxide in atmospheric chemistry, there is available in the literature neither theoretical nor experimental study of complexes pairing them together. This complex is of fundamental interest not only in that it pairs a radical with a neutral, but also that it is a highly oxygen-enriched system which presents a multitude of H-bonding options. The present work reports, for the first time, a detailed examination of the stabilities, electronic structure, and vibrational frequencies of HOO...HOOOH complexes.

2. Computational details

The geometries of the isolated HOO and HOOOH species and their dimer complexes were fully optimized at the UMP2/6-311++G(2d,2p) and M05-2x/6-311++G(2d,2p) computational levels. Additional calculations were carried out at the CCSD(T) level, using a cc-pVTZ basis set. The Atoms in Molecules (AIM) methodology was used to analyze the electron density of the systems considered at the UMP2/6-311++G(2d,2p) computational level. The Natural Energy Decomposition Analysis (NEDA) within the Natural Bond Orbital methodology has been performed to obtain insight of the source of the interaction energy.

3. Results and discussion

The HOOOH molecule can occur in two different conformations: cis and trans conformers. Each of these two configurations can form a complex with the HOO radical, in several different structures. Three minima, designated S1, S2 and S4, were identified for the trans HOOOH conformer, and the cis conformer also coupled with HOO in three different minima (S3, S5, and S6). All three S1, S2, and S4 complexes containing trans HOOOH involve the donation of one HOOOH proton to the terminal O atom of HOO. Where they differ is related to the second H-bond. HOO donates a proton to the terminal O atom of HOOOH in S1, to the central O atom in S2, and to the first O in S4, the O atom that is also the proton donor in the other H-bond. Three structures of S3, S5, and S6 complexes are rather distinct from one another. S3 involves a pair of H-bonds, both angularly distorted, in which each molecule serves simultaneously as both proton donor and acceptor. There are also two H-bonds in S5, and both fairly linear. However, HOOOH serves as double donor, and HOO as double acceptor. This sort of arrangement typically involves negative cooperativity so it is not surprising that S5 is less stable than S3. There is only a single H-bond present in S6, accounting for its comparatively weak binding. S3 is the most stable of this set. A topological analysis of the electron density within the Atoms in Molecules (AIM) framework provides a variety of graphs illustrated in Fig. 1. The small values of the electron density and the positive values of the Laplacian and total energy density indicate that these intermolecular bonds correspond to weak interactions. The results of NEDA calculations indicate that charge transfer makes the largest contribution to the interaction in all cases, followed thereafter by electrostatic, and then exchange and polarization.

4. Conclusions

There are six minima on the potential energy surface of the OOH + HOOOH dimer. Three of these involve the cis and three the trans configuration of HOOOH. In four of these structures, the OOH radical acts as H-donor and H-acceptor simultaneously. Both molecules act simultaneously as proton donor and acceptor in the most stable dimer. Stabilization energies of studied complexes including BSSE and ZPE are in the range between 12 and 26 kJ mol⁻¹.

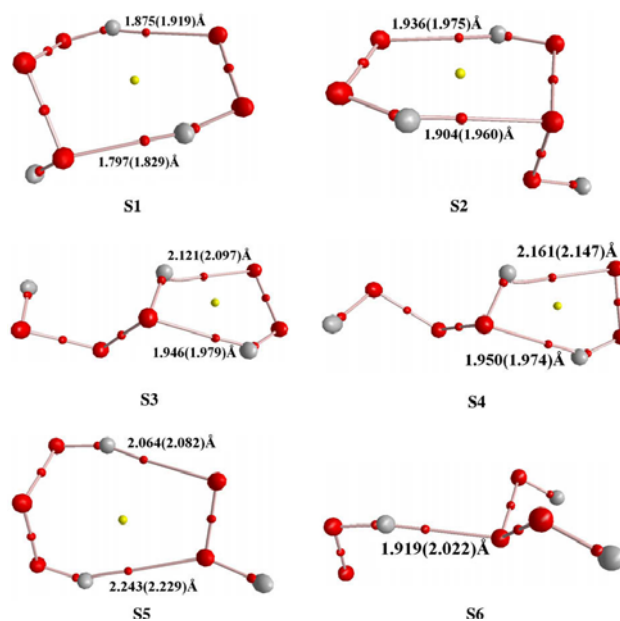


Fig 1. Molecular graph of the dimer minima obtained at the UMP2/6-311++G(2d,2p) computational level. The interatomic distances (Å) of those atoms that shows intermolecular interactions calculated at M05-2x/6-311++G(2d,2p) are shown in parenthesis.

References

- [1] R.L.T. Parreira, S.E. Galembeck, J. Am. Chem. Soc. 125 (2003) 15614.
- [2] J.M. Anglada, J. Am. Chem. Soc. 126 (2004) 9809. [3] S. Aloisio, J.S. Francisco, J. Am. Chem. Soc. 122 (2000) 9196.
- [3] M. Torrent-Sucarrat, J.M. Anglada, Chem. Phys. Chem. 5 (2004) 183.
- [4] B. Wang, H. Hou, Chem. Phys. Lett. 410 (2005) 235.
- [5] J. Espinosa-Garcia, J. Am. Chem. Soc. 126 (2004) 920.
- [6] R.P. Wayne, Chemistry of Atmospheres, second ed., Oxford University Press, Oxford, 1991.
- [7] P.T. Nyffeler, N.A. Boyle, L. Eltepu, C.-H. Wong, A. Eschenmoser, R.A. Lerner, P. Wentworth Jr., Angew. Chem. Int. Ed. 43 (2004) 4656.
- [8] K. Suma, Y. Sumiyoshi, Y. Endo, J. Am. Chem. Soc. 127 (2005) 14998.

Surface study and adsorption mechanism of 2-butanol over the (100) surface of γ -alumina: a dft study

H.A. Dabbagh*, M. Zamani

Catalysis Research Lab, Department of Chemistry, Isfahan University of Technology, Isfahan, Iran, 84156-83111

E-Mail: (dabbagh@cc.iut.ac.ir, m.zamani@ch.iut.ac.ir)

Keywords: γ -Alumina (100) surface, Adsorption, Dissociation, H-shift, DFT**1. Introduction**

Several papers have been reported for the adsorption of alcohols over the γ -alumina [1-3]. De Vito et al. [1] has been studied the adsorption of methanol. They have concluded that the methanol adsorbs on a tetrahedral aluminum ion forming a covalent bond. Cai and Sohlberg [2] computed the adsorption of methanol, ethanol, propanol, and iso-propanol over the γ -alumina (110) surface. They have show that all four alcohols considered chemisorb to the alumina surface when they come sufficiently close to surface with suitable orientation. Feng et al. [3] present a detailed theoretical study on isopropanol adsorption on both clean and hydrated γ -alumina (100) and (110) surfaces. They have considered all possible adsorption configurations in their calculation. In this study mechanism of adsorption, dissociation, and hydrogen-shift of adsorbed 2-butanol over the defect spinel (100) surface was investigated at DFT/BLYP (Becke-Lee-Yang-Parr) level of calculation.

2. Methods

DFT calculations were performed using the DMOL³ program [4,5]. The Double Numerical Plus Polarization function (DNP) and BLYP generalized gradient approximation were used in all calculations. To determine the activation energy for a specific reaction path, a transition state was identified by the complete linear synchronous transit (LST) method, and the quadratic synchronous transit (QST) method. Simulation of all reactions was performed under thermal condition.

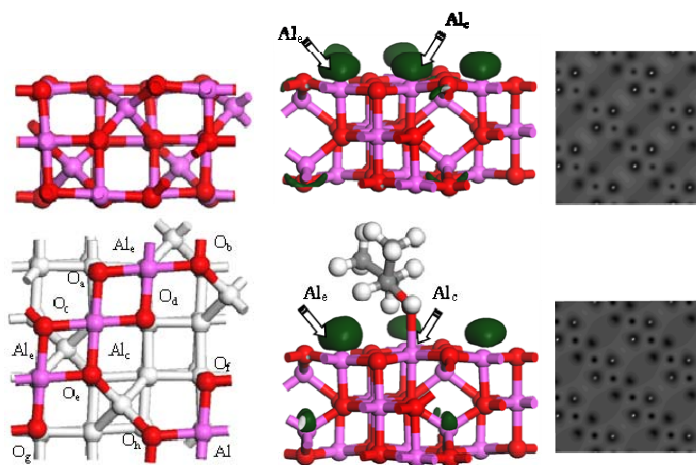


Fig. 1. Optimized geometry of bare γ -alumina (100) surface (left), front view (middle) and top view (right) of LUMO electronic contour of alumina surface before and after the adsorption of 2-butanol.

3. Results and discussion

2-Butanol is physisorbed on the surface at a distance of 2.05 Å. This distance is longer than that between Al and O atoms of the surface. By changing the central penta-coordinated aluminum atom (Al_c) into a hexa-coordinated aluminum atom, the surface bond lengths changed from 1.881 to 1.952 Å. The OH bond of the 2-butanol molecule formed a staggered conformation with Al-O bonds of the cluster (Fig. 1). For the adsorbed 2-butanol surface, the charge density of Al_c is 1.551 and for Al_e the charge densities are 1.384, 1.399. The charge density for pure hexa-coordinated aluminum is 1.635. This indicates that adsorption of 2-butanol on the surface reduces the charge density of Al_c , but increases the charge density (stronger Lewis acid site) on Al_e adjacent to Al_c . The charge density of Al_e of after adsorption of 2-butanol is higher than Al_e of bare surface. This feature was confirm by the lowest unoccupied molecular orbital (LUMO) electron contours of (100) surface before and after adsorption (Fig. 1). It was clear that the LUMO electron contour is reinforce on Al_e site after adsorption. The adsorption energy

of 2-butanol is $-29.95 \text{ kcal mol}^{-1}$. Dissociation energies for 2-butanol at different oxygen sites O_a and O_c are -35.14 and $-19.12 \text{ kcal mol}^{-1}$. The feasibility of proton migration of adsorbed alcohol $[R-O(H)-Al-O_{(a-h)} \rightarrow R-O-Al-O_{(a-h)}H]$ to adjacent oxygen of the surface was investigated (Fig. 2). Migration of the proton of alcohol to oxygen O_c is an endothermic process ($+9.19 \text{ kcal mol}^{-1}$) with a small activation energy ($13.56 \text{ kcal mol}^{-1}$). Migration of the proton to oxygen O_a is an exothermic process ($-6.83 \text{ kcal mol}^{-1}$) with a large activation energy ($69.34 \text{ kcal mol}^{-1}$). The proton shift is a kinetically controlled process. The pathway with larger E_a leads to a more stable product ($\Delta H^\circ = -6.83 \text{ kcal mol}^{-1}$) and the one with smaller E_a is responsible for the formation of a less stable product ($\Delta H^\circ = +9.19 \text{ kcal mol}^{-1}$). The distance that the proton must migrate to oxygen (O_a or O_c) of the surface controls this process. The distance for migration of the proton to site O_c is shorter than to site O_a . This makes the former proton transfer pathway more feasible. The $Al-O_{\text{alcohol}}$, $H-O_c$, bond lengths and H-bonding bond distance between H and O_{alcohol} [$Al-O_c-H \cdots O_{\text{alcohol}}-R$] are 1.818 , 1.033 and 1.578 \AA , respectively. This makes the $H-O_c$ bond longer than the normal $O-H$ bond. This type of hydrogen bonding was not observed for migration of the proton to O_a . The bond lengths of $Al-O_{\text{alcohol}}$ and $H-O_a$, were 1.758 and 0.985 \AA , respectively. The H-shift to site O_c will be much faster than to site O_a (higher E_a). The former is a kinetically controlled process and the latter a thermodynamically controlled process. The second factor that makes migration to O_c more favorable is the larger $HO_{\text{alcohol}}-AlO_c$ dihedral angle. The angles for proton migration to O_c and O_a are 49.80 and 48.60° , respectively. The third factor for the ease of proton migration to site O_c is the higher basic strength of the O_c oxygen. The Mulliken charge on O_c and O_a is -1.000 and -0.977 , respectively.

4. Conclusions

These results indicate that the physical adsorption of 2-butanol over the (100) alumina surface is exothermic. This process is more favor than chemical adsorption. The dissociation of physically adsorbed alcohol occurs by a hydrogen shift mechanism.

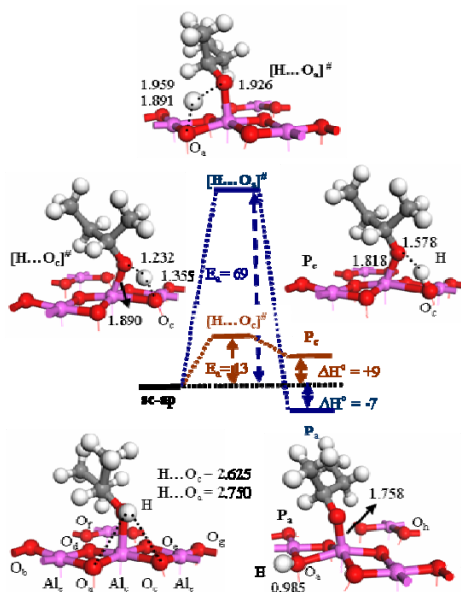


Fig. 2. Adsorption and calculated H-shift mechanism via oxygen atoms (O_c and O_a) of 2-butanol over (100) surface (E_a and ΔH° in kcal mol^{-1}).

References

- [1] D.A. De Vito, F. Gilardoni, L. Kiwi-Minsker, P.Y. Morgantini, S. Porchet, A. Renken, J. Weber, J. Mol. Struct., Theochem. 469 (1999) 7.
- [2] S. Cai, K. Sohlberg, J. Mol. Catal. A Chem. 193 (2003) 157.
- [3] G. Feng, C. Huo, C. Deng, L. Huang, Y. Li, J. Wang, H. Jiao, J. Mol. Catal. A Chem. 304 (2009) 58.
- [4] B. Delley, J. Chem. Phys. 92 (1990) 508.
- [5] B. Delley, J. Chem. Phys. 113 (2000) 7756.
- [6] B. Shi, B.H. Davis, J. Catal. 157 (1995) 359.

**NICS-rate as a new measure of aromaticity**

S. Noorizadeh* and M. Dardab

Chemistry Department, College of Sciences, Shahid Chamran University, Ahvaz, Iran

(E-mail: noorizadeh_s@scu.ac.ir)

Keywords: Aromaticity, Nucleus independent chemical shift (NICS), NICS scan**1. Introduction**

Aromaticity, the property resulting from cyclic conjugation, is an important concept in organic chemistry and has been subject of debate since the 19th century and is still an attracting considerable interest. Theoretical investigation for the origin of this concept has gained a rapid development. One of the most widely used magnetism-based index is the Nucleus-Independent Chemical Shift (NICS). This index [1] has been used extensively to assess the aromaticity and antiaromaticity of many organic and inorganic compounds. In some cases, however, using NICS values at the geometrical center of the ring (NICS(0)) may mislead or contradict other indices of aromaticity and therefore it seems that single NICS(0) value is not a very good tool for assessing whether a molecule is aromatic or not. Therefore, due to its conceptual imperfections, NICS has been refined considerably. Recently Stanger [2] developed the scheme of scanning the NICS values (NICS scan) up to a certain distance from the ring center.

The purpose of this paper is to introduce a new method for indication of aromaticity in cyclic compounds based on the analysis of NICS index variation at different distances from the center of the ring. This method, which is denoted as NICS-rate, is applied for both monocyclic and polycyclic molecular systems to assess the aromaticity and local aromaticity in these systems.

2. Theoretical Section

Overall 30 molecules are selected in this study, which are included aromatic, antiaromatic and nonaromatic systems with both monocyclic (20 molecules) and polycyclic (10 molecules) structures. The geometries of these molecules were optimized at the MP2 level with the 6-311++G** basis set, which was found to be the minimal satisfactory level. Using the MP2 optimized structures, NICS values were calculated at the HF/6-31+G* level of theory using the GIAO method. The probe (ghost atom, Bq) was placed at the ring center of each molecule (0.0 Å) and its distance was varied (up to 4 Å) perpendicular to the molecular plane at an interval of 0.2 Å. Gaussian 03 program was applied to perform all the calculations. The NICS-rate at a given distance from the center of the ring (*r*) was calculated using the difference between NICS values of two successive points ($\Delta\text{NICS} = \text{NICS}(r+0.2) - \text{NICS}(r)$) divided by interval ($\Delta r = 0.2$). Therefore:

$$\text{NICS-rate} = \frac{\Delta \text{NICS}}{\Delta r} \approx \frac{\partial \text{NICS}}{\partial r} \quad (1)$$

These NICS-rates ($\frac{\partial \text{NICS}}{\partial r}$) are finally plotted against the corresponding distances (*r*).

3. Results and discussion

The evaluated NICS-rate as a function of distance for furane, thiophene and pyrrole are given in Fig. 1. It is clear that NICS-rate values are distance-dependent and all curves pass through a maximum observed nearly at 1 Å above the ring centers. The maximum NICS-rates for furane, thiophene and pyrrole are 6.6225, 7.4805 and 8.7095, respectively; which are in the same order of aromaticity predicted by NICS. For 8 other aromatic molecules the same maximum is observed in NICS-rate curves.

Fig. 2 shows that in cyclobutadiene, the NICS-rate curve passes through a minimum observed at nearly 1 Å above the ring center. It seems that the presence of a minimum in NICS-rate graph imply to the antiaromatic characters for the molecule. For 9 other antiaromatic molecules such a minimum is observed in NICS-rate curves.

The obtained NICS-rate curve for benzene, as a paradigm of aromaticity, is given in Fig. 3. The presence of both maximum and minimum in NICS-rate, implies to the competition between σ - and π -electrons in the NICS values. It seems that the effect of σ -electrons in NICS is rapidly diminished; whereas the π -electrons contribution is increased until it reaches to a maximum influence (which is seen as NICS-rate=0 at nearly 1 Å) and thereafter it decreases, which causes a rapid increase in the NICS-rate values. It is clear that the magnitude of maximum (6.9175) is more than the minimum (-12.068). The absolute ratio of these two NICS-rates is 1.48. This ratio is symbolized with NRR (NICS-Rate Ratio). Therefore:



$$NRR = \frac{NICS\text{-rate (Max)}}{NICS\text{-rate (Min)}}$$

(2)

The same shape is observed for the graph of pyridine; i.e. both of maximum and minimum NICS-rates are observed at 1.6 Å and 0.4 Å, respectively. NRR index value for pyridine is 1.24, respectively. Since it is clear that benzene is more aromatic than pyridine, therefore it seems that the magnitude of NRR may have some relations to the aromaticity of the system. This point is checked for more than 18 molecules, which the corresponding NRRs are gathered in Table 1. In all cases the evaluated NRR are in good agreement with the aromaticity of molecules.

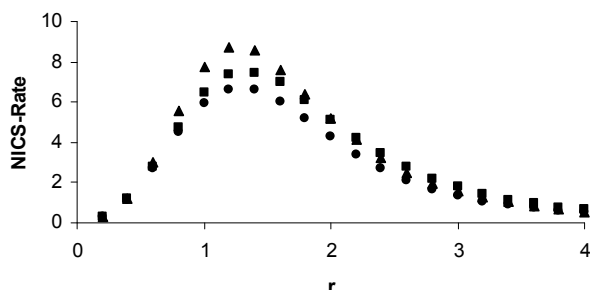


Fig. 1. NICS-Rate as a function of distance for furan (•), thiophene (■) and pyrrole (▲) molecule.

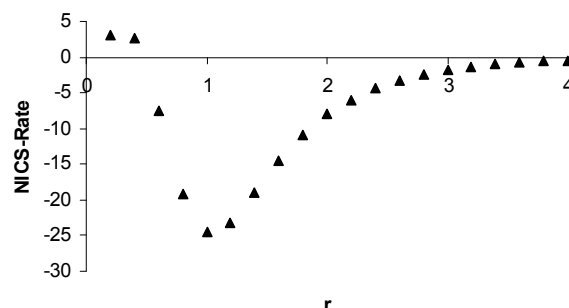


Fig. 2. NICS-Rate as a function of distance for cyclobutadiene molecule.

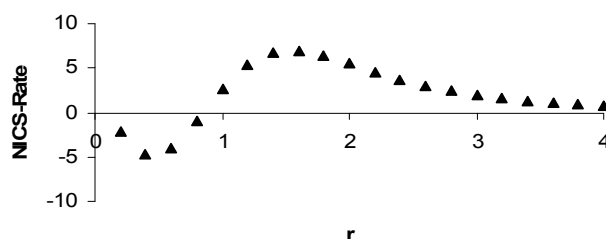


Fig. 3. NICS-Rate as a function of distance for benzene molecule.

Table 1. Calculated NICS(0) and NICS-Rate Ratio (NRR) for those molecules which show both maximum and minimum in their curves.

Molecule	NICS(0)	NRR	Molecule	NICS(0)	NRR
Cyclopentadiene	-3.184	0.911	naphthalene	-9.989	1.452
Benzene	-9.702	1.468	azulene(5)	-19.592	1.968
Pyridine	-8.144	1.200	azulene(7)	-6.993	1.216
ZZ-squaric acid	-2.572	0.590	benzocyclobutadiene(6)	-2.396	0.886
ZE-squaric acid	-3.207	0.650	biphenylene(6)	-4.986	1.222
EE-squaric acid	-3.329	0.654	acenaphthylene(6)	-8.643	1.361
tropylium cation	-7.53	1.133	acenaphthylene(5)	2.981	0.130
cycooctatetraenyl dication	-7.435	1.133	calicene(5)	-7.003	2.263
anthracene(1)	-8.413	1.241	bicyclobutadienobenzene(4)	-12.282	0.872
anthracene(2)	-13.239	1.756	bicyclobutadienobenzene(6)	-10.088	2.243
phenanthrene(1)	-10.224	1.487	pyracycene(6)	-2.662	0.705
phenanthrene(2)	-6.533	1.240			

4. Conclusions

It is shown that the NICS-rate, which presents the variation of NICS index by changing the distance from the center of the ring, is a useful tool for prediction of aromaticity in cyclic compounds. . From the scan curve it is proposed that for aromatic systems, the NICS-rate values will pass through a maximum while for antiaromatic species a minimum is expected. Those systems which show both minimum and maximum in their NICS-rate curves could be classified according to their NRR index (NICS-Rate Ratio); which is the absolute ratio of maximum to minimum NICS-rates. NRRs for aromatic and nonaromatic systems are more than and less than unity, respectively. Also the NICS-rate curve can successfully predicts the local aromaticity of polycyclic compounds.

References

- [1] Schleyer, P.v.R. Maerker, C. Dransfeld, A. Jiao, H. Hommes, N.J.R.v.E. J. Am. Chem. Soc. 118 (1996) 6317.
- [2] Stanger, A. J. Org. Chem. 71 (2006) 883.

**Evaluation of ground-state correlation energies using an empirical model**

S. Noorizadeh*, H. Parsa

Chemistry Department, College of Sciences, Shahid Chamran University, Ahvaz, Iran

(E-mail: noorizadeh_s@scu.ac.ir)

Keywords: Correlation energy, Electron correlation, Atomic number, Empirical formula.**1. Introduction**

The difference between Hartree-Fock limit energy and exact non-relativistic ground-state total electronic energy ($E_{\text{corr}} = E_{\text{ex}} - E_{\text{HF Limit}}$) is called correlation energy, which arises from the replacing of the exact antisymmetric wave function by single Slater determinant. Since an explicit handling of electron correlation is required for proper description of atomic and molecular properties such as exact electronic energy and chemical bonding, therefore accurate evaluation of this quantity is central problem in many areas of modern theoretical chemistry and physics researches. Large number of recent papers appeared in the literature offering various models to calculate this property. More recently Liu and Parr [1] estimated the ground-state atomic correlation energies using an empirical formula and evaluated the kinetic and potential energy components of these correlations. Using cusp approximation, Mohajeri and Alipour [2] have also introduced a new method based on electron density at the nucleus to determine electron correlation energies for isoelectronic atomic ion series by different power of atomic number.

In this research it is attempted to introduce a new empirical model to estimate the ground-state correlation energies per electron for isoelectronic atomic ions in terms of their atomic numbers.

2. Theoretical section

By considering the plots of experimental correlation energies against atomic numbers for different series of isoelectronic atomic ions ($N=2-18$), two categories are recognized. In some series ($N=4-6$ and $12-18$), the correlation energies show nearly a linear relationship with the atomic numbers and in the other series ($N=2, 3$ and $7-11$) the correlation energies for the systems with low atomic numbers, increase linearly with the increasing the nuclear charges; whereas for ions with large atomic numbers, this curve asymptotically goes to a constant. It is the same as the variation of reaction rate with the concentration of enzyme substrate (Michaelis-Menten Mechanism). In the basis of these observations we speculate that there may be a *Michaelis-Menten like* relation, which can properly, expressed the correlation energies in terms of atomic numbers. Therefore:

$$E_c/N = \frac{a+bZ}{c+Z} \quad (1)$$

where Z and N are the atomic number and the number of electrons, respectively. To find the adjustable parameters (a , b , c and d) by using a simple least squares procedure, the experimental correlation energies for different isoelectronic series are fitted to the corresponding atomic numbers according to the above empirical relation. The ability of this relation in predicting the correlation energies per electron (E_c/N) is checked for different isoelectronic series included of both neutral and charged atoms. All over this work the correlation energies are taken as positive quantities for simplicity.

3. Result and discussion

To test the reliability of the suggested formula in reproducing the correlation energies, the data needed are Z , N and accurate values of ground state correlation energy (E_c) for each species. These data are taken from Chakravorty *et al.* work [3]. The best fitting results including adjusted parameter values, regression coefficients and Average Absolute Deviations (AADs) are collected in table 1; together with the reported AADs by Liu [1] for comparison. It is clear that in all cases (with one exception $N=9$) the evaluated AADs are less than those reported previously. The corresponding fitted parameters are different for various isoelectronic series; but for species with $N=2$, and 3 , these values are almost close, through the series with $N=4-6$, and $12-18$, each parameter is constant, and also for $N=7-11$, the difference between each of them is completely negligible. The correlation between computed and experimental energies for total 315 species is depicted in figure 1. Note that the obtained linear relation (with $R^2=0.999$), has intercept=0.00 and slope= $0.997 \approx 1$, which indicate to closeness of the predicted and experimental energies.

Table 1: Fitted adjustable parameters of Eq. (1), regression coefficients, and absolute average deviations (kcal/mol) for different isoelectronic series.

N	Number of data points	a	b	c	d	R ²	AAD	AAD ^a
2	19	-0.01100	0.0614	0.0662	2.6339	0.999	0.0062	0.40
3	26	-0.02070	0.0467	0.0658	2.6118	1.000	0.0127	0.17
7	22	0.00001	0.1101	5.9009	3.2180	0.998	0.1872	0.46
8	21	0.00001	0.1388	5.8218	3.6164	0.998	0.1257	0.17
9	20	0.00001	0.1499	5.8166	3.6278	0.986	0.8252	0.33
10	19	0.08121	0.1398	5.8752	3.2888	0.944	0.5712	0.74
11	18	0.00001	0.1351	5.8771	3.2220	1.000	0.0239	0.24
4	25	0.12041	0.0404	11.2572	0.0505	0.999	0.6273	3.36
5	24	0.20624	0.0234	11.4550	0.0816	0.998	0.7278	2.24
6	23	0.22203	0.0239	11.4711	0.3334	0.998	0.5953	0.92
12	17	0.23009	0.0389	11.4797	0.6025	0.999	0.4472	0.48
13	16	0.19452	0.0375	11.4774	0.5461	0.998	0.6284	0.98
14	15	0.16732	0.0389	11.4801	0.5707	0.998	0.5803	0.96
15	14	0.16079	0.0372	11.4845	0.5520	0.999	0.4251	0.79
16	13	0.17102	0.0345	11.4571	0.4672	0.999	0.5611	0.85
17	12	0.16586	0.0342	11.4751	0.4427	0.999	0.3132	0.59
18	11	0.15405	0.3482	11.4755	0.4421	0.999	0.1744	0.28

a. Data taken from Ref. 1

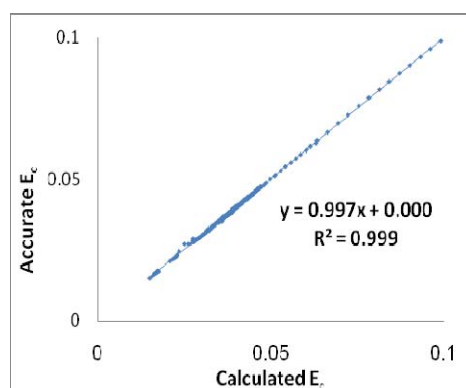


Fig. 1. Accurate versus calculated correlation energies for all atoms and ions considered in this study (a total 315 species).

4. Conclusions

Using Michaelis–Menten equation for enzyme reaction rates, an empirical relation is introduced for correlation energies in terms of the atomic numbers. This relation successfully predicts the correlation energies of atoms in both of neutral and ionic forms with low deviation from experimental energies. For some isoelectronic series the evaluated fitting parameters are nearly the same.

References:

- [1] Liu, S. Parr, R.G. J. Phys. Chem. A 111 (2007) 10422.
- [2] Mohajeri, A. Alipour, M. J. Mol. Struc. (THEOCHEM) 907 (2009) 115.
- [3] Chakravorty, S. J. Gwaltney, S.R. Davidson, E.R. Phys. Rev. A 47 (1993) 3649.

Ground state correlation energies and absolute hardness in atomic systems

S. Noorizadeh* and M. Mondanizadeh

Chemistry Dept., College of Sciences, Shahid Chamran Univ., Ahwaz, Iran

(E-mail: noorizadeh_s@scu.ac.ir)

Keywords: Correlation energy, Absolute hardness, Koopman's theorem.

1. Introduction

The calculation of the electron correlation energy, which is defined as the difference between the exact nonrelativistic energy and the best possible Hartree-Fock energy obtained by using the complete basis set ($E_{\text{corr}} = E_{\text{exact}} - E_{\text{HF}}$), plays a very important role in quantum chemistry and has been always the most active research field in modern theoretical chemistry. The



HF-SCF method provides an excellent starting point, which accounts for about 99% of the total energy of the system. However, the neglect of correlations between electrons, leads to rather poor description in the chemical sense because the energy of the chemical bond is comparable to that 1% of the HF-SCF method. This is why the inclusion of the electron correlation is critical for the accurate and quantitative evaluation of molecular energies. Many attempts have been made to examine the problem of estimating accurate correlation energy. In many of these works, E_{corr} is considered as a function of Z (atomic number), N (number of electrons) and ρ (charge density) of the system [1-3].

One of the most widely used concepts in Density Functional Theory is absolute hardness, which is defined as the second derivative of total energy with respect to the number of electrons; i.e.:

$$\eta = \left(\frac{\partial^2 E}{\partial N^2} \right)_{V(r)} \quad (1)$$

Using Koopman's theorem, this quantity could be expressed in terms of the Highest Occupied and Lowest Unoccupied Molecular Orbitals as the following equation:

$$E_{\text{corr}} = -\frac{\epsilon_H - \epsilon_L}{2} \quad (2)$$

Since this quantity is related to the stability of system and the correlation energy may have the same characteristic, it comes in mind that there may be a relation between E_{corr} and η .

In the present study, an empirical relation is proposed to estimate the electron correlation energies of atomic systems using their calculated absolute hardness values.

2. Theoretical section

For more than 300 atomic species in both neutral and ionic forms, the frontier orbital energies (HOMO and LUMO) are evaluated using the accurate and known method G2. By considering the correlation energies v.s. calculated hardnesses curves it is found that for some isoelectronic series ($N=2,3, 9-11$) a linear curve is observed, whereas for the other series ($N=4-8$ and $12-18$) a logarithmic graph is expected. Therefore the following relation is considered between the E_{corr} and η values:

$$E_{\text{corr}} = \frac{a+b\eta}{1+c\eta+d\eta^2} \quad (3)$$

where the adjustable parameters can be find using a simple fitting procedure. Note that this equation shows both linear (for negligible c and d parameters) and nonlinear relations (significant c and d parameters); which is suitable for investigation of correlation energies in different isoelectronic series.

3. Results and discussion

The obtained adjustable parameters (a , b , c and d) for different isoelectronic series are collected in Table 1 together with the corresponding regression coefficients and calculated Average Absolute Error (AAD) values. The reported AADs by Liu [2] for the estimated correlation energies from atomic numbers are also given in this table for comparison. It is clear from this table that in those cases in which $N < 12$ (bolded face in table), the estimated energies from the hardness values are more accurate and for isoelectronic series with $N > 12$ this empirical equations could not reproduce the correlation energies as accurate as the Liu relation. This difficulty may arises from the Janak's approximation which is used for calculation of hardness values. The correlation between all calculated and experimental E_{corr} (315 points) are shown in Fig. 1. Very small intercept (intercept = 0.00003), the slope close to unity (slope = 0.999) and $R^2 = 0.9999$, all imply to the closeness of the reported and experimental correlation energies.

Table1. Adjustable parameters of the considered empirical relation, correlation coefficients and calculated Average Absolute Deviations in Kcal/mole, AAD, for the isoelectronic series considered in this study.

N	N.O.P	a	b	c	d	R ²	AAD	AAD ^a
2	19	0.0254	0.2512	5.4691	-0.0011	0.991	0.05	0.40
3	26	0.0404	0.2768	5.0485	0.0449	0.997	0.03	0.17
4	25	0.0756	0.1380	0.1356	-0.0304	0.998	1.91	3.36
5	24	0.0875	0.2969	0.7778	-0.1027	0.995	1.50	2.24
6	23	0.1152	0.5236	2.0584	-0.2148	0.997	0.65	0.92

7	22	0.1461	0.8561	3.5399	0.0386	0.995	0.31	0.46
8	21	0.2342	0.3720	1.1205	0.0282	0.998	0.16	0.17
9	20	0.3122	0.0251	-0.1041	0.0243	0.997	0.12	0.13
10	19	0.3870	0.0249	0.0561	0.0001	0.991	0.25	0.74
11	18	0.3852	0.1069	-0.0114	0.1371	0.997	0.23	0.24
12	17	0.4099	0.7289	1.2135	-0.0539	0.999	0.60	0.48
13	16	0.4399	-0.598	-1.9298	0.8086	0.991	1.76	0.98
14	15	0.4607	-0.528	-1.9037	1.0180	0.996	1.22	0.96
15	14	0.4872	-0.7921	-2.3630	1.2744	0.996	0.93	0.79
16	13	0.5345	-0.5439	-1.7405	0.8702	0.998	0.90	0.85
17	12	0.5822	0.3499	-0.0299	-0.0741	0.998	0.72	0.59
18	11	0.6966	0.2424	0.2445	-0.0354	0.998	0.71	0.28

^a Data taken from Ref. [2].

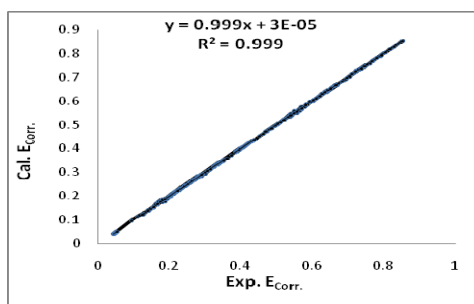


Fig. 1. Correlation between calculated and experimental E_{corr} for all species considered in this study.

4. Conclusion

It seems that the ground state correlation energies for atomic species in both neutral and charged forms can be correlated with the hardness values evaluated using Janak's approximation. This relation for species with small number of electrons ($N < 12$) successfully reproduced the experimental energies.

References

- [1] Kristyan, S. J. Chem. Phys. 102 (1995) 278.
- [2] Liu, S. Parr, R. J. Phys. Chem. A 111 (2007) 10422.
- [3] Mohajeri, A. Alipour, M. J. Mol. Struct. (THEOCHEM) 907 (2009) 115.



The study of structure and electron configuration of *closo*- B₅H₅⁻² and related isolobal compounds: *ab initio* study and NBO analysis

S.Jameh-Bozorghi^a, E.jalali^{b,a}, H. R. Namdari^c, A.ghaempanah^a

a-chemistry Department, science faculty, Islamic Azad university, Arak Branch, Arak, Iran

b- chemistry Department, science faculty, Islamic Azad university, Damghan, Branch, Damghan, Iran

c- chemistry Department, science faculty, Islamic Azad university, Shar-e-rey Branch, Tehran, Iran

1. Introduction

The molecular formulas of close and Nido and Arachno and Hypo Hydro Borane and the Isolobal composites are listed below:

Type	Formula
Closo	[B _n H _n] ⁻² or [B _p H _{p+2}]
Nido	[B _n H _{n+4}] or [B _p H _{p+4}]
Arachno	[B _n H _{n+6}] or [B _p H _{p+6}]
Hypso	[B _n H _{n+8}] or [B _p H _{p+8}]

In this research theoretical study of *closo*- B₅H₅⁻² (**1**), *closo*- CB₄H₅⁻ (**2**), *closo*- C₂B₃H₅⁻² (**3**), *closo*- NB₄H₅ (**4**) and *closo*- N₂B₃H₅⁺² (**5**) was performed. All of the compounds **1** to **5** must to have *closo* structure and be Isolobal together. All these five compounds are synthesized and characterized by R.Hoffmann *et al* [1] and H. C.Brown *et al* [2] and Marek Zuidelewise[3] respectively.

2. Calculation methods

The DFT calculations were carried out using B3Lyp/6+311+G** with the GAUSSIAN 03 package of programs implemented on a Pentium PC computer with a 703 GHZ processor.

3. Results and discussion

Our idea is to structure of B₅H₅⁻² was close and bonds Length and electron density of the (B-B) bonds were 1.6865 Å and 1.64929 electrons respectively. In CB₄H₅⁻ and NB₄H₅ compounds the bond Length of (B-B) was similar to previous one. But bond Length and electron density of (B-C) 1.5545 Å, 1.81356 electron and (B-N) are 1.5145 Å, 1.89898 electron respectively.

The study of Homo and Lumo orbital shapes showed that they have the same electron arrangement.

4. Conclusions

The study of structure and orbital shapes of the composites of number 1 to **5** shows that they have the same chemical properties. In the other words they are Isolobal.

Reference

- [1] R.Hoffmann, Angew. Chem. Int. Ed.21 (1982).
- [2] H. C.Brown, J. V.B kanth, p. V.Dalvi J. Phys. Chem. A 113 (2009) 12079
- [3] M. Zuidelewise, J. Org. Chem. 64 (1999) 6263.
- [4] M. Elian, M.M.L. Chen. D.M.P. Mingos and R. Hoffmann, Inorg. Chem. 15 (1970) 1148.
- [5] Zdelewise, A.O. J. Chem .phys. 128 (2008) 1843.



**Theoretical calculations of relative pK_a values for some of substituted amines in aqueous solution**A. Ebady^a, R. Behjatmanesh-ardakani^a^aDepartment of chemistry, payame Noor University (PNU), ardakan, Iran

(E-mail: ebadi5455@yahoo.com)

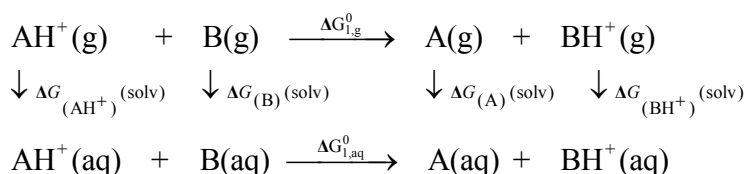
Keywords: pK_a , B3LYP, Cluster, Amine, CPCM.**1. Introduction**

The quantitative behavior of acids and bases in solution can only be understood if their pK_a values are known. In particular, the pH of a solution can be predicted when the analytical concentration and pK_a values of all acids and bases are known. So far for many of molecules consist of various functional groups, electronic structure studies and prediction of pK_a values, have been performed in aqueous solution using semi empirical or ab initio methods [1-5]. In this work, we consider the effects of specific solute-solvent interactions using forming the clusters of amine-water by introduction one and two explicit water molecules around the amine and consider the obtained cluster as a compound solvated by dielectric continuum. This model predicts the pK_a values in good agreement with experimental data than pure continuum models.

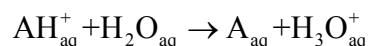
2. Methods

The initial structures of the water-amine clusters were built with HyperChem 7.0 software and PM3 [6] semi-empirical method. The geometries were then optimized at B3LYP level in gas phase using the 6-31+G* basis set. The gas phase free energies (G_{gas}) and solvation free energies changes (ΔG_{solv}) values were calculated by B3LYP/6-31+G*/B3LYP/6-31+G* levels of theory. The absence of imaginary frequencies verified that all structures were true minima at their respective levels of calculation. In addition, for comparison purpose, the geometries of all of neutral and cation species after optimization in gas phase were optimized in solution again and then the solvation free energies were calculated.

The thermodynamic cycle used for calculation of the relative pK_a values is shown in scheme1. The expressions utilized for the pK_a calculations are given below:

**Scheme1.** The thermodynamic cycle employed for pK_a calculations.

A compound is defined as AH^+ acids in aqueous solution if it dissociates as follows:



$$pK_a(\text{AH}^+) = \frac{\Delta G_{\text{aq}}^0}{2.303RT} - 1.74 \quad (1)$$

or following nascimento [7,8], a simpler form of Eq.(1) can be used:

$$\Delta G^0(\text{kcal.mol}^{-1}) = 1.36pK_a + 2.36 \quad (2)$$

For relative pK_a values calculation, where we have two amines (given by AH^+ and BH^+), and the following equation was used:

$$pK_a(\text{AH}^+) = pK_a(\text{BH}^+) + \Delta pK_a \quad (3)$$

Where $pK_a(\text{AH}^+)$ is the pK_a of the unknown amine, $pK_a(\text{BH}^+)$ is the pK_a of the known amine and ΔpK_a is the difference in pK_a of two amines. In the relative pK_a calculations, the values for $G_{\text{gas}}(\text{H}^+)$ and $\Delta G_{\text{solv}}(\text{H}^+)$ cancel out, so any inaccuracies in calculated or literature values used for these species are irrelevant [10]. In this paper, we used propylamine as the reference molecule. The experimental pK_a of propylamine has been measured ($pK_a=10.57$). All calculations were performed using Gaussian 98 software.



3. Results and discussion

The gas phase free energy changes, solvation free energies and the calculated pK_a values are showed in Table 1. According to the Table 1, the second method has higher accuracy in comparison to the first method. It is easily observable that considering explicit water molecules near the bases, and also optimization in solution lead to a good agreement with experimental values. Especially, while the neutral species in solution are optimized, continuum models ignore strong specific interactions, such as hydrogen bonds, therefore, introducing explicit water molecules (and so hydrogen bonds) as a first shell of solvation in the cavity of solute leads to the change in free energy of solvation. Optimization in solution causes to increase the value of solvation free energy. In other hand, with optimization in solution the value of solvation free energy would be in good agreement with experimental data.

4. Conclusions

The relative pK_a 's for several of amine-water clusters have been predicted in solution by density functional theory in combination with polarizable continuum model (PCM). The free energy of solvation has been calculated with consideration both of optimized geometry of molecules in gas phase and in solution phase. Good agreement to experimental data has been observed with optimized geometry in solution especial with optimized geometry of neutral species.

Table1. Calculated and Experimental pK_a 's in water at B3LYP level

	^a pK_a (calc.)	^a pK_a (calc.)	^b pK_a (calc.)	^c pK_a (calc.)	pK_a (exp.)
methylamine.(H ₂ O)	9.46		10.26	10	10.62
methylamine.(H ₂ O) ₂		10.71			10.62
ethylamine.(H ₂ O)	10.25		11.1	10.96	10.63
ethylamine.(H ₂ O) ₂		10.87			10.63
propylamine (H ₂ O)	10.57		10.57	10.57	10.57
propylamine (H ₂ O) ₂		10.57			10.57
2-aminoethanol.(H ₂ O)	8.85		9.43	11.18	9.5
2-aminoethanol.(H ₂ O) ₂		6.89			9.5
1,2-ethanediamine.(H ₂ O)	10.28		10.1	10.55	10.7
1,2-ethanediamine.(H ₂ O) ₂		8.52			10.7
Dimethylamine.(H ₂ O)	9.78		10.59	10.63	10.77
Dimethylamine.(H ₂ O) ₂		11.34			10.77
Diethylamine.(H ₂ O)	10.69		11.5	11.39	10.8
Diethylamine.(H ₂ O) ₂		11.21			10.8
MAD	0.53	0.87	0.34	0.5	

a. With optimized geometry at gas phase, b. With optimized geometry of neutral species in solution phase, c. With optimized geometry of neutral and cation species in solution.

References

- [1] Schuurmann, G. Quant. Struct-Act. Relat. 15 (1996) 121.
- [2] Schuurmann, G. Quantitative Structure-Activity Relationship in Environmenta.
- [3] Pliego, J. R. J. Chem. Phys. Lett. 367 (2003) 145.
- [4] Saracino, G. A. A.; Improta, R.; Barone, V. Chem. Phys. Lett. 373 (2003) 411.
- [5] Pliego, J. R. Jr.; Riveros, J. M. J. Phys. Chem. A 106 (2002) 7434.
- [6] Stewart, J. J. P. J. Comput. Chem. 10 (1989) 209.
- [7] Silva, C. O.; da Silva, E. C.; Nascimento, M. A. C. J. Phys. Chem. A 104 (2000) 2402.
- [8] Silva, C. O.; da Silva, E. C.; Nascimento, M. A. C. J. Phys. Chem. A 103 (1999) 11194.
- [9] Toth, A. M.; Liptak, M. D.; Phillips, D. L.; Shields, G. C. J. Chem. Phys. 114 (2001) 4595.



The investigation of hydrogen bonding effects on the calculated relative pK_a values for several compounds in aqueous solution

R. Behjatmanesh-ardakani^a, A. Ebady^a

^aDepartment of chemistry, payame Noor University (PNU), ardakan, Iran

(E-mail: ebadi5455@yahoo.com)

Keyword: Hydrogen bonding, solvation, CPCM, Solvation free energies.

1. Introduction

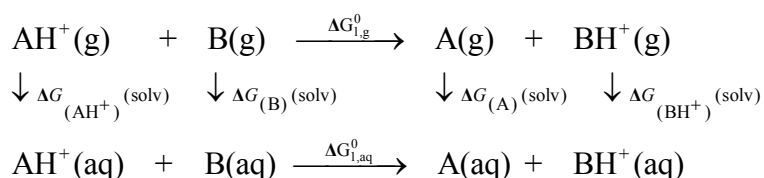
A reliable theoretical calculation of the pK_a values in solvent is very important in the modeling of chemical reactions in the solution phase. In living organisms, acid-base homeostasis and enzyme kinetics are dependent on the pK_a values of the many acids and bases present in the cell and in the body. The structural factors that influence the magnitude of the acid dissociation constant include Pauling's rules for acidity constants, inductive effects, resonance effects, and hydrogen bonding. Solvent effects are essential components of all liquid-state chemistry, and it is impossible to understand liquid-phase organic, biological, or inorganic chemistry without including them. Dielectric continuum solvation models [1] are widely used, because they are computationally good and simple way to simulate equilibrium properties of solutes but they ignore specific solute-solvent interactions. In this work the focus is on the effects of specific solute-solvent interactions using clusters of amine-water by introducing explicit water molecules to the amines and related cations. Then the obtained clusters are considered as compounds solvated by dielectric continuum. The proposed model provides a tool to predict pK_a values in good agreement with experimental data than pure continuum models.

2. Methods

The acidity constant is a measure of a molecule's propensity to become deprotonated in aqueous solution. It is directly related to the free energy of the deprotonation reaction:

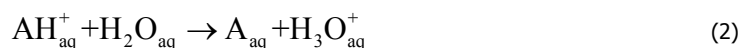
$$pK_a = \frac{\Delta G_a}{2.303RT} \quad (1)$$

The deprotonation of a compound in aqueous solution can be represented as part of a thermodynamic cycle. The thermodynamic cycle used for calculation of the relative pK_a values is shown in scheme1.



Scheme1. The thermodynamic cycle employed for pK_a calculations.

A compound is defined as AH^+ acids in aqueous solution if it dissociates as follows:



$$pK_a(\text{AH}^+) = \frac{\Delta G_{\text{aq}}^0}{2.303RT} - 1.74 \quad (3)$$

Alternatively, a simple form of Eq. (1) can be used according to Nascimento [2,3].

$$\Delta G^0 (\text{kcal.mol}^{-1}) = 1.36pK_a + 2.36 \quad (4)$$

The initial structures of the water-amine clusters were built with hyperChem 7.0 software and PM3 [4] semiempirical method. The geometries were then optimized at MP2 (FULL) level in gas phase using the 6-31G* basis set.

In the relative pK_a calculations, the values for $G_{\text{gas}}(\text{H}^+)$ and $\Delta G_{\text{solv}}(\text{H}^+)$ cancel out [5]. In this paper, we used propylamine as a reference molecule. The experimental pK_a equal to 10.57 for propylamine has been obtained from NIST [6]



The gas phase calculations were performed using standard procedures, and, for the zero point energy corrections, the frequencies were scaled by a factor 0.942 taken by NIST website [6] which is suitable to the basis set and level of calculation employed.

Free energy of solvation values were calculated by using the CPCM implicit solvation model [7], based on the polarized continuum model (PCM) of Tomasi and co-workers [8]. In the Barone and Cossi implementation of this method, the cavities are modeled based on the molecular shape, using optimized parameters, and both electrostatic and nonelectrostatic contributions to the energies. The total free energy is the sum of the free energies obtained for electrostatic interactions, formation of the cavity in the continuum medium, dispersion interactions, and repulsion interactions. All calculations were performed using GAUSSIAN 98 [9].

3. Results and discussion

The results of the calculation are displayed in Table 1. It is observable that consideration of water molecules around the neutral and cation species of the investigated molecules show better results than consideration water molecules around the cation species by comparison with experimental data.

4. Conclusions

In this paper, we have used MP2(Full)/6-31G* in conjunction with CPCM method to predict relative pK_a s of several amines. Results show that introducing water molecules in the first shell of all species containing neutral and cations give better results in comparison with the state that only cations are considered.

Table 1. The calculated and Experimental pK_a values in water at MP2 (FULL) level.

Compound	(H ₂ O) ^a	(H ₂ O) ₂ ^a	(H ₂ O) ^b	(H ₂ O) ₂ ^b	pK_a (exp.)
methylamine	10.06	10.68	10.41	10.97	10.62
propylamine	10.57	10.57	10.57	10.57	10.57
2-aminoethanol	8.96	9.25	8.59	9.48	9.5
1,2-ethanediamine	10.31	10.54	9.63	10.14	10.7
1,3-propanediamine	9.73	10.93	10.16	11.02	10.9
Dimethylamine	10.62	11.12	10.78	10.75	10.77
Diethylamine	9.93	10.17	12.79	12.02	10.8
pipridine	11.41	10.51	11.55	10.32	11.1
2,5-diazahexane	10.25	9.66	11.71	11.1	10.4
MAD	0.46	0.31	0.74	0.41	
a. $BH^+(H_2O)_n + Ref(H_2O)_n \rightarrow B(H_2O)_n + Ref^+(H_2O)_n$					
b. $BH^+(H_2O)_n + Ref \rightarrow B + Ref^+(H_2O)_n$					

References

- [1] Tomasi, J.; Persico, M. Chem. Rev. 1994, 94, 2027.
- [2] Silva, C. O.; da Silva, E. C.; Nascimento, M. A.C. J. Phys. Chem. A. 104 (2000) 2402.
- [3] Silva, C. O.; da Silva, E. C.; Nascimento, M. A. C. J. Phys. Chem. A 103 (1999) 11194.
- [4] Stewart, J. J. P. J. Comput. Chem. 10 (1989) 209.
- [5] Toth A.; Liptak, M. D.; Phillips, D. L.; and Shields, G. C. J. Chem. Phys. 114 (2001) 4595.
- [6] [http:// webbook.nist.gov](http://webbook.nist.gov)
- [7] Barone, V.; Cossi, M. J. Phys. Chem. A. 102 (1998) 1995.
- [8] Miertus, S.; Scrocco, E.; Tomasi, J. Chem. Phys. 55 (1981) 117.
- [9] Frisch, M. J.; Gaussian, Inc., Pittsburgh, PA 1998.

Prediction of decomposition mechanism of compound 2-fluoropyridine; A Density Functional StudyS. Jameh-Bozorgi^{a,b,*}, M. darvishpour^b, M. H. Fekri^c

a- Chemistry Department, science faculty, Islamic Azad University, Touyserkan Branch, Touyserkan, Iran

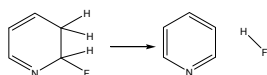
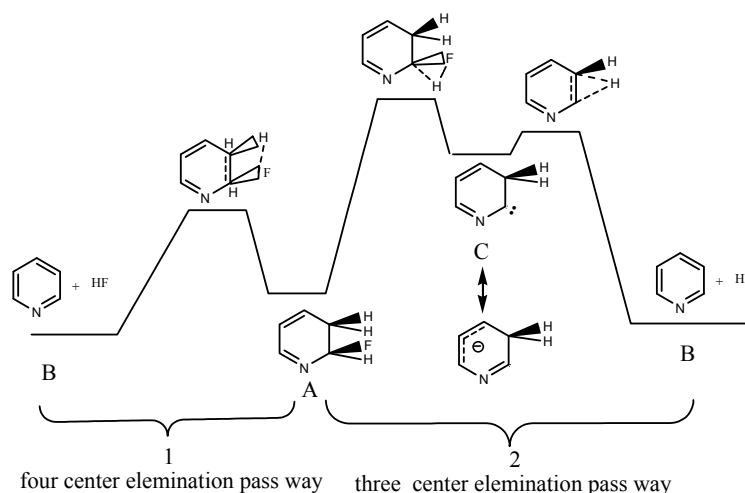
b- Chemistry Department, science faculty, Islamic Azad University, Arak Branch, Arak, Iran

c- Chemistry Department, science faculty, Islamic Azad University, Khorram abad Branch, Khorram abad, Iran

(E-mail address:Fekri_1354@yahoo.com)

Keyword: DFT, ZPE, Ea, Four-centered, 2-Flouro-2,3-dihydropyridine.**1. Introduction**

The experimental study of the kinetic of dissociation process of 3-halo-2,3-dihydropyridinies , investigated by Liu [1], showed that the decomposition reaction is a unimolecular process and the occurred from two pass ways, three centered and four centered transition state. Their results suggested a four-membered transition state is better than three-membered transition state structures relatively.

**Scheme 1.****Scheme 2.**

DFT methods have been used as a powerful tool of computational study on a variety of molecules, especially those that could not be studied by either HF-SCF methods because of the poor evaluation of the predicted molecular properties or MPn perturbation theory methods because of the prolonged time of calculations [2,3].

2. Calculation methods

Structures of all compounds were fully optimized using hybrid density functional B3LYP levels of theory using the 6-311+G** basis set as implemented in the Gaussian 98 program package (G98W).

The geometries are optimized using standard gradient techniques with default parameters set in G98W.



3. Results and discussion

Initial estimation of the structural geometry of the compound **A**, **B** and **C** were obtained by a molecular mechanic program; PM3 method of the MOPAC 7.0 computer program [4,5]. The GAUSSIAN 98 package of programs were finally used to perform ab initio calculations at the B3LYP/6-311+G** level.

Geometries of the transition states were obtained by keyword SADDLE in MOPAC 7.0 program, were reoptimized by the QST2 subroutine at the B3LYP/6-311+G** level. For further optimization, TS subroutine was used.

The nature of the stationary points for compounds **A**, **B** and **C** and transition state structures has been fixed by means of the number of imaginary frequencies. For minimum state structure, only real frequency values, and in the transition-state, only single imaginary frequency values, were accepted [6,7]. Zero point (*ZPE*) and total electronic (*E_{el}*) energies (*E₀* = *ZPE* + *E_{el}*) for the energy minimum and energy maximum geometries of the decomposition of compound **A** to pyridine as calculated on the B3LYP/6-311+G** level of theory. For single-point energy calculations were used and are given in Table 1.

Studies on B3LYP /6-311+G** of theory show that the barrier height of the decomposition of the compound **A** to pyridine for pass way (1) is lower than (2). It is good agriment with experimental methods.

Table 1. Calculated Total Energies (*E*), Zero-Point Energies *ZPE*, and Relative Energies ΔE : Hartree (Kcal mol⁻¹) for the energy minima structures of compounds **A**- **C** and transition structures for two reaction pass ways (Scheme 1).

<i>Pass way</i>	<i>Geometry</i>	<i>ZPE</i>	<i>E_{el}</i>	<i>E₀</i>	ΔE_0
	A	0.102672	-348.801201	-348.698529	0.000000 (0.000000)
	B	0.099280	-348.837475	-348.738195	-0.039666 (-24.890415)
1	[A → B] [#]	0.096742	-348.838839	-348.742097	0.053174 (33.36668)
2	[A → C] [#]	0.094794	-348.697724	-348.602930	0.095599 (59.98837)
	C	0.096284	-348.715791	-348.619507	0.079022 (49.586305)
	[C → B] [#]	0.096518	-348.712559	-348.616041	0.082488 (51.76122)

References

- [1] B. Liu, J. Chem. Phys. 80, (1984) 581.
- [2] Englisch, H.; Fieseler, H.; Haufe, A. Phys. Rev. A 37 (1988) 4570.
- [3] Von Barth, U. Phys. Rev. A, 20 (1979) 1693.
- [4] J. J. P. Stewart, QCPE 581, Department of Chemistry, Indiana University, Bloomington, IN, USA.
- [5] J. J. P. Stewart, J. Comput.-Aided Mol. Des. 4 (1990) 1.
- [6] J. W. McIver, Jr, Acc. Chem. Res. 7 (1974) 72.
- [7] O. Ermer, Tetrahedron 31 (1975) 1849.

**Effect of floating basis set on the electronic properties of adamantane**

H. Sabzyan* and B. Saed

Department of Chemistry, University of Isfahan, Isfahan 81746-73441, I. R. Iran

sabzyan@sci.ui.ac.ir / saed@chem.ui.ac.ir

Keywords: Adamantane, Floating Basis Set, Molecular Cage, DFT**1. Introduction**

Adamantane is a colorless crystalline cycloalkane with the formula $C_{10}H_{16}$ which was discovered in petroleum in 1933 and has been used in solid-state NMR spectroscopy as a chemical shift reference, and as a stabilizer of the dye lasers media. Numerous experimental, computational and theoretical studies have been carried out on the characteristics of adamantane in the solid state [1-4]. However, no computational or theoretical investigation has been carried out on the electronic characteristics over the cage space. The aim of this paper is to present results of a theoretical study on the electronic and binding characteristics of the neutral and charged adamantanes, with special stress on the molecular cage, using floating basis sets (FBS).

2. Computation Method

Geometry optimization (within T_d symmetry) and calculation of the properties of the neutral and charged adamantanes (A , A^+ and A^-) were carried out at the DFT level of theory with B3LYP functional using 6-311++G(d,p) basis set.

Position of the cage center (distance from the tertiary (-CH) carbon atoms, h) is obtained using the equality $h = \sqrt{3/8}R$ in which R is the average of the six distances between tertiary carbons (-CH). Due to the high number of geometric constraints in the standard z-matrix of the cage molecules like adamantane, At least three cycles of optimizations were needed to fully optimize structures of these three cage species within T_d symmetry prior to the application of the floating basis set (FBS).

The optimized structural parameters obtained for neutral and charged adamantanes are analyzed. Effects of the type (size and exponent) of the floating basis functions located at the center of the cage on the orbital densities and energies, and total electronic energies are studied with these (frozen) optimized geometries. For the neutral, and positively and negatively charged adamantanes, the SCF calculations could be accomplished only up to the 6-311++G(d,p) FBS of the C, H and B atoms, respectively.

Atoms-in-molecules theory of Bader is used (as implemented in the AIM2000 software) to visualize electron densities and its variations with the applied FBS.

3. Results, Discussion and Conclusions

Calculated total stabilization energies due to the inclusion of different FBSs (Fig. 1) are larger for the anion (A^-) as compared to those for the neutral (A) adamantane; The largest stabilization energies for A^- and A are obtained with the 6-311++G(d,p) FBS of the Li and Be atoms, respectively. In Fig. 1, different FBSs are denoted by the atomic numbers of the corresponding atoms.

Application of the FBS in the calculation of the electronic energies of A , A^- and A^+ results respectively in changes of -0.243 to 0.012 eV, -0.006 to -1.035 eV (for α electrons) & -0.009 to -0.994 eV (for β electrons), and -0.190 to -0.149 eV (for α electrons) & -0.366 to +0.239 (for β electrons) in the single-electron orbital energies, such that the maximum shift in the HOMO-LUMO transition wavelength is 5.2 nm and 6.9 nm for the A and A^- , respectively. Furthermore, in some cases, the order of the quasi-degenerate states near the Fermi level is changed after the inclusion of FBS.

The effects of the FBS on the shape and spatial extent of the active orbitals are visualized. Presence of the FBS at the center of the cage leads to more concentration of the probability density towards the center of the cage for all three species. This effect is larger and more evident for the A^- species. Further analysis of the FBS effect (demonstrated for the A^- in Fig. 2) shows that the type of FBS can have significant effect on the shape of the boundary surfaces of the frontier orbitals.

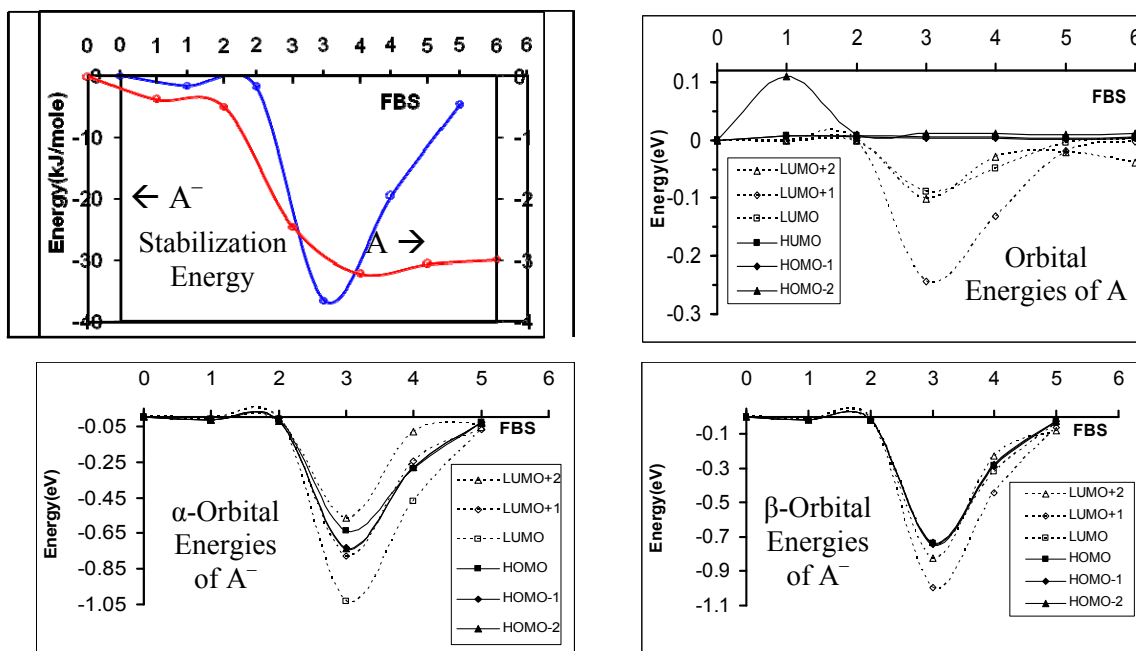


Fig. 1. Stabilization and orbital energies of A and A⁻ obtained with the inclusion of the 6-311++G(d,p) FBS of different atoms H to C (labeled with their atomic numbers).

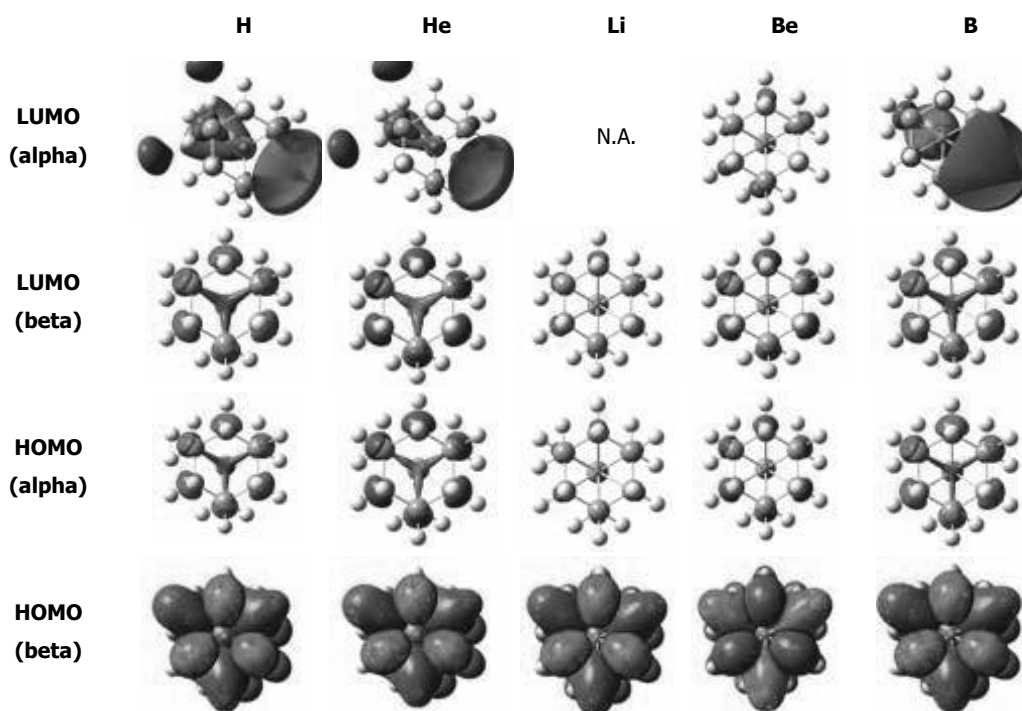


Fig. 2. Orbital boundary surfaces of A⁻ obtained with different 6-311++G(d,p) FBSs.

References

- [1] P. K. Madhu, X. Zhao, H. L. Malcolm, Chem. Phys. Lett. 346 (2001) 142.
- [2] J. Filik, J. N. Harvey, N. L. Allan, P. W. May, J. E. P. Dahl, S. Liu, R. M. K. Carlson, Phys. Rev. B. 74 (2006) 035423.
- [3] G. P. Zhang, T. F. George, G. A. Mansoori, Phys. Rev. B. 75 (2007) 035413.
- [4] K. K. Irikura, J. Org. Chem. 73 (2008) 7906.



DFT and ab initio study of metallotropic shift and prototropic shift mechanism of 5-terth-butylcyclopenta-1,3-diene and their analogs

S. Rafatpanah¹, S. Jameh - Bozorgchi¹, V. Daneshdoost¹

1. Chemistry department, faculty of sciences, Islamic Azad university, Arak branch, Arak, Iran.

Rafat_420@yahoo.com

Keyword: Ab initio, DFT, Natural bond orbital, NICS, Metallotropic, Prototropic, 5-terth-butylcyclopenta-1, 3-diene.

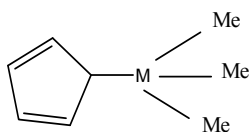
1. Introduction

Cyclopentadiene is a liquid with a low boiling point. It cannot be stored at room temperature because it spontaneously undergoes a Diels–Alder reaction with itself that forms the bridged dimer dicyclopentadiene. This reaction is reversible at elevated temperatures, so the most convenient way to obtain cyclopentadiene is to distill the commercially available dimer. Cyclopentadiene reacts with strong bases to form the cyclopentadienyl anion, which acts as a ligand in ferrocene and other sandwich complexes.

2. Methods

Ab initio calculation were carried out using density functional theory at B3LYP 3-21G*//B3LYP /3-21G* and B3LYP/6-311G**// B3LYP6-311G** levels of theory and molecular orbital (MO: Mp2/3-21G*//B3LYP/3-21G*) and NBO analysis, density functional theory (DFT: B3LYP/3-21G*//B3LYP/3-21G*) based methods were used to study of metallotropic shift and prototropic shift mechanism of 5-tert-butylcyclopenta-1,3 diene(1), cyclopenta-2,4 dienyl trimethyl silan(2) , cyclo penta -2,4 dienyl trimethyl german(3) and cyclo penta -2,4 dienyl trimethyl stannane(4), (see scheme1) .also thermodynamic parameters and geometric parameters based on the optimized ground state geometers using B3LYP/3-21G* method are calculated.

Further the aromaticity of compounds 1-4 evaluated by their the nucleus – independent chemical shifts (NICS).



Scheme1. [M: C (1), Si (2), Ge (3), Sn (4)].

3. Results and discussion

the ground state and transition state structure of compounds 1-4 have been optimized by the density functional theory (DFT) based method at B3LYP/3-21G* level of theory using the GAUSSIAN 98 package of programs[1-5]. Calculated energy (ΔE_0) of metallotropic decrease from compound 1 to 4 (scheme 1) the quantity of (ΔE_0) for compounds 1-4 is consequently equal with: 42.13 kcal/mol, 15.97 kcal/mol, 11.68 kcal/mol, and 4.88 kcal/mol, which thee quantity show the required energy for metallotropic in compound 4 is minimum and its metallotropic has done easily. Also the required energy for prototropic at all compound is less than metallotropic.

NBO analysis is [6, 7] reveal that the stabilization energy (E_2) associated with the electronic delocalization from bonding orbital [σ_{C5-M6}] to antibonding orbital [π^*_{C1-C2}] is increased from compound 1 to 4 in this manner: 1.45, 6.58, 9.08 and 14.11. These result detect that increasing of E_2 values were caused decreasing of ΔE_0 values.

Also with increasing the quantity of E_2 , the occupancy of bonding molecular orbital [σ_{C5-m6}] is reduced and the occupancy of antibonding molecular orbital [π^*_{C1-C2}] is increased. The aromatic property [8, 9] has direct relation with the stabilization energy.

The computation of nucleus independent chemical shift (NICS) [10] for compounds 1-4 has done with GIAO-HF/3-21G*. The obtained results revealed that the minimum values of NICS for compounds 1 to 4 are corresponded to center of rings and equal with: -3.60 ppm -6.70 ppm, -7.26 ppm and 9.30 ppm, respectively. Also the maximum values of NICS are corresponded to 0.7 Å above the ring centers and equal with: -6.72 ppm, -9.68 ppm, -10.22 ppm and -12.07 ppm



References

- [1] M. J. Frisch, G.W. Trucks, H. B. Schlegel, G. e Scuseria, M. A. Robb, R. Cheeseman, V. G. Zakrzewski, J. A. Montgomery, R. E. Startmaan, J. C. Burant, s. Dapprich, J. M. Millam, A.D. Daniels, K. N. Kudin, M. C. Strain, O. Farkas, J. Tomasi, V. Barone, M. Cossi, R. Cammi, Q.C. K. Morokuma, D. k. Malick, A. D. Rabuck, k. Raghavachary, . B. Foresman, R. Gomperts R. I. Martin, D. J. Fox, T. Keith, M. A. Al-Laham, C. Y. Peng, A. Nanayakkara, C. Gonzalez, M. Challacombe, P. M. W. Gill, B. Johnson, W. Chen, M. W.Wong, J. I. Andres, M. Head-gordon, E. S. Replogle and J. A. Pople. GAUSSIAN 98 (revision a. 3) Gaussian inc. Pittsburgh, pa, USA, 1998.
- [2] A. D. becke, J. Chem. Phys. 98 (1993) 5648.
- [3] C. Lee, W.Yang and R .G. Parr, Phys. Rev. B 37 (1998) 785.
- [4] W.J. Hehre, I. Random, P.Y R. Schleyer and J. A. Pople. Ab initio molecular orbital theory, Wiley, New York, 1986.
- [5] J. M. Seminario and P. Politzer, (Eds), Modern Density Function Theory, A Tool for chemistry, Elsevier, Amsterdam, 1995.
- [6] E. D. Glendening, A. E. Reed, J.E. Carpenter and F. Weinhold, NBO version 3.1.
- [7] A. E. Reed, L.A. Curtiss and F. Weinhold, Chem. Rev. 88 (1988) 889.
- [8] (a) P. G. Garret, Aromaticity, Wiley, New York, 1986; (b) A. R. Katritzky, P. Barczynsky, G. Musumarra, D. Pisano and M .Szarfan, J. Am. Chem. Soc. 111(1989) 7; (c) A.R. Katritzky, V. Feygelmanm, G. Musumarra, P. Barczynsky, and M. Szarfan, J.Parkt. Chem. Chem. Ztg. 332(1990)853; (d) D. Jug, A. M. Koster, J. Phys. Org. Chem. 4 (1991) 163.
- [9] (a) V.I. Minkin, M. N. Glukhovstsev and B. Y. Simkin. Aromaticity and antiaromaticity. Wiley. New York, 1904; (b) P. V. R. Schleyer and H. jiao, Pure Appl. Chem. 68 (1996) 209.
- [10] P. V. R. Schleyer, C. Maerker, A. Dransfeld, H. jiao and N. J. V. E. Hommes, J. Am. Chem. Soc. 118 (1996) 6317.

**Determination of the pK_a values of Glycine, Phenylalanine and glycylphenylalanine using DFT method**Farhoush Kiani,^{a,*} Abbas Ali Rostami^b Sasan Sharifi,^c and Azar Bahadori^c^a Department of chemistry, Islamic Azad University, Ayatollah Amoli Branch, Amol, Iran.^b Department of Physical and Inorganic Chemistry, Faculty of Chemistry, University of Mazandaran, Mazandaran, Iran^c Department of Chemistry, Faculty of Sciences, Islamic Azad University, Arak Branch, Arak, Iran.

* E-mail: farhosh_kiani@yahoo.com

Keywords: dissociation constant, hydrogen-bond-donor, DFT method, solvation free energy**1. Introduction**

The peptides are an amazing class of compounds. Although they are all constructed from relatively simple building blocks (the amino acids), they exhibit a remarkable range of biological properties: peptides can act as antibiotics, hormones, food additives, poisons or pain-killers and it is primarily because of their medicinal properties that the study of peptides has become one of the most active areas of current research.¹ With an amino and a carboxylic acid group being present in these molecules there is both a basic and an acidic component in them. Both functional groups can be ionized. Although peptides are composed of amino acids, the amide bond itself shows neither the properties of the amino group, nor those of the carboxylic acid group. In fact, the properties of the amide group are governed by the conjugation of the nitrogen lone pair with the carbonyl group—this mesomeric effect which can be expressed as a resonance between two canonical forms.¹ Different experimental procedures are frequently used for the determination of acidity constants. For example, high-pressure liquid chromatography, liquid-liquid partition, and methods that involve potentiometric titrations or spectrometric determinations in water or in mixtures of solvents. The determination of the ionization constant by UV-Vis spectrometry is more time-consuming than by potentiometry. However, spectroscopy is an ideal method when a substance is too insoluble for potentiometry or when its pK_a value is particularly low or high.² On the other hand, during the last two decades there has been much interest in developing a methodology enabling theoretical prediction of pK_a values, employing various quantum theoretical techniques. Kinds of polarizable continuum models have been applied to calculate free energy differences for cations, neutral compounds and their anions. On the basis of solvation free energies, the pK_a values were obtained for the compounds in question by using thermodynamic equations; involving the combined experimental and calculated data.³ This paper deals with the influence of factors such as the SCRF model applied, choice of a particular thermodynamic equations, atomic radii used to build a cavity in the solvent (water), optimization of geometry in water, inclusion of electron correlation, and the dimension of the basis set on the solvation free energies and on the calculated pK_a values. In this study, pK_a values of glycine, phenylalanine and glycylphenylalanine were determined in aqueous solution by ab initio method and temperature 25°C. In order to explain the acidic dissociation constants obtained, we investigated the molecular conformations and solute-solvent interactions of the cation, anion and neutral species of glycine, phenylalanine and glycylphenylalanine, using ab initio and density functional theory (DFT) methods.

2. Computational method

Fig. 1 shows the structures of glycine, phenylalanine and glycylphenylalanine and the practical numbering system adopted for performing the calculations. The initial geometries of the molecules by the semi empirical PM3 method are included in program CS Chem3D version 5.0.⁴ These geometries were optimized with the Gaussian 98 program packages using the B3LYP/6-31+G(d) methods and the default convergence criteria. To analyze the solvent effects on all the specimen involved in the selected ionization reaction, the polarized continuum model (PCM) of Tomasi et al. was used.⁵ Furthermore, to shed light on the experimental pK_a values of amino acids and dipeptide in water, we selected the solvation of the specimen by means of intermolecular hydrogen bonds (IHB) that involves one molecule of the mentioned specimen and some molecules of water.

3. Results and discussion

The tendency of a molecule to lose its hydrogen atom as an acidic proton is quantified as pK_a . The acidic dissociation constants of amino acids and dipeptides have been extensively studied in different kinds of background electrolytes.⁶ It is known that, in general, potentiometry and spectroscopic methods are highly sensitive and as such are suitable for studying chemical equilibria solutions. These methods involve the direct determinations of the mole ratio of acid-base conjugate pairs in a series of buffered solutions of known pH. If the components involved in the equilibrium can be obtained in pure form, and if

their spectral responses do not overlap, the analysis is very simple.^{2,7} The values of total energy and dissociation constants of glycine, phenylalanine and glycyphenylalanine are listed in Table 1 and Table 2 together with the calculated values using the Tomasi's method at the B3LYP/6-31+G(d) level of theory, respectively.

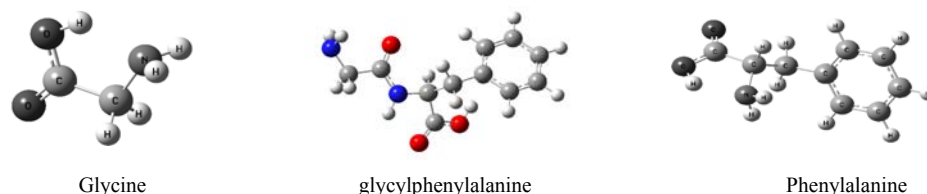


Fig. 1. Optimized Structures of glycine, phenylalanine and glycyphenylalanine for carrying out the calculations.

Table 1. Calculated total energy using the Tomasi's method at the B3LYP/6-31+G(d) level of theory for cationic, neutral and anionic specimen of glycine, valine, phenylalanine, glycyphenylalanine and glycyvaline, at 298.15 K.

N	Solvated Specimen	G_{sol}° (Hartree)	G_{sol}° /molecule (kJ mol ⁻¹)	Solvated Specimen	G_{sol}° (Hartree)	G_{sol}° /molecule (kJ mol ⁻¹)
Glycine				Phenylalanine		
0	H ₂ L ⁺	-5.5529E+02	-1.4579E+06	H ₂ L ⁺	-5.5529E+02	-1.4579E+06
1	H ₂ L ⁺ (H ₂ O)	-6.3174E+02	-8.2931E+05	H ₂ L ⁺ (H ₂ O)	-6.3174E+02	-8.2931E+05
0	HL	-5.5484E+02	-1.4567E+06	HL	-5.5484E+02	-1.4567E+06
1	HL(H ₂ O)	-6.3127E+02	-8.2870E+05	HL(H ₂ O)	-6.3127E+02	-8.2870E+05
2	HL(H ₂ O) ₂	-7.0773E+02	-6.1938E+05	HL(H ₂ O) ₂	-7.0773E+02	-6.1938E+05
0	L ⁻	-5.5439E+02	-1.4555E+06	L ⁻	-5.5439E+02	-1.4555E+06
1	L ⁻ (H ₂ O)	-6.3082E+02	-8.2811E+05	L ⁻ (H ₂ O)	-6.3082E+02	-8.2811E+05
2	L ⁻ (H ₂ O) ₂	-7.0726E+02	-6.1897E+05	L ⁻ (H ₂ O) ₂	-7.0726E+02	-6.1897E+05
3	L ⁻ (H ₂ O) ₃	-7.8370E+02	-5.1440E+05	L ⁻ (H ₂ O) ₃	-7.8370E+02	-5.1440E+05
4	L ⁻ (H ₂ O) ₄	-8.6011E+02	-4.5165E+05	L ⁻ (H ₂ O) ₄	-8.6011E+02	-4.5165E+05

N: total number of solvation water molecules; G_{sol}° : total free energy in solution; G_{sol}° /molecule,: total energy of solvated specimen per water molecule; H₂L⁺: cation species; HL: neutral; L⁻: anion species.

Table 2. Values of pK_a for the protonation of glycine, valine, glycyvaline, phenylalanine and glycyphenylalanine obtained using the Tomasi's method at the B3LYP/6-31+G(d) level of theory, at 298.15 K.

Specimen	Selected equations	pK _a (Calculated)	pK _a (Experimental) ^a
Glycine	H ₂ L ⁺ (H ₂ O) + H ₂ O = HL(H ₂ O) + H ₃ O ⁺	2.2916	2.34
	HL(H ₂ O) ₂ = L ⁻ (H ₂ O) + H ₃ O ⁺	9.6432	9.73
Phenylalanine	H ₂ L ⁺ (H ₂ O) = HL + H ₃ O ⁺	2.2799	2.50
	HL(H ₂ O) = L ⁻ + H ₃ O ⁺	8.8079	9.50
Glycyphenylalanine	H ₂ L ⁺ (H ₂ O) + 2H ₂ O = HL(H ₂ O) ₂ + H ₃ O ⁺	3.9151	3.23
	HL(H ₂ O) ₂ + H ₂ O = L ⁻ (H ₂ O) ₂ + H ₃ O ⁺	7.2077	8.14

^a Experimental data collected from Ref. ^{2,6}

References

- [1] Bailey, P. D. "An Introduction to Peptide Chemistry," (John Wiley and Sons, New York, 1992).
- [2] Sharifi, S. Nori-shargh, D. Bahadory, A. J. Braz. Chem. Soc. 18 (2007) 1011.
- [3] Sosnowska, N. S. Theor. Chem. Acc., 118 (2007) 281.
- [4] Program CS Chem3D 5.0; Program for Molecular Modeling and Analysis; Cambridge Soft Corporation: MA, USA, 2000.
- [5] Miertus, S. Scrocco, E. J. Tomasi, Chem. Phys. 65 (1982) 239.
- [6] Monajjemi, M. Garib, F. Aghaei, H. Shafiee, G. Thghvamanesh, A. Shamel, A. Main Group Met. Chem. 26 (2003) 39.
- [7] Blanco, S. E. Almandoz, M. C. Ferretti, F. H. Spectrochim. Acta, Part A. 61 (2005) 93.



Host-guest inclusion complex formation of cucurbit [6]uril with some aliphatic alcohols: Ab initio calculations study

Z. B. Nojini^{a*}, A. A. Rafati^b, S. M. Hashemianzadeh^c

^aDepartment of Chemistry, Faculty of Science, Shahid Chamran University, Ahwaz, Iran

^bFaculty of Chemistry, Bu-Ali Sina University, Hamedan, Iran

^cDepartment of Physical Chemistry, College of Chemistry, Iran University of Science and Technology, Tehran, Iran

E-mail: zb_nojini@scu.ac.ir and zb.nojini@gmail.com

Keywords: Cucurbit [6] uril, Inclusion complex, Reactivity indexes, Ab initio.

1. Introduction

Similar to the well known macrocyclic host compounds, such as crown ethers, cyclodextrins and so on, the cucurbit[n]uril homologues display remarkable affinity and selectivity due to the rigid macrocyclic structure with a unique cavity, rimmed by carbonyl oxygen. CB[6] was first synthesized in 1905 [1, 2]. CB[6] is a macrocyclic cavitands comprising six glycoluril units linked through 12 methylene bridges, which defines a hydrophobic cavity guarded by two carbonyl fringed portals.

2. Computational Method

Computational analysis of host-guest inclusion complex formation of the CB[6] with aliphatic alcohols were carried out, using the ab initio calculation at the level of HF/6-31G. The CB[6] was built and optimized by ab initio calculations.

3. Results and discussion

The penetrations of alcohols in cavity of CB[6] were studied. The potential energy surface plots (energy of the inclusion complex vs. the z coordinate) for all complexes of CB[6] with alcohols are shown in Figure. 1. The structures of all complexes at the minimum energy of complexation optimized by ab initio calculations at the level of HF/6-31G. Typically structures at each energy minimum obtained from HF/6-31G for the CB[6]-guest complexes are illustrated in Figure. 2.

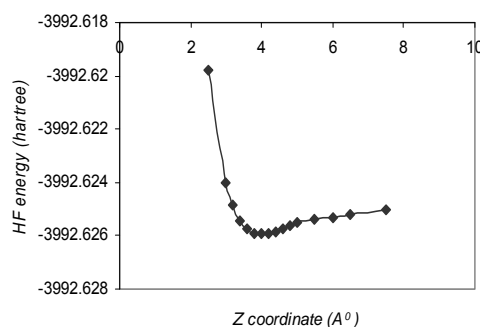


Fig. 1. Graphic diagram for emulation of the inclusion complexation of C₉-OH into CB[6].

The stability energy values for the complexes as well as each components, and HOMO, LUMO, and energy gap for complex formation between CB[6] and alcohols are listed in Table 1. To examine the binding properties of these complex formations, we calculated the total energy of the CB[6]-alcohol as well as the pristine CB[6] and alcohol molecules. The complex formation energy, E , was calculated using the following expression:

$$E = E_{(\text{complex})} - (E_{\text{CB}[6]} + E_{\text{alcohol}}) \quad (1)$$

Results show that the complex formation is stable than isolated molecules. Secondly, all the calculated formation energies are negative. As defined by Eq. (1), this means that the complex formation of the alcohols molecules is exothermic for CB[6].

Table 1. Electronic energies and HOMO, LUMO, and gap energies of the inclusion complexations of CB[6] with aliphatic alcohols of the HF optimized structures.

Type	E	ΔE	HOMO	LUMO	Gap energy
CB[6]	-97021.7	-	-9.43011	-0.0468	9.38331
C ₄ -OH/CB[6]	-103337	0.36707	-9.32562	-0.03048	9.29514
C ₅ -OH/CB[6]	-104398	0.32767	-9.30439	0.045715	9.350105
C ₆ -OH/CB[6]	-105460	0.37174	-9.29677	0.052790	9.349565
C ₇ -OH/CB[6]	-106522	0.46611	-9.42031	-0.0947	9.32561

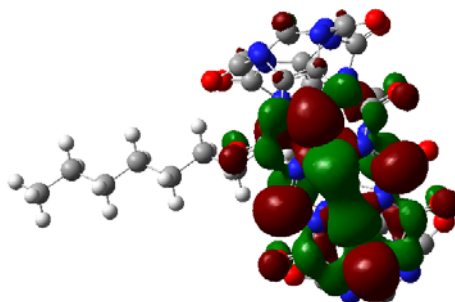


Fig. 2. Typically structures at each energy minimum obtained from HF/6-31G for the CB[6]-guest complexes.

4. Conclusions

The results of potential energy surfaces show that the alcohol molecules penetrate into the cavity of the CB[6] by the hydroxyl group with 1:1 stoichiometry, and the formed complex have minimum energy.

References

- [1] R. Behrend, E. Meyer, F. Rusche, J. Liebigs, Ann. Chem. 339 (1905) 1.
- [2] W. L. Mock, Top. Curr. Chem. 175 (1995) 1.

**The relation structure and detonation performance of explosives**

M.J. Gohar, H.R. Shamlouei*

Faculty of Science, Islamic Azad University of Gachsaran, Gachsaran, Iran

*shamluei@iaug.ac.ir

Keywords: Ab initio, Explosive performance, Nitramine**1. Introduction**

There is a need to synthesis, evaluate and application of new explosives to produce munitions with special applications.

In order to test these explosives various test methods is available but they are so expensive, and dangerous. So development of new high energy materials (HEMs) needs reliable prediction of desired properties such as performance, and vulnerability of them by computational methods. Methods for predicting the performance of new energetic materials before synthesis or formulation are recognized to be cost-effective, environmentally desirable and time-saving capabilities to use in the early stages of the development process [1,2]. The performance of explosives depends on some parameters such as enthalpy of detonation, detonation temperature, velocity and pressure. Various theoretical methods are employed to predict these parameters to calculate the performance of explosives. The heat [3,4], temperature [5], velocity and pressure of detonation [6,7], can be computed by various methods.

The enthalpy of formation of explosives can be calculated by the computational chemistry so the heat of detonation is derived by Eq1.

$$Q_{\text{det}} = \frac{\Delta_f H(\text{Detonation Products}) - \Delta_f H(\text{Explosives})}{M} \quad (1)$$

The density of explosive with the chemical formula of CaHbNcOd can be computed by ab initio method [8] and can be obtained by experimental equations such as Eq2 [Error! Bookmark not defined.].

$$\rho_0 = \frac{13.1466a - 5.3031b + 39.7241c + 29.3395d}{M_w} \quad (2)$$

The detonation temperature can be calculated by using the heat of detonation and average heat capacity of gaseous products. The detonation velocity and pressure is reported as Eq.2 and 3[Error! Bookmark not defined.].

$$D = A\phi^{0.5}(1 + B\rho_0) \quad A = 1.01 \quad B = 1.30 \quad (3)$$

$$P = K\rho_0^2\phi \quad K = 15.58, \quad \phi = NM^{0.5}Q^{0.5} \quad (4)$$

where N is mole number of gaseous products, and M is average molar mass of gaseous product

In this research, the heat, velocity and pressure of detonation for 6 nitramines were calculated and compared with each others.

2. Methods

The structures and enthalpies of formation for 6 nitramines with 1-6 N-NO₂ groups were calculated by HF and B3LYP method with the 6-311++g** basis set and then by using Eq1 to 4, the explosive performance was calculated. In table1 a list of 6 nitramine can be seen.

Table1. The list of selected nitramines.

$\text{C}_5\text{H}_{10}\text{N}_2\text{O}_2$	$\text{C}_4\text{H}_8\text{N}_4\text{O}_4$	$\text{C}_3\text{H}_6\text{N}_6\text{O}_6$
$\text{C}_2\text{H}_4\text{N}_8\text{O}_8$	$\text{CH}_2\text{N}_{10}\text{O}_{10}$	$\text{N}_{12}\text{O}_{12}$

3. Results and discussion

The structure of each material in table1 was optimized. For instance, the optimized structure of $\text{C}_2\text{H}_4\text{N}_8\text{O}_8$ is presented in Fig. 1.

The heat of detonation was calculated by Eq1 and then the densities of 6 nitramines were calculated by Eq2. By using the heat of detonation and the density for each nitramines, the velocity and pressure of detonation as two important parameters in explosives efficiency were calculated. The results are shown in table2.



Fig. 1. Optimized structure for $C_2H_4N_8O_8$.

Table 2. Calculated Density, heat Pressure and Velocity of Detonation for nitramines with different N-NO₂ number.

Number of N-NO ₂	Heat of Detonation (kJ.mol ⁻¹)	Density g.cm ³	mole number of produced gas	Detonation Velocity m.s ⁻¹	Detonation Pressure kbar
1 N-NO ₂	1121.559	1.159971	8	-	-
2-N-NO ₂	-966.616	1.627214	10	27000	36
3N-NO ₂	-1937.22	1.900824	9	32000	52
4N-NO ₂	-3842.93	2.080509	9	40000	72
5N-NO ₂	-4999.13	2.207547	10.5	44000	86
6N-NO ₂	-1381.61	2.30212	12	22000	46

The density and heat of detonation is plotted in Fig 2 and 3. The results show that by increasing the number of N-NO₂ groups, the density and heat of detonation increases.

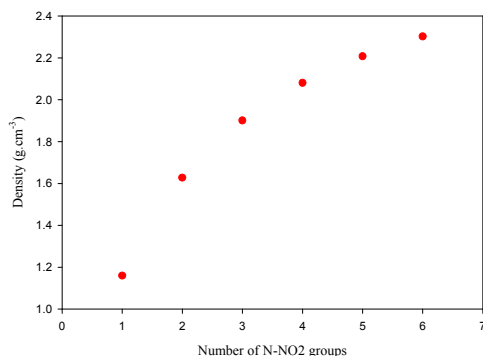


Fig. 2. Predicted density versus number of N-NO₂.

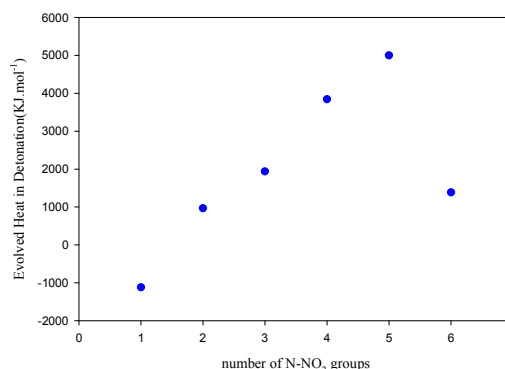


Fig. 3. Predicted evolved heat in detonation versus number of N-NO₂.

4. Conclusions

In this research the effort to correlating the structure and detonation properties of explosives was done. Although the predicted numbers are not completely correct but the results are comparable and the effect of structure is obviously seen. The continuing work is done to correct the models and so the obtained result to be reliable.

References

- [1] M.S. Miller, B.M. Rice, A.J. Kotlar, R.J. Cramer, Clean Products and Processes, 2 (2000) 37.
- [2] M.J. Kamlet, S.J. Jacobs, J. Chem. Phys. 48 (1968) 23.
- [3] M. H. Keshavarz, Propellants Explos., Pyrotech. 33 (2008) 448.
- [4] B.M. Rice, J. Hare, Thermochimica Acta, 384 (2002) 377.
- [5] M. H. Keshavarz, H. R. Nazari, Journal of Hazardous Materials, B133 (2006) 129.
- [6] M.J. Kamlet, S.J. Jacobs, Journal of Chemical Physics, 48 (1968), 20.
- [7] M. H. Keshavarz, Journal of Hazardous Materials 141 (2007), 536.
- [8] C.K. KIM, S.G. CHO, C.K. KIM, H.Y. PARK, H. ZHANG, H.W. LEE, Journal of Computational Chemistry, 29 (2008) 182.



A mathematical model for correlation rate constant of inorganic reactions with compositions in binary aqueous-organic systems

A. Habibi-Yangjeh^a, M.Esmaili-Taramsari^{b*}

Department of Chemistry, University of Mohaghegh Ardabili, Ardabil, Iran

^a(E-mail: ahabibi@uma.ac.ir)

^b(E-mail: esmaili_23@yahoo.com)

Keywords: Kinetic, Inorganic reaction, solvent effects.

1. Introduction

Solvent effects play a key role in many chemical and physical processes in solutions [1-3]. The study of solute-solvent interactions in binary mixtures is more complex than in pure solvents. Very recently, we have correlated various solvatochromic parameters with composition in aqueous and organic binary solvent systems using combined nearly ideal binary solvent/Redlich-Kister (CNIBS/R-K) equation [4].

In the presence work, to evaluate the accuracy and applicability of the CNIBS/R-K model for calculating $\ln k$ of inorganic reactions in binary aqueous-organic solvent systems, 110 experimental data sets at temperatures ranging 20-65 °C were used.

2. Theoretical treatment

The proposed model to calculate the $\ln k$ of inorganic reactions in binary mixed solvent system at a constant temperature is expressed as:

$$\ln k_m = f_w \ln k_w + f_o \ln k_o + f_w f_o \sum_j M_j (f_o - f_w)^j \quad (1)$$

In some cases, the numerical values of $\ln k_o$ are not available. To overcome this, it is possible to consider $\ln k_o$ as a model constant, B, and rewrite equation (1) as:

$$\ln k_m = f_w \ln k_w + B f_o + f_w f_o \sum_j M_j (f_o - f_w)^j \quad (2)$$

In similar way, if the value of $\ln k_w$ was not available, the model is written as:

$$\ln k_m = A f_w + B f_o + f_w f_o \sum_j M_j (f_o - f_w)^j \quad (3)$$

To assess the accuracy of the equations, the experimental values of the $\ln k$ were fitted into the equation and the mean percentage deviation (MPD) and individual percentage deviation (IPD) between experimental and calculated values is considered as an accuracy criterion.

3. Results and discussion

In order to evaluate the accuracy of the model, rate constants for various inorganic reactions in binary aqueous-organic solvent systems in temperatures ranging 20 to 65 °C were applied. To evaluate the correlation ability of the model, whole data points (n=753) in each set have been fitted to the model and back-calculating $\ln k$ values have been used to calculate MPDs.

As can be seen approximately 79.5% of the calculated $\ln k_m$ values have IPD lower than 0.5%. For the correlation equations the MPD values are between 1.2105×10^{-5} and 1.01328. In (FIG. 1) the calculated values of $\ln k_m$ in various binary solvent systems were plotted vs. the experimental values of them.

For this correlation, the following equation can be obtained:

$$\ln k_{cal} = 0.99967 \ln k_{exp} - 0.00157 \quad (4)$$

(n = 753, R² = 0.999640, s.e = 0.03977, F = 2060573.18, MPD = 0.31043)

As can be seen from the statistics of the proposed equation, the model is statistically valuable. Correlative equations at various temperatures are also acceptable. The distribution of IPD values for the correlative equations in different groups (IPD < 0.5, 0.5-1, 1-1.5 and > 1.5%) have been calculated (FIG. 2).

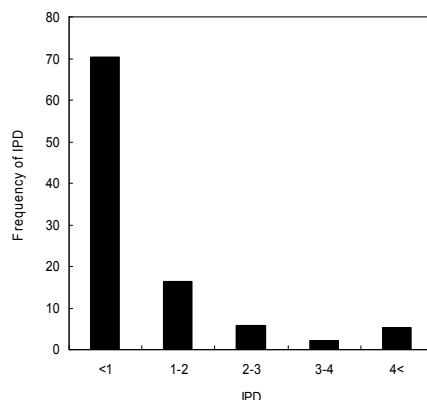


Fig. 1. Plot of frequency of individual percentage deviations (IPD) vs. different groups of IPD (IPD<0.5, 0.5-1, 1-1.5 and >1.5) for the proposed equations.

The model did not show proportional and systematic error, because the slope ($a = 0.99967$) and intercept ($b = 0.00157$) are not significantly different from unity and zero, respectively and the propagation of errors in both sides of zero are random (FIG. 2). As expected, the model shows a strong correlation between predicted and experimentally measured values.

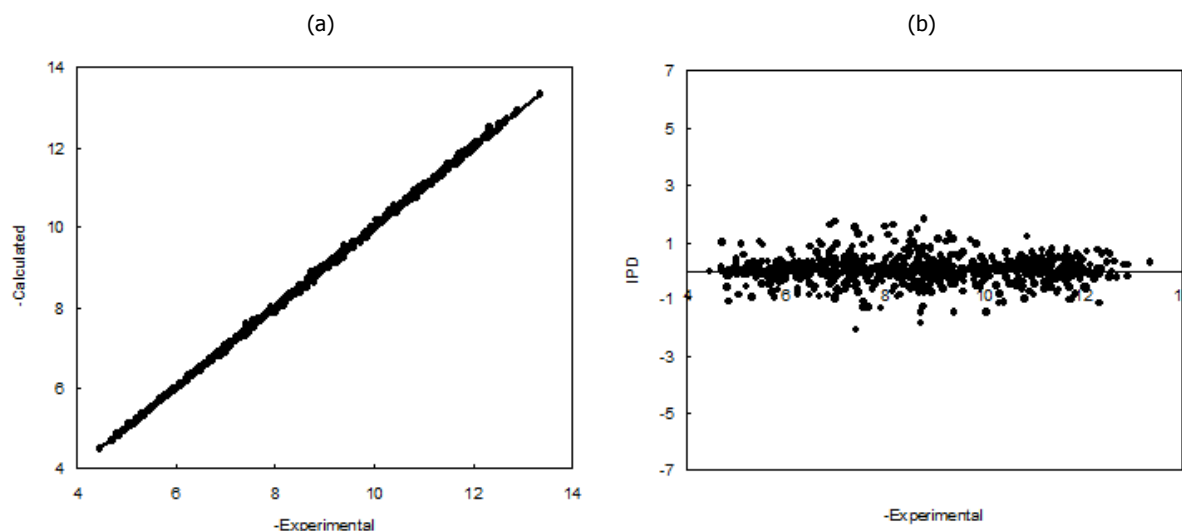


Fig. 2. Plot of the calculated values of $\ln k$ from the correlation equations vs. the experimental values of it for various binary aqueous-organic solvent systems(a) and plot of IPD of $\ln k$ vs. the experimental values of it (b).

4. Conclusions

The model provides a simple computational model to correlate/predict the $\ln k$ values in various binary aqueous-organic solutions. For the proposed model, MPD is about 0.31. Approximately 79.5% of the calculated values of $\ln k$ have IPD lower than about 0.5% to predict unmeasured values by using only five experimental data.

References

- [1] Reichardt, C, Solvents and Solvent Effects in Organic Chemistry, 3rd ed, VCH, (2003).
- [2] Marcus, Y, Chem. Soc. Perkin Trans. 2 (1994) 1015.
- [3] Engberts, J. B. F. N. Blandamer, M, Phys. Org. Chem. 11 (1998).
- [4] Habibi-Yangjeh, A, Bull. Korean. Chem. SOC. 25 (2004) 1165.

Intramolecular Hydrogen Bond in the Hydrazinoturns

E. Rasti, H. A. Dabbagh*

Department of Chemistry, Isfahan University of Technology, 8415483111, Isfahan, Iran

(E-mail: dabbagh@cc.iut.ac.ir)

Key words: Intramolecular hydrogen bond, Hydrazinoturn, Conformational analysis.**1. Introduction**

Hydrogen bonding always is an important subject in old and modern chemistry [1], because it has an essential role in life science. It is a fundamental for molecular recognition and supramolecular synthesis. Recently, there has been increasing interest in unconventional hydrogen bonds in modern chemistry [2]. One of the challenging issues in molecular design is the control of three-dimensional structures [3]. Extensive molecular dynamics studies describe folding phenomena in these oligomers. Even in γ -peptides, characteristic folding patterns were found [4]. In this research, we studied of hydrazino acetamides in gas phase at the DFT at 6-31+G** levels of theory in order to speared hydrogen bond network. Quantum chemical conformational analysis was performed by rotating around the appropriate bond for each compound studied in this paper.

2. Methods

All of the structures studied in this work were optimized by density functional method (DFT) at B3LYP level applying 6-31+G** basis sets individually. All calculations reported in the present study were carried out using the GAUSSIAN 03 software. Potential energy scan (PES) studies of these compounds were performed at HF/6-31G level.

3. Results and discussion

The 8 molecules selected for this study are listed in (Scheme 1). These molecules are selected, because, **1a**, **1b**, **5a** and **5b** are presumed to show eight-membered bifurcated hydrogen bonded pseudo cycle network. Molecules **2** and **3** show only O...H hydrogen bond. Molecules **4a** and **4b** show only.

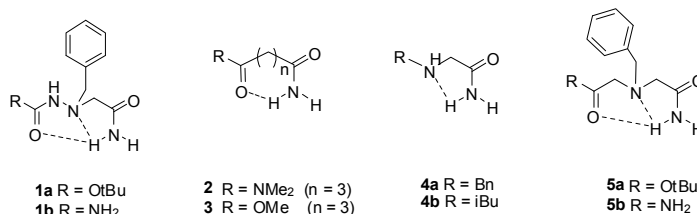
**Scheme 1.** The 8 molecules for which structures have been investigated in this study.

Table 1 lists the figures related to intramolecular hydrogen bonding was calculated at B3LYP/6-31+G** levels. The structural parameters of minima conformers of compounds **1-5b** are listed in Table2.

Table 1. Geometrical properties of the hydrogen bond network of molecules **1-5b** noticed in this work.

Com.	B3LYP/6-31 +G**			
	-O...H-N (Å)	-O...H-N (°)	-N...H-N (Å)	-N...H-N (°)
1a	2.09	163.4	2.39	100.4
1b	2.00	162.2	2.44	98.4
2	1.96	158.4	-	-
3	2.17	152.5	-	-
4a	-	-	2.27	105.2
4b	-	-	2.25	106.8
5a	2.19	151.4	2.50	97.3
5b	2.12	153.5	2.52	96.4

Molecules **1a**, **1b**, **5a** and **5b** are very similar. Molecule **1a** and **1b** experiences stronger internal hydrogen bonding and this could be due to the presence of a β nitrogen atom in molecule **1a** and **1b**. This nitrogen atom is not present in molecules **5a** and **5b**. For molecules **2** and **3**, which prefer the eight-membered hydrogen-bonded pseudo cycle, the reading of Table 1 indicates strong intramolecular hydrogen bonding, particularly for molecule **2**. Molecules **4a** and **4b** exhibit similar intramolecular hydrogen bond network. A clear intramolecular hydrogen bond exists between H and N, thus forming a C₅ pseudo ring. The PES trajectories from HF/6-31G of Molecules **1a** and **5a** are shown in Fig.1. This plot shows us similar stability

and instability especially for two compounds **1a** and **5a**. The PES plot of **1b** and **5b** predicts similar stability for all two compounds (Fig. 1). The energy minima of **1a**, **1b**, **5a** and **5b** indicate strong intramolecular hydrogen bonding for both compounds. The energy barrier for rotation of conformers of **1a**, **1b**, **5a** and **5b** are approximately 15.5, 11.0, 14.0 and 9.0 kcal/mol, respectively.

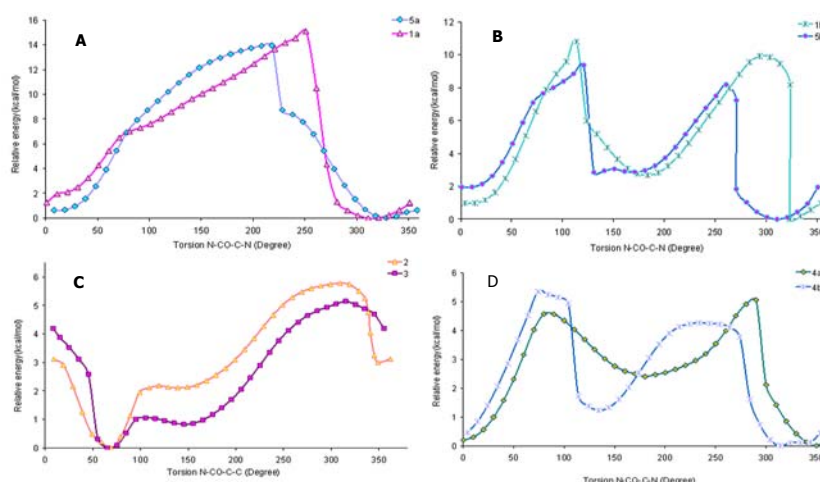


Fig. 1. (A) PES for **1a** and **5a**, (B) PES for **1b** and **5b**, (C) PES for **2** and **3** and (D) PES for **4a** and **4b**.

Table 2. Structural parameters (H-bond length and H-bond angle) of minima conformers which obtained from PES plot at HF/6-31G level.

Com.	Conf.	HF/6-31G			
		Dihedral φ^a	-O...H-N (Å)	-O...H-N (°)	-N...H-N (°)
1a	328.1		2.08	162.9	2.45
1b	323.7		1.99	164.0	2.48
2	69.0		2.09	151.9	-
3	65.2		2.16	151.4	-
4a	350.2		3.79	70.3	2.34
4b	314.1		4.31	40.2	2.31
5a	310.8		2.06	158.9	2.62
5b	310.8		2.01	158.8	2.62

^a φ is dihedral angle (°) corresponding the rotation around the amidic group.

Thus, molecule **1a** and **5a** both present a high energy rotation barrier, resulting in a highly stable "hydrazinoturn" conformation. The PES trajectory plot for -CONH₂ group of molecules **2** and **3** are shown in Fig. 1. This plot predicts similar stability for all two compounds which is a result of similar interactions. The energy barrier of **2** and **3** are 6.0 and 5.0 kcal/mol, respectively, which indicates a much smaller barrier than molecule **1a** and **1b**. The O...H hydrogen bonding C₈ pseudocycle pattern thus results in a more flexible dynamic pattern than the "hydrazinoturn". The PES trajectory of amidic group of **4a** and **4b** shows energy minima conformers appearing at similar dihedral angle region (Fig. 1). The energy barrier for the conformers of **4a** and **4b** was calculated less than 4.5-5.5 kcal/mol indicating that N...H-N of the C₅ pseudocycle hydrogen bonding pattern is also more flexible than the "hydrazinoturn".

4. Conclusions

This study confirms that the hydrogen bond network in conformer with minimum energy in molecule **1a** and **1b** is stronger than the one in molecules **3**, **4a**, **4b**. It was also concluded that molecules **1a**, **5a** and **5b** behaves a bifurcated hydrogen bond network is observed in both cases. The hydrogen bond network of Molecules **1a**, **1b**, **5a** and **5b** is actually relatively stronger than the mere O...H bond (as in **3**) but dramatically stronger than the mere N...H hydrogen bond (as in **4a** and **4b**).

References

- [1] Jeffrey, G. A, An Introduction to hydrogen bonding, Oxford University Press, Oxford, 1997.
- [2] Steiner, T, Crystallogr. Rev. 6 (1996) 1.
- [3] Goodman, M. Ro, S. In Burger's Medicinal Chemistry and Drug Discovery, John Wiley & Sons, 1995.
- [4] Hintermann, T. Gademann, K. Jaun, B. Seebach, D, Helv. Chim. Acta 81 (1998) 983.



Investigation of interaction host-guest chemistry of Cucurbit[6]uril-Ethylamine using DFT calculations of NQR parameters

*N. Ahmadian^a and A. Karamiyar^b

^aIslamic Azad University Ghaemshahr Branch

(E-mail:nsm_ahmadian@yahoo.com)

^bDepartment of chemistry, University of Urmia, Urmia, Iran

Keywords: NQR, Cucurbit[6]uril, Ethylamine, Host-guest, DFT.

1. Introduction

Cucurbituril (CB[6]) a macrocyclic cavitand comprising six glycoluril units, has a hydrophobic cavity that is accessible through two identical carbonyl-fringed portals [1]. Cucurbiturils were first synthesized in 1905 by Behrend [2], but structure was not defined until 1981 [3]. Crystal structure analyses indicate that the cavity of this macrocycle has enough room to host a variety of molecules inside it. So far, several inclusion compounds, (pseudo)rotaxanes and molecular necklaces have been prepared thereby opening novel perspectives in the design of supramolecular architectures [4]. Such cavities are also important building blocks for nanostructure materials and nanocapsules [5]. When an intramolecular cavity exists in a molecule, it can trap another chemical species to form a host-guest complex. Host-guest chemistry is the name given to the study of the encapsulation of one compound (the guest) by a second compound (the host) through non-covalent interactions [6]. On the other hand, nuclear quadrupole resonance (NQR) spectroscopy is a very direct and experimentally quite simple method for studying the interaction between the electric quadrupole moment of a nucleus and the electric field gradient at its site. This approach provides a great deal of information about charge distribution [7]. To the best of our knowledge, there is no report on the prediction of quadrupole coupling constant, asymmetry parameter, η , and resonance frequencies of cucurbituril homologues and/or inclusion compounds, so far. Therefore in this work, NQR parameters of ethylamine-cucurbit[6]uril inclusion complex were predicted by using quantum mechanical calculations, see Fig. 1.

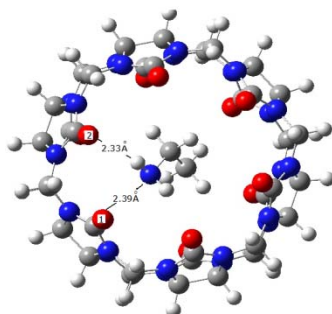


Fig. 1. Cucurbit[6]uril-ethylamine host-guest complex.

2. Method

The electrical quadrupole moment eQ , is a characteristic of a particular nucleus with spin angular momentum, I , equal or greater than one ($I \geq 1$). This is a measure of the deviation of the nuclear charge distribution from spherical shape. The electric quadrupole moment interacts with electric field gradient (EFG). This originates from the internal electrostatic charges at the site of the nucleus [8]. Since, ^{14}N , ^{17}O and ^2H nuclei have spin angular momentum greater than one, therefore it is expectable that the molecules contain these kind of nuclei can be studied by using NQR spectroscopy from both experimental and theoretical point of views. All quantum chemical calculations were carried out using Gaussian 98 Program. First cucurbit[6]uril and ethylamine molecules were drawn in HyperChem program and then were partially optimized at molecular mechanic level and finally were feed into Gaussian package. After that these molecular structures were optimized from chemical intuitive geometries with the semi-empirical PM3 method and then refined at B3LYP/6-31G(d) and B3LYP/6-311G levels for reaching the best optimization with D_{nh} ($n=6$) and C_1 symmetries and also for the calculation of the EFG tensors. Finally, geometrically optimized ethylamine at B3LYP/6-31G(d) level was included into geometrically optimized cucurbit[6]uril at B3LYP/6-31(d)G level which then were optimized again by using Gaussian package for obtaining DFT nuclear quadrupole resonance (NQR)



parameters. Quadrupole coupling constant, χ_{zz} , and asymmetry parameter, η , of the EFG tensor carry the structural information of the chemical environment surrounding the nucleus under study which are defined as follows:

$$\chi_{zz} = \left(\frac{e^2 Q q_{zz}}{h} \right) \quad \text{with} \quad eq_{zz} = V_{zz} \quad (1)$$

$$\eta = \left| \frac{V_{xx} - V_{yy}}{V_{zz}} \right| \quad (2)$$

where V is the electrostatic potential at the nucleus, due to the surrounding charges, e the electronic charge, q the largest principle value of the EFG tensor, Q electric quadrupole moment and h is Planck's constant.

3. Results and discussion

Table 1 shows the ^{14}N and ^{17}O quadrupole coupling constant, (χ_{zz} , in kHz), and asymmetry parameter, η , and resonance frequencies (in kHz) of cucurbit[6]uril and ethylamine at DFT/6-311G and DFT/6-31G(d) theoretical quantum mechanic calculation levels. It seems that due to hydrogen bond formation between hydrogen atoms of ethylamine molecule and oxygen atoms of cucurbit[6]uril, the electrical charge gradient surrounding nitrogen atom of ethylamine reduces which in turn causes to decrease in quadrupole coupling constant, χ_{zz} , which is clear in obtained results. Besides, this decrease leads to an increase in asymmetry parameter (η) of ethylamine molecule.

Table 1. ^{17}O and ^{14}N NQR parameters of interaction host-guest chemistry of Cucurbit[6]uril-Ethylamine.

Method	Ethylamine		Cucurbit[6]uril			Cucurbit[6]uril-Ethylamine		
	N	O ₁ O ₂		N	O ₁ O ₂			
η	B3LYP/I		0.093	0.516	0.516	0.200	0.542	0.558
	B3LYP/II	0.102	0.420	0.420		0.167	0.441	0.459
χ_{zz}	B3LYP/ I		6.904	9.23	9.23	5.88	9.36	9.33
	B3LYP/II	4.91	7.72	7.72		4.90	7.84	7.78

I: 6-311G and II: 6-31G(d)

4. Conclusion

From our findings, it could be concluded that hydrogen bond formation between hydrogen atoms of ethylamine and portal oxygen atoms of cucurbit[6]uril can changes the charge distribution surrounding nitrogen atom of ethylamine which in turn can changes the nuclear coupling constant, asymmetry parameters and resonance frequencies. Therefore, hydrogen bonding plays an important role in NQR spectroscopy of host-guest chemistry.

References

- [1] S. Y. Jon, N. Selvapalam, D. H. Oh, J.-K. Kang, S.-Y. Kim, Y. J. Jeon, J. W. Lee, K. Kim. J. Am. Chem. Soc. 125 (2003) 10187.
- [2] B. E. Meyer, F. Rusche, Liebigs Ann. Chem. 339 (1905) 1.
- [3] W. A. Freeman, W. L. Mock, N.-Y. Shih, J. Am. Chem. Soc. 103 (1981) 7367.
- [4] Fabio Pichierri, Chemical Physics Letters 390 (2004) 214.
- [5] J. Lagona, P. Mukhopadhyay, S. Chakrabarti, L. Isaacs, Angewandte Chemie-International Edition, 44 (2005) 4844.
- [6] Fabio Pichierri, Chemical Physics Letters, 403 (2005) 252.
- [7] F. Elmi, N. L. Hadipour, F. Safinezhad, Chemical Physics Letters, 375 (2003) 273.
- [8] M. Mirzaei, N. L. Hadipour, Chemical Physics Letters, 438 (2007) 304.

**Theoretical Study of the Antioxidant Properties of Trolox in the Gas Phase and Solvent Environment**

Elyas Nazarpour, Mehdi D. Davari, Mansour Zahedi*

Department of Chemistry, Faculty of Sciences, Shahid Beheshti University, G.C., Evin, 19839-6313, Tehran, Iran

(E-mail: elyasnazarpour@yahoo.com)

Keywords: trolox (TrOH), Bond dissociation enthalpy (BDE), Ionization potential (IPr), Proton dissociation enthalpy (PDE), Proton affinity (PA), Electron transfer enthalpy (ETE).

1. Introduction

Trolox (TrOH), a phenolic antioxidant originally designed for food preservation [1], has a chromane structure similar to α -tocopherol (α -TOH), but without the polyisoprenoid hydrophobic tail. It is both water and lipid soluble [2] and has been studied chemically for its stabilizing radical-trapping activity [3] and therapeutically for its capacity to limit myocardial infarction [4] and prevent liver necrosis caused by lipid peroxidation [5]. TrOH has advantages over α -tocopherol, the latter being only lipidsoluble due to the presence of a carboxyl group *in lieu* of a phytol chain which imparts TrOH with water solubility. TrOH is used as a standard antioxidant in biochemical studies against which the antioxidant capacity of compounds is compared. To provide more insight into the antioxidant properties of TrOH, we here present a theoretical study of its capacity as a trapper of free radicals within the DFT framework. In this paper, we focus on the reaction mechanisms between TrOH and hydroperoxyl radical. Besides the two generally accepted mechanisms of phenolic antioxidants action [6,7], recently discovered sequential proton loss electron transfer (SPLET) mechanism [8,9] have been also studied. Further important goal of this paper is to estimate the solvent effect on the antioxidant related parameters of TrOH through these three possible mechanisms. Thus, the effect of solvent and the role of them on the energetics of these three types of reactions were also investigated.

2. Methods

The hybrid B3LYP functional and the 6-31G(d) basis set was used for the optimization of all of the stationary points in the gas phase. Frequency calculations were used to characterize stationary points as minima or first-order saddle points. Single point calculations have been carried out using 6-311+G(2d,2p) basis set. All reactions and activation enthalpies reported were zero-point (ZPE) corrected with unscaled frequencies. Net atomic charges and spin densities were obtained using the natural population analysis of Weinhold et al. [10]. To analyze the hydrogen bondings we have used the natural bond orbital (NBO) [11]. The solvent effect was taken into consideration in all of the calculations by employing the self-consistent reaction field (SCRF) method [12] with a polarized continuum model (PCM). The effectiveness of the model has been verified in previous studies. All calculations were performed with Gaussian 98 program [13].

3. Results and discussion

A proposed mechanism [5] which can be envisioned for sequential hydrogen abstractions from TrOH has been presented in Fig. 11. In this mechanism **TrOH** is trolox, **TrO[•]** is the phenoxy radical, **TrSQ** is trolox semiquinone, **TrKD** is trolox ketodiene and **TrQ** is the trolox quinone. As can be seen in this figure, mechanism starts with transformation of **TrOH** to **TrO[•]** in the presence of hydroperoxyl radical which is subsequently converted to a **TrSQ** after second hydrogen abstraction. Then, the formation of **TrSQ** is followed by production of a **TrKD** and finally **TrQ**. Thomas and Bielski [14] have also described this sequence of events after the one-electron oxidation of TrOH by pulse radiolysis. As has been reported by Liu and coworkers [15], from the isolated reactants, an H-bonded intermediate is initially formed in each reaction. As one can see, these intermediates have been named **INT-1H** and **INT-2H** respectively. There is an H-bonded intermediate before isolated products in each reaction, too. These intermediates have been named **INTp-1H** and **INTp-2H**, respectively. The calculated transition states **TS1** and **TS2** correspond to two hydrogen abstraction pathways. The mechanism shown in Figure 1 involves the phenolic hydrogen (H1) and the acidic hydrogen (H2) abstractions from TrOH by hydroperoxyl radical. The activity of the phenolic antioxidants is determined by O–H bond dissociation enthalpy (BDE), and O–H BDE is mainly governed by the stability of the phenoxy radical. In other word, the higher the stability of phenoxy radical or the weaker the strength of the O–H bond, the higher the antioxidant activity will be. These data, together with the fact that the primary oxidation products of monophenolic compounds formed by hydroperoxyl are phenoxy radicals, indicate that TrOH radical must evolve chemically to

the **TrKD** form through a series of intermediates starts with a hydrogen abstraction reaction of the **TrO[•]** radical to form a ketodiene, which is subsequently hydrolyzed to trolox quinone, **TrQ**.

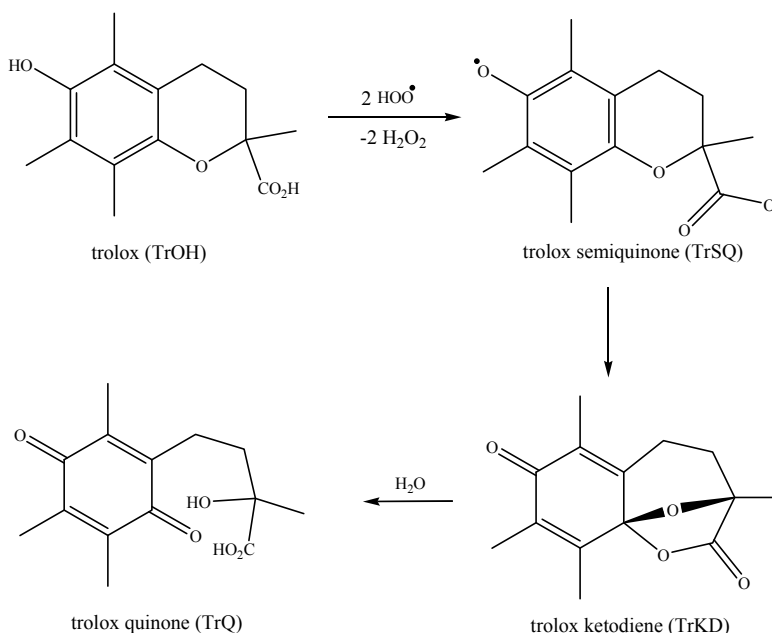


Fig. 1. Proposed mechanism for the sequential hydrogen absorption from TrOH by hydroperoxyl radical in reference [5]. Different species in the oxidation pathway has been shown.

4. Conclusions

Density functional calculations have now been performed with B3LYP functional to investigate the mechanism of hydrogen abstraction from TrOH by the hydroperoxyl radical (HOO[•]). The calculated O–H bond dissociation enthalpies (BDEs) and ionization potentials (IPs) for this compound in the gas phase as well as different solvents show that in the gas phase or in the presence of apolar solvents the hydrogen transfer is the predominant mechanism. Whereas, the antioxidant activity of TrOH was found to be dominated by the electron transfer in the polar solvent. The results obtained are in good agreement with experimental study of antioxidants effectiveness of trolox.

References

- [1] J. W. Scott, W.M. Cort, H. Harley, J. Am. Chem. Soc. 51 (1974) 200.
- [2] D. Metodiewa, H. B. Dunford, Biochem. Int. 25(1991) 895.
- [3] M. J. Thomas, B. H. J. Bielski, J. Am. Chem. Soc. 111(1989) 3315.
- [4] K. Lee, P. Canniff, D. Hawel, P. Silver, A. Ezrin, Gen. Pharmacol. Ther. 47(1990) 174.
- [5] T. Doba, G. W. Burton, K.U. Ingold, Biochim. Biophys. Acta. 899(1985) 76.
- [6] J. S. Wright, D. J. Carpenter, D. J. McKay, K. U. Ingold, J. Am. Chem. Soc. 119 (1997) 4245.
- [7] E. G. Bakalbassis, A. T. Lithoxoidou, A. P. Vafiadis, J. Phys. Chem. A. 107 (2003) 8594.
- [8] E. Klein, V. Lukes, M. Ilcin, Chem. Phys. 336 (2007) 51.
- [9] V. B. Luzhkov, Chem. Phys. 314 (2005) 211.
- [10] F. Weinhold, J. E. Carpenter, The structure of small molecules and ions; Plenum: New York, 1988.
- [11] A. E. Reed, L. A. Curtiss, F. Weinhold, Chem. Rev. 88 (1988) 899.
- [12] M. W. Wong, M. J. Frisch, K. B. Wiberg, J. Am. Chem. Soc. 114 (1992) 1645.
- [13] M. J. Frisch et al., Gaussian 98, revision A.9; Gaussian, Inc.: Pittsburgh, PA, 1998.
- [14] M. J. Thomas, B. H. J. Bielski, J. Am. Chem. Soc. 111 (1989) 3319.
- [15] S. Xu, G. Wang, H. M. Liu, L. J. Wang, H. F. Wang, J. Mol. Struct.: THEOCHEM 809 (2007) 79.

Study of the electric field effect on the electronic properties of Au/Cytosine/Au structure

S. Azimi^a, H. Milani Moghaddam^b

^a Physics Department, Payame Noor University of Mashhad ,Mashhad ,Iran

^b Physics Department, Mazandaran University, Babolsar,Iran

(E-mail: s_a495@yahoo.com)

Keywords: Molecular electronics, Cytosine, Density functional theory, Density of states.

1. Introduction

With the emergence of molecular electronics, industry circuits by decreasing the size of devices and so simultaneously increase the speed [1,2]. That is due to the fact that devices in molecular electronics are strongly dependent on the quality and nature of the contacts [3]. In the last decade of the 20th century experiments on DNA charge transfer either single molecule or in solution showed diverse behaviors. One of the bases of DNA is Cytosine which further details will be provided in subsequent sections [4]. In this work, we have performed Density Functional theory (DFT) method to study the electric field effect on the electronic properties of Au/MSC/Au structure, especially in the MSC/Au contact where the MSC is S-Cytosine-S Molecule. We also investigate that how HOMO-LUMO gap (highest occupied molecular orbital and lowest unoccupied molecular orbital) and density of electronic states (DOS) in Au/MSC/Au and 3Au/MSC/3Au structures change by applying an electric field.

2. Methods

All calculations are performed using Gaussian03 program. The following structures are optimized at DFT-B3LYP level of theory. We choose the basis set 6-31G(d) for C, N, H, O and S atoms and LanL2DZ for Au atom. We consider any Au/MSC contact as model with $n = 1, 3$ atoms, where n is the number of Au atoms (Figure 1:a-b).

3. Results and discussion

Electric fields are applied in the greatest dipole moment direction. We apply the electric fields in the +X and -X axis direction for the AU/MSC/Au and 3AU/MSC/3Au structures, respectively. Figure 2 and 3 show HOMO-LUMO gap (HLG), $HLG = E_{LUMO} - E_{HOMO}$, for the AU/MSC/Au and 3Au/MSC/3Au structures, in that order. We also study the effect of different electric fields on DOS of the Au/MSC/Au and 3Au/MSC/3Au structures. (see figures 4 and 5). By attaching more Au atoms to MSC, HLG behavior with field resembles more to semiconductors behavior. According to panels (a), (b) in figures 4 and 5, HLG decrease by increasing the number of Au atoms in the same electric field.

4. Conclusions

We have seen that by attaching Au atoms to MSC a semiconductor-like behavior can be achieved. We can also see that HLG of the Au/MSC/AU and 3Au/MSC/3AU structure decrease by increasing the applied electric field. The HLG of the Cytosine molecule is 0.192 eV without applied electric field.

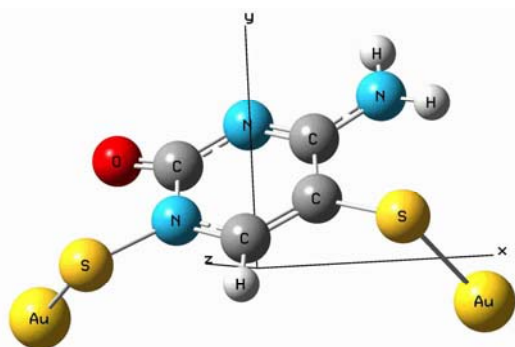


Fig. 1-a. The AU/MSC/AU.

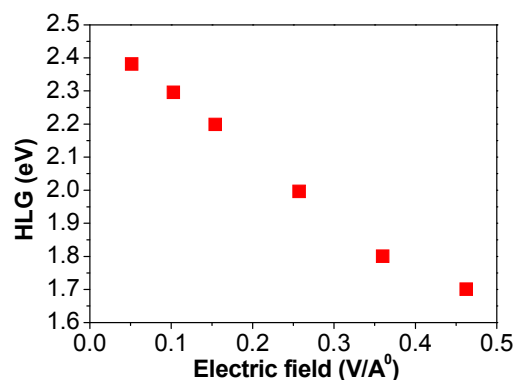


Fig. 2. HLG vs. electric field for the AU/MSC/Au structure.

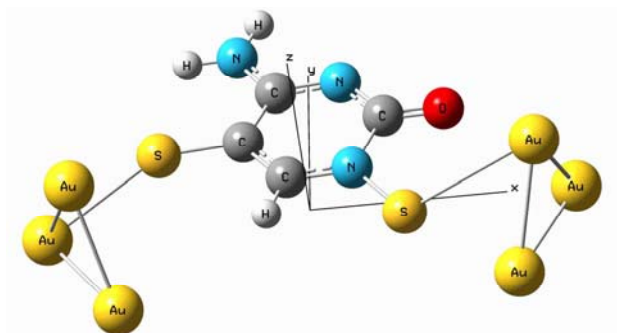


Fig. 1-b. The 3AU/MS/3AU structure.

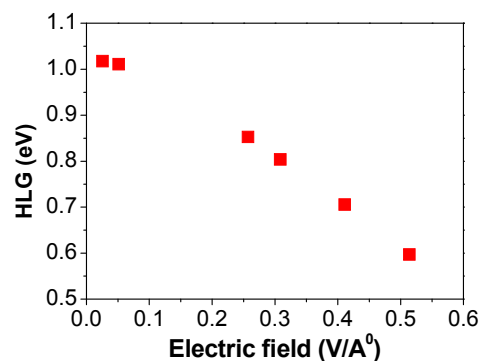


Fig. 3. HLG vs. electric field for 3AU/MS/3AU structure.

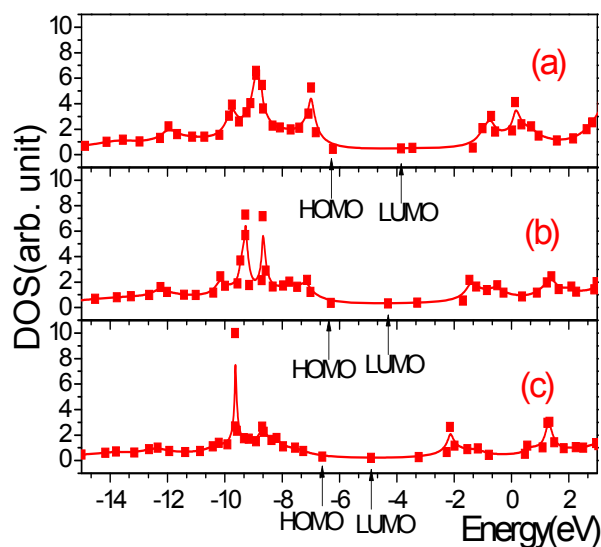


Fig. 4. DOS of the AU/MS/AU structure vs. electric fields: field for figure (a) 0.05 (V/A⁰), (b) 0.25 (V/A⁰), (c) 0.46 (V/A⁰).

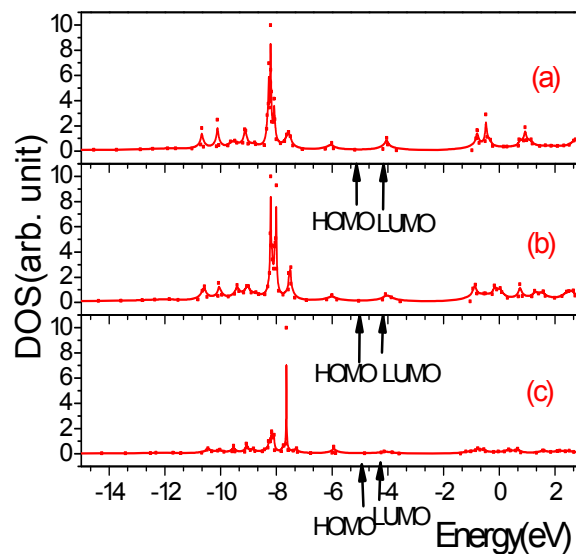


Fig. 5. DOS of the 3AU/MS/3AU structure vs. electric fields: field for figure (a) 0.05 (V/A⁰), (b) 0.25 (V/A⁰), (c) 0.51 (V/A⁰).

References

- [1] James R. Heath, Mark A. Ratner, Molecular Electronics, Physics Today, May 2003.
- [2] J. M. Seminario, Molecular and Nano Electronics: Analysis, Design and Simulation, Elsevier, 2007.
- [3] G. Cuniberti, F. GroBmann, R. Guti rrez, The Role of Contacts in Molecular Electronics.
- [4] T. Chakraborty, Charge Migration in DNA, Springer, 2007.

The complexation of tetracycline with Ca²⁺: A DFT study

S. Omid¹, S. Javadian², M. Noorinezhad³

^{1,3} Department of Ecology, Shrimp Research Center, Bushehr, Iran

² Department of Chemistry, University of Tarbiat Modarres, Tehran, Iran

(E-mail: smomidi@gmail.com)

Keywords: Tetracycline, Calcium cation, Antibiotic, Electronic structure.

1. Introduction

Tetracycline is the parent compound of a family of antibiotics in widespread clinical use [1]. Numerous studies have been undertaken on the mechanism of the antibacterial action of tetracyclines [2]. These have demonstrated that tetracycline is a metal-dependent antibacterial agent that inhibits bacterial protein synthesis by binding to the ribosome [3]. With respect to the microbiological action of tetracyclines, Mg²⁺ and Ca²⁺ are probably the most relevant divalent cations to be considered for chelation [4].

2. Computational method

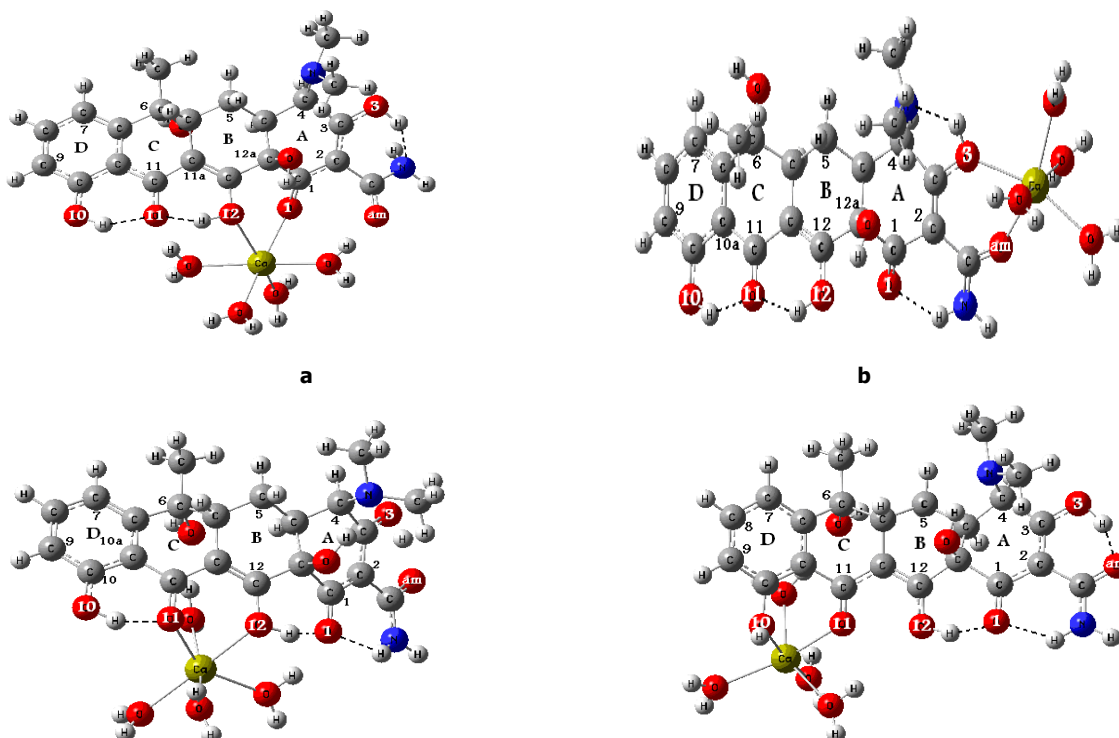
In the present study, we are interested in studying the interaction of Ca²⁺ and its hydrated forms with tetracycline. The all calculations were carried out using GAUSSIAN 98 package. The geometry of the [Ca(H₂O)₆]²⁺, [Ca(TC)]²⁺ and [Ca(TC)(H₂O)₄]²⁺ were optimized at B3LYP/6-31G* level. The binding energy in the gas phase, E_b, was calculated according to Eq. 1:

$$E_b = E_{AB} - E_A - E_B \quad (1)$$

Where E_{AB}, E_A and E_B corresponds to the total energy of the optimized complex, [Ca(H₂O)₆]²⁺ and tetracycline, respectively.

3. Results and discussion

Tetracycline is able to displace two water units from the hexahydrated complex (Scheme 1) and the most positions of tetracycline have suitable condition for binding with calcium ion. The preference of tetracycline by Ca²⁺ is enlightened by these results. Moreover, its electronic structure, as shown by huge changes in the atomic populations, is perturbed by Ca²⁺. The stability of the studied systems is accounted for in terms of the calculated structure and electronic properties: Ca-O bond lengths, charge transfers, and binding energies (Table 1).





c

d

Scheme 1. Optimized structures of $[\text{TC-Ca}-(\text{H}_2\text{O})_4]^{+2}$ Using B3LYP and 6-31G* Basis Set.

Table 1. Calculated B3LYP/6-31G* Binding Energies (BE), for the Tetracycline Complexes.

Complex	BE (kcal/mol)
$[\text{Ca}(\text{H}_2\text{O})_6]^{+2}$	278.34
$[\text{TC}(\text{O}_{10}\text{-O}_{11})\text{-Ca}-(\text{H}_2\text{O})]^{2+}$	325.59
$[\text{TC}(\text{O}_{11}\text{-O}_{12})\text{-Ca}-(\text{H}_2\text{O})]^{2+}$	338.02
$[\text{TC}(\text{O}_{12}\text{-O}_1)\text{-Ca}-(\text{H}_2\text{O})]^{2+}$	330.29
$[\text{TC}(\text{O}_3\text{-O}_{\text{am}})\text{-Ca}-(\text{H}_2\text{O})]^{2+}$	340.79

4. Conclusion

It was found that most positions of tetracycline have suitable condition for binding with calcium ion. The octahedral $[\text{Ca}(\text{TC})(\text{H}_2\text{O})_4]^{2+}$ complex is more stable than hexahydrated $[\text{Ca}(\text{H}_2\text{O})_6]^{2+}$ complex.

References

- [1] I. Chopra, M. Roberts, Am. Soc. Microbial. (2001) 232.
- [2] L. A. Mitscher, The chemistry of the tetracycline antibiotics. Marcel Dekker Inc., New York, 1978.
- [3] O. G. Othersen, F. Beierlein, H. Lanig, T. Clark, J. Phys. Chem. B 107 (2003) 13743.
- [4] K. Meindl, T. Clark, J. Phys. Chem. B 109 (2005) 4279.

Ab initio thermodynamic evaluation of the DFTHP (the intermediate in TEX production)

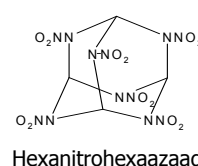
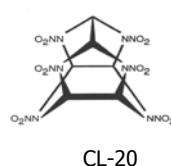
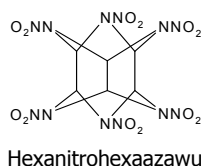
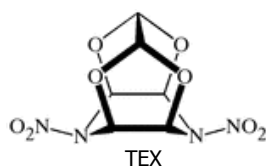
M. Mohammadi, H. R. Shamlouei*, K. Asad Samani and R. Karimian

Faculty of Science, Islamic Azad University of Gachsaran, Gachsaran, Iran

(E-mail: shamluei@iaug.ac.ir)

Keywords: DFTHP, TEX, Ab initio.**1. Introduction**

Military researchers try to produce new explosives with higher performance and lower sensitivity. The computational methods predict high density and high performance for the cage nitramines. The example of cage nitramines are CL-20, Hexanitrohexaazawurtzitane, Hexanitrohexaazaadamantane and 4,10-dinitro-2,6,8,12-tetraoxa-4,10-diazatetrocyclo [5.5.0.05,903,11] -dodecan (TEX). These explosives were developed by Thiokol Company [1].



Unfortunately, a competition exists between the efficiency and the sensitivity of explosives. Higher efficiency leads to higher sensitivity so production, handling, storage and transformation of high performance explosives are limited and dangerous.

The TEX is a special new explosive that have high performance and low sensitivity. It seems as yellow crystalline in pure form or brown crystals with small impurity. High density of TEX is considerable and very attractive. The high density of it is due to compact crystalline unit cell that fills vacancy between the cages [2]. In addition to high density, the TEX has high thermal stability and has good compatibility with conventional explosive such as RDX and HMX [3]. Despite of inexpensive raw materials for production of TEX, low information about it, is mysterious and it seems that research about it is highly secreted. In other references it is noted that the production and application of the TEX [4] and FOX-7 [5] are under developing and attracted to the scientists [6].

In addition to high performance comparable to other high explosives such as HMX, RDX, NQ, the TEX has low sensitivity under various stimulations such as impact, temperature and vice versa. In table2, some of explosive properties of TEX are compared with other high explosives.

Table 1. Comparison of explosive properties of TEX with other high energy explosives [7].

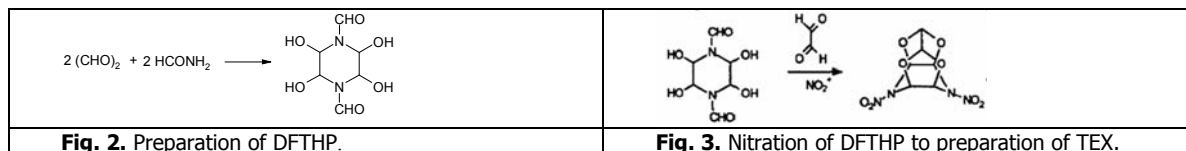
Characteristics	RDX	HMX	NQ	FOX-7	TEX
Molecular Weight (g/mol)	222.10	296.16	104.07	148.08	262.13
Melting Point (°C)	204	275	232	215	250
Density (g/cm ³)	1.82	1.96	1.71	1.86-1.88	1.99
Detonation Rate (m/s)	8750	9100	8200	9000	8665
Vacuum Stability(ml)	<0.1	0.06	-	<0.1	0.05
Impact Sensitivity (J)	7.5	7.4	49	25	22.5
Ignition Temperature (°C)	220	287	232	215	>252
Evolved Gas Volume (L/kg)	903	902	1042	-	940[8]

In addition of explosive properties, significant volume of gases is evolved during decomposition of the TEX. As the result of high gas volume production, it is a suitable candidate for using in propellant. Furthermore, the semiempirical calculation showed that the flame temperature of TEX detonation is considerably low in comparison of other oxidizers such as HMX and RDX. This is the other advantage of TEX for using in propellants. In two-step synthesis of TEX firstly, the DFTHP is prepared and nitrated by mixture of nitric and sulfuric acid. In Figures 2 and 3 the two-step process for preparation of TEX is shown.

According to importance of the TEX, the thermodynamical and explosive property of it was computed by semiempirical method previously [9]. In this research the optimum structure of DFTHP was calculated and the stability of it was estimated. The nitration reaction of DFTHP was studied. Finally the heat of reaction in Fig. 2 was calculated.

2. Computational methods

The structure of materials were optimized by Hartree-Fock method using the 6-311++G** basis set. The thermodynamical properties and vibrational spectrum of them were then calculated by the same method.



3. Results and discussion

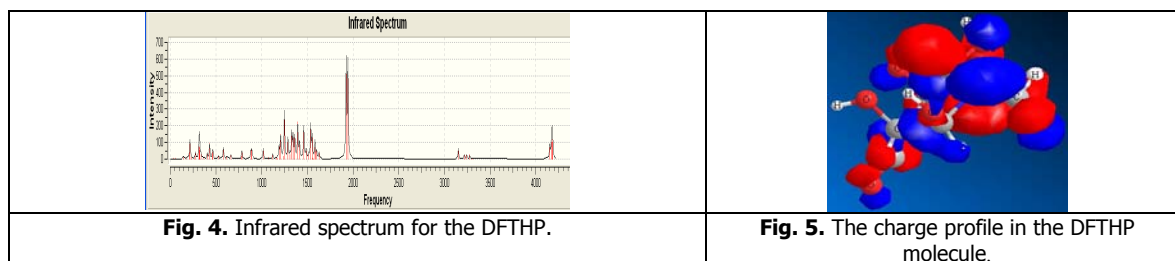
Optimized structure of DFTHP and other material involved in reaction 1 and 2 is calculated. The list of materials is shown in table 2.

Table 2. Name and calculated energy for the materials.

	Name	Energy (kJ.mol ⁻¹)		Name	Energy (kJ.mol ⁻¹)
1	TEX	-2748858	4	HCONH ₂	-594856
2	DFTHP	-2075873	5	H ₂ SO ₄	-1831692
3	(CHO) ₂	-444886	6	HNO ₃	-733621
7	NO ₂ ⁺	-533836			

After the optimization of structure, the enthalpy of formation for DFTHP was calculated. The calculated energy for each of material is shown in table2. By using the data in table2, the enthalpy of formation for DFTHP was calculated as 1286.542 kJ.mol⁻¹.

The vibrational spectrum of DFTHP was studied to investigate the negative vibrational mode and stability of it. The result of calculated infrared Spectroscopy is shown in Fig4. No negative mode exists in vibrational spectrum means that the DFTHP is stable under usual medium.



For understanding the chemistry of nitration of DFTHP to produce TEX, the density of electron was calculated for NO₂⁺ and DFTHP for investigating the site in which the NO₂⁺ is attacked to it. The density of electrons in DFTHP is shown in Fig5. In this figure, it is clearly seen that the negative charge (attack site) locates on nitrogen atom so the positive charge on NO₂⁺ (located on oxygen atom) attach to nitrogen as first step of nitration reaction.

4. Conclusions

The structure and stability of DFTHP molecule is studied by computational methods in which it is showed that the intermediate is stable under usual situation. Electron density analysis showed that the nitrogen atoms in this molecule have high density electron and is capable to attract the NO₂⁺ group.

References

- [¹] G. Lund, T. Highsmith, P. Braithwaite, US Patent NO 5529649, 1996.
- [²] K. Karaghiosoff, T. Klapötke, A. Michailovski, G. Holl, Acta Crystal. 58 (2002) 580.
- [³] Y. Zuo, R.Xu, K. Chang, Q. Peng, China Academy of Engineering Physics, Energetic Materials, 13 (2005) 110.
- [⁴] P. C. Braithwaite, W.W. Edwards, R. M. Hajik, T.K. Highsmith, G. K. Lund, 29th Int. Annu. Conf. ICT Proc. Karlsruhe, Germany, 62 (1998) 1.
- [⁵] N.V. Latypov, J. Bergman, A. Langlet, U. Wellmar, U. Bemm, Tetrahedron, 54 (1998) 1125.
- [⁶] Z. Jalový, R. Matyáš, Proc. 5th Int. Seminar, New Trends in Research of Energetic Material, Pardubice, April (2002) 92.
- [⁷] R. Meyer, J. Kohler, A. Homburg, "Explosives."; Wiley –VCH verlag GmbH & Co. KGaA, 5th Ed. (2002) 70.



Quantum mechanical study of electrophilic substitution reaction in diazole and their Analogs, NICS, and NBO analysis

V. Daneshdoost, S. Jameh-Bozorgi, S. Rafatpanah

Chemistry Department, Faculty of Sciences, Islamic Azad University Arak branch, Arak, Iran

Vahid712@yahoo.com

Keyword: Ab initio, DFT, Natural Bond Orbital, NICS, Azole, Electrophilic substitution reaction.

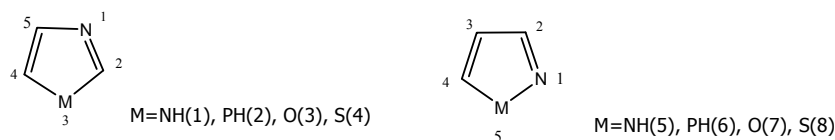
1. Introduction

Diazoles are compounds that contain a nitrogen atom and a heteroatom in the five-member ring. Their aromaticity is obtained from delocalization of electron pair of heteroatom. The alkali property of 1, 2-azoles is less than 1, 3-azoles because they have a heteroatom in the vicinity of nitrogen which has electron withdrawing effect.

2. Methods

Ab initio MO and DFT methods [1-4] and NBO(Natural Bond Orbital) [5,6] and NMR analysis have used for review of structural properties and effects of directional of electrophilic substitution reaction and aromatic nature of combination ,Imidazole(1), Phosphazole(2), Oxazole(3) [7], Thiazole(4) [8], Pyrazole(5), Isophosphazole(6) , Isoxazole(7) [9] , Isothiazole(8) [10] (Scheme1).

All calculations have done with the GAUSSIAN 98 package of program [11].



Scheme 1.

3. Results and discussion

The result of calculation in theoretical level B3LYP/ 6-311+G**//B3LYP/6-311+G** for calculated energy shows that , the quantity of ΔE_0 For compounds 2,5,7,8 is consequently equal with: 10.5661 kcal/mol, 6.4520 kcal/mol, 22.8200 kcal/mol and 4.0669 kcal/mol which these quantities shows that ,Imidazole(1), Oxazole(3), Thiazole(4),Isophosphazole(6) are more stable than Their isomers and the most stable compound is Isoxazole. NMR calculation which have done with GIAO-HF/6-311+G** for 1-8 combination show that: 1) aromatic property in compositions 1, 5 is increasing from 2, 6 and in compositions 4, 8 is increasing from 3, 7. 2) according to NICS (nucleus independent chemical shift) [12] values, aromatic property of 1, 2-azoles is more than 1, 3-azoles and procedure of aromaticity is: 5>8>7>6 (table1).

Table 1.

Compounds	Pyrazole(5)	Isothiazole(8)	Isoxazole(7)	Isophosphazole(6)
NICS	-14.60	-13.36	-12.19	-5.27

NBO calculations have done whit B3LYP/6-311+G** theoretical level. The results of NBO calculation confirm the result of NICS.

The aromatic character could be increased by the increase of the stabilization Energy associated with $LP_M \rightarrow \pi^*_{N1-C2}$ Delocalizations (E_2). E_2 values have inverse ratio with electronic occupancy. The electronic occupancy of donor orbital is decreased with increase E_2 .

The electronic occupancy of donor orbital is increased with increase E_2 (Tables 2 and 3).

Table 2.

Compounds	Resonance Energy(E_2)	Occupancy	
	$LP_{(1)M} \rightarrow \pi^*_{N1-C2}$	$LP_{(1)M}$	π^*_{N1-C2}
Pyrazole ₍₅₎	3.30	1.60870	0.33449
Isophosphazole ₍₆₎	3.06	1.86585	0.19021

**Table 3.**

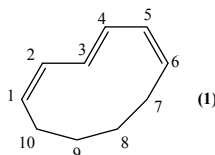
Compounds	Resonance Energy(E ₂)	Occupancy	
	LP _{(2)M} → π* _{N1-C2}	LP _{(2)M}	π* _{N1-C2}
Isothiazole ₍₈₎	17.20	1.59651	0.32887
Isoxazole ₍₇₎	16.91	1.69802	0.28871

References

- [1] D. Becke, J. Chem.Phys. 98, 5648 (1993).
- [2] C. Lee, W. Yang, R.G. Parr, Phys. Rev. B, 37, 785 (1988).
- [3] A.W.J. Hehre, I. Random, P.V. R. Schleyer, J. A. Pople, Ab initio Molecular Orbital Theory(Wiley, New York,1986).
- [4] J. M. Seminario And P. Politzer, Eds, Modern Density Function Theory, A Tool for Chemistry (Elsevier, Amsterdam, 1995).
- [5] E. D. Glendening, A. E. Reed, J. E. Carpenter, F. Weinhold, NBO version 3.1.
- [6] A. E. Reed, L. A. C. Curtiss F. Weinhold, Chem. Rev, 88, 899(1988).
- [7] I. Turchi, Wiley-Interscience, New York, 1986, A. Hassner and B. Fischer, Heterocycles, 35, 1441(1993).
- [8] J. V. Metzger, Wiley-Interscience, New York, 1979, J. V. Metzger, In Comprehensive Heterocyclic Chemistry, vol. 6, ed. K. T. Potts, Pergamon Press, Oxford, P. 235, 1984.
- [9] S. A. Lang, Jrand Y-I. Lin, In comprehensive Heterocyclic Chemistry, vol. 6, ed. K. T. Potts, Pergamon Press, Oxford, P. 1, 1984.
- [10] D. L. Pain, B.J. Peart And K.R.H. Wooldridge, Comprehensive Heterocyclic Chemistry, Vol. 6, Ed. K. T. Potts, Pergamon Press, Oxford, P. 131, 1984.
- [11] C. Lee, W. Yang and R.G. Parr, Phys. Rev. B37 (1988) 785.
- [12] P. V. R. Schleyer, C. Maerker, A. Dransfeld, H. jiao and N. J. V. E. Hommes, J. Am. Chem. Soc. 118 (1996) 6317.

Conformational study of (E,E,Z)1,3,5-cyclodeatriene using ab initio molecular orbital methodR. Soleymani^a and S. Jameh-bozorgchi^{b,*}^aChemistry Department, Faculty of sciences, Islamic Azad University, Touyserkan branch, young researchers club, Touyserkan, Iran^bChemistry Department, Faculty of sciences, Islamic Azad University, Touyserkan branch, Touyserkan, Iran
(E-mail:nima_soleimany@yahoo.com)**Keywords:** DFT, Ab initio calculation, Conformational properties, (E,E,Z)-cyclodeca-1,3,5- triene.**1. Introduction**

The cyclodecatriene collinolactone is a new microbial natural product from treptomyces sp. Gö 40/10 and represents a hitherto unknown chemical class of substances. The structure elucidation was performed with modern spectroscopic methods (1D/2D-NMR, HR-ESI-MS, IR, UV).[1] Theoretical study about many isomers and configurations of cyclodeatriene were performed recently[2,3], but this studies for (E,E,Z)-1,3,5-cyclodeatriene not exist. This study was undertaken to investigate the structural optimization and conformational interconversion pathways of (E,E,Z)1,3,5-cyclodeatriene (**1**) using ab initio method at HF/6-31G* level of theory.

**2. Calculation method**

Quantum mechanical calculations at UHF/6-31G* level of theory using to investigation structural, conformational and energetic study of (E,E,Z)1,3,5-cyclodeatriene (**1**). Also, energetic single point calculations at DFT-B3LYP/6-31G*//UHF/6-31G* level were performed to comparison with HF method.

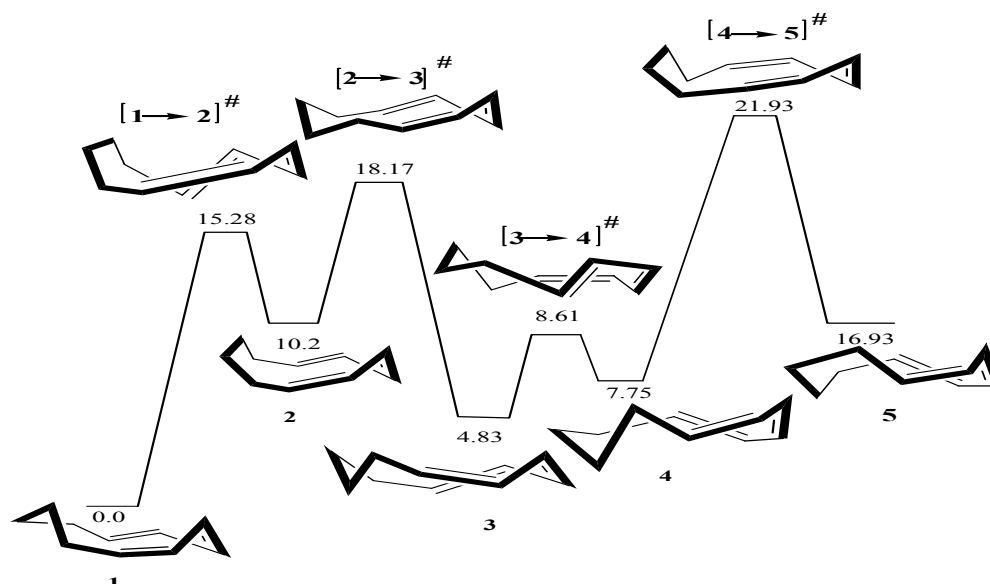


Fig. 1. Calculated HF/6-31G* profile for ring inversion of (E,E,Z)- cyclodeca-1,3,5-triene (**1**).

2. Results and discussion



The results of ab initio calculations for structure optimization and conformational interconversion pathways of (E,E,Z)1,3,5-cyclodeatriene (**1**) are shown in Fig. 1. Five potential energy minima and four transition states were found important for a description of the conformational features of **1**.

Table 1. Calculated energies (in kcal mol⁻¹) for the important geometries of (E,E,Z)-cyclodeca-1,3,5-triene.

Conformer	Method	HF/6-31G*//HF6-31G*	B3LYP/6-31G*//HF6-31G*
		ΔE_0^a	ΔE_0^a
1		0.000000	4.702434
2		10.028049	2.900163
3		4.834839	0.000000
4		7.756390	3.183358
5		16.932729	10.780621
[1 → 2] [#]		15.28012	9.781375
[2 → 3] [#]		18.170054	12.642883
[3 → 4] [#]		8.606764	3.636420
[4 → 5] [#]		21.934486	16.20406

4. Conclusion

In conclusion, HF/6-31g* calculations provide a fairly clear picture of the conformational properties of (E,E,Z)-cyclodeca-1,3,5-triene (**1**) from the structural and dynamic points of view. According to the obtained results by HF/6-31G*//HF6-31G* level of theory, the energy barrier for ring inversion of this conformation is about 21.93 kcal.mol⁻¹.

Reference

- [1] L. Hoffmann, doctoral dissertation, Georg-August-Universität Göttingen 2006-05-03.
- [2] I. Yavari, H. Kabiri Fard and S. Moradi; Journal of the Iranian Chemical Society, 1 (2004) 71.
- [3] G. Buemi, F. Zuccarello, A. Raudino and D. Grasso Journal of Molecular Structure, 69 (1980) 201.



Computational study on the stability of ternary (5, 7-dichloroquinoline-8-ol and 4- vinyl pyridine) Ln complexes (Ln: La, Ce, Nd, Sm)

T. Hosseinnjad*, S. J. Ahmadi, S. Shirvani-arani, M. H. Karimi-Jafari

Computational Chemistry Laboratory, NSTRI, Tehran, Iran

(E-mail: Tayebah.Hosseinnjad@Gmail.com)

Keywords: Lanthanides, Ionic imprinted polymers, Stability, HF calculation, Sparkle PM3.

1. Introduction

Selective complexation of lanthanide cations with ligands represents a challenging task in important processes such as ion extraction and separation; because rare-earth elements often coexist in their minerals and nuclear waste. Ionic imprinted polymers (IIPs) provide a new class of materials processing high selectivity and affinity for target ion. Synthesis of IIPs involves arranging of functional monomers (ligands) around the ion-template as a complex. Subsequent polymerization results in trapping ion-ligands complex in highly cross-linked polymer matrix. Extraction of the imprint ions from polymer matrix leaves predetermined arrangement of ligands and a tailored binding pocket on polymers. The interaction energy between metal cations and functional groups of ligands (involved in the imprinting and rebinding steps) affects strongly the affinity and selectivity of IIPs [1]. In order to gain insights into the computational design of IIPs and studying conformational stability of pre-polymerization complexes, calculation of binding energy ($\Delta E_{\text{binding}}$) between ion-template and ligands seems to be essential. The main goal of this research is a quantum-mechanical study on the stability of ternary complexes of some lanthanide cations (La^{+3} , Ce^{+3} , Nd^{+3} , Sm^{+3}) with 5,7-dichloro quinoline-8-ol (DCQ) and 4- vinyl pyridine (VP) ligands which have been prepared in a recently synthesized IIP for selective separation of Sm^{+3} from other lanthanides such as La^{+3} , Ce^{+3} and Nd^{+3} cations [2]. All complexes and ligands were fully optimized by quantum mechanical calculations at the Hartree-Fock (HF) level of theory, using parallel computation by Gamess software. As a results of calculations, we have obtained the trend in stability of lanthanide complexes $[\text{Ln}(\text{VP})_2(\text{DCQ})_3]^{+3}$ by calculation of binding energy of lanthanide ions which coordinated with VP and DCQ ligands at the optimized geometry of clusters.

2. Computational method

The *ab initio* calculations were performed at the HF level using Gamess package. In order to reduce computational cost, the 46+4fⁿ core electrons of lanthanide cations were described by quasi relativistic pseudo-potentials (RECPs) of Dolg et al.[3] and the valence electrons by a (7s,6p,5d)/[5s, 4p, 3d] basis set. The other atoms (H, C, N, O, Cl) were described by 6-31G basis set.

3. Results and discussion

The geometries of ligands (VP, DCQ) and $[\text{Ln}(\text{VP})_2(\text{DCQ})_3]^{+3}$ ternary complexes were fully optimized at HF level of theory without imposing symmetry constraints. The optimized structure of ligands and Sm-complex $[\text{Sm}(\text{VP})_2(\text{DCQ})_3]^{+3}$ together with the definition of binding energies has been displayed in Fig.1.

It is noteworthy that the initial conformation of $[\text{Ln}(\text{VP})_2(\text{DCQ})_3]^{+3}$ was deduced by conformational analysis procedure based on sparkle PM3 semi-empirical method [4]. The choice of sparkle PM3 method for prediction of initial geometry was motivated by the fact that the bonds between lanthanides and ligands essentially possess an electrostatic character which could be well represented as the sparkle model. The conformational analysis procedure was concerned by definition of coordination sphere variables that control the relative orientation of ligands around the lanthanide cations.

In the next step, the force constant calculations have been performed to ensure that the optimized structures are true minima. Also consideration of force constants reveals thermochemical information (Such as Gibbs free energies) and zero point energies for optimized complexes. Our HF level calculated results for energies of lanthanides, ligands, Ln-Complexes and consequently binding energies have been presented in Table 1.

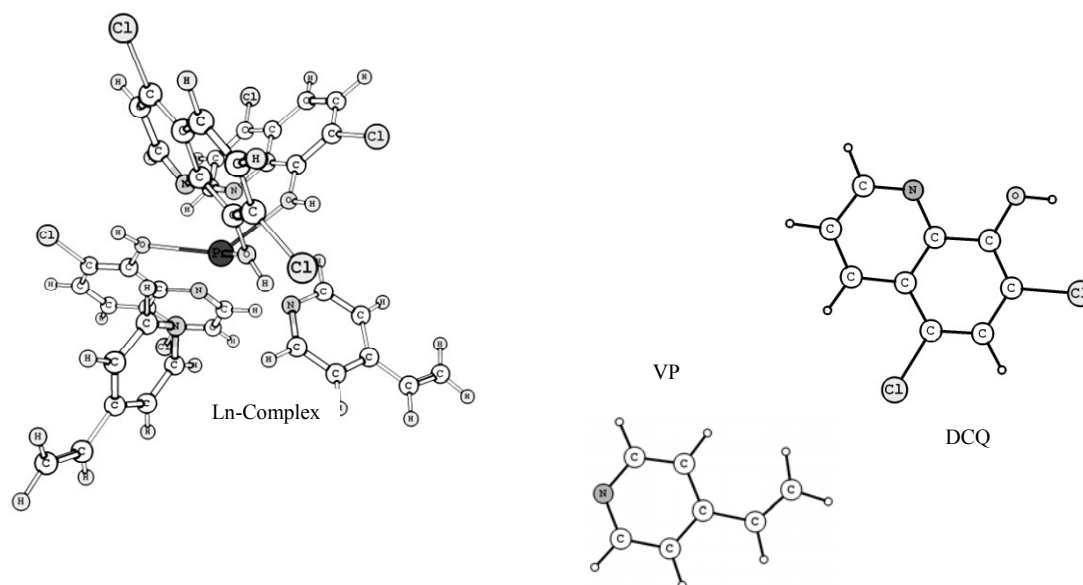


Fig. 1. The optimized geometries of ligands and Sm-complex $[\text{Sm}(\text{VP})_2 (\text{DCQ})_3]^{+3}$.

Table 1. The energies of lanthanides, ligands, Ln-Complexes and consequently binding energies obtained at the HF level calculations.

	Lanthanides (hartree)	2(VP) (hartree)	3(DCQ) (hartree)	$[\text{Ln} (\text{VP})_2 (\text{DCQ})_3]^{+3}$ (hartree)	Binding energy (Kcal.mol ⁻¹)
La	-29.8641	-646.898	-4175.28	-4852.93	-556.902
Ce	-30.4993	-646.898	-4175.28	-4853.58	-567.246
Nd	-31.7283	-646.898	-4175.28	-4854.84	-583.793
Sm	-32.9225	-646.898	-4175.28	-4856.05	-598.516

4. Conclusion

Our calculated results via sparkle PM3 conformational search demonstrated that the stability of aforementioned lanthanide complexes depends strongly on the bonding angle between the nitrogen atoms of VP ligands with lanthanides. We have also presented the binding energies of $[\text{Ln} (\text{VP})_2 (\text{DCQ})_3]^{+3}$ ternary complexes that govern the stability of Ln- complexes and also can be useful in the computational design of lanthanides imprinted polymers.

References

- [1] Y.Liu, F. Wang, T. Tan, M. Lei, Anal. Chim. Acta. 581(2007) 137.
- [2] S. Shirvani-Aranya, S. J. Ahmadi, A. Bahrami-Samani, M. Ghannadi-Maragheh, Anal. Chim. Acta. 623 (2008) 82.
- [3] M. Dolg, H. Stoll, A. Savin, H. Preuss, Theor. Chim. Acta., 75 (1989) 173.
- [4] A. V. M. Andrade, N. B. da Costa Jr, A. M. Simas, G. F. de Sa, Chem. Phys. Lett. 227 (1994) 349.

**An analytical potential energy surface for CO – N₂ dimer from ab initio calculations**A. Farjamnia^{a,b}, A. Maghari^b, M. H. Karimi-Jafari^{a*}^a Computational Chemistry Laboratory, NSTRI, Tehran, Iran^b Department of Physical Chemistry, College of Science, University of Tehran, Tehran, Iran

(E-mail: mhkarimijafari@gmail.com)

Keywords: Van der Waals complex, Intermolecular forces, Second virial, CO-N₂ dimer.**1. Introduction**

Van der Waals complexes containing CO and/or N₂ are of longstanding interest, especially in atmospheric science and astrophysics. However there is not an analytical potential energy surface for description of weak interactions between CO and N₂ molecules. To our knowledge the only ab initio investigation of this system is due to Fiser and Polak [1]. Ab initio calculations of the potential energy surfaces of Van der Waals complexes initially reproduce the PES in the form of tables of numbers and these numbers have to be interpolated or extrapolated for desired applications. This is not a simple task when one attempts to reproduce the correct anisotropy of interaction at a spectroscopic level of accuracy. The CO-N₂ complex was first detected spectroscopically in the infrared region of the CO stretching vibration [2]. Other similar observations indicate that the orientation of the CO subunit relative to the N-N bond is nearly perpendicular [3]. Electron correlation contributions to intermolecular interactions have a central role in the structure and energetics of van der Waals complexes. It can commonly be described adequately when one applies a high level post Hartree-Fock method in conjunction with an extended basis set. To overcome these difficulties, application of bond functions located somewhere between monomers seems to be a wise solution.

2. Computational details

The intermolecular interaction energy between two rigid linear molecules can be expanded as follows:

$$U(R, \theta_a, \theta_b, \varphi) = \sum_{\Lambda} V_{\Lambda}(R) A_{\Lambda}(\theta_a, \theta_b, \varphi)$$

where $\Lambda \equiv L_a, L_b, M$. The expansion coefficients can then be written as:

$$V_{\Lambda}(R) = \int A_{\Lambda}(\theta_a, \theta_b, \varphi) U(R, \theta_a, \theta_b, \varphi) d\omega$$

where $d\omega$ is the integration over the angular coordinates. The actual calculation of these coefficients can be performed by calculating for a given value of R the potential $U(R, \theta_a, \theta_b, \varphi)$ in a grid of points such that the integrations can be carried out by numerically quadrature. Thus the ab initio calculations were performed in a $10 \times 10 \times 10$ points Gauss-Legendre grid for θ_a , θ_b and φ . This integration rule seems to be natural for our functional and coordinate system. Angular basis functions are:

$$A_{L_a, L_b, M}(\theta_a, \theta_b, \varphi) = P_{L_a}^M(\cos\theta_a) P_{L_b}^M(\cos\theta_b) \cos(M\varphi)$$

where $P_L^M(\cos\theta)$ stands for the associated Legendre polynomials. Using the full symmetry of the system 500 angular points were calculated for 14 unequally spaced R values between 5 and 22. The angular expansion is truncated at $L_A = 8$, $L_B = 9$ and M is constrained to be less than 4. Thus there is 139 term in our expansion. The full potential is obtained by fitting the radial coefficients over the grid of R points with the following general form:

$$V_{\Lambda}(R) = e^{a-bR} \left(\sum_m g_m R^m \right) - \sum_n \frac{C_n}{R^n} F_n$$

The interaction is described in the body-fixed Jacobi coordinates system. Before complete exploration of the PES the efficiency of different computational levels was investigated by some test calculations along an angular slice of PES. Accordingly the best compromise between accuracy and computational cost is achieved at the MP4/aQZD+b level of theory. In Figure 1 the radial dependence of the isotropic part of the PES (V_{000}) is compared with the minimum and maximum values of interaction energy over the angular grid. Some of the important expansion coefficients as emerged from numerical integration are depicted in Figure 2 and are compared with their fitted functions. Our investigation shows that the global minimum of the PES is corresponded to $\theta_a = 21.83^\circ$, $\theta_b = 114.14^\circ$ and $\varphi = 180^\circ$, with a well depth of -123.548 cm^{-1} . As a pure two body interaction



property, the second virial coefficient $B(T)$ is calculated to give a first, simple test of the quality of constructed PES. Values of $B(T)$ was calculated from

$$B(T) = \frac{N_A}{4} \int_0^\infty R^2 dR \int (1 - e^{-U/k_B T}) d\omega$$

via a $8 \times 8 \times 8$ points Gause-Legendre integration over θ_a , θ_b and φ followed by a multi panel Gauss-Kronrod quadrature over R . In Figure 3 calculated second virial coefficients are compared with experimental results.

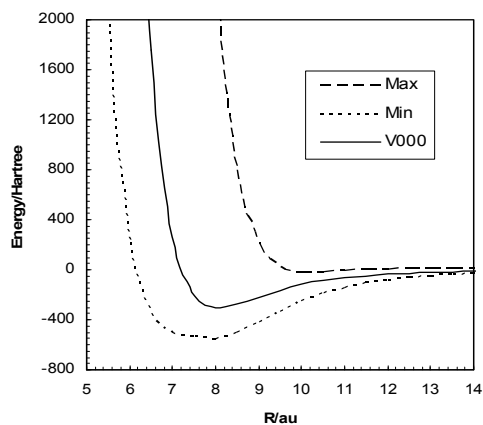


Fig. 1.

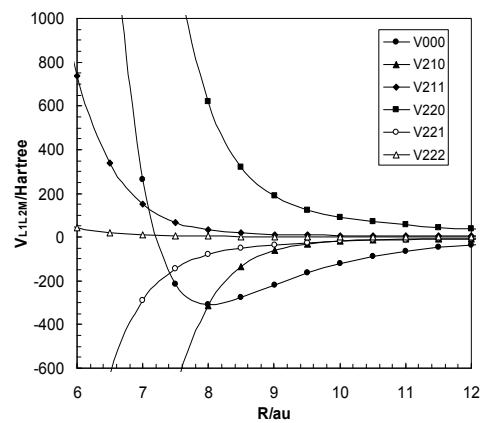


Fig. 2.

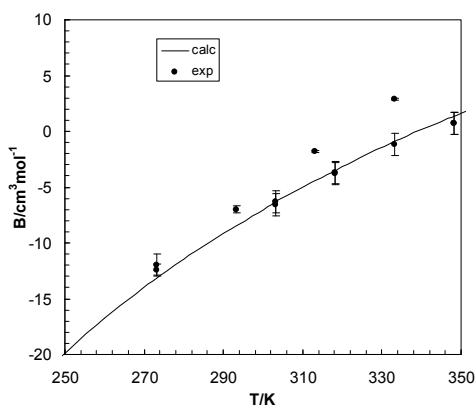


Fig. 3.

References

- [1] J. Fiser, R. Polak, Chem. Phys. Lett. 360 (2002) 565.
- [2] Y. Kawashima, k. Nishizawa, Chem. Phys. Lett. 249 (1996) 87.
- [3] Y. Xu, A.R.W. McKeller, J. Chem. Phys. 104 (1996) 2488.

Proton transfer reaction in variously substituted Aniline-OH/Anilide-(H₂O)_n complexesH. Roohi^{a, b}, B. Moghadam^{a,*}^aDepartment of Chemistry, Faculty of Science, University of Sistan & Baluchestan, P.O. Box 98135-674, Zahedan, Iran^bDepartment of Chemistry, Faculty of Science, University of Guilan, Rasht, Iran.

(E-mail: b.moghadam87@yahoo.com)

Keywords: Aniline, Anilide, Proton transfer, Substitution effect.**1. Introduction**

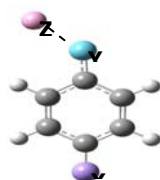
Aniline contains an amine group which can acts as both the donor and acceptor of hydrogen bonds. This group lies in close proximity to the aromatic ring, which provides an opportunity to study the influence of subsistent effects on the intermolecular hydrogen bond and proton transfer reaction [1,2]. Additionally, aniline can form the anilide anion in which, negatively charged, the nitrogen atom acts as a strongly basic center. Proton transfer reactions play a central role in a large number of chemical and biological phenomena and have been the subject of numerous studies [3]. The change in the relative acidity of molecules involved in proton transfer can be induced by the extent of salvation. The aim of the present study is to compare the proton transfer reaction in the p-substituted Aniline-OH/Anilide-(H₂O)_n complexes.

2. Methodology

In this study, proton transfer reaction in compounds representing various p-substituted Anilines/Anilide was investigated. The isolated molecules and complexes were studied using DFT quantum chemical methods at the B3LYP/6-311++G (2d, 2p) level of theory. The binding energies have been corrected for BSSE.

3. Results and discussion

The purpose of this study was to investigate effect of the various substitutions on proton transfer reaction in Aniline/Anilide derivatives complexes. The geometry of the investigated X-Aniline-OH⁻ complex and X-Anilide-(H₂O)_n complexes was optimized by using of the B3LYP method with 6-311++G (2d, 2p) and 6-311++G (3df, 2pd) basis sets. The results obtained from proton transfer reaction analyzing showed a higher stability of Aniline-OH/Anilide-H₂O complexes with CH₃ substitution than the other complexes. The stability of substituted complexes for single H₂O can be arranged as CH₃-A > Anilide > OCH₃-A > CHO-A > NO₂-A > NO-A. It seems that, when a substituted group behaves as an electron donor then formed complex is more stable in proton transfer reaction and vise versa (Table 1). On the other hand, we observed remarkable effect of H₂O group on proton transfer reaction. Upon to increase of H₂O molecule surrounding an Anilide, obviously increase in proton transfer is occurred from H₂O to NH⁻. The order of stability of complexes does not change by BSSE correction. We observed an increase in C-N bond length in Anilide upon to proton transfer from H₂O to NH⁻.

X= CH₃, OCH₃, NO, NO₂, CHO, HY=NH⁻, NH₂Z= OH⁻, (H₂O)_n n=1-4**4 Conclusions**

Our results show the effect of different substituted groups on proton transfer reaction in Aniline-OH/Anilide-(H₂O)_n complexes. In addition our results show importance of surrounding H₂O molecules in proton transfer reaction in substituted Aniline/Anilide complexes.

Table 1. The binding energies (kJ mol⁻¹) and Bond Length C-N (Å) obtained for the X-Aniline-OH and X-Anilide-(H₂O)_n (n =1-4) complexes at B3LYP/6-311++G (2d, 2p) level.

X	Ph-Y	Z	ΔE	C-N
P-CH ₃	C ₆ H ₄ NH ⁻	H ₂ O	-75.15	1.340
P-CH ₃	C ₆ H ₄ NH ⁻	2H ₂ O(linear)	-108.87	1.344
P-CH ₃	C ₆ H ₄ NH ⁻	2H ₂ O(trans)	-114.95	1.352
P-CH ₃	C ₆ H ₄ NH ⁻	3H ₂ O	-138.11	1.367
P-CH ₃	C ₆ H ₄ NH ⁻	4H ₂ O	-137.02	1.375
P-OCH ₃	C ₆ H ₄ NH ⁻	H ₂ O	-74.14	1.340
P-OCH ₃	C ₆ H ₄ NH ⁻	2H ₂ O(linear)	-107.64	1.344



P-OCH ₃	C ₆ H ₄ NH ⁻	2H ₂ O(trans)	-113.35	1.352
P-OCH ₃	C ₆ H ₄ NH ⁻	3H ₂ O	-136.33	1.373
P-OCH ₃	C ₆ H ₄ NH ⁻	4H ₂ O	-133.06	1.375
P-CHO	C ₆ H ₄ NH ⁻	H ₂ O	-61.61	1.322
P-CHO	C ₆ H ₄ NH ⁻	2H ₂ O(linear)	-88.19	1.325
P-CHO	C ₆ H ₄ NH ⁻	2H ₂ O(trans)	-90.31	1.332
P-CHO	C ₆ H ₄ NH ⁻	3H ₂ O	-90.79	1.340
P-CHO	C ₆ H ₄ NH ⁻	4H ₂ O	-80.95	1.347
P-NO	C ₆ H ₄ NH ⁻	H ₂ O	-57.52	1.317
P-NO	C ₆ H ₄ NH ⁻	2H ₂ O(linear)	-81.84	1.320
P-NO	C ₆ H ₄ NH ⁻	2H ₂ O(trans)	-81.69	1.326
P-NO	C ₆ H ₄ NH ⁻	3H ₂ O	-73.16	1.332
P-NO	C ₆ H ₄ NH ⁻	4H ₂ O	-60.15	1.340
P-NO ₂	C ₆ H ₄ NH ⁻	H ₂ O	-57.78	1.319
P-NO ₂	C ₆ H ₄ NH ⁻	2H ₂ O(linear)	-82.27	1.322
P-NO ₂	C ₆ H ₄ NH ⁻	2H ₂ O(trans)	-82.44	1.328
P-NO ₂	C ₆ H ₄ NH ⁻	3H ₂ O	-75.20	1.335
P-NO ₂	C ₆ H ₄ NH ⁻	4H ₂ O	-62.06	1.344
P-H	C ₆ H ₄ NH ⁻	H ₂ O	-74.71	1.338
P-H	C ₆ H ₄ NH ⁻	2H ₂ O(linear)	-108.26	1.343
P-H	C ₆ H ₄ NH ⁻	2H ₂ O(trans)	-114.05	1.350
P-H	C ₆ H ₄ NH ⁻	3H ₂ O	-135.80	1.364
P-H	C ₆ H ₄ NH ⁻	4H ₂ O	-134.33	1.373
P-CH ₃	C ₆ H ₄ NH ₂	OH ⁻	-165.88	1.340
P-OCH ₃	C ₆ H ₄ NH ₂	OH ⁻	-172.62	1.340
P-CHO	C ₆ H ₄ NH ₂	OH ⁻	-237.83	1.322
P-NO	C ₆ H ₄ NH ₂	OH ⁻	-171.47	1.317
P-NO ₂	C ₆ H ₄ NH ₂	OH ⁻	-191.41	1.319
P-H	C ₆ H ₄ NH ₂	OH ⁻	-170.04	1.338

References

- [¹] H. Szatyłowicz, T. M. J. Krygowski, Phys. Chem. A 111 (2007) 170.
 [²] M. Cheng, X. Pu, N.-B. Wong, M. Li, A. Tian, New J. Chem. 32 (2008) 1060.
 [³] D. Marx, Chem. Phys. Chem. 7 (2006) 1848.

DFT study of gas-solid interaction in oxidative coupling of methane reactions: CH₄ + BaTiO₃ perovskite catalyst

Mahtab Gharibi^{*1,2}, Maryam Motalebipour¹

¹National Petrochemical Company, Research & Technology Co. (NPC-RT), Tehran center- Iran

²Department of Chemistry, Tarbiat Moallem University, 49 Mofateh Avenue, Tehran-Iran

(E-mail: m.gharibi@npc-rt.ir)

Keywords: DFT calculations, BaTiO₃ catalyst, Oxidative coupling of methane (OCM), Bond energy.

1. Introduction

A vast variety of metal oxides has been tested as potential catalysts. Rare-earth compounds, alkali and alkaline-earth metal compounds, and multivalent metal oxides such as Mn/Na₂WO₄/SiO₂ have been reported as catalysts effective in exothermic OCM process: CH₄ → CH₃[•] Catalytic activation-hydrogen abstraction, CH₃[•] → C₂H₆ Rapid gas-phase coupling, C₂H₆ → C₂H₅[•] Catalytic activation and activation by various radicals, C₂H₅[•] → C₂H₄ Rapid gas-phase reactions, C₂H₄ → CO Catalytic activation and activation by various radicals, CO → CO₂ Mainly catalytic oxidation.

The theoretical efforts on BaTiO₃ towards an understanding of elastic constants, phase transfer, oxygen vacancies, relaxation, optical band gaps and Ferro electricity, bulk modulus and band structure [1-2]. However, in this work we attempt to find optimized bulk model BaTiO₃ catalyst on OCM process by using hybrid DFT (B3PW, B3LYP) as a new screening and suggest a catalytic cycle mechanism over BaTiO₃ that is more consistent with Ito-Lunsford mechanism on Li/MgO oxide catalyst. Fig. 1 shows the good catalytic performance on BaTiO₃ for OCM process [3].

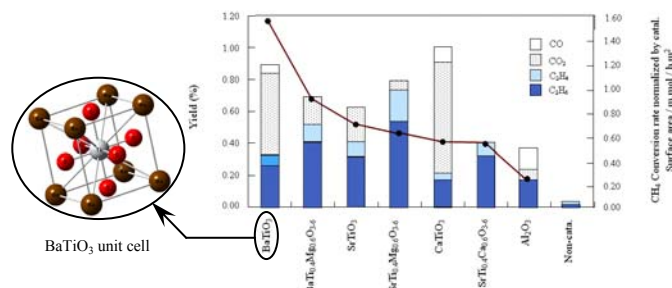


Fig. 1. Activity of methane conversion with various perovskite catalysts. The optimized geometry for 1×1×1 cubic BaTiO₃ unit cell is also shown.

2. Methods

The Gaussian 98 program package has been used for all calculations. The strategy employed in this work is first optimizing catalyst geometries by making use of *ab initio* density functional theory (DFT) applying a number of different exchange-correlation functional, which describes well the lattice structure of perovskite crystals, including *hybrid* B3LYP or B3PW with the SSD and LANL2DZ basis sets and then obtaining bulk properties. For calculation of bulk crystal, the BaTiO₃ catalyst was modeled as a finite lattice Ba_nTi_nO_{3n} (n=8) molecular cluster. This cluster size is significantly larger than the molecular sizes of CH₄, O₂ and OCM products, so that the chemisorption's properties of the surface should be minimally altered.

3. Results and discussion

We investigated methane adsorption on different reaction sites of its surface while considering lattice fixed during adsorption via calculation of energies. In Fig. 2 the relative energy of the BaTiO₃+CH₄ complex is plotted as a function of the C-H distance to illustrate the dissociation and migration of the CH₄ molecule upon adsorption.

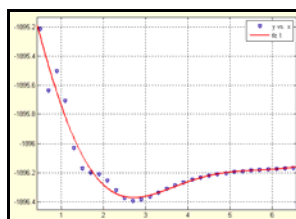


Fig. 2. Relative energy of the BaTiO₃+CH₄ complex as a function of the C-H distance.



Table 1 gives the calculated properties for bulk crystal BaTiO₃ and CH₄ at the B3PW level, together with experimental data. Standard DFT functional (LDA, BLYP, B3LYP, PW) and uncorrected HF are also added for comparison. Our results confirm that B3PW/LANL2DZ can be confidently used, the agreement with experiment being of the same order as that achieved by using the more extended theoretical levels.

Table 1. Comparison of the results for bond lengths and lattice parameter on cubic BaTiO₃ (^a Ref. [5], ^b Ref. [6], ^d Ref. [4].)

	Bond Lengths (Å)		Lattice Parameter (Å)	
	This work	Expt. ^b	Cubic (<i>a</i> = <i>b</i> = <i>c</i>)	
Ba-O	2.8453	2.8365	This work	4.0145
Ti-O	2.0069	2.0057	LDA ^a , PW91 ^d	3.96, 3.996
Ti-Ba	3.4767	3.4739	BLYP, PBE ^a , B3LYP, HF ^a	4.08, 4.03, 4.01, 4.01
CH ₃ -H	1.08	1.08	Expt.	4.0185 ^b

As an indication of the quality of the chosen correlation method, pseudo potential, and basis sets, in Table 2 the calculated bond energies (kcal/mol) of relevant gas phase molecules, such as CH₄ → CH₃ + H, C₂H₆ → CH₃ + CH₃, O₂ → O + O, with experimental or series of *ab initio* data at the HF, MP2, BLYP, G2, and G3MP2B3 levels are compared. Experimentally, the reaction 4CH₄ + O₂ → 2C₂H₆+2H₂O is exothermic by -84.5 kcal/mol. Using DFT/B3PW level we get -76.23 kcal/mol which is good agreement with experimental data. We investigated methane adsorption on different reaction sites of its surface while considering lattice fixed during adsorption via calculation of energies. We investigated methane adsorption on different reaction sites of its surface while considering lattice fixed during adsorption via calculation of energies.

Table 2. Bond energies (kcal/mol) for some gas phase molecules and reaction energy for methane conversion to ethane.

Reaction Step	Theoretical Refs.	This work	Expt.
O ₂ → O + O	22 (HF) ^a , 113 (MP2) ^a	116.74	119.106 ± 0.048 ^b
H ₂ O → OH + H	89 (HF) ^a , 119 (MP2) ^a , 123.0 (B3LYP) ^c	98.09	119 ± 1 ^b
OH → O + H	68 (HF) ^a , 96 (MP2) ^a , 102.39 (B3LYP) ^d	100.45	101.0 ± 0.2
CH ₄ → CH ₃ + H	88 (HF) ^a , 107 (MP2) ^a , 104.76 (G3MP2B3) ^b	103.7	104 ± 1 ^b
C ₂ H ₆ → CH ₃ + CH ₃	67 (HF) ^a , 92 (MP2) ^a , 90.81 (G2) ^b	90.65	90.2 ± 0.2
4CH ₄ + O ₂ → 2C ₂ H ₆ + 2H ₂ O	-74 (HF) ^a , -73 (MP2) ^a	-76.23	-84.5 ^b

^a Ref.[7], ^b Ref.[10], ^c Ref. [9], ^d Ref. [8].

References

- [1] S. Piskunov, E. Heifets, R. I. Eglitis, and G. Borstel, *Comp. Mater. Sci.* 29 (2004) 165.
- [2] F. Cora, *Mol. Phys.* 103 (2005) 2483.
- [3] X. Li, K. Tomishige and K. Fujimoto, *Catal. Lett.* 36 (1996) 21.
- [4] G. Rakotovelof, P. S. Moussounda, M. F. Haroun, P. Legare, A. Rakotomahevitra, and J. C. Parlebas, *Eur. Phys. J. B* 57 (2007) 291.
- [5] S. Tinte, and M. D. Stachiotti, *Atomistic simulation of surface effects in BaTiO₃*, *AIP. Conf. Proc.* 535 (2000) 273.
- [6] Y.-Il Kim, K.-S. Ryu, S.-H. Nahm, and J.-S. Park, *Current Applied Physics*, 6S1 (2006) e266.
- [7] M. A. Johnson, E. V. Stefanovich, and T. N. Truong, *J. Phys. Chem. B* 101 (1997) 3196.
- [8] R. Janoschek, *Pure Appl. Chem.* 73 (2001) 1521.
- [9] B. Jursic, and R. Martin, *International Journal of Quantum Chemistry*, 59 (1 996) 495.
- [10] *Handbook of Chemistry and Physics*, 79th Ed., CRC Press, NY, 1998, pp. 9-80.

Theoretical study for reaction between triphenylphosphine and activated acetylenic esters in the presence of SH heterocyclic compounds

S. M. Habibi Khorassani^a, M. T. Maghsoodlou^a, A. Ebrahimi^a, H. Ghasempour^a and Z. Ghahghayi^a

^aDepartment of Chemistry, University of Sistan and Baluchestan, P.O. Box 98135-674, Zahedan, Iran

(E-mail: ghasempour2@yahoo.com)

Keywords: Stable phosphorus ylides, Dialkyl acetylenedicarboxylates, **Z** and **E** rotamer, AIM method.

Introduction

In the current work, the stability of the **Z** and **E** isomers was undertaken for the two rotamers of a phosphorus ylide by means of atoms in molecules (AIM) analysis. Phosphorus ylides are important reagents in synthetic organic chemistry, especially in the synthesis of naturally occurring products, compounds with biological and pharmacological activity [1-6]. Most of the phosphonium salts are usually made from the reaction of phosphine and an alkyl halide [4-6], though they can be obtained by Michael addition of phosphorus nucleophiles to activated olefins [2,3]. A facile synthesis of the reaction between triphenylphosphine **1**, dialkyl acetylenedicarboxylates **2** and 2-aminothiophenol **3** (as a SH-acid) has been earlier reported [7]. The reaction is shown in Figure 1. The **Z** and **E** isomers were optimized for all ylide structures at HF/6-31G(d,p) level of theory by Gaussian 98 package program. The energy of both conformers have been calculated at B3LYP/6-311++G** level. Atoms in molecules (AIM) analysis at HF/6-31G(d,p) level of theory have been performed in order to gain a better understanding of most geometrical parameters of both **E-4(a, b)** and **Z-4(a, b)** of phosphorus ylides. The numbers of critical points and intramolecular hydrogen bonds as well as the charge of atoms that constructed on the **Z** and **E** isomers have been recognized. The results altogether reveal the effective factors on stability of **Z** and **E** ylide isomers.

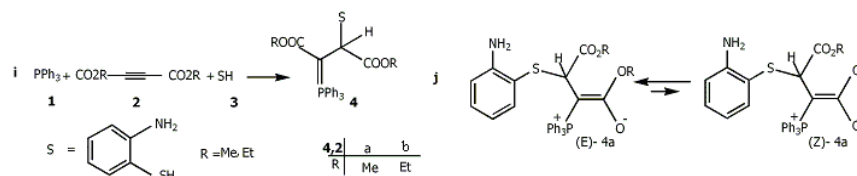


Fig. 1. (i) The reaction between triphenylphosphine **1**, dialkyl acetylenedicarboxylate **2** (**2a** or **2b**) and 2-aminothiophenol **3** for generation of stable phosphorus ylides **4** (**4a** or **4b**), **(j)** Two isomers (**Z-4a** and **E-4a**) (major and minor) of ylide **4a**

2. Theoretical study and calculations

In order to determine more stable form of both geometrical isomers [**Z-4(a, b)** or **E-4(a, b)**] of ylides (**4a** or **4b**), first their structures were optimized at HF/6-31G(d,p) level of theory [8] by Gaussian 98 program package [9]. Also relative energy of the two rotamers has been calculated at HF/6-31G(d,p) and B3LYP/6-311++G(d,p) levels (See Figure 2). The relative stabilization energies for both [**Z-4(a, b)** and **E-4(a, b)**] isomers are reported in Table 1, as can be seen, **E-4a** and **E-4b** isomers are more stable than **Z-4a** and **Z-4b** forms (0.60 and 0.77 kcal/mol respectively) at B3LYP level.

Table 1. The relative energy (kcal/mol) for both **Z** and **E** isomers of ylides **4a** and **4b**, obtained as HF/6-31G(d,p) and B3LYP/6-311++G(d,p) levels.

Conformer	HF	B3LYP
Z-4a	1.04	0.60
E-4a	0.00	0.00
Z-4b	1.09	0.77
E-4b	0.00	0.00

Further investigation was undertaken in order to determine more effective factors on stability of both isomers, on the basis of AIM calculations [10] at HF/6-31G(d,p) level of theory by the AIM2000 program package [11]. As noted in the literature the ranges of $\rho(r)$ and $\nabla^2\rho(r)$ are 0.002-0.035e/a₀³ and 0.024-0.139 e/a₀⁵, respectively, if H-bonds exist. The number of hydrogen bonds in both categories (**E-4a** and **Z-4a**) and (**E-4b** and **Z-4b**) are (8 and 8) and also (8 and 8), respectively (See Table 2 and 3). In addition, the ranges of their electron densities are in (0.002 - 0.014 and 0.002 - 0.013 au) and also (0.002 - 0.014 and 0.001 - 0.014 au), respectively (See Tables 2 and 3). With respect to the large number of hydrogen bonds in both **Z** and **E** isomers it is difficult to make a precise decision for determination of more stable isomer.

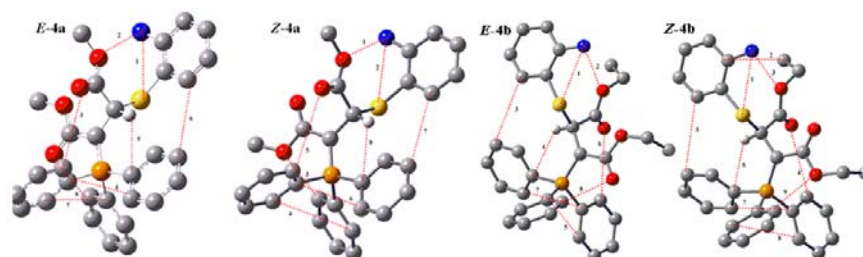


Fig. 2. Intramolecular hydrogen bonds (dotted lines) in E-**4a**, Z-**4a**, E-**4b** and Z-**4b** isomers of stable ylide **4a** and **4b** respectively.

Table 2. The values of $\rho \times 10^{-3}$, $\nabla^2\rho \times 10^{-3}$ and Hamiltonian (H) for both Z-**4a** and E-**4a** isomers of ylide **4a** calculated at the hydrogen bond critical points. All quantities are in atomic units

E	ρ	$\nabla^2\rho$	H	Z	ρ	$\nabla^2\rho$	H
1	14.01	-13.71	-1.80	1	8.89	-8.44	-0.59
2	8.51	-7.99	-0.52	2	13.91	-13.79	-1.86
3	8.39	-7.48	-0.63	3	9.27	-9.35	-1.23
4	9.44	-8.93	-1.73	4	9.29	-8.04	-1.43
5	11.48	-10.44	-1.68	5	8.58	-7.61	-0.61
6	2.98	-2.27	-0.51	6	9.22	-8.62	-1.68
7	9.06	-7.88	-1.49	7	2.58	-1.99	-0.47
8	12.72	-11.75	-0.087	8	11.38	-10.50	-1.74

Table 3. The values of $\rho \times 10^{-3}$, $\nabla^2\rho \times 10^{-3}$ and Hamiltonian (H) for both Z-**4b** and E-**4b** isomers of ylide **4b** calculated at the hydrogen bond critical points. All quantities are in atomic units

E	ρ	$\nabla^2\rho$	H	Z	ρ	$\nabla^2\rho$	H
1	14.09	-13.76	-1.79	1	14.00	-13.84	-1.85
2	8.24	-7.73	-0.50	2	8.72	-8.25	-0.56
3	2.93	-2.24	-0.51	3	8.86	-7.79	-0.57
4	11.46	-10.41	-1.68	4	2.60	-2.00	-0.47
5	9.43	-8.95	-1.74	5	11.36	-10.49	-1.74
6	8.50	-7.56	-0.62	6	9.29	-8.85	-1.65
7	9.04	-7.85	-1.49	7	9.31	-8.06	-1.44
8	12.71	-11.74	-0.87	8	9.44	-9.50	-1.24

On the basis of theoretical calculations (Table 1), the difference between the relative stability of the E-**4a**, Z-**4a**, E-**4b** and Z-**4b** isomers in gas phase are small (0.60 and 0.77 kcal/mol respectively). Perhaps this negligible difference is not taken more considerably in solution media for **4a** and **4b**, for this reason it is possible to see the two isomers of **4a** and **4b** (both Z and E isomers). Experimental results [7] obtained from the ^1H , ^{13}C , ^{31}P NMR data showed the two isomers for the ylides **4a** and **4b** which are consistent with the results of the theoretical investigations.

3. Conclusion

The assignment of the Z and E isomers as a major or minor form in both ylides **4a** and **4b** were undertaken by AIM method. Quantum mechanical calculation was clarified how ylides **4a** and **4b** exist in solution as a mixture of two geometrical isomers.

References

- [1] Wittig, G. Science, 210(1980) 600.
- [2] Johnson, A. W. Ylide Chemistry, Academic Press, London, 1966.
- [3] Cadogan, J. I. G. Organophosphorus Reagents in Organic Synthesis, Academic Press, New York, 1979.
- [4] I. Yavari, L. Ahmadian-Razlighi, Phosphorus, Sulfur, and Silicon. 181 (2006) 771.
- [5] M. T. Maghsoodlou, N. Hazeri, G. Afshari, U Niroumand. Phosphorus, Sulphur, and Silicon. 181 (2006) 2681.
- [6] S. M. Habibi-Khorassani, M. T. Maghsoodlou, H. Roohi, M. Zakarianejad, M. Moradian, Progress in Reaction Kinetics and Mechanism 30 (2005) 127-144.
- [7] A. A. Esmaili, M. Ghareghloo, M.R. Islami, H.R. Bijanzadeh, Tetrahedron, 59 (2003) 4785.
- [8] M. J. Frisch, et al. Gaussian 98, Revision A. 7, Gaussian, Inc., Pittsburg h, PA, 1998.
- [9] A. E. Reed, R. B. Weinstock, F.J. J. Weinhold, Chem. Phys, 83 (1985) 735.
- [10] R. F. W. Bader, Atoms in molecules A Quantum Theory, Oxford University, New York, (1990).
- [11] F. W.Biegler König, J.Schönbohm, D. J. Bayles, Comput. Chem. 22(2001) 545.

Quantum chemical study of the interaction between O₃ and H₂O₂B. makiabadi^{a,c,*}, H. Roohi^{a,b}^aDepartment of Chemistry, Faculty of Science, University of Sistan & Baluchestan, P.O. Box 98135-674, Zahedan, Iran^bDepartment of Chemistry, Faculty of Science, University of Guilan, Rasht, Iran.^cSirjan Engineering College, Shahid Bahonar University, P.O. Box 78185439, Sirjan, Iran

(E-mail: bmakiabadi@yahoo.com)

Keywords: Red-shifted H-bond, Excitation energy, NBO and QTAIM analyses**1. Introduction**

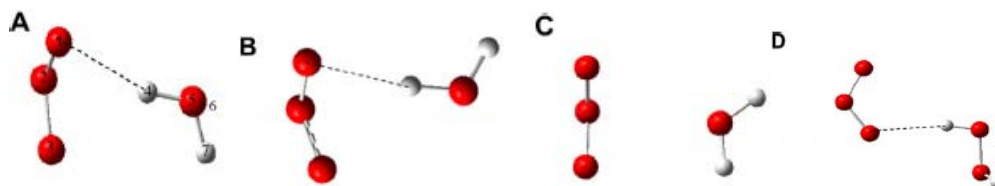
Molecular complexes are of importance in atmospheric chemistry. The reaction of ozone with other species is one of the best investigated chemical reactions as is reported in many research papers published in the recent years [1–3]. The H₂O₂ complexes have received considerable attention [4–6]. In the present study, high level quantum chemical calculations carried out for the O₃–H₂O₂ complexes in order to elucidate the structural characteristics and energetics of the O₃–H₂O₂ complexes. In addition, natural bond orbital (NBO) [7] analysis and the Bader's quantum theory of atoms in molecules (QTAIM) [8] have been employed to elucidate the interaction characteristics of the O₃–H₂O₂ complexes.

2. Methods

All the structures studied in this work were optimized by using B3LYP method with 6-311++G(d,p), 6-311++G(df,pd) and aug-cc-pVDZ basis sets, MP2(FC) method with 6-311++G(d,p) and aug-cc-pVDZ basis sets, and QCISD(FC) method with 6-311++G(d,p) basis set. In addition, structures were optimized at MP2(FC)/aug-cc-pVTZ level of theory. The counterpoise procedure (CP) [9] was used to correct basis set superposition error (BSSE) in the calculation of binding energies. Geometries, energies, and frequencies were determined by using the GAUSSIAN-98 program package [10] on a Pentium 4 computer with a single processor. The excitation energy of the O₃–H₂O₂ complexes was calculated using time-dependent density functional theory. Natural bond orbital (NBO) analysis was carried out with version 3.1 included in GAUSSIAN-98 program at the QCISD/6-311++G(d,p) level of theory. In addition, topological properties have been calculated using AIM method on the wave functions obtained at QCISD/6-311++G(d,p) level by AIM method.

3. Results and discussion

Four minima structures, which are illustrated in Fig. 1, obtained for O₃–H₂O₂ complex. The A–C complexes have pseudo cyclic configuration and D complex has pseudo linear one. The A and B structures contain two O₁...O₆ interactions and one H...O hydrogen bond interaction. C structure contains two O...O type interactions (O₂...O₅ and O₃...O₆). Finally, D structure exhibits only one H...O hydrogen bond interaction with other hydrogen atom (H7) in out of the O₃ plane.

**Fig. 1.** Equilibrium structures for H₂O₂–O₃ complexes (top view).

From electronic binding energy all calculations indicate that the complex D is less stable complex in complexes including HB (A, B and D). In addition to H...O hydrogen bond (HB) interaction that exists in complexes A, B and D, complexes A and B have also two O...O type interactions. These results suggest that the formation of O...O interaction enhances the stability of the complexes formed between O₃ and H₂O₂. The order of stability of complexes does not change by employing BSSE correction. To elucidate the effect of complexation on the absorption spectrum of O₃ molecule, excitation energy of the O₃–H₂O₂ complex, H₂O₂ and O₃ were calculated using time-dependent density functional theory (TD-DFT). The excitation energy of O₃, H₂O₂ and complexes A–D at B3LYP/6-311++G(df,pd) level of theory show that the excitation energies correspond to transition from the ground state (1A1) to the excited states 1B1, 1A2 and 1B2 for ozone are 2.059, 2.310 and 5.328 eV, respectively. The



computed excitation energies are comparable well with the experimental values (2.1, 1.6 and 4.86 eV). The first and second excitation energies are 1.653 and 2.169 for A and 1.487 and 2.148 eV for B, respectively, indicating that the excitation energies of O₃ are red-shifted upon complexation. The complex formation also influences the vibrational frequencies of O₃ and H₂O₂. Both B3LYP/aug-cc-pVDZ and QCISD/6-311++G(d,p) computations predict that the vibrational frequencies of O₅-H₄ bond of H₂O₂ in complexes A, B and D are red-shifted with respect to the H₂O₂ (3751.5, 3855.8 cm⁻¹). The amount of red-shift in the complexes A, B and D is 48.8, 40.4 and 43.0 cm⁻¹ at B3LYP/aug-cc-pVDZ level, respectively, which are in good agreement with the experimental value of 26.6 cm⁻¹. In HB complexes A, B and D, results show that O₂ and O₃ atoms of ozone lose and O1 atom involved in HB gains electronic charge, resulting in a charge transfer of 0.0040, 0.0073 and 0.0124 e from proton acceptor O₃ to proton donor H₂O₂, respectively. We must note that the amount of charge transfer is not correlated to the binding energy. The NBO results predict that the lp(O1) →*(O₅-H₄) donor acceptor interaction is the most important interaction in A, B and D systems. The most important interaction in complex C is σ(O₅-O6)→RY*(O₂) interaction. The comparison of QTAIM data of O₅-H₄ bond of complexes A, B and D with monomer H₂O₂ shows that the q(r) decreases upon H-bonding, in agreement with the increase of its bond distance as well as red shift of corresponding vibrational frequency. ∇²q(r) and H(r) values at O₅-H₄ bonds involved in hydrogen bonds are negative, this is the indication of covalency of this bond. In complexes A, B and D, one BCP exist in O₁...H₄ distance, indicating interaction between H₂O₂ and O₃ through the hydrogen bonding. The small electron density and positive values of ∇²q(r) as well as H(r) at O...H BCPs are typical for closed-shell interaction or charge depletion between the nuclei, indicating the electrostatic nature of the O1...H₄ hydrogen bonding.

4. Conclusions

The quantum chemical calculations carried out for the O₃-H₂O₂ complexes in order to examine the structural characteristics and energetics of the ozone-molecule complexes. From the obtained results, it can be concluded that among the methods used in this work the MP2/aug-cc-pVTZ, MP4/aug-cc-pVTZ and B3LYP/aug-cc-pVDZ levels of theory are sufficient to describe the O₃-H₂O₂ complex. The natural bond orbital (NBO) analysis and theory of atoms in molecules have been employed to elucidate the interaction characteristics of the O₃-H₂O₂ complexes. Four complexes were found as stable structures of O₃-H₂O₂. The first and second excitation energies of O₃ are red shifted upon complexation. The computations predict that the vibrational frequencies of O₅-H₄ bond of H₂O₂ involved in HB in complexes A, B and D are red-shifted with respect to the H₂O₂. Two different intermolecular interactions were predicted that participate in the formation of complexes, namely: conventional O...H hydrogen bond and O...O connection. The NBO analysis shows that the electronic charge is transferred from O₃ to H₂O₂ in three complexes which have conventional hydrogen bond. The QTAIM results reveal that the both intermolecular interactions have electrostatic character.

References

- [1] Y. Bedjanian, G. Poulet, Chem. Rev. 103 (2003) 4639.
- [2] H. Tachikawa, S. Abe, Inorg. Chim. Acta 358 (2005) 288.
- [3] H. Roohi, B. Mackiabadi, Bull. Chem. Soc. Jpn. 80 (2007) 1914.
- [4] T. Zeegers-Huyskens, J. Phys. Chem. A 107 (2003) 8730.
- [5] B. Wang, H. Hou, Y. Gu, Chem. Phys. Lett. 309 (1999) 274.
- [6] H.M.T. Nguyen, M.T. Nguyen, J. Peeters, T. Zeegers-Huyskens, J. Phys. Chem. A 108 (2004) 11101.
- [7] A.E. Reed, L.A. Curtiss, F. Weinhold, Chem. Rev. 88 (1988) 899.
- [8] R.F.W. Bader, Atoms. In Molecules A Quantum Theory, Clarendon Press, Oxford, UK, 1990.
- [9] S.F. Boys, F. Bernardi, Mol. Phys. 19 (1990) 553.
- [10] M.J. Frisch et al. GAUSSIAN 98, Revision A.7, Gaussian, Inc., Pittsburgh, PA, 1998.

**Study of the origin of rotational barrier in NH₂-X (X = NO, NS)**H. Roohi ^{a,b}, B. makiabadi^{a,c*}, M. Hagealirezahi^a^aDepartment of Chemistry, Faculty of Science, University of Sistan & Baluchestan, P.O. Box 98135-674, Zahedan, Iran^bDepartment of Chemistry, Faculty of Science, University of Guilan, Rasht, Iran.^cSirjan Engineering College, Shahid Bahonar University, P.O. Box 78185439, Sirjan, Iran

(E-mail: bmakiabadi@yahoo.com)

Keywords: Rotational barrier, N-Thionitrosamine, NBO, AIM.**1. Introduction**

N-Thionitrosamines, R₂NAN=S, are rare examples of compounds which contain bonds between nitrogen and bivalent sulfur [1]. Despite their instability in the free state, preparation of a number of complexes containing N-thionitrosamines bound to some metals have been reported [2,3]. Although, rotational energy barrier in the nitrosamine compounds have been most studied by various groups of investigations using the dynamic NMR and theoretical techniques [4–6], the origin of rotational barrier in N-thionitrosamine compounds seems to be unknown. In the present work, we attempt to analyze the origin of the N-N rotational barrier in NH₂NO and NH₂NS by AIM analysis [7] and the charge transfer effects on the rotational barrier by means of NBO analysis [8].

2. Methods

All structures were fully optimized at the MP2/6-311++G** level. The Gaussian 98 package [9] was used to carry out all ab initio calculations. The thermal corrections to the enthalpy (H), and Gibbs free energy (G) were obtained from the vibrational frequency analysis at the MP2/6-311++G** levels. NBO analysis was carried out with version 3.1 included in Gaussian 98 program at the MP2/6-311++G** level of theory. AIM analysis was also performed by at the MP2/6-311++G** level.

3. Results and discussion

The other structural changes associated with rotation are an elongation of the N-N bond length and a shortening of the N-S bond length. The main change occurs in the N-N bond length and the N-S bond is relatively unaffected on rotation. The MP2/6-311++G** calculated rotational barrier on going from ground state to TS1 for TNA and NA is 79.6 and 76.3 kJ/mol, respectively. Fig.1(a), presents the molecular graphs of TNA in ground state (GS) and transition states TS1 and TS2. Fig. 1(b) present the contour maps of Laplacian of charge density $\nabla^2\rho$ for TNA. In TNA, the rotation about the N-N bond leads to a large decrease in the charge density of N-N bond critical point along with a small increase in the charge density of N=S bond critical point. The $\nabla^2\rho$ value at N-N bond critical point was found to be negative indicating that the electronic charge is concentrated in the internuclear region. While, the $\nabla^2\rho$ value of N-N bond critical point increases on rotation, the $\nabla^2\rho$ value at N=S bond critical point decreases. The ρ value at N-N and N=O(S) BCPs of both compounds decrease on rotation. While, the change of charge density ($\nabla\rho$) on rotation at N-N BCP of both compounds is approximately equal (-0.108 au), the $\nabla\rho$ value at the N=O BCP of NA (0.033 au, 9)) is greater than corresponding value of N=S bond (0.021 au) in TNA. Analysis of data also suggests that the ρ and $\nabla^2\rho$ values of N=S BCPs of TNA on rotation does not change much and the major changes are found with the corresponding values of N-N bond. The dependence of electronic population on atomic size invalidates some objections to resonance. The electronic populations in TNA are 7.673 at N1, 7.570 at N, and 15.484 at S, changing to 7.656, 7.807 and 15.154, respectively upon rotation. Resonance would require a partial positive charge on N1, not a negative one (denoted as an electronic opulation $N > 7$). Besides, the greater electronic population of N in GS than in TS1 may be as further evidence against resonance stabilization in TNA. The comparison between charge transfer energy of NA and TNA shows that the LP(N1) \rightarrow BD*(N-X) (X = O, S) delocalization increases in the order O < S; this is responsible for the increasing N-N rotational barrier in TNA. Thus the differences between the total delocalization energies of NH₂NO (134.8 kcal/mol) and NH₂NS (138.8 kcal/mol) compounds in ground state are mainly related to the changes in LP(N1) \rightarrow BD*(N-X) interactions. The difference $\Delta E_{\text{del}} = E_{\text{total}} - E_{\text{Lewis}}$ measures the loss of stabilization associated with the deletion of all hyperconjugative interactions. The relative total energies of the various conformers as well as the Lewis and delocalization energy contributions to the relative energies upon rotation are presented in Fig.1(c).

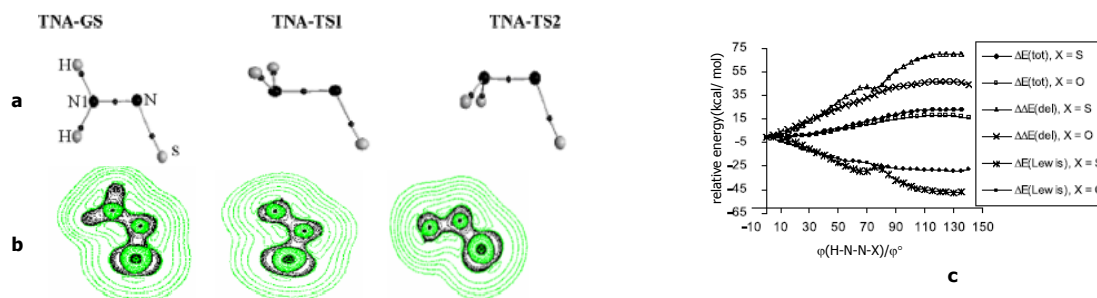


Fig. 1. The molecular graphs of TNA. BCPs are given as small spheres. (b) The contour plots of the Laplacian of the charge density in N-N-S plane. (c) Total (E_{tot}), Lewis (E_{Lewis}) and delocalization (E_{del}) energies versus dihedral angle ϕ ($X = O, S$).

4. Conclusions

The results of a detailed study of the origin of internal rotational barrier of $N(C)=S(O)$ group in TNA, NA and TFA compounds, using NBO and AIM analyses, were presented. AIM results show that the electronic population of amino nitrogen atom of NA and TNA decreases on rotation. Besides, the change of electronic population of middle N atom in TNA is greater than NA on going from TS1. In addition, loss of electronic population of oxygen atom in NA is smaller than corresponding value of sulfur atom of TNA. NBO analysis reveals that the greater rotational barrier for TNA is due to more charge transfer from nitrogen of amino group to sulfur in TNA than from nitrogen to oxygen in NA. The increasing of rotational barrier when passing from NA to TNA mainly due to difference between delocalization energies of $LP(N1) \rightarrow BD^*(N-X)$ interactions in ground states. From NBO results it seems that the strong delocalization in TNA is due to the small energy difference $\Delta\epsilon$ and great Fock matrix element $F(i,j)$ between the interacting orbitals. Although, the $F(i,j)$ is also decreasing from TNA to NA, the influence of the decrease in $\Delta\epsilon$ is very important. Besides, pyramidalization of nitrogen atom leads to decrease of delocalization energy contribution and increase of Lewis energy contribution on total energy. Amount of these energy contributions in TNA is greater than NA. The variation of delocalization contribution upon rotation is greater than Lewis energy contribution. Therefore, the electrostatic and steric contributions included in the Lewis term are less important than delocalization on rotation. In agreement with the higher barrier for TNA compared with NA, the larger change in structure, electron delocalization and electronic population of the nitrogen atom in TNA can be attributed to the greater change in the hybridization of nitrogen atom of amino group upon rotation.

References

- [1] W.J. Middleton, J. Am. Chem. Soc. 88 (1966) 3842.
- [2] M. Herberhold, A.F. Hill, J. Organomet. Chem. 315 (1986) 105.
- [3] A. Gieren, C. Ruiz-Perez, T. Hu"bner, M. Herberhold, A.F. Hill, J. Chem. Soc. Dalton Trans. (1988) 1693.
- [4] M. _OKi, Application of Dynamic NMR Spectroscopy to Organic Chemistry, VCH, New York, 1985, p.75.
- [5] J.E. Haky, J.E. Saavedra, B.D. Hilton, Org. Magn. Reson. 21 (1983) 79.
- [6] R. Glaser, J. Am. Chem. Soc. 121 (1999) 5170.
- [7] R.F.W. Bader, Atoms in Molecules. A Quantum Theory, Clarendon, Oxford, UK, 1990.
- [8] A.E. Reed, L.A. Curtiss, F. Weinhold, Chem. Rev. 88 (1988) 899.
- [9] M.J. Frisch, et al., Gaussian 98, Revision A.7, Gaussian, Inc., Pittsburgh PA, (1998).

**Substituent effect on local aromaticity in mono and di-substituted aza analogs of Indole**

A. Mohajeri *and M. Shahamirian

Department of Chemistry, College of Sciences, Shiraz University, Shiraz, Iran

(E-mail: mozhgan_org@yahoo.com)

Keywords: Aromaticity, Substituent effect, ATI, Indole.**1. Introduction**

Aromaticity is a concept of key importance in physical organic chemistry [1] and because of its significant implications in organic chemistry, has been the subject of a large number of studies [2]. Among these, the heteroaromatic ring systems are the most interesting and the quantitative assessment of the aromaticity of heterocycles has been considered [3, 4]. The aromatic character of furan and pyrrole families was studied in order to understand the effects of different heteroatoms on the electronic structure of ring systems [5]. The aim of the present study is to investigate the π -electron delocalization, substituent effect and the consequences of its position on the aromaticity of mono- and di-substituted heterocyclic analogs of Indole.

2. Computational methods

The calculations carried out in this research have been done using GAUSSIAN 03 program [6]. The Becke's three-parameter exchange functional with LYP correlation functional (B3LYP) and basis set 6-311++G** were used. The molecular geometries of aromatic rings in Fig.1 and their derivatives have been fully optimized and each stationary point was then characterized by computing the vibrational frequencies to ensure that the resulting structures were the minima. Moreover, their wave functions at the same level of theory have been used to characterize the topological properties of the electronic charge density. Calculation of the atomic overlap matrices (AOM) and delocalization indices have been performed with AIM2000 [7].

3. Results and discussion

We studied the aromaticity and π -electron delocalization in mono and di-substituted heterocyclic analogs of Indole. Two typical systems of aromatic rings depicted in Fig.1 have been analyzed. Three substituents (Cl, OCH₃, and CN) with different behavior in inductive (F) and resonance (R) effects have been selected to evaluate aromaticity variation using electronically based indices such as ATI [8] and FLU [9]. Table 1 lists data for the quantitative measure of aromaticity for individual rings of the considered systems in mono substituted derivatives. Generally, two indices give a similar trend for the aromaticity variation. But only ATI shows that inserting a substituent on all of the possible positions in a ring decreases the aromaticity in both rings when comparing with its unsubstituted ring. This result is in line with the works reported by Solà [10] in which it has been shown that substituents perturb π -electron delocalization indicating a partial π -localization and therefore the symmetry and aromaticity characteristics are lost. Therefore, we preferred to apply ATI for analyzing the local aromaticity in our considered systems. Also, the effect of substituent position on the π -electron delocalization is investigated. It results from the data in Tables 1 that the inclusion of substituent, independent of its resonance or inductive effect, in some specific positions (5, 8) causes less decrease in aromaticity in comparison to other positions for ring A. These observations can be interpreted by resonance structures which shows substituent prefers to select specific position leading to produce maximum number of rings with $6n$ electrons among resonance structures. In another approach, the variation of aromaticity has been investigated when we consider a specific position in a ring and change the type of substituent. The results show that the maximum aromaticity exhibits the similar trend of Cl > CN > OCH₃ for all rings studied here. It means that OCH₃ with a lone pair available for resonance with the ring has strong influence on π -electron delocalization. In another part, the effect of interaction between two substituents via the aromatic rings has been studied. The results reveal that in di-substituted derivatives, the π -electron delocalization significantly decreases compared to the corresponding mono-substituted ones which results from intramolecular interaction between the two substituents. Here, the substituents such as OCH₃ and Cl with strong resonance power and less negative inductive effects are considered as the first substituents. It was indicated that the first substituent preferably locates on the heterocycle while the second locates where it has the best cooperation with the first substituent to increase aromaticity irrespective of whether para or meta isomer is established.

4. Conclusion

In this work, it has been shown that ATI can reasonably describe the substituent effect and consequences of its position on aromaticity variation in these biheterocycle compounds. Almost in all cases, maximum aromaticity is characterized when substituent is placed in specific position with respect to heteroatom which makes maximum number of five-membered with 6n electrons in the resonance form. Also, it results from our study that in di-substituted derivatives, irrespective of whether the two substituents form meta or para isomer, they preferably choose the position which leads to maximum aromaticity.

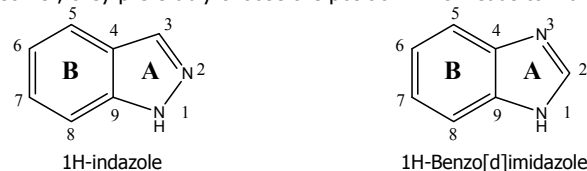


Fig. 1. Labels and numbering for the ring studied.

Table 1. Calculated ATI and FLU values for mono-substituted derivatives of 1-H Indazole and 1H-Benzo[d]imidazole.

	OCH ₃		Cl		CN	
	ATI	FLU	ATI	FLU	ATI	FLU
1-H Indazole						
3 (A)	1.183389	0.032324	1.210881	0.027490	1.211647	0.024973
(B)	1.313532	0.008682	1.313827	0.008958	1.314984	0.008822
5 (A)	1.227782	0.025017	1.224601	0.026614	1.227943	0.025439
(B)	1.287543	0.011825	1.301492	0.009120	1.295409	0.009606
6 (A)	1.222500	0.027518	1.223349	0.026824	1.224788	0.026789
(B)	1.295951	0.009064	1.304802	0.009637	1.302552	0.009576
7 (A)	1.220091	0.028763	1.223024	0.026316	1.225670	0.025858
(B)	1.292896	0.009721	1.303223	0.009741	1.300034	0.009615
8 (A)	1.231962	0.024210	1.225603	0.026313	1.228154	0.025679
(B)	1.290413	0.011889	1.303883	0.009249	1.294377	0.009449
1H-Benzo[d]imidazole						
2 (A)	1.108847	0.044205	1.143627	0.040005	1.142579	0.035160
(B)	1.315065	0.006209	1.310568	0.007154	1.306847	0.008812
5 (A)	1.155669	0.034762	1.151432	0.035532	1.155009	0.033302
(B)	1.288021	0.010337	1.302763	0.008119	1.295793	0.008455
6 (A)	1.152252	0.035725	1.149492	0.036265	1.151922	0.036255
(B)	1.297196	0.008436	1.302896	0.008209	1.296369	0.008835
7 (A)	1.148177	0.039099	1.151450	0.036702	1.154203	0.035415
(B)	1.293018	0.008645	1.304033	0.007910	1.297422	0.008894
8 (A)	1.158690	0.033962	1.154135	0.035327	1.156076	0.034922
(B)	1.292139	0.009890	1.304897	0.008126	1.294275	0.008581

References

- [1] P. v. R. Schleyer, Chem. Rev. 101(2001) 1115.
- [2] V. I. Minkin, M. N. Glukhovtsev, B. Y. Simkin, Aromaticity and Antiaromaticity, Wiley, New York, 1994.
- [3] M. K. Cyrański, T. M. Krygowski, A. R. Katritzky, P. v. R. Schleyer, J. Org. Chem. 67 (2002) 1333.
- [4] D. Baric, Z. B. Maksic, J. Phys. Org. Chem. 16 (2003) 753.
- [5] P.v.R. Schleyer, P.K. Freeman, H. Jiao, B. Goldfuss, Angew. Chem., Int. Ed. Engl. 34 (1995) 337.
- [6] M. J. Frisch, et al., Gaussian 03, Revision A.03. Gaussian, Inc., Pittsburgh, PA, (2003).
- [7] R. F. W. Bader, AIM2000 Program, ver 2.0, Hamilton, McMaster University, 2000.
- [8] X. Fradera, M. A. Austen, R. F. W. Bader, J. Phys. Chem. A 103 (1999) 304.
- [9] E. Matito, M. Duran, M. Solà, J. Chem. Phys. 125 (2006) 059901.
- [10] F. Feixas, E. Matito, J. Poater, M. Solà, J. Comp. Chem. 29 (2008)1543.



Conformational study for investigation of structure-function relationships in protein-based elastomeric materials

B. Chahkandi^a, *B. Seyed Hosseini^a

^aDepartment of Chemistry, Islamic Azad University of Shahrood, Shahrood, Iran

(E-mail: bchahkandi@gmail.com, bshosseini29@yahoo.com)

Keywords: Tripeptide, Elastine, Conformation, Ab initio.

1. Introduction

Proteins are fundamental components of all living cells. The specific functionality of a protein is usually determined by its three-dimensional native structure. Understanding the protein structure-function relationship and protein folding is an important research subject in the current post-genomic era. Whereby if we could pronounce the low by which proteins fold, we would be able to proceed with unprecedented speed and efficiency in answering medical questions and remove the many obstacles behind sophisticated drug discovery. The temporal and the spatial resolutions of the state of the art experiments are not accurate enough to observe the microscopic protein folding directly on an atomic scale [1]. Computer simulation is a complementary tool that helps us understand the kinetic processes and the thermodynamic stabilities of protein folding. Peptides and proteins are basically the polymers of amino acids. A relatively small and emerging class of protein-based materials is elastomeric materials. With respect to that the polypeptides from these materials, they are mainly formed by sequences with regular repetitions and little complications.

Elastin protein is a kind of elastomeric material that is mainly formed by glycine, valine, alanine and proline amino acids. One of the parent repeating polymers in elastin is (Val-Pro-Gly-Val-Gly)_n [2,3]. The study of dipeptide pro-Gly conformational properties in elastin polypeptide was performed to define and describe the relation between proline application relevance with elastomeric mechanical behavior of penta-peptide in this group of materials [4]. Usually, secondary structures for peptides and proteins can be described by torsion angles (mostly, backbone torsion angles, Φ and Ψ angles).

2. Methods

Ab initio calculations were carried out on the selected conformations of the tripeptide model HCO – Gly – L – Val – Gly – NH₂ shown in Figure 1, at the HF/6-31G(d) level in gas phase at 1 atm and 298K. The Gaussian 98 program was used for the geometry optimization of HCO – Gly – L – Val – Gly – NH₂ tripeptide [5]. So the backbone torsional angles ($\Phi_1, \Psi_1, \Phi_2, \Psi_2, \Phi_3, \Psi_3$) as a variable of the energy function was changed at 30° intervals from 0 to 360° of (g) conformer. For this purpose all backbone torsional angles has been kept fix in $\beta_L(\Phi_i = \Psi_i = \pm 180^\circ)$ conformation and only one one of them was variable at 30° intervals from 0° to 360°.

3. Results and Discussion

In the present work we study the different conformers that obtained from the rotation of backbone torsional angles (Φ_i, Ψ_i) in protected tripeptide "HCO – Gly – L – val – Gly – NH₂" in elastin penta peptide which has a chiral center and one prochiral sidechain. (see Figure 1) Tripeptides were chosen as an ideal model because they allow all N-acetyl and N-methyl interactions and resultant conformations possible with a central peptide to be evaluated. The studied tripeptide structure is shown in Figure 1 which is presented by an internal coordinate system of z-matrix, numbering atoms and every possible torsional angle of the structure and the side chain (χ) dihedral angle. In this study A and B are considered as H atom. We added HCO and NH₂ groups to tripeptide separately for keeping α -carbon during the peptide bond and modeling the bigger polypeptide structures. Adding these groups doesn't change the special internal parameters of the main structure of tripeptide.

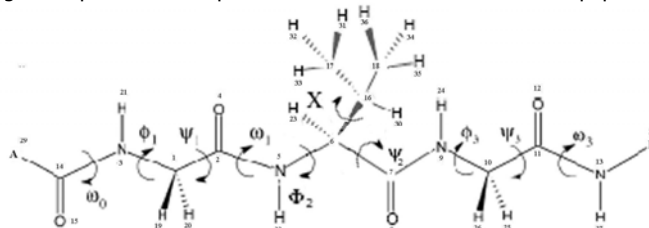


Fig. 1. Schematic of the numbering system applied to the tripeptide HCO-Gly-L-Val-Gly-NH₂. showing all side chain and backbone torsional angles.

Among studied conformations, $\beta_L\beta_L\beta_L$ extended conformer was found highest stability. When Φ_1, Ψ_1, Φ_3 and Ψ_3 of the terminal glycine residues of HCO-Gly-L-Val-Gly-NH₂ were 180°, were found lowest energy, but, when valine torsional angles

were Φ_2 , Ψ_2 ($180^\circ, -120^\circ$) and ($150^\circ, 180^\circ$), respectively, were found lowest energy. Glycine side chain is consisting of only a H atom so, backbone dihedral angles lead to less values of 180° by larger sidechain groups. (see Figure2)

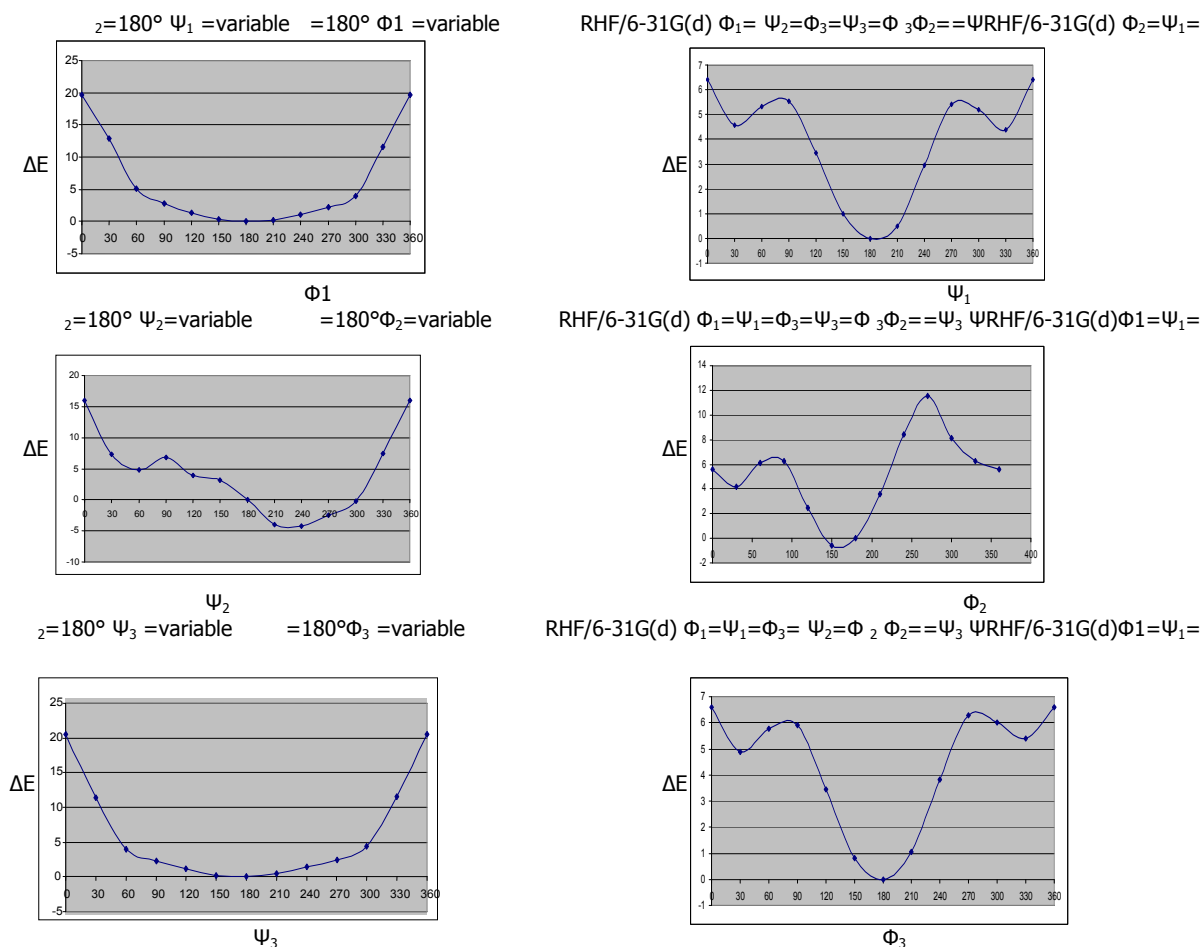


Fig 2. one dimensional PES for HCO-Gly-L-Val-Gly-NH₂. All values are relative to the bLbLbL ($\Phi_i = \Psi_i = \pm 180^\circ$) geometry on the PES.

4. Conclusions

When $\Phi_2 = 0^\circ$ and $\Psi_2 = 180^\circ$ there is a coupling between two oxygen atoms in peptide plane and if $\Phi_2 = 180^\circ$ And $\Psi_2 = 0^\circ$ There is an interference between two Hydrogen atoms, and this fact prevents the formation of such angles. If both Φ_2 and Ψ_2 are 180° and $\Phi_2 = \Psi_2 = 0^\circ$ we'll have an interference between carbonyl oxygen atoms and Hydrogen atom which is the favorable factor. So dipole-dipole attraction interactions play the main role in producing this stability. According to the biophysical studies calculations analysis, the natural elastin shows the existence of pleated sheet β conformer (extended) which plays the main role in developing elastomeric behavior [6,7]. Although proline and glycine amino acids in elastin prefer spiral structures β turn(II), but valine amino acid existence with a large sidechain can play a role in forming pleated sheet β (extended) structure.

References

- [1] G.A. Chass, A.M. Rodriguez, M.L. Mak, E. Deretey, A. Perezel, C.P. Rose, R.D. Enriz, I.G. Csizma, J. Mol. Struet. (Theochem) 500 (2000) 5.
- [2] Indik, Z.Yeh, H.N.Ornstein – Goldstein, Sheppar, P. Anderson, NO. Rosen bloom, J.C. Peltonen, L. Rosenbloom, J. proc. Natl. Acad. Sci. Usa 84 (1981) 5680.
- [3] B.H. Doeswamy, M. mahendra, K. Abiraj, D. Channe Gowda, M.A. Sridhav, J. Shashidhava Prasad. Synthesis, J. Chem. Crystallography 35 (2005) 10.
- [4] W. Kim, V.P. Conticello, J. Maeromoleculav Science, Part C: Polymer Reviews 47(2007) 93.
- [5] Frish .MJ, Trueks .G.E, Schlegel .H.B Scuseria. G.E, Robb. M.A, Cheesmsn .M, Scalmani .G, Rega.N, petersson.c, pople.Y.A (2003) GAUSSIAN o3, Rev.B, Gaussian. Pittsburgh. PA.
- [6] P.C. Gross, W. Possart, M.Zeppezauer, Z. Naturforsch. C 58 (2003) 58, 873.
- [7] A.J. Alix, J. Soc. Biol. 195 (2001) 181.

The effect of hydrogen bond interactions on N-glycosidic bond in 3-methyl-2'-deoxyadenosine modelAli Ebrahimi^a, Mostafa Habibi-Khorassani^a and Sophia Bazzi^{a*}

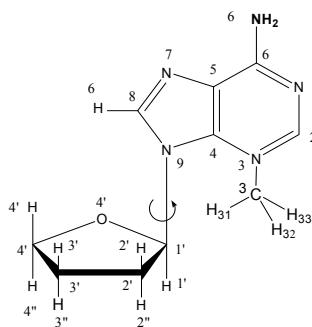
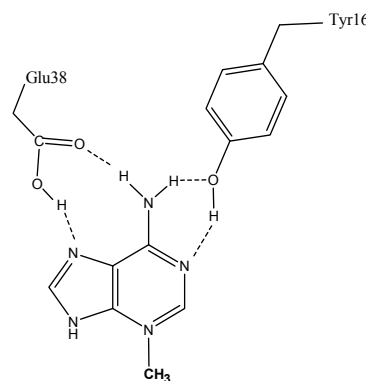
Department of Chemistry, University of Sistan & Baluchestan, P.O. Box 98135-674, Zahedan, Iran

(E-mail: sophia.bazzi@yahoo.com)

Keywords: DNA damage, 3-Methyl-2'-deoxyadenosine, 3-Methyl adenine DNA glycosylase I (TAG), Hydrogen bonding, N-Glycosidic bond.

1. Introduction

DNA is vulnerable to certain types of disruptive forces like alkylation that is a process in which the electrophilic substances attack the molecules that possess an unshared pair of electrons. Adenine and guanine are especially susceptible to alkylation [1]. Depurination is an alternation of DNA in which the purine base (adenine or guanine) is removed from the deoxyribose sugar by hydrolysis of N-glycosidic bond. The cleavage of the N-glycosidic bond in deoxy (nucleosides) and –nucleosides is a common reaction in DNA damage and repair [2], toxicity mechanisms [3], and nucleobase salvage [4,5]. 3-Methyl adenine DNA glycosylase I (TAG) is an alkylated purine-specific DNA glycosylase which is unique for 3-methyl-2'-deoxyadenosine (3-MDA) and 3-methyl deoxyguanosine [6]. The 3-MDA binding pocket of TAG that suggested by Chunyang Cao, et al [7] is given in Scheme 1.

**Scheme 2****Scheme 1**

TAG has glutamic acid (Glu38) and tyrosine residues that form hydrogen bonds with the N1, N6 and N7 positions of 3-MDA in which N1 and N7 are proton acceptor and N6 is proton donor. In the present work, in order to study the effect of different H-bonds on N-glycosidic bond cleavage, the effect of H-bond interactions between a simple molecule, HF, and different sites of damaged base has been investigated by means of density functional theory (DFT) calculations.

2. Methods

3-MDA has been modeled by replacing the sugar phosphate backbone and 3'-hydroxyl group with hydrogen atoms (Scheme 2). All geometries have been optimized at B3LYP [8] level in conjunction with the 6–31 G** basis set using Gaussian03 program package [9]. The AIM analysis has been performed on the wave functions obtained at B3LYP/6–31G** level of theory by AIM2000 [10] program package.

3. Results and discussion

Two intermolecular hydrogen bonds are predicted by the results of AIM analysis in structures **1** (with N7 and H26) and **2** (with N1 and H16). As can be seen in Table 1, the order of N-glycosidic bond length is: **1** > **2** > 3-MDA, which the reverse is true for the electron densities calculations at C–N bond critical point (BCP), ρ_{BCP} .

The values of ρ calculated at N...H and H...F BCPs in **1** are more than those in **2**. On the other hand, N...H and H...F distances in **1** are less than those in **2**. As a result, hydrogen bond interactions in **1** are stronger than those in **2** while the N-glycosidic bond in structures **1** and **2** is longer than that in 3-MDA. Thus, the hydrogen bonds in structures **1** and **2** causes N-glycosidic bond lengthening.



Why the effect of hydrogen bonds on N-glycosidic bond in **1** is more than that in **2**? The N7 atom is closer to N-glycosidic bond relative to the N1 atom such that the N7...H influences the N-glycosidic bond more, relative to N1...H hydrogen bond. In addition, N7 atom is placed in a nonaromatic five-membered ring while N1 atom is placed in an aromatic six-membered ring. Due to the more stability of an aromatic ring related to none aromatic one, the bonds of five membered ring bear more changes than those in aromatic ring.

Table1. The most important parameters optimized at B3LYP/6-31D** level of theory.

structure	C1'-N9	N7...HF	Distance		H16...FH	C8-N7	C8-N9
			H26...FH	N1...HF			
1	1.507	1.703	1.734			1.309	1.381
2	1.504			1.844	1.823	1.307	1.393
3-MDA	1.500					1.303	1.392
ρ							
1	0.234	0.050	0.038				
2	0.236			0.037	0.032		
3-MDA	0.237						

Comparison between **1**, **2** and 3-MDA shows that the hydrogen bond interactions lead to elongation of C8-N7 in structures **1** and **2** that is accompanied by C8-N9 contraction. As a general role, elongation of one bond leads to contraction of some other bonds while all bonds correspond to one atom. Increasing the C8-N7 bond length by hydrogen bond in **1** is more than that in **2**, such that the N-glycosidic bond length in **1** is longer than in **2**.

4. Conclusions

The C8-N7 and C8-N9 bond lengths play a critical role in the length of N-glycosidic bond. The effect of hydrogen bond interactions on the N-glycosidic bond length in **1** is stronger than those in **2**. Thus the (Glu38) may be more effective than (Tyr16) in the lengthening of N-glycosidic bond.

References

- [1] McKee, T. McKee, J. R. Biochemistry, McGraw-Hill Companies, New York, 2003.
- [2] McCann, J. A. B., Berti, P. J. 130 (2008) 5789.
- [3] Robertson, A. B. Klungland, A. Rognes, T. I. Leiros. 66 (2009) 1420.
- [4] Bzowska, A. Kulikowska, E. Shugar, D. Pharmacol. Ther. 88 (2000) 349.
- [5] Versées, W. Ioverix, S. Vandemeulebroucke, A. Geerlings, P. Steyaert, J. J. Mol. Biol. 338 (2004) 1.
- [6] Drohat, A. C. Kwon, K. Krosky, D. J. Stivers, J. T. Nat. Struct. Biol. 9 (2002) 659.
- [7] Cao, C. Kwon, K. Lin Jiang, Y. Drohat, A.C. Stivers, J. T. J. Biol. Chem. 278 (2003) 48012.
- [8] Becke, A. D. J. Chem. Phys. 98 (1993) 5648.
- [9] Frish M. J. et al. Gaussian 03 (Revision B.03), Gaussian, Inc, Pittsburgh, PA, 2003.
- [10] Biegler König, F. W. Schönbohm, J. Bayles, D. J. Comput. Chem. 22 (2001) 545.

Theoretical investigation on bailes-hillman reaction

S. Z. Mohammadi and M. Zamani

Chemistry Dept., College of Sciences, Payame Noor Univ., Kerman, Iran

(E-mail: szmohammadi@yahoo.com)

Keywords: Bailes-Hillman reaction, Minimum electrophilicity principle, Maximum hardness principle, Minimum polarizability principle.

1. Introduction

The description of chemical processes in terms of reactivity indexes has become a current approach in theoretical chemistry. Several local and non local reactivity indices are defined in the form of static density response functions, namely, chemical potential (μ) and hardness (η). In recent years, computational methods based on quantum mechanics (such as Density Functional Theory; DFT) have become important tools for studying chemical reactions. Two DFT based reactivity indexes, which are now being applied for interpretation and rationalization of chemical mechanism and the other chemical aspects, are electronic chemical potential and chemical hardness and defined as:

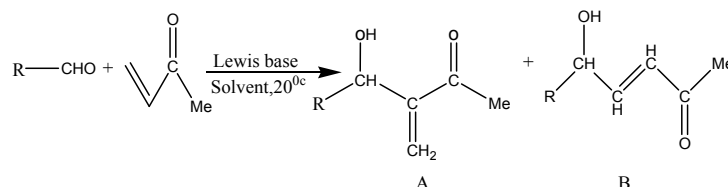
$$\mu = \left(\frac{\partial E}{\partial N} \right)_v \quad (1)$$

$$\eta = \left(\frac{\partial^2 E}{\partial N^2} \right)_v = \left(\frac{\partial \mu}{\partial N} \right)_v \quad (2)$$

Maximum Hardness Principle (MHP) states that under constant μ and v , η should be maximum when energy has the minimum value. The other parameter that is related to η and μ and is used for the study of a given molecular system is electrophilicity parameter (ω), which is expressed as:

$$\omega = \frac{\mu^2}{2\eta} \quad (3)$$

In this paper it is attempted to check the validity of most popular principles (Maximum Hardness, MHP, Minimum Electrophilicity, MEP and Minimum Polarizability, MPP) in predicting the direction of a Bailes-Hillman reaction, which is shown in Scheme 1.

**Scheme 1.** Bailes-Hillman Reaction.**2. Theoretical section**

All geometry optimizations of the reactant and product structures were performed at both HF and B3LYP levels of theory with different basis sets (6-31G** and 6-31+G**). Frequency analysis was also performed at the same level of theory to make sure that are minimum structure.

By assuming that the energy varies quadratically with the number of electrons and applying the finite difference approximation, chemical potential and hardness gets the following operational definitions [1]:

$$\mu = \frac{(IE + EA)}{2} \quad (4)$$

$$\eta = \frac{(IE - EA)}{2} \quad (5)$$

IE and EA values are the vertical ionization potential and electron affinity, respectively. To save computational time, many authors have calculated μ and η by using Janak's theorem [2]:

$$\mu = \frac{(E_{lumo} + E_{homo})}{2} \quad (6)$$

$$\eta = \frac{(E_{lumo} - E_{homo})}{2} \quad (7)$$



3. Results and discussion

The listed molecules in Table 1 are the considered molecules in this study (see Scheme 1). It is clear that both electron-donating and electron-releasing substituents are considered in this list. The obtained results for both hardness and electrophilicity indicate that the MHP and MEP are not successful in predicting the direction of reaction, when Janak's approximation is used; i.e. in most cases the product has less hardness and more electrophilicity than the product. Therefore these principles are failed. By removing Janak's approximation and using the IE and EA for calculations of chemical potential and hardness values, this difficulty is not removed. But the Minimum Polarizability Principle in all cases correctly predicts the stability of products with respect to the reactants. This conclusion is not depending on the basis set and method (see Table 2).

The evaluated charges and fukuies for those atoms which are attached in this reaction are gathered in Table 3. It is clear that the fukui values for those atoms which produce the main product of this reaction are close to each other. Therefore it seems that the Bailes-Hillman reaction is a frontier molecular orbital controlled and not charge controlled.

Table 1. Considered substituents in this study.

NO	R	NO	R
1	m – NO ₂ C ₆ H ₆	5	C ₆ H ₆
2	o– NO ₂ C ₆ H ₆	6	p – Et C ₆ H ₆
3	p – Br C ₆ H ₆	7	C ₆ H ₅ CH=CH
4	p – Cl C ₆ H ₆	8	CH ₃ (CH ₂) ₃

Table 2. Calculated polarizability components and mean polarizability using B3LYP/6-31+G**.

Molecule	α_{xx}	α_{yy}	α_{zz}	α
A1	118.856	143.556	195.473	152.628
B1	209.598	138.204	125.405	157.7357
A2	131.107	150.079	167.314	149.500
B2	161.004	133.599	163.409	152.671
A3	207.671	128.965	132.593	156.410
B3	160.441	111.482	216.519	162.814
A4	202.383	124.790	116.901	148.024
B4	182.084	99.8677	176.614	152.855
A5	129.237	109.979	91.158	110.125
B5	133.849	104.2946	177.158	138.433
A6	134.164	147.471	220.680	167.438
B6	134.670	133.603	250.563	172.945
A7	131.022	19.7335	236.744	129.166
B7	171.729	114.724	237.243	174.565
A8	110.117	118.107	114.925	114.383
B8	120.860	125.123	108.156	118.046

Table 3. Computed Mulliken Charges and negative fukuies using B3LYP/6-31+G** level of theory for the attached atoms.

Method	C ₁	C ₂	C ₃	
HF/6-31G**	-0.2231	-0.2191	0.5072	
HF/6-31+G**	-0.1290	-0.2765	0.3952	
B3LYP/6-31G**	-0.2000	-0.0954	0.4107	
B3LYP/6-31+G**	-0.3427	0.0661	0.3515	
C ₂ ⁺	C ₃ ⁺	f ₁ ⁻	f ₂ ⁻	f ₃ ⁻
0.1782	-0.2190	0.1311	0.3974	-0.726
0.1964	-0.2041	0.0208	0.4730	-0.599
0.1386	-0.0566	0.1690	0.2341	-0.467
0.1460	-0.0378	0.3025	0.0799	-0.389

4. Conclusion

It seems that the electrophilicity and Minimum Electrophilicity Principle is more successful in predicting the direction of Bailes-Hillman reaction than the other commonly used principles such as Maximum Hardness and Minimum Polarizability Principles. The obtained charges and fukuies indicate to this fact that the considered reaction is a frontier molecular orbital controlled and not charge controlled.

References

- [1] Pearson, R.G. J. Am. Chem. Soc. 107 (1985) 6801.
- [2] Janak, F. Phys. Rev. B 18 (1978) 7165.

Study of the electric field effect on the electronic properties of the 6Au/S-Guanine-S/6Au structureF. Hashemi, H. Milani Moghaddam, M. Tayaran, F. Shariati^b^a Physics Department, Khayyam University of Mashhad, Mashhad, Iran^b Physics Department, Mazandaran University, Babolsar, Iran

(E-mail: seidehfaezeh_hashemi@yahoo.com)

Keywords: Molecular wires, DNA, Guanine, Density function theory.**1. Introduction**

The progress of molecular wires [1] attracts much attention on their transport behaviors. DNA (Deoxyribonucleic Acid) molecule might be used as an insulator, semiconductor or conductor in the molecular wires [2]. A number of experimental groups have reported measurements of the current-voltage characteristics of molecules specially DNA [3,4].

In this study, we are modeling a molecular wire like metal/molecule/metal that the molecular bridge is one of the bases of DNA which called Guanine. We have performed Density Functional Theory (DFT) method to study the effect of the electric field on the electronic properties of the 6Au/SGM/6Au wire which the SGM stands for Sulfur-Guanine Molecule. We investigate that how HOMO-LUMO gap (Highest Occupied Molecular Orbital and Lowest Unoccupied Molecular Orbital, HLG), the Density of Electronic States (DOS) and the band length between S and Au₁₇ in the 6Au/SGM/6Au structure change by applying an electric field.

2. Methods

All calculations are performed using Gaussian03 program. The 6Au/SGM/6Au structure is optimized at DFT-B3LYP level of theory. We choose the basis set 6-31G* for C, N, H, O and S atoms and LanL2DZ for Au atom.

3. Result and discussion

The electric fields are applied in the greatest dipole moment direction that in the 6Au/SGM/6Au wire is along the -Z axis. Figures 2 and 3 show the DOS in the absence of an applied field and for different electric fields, respectively. The band length between S and Au₁₇ decrease sharply in the 6Au/SGM/6Au structure as the electric field increase (see figure 4). After applying different electric fields the HLG increase (see figure 5).

4. Conclusions

In the 6Au/SGM/6Au structure, the HLG of the 6Au/SGM/6Au structure is 1.032 (eV) in the absence of an applied electric field. After applying the electric field, the HLG increase. The band Length between S and Au₁₇ become shorter when we apply the electric field. We have seen that by attaching Au atoms to SGM a semiconductor-like behavior can be achieved. We can see that Guanine will be useful as an element in the molecular wires.

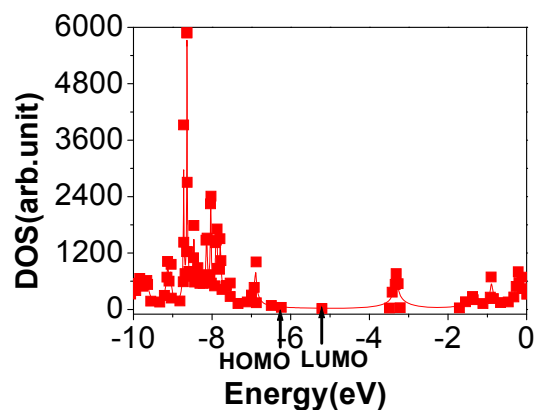
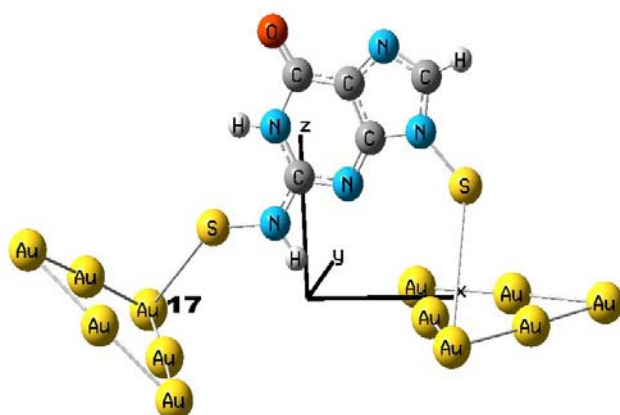


Fig. 1. The 6Au/SGM/6Au structure.

Fig. 2. The DOS of the 6Au/SGM/6Au structure vs. Energy.

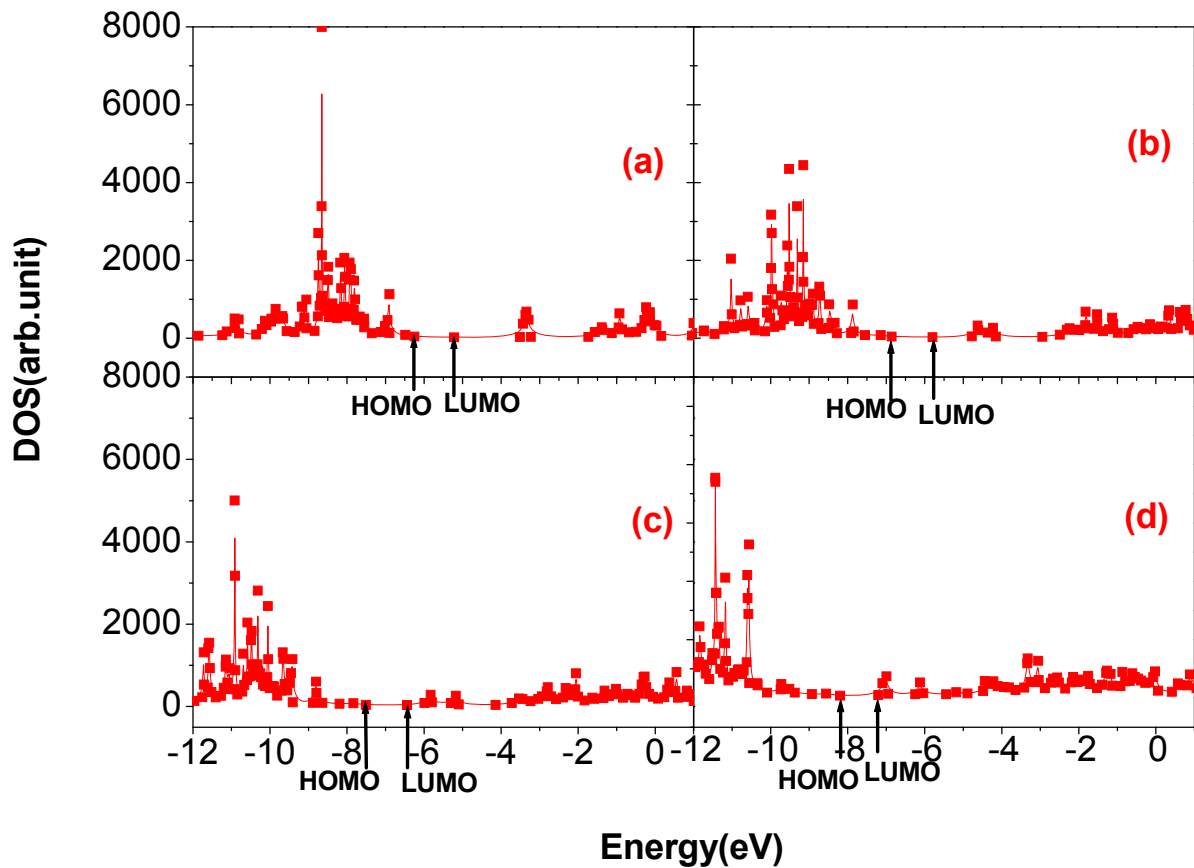


Fig. 3. The DOS of the 6Au/SGM/6Au structure vs. energy in different electric fields. The electric field for figures: (a) 0.005(V/Å), (b) 0.25(V/Å), (c) 0.51(V/Å), (d) 0.77(V/Å).

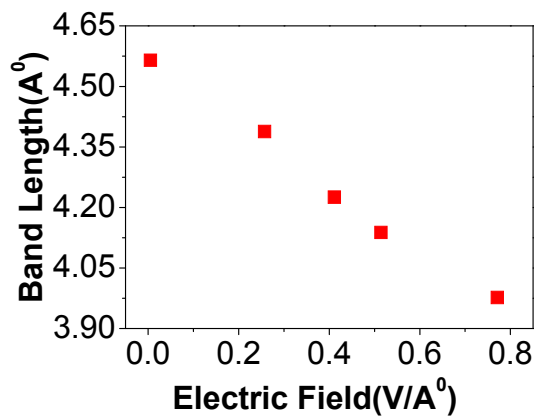


Fig. 4. The band Length between S and Au₁₇.

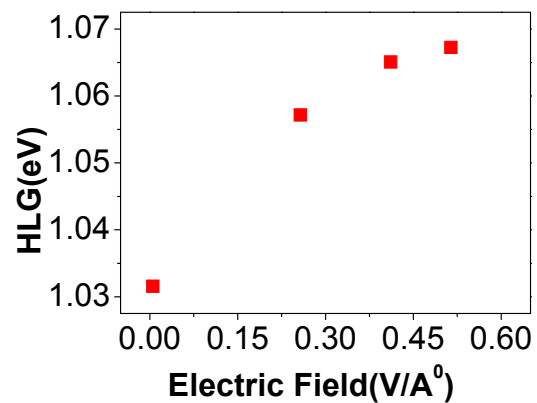


Fig. 5. The HLG of 6Au/SGM/6Au structure vs. the electric fields vs. the electric fields in the 6Au/SGM/6Au structure.

References

- [1] R. F. Service, Science, 295 (2002) 2398.
- [2] Yuri A. Berlin, Alexander L. Burin, Mark A. Rantner, Superlattices and Microstructures, 28 (2000) 4.
- [3] A. Rakitin, et al. Phys. Rev. Lett, 86 (2001) 367.
- [4] K.-H. Yoo, et al. Phys. Rev. Lett. 87 (2001) 198102.

**Spin separation of deformation density in doublet state of Li@C₆₀**S. Fakhraee ^{a,*}^aDepartment of Chemistry, College of Sciences, Payame Noor University (PNU), Shiraz, Iran
(E-mail: Fakhraee@spnu.ac.ir, Fakhraee@yahoo.com)**Keywords:** Li@C₆₀, fullerene, deformation density, spin.**1. Introduction**

Since the discovery of nanomaterials such as carbon nanotubes (CNT), graphenes and fullerenes, numerous research studies have been centralized on the determination of physical and chemical characteristics of these compounds. The remarkable properties of these structures are appeared by intercalating atoms or molecules. This has an important role in changing the ability of accepting and donating electrons in nanostructures. Among the well known carbon nanostructures, cage-like structure fullerenes and especially buckminsterfullerene C₆₀ has significant ability to encapsulate metal and non-metal atoms. Nanocarbon systems such as fullerenes and geraphenes have wide applicability to drug delivery in biological applications which can be intensified by intercalating alkali metals. It has been shown that lithium is perfectly capable of transferring charge density to the surface which increases the ability of interaction of nanostructures with biochemical substances. Despite, Numerous theoretical and experimental studies on properties of alkali metals intercalated C₆₀, the quality and quantity of charge transfer in these complexes, especially for multiplet spin states, has not yet been determined.

In a recent work by our group, a new computational technique was introduced for analysis of interatomic or intermolecular interactions based on deformation density matrix [1,2]. In the present work, we wish to specify the qualification and quantification of reorganization of electron density for interaction of Li encapsulated in C₆₀ by the help of mentioned method. Then the results are compared for α and β spins.

2. Theoretical method

Electron density reorganization of fragments changes, while a complex forms. The density difference between complex and those of fragments are defined as deformation density, $\Delta\rho$, which is obtained by following equation:

$$\Delta\rho = \rho_{\text{complex}} - \sum \rho_{\text{fragments}} \quad (1)$$

Digonalization of deformation density matrix among complex formation results in deformation natural orbitals (DNOs) as eigenvectors, $\theta_{\Delta,i}$ and displaced charged as eigenvalues, $n_{\Delta,i}$. In fact, DNOs demonstrate the space responsible for reorganization in electron density. Decomposition of deformation density in terms of $\theta_{\Delta,i}$ and $n_{\Delta,i}$ gives Eq. 2 as:

$$\Delta\rho = \sum_i^m n_{\Delta,i} |\theta_{\Delta,i}|^2 \quad m : \text{number of DNOs.} \quad (2)$$

Two essential factors that govern the deformation density in complex are as follows:

1- Virtual pressure imposing on orbitals to achieve mutual orthogonality which called kinetic energy pressure (KEP) or stric effect. This part is originated from Pauli repulsion principle [3,4]. 2- Orbital relaxation which is originated from inter-fragment physical attraction and repulsion; and will be showed by 'relax' as lower index. Eq. 2 can be defined for both above individual parts and also for the total interaction including KEP and relaxation as:

$$\Delta\rho_{\text{total}} = \Delta\rho_{\text{KEP}} + \Delta\rho_{\text{relax}} = \sum_i^m n_{\Delta,i}^{\text{KEP}} |\theta_{\Delta,i}^{\text{KEP}}|^2 + \sum_i^m n_{\Delta,i}^{\text{relax}} |\theta_{\Delta,i}^{\text{relax}}|^2 = \sum_i^m n_{\Delta,i}^{\text{tot}} |\theta_{\Delta,i}^{\text{tot}}|^2 \quad (3)$$

Diagonalization of the density matrices corresponding to the above densities will thus result in the corresponding deformation natural orbitals (DNO) and displaced charges as eigenvalues:

$$\mathbf{P}_{\Delta}^X \xrightarrow{\text{digonalization}} \mathbf{P}_{\Delta}^X \mathbf{S} \mathbf{C}_{\Delta}^X = \mathbf{C}_{\Delta}^X \mathbf{n}_{\Delta}^X \quad \mathbf{x} = \text{total, KEP, relax} \quad (4)$$

where, X stands for total, KEP and relax DNOs.

The sign of eigenvalues n_{Δ}^X has an important physical concept. DNOs with $n_{\Delta}^X > 0$ and $n_{\Delta}^X < 0$ refers to accumulation and depletion of charge, respectively, in the space provided by the corresponding DNO.

In the present work, reorganization of electron density is quantified for Li-C₆₀ interaction for α and β spins. All molecular geometry optimizations are performed at HF/6-31G* level of theory utilizing Gaussian 03 suite of programs. Basis set superposition error (BSSE) is also considered to obtain wave functions of the fragments.

3. Results and discussion

The KEP, relax and total DNOs ($\theta_{\Delta,i}^{KEP}$, $\theta_{\Delta,i}^{relax}$ and $\theta_{\Delta,i}^{total}$, respectively) and their eigenvalues for Li@C₆₀ complex are obtained by diagonalization of their deformation density matrices and analyzed. Only DNOs with significant eigenvalues are reported and compared in Table 1 for α and β spins. Also, degenerate DNOs with respect to their $n_{\Delta,i}^X$ are omitted to save space. The obtained eigenvalue for each DNO, $n_{\Delta,i}^X$, are demonstrated in the parenthesis below corresponding DNOs in Table 1.

The comparison of $\theta_{\Delta,i}^{total}$ with $\theta_{\Delta,i}^{KEP}$ and $\theta_{\Delta,i}^{relax}$ in Table 1 reveals that the $\theta_{\Delta,i}^{relax}$ orbitals are more similar to $\theta_{\Delta,i}^{total}$ with regards to the corresponding symmetry and their eigenvalues than the $\theta_{\Delta,i}^{KEP}$, so these orbitals have more contribution to the interaction of Li and C₆₀ than the others. Also the scheme of orbitals in Table 1 confirms that electron density is depleted on the Li atom and concentrated on the surface of fullerene in complex formation.

As the α -atomic orbitals can be considered as frontier orbitals for lithium atom interacting with C₆₀, it is expected that α DNO orbitals play most significant role than β orbitals in both $\theta_{\Delta,i}^{KEP}$ and $\theta_{\Delta,i}^{relax}$. The results show α -DNOs of $\theta_{\Delta,i}^{relax}$ are more similar to those of $\theta_{\Delta,i}^{total}$. Therefore these orbitals play an important role in Li and C₆₀ interaction than β -DNO orbitals. On the other hand the beta electron of Li atom is located in the core 1s orbital and consequently, 1s β -electron dose not significantly contribute to the deformation density.

Table 1. $\theta_{\Delta,i}^{KEP}$, $\theta_{\Delta,i}^{relax}$, and $\theta_{\Delta,i}^{total}$ DNOs for Li@C₆₀ interaction for α and β spins with their corresponding eigenvalues located in the parenthesis below each orbital.

4. Summary and concluding remarks

Deformation density analysis of complexation of Li@C₆₀ is inspected and decomposed into KEP, relaxation components. Diagonalization of the corresponding density matrices revealed the reorganized charge due to KEP and relaxation interactions. The results show that the charge reorganization on the surface fullerene. This observation provides new insights in nanobiotechnology. Since encapsulation of alkali atoms inside the fullerenes forces the fullerene's electrons to concentrate on the surface to make stronger interactions with biomolecules. Also separated results for α and β spin orbitals demonstrate that α -spin deformed density due to relaxation part has main contribution to complexation at Li@C₆₀.

References

- [1] A. H. Pakiari, S. Fakhraee, S. M. Azami, Int. J. Quantum Chem., 108 (2008) 415.
- [2] S. Fakhraee, S. M. Azami, J. Chem. Phys., 130 (2009) 084113-1.
- [3] V.F. Weisskopf, Science, 187 (1975) 605.
- [4] J.K. Badenhoop, F. Weinhold, J. Chem. Phys., 107 (1997) 5406.

$\theta_{\Delta,i}^{relax}$		$\theta_{\Delta,i}^{total}$		$\theta_{\Delta,i}^{KEP}$	
α	β	α	β	α	β

**Study of hydrogen bonding in Pyridine-2,6-dicarboxylic acid(dipic) using computational methods**S. Jameh-Bozorgi^{*,1}, H. Esfandiari²¹Department of Chemistry, Azad University - Touyserkan Branch²Department of Chemistry, Islamic Azad University - Neyriz Branch

E-mail: (sjamehbozorgi@gmail.com)

Keywords: Intramolecular hydrogen bond, ab-Initio, AIM and NBO.**1. Introduction**

Pyridine-2,6-dicarboxylic acid (dipicolinic acid, H₂dipic) is a water-soluble, commercially available, cheap and versatile N,O-chelator possessing diverse coordination modes, with a recognized biological function in the body metabolism, namely as a major component of bacterial spores, and in a variety of processes as an enzyme inhibitor, plant preservative, food sanitizer, etc [1,2].

2. Methods

The strong intramolecular hydrogen bond in dipic was studied with ab-initio calculations. All possible conformations of dipic were fully optimized at HF, MP2 and B3LYP levels with 6-311++G** basis set in order to determine the conformational equilibrium. The nature of the strong intramolecular hydrogen bond in the most stable chelated conformers has been studied by using the atoms in molecules (AIM) theory of Bader by mean of AIM2000 software and NBO analysis, calculated at the MP2/6-311++G** level [3,4]. These wave functions obtained from the geometries at the same level. In AIM analysis, we have located the bond critical points and acquired detailed information on the relative strength of the hydrogen bond can be obtained in term of electron density (ρ), and Laplacian ($\nabla^2\rho$). Finally, for better understanding the nature of intramolecular hydrogen bond and conformational preference, the natural bond orbital(NBO) analysis was performed.

3. Results and discussion

Theoretically, H₂dipic has about 10 different plausible conformers. The results of Table 1, it can be concluded that, the energy order is independent from the computational level and also electron correlation energy. It is obvious from this table, although the relative stability at MP2 and B3LYP levels is identical but this stability order at HF method is different. All of the structures were fully optimized, except 1,9,10 conformers that full optimization gave no planar structures. In 9, the two hydroxyl hydrogens are in a suitable position for hydrogen bond formation with nitrogen. In 10 conformer one of the hydroxyl hydrogens is outside rotated by 180° and can not form hydrogen bond. Only one hydrogen bond and one ring are formed. The AIM is a very useful tool in analyzing the hydrogen bond. In all of the HB critical points, the values of ρ_{BCP} and $\nabla^2\rho_{BCP}$ are in the range 0.0234 - 0.0274 a.u. and (-0.0247) - (-0.0280) a.u. respectively. These electronic charge transfers are well estimated by NBO approach by second order perturbation theory. The total values of charge transfer energies for 6, 7, 9 and 10 conformers are about 1298.4, 1407, 864.48 and 1484.74 kcalmol⁻¹, respectively.

Tabel 1. Stability order between conformers.

Level	Energy order
HF	10 < 7 < 1 < 9 < 2 < 3 < 6 < 8 < 4 < 5
B3LYP	10 < 7 < 9 < 1 < 2 < 3 < 6 < 8 < 4 < 5
MP2	10 < 7 < 9 < 1 < 2 < 3 < 6 < 8 < 4 < 5

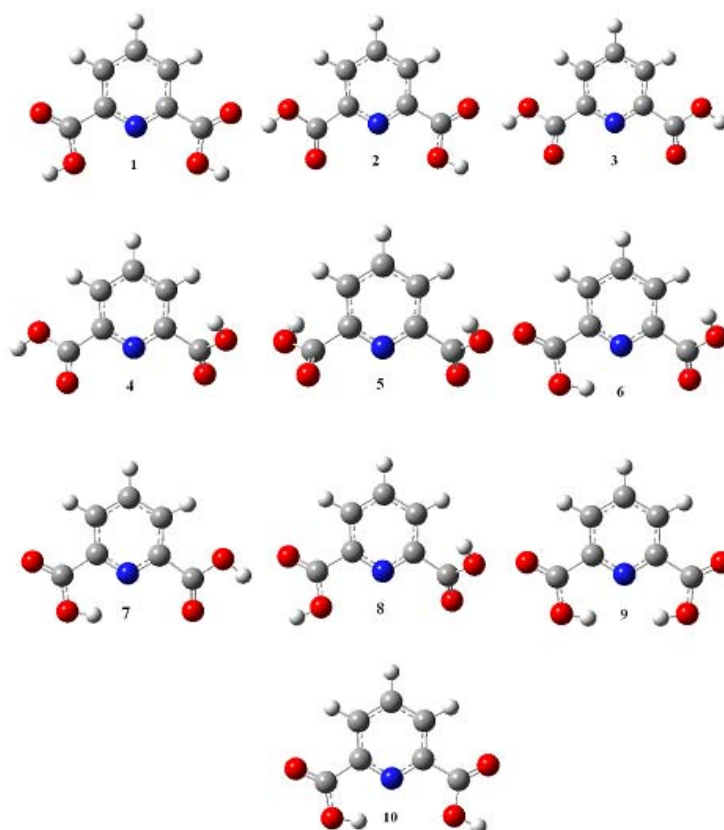


Fig. 1. The optimized structures of dipicolinic acid conformers at MP2/6-311++G (d, p) level.

4. Conclusions

MP2 and B3LYP theoretical methods are employed to optimize all of the dipicolinic acid conformers with the most popular basis sets. The NBO and AIM analyses were used in order to discuss the origin of conformational preference and hydrogen bond strength. According to results, dipicolinic acid can have been 10 stable conformers and therefore 10 local minimum and all of the computational levels emphasized on E11 as global minimum.

Reference

- [1] M. Chatterjee, M. Maji, S. Ghosh, T.C.W. Mak, J. Chem. Soc., Dalton Trans. (1998) 3641.
- [2] L.C. Nathan, T.D. Mai, J. Chem. Cryst. 30 (2000) 509.
- [3] U. Koch, P.L.A. Popelier, J. Phys. Chem. 99 (1995) 9747.
- [4] R.W.F. Bader, Chem. Rev. 91 (1991) 893.



The theoretical study of ¹³C NMR chemical shielding tensors in 3- amino-2-nitrobenzo[b]thiophenes and comparison with experimental values

Mahdi Rezaei-Sameti*

Department of Chemistry, Faculty of Science, Malayer University, Malayer, Iran

(E-mail: mrsameti@gmail.com)

Keywords: Ab initio, NMR, ¹³C, Shielding Tensor, CSGT, GIAO, Density functional theory, 3- amino-2-nitrobenzo[b]thiophenes .

1. Introduction

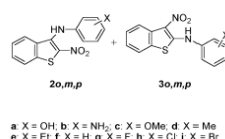
NMR spectroscopy of ¹³C has an enormous potential for investigating conformations and configurations in organic compounds. After the discovery of NMR, such potential rapidly increased to cover various kinds of compounds, including biological, inorganic and organometallic compounds [1]. The GIAO/DFT (gauge including atomic orbital/density functional theory) approach is extensively used for the calculations of chemical shifts for different types of compounds. DFT calculations are hardly expensive and they enable accurate calculations on systems such as large organic molecules [2]. At present with this methodology, a variety of spin- spin coupling constants can be calculated with good accuracy in polyatomic systems [3-4].

2. Computational methods

Geometry of all compounds are optimized by employing DFT method using a 6-311++G(2d,2p) basis set and using the GAUSSIAN 98 program. Calculations were performed on a Pentium-PC computer with a 3000 MHz processor (Figure 1). The ¹³C NMR shielding results presented were obtained using B3LYP methods and the 6-311++G (2d,2p) , 6-31++G(2d,2p), 6-31G(2d,2p) basis set and the calculations of NMR shielding tensors were done using two of the most common procedures, namely GIAO and CSGT.

3. Results and discussions

In this work we used the *ab initio* computational techniques to study the effect of some ortho-substituted *aniline* such as :{ x=OH, NH₂, OMe, Me, Et, H, F, Cl , Br} on the ¹³C NMR spectroscopy of 3- amino-2-nitrobenzo[b]thiophenes with two conformer 2O and 3O.



The calculations of NMR shielding tensors were done using two of the most common procedures, namely GIAO and CSGT. The isotropic value, anisotropy of the tensor and shielding tensor asymmetry parameter are calculated:

a) The isotropic value (or trace), σ_{iso} , of the shielding tensor which is defined as:

$$\sigma_{iso} = \frac{1}{3}(\sigma_{11} + \sigma_{22} + \sigma_{33}) \quad (1)$$

b) The anisotropy ($\Delta\sigma$) of the tensor,

$$\Delta\sigma = \sigma_{33} - \frac{1}{2}(\sigma_{22} + \sigma_{11}) \quad (2)$$

c) The shielding tensor asymmetry parameter (η) given by

$$\eta = \frac{(\sigma_{22} - \sigma_{11})}{(\sigma_{33} - \sigma_{iso})} \quad (3)$$

The assignment or ordering of the principal components in the ¹³C CSA tensor depends on the convention used, but for this manuscript the principal components are defined using:

$$|\sigma_{33} - \sigma_{iso}| \geq |\sigma_{22} - \sigma_{iso}| \geq |\sigma_{11} - \sigma_{iso}| \quad (4)$$

The relations between the experimental ¹³C chemical shift (δ_{exp}) and GIAO and CSGT magnetic isotropic shielding tensors (σ_{calc}) which are now widely used in efficient implementation , are usually linear and described by following equation given as:

$$\delta(exp) = a + b\sigma(cal) \quad (5)$$

The slope and intercept of the least-square correlation line is used to scale GIAO and CSGT absolute shielding, σ , and to predict chemical shifts,

$$\delta(pred) = a + b\sigma(cal) . \quad (6)$$

The shielding tensor asymmetry parameter (η) is variable ranging from -80.25 to 11.21 and the anisotropy ($\Delta\sigma$) of the tensor is variable ranging from -148.1 to -3.31 respectively. The computational results for all conformers are given in tables (1-18). The comparison the calculated and experimental values show a good agreement.

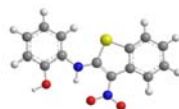


Fig. 1. Optimized structures of conformer A.

Table 1. Ab initio NMR ^{13}C shielding tensors with GIAO method for geometry optimized 3- amino-2-nitrobenzo[b]thiophenes {conformer A} with B3lyp/6-311++G(2d,2p).

Compounds	σ_{33}	σ_{22}	σ_{11}	σ_{iso}	$\Delta\sigma$	η
C1	-6.2073	-2.6072	170.0467	53.7440	-89.9271	2.8799
C2	24.4064	-51.8944	168.5658	47.0259	-33.9293	9.7465
C3	-49.3377	28.0740	169.4639	49.4001	-148.1067	1.4320
C4	-38.0862	35.8910	166.5880	54.7976	-139.3257	1.4071
C5	23.0412	-22.8246	141.9849	47.4005	-36.5390	6.7658
C6	-26.0260	-23.9354	146.1677	32.0688	-87.1422	2.9280
C7	17.1733	-42.6667	120.7160	31.7408	-21.8514	11.2156
C8	19.7451	32.5187	76.9150	43.0596	-34.9718	1.9042
C9	-8.9689	104.9112	55.8626	50.6016	-89.3558	-0.8234
C10	2.5224	142.1463	0.6523	48.4403	-68.8769	-3.0815
C11	9.4064	102.0157	-51.5416	19.9602	-15.8307	-14.5500
C12	55.5559	147.8888	-30.1509	57.7646	-3.3131	-80.6084
C13	18.8596	148.6340	18.2844	61.9260	-64.5996	-3.0267
C14	-38.0966	142.6747	35.1953	46.5911	-127.0316	-1.2691

Table 2. Ab initio NMR ^{13}C shielding tensors with CSGT method for geometry optimized 3- amino-2-nitrobenzo[b]thiophenes {conformer A} with B3lyp/6-311++G(2d,2p).

Compounds	σ_{33}	σ_{22}	σ_{11}	σ_{iso}	$\Delta\sigma$	η
C1	-4.2375	-1.1521	170.1892	54.9332	-88.7561	2.8957
C2	24.9015	-49.7355	169.3717	48.1792	-34.9166	9.4128
C3	-46.7387	29.2938	170.1565	50.9038	-146.4639	1.4426
C4	-33.1922	36.0661	165.8084	56.2274	-134.1295	1.4509
C5	25.7512	-19.8238	143.6330	49.8535	-36.1534	6.7818
C6	-24.2116	-23.4736	146.9646	33.0931	-85.9571	2.9742
C7	17.8431	-39.1195	121.3596	33.3611	-23.2770	10.3415
C8	20.7810	32.7232	79.9867	44.4970	-35.5740	1.9929
C9	-7.5231	107.2175	57.8929	52.5291	-90.0783	-0.8214
C10	4.5324	143.7878	2.3496	50.2233	-68.5363	-3.0955
C11	11.0529	103.9553	-49.4067	21.8672	-16.2214	-14.1814
C12	55.1743	148.0977	-27.9855	58.4289	-4.8818	-54.1029
C13	20.9461	148.9426	19.5867	63.1585	-63.3186	-3.0644
C14	-36.9833	143.4542	35.5091	47.3267	-126.4650	-1.2803



Gas-Phase theoretical study on thermodynamic parameters (ΔG and ΔH) of binary mixtures $((CH_3OH)_m (H_2O)_n (m+n) 9-17)$ at various temperature

Mehdi Rezaei Sameti,^a Sadegh Salehzadeh,^b Mehdi Bayat^b

^a Department of Chemistry, Faculty of Science, Malayer University, Malayer, Iran

^b Faculty of Chemistry, Bu-Ali Sina University, Hamedan, Iran

(E-Mail: mrsameti@gmail.com)

Keywords: Ab initio, Binary mixture, Thermodynamic parameter, Methanol, Water.

1. Introduction

The excess enthalpy can be measured with a flow mixing calorimeter either isothermally or adiabatically. Using the adiabatic method the excess enthalpy is obtained from the temperature change of the mixing process and on the one hand from the heat capacity c_p of the mixture and on the other hand from the heat capacities $c_{p,i}$ of the pure components[1-4].

In this work for calculating the experimental enthalpy, we used the ab initio method for this reason, and in an attempt to understand the phase behavior of aqueous methanol, the clustering in the mixture is investigated at the gas phase. The study is performed at the B3LYP/6-31G* level of theory.

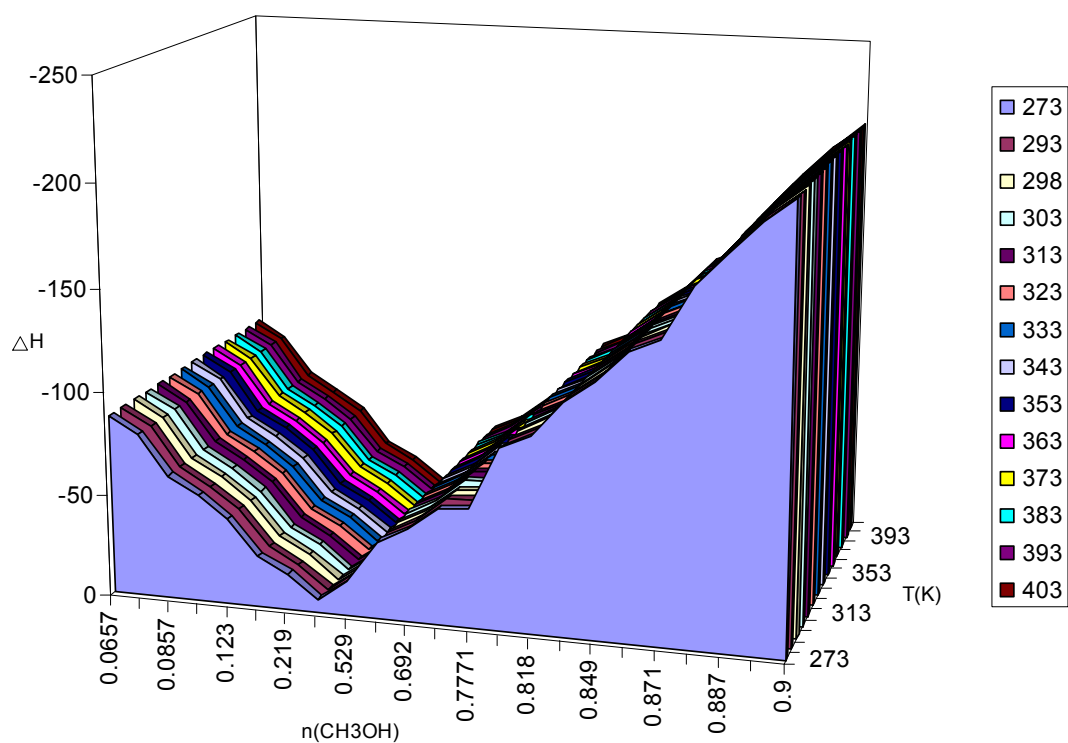
Several previous studies attempted to describe the formation of hydrogen bond between one, two and three C_2H_5OH with water in the gas phase, but according to our best knowledge there are no reports on theoretical description of hydrogen bond formation between the CH_3OH and H_2O in various mol fractions in mixture.

2. Computational details

The geometries of all compounds at gas phase were fully optimized at DFT (B3LYP) levels of theory using the Gaussian 03 set of programs. The standard 6-31G* basis set was used for all atoms. Vibrational frequency analyses, calculated at the same level of theory, in various temperature (between 278.15-403.15 K) indicate that optimized structures are at the stationary points corresponding to local minima without any imaginary frequency. A starting molecular-mechanics structure for the ab initio calculations was obtained using the HyperChem 5.02 program.

3. Result and discussion

Herein for first time we want to report the thermodynamic properties such as ΔG and ΔH of binary mixture $(CH_3OH)_m(H_2O)_n (m+n)$ mixture, with $m+n$ as high as 9-17, at various mol fraction and temperatures. For each mixture combination in each mol fraction, two different conformations cyclic and chain structures are investigated. The results indicate that the cyclic structures are more stable when compared with chain structures. Also the trend of ΔG and ΔH of these mixtures were investigated in various mol fractions and temperatures. The result shows that the ΔH of these mixtures in all mol fractions was decrease with increase in temperature. Experimental results show that in the binary mixture of Methanol and water, the excess molar volumes, excess enthalpy and excess Gibbs free energy are negatives at the whole mole fractions. The comparison between experimental data and the theoretical show that a good agreement.



References

- [1] Kuo, J. L. Fujii, A. Mikami, N. J. Phys. Chem. A 111 (2007) 9438.
- [2] Mejia, S. M. Espinal, J. F. Restrepo, A. Mondragon, F. J. Phys. Chem. A, 111 (2007) 8250.
- [3] Dettmann, C. Ernst G., Wirbser, H. J. Chem. Thermodynamics 38 (2006) 56.
- [4] Wormald, C. J.; Badock, L.; Lloyd, M. J. J. Chem. Thermodynamics 28 (1996) 603.



Comparison between the experimental and theoretical vibrational frequencies of some halo-derivatives of aniline

M. Rezaei-Sameti

Department of Chemistry, Faculty of Sciences, Malayer University, Malayer, Iran

(E-mail: mrsameti@gmail.com)

Keywords: DFT, Halo aniline derivatives, Infrared spectra, Vibrational frequencies.

1. Introduction

In recent years, aniline and its derivatives have been subjected to many different types of scientific studies up to now [1]. They have been widely used in a variety of industrial and commercial purposes, including dyestuff, pesticide and pharmaceuticals manufacturing [2]. Some of the *para*-substituted derivatives of anilines are local anesthetics and the amino group in these molecules plays an important role in the interaction with the receptor [3]. In best of our knowledge, the first complete study on aniline has carried out by Evans [4], the assignments of the infrared spectra in the vapor, solution and liquid phases and the Raman spectra in the liquid state have been reported by other authors [5].

2. Computational methods

Calculations have been done at B3LYP employing the 6-31G (d), 6-31G (2d,2p), 6-31++G(2d,2p), and 6-311++G(2d,2p) levels of theory. The optimized structures were used for calculation of vibrational frequencies at B3LYP/6-311++G (2d,2p) level of theory. All the calculations are performed by using GAUSSSIAN 98 program package on the personal computer.

3. Results and discussion

This paper is a continuation of my former works for predicting of the experimental parameters of some known compounds using theoretical calculation [6]. For this reason, in this work we study the vibrational frequencies of all possible isomers of some aniline derivatives with general formula $C_6H_{5-n}X_nNH_2$ ($n=1-5$; $X=F, Cl, Br$).

The resulting data were scaled by 0.952 for N-H stretching bond and 0.981 for C-N, C-X ($X=F, Cl, Br$), C=C, N-H (bending) bonds. The results showed that, there is a good agreement between the scaled theoretical frequencies and experimental data for this type of compounds. The comparison the frequencies show the flowing trends for all aniline derivatives:

1- For one substitute of halo aniline derivatives the trends of frequency for N-H bending-X ($X=F, Cl, Br$), C-N in Orto, Meta and para positions are:

$$V_{(F)} > V_{(Cl)} > V_{(Br)}$$

2- For two substitute of halo aniline derivatives for N-H bending-X ($X=F, Cl, Br$), C-N bonding in (2,3), (2,5), (2,6),(3,4) and (3,5) positions are:

$$V_{(F)} > V_{(Cl)} > V_{(Br)}$$

3- For three substitute of halo aniline the trends of frequency for N-H bending and C-N bonding in the (2,3,4),(2,3,5) and (2,4,5) are:

$$V_{(Cl)} > V_{(Br)} > V_{(F)}$$

Figures 1 and 2 show the comparison between experimental and theoretical frequencies for the para halo aniline and 2,5 di halo aniline for an example. As it can be seen in this Figure, there is a good correlation between the experimental and calculated frequencies for these components.

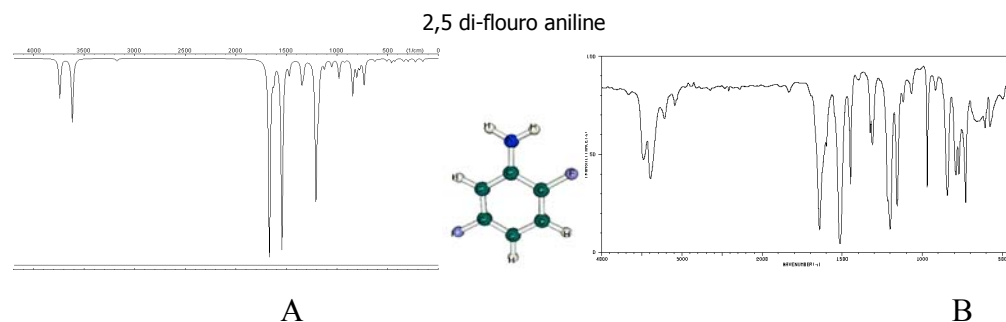


Fig. 1. A) Theoretical IR spectra, optimized structure by DFT/ ((B3LYP//6-311++G(d,p)). (B) Experimental IR spectra of para fluoro aniline and 2,5 di- fluoro aniline derivatives.

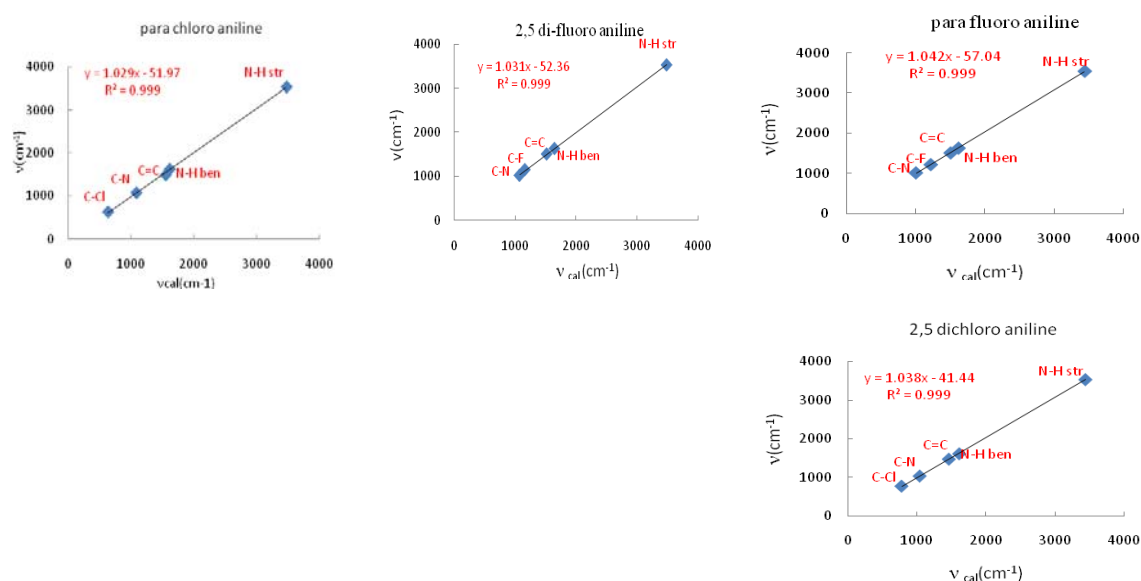


Fig. 2. Correlation of the theoretical and experimental vibrational frequency of para halo aniline and 2,5 di-halo aniline derivatives by DFT/((B3LYP//6-311++G(2d,2p)) .

References

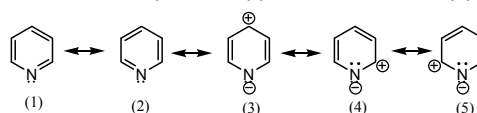
- [1] Rappoport, Z. The chemistry of aniline, part 1, 2007.
- [2] Altun, A. Gölcük, K. Kumru, M. J. Mol. Struct. Theochem. 625 (2003) 17.
- [3] Kurt, M. Yurdakul, M. Yurdakul, S. Journal of Molecular Structure Theochem. 711 (2004) 25.
- [4] Evans, J.C. Spectrochim. Acta 16 (1960) 428.
- [5] Dove, A.P. Gibson, V.C. Marshall, E.L. Rzepa, H.S. White, A.J.P. Williams, D. J. J. Am. Chem. Soc. 128 (2006) 9834.
- [6] Rezaei-Sameti, M. Journal of Molecular Structure: THEOCHEM 867 (2008) 122.

Ab initio and DFT study of dehydrogenation of 1,2-Dihydro-pyridine, ASE and NICS analysisS. Jameh-Bozorgi^{a,b*}, V. daneshdoost^b, S. Rafatpanah^b and N. Zolfaghar^ba- Chemistry Department, science faculty, Islamic Azad University,
Touyserkan Branch, Touyserkan, Iranb- Chemistry Department, science faculty, Islamic Azad University, Arak Branch, Arak, Iran
(E-mail: sjamehbozorgi@gmail.com)**Keywords:** Ab initio, NICS, ASE, Elimination, Dehydrogenation.**1. Introduction**

Pyridine (**1**) is a heterocyclic system which most closely resembles benzene in terms of structure and overall stability. For example, pyridine, like benzene, is extremely resistant to oxidation and is frequently employed as a solvent in conjugation with such oxidizing agents as chromium trioxide to effect the oxidation of organic molecules.¹

Cyclic conjugation in (**1**) is apparent from its stabilization energy of 21 Kcal/mole² and from the measured C-C and C-N bond lengths which lie intermediate between those known for authentic single and double bonds.³

In the alternative valence -bond description of pyridine, structures (1)-(5) are considered to contribute to the resonance hybrid.

**Scheme 1.**

The zwitterionic forms in the present instance are believed to contribute substantially to the hybrid, chiefly on the basis of the large dipole moment for this substance, 2.26D⁴, which is appreciably greater than that of piperidine (1.17 D), its perhydro counterpart. On the basis of these resonance structures, it must be noticed that the relatively more electronegative nitrogen atom produces by electron attraction a deficiency of charge in the ring carbon atoms.

2. Calculation methods

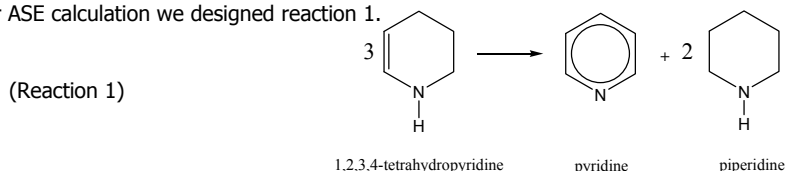
The DFT calculations were carried out using B3LYP/6-311+G**//B3LYP/6-311+G** and MP2/6-311+G**// B3LYP /6-311+G** levels of theory with the GAUSSIAN 03 package of programs implemented on a Pentium-PC computer with a 7.3 GHz processor.

3. Results and discussion

Calculated relative energy minimum and energy maximum structures for reaction compound as calculated at the DFT-B3LYP/6-311+G** level of theory are given in Fig.1. For single-point energy calculations, MP2/6-311+G**// B3LYP /6-311+G** was used. B3LYP /6-311+G**// B3LYP /6-311+G** results showed that dehydrogenation reaction is exothermic. (Fig. 1) B3LYP and MP2 results revealed that ΔH of this reaction is -9.8 and -11.3 Kcal mol⁻¹, respectively.

Studies on the B3LYP /6-311+G**// B3LYP /6-311+G** and MP2/6-311+G**// B3LYP /6-311+G** levels of theory show that the barrier height of the Dehydrogenation of 1,2-dihydropyridine is 71.16 and 80.02 kcal mol⁻¹, respectively (see Figure 1).

It has long been of interest to define the produced energy (ΔH) in reaction is the same Aromatic Stabilization Energy (ASE). For ASE calculation we designed reaction 1.



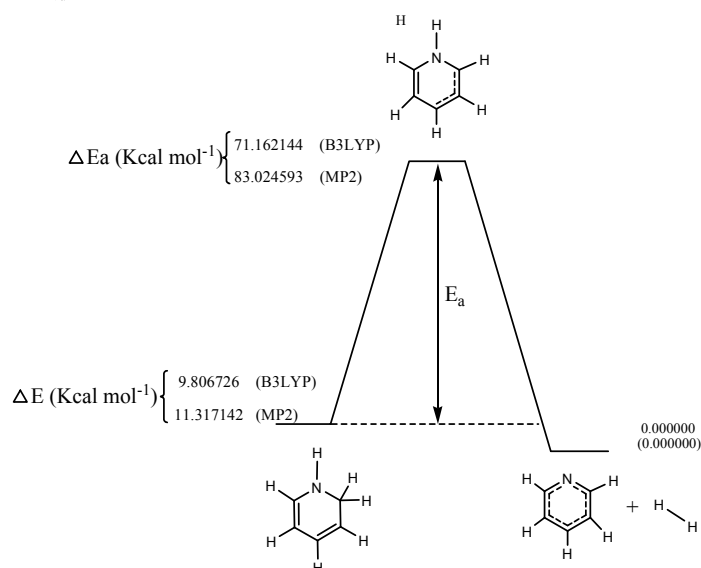


Fig. 1. B3LYP and MP2 energy diagram.

B3LYP /6-311+G**// B3LYP /6-311+G** and MP2/6-311+G**// B3LYP /6-311+G** results showed that ASE of pyridine is 27.47 and 34.41 Kcal mol⁻¹ respectively. These results have a good agreement with experimental data, but different from ΔH . NMR study results revealed that 1,2,3,4-Tetrahydropyridine and Pipyridine are non aromatic but Pyridine is aromatic.

The Nucleus Independent Chemical Shift (NICS)⁵ values in the center of ring (NICS(0)) and also 0.5 Å (NICS(0.5)) and 1 Å (NICS(1)) from over the ring were calculated. The obtained result revealed that the product NICS values are higher than reactant. Also the NICS(1) value of pyridine (-10.21ppm) is highest amount.

References

- [1] G.I.Poos, G.E.Arth, R.E.Beyler and L.H.Sarett, J. Am. Chem. Soc. 75 (1953) 422.
- [2] J.D.Roberts and M.C.Caserio, Basic Principles of Organic Chemistry, W.A. Benjamin, Inc., New York, 1964.
- [3] V.Schomaker and L.Pauling, J.Am.Chem.Soc., **61**, 1769(1939); B.B.Demore, W.S.Wilcox, and J.H.Goldstein, J. Chem. Phys. **32** (1954) 876; B.Bak, L.Hansen, and J.Rastrup-Andersen, ibid. 22 (1954) 2013.
- [4] B.A.Middelton and J.R.Partington, Nature, 141 (1938) 516; L.E.Orgel, T.L.Cottrell, W.Dick, and L.E.Sutton, Trans.Faraday. Soc., 47 (1951) 113.
- [5] P.v.R.Schleyer, C.Maerker, A.Dransfeld, H.Jiao and N.J.R.v.E.Hommes, J. Am. Chem. Soc., 118 (1996) 6317.

Electric field effect on the HOMO-LUMO gap of the Au/S-Thymine-S/Au structureF.Shariatii, H. Milani Moghaddam, M.Tayarani, F.Hashemi^b^a Physics Department, Khayyam University of Mashhad, Mashhad, Iran^b Physics Department, Mazandaran University, Babolsar, Iran

(E-mail: fatemeh.shariatii64@gmail.com)

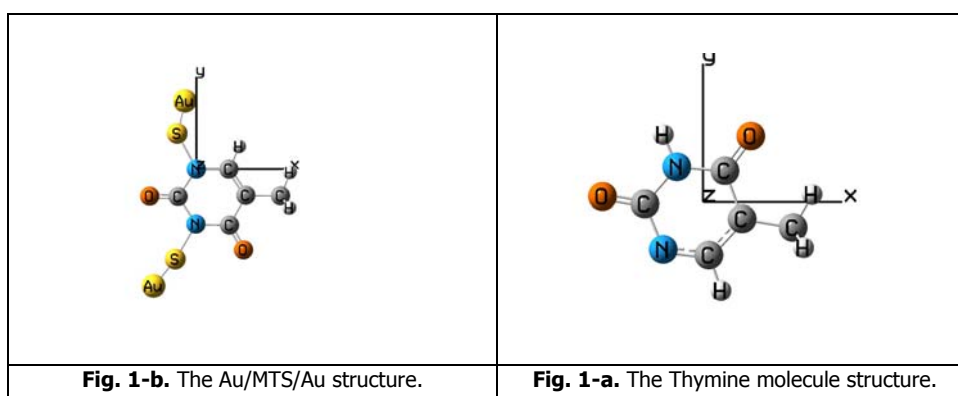
Keyword: Molecular wires, Thymine, Density of state, Density Functional Theory**1. Introduction**

Molecular electronic involves the search for single molecular or small groups of molecules that can be used as the fundamental units for computing [1-2]. DNA (Deoxyribonucleic Acid) can be used as a molecular bridge in the molecular wires [3]. DNA molecule is used as an insulator, semiconductor or conductor in the molecular wires [4].

One of the bases of DNA is Thymine. In this study, we consider the effect of the electric field on electronic properties of the Au/MTS/Au structure (Figure 1) where the MTS stands for Sulfur-Thymine-Sulfur molecule. We have used Density Functional theory (DFT) method to calculation. We consider that how HOMO-LUMO gap (highest occupied molecular orbital and lowest unoccupied molecular orbital, HLG) and density of electronic states (DOS) in Au/MTS/Au structure change by applying an electric field.

2. Methods

We perform all calculations using Gaussian03 program. The Au/MTS/Au structure is optimized at DFT-B3LYP level of theory. We choose the basis set 6-31G* for C, N, H, O and S atoms and LanL2DZ for Au atom.

**3. Results and discussion**

In Thymine structure, HLG is 2.4 eV in the absence of an applied electric field. We apply different electric fields in the greatest dipole moment direction to the Thymine structure i.e. along the +X axis direction. The HLG increases by applying the electric field. The HLG reaches 3.5 eV in the electric field less than 3 V/Å (see Figure 2-a). Figure 2-b shows the DOS of the Thymine structure in the absence of an applied electric field.

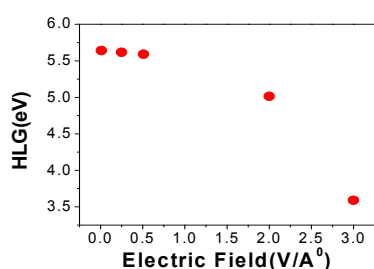


Fig. 2-a. HLG vs. different electric fields
DOS of the Thymine molecule vs. energy
for the Thymine molecule.

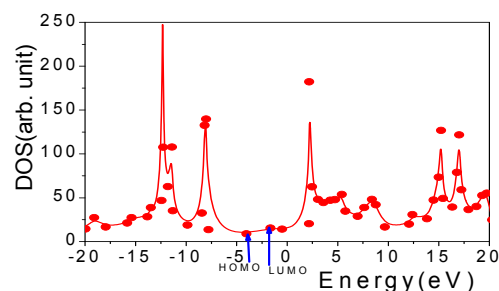


Fig. 2-b. The
in the absence of an applied electric field.

In MTS structure, HLG is 2.7 eV in the absence of an applied electric field. We apply different electric fields in the greatest dipole moment direction to the MTS structure along the +Y axis direction. The HLG decreases in the electric field. The HLG reaches 0.9 eV in the electric field less than 1 V/Å (see Figure 3-a). Figure 3-b shows the DOS of the MTS structure in the absence of an applied electric field. We also study the effect of different electric field on DOS of the Thymine and Au/MST/Au structures (see Figures 4 and 5).

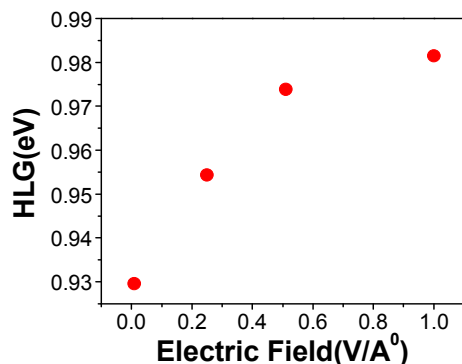


Fig. 3-a. HLG vs. different electric fields
Au/MTS/Au structure vs. energy
for the Au/MTS/Au structure.

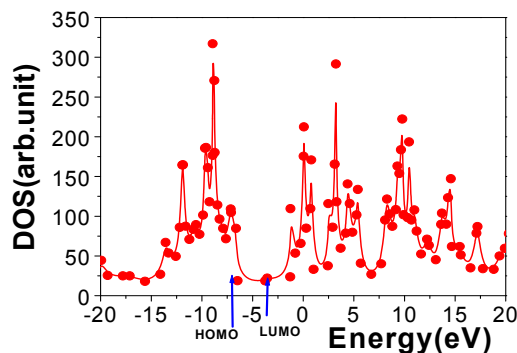


Fig. 3-b. The DOS of the
in the absence of an applied electric field.

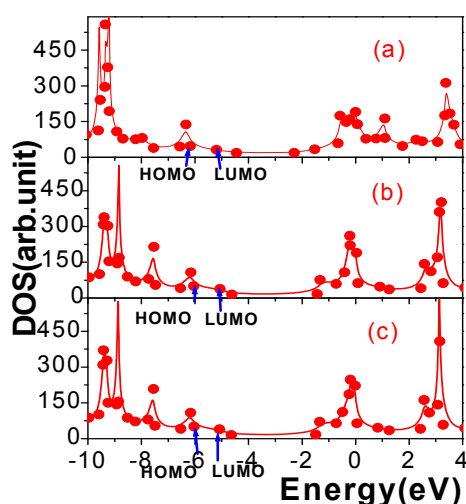


Fig. 5. The DOS of the Au/MST/Au structure vs. electric fields:
Field for figures: (a) 0.25(V/Å), (b) 0.51(V/Å), (c) 1(V/Å).

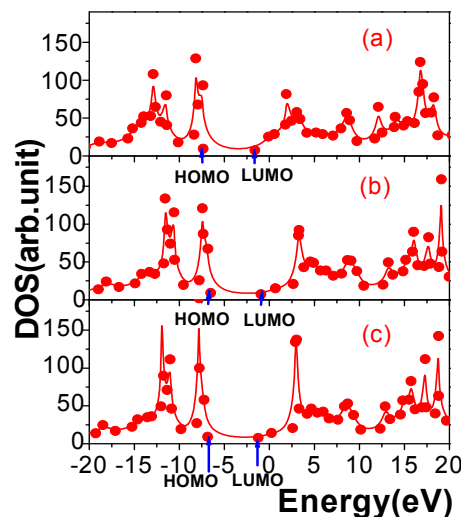


Fig. 4. The DOS of the Thymine molecule vs. electric fields:
Field for figures: (a) 0.25(V/Å), (b) 0.51(V/Å), (c) 1(V/Å).

4. Conclusions

We consider that how HLG (HOMO-LUMO gap), $HLG = E_{LUMO} - E_{HOMO}$ and DOS (density of electronic states) in the Thymine molecule and Au/MTS/Au structure change by applying the electric field. By attaching Au atom to the MST structure, we could observe a semiconductor-like behavior for the MST structure in electrical field but the Thymine molecule has an insulator-like behavior in the electrical field. Also the HLG has extremely changes in the electric field.

References

- [1] R.E. Service Science 294 (2001) 2442.
- [2] F. Patolsky, C.M. Lieber. Materials today 8 (2005) 20.
- [3] A. Gorodetsky, J. Hone, J. Barton, C. Nuckoll S. Nature nanotechnology 3 (2008) 163.
- [4] A. Berlin, L. Burin, A. Ranter Superlattices and Microstructures 4 (2000) 28.

Aromaticity variation in stacked nucleic acid base pairs

A. Mohajeri*, N. Davari

Department of Chemistry, College of Sciences, Shiraz University, Shiraz 71454, Iran

(E-mail: nazanin.davari@gmail.com)

Keywords: DNA stacking, DNA aromaticity, PDI, ATI, FLU.**1. Introduction**

Stacking is a special vertical arrangement of aromatic systems characterized by their parallel orientation [1]. In DNA, stacking is a non-covalent interaction between adjacent nucleic acid bases which are positioned nearly perpendicular to the length of the DNA strands. Stacking interaction is mostly due to the dispersion energy which originates from the formation of instantaneous dipole-dipole interactions [2]. Stacking interactions in NAB pairs is the subject of numerous studies [3-5], but the variation of aromaticity in nucleic acid base pairs due to stacking interaction has not been yet published. However, changes in the aromaticity of stacked nucleic acid base pairs have significant effect on the interaction of enzymes with nucleic acid substrates. So the aromaticity is important parameter used as a reactivity measure of nucleic acid molecules. In this work, the interactions in fifteen stacked complexes of five nucleic acid bases have been studied using density functional theory. Our main goal is to investigate to what extent the aromatic character of nucleic acid bases depends on the intermolecular interactions, specifically stacking interaction. To do so we have analyzed the molecular geometries of both isolated and stacked complexes and aromaticities have been evaluated by three electronically-based indices (PDI, ATI and FLU).

2. Computational methods

MPWB1K was applied to study energies, geometries and wave functions, aromaticities as well as harmonic vibrational frequencies for all isolated base pairs and their stacked [6]. The basis set is 6-31+G* IOP(3/76=0560004400) and the calculation were carried out with Gaussian 03 [7]. The interaction energies were evaluated by using supra-molecular method as the difference between the energy of a stacked complex and energies of the isolated base pairs. The obtained wave functions were used for the topological analyses of the electron densities. The AIM2000 program was employed for calculating the bond critical points and visualizing the bond paths [8]. For the characterization of the aromaticity we employed three relatively recent approaches (ATI, PDI and FLU), which all are in a sense based on extracting the information from the molecular electron density, to determine the aromaticities of 6-membered rings in isolated NABs and their stacked complexes [9-12]. The geometries are optimized without any constraints and the bases were not kept frozen or rigid.

3. Result and discussion

The optimized distance between the 6-membered rings of stacked pairs are ranges from 3.27 for GU to 4.38 for AA (Figure 1). In GC, GU, GT, UT and TT hydrogen bonding occurs inevitably. The contribution of hydrogen bonding in the stability of base pairs is in the range -0.8948 to -3.8586. AIM analysis shows that carbon-carbon bond of both stacked pairs have the most decrease in delocalization index. Therefore the obvious conclusion is that the carbon-carbon bond has the most contribution in stacking interaction. Energy and aromaticity values in isolated and stacked bases are summarized in Table 1 and 2. The same energy order is seen for both isolated nucleic acid bases and the nucleic bases in stacked pairs. Stacking interaction is in the following sequence: GG> GU> GT> GC> UC> TC> CC> AC> GA> AT> AU> TT> AA> UU> UT. Aromaticity analysis of stacked pairs based on FLU descriptor exhibits decrease in aromaticity in all bases. ATI is in agreement with FLU in all stacked pairs. They both indicate decrease in aromaticity. On the contrary, PDI does not indicate exact trend. The aromaticity order of nucleic acid bases in stacked pairs using FLU index is the same as isolated nucleic acid bases: A> C> G> U> T. The ATI order for nucleic acid bases in stacked pairs is: A>C>G≈U≈T. In most cases PDI index shows increase in aromaticity. Therefore PDI is not a reliable index for measuring the aromaticity of nucleic acid bases.

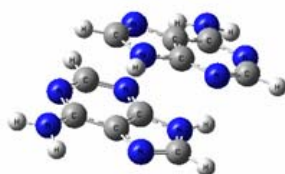


Fig. 1. Structure of A...A stacked pair.**Table1.** Energy and aromaticity values of isolated nucleic acid bases.

	E(hartree)	PDI	ATI	FLU
A	-467.124729	0.0588	1.1233	0.0268
C	-394.761090	0.0426	1.0842	0.0622
G	-542.333715	0.0319	1.0098	0.0689
T	-453.943759	0.0265	1.0035	0.1046
U	-414.647501	0.0264	1.0131	0.0992

Table2. Stacking energy and aromaticity values of stacked base pairs.

molecules	Stacking energy(Kcal/mol)	PDI		ATI		FLU	
		X	Y	X	Y	X	Y
X...Y							
A...A	-6.8889	0.0589	0.0575	1.0835	1.0812	0.0378	0.0445
A...C	-9.5193	0.0588	0.0424	1.0925	1.0425	0.0347	0.0743
A...T	-8.4369	0.0572	0.0265	1.0914	0.9720	0.0360	0.1205
A...U	-7.4696	0.0570	0.0267	1.0894	0.9801	0.0364	0.1171
C...C	-9.5531	0.0439	0.0441	1.0610	1.0571	0.0705	0.1029
G...A	-9.1633	0.0315	0.0580	0.9787	1.0803	0.0834	0.0393
G...C	-11.8405	0.0319	0.0413	0.9784	1.0368	0.0836	0.0761
G...G	-14.0151	0.0322	0.0322	0.9787	0.9770	0.0830	0.0851
G...U	-12.7920	0.0201	0.0280	0.9800	0.9720	0.0832	0.1129
U...C	-10.0904	0.0270	0.0427	0.9843	1.0493	0.1111	0.0708
U...T	-5.9845	0.0263	0.0270	0.9756	0.9796	0.1159	0.1150
U...U	-6.2593	0.0270	0.0264	0.9847	0.9796	0.1025	0.1137
G...T	-11.9076	0.0321	0.0284	0.9812	0.9663	0.0833	0.1181
T...C	-9.5816	0.0274	0.0425	0.9721	1.0447	0.1177	0.0708
T...T	-7.0693	0.0268	0.0268	0.9724	0.9745	0.1162	0.1161

4. Conclusion

The values which are reported in Table 2, leads to a general conclusion that aromaticity of nucleic acid bases decreases as stacking interaction takes place. Each nucleic base shares its n -electrons with the other fragment to form stacking interaction, thus decrease in aromaticity definitely occurs.

References

- [1] M. L. Główska, D. Martynowski, K. Kozłowska, J. Mol. Struct. 474 (1999) 81.
- [2] P. Hobza, J. Šponer, Chem. Rev. 99 (1999) 3247.
- [3] J. Šponer, J. Leszczynski, P. Hobza, J. Phys. Chem. A 101 (1997) 9489.
- [4] J. Šponer, P. Jurečka, I. Marchan, F. J. Luque, M. Orozco, P. Hobza, Chem. Eur. J. 12 (2006) 2854.
- [5] S. Samanta, M. Kabir, B. Sanyal, D. Bhattacharyya, Int. J. Quant. Chem. 108 (2008) 1173.
- [6] Y. Zhao, D. G. Truhlar, J. Chem. Theor. Comput. 1 (2005) 415.
- [7] Frisch, M. J. et al., Gaussian 03, Revision B03, Gaussian Inc., Pittsburgh PA, 2003.
- [8] F. W. Bader, AIM Program, ver 2.0; Mc. Master University: Hamilton, Canada, 2000.
- [9] J. Poater, X. Fradera, M. Duran, M. Solà, Chem. Eur. J. 9 (2003) 400.
- [10] P. Bultinck, R. Ponc, S. Van Damme, J. Phys. Org. Chem. 18 (2005) 706.
- [11] E. Matito, M. Duran, M. Solà, J. Chem. Phys. 122 (2005) 014109.
- [12] E. Matito, M. Duran, M. Solà, J. Chem. Phys. 125 (2006) 059901.

**Introduction a new high energetic compound to improve performance of solid propellants**F. Seif^a, M. A. Ghasemi^a and M. H. Keshavarz^a^aDepartment of Chemistry, Malek-ashtar University of Technology, Shahin-shahr, Isfahan, Iran

(E-mail: seif.farhad@gmail.com)

Keywords: Energetic compound, Solid propellant, Heat of formation, Specific impulse, Computer code.**1. Introduction**

The search for new energetic compounds with high content of energy and desirable properties is one of the major challenges to the chemical industry. In this work, a new energetic compound 1,4-dinitro-1,2,4,5-terazine will be introduced, which is suitable its usage in solid propellants to improve their performance. A new theoretical model is used to calculate the condensed phase heat of formation of this compound [1]. The performance of 1,4-dinitro-1,2,4,5-terazine has been computed by complex computer code ISPBKW [2] and compared with those of hexahydro-1,3,5-trinitro-1,3,5-triazine and octahydro-1,3,5,7-tetranitro-1,3,5,7-tetrazocine as two common energetic oxidizers in solid propellants.

2. Method

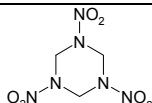
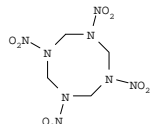
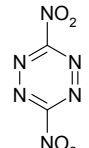
The complex computer code ISPBKW [2] can be used to compute specific impulse of hexahydro-1,3,5-trinitro-1,3,5-triazine, octahydro-1,3,5,7-tetranitro-1,3,5,7-tetrazocine and 1,4-dinitro-1,2,4,5-terazine. The predicted results are given in Table 1. We have used a suitable theoretical method for calculation of the condensed phase heat of formation of 1,4-dinitro-1,2,4,5-terazine [1]. The calculated condensed heat of formation of this novel compound is 159.95 kJ/mol.

3. Results and discussion

Solid propellants are energetic materials with low burning rate that will burn ideally at uniform rate of ignition without using of oxygen in atmosphere [3]. The discharge of hot gaseous products during combustion of solid propellants can develop thrust. The specific impulse can be used for predicting the performance of solid propellants. It can be defined as the integral of thrust per unit weight of propellant over the time of combustion [3].

Energetic compounds such as hexahydro-1,3,5-trinitro-1,3,5-triazine and octahydro-1,3,5,7-tetranitro-1,3,5,7-tetrazocine are used in solid propellants to improve their performance. The new energetic compound 1,4-dinitro-1,2,4,5-terazine is a suitable candidate in using solid propellants, which has not been synthesized yet.

Table 1. Comparison of performance of 1,4-dinitro-1,2,4,5-terazine with respect to hexahydro-1,3,5-trinitro-1,3,5-triazine and octahydro-1,3,5,7-tetranitro-1,3,5,7-tetrazocine

Name	Molecular structure	The condensed phase heat of formation (kcal/mol)	Specific impulse (s)
hexahydro-1,3,5-trinitro-1,3,5-triazine		15.99	260.2
octahydro-1,3,5,7-tetranitro-1,3,5,7-tetrazocine		17.92	259.2
1,4-dinitro-1,2,4,5-terazine		159.95	289.0



4. Conclusions

As seen, the condensed phase heat of formation of 1,4-dinitro-1,2,4,5-terazine is relatively high with respect to the other energetic compounds, which can increase the heat of combustion in using it in solid propellant [4]. High energy content of 1,4-dinitro-1,2,4,5-terazine can introduce it as a suitable oxidizer and energetic component in solid propellant. The calculated specific impulse of 1,4-dinitro-1,2,4,5-terazine is higher than the other compounds, which is consistent with its condensed phase heat of formation. Thus, it would be expected that the performance of solid propellants can be increased through introducing of 1,4-dinitro-1,2,4,5-terazine.

References

- [1] M. H. Keshavarz, Predicting condensed phase heat of formation of nitroaromatic compounds, *J. Hazard. Mater.*, 169 (2009) 890.
- [2] C. L. Mader, "Numerical Modeling of Explosives and Propellants", 2nd Ed., CRC Press (1998).
- [3] G. P. Sutton and O. Biblarz, "Rocket Propulsion Elements", John Wiley & Sons, New York (2001).
- [4] M. H. Keshavarz, in "New Research on Hazardous Materials", Chapter 9, A Simple Theoretical Prediction of Detonation Velocities of Non-Ideal Explosives Only from Elemental Composition, pp. 293-310, Nova Science Publishers, Inc. (2007).

**Complexation of Glycine by Manganese (II) in the Gas Phase: A Theoretical Study**M. Hassan Khodabandeh^a, Mehdi D. Davari^a, Karim Zare, Mansour Zahedi^{a*}, Gilles Ohanessian^{b*}^aDepartment of Chemistry, Faculty of Sciences, Shahid Beheshti University, G.C., Evin, 19839-6313, Tehran, Iran^bLaboratoire des Mécanismes Réactionnels, Département de Chimie, Ecole Polytechnique, CNRS, 91128 Palaiseau Cedex, France

(E-mail: mh.khodabandeh@yahoo.com)

Keywords: Glycine, Mn²⁺, Complexation, Gas phase metal ion chemistry, Ab initio calculations, Density functional theory.**1. Introduction**

Recently, transition metal cationization has proven to be a very useful tool for the elucidation of the primary structure of amino acids [1]. The interaction of different metal cations with glycine (Gly), the prototype compound of ions with amino acids, have been studied extensively by several authors from experimental and theoretical points of view [2,3]. Despite numerous studies [4] on gaseous metal cationized glycine, however, to the best of our knowledge, the interaction of manganese and amino acids has not been studied theoretically. The aim of this work is to study the structure of Mn(II) complexes with glycine as a typical amino acid. To obtain a comprehensive understanding of manganese complexation three possible spin states namely high, low and intermediate spin states have been investigated using quantum chemical methods. The examination of gas phase glycine-manganese (Gly-Mn²⁺) complexes provides fundamental information about the probable manganese spin state and glycine coordination sites.

2. Methods

We have performed geometry optimization and vibrational frequency calculations at the MP2 level, and also single-point energy calculations on some B3LYP geometries using the MP2 and CCSD(T) methods. Geometry optimization and frequency calculations have been performed using the 6-31G(d,p) basis set for all atoms without constraints by applying an unrestricted formalism. Single point calculations have been carried out using the 6-311+G(3df,2p) basis set for the O, N, C, and H atoms, and the [14s11p6d3f/8s6p4d1f] Wachters basis set for Mn [5]. All the calculations were performed by means of the Gaussian 98 program [6].

3. Results and discussion

The interaction of Mn²⁺, being in three possible spin states, with glycine has been studied using quantum chemical calculations in the gas phase. Seven modes of interaction have been considered in all cases. Investigation of manganese complexes having various possible spin state including high, intermediate and low spins shows that the most stable complexes are high spin (total electron spin $S=5/2$). Calculations show that the most stable mode of binding involves the simultaneous interaction of Mn²⁺ with two oxygen atoms of the zwitterionic conformers of glycine ($\eta^2\text{-O,O (CO}_2^-)$) (Figure 1), while the second preferred binding site consists of chelation between the carbonyl oxygen and the amino nitrogen ($\eta^2\text{-O,N}$). These results indicate that the relative affinity of Mn²⁺ and the glycine zwitterion makes this isomer of glycine more stable than others, even though it is not stable in its isolated form. The results are in accord with those of previous reports for some doubly charged cations and in some cases with monocations. The nature of the interaction between manganese metal cation and glycine is also discussed employing natural population and molecular orbital analyses. It has been found that electrostatics contribution plays a crucial role in this interaction. Complexation energy (D_0) of the low lying energy isomer, for the most stable sextet spin state, has been obtained as about 156 kcal/mol. It has also been shown that the computed vibrational frequencies could aid in identification of the most stable Mn²⁺-glycine complex.

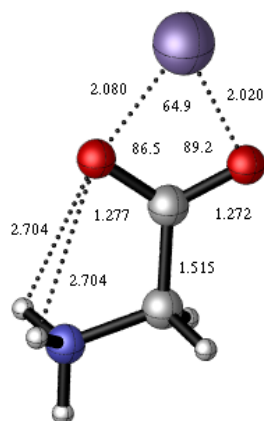


Fig. 1. Molecular geometry of optimized structure for high spin ($S=5/2$) Gly- Mn^{2+} complexes at B3LYP/6-31G(d,p) level; Distances and angles are given in angstrom and degree, respectively.

4. Conclusions

Quantum chemical calculations have been performed in order to identify the Mn^{2+} binding sites of glycine. Seven modes of Gly- Mn^{2+} interaction were considered as starting structures in each case. Stable complexes on the potential energy surface have been located. It has been found that among three possible spin state of Mn^{2+} including high, low, and intermediate spins in Gly- Mn^{2+} complex, the most stable complex is high spin. Two low energy complexes were characterized in each spin state: one in which the metal ion interacts with the carboxylate terminus of zwitterionic glycine ($\eta^2\text{-O,O (CO}_2^-)$), and another in which it chelates with the amino nitrogen and the carbonyl oxygen of neutral glycine ($\eta^2\text{-O,N}$). Analysis of the nature of metal-glycine binding shows that the large electrostatic interaction established with the zwitterionic conformation of glycine makes the bidentate coordination with carboxylate group the most stable structure. The gas phase interaction energy of manganese cation (Mn^{2+}) with glycine (6) was established at B3LYP, MP2 and CCSD(T) levels of theory. Finally, the computed IR spectra of the most stable structures of the high spin Gly- Mn^{2+} complexes were discussed.

References

- [1] F.W. McLafferty, H.D.R. Schuddehage, J. Am. Chem. Soc, 62 (1969) 1866.
- [2] J. Bertran, L. Rodriguez-Santiago, M. Sodupe, J. Phys. Chem. B 103 (1999) 2310.
- [3] S. Hoyau, G. Ohanessian, J. Am. Chem. Soc. 119 (1997) 2016.
- [4] E. Constantino, L. Rodriguez-Santiago, M. Sodupe, J. Tortajada J. Phys. Chem. A 109 (1) (2005) 224.
- [5] A.J.H. Wachters, J. Chem. Phys. 52 (1970) 1033.
- [6] M.J. Frisch et al., Gaussian 98, Gaussian, Inc., Pittsburg, PA, 1998.

AIM analysis for the ylide rotamers from the reaction between triphenylphosphine and dialkyl acetylenedicarboxylates in the presence of 2-mercapto-1-methylimidazole

S. M. Habibi Khorassani^a, M. T. Maghsoodlou^a, A. Ebrahimi,^a Z. Ghahghayi^a, H. Ghasempour^a

^aDepartment of Chemistry, University of Sistan and Baluchestan, P.O. Box 98135-674, Zahedan, Iran

(E-mail: ZahraGhahghayi@gmail.com)

Keywords: Stable phosphorus ylides; Dialkyl acetylenedicarboxylates; Rotamer; AIM method, Heterocyclic SH compound.

1. Introduction

In the recent work, the stability of the Z and E isomers was undertaken for the two rotamers of a phosphorus ylide by means of atoms in molecules (AIM) analysis. phosphorus ylides are important reagents in synthetic organic chemistry, especially in the synthesis of naturally occurring products, compounds with biological and pharmacological activity [1]. The synthesis of phosphorus ylides is an important reaction in organic chemistry because of the application of these compounds in the synthesis of organic products [2-8]. A facile synthesis of the reaction between triphenylphosphine **1**, dialkyl acetylenedicarboxylates **2** and 2-mercapto-1-methyl imidazole **3** (as a SH-acid) have been earlier reported [9]. The reaction is shown in Figure 1.

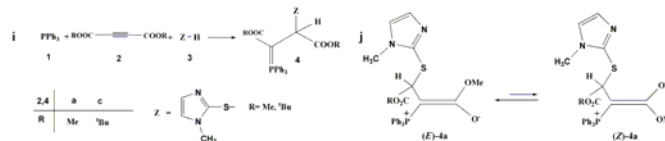


Fig. 1 (i) The reaction between triphenylphosphine **1**, dialkyl acetylenedicarboxylate **2** (**2a** or **2c**) and 2-mercapto-1-methyl imidazole **3** for generation of stable phosphorus ylides **4** (**4a** or **4c**), **(j)** Two isomers (Z)-**4a** and (E)-**4a** (Major and Minor) of ylide **4a**.

2. Methods

The Z and E isomers were optimized for all ylide structures at HF/6-31G(d,p) level of theory by Gaussian 98 package program. The energy of both conformers have been calculated at B3LYP/6-311++G** level. Atoms in molecules (AIM) analysis at HF/6-31G(d,p) level of theory have been performed in order to gain a better understanding of most geometrical parameters of both E-**4(a, c)** and Z-**4(a, c)** of phosphorus ylides. The numbers of critical points and intramolecular hydrogen bonds as well as the charge of atoms that constructed on the Z and E isomers have been recognized. The results altogether reveal the effective factors on stability of Z and E ylide isomers.

3. Results and discussion

In order to determine more stable form of both geometrical isomers [Z-**4(a, c)** or E-**4(a, c)**] of ylides (**4a** or **4c**), first their structures were optimized at HF/6-31G(d,p) level of theory [10] by Gaussian 98 program package [11]. Also relative energy of the two rotamers has been calculated at HF/6-31G(d,p) and B3LYP/6-311++G(d,p) levels (See Figure 2). The relative stabilization energies for both [Z-**4(a, c)** and E-**4(a, c)**] isomers are reported in Table 1, as can be seen, E-**4a** and E-**4c** isomers are more stable than Z-**4a** and Z-**4c** forms (2.97 and 1.73 kcal/mol respectively) at B3LYP level.

Table 1. The relative energy (kcal/mol) for both Z and E isomer of ylides **4a** and **4c**, obtained as HF/631G (d,p) and B3LYP/6311++G(d,p) levels.

Conformer	HF	B3LYP
Z-4a	4.22	2.97
E-4a	0.00	0.00
Z-4c	2.43	1.73
E-4c	0.00	0.00

Further investigation was undertaken in order to determine more effective factors on stability of both isomers, on the basis of AIM calculations [40] at HF/6-31G(d,p) level of theory by the AIM2000 program package. As noted in the literature, the ranges of $\rho(r)$ and $\nabla^2\rho(r)$ are 0.002-0.035e/a₀³ and 0.024-0.139 e/a₀⁵, respectively, if H-bonds exist. The number of hydrogen bonds in both categories (E-**4a** and Z-**4a**) and (E-**4c** and Z-**4c**) are (7 and 8) and also (15 and 13), respectively (See Table 2 and 3). In addition, the ranges of their electron densities are in (0.004-0.022 and 0.005-0.012au) and also (0.002-0.013 and 0.002-0.013au), respectively. With respect to the large number of hydrogen bonds in both Z and E isomers it is difficult to make a precise decision for determination of more stable isomer.

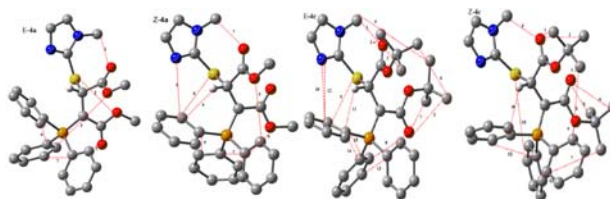


Fig. 2. Intramolecular hydrogen bonds (dotted lines) in E-**4a**, Z-**4a**, E-**4c** and Z-**4c** geometrical isomers of stable ylide **4a** and **4c** respectively.

Table 2. The values of $\rho \times 10^{-3}$, $\nabla^2\rho \times 10^{-3}$ and Hamiltonian (H) $\times 10^{-3}$ for both Z-**4a** and E-**4a** isomers of ylide **4a** calculated at the hydrogen bond critical points. All quantities are in atomic units

E	ρ	$\nabla^2\rho$	H	Z	ρ	$\nabla^2\rho$	H
1	4.34	-4.37	-0.89	1	9.74	-9.21	-0.85
2	21.55	-19.21	-0.43	2	5.84	-5.97	-0.92
3	5.64	-6.06	-1.11	3	4.67	-4.45	-0.84
4	13.40	-12.00	-1.61	4	11.11	-10.15	-1.74
5	14.74	-14.92	-1.70	5	12.03	-11.66	-1.22
6	11.03	-9.57	-1.59	6	11.70	-10.76	-1.83
7	10.96	-10.19	-1.82	7	10.19	-8.84	-1.53
				8	9.23	-7.68	-1.20

On the basis of theoretical calculations (Table 1), the difference between the relative stability of the E-**4c** and Z-**4c** isomers in gas phase is (1.73 kcal/mol) while it is considerably greater in the E-**4a** and Z-**4a** (2.97 kcal/mol). Perhaps this noticeable difference is taken more in solution media for **4c**, because of the more hydrogen bonds in E-**4c** (15) with respect to the E-**4a** (7) and also bulky groups(di-tert-butyl acetylendicarboxylates) in E-**4c** in comparison with methyl groups in E-**4a**, for this reason it is possible to observe only one isomer of **4c** (E). In recent case (synthesis of ylide **4c**) [9], the ^1H , ^{13}C , ^{31}P NMR data showed the only one isomer for the ylide **4c**. Nevertheless, the result is different for **4a** ylide (observed as the two isomers) which may be attributed to the difference in relative stability of E-**4a** and Z-**4a** isomers. Perhaps this difference is not taken more considerably in solution media (less hydrogen bonds and small groups in di-methyl-diacetylendicarboxylates) for **4a** and for this reason it is possible to see the two isomers of **4a** (both Z and E isomers).

4. Conclusions

The assignment of the Z and E isomers as a Major or Minor form in both ylides **4a** and **4c** were undertaken by AIM method. Quantum mechanical calculation was clarified how ylides **4a** and **4b** (its results as same as **4a**) exist in solution as a mixture of two geometrical isomers. These results have also provided useful evidence for the ylide involving **4c**. Noticeable differences between the most important geometrical parameters (for instance, relative energy) provide a suitable chance for ylide **4c** which appears as a single geometrical isomer (Z-**4c**) in solution.

References

- [1] Wittig, G. *Science*, 210 (1980) 600.
- [2] Laszo, P. *Organic Reaction, Simplicity and Logic*, Wiley, New York, 1995.
- [3] Johnson, A. W. *Ylide Chemistry*, Academic Press, London, 1966.
- [4] Cadogan, J. I. G. *Organophosphorus Reagents in Organic Synthesis*, Academic Press, New York, 1979.
- [5] I. Yavari, L. Ahmadian-Razlighi, *Phosphorus, Sulfur and Silicon*. 181 (2006) 771.
- [6] M. T. Maghsoodlou, S. M. Habibi-Khorassani, M. K. Rofouei, S. R. Adhamdoust, M. Nassiri, *Arkivoc*. xii (2006) 145.
- [7] S. M. Habibi-Khorassani, M. T. Maghsoodlou, M. Nassiri, M. Zakarianezhad, M. Fattahi, *Arkivoc* xvi (2006) 168.
- [8] S. M. Habibi-Khorassani, M. T. Maghsoodlou, A. Ebrahimi, M. Zakarianezhad, M. J. Fattahi, *Solution Chem*. 36 (2007) 1117.
- [9] M. T. Maghsoodlou, N. Hazeri, S. M. Habibi Khorassani, M. Nassiri, Marandi, G. Afshari, U. Niromand, *J. Sulfur. Chem*. 26 (2005) 261.
- [10] M. J. Frisch, et al. *Gaussian 98*, Revision A. 7, Gaussian, Inc. Pittsburg h, PA, 1998.
- [11] A. E. Reed, R. B. Weinstock, F.J. J. Weinhold, *Chem. Phys*. 83 (1985) 735.
- [12] R. F. W. Bader, *Atoms in molecules A Quantum Theory*, Oxford University, New York, (1990).

**Vibrational analysis and theoretical study on NMR shielding and physical properties of triamantane**Z. Bayat*, S. J. Mehdizade^a, M. Emadian, M. Nejatpoor, S. Vahdani

Department of Chemistry, Islamic Azad University Quchan Branch, Iran

^aDepartment of Chemistry, Ferdowsi University, Mashhad, Iran

(E-mail: z.bayat@gmail.com)

Keywords: Triamantane, Assignment, DFT, HF, NMR, Physical properties.**1. Introduction**

Since the discovery of Adamantane from petroleum in 1933[5], there has been great interest in the properties of this once unique cage-structured molecule. Some years later it was joined by Diamantane [6] to form the two smallest examples of a series of molecules known as "diamond hydrocarbons" or diamondoids. Synthetically, chemists managed to reproduce these structures in the laboratory [7] and go two steps further, producing both Triamantane (see Fig.1)[8]. Triamantane which has 120 vibrational modes, $35A_1 + 25A_2 + 29B_1 + 31B_2$. Again, the addition of another unit has reduced the symmetry of the molecule. In Triamantane, the symmetry has decreased to C_{2v} , so all modes are now Raman active, producing 120 possible signals in the Raman spectrum. This increase in molecule size and decrease in symmetry means we now have 20 intense CH stretch vibrations in the same 100 cm^{-1} region, which produces a very poorly resolved experimental signal. The calculated spectrum for Triamantane still has the same discrepancies as the Adamantane and Diamantane calculations but there is also disagreement in the intensity of vibrations in the region around ~ 1300 and $\sim 1100\text{ cm}^{-1}$.

**Fig. 1.** Structure of Triamantane**2. Method**

Theoretical methods have been applied to predict the vibrational spectra of some of these molecules. Calculations were performed using either Hartree-Fock theory or the three-parameter hybrid functional of Becke and the correlation functional of Lee, Yang, and Parr_B3LYP_. A range of basis sets were used, a selection found as standard in the GAUSSIAN03 [9] software.

3. Results

CH_2 scissoring motions was calculated at 1468 and 1462 cm^{-1} (scaled frequencies are reported) in B3LYP/6-311+G** and HF/6-311+G** respectively and analogous experimental signal was appeared at 1436 cm^{-1} . A strong Raman band at 1222 cm^{-1} was assigned as CH_2 twisting (coupled with CH bending) motion and was calculated at 1235 and 1238 cm^{-1} in B3LYP/6-311+G** and HF/6-311+G** respectively. Another strong Raman band at about 1200 cm^{-1} was assigned as CH_2 wagging motion (coupled with CH bending and CH_2 twisting) and was calculated at 1088 and 1091 cm^{-1} in B3LYP/6-311+G** and HF/6-311+G** respectively. The isotropic chemical shifts δ with respect to TMS are 42.2302 , 31.5446 , 1.3818 , 1.0855 (HF) and 45.9558 , 34.9148 , 1.7275 , 1.3649 (B3LYP) of C(2), C (3), H(2) and H (3) respectively. The ΔG_{solv} of Diamantane is 1.76-kcal/mol at b3lyp/6-311+g** and -1.83kcal/mol at HF/6-311+G**.

4. Conclusion

The vibrational spectrum of Triamantane reliably reproduced by calculation at B3LYP/6-311+G** and HF/6-311+G** computational level. The results obtained are in excellent agreement with the experimental data. Strong Raman band in the $681\text{-}1222\text{ cm}^{-1}$ region may be attributed to breathing (C-C stretching), C-H bending and CH_2 twisting (coupled with CH bending and CH_2 wagging) and CH_2 twisting (coupled with CH bending) motions. Also some of the properties for Triamantane were calculated.

Reference

[1] Hart, J.N. May, P. W. Allan, N. L. Dahl, J.E.P. Liu, S. Carlson and R. M.K. Adcock, J. L, Chemical Physics Letters 460 (2008) 237.



[2] <http://www.chm.bris.ac.uk/pt/diamond/diamondoids.htm>

[3] Oomens, J. Polfer, N. Pirali, O. Ueno, Y. Maboudian, R. May, P. W. Filik, J. Dahl, J. E. Liu and S. Carlson, R. M.K, J. Molecular Spectroscopy 238 (2006) 158.

[4] Bayat, Z. Monajjemi, M, J. Phys. Theoretical Chem. 5 (2008) 85.

[5] Landa, S. Machacek, V. Collect. Czech. Chem. Commun. 5 (1933) 1.

[6] HaIa S., Landa, S. Hanus, V. Angew. Chem. Internat. Edit. 5 (1966) 1045.

[7] von Schleyer, P.R. Olah G.A. (Eds.), Cage Hydrocarbons, Wiley, New York, 1990, p. 138.

[8] Williams Jr., V.Z. von Schleyer, P.R. Gleicher, G.J. Rodewald, L.B. J. Am. Chem. Soc. 88 (1966) 3862.

[9] Bisticic, L. Pejovb, L. Baranovic, G.J. Mol. Struct.-Theochem. 594 (2002) 79.



The one-dimensional model for anharmonic vibrations of a nano-sized oscillator using Rydberg potentials and Casimir force with fractional damping

M. Dehestani*, M. Mansoori Kermani

^aDepartment of Chemistry, Shahid Bahonar University of Kerman

(E-mail: dehestani2002@yahoo.com, mansoori.2002@yahoo.com)

Keywords: Nano oscillator, Fractional damping, Adomian's method, Rydberg function, Casimir force.

1. Introduction

Nanosystems can have properties which are distinctly different from those of macroscopic systems: properties that are well defined and clearly fixed in the bulk are very often no longer typical features in nanophysics and nanotechnology.

For sufficiently small systems, that is, systems with a particle number not larger than a few hundred, the methods of theoretical quantum chemistry are useful.

The mechanical motion of the nano-devices can be explained in terms of quantum mechanics and examined by considering that these objects are subjected to nonlinear forces like Casimir force, and the anelastic properties of materials are nonlinear. The Casimir effect consists in the electrical polarization of two perfectly conducting bodies and it was found in materials like plastics and nano-wires. The mathematical modelling of the mechanical motion of the nano- and micro-devices subjected to nonlinear forces and fractional damping is a hard task, which currently requires computational methods like decomposition, numeric and homotopy methods. Dra̧ga̧nescu et al. investigated anharmonic vibrational of a nano-sized oscillator [1].

2. The anharmonic vibrations model

In this work we will consider the elastic force acting in the case of oscillators of the nano-devices to originates from Rydberg potential

$$V_r(x) = -D_e(1 + bx)\exp(-bx) \quad (1)$$

where D_e is the dissociation energy, b is the anharmonicity constant and x is the displacement from the equilibrium position d_e . The Casimir force between a sphere and a plate without roughness is given by

$$F = \frac{\pi^3 \hbar c R}{360 z^3} \quad (2)$$

here $\hbar = h/2\pi$, h , c , R , and z are the Plank constant, the velocity of light, the area of the plates, the radius of the sphere, and the distance between the sphere and the plate, respectively. This model is one-dimensional oscillator consisting of a sphere with mass m and radius R , which is suspended by means of vertical elastic wire which produces a force originating in a Rydberg potential, on a horizontal conducting surface. For fractional damping force, λ is the damping constant. The distance between centre of sphere and surface is $d_e \gg R$. The motion is possible for $x(d_e - R)$. Let us consider a very minute perturbing force $F(t)$ acts on the sphere

$$F(t) = f_0 \sin(t\omega) \quad (3)$$

here f_0 is the amplitude of the force and ω is angular frequency in harmonic excitation. The motion of sphere, with attention the second Newton law, relinquished of weigh force and also expanding the nonlinear term into series yield:

$$\frac{d^2 x}{dt^2} + \frac{\lambda d^\mu x}{mdt^\mu} - \frac{D_e b^2}{m} \left(-x + bx^2 - \frac{b^2 x^3}{2} + \frac{b^3 x^4}{6} \right) - \frac{c}{md_e^3} \left(1 + \frac{3}{d_e} + \frac{6x^2}{d_e^2} + \frac{10x^3}{d_e^3} + \frac{15x^4}{d_e^4} \right) = \frac{f_0}{m} \sin(t\omega) \quad (4)$$

The fractional derivative operator (d^μ/dt^μ) is used for expression fractional damping, where μ is a fractional number.

3. Decomposition method

The Adomian's decomposition method can be used to solve differential equations,

$$Lx(t) + Rx(t) + Nx(t) = g(t) \quad (5)$$



here L , R , N , and $g(t)$ are a linear invertible operator, a linear residual operator, a nonlinear operator, and a given function, respectively. $x(t)$ is a unknown function. The solution of the equation can be considered as:

$$x(t) = A + Bt + L^{-1}g(t) - L^{-1}Rx(t) - L^{-1}Nx(t) \quad (6)$$

here A , and B are integration constants and the solution can be written as a series:

$$x(t) = \sum_0^{\infty} x_n(t) \quad (7)$$

$$x_0(t) = x(0) + t\dot{x}(0) + L^{-1}g(t) \quad (8)$$

$$x_{n+1}(t) = -L^{-1}Rx_n(t) - L^{-1}A_n \quad (9)$$

$$A_n = \frac{1}{n!} \frac{d^n N}{d\lambda^n} \sum \lambda^i x_i(t) \quad (10)$$

4. Results and discussion

We could illustrate the possibility of obtaining approximate solutions of the equations of motion for NEMS /MEMS devices [2] having nonlinearity and fractional damping, by decomposition method. For $\mu = 1$, $x(t) = A_e$, $\dot{x}(0) = 0$ we obtain:

$$x_1(t) = \frac{f_0 \lambda}{m^2 \omega^3} \cos(t\omega) - \frac{D_e b^2}{m} Z - \frac{c}{m d_e^3} M \quad (11)$$

$$\begin{aligned} M = & \frac{1}{1152m^4 \omega^{10} d_e^4} (8640m^4 t^2 \omega^{10} A_e^4 + 5760m^4 t^2 \omega^{10} A_e^3 d_e + 3456m^4 t^2 \omega^{10} A_e^2 d_e^2 + 1728m^4 t^2 \omega^{10} d_e^3 \\ & + 576m^4 t^2 \omega^{10} d_e^4 + 69120m^3 \omega^6 \sin(t\omega) A_e^3 f_0 + 34560m^3 \omega^6 \sin(t\omega) A_e^2 d_e f_0 + 13824m^3 \omega^6 \sin(t\omega) A_e d_e^2 f_0 \\ & + 25920m^2 t^2 \omega^6 A_e^2 f_0^2 + 12960m^2 \omega^4 \cos(2t\omega) A_e^2 f_e^2 + 8640m^2 t^2 \omega^6 A_e d_e f_0^2 + 4320m^2 \omega^4 \cos(2t\omega) A_e d_e f_0^2 \\ & + 1728m^2 t^2 \omega^6 d_e^2 f_0^2 + 864m^2 \omega^4 \cos(2t\omega) d_e^2 f_0^2 + 51840m \omega^2 \sin(t\omega) A_e f_0^3 - 1920m \omega^2 \sin(3t\omega) A_e f_0^3 \\ & + 8640m \omega^2 \sin(t\omega) d_e f_0^3 - 320m \omega^2 \sin(3t\omega) d_e f_0^3 + 3240t^2 \omega^2 f_0^4 + 2160 \cos(2t\omega) f_0^4 - 135 \cos(4t\omega) f_0^4) \\ Z = & \frac{1}{6912m^4 \omega^{10}} (-3456m^4 t^2 \omega^{10} A_e + 3456bm^4 t^2 \omega^{10} A_e^2 - 1728b^2 m^4 t^2 \omega^{10} A_e^3 + 576b^3 m^4 t^2 \omega^{10} A_e^4 \\ & - 6912m^3 \omega^6 \sin(t\omega) f_0 + 13824bm^3 \omega^6 \sin(t\omega) A_e f_0 - 10368b^2 m^3 \omega^6 \sin(t\omega) A_e^2 f_0 + 4608b^3 m^3 \omega^6 \sin(t\omega) A_e^3 f_0 \\ & + 1728bm^2 t^2 \omega^6 f_0^2 + 864bm^2 \omega^4 \cos(2t\omega) f_0^2 - 2592b^2 m^2 t^2 \omega^6 A_e f_0^2 - 1296b^2 m^2 \omega^4 \cos(2t\omega) A_e f_0^2 \\ & + 1728b^3 m^2 t^2 \omega^6 A_e^2 f_0^2 + 864b^3 m^2 \omega^4 \cos(2t\omega) A_e^2 f_0^2 - 2592b^2 m \omega^2 \sin(t\omega) f_0^3 + 96b^2 m \omega^2 \sin(3t\omega) f_0^3 \\ & + 3456b^3 m \omega^2 \sin(t\omega) A_e f_0^3 - 128b^3 m \omega^2 \sin(3t\omega) A_e f_0^3 + 216b^3 t^2 \omega^2 f_0^4 + 144b^3 \cos(2t\omega) f_0^4 - 9b^3 \cos(4t\omega) f_0^4) \end{aligned}$$

5. Conclusion

A nonlinear oscillator model with fractional damping and nonlinearity due to Casimir force and anharmonic elastic force deriving from a Rydberg equation, with the aid of Adomian's decomposition method was investigated.

Reference

- [1] G. E. Dra~ga~nescu, L. Bereteu, A. Ercut, G. Luca, Commun Nonlinear Sci Numer Simulat ,(2009) doi:10.1016/j.cnsns.2009.05.006.
- [2] D. P. Sheehan, J. H. Wright, A. R. Putnam, E. K. Perttu Physica E 29 (2005) 87.



The effect of the ring size and Benzene Ring Addition on Cyclic Ketones: FT-IR, FT-Raman, NMR spectra, and molecular structure investigation

H. Hooshyar^a, K. Zare^b, S. Khanahmadzadeh^a, R. Sadeghi^c

^a Department of Chemistry, Islamic Azad University Mahabad Branch, Islamic Azad University Mahabad, Iran

^b Department of chemistry Science of Research Campus, Islamic Azad University, P.O.Box14515-775, Iran, Shahid Beheshti University, Tehran, Iran

^c Department of Chemistry, Faculty of Science, University of Kurdistan, Sanandaj, Iran

^{*}(E-mail: h_hshyr@yahoo.com)

Keywords: Cyclic Ketones, Ring size, Benzene Ring, Molecular structure.

1. Introduction

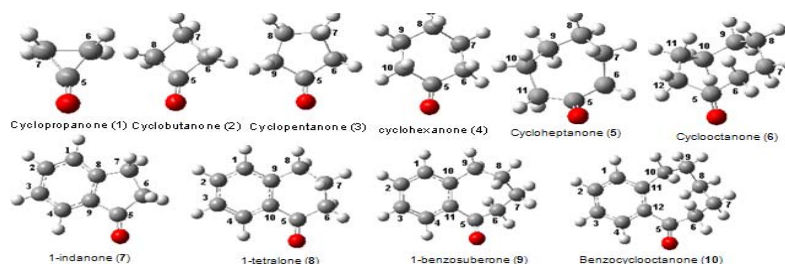
The geometries, dipole moments, moments of inertia, vibrational frequencies and thermo chemistry parameters were parameterized for the cycloketones in the same manner as for the acyclic ketones by the molecular mechanics (MM4) calculations [1] and ab initio [2] discussed in previous articles. This report describes a study of the effect of ring size and benzene addition on the geometry parameters, vibrational frequencies and thermochemistry parameters and comparison of Basis Sets & Methods. Various parameters of these molecules were evaluated including the minimum energy of the molecule (as obtained from a geometry optimization of an initial input structure), vibrational modes and thermochemical data. In addition a comparison of basis sets and methods was made using the energy as an indicator of the effectiveness of a given basis set and/or method in describing a molecular property.

2. Computational methods

Ab initio calculations were performed with the Gaussian03 program. The geometry optimizations were carried out at the Hartree-Fock (HF) [3] and second order Moller-Plesset perturbation theory levels (MP2) [4] and with density functional theory (DFT). The structure of the molecule was completely optimized without any symmetry in all the levels. The harmonic vibrational frequencies and the infrared intensities were calculated analytically on the resulting ground-state optimized molecular geometries. ¹H- and ¹³C- chemical shifts were calculated with GIAO method using corresponding TMS shielding calculated at the B3LYP/6-311G (d,p) level.

3. Results and discussion

The Cyclic Ketones 1-10 chosen for study are illustrated in **Scheme 1**. Variations of Potential Energy (Hartree), of title compounds are given in **figure1**. As clearly seen from the values on the calculated energies, there is a little difference between basis sets for 6-311 (or 6-31), use of the basis sets of larger sizes give rise to increases in the differences between the calculated energies of the title molecule.



Scheme 1. Molecular models and numbering scheme of Cyclic Ketones $n = 3-8$ (n -member ring ketones) and benzocycloketones forms of the studied molecules

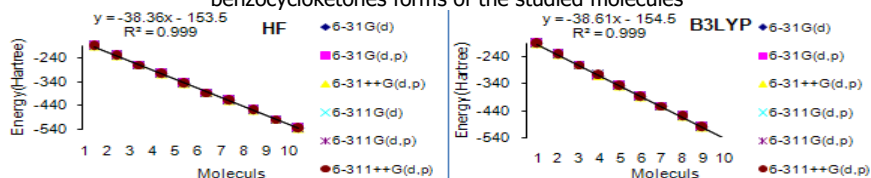


Fig. 1. Comparison of potential energy (Hartree) for series cyclic ketones and benzocycloketones with levels of Calculation.

3.1 Geometric parameters

The structural parameters which are responsible and have the most effect on the ring strain are C=O bond length and C-C=O bond angle. The decrease in the C=O bond length and the increase in the C-C=O bond angle increase the ring strain. Calculations at all applied levels indicate that the C=O, C-C-C bond length and angle increases by increasing the ring size.

3.2 Vibrational Spectra

Vibrational analysis is performed by the density functional and ab initio correlated methods. The calculated and experimental C=O stretching vibrational frequencies for series cyclic ketones and benzocycloketones are summarized in **Table1**. C=O bond length decreases as ring size decreases then the strength of the bond increase and therefore vibrational frequency increases, this can be seen in **Figure2**.

Table1. Carbonyl stretching frequencies for Cycloketones (cm⁻¹).

No. Carbons in Ring	B ₃ LYP				MP ₂				Expt. ^a (Gas)
	A	B	C	D	A	B	C	D	
1	1792	1782	1882	1870	1730	1722	1871	1857	1850
2	1715	1701	1818	1803	1638	1630	1799	1780	1816
3	1665	1649	1772	1755	1597	1583	1753	1734	1771
4	1641	1623	1743	1727	1578	1562	1724	1704	1738
5	1628	1609	1730	1712	1564	1547	1708	1688	1721
6	1626	1609	1727	1712	1561	1547	1708		1718
7	1641	1626	1741	1707	1595	1582	1733		1742
8	1613	1603	1707	1692	1586				1714
9	1606	1596	1700	1686	1579				1698
10	1600	1594	1686	1680	1578				1683

^aFrom Ref.5. 6-311G (A), 6-311G** (B), 6-311++G (C), 6-311++G** (D)

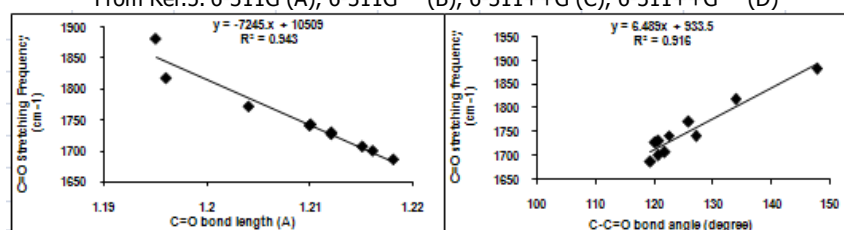


Fig. 2. B3LYP/B calculated variation of the C=O stretching mode with C=O and C-C=O bond length and angle.

3.3 Dipole moments

The calculated dipole moments at the different theory levels are given in **Table 2**. For cyclic ketones $n = 3-8$ (n -member ring ketones): $1 < 2 < 3 < 4 > 5 > 6$, For benzocyclic ketones: $7 > 8 > 9 > 10$.

Table 2. Experimental and calculated dipole moments (D).

No. Carbons in Ring								
	Exp.	Method	State or Solvent	Ref.	B ₃ LYP/ B	B ₃ LYP/ D	HF/B	HF/D
1					2.7700	3.0579	3.0940	3.3070
2	2.89	MW-S	Gas	18	2.7658	3.1062	3.1362	3.3891
3	3.30	MW-S	Gas	19	2.9282	3.2940	3.2928	3.5475
4	3.25	MW-S	Gas	20	3.2099	3.5741	3.4036	3.6562
5	3.07	DE	Benzene	21	3.2237	3.5732	3.4011	3.6396
6	2.96	DE	Benzene	21	2.7578	3.3371	3.0578	3.2840
7					3.4703	3.7908	3.7098	3.9078
8					3.3379	3.6206	3.5742	3.7590
9					3.3318	3.4611	3.4159	3.5778
10					3.0114	3.3190	3.4727	3.6373

4. Conclusions

The results of the study lead to the following conclusions:

(i) Calculations at all applied levels indicate that the C=O bond length increases by increasing the ring size. (ii) According to these calculations, $\nu_{C=O}$ decreases by increasing the ring size whereas $\mu_{C=O}$ and $\alpha_{C=O}$ have parallel effect. (iii) The C=O, C-C-C bond length and angle increases by increasing the ring size. (iv) By the addition benzen to the cycloketones we have decreases potential energy (about -150 Hartree) and addition stability.

References

- [1] C.H. Langley, N.L. Allinger, J Comput Chem. 22 (2001) 1426.
- [2] H. Hooshyar, H. Rahemi, K.A. Dilmagani, S.F. Tayyari, J Theoretical and Computational Chemistry 6 (2007) 459.
- [3] W.J. Hehre, L. Radom, P.R. Schleyer, J.A. Pople, Ab initio molecular orbital theory, 1st edn. Wiley, New York, 1986.
- [4] M.J. Frisch, M. Head-Gordon, J.A. Pople, Chem Phys Lett. 166 (1990) 275.
- [5] National Institute of Standard and Technology (NIST), Chemistry, 69, June, 2005.

Ab initio and density functional studies on the structure and vibrational Spectra of 2-(4-methyl-2-biphenyl)-4-amino-1, 2, 4-triazole-3-thiol

H. Hooshyar^a, R. Sadeghi^b, D. Setamdideh^a, H. gyan^a

^aDepartment of Chemistry, Islamic Azad University Mahabad Branch, Islamic Azad University Mahabad, Iran

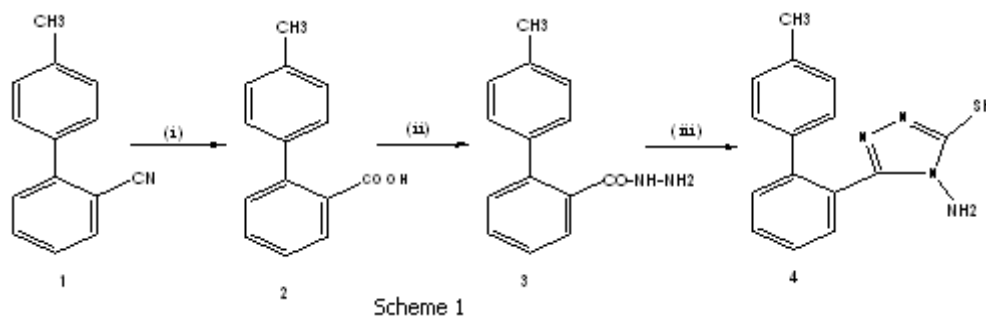
^bDepartment of Chemistry, Faculty of Science, University of Kurdistan, Sanandaj, Iran

(E-mail: h_hshyr@yahoo.com)

Keywords: X-ray crystal structure, Vibrational assignments, NMR spectra, Molecular structure.

1. Introduction

Compounds of 1, 2, 4-triazole derivatives exhibit diverse pharmacological activities such as fungicidal, insecticidal, bactericidal, herbicidal, anti-tumour [1], anti-inflammatory [2], CNS stimulant. They also find applications as dyes, lubricants, analytical reagents and antiviral agents. In the light of the above observations, the incorporation of the active 1, 2, 4-triazole nucleus to the biphenyl ring is part of our continued effort towards the synthesis and study of the biological properties of condensed nitrogen and sulphur heterocycles [3–5]. In the present study we started the theoretical studies of 2-(4-methyl-2-biphenyl)-4-amino-1, 2, 4-triazole-3 thiol. This molecule was chosen as the model for the present study, because the synthesis and X-ray crystal structure analysis of a possible bioactive molecule, 2-(4-methyl-2-biphenyl)-4-amino-1, 2, 4-triazole-3 thiol have been reported. The synthesis of 2-(4-methyl-2-biphenyl)-4-amino-1, 2, 4-triazole-3-thiol 4 was obtained by using 4-methyl-2-cyanobiphenyl as shown in **Scheme 1**.



(i) 30% NaOH, Methanol (ii) H₂SO₄, Methanol; Ethanol, NH₂-NH₂ (iii) CS₂, KOH; NH₂-NH₂, Ethanol

2. Calculations details

All the calculations were performed with the Gaussian 03W program package on a double Xeon/3.2 GHz processor with 8 GB Ram. The molecular structure of the 2-(4-methyl-2-biphenyl)-4-amino-1, 2, 4-triazole-3-thiol, in the ground state are optimized by using the Hartree-Fock (HF)[6], density functional using Becke's three-parameter hybrid method with the Lee, Yang, and Parr correlation functional methods [7] (B3LYP) with the standard 6-31G* and 6-31+G* basis sets. The vibrational frequencies were also calculated with these methods.

3. Results and discussion

3.1 Geometric parameters:

X-ray diffraction and calculated for the isolated state structures of the 2-(4-methyl-2-biphenyl)-4-amino-1, 2, 4-triazole-3-thiol molecules with atom numbering are presented in **Fig. 1**.

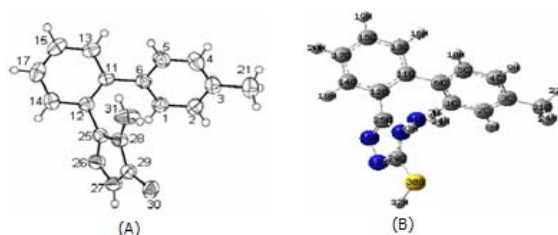


Fig. 1. The structure of 2-(4-methyl-2-biphenyl)-4-amino-1, 2, 4-triazole-3-thiol molecules: (A) X-ray experimental [11] with atom numbering; (B) calculated for the isolated molecules in the gas phase.

As follows from this comparison, the bond lengths and angles calculated for title compound show quite good agreement with experimental values. The agreement for bond angles is not as good as that for the bond distances (**Fig. 2**).

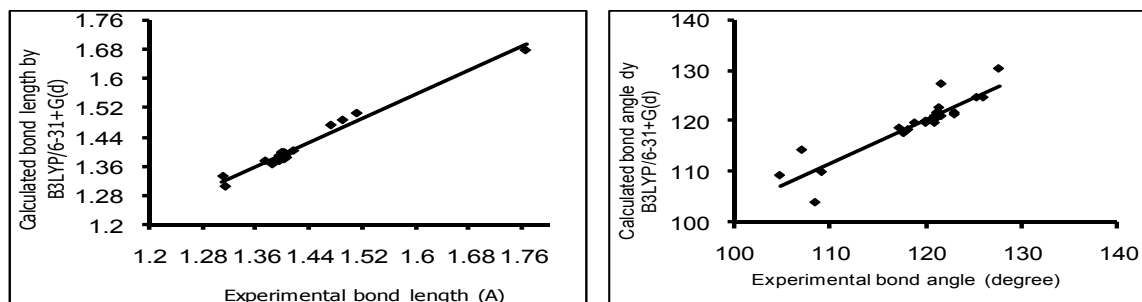


Fig. 2. Calculated B3LYP/6-31+G(d) bond lengths and bond angles in comparison with experimental data.

4.2 Vibrational assignments

The literature search has revealed that DFT calculations and vibrational analysis have not been reported so far on 2-(4-methyl-2-biphenyl)-4-amino-1, 2, 4-triazole-3-thiol. Therefore, we have calculated the theoretical vibrational spectra of 2-(4-methyl-2-biphenyl)-4-amino-1, 2, 4-triazole-3-thiol by using HF and B3LYP, methods with 6-31G (d) basis set. Title compound contains 34 atoms so that, it has 96 normal modes.

4.4 ¹H and ¹³C NMR

NMR spectra were recorded on a Shimadzu AMX400, spectrometer by using CDCl₃ as solvent and TMS as an internal standard (Chemical shift in ppm). Calculated NMR chemical shifts at HF and B3LYP/6-31G (d) levels of 2-(4-methyl-2-biphenyl)-4-amino-1, 2, 4-triazole-3-thiol after subtraction of the value of tetramethylsilane calculated at the same level of theory.

5. Conclusions

The results of the study lead to the following conclusions:

(i) The ground state geometries were optimized using the HF and B3LYP methods with the 6-31G (d), 6-31+G (d) basis set and geometries reported within the limits of accuracy of available experimental data. The bond lengths and angles calculated for title compound show quite good agreement with experimental values. The agreement for bond angles is not as good as that for the bond distances. (ii) The frequency assignments performed for the first time from FTIR and FT-Raman spectra recorded were for 2-(4-methyl-2-biphenyl)-4-amino-1,2,4-triazole-3-thiol. (iii) Mulliken charges of dacarbazine at different levels were calculated and the results discussed. (iv) calculated NMR chemical shifts and thermodynamic properties at HF and B3LYP/6-31G(d) levels of 2-(4-methyl-2-biphenyl)-4-amino-1, 2, 4-triazole-3-thiol were discussed and reported.

References

- [1] B. H. Shivarama, K.P.Narayana, B.R. Sooryanarayana, M.K. Shivananda Eur J. Med. 37 (2002) 511.
- [2] K. Cooper, J. Steele. Chem Abstr.112 (1990) EP 329357, 76957.
- [3] B. Prabhuswamy, S.Y. Ambekar. Synth Commun. 29 (1999) 3487.
- [4] Basappa, M. Sathish Kumar, S. Nanjundaswamy, M. Mahendra, B.S. Vishwanath, J. Shashidhara Prasad, K.S. Rangappa. Bioorg Med. Chem. Lett. 14 (2004) 3679.
- [5] S.Nanjunda Swamy, S. Basappa, M.A. Sarala, Sridhar, J. Shashidhara Prasad, K.S. Rangappa. J. Chem. Res. 357 (2005) 291.
- [6] M. Begtrup, G. Boyer, P. Cabildo, C. Cativiela, R.M. Claramunt, J. Elguero, J.I. García, P. Toiron, Vedsø, Magn Reson. Chem. 31 (1993) 107.
- [7] C.T. Lee, W.E. Yang, R.G. Parr Development of the Colle–Salvetti Correlation Energy Formula into a Functional of the Electron–Density. Phys Rev. 37 (1988) 785.

**Direct derivation of Lennard-Jones parameters for CO using the DFT calculations**

Jaber Jahanbin Sardroodi, Alireza Rastkar Ebrahimzadeh, Mina Yaghoobi notash

Molecular Simulations Lab. Azarbaijan University of Tarbiat Moallem

(E-mail: mina_yaghoobi@yahoo.com)

Keywords: DFT method, Lennard-Jones parameters, vdw energy, Mulliken population, Lowdin population.**1. Introduction**

Van der Waals force field parameters are difficult to determine from only experimental data, because of the insufficient data-to-parameter ratio. We present a method which exploits virtually unlimited number of DFT calculations, as compared with experimental data, and does not have to rely on unphysical combination rules used by most force fields. A wide variety of functional forms for the vdw potential have been used in the literature including the Lennard-Jones (LJ) 12-6, Exp-6 and Morse and buffered-14-7 potentials [1]. Because the 12-6 potential included simulations are faster than others, we use the Lennard-Jones 12-6 potential written as:

$$E_{vdw} = 4\epsilon_{ij} \left[\left(\frac{\sigma_{ij}}{r_{ij}} \right)^{12} - \left(\frac{\sigma_{ij}}{r_{ij}} \right)^6 \right] \quad (1)$$

This interaction energy have been calculated as the difference between dimer interaction energies and electrostatic energy resulted from the atomic charges.

We assume that the interaction energy of CO-CO pair is the sum of the vdw and electrostatic energies:

$$E_{ij} = E_{vdw} - E_{elec} \quad (2)$$

Therefore, in order to evaluation vdw energy, we have to obtain the difference between interaction and electrostatic energies. We have used density functional theory computations for obtaining the interaction energy of CO-CO pair and electrostatic energy between CO's have also been evaluated by the help of Coulomb equation. The charges on the atoms have been obtained by two methods, one is the direct DFT calculations of the atomic charges done on the optimized structure and the other is the using the dipole moment obtained from the SCF computations.

Finally the interaction parameters have been evaluated using a non linear regression least squares method as fitting the function F defined below to the E_{vdw} .

$$F = \sum_{i,j, i \neq j} E_{vdw}(i,j) \quad (4)$$

2. Computational details

All DFT calculations in this paper were performed with The General Atomic and Molecular Electronic Structure System (GAMESS-US) [2]. The structure of CO was first optimized using different DFT methods including LYP, BLYP, B3LYP, PBE, PW91, and GPW91. Then the results of computations were compared to the existing experimental data and the B3LYP/6-31G (d, f) method was chosen as the most reliable method. This comparison has been shown at Table 1 for the B3LYP method. At the next, atom-centered charges were calculated for the optimized reliable structure. The atomic charges have been computed using three methods including Mulliken population analysis, Lowdin population analysis [3,4] and fitting the electrostatic potential (CHELPG) [4]. The dipole moment of the CO was evaluated using these calculated atomic charges by the well-known equation:

$$p = \sum_i q_i r_i \quad (5)$$

However, dipole moment of CO was also calculated directly by pure SCF computations and compared with those obtained from atomic charges. The results have been collected as Table 2.

**Table 1.** C-O bond-length (angstrom), in B3LYP method, from various basis sets.

Basis set	6-311G(d)	6-311G(d, f)	6-31G(d)	6-31G(2d)	6-31G(3d)	6-31G(d, f)	experimental
C-O bond- length	1.1264581	1.1250761	1.1381244	1.1325597	1.1307016	1.1292413	1.1283

Table 2. Configuration energies (au), SCF dipole moments (D) and carbon atom charges (in electronics) from three method for B3LYP/6-31G(d, f) optimized bond length.

DFT method	Energy	Dipole- moment	Mulliken Charge	Lowdin charge	ChelpG
BLYP/6-31G(d, f)	-113.30483194	0.128141	0.186507	-0.115305	-0.0236
BLYP/6-31G(3d)	-113.30523151	0.118121	0.264465	-0.111686	-0.0218
B3LYP/6-311G(d)	-113.29543563	0.108119	0.112338	-0.109554	-0.0199
B3LYP/6-311G(d, f)	-113.29965715	0.101010	0.062129	-0.205922	-0.0186

For evaluation vdw energy of CO dimers we fixed configuration of individual CO's to the optimized structure, and the relative orientations in dimer configuration were varied. For evaluation the dimer interaction energy, we produced at least 10^5 different configurations. The variations of relative orientations of CO molecules have been carried on using coordinates defined relative to the center of C-O bond. The configurations have been produced by a linux script. This script has been written on a template provided at the web page of google GAMESS group. The script changes the distance and relative orientation of CO molecules and automatically produce GAMESS input files and run the program and collect the results and output data (especially interaction energy, E_{ij}) for each configuration. Finally the vdw energy was obtained in each configuration from the following relation:

$$E_{vdW} = E_{ij} - E_{elec} \quad (6)$$

The LJ parameters σ_{ij} and ϵ_{ij} for C and O atoms were determined simultaneously by using a nonlinear regression method implemented as genfit function in Mathcad-14 package. Table 3 have been contained the calculated LJ parameters for O-O, C-O and C-C occurring in a CO-CO interaction along with the experimental values [5] in order to the comparison purpose. The results show that the agreement between the calculated values and the experimentally derived parameters are reasonable.

Table3. Site-specific Lennard-Jones parameters for carbon monoxide

$\sigma_{O-O} / \text{\AA}$	$\epsilon_{O-O} / \text{kcal} \cdot \text{mol}^{-1}$	$\sigma_{C-C} / \text{\AA}$	$\epsilon_{C-C} / \text{kcal} \cdot \text{mol}^{-1}$	$\sigma_{C-O} / \text{\AA}$	$\epsilon_{C-O} / \text{kcal} \cdot \text{mol}^{-1}$
3.0058	0.1029	3.5638	0.0627	3.2848	0.0803

3. Results and discussions

The Van der Waals interaction parameters for CO-CO interaction have been determined using density functional theory computations. The vdw energy has been defined as the difference between total interaction energy and electrostatic interaction energy between two CO molecules. The atomic charges needed for evaluation electrostatic energy have been obtained successfully from either direct DFT calculations or calculations via SCF dipole moment. The calculated vdw parameters are in good agreement with experimentally derived parameters.

References

- [1] Halgren, T. J. Am. Chem. Soc. 1992, 114, 7827-7843.
- [2] General Atomic and Molecular Electronic Structure System, M. W. Schmidt, et al. J. Comput. chem. 14, 1347-1363 (1993).
- [3] Frank Jensen, Introduction to Computational Chemistry, 2nd. Ed, John Wiley & Sons, Ltd. Chichester, 2007.
- [4] K. I. Ramachandram, G. Deepa, K. Namboori. Computational Chemistry and Molecular Modeling, Principles and Applications, 2008 Springer-Verlag Berlin Heidelberg.
- [5] J. P. Bovanich, J. Quant. Spectrosc. Radiat. Transfer Vol. 47, No. 4, PP. 243-250, 1992.

**Aromaticity in terms of ring critical point properties**

A. Mohajeri* and A. Ashrafi

Department of Chemistry, College of Sciences, Shiraz University, Shiraz 71454, Iran

(E-mail: abolfazlashrafi@gmail.com)

Keywords: Aromaticity, RCP properties, AIM, Polycyclic aromatic hydrocarbon.**1. Introduction**

Although aromaticity is not a directly observable quantity and there is no exact quantum chemical definition, it is a widely used concept in physical organic chemistry [1]. According to the most definition of Schleyer and co-workers [2], aromaticity is a manifestation of electron delocalization in closed circuits, results in energy reduction. The main problem, of course, is that delocalization is not directly measurable and there is no single definition underlying the use of this concept throughout chemistry. Aromaticity is usually evaluated indirectly by measuring a physicochemical property that reflects the aromatic character of a molecule. The present study is directed to show how the properties derived from the topological analysis of the electron density can be applied for description of different aromaticity indices. Our main goal is to provide local measure of aromaticity by use of density based properties estimated in the RCP for a series of 43 six-membered rings.

2. Computational details

The calculations carried out in this research have been done with Gaussian 98 program [3]. The Becke's three-parameter exchange functional with LYP correlation functional (B3LYP) and basis set 6-311++G** were used. The molecular geometries of 43 aromatic rings (Figure 1) have been fully optimized and their wavefunctions have been used to characterize topological properties of the electronic charge density. The AIM2000 program [4] was used for topological analysis of electron density. The following characteristics of ring critical points (RCPs) are taken into account: density at RCP, its Laplacian, the eigenvalues of the Hessian matrix of density, the ellipticity, the electronic kinetic energy density and the total energy density. The gauge including atomic orbital (GIAO) method [5] has been used to perform calculations of NICS(1).

3. Results and discussion

The characteristics of the electron density at the RCP are analyzed in the present study as possible descriptors describing the aromaticity of a given ring. We have chosen molecules containing 1 to 4 six-membered rings, some of them incorporating heteroatom in their structures (Figure 1). The RCP properties and the values of HOMA, NICS(1), PDI, ATI, FLU and A_6^{π} indices for the rings were calculated. The correlations between different aromaticity indices and eight RCP properties have been checked for two separate sets. The first set includes just benzenoid hydrocarbons and the second set is our total aromatic systems including both benzenoid rings and heterocyclics. The investigation correlation matrices for the correlation between aromaticity indices and RCP properties is illustrated that various aromaticity indices correlate with RCP properties in different manner. Among six aromaticity indices, HOMA shows the best correlation with most of RCP properties (with correlation coefficients greater than 0.9) whereas other indices such as PDI, ATI, FLU and A_6^{π} are found to be less correlated with RCP properties, however their correlation coefficients are in acceptable range, and finally the correlation between RCP parameter and NICS(1) seems to be failed completely (Table 1). The correlation trend for the second set are similar to the benzenoid rings in the first set the correlation coefficients become clearly smaller. In the case where we have a set of different aromatic rings including heterocyclics, individual RCP properties may not reveal high correlation with aromaticity indices. We suggested using combination of RCP properties to model of the aromaticity indices and described the aromaticity of a given set including rings with one or more heteroatom(s). Since the intercorrelation between RCP parameters themselves are quite good, the RCP properties can be used together in a vector serving as a descriptor for a ring.

Indeed, $P = (\rho(r_c), \nabla^2 \rho(r_c), \lambda_1, \lambda_2, \lambda_3, G(r_c), H(r_c), \varepsilon)$ is an eight-dimensional vector of properties evaluated at the ring critical point and the data matrix of RCP properties for 43 aromatic rings has a dimension of (43 x 8). To handle the RCP data matrix, it is subjected to principal component analysis (PCA) which involves a mathematical procedure that transforms a number of correlated variables into a number of uncorrelated variables called principal components [6]. The first principal

component accounts for as much of the variability in the data as possible, and each succeeding component accounts for as much the remaining variability as possible. The results of the application of PCA on the RCP descriptors data matrix are listed in Table 2. In this Table, the eigenvalues, the percent of variances in the RCP data matrix explained by each eigenvalue and the cumulative percent of variances have been listed for the first to three principal components. As is observed, the largest variances have been explained by the first PC (about 93%) and the first three PCs can explain more than 99% of variances in the data matrix. In this work, multiple linear regressions are used to model each aromaticity indices as a function of the first three PCs. The values of correlation coefficients indicate that the resulted models can be well applied for all indices except NICS(1). It can be concluded that although individual RCP parameters cannot be considered as useful descriptors for aromaticity of heterocyclic compounds, combination of RCP properties lead to significant improvement in the correlation coefficients.

4. Conclusions

In the present study, the use of topological electron density properties in the ring critical points of the aromatic systems has been investigated as a way of quantifying aromaticity indicators. Inclusion of heterocyclic compounds in the set of aromatic rings under investigation may cause obvious discrepancy in the correlation between RCP properties and aromaticity indices. Thus, because of multidimensional character of aromaticity, individual RCP properties cannot be considered as reliable quantitative characteristics of π -electron delocalization in heterocyclic compounds. However, principal component analysis has been analysis has been used to compress the RCP data matrix of 43 aromatic rings into principal components and each aromaticity indices were modeled as a function of the first three PCs using multiple linear regressions.

Index	HOMA	NICS(1)	FLU	PDI	ATI	Δ^{π}	$\rho(r_c)$	$\nabla^2\rho(r_c)$	G(r _c)	H(r _c)	λ_1	λ_2	λ_3	ϵ
HOMA	1													
NICS(1)	0.672	1												
FLU	0.894	0.641	1											
PDI	0.867	0.527	0.884	1										
ATI	0.581	0.299	0.685	0.650	1									
Δ^{π}	0.850	0.460	0.939	0.929	0.720	1								
$\rho(r_c)$	0.703	0.387	0.553	0.701	0.284	0.616	1							
$\nabla^2\rho(r_c)$	0.754	0.418	0.627	0.766	0.357	0.698	0.993	1						
G(r _c)	0.744	0.409	0.611	0.752	0.340	0.681	0.996	0.999	1					
H(r _c)	0.834	0.510	0.793	0.876	0.529	0.856	0.895	0.939	0.928	1				
λ_1	0.606	0.339	0.450	0.613	0.189	0.519	0.990	0.970	0.976	0.841	1			
λ_2	0.692	0.417	0.592	0.730	0.349	0.670	0.947	0.962	0.957	0.946	0.927	1		
λ_3	0.730	0.386	0.584	0.725	0.309	0.648	0.987	0.983	0.987	0.879	0.972	0.897	1	
ϵ	0.454	0.239	0.261	0.425	0.019	0.303	0.891	0.841	0.856	0.620	0.926	0.718	0.909	1

Table 1. Correlation matrix for the correlation between aromaticity indices and RCP properties for all rings of the systems shown in Figure 1.

Table 2. Results of application of PCA on the RCP data matrix of all aromatic rings in Figure 1.

Principal component	Eigenvalue	Percent of variance	Cumulative percent of variance
PC ₁	7.447	93.09	93.09
PC ₂	0.470	5.87	98.97
PC ₃	0.071	0.89	99.86

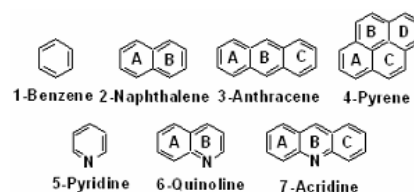


Figure 1. Some of studied aromatic molecules with ring labeling.

References

- [1] Matito, E. Feixas, F. Solà, M. J. Mol. Struct. (Theochem) 811 (2007) 3.
- [2] Chen, Z. Wannere, C. S., Corminboeuf, C. Puchta, R. Schleyer, P. v. R. Chem. Rev. 105 (2005) 3842.
- [3] Frisch, M. J. et al Gaussian 98, Revision A.7, Gaussian, Inc., Pittsburgh PA, 1998.
- [4] Bader, R. F. W. AIM2000 Program, ver 2.0, Hamilton; McMaster University, (2000).
- [5] Wolinski, K. Hinton, J. F. Pulay, P. J. Am. Chem. Soc. 112 (1990) 8251.
- [6] Malinowski, E.R. Factor Analysis in Chemistry, John Wiley & Sons, New York, 2002.

Hydrogen bonds in methylimidazolium-tetrafluoroborate ionic liquidH. Roohi^{a,b}, R. Salehi^{a*}^aDepartment of Chemistry, Faculty of Science, University of Sistan & Baluchestan, P.O. Box 98135-674, Zahedan, Iran^bDepartment of Chemistry, Faculty of Science, University of Guilan, Rasht, Iran

(E-mail: R.salehi88@ymail.com)

Keywords. Methylimidazolium, tetrafluoroborate, Hydrogen bond, ion pair, binding energies.**1. Introduction**

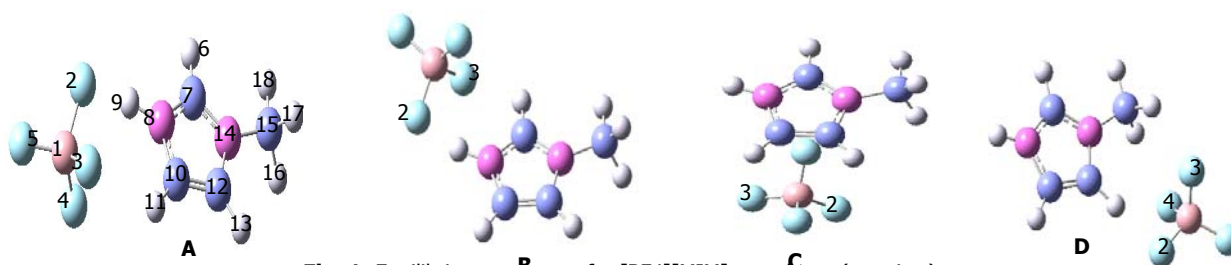
Ionic liquids are a class of novel composed exclusively of organic cations and inorganic anions. They possess appealing features such as low melting points, negligible vapor pressure, nonvolatile, nonflammable, wide electrochemical windows, and so on [1-5]. Their physical properties could be tailored by adjusting the structures and species of cations and/ or anions for a given end use, therefore ionic liquids have been referred to as "designed solvents" [6]. The structural [7-8], thermodynamic properties [9-10], of both pure ionic liquids and their mixtures with other compounds have been studied extensively by computer simulations. It has been recognized that the hydrogen bonds have a significant influence on the physical properties of imidazolium ionic liquids; however, most of the simulations were limited to single ionic species and/or single ion-pairs of some specific ionic liquids. In present study, we have calculated the intermolecular interaction energies and geometrical features of [MIM] [BF₄] ion pair by using DFT method at the B3LYP/6-311(2d2p) level.

2. Calculation methods

All the structures studied in this work were optimized by using B3LYP method with 6-311++G(2d,2p) basis set. Geometries and energies were determined by using the Gaussian 03 program package [12].

3. Results and discussion

The Figure 1 illustrates the optimized geometries of the [MIM][BF₄] complex obtained through the B3LYP/6-311++G(2d,2p) calculations. The electronic binding energies, as well as the results of the BSSE-corrected binding energies and zero-point corrected energies for different structures of [MIM][BF₄] complex are listed in Table 1. From Table 1, binding energies obtained using 6-311++G (2d,2p) basis set are -374.74 kJ mol⁻¹ for isomer **A**, -386.42 kJ mol⁻¹ for isomer **B**, -317.87 kJ mol⁻¹ for isomer **C**, -332.48 kJ mol⁻¹ for isomer **D**. The stability of isomers decreases in the order of **B** > **A** > **D** > **C** >. The inclusion of BSSE correction has a minor effect on the binding energy, so this correction is not discussed. In all complexes of the [MIM][BF₄] ion pair, hydrogen bonds between the [MIM]⁺ cation and the BF₄⁻ anion are observed. The main structural parameters of these complexes are given in Table 2. In **A** and **B** complexes, the H9...F2 distances are 1.514 and 1.570 Å, respectively, which are longer than the covalent bond distance of H-F (1.07 Å) and shorter than the van der Waals distance of H...F (2.670 Å) [13]. The results suggest that the most stable hydrogen bonds of N-C-H...F are formed in the **A** and **B** isomers. The two and three hydrogen bonds for **C** and **D** isomers, respectively, are also reported in Table 2. As a result, stability of these isomers increases with increment of the number of C-H...F type hydrogen bonds.

**Fig. 1.** Equilibrium structures for [BF₄][MIM] complexes (top view).**4. Conclusions**

Quantum chemical calculations have been performed for the various isomers of [BF₄][MIM] ion pair in order to examine their structural characteristics and energetics at the B3LYP/6-311++G(2d,2p) level of DFT theory. The stability of complexes



decreases in the order of **B** > **A** > **D** > **C**. The hydrogen-bond interaction in complexes **A(B)** is stronger than in complexes **D(C)**.

Table1. Binding energies (kJ mol⁻¹) of [MIM] [BF₄] complexes

Complex	ΔE	ΔE^a	ΔE^b
A	-374.74	-372.56	-371.30
B	-386.42	-384.00	-374.80
C	-317.87	-316.01	-308.08
D	-332.48	-329.99	-318.86

ΔE^a =Electronic binding energy (ΔE) + BSSE, ΔE^b = ΔE^a + ΔZPE

Table2. Optimized geometrical parameters of [MIM] [BF₄] complexes.

parameter	A	B	C	D
H6...F3		2.157		
H9...F2	1.514	1.570		
H11...F3	2.275		1.974	
H13...F2			2.057	1.887
H16...F3				2.214
H17...F4				2.214
C7-H6...F3		124.9		
N8-H9...F2	172.4	164.4		
C10-H11...F3	122.2		140.4	
C12-H13...F2			131.1	178.3
C15-H16...F3				126.2
C15-H17...F4				126.1

References

- [1] T. Welton, Chem. Rev. 99 (1999) 2071.
- [2] P. Wassercheid, W. Keim, Angew. Chem., Int. Ed. 39 (2000) 3772.
- [3] K. R. Seddon, J. Chem. Technol. Biotechnol. 68 (1997) 351.
- (4) R. Hagiwara, Y. Ito, J. Fluorine Chem. 105 (2000) 221.
- (5) J. G Huddleston, A. E. Visser, W. M. Reichert, H. D Willauer, G. A. Broker, R. D. Rogers, Green Chem. 3 (2001) 156.
- [6] M. J. Earle, K. R. Seddon, Pure Appl. Chem. 72 (2000) 1391.
- [7] C. G. Hanke, S. L. Price, R. M. Lynden-Bell, Mol. Phys. 99 (2001) 801.
- [8] M. G. Del Po' polo, G. A. Voth, J. Phys. Chem. B 108 (2004) 1744.
- [9] J. Shah, J. Brennecke, E. Maginn, Green Chem. 4 (2002) 112.
- (10) R. M. Lynden-Bell, N. A. Atamas, A. Vasilyuk, C. G. Hanke, Mol. Phys. 100 (2002) 3225.
- [11] Y. U. Paulechka, G. J. Kabo, A. V. Blokhin, O. A. Vydrov, J. W. Magee, M. J. Frenkel., Chem. Eng. Data 48(2003) 457.
- [12] Frish M. J., et al. Gaussion03 (Revision B.03), Gaussion, Inc, Pittsburgh, PA, 2003.
- [13] A. Bondi, J. Phys. Chem. 68(1964) 441.

Theoretical Study, Kinetics and Mechanism Investigation of the Reactions between Triphenylphosphine, Dialkylacetylenedicarboxylates and N-H Acid such as Benzhydrazide

M. A. Kazemian, S. M. Habibi Khorassani, M. T. Maghsoodlou and A. Ebrahimi*

Department of Chemistry, University of Sistan and Baluchestan, P.O. Box 98135-674, Zahedan, Iran

(E-mail: kazemean@yahoo.com)

Keywords: Benzhydrazide, Dialkyl acetylenedicarboxylates, Triphenylphosphine, Two dimensional scanning, Mechanism.

1. Introduction

In the present work in gas phase, the variable mechanisms were investigated for the reaction between Triphenylphosphine, Dialkyl acetylenedicarboxylates in the presence of N-H acids such as Benzhydrazide for generation of phosphorus ylides (see Figure 1). Suitable mechanism was determined with respect to the potential energy surface. Phosphorus ylides are reactive systems which have a role in many valuable reactions of organic synthesis [1-2]. These are most often obtained in excellent yields from the 1:1:1 addition reaction between triphenylphosphine, dialkyl acetylenedicarboxylates, in the presence of CH, SH or NH-compound [3-4]. A facile synthesis investigated for the reaction between triphenylphosphine **1** (TPP), dimethyl acetylenedicarboxylates **2** (DMAD) and Benzhydrazide (as NH-acid). Useful information was obtained from studies of the effect of solvent, structure of reactants (different alkyl groups within the dialkyl acetylenedicarboxylates and SH-acids) and also concentration of reactants on the rate of reactions [7-9]. Rate determining step and fast step of the reaction were experimentally recognized in our research works. In addition, mechanism of the reaction and rate of equation which were obtained from the experimental results were in successfully agreement with the study state approximation. In the present work, various mechanisms were also theoretically investigated for the reaction between Triphenylphosphine, Dialkyl acetylenedicarboxylates in the presence of N-H compounds such as Benzhydrazide, in comparison with the experimental mechanism.

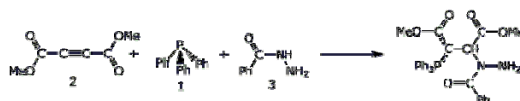


Fig. 1. The reaction between triphenylphosphine **1**, dialkyl acetylenedicarboxylate **2** and benzhydrazide for generation of stable phosphorus ylides **4**.

2. Methods

All calculation were performed using Gaussian98 at HF/6-31G(d,p) level of theory. In addition, extra basis set 6-31+G(3df,3pd) was employed for the phosphorous atom and also single point energy calculations were achieved at B3LYP/6-31G(d,P) level. Two dimensional scanning techniques were applied to determine the transition state structures. However, scan keyword in Gaussian package was not usable because the molecular structures were too big with large number of atoms; to overcome this problem, full scan (manual scan) was employed instead of scan keyword.

3. Results and discussion

Three proposed mechanism were theoretical studied for mentioned reaction. Only one of them was discussed as follows:

Proposed mechanism 1:

In order to study this mechanism (which depicted in Figure 2) all structures were drawn by gaussview and the calculations were performed with Gaussian98 software. For all atoms, level of calculations was HF/6-31G(d,p). However, HF/6-31+G(3df,3dp) level of theory was specially utilized for phosphorous atom. In the first step (step1-1) of proposed mechanism 1 (Figure 1), **2** and **1** were considered together for investigation of probable interactions.

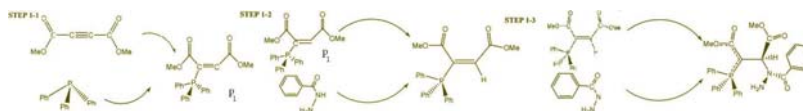


Fig. 2. Steps of proposed mechanism 1

Then intermediate p_1 (see Figures 2) was drawn and optimized at mentioned level. Under this condition P-C bond was longed in 0.1Å^o magnitudes step by step with full-scan. The results are shown in Figure 3 and amount of E_a , 29.08 kcal/mol, obtained for this stage. The procedure was then repeated for the second step in accord with the first step of the reaction mechanism. In this step (step1-2), hydrogen atom of benzhydrazide is brought to carbon atom of intermediate 1 (p_1) to reduce the distance between the two atoms from 4.2 Å^o to 0.80 Å^o for generation of energy profile. As can be seen from Figure 4, the required energy for this step is about 28.54 kcal/mol.

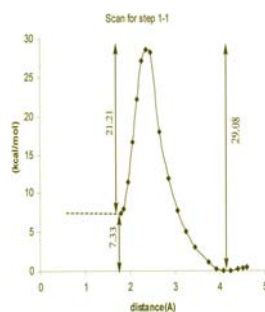


Fig. 3. The changes of energy with respect to (C1-P9) distance and the transition states structure optimizations were conducted at the HF/6-31G(d,p) level.

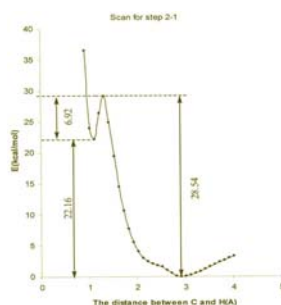


Fig. 4. The changes of energy with respect to (C1-H2) distance and the transition states structure optimizations were conducted at the HF/6-31G(d,p) level.

Because of the fast reaction between two ions in third step (step1-3), Transition State (T.S) is not theoretically observed in this stage. Due to the some species ionic are reacted together with no activation energy, the energy profile is not obtainable for the third step. With respect to the obtained activation energy for each step of proposed mechanism 1 overall activation energy was calculated about 57.62 kcal/mol. Hence the first step of the reaction ($E_a=29.09$ kcal/mol) is rate determinant step for proposed mechanism 1 in comparison with second step. The obtained result from theoretical calculation for proposed mechanism 1 was in good agreement with the experimental mechanism. Same procedure was considered for the other probable mechanism (mechanism 2 and mechanism 3). The results indicated that probable mechanism 2 and 3 are not consistent with the experimental data.

4. Conclusions

In our research work, three mechanisms of the reaction between Triphenylphosphine, Dialkyl acetylenedicarboxylates and benzhydrazide were theoretically studied in the gas phase. Two dimensional scanning techniques were employed to determine the transition state structures. The result can be summarized as follows: (1) proposed theoretical mechanism 1 was confirmed by the experimental mechanism, because the total activation energy was less than other probable mechanism 2 and 3.

References

- [1] Johnson, A. W. *Ylied Chemistr.*, Academic Press, London. (1966).
- [2] Cadogan, J. I. G. *Organophosphorus Reagents in Organic Synthesis*, Academic Press, New York. 1979.
- [3] Yavari, I., Ramazani, A. *Phosphorus, Sulphur, and Silicon*, 130 (1997) 73.
- [4] Yavari, I., Alizadeh, A., Anvary-Abbasnejad, A. M. *Phosphorus, Sulphur and Silicon*, 177 (2002) 81.
- [5] Maghsoodlou, M.T., Hazeri, N., Habibi Khorasani, S.M., Shahzadeh, A., Nassiri, M., *Phosphorus Sulphur and Silicon*, 3 (2006) 4.
- [6] Maghsoodlou, M.T., Hazeri, N., Habibi Khorasani, S.M. et al. *Phosphorus, Sulphur, and Silicon*, 181 (2006) 3.
- [7] Habibi Khorasani, S.M., Maghsoodlou, M.T., Hazeri, N., Nassiri, M., Marandi, G., Shahzade, A., *Phosphorus. Sulfur and Silicon*, 181 (2006) 3.
- [8] Habibi Khorasani, S.M., Maghsoodlou, M.T., Ebrahimi, A., Roohi, H., Zakarianezhad, M., Moradian, M., *progress in Reaction Kinetics and Mechanism*, 30, 1/2 (2005).
- [9] Habibi Khorasani, S.M., Maghsoodlou, M.T., Ebrahimi, A., Roohi, H., Zakarianezhad, M., *J. Iranian Chem. Soc.* 3 (2006) 3.

**A computational study of molecular transport through carbon nanotubes**Zahra Tavangar^a and Hassan Sabzyan^b^aFaculty of Chemistry, University of Kashan, Kashan, Iran

(E-mail: tavangar@chem.ui.ac.ir)

^bFaculty of Chemistry, University of Isfahan, Isfahan, Iran**Keywords:** CNT, MD Simulation, Projected Radial Distribution, diffusion.**1. Introduction**

Fluid flow through CNTs can be fast and selective, similar to the selective and extraordinary fast flows in biological cellular channels, and thus has considerable importance in many biological and nano-electromechanical processes as well as in pharmaceutical industries. It is difficult to detect and trace the behavior of molecules inside nanopores and nanotubes. Therefore, computational methods, such as molecular dynamics (MD) or Monte Carlo (MC) simulations, have been widely used to determine the mechanisms of flow, diffusion, adsorption, and separation of multicomponent molecular mixtures in ideal nanoporous materials as well as in real systems such as carbon nanotube [1-3]. A detailed study of the gas and liquid flows in the CNTs can open the way towards the study of the flow of reaction mixtures in prospective nano-reactors [4].

In this work, we have carried out molecular dynamic simulation on the flow of carbon monoxide (CO) and carbon dioxide (CO₂) simple molecular fluids inside various SWCNTs. The effects of the size and type of these nano-conduits on the flow dynamics of the pure CO and CO₂ gases and their mixtures have been studied in detail.

2. Computational details

Molecular dynamics (MD) simulations of the diffusive flow of CO/CO₂ gases in individual CNTs are carried out using DL_POLY software in which the inter-molecular potential energies and short range interactions are described by the AMBER force field parameters [5]. Geometries of all CNTs are left relaxed (flexible) throughout the simulations. The periodic boundary condition is employed only along the CNTs' axes. The velocity Verlet algorithm with a time step $\delta t = 0.1$ fs is used to integrate the differential equations of motion. Runs are taken up to 10⁶ time steps summing up to a simulation time of 100 ps. The molecules are initially distributed randomly throughout the CNT.

3. Result and Discussion

The diffusion (or mobility) coefficient, D_μ , calculated for the flow of the CO and CO₂ molecules inside different CNTs using Eq. (1) are reported in Table 1.

$$D_\mu = \langle [Z_\mu(t) - Z_\mu(0)]^2 \rangle / 2t^\alpha \quad (1)$$

In this Equation, $Z_\mu(t)$ is the coordinate of a molecule of type μ at time t . Analysis of the calculated diffusion coefficients shows that the flow of the CO molecules through the (13,0) and (10,6) CNTs is in accelerated mode, while through the other CNTs is in the transition mode. Table 1 shows also that flow of the CO₂ molecules through the (21,0) CNT can be described as a normal mode diffusion ($\alpha = 1$), while, through the (8,8) and (12,8) CNTs is in the single file diffusion ($\alpha = 0.5$), and through the (10,6) and (12,12) CNTs is in the transition mode diffusion ($0.5 < \alpha < 1.0$).

Table 1: Diffusion (or mobility) coefficients calculated for the flow of the CO and CO₂ gases in various CNTs.

CNT	D_{CO_2}	D_{CO}
(8,8)	$1.51 \times 10^{-10} \text{ cm}^2/\text{s}^{0.50}$	$6.14 \times 10^{-5} \text{ cm}^2/\text{s}^{0.96}$
(10,6)	$5.52 \times 10^{-7} \text{ cm}^2/\text{s}^{0.79}$	$0.02 \times 10^0 \text{ cm}^2/\text{s}^{1.16}$
(13,0)	$1.49 \times 10^{-13} \text{ cm}^2/\text{s}^{0.24}$	$1.37 \times 10^0 \text{ cm}^2/\text{s}^{1.31}$
(12,8)	$6.45 \times 10^{-10} \text{ cm}^2/\text{s}^{0.50}$	$2.38 \times 10^{-5} \text{ cm}^2/\text{s}^{0.89}$
(21,0)	$8.00 \times 10^{-4} \text{ cm}^2/\text{s}^{1.00}$	$4.79 \times 10^{-6} \text{ cm}^2/\text{s}^{0.81}$
(12,12)	$1.10 \times 10^{-9} \text{ cm}^2/\text{s}^{0.59}$	$1.68 \times 10^{-6} \text{ cm}^2/\text{s}^{0.77}$

The average cross-sectional projection of the radial distribution of the CO and CO₂ molecules in the simulation of the pure gas flows through various CNTs are plotted in Fig. 1. Except for the (13,13) CNT, the maxima of the CO and CO₂ peaks occur at the same distances from the CNT axis. The sharp peaks of the projected radial distributions of the CO and CO₂ molecules in the (12,12), (21,0) and (12,8) CNTs indicates that distribution of both species are annular along the axis. The similarity of the radial distribution peaks in the (12,12) and (21,0) CNTs (having almost equal radii) show that with this diameter of the CNTs, their helicity type does not have important role in the radial distribution of the gas molecules. Figure 1, clearly shows that in the (13,0) CNT, the radial distributions of the CO and CO₂ molecules are fundamentally different. The radial distribution of the CO₂ molecules has a relatively sharp peak, while the peak of the radial distribution of the CO molecules is boarder. This emphasizes that the CO₂ molecules distribute on one column in the flow through the (13,0) CNT. Note that appearance of the two sets of peaks around the axes of this CNT is due to the projection of the distributions along the CNTs onto a single cross section.

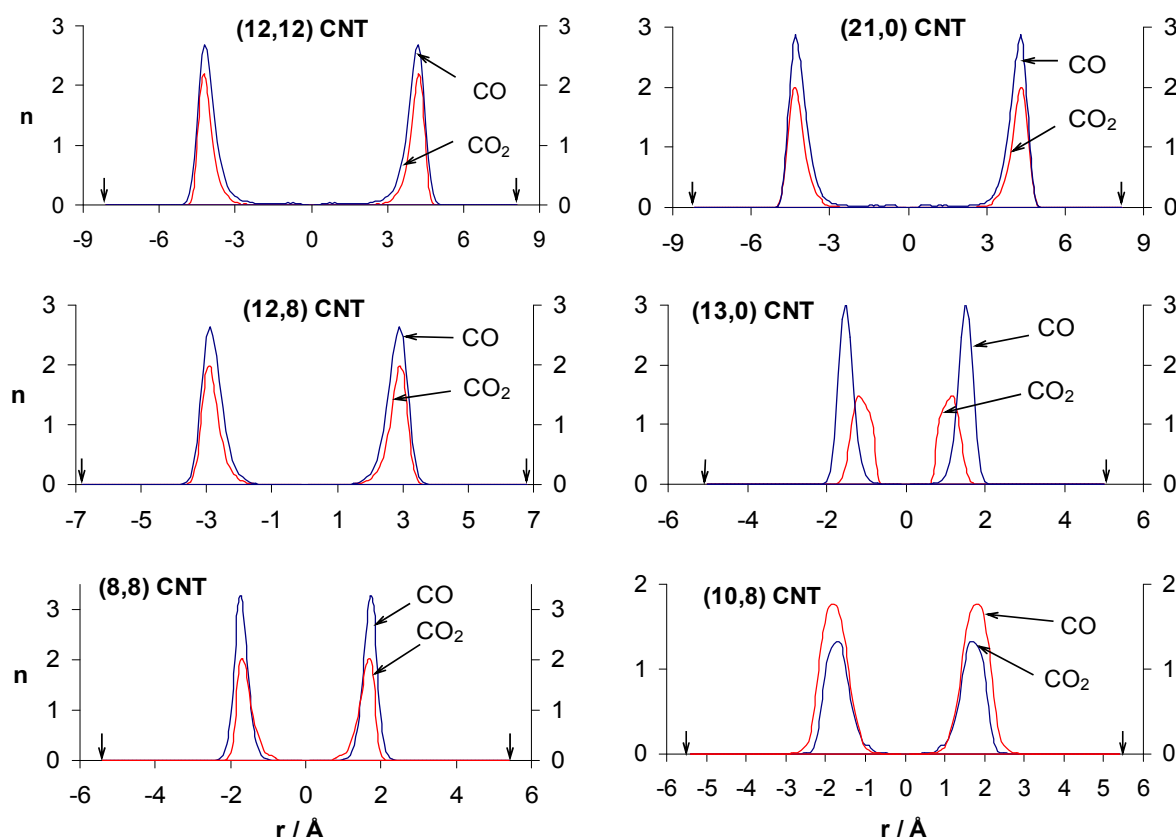


Fig. 1. Cross sectional projection of the radial distribution of gas molecules obtained for the flow of the pure CO and CO₂ gases through various CNTs. Arrows point to the CNTs wall.

References

- [1] Z. Mao, S.B. Sinnott, J. Phys. Chem. B 104 (2000) 4618.
- [2] K.-H. Lee, S.B. Sinnott, Nano Lett. 5 (2005) 793.
- [3] V.P. Sokhan, D. Nicholson, N. Quirke, J. Chem. Phys. 120 (2004) 3855.
- [4] C. Pham-Huu, N. Keller, C. Estournes, G. Ehret, J.M. Grenèche, M.J. Ledoux, Phys. Chem. Chem. Phys. 5 (2003) 3716.
- [5] W.D. Cornell, P. Cieplak, C.I. Bayly, I.R. Gould, K.M. Merz, D.M. Ferguson, D.C. Spellmeyer, T. Fox, J.W. Caldwell, P.A. Kollman J. Am. Chem. Soc. 117 (1995) 5179.



Thermodynamics of vapor-liquid equilibria of aqueous polymer solutions from the experimental vapor pressure osmometry and molecular thermodynamics modelling

R. Sadeghi^{*a}, Y. Shahebrahimi^b

^aDepartment of Chemistry, University of Kurdistan, Sanandaj, Iran

(E-mail: rsadeghi@uok.ac.ir)

^bDepartment of Chemical Engineering, University of Kurdistan, Sanandaj, Iran

(E-mail: yas_shahebrahimi@yahoo.com)

Keywords: Polymer solution, Vapor-liquid equilibria , Water activity, Vapor pressure, Model.

1. Introduction

Water soluble polymers have, for many years, received less than their share of the considerable scientific effort which has been devoted to the study of the structure and properties of the broad mass of macromolecular systems. The effect of this has been that the study of water soluble polymers has been something of a "Cinderella" subject, in spite of the importance of the polymers in biological systems, foods, and industrial products where the advantages (and low cost) of water as a solvent can be employed [1]. Phase equilibria is as important in the polymer processing and polymer applications industries as in the petroleum and chemical industries. This is primarily so because many polymeric materials are produced in a solution with a solvent or contain a substantial portion of monomers, dimers, and so forth. The usefulness of the materials depends on the amount of low molecular weight material contained in the polymer, whether the low molecular weight material will diffuse from the polymer solution, and how fast this diffusion will take place [2]. From the theoretical viewpoint, accurate modelling of phase behavior of polymer-solvent mixtures is necessary for proper design of separation processes such as removal of low-molecular weight substances from polymers by devolatilization, or polymer fractionation. It was found that the segment-based models provide the most flexible and convenient thermodynamic framework for researchers to characterize the nonideal behavior of polymer solutions [3,4]. In the first part of this work, vapor-liquid equilibria behavior of the aqueous solutions of wide range of water soluble polymers including poly(ethylene glycol) (200 and 6000), poly(ethylene glycol dimethyl ether) (250, 500 and 2000), poly(ethylene glycol monomethyl ether) (350) and poly(propylene glycol) (400) have been determined at different temperatures by both vapor pressure osmometry and isopiestic method. In the second part of this work, a new molecular thermodynamics model based on the Flory-Huggins-Hydration theory (for chemical interactions) and a segment based local composition model (for physical interactions) has been presented for the prediction of the vapor-liquid equilibrium data of the polymer solutions.

2. Methods

In this work, water activities of investigated polymer solutions were obtained from the vapor pressure osmometry and improved isopiestic method. The vapor pressure osmometry was performed with the help of an osmomat K-7000 (Knauer). With this method, the vapor pressure is measured indirectly by using thermistors to measure voltage changes caused by changes in temperature. First the osmometer was calibrated using aqueous NaCl solutions, yielding a function which correlates the panel reading to the corresponding concentrations of the sodium chloride solution. Then the measurements for the different polymer solutions were carried out. The water activity for the standard aqueous NaCl solutions at different concentrations and temperatures has been calculated from the correlation of Colin et al [5]. The used isopiestic apparatus consisted of five-leg manifold attached to round-bottom flasks. Two flasks contained the standard NaCl solutions, two flasks contained the polymer solution and the central flask was used as a water reservoir. The apparatus was held in a constant-temperature bath for at least 120 h for equilibrium. After equilibrium had been reached, the manifold assembly was removed from the bath, and each flask was weighed with an analytical balance with a precision of ± 0.0001 g. From the weight of each flask after equilibrium and the initial weight of NaCl and polymer, the mass fraction of each solution was calculated.

We model the excess Gibbs free energy G^E as consisting of two additive parts chemical contribution, G_{chem}^E , and physical contribution, G_{phys}^E :

$$G^E = G_{chem}^E + G_{phys}^E \quad (1)$$



The chemical contribution incorporates both chemical association theory to account for the hydrogen bonds and Flory-Huggins theory for the volume difference between components. The physical contribution is represented by a segment based local composition model.

3. Results, Discussion and Conclusions

The effect of temperature, molecular weight and structure of polymer on the vapor-liquid equilibrium behavior of aqueous polymer solutions were investigated. It was found that for a certain polymer mass fraction, water activities of aqueous polymer solution increase by increasing molecular weight of polymer and temperature. Vapor pressure osmometry and isopiestic method are two well known techniques for the determination of vapor-liquid equilibria of solutions. In this work, both techniques have been used for the determination of vapor-liquid equilibria of the investigated polymer solutions and a comparison between the vapor-liquid equilibrium data such as water activity and vapor pressure obtained from these techniques was investigated. A new molecular thermodynamics model has been used for the prediction of the vapor-liquid equilibrium data of the investigated polymer solutions. The model gives a good representation of water activities over wide concentration range.

References

- [1] M. Yu, H. Nishiumi, J. de S. Arons, *Fluid Phase Equilibria*, 83 (1993) 357.
- [2] M. S. High, R. P. Danner, *Fluid Phase Equilibria*, 55 (1990) 1.
- [3] R. Sadeghi, *Polymer*, 46 (2005) 11517.
- [4] R. Sadeghi, M. T. Zafarani-Moattar, A. R. Salabat, *Ind. Eng. Chem. Res.*, 45 (2006) 2156.
- [5] E. Colin, W. Clarke, D. N. Glew, *J. Phys. Chem. Ref. Data* 14 (1985) 489.



Determination of the melting point of the equimolar ionic liquid–benzene inclusion crystal by molecular simulation

M. H. Kowsari^{a,b,*}, S. Alavi^c, M. Ashrafzaadeh^{b,d} and B. Najafi^a

^a Department of Chemistry, Isfahan University of Technology, Isfahan, 84156-83111, Iran

^b Supercomputing Center, Isfahan University of Technology, Isfahan, 84156-83111, Iran

(E-mail: mohammad.kowsari@gmail.com)

^c Department of Chemistry, University of Ottawa, Ottawa, Ontario K1N 6N5, Canada

^d Department of Mechanical Engineering, Isfahan University of Technology, Isfahan, 84156-83111, Iran

Keywords: Melting Point, Molecular dynamics, Ionic liquids, Inclusion crystal, Simulation.

1. Introduction

A broad and rapidly growing range of applications are being developed for ionic liquids (ILs) and their mixtures. The melting point is one of the most important properties for the design and application of ionic liquids and their mixtures in academia and industry. However, despite much research activity on ionic liquids, relatively little is understood about of the connection between the chemical structure of the ILs and their mixtures with the melting point. The accurate experimental and theoretical melting point determination of ILs is also made difficult by the presence of polymorphism, eutectics, glass formation, and super cooling in the solid state.

2. Methods

The force field of the 1-ethyl-3-methylimidazolium cation and bis(trifluoromethanesulfonyl)imide anion, [NTf₂]⁻ (or [(CF₃SO₂)₂N]⁻) used in this work is from the systematic all-atom force field developed by Canongia Lopes et al. [2] based on the OPLS-AA and AMBER framework. For the benzene molecule, we have used force field parameters from the general AMBER force field (GAFF) [3]. All species in the simulations are fully flexible. The reader is referred to the published papers by Canongia Lopes et al. for further details of the force field [2].

Constant pressure and temperature (NpT) molecular dynamics simulations of 3×3×3 replica of the unit cell with 108 [emim][NTf₂] ion pairs plus 108 benzene molecules were performed for a total of 4968 atoms. The simulations were done with the Nosé–Hoover thermostat/barostat algorithm as implement in the DL_POLY program [4] version 2.18. The relaxation times used for the thermostat and barostat are 0.1 and 2.0 ps, respectively. Periodic boundary conditions were employed, and the equations of motion were integrated using the Verlet leapfrog scheme. The time step of the simulations was 2.0 fs and cutoff distance of $R_{\text{cutoff}} = 15 \text{ \AA}$. The electrostatic long-range interactions were calculated using the Ewald summation method.

The initial configurations of the cations, anions, and benzene molecules in the simulation supercell are derived from the crystallographic x-ray structure of equimolar inclusion crystal of [emim][NTf₂]•C₆H₆ at 110 K reported by Łachwa et al. [5]. Initial MD simulations were performed at $p = 1 \text{ atm}$ and $T = 110 \text{ K}$ with 2 ns simulation time needed for total energy convergence of the system. The final configuration of this stage was used as the starting point for the further stages of the melting simulations. We performed MD simulations of the solid and liquid phases from 110 K up to 440 K. After simulations of the perfect inclusion crystal, the void induced melting method was used to eliminate superheating and reduce calculated melting point. Each void corresponds to the removal of an ion-pair with one benzene molecule from a random location in the supercell. We introduced 2 to 8 "formula unit voids" (out of a total of 108 formula units in the initial simulation) in the simulations of the melting point.

3. Results and Discussion

Starting from an equilibrated the solid-state binary system at 110 K, we heat the system of perfect crystals to different temperatures to detect the melting transition. We observed a jump in the equilibrated thermodynamic properties (e.g., in volume or energy) for temperatures above 400 K indicating the melting transition for the perfect crystal simulations. Changes in the molecular arrangement, radial distribution functions (RDFs), density, configurational energy, and the dynamic behavior of species are used to detect and characterize the melting process [6]. The reported experimental melting point for this system was $\sim 288 \text{ K}$ [5]. Therefore, the simulations of the perfect crystal are superheated. To remove the activation barrier to melting, simulations were performed for the super cell with 2, 4, 5, 6, 7, and 8 voids. As the number of voids in the super cell increases,

the calculated melting points drop to lower temperatures (see Fig. 1). The melting temperatures for simulations with 6 and 7 voids converge to a value of ≈ 290 K and for 8 voids the calculated melting point is 280 K.

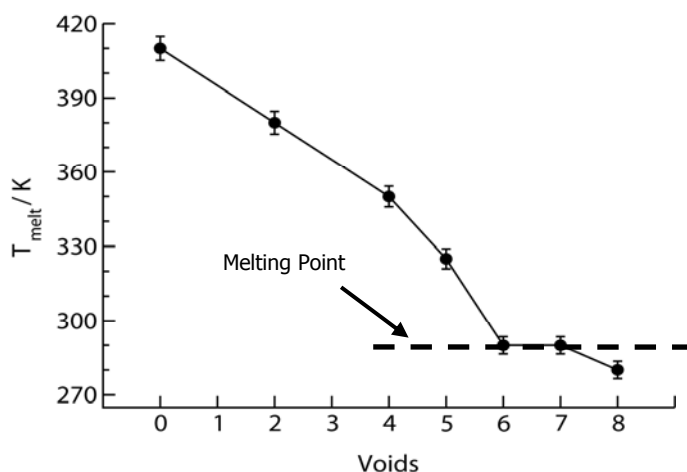


Fig. 1. The average calculated melting points of solids as a function of the number of voids introduced in the simulation cell.

4. Conclusions

We have simulated the melting for $[\text{emim}][\text{NTf}_2] \cdot \text{C}_6\text{H}_6$ and determined the melting point by the "void induced melting" method. The voids become sites for heterogeneous nucleation of the melting process and reduce the free energy barrier to melting seen in perfect crystals. The simulations correctly predict that the melting of the equimolar mixture occurs at a single temperature (not over a range of temperatures) and the calculated melting point of 290 K (see Fig. 1) is in excellent agreement with the experimental melting point of 288 K. We predict that $\Delta H_m = 37.7 \pm 2.2 \text{ kJ mol}^{-1}$ for the equimolar inclusion mixture at calculated melting point, which is in good agreement with the differential scanning calorimetry (DSC) experimental results of $42 \pm 2 \text{ kJ mol}^{-1}$. Additionally, we studied the effects of introducing the benzene molecules in the $[\text{emim}][\text{NTf}_2]$ lattice. The structures of the solid and liquid states have been characterized by calculating RDFs.

References

- [1] S. Alavi and D. L. Thompson, *J. Chem. Phys.* 122 (2005) 154704.
- [2] J. N. Canongia Lopes, J. Deschamps, and A. A. H. Pádua, *J. Phys. Chem. B*, Vol. 108 (2004) 2038; erratum: Vol. 108 (2004) 11250; also: J. N. Canongia Lopes and A. A. H. Pádua, *J. Phys. Chem. B* 108 (2004) 16893.
- [3] J. Wang, R. M. Wolf, J. W. Caldwell, P. A. Kollman, and D. A. Case, *J. Computat. Chem.* 25 (2004) 1157.
- [4] W. Smith, T. R. Forester, and I. T. Todorov, *The DL_POLY Molecular Simulation Package*, v. 2.18 (2007). Daresbury Laboratory, U.K., http://www.cse.clrc.ac.uk/msi/software/DL_POLY/
- [5] J. Łachwa, I. Bento, M. T. Duarte, J. N. Canongia Lopes, and L. P. N. Rebelo, *Chem. Commun.*, (2006) pp. 2445.
- [6] M. H. Kowsari, S. Alavi, M. Ashrafizaadeh, and B. Najafi, revisions send to *J. Chem. Phys.*, October 2009.



Effects of temperatures, pressures and pore size on the adsorption/separation of CO₂/N₂ gas mixture through carbon nanotube: canonical monte carlo simulation

*Saleheh Razavi^a, S.Majid Hashemianzadeh^a, Sahra balilehvand^b

^a Molecular Simulation Research Laboratory, Department of Chemistry, Iran University of Science and Technology, Tehran, Iran

(E-mail: srazavi@chem.iust.ac.ir)

^b Department of chemistry, university of alzahra, Tehran, Iran

Keywords: Molecular simulation, Carbon nanotube, Gas adsorption, Adsorption isotherm, Lennard-Jones potential.

1. Introduction

Carbon nanotubes have many fascinating properties. Their well-defined structures with hollow nanosize interiors suggest their potential use as sorbents for gas adsorption and separation. The internal and external adsorption sites of the curved nanotubes enhance surface proximity for adsorbates and hence influence the extent of adsorption. A large number of experimental studies have been carried out thus far on the adsorption of hydrogen on carbon nanotubes as part of the development of the next-generation fuel cell technology. Recently, there have been a few simulations examining the effect of the external surface of a nanotube bundle on the adsorption of hydrogen at supercritical temperatures and the adsorption of neon, argon, krypton, xenon, and methane at subcritical temperatures. [1,2]. There has been a number of molecular simulations of adsorption of gases in carbon nanotubes. This present work is focused on the capability of carbon nanotube for separation of CO₂/N₂ binary mixture using (N,V,T) Canonical Monte Carlo simulation. In this case, in order to gain better insight into simulation results, the virial equation of state with second and third virial coefficients, obtained from experimental measurements, was considered. The main objective of this study is to evaluate the effect of different factors such as temperature, pressure and pore size on the adsorption and separation performance of the carbon nanotube with the intent of finding the optimum condition for adsorption separation of CO₂/N₂ mixture in the carbon nanotube.

2. Model and Simulation details

A standard Canonical Monte Carlo simulation at fixed volume, temperature and sum of the species were carried out for the adsorption of CO₂/N₂ mixture in the carbon nanotube. The carbon dioxide and nitrogen molecules are modeled as spherical particles which interact with each other via the Lennard-Jones 12-6 potential. Lorentz-Berthelot combining rules were used for all cross interactions:

$$\phi_{LJ}(r) = 4\epsilon_{ij} \left[\left(\frac{\sigma_{ij}}{r} \right)^{12} - \left(\frac{\sigma_{ij}}{r} \right)^6 \right], \quad \epsilon_{ij} = \sqrt{\epsilon_i \epsilon_j}, \quad \sigma_{ij} = (\sigma_i + \sigma_j)/2$$

Where $\epsilon_{\text{CO}_2} = 225.3 \text{ k}$, $\sigma_{\text{CO}_2} = 3.91 \text{ \AA}$, $\epsilon_{\text{N}_2} = 71.4 \text{ k}$, $\sigma_{\text{N}_2} = 3.791 \text{ \AA}$ and $\epsilon_c = 28.2 \text{ k}$, $\sigma_c = 3.4 \text{ \AA}$ [3].

The cut off radius was 2.5 times the collision diameter. For every state, 5×10^7 configurations were generated. The first 2×10^7 configurations were discarded to guarantee equilibration, whereas the remaining 3×10^7 configurations were used to average the desired thermodynamic properties. The simulation box ($100.0 \text{ \AA} \times 100.0 \text{ \AA} \times 45.0 \text{ \AA}$) contains one SWNT. It is worthy to point out that in this work the virial equation of state with second and third virial coefficients was used [14] to estimate the number of fluid molecules at different temperatures and pressures.

$$PV/NRT = 1 + B_{\text{mix}} P + C_{\text{mix}} P^2 \quad (1)$$

B_{mix} and C_{mix} are the mixture second and third virial coefficients with B_{ij} and C_{ijk} that are functions of temperature only. The comprehensive information has been explained in details in J.F. Estela-Urbe. et al work (4).

$$B_{\text{mix}} = \sum_i \sum_j x_i x_j B_{ij} \quad (2) \quad C_{\text{mix}} = \sum_i \sum_j \sum_k x_i x_j x_k C_{ijk} \quad (3)$$

3. Result and discussion:

3.1. Adsorption isotherms for equimolar mixture of CO₂/N₂

The results are shown in Fig 1, Represent that the adsorption capacity is an increasing function of pressures for all CNTs with the greater magnitude of CO₂ relative to N₂ in all simulation condition. This result is consistent with the fact that stronger interaction of carbon dioxide with nanotube surface results in higher adsorption capacity compared to nitrogen. Additionally, from this figure, it is clear that the effect of pore size is more significant to the adsorption capacity of carbon dioxide whereas it is

hardly exert its influence to the adsorption capacity of nitrogen. Additionally the volumetric density is a decreasing function of pore width due to the definition of volumetric density in this literature (n/V) where n is a total number of gas molecules and V is an inner volume of CNTs

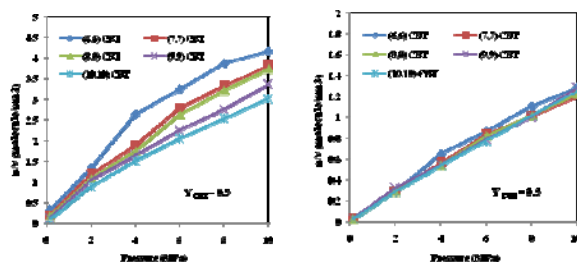


Fig. 1. Adsorption capacity isotherms of a) carbon dioxide b) nitrogen in carbon dioxide with different pore size at 323K.

3.2 .Selectivity:

In last section, the simulation reveals that there is an optimum pore size of $d=8.45$ nm in which the carbon nanotubes show maximum adsorption of gases, therefore, we take $d=8.45$ when we are investigating the effect of other factors on the adsorption behavior of gasses in this section, the effect of temperature, pressure and pore size were investigate in order to find the optimum condition for separation of CO_2/N_2 by means of carbon nanotube. Simulation results show that under identical condition the selectivity of carbon nanotube is greater than other materials considered in other works.

Fig. 2. depicts the dependence of adsorption selectivity of carbon dioxide and nitrogen with the increase of pressure from 0.15 MPa to 10 MPa when the pore width is $D=6.6$ nm. the selectivity is a decreasing function of pressure. In addition we can see from fig .2 that the selectivity of carbon dioxide over nitrogen increases when temperature falls. Additionally,

The pore width is a increasing function of pressure. From this fig it is clear that the optimum condition for carbon dioxide separation when $Y_{CO_2} = 0.5$ is $t=300K$, $p=0.15$ and pore size related to (6,6) CNT.

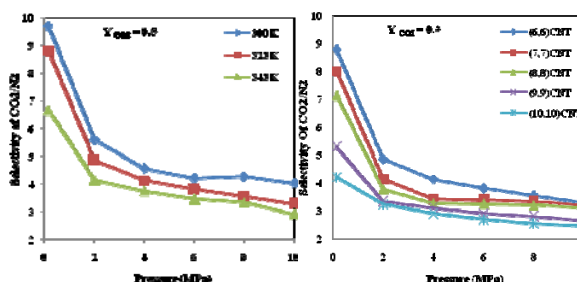


Fig. 2. Selectivity of carbon dioxide relative to nitrogen at various pressure at bulk composition of carbon dioxide $Y_{CO_2}=0.5$ (a) at pore size of $D=6.6$ nm and three temperatures, (b) $T=323$ K and different pore size of carbon nanotube.

4. Conclusion

Canonical Monte Carlo simulation was studied to investigate the adsorption and separation behavior of Carbon dioxide and nitrogen in carbon nanotubes. The effects of temperature, pressure and pore width on adsorption and separation behavior were explored. The Simulation results show that CO_2 is preferentially adsorbed over N_2 in CNTs. The most basic conclusion is, the selectivity is greater than unity in all cases, in consistent with the adsorption isotherms of both components. The selectivity of carbon dioxide over nitrogen versus pressure in different CNTs was obtained at three different temperatures. Results indicate that the selectivity is a decreasing function of pressure and pore width at investigated condition. In addition, increasing the temperature results the decreases of selectivity .it is because, when the temperature increases, the properties of two components approximately seems to become closer compared to lower temperatures. Finally, the optimum condition for selectivity of equimolar mixture of CO_2/N_2 via carbon nanotube was investigated.

References

- [1] Calbi, M. M. Cole. M. W. Phys. Rev. B 66 (2002) 115413.
- [2] Gatica.S. M. Bojan. M. J.. Stan,.G.. Cole.M. W. J. Chem. Phys. 114 (2001) 3765.
- [3] Yuxiang Jia.Meng Wang.and Lianying Wu. Separation Science and Technology. 42 (2007) 3681.
- [4] J.F. Estela-Urbe. J. Jaramillo. M.A. Salazar. J.P.M. Trusler. Fluid Phase Equilibria 204 (2003) 169.
- [5]

**Molecular dynamics studies on PolyG and PolyA in the presence of guanidine chloride**^aShahrbano Ghalehaghbabaei, ^aDavood Ajloo*^a Laboratory of Computational Biophysical Chemistry, School of Chemistry, Damghan University of Basic Science, Damghan, Iran
(ajloo@dubs.ac.ir, banoo.ghaleh@gmail.com)**Keywords:** Secondary structure, Polyalanine, Polyglutamine, Chemical denaturation, Molecular dynamics.**1. Introduction**

Homo-oligopeptides (HOPs) are multimers of the same amino acid. The peptides poly-(Ala) and poly-(Gln) are probably the best known representatives of HOPs because they possess important biological effects, and can cause various human illnesses, playing a relevant role in the formation of several neurodegenerative diseases [1–3]. Therefore, detailed structural investigation of poly-(Ala) and poly-(Gln) peptides is important in order to identify their conformational properties, which can help in understanding the mechanisms underlying these human illnesses and neurodegenerative diseases. The denaturing agents most largely employed in folding/unfolding experiments are urea and guanidinium chloride (GdmCl). The situation is further complicated by the fact that the molecular basis for denaturation by urea and GdmCl is still unclear. Two models have been proposed, one based on a direct, favorable interaction between the denaturant and the protein [4,5] and the other based on a modification of the hydrogen-bond structure of water and a consequent weakening of hydrophobic interactions [6]. In this work Denaturation of Poly-(Ala) and poly- (Gln) at alkaline pH and different temperatures in the absence and presence of different concentration of guanidine chloride was studied by molecular dynamics (MD) implemented in Gromacs 3.3.1. One molecule of poly- (Gln) including 21 amino acid and 21 negative charge immersed in a box with 4.5×4.5×4.5 nm³ and One molecule of Poly-(Ala) including 21 amino acid immersed in a box with 4.2×4.2×4.2 nm³. This was done by inserting one molecule of polypeptide and different number of sodium, chloride and guanidine ions at the wide range of time. After preparing the input files, the system optimized at 273, 285, 300, 315, 330, 360, 375 and 390K, also in concentration 10, 20, 30, 40, in the 20000 ps time scale. Physico-chemical parameters, such as, radial distribution function(RDF), radius of gyration(R_g), circular dichroism at 222 nm (CD222), solvent accessible surface area (SASA), midpoint of transition temperature (T_m), number and distance of hydrogen bond (HB)were obtained from analyzing output of molecular dynamics.

2. Materials and method

Structure of helix poly (21-Ala) and poly (21-Gln) peptides and GdmCl were constructed by hyperchem. The N and C termini of Poly (Ala) and poly- (Gln) are capped, respectively, by neutral acetyl and amide groups. Force field parameters and the topology for the Guanidinium Chloride molecule were generated using the PRODRG2 server (http://davapc1.bioch.dundee.ac.uk/cgi-bin/prodrg_beta). [7]. All MD simulations were carried out using the GROMACS 3.3 package [8]. The peptide was first placed in a cubic box with periodic boundary conditions. Water is described with the SPC model. As a rule, the electrostatic interaction implemented with PME, the thermal bath is coupled with the Nose-Hoover algorithm, and the time step is set to 20ns. Pressure coupling is Parrinello-Rahman. A nonbond pair list cutoff of 0.9 nm was used, and the nstlist was updated every ten steps. The box is a cubic with a volume of 74 and 91 nm³ for poly-(Ala) and poly-(Gln) respectively. the distance between the peptide and the box edges was chosen to be about 1 nm. This allows us to rule out any unwanted effects, which may arise from the applied periodic boundary conditions. Then, guanidine ions were located and oriented randomly around the peptides. Finally, water molecules nonoverlapping and certain ions were randomly added into the simulation box. The simulation trajectories were analyzed using several auxiliary programs provided with the GROMACS 3.3 package. After complementing the MD calculation CD222 nm, RDF, SASA and number and distance of hydrogen bond were obtained by g_helix, g_rdf, g_sas and g_hbond, respectively. For all simulations, the atomic coordinates were saved every 50 ps for analysis simulations were run on a 40-CPU.

3. Results and discussion

By averaging of CD222 at different temperatures and plotting versus temperature then by differentiation, inflection point can be obtained. Temperature at inflection point, T_m , is 348 and 366 K for poly-alanine (PA) and poly-glutamate (PG), respectively. That is mean; PG is more thermodynamic stable than PA. On the other hand, the transition state appears in the PA while in the PG does not observe. In addition, existence of cited transition state becomes more probable due to temperature



increasing. Protein-solvent hydrogen bond (1HB_{np}-sol) was plotted for both polypeptides. It increases and decreases by temperature for PA and PG, respectively. Protein-protein HB increases for both poly peptide while decreases. Reducing in PA or scattering water molecules from the protein surrounding make enhancing the beta structure. Radius of gyration, R_g, in PG increases while in the PA case it decreases due to formation of beta. Radial distribution functions (RDF) are similar in two polypeptides. Protein-denaturant RDF decreases at 3 Å in the presence of denaturant (DRG). RDF protein-solvent, ligand-solvent and protein- Na decrease, decreases, and increases respectively in charge of increasing the ligand. Root mean square deviation (RMSD) decreases for both poly-peptide. Hydrophobic surface increases by temperature for PG and it decreases for PA in why of difference between polypeptide structures.

References

- [1] Brown, L. Y. Brown, S. A. Trends Genet 20 (2004) 51.
- [2] Perutz. M. F. Curr Opin Struct Biol 6 (1996) 848.
- [3] Perutz, M. F. Trends Biochem Sci 24 (1999) 58.
- [4] Shellman, J. A. C. R. Trav. Lab. Carlsberg. 29 (1955) 223.
- [5] Kresheck, G. C. Scheraga, H. A. Phys. Chem. 69 (1965) 1704.
- [6] Frank, H. S. Franks, F. Chem. Phys. 48 (1968) 4746.
- [7] Schüttelkopf, A. W. van Aalten, D. M. Acta Crystallogr. Sect D, (2004) 60.
- [8] Van Der Spoel, D. Lindahl, E. Hess, B. Groenhof, G. Mark, A. E. Berendsen, H. J. J. Comput. Chem. 26 (2005) 1701.

Interaction between amylin peptide and dioleoylphosphatidylcholine: a molecular dynamics studyS. Jalili^a, B. Najafi^{b,*}, A. Maleki^b^aDepartment of Chemistry, K. N. Toosi University of technology, P. O. BOX 1587-4416, Tehran, Iran^{b,*}Department of Chemistry, University of Isfahan university of Technology, Isfahan, Iran^b(E-mail: a. maleki@ ch. iut. ac. Ir)**Keywords:** Amylin, Bilayer, Area per lipid, Lateral diffusion, Dioleoylphosphatidylcholine, DOPC.**1. Introduction**

Amylin is an endocrine hormone that regulates metabolism. In patients afflicted with type 2 diabetes, amylin is found in fibrillar deposits in the pancreas. Membranes are thought to facilitate the aggregation of amylin, and membrane-bound oligomers may be responsible for the islet beta-cell toxicity that develops during type 2 diabetes [1]. Amylin polypeptide consists of 37 amino acids with the sequence LYS¹-CYS²-ASN³-THR⁴-ALA⁵-THR⁶-CYS⁷-ALA⁸-THR⁹-GLN¹⁰-ARG¹¹-LEU¹²-ALA¹³-ASN¹⁴-PHE¹⁵-LEU¹⁶-VAL¹⁷-HIS¹⁸-SER¹⁹-SER²⁰-ASN²¹-ASN²²-PHE²³-GLY²⁴-ALA²⁵-ILE²⁶-LEU²⁷-SER²⁸-SER²⁹-THR³⁰-ASN³¹-VAL³²-GLY³³-SER³⁴-ASN³⁵-THR³⁶-TYR³⁷.

Its structure has been determined to a high resolution by NMR spectroscopy with the protein data bank (PDB) code of 2kB8.

As the number of membrane proteins in the Protein Data Bank increases, efforts to understand how they interact with their natural environment are increasing in importance. The results of experiments using model systems are revealing how these interactions contribute to the stability of both the protein and the membrane in which it is embedded [2]. MD simulations are rapidly becoming popular tools that complement experimental techniques in structural biophysics, such as neutron diffraction and NMR [3].

2. Methods

The simulation was performed using the GROMACS v 4.0.5 MD simulation package. Amylin (pdb code 2kB8) embedded in the lipid bilayer containing 126 dioleoylphosphatidylcholine (DOPC). The system was solvated with SPC (simple point charge) water and system-neutralizing sodium and chloride ions (corresponding to ~ 0.1 M NaCl) were added (Fig. 1). Electrostatic interactions were calculated using PME (Particle Mesh Ewald). The simulation was performed at constant temperature, pressure and number of particles (NPT). The LINCS algorithm was used to restrain bond lengths. The united atom lipid parameters were adapted from the work of Berger and co workers [4] and the parameters peptide used the GROMOS force field. Energy minimization (EM) by the steepest descent method was used to remove bad contacts and reduce the potential energy of the system. The system was subjected to a 1ns MD simulation using the NVT ensemble and then NPT ensemble.

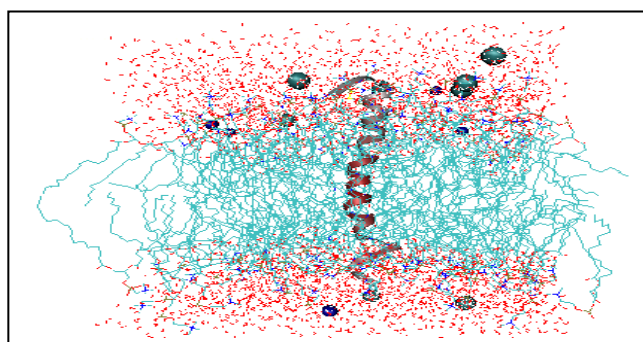


Fig . 1. Simulation snapshot of the Amylin in a DOPC bilayer

3. Results and discussion

The mean square displacement (MSD) contains information on the atomic diffusivity. From MSDs curves (Fig. 2), it is possible to obtain lateral diffusion coefficient. The lateral diffusions obtained are in the order of $10^{-8} \text{ cm}^2 \text{ s}^{-1}$. The trend in the lateral diffusion is tail > lipid > headgroup. It is found that the lipid tail determine the lateral diffusion, with negligible influence of the head group.

Typically Root mean square deviation (RMSD) is used to make a quantitative comparison between the structure of partially fold protein and the structure of native state. The calculated RMSD is higher for the protein than the protein backbone (Fig. 3) that is due to the higher flexibility of side chain atoms.

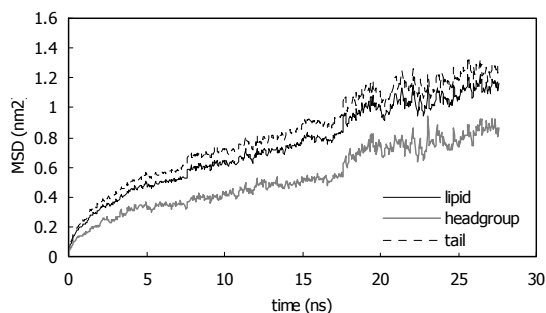


Fig. 2. The calculated MSDs of lipid (black line), Headgroup (Gray line) and tail (dash line) in the range of 27 ns.

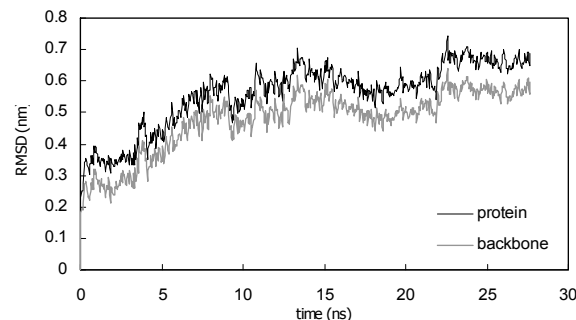


Fig. 3. RMSDs as the function of time for protein (black line) and back bone of the protein (gray line).

Lipid order parameter is a measure of the orientational mobility of the C-H bond and is defined as follow:

$$S = \left\langle \frac{3 \cos^2 \theta - 1}{2} \right\rangle \quad (1)$$

where θ is the (time depended) angle between the C-H bond vector and a reference axis. The angular brackets denote a time and ensemble average [5]. In this work order parameter decrease from the interface region to the bilayer center, also the difference between the Sn1 and Sn2 chain reveals that the Sn1 tail in DOPC is more ordered in the beginning of the chain, while the Sn2 is more ordered at its end (Fig. 4).

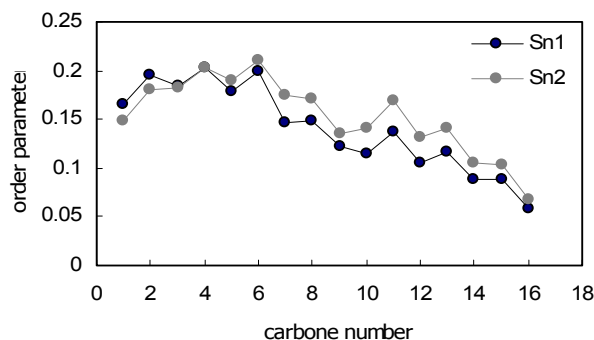


Fig. 4. Order parameter as the function of carbon number. Sn1 and Sn2 represen the two hydrophobic parts.

4. Conclusions

In this work we obtained mean square displacement (MSD), RMSD, lateral diffusion and order parameter. There are several types of analyses that we want to obtain such as density of the membrane environment, area per lipid head group, bilayer thickness (vertical dimension), number of contacts and H bonds between protein and lipid.

References

- [1] S. M. Patil, S. Xu, S. R. Sheftic, A. T. Alexandrescu, J. Biol. Chem. 284 (2009) 11982.
- [2] M. Sanderson, Peptide–lipid interactions: insights and perspectives, Org. Biomol.Chem. 3 (2005) 201.
- [3] K. Balali-Mood, T. A. Harroun, J. P. Bradshaw, Eur. Phys. J. 12 (2003) 135.
- [4] O. Berger, O. Edholm, F. Jahnig, Biophys. J. 72 (1997) 2002.
- [5] L. S. Vermeer, V. Reat, A. Milon, J. Czaplicki, Eur. Biophys. J. 36(2007) 919.

**Molecular dynamics simulation of nanoconfined fluids in napt ensemble**Farkhondeh Mozaffari^a, Hossein Eslami^b, Jalil Moghadasi^{c,*}^aDepartment of Chemistry, Islamic Azad university, Firoozabad branch, Firoozabad, Fars, Iran^bDepartment of Chemistry, College of Sciences, Persian Gulf University, Boushehr 75168, Iran^cDepartment of Chemistry, College of Sciences, Shiraz University, Shiraz 71454, Iran

E-mail: mozaffarif@yahoo.com

Keywords: Local density, Parallel component of pressure, Solvation force.**1. Introduction**

Understanding the properties of fluids at interfaces is of basic importance in many processes such as lubrication, adhesion, coating, chromatography, and membrane separation. In fact confining a fluid between two solid surfaces, whose separations are just a few molecular diameters affects significantly both equilibrium and nonequilibrium properties of fluids. In this work we extend the MD simulation method of Berendsen et al. [1] with coupling to an external bath to propose a new MD simulation method in the NAPT ensemble.

2. Method

The physical system of interest is a confined fluid consisting a fixed number of particles, between two parallel surfaces at a separation distance h . Coupling of the system to a heat bath with a fixed temperature T_0 is occurred as it is explained by Berendsen et al. [1] Coupling to a constant pressure bath can also be accomplished according to the similar method developed by Berendsen et al. [1] The pressure change is written as:

$$\left(\frac{dP_{||}}{dt} \right)_{bath} = \frac{P_{0,||} - P_{||}}{\tau_P} \quad (1)$$

where $P_{||}$ and $P_{0,||}$ are the instantaneous and target values of the parallel component of pressure, respectively, and τ_P is the time constant for pressure coupling, determining the strength of coupling to the barostat. $P_{||}$ is defined as:

$$P_{||} = \frac{P_{xx} + P_{yy}}{2} \quad (2)$$

$$= \frac{1}{3V} \sum_i m_i v_i^2 + \frac{1}{2V} \left[\sum_i \sum_j (X_{ij} \cdot F_{x,ij} + Y_{ij} \cdot F_{y,ij}) + \sum_i \sum_s (X_{is} \cdot F_{x,is} + Y_{is} \cdot F_{y,is}) \right]$$

where P_{xx} and P_{yy} are the x- and y-components of pressure tensor, respectively, m is the atomic mass, v is the velocity, V is the volume, subscripts i and j show the atoms in the confined region, subscript s stands for the surface atoms, X and Y are the relative distances between particles in the x and y directions, respectively, and F_x and F_y are their corresponding forces. The pressure change can be accomplished by changing the virial through scaling of interparticle distances in the z direction.

As the original algorithm proposed by Berendsen et al., [1] we incorporated the scaling terms for velocities and coordinates into a leap-frog algorithm [2]. Therefore, the algorithm is essentially the same as that of Ref. 1, except by comparing the parallel pressure to its pre-specified value we did coordinates scaling, just for z-coordinates of the particles

In this simulation only the confined region at constant NAPT is simulated. Here $P_{||}$ is fixed to the corresponding bulk pressure. To validate the simulation method outlined in this work, we chose a well-known system for which we can compare the results of our method. We chose the same system chosen by Schoen et al. [3-5] in their GCEMC simulation and Wang and Fichthorn [6] in their NAPT ensemble MD simulation. The system is liquid Ar confined between two solid surfaces of Ar, each of which composed of five layers of fcc (100) with a lattice constant of 0.5443 nm. The surfaces are made by replicating the fcc (100) unit cell in x, y, and z directions by 5×5×5, therefore each layer has 50 Ar atoms separated by lattice constant in each dimension and the corresponding box size in x and y dimensions are each 2.72 nm. It is assumed that the fluid-fluid and fluid-surface interactions are of Lennard-Jones (LJ) type.

$$U = 4\varepsilon \left[\left(\frac{\sigma}{r} \right)^{12} - \left(\frac{\sigma}{r} \right)^6 \right] \quad (3)$$

where U is the potential energy of interaction between a pair of particles, r is their separation distance, ε is the potential energy



well depth, and σ is the distance at which $U=0$. The LJ parameters for Ar are the conventional ones; $\sigma=0.3405$ nm and $\varepsilon=0.996$ kJmol⁻¹. In this simulation the cutoff distance was 1.2 nm (3.5σ) and long-range corrections were performed according to the formulation of Wang and Fichthorn.[6] The temperature was set at 119.8 K and two set of simulations were performed at 20.37 MPa and 1.675 GPa in order to compare the results with Wang and Fichthorn's results [6] and previous GCMC simulation results [3-5]. As it is described in the former section a Berendsen thermostat was used to keep the temperature constant and the method explained was used to keep the parallel component of pressure fixed.

3. Results and discussion

A large number of systems in which the number of Ar atoms varies between 50 to 350 were chosen and two set of simulations were performed; one at $T=119.8$ K and $P_{||}=20.37$ MPa and another one at $T=119.8$ K and $P_{||}=1.675$ GPa. As a result the surface distance, h , was varied during the simulation until getting the pre-specified $P_{||}$. The fluid molecules were treated dynamically while the surface atoms were static. Periodic boundary conditions were applied in the x and y directions.

The equilibrium local density profiles extracted over a 2 ns span. The local density oscillates with respect to the distance between the confining surfaces. The results are the same as the NAPT ensemble MD simulation results of Wang and Fichthorn [6].

Specifying the parallel component of pressure, we can calculate the vertical component of pressure, P_{\perp} , which is an important quantity in calculating the solvation force. The solvation force, which is the required force to hold the two surfaces at a specified separation, is calculated as the difference between the vertical and the parallel components of pressure. Our results are in agreement with the previously reported results generated using GCEMC simulation [3-5] and with the results reported by Wang and Fichthorn [6] using NAPT ensemble MD simulation method. It is known that better layered structures with sharper density peaks correspond to higher, more repulsive, solvation forces.

Also the dependence of N on the surface separation is in complete agreement with NAPT ensemble MD simulation results of Wang and Fichthorn [6] and with the former GCEMC simulation results [3-5]. The results show that as the distance between the confining surfaces changes gradually, the fluid particles are adsorbed into or desorbed out of the confining region. When the particles desorbs from a layer in a confined region, a new layer will be made and vice versa.

4. Conclusions

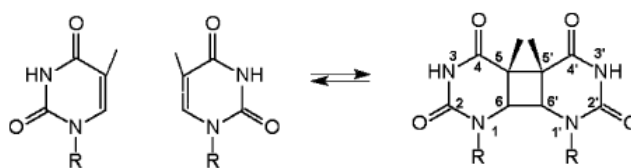
We have presented a new simulation method for simulating confined fluids. The method is able to control pressure or stress in any desired direction. Although the method has been employed here to simulate the confined fluids, it can also be useful in such fields as molecular ultra thin films at interfaces and the elasticity and failure in solids. The method has been validated against the GCEMC simulation results [3-5] and the constraint NAPT ensemble MD simulation results of Wang and Fichthorn [6]. The method is very convenient for calculating the solvation force and the effect of pressure on solvation force. Here it is assumed that the parallel component of pressure is uniform throughout the confining region and is equal to the bulk pressure in surface force measurements. Unlike the method of Wang and Fichthorn [6] which uses a constraint method to keep the pressure constant, the present method keeps the pressure constant via coupling to an external bath.

References

- [1] H. J. C. Berendsen, J. P. M. Postma, W. F. Van Gunsteren, A. DiNola, and J. R. Haak, J. Chem. Phys. 81 (1984) 3684.
- [2] M. P. Allen, D. J. Tildesley, Computer Simulation of Liquids, Clarendon Press: Oxford, 1987.
- [3] M. Schoen, D. J. Diestler and J. H. Cushman, J. Chem. Phys. 100 (1994) 7707.
- [4] M. Schoen, D. J. Diestler and J. H. Cushman, Phys. Rev. B, 47 (1993) 5603.
- [5] M. Schoen, D. J. Diestler and J. H. Cushman, J. Chem. Phys. 87 (1987) 5464.
- [6] J. C. Wang and K. A. Fichthorn, J. Chem. Phys. 112 (2000) 8252.

Investigation of damaged DNA double strand using molecular dynamics simulationAmin Arabbagheri^a, Gholam Abbas Parsafar^{b,*}^{a,b} Department of chemistry and nanotechnology research center, Sharif university of Technology, Tehran, Iran
(E-mail: amin_arab@yahoo.com)**Keywords:** Molecular dynamics, Amber, Thymine, DNA double strand**1. Introduction**

Dimerization of thymine groups in DNA has been reported as a major damage in biological cells. It occurs by radiation of UV light for example in human skins[1], shown schematically in Figure 1. Formation of T<>T takes place where a thymine group is next to another one in a DNA double strand sequence. Special type of enzyme, photolyase, efficiently repairs such damage. Lack of suitable experiments, quantum chemical computations mixed with molecular dynamics has been employed to investigate such mechanisms [2]. It is interesting to find out which dynamical behavior of a damaged double strand, makes it unstable, in a way that it causes photolyase to repair it.

**Fig. 1.** Formation of thymine dimer caused by UV radiation.**2. Method**

We are using AMBER99 as the force field, it works properly for biological system and specially for DNA simulations [3]. We used rectangular periodic boxes which contain TIP3P water models as solvent. We took as initial configuration, the X ray structure of a DNA double strand containing a cis-syn thymine dimer, d[GCTTAATTTCG]d[CGAAT<>TAAGC] , with PDB entry 1N4E. This system has been neutralized with eighteen sodium counter ions. The engine Gromacs , which has been developed in the university of Groningen [4], has been employed for this work.

In this work we will use also non-invasive technique to couple only solvent with the thermostat, instead of using a thermostat per each part of the system. It has given more realistic results in some cases.

3. Results and discussion

Figure 2 shows twisted region of the double strand after 1 ns simulation. After a short simulation there is a relative stability for the damaged strand which is necessary to obtain longer trajectories. There is another possibility for cytosine groups to act like thymine groups and also to form a cyclobutane between T and C groups, but it needs parameters for bond lengths, angels, dihedrals, etc which are obtainable from restrained electrostatic potential fit calculations, which is compatible with AMBER philosophy [4].

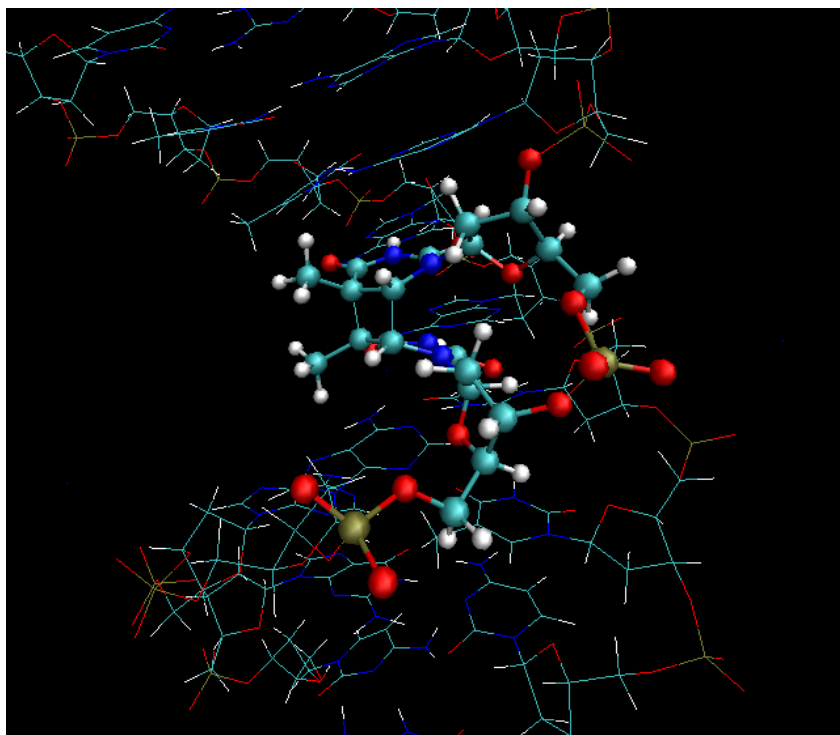


Fig. 2. Coordinates of T15 and T16 after 1 ns simulation.

References

- [1] M. R. Holman, T. Ito, S. E. Rokita, J. AM. CHEM. SOC, 129 (2006) 6.
- [2] F. Masson, T. Laino, U. Rothlisberger, J. Hutter, ChemPhysChem 10 (2009) 400.
- [3] F. Masson, T. Laino, I. Tavernelli, U. Rothlisberger, J. Hutter, journal of American chemical society, 130 (2008) 3443.
- [4] D. Van der Spoel, E. Landahl, B. Hess, G. Groenhof, A. E. Mark, H. J. C. Berendsen, J Comput Chem, 26 (2005) 1701.

**Diffusion of different refrigerants in zeolite FAU: A molecular dynamics study**R. Rabiei^a, M. Loghavi^a, F. Amirseifadini^a, S. Alavi^b, H. Mohamadimanesh, B. Najafi^{a,*}^aDepartment of chemistry, Isfahan University of Technology, Isfahan, Iran^bDepartment of chemistry, University of Ottawa, Ottawa, Canada

(E-mail: rzh.rabiei@gmail.com)

Keywords: FAU zeolite, Simulation, CF₂Cl₂, Molecular dynamics, Diffusion.**1. Introduction**

The diffusion of halocarbons refrigerants in zeolites is attracting a great deal of attention at present due to its relevance to environmental issues concerning ozone-depleting chlorofluorocarbons (CFCs) [1] and the removal of chlorinated solvent residues from contaminated groundwater and soils [2]. For example, NaY zeolite can be used to separate various hydrofluorocarbons (HFCs) during the manufacture of CFC substitutes [3]. This paper deals with the diffusion of CF₄, CF₃Cl, CF₂Cl₂, and CFCI₃ in FAU zeolite by means of molecular dynamics simulation.

The suitable potential parameters were used [4],[5] to describe the interaction between the guest molecules, guest molecules and zeolite and within the zeolite framework. Using these interatomic potentials, diffusion coefficients for different refrigerants and also activation energy for the adsorbate motions within FAU zeolite are evaluated.

2. Methods

The zeolite host were modeled as follows: siliceous faujasite (FAU), Si₁₉₂O₃₈₄ (Si:Al=∞), with q(Si)=+2.4 and q(O)=-1.2. Charges for guest molecule (CF₂Cl₂) consist of: q(C)=+0.210, q(F)=-0.086, and q(Cl)=-0.019 [5].

The interatomic potentials previously described for modeling the whole system were implemented in the DL_POLY program in the NVT ensemble and then NVE ensemble. A time step of 1fs was selected, with simulation run at loading of 8 molecules per unit cell. The simulations spanned a range of temperatures between 200 and 700 K, each for 5×10⁶ steps, following 3×10⁶ steps of equilibration (NVT ensemble). A cutoff 13 Å was used. The trajectory was recorded every 20000 steps during the production stage. The mean square displacements (MSDs) of CF₂Cl₂ molecules at different temperatures were evaluated by means of the following classical equation:

$$MSD(t) = \left\langle \Delta r_j^2(t) \right\rangle = \frac{1}{N} \sum_{j=1}^N \Delta r_j^2(t) = \frac{1}{N} \sum_{j=1}^N [r_j(t) - r_j(0)]^2$$

where N corresponds to the number of CF₂Cl₂ molecules considered in the computation of the MSD.

The diffusion coefficients were obtained by fitting the MSD plots as a function of the time, assuming the following Einstein relation:

$$MSD(t) = A + 6Dt$$

The activation energy corresponding to the self-diffusion processes were then evaluated from the linear least-squares fit to the Arrhenius plots assuming the following relation:

$$D = D_0 \exp\left(-\frac{E_a}{RT}\right)$$

where D₀ is the diffusion coefficient at infinite temperature.

3. Results and discussion

The diffusion coefficients of different refrigerants in zeolite FAU are calculated and the effect of increase of F atom in molecules is investigated. For example, Figure 1 reports the MSDs for CF₂Cl₂ in FAU zeolite as a function of the temperature. As is shown, the MSDs increase with temperature.

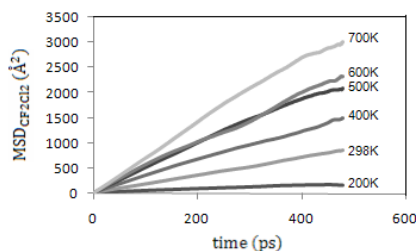


Fig. 1. MSD plots for CF_2Cl_2 in FAU at various temperatures.

The values of the diffusion coefficients derived from the MSDs are reported in Table 1.

T (K)	Diffusion coefficient (m^2s^{-1})
200	6.78×10^{-10}
298	3.407×10^{-9}
400	4.291×10^{-9}
500	6.936×10^{-9}
600	9.961×10^{-9}
700	1.001×10^{-8}

Table 1. Diffusion coefficients (m^2s^{-1}) calculated for CF_2Cl_2 in FAU at various temperatures.

The data for 8 CF_2Cl_2 molecules per unit cell are shown as Arrhenius plot in figure 2, which yields an approximate value of 2.7 kJ mol^{-1} for CF_2Cl_2 at this loading.

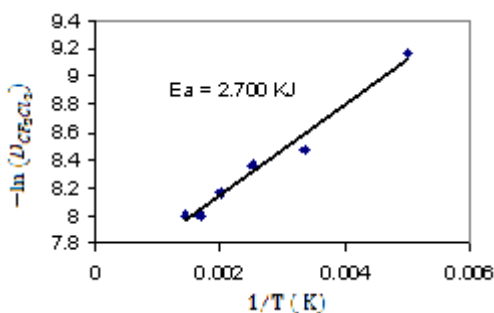


Fig. 2. Arrhenius plot showing activation energy.

References

- [1] Manzer, L. E. Science. 24 (1990) 931.
- [2] Hutchings, G. J., Heneghan, C. S., Ian, D. H. and Taylor, S. H. Nature. 384 (1996) 341.
- [3] Corbin, D. R., Mahler, B. A. World Patent, W. O. 94 (1994) 24.
- [4] Plant, D. F., Maurin, G. and Bell, R. G. J. Phys. Chem. B.111 (2007) 2836.
- [5] Mellot, C. F. and Cheetham, A. K. J. Phys. Chem. B.103 (1999) 3864.



Study properties of imidazolium-based bromide ionic liquid's and effect of alkyl chain length by molecular dynamic simulation

V. Sokhanvaran, S. Yeganegi, A. Soltanabadi

Department of Physical and Inorganic Chemistry, Faculty of Chemistry, University of Mazandaran, Babulsar, Iran.

(E-mail: v.sokhanvaran@gmail.com)

1. Introduction

Ionic liquids represent a class of chemicals that composed of large asymmetric organic cation and inorganic anion. Room temperature ionic liquids or briefly ionic liquids that remain in the liquid state in a wide range of temperatures (ILs) have attracted much attention due to their peculiar chemical and physical properties such as near-zero vapor pressure, large liquid range, nonflammability, thermal stability, high ionic conductivity, large electrochemical Window, controllable polarity, and the ability to solvate compounds of widely varying polarity [1-2]. Applications of ionic liquids can be numerous, from catalysis, synthesis, separations, and electrochemistry to polymers and magnetic or nanostructures materials. Understanding the physical properties of ionic liquids (ILs) via computer simulation is important for their potential technological applications [3]. In principle molecular dynamics (MD) simulations can be a powerful tool to obtain structural, dynamical properties systematic [4]. The imidazolium ionic liquids have been subject of many simulation studies although; the experimental and theoretical investigations on the imidazolium bromide are rare. Recently Sadeghi et al. [5] have studied mixtures of imidazolium bromide ILs and water experimentally. This has motivated us to perform a systematic study on the structural and dynamical properties of this ILs by MD simulations.

2. Method and Simulation details

We have chosen the united atom force field functional form for the potential energy. This UA model was derived from their all atom force field with the same functional form given by below equation.

$$U = \sum_{bonds} k_r (r - r_0)^2 + \sum_{angles} k_\theta (\theta - \theta_0)^2 + \sum_{dihedrals} k_\chi [1 + \cos(n\chi - \delta)] + \sum_{i < j} 4\epsilon_{ij} \left[\left(\frac{\sigma_{ij}}{r_{ij}} \right)^{12} - \left(\frac{\sigma_{ij}}{r_{ij}} \right)^6 \right] + \sum_{i < j} \frac{q_i q_j}{r_{ij}}$$

where U represents the total energy of the system. All these parameters for the intra-and intermolecular interactions are given by Liu et.al [6]. Molecular dynamic simulations of ionic liquid [RMIM][Br] were performed using the DL_POLY package with the following protocol: (a) the simulations were carried out in the NPT ensemble; (b) a Nose-Hoover thermostat was used to maintain the temperature $T = 298.15$ K and a Berendsen pressure coupling kept the pressure $p = 1$ atm; (c) the initial configuration was obtained by randomly disposing 216 [RMIM][Br] ion pairs in a cubic box. Standard periodic boundary conditions and the minimum image convention were applied. A time step of $t = 0.001$ ps and cut off distance of 1.4 nm was used and The Ewald summation was used for the long range electrostatic interactions. The trajectories were integrated by the leapfrog algorithm. The equilibration period consists of a 4ns NPT trajectory follows by 1ns production phase.

3. Results and Discussion

At first the structures of cation were optimized at B3LYP/6-31++G(d,p) level by using Gaussian 03 package, and the minimized structures were used in classical MD simulations. The structures, thermodynamics, and dynamical properties of three ionic liquids, 1-alkyl-3 methyl imidazolium bromide were studied. The liquid density calculated can be used to validate the force field proposed in MD simulation. The value of density was obtained directly in NPT ensemble. Each simulation required over 4 million MD configurations to properly equilibrate the periodic boxes. The computed densities for three ionic liquid [HMIM][Br], [BMIM][Br], [EMIM][Br] are given in Table (1).

Table1. Simulated densities (gr/cc) of [RMIM][Br] ionic liquids at 298.15 K

[EMIM]Br	[BMIM]Br	[HMIM]Br
1.42812	1.31037	1.23393

A correlation between liquid density and the carbon atom number of $[C_n\text{mim}][\text{Br}]$ are shown in Fig. 1. Radial distribution

functions (RDFs) is a kind of distribution functions, which can be used to characterize the microscopic structure of the ionic liquids. It represents the distance-dependent relative probability of observing a given site or atom relative to some center sites or atoms. In order to investigate the influence of the anion on different ionic liquids, radial distribution functions (RDF) obtained for anion-anion are shown in Fig. 2 and Fig. 3 shows that RDFs for characteristic sites of the [RMIM][Br] ILs at 298.15 K as a function of the cation size: tail-tail (CT3-CT3). The first maxima of the CT3-CT3 RDFs on the other side are remarkably increasing with increasing length of the alkyl side chain, indicating again the tendency of the tails to aggregate.

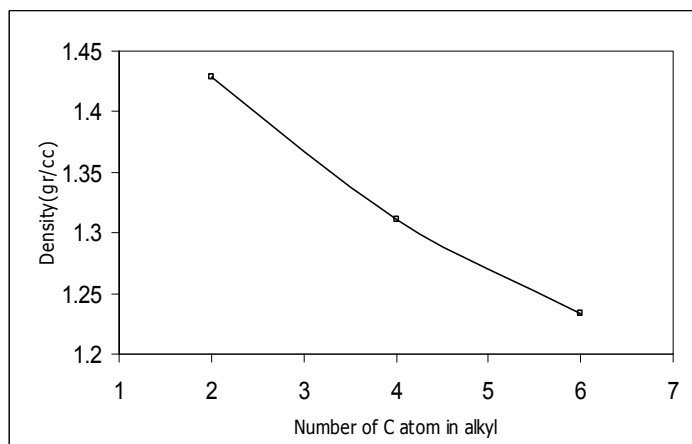


Fig. 1. Calculated density as a function of ILs chain length at 298.15 K and 1 atm.

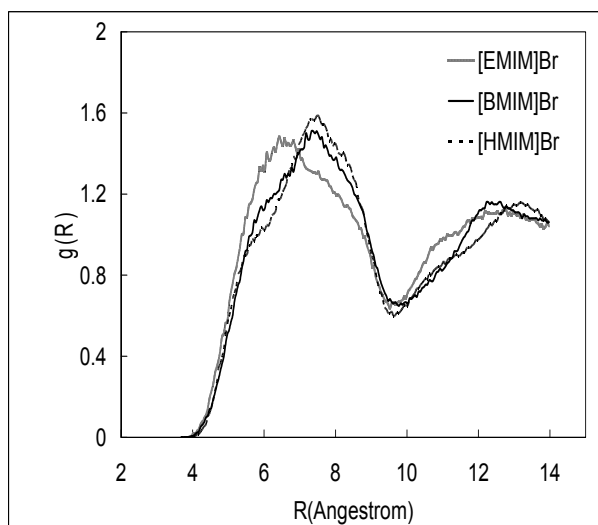


Fig. 2. Br-Br RDFs for various ILs at 298.15 K and 1atm.

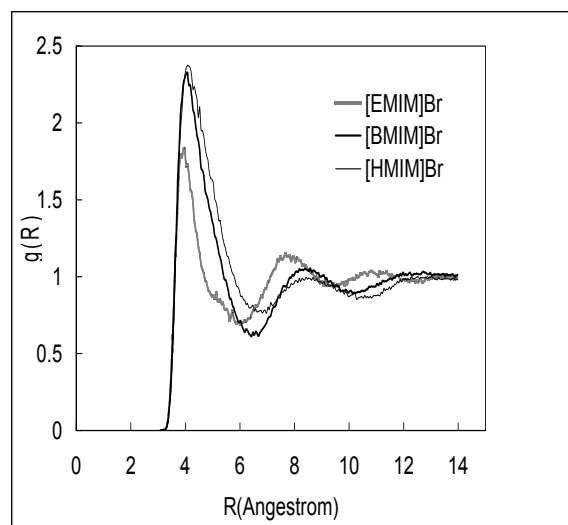


Fig. 3. Tail-Tail RDFs for various ILs at 298.15 K and 1atm.

References

- [1] W. Zhao, B. Heggen, S. Zahn, B. Kirchner, S. Balasubramanian, *J. Am. Chem. Soc.* 131 (2009) 15825.
- [2] X. Liua, G. Zhouab, S. Zhanga, G. Yu, *J. Molecular Simulation.* (2009) DOI: 10.1080/08927020903124569.
- [3] Y. Wang, W. Jiang, T. Yan, G.A. Voth, *J. Acc. Chem. Res.* 40 (2007) 1193.
- [4] G. Raabe, J. Kohlr, *J. Chem. Phys* 128 (2008) 154509.
- [5] H. Shekaari, Y. Mansoori, R. Sadeghi, *J. Chem. Thermodynamic* 40 (2008) 852.
- [6] Z. Liu, X. Wu, W. Wang, *Phys. Chem. Chem. Phys.* 8 (2006) 1096.

**Molecular dynamics simulation of hydrated nafion in sandwich model**H. Abroshan ^a, H. Akbarzadeh ^a, G.P. Parsafar ^a, E. Alizadeh ^b, S.A. Mousavi ^c^a Department of chemistry, Sharif University of Technology, Tehran, Iran^b NDSTRI, Malek-Ashtar University of Technology, Fereydoon Kenar, Iran^c Department of chemical engineering and petroleum, Sharif University of Technology, Tehran, Iran

(E-mail: hadi.abroshan@yahoo.com)

Keywords: Nafion, Water molecules, Molecular dynamics, NAMD, Sandwich model.**1. Introduction**

The last decade has seen greatly increased activity in the search for stable and cost-effective ion-exchange membranes for use in the proton exchange membrane fuel cells (PEMFC) [1]. These materials must fulfill a range of demanding requirements: high protonic and low electronic conductivity; hydrolytic, oxidative and thermal stability, and low fuel permeability. The environment within the membrane is aqueous, strongly acidic and tolerant to relatively high temperatures (ca. 100 °C) – with peroxides formed as reaction products at the catalyst [2]. Nafion has received a considerable amount of attention as a proton conductor for proton exchange membrane (PEM) fuel cells because of its excellent thermal and mechanical stability. It has the following structure. $-(CF_2-CF_2)_m-CF_2-CF(R-SO_3^-)$. The chemical basis of Nafion's superior conductive properties remains a focus of research. The morphology of Nafion membranes is a matter of continuing study to allow for greater control on its properties. Other properties must be related to the Nafion structure such as water management, hydration stability at high temperatures, electro-osmotic drag, as well as the mechanical, thermal, and oxidative stability. There are some proposed models for Nafion, Cluster-Channel or Cluster-Network Model, core-shell model, rod model [3]. The sandwich model has recently been proposed in which the polymer forms two layers whose sulfonic groups attract across an aqueous layer where transport occurs [4]. In this study we performed molecular dynamics simulation of five hydrated Nafion with different value of *m* (5-9) in order to get insights about this model and equilibrium and dynamics properties of its components.

2. Methods

Single chains of Nafion was created using Gaussview software and was minimized and equilibrated with NAMD package [5] and GAFF force field [6]. The resulting structure was replicated using VMD package [7] to form a sandwich structure of Nafion. Water molecules and appropriate number of hydronium ions were added to the systems, considering the hydrated coefficient in all systems to be 15 and then the energy minimization was done. This has been followed by a simulated annealing procedure that involved four steps: (a) the final structure obtained from the minimization step was heated from 300 to 550 K over a period of 50 ps using the NVT ensemble. (b) The final configuration obtained from the NVT simulation of step (a) was used as an input for a subsequent MD simulation performed at 1000 K using the NPT ensemble for a period of 50 ps. (c) The final configuration from the NPT simulation of step (b) was taken as the initial configuration for MD simulation with cooling from 550 to 300 K over a period of 50 ps using the NVT ensemble. (d) Finally, a MD simulation using the NPT ensemble was performed at 300 K for 50 ps. The annealing procedure was repeated three times, and a final density of 1.7 g/cm³ was obtained for this model. Molecular dynamics simulation was then continued for 2 ns.

3. Results and discussion

Structural analysis shows that relationship among sulfonated groups seems to be like a W shape. Increasing in *m* may lead to form a stretched W shape. On the other hand hydronium ions are located among sulfonated groups to form a bridge among them. Root mean square deviation (RMSD) results, which has an intimate relationship with the diffusion coefficient, show a high value when *m* is chosen to be 6. Interaction energy calculation between different parts of model was done and result shows that the stabilizing interaction of all systems are considerable but it will be decreased with *m* which means, there is a reverse relationship between the stabilizing interaction energy and *m*. It should be noted that the most interaction is electrostatic type and the van der Waals interactions dose not contribute as the electrostatic one.



References

- [1] J. Larminie, A. Dicks, Fuel cell systems explained. Wiley, Chichester, UK, 2003.
- [2] B. Smitha, S. Sridher, A. A. Khan, J. Memb. Sci. 259 (2005) 10.
- [3] K. A. Mauritz, R. B. Moore, Chemical Reviews, 104 (2004) 4535.
- [4] H.G. Haubold, Th. Vad, H. Jungbluth, P. Hiller, Electrochimica Acta, 46 (2001) 1559.
- [5] J.C. Phillips, R. Braun, W. Wang, J. Gumbart, E. Tajkhorshid, E. Villa, C. Chipot, R.D. Skeel, L. Kale, K.J. Schulten, Comput. Chem., 26 (2005) 1781.
- [6] J. Wang, P. Cieplak, P.A. Kollman, J. Comput. Chem. 21 (2000) 1049.
- [7] W. Humphrey, A. Dalke, K. Schulten, J. Molec. Graphics. 14 (1996) 33.



Canonical Monte Carlo simulation of adsorption of pure and binary mixture of hydrogen and methane on silicon nanotube: temperature, pressure and bulk composition effects

*Sahra Balilehvand ^a, S.Majid Hashemianzadeh ^b, Saleheh Razavi ^b

^a Department of Chemistry, University of alzahra, Tehran, Iran

^b Molecular Simulation Research Laboratory, Department of Chemistry, Iran University of Science and Technology, Tehran, Iran

(E-mail: sahra_balilehvand@yahoo.com)

Keywords: Single-walled silicon nanotube, Molecular simulation, Gas adsorption, Adsorption isotherm, Lennard-Jones potential.

1. Introduction

With the development and progress of human society, the fossil fuels of coal, petroleum, and others are consumed drastically. Exploiting new and effective alternative energy sources is urgently required. Both H₂ and CH₄ are renewable clean energy sources. But a storage technology with low cost and high energy density is of critical importance. Compared to compressed natural gas (CNG) technology, adsorption natural gas (ANG) technology is very promising and efficient, because ANG requires a relatively low pressure of about 4 M Pa to be stored in lightweight carrier, whereas CNG is often stored in heavy steel cylinders at high pressures, 20-30 M Pa. Novel carbon-based nanomaterials, such as single-walled carbon nanotubes (SWNTs), worm-like SWNTs, double-walled carbon nanotubes (DWNTs), stacked-cup carbon (SCCNT), doped fullerenes, and ordered porous carbons have been regarded as promising media for efficient reversible storage of chemical species[1]. With the successful synthesis of silicon nanotubes (SiNTs) by the chemical vapor deposition (CVD) method in 2002 [2] and because of silicon Compared to carbon, has more electrons in the outer shells, which leads to higher polarizability and a stronger dispersion force, the SiNT may exhibit a stronger van der Waals (VDW) attraction to gasses than CNTs. In this paper, we present the standard CMC simulation to reveal the adsorption behaviour of pure H₂ and CH₄ and their mixture on the outer and inner surface of (14,14) SWSiNT. In addition the effect of temperature, pressure and bulk composition on the adsorption isotherms was studied.

2. Model and Simulation details

A standard canonical Monte Carlo simulation is employed in this work. We considered here the ideal (14,14) SiNT models that was selected to be studied exhibit a diameter of about 30 Å, and heights of about 37 Å [3,4]. In this study, the interactions between fluid molecules are described by a (12-6) LJ potential [5]. For interactions between fluids and silicon nanotube a Lennard-Jones type of potential of (9 - 6) functional form was used [5]. The Lennard-Jones parameters for SiNT were estimated by Lorentz-Berthelot mixing rules where $\sigma_{H_2}=2.958$ (Å⁰), $\epsilon/k_B H_2=36.7$ (K), $\sigma_{CH_4}=3.81$ (Å⁰), $\epsilon/k_B CH_4=148.1$ (K), $\sigma_{SiNT}=4.482$ (Å⁰) and $\epsilon/k_B SiNT=127.96$ (K).

The cut off radius was 2.5 times the collision diameter. For every state, 2*10⁷ configurations were generated. The first 1*10⁷ configurations were discarded to guarantee equilibration, and the remaining 1*10⁷ configurations were used to ensemble average values of thermodynamic properties. The simulation box (200.0 Å × 100.0 Å × 45.0 Å) contains one SWNT. For achieve more accurate result the virial equation of state with second and third virial coefficients was used to estimate the number of fluid molecules at different temperatures and pressures as shown in the following equation [6].

$$PV/NRT=1+B_{mix}P+C_{mix}P^2 \quad (1)$$

B_{mix} and C_{mix} are the mixture second and third virial coefficients, which are functions of temperature and composition through the relations:

$$B_{mix} = \sum_i \sum_j x_i x_j B_{ij} \quad (2)$$

$$C_{mix} = \sum_i \sum_j \sum_k x_i x_j x_k C_{ijk} \quad (3)$$

In Eq. (2) and (3), x_i, x_j and x_k are the mole fractions of the ith, jth and kth components of the mixture. B_{ij} and C_{ijk} are, respectively, interaction second and third virial coefficients, which are functions of temperature only and reported by Estela Uribe [6].

3. Results and discussion

3.1 Effect of pressure and temperature on the adsorption of pure CH₄ and H₂

Isotherms adsorption of H₂ and CH₄ on (14, 14) SWNT are obtained at supercritical temperatures (283, 293, 303 and 313K) (Fig.1). Results disclose that all adsorption isotherms increase with gas pressure. Both H₂ and CH₄ gravimetric densities exhibit similar behaviour, our results reveal that the amount of H₂ and CH₄ adsorbed on the inner surface of SWNT is more than outer side. It should be mentioned that gravimetric storage capacity for CH₄ is larger than that of H₂ in the same SiNT. This may be related to the competitive adsorption between methane and hydrogen on the pore surface.

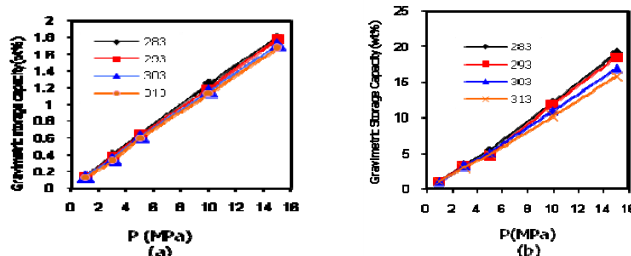


Fig. 1. Adsorption isotherms of pure H₂ on (14, 14) SWSiNT at different temperatures (a) total H₂ gravimetric capacity.(b) total CH₄ gravimetric capacity.

3.2 Effect of pressure and temperature on the adsorption of equimolar CH₄/ H₂ mixture.

Gravimetric storage capacity of an equimolar mixture of real H₂ and CH₄ gasses is plotted versus pressure at 298, 313 temperatures (Fig2). It can be observed that all adsorption isotherms show a Langmuir shape (type I). It can be concluded that all adsorption isotherms behave the same as that for pure gasses.

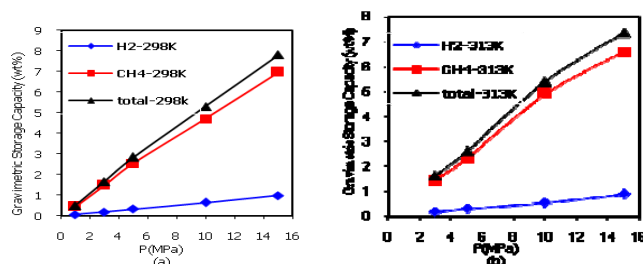


Fig.2. Adsorption of an equimolar H₂ and CH₄ mixture at (a) 298K and (b) 313K as a function of bulk pressure.

3.3 Effect of bulk composition on the adsorption of CH₄/ H₂ mixture

The effect of the bulk composition on the adsorption of CH₄/H₂ system, when the temperature is 298K and the pressure is 15 MPa, were studied. It can be seen that a higher adsorption capacity can be achieved with the increase of mole fraction of methane in the bulk.

4. Conclusion

Canonical Monte Carlo Simulations were performed to investigate the adsorption behaviour of pure and an equimolar H₂/CH₄ mixture in SiNT. All adsorption isotherms at supercritical temperatures exhibit Langmuir isotherm shape (type I). Both CH₄ and H₂ can be adsorbed on the inner surface of tube more strongly compared to the outer surface. Gravimetric storage capacity for CH₄ is larger than that of H₂. It is based on the more interaction between methane and pore surface than hydrogen interaction. It can be concluded that a higher adsorption capacity can be achieved with the increase of mole fraction of methane.

References

- [1] Mu, C.; Yu, Y. X.; Liao, W.; Zhao, X. S.; Xu, D. S.; Chen, X. H.; Yu, D. P. Appl. Phys. Lett. 87 (2005) 113104.
- [2] Sha, J.; Niu, J. J.; Ma, X. Y.; Xu, J.; Zhang, X. B.; Yang, Q.; Yang, D. R. Adv. Mater. 14 (2002) 1219.
- [3] Darkrim, F.; Levesque, D, J. Chem. Phys. 109 (1998) 4981.
- [4] J.F.EstelaUribe, J. Jaramillo, M. A.Salazar, J.P.M.Trusler, Fluid Phase Equilib. 204(2003) 169.
- [5] George P. Lithoxoos, Jannis Samios, J. Phys. Chem. C 112 (2008) 43.
- [6] J.F. Estela-Uribe, J. Jaramillo, M.A. Salazar, J.P.M. Trusler, Fluid Phase Equilib. 204 (2003) 169.



Molecular dynamics simulation of the viscosity of ionic liquids

Nargess Mehdipour* and Hossein Eslami

Department of Chemistry, College of Sciences, Persian Gulf University, Boushehr 75168, Iran

(E-mail: mnargess@hotmail.com)

1. Introduction

The room temperature ionic liquids (RTILs) are being considered as new organic and inorganic solvents and materials of practical importance. Although the RTILs have been the subject of considerable experimental measurements, still less is known about the connection of their macroscopic properties to their molecular properties. However, molecular simulations of pure ionic liquids and their mixtures have been applied to describe their structure-property relations [1]. Application of highly viscous ionic liquids is hindered due to the difficulties in their handling in such processes as pumping, mixing, and stirring. Therefore, the shear viscosity of RTILs is of fundamental importance for their practical applications. This work is planned to perform molecular dynamics (MD) simulation to calculate the shear viscosity of a recently parameterized RTIL, 1-n-Butyl 3-Methylimidazolium bis(Trifluoromethylsulfonyl)imide, [bmim][Tf₂N], [2].

2. Method

The viscosity coefficient can be calculated using equilibrium or non-equilibrium MD simulations, in which an appropriate perturbation is applied and the ensemble average of the resulting flux is measured. Recently, Müller-Plathe et al. [3] have developed a reverse nonequilibrium MD (RNEMD) technique, in which the flux is imposed and the corresponding force is measured. Because of the fact that in this method the cause and effect are reversed with respect to experiment and the conventional nonequilibrium simulation methods, it is called "reverse".

Partitioning the simulation box into a number of slabs along, the z direction, in a way that the central slab locates at z=0 and the last slab locates at z=L_z/2, where L_z is the box dimension along the z dimension, the momentum flux is imposed on the system in an unphysical way, as follows. The atoms inside the central slab and its periodic image are propelled in the +x direction. Similarly, the atoms inside the last slab and its period images are propelled in the -x direction.

Periodically repeating momentum swaps, the total momentum transferred in a simulation is known. The physical momentum flow, in the opposite direction, occurs in the system as the result of system's response to nonequilibrium situation. In the steady state, the rate of momentum transferred, unphysically by momentum swaps, is equal to that of momentum flowing back through the fluid by friction. Therefore, $j(p_x) = \frac{P_x}{2At}$, where j(p_x) is the momentum flux, P_x is the total momentum transferred in time t of simulation, A=L_xL_y, and factor 2 arises because of the periodicity of the system.

3. Simulation

The force-field parameters for [bmim][Tf₂N] are reported elsewhere [2]. All simulations were performed using the MD simulation package, YASP [4], at 323 K and 1.013 kPa. All nonbonded interactions were truncated at 0.95 nm with a reaction field correction for the Coulombic interactions. An atomic Verlet neighbor list was used, which was updated every 15 time steps, and the neighbors were included if they were closer than 1.0 nm. The time step for the leapfrog integration scheme was 1.0 fs. After an equilibration time of 2 ns, RNEMD calculations were performed for 5 ns.

4. Results

4.1 Velocity profiles

Adjusting the exchange frequency empirically, we performed long enough simulations to achieve the steady state. After this initial time to achieve the steady state, we performed simulations for 5 ns and averaged the velocity of atoms in each slab. Following the observation of Zhao et al. [5], the bmim cations were chosen as the species for momentum exchange. The results on the velocity profiles of bmim cations are shown in Figure (1) at different exchange frequencies. The results in Figure (1) show that at strong perturbations, exchange periods of 5 and 10 time steps, nonlinear velocity profiles are observed. However, at weaker perturbations, the results show that a linear velocity profile is observed.

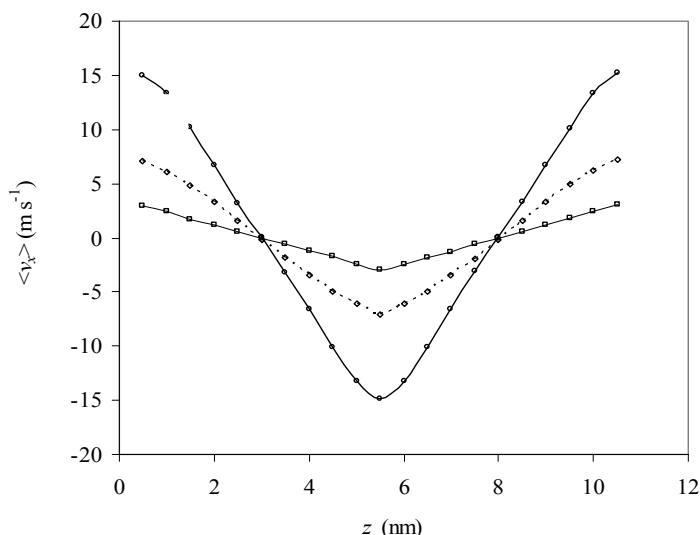


Fig. 1. Calculated velocity profiles for [bmim][Tf₂N]. The curves represent the results at exchange frequencies of 5 (○) and 10 (◇), and 20 (□) time steps.

4.2 Shear viscosity

The results of previous sections, linear and nonlinear velocity profiles at different perturbations, show that weaker perturbations are required to locate in the linear-response domain. This, however, requires longer simulations to achieve the steady state. The longer simulations, at weaker perturbations, are still going on. Here, it is just sufficient to point out that from the results of such simulations (linear velocity profiles) the viscosity coefficient can be calculated. But, the calculated viscosity coefficients will be shear rate dependent, as it is known that ionic liquids do not show Newtonian behavior at the shear rates accessible in molecular dynamics simulation methods [5]. However, the proper extrapolation lets us to calculate the zero-shear rate viscosity coefficients from the shear-rate dependent viscosity coefficients.

References

- [1] C. J. Margulis, H. A. Stern, and B. J. Berne, *J. Phys. Chem. B* 106 (2002) 12017.
- [2] W. Zhao, H. Eslami, W. L. Cavalcanti, F. Müller-Plathe, *Z. Phys. Chem.* 221 (2007) 1647.
- [3] F. Müller-Plathe, *Phys. Rev. E* 59 (1999) 4894.
- [4] F. Müller-Plathe, *Comput. Phys. Commun.* 78 (1993) 77.
- [5] W. Zhao, F. Leroy, S. Balasubramanian, F. Müller-Plathe, *J. Phys. Chem. B* 112 (2008) 8129.

**Study of the Solvent Effects on Hydrogen bonds of DNA base pairs using Molecular Dynamics Simulation**

S. Jalili*, H. Fallah

Department of Chemistry, K. N. Toosi University of Technology, Tehran ,Iran

(E-mail:hengame.fallah@gmail.com)

Keywords: Molecular dynamics, Hydrogen bond, Solvent effect, Base pair.**1. Introduction**

The hydrogen bonds between base pairs in DNA are arguably the most important ones in all of biological chemistry. [1] The structure of DNA is depended on the H-bonds of its base pairs. Solvents may effect on the number of H-bonds and also on their stability or rigidity. In this study, our purpose is to survey the various solvent effects on hydrogen bonds in the DNA structure.

2. Method

AMBER 9.0 package of molecular dynamics simulation and the AMBER99 force field were used for the molecular dynamics simulation. The initial structure of the 18-mer DNA was extracted from Protein Data Bank (PDB entry: 1TRO) [2]. The modified structure is shown in Fig1. Details of the simulation are listed in Table1.

Table 1. Summary of simulation.

Force field	AMBER99
Water model	TIP3P
Cut off	13Å
Time step	0.002 ps
Time of heating	10 ps
Time of MD simulation	200 ps

First, the solvent and ions were optimized while keeping solute fixed. Then, the whole system was optimized. The simulation was done in two stages. First, the system heated from 0K to 300K in 10 ps. Then, the simulation was continued for 200 ps. The simulations were done in both water and methanol as solvent.

3. Results and discussion

As seen in Fig. 1, DNA in water is more stable than DNA in methanol. Fig. 2 shows the comparison of the root mean square deviation (rmsd) for DNA in water and DNA in methanol. In addition, we chose one of hydrogen bonds in DNA, H1...N3 in the first G-C base pair, and calculated the distance of these atoms during the simulation (Fig. 3).

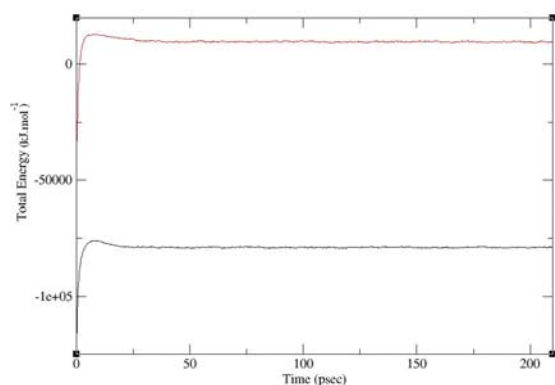


Fig. 1. Total energy of the system during the simulation.
DNA in water (black), DNA in methanol (red).

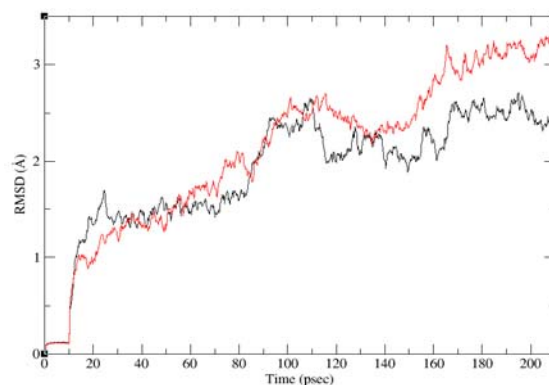


Fig. 2. RMSD for DNA in water (black) and DNA in methanol (red).

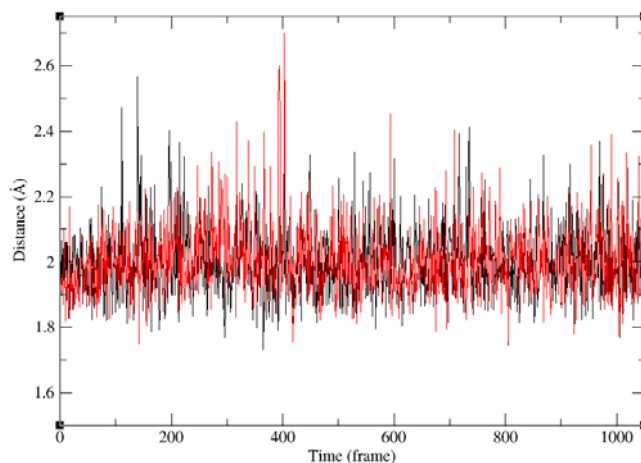


Fig. 3. Distance of H1 in DG1 to N3 in DC36 during the simulation for DNA in water (black) and DNA in methanol (red).

The average distance between H and N in DNA in water is 1.99605 Å and in DNA in methanol is 2.00530 Å. So, the difference is not so much (~ 0.01 Å).

DNA in water is more stable than DNA in methanol. Changes of distance in hydrogen bond (H1...N3) during simulation show same trend for both DNA in water and DNA in methanol systems.

References

- [1] Gould, I. R. Kollman, P. A., J. Am. Chem. 116 (1994) 2493.
- [2] Suenaga, A. Yatsu, C. Komeiji, Y. Uebayasi, M. J. Molecular Structure. 526 (2000) 211.

Molecular dynamics study of hydrogen adsorption on nitrogen doped graphene

S.Jalili*, A.Vahidi Ferdowsi

Department of Chemistry, K. N. Toosi University of Technology, P.O. Box 15875-4416, Tehran, Iran,

(E-mail: a.v.ferdowsi@gmail.com)

Keywords: MD simulation, Adsorption, N-doped Graphene, Isotheric heat, Self-diffusivity.**1. Introduction**

Hydrogen as an ideal energy carrier has attracted a great deal of attention in recent years. An enormous challenge to have a safe and efficient way for reversible hydrogen adsorption is the efficient hydrogen storage.

One of the possible ways for such storage is the efficient hydrogen physisorption in a different material. Carbon based materials for high surface areas, thermal stability, economical production and mechanical properties are still important issue.[1]

Most of efforts are far to reach the target of 6.5 wt% at ambient temperature and modest pressure for commercial applications specified by DOE [2].

Generally adsorption on solid introduce two category; adsorption on Perfect surface and defective surface. We think that the structural deformations in nitrogen doped graphene sheets [3] are so localized around the nitrogen sites, and can polarized hydrogen molecule to electronegative nitrogen then cause to higher and strong adsorption in this surface.

We used the MD simulation to investigate the effects of temperature and pressure on the adsorption and measure some useful thermodynamic parameter.

2. Method

The structure of N-doped graphene sheet which is used in this work is shown in above figure 1.

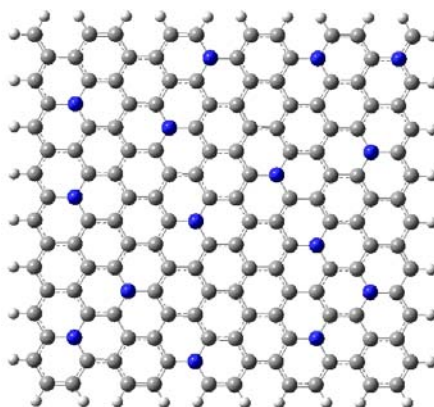


Fig. 1. N-doped graphene sheet.

The Gaussian 03 package was used for optimization of the considered structure. MD simulations were performed in the canonical NVT ensemble, using the GROMACS program. The unit cell contained one N-doped graphene sheet in simulation box which is filled with H₂ molecules.

3. Results and discussion

Hydrogen adsorption isotherms graphene sheet were studied using molecular dynamics simulation. Adsorption isotherms were obtained graphene surface at several temperatures from 77K up to 400 K. The results were compared with the graphene without defects at the same conditions. Adsorption coverage, isosteric heat, binding energy, were calculated.

References

- [1] Jalili, S. et al. Int. J. Nano. Sci. 8 (2009) 425.
- [2] Liu, W. Zhao, H. Li, Y. Jiang, Q. Lavernia, E.J. J. Phys. Chem. C. 113 (2009) 2028.
- [3] Wei, D. Liu, Y. Wang, Y. Zhang, H. Huang, L. Gui, Y. Nano. Lett. 9 (2009) 1752.



**Molecular dynamics simulation of hydrogen adsorption in double-walled carbon nanotubes**

S. Jalili and A. Gorji*

Department of Chemistry, K. N. Toosi University of Technology, Tehran, Iran

(E-mail: cagorji@yahoo.com)

Keywords: Double-walled carbon nanotubes, Hydrogen storage, Functionalized nanotubes, Molecular dynamics simulations.**1. Introduction**

Hydrogen is a clean energy source that has been attracted much attention as an alternative for fossil fuels to solve the problem of urban pollution through the application of hydrogen fuel cells in motors of vehicles. The storage of this gas is therefore an essential problem that has not been yet solved up. Many kinds of materials have been proposed as hydrogen storage media, such as metal-hydride structures and carbon-based nanoporous materials.

Carbon nanotubes are hollow structures which are of special interest to use for hydrogen storage. There are considerable published papers on the application of carbon nanotubes in this field. Although pure carbon nanotubes have been shown to have a low hydrogen adsorption capacity, the researchers are attempting to increase their capacity through various methods such as metal decoration [1] and covalent functionalization [2].

2. Method

In this work, we have studied the hydrogen adsorption in bare and functionalized double-walled carbon nanotubes. A number of hydrophobic ($-\text{CH}_3$) and hydrophilic ($-\text{OH}$, $-\text{COOH}$) functional groups have been covalently substituted on sidewalls at internal and external surfaces of nanotubes in order to reach the maximum storage capacity.

The double-walled nanotube (DWNT) studied was composed of concentric (6,6) and (16,16) nanotubes with 30 unit cells (an average length of 75 Å), whose ends are blocked with hydrogen atoms. This system was placed in a rectangular periodic box with the dimensions of $50 \times 50 \times 150$ Å, filled with hydrogen molecules (Fig. 1). The nanotubes were modeled as flexible, uncharged molecules with the bonded parameters from the Charmm27 force field. Hydrogen molecules were represented as one-particle bodies. The Lennard-Jones parameters for C-C and $\text{H}_2\text{-H}_2$ interactions were taken from the literature [3].

The simulations were performed in NPT ensemble at 77 K and 15 MPa using the Gromacs 4.0.5 simulation package. The equations of motion were integrated using the leap-frog algorithm with a time step of 2 fs. Periodic boundary conditions were applied in three dimensions with a cutoff of 10 Å for nonbonded interactions.

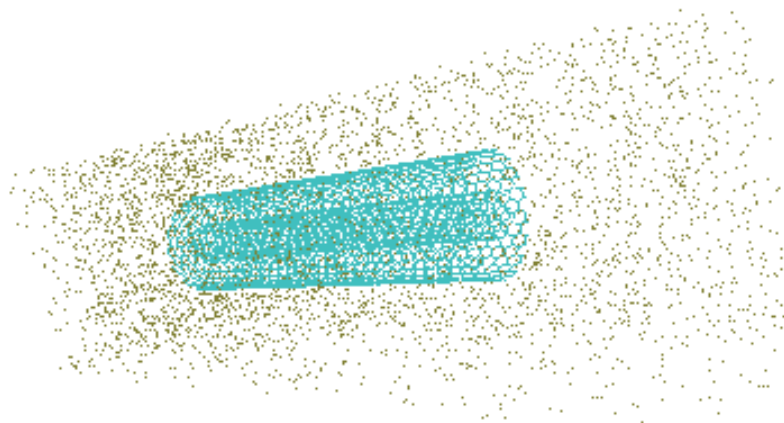


Fig. 1. The initial simulation box containing a DWNT and 4200 hydrogen molecules.

3. Results and discussion

The amount of adsorbed hydrogen in different places was calculated and compared for bare and functionalized nanotubes. There are three possible adsorption sites for hydrogen molecules. Most of hydrogen molecules are adsorbed on external walls of nanotube. The adsorption pattern changes upon the functionalization of nanotubes.



4. Conclusions

Since hydrogen molecules are small, it is possible for a number of them to adsorb on internal walls of smaller nanotubes and/or the region between two nanotubes. This increases the hydrogen uptake in comparison to single-walled nanotubes. The hydrophobic and hydrophilic functional groups examined may help to design new materials with higher hydrogen storage capacity.

References

- [1] S. Jalili, A. Jaber, M. G. Mahjani, M. Jafarian, *Int. J. Nanosci.* 8 (2009) 425.
- [2] A. Hirsch, *Angew. Chem. Int. Ed.* 41 (2002) 1853.
- [3] C. Gu, G.-H. Gao, Y.-X. Yu, Z.-Q. Mao, *Int. J. Hydrogen Energy* 26 (2001) 691.

**Comparison of the diffusion of CO and N₂ in ITQ-7 zeolite via Molecular dynamics simulation**F. Amirseifadini^a, M. Loghavi^a, R. Rabiei^a, S. Alavi^b, and H. Mohammadimanesh^a, B. Najafi^{a,*}^aDepartment of chemistry, Isfahan University of Technology, Isfahan, Iran^bDepartment of chemistry, University of Ottawa, Ottawa, Canada

(E-mail: f.amirseifadini@gmail.com)

Keywords: ITQ-7 zeolite, Simulation, Carbon monoxide, Nitrogen, Molecular dynamics, Self-diffusivity.**1. Introduction**

Zeolites are porous crystalline structures with very regular well-defined shapes. In their most simple form, zeolites consist of silicon (Si) and oxygen (O) in a proportion SiO₂. Silicon atoms bind four oxygen atoms, in a tetrahedral arrangement[1]. The diffusion of molecules inside the nanometer-scale pores of zeolites controls the performance of zeolites in many applications of these materials for chemical separations and catalysis[2]. Molecular simulations have played a useful role to the study of diffusion in these materials

2. Methods

In this study, we used molecular simulations to predict the diffusion of CO and N₂ in ITQ-7 zeolite. ITQ-7 (structure type ISV) has a three-dimensional system of large pores defined by windows containing 12 member rings of about 6 Å in diameter[2]. The main purpose of this study is to compare the diffusion of CO and N₂ in ITQ-7, the effect of the loading and temperature on the dynamics behavior and diffusion coefficient and also the relationship between the diffusion coefficient and the activation energies. The last purpose of the work is to determine the adsorption energies of CO and N₂.

In this study, we modeled interactions between adsorbed molecules and the zeolite framework atoms following the method of Makrodimitris et al. [3].(Table 1)

Table 1. Potential parameters used to represent the zeolite framework and guest molecules.

		ϵ/k_b (K)	σ (Å)	Partial Charges (e)
Zeolite	Si	18.62	0.0677	+2
	O	101.65	0.2708	-1
CO	C	1.278	3.55	+0.0223
	O	2.118	2.95	-0.0223
N₂	N	36.0	3.31	-0.482
	CofM	0.0		+0.964

The simulations are initially performed in the NVT ensemble at p=1 bar and at a range of temperatures between 200 and 700 K, each for 300000 steps at loadings of 2,4,6,8,10,12,14,16,18 and 20 for N₂ and loadings of 2,12 and 20 for CO, with the Nose-Hoover thermostat algorithm. The DL_POLY molecular program version 2.18 was used for these simulations. In the molecular dynamics simulations, the equations of motion for the CO and N₂ motions were integrated with a time step of 1 fs using the Verlet leapfrog algorithm and a thermostat relaxation time of 0.1 ps. Long-range electrostatic interactions were calculated using the Ewald summation method with a precision of 1×10^{-6} and all intermolecular interactions in the simulation box were calculated within a cut off distance of $R_{\text{cutoff}} = 13$ Å. For the calculation of the mean-square displacement and diffusion coefficient, 500 ps NVE simulations were performed on the equilibration configurations of the NVT simulations. Self-diffusion coefficients were calculated from the Einstein relationship as follows [4]:

$$D_{\alpha} = \frac{1}{6N_{\alpha}} \lim_{t \rightarrow \infty} \frac{d}{dt} \sum_{i=1}^{N_{\alpha}} \langle |\mathbf{r}_i(t) - \mathbf{r}_i(0)|^2 \rangle \quad (1)$$

where N_{α} is the number of diffusing molecules of type α , $\mathbf{r}_i(0)$ and $\mathbf{r}_i(t)$ are the initial and final positions of the center of mass of molecule i over the time interval t , and $\langle |\mathbf{r}_i(t) - \mathbf{r}_i(0)|^2 \rangle$ is the averaged mean-square displacement (MSD) of the ensemble.

The activation energies were calculated using the Arrhenius equation:



$$D = D_0 \exp\left(-\frac{E_a}{RT}\right) \quad (2)$$

where E_a is the Arrhenius activation energy.

The adsorption energies were calculated using:

$$E_{\text{ads}} = E_{\text{tot}} - (E_{\text{zeo}} + E_{\text{gas}}) \quad (3)$$

3. Results and discussion

Table 2 reports the diffusion coefficients for N_2 in ITQ-7 at the various loadings investigated (2, 4, 6, 8, 10, 12, 14, 16, 18 and 20 nitrogen molecules / unit cell) as a function of the temperature. At all of these loadings, we observed that the diffusion coefficients increase with temperature because of increase of kinetic energy of particles and decrease of the diffusion coefficients decrease with increase of loading due to steric hindrance.

Table 2. Diffusion coefficients (in $10^{-8} \text{ m}^2/\text{s}$) for N_2 .

Loading (molecules/u.c)	200 K	298 K	400 K	500 K	600 K	700 K
2	1.63	2.77	3.49	4.22	4.62	4.85
4	1.55	2.21	3.10	3.46	4.51	4.74
6	1.29	1.78	2.41	3.05	3.15	3.41
8	0.96	1.45	2.17	2.49	2.67	3.02
10	0.89	1.22	1.54	1.64	2.24	2.37
12	0.79	1.12	1.47	1.60	1.94	2.10
14	0.60	0.96	1.21	1.41	1.74	1.91
16	0.58	0.84	1.08	1.21	1.48	1.66
18	0.51	0.70	0.88	1.09	1.28	1.51
20	0.42	0.62	0.86	1.02	1.27	1.42

The diffusion activation energies were obtained from the slope of $\ln(D)$ versus $1/T$ (Arrhenius equation, Eq. 2).

For comparison, diffusion coefficient of both CO and N_2 at the same loading and temperature range are shown in table 3. As shown, both gases have nearly the same coefficient, mostly due to the same molecular weight.

Table 3. Diffusion coefficients (in $10^{-8} \text{ m}^2/\text{s}$) for N_2 and CO, at loading 12.

Guest	200 K	298 K	400 K	500 K	600 K	700 K
CO	0.71	0.93	1.21	1.54	1.85	2.00
N_2	0.79	1.12	1.47	1.60	1.94	2.10

References

- [1] D. J. Earl, M. W. Deem, Ind. and Eng. Chem. Res. 45 (2006) 5449.
- [2] D. Selassie, D. Davis, J. Dahlin, E. Feise, G. Haman, D. S. Sholl, D. Kohen, J. Phys. Chem. C. 112 (2008) 16521.
- [3] K. Makrodimitris, G. K. Papadopoulos, D. N. Theodorou, J. Phys. Chem. B. 4 (2001) 105.
- [4] M. U. Ari, M. G. Kutug, A. M. Yurtsever, A. E. enatalar. J. Phys. Chem. B. 23 (2009) 113.

**Investigation of surface free energy of platinum nanoparticles via molecular dynamics simulation**

H. Akbarzadeh, H. Abroshan, G. A. Parsafar*

Department of Chemistry and Nanotechnology Research Center, Sharif University of Technology, Tehran, Iran

(E-mail: akbarzadehhamed@yahoo.com)

Keywords: Molecular dynamics, Nanoparticle, Thermodynamic integration, Platinum.**1. Introduction**

Metal nanoparticles exhibit physical, chemical, and electronic properties different from those of the bulk and single molecules due to the large fraction of surface atoms. The results reveal that the total surface free energy of a nanoparticle increases with decreasing the particle size [1,2]. We have used molecular dynamics (MD) simulation to study the surface free energy of a Pt nanoparticle. Therefore our aim is to extend the MD simulation, to investigate the thermodynamic properties of nanoparticles with a relatively simple strategy.

2. Method

In the work study, molecular dynamic simulation on a solid platinum nanoparticle was done using the DL-POLY-2.20 program [3]. We used the quantum Sutton-Chen (QSC) potential in these simulations [4,5]. The MD simulations are carried out in a NPT ensemble with a constant number of atoms N and pressure P and temperature T . Temperature is controlled by a Nose-Hoover thermostat and pressure kept at the 0 Pa. The equations of motion are integrated using the Verlet Leapfrog algorithm with a time step of 0.001 ps for a system of 3430 atoms. The samples are heated in successive runs between 298.15 and 2000 K and cooled down to 298.15 K, with a temperature interval of 50 K. In each run, the first 5×10^4 time steps are used to equilibrate the sample, the statistical average of the thermodynamic variable (the internal energy in this case) is obtained on an additional set of 5×10^4 time steps. All calculations of the surface free energy are performed in the NVT ensemble. We have employed finite slabs with the periodic boundary conditions in the lateral cells. The solid slabs contain 1836, 2152 and 2212 atoms for the Pt (111), Pt (100), and Pt (110) surfaces and consist of 13, 17, and 23 atomic layers with zero pressure lattice constants from the NPT simulation. For instance the former slab has 13 layers with a total of 1836 atoms. An odd number of atomic layers are taken for the sake of symmetry of the upper and lower surfaces. The three systems are chosen to have approximately equal spatial dimensions and the z axis is normal to the surface.

3. Result and discussion

In this paper, the procedure used is similar to that introduced in references 1 and 2. Firstly, we calculate the Gibbs free energy of the platinum bulk material from equation (1).

$$G(T, P=0) = T_0 \left[\frac{G(T_0, P=0)}{T_0} - \int_{T_0}^T \frac{U(T, P=0)}{T^2} dT \right] \quad (1)$$

where T_0 is a predetermined reference temperature. In order to calculate $G(T, P=0)$, the temperature dependence of $U(T, P=0)$ is needed. For such a task, we have used the constant-pressure simulation to obtain the internal energy at different temperatures. In order to use equation (1), the Gibbs free energy at the reference temperature must be obtained separately by the thermodynamic integration (TI) method for a suitable ideal reference state. To do so, we consider a system with the switching Hamiltonian $H = (1 - \lambda) H_1 + \lambda H_2$, where H_2 describes the actual system and H_1 is the Hamiltonian of the reference system, with known free energy, and λ is the switching parameter. For the solid, the reference system H_1 is a set of Einstein oscillators centered on the average positions of the atoms in the ensemble corresponding to the Hamiltonian H_2 . Secondly, we calculate the surface free energy. By taking the total Gibbs free energy as the sum of the central bulk and surface free energies, we have calculated the free energy of a platinum nanoparticle as a function of temperature. The calculated results are in good agreement with experimental values [6], with the average percent difference of 2.89. Using the thermodynamic integration method, we have calculated the solid surface free energy of the (111), (100) and (110) faces. The results are depicted in Figure 1. It can be seen that the free energy of the faces at low temperatures are ordered precisely as expected from the packing of the atoms in the layers. The close-packed (111) face has the lowest and loosely-packed (110) face has the highest free energy.

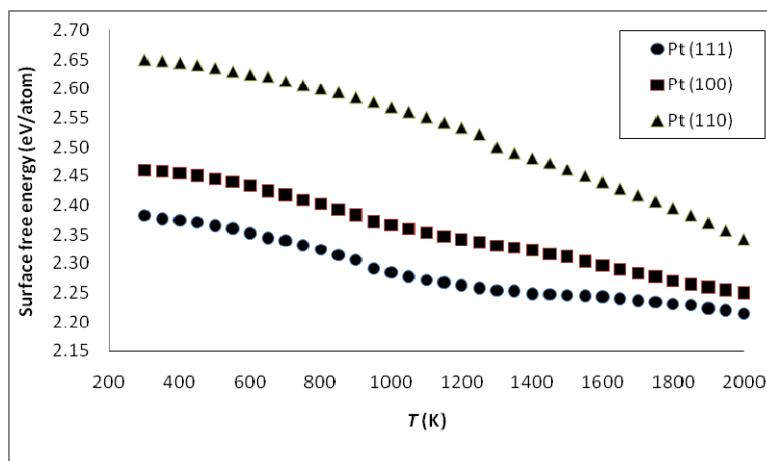


Fig. 1. Solid surface free energy versus temperature for the (111), (100) and (110) faces.

4. Conclusions

Using MD simulation with the QSC potential, we have studied the surface energy of a platinum nanoparticle. It is shown that the free energy of the faces at low temperatures is ordered precisely as expected from the packing of the atoms in the layers. The close-packed (111) face has the lowest free energy, while the loosely-packed (110) face has the largest value. As the temperature increases, the anisotropy of the surface free energy becomes lower, because the crystal becomes slowly disordered. The free energy of a nanoparticle can be divided into two parts, namely the bulk and surface. The impact of the size on the thermodynamic properties of a particle is determined by its surface atoms.

References

- [1] J. B. Sturgeon, B. B. Laird, Phys. Rev. B. 62 (2000) 14720.
- [2] E. O. Arregui, M. Caro, A. Caro, Phys. Rev. B. 66 (2002) 054201.
- [3] W. Smith, I. T. Todorov, Molecular Simulation 32 (2006) 935.
- [4] A. P. Sutton, J. Chen, Philos. Mag. Lett. 61 (1990) 139.
- [5] T. Cagin, Y. Kimura, Y. Qi, H. Li, H. Ikeda, W. L. Johnson, and W. A. Goddard, Mat. Res. Soc. 554 (1999) 43.
- [6] R. Hultgren, P. D. Desai, D. T. Hawkins, M. Gleiser, K. K. Kelly and D. D. Wagman, Selected Values of the Thermodynamic Properties of the Elements (Metals Park, OH: American Society for Metals) 1973.

Study of methane adsorption in single-walled carbon nanotube bundlesS. Jalili^{a,*}, N. Alizadeh^b, and M. Vahedpour^b^aDepartment of Chemistry, K. N. Toosi University of Technology, Tehran, Iran^bDepartment of Chemistry, Zanjan University, Tehran, Iran

(E-mail: nasibeh.alizadeh@yahoo.com)

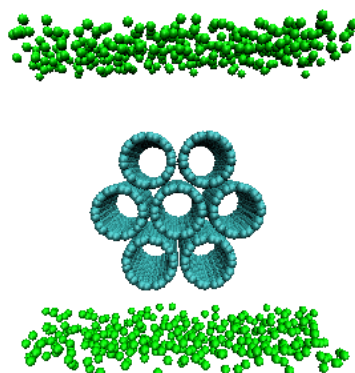
Keywords: Methane storage, Adsorption isotherm, Nanotube bundles, Molecular dynamics.**1. Introduction**

Single-walled carbon nanotubes (SWNTs) are cylindrical structures that have drawn much attention as novel nanomaterials for storage and transport of gases, such as hydrogen and methane. Methane is a major component (70-90 wt.%) of natural gas, which is considered as a suitable, non-polluting energy source for the future [1]. SWNTs are usually synthesized in the form of bundles, in which several nanotubes are held together by van der Waals attractions. These bundles provide several internal and external adsorption sites. In this work, we have studied the adsorption of methane on an infinitely long, seven-tube bundle of (10,10) SWNTs with 15 unit cells, with an approximate diameter of 47 Å.

2. Method

Simulations were performed using the Gromacs 4.0.5 simulation package. The methane molecules were considered as single particles with the Lennard-Jones parameters of $\sigma = 3.81$ Å and $\epsilon/k = 148.1$ K. For the carbon atoms of nanotubes, the Lennard-Jones length and energy parameters were taken 3.4 Å and 28 K, respectively [2]. The geometry of nanotubes was kept rigid during the simulations, excluding the need for bonded parameters. The seven-tube bundle was initially placed in a rectangular simulation box with a z-axis length of 36.9 Å. The box vectors in the directions normal to the nanotube axis were taken equal to 100 Å to avoid the interactions of bundle with its periodic images. The methane molecules were initially placed in the two sides of simulation box, above and below the bundle (Fig. 1). The required number of methane molecules was calculated using the van der Waals equation of state at 300 K and 6 MPa.

Equations of motion were integrated using the leap-frog algorithm with a time step of 2 fs. Periodic boundary conditions were applied in all directions using a cutoff distance of 12 Å. The temperature was kept constant at 300 K using the Nose-Hoover thermostat.

**Fig. 1.** The initial simulation box.**3. Results and discussion**

The amount of adsorbed methane, along with the adsorption isotherms [3] were studied from the trajectories. There are several adsorption sites on a nanotube bundle. These are intratubular sites, interstitial sites, external grooves and the exposed surface of individual nanotubes. Since the nanotubes are infinite, there is no internal adsorption and it is possible to study the external and/or interstitial adsorption.



4. Conclusions

In this work, we have reported the amount of adsorbed methane on single-walled nanotube bundles. Methane molecules are moved from their initial positions far from the bundle and adsorb on various sites. The simulations have been performed at room temperature, which is similar to experimental conditions. It is also possible to treat nanotube bundles with capped ends as finite tubes to study the internal adsorption. The results of such studies are useful to devise suitable gas storage media for future applications.

References:

- [1] X. Zhang, W. Wang, *Fluid Phase Equilib.* 194-197 (2002) 289.
- [2] F. J. A. L. Cruz, I. A. A. C. Esteves, J. P. B. Mota, *Colloids Surf. A*, 2009, in press, doi:10.1016/j.colsurfa.2009.09.002.
- [3] S. Jalili, R. Majidi, *Physica E* 39 (2007) 166.

**GCMC simulations of hydrogen adsorption in single-walled SiC nanotubes**M. Rahimi Galugahi ^a, S. Yeganegi ^b, M. Shadman ^b^a Department of Chemistry, Faculty of Science, Islamic Azad University, Shahrood branch, Shahrood, Iran^b Department of Physical and Inorganic Chemistry, Mazandaran University, Babulsar, Iran

(E-mail: sdyeganegi@gmail.com)

Keywords: GCMC, Hydrogen adsorption, SiCNT.**1. Introduction**

In last two decades, most of the scientists working is on the one of the major problems that is the difficulty of finding efficiency storage and adsorption capacity of nanotubes with theoretical or experimental procedures. One of the important types of nanotubes is silicon carbon nanotubes (SiCNT). The first preparation of Silicon Carbide (SiC) nanotubes (NTs) by shape memory synthesis have reported in 2001 [1] and then it has been improved to grow for several kinds of one-dimensional nanostructures of SiCNTs via the disproportionation reaction of SiO with carbon nanotubes (as templates) in a tube furnace in 2002 [2]. A SiCNT is a structural analogue of a carbon nanotube in nature: alternating Si and C atoms entirely substitute for C atoms in a graphitic like sheet with almost no change in atomic spacing.

In order to compare the hydrogen storage capability of SiCNTs with that of CNTs and BNNTs, we have considered the SiCNTs as an ideal one-dimensional nanopores model in the framework of GCMC simulations to reveal, at the molecular level, the adsorption behaviors of pure hydrogen in SiC nanopores. In this paper we have investigate the effect of pore size, temperature, and pressure on the adsorption isotherm and adsorption selectivity of the confined mixtures. Understanding of the adsorption behavior, at the molecular level, will guide one to design new materials for H₂ storage/separation enhancing industry.

2. Potential models and simulation details

In this work, it is assumed that the nanotube has a rigid structure and no geometry variation of the adsorbent is considered, since the induced geometric variation of nanotubes by gases can be neglected at room temperature. In the GCMC simulation, the temperature, volume, and chemical potential kept constant during the simulation. Here, the fluid-fluid interaction was described using the typical 12-6 Lennard-Jones pair potential:

$$U(r_{ij}) = 4\epsilon_{ij} \left[\left(\sigma_{ij}/r_{ij} \right)^{12} - \left(\sigma_{ij}/r_{ij} \right)^6 \right]. \quad (1)$$

where ϵ_{ij} and σ_{ij} are the energy and length parameters in LJ potentials, and r_{ij} denotes the distance between the centers of particle *i* and particle *j*. The parameters ϵ_{ij} and σ_{ij} between different particles are calculated by the following Lorentz–Berthelot rules.

$$\epsilon_{ij} = \sqrt{\epsilon_i \epsilon_j}, \sigma_{ij} = (\sigma_i + \sigma_j)/2. \quad (2)$$

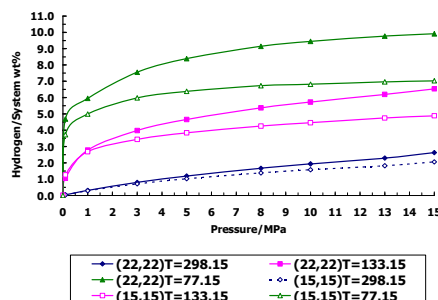
In actual calculation, the spherical cutoff is adopted, and the cutoff distance is set to $5\sigma_{ij}$. Three types of operations with equal probability are performed in the GCMC simulation cell: displacement, creation and deletion [3]. The moves are repeated until the number of hydrogen molecules in the simulation cell comes to the equilibrium. The molecular diameter for hydrogen, methane and nitrogen molecules were 0.289, 0.38 and 0.316 nm respectively and the Si–C bond length in a Silicon carbon hexagon has set as 0.187 nm. The nanotube wall can screen fluid molecules, that is, hydrogen, methane and nitrogen molecules inside the tube cannot cross the tube walls. Furthermore, periodic boundary conditions are set on the open end of single-wall (SW) SiCNT during displacement [4]. GCMC simulation of hydrogen physisorption in SWCNTs and SWBNNTs are similar to that in SWSiCNTs [3]. In this research, each simulation consists of 4×10^7 GCMC moves. The first 2×10^7 moves was as equilibration and have been discarded, and last 2×10^7 moves have been used for calculating ensemble averages of thermodynamics parameters. The MuSiC molecular simulation package was used for GCMC simulations [5].

3. Results and discussion

The simulation were performed at a fixed length (40 Å) of two chiral nanotubes (15, 15) and (22, 22) for ranges of temperature (298.15 K, 133.15 K and 77.15 K), pressure (0 – 15 MPa) and tube. Thus, we can plot the adsorption isotherms of hydrogen physisorption in SWSiCNTs. Figure 1 shows that the hydrogen storage capacity of SWSiCNTs increases with pressure and decreases with temperature. The variation of the adsorption of hydrogen with pressure is more pronounced for lower temperatures; also the difference of adsorption between different nanotubes is larger for the lowest temperature and the highest pressure.

Figure 2 presents the adsorption isotherms for two types SWSiCNT, SWCNT and SWBNT as a function of pressure at 293 K. Hydrogen adsorption or storage capacity of SWSiCNTs is greater than that of SWBNNTs and SWCNTs at all pressures when their diameters are equal and have same conditions (See figure. 2). Figures 1 and 2 show that the adsorption isotherms of hydrogen physisorption in (22, 22) and (15, 15) almost accord with each other. That is, the influence of tube chirality on hydrogen storage capacity of SWSiCNTs can be ignored such as SWBNNTs and SWCNTs [3-7].

By fixing temperature, pressure and tube diameter, we investigate the dependence of hydrogen storage capacity of SWSiCNTs on the nanotube length. Some of our results are drawn in figure 3. Figure 3 compares influence of nanotube length for (15,15) nanotube on hydrogen physisorption in SWBNNTs and SWCNTs and SWSiCNTs at 293 K and 10 MPa. The hydrogen storage capacity of SWSiCNTs almost hold the line when the tube length increases, that is to say, the axial distribution of hydrogen molecules stored in the nanotubes is approximately uniform. Therefore, only by changing tube length, one cannot vary the weight percent of adsorbed hydrogen in SWSiCNTs and SWCNTs. Similarly, these results have been observed for



SWBNNTs and SWCNTs before [3-7].

Fig. 1. The hydrogen storage capacity of (15,15) and (22,22) SWSiCNTs at 77.15 and 298.15 K

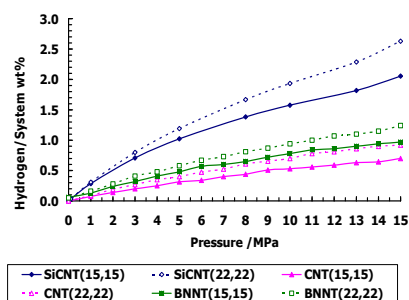


Fig. 2. The comparison between hydrogen physisorption of SWSiCNTs, SWBNNTs and SWCNTs.

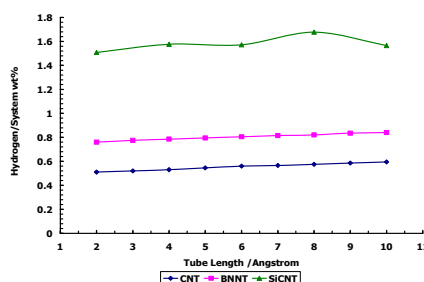


Fig. 3. The effect of tube length on hydrogen physisorption in SWSiCNTs, SWBNNTs and SWCNTs.

References

- [1] C. Pham-Huu, N Keller, G. Ehret, M. J. Ledoux, J. Catalysis 200 (2001)400.
- [2] X. H. Sun, C. P. Li, W. K. Wong, N. B. Wong, C. S. Lee, S. T. Lee, B. K. Teo, J. Am. Chem. Soc. 124 (2002:14464.
- [3] J. Cheng, X. Yuan, L. Zhao, D. Huang, M. Zhao, L. Dai, R. Ding, Carbon 42 (2004) 2019.
- [4] A. P. Allen, D. J. Tildesley, Computer simulation of liquids. New York: Oxford University Press; 1987.
- [5] A. Gupta, S. Chempath, M.J. Sanborn, L. A. Clark, R. Q. Snurr, Molecular Simulation 29 (2004) 29.
- [6] J. Cheng, R. Ding, Y. Liu, Z. Ding, L. Zhang, Computational Materials Science 40 (2007) 341.
- [7] J. Cheng, L. Zhang, R. Ding, Z. Ding, X. Wang, Z. Wang, International Journal of Hydrogen Energy 32 (2007) 3402.

**MD simulation of the dynamics of molecular motion in the equimolar mixture of [emim][NTf₂] \cdot C₆H₆**M. H. Kowsari^{a,b}, S. Alavi^c, M. Ashrafizaadeh^{b,d}, and B. Najafi^{a,*}^a Department of Chemistry, Isfahan University of Technology, Isfahan, 84156-83111, Iran^b Supercomputing Center, Isfahan University of Technology, Isfahan, 84156-83111, Iran^c Department of Chemistry, University of Ottawa, Ottawa, Ontario K1N 6N5, Canada^d Department of Mechanical Engineering, Isfahan University of Technology, Isfahan, 84156-83111, Iran

(E-mail: mohammad.kowsari@gmail.com)

Keywords: Molecular dynamics, Ionic liquids, Rotational motion, MSD, OACF, Simulation.**1. Introduction**

Recently, the structure and temperature/composition phase diagrams of the binary mixtures of imidazolium-based ionic liquids with benzene and alkylbenzenes have been investigated [1]. When imidazolium-based ILs mixed with aromatic hydrocarbons such as benzene, toluene, and xylenes, it can form "inclusion complexes" and/or clathrate (cage-like) structures. We use MD simulations to perform detailed analysis of the structure, rotational and translational motions for the solid and liquid states of the equimolar mixture of [emim][NTf₂] \cdot C₆H₆.

2. Methods

The systematic all-atom force field developed by Canongia Lopes et al. [2] based on the OPLS-AA and AMBER framework used for definition of intra- and intermolecular interactions in the 1-ethyl-3-methylimidazolium cation and bis(trifluoromethanesulfonyl)imide anion, [NTf₂]⁻ (or [(CF₃SO₂)₂N]⁻). Also, the general AMBER force field (GAFF) is used for the benzene molecule. The reader is referred to the published papers by Canongia Lopes et al. for further details of the force field [2].

Constant pressure and temperature (NpT) molecular dynamics simulations of 3 \times 3 \times 3 replica of the unit cell with 108 [emim][NTf₂] ion pairs plus 108 benzene molecules were performed for a total of 4968 atoms. The initial configuration of the simulation supercell is derived from the crystallographic x-ray structure of this binary mixture reported by Łachwa et al. [1]. The simulations were done with the Nosé–Hoover thermostat/barostat algorithm as implement in the DL_POLY program [3] version 2.18. The relaxation times used for the thermostat and barostat are 0.1 and 2.0 ps, respectively. Periodic boundary conditions were employed, and the equations of motion were integrated using the Verlet leapfrog scheme. The time step of the simulations was 2.0 fs and cutoff distance of $R_{\text{cutoff}} = 15$ Å. The electrostatic long-range interactions were calculated using the Ewald summation method.

3. Results and discussion

The detailed nature of the motions of three species [emim]⁺, [NTf₂]⁻, and benzene are explicitly studied at different temperatures during the simulation to explore the atomic-level details of the melting. In particular, the possibility of benzene rotations about their C₆ axes in the solid phase prior to melting is of interest. To quantitatively study the rotation of benzene, we calculate the orientational autocorrelation function (OACF) for the benzene molecules in the simulation supercell at different times. The OACF is defined as,

$$M(t) = \frac{\langle \boldsymbol{\mu}(t) \cdot \boldsymbol{\mu}(0) \rangle}{\langle \boldsymbol{\mu}(0) \cdot \boldsymbol{\mu}(0) \rangle} \quad (1)$$

where $\boldsymbol{\mu}(t)$ is a unit vector directed from one of the C atoms of benzene to the H atom connected to it. The brackets $\langle \rangle$ represent an ensemble average over all benzene molecules and time origins.

The time decays of the OACFs for benzene at several temperatures from simulations are shown in Fig. 1. At low temperature (110 K), the benzene molecules retain their orientations and the vector $\boldsymbol{\mu}(t)$ has a fixed direction at different times. As the temperature increases, the benzene molecules undergo changes in orientation and $M(t)$ begins to decay. The OACFs for benzene molecules in the solid phase at temperatures up to the experimental melting point of 288 K are shown [4].

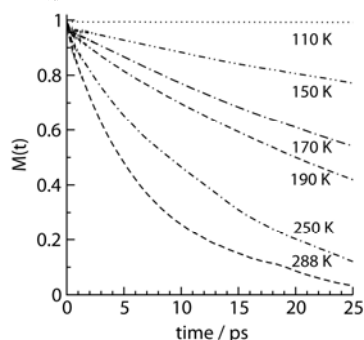


Fig. 1. The time decays of OACFs for benzene.

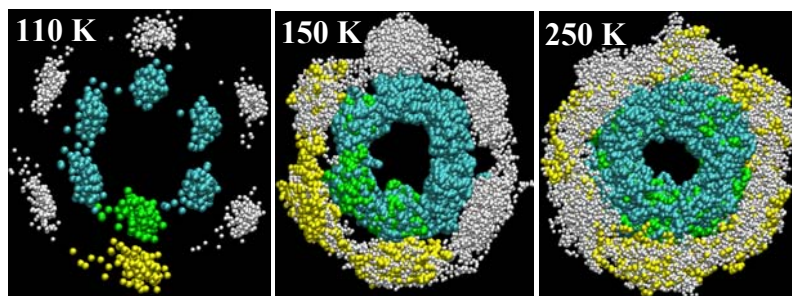


Fig. 2. Traces show for the motions of the selected benzene molecule from several trajectories at different temperatures. One of the C–H sites of benzene ring shown by green and yellow colors for cleared the rotational motions of ring.

To determine more details, overlaid snapshots for the motion of a selected benzene molecule are shown for four temperatures (110, 150, 250 K) in Fig. 2. These traces are prepared by superimposing the benzene positions along the 800 ps simulation trajectory. At 110 K, the in-plane rotation of the benzene molecule is constrained. At 150 K, a single hop of $\pm 60^\circ$ is observed. The benzene molecule rotates fairly uniformly at 250 K. We fit the time decay of the OACFs with a single exponential decay function, $M(t) = ae^{-t/\tau}$. A rotation rate constant can be defined as $k = 1/\tau$. Thus, the temperature dependence of the rotation rate constant can be expressed by an Arrhenius equation ($\ln k(t) = -E_{act}/RT + \text{const.}$).

The Arrhenius plot for the rate constant is linear to a good degree and activation energy of 6.4 kJ/mol is obtained for the rotation of benzene in its lattice sites. The linearity of the Arrhenius plot shows that the benzene molecule only hops 60° in each move. If there were hops $n \times 60^\circ$ at higher temperatures, a simple linear Arrhenius plot would not be sufficient to represent the data.

4. Conclusions

The dynamics of the ions and benzene molecules have been studied by calculating the MSDs and OACFs. The MSDs of the cation and anion are generally very close to each other in the liquid phase which indicates the strong association between ion-pairs in the inclusion mixture. Prior to melting, the benzene molecules rotate about their C_6 symmetry axes in their lattice sites. The activation energy for this rotation is determined to be 6.4 kJ/mol.

References

- [1] J. Łachwa, I. Bento, M. T. Duarte, J. N. Canongia Lopes, and L. P. N. Rebelo, Chem. Commun. (2006) 2445.
- [2] J. N. Canongia Lopes, J. Deschamps, and A. A. H. Pádua, J. Phys. Chem. B 108 (2004) 2038; erratum: 108 (2004) 11250; also: J. N. Canongia Lopes and A. A. H. Pádua, J. Phys. Chem. B 108 (2004) 16893.
- [3] W. Smith, T. R. Forester, and I. T. Todorov, The DL_POLY Molecular Simulation Package, v. 2.18 (2007). Daresbury Laboratory, U.K., http://www.cse.clrc.ac.uk/msi/software/DL_POLY/
- [4] M. H. Kowsari, S. Alavi, M. Ashrafizaadeh, and B. Najafi, revisions send to J. Chem. Phys., October 2009.

Molecular dynamics analysis of Proline-Rich Homeodomain (PRH) – DNA interaction

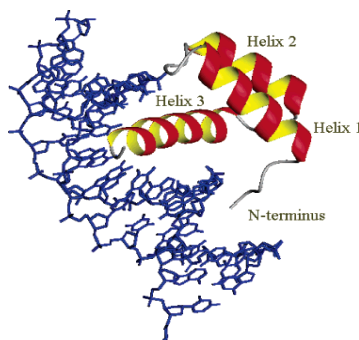
S. Jalili*, L. Karami

Department of Chemistry, K. N. Toosi University of Technology, P.O.BOX 1587-4416, Tehran, Iran

(E-mail: karami.leila1@gmail.com)

Keywords: Molecular dynamics simulation, Proline-Rich Homeodomain (PRH) – DNA interaction, Flexibility.**1. Introduction**

In a biological cell, DNA-binding proteins affect several crucial processes such as cell division, differentiation, and protein expression. The homeodomain proteins are a family of gene regulatory proteins which control cell differentiation during the early stages of embryo development of many eukaryotic organisms. Proline-Rich Homeodomain (PRH) protein contains an N-terminal domain that is 20% proline-rich, a central homeodomain that is essential for binding to DNA, and an acidic C-terminal domain. Proline-Rich Homeodomain (Fig. 1) of 70 aminoacids consists of three helices, the third of which is inserted into the major groove of the DNA in a conserved manner. The third helix is also called recognition helix. On the minor groove side, the N-terminal arm of this domain is also contributing to DNA binding [1]. Experimental studies represent DNA consensus sequence recognized by PRH is 5'-ATTAA-3' [2].

**Fig. 1.** Structure of Proline-Rich homeodomain–DNA complex**2. Methods**

Molecular Dynamics (MD) simulations were performed on PRH-DNA complex. Starting coordinates of the PRH and DNA were obtained from PDB (PDB code: 2E1O and 167D respectively) then with regarding to experimental studies, input file for gromacs was obtained. AMBER force field was applied for protein and DNA parameters. The MD simulations were performed with GROMACS package [3] version 4.0.5. System was first (energy) minimized. The box was then equilibrated for 1 ns in NVT ensemble. Production run was performed for 5 ns in NPT ensemble and configurations of the systems were saved every 2 ps. In this work, we analyze structural properties of Proline-Rich Homeodomain interacting with DNA by RMSD and RMSF.

3. Results and discussion

The root mean square deviations (RMSD), as a measure of the global structural properties, for the protein backbone in free and complex status are shown in Fig. 2a. During the simulations, the RMSD value of the protein fluctuated around 0.3 nm in homeodomain–DNA complex and protein become stable after 1.1 ns, whereas RMSD value is more for the free protein. The difference in RMSD values between protein in free and bound status is considerable. Since DNA binding necessarily restricts molecular motions, the protein in the complex shows the lowest average RMSD (average value is 0.62 nm for the free protein and 0.31 nm for the bound conformation).

The residue-based RMS deviations in Fig. 2b display that the terminals of the protein are more flexible. The least fluctuating segments are helix-3 (residues 46–60, except for Ser 48) and then residues 18–38. The protein side chains are more flexible than the backbone.

Distance deviations from the starting structure may not necessarily mirror the mobility of structural elements. More comprehensive information on flexibility is achieved by comparing root mean square fluctuations [4].

Root mean square fluctuations per residue basis for the protein backbone in free and complex status are shown in Fig. 3. Excluding the residues of N- and C- terminal arm (residues 1-8 and 61-70), the RMSF for two simulations does not exceed 0.5

nm. The helix-3 region (residues 46–60) of the homeodomain protein that recognizes the core DNA sequence has low fluctuations. In fact, the recognition helix-3 of the homeodomain–DNA complex has small difference in fluctuation, their values ranging from 0.08 to 0.1 nm, and the values for free homeodomain from 0.0.15 to 0.23 nm. These indicate the helix-3 is low flexible and a rigid region in two systems. On the other hand, N- and C-terminal arms (residues 1-8 and 61-70, respectively) show larger fluctuation in free homeodomain.

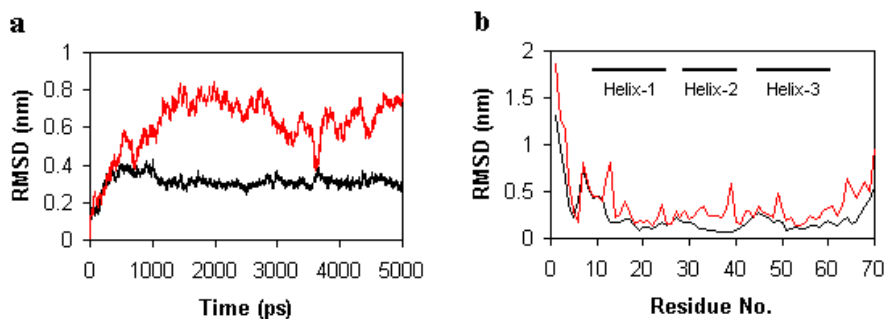


Fig. 2. (a) RMSD (root mean square deviation) of protein backbone in the homeodomain–DNA complex (black) and free homeodomain (red) and (b) RMSD of protein sidechains (red) and backbone (black) in the homeodomain–DNA complex

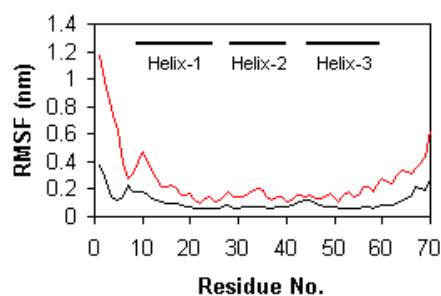


Fig. 3. RMSF (root mean square fluctuation) of protein backbone in the homeodomain–DNA complex (black) and free homeodomain (red)

Conclusions

In the present work, a molecular dynamics simulation of Proline-Rich Homeodomain (PRH) – DNA was carried out to investigate the structural properties such as RMSD and RMSF. From the mentioned results above, the following conclusions may be drawn: homeodomain protein in the protein–DNA complex is more stable than the unbound homeodomain protein due to DNA restricting molecular motions. The fluctuations of protein backbone specially N- and C- terminal arm are reduced upon binding.

References

- [1] A. Soufi, P-S Jayaraman, *Biochem. J.* 412 (2008) 399.
- [2] M. R. Crompton, T. J. Bartlett, A. D. MacGregor, *Nucleic Acids Research.* 20 (1992) 5661.
- [3] E. Lindahl, D. van der Spoel, B. Hess, *J. Mol. Mod.* 7 (2001) 306.
- [4] A. Caflisch, I. Jelesarov, *J. Mol. Recognit.* 17 (2004) 120.

**Quantifying the anisotropy of potential energy surfaces with the aim of statistical central moments**

M. Ashouri, M. H. Karimi-Jafari*

Computational chemistry laboratory, NSTRI, Tehran, Iran

(E-mail: mhkarimijafari@gmail.com)

Keywords: Anisotropy, Intermolecular interaction, Skewness, kurtosis, Central moment.**1. Introduction**

Anisotropy of the potential energy surfaces of van der Waals complexes is a challenge in their ab initio calculations and analytical representations. Qualitatively, anisotropy is interpreted as dependency of interaction energy on the relative orientation of interacting monomers. However, there is not a quantitative definition that provides a unique measure for comparison of anisotropy of different PESs. Recently via an ab initio investigation of the Cl₂ dimer [1] it was proposed to apply simple statistical measures for comparison of the anisotropy of potential energy surfaces of different systems at different intermolecular distances. In present work this idea is extended and generalized as a convenient tool for quantifying the anisotropy at least in a relative measure. In statistics, the term central tendency relates to the way in which quantitative data tend to cluster around some value. A measure of central tendency is any of a number of ways of specifying this "central value". Thus an initial objective might be to "choose an appropriate measure of central tendency". In the simplest cases, the measure of central tendency is an average of a set of measurements, the word average varies as mean, median, or other measure of location, depending on the context. The term is applied to multidimensional data as well as to univariate data. After choosing the mean as a measure of central tendency we can focus on the shape of the distribution of data set around the mean value. The moments describe the nature of the distribution. Any distribution can be characterized by a number of features such as the mean, the variance, the skewness and the kurtosis. The first moment about zero, if it exists, is the expectation of variable, i.e. the mean of the distribution. In higher orders, the central moments are more interesting than the moments about zero. The n^{th} central moment is defined as follows:

$$\mu_n = \int (x - \bar{x})^n f(x) dx$$

where \bar{x} is the mean and usually, the function $f(x)$ will be a probability density function. The first central moment is thus 0. The second central moment is the variance, the positive square root of which is the standard deviation, σ . The normalized n^{th} central moment or standardized moment is the n^{th} central moment divided by σ^n which are dimensionless quantities. The third central moment is a measure of the lopsidedness of the distribution; any symmetric distribution will have a third central moment, if defined, of zero. The normalized third central moment is called the skewness, often γ . A distribution that is skewed to the left (the tail of the distribution is heavier on the right) will have a negative skewness. A distribution that is skewed to the right (the tail of the distribution is heavier on the left), will have a positive skewness. The fourth central moment is a measure of whether the distribution is tall and skinny or short and squat, compared to the normal distribution of the same variance. Since it is the expectation of a fourth power, the fourth central moment, where defined, is always non-negative. The kurtosis κ is defined to be the normalized fourth central moment. If a distribution has a peak at the mean and long tails, the fourth moment will be high and conversely.

2. Results and Discussion

Considering the calculated points on the PES at a fixed value of R as a data set or distribution the following definitions are used for mean, \bar{U} , standard deviation, σ^2 , skewness, γ , and kurtosis, κ :

$$\begin{aligned} \bar{U} &= \frac{1}{N} \sum_{i=1}^N U_i & \sigma^2 &= \frac{1}{N-1} \sum_{i=1}^N (U_i - \bar{U})^2 \\ \gamma &= \frac{1}{N-1} \frac{\sum_{i=1}^N (U_i - \bar{U})^3}{\sigma^3} & \kappa &= \frac{1}{N-1} \frac{\sum_{i=1}^N (U_i - \bar{U})^4}{\sigma^4} \end{aligned}$$



These definitions are grid dependent and any comparison of anisotropy according them is meaningful when the applied grids are the same. By analogy we can extend these definitions to the continuous and grid independent cases as follows:

$$\bar{U} = \frac{1}{\int d\omega} \int U(\omega) d\omega \quad \sigma^2 = \frac{1}{\int d\omega} \int (U(\omega) - \bar{U})^2 d\omega$$

$$\gamma = \frac{1}{\sigma^3 \int d\omega} \int (U(\omega) - \bar{U})^3 d\omega \quad \kappa = \frac{1}{\sigma^4 \int d\omega} \int (U(\omega) - \bar{U})^4 d\omega$$

where $\int d\omega$ is the integration over the angular coordinates. With the aim of these tools we compare some of the analytical potential energy functions available in the literature for N₂ dimer [2-5]. The results obtained for the skewness and kurtosis are depicted in Figures 1 and 2. As can be seen the full ab initio PES of Ref. 5 is more anisotropic than the others at short range and the experimentally derived PES of Ref. 4 is less anisotropic in all distances.

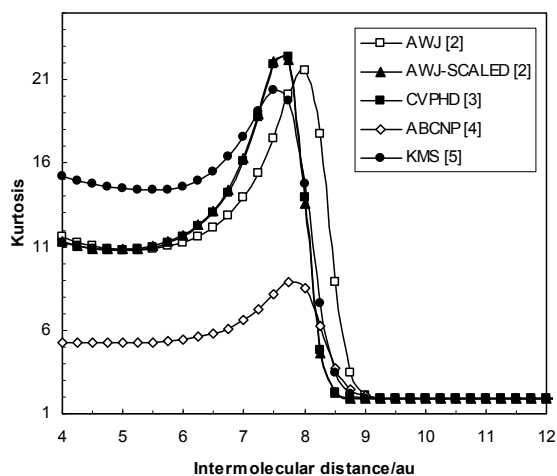


Fig. 1.

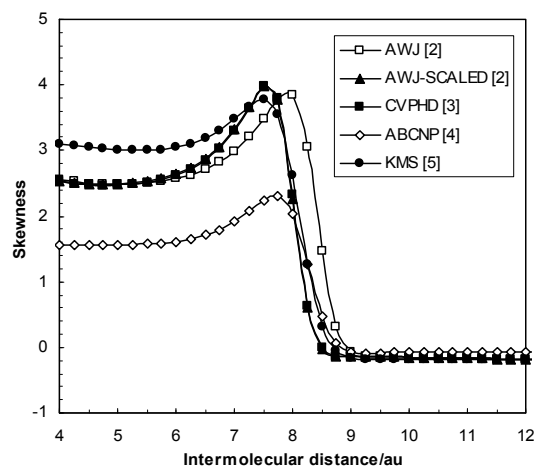


Fig. 2.

References

- [1] M. H. Karimi-Jafari, M. Ashouri, A. Yeganeh-Jabri, *Phys. Chem. Chem. Phys.*, 11 (2009) 5561.
- [2] A. Van der Avoird, P. E. S. Wormer, A. P. J. Jansen, *J. Chem. Phys.*, 84 (1986) 1629.
- [3] D. Cappelletti, F. Vecchiocattivi, F. Pirani, E. L. Heck, *Molec. Phys.*, 93 (1997), 485.
- [4] V. Aquilanti, M. Bartolomei, D. Cappelletti, E. Carmona-Novillo, F. Pirani, *J. Chem. Phys.*, 117 (2002) 615.
- [5] M. H. Karimi Jafari, A. Maghari, S. Shahbazian, *Chem. Phys.*, 314 (2005), 249.

**Prediction of thermodynamic properties of ketones using artificial neural network**

Z. Kalantar, M. Arab Chamjangali, H. Nikoofard, M. Sabouri*

Faculty of chemistry, Shahrood University of Technology, Shahrood, Iran

(E-mail: zkalantar@shahroodut.ac.ir, zahrakalantar@yahoo.com)

Keywords: Ketones, Thermodynamic properties, Artificial neural network (ANN), Multi linear regression (MLR), Density.**1. Introduction**

The liquid density is a very important parameter for both heat transfer and mass transfer calculations in the design of chemical processes. Although experimental data can be very accurate, it is difficult to provide all the data needed for every compound. For this reason, several methods have been developed for predicting liquid densities such as group contribution method or correlation function. In the past decade, the topic of neural network (NN) has generated widespread interest and popularity. The popularity of this technique is due to their success in data analysis because they are indeed self learning mechanisms which don't require the traditional skills of a programmer. In this work we used artificial neural network (ANN) for density prediction of ketones over a wide range of temperature and pressure.

2. Methodes

The pvT data for different ketones (acetone [1], butan-2-one [2], pentan-2-one [3], pentan-3-one [4], 4-methylpentan-2-one [3], hexan-2-one [3]) was randomly divided into 3 groups: training set, validation set and test set consisting of 597, 132 and 66 data, respectively. In order to calculate the theoretical descriptors, the molecular structures were constructed with the aid of Hyperchem 7.1 and were optimized using AM1 algorithm. The molecular geometries of compounds were further optimized by Dragon package 2.1. As a result, total of 1481 theoretical descriptor were calculated for each compound in the data set. The method of stepwise MLR was used to select the most important descriptor and to calculate the coefficient relating the density to the descriptors. Three layer network with a sigmoid transfer function was designed the optimization of the weights and biases was carried out Levenberg-Marquardt algorithm.

3. Results and discussion

Multi-parameter linear correlation of density values for different ketones versus the molecular descriptors gives the results in Table 1.

Table 1. name of descriptor, its symbol and coefficient in multi-parameter linear correlation.

Name of descriptor	symbol	coefficient
pressure	p	0.440
temperature	T	-0.741
Sub polarity parameter	SPP	-1739.014
Average molecular weight	AMW	-27.841
Average connectivity index chi_4	X4A	-13.228
Constant	-----	2081.094

An artificial neural network (ANN) was constricted using 5 input including SPP, AMW and X4A (the same descriptors in the MLR model), temperature and pressure and 1 neuron in output layer that predicts density by network. The number of neuron in a hidden layer is unknown and need to be optimized. Plots of RMSET and RMSEV versus the number of node in the hidden layer show that 5 nodes in hidden layer is optimum value. Also the results demonstrate that overfitting does not exist for this artificial neural network (ANN) model and training is stopped after 180 iterations. The capability of the model has been evaluated by predicting values of density by the optimized artificial neural network (ANN) model for the validation and test sets. The excellent prediction results, reveals the capability of this model. Also, the performance of this model was evaluated by plotting the estimated values versus the experimental values of density for the validation and test sets, see Fig. 1.

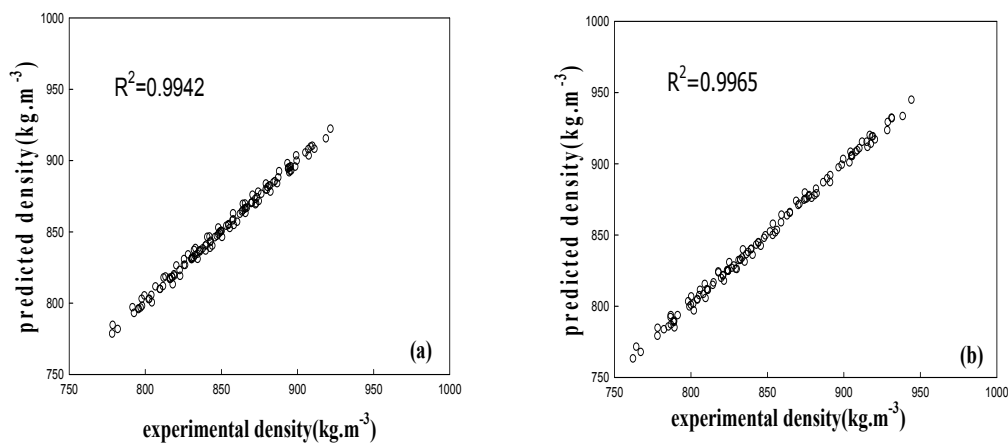


Fig. 1. Plot of predicted density versus experimental density for (a) validation set and (b) test set.

4. Conclusions

As a result, it was found that properly selected and train artificial neural network (ANN) could fairly represent dependents of the density for ketones to the molecular descriptors.

References

- [1] R. Malhotra, L. A. Woolf, J. Chem. Thermodynamics 23 (1991) 867.
- [2] R. Molhatra, L. A. Woolf, J. Chem. Thermodynamics 24 (1992) 1207.
- [3] R. Molhatra, L. A. Woolf, J. Chem. Thermodynamics 28 (1996) 1411.
- [4] R. Molhatra, W. E. Price, L. A. Woolf, J. Chem. Thermodynamics 25 (1993) 361.

**Molecular dynamics simulation study of self-diffusivity of carbon disulfide gas in ITQ-7 zeolite**M. Loghavi^a, F. Amirseifadini^a, R. Rabiei^a, S. Alavi^b, H. Mohammadimanesh^a and B. Najafi^{a,*}^aDepartment of chemistry, Isfahan University of Technology, Isfahan, Iran^bDepartment of chemistry, University of Ottawa, Ottawa, Canada

(E-mail: mohsen.loghavi@gmail.com)

Keywords: ITQ-7 zeolite, Molecular dynamics, Simulation, Self diffusion, Carbon disulfide.**1. Introduction**

Zeolites are an important class of molecular sieves in which separations are obtained by selecting the pore size such that in mixtures molecules that are too large are being blocked. The basic building blocks of zeolites are corner sharing TO₄ units, where the T-atoms usually refer to Si, Al, or in some cases also P. These tetrahedrals can form different types of units, such as 6-rings, 8-rings, or 12-rings [1]. From a scientific point of view, zeolites are challenging. As most of the activity occurs inside the material, it is very difficult to carry out experiments that provide us information at the molecular level. Molecular dynamics simulations are used to give a comprehensive view of adsorption, diffusion and loading selectivity of carbon disulfide gas in ITQ-7 zeolite.

2. Methods

Siliceous zeolite-ITQ-7- and carbon disulfide have been chosen as the host and guest respectively. ITQ-7 (structure type ISV) has a three-dimensional system of large pores defined by windows containing 12 member rings of about 6 Å in diameter [2]. CS₂, is very toxic and is harmful by inhalation of the vapor, skin absorption of the liquid, or ingestion [8]. Interactions between adsorbed molecules and the zeolite framework atoms have been modeled by method of Makrodimitris et al [3] and Rabinson et al [4]. That is, each atom in the zeolite is assumed to interact with each site on the adsorbed molecules through both a Lennard-Jones potential and electrostatic interactions. All interatomic interactions between the atoms in the simulation box and the nearest image sites were calculated within a cutoff distance of R_{cutoff}= 13 Å for all simulated systems. The electrostatic interactions were evaluated using the Ewald method with a precision of 1×10⁻⁶. Molecular dynamics simulations were performed on the periodic 3×3×3 replica of the ITQ-7 unit cell at loadings of 2, 4, 6, 8, 10, 12, 14 and 16 molecules per unit cell and different temperatures-200 K, 298 K, 400 K, 500 K, 600 K and 700 K via the DL_POLY program version 2.18. Periodic boundary conditions were applied and the time step and pressure in all simulations were 1 fs and 1 bar respectively. Each MD simulation started with an equilibration (300 000 time steps in the NVT ensemble) followed by MD runs (500 000 time steps) in the NVE ensemble for data collecting. The trajectory was recorded every 200 steps during the production stage, and radial distribution functions were recorded every 500 steps [5]. The mean square displacements (MSDs) of the CS₂ molecules at each loading and at the different temperatures were evaluated by means of the following classical equation:

$$MSD(t) = \langle \Delta r_j^2(t) \rangle = \frac{1}{N} \sum_{j=1}^N \Delta r_j^2(t) = \frac{1}{N} \sum_{j=1}^N [r_j^c(t) - r_j^c(0)]^2 \quad (1)$$

Where N corresponds to the number of CS₂ molecules considered in the computation of the MSD and $r_j^c(t)$ is the location of the center of mass of molecule j at time t. The self-diffusion coefficient can also be obtained from the long-time limit of the MSD using the well-known Einstein relation [6]:

$$D_j = \frac{1}{6} \lim_{t \rightarrow \infty} \frac{d}{dt} \langle [r_j^c(t) - r_j^c(0)]^2 \rangle \quad (2)$$

The activation energies corresponding to the self-diffusion processes were then evaluated from the Arrhenius relation [7]:

$$D = D_0 \exp\left(-\frac{E_a}{RT}\right) \quad (3)$$

where E_a is the Arrhenius activation energy for the diffusion process. When ln(D) is plotted vs 1/T, activation energy can be extracted from slope of Arrhenius plot.

The adsorption energy for the ITQ-7 with nCS₂ molecules per unit cell can be defined as:

$$E_{ads} = E_{tot} - (E_{zeolite} + E_{gas}) \quad (4)$$



where E_{tot} and E_{zeolite} have been obtained from MD simulations and E_{gas} has been calculated by the ideal gas relation-
 $E_{\text{gas}} = 3nRT/2$.

3. Results and discussion

The MSDs for center of mass of CS_2 in ITQ-7 were calculated at the various different loadings (2, 4, 6, 8, 10, 12, 14, 16 carbon disulfide molecules/ unit cell) as a function of temperature in the range of 0–480 ps. At all of these loadings, the MSDs increase with temperature.

The diffusion coefficients have been evaluated from the linear slope of MSD (t) functions in the diffusive regime (Eq. 2). Figures 1 and 2 illustrate these coefficients as a function of the temperature and loading respectively. As can be seen in Figure 1, the self-diffusivity increases as the temperature is increased, due to the increase of mobility of particles by increasing of temperature.. Figure 2 shows the guest diffusivity in ITQ-7 decreases with increasing loading because of mutual hindrance.

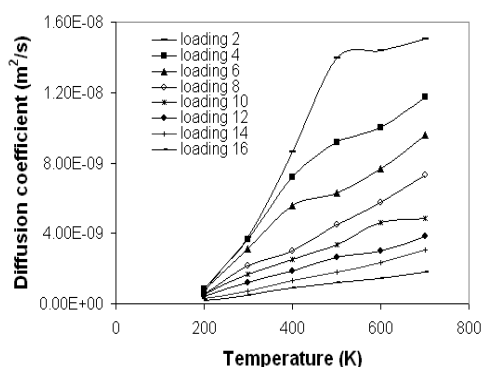


Fig. 1. Diffusion coefficient vs Temperature.

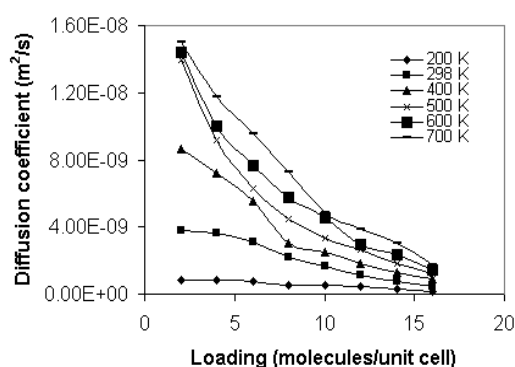


Fig. 2. Diffusion coefficient vs Loading.

Diffusion activation energy is obtained as the slope of $\ln(D)$ vs $1/T$ plot at each loading. These activation energies are about 5.4 kJ/mol at most loadings except of 2 and 4 loadings.

The radial distribution functions (RDFs) were calculated at several temperatures and loadings for C-C, Si-C and O-C sites. The RDF of C-C were changed with increasing temperature and loading, while RDF of Si-C and O-C RDFs remains nearly constant, because Si and O atoms were frozen in the simulations.

The adsorption energies per guest molecule at all loadings were calculated. These energies increase as a function of loading for the presence of more number of guests. The adsorption energies decrease with temperature for the increase of kinetic energy of the molecules.

4. Conclusion

Diffusion of CS_2 molecules in ITQ-7 zeolite was investigated via the molecular dynamics simulation. Some dynamic and structural properties such as MSDs, diffusion coefficients, activation energies, RDFs and adsorption energies were calculated at different loadings and temperatures.

References

- [1] B. Smit, T. L. M. Maesen, Chem. Rev.10 (2008) 108.
- [2] D. Selassie, D. Davis, J. Dahlin, E. Feise, G. Haman, D. S. Sholl, D. Kohen, J. Phys. Chem. C. 42 (2008) 112.
- [3] K. Makrodimitris, G. K. Papadopoulos, D. N. Theodorou, J. Phys. Chem. B. 4 (2001) 105.
- [4] S. B. Zhu, J. Lee, G. W. Robinson, Molecular Physics, 1 (1988) 65.
- [5] D. F. Plant, G. Maurin, R. G. Bell, J. Phys. Chem. B. 11 (2007) 111.
- [6] M. H. Kowsari, S. Alavi, M. Ashrafizaadeh, B. Najafi, The Journal Of Chemical Physics. (2008) 129.
- [7] P. Demontis, G. B. Suffritti, E. S. Fois, S. Quartieri J. Phys. Chem. 3 (1992) 96.
- [8] H. F. Mark, D. F. Othmer, C. G. Overberger, G. T. Seaborg, Encyclopedia of chemical technology, John Wiley & Sons, New York, 1978.

The effect of using two different water models on the pressure-area isotherm of DPPC monolayer

Delara Mohammad-Aghaie^{*}, Fernando Bresme^b

^{*}Department of Chemistry, College of Sciences, Shiraz University of Technology, Shiraz, 71555-313, Iran

^bDepartment of Chemistry, Imperial College London, SW7 2AZ, London, United Kingdom

(E-mail: d_aghahie@sutech.ac.ir)

Keywords: Molecular dynamics simulation, Pressure-area isotherm, DPPC, TIP4P-2005, SPC/E.

1. Introduction

Lung surfactant is the surface-active lining of the alveoli and consists of ~90% lipids and 5-10% proteins. The major component of surfactant lipids is DPPC (Dipalmitoyl Phosphatidyl Choline), a phospholipid with two palmitic acid tails.

Not only is DPPC, the primary component of lung surfactant, but it is also thought to be primarily responsible for the reduction of surface tension in the lungs to near-zero which is essential for breathing [1].

In our previous work, we investigated the phase behavior of DPPC monolayers at the air-water interface, using atomistic molecular dynamics simulations [2]. There we reported pressure-area isotherms of DPPC monolayers at four different temperatures, ranging from 273K to 310K. We could show obvious liquid condensed (LC) to liquid expanded (LE) phase transition on a time scale of almost 50 ns. Sufficient structural analysis confirmed the existence of this phase transition.

Knowing that different factors can affect the shape and position of obtained pressure-area isotherms of phospholipid monolayers, we decided to explore the effect of two different water models (SPC/E and TIP4P-2005) on the obtained isotherms at temperature 310 K.

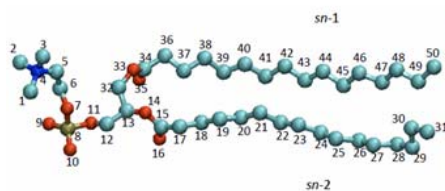


Fig. 1. The molecular model of the DPPC molecule.

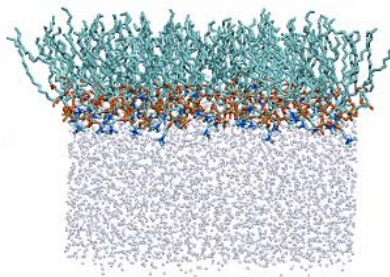


Fig. 2. The snapshot of the simulation setup.

2. Computational details

Molecular dynamics simulations of DPPC monolayers adsorbed at the water-air interface were performed with two different water models to assess their effect on the obtained pressure-area isotherms. The initial configuration of DPPC monolayer was prepared by 64 times replicating a single DPPC molecule. The phospholipids were arranged in a square two dimensional lattice and the head groups were partially immersed in one of the water surfaces of a pre-equilibrated water film containing 4×10^3 water molecules. Fig. 1 shows the molecular model of one DPPC molecule, where Fig.2 represents the snapshot of the simulation setup. The Berger et. al. force field [3] which uses a united atom approach to represent the CH₂ and CH₃ groups, was the one that we selected to model our phospholipids. All the interatomic bonds are rigid, and the angles and improper dihedrals are modeled through the GROMOS force field. The torsional interactions of the hydrocarbon chains were modelled through the Ryckaert-Bellemans potential. Non bonded interactions were handled through a combination of Lennard-Jones and Columbic terms and we employed full periodic boundary conditions in all the simulations. The short Lennard-Jones interactions were truncated at 1.7 nm.

Two selected water models are SPC/E and TIP4P/2005. The latter model provides a more accurate representation of the water surface tension in comparison to other proposed models for the water. The SPC and its variant SPC/E water models, predict surface tensions that are too low in comparison with the actual surface tension of water. We expect this has an impact on the surface pressure computations, shifting the pressure area isotherms to lower values.

In order to obtain surface pressure (Π)-Area isotherms, the following equation was used to calculate the surface pressure:

$$\Pi(A, T) = \gamma_w(T) - \gamma_m(A, T) \quad (1)$$

Where A is the area per phospholipid, $\gamma_w(T)$ is the surface tension of the water model at temperature T , and $\gamma_m(A, T)$ is the surface tension of the monolayer which was extracted from simulations as follows:

$$\gamma_m(A, T) = \gamma_t(A, T) - \gamma_w(T) \quad (2)$$

Here $\gamma_t(A, T)$ is the total surface tension imposed on the DPPC-water layer. The constant surface tension and temperature simulations were performed using the Berendsen barostat/thermostat with coupling constants 1 and 0.1 picoseconds respectively. The initial configurations were equilibrated using the Berendsen thermostat at $T=310K$ for tens of nanoseconds, before performing the main simulations. We used a time step of 2 femtoseconds for all of the simulations which were performed with the code GROMACS 3.3.

3. Results and discussion

In our calculations we need the surface tension of the pure selected water models. In this respect we performed two distinct simulations each for one of the water models at $T=310K$. The surface tension of SPC/E model was found to be 58.456 mN/m and for the TIP4P-2005 model it became 64.558 mN/m. Then we started two sets of constant surface tension and temperature simulations for the DPPC monolayers adsorbed at SPC/E and TIP4P-2005 water models. As it can be seen in Fig. 3 in order to have the surface pressure-area isotherms, we need some points corresponding to different surface pressures and area per phospholipids. Each point shown on the isotherms has been obtained after 60 ns of simulation. The last 20 ns of the simulations have been used to extract the results.

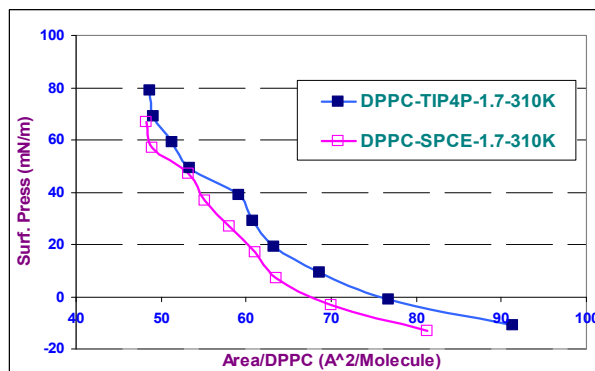


Fig. 3. Surface pressure-area isotherms of DPPC monolayers adsorbed at the SPC/E and TIP4P-2005 water models.

The isotherms clearly show the lowering of the surface pressures due to using the SPC/E water model. It is because the SPC/E water model gives lower value for the water surface tension. According to Eq. 2 at constant total surface tension, this leads to greater monolayer surface tension and then based on Eq. 1 lower surface pressures will be obtained. The DPPC TIP4P-2005 isotherm shows better correspondence with the experimental isotherms.

The radial distribution functions were obtained using three carbon atoms in the middle of sn-1 and sn-2 chains of the DPPC molecule. (Carbons 21, 22, 23 of the sn-1 chain and 40, 41, 42 of the sn-2 chain). Although the carbon atoms of DPPC molecule have been used to obtain the RDF plots, again the effect of water model is evident here. In the case of TIP4P-2005 model, the RDF plots corresponding to the points with lower area per DPPC, exhibit more long range order which is characteristic of the liquid condensed phase. It shows that the LC phase of DPPC monolayer can be nucleated more easily in the presence of TIP4P-2005 model. The effect of changing water model also is obvious in other structural properties such as the distance between carbons C15 - C31 in the sn-2 chain, and carbons C34 - C50 in the sn-1 chain which are considered as the lengths of two hydrocarbon chains. In the case of TIP4P-2005 model, these lengths are longer, again showing better nucleation of the liquid condensed phase.

References

- [1] Knecht, V., Müller, M., Bonn, M., Marrink, S. J., Mark, A. E. J. Chem. Phys. 122 (2005) 24704.
- [2] Mohammad-Aghaie, D., Macé, E., Sennoga, C., Seddon, J., Bresme, F. J. Phys. Chem. B. (In Press)
- [3] Berger, O., Edholm, O., Jähnig, F., Biophys. J. 72 (1997) 2002.

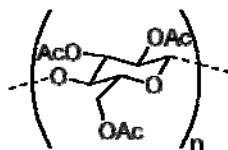
Molecular dynamic simulation of amorphous cellulous triacetate membraneMuhammad Shadman ^a, Saeid Yeganegi ^{a,*}, Farhood Ziaie ^b^a Department of Physical and Inorganic Chemistry, Faculty of Chemistry, University of Mazandaran, Babulsar, Iran^b Agricultural, Medical and Industrial Research School (AMIRS), Karaj, Iran

(E-mail: yeganegi@umz.ac.ir)

Keyword: Penetration, Membrane, Molecular dynamic, CTA.**1. Introduction**

The adsorption of small molecules in polymeric matrices is of great scientific interest for applications ranging from catalysis to separation technology, to development of new polymeric membranes with improved barrier properties [1]. The question that most naturally occurs is what makes a polymeric membrane a good barrier? This work tries to check out one type of polymer as host matrix to investigate and calculate the ability of it to compare with other polymeric membranes by theoretically procedure. Therefore, the most commercially important cellulosic polymer, Cellulous Triacetate (CTA) is selected. According to our knowledge, there are not any investigations to the correlations between the structural organization and the properties of this polymer theoretically or experimentally.

In recent years, molecular modeling simulations have been advanced to such a level to predict the properties of polymers. Molecular dynamic simulations of the oligomers of polymers can perform at ambient temperature over wide range of polymeric chain lengths. However, the force field such as COMPASS, amber, UFF or Dreiding can applied for this interest researches. The main aim of this paper is to investigate the sorption and diffusion of methane and nitrogen in the mesomorphic of CTA. The monomer of CTA has shown in figure 1.

**Fig. 1.** The CTA monomer**2. Method and simulation details**

In this work, NVE and NPT molecular dynamics, and GUI analysis module of DL_POLY software were used in order to perform the computations and to calculate the density, diffusion coefficient and to predict the correlation between these properties [2]. The computational procedure used in this research includes the following main steps shown in Figure 2.

Here, we also use the Dreiding force field for all simulations. The Dreiding force field provides a potential energy interaction function (E_{total}) that accounts for both bonded (E_b) and non-bonded (E_{nb}) interactions: $E_{total}=E_b+E_{nb}$. The bonded terms typically include harmonic bond stretching (E_s), harmonic angle bending (E_a), torsional (E_t), and inversion (E_i) energies: $E_b=E_s+E_a+E_t+E_i$. Non-bonded terms typically contain van der Waals (E_{vdW}), electrostatic (Coulombic) (E_q) and hydrogen bond (10–12 potential) (E_{hb}) interactions: $E_{nb}=E_{vdW}+E_q+E_{hb}$ [3]. The 14 Å cut off distance and the Lennard-Jones (LJ) 6–12 potential was used to calculate the non-bonded van der Waals interactions. In this work, we have used the LJ parameters that obtained from previous work for CH₄ and N₂ [4]. The charge distribution in the molecule, due to Coulombic (electrostatic) interactions, of the simulated polymers was obtained with the charge equilibration method described by Rappe and Goddard using the applied force field. The NPT and NVE molecular dynamics simulations were performed at different temperatures for each constructed and minimized polymer system. In order to ensure that the simulations are carried out for sufficient time, that is one of the most important criteria in equilibrating the system [5], the number of steps of MD simulations was 3 ns, and the output frequency was every 250 steps. The time steps of 0.001 to 0.003 ps are taken to be constant for all the simulations of this study. The non-canonical 'T-damping' thermostat described by Berendsen et al. was used for isothermal-isobaric NPT-MD simulations. Figure 3 shows the cubic periodic boundary conditions of 10 nitrogen and 5 oligomers of 25 monomeric chain length.

3. Results and discussions

As was indicated above and figure 2, the simulations were performed in three parts. First part is related to compact the polymeric matrix, second is concerned about equilibration and third is productions portion of MD simulations. After each production, the history of dynamics of each atom is presented to analysis of thermodynamic properties of it.

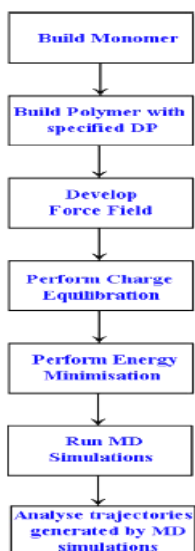


Fig. 2. Steps in the computational procedure used in this research.

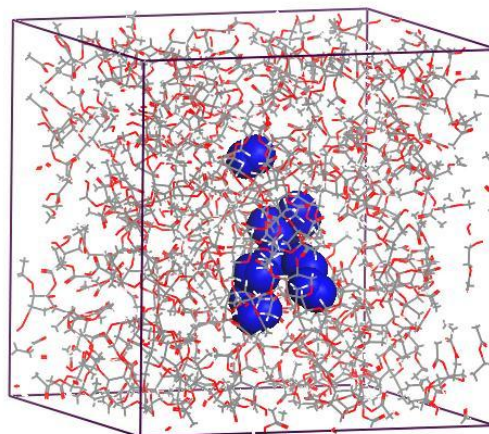


Fig. 3. The PBC of N₂ in amorphous CTA with 37 Å box dimension.

In the first step, we have simulated polymeric membrane to exact the same as used for industrial propose. It means, it should examine the real density and some physical properties from simulations and experimental report. Next, it is necessary to the polymeric host matrix and gases guest molecules equilibrate in interest temperatures. The result at 298.15 K and 0.001 GPa for CTA and N₂ as penetrant molecules, observed in Figure 4 and 5 respectively to indicated the equilibration step.

It should be described to readers that our MD researches to clear the CTA properties would be continued.

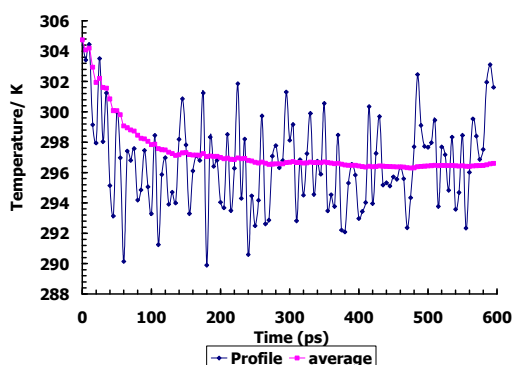


Fig. 4. The temperature history file from NPT-MD

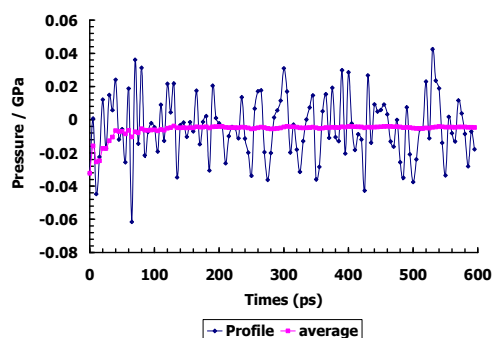


Fig. 5. The pressure history file from NPT-MD

References

- [1] I. Cozmuta, M. Blanco, W. A. Goddard III, J. Phys. Chem. B 111 (2007) 3151.
- [2] I. T. Todorov, and W. Smith. Philosophical Transactions of the Royal Society of London A, 362 (2004) 1835.
- [3] A. Alentiev, I. G. Economou, E. Finkelshtein, J. Petrou, V. E. Raptis, M. Sanopoulou, S. Soloviev, N. Ushakov, Y. Yampolskii Polymer 45 (2004) 6933.
- [4] M. Shadman, S. Yeganegi, F. Ziaie, Chemical Physics Letters 467 (2009) 237.
- [5] M. P. Allen, D. J. Tildesley, Computer simulation of liquids Oxford University Press, Oxford, (1987).

Molecular Dynamics Simulations of the Protein-Micelle Interaction

S. Jalili and M. Akhavan*

Department of Chemistry, K. N. Toosi University of Technology, Tehran, Iran

(Emails: sjalili@kntu.ac.ir, mojdeh@dena.kntu.ac.ir)

Introduction

Amyloid- β ($A\beta$) peptide is the major component of the senile plaques found in the brain of Alzheimer's disease (AD) patients. One mechanism for the toxicity of $A\beta$ oligomers is the formation of pores or ion channels through the interaction with cell membrane. Experimental and Molecular dynamics (MD) studies of $A\beta$ peptides in membrane-mimicking environments (such as micelles) all show two helical regions connected by a loop. However, contradicting results are obtained about the positioning of $A\beta$ in these environments. Some people suggest that the C-terminal helix of $A\beta$ is imbedded in the core of micelle [1], while others report that the peptide resides on the micelle surface and do not insert into its hydrophobic core [2]. In this work, we have reported the results of MD simulations on the interaction of $A\beta_{40}$ with a sodium dodecyl sulfate (SDS) micelle. Knowledge about the structure and positioning of $A\beta$ monomers in SDS micelles is essential for an understanding of the initial events in the oligomerization process of $A\beta$ in biological membranes.

Methods

Simulations of $A\beta_{40}$ peptide in preformed SDS micelles were performed using two different initial positions for the peptide; one in the micelle core (S1) and one in water phase (S2), far from the micelle. In the 3rd simulation (S3), the process of spontaneous self-association of SDS molecules around the peptide was followed.

All MD simulations were performed using the GROMACS 4.0 simulation package. The GROMOS96 force field with the 43a2 parameter set was used throughout. The SDS charges and bonded parameters were taken from previous simulations [3]. Every system was first energy minimized, followed by 1 ns NVT simulation for equilibration. During this run, the coordinates of the peptide were harmonically restrained with to their initial positions. The production runs were performed for 50 ns at constant temperature, pressure and number of particles (NPT) and the coordinates were saved every 10 ps. The temperature of the system was maintained at 300 K, using the Nose-Hoover thermostat and the pressure coupling was performed at 1 bar with the Parrinello-Rahman barostat. Long range electrostatic interactions were treated using the PME method. Periodic boundary conditions were applied with a van der Waals cutoff of 1 nm. All bond lengths were constrained using the LINCS algorithm, allowing an integration time step of 2 fs.

Results and Discussion

The time evolution of the peptide's secondary structure in S1 and S2 simulations are shown in Fig. 1. There are two helical regions in the peptide, which are connected through a structureless link. The first 14 residues in both systems are more or less unstructured and appear as coils or bends. This structure is in agreement with the experimental studies. For S1 system, there are two α -helices between residues 15-24 and 29-36, connected by residues 25-27. For S2, the helical regions are mainly of 5-helix type. The final structures obtained from S1 and S2 simulations are shown in Fig. 2. In S1, the C-terminal helix of the peptide is located in the micelle core, whereas in S2 this section is outside the core and can interact with both water and head groups.

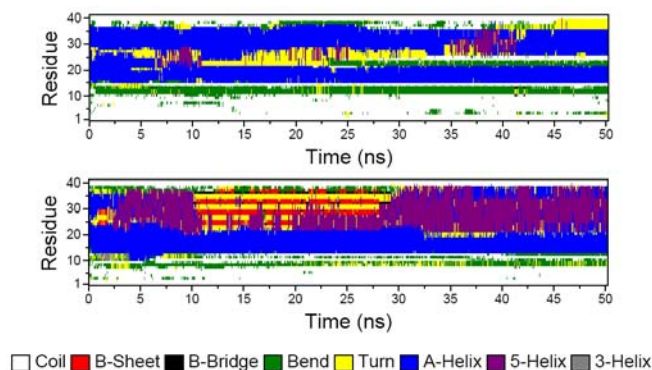


Fig. 1 Time evolution of the peptide's secondary structure in S1 (top) and S2 (bottom) simulations.

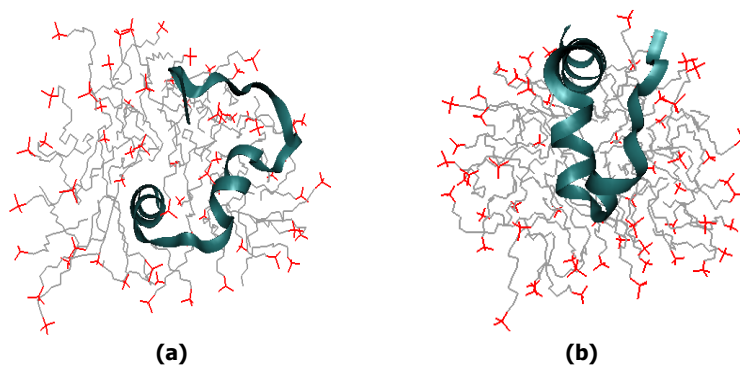


Fig. 2 Final structures from the S1 (a) and S2 (b) simulations.

Fig. 3 shows the main steps of the spontaneous self-assembly of SDS molecules around the peptide, as obtained from the S3 simulation. At the zero time, when the equilibration of the system is accomplished, there exist sparse collections of 10-15 dodecyl sulfate molecules at different places around the peptide in the simulation box. These collections are joined together during the simulation and eventually form a 38-molecule micelle around the peptide at the end of simulation. The association of these assemblies normally proceeds via head group interactions. The rest of SDS molecules are ordered in the form of two 7-molecule globules and some individuals. The peptide position relative to the micelle is similar to the S2 simulation, as revealed from radial density plots (data not shown).

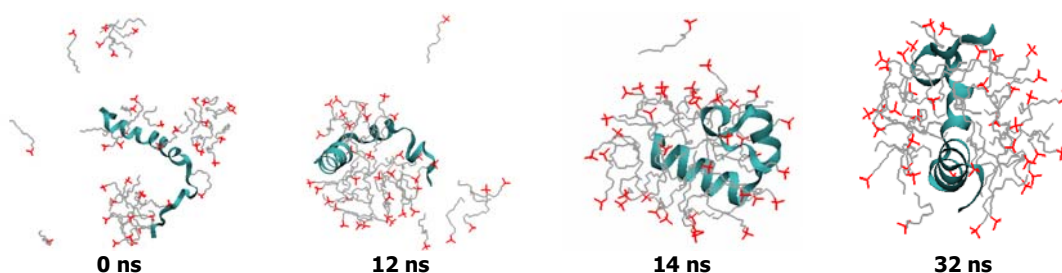


Fig. 3 The structure of the peptide and the 38 molecules of main micelle at different times.

Conclusions

In this paper, we studied the interaction of the Alzheimer's A β 40 peptide with SDS micelles. Our results showed that the experimental conformation of the peptide in SDS micelles is well reproduced using the molecular dynamics simulations. The simulation result was shown to be dependent on the initial positioning of the peptide with respect to the micelle. This difference may be caused by insufficient sampling and convergence problems. However, there is no idea about the times required for it to converge. The continuation of the S1 simulation for a further time of 50 ns did not make any difference in the results. It seems that the required time may be beyond the scope of atomistic simulations.

Keywords: Alzheimer's Disease, Amyloid Beta Peptide, Sodium Dodecyl Sulfate, Protein-Micelle Interaction, Molecular Dynamics Simulation.

References

- [1] H. Shao, S. Jao, K. Ma, M. G. Zagorski, *J. Mol. Biol.* 285 (1999) 755.
- [2] J. Jarvet, J. Danielsson, P. Damberg, M. Oleszczuk, A. Gräslund, *J. Biomol. NMR* 39 (2007) 63.
- [3] M. Sammalkorpi, M. Karttunen, M. Haataja, *J. Phys. Chem. B* 111 (2007) 11722.



New aldehyde as a new pre-material for synthesis of new liquid crystals, synthesis, Ab initio DFT study, characterization and structure

Omid Dadfar*, Razieh Samimi, Eslam Alizadeh

Department of Chemistry, Shahid Rajaei Teacher Training University, P.O.Box 16785- 163,
Tehran, Iran

* Omid Dadfar, omid.dadfar@yahoo.com, Tel: +98-731-2227629, Mob: +989171358533

1. Introduction

Metallomesogens, metal complexes of organic ligands which exhibit liquid crystalline characters have been important field of studies in the optical tools. [1-2]. Salicylaldehyde-based ligands have been widely used in synthesis of these complexes. There are many studies about using copper(II) in synthesis of mesogenic complexes [3-5]. ((alkoxy)phenyl)diazenyl hydroxyl benzaldehydes are one of important reactants to synthesis of complexes with liquid crystal characters. In this work, we have studied the synthesis and characterization of (E)-5-((4-(dodecyloxy)phenyl)diazenyl)-2-hydroxybenzaldehyde that can be used to syntheses of Cu(II) and Ni(II) complexes have crystal liquid properties.

2. Experimental Methods

Synthesis of this ligand is depended on preparing some components. As the scheme, 4-dodecyloxynitrophenol and 4-(dodecyloxy)aniline should be prepared.

2-3-1) preparation of 4-dodecyloxynitrophenol

4-dodecyloxynitrophenol is preparing in the etherification of 4-nitrophenol with 1-bromododecan in the standard method [6]. In this method, according to stoichiometry amounts, one mole of 1-bromododecan and one mole of 4-nitrophenol in the one mole of solvent of DMF and half mole of potassium carbonate (for pH control in 10-11) are refluxed during 3 hour. It yields to a brown product. After washing it with ethanol 96%, and recrystallization, white needle shape crystals will appear.

2-3-2) preparation of 4-(dodecyloxy)aniline

Synthesis of 4-(dodecyloxy)aniline, is the result of reduction of 4-dodecyloxynitrophenol with SnCl_2 in the acidic media that is prepared according to standard method [7]. In this method, according to stoichiometric amounts, one mole of 4-dodecyloxynitrophenol and three mole of SnCl_2 in presence of six mole of HCl (6M) is refluxed during 3 hour and yield to brown aminic product. This product can be extracted by diethylether after a short time.

2-3-3) Preparation of (E)-5-((4-(dodecyloxy)phenyl)diazenyl)-2-hydroxybenzaldehyde

(E)-5-((4-(dodecyloxy)phenyl)diazenyl)-2-hydroxybenzaldehyde is synthesized of diazotation of 4-(dodecyloxy)aniline. For this propose, pure 4-(dodecyloxy)aniline have been solved in HCl (6M) at the controlled temperature at 0-5 C and after 30 minutes should react with solution of sodium nitrite that is dropping slowly into the reaction media. It yield to diazonium halite. Then obtained solution adds to the balloon contained 2-hydroxy benzaldehyde. After adding NaOH(10%) it stir with magnetic stirrer during 3 hours. Yellow-brown residual will precipitate.[8]

3. Computational methods

Geometry optimization is performed using Gaussian 03 package (G03W) [9] at the level of density functional theory with B3LYP/6-31G(d,p) and IR spectrum is computed in B3LYP/6-31G(d) level. This level use Beck's three-parameter hybrid functional combined with the Lee-Yang-Parr correlation functional (B3LYP) level of theory with 6-31G(d,p) basis set [10-11]. IR frequency computations is performed with B3LYP method and 6-31G(d) basis set.

4. Result and desiccations

Temperature controlling in rang of 0-5C is very important and pH should be more than 7 in this synthesis. After this process, product is analyzed about melting point, IR and HNMR spectrums in experimental analyses and it is studded about optimization and the IR spectrums by Gaussian 2003 in computational analysis. Melting point of final product is 128.51 C.

5. Computational results:

Structure of product is optimized in Gaussian 03 package. IR frequency calculations yield to results that its graphical scheme is

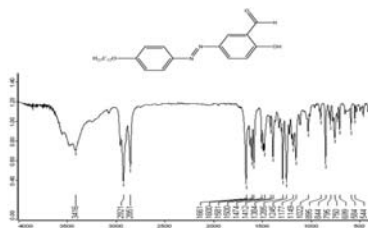


Fig. (1)



Fig. (2)

Fig. (1): Instrumental IR spectrum of (E)-5-((4-(dodecyloxy)phenyl)diazenyl)-2-hydroxybenzaldehyde

Fig. (2): IR spectrum obtained From Freq Calculation of (E)-5-((4-(dodecyloxy)phenyl)diazenyl)-2-hydroxybenzaldehyde

6. Conclusion

(E)-5-((4-(dodecyloxy)phenyl)diazenyl)-2-hydroxybenzaldehyde synthesis is studied in this work. Results of experimental and computational scrutinizing shows that synthesis is yielded to the favorite product. NMR and IR spectrums obtained from instrumental and computational analyses in ab initio DFT methods are coordinated to each other. There are new series of ligands can be synthesized of this aldehyde that can be used in product CDs, DVDs and B-rays. This synthesis yield to 71% product.

References

- [1] A. A. Khandar, Z. Rezvani, *Polyhedron*, 1999, 18:129
- [2] Giroud AM, Maitlis PM. *Angew. Chem. Int. Ed.Eng.* 1991;30:375.
- [3] Piecoki C, Simon J, Skoulios A,Guillon D, Weber P. *J. Am. Chem. Soc.* 1982;104:5254.
- [4] Marcos M, Romero P, Serrano JL, Barbera J, Levelut AM. *Liq. Cryst.* 1990;7:251.
- [5] Marcos M, Romero P,Serrano JL. *J. Chem[Soc., Chem. Commun.,* 1989,1641.
- [6] F. Wurthner, R. Wortmann, *Angew. Chem.,* 1997, 109, 2933.
- [7] E. C. Horing, *Organic. Synthesis*, Jhon Willy & sons, New York, 1995, 2, 130.
- [8] Gang Wang; Ying Qian; Guomin Xiao; Baoping Lin; Yiping Cui, *Dyes and Pigments*, 2006, 1
- [9] M. J. Frisch, G. W. Trucks, H. B. Schlegel, G. E. Scuseria, M. A. Robb, J. R. Cheeseman, J. A. Montgomery, Jr., T. Vreven, K. N. Kudin, J. C. Burant, J. M. Millam, S. S. Iyengar, J. Tomasi, V. Barone, B. Mennucci, M. Cossi, G. Scalmani, N. Rega, G. A. Petersson, H. Nakatsuji, M. Hada, M. Ehara, K. Toyota, R. Fukuda, J. Hasegawa, M. Ishida, T. Nakajima, Y. Honda, O. Kitao, H. Nakai, M. Klene, X. Li, J. E. Knox, H. P. Hratchian, J. B. Cross, C. Adamo, J. Jaramillo, R. Gomperts, R. E. Stratmann, O. Yazyev, Martin, D. J. Fox, T. Keith, M. A. Al-Laham, C. Y. Peng, A. Nanayakkara, M. Challacombe, P. M. W. Gill, B. Johnson, W. Chen, M. W. Wong, C. Gonzalez, and J. A. Pople, *Gaussian, Inc., Pittsburgh PA*, 2003.
- [10] Becke, J. *Chem. Phys. Rev. B* 37 (1993) 5648.
- [11] Lee, W. Yang, R. G. Parr, *Phys. Rev. B* 37 (1988) 785.

Simulation Studies on the Diffusion of Argon in Nanoporous PVB Membranes

Muhammad Shadman ^a, Saeid Yeganegi ^{a, *}, Farhood Ziaie ^b

^a Department of Physical and Inorganic Chemistry, Faculty of Chemistry, University of Mazandaran, Babolsar, Iran.

^b Agricultural, Medical and Industrial Research School (AMIRS), Karaj, Iran

(* e-mail: yeganegi@umz.ac.ir)

Keyword: Molecular simulation, PVB, diffusion, nanopore

1. Introduction

A great portion of research effort in the membrane gas separation is still being focused on the development of membrane material. In the past decades, considerable attention has been paid to the studies of the intrinsic permeation properties of polymers as a consequence of the ever growing use of these materials for permselective membranes for gas separation, protective coatings, and food packing. Gas transport is governed by the solubility and diffusion coefficients of gases in the membranes [1-4]. Computer simulation studies of permeation of small gas molecules through polymeric materials have undergone a remarkable development over the past few years. Detailed molecular dynamics simulations have become a widely used method for the investigation of the molecular structure of amorphous polymers and of the diffusion of small molecules through these materials [5].

This is aim of this report to give some new results and additional interpretations of molecular dynamics (MD) simulations concerning the diffusion processes in nanoporous polymeric materials. In this work, we explore and investigate the diffusion of argon molecules through bulk amorphous poly vinyl butiral (PVB) as the commercially polymeric product.

2. Computational methodology

The amorphous bulk polymer is modeled as 5 linear chains of 20 monomer contains 4310 atoms and the length of the sides of the cubic unit cells was 32–36 Å. Different configurations of the polymer chains were generated and placed in a cubic box. The PVB monomer is shown in figure 1. Cubic periodic boundary conditions have been applied (figure 2). To estimate the density of the material for an infinite chain length, models of increasing chain lengths have been simulated $(-C_{14}H_{26}O_5-)_n$ with $n=4, 6, 8, 10, 15$ and 20 and the density computed using 200 ps of NPT molecular dynamics. The “calculated” density of amorphous PVB is the extrapolated density considering an infinite chain. Figure 3 shows the projected density for the “infinite” chain length

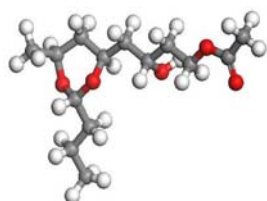


Fig. 1: the Gray atoms are C, the white are H and the red are O.

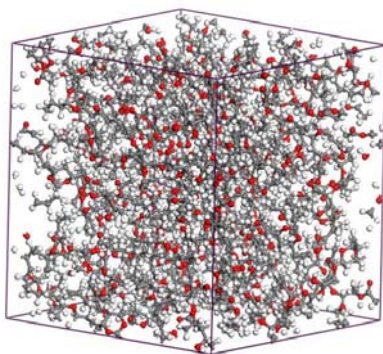


Fig. 2. A snapshot of simulation box. PBC applied for 4320 atoms of PVB and Ar

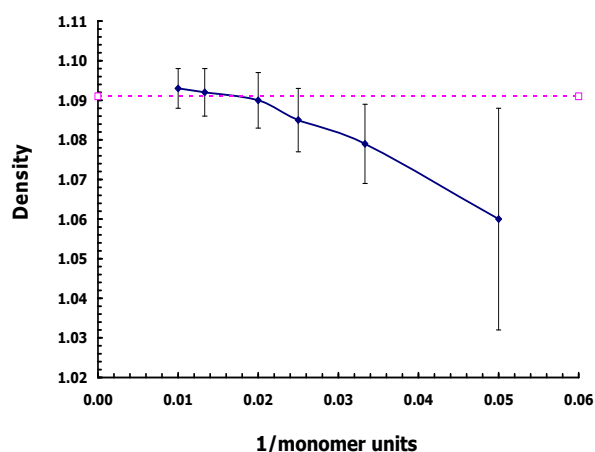


Fig. 3. Density variation as a function of polymer chain length. For $n = \infty$ the calculated density is 1.093 g/cm³. The experimental density of PVB is 1.09 g/cm³.

In all simulations, Dreiding force field with a atom based cutoff of 12.5 Å for polymer atoms and lennard-jones potential for argons were employed. Long-range interactions were treated by Ewald summation technique. Equilibration is ensured by following a heating and cooling temperature cycle protocol is named annealing procedure: a stepwise procedure of constant pressure molecular dynamics (NPT) cycles of heating and cooling from 400 to 250 K by a step of 25 K, each of 10 ps, with 5 cycles were performed. This was followed by long NPT simulation runs of 0.3 ns at a given temperature 248.15, 273.15, 298.15, 313.15 and 333.15 K and a pressure of 1 bar. A time step of 1 fs was employed. The production runs consisted of 2 ns of NVT dynamics at each temperature. A time step of 3 fs was employed. To run the simulation with greater time step than 1 fs, chemical bond lengths have been constrained using the RATTLE algorithm which is the velocity version of the SHAKE algorithm. In this work, all simulations carried out with DL_POLY molecular dynamic package Material studio [6], and temperature and pressure were controlled by the Berendsen's method [7].

3. Results and discussions

Trajectory file data generated from MD simulation has been used in all the polymer property calculations and analyses presented in this research. The history files were analysed by GUI analysis module. The self diffusion coefficient of argon can be evaluated from the limiting slope of the mean-square displacement (MSD) as a function of time [8]. The GUI of the package can help us to analysis of the history data for calculation of MSD for argon in different temperatures. Figure 4 presents log (MSD) vs log (t) of argon molecules in different temperatures. The slope of the log (MSD) as a function of log (t) must be close to unity [8]. Then, the slopes of the best line fitted for MSDs of 248.15, 273.15, 298.15, 313.15 and 333.15 K are 0.9465, 1.06, 0.9551, 0.9881 and 0.9744 respectively. Therefore, the self diffusions for these temperatures are 1.163, 2.52, 1.95, 1.44 and 1.95 ($\times 10^{-9} \text{m}^2 \text{s}^{-1}$) respectively. It seems increasing temperature, increases MSD and diffusion to around 298.15 K and then MSDs decrease with increasing the temperatures. It is should be noted that our simulations have not completed and would be continued.

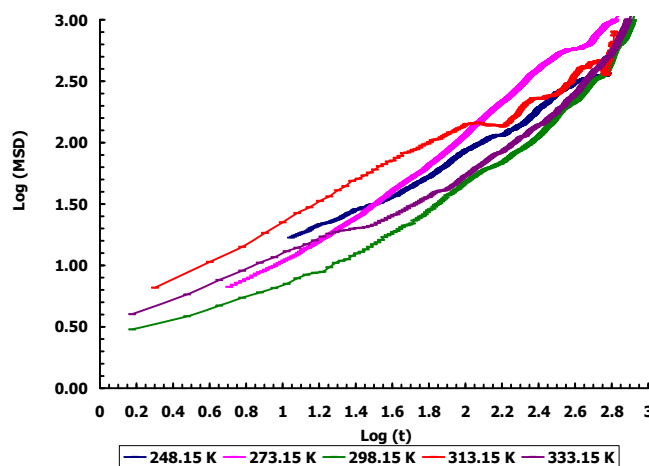


Fig. 4. Log (MSD) vs log (t) of ten argon molecules

References:

- [1] M. López-González, E. Saiz, J. Guzmán, E. Riande, *Macromolecules* 34 (2001) 4999-5004.
- [2] M. F. Laguna, J. Guzmán, E. Riande, *Macromolecules* 31 (1998) 7488-7494.
- [3] D. Pavel, R. Shanks, *Polymer* 44 (2003) 6713-6724.
- [4] D. Pavel, R. Shanks, *Polymer* 46 (2005) 6135-6147.
- [5] E. Tocci, D. Hofmann, D. Paul, N. Russo, E. Driolia, *Polymer* 42 (2001) 521-533.
- [6] I. T. Todorov, and W. Smith. *Philosophical Transactions of the Royal Society of London A*, 362 (2004) 1835.
- [7] H. J. C. Berendsen, J. P. M. Postma, W. F. van Gunsteren, A. DiNola, J. R. Haak, *J. Chem. Phys.* 81 (1984) 3684.
- [8] M. P. Allen, D. J. Tildesley, *Computer simulation of liquids* Oxford University Press, Oxford, (1987).



Electrochemistry





Investigation of interaction ct-DNA with 10-molybdo 2- vanado phosphoric acid by UV/Vis spectroscopy and cyclic voltammetry

N. Sohrabi^{a,b,*}, H. R. Zare^a, S. Shiralinasab^a

^aDepartment of Chemistry, Yazd university, Yazd, Iran ^bIsfahan Payamenoor University, Nabavimanesh Avenue, Isfahan, Iran
(Email: * nasrinsohrabi@yahoo.com)

Keywords: polyoxometalate, DNA, UV/Vis spectroscopy, cyclic voltammetry, interaction

1. Introduction

Polyoxometalates (POMs) are early transition metal oxygen clusters such as Mo, V and W [1] which contained potential applications in materials [2], biochemistry [3], medicine [4] and catalysis [5]. The interactions of some anticancer drugs with DNA have been studied with a variety of techniques. The electrochemical investigations of DNA binding molecule interactions can provide a useful complement to spectroscopic methods.

As DNA is heated, it reaches a temperature where the strand separated (DNA melts). This leads to a significant increase in the ultraviolet absorption at around 260 nm. The melting point (T_m) is the temperature at which half the DNA is unwound [6].

The physicochemical properties of $[H_5PMo_{10}V_2O_{40}]$, (POMo), and its interaction with ct-DNA at various temperatures and 5mM phosphate buffer pH=7 by two techniques include UV/Vis and electrochemical methods.

Small shift in potential and decrease of current represent outside binding mode of DNA to POMo.

2. Methods

1. UV/Vis spectroscopy

We used the UV/Vis spectroscopy for studied physicochemical properties of 10-molybdo 2-vanado phosphoric acid, $[H_5PMo_{10}V_2O_{40}]$, at various environmental conditions, such as concentration, temperature and ionic strength. Then the interaction of $[H_5PMo_{10}V_2O_{40}]$ with calf thymus deoxyribonucleic acid (ct-DNA) was investigated.

2. Voltammetry

Preparation and voltammetric studies of an polyoxomolybdate modified glassy carbon electrode have been investigated. The properties of a modified glassy carbon electrode with polyoxomolybdate, ($[H_5PMo_{10}V_2O_{40}]$), during preparation under different conditions were examined. Interaction of CT-DNA with GCE/POMo was investigated by DPV.

3. Results and discussion

The UV/Vis spectrum of $[H_5PMo_{10}V_2O_{40}]$ at phosphate buffer with pH=7 and 25 °C shown an increase in Absorbance without change in λ_{max} in present of DNA. The denaturation of CT-DNA in different mol ratio 0, 0.024, 0.047 and 0.088 of POMo to DNA was studied. The T_m values were determined for these mol ratios with Igor software. Then using these parameters, we calculated ΔH_m according eq 1 [7]:

$$-\Delta \epsilon_{260}(T) = \frac{(a_N + b_N T) + (a_D + b_D T) \exp\left[-\frac{\Delta H_m}{R} \left(\frac{1}{T} - \frac{1}{T_m}\right)\right]}{1 + \exp\left[-\frac{\Delta H_m}{R} \left(\frac{1}{T} - \frac{1}{T_m}\right)\right]} \quad (1)$$

We fitted this equation with a good nonlinear regression equation with Sigma Plot software and calculated its parameters. Table 1 shown ΔH_m value for various T_m . By using of ΔH_m we calculated ΔG_D .

Table 1. the parameter of fit eq 1

$\frac{[H_5PMo_{10}V_2O_{40}]}{[ct-DNA]}$	0	0.024	0.047	0.088
T_m (K)	338.726±0.01	338.195±0.01	342.799±0.01	338.195±0.01
ΔH_m (kJ/mol)	314.9±1.692	378.0±2.798	402.2±3.688	277.5±1.538

The small change in T_m values confirm the outside binding mode.

We studied pH effect on the modified glassy carbon electrode. The pH dependence of redox activity of this film one linear segment was shown with slop values of 55.2 m V/pH. Figure 1 shown modified electrode voltammograms in different pH.

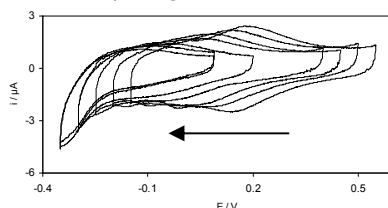


Fig. 1. voltammograms of modified electrode in phosphate buffer with different pH

The charge transfer coefficient (α) and the charge transfer rate constant, k_s , for electron transfer between $[H_5PMo_{10}V_2O_{40}]$ and glassy carbon electrode were calculated from the slop of E_p versus $\log(u)$ plot, as 0.514 and 25.203 s^{-1} respectively.

The addition of CT-DNA into the POM/GCE caused a considerable decrease in peak current (Fig 2) without change in potential that represent outside binding mode of interaction.

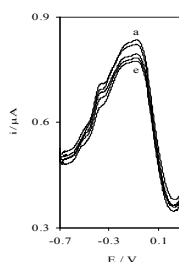


Fig. 2. DVP for modified glassy carbon electrode (a-e) in present different constant of DNA, 0, 0.5, 0.1, 0.13 and 0.195 mM respectively.

the distribution of bound and free forms depends on the square of the measured current, so we can therefore calculate the mole fraction of bound complex as [8]:

$$X_b = (i^2 - i_{sat}^2) / (i_0^2 - i_{sat}^2) \quad (2)$$

Binding constants (K) and binding site sizes (s) were determined from the voltammetric data, i.g., shifts in potential and changes in limiting current with the addition of DNA. For determination of these parameter, we used equation 3 [8]:

$$\frac{C_b}{C_t} = \frac{b - (b^2 - \frac{2K^2 C_t [DNA]}{s})^{1/2}}{2KC_t} \quad , \quad b = 1 + KC_t + K[DNA]/2s \quad (3)$$

Fitting the simulated isotherm to eq 3 gave a very good fit. The fit of data with two parameter gave $K = 465 \times 10^4 \text{ M}^{-1}$ and $s = 0.5$

4. Conclusions

Small shift in potential and decrease of current represent outside binding mode of DNA to POM. The small change in T_m values confirms the outside binding mode [9].

References

- [1] A. Tian, Z. Han, J. Peng, J. Ying, J. Sha, B. Dong, J. Zhai, H. Liu, *Inorganica Chimica Acta*. 361 (2008) 1332.
- [2] M.T. Pope, A. Muller, *Chem. Int. Ed. Engl.* 30 (1991) 34.
- [3] P.J. Kulesza, B. Karwowska, B. Grzybowska, A. Wieckowski, *Electrochim. Acta*. 44 (1998) 1295.
- [4] F. Caruso, D.G. Kurth, D. Vollmer, M.J. Koop, A. Muller, *Langmuir*, 14 (1998) 3462.
- [5] C. L. Hill, R. B. Bown, *J. Am. Chem. Soc.* 108 (1986) 536.
- [6] C. N. Pace, K. L. Show, *Proteins. Struct. Funct. Genet. Suppl.* 4 (2000) 1.
- [7] E. Ahmad, V. Rishi, F. Anjum, W. Pfeil, *J. Biochem.* 329 (1998) 137.
- [8] M. T. Carter, M. Rodriguez, A. J. Bard, *J. Am. Chem. Soc.* 111 (1989) 8901.
- [9] A. A. Ghazaryan, Y.B. Dalyan, *J. Biomol. struct. And Dynam.* 24 (2006) 67.

**Corrosion and passivation of Ti-6Al-4V in acid -organic inhibitor**

S. M. A. Hosseini*, M. Salari, M. Mohammad Alizadeh

Department of Chemistry, Faculty of Science, Shahid Bahonar University of Kerman, 22 Bahman, Kerman 76175, Iran

(Email: s.m.a.hosseini@mail.uk.ac.ir)

Keywords: Titanium alloy, Inhibitor, passivation, SEM**1. Introduction**

Industrial applications of titanium and its alloys have been expanding widely in various areas. The advantages of titanium materials over many metals are their excellent corrosion resistance and high strength-to-weight ratio as demonstrated in the aerospace applications. Titanium and some of its alloys have been subjected to investigations in different reducing acid media [1-2]. It has been reported [3] that the addition of alloying elements such as Al, V, Mo, and Nb to titanium increases the steady dissolution currents in the passive state, through a change of defectness degree of passive films when the alloying atoms enter its lattice. Additionally single phase β -structure alloys have better corrosion resistance than two phase $\beta+\alpha$ alloys. Furthermore, the electrochemical behavior of titanium was interpreted in terms of a two layer structure of the passive film. A barrier film, next to the metal, inhibits the metal dissolution thanks to its low cationic conductivity and a porous outer layer. Most organic inhibitors used to protect titanium against corrosion function as oxidizers which are principally reduced on the metal surface and then enhance the effectiveness of the cathodic process [4]. The present investigation relates to the studies of corrosion behavior of Ti-alloy in sulfuric acid solution at different temperatures, using organic compound of (4-[1-(5-nitro-2-furyl) methylidene]-2-phenyl-5(4H)-oxazolone) (NFP) by potentiostatic technique.

2.. Methods

Titanium alloy (Ti-5.47Al-4.02V) sheet was cut into pieces of 2cm² area. Prior to immersion in the electrolyte, the individual specimens were mechanically polished with different grades (1/0 to 4/0) of emery paper. After polishing, specimens were etched in an aqueous mixture of HF (2 v/o) and HNO₃ (4 v/o) for a few seconds at room temperature and washed with double distilled water. The specimens were finally degreased with acetone in an ultrasonic cleaner. The polarization studies were performed potentiostatically (Pos 73, Wenking Model) in different concentrations of sulfuric acid solution and NFP at different temperatures (20-50±1°C). The electrode surface was examined by SEM (JEOL 840 A) before and after polarization studies.

3. Results and discussion

The test samples were left exposed under ocp conditions in different concentrations (1-17M) of H₂SO₄ solution at different temperatures for stabilization and the stable ocp was noted. The ocp values ranged between -450 to -650 mV. Cathodic curves show that the current density increased as the applied potential was made more and more negative at each concentration and temperature. Cathodic Tafel slope, derived from the curves, were found to range between 100 and 130 mV/dec I. The cathodic and anodic curves obtained in few selected concentration of acid in the presence of inhibitor at different temperatures indicate that the decrease in cathodic current density was pronounced in most of the cases with increasing inhibitor concentration reflecting lower rate of the cathodic and anodic reaction. The critical current density was found to decrease in direct proportion to the inhibitor concentration. The critical potential for passivity shifted towards noble direction with increasing inhibitor concentration. The effect of temperature show that with increasing temperature the critical current density and passivity current density increased in each case. However, the increase in critical current density is much pronounced than the increase in passivity current density. The critical potential for passivity did not vary noticeably with change in the temperature. It is found that with increasing concentration of inhibitor the activation energy increases in the active and passive region. SEM studies of alloy surface, after polarization was performed to examine the nature of the film on the surface. It is observed that the film formed on the surface of the alloy in presence of inhibitor is enough protective and uniform to keep the alloy safe.

4. Conclusion

The alloy undergoes active dissolution and turns passive in the negative potential region in entire range of acid concentration containing different amount of inhibitor.

The inhibitor affected cathodic and anodic parameters by suppressing cathodic reaction and reducing anodic current densities.



The film formed on the surface of the alloy in presence of inhibitor is enough protective and uniform to keep the alloy safe.

References

- [1] R.S. Glass and Y.K. Hong, *Electrochim.Acta* 29, (1984) 1465.
- [2] D.D.N. Singh, M.K. Banerjee and P.S.Nag, *NML Tech.J.* 22 (1983) 33.
- [3] N.D.Tomashov, G.P.Chernova, Yu.S.Ruscol, G.A.Ayuyan, *Electrochim.Acta*, 19 (1974) 159.
- [4] J.A.Petit, G.Chatainier and F.Dabost, *Corrosion Science*, 21 (1981) 279.

**Dependence on ionic strength of phenylalanine protonation constants in NaClO₄ aqueous solution**

Farrokh Gharib, Faezeh Mofidi*

Department of Chemistry, Shahid Beheshti University, Tehran, Evin, Iran

(Email: fa.mofidi@gmail.com)

Keywords: Phenylalanine, Ionic strength, Protonation constant, SIT model.**1. Introduction**

The intrinsic acid-bases properties of the 20 naturally occurring α -amino acids have attracted the interest of a number of researchers for several decades. Amino acids are units for proteins and for this reason the effect of salt on protonation constants is very important in an understanding of the role of electrostatics in protein stability [1]. Past studies revealed the absence of systematic studies on the Influence of ionic strength on acid-base equilibrium constants, particularly at moderate to high ionic strength values.

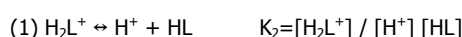
The present work deals with the study of L- Phenylalanine in aqueous solution and at different ionic strengths, 0.1 to 2 mol dm⁻³ sodium perchlorate as supporting electrolyte, using a potentiometric technique.

2. Methods

Potentiometric measurements carried out in a double-walled thermostated reaction vessel at 20 °C and ionic strength of mixtures was maintained to 0.1-2 M with sodium perchlorate. A Jenway research potentiometer, model 3520, with a combined pH electrode was used for e.m.f measurement in potentiometric titrations of acidic solution mixtures. In this work, 30 mL of the solution containing the amino acid under study (4 – 5 mmol L⁻¹), a small excess of HClO₄ (10 mmol L⁻¹), and the background salt (NaClO₄: 0.1 ≤ I ≤ 2 mol L⁻¹) was titrated with standard NaOH solution in the same ionic strength. Prior to each experiment, independent titration of perchloric acid solution with standard NaOH was carried out to determine of the specific constant of the potentiometric cell (E⁰). Protonation constants were determined by curve fitting method. In all cases, the procedure was repeated at least three times.

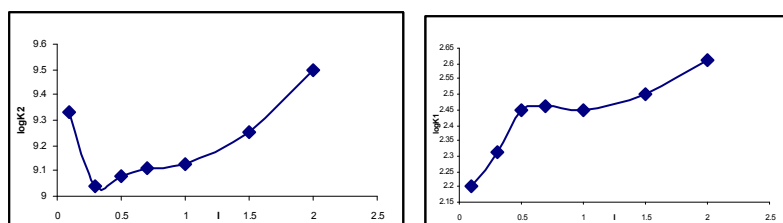
3. Results and discussion

Phenylalanine protonation constants are expressed as K₁ and K₂ according to the reactions:



In this work, the protonation constants of phenylalanine were determined at different ionic strengths of sodium perchlorate using potentiometric technique and calculated using a computer program (Microsoft Excel Solver) which employs a nonlinear least-squares method.

The dependence of logK on I is shown in figure:



Both the first and second protonation constants are strongly dependent on I .

At low ionic strength (possibly less than 0.1 mol dm⁻³) the Coulomb interactions between ions of the atmosphere and amino acid are of primary importance. However, as the ionic strength increases, the ionic atmosphere becomes more compressed and



screens the ionic charges more effectively. So, at higher concentration of the supporting salt the intermolecular interactions (such as dipole–dipole or multipole–multipole) become more important and possibly have a primary role between the ions.

The dependence on ionic strength on protonation constant was taken into account by using the specific ion interaction theory, SIT model [2]. In this work, SIT model was used to extrapolate the formation constants of all species found at infinite dilution and calculating the specific interaction coefficients.

References

- [1] Joanna Makowska, Katarzyna Baginska, Adam Liwo, Lech Chmurzynski, Harold A. Scheraga, *Peptidescience*, 30 (2008) 724
- [2] F. Gharib and A. Farajtabar, *J. Mol. Chem.* 135 (2007) 27.

**The corrosion inhibition of austenitic chromium- nickel steel in H₂SO₄ + L-OH compound**M. Amiri^a, S.M.A. Hosseini^a, R. Razavi^{*a}^aDepartment of Chemistry, Shahid Bahonar University of Kerman, Kerman, Iran

(Email: raz8122000@yahoo.co.in)

Keywords: Corrosion; Inhibitor; Steel**1. Introduction**

Acid solutions are widely used in various industries. The most important applications are acid pickling, industrial acid cleaning, acid decaling and oil-well acidizing [1].

Adsorption inhibitors are usually organic substances containing polar functions with nitrogen, sulphur and/or oxygen in the conjugated system [2,3]. Generally, inhibitor molecules either physically or chemically adsorb on a corroding metal surface. It has been suggested [4,5] that physisorbed molecules are attached to the metal at local cathodes and essentially retard metal dissolution by stifling the cathodic reaction, whereas chemisorbed molecules protect anodic areas and reduce the inherent reactivity of the metal at the sites where they are attached. The present work aims to investigate the inhibition properties of dimethyl 2 - (2 - hydroxy phenyl amino)-3-(tri phenyl phosphoranilidin) butane dioate (L-OH) that synthesized according to published methods [6] on the austenitic chromium- nickel steel in sulfuric acid media.

2. Methods

The rode type steel of 3 mm in diameter, was mechanically polished with different grades (800, 1200, 1500) emery papers, washed with distilled water and acetone then placed in a test solution. A saturated calomel electrode (SCE) was used as reference electrode and a platinum plate was used as the counter electrode, all potentials were reported versus SCE. H₂SO₄ solutions were prepared from sulfuric acid (97% Merck) with bidistilled water and were used as corrosion media in this study. The concentrations of inhibitor were chosen as 1×10^{-3} , 2×10^{-3} , 5×10^{-3} , 1×10^{-2} M and were studied from 298 to 343 ± 1K.

3. Results and discussion

Inspection of the Figures reveal that the polarization curves shift toward less negative potential and lower current density values upon the addition of the L-OH. This behavior reflects the inhibitive action of the inhibitor. The corrosion potentials gained more positive values as the concentration of added inhibitor is raised. With the increase of L-OH concentration, both anodic and cathodic current densities were inhibited, but the reduction of anodic currents was more significant than that of cathodic current. This behavior reflects that the compound acts as an anodic inhibitor for the austenitic chromium- nickel steel in 0.5 M H₂SO₄. Moreover the numerical values of inhibition efficiency increased as the concentration of L-OH were increased. L-OH inhibited corrosion by adsorption from acid solution on steel surface which followed Timken's adsorption isotherm. It can be easily seen that the $-\Delta G_{ads}^0$ decrease in the range of 298-343 K. The large negative values of ΔG_{ads}^0 reveal the spontaneous adsorption of the inhibitor and are usually characteristics of strong interaction with the metal surface. Accordingly, the trend of inhibition efficiency with temperature suggests that L-OH molecules were chemically adsorbed on the surface. The effect of temperature show that the corrosion rate of steel increase with increasing temperature. The effect of pH on the inhibition efficiency, some experiments were carried out with L-OH at different concentrations. The values show that, when the pH increases, the inhibition effect is decreased. An overall investigation of the results shows that this inhibitor is effective in acid media.

4. Conclusions

L-OH effects as an anodic inhibitor on the corrosion of austenitic chromium- nickel steel in sulfuric acid media.

The negative value of ΔG_{ads}^0 indicates the spontaneous adsorption of the inhibitor on the surface of austenitic chromium-nickel steel.

Inhibition of austenitic chromium- nickel steel in H₂SO₄ by L-OH is attributed to adsorption of this compound onto steel surface via double bond of carbon atoms and lone pair of electrons present on nitrogen and oxygen in conjugated system.

The adsorption of L-OH is found to obey Temkin isotherm.

Inhibition efficiency increase with increasing the concentration of inhibitor (L-OH) at all temperatures studied.

The trend of inhibitor adsorption with temperature suggests those L-OH molecules are chemically adsorbed on the alloy surface.



References

- [1] G. Schmitt, Br. Corros. J. 19 (1984) 165.
- [2] E.E. Ebenso, Mater. Chem. Phys. 71 (2002) 62.
- [3] H. Ashassi-Sorkhabi and S.A.Nabavi-Amri, Acta Chim Slov. 47 (2000) 587.
- [4] E.E. Oguzie, C. Unaegbu, C.E. Ogukwe, B.N. Okolue and A.I. Onuchukwu, Mater.Chem. Phys. 84 (2000) 364.
- [5] E.S. Ferreira, C. Giacomelli, F.C. Gicomelli and A. Spinelli, Mater. Chem. Phys. 83 (2004) 129.
- [6] I. Lukovits, E .Kalman and F. Zuchi, Corrosion. 57 (2001) 3.

**Inhibition action of some thiosemicarbazones on the corrosion of mild steel in 1 M H₂SO₄ solution**Nasrin Soltani^{*a}, Abbas Teimouri^b

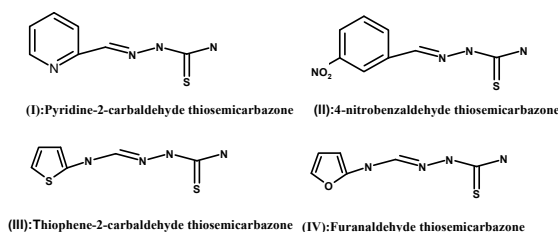
a. Payame Noor University (PNU), Shahin Shahr Branch, Isfahan, Iran

b. Payame Noor University (PNU), Isfahan, Iran

(Email: soltani@kashanu.ac.ir)

Keywords: Acid inhibition; Mild steel; Polarization; EIS; Kinetic parameters**1. Introduction**

Acid solutions are widely used in various industries for the pickling of ferrous alloys and steels. To avoid base metal attack and to ensure the removal of corrosion products/scales alone, inhibitors are extensively used [1, 2]. Thiosemicarbazone and their derivatives have continued to be the subject of extensive investigation in chemistry and biology owing to their broad spectrum of anti-tumor [3], and in many other applications including corrosion inhibition of metals [4]. The inhibiting action of Thiosemicarbazone derivatives has been mainly attributed to adsorption of thiocarbonyl group (>C=S) on the surface of metal [5]. The purpose of the present work is to study the inhibition effect of four derivatives of thiosemicarbazone (Fig. 1) on the corrosion of mild steel in 1 M H₂SO₄ using polarization, electrochemical impedance spectroscopy (EIS) and weight loss measurements. The nature of inhibitor adsorption process and the effect of temperature are also studied and discussed.

**2. Methods**

Polarizations and Impedance measurements were carried out using AUTOLAB model PGSTAT 35. Electrochemical experiments were performed in a conventional three electrodes electrochemical cell at 25°C with the mild steel as a working electrode, a platinum counter electrode and silver–silver chloride (Ag/AgCl) electrode as reference electrode. Working electrode was first immersed into the test solution for 30 minutes to establish a steady state open circuit potential. Polarization studies were performed with a scan rate of 0.5 mVs⁻¹ in the potential range from -500 to +500 mV relative to the corrosion potential. Polarization data was analyzed using GPES electrochemical software. Electrochemical corrosion parameters, such as corrosion potential (E_{corr}), cathodic and anodic Tafel slopes (b_a and b_c) and corrosion current (I_{corr}), obtained by extrapolation of the Tafel lines and The inhibition efficiency was calculated from the following equation:

$$IE_p (\%) = \left(\frac{I_0 - I}{I_0} \right) \times 100$$

where I_0 and I are the corrosion current densities in absence and presence of inhibitor, respectively.

Electrochemical impedance spectroscopy measurements were performed at corrosion potentials, E_{corr} , over a frequency range of 100 kHz to 0.1 Hz with a signal amplitude perturbation of 5 mV. Impedance data were analyzed using a Pentium IV computer and FRA software. Nyquist plots of steel in uninhibited and inhibited acidic solutions obtained for solutions containing various concentrations of Thiosemicarbazone and then The impedance parameters derived from these plots.

3. Results and discussion

Anodic and cathodic polarization curves for mild steel in 1M H₂SO₄ with and without various concentrations of used inhibitor (IV) are shown in Fig 2 a (the same figures obtained for other compounds). From Fig. 2 a, it is clear that both anodic metal dissolution and cathodic reduction reactions were inhibited when the Thiosemicarbazones compounds were added to the acid solution and this inhibition was more pronounced with increasing inhibitor concentration. The presence of compound IV in H₂SO₄ solution resulted in shift of corrosion potential towards more noble direction in comparison with that obtained in the absence of inhibitor. These results indicate that all investigated inhibitors act as mixed type inhibitor with predominant control of anodic reaction [2].

Nyquist plots of mild steel in uninhibited and inhibited acid solutions containing various concentrations of inhibitor (IV) in the 1M H₂SO₄ solution are given in Fig. 2b (the same figures obtained for other compounds).

The recorded EIS spectrum for mild steel in the presence of all of inhibitors consists of a large capacitive loop at high frequencies (HF) and a small inductive one at low frequency values (LF). The equivalent circuit of Fig. 2 c, which has been previously used, fits well our experimental results.

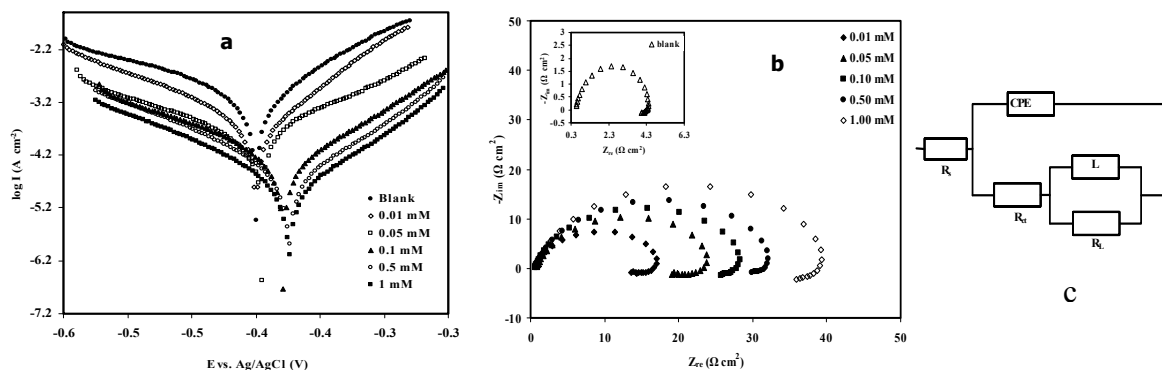


Fig. 2. (a) Polarization curves for mild steel in 1 M H₂SO₄ in the absence and presence of different concentrations of compound IV at 25 °C, (b) Nyquist plot for mild steel in 1 M H₂SO₄ in the absence and presence of different concentrations of compound IV at 25°C and c . The equivalent circuit used to fit the obtained impedance spectra for mild steel in the absence and presence of the inhibitors

4. Conclusions

The following results can be drawn from this study:

- 1- All the Thiosemicabazoness, perform well as corrosion inhibitors in hydrochloric acid solutions and the inhibiting efficiencies follow the order IV > III > II > I
- 2-Tafel behaviour indicates that all inhibitors are of mixed anodic-cathodic type.
- 3-Adsorption of the Thiosemicabazoness on the steel surface obeys the Langmuir's isotherm.
- 4-The values of free energy of adsorption and the relationship between the inhibition efficiency values and calculated quantum chemical parameters suggest that these Thiosemicabazoness can be adsorbed on mild steel surface by physicalmechanism.

References

- [1] M. Behpour, S.M. Ghoreishi, N. Soltani, M. Salavati-Niasari, M. Hamadani, A. Gandomi, Corros. Sci. 50 (2008) 2172.
- [2] M. Behpour, S.M. Ghoreishi, M. Salavati-Niasari, B. Ebrahimi, Mater. Chem. Phys. 107 (2008) 153.
- [3] S. Singh, F. Atar, A. Azam, Bioorg. Med. Chem. Lett.15 (2005) 5424.
- [4] S. T. Arab, Mater. Res. Bull. 43 (2008) 510.
- [5] L. Larabi, K. Y. Hare, O. Benali, S. Ghalem, Progr. Org. Coat. 54 (2005) 256.

Application of a new dioxime to potentiometric and its computational Studies

M. H. Fekri^{a*}, M. Darvishpour^b

^aDepartment of Chemistry, Islamic Azad University, Khorramabad Campus, Khorramabad, Iran.

^bDepartment of Chemistry, Islamic Azad University, Arak Campus, Arak, Iran.

(Email: Fekri_1354@yahoo.com)

Keywords: Ion selective electrode, PVC membrane, Ni(II) determination, α -dioxime, ab initio.

1. Introduction

The dioxime ligands are known to coordinate metal ions as neutral dioximes [1,2]. The chemistry of the bis-dioxime complexes of transition metal ions has attracting continues attention because of their importance with reference to dioxygen carriers [3], catalysis in chemical transformations [4], intramolecular hydrogen bonding and metal-metal interaction [5]. The ion selective electrode (ISE) approach to trace analysis is advantageous because of the speed and ease of ISE procedures in which little is required. Further, ISE possess wide dynamic ranges, an are relatively low in cost. Ion selective electrodes based on neutral carrier ligands are well established for alkali and alkaline-earth metal cations [6-7].

In this work, the ligand (Fig.1) used as an ionophore in fabrication of ISE_s for determination if Ni(II) and studied its structure by ab initio HF calculations using a standard 6-31G* basis set and LanL2DZ.

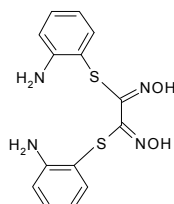


Fig. 1. structure of (1E,2E)-bis(2-aminophenyl)N'1,N'2-dihydroxyethanebis (imidothioate) used as ionophore.

2. Methods

A mixture of PVC, oleic acid, acetophenone and ionophore to give a total mass of 100 mg, was dissolved in about 2 mL of THF and the solution was mixed well. The resulting clear mixture was transferred into a glass dish of 2 cm diameter. The solvent was evaporated slowly until an oily concentrated mixture was obtained. A full optimization of the structure of ligand and its complexe are performed at the ab initio HF level of theory using gradient techniques with the Gaussian 98 set of programs[8].

3. Results and discussion

1. Effect of membrane composition on the electrode response

The potential responses of various ion-selective electrodes based on dioxime are in Fig. 2. Expect for the Ni(II) ion selective electrode, in all other cases the slope of the corresponding potential-pM plots is much lower than the expected Nernstain slopes.

Besides the critical role of the nature of the ion carrier in preparing membrane-selective sensors, some other important features of the PVC membrane are known to significantly influence the sensitivity, linearity range and selectivity of ion-selective electrodes. These include the amount of ionophore, the nature of solvent mediator, the plasticizer/PVC ratio and especially the nature of additives used .

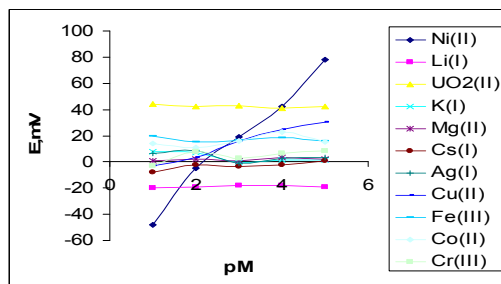


Fig. 2. Response at pH 3 against some of cations for ion-selective electrodes containing BTD as ionophore.

2.ab initio calculations

We performed a full geometry optimization at HF level of theory, using 6-31G* basis set for dioxime and for formed Ni(II) complex. We used effective core potential (ECP) standard basis set, LanL2DZ basis set, for Ni(II) and 6-31G* for all other atoms. Stabilisation energy for ligand and its complex obtained $-1700.32 \text{ Hartree mol}^{-1}$ and $-2500.67 \text{ Hartree mol}^{-1}$ respectively. Calculated cartesian atomic coordinates, bond length, angle and torsion angles of ligand and its complex are obtained. The calculations predicted planar structure for dioxime. Also calculations on complex showed that the Ni(II) complex is as mononuclear complex that Ni was coordinated to N and O [9].

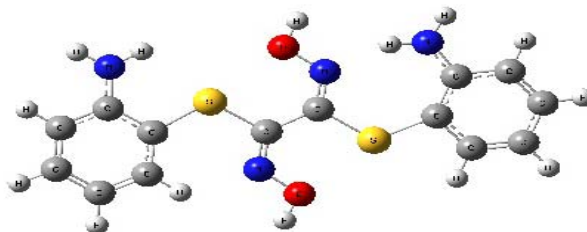


Fig. 3. The ab initio optimized structure of the used dioxime

References

1. Ovcharenko, V., Fokin, S., Reznikov, V., Ikorskii, V., Romanenko, G., Sagdeev, R., Nonclassical packing of metal dioximates superexchange through a diamagnetic metal cation *Inorg.Chem.* 37, (1988), 2104-2110
2. Chakravorty, A., Structural chemistry of transition metal complexes of oximes, *Coord. Chem. Rev.* 13, (1974), 1-46.
3. Lance, K.A., Goldsby, K.A., Busch, D.H., Effective new cobalt(II) dioxygen carriers derived from dimethylglyoxime by the replacement of the linking protons with difluoroboron, *Inorg. Chem.* 29, (1990), 4537-4544.
4. Taqui Khan, M., Ramachandraiah, G., Kumar, S., Mononuclear bis(dimethylglyoximate)ruthenium(III) complexes with different addended axial groups: highly efficient catalysts for water oxidation, *J. Mol. Catal.* 45, (1990), 199-205.
5. Schlemper, E.O., *Acta Crystallogr., Sect. B* 33, (1977), 2482.
6. Nieman, T.A., Horvai, G., *Anal. Chim. Acta*, (1985), vol. 170, p. 359.
7. Kitazawa, S., Kimura, K., Yano, H., Shono, T., *Analyst*, (1985), vol. 110, p. 295.
8. M. J. Frisch, et al., GAUSSIAN 98 (Revision A3), Gaussian Inc, Pittsburgh, PA, (1998).
9. O. Jimenez-Sandoval, D. Ramirez-rosales, M. D. J. Rosales-Hoz, M. E. Sosa-Torres and R. Zamorano-Ulloa, *J. Chem. Soc., Dalton Trans.*, 1551 (1998).

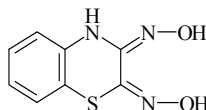
Cr(III) ion selective electrode based on 2H-1,4-benzothiazine-2,3(4H)dione dioxime as a natural carrierM. H. Fekri^{a*}, M. Darvishpour^b^aDepartment of Chemistry, Islamic Azad University, Khorramabad Campus, Khorramabad, Iran.^bDepartment of Chemistry, Islamic Azad University, Arak Campus, Arak, Iran.

(Email address: Fekri_1354@yahoo.com)

Keywords: Ion selective electrode, PVC membrane, Cr(III) determination, α -dioxime**1. Introduction**

Ion selective electrodes (ISEs) are membrane electrodes that respond selectively to ions in the presence of others. These include probes that measure specific ions and gasses in solution. The most commonly used ISE is the pH probe. For this type of electrodes, the formation constant of the ion-ionophore complex within the membrane phase is very important parameter that dictates the practical selectivity of the sensor [1].

The first report on Cr(III) was in 1980 [2]. In 1987 a Cr(III) selective electrode with PVC membrane based on 8-quinoline-dithiocaboxilate was described [3]. In 1989 another ion selective electrode based on chromium dithizonate was built that was a precipitate based selective electrode [4]. A PVC-based Cr(III)-selective electrode, which was recently been prepared, is based on 4-methylaminoazobenzene [5]. Gholivand et al. used a Cr(III)-selective electrode based on glyoxal bis(2-hydroxyanil) [6].

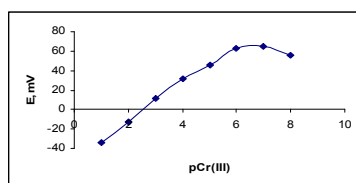
**Fig. 1.** structure of 2H-1,4-benzothiazine-2,3(4H)dione dioxime (BTD) used as ionophore.**2. Methods**

A mixture of PVC, oleic acid, acetophenone and ionophore to give a total mass of 100 mg, was dissolved in about 2 mL of THF and the solution was mixed well. The resulting clear mixture was transferred into a glass dish of 2 cm diameter. The solvent was evaporated slowly until an oily concentrated mixture was obtained.

3. Results and discussion

The 2H-1,4-benzothiazine-2,3(4H)dione dioxime as a carrier was found to be highly responsive to Cr(III) with respect to several other metal ions. Therefore, we studied in detail the performance of the plasticized PVC membrane containing this Ionophore for Cr(III) in aqueous solution. In order to test the performance of the membrane characteristics, various operation parameters including selectivity, response time, sensitivity, lifetime, linear range, the influence of pH and the membrane composition on the response of the electrode were investigated.

Effect of membrane composition on the electrode response. It is well Known that the sensitivity and selectivity of the ion-selective sensors not only depend on the nature of ionophore used, but also significantly on the membrane composition and the properties of plasticizers and additives used. Thus, the influences of the membrane composition, the nature and amount of plasticizers and amount of oleic acid as an additive on the potential response of the Cr(III) sensor were investigated.

**Fig. 2.** Calibration plot of the Cr(III)-ISE based on BTD.

Among the different composition studied, membrane incorporating 28 % PVC, 62 % AP, 5.3 % OA and 4.7 % ionophor shows the best sensitivity. The calibration plot is shown in Fig. 2, which indicates a linear range from 1.0×10^{-6} to 1.0×10^{-1} M Cr(III) with a Nernstian slope of 19.5 ± 0.5 mV/decade of Cr(III) concentration.

Effect of pH. The influence of pH on the response of the PVC membrane electrode at 1.0×10^{-4} M concentration of Cr(III) is performed (Fig. 3). The potential remain constant from pH of about 1.5 to 5.5 variation of the potential at pH < 1.5 could be related to protonation of the ligand in the membrane phase, which results in a loss of its ability to complex with Cr(III) ions. At pH > 5.5, the potential drope may be due to the hydrolysis of the Cr(III) ions and therefore, all of measurements were performed at pH = 3.0. The working pH range is slightly reduced at lower Cr(III) concentration, and therefore, all of the measurements were performed at pH = 3.0.

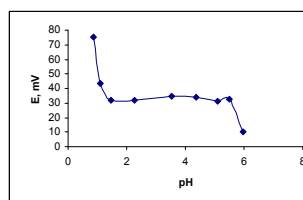


Fig. 3. The pH response of the Cr(III)-ISE based on BTM.

Application. The new Cr(III)-selective electrode was satisfactorily applied to the determination of Cr(III) in tea leaves, cacao powder and coffee. The analyses were performed by direct potentiometry using the standard addition technique. In the absence of samples containing Cr(III), known amounts of Cr(III) were added. The results obtained are summarized in Table 4. Good recoveries in all matrices were obtained.

Table 1. Practical applications of proposed sensor

Sample	Average chromium concentration ($\mu\text{g/g}$)	
	Proposed sensor	AAS
Coffee	2.6 ± 0.1	3.1 ± 0.1
Cacao powder	1.9 ± 0.1	2.3 ± 0.1
Tea leaves	1.4 ± 0.1	1.8 ± 0.1

References

1. Morf, W.E., The Principles of Ionselective Electrodes and of Membrane Transport, Elsevier, New York, 1981.
2. Masuda, Y., Shida, E.I., Hivaga, K., Nippon Kagaku kaishi, 1980, vol. 10, p. 1453.
3. Lebedeva, O.A., Yu Yanson, E., Fromotkrtiya Izobret, 1987, vol. 39, p. 195.
4. Chattopadhyaya, M.C., J. Indian Chem. soc., 1989, vol. 66, p. 54.
5. Abbaspour, A., Izadyar, A., Talanta, 2001, vol. 53, p. 1009.
6. Gholivand, M.B., Sharifpour, F., Talanta, 2003, vol. 60, p. 707.

**Activity coefficients of NiCl₂ in (Glucose + water) mixtures at 298.15 K**

B.Ghalami –Choobar, T.Nasiri

Department of Chemistry, Faculty of Science, University of Guilan, P.O. Box: 19141, Rasht, Iran

(Email: B-Ghalami@guilan.ac.ir)

Keywords: Activity coefficients, Potentiometric method, Glucose, NiCl₂**1. Introduction**

Recently, there has been an increasing amount of work concerning the measurement of thermodynamic properties of electrolytes in mixtures of solvents, due to their composition are important in industrial, chemistry, biological and other fields. Within electrolytes systems, those of the type electrolyte + sugar + water are especially important for understanding the behavior of saccharides. In this work, the results relating to the mean activity coefficient measurements for NiCl₂ in (glucose + water) mixtures using the potentiometric method are reported. The mean activity coefficient of NiCl₂ in the NiCl₂ + glucose + water systems were determined on a galvanic cell containing a solvent polymeric (PVC) Ni- ISE and Ag/AgCl electrodes at T = 298.15 K. We have reported in our previous papers the ability of the solvent polymeric membrane electrode for determination of activity coefficient for binary and ternary electrolyte solutions [1-3]. In the present study, the determination of activity coefficient for NiCl₂ in various glucose / water mixed solvent systems containing 0, 10, 20, 30, and 40 % mass fraction of glucose over ionic strength range from 0.0001 to 5 mol kg⁻¹ are reported. The modeling of these ternary systems was made based on the Pitzer ion-interaction model. The resulting values of the mean activity coefficients together with Pitzer ion-interaction parameters ($\beta^{(0)}$, $\beta^{(1)}$ and C^ϕ) for the series under investigated systems are reported.

2. Methods

All of the potentiometric measurements were made by using a multimeter (Martini instruments Mi 180) whose resolution was 0.1 mV. The output of the multimeter was connected to a personal computer (AMD) by the RS232 connector for data acquisition. In this work, the potentiometric measurements were performed for the ternary NiCl₂ + glucose + H₂O systems on the galvanic cell of the type: Ag | AgCl | NiCl₂ (m) , glucose (w %), H₂O (1-w) % | Ni-SE over total ionic-strengths from 0.001 to 5000 mol kg⁻¹. The electrodes used in this work were prepared in our laboratory in accordance with the general procedure of PVC membrane construction and had a reasonably good Nernst response. In each series of the glucose- water as a mixed solvent and for each standard addition step, data collection was performed every 10 s interval and during 15 (for concentrated solutions) to 20 min (for dilute solutions) by using a multimeter connected to personal computer. As usual, all measurements were performed under stirring conditions and the temperature was kept constant at 298K (±0.1 K), employing a double-wall container enabling the circulation of thermostat water from a Model GFL circulation.

3. Results and discussion

The experimental mean activity coefficients of NiCl₂ in the mixtures were determined by using Nernst equation:

$$E = E^0 + s \log(\gamma_{\pm, \text{NiCl}_2} m) \quad (1)$$

Where E⁰ and s indicate the cell constant potential and the Nernstian slope, respectively. The emf of the galvanic cell was measured at different series of electrolyte molalities in pure water and in glucose-water mixed solvents through changing of electrolyte concentration by standard addition method. Fig. 1 presents the emf of galvanic cell versus the activity in glucose-water mixed solvent system containing 10% mass fraction of glucose (The values of molality, mean activity coefficient and emf data were illustrated in Table 1). The Pitzer ion -interaction parameters together with E⁰ and s were determined by combining equations 1 and 6 by an iteration minimization procedure.

$$\ln \gamma_{\pm \text{NiCl}_2} = f^\gamma + \frac{4}{3} B_{\text{NiCl}_2}^\gamma m + \frac{4\sqrt{2}}{3} C_{\text{NiCl}_2}^\phi m^2 \quad (2)$$

where

$$f^\gamma = -2A_\phi \left[\frac{\sqrt{I}}{(1+b\sqrt{I})} + \left(\frac{2}{b} \right) \ln(1+b\sqrt{I}) \right] \quad (2a)$$

$$B_{\text{KCl}}^\gamma = 2\beta_{\text{KCl}}^{(0)} + \left(2\beta_{\text{KCl}}^{(1)} / \alpha^2 I \right) \left[1 - (1 + \alpha\sqrt{I} - \alpha^2 I / 2) e^{-\alpha\sqrt{I}} \right] \quad (2b)$$

Table 2 shows some of the resulting $\beta^{(0)}$, $\beta^{(1)}$ and C^ϕ Pitzer ion -interaction parameters from iteration minimization procedure for the investigated systems. Fig. 2 presents the variation of the NiCl_2 mean activity coefficients versus the molality in water, and different mass fraction of glucose in mixed solvents. As, it can be concluded the activity coefficients decrease when mass fraction (%) of glucose increase in glucose -water mixed solvent. it can be concluded the activity coefficients decrease when mass fraction (%) of glucose increase in glucose -water mixed solvent.

Table 1. The values of the molality, mean activity coefficient and emf data

m	γ	E
0.0007	0.8955	-129.9
0.0022	0.8335	-102.6
0.0059	0.7580	-75.7
0.0132	0.6834	-50.5
0.0205	0.6401	-38.5
0.0561	0.5418	-11.2
0.1234	0.4754	10.3
0.2447	0.4343	31.5
0.3508	0.4229	43.6
0.5276	0.4244	58.1
0.7000	0.4405	68.3
0.9436	0.4807	80.2
1.1705	0.5350	89.6
1.3499	0.5899	96.1

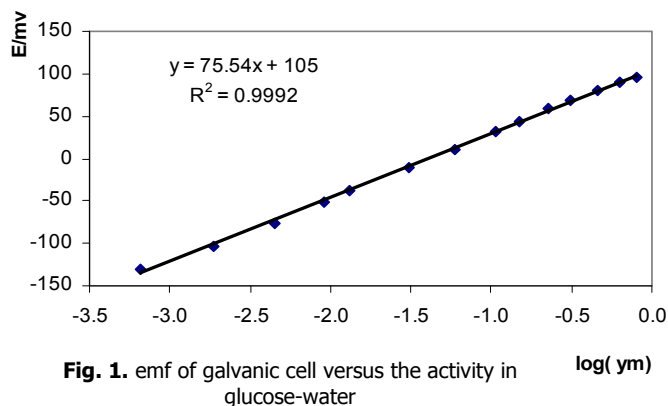


Fig. 1. emf of galvanic cell versus the activity in glucose-water

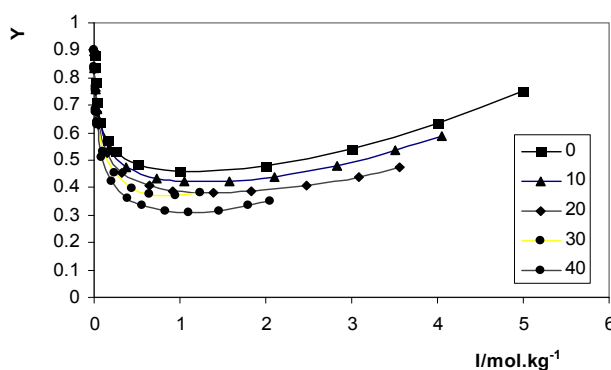


Fig. 2. The mean activity coefficients versus the ion strength in glucose –water mixed solvents

Table 2. The values obtained of Pitzer parameters

parameters	0%	10%	20%
A_ϕ	0.3915	0.4183	0.4503
$\beta^{(0)}$	0.3499	0.353931	0.3588
$\beta^{(1)}$	1.53	1.5866	1.6543
C^ϕ	-0.00471	0.006146	0.007691

4. Conclusions

The mean activity coefficients of NiCl_2 in the NiCl_2 + glucose + water systems were determined by a potentiometric method using a solvent polymeric ion-selective membrane electrode and Ag-AgCl electrodes at temperature 298.15 K. The adjustable parameters were determined. The results show that The adjustable parameters in ecrease when mass fraction (%) of glucose increase in glucose -water mixed solvent.

References

- [1] B.Ghalami-Choobar, M.Arvand , M. Moghimi, M. A. Bagherinia, Phys. Chem. Liq 47(2009) . 553 -563
- [2] F. Deyhimi, B. Ghalami-Choobar, Fluid Phase Equilib. 246 (2006) 185-190
- [3] B. Ghalami-Choobar, M. Moghimi, N.Mahmoodi , M. Mohammadian J. Chem. Thermodyn in press (2009)



Investigation of stress corrosion cracking of sensitized stainless steel 304 in chloride media by using electrochemical impedance spectroscopy

B.Adib^a, J.Neshati^b,*A.Sardashti^c

^aDepartment of chemistry ,Azad university ,Tehran ,Iran.

^bDepartment of corrosion ,Research institute of petroleum industry ,Tehran ,Iran.

^cDepartment of chemistry ,Azad university ,Tehran ,Iran.

(Email: Azadeh.sardashti@yahoo.com)

Keywords: Stress corrosion cracking; EIS; Stainless steel 304; U-bend; Monitoring

1. Introduction

Stress corrosion cracking (SCC) is well-known corrosion process. In the past time BOSCH et al have used EIS during slow strain rate tensile(SSRT) tests of 304 specimen in a 5 mol/L H₂SO₄+ 0.1 mol/L NaCl solution at room temperature. In this study electrochemical impedance spectroscopy(EIS) has been used as a tool to detect stress corrosion cracking in a stainless steel sample exposed to an aqueous environment that containing 40 weight percent magnesium chloride(PH=4.5) at 120°C. In this study EIS measurement was performed during the u-bend tests. In the EIS experiments ,phase shifts at particular frequencies show a clear difference between the stressed and non-stressed specimens. The purpose of this research is to figure out whether it is possible to use EIS for monitoring stress corrosion cracking by u-bend tests.

2. Methods

u-bend specimens were provided by ASTM G30 standard and specimens were annealed at 750 C for 1 hour. The cell consisted of the sample , used as the working electrode(WE) a platinum as the reference electrode (RE) and counter electrode(CE).

The morphology of the fractured specimens was examined through metallography a scanning electron microscopy(SEM). EIS measurements were always performed simultaneously on two identical samples: one stress with a u-bend test and one free of stress.

3. Results and discussion

Results were shown that changes in phase shift in the two samples versus time could be related to the stress corrosion cracking process. Fig 1 shows that At 23.95 Hz a clear difference between the phases of the stressed and non-stressed tests can be seen from approximately 142 hours on wards. For application of EIS to the monitoring of stress corrosion cracking under these circumstances a frequency between 1 and 100 Hz seems the most appropriate choice. The model of cracks impedance can be described by an equivalent circuit as shown in Fig.2.

Fig.3. shows that analysis of fracture surface with SEM confirmed that stress corrosion cracks were formed in this case.

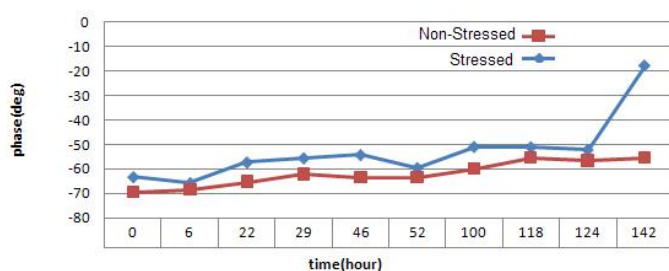


Fig. 1. Phase by time Chart (23.95Hz).

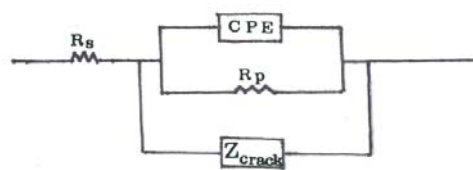


Fig. 2. Equivalent circuit for stressed sample.

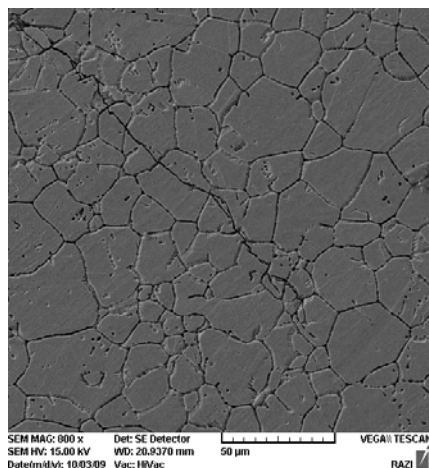


Fig. 3. Fractured surface with SEM microscope

4. Conclusions

1. Intergranular and transgranular SCC are observed when stainless steel 304 alloy shaped u-bend in the chloride solution at 120°C.
2. The EIS measurements was shown that the evolution of the phase shift of the impedance at various frequencies could be related to the stress corrosion cracking of the sample with stressed so electrochemical impedance spectroscopy could be used to detect stress corrosion cracking in chloride environment.
3. For electrochemical impedance spectroscopy to the monitoring of stress corrosion cracking under these circumstances a frequency between 1 and 100 seems the most appropriate choice.

References

- [1] R. Oltra, M. Keddad, Corrosion Science 28 (1) (1998) 1.
- [2] M.C. Petit, M. Cid, M. Puiggali, Z. Amor, Corrosion Science 31 (1990) 491.
- [3] R.W. Bosch, F. Moons, J.H. Zheng, W.F. Bogaerts, Corrosion 57 (2001) 532.
- [4] M.E. Inding, A.R. McIlree, Corrosion 35 (1979) 288.
- [5] G. Cragolino, D.D. Macdonald, Corrosion 38(8) (1982) 406.
- [6] E. McCafferty, Corrosion Science 47(2005) 3202-3215.
- [7] D.O. Condit, Corrosion 28 (1972) 95-100.
- [8] F. Bentiss, M. Lebrini, M. Lagrenee, Corrosion Science. 47 (2005) 2915-2931.
- [9] M.S. Morad. Corrosion Science. 42 (2000) 1307-1326.
- [10] R.W. Bosch. Corrosion Science , 47 (2005) 125-143.
- [11] A. Li-juan, L. Qing-fen. Transactions of Nonferrous Metals Society of China. 17 (2007) 184-188.

Thermochemistry of natural hypersaline water systems using the urmia lake as a case

S. Sakeni Alvanag ^a, N. Heidari ^b, M. Mokhtarpour ^c

^aMsc Graduate, Department of Chemistry, University of Urmia, Urmia, Iran

^bAssistant Professor, Department of Chemistry, University of Urmia, Urmia, Iran

^cMsc Graduate, Department of Chemistry, University of Urmia, Urmia, Iran

(Email: somayeh_sakeni@yahoo.com)

Keywords: Urmia Lake, Heat of mixing, Heat of dilution, Heat of evaporation

1. Introduction

All physical and chemical phenomena in natural water bodies are accompanied by thermal effects, which may have considerable practical and theoretical importance. Two examples of such effects are heat of dilution and heat of evaporation. ⁽¹⁾

One method for the calculation of the partial heat of water evaporation from natural brine can be based on the use of the heat of dilution of this brine by fresh water. Let us consider the isothermal cycle of the dilution of Urmia lake water: a) by the addition of one mole of liquid fresh water to urmia lake water; and b) by the evaporation of one mole of fresh water and by the addition of the obtained steam to urmia lake water ⁽²⁾.

Under such conditions, the obtained thermodynamic functions are partial ones. The discussed cycle is given in Fig. 1

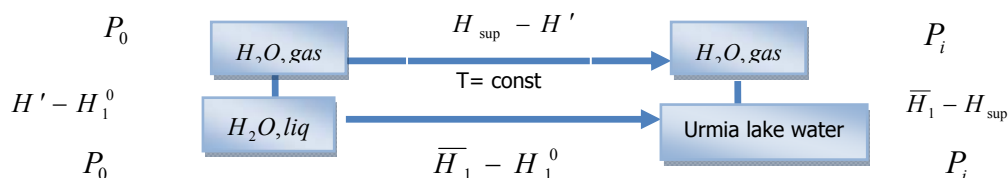


Fig. 1. Isothermal cycle of the dilution of Urmia lake water.

The symbols used in this cycle are as follows:

1. P_0 and P_i are the vapor pressure over pure water and over Urmia lake water;
2. H_1^0 and H_1 are the enthalpy of pure water and the partial enthalpy of water in a particular solution;
3. H' and H_{sup} are the enthalpy of the water steam and enthalpy of superheated water steam;

According to the thermodynamic definition

$$\Delta \bar{H}_{evap}^0 = H_{sup} - \bar{H}_1 \quad (1)$$

$$\bar{L}_1^0 = \bar{H}_1 - H_1^0 \quad (2)$$

where \bar{L}_0 is the partial heat of dilution. Considering the above-discussed thermodynamic cycle, we can write:

$$(H' - H_1^0) + (H_{sup} - H') + (-\Delta \bar{H}_{evap}^0) = \bar{L}_1^0 \quad (3)$$

$$\Delta \bar{H}_{evap}^0 = -\bar{L}_1^0 + (H_{sup} - H_1^0) \quad (4)$$

Equation (4) can be used for the calculation of the partial heat of water evaporation from Urmia lake water. The values of H_{sup} and H_1^0 can be taken from any tables of the thermodynamic properties of water and water vapor, but the heat of dilution should be experimentally measured. The study of the heat of dilution of Urmia lake water by fresh waters is important not only for $\Delta \bar{H}_{evap}^0$ calculation.

2. Methods

at the first, the concentration of ions in Urmia lake water has been measured. The heats of mixing of Urmia lake water with distilled water (ΔH_{mix}) have been measured on a thermoanalyse VP-ITC Microcalorimeter. Before injection of sample, distilled water Microcalorimeter apparatus, sample and distilled water are poured to separate cells and for five minute enter to the Thermo Vac that has degassing and thermostatic effect and then we inject 1.5 ml of Urmia lake water with syringe to sample

cell and also we inject the same amount of deionized water to reference cell in Microcalorimeter and also distilled water with the help of auto-pipette in the time interval has been injected to the working cell. The volume of auto-pipette is 300 $\mu\text{L}^{(4)}$.

3. Results and discussion

Table 1: The ionic concentration (in molality units) of the urmia lake water:

	Ca^{2+}	Mg^{2+}	Na^+	K^+	Cl^-	HCO_3^-	SO_4^{2-}	I_m
Urmia lake water(ULW)	0.014	0.5	5.39	0.069	6.18	0.016	0.224	7.307

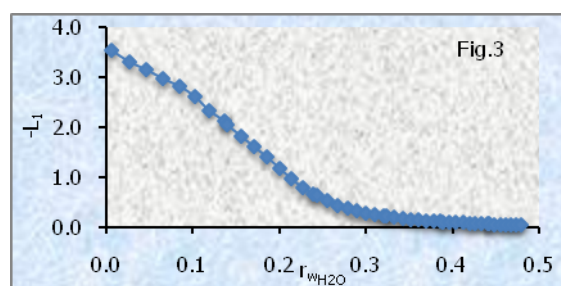
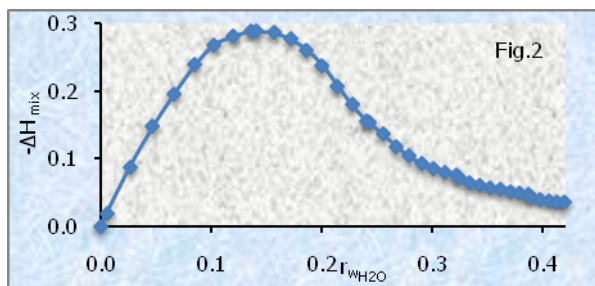


Fig. 2 , 3. Heat of mixing of Urmia lake water with fresh water function of weight fraction of fresh water in the formed mixture, Heat of dilution of Urmia lake water with fresh water function of weight fraction of fresh water in the formed mixture, respectively.

Here, $r_{W_{H_2O}}$ is the weight fraction of fresh water in the particular mixture obtained.

$$r_{W_{H_2O}} = \frac{g_{H_2O}}{G_{total}} \quad (G_{total} = g_{ULW} + g_{H_2O}) \quad (5)$$

where, g_{ULW} and g_{H_2O} are the amounts of Urmia Lake water (ULW) and bidistilled water, respectively and:

$$\Delta H_{mix} = \frac{\Delta Q_i}{G_{total}} \quad (6)$$

ΔQ_i is the heat effect of the one-step mixing for the particular amount of the mixture. Let us consider some thermal effects measured during the mixing of urmia lake water and H_2O experiments. the heat of solution (dilution) L_1 of fresh water in urmia lake water

$$L_1 = \frac{\Delta Q_i}{g_{H_2O}} \quad (7)$$

4. Conclusions

The curve in Fig. 2 is exothermic and shows asymmetry with maxima placed near $r_w = 0.1362$ and $\Delta H_{mix} = -0.2894$. The extrapolation of the relationship of $L_1 = f(r_w)$ to $r_w = 0$ gives the \bar{L}_1^0 equal to about $-3.6 \text{ kJ} \cdot (\text{kgH}_2\text{O})^{-1}$. For the calculation of the heat of evaporation of water from urmia lake water (ΔH_{evap}^0) at 25°C by Eq. (4), we used $\bar{L}_1^0 = -3.6 \text{ kJ} \cdot (\text{kgH}_2\text{O})^{-1}$, found above, and the known values⁽³⁾ of $H_{sup} = 2544.71 \text{ kJ} \cdot (\text{kgH}_2\text{O})^{-1}$ and $H_1^0 = 104.73 \text{ kJ} \cdot (\text{kgH}_2\text{O})^{-1}$. Then using Eq.(4) we obtain:

$$\Delta H_{evap}^0 = -(-3.6) + (2544.71 - 104.73) = 2443.58 \text{ kJ} \cdot (\text{kgH}_2\text{O})^{-1}$$

References

- [1] Krumgalz, B.S. Bury, R. Treiner C, Marine Chemistry, 19,9-16, 1986.
- [2] Krumgalz, B.S. Bury, R. Treiner C, Journal of Solution Chemistry,1199-1210, 1990.
- [3] Handbook of Chemistry and Physics, 63rd edn., R. C. Weast, ed., CRC Press, Boca Raton, FL, 1982/1983.
- [4] Sakeni, S, a thesis for the degree of master of Science in the Physical Chemistry, University of Urmia, 1386.



physical chemistry of urmia lake, The carbonate system in hypersaline solutions: Alkalinity and CaCO₃ solubility of evaporated seawater

M.Mokhtarpour^a, N.Heidary^b, S.Sakeni^c

^aMsc Graduate, Department of Chemistry, University of Urmia, Urmia, Iran

^bAssistant Professor, Department of Chemistry, University of Urmia, Urmia, Iran

^cMsc Graduate, Department of Chemistry, University of Urmia, Urmia, Iran

(Email: M.mokhtarpour@gmail.com)

keywords: Brine, Carbonate system, Apparent dissociation constant, Apparent solubility product, Ionic strength.

1. Introduction

The chemical evolution of seawater upon evaporation has been studied mainly in relation to major ion composition. Evaporation progresses in well defined steps at which distinct mineral precipitations are detected. The early precipitation of CaCO₃ is followed by gypsum precipitation at about threefold evaporation and by halite precipitation when the volume is reduced to about a tenth of the original seawater. It is also generally recognized that evaporation of seawater should affect the carbonate system in various ways. CO₂ solubility should decrease, due to the salting-out effect, and the apparent dissociation constants of carbonic acid as well as the apparent solubility product of CaCO₃ should vary as the ionic composition and ionic strength change. Our objective was to investigate the effect of evaporation on seawater alkalinity and CaCO₃ solubility by running evaporation experiments in the laboratory and measuring the ionic composition, pH, and alkalinity of seawater samples evaporated to various degrees. CaCO₃ solubility was evaluated by running parallel experiments on samples in which aragonite powder was suspended.

2. Methods

The solutions investigated consist of natural seawater samples which were evaporated to various degrees under laboratory conditions: a) Evaporation procedure: Seawater was evaporated in a continuously ventilated fume hood, at " 25±3 °C" in open pyrex beakers, in the presence or absence of aragonite; the solutions were homogenized several times per day by manual stirring with glass rods. After the desired degree of evaporation was attained, the solutions, including precipitated salts, were quantitatively transferred to tightly sealed bottles and stored until analysis in a thermostatic shaking bath at " 25±1°C" . b) Analytical procedure: The experimental solution was filtered with a 50-ml all-glass syringe, via a membrane filter. Fifty milliliters of the filtrate were titrated with a 0.02 N HCl solution. Mg and Ca were analyzed by titration with EDTA, Chloride ion concentrations were measured by Mohr titration, Na and K analyzed by flame photometry, Sulfate was determined gravimetrically as BaSO₄.^[1]

3. Results and discussion

The alkalinities were calculated from the titration data by a modification of Sass and Ben-Yaakov's (1977) calculation procedure in which the carbonate system is completely described during the titration by:

$$\frac{1}{V_0} \left[TA V_0 + \frac{a_{H^+}}{\gamma_{H^+}} (V_0 + V_a) - N_a V_a \right] = C \frac{K_1' a_{H^+} + 2K_1' K_2'}{a_{H^+}^2 + K_1' a_{H^+} + K_1' K_2'} \quad (1)$$

where V₀ is the volume of the sample before titration, V_a is volume of hydrochloric acid added, N_a is normality of HCl, γ_{H⁺} is activity coefficient of the H⁺, TA is total alkalinity, C is total concentration of CO₂ and K₁', K₂' are first and second dissociation constants of carbonic acid. The right-hand term in Eq.1 represents the charged carbon species in the solution, At sufficiently low pH values beyond the equivalence point, the concentrations of these species become very small and, after we neglect the right-hand term, Eq. 1 is reduced to a simple Grantype equation:

$$a_{H^+} (V_0 + V_a) = -TA V_0 \gamma_{H^+} + N_a \gamma_{H^+} V_a V_0 \quad (2)$$

In Eq.2, the product a_{H⁺}(V₀+V_a) is a linear function of the titration variable V_a. For any given titration point below the equivalence point, a_{H⁺} can be calculated from the measured pH, and V₀+V_a are known. Hence, the total alkalinity of the sample and γ_{H⁺} can be calculated from the line slope and intercept, which are obtained by linear regression analysis on several titration points in this region.^[2]



The degree of evaporation (DE) is henceforth defined as the ratio between the molal concentrations of magnesium in the evaporated solution and that in "mean" seawater [3]:

$$DE = \frac{C_{Mg^{2+}, \text{insolution}}}{C_{Mg^{2+}, \text{inseawater}}} \quad (3)$$

Calculation of ionic strength: Samples ionic strength and carbonate solubility were calculated via equations :

$$I = \frac{1}{2} \sum m_i z_i^2 \quad (4)$$

$$S_{CaCO_3} = \frac{TA}{2} \quad (5)$$

Ionic strength of samples without aragonite

	Cl^-	Ca^{2+}	Mg^{2+}	Na^+	K^+	SO_4^{2-}	HCO_3^-	DE	I
original	5.14	0.0175	0.185	1.616	0.0253	0.0881	0.00046	1	3.9721
1day	5.27	0.0175	0.1875	2.02	0.0317	0.0993	0.000485	1.0135	4.2697
3days	5.3	0.0175	0.195	2.423	0.038	0.139	0.000524	1.0541	4.5838
6days	5.34	0.0175	0.2125	2.644	0.0506	0.147	0.000551	1.1487	4.7716
8days	5.37	0.015	0.345	2.87	0.0633	0.176	0.00118	1.8649	5.2242
13days	5.49	0.015	0.36	2.857	0.0696	0.288	0.00103	1.946	5.5348
18days	5.52	0.0125	0.3725	3.071	0.0745	0.296	0.00113	2.0135	5.6953
25days	5.76	0.01	0.385	3.503	0.0796	0.309	0.00123	2.0811	6.0799
30days	5.91	0.0075	0.445	3.122	0.0823	0.366	0.00161	2.4054	6.195

Ionic strength of samples with aragonite

	Cl^-	Ca^{2+}	Mg^{2+}	Na^+	K^+	SO_4^{2-}	HCO_3^-	DE	I
original	5.11	0.0175	0.365	5.25	0.0696	0.0278	0.000937	1	6.0359
1day	5.22	0.01625	0.414	5.45	0.076	0.0514	0.001026	1.134	6.3368
3 days	5.33	0.01375	0.4335	5.66	0.0823	0.082	0.001131	1.188	6.5952
6 days	5.43	0.0125	0.4475	5.66	0.0886	0.107	0.001101	1.226	6.7238
8 days	5.5	0.0125	0.465	5.45	0.101	0.176	0.001344	1.274	6.8332
13 days	5.6	0.0075	0.5325	5.25	0.114	0.686	0.001475	1.459	7.9347
18 days	5.64	0.0075	0.655	4.44	0.14	0.822	0.001665	1.794	8.0798
25 days	5.65	0.005	0.66	4.44	0.114	1.276	0.001803	1.808	8.9849
30 days	5.8	0.005	1.05	5.1	0.248	1.29	0.00191	2.877	10.265

Results of alkalinity and carbonate solubility in samples

samples	pH in samples without aragonite	TA in samples without aragonite	S_{CaCO_3} in samples without aragonite	pH in samples with aragonite	TA in samples with aragonite	S_{CaCO_3} in samples with aragonite
original	8.3	0.413	0.2065	8.06	0.688	0.344
1day	8.29	0.425	0.2125	8.08	0.718	0.359
3days	8.23	0.491	0.2455	8.08	0.756	0.378
6days	8.17	0.491	0.2455	8.09	0.753	0.3765
8days	8.07	0.863	0.4315	8.02	0.911	0.4555
13days	8.03	0.797	0.3985	8.02	0.972	0.486
18days	7.99	0.705	0.3525	7.98	1.1	0.55
25days	7.94	0.945	0.4725	7.79	1.4514	0.7257
30days	-	1.169	0.5845	-	-	-

4. Conclusions

Carbonate solubility in Urmia lake is calculated. With increasing the carbonate solubility, pH decreased. the apparent dissociation constants and solubility of the carbonate system in sea water are explicitly dependent upon solution composition. any variation in composition of solution which involves a departure in the major ion ratio would be reflected in a change in k' from sea water values.

With increasing the lake concentrations, pH decreases and ion strength increases .carbonate system is the important parameter of pH changes.[4]

References

- [1] B.Lazar, A.Starinsky, A.Katz, E.Sass and S.Ben-Yakoov. American Society of Limnology and Oceanography, Inc, 1983.
- [2] Eytan Sass and Sam Ben Yakoov, Marine Chemistry, 5(1977)183-199, 1976 .
- [3] S.Ben-Yakoov and M.B.Goldhaber. Deep-Sea Research, Vol.20, pp.87 to 99, 1972.
- [4]] Mokhtarpoor.M, a thesis for the degree of master of Science in the Physical Chemistry, University of Urmia, 1388



Determination of thermodynamic properties of aqueous mixtures of MgCl_2 and $\text{Mg}(\text{NO}_3)_2$ by the EMF method at $T=298.15$

M. Giah^{a*}, M. Pournaghdy^b, H. Aghaie^b

^aDepartment of Chemistry, Faculty of Science, Islamic Azad University, Lahidjan Branch, Lahidjan, Iran.

^bDepartment of Chemistry, Islamic Azad University, Science and Research Branch, Tehran, Iran.

(Email: giah_i_m@yahoo.com)

Keywords: Thermodynamic property, MgCl_2 , $\text{Mg}(\text{NO}_3)_2$, Pitzer model, EMF, activity coefficients.

1. Introduction

Although the thermodynamic properties of various electrolyte solutions, and particularly mixed-electrolyte solutions, have been widely studied [1–5] in the past 100 years, there remain numerous electrolytic systems for which these data are unreported or scarce. In the last decades, a series of ion-interaction models for electrolyte solution have been proposed to predict activity coefficient of each solute and osmotic coefficient of aqueous systems. One of the most famous and useful models is that proposed by Pitzer [3, 6].

2. Methods

Preparation of PVC membrane electrode and Ag-AgCl electrode

The 1, 4- bis (2-(5- methyl-4- phenylthiazol-2-yl) hydrazinyl) benzene (BMPHB) is used as the ionophore which acts as neutral ion carrier in plasticized polymeric membrane for fabrication of Mg^{2+} -selective electrode. The Ag-AgCl wire was used as both internal reference electrodes and chloride selective electrode.

Potentiometric measurement and procedure

The cell arrangements in this work were as follows:

(A) $\text{Mg-ISE} / \text{MgCl}_2 (m_{A0}) / \text{Ag-AgCl}$

(B) $\text{Mg-ISE} / \text{Mg}(\text{NO}_3)_2 (m_{B0}) / \text{Ag-AgCl}$

(C) $\text{Mg-ISE} / \text{MgCl}_2 (m_A), \text{Mg}(\text{NO}_3)_2 (m_B) / \text{Ag-AgCl}$

The above galvanic cells are without liquid junction. Here m_{A0} and m_{B0} were molalities of MgCl_2 and $\text{Mg}(\text{NO}_3)_2$ as single salts in water, respectively. The m_A and m_B were the molalities of MgCl_2 and $\text{Mg}(\text{NO}_3)_2$ in the mixture, respectively. Firstly, the electromotive force (emf) of cells (A) and (B) were measured and finally the emf of cell (C) was measured in the sequence of ionic strength fraction (y) of $\text{Mg}(\text{NO}_3)_2$ in the solutions.

Pitzer equation

The Pitzer ion interaction model was used for the experimental data correlation and calculation of thermodynamic properties for mixed electrolyte solutions.

3. Results and discussion

The calibration of electrode pair of Mg^{2+} -ISE and Ag-AgCl

As a preliminary step, the amount of m_{A0} from 0.00033 to 4.000 mol. kg^{-1} were selected to determine each corresponding potential (E_A) using the cell (A). The Nernst equation for cell (A) is:

$$E_A = E^0 + k \log m_{A0}^3 \cdot \gamma_{\text{MgCl}_2}^0 \quad (8)$$

Where the $\gamma_{\text{MgCl}_2}^0$ is the mean activity coefficient of pure MgCl_2 in water. The E^0 is the experimental standard potential of cell (A). Then determined potentials were plotted against $\log a_{\text{MgCl}_2}$ (figure 1) to check the Nernst response and the linear correlation coefficient (R^2). The mean activity coefficients of pure MgCl_2 ($\gamma_{\pm \text{MgCl}_2}^0$) in water were calculated.

Experimental mean activity coefficient of MgCl_2 in the mixture

The cell (C) was used to determine the emf values (E_c) of the mixed salts in the mixture at $T = 298.15$ K at different ionic strengths I and mole fraction y . The mean activity coefficients of $MgCl_2$ calculated and are shown in figure 2.

Calculation of thermodynamic properties

The osmotic coefficients (ϕ), the mean activity coefficients of $Mg(NO_3)_2$ and the excess Gibbs free energy calculated for all of the series under investigation with common cation $[(1-y) MgCl_2 + y Mg(NO_3)_2]_{(aq)}$.

4. Conclusions

The thermodynamic investigation of the system $[(1-y) MgCl_2 + y Mg(NO_3)_2]_{(aq)}$ was studied by a potentiometric method using a solvent polymeric Mg^{2+} -selective membrane electrode with an Ag-AgCl electrode at temperature 298.15 K. The activity coefficients of $MgCl_{2(aq)}$ in pure solution and in the mixture were measured by galvanic cells without liquid junction. The activity coefficients of $Mg(NO_3)_{2(aq)}$ in the mixture and the excess Gibbs free energy were also calculated.

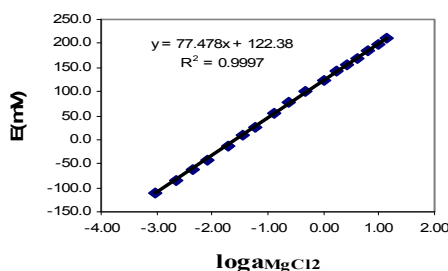


Fig. 2. Plot of The emf versus $\log a_{MgCl_2}$ for calibration of Mg-ISE and Ag-AgCl electrode pair at 298.15K.

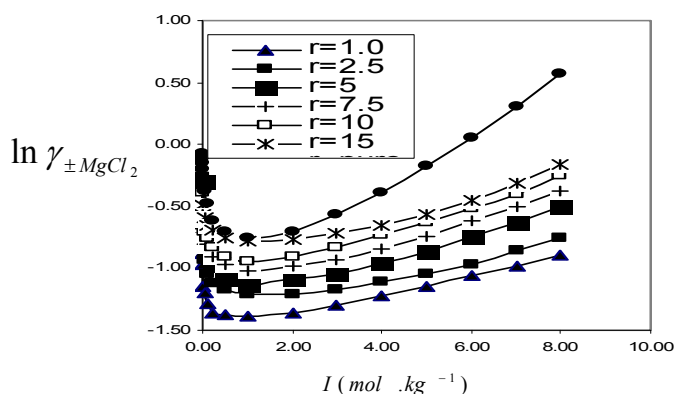


Fig. 3. Plot of the values of natural logarithm mean activity coefficients for $MgCl_2$ versus total ionic strength at different molar ratio ($r = m_{MgCl_2} / m_{Mg(NO_3)_2}$) at 298.15 K.

References

- [1] P. Debye, E. Huckel, Phys. Zeit. 24 (1923) 185–195.
- [2] R.A. Robinson, R.H. Stokes, J. Am. Chem. Soc. 70 (1948) 1870–1878.
- [3] K.S. Pitzer, J. Phys. Chem. 77 (1973) 268–277.
- [4] R.A. Robinson, R.N. Roy, R.G. Bates, J. Solution Chem. 3 (1974) 837–846.
- [5] J. Zhang, S.Y. Gao, S.P. Xia, J. Chem. Thermodyn. 35 (2003) 1383–1392.
- [6] K.S. Pitzer, Activity Coefficients in Electrolyte Solutions, second, ed., CRC Press, Boca Raton, FL, 1991, p. 75.

**Oxidation of Methanol at Nickel Chloride Modified Carbon Paste Electrode (NCMCPE) in Alkaline Medium**

J. Shabani shayeh , M. Jafarian* , M.G. Mahjani ,M. Rashvand avaei

Department of chemistry, K.N. Toosi University of Technology, P.O. Box 15875-4416, Tehran, Iran

(Email: mjafarian@kntu.ac.ir)

Keywords: Carbon paste, methanol, nickel chlorid, electro oxidation**1. Introduction**

Carbon paste electrode (CPE) is a special kind of heterogeneous carbon electrode consisting of mixture prepared from carbon powder and a suitable water-immiscible or non-conducting binder. Advantageous properties and characteristics of CPE can be listed as: facility to prepare, low cost, large potential window, simple surface renewal process and incorporation different substances during the paste preparation that allow the fabrication of electrodes with desired composition, and hence, with pre-determined properties [1,2]. In this study, in order to investigation of electro catalytic characteristics of NCMCPE for electro-oxidation of methanol, the methods of cyclic voltammetry (CV), chronoamperometry (CA) and impedance spectroscopy (EIS) were employed.

2. Methods

Electrochemical studies were carried out in a conventional three electrode cell powered by an electrochemical system comprising of EG&G model 273A potentiostat/galvanostat. A saturated Ag/AgCl electrode and a Pt wire were used as the reference and counter electrodes, respectively. Nickel modifies carbon paste electrode was made by mixing nickel chlorid and graphite powder by dissolving them in some distilled water and were dried in oven at 80-90 °C for 6 hours.

3. Results and discussion

Fig. 1 presents cyclic voltammograms of carbon paste electrode (CPE) and the same electrode that was modified with nickel chloride in 1 M NaOH solution in the range of 0 to 600 mV vs. Ag/AgCl recorded at a potential sweep rate of 10 mVs⁻¹.

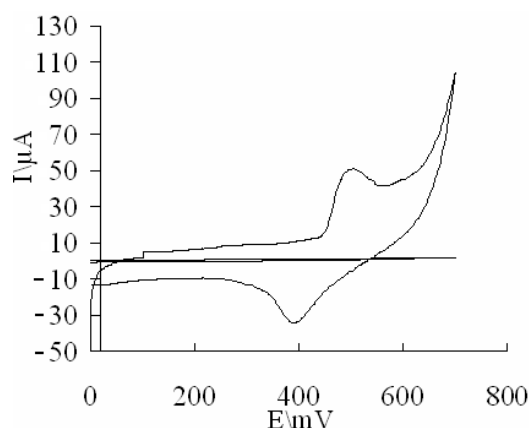
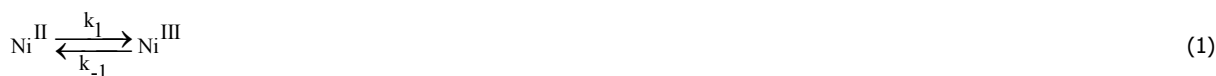


Fig. 1. presents cyclic voltammograms of CPE in the absence of Nickel chloride and presence of Nickel chloride in CPE.

At nickel chloride modified carbon paste electrode (NCMCPE), oxidation of methanol appeared as a typical electrocatalytic response. This phenomenon was attributed to the electrocatalytic activity of Ni^{II} and Ni^{III} species. The redox reaction of nickel species present in the carbon paste matrix is



and methanol is oxidized on the modified surface via the following reaction [3]:



In Fig. 2 the effect of the methanol concentration on the cyclic voltammograms of NMCPE was investigated. As can be seen, increasing methanol concentration causes a proportional enhancement of the irreversible oxidation peak of methanol, Fig. 2 (inset).

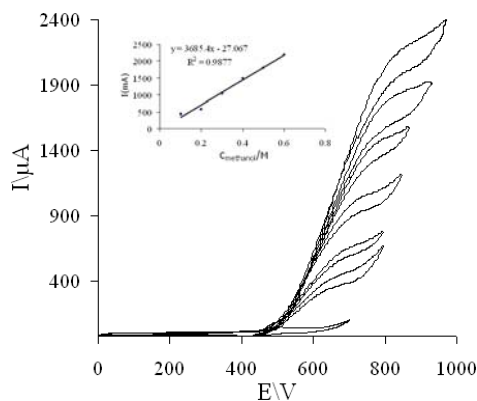


Fig. 2. shows cyclic voltammograms of CPE in 1 M NaOH solution in the presence of 0.1, 0.2, 0.3, 0.4, 0.5 and 0.6 M methanol at a potential sweep rate of 10 mVs⁻¹.

Results of the double-step chronoamperograms indicated a diffusion controlled process. The transition current is obviously due to the mediated oxidation of methanol by NiI^{III} species and is substantiated upon increasing the concentration of methanol. Also, as the electrolysis potential is stepped down to 0 mV vs. Ag/AgCl, no significant current is obtained indicating the irreversibility of the process (not shown here). This result has been confirmed by chronoamperometry (CA) and impedance spectroscopy (EIS) techniques.

4. Conclusions

The preparation and usefulness of nickel chloride modified carbon paste electrode (NMCPE) for methanol electro-oxidation in alkaline media investigated. The electrode was electro-catalytically active around 677 mV vs. Ag/AgCl where the carbone paste electrode possessed no activity.

References

- [1] J. Tashkhourian, M.R. Hormozi Nezhad, J. Khodavesi, S. Javadi, L. Electroanal. Chem. 633 (2009) 85.
- [2] S. Shahrokhian, M. Ghalkhani, M.K. Amini, Sens. Actuators B 137 (2009) 669.
- [3]. I. Danaee, M. jafarian, F. Forouzandeh, F. Gobal, M.G. Mahjani, Electrochim. Acta 53 (2008) 6602.

**Modification of glassy carbon electrode by electrochemical reduction in situ generated diazonium salts**

N.Yazdizade*, A.A.Rostami. A. Omrani

Faculty of Chemistry, University of Mazandaran, Babolsar, Iran

(Email: n_chem_y@yahoo.com)

Keywords: Modification, In situ, diazonium salt, grafting, barrier effect.**1. Introduction**

The functionalization of surfaces including electrodes and powders via the reduction of diazonium cations has been widely investigated during the past decade.¹⁻² The modification of surfaces with specific chemical functionalities can result in potential application in chemical sensing, microelectronics, protection against corrosion, and biosensing. Since the past decade, the electrochemical reduction of aryl diazonium salts on conductive surfaces has been widely investigated.³⁻⁴ This technique allows the covalent attachment of aryl groups bearing a terminal functionality and halogenated groups to various surfaces (carbon,⁵ metals including gold, semiconductors, and silicon) through the generation of an aryl radical which then covalently binds to the electrode. In this paper, we report the direct electrochemical functionalization of a carbon electrode with a diamine.

2. Methods

Reagents. Sodium nitrite, potassium hexacyanoferrate(III), potassium chloride, hydrochloric acid and diamines (1,2-phenylenediamine and N,N-dimethyl-1,4-phenylenediamine) used for diazonium salt in situ synthesis were used as received from MERCK.

Electrode preparation before modification. A one-compartment electrochemical cell was used with a three-electrode configuration. Glassy carbon electrode was used as working electrode. The reference electrode was Ag/AgCl (saturated KCl), and the platinum gauze was used as the counter electrode. The glassy carbon electrode surface was cleaned by polishing with Buehler 0.3 μm alumina slurry. After each polishing step, the electrode was washed with Nanopure water.

Electrochemical modification. The in situ diazonium reduction experiments were carried out in deaerated water at room temperature. A total of 400 μL of 0.1 M NaNO_2 (final concentration: 2 mM) was added to the electrolytic solution (20 mL) containing 2 mM phenylenediamine and 0.5 M HCl under stirring. The mixture was left to react for about 5 min prior to the electrochemical functionalization. The modification was done using cyclic voltammetry during 10 cycles at the potential between 0.9, -1.1 for 1,2-phenylenediamine. All solution was deaerated by bubbling with ultrapure nitrogen for 10 min prior to each experiment. The barrier properties of unmodified and modified carbon electrodes were evaluated using 5 mM $\text{Fe}(\text{CN})_6^{3-/4-}$ in 0.1 M KCl aqueous solution.

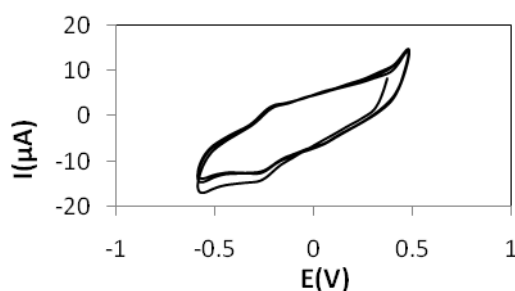


Fig. 1. Cyclic voltammograms at a scan rate of 50 mV/s for a glassy carbon electrode in a solution containing (1,2-phenylenediamine) (2 mM) and 2 mM NaNO_2 in aqueous 0.5 M HCl.

3. Results and discussion

The amine group on the phenyl ring "aromatic amine" is known to be selectively oxidized by nitrosonium ions in the presence of aliphatic⁵ amine on the molecule, but the effect of the aliphatic amines (primary, secondary, or tertiary) of the diamine on the grafting by the "diazonium chemistry" has not been investigated except for 4-amino-N,N-diethylaniline⁴ and 4-aminobenzylamine.⁶ Electrochemical reduction in aqueous acidic medium of diazonium cations generated in situ from 1,2-phenylenediamine (Figure 1) and N,N-dimethyl-1,4-phenylenediamine was investigated by cyclic voltammetry at a glassy carbon electrode. The first cycle of each voltammogram presents two chemically irreversible reduction processes. A shift of the wave

to more negative potential is also observed. This cyclic voltammetry behavior is reminiscent of that observed for the reduction of other diazonium cations, and this was explained by the formation of an organic film, which passivates the electrode surface. The blocking behavior of the resulting modified glassy carbon electrodes was investigated by electrochemical measurements in the presence of $\text{Fe}(\text{CN})_6^{3-/4-}$ as an electroactive redox probe.^{7,8} Figure 2 shows CVs before and after the modification of glassy carbon electrode by the electrochemical reduction of in situ generated diazonium cations.

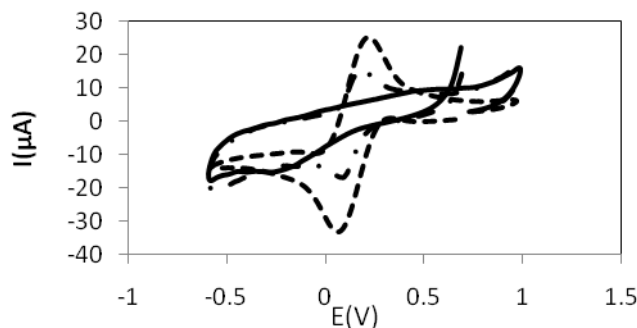


Fig. 2. Cyclic voltammograms recorded in aqueous 5mM $\text{Fe}(\text{CN})_6^{3-/4-}$ /0.1 M KCl a scan rate of 50 mV/s for a bare glassy carbon electrode (---), a modified electrode after 1 min of rinsing in water (—), and after 1 min of rinsing in acetonitrile (— · —). The electrode was modified under cyclic voltammetry of 1,2-phenylenediamine, for 10 cycles. Deposition solution: see the Experimental Section.

The cyclic voltammograms recorded for the modified electrodes following rinsing in water exhibited a significant blocking behavior as demonstrated by the suppression of the electrochemical response for the redox probe and the increase of the potential peak separation between the anodic and cathodic peaks, but following rinsing treatment in acetonitrile modified electrode showed a dramatic decrease of this effect.

References

- (1) Brooksby, P. A.; Downard, A. J. *Langmuir* **2004**, 20, 5038.
- (2) Baranton, S.; Be' langer, D. J. *Phys. Chem. B* **2005**, 109, 24401.
- (3) Pinson, J.; Podvorica, F. *Chem. Soc. Rev.* **2005**, 34, 429 and references therein.
- (4) Liu, G.; Liu, J.; Bocking, T.; Eggers, P. K.; Gooding, J. J. *Chem. Phys.* **2005**, 319, 136.
- (5) Kornblum, N.; Iffland, D. C. J. *Am. Chem. Soc.* **1949**, 71, 2137.
- (6) Corgier, B. P.; Laurent, A.; Perriat, P.; Blum, L. J.; Marquette, C. A. *Angew. Chem., Int. Ed.* **2007**, 46, 4108
- (7) D'Amours, M.; Be' langer, D. J. *Phys. Chem. B* **2003**, 107, 4811.
- (8) Downard, A. J.; Prince, M. J. *Langmuir* **2001**, 17, 5581. (7) For example: (a) Downard, A. J. *Electroanalysis* **2000**, 12, 1085.



Ability of the potentiometric method on the thermodynamic modeling of the concentrated mixed electrolyte system

Farzad Deyhimi, Maryam Abedi

Department of Chemistry, Shahid Beheshti University, Evin-Tehran 1983963113, Iran.

(Email: M.Abedi85@gmail.com)

Keywords: Thermodynamic Properties, Activity Coefficient, Potentiometric, Mixed Electrolytes.

1. Introduction

The knowledge of the thermodynamic properties of aqueous mixed electrolyte solutions are needed for understanding the nature of various ionic interactions and controlling many industrial and environmental processes [1]. The customary experimental techniques used for these purposes are vapor pressure or solvent activity based methods. Nevertheless, the more recent development of different carrier-based solvent polymeric ion-selective membrane electrodes (ISEs), has led to an attractive and alternative rapid method for the investigation of the thermodynamic properties of electrolyte systems through the determination of the activity coefficients [3-6]. However, it is well known that in mixed electrolyte system the response of ISEs could be more or less affected by the presence of interfering ion, as expressed by the potentiometric selectivity coefficient (K_{ij}) of the ISE. In view of usefulness of this device, we have used, for many years, different types of ISE, and particularly, solvent polymeric ISE membrane for the determination of mean activity coefficients in mixed solvents and in mixed electrolyte systems [2-5 and refs. therein]. In this context, it seemed interesting to investigate the applicability of typical solvent polymeric ISE membrane in critical conditions for the determination of activity coefficient in mixed electrolyte systems. For this purpose, two mixed 1:1 electrolyte systems with common anions, namely the ternary $\text{NH}_4\text{Cl}+\text{KCl}+\text{H}_2\text{O}$ and $\text{KCl}+\text{NH}_4\text{Cl}+\text{H}_2\text{O}$ electrolyte systems were selected, in which the corresponding NH_4^+ and K^+ cations are considered as the strongest interfering ion for K^+ ISE and NH_4^+ ISEs, respectively. In addition, Pitzer semi-empirical ion-interaction theory for mixed salts was used for the determination of thermodynamic properties of these ternary electrolyte systems over the ionic strength ranging from 0.01 up to 5 mol/kg, at 298 K, and in different series of mixed electrolyte systems with similar ionic strengths, and each characterized by different defined molal ratio ($r = m_1 (\text{MX}_1) / m_2 (\text{MX}_2)$).

2. Method

In Pitzer ion-interaction theory, the non-ideal behavior of the electrolyte system is conveniently described by the related activity and excess Gibbs free energies [1-4]. For a single $M_{\nu+}X_{\nu-}$ electrolyte (e.g. NH_4Cl or KCl), and for a (1:1) mixture of MX and NX electrolytes, the corresponding Pitzer equations are written respectively as

$$\ln \gamma_{\pm} = |z_+ z_-| f^{\gamma} + m \left(\frac{2\nu_+ \nu_-}{\nu} \right) B^{\gamma} + m^2 \left(\frac{2(\nu_+ \nu_-)^{3/2}}{\nu} \right) C^{\gamma} \quad (1)$$

$$\ln \gamma_{\pm \text{MX}} = f^{\gamma} + I \left\{ B_{\text{MX}}^{\gamma} + y_2 (B_{\text{NX}}^{\phi} - B_{\text{MX}}^{\phi} + \theta_{\text{MN}}) \right\} + I^2 \left\{ \left(\frac{3}{2} C_{\text{MX}}^{\phi} \right) + y_2 \left(C_{\text{NX}}^{\phi} - C_{\text{MX}}^{\phi} + \frac{\psi_{\text{MNX}}}{2} \right) + y_2 (1 - y_2) \frac{\psi_{\text{MNX}}}{2} \right\} \quad (2)$$

The Pitzer graphical method [1] could also be used for the determination of the mixed ionic interaction parameters ($\theta_{\text{MN}}, \psi_{\text{MNX}}$) for the studied ternary systems. Using the obtained Pitzer parameters the value of osmotic coefficients (ϕ), excess Gibbs free energies (G^{E}), and water activities (a_w) were determined for all series of investigated mixed electrolyte solutions.

3. Results and discussion

Using the reported Pitzer parameter ($\beta^{(0)}, \beta^{(1)}$ and C^{ϕ}) for aqueous pure NH_4Cl and KCl solutions [1], the potentiometric selectivity coefficient of the NH_4^+ (1) ISE toward the K^+ (2) and K^+ (1) ISE toward the NH_4^+ (2) interfering ions were determined.



In order to check the impact of the interfering term ($K_{12}^{\text{Pot}} a_2/a_1$) on the results, its value was evaluated in the corresponding concentration range for the whole studied series of the ternary electrolyte systems. The range of variability of the magnitude of the interfering term for each series of solutions, and its influence ($\square \log a_1$) on the determined $\log a_1$ values were also calculated. As can be seen, the magnitude of this term increases as the molal fraction (r) decreases, however, the calculations confirm that for the series of solutions with different molal ratio $r = m_1/m_2$, the corresponding logarithm of the mean activity coefficients could conveniently be determined, up to their fourth decimal place values by the Nernst equation. Accordingly, the resulting value of these interaction parameters for each series of mixed electrolyte solutions with a defined $r = m_1/m_2$, along with their resulting mean values (\pm SD), were calculated for the whole series of solutions. By comparison of the reported data, when the related values of the interaction parameters ($\theta_{\text{NH}_4\text{Na}}, \psi_{\text{NH}_4\text{NaBr}}$) for the series of solutions with a defined $r = m_1/m_2$, were significantly different from the resulting mean values of the remaining series of solutions, the data series of the corresponding solution were excluded in the evaluation of the final mean values of these parameters.

Finally, based on the obtained Pitzer ion-interaction parameters the value of osmotic coefficients (ϕ), excess Gibbs free energies (G^E), and water activities (a_w) were, as well, determined for the whole series of investigated mixed electrolyte systems.

4. Conclusions

The impact of the magnitude of the potentiometric selectivity coefficient of the ISE membrane (K_{12}^{Pot}) on the estimation of the activity coefficient was analyzed. Accordingly, the limitation due to the interfering effect of the secondary ion (2) present in mixed electrolyte systems is expressed by the magnitude of $K_{12}^{\text{Pot}} \frac{a_2}{a_1}$. The obtained results confirm experimentally that the restrictive role of interfering ions on the ISE measurements could, to a certain extent, be counterbalanced by the convenient choice of the molal fraction for the investigated mixed electrolyte systems. As shown by the reported data, for the investigated electrolyte systems, reliable mean activity coefficients values up to 4 decimal significant numbers correspond to the mixed electrolyte systems with higher molal ratio. The appropriate values of the two and three particles Pitzer interaction parameters (θ_{MN}, ψ_{MNX}) values corresponding to each series of solution with a defined molal ratio ($r = m_1/m_2$), were also determined based on the magnitude of their deviation from the resulting mean values of the other series of solutions ($r = m_1/m_2$). The final series of selected Pitzer parameters permit the evaluation of the other thermodynamic properties such as the osmotic coefficients (ϕ), excess Gibbs free energies (G^E), and water activities (a_w) for the whole series of investigated ternary electrolyte systems.

References

- [1] K. S. Pitzer (Ed.), Activity Coefficients in Electrolyte Solutions, 2nd ed., CRC Press, Boca Raton, FL, 1991.
- [2] F. Deyhimi, A. Ebrahimi, H. Roohi, K. Koochaki, J. Chem. Eng. Data 49 (2004) 1185.
- [3] F. Deyhimi, R. Salamat-Ahangari, B. Ghalami-Chooobar, Phys. Chem. Liq 41 (2003) 605.
- [4] F. Deyhimi, R. Salamat-Ahangari, Fluid Phase Equilibria 264 (2008) 113.
- [5] F. Deyhimi, Z. Karimzadeh, Fluid Phase Equilibria 287 (2010) 155.
- [6] K. S. Pitzer, J. Phys Chem. 77 (1973) 268.
- [7] K. S. Pitzer, J. J. Kim, J. Am. Chem. Soc. 96 (1974) 5701.
- [8] K. S. Pitzer, G. Mayorga, J. Phys Chem. 77 (1973) 2300.

**Electrochemical impedance study on anomalous diffusion in poly pyrrole film**

A. Sharifi, M.G. Mahjani*, A. Ehsani, M. Jafarian

Department of Chemistry K. N. Toosi University of Technology, Tehran, Iran

(Email: mahjani@kntu.ac.ir)

Keywords: impedance, anomalous diffusion, polypyrrole**1. Introduction**

Film electrodes are being investigated intensively in electrochemistry in relation to several attractive applications. These cells operate on the basis of two mobile charge carriers in a thin layer restricted by two planar interfaces which are permeable to different species (finite diffusion or diffusion with general boundary conditions). Electrode coated with electroactive polymer films and electrochromic devices both fall into this class. Usually in a solution/film/metal arrangement, with one ionic and one electronic mobile carrier in the film. Electrochemical impedance is one of the best techniques for monitoring the properties of film-based systems[1,2,3].

2. Methods

Polypyrrole (PPY) film on graphite working electrode were prepared by cycling the potential from -0.5 to 0.9V vs SCE in solution of KClO₄, KCl, KNO₃, K₂SO₄ and 0.1M monomer. The electrochemical properties of PPY film investigated by impedance spectroscopy in frequency range of 100KHz to 5mHz in different dc offset potential and 5mv alternating potential. Fractal dimension of the film are obtained in different electrolyte from constant phase element (CPE), or fractal capacitors[4].

3. Results and discussion

Nyquist plots of film in low frequency show generalize Warburg (semi infinite one dimensional diffusion($D/\text{cm}^2\text{s}^{-1}$) and anomalous warburg (finite diffusion, $D/\text{cm}^2\text{s}^{-\gamma}$). Conventional boundary conditions related to totally reflecting or totally absorbing boundaries. The high frequency Warburg part is not affected by the particular type of boundary at the end of the diffusion zone. In the presence of an ion-blocking contact the low frequency part of the spectra is determined by a non-trivial combination of a diffusion capacitance and the effect of the boundary (CPE-restricted diffusion). Influence of fractal dimension, supporting electrolyte nature and thickness of the film in different dc offset potential was obtained from the value of equivalent-circuit parameters were determined by using non-linear least square fitting procedures and MATLAB software with below equation (real and imaginary part) for determining γ value:

$$Z(\omega) = R_d \frac{\coth(i\omega\tau_d)^{\gamma/2}}{(i\omega\tau_d)^{1-\gamma/2}}, \gamma \leq 1.$$

$$\text{Re } Z^*(u) = \frac{u^{\frac{\gamma}{2}-1} \left(\cos\left(\frac{\pi\gamma}{4}\right) \sin\left(2u^{\frac{\gamma}{2}} \sin\left(\frac{\pi\gamma}{4}\right)\right) - \sin\left(\frac{\pi\gamma}{4}\right) \sinh\left(2u^{\frac{\gamma}{2}} \cos\left(\frac{\pi\gamma}{4}\right)\right) \right)}{\cos\left(2u^{\frac{\gamma}{2}} \sin\left(\frac{\pi\gamma}{4}\right)\right) - \cosh\left(2u^{\frac{\gamma}{2}} \cos\left(\frac{\pi\gamma}{4}\right)\right)}$$

$$\text{Im } Z^*(u) = \frac{u^{\frac{\gamma}{2}-1} \left(\sin\left(\frac{\pi\gamma}{4}\right) \sin\left(2u^{\frac{\gamma}{2}} \sin\left(\frac{\pi\gamma}{4}\right)\right) + \cos\left(\frac{\pi\gamma}{4}\right) \sinh\left(2u^{\frac{\gamma}{2}} \cos\left(\frac{\pi\gamma}{4}\right)\right) \right)}{\cos\left(2u^{\frac{\gamma}{2}} \sin\left(\frac{\pi\gamma}{4}\right)\right) - \cosh\left(2u^{\frac{\gamma}{2}} \cos\left(\frac{\pi\gamma}{4}\right)\right)}$$

Where 'u' is a function of frequency(ω). The values of the γ were obtained between 0.5-1 in different electrolyte for the anomalous diffusion of dopant anions in the films.

References:

- [1] J. Bisquert, A. Compte, J. Electroanal. Chem. 499(2001)112.
- [2] R.D. Armstrong, J. Electroanal. Chem. 198(1986)177.
- [3] Z.Hens. W.P. Gomes. J. Phys. Chem. B101(1997)5814.
- [4] I.D. Raistrick, in: R.S. MacDonald(Ed.), Impedance spectroscopy Emphasizing Solid Materials and systems, Wiley, New York, 1987.





Electropolymerization of PEDOT films on the glassy carbon electrode and study of ions transport during the redox process

A. A. Rostami, A. Omrani, A. Moradi*

Faculty of Chemistry, University of Mazandaran, Babolsar, Iran, P.O.Box: 47416-95447.

(Email: Dara_mo1363@yahoo.com)

Keywords: electropolymerization, Poly (3, 4-ethylenedioxythiophene), Counter ions, morphology

1. Introduction

During the last 25 years, the field of conductive polymers has grown enormously. poly(3,4-ethylenedioxythiophene) (PEDOT) has been the subject of both fundamental and applied research due to its unique and well-known properties such as low oxidation potential, good stability in the oxidized state and high conductivity [1]. This material has application as anti-static and anti-corrosive coatings [2, 3], sensors and biosensors [4], electrochromic devices [5] and solar cells photoactive component [6]. Studies on the galvanostatic polymerisation of EDOT in organic media have shown the influence of the supporting electrolyte, namely the counter-anion nature on the polymer morphology; it has been observed that the PEDOT granules size increases with the molar mass of the anion [7]. The effect of the counter-anion type on the conductivity of the obtained polymer has also been reported [8].

2. Methods

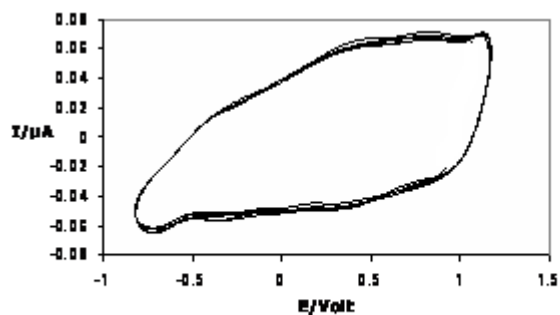
The monomer 3, 4-ethylenedioxythiophene, EDOT, and the solvent, acetonitrile, ACN (99.93%) were used as received. Lithium perchlorate, LiClO_4 (99%), lithium hexafluorophosphate, LiPF_6 ($\geq 99\%$), and lithium tetrafluoroborate, LiBF_4 , were used as supporting electrolyte. Prior to the measurements, the solutions were deaerated by bubbling N_2 (high purity, dried) for 10 min. PEDOT films were potentiodynamically grown in a conventional three-electrode cell, at a sweep rate (ν) of 120 mV s^{-1} , in a solution of 50 mM EDOT + ACN in 0.01 M of several supporting electrolytes: LiClO_4 , LiBF_4 and LiPF_6 . The potential was cycled, during 120 cycles, between -0.95 and 1.26 V for the films formed in the last three electrolytes. After polymerisation, the films were electrochemically characterised in the same electrolyte solution used in the growth but without monomer (0.01 M of supporting electrolyte in ACN), in the potential range [-0.85; 1.10] V at $\nu=50 \text{ mV s}^{-1}$. The electrochemical cell consisted of three electrodes, GC as working electrode. Ag/AgCl as reference electrode and Pt as counter electrode were used.

3. Results and discussion

The polymer was generated by cyclic voltammetry from a 50 mM monomer solution in acetonitrile with different electrolytes. The cyclic voltammograms (CVs) of the polymers recorded in monomer-free solutions are shown in (Fig.1a to c). The electrochemical processes are similar, independent of the type of counter ion. Oxidation occurs for counter ions in the potential range [0.81; 0.60; 0.55] respectively. The conductivity values follow the sequence $\text{ClO}_4^- > \text{BF}_4^- > \text{PF}_6^-$. Comparing this study with our results, it seems that PEDOT films doped with ClO_4^- show the highest conductivity values. Substitution of smaller anions in the films leads to increasing of oxidation. This fact can explain the higher doping of the polymer obtained when LiClO_4 is used comparatively to LiBF_4 and LiPF_6 .

4. Conclusions

PEDOT films were electrochemically oxidized at 1.26V with different counter ions and their in situ conductivity values were determined. ClO_4^- appeared to produce the highest conductivity values for both types of polymers. In addition to the nature of the counter ion, the oxidation potential also appeared to have a strong effect on the morphology and, thus, on the conductive properties of the material.


a) LiClO₄

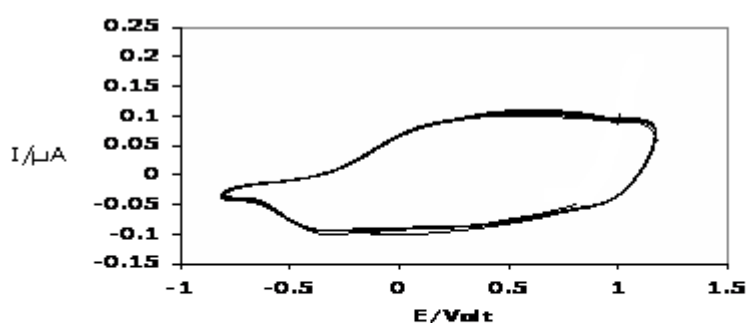
b) LiBF₄

c) LiPF₆

Fig. 1. Cyclic voltammograms of PEDOT_h films in a monomer-free solution of **a)** 0.01 M LiClO₄ **b)** 0.01 M LiBF₄ **c)** 0.01 M LiPF₆ $\nu=50 \text{ mV s}^{-1}$; initial polarization at $E=-0.85 \text{ V}$.

References

- [1] Groenendaal, L. Zotti, G. Aubert, P. H. Waybright, SM. Reynolds, JR, *Adv. Mater.* 15 (2003) 855.
- [2] Randriamahazaka, H. Plesse, C. Teyssié, D. Chevrot, C, *Electrochem. Commun.* 5 (2003) 613.
- [3] Armelin, E. Oliver, R. Liesa, F. Iribarren, JI. Estrany, F. Alemán, C, *Prog. Org. Coat.* 59 (2007) 46.
- [4] Bendikov, TA. Harmon, TC, *Anal. Chim. Acta.* 551 (2005) 30.
- [5] Cho Ko, H. Park, S. Lee, H, *Synth. Met.* 143 (2004) 31.
- [6] Saito, Y. Fukuri, N. Senadeera, R. Kitamura, T. Wada, Y. Yanagida, S, *Electroch. Comm.* 6 (2004) 71.
- [7] Blanchard, F. Carré, B. Bonhomme, F. Biensan, P. Pagès, H. Lemordant, D, J. *Electroanal. Chem.* 569 (2004) 203.
- [8] Aubert, P. H. Groenendaal, L. Louwet, F. Lutsen, L. Vanderzande, D. Zotti, G, *Synth. Met.* 126 (2002) 193.

**Effect of nano-TiO₂ particles on the corrosion behaviour of epoxy polyaniline coatings on aluminium**M. G. Hosseini^a, P. Zardari^b, R. Najjar^c^aDepartment of Physical Chemistry, University of Tabriz, Tabriz, Iran^bDepartment of Physical Chemistry, University of Tabriz, Tabriz, Iran^cDepartment of Organic Chemistry, University of Tabriz, Tabriz, Iran

(Email: mg-hosseini@tabrizu.ac.ir)

1. Introduction

Aluminium, due to its widespread applications is an obvious substrate for corrosion studies. Many of its applications are practicable due to its natural tendency to form an activating oxide layer, which can artificially be generated by anodizing the substrate. However, this activating layer is deteriorated in aggressive media, such as chloride, which results in pitting corrosion. Therefore, coatings are required to protect the aluminium surface in order to obtain higher protection levels. The use of polymers as anticorrosion coating has been explored as a potential candidate to replace the chromium-containing materials, which have adverse health and environmental concerns [1]. PANI due to non-toxic properties, good environmentally friendly specification, and stability has been studied for the development of the aforementioned technological applications [2]. It is thought worthwhile to use nano-particulate titanium oxide (TiO₂) as a metal oxide additive in the composite. In this contribution, we have prepared Nano-TiO₂-PANI epoxy hybrid composite thick films and investigated their suitability for anticorrosive coatings.

2. Methods

Nano-TiO₂ powder dissolved in distilled water, concurrently dodecylbenzene sulfonic acid (DBSA) dissolved in distilled water was mixed with 4.5ml aniline monomer solution stirring for 2 hour. When the emulsion was formed, with this emulsion as a base matrix, a nano-composite coating was formed by adding nano-TiO₂ in various concentrations. Then 0.8M ammonium persulphate (APS) solution was dropped into the reactor, and the solution is vigorously stirred for 12 hour. The particles were finally obtained from the sequential after treatments, i. e. washing, filtering, drying and milling. For preparation of coating, PANI-TiO₂ nanocomposite powder was suspended in tetraethylenepentamine (TEPA) to make a suspension mixture, followed by proper mixing using a magnetic stirrer. An appropriate amount of epoxy to obtain a uniform matrix was added and the mixture was stirred again. After vigorous stirring, the homogeny composite was obtained. Specimens of aluminium 5000 series alloys in the form of 1×1 cm taken sheets were mounted to the working electrode. The test aluminium panels were pre-treated by degreasing in solution of [5g.dm⁻³ (NaOH), 30 g.dm⁻³ (Na₂CO₃), and 20 g.dm⁻³ (Na₃PO₄.10H₂O), at 50°C; for 40s]; then rinsing with 5% (NaOH), at 50°C for 30s and 10% (HNO₃), at room temp for 15s and recently rinsing with distilled water. The previously pretreated aluminium were electrochemically anodized in 20% H₂SO₄ ($j = 1.8 \text{ A. dm}^{-2}$, $\tau = 12.5 \text{ min}$, $\delta = 5\mu\text{m}$, room temp.). Anodized aluminium was rinsing with distilled water and dried with air. Untreated aluminium panels were used for comparison. The liquid paints were coated on substrate by dipping and then dried in 60°C for 8h. In order to evaluate the electrochemical properties of the coatings; electrochemical impedance spectroscopy (EIS) measurements were performed in saline medium at 65°C. The impedance measurements were carried out over a frequency range of 100 KHz-0.01 Hz, using $\pm 5\text{mV}$ amplitude of sinusoidal voltage. Experimental data have been fitted and analyzed by Zview (II) software.

3. Results and discussion**Fourier transform infra-red (FTIR) spectroscopic study**

Fig. 1 shows the overlay FTIR spectra of (a) pure PANI and (b) PANI/nano-TiO₂ composite at the loading levels of 0.5 (b) and 1wt. % (c), respectively. The band at 3750 cm⁻¹ corresponds to OH group, peaks at 1504 cm⁻¹ and 2360 cm⁻¹ are assigned to C=N and

C≡N stretching vibrations. The band at 3420 cm⁻¹ corresponds to interaction between TiO₂ and PANI.

The surface morphology

Fig. 2 shows the SEM of PANI/nano-TiO₂ (1%) powder. The SEM shows that the nano-TiO₂ particles are well dispersed with few agglomerations. Fig. 2 demonstrates that the nanoparticles were successfully prepared in polymer matrix.

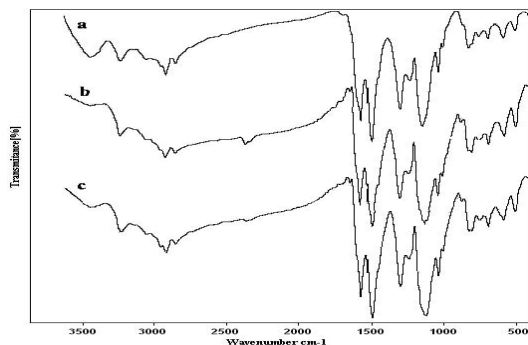


Fig. 1. the FTIR spectra of (a) pure PANI
(b) PANI-TiO₂ (0.5%) and (c) PANI-TiO₂ (1%)

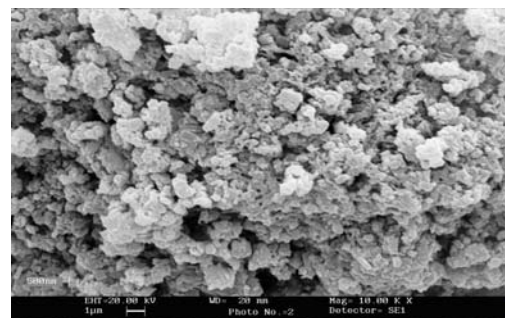


Fig. 2. SEM micrograph of PANI-TiO₂ (1%)

Electrochemical impedance spectroscopy (EIS) measurements

The coated samples were exposed to saline at 65°C for periods of 100h and (EIS) measurements were performed. The Bode plots for anodized and untreated aluminium coated with PANI-TiO₂ (1%) were shown in Fig. 3. It can be seen that, nanocomposite coating on treated aluminium by anodized has better corrosion protection than untreated aluminium. Fig. 4 shows the variation of coating resistance verses time, for different concentration of nanocomposite coatings. The results demonstrated that anodized aluminium coated with 1% of nano- TiO₂ in PANI has the best resistance in saline. The exceptional improvement of performance of these coatings has been associated with the increase in barrier to diffusion, prevention of charge transport by the nanosize TiO₂, redox properties of polyaniline as well as very large surface area available for the liberation of dopant due to nano-size additive.

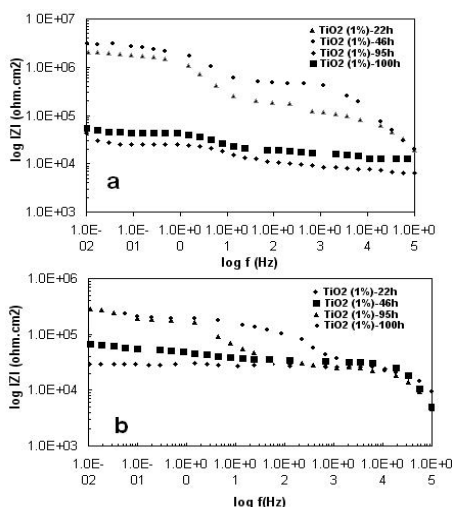


Fig. 3. Bode plots for PANI/ TiO₂ (1%) deposited on (a) anodized (b) untreated aluminium during 100h immersion in 3.5% NaCl solution at 65°C.

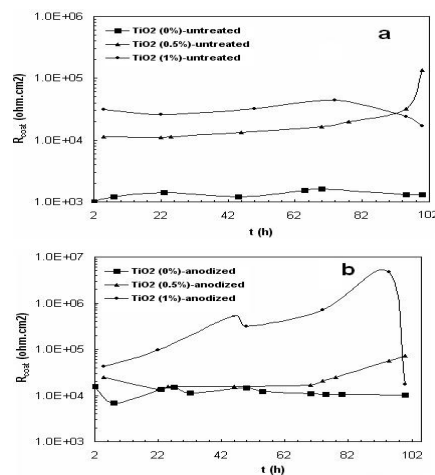


Fig. 4. Evolution of coating resistance of PANI coating loading with different content nano-TiO₂ particles for (a) anodized (b) untreated aluminium during 100h immersion in 3.5% NaCl solution at 65°C.

4. Conclusions

The SEM photograph shows the composite has a mixed nanomorphology, and nanoparticles are successfully prepared in polymer matrix. The effect of nano- TiO₂ addition on the corrosion performance of PANI coatings was investigated by EIS. It was found that addition of extremely small concentration of nano- TiO₂ can significantly improve the corrosion resistance of coating. The results demonstrated that anodized aluminium coated with 1% of nano- TiO₂ in PANI has the best resistance in saline.

References

- [1] M.G. Hosseini, M. Raghbi-Boroujeni, I. Ahadzadeh, R. Najjar, M.S. Seyed Dorraji, **Prog. Org. Coat.** 66 (2009) 321.
- [2] M. Sabouri, T. Shahrabi, H.R. Faridi, M.G. Hosseini, **Prog. Org. Coat.** 64 (2009) 429.

**Electroless plating of Ni-Cu-B on Al and corrosion behaviours of the deposit***S.Rahmani^a, S.A.Seyedsadjadi^a^aDepartment of Chemistry, Iran University of Science and Technology, Tehran, Iran

(Email: s_rahmani86@chem.iust.ac.ir)

Keywords: Electroless Coating; Aluminium; Amorphous Coating; EDAX Analyzes; SEM Microscopy; Polarization Test.**1. Introduction**

Electroless deposition process has undergone numerous modifications to meet the challenging needs of a variety of industrial applications since Brenner and Riddell invented the process in 1946. Amorphous Ni-B binary alloys have been studied extensively [1]. For electroless plating of Ni-B alloy deposits, boron-containing reducing agents such as sodium borohydride or dimethylamine borane are commonly used [2]. The choice of the additional element is made on the basis of the chemically physical property to be imparted to the deposit [3]. Adding a third element to form a ternary system may change their amorphous forming tendency and crystallization characteristics greatly. The purpose of this work is to study the microstructure Physical properties and corrosion behavior of electroless plating Ni-Cu-B deposits [4]. It was mentioned that the addition of copper into electroless Ni-P matrix improves the corrosion resistance of the coatings [5].

2. Methods

Aluminium sheet was used as the substrate material for the preparation of electroless Ni-Cu-B coatings. The substrates were ground on #2000 emery paper and then polished with α -Al₂O₃ polishing medium, degreased in an alkaline solution, cleaned by distilled water, activated in diluted H₂SO₄ acid, and rinsed in distilled water in sequence prior to a deposition cycle. The plating occurred under agitation for 60 min. The bath composition and operating conditions were as follow: 0.1mol/l (NiCl₂·6H₂O), 1mol/l (C₂H₄(NH₂)₂·H₂O), 0.06 mol/l (KNaC₄H₄O₆·4H₂O), 1.5mol/l (NaOH), 18.5mmol/l (NaBH₄) and 0–4mmol/l (CuCl₂·2H₂O) and some stabilizer. The initial pH value of the bath was 14 and temperature was controlled at 90±1 °C. The plating time was 1h. During plating, the bath solution was agitated using a magnetic stirrer at 300 rpm.

3. Results and discussion

The Cu/Ni atomic percent ratio in the deposits was analysed (EDAX). The boron content of the specimens was determined by inductively coupled plasma (ICP). It can be seen that with increasing the Cu concentration in the bath, the copper content of the deposit increases with a simultaneous decrease in the nickel content. There is only a slight change in boron content of the electroless Ni-Cu-B deposit. Scanning electron micrograph (SEM) analysis was performed (Figure 1). All types of deposits are perfectly uniform and adherent on the aluminum substrate. The SEM micrograph of Ni-Cu-B coating exhibits typical cauliflower type structure. The XRD patterns of Ni-Cu-B deposits show that their structures are amorphous. All types of deposits are perfectly uniform and adherent on the aluminum substrate. X-Ray diffraction pattern of these alloy coatings exhibits a single broad peak. Measurements carried out according to Debye-Scherrer equation, revealed that the coatings have nano-crystalline structure. The grain size of the coatings is about 1.3 nm. In other word we can say that the coatings are amorphous and contain nano crystallites (Figure 2). Theoretically, a disorder in arrangement of atoms manifests itself as a broad peak in XRD. Corrosion behaviours were investigated using a Parstat 2273 potentiostat. The potentiodynamic polarization curves were measured in 3.5 wt% NaCl solution at room temperature in a three-electrode cell with saturated calomel reference electrode (SCE), a platinum grid as a counter electrode, the third electrode being the tested specimen. The coatings were masked so that only a 1cm² area was exposed to the electrolyte. The electrode potential was scanned from ±400 mV vs. open circuit potential (OCP) at the rate of 1mVs⁻¹ after a settling time of 15min to stabilize the open circuit potential. By increasing copper content of the deposits corrosion resistance of the coating was increased because of passivity effect of copper.

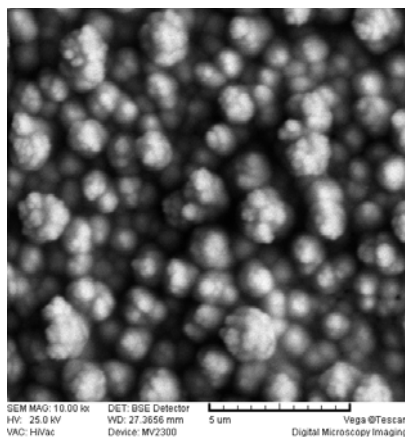


Fig. 1. Microstructure of electroless plating alloys Ni-4Cu-B

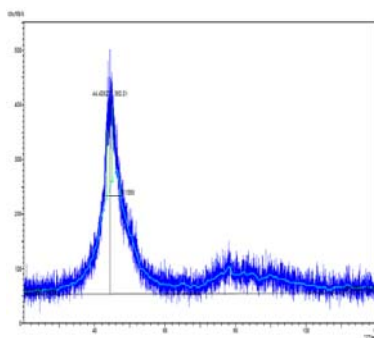


Fig. 2. X-Ray diffraction pattern of electroless Ni –B Deposit

4. Conclusions

1. by increasing molar content of CuCl_2 in the plating bath elemental composition of the coatings changed.
2. XRD patterns suggest that the deposits of electroless Ni–Cu–B alloy are amorphous and contain nano crystallites in the as-deposited condition.
3. When the CuCl_2 concentration was 4mol/l in plating bath, the anti-corrosion performance of the Ni–Cu–B coatings was the best.

References

- [1] V. Vitry, F. Delaunois, C. Dumortier, Surface & Coating Technology. 202 (2008) 3316-3324.
- [2] K. Krishnavini, T.S.N. Sankara Narayanan, S.K. Seshadri, Surface & Coatings Technology. 190 (2005) 115– 121.
- [3] T.S.N. Sankara Narayanan, A. Stephan, a, bS. Guruskanthanb, Surface and Coatings Technology. 179 (2004) 56–62.
- [4] Wangyu Hu, Lijun Wu, Lingling Wang, Bangwei Zhang, Hengrong Guan, Physica B. 212 (1995) 195-200.
- [5] E. Valovaa, J. Dilleb, S. Armyanova, J. Georgievaa, D. Tatcheva, M. Marinova, J. L. Delplanckeb, O. Steenhautc, A. Hubinc, Surface & Coatings Technology. 190 (2005) 336– 344.

Investigation on Cathodic Disbonding of High Solid Thick Polyurethane Pipeline Using Electrochemical Impedance Spectroscopy (EIS)

J. Neshati^a, J. Mofidi^b, F. Akvan^b

^a Corrosion Department, Research Institute of Petroleum Industry (RIPI), P. O. Box 18745-4163, Tehran, Iran.

^b Faculty of Chemistry, North Tehran Branch, Islamic Azad University, Tehran, Iran.

(Email: f.akvan@gmail.com)

Keywords: Cathodic disbonding, Modeling, Cathodic protection, Polyurethane coating, Electrochemical impedance spectroscopy (EIS), Pipeline.

1. Introduction

Cathodic disbonding is one of the main problems in the pipelines for organic coatings on steel substrates under cathodic protection. Cathodic flow produces alkalinity at the interfaces. The alkalinity is the result of cathodic activity under coating. It is made with faults, either inherent or induced electrolyte in coating [1]. Pipeline corrosion and stress corrosion cracking (SCC) occur in electrolytes under disbonded coatings [2-4]. Cathodic disbonding tests were developed in the 1960s [5,6], and leading to the publication of ASTM G8-1969 [7] in which an artificial defect was introduced to simulated the damaged area of a coating. Coating disbondment could be resulted from several reasons [8]. The main mechanisms of anticorrosion to metals include three aspects [9]: (1) the organic coatings act as a barrier layer to decrease the diffusion of the aggressive species towards the interface of metal/coating; (2) the inhibitive pigments contained in the organic coatings can impede the corrosion of the metallic substrate when the aggressive species reach the interface of metal/coating; (3) there is usually a good adhesion between metal and coatings to prevent the coatings from disbonding due to corrosion.

2. Method

In this research three parameters including the coating thickness, the artificial holiday (defect) and electrolyte type were investigated according to ASTM G8 using Electrochemical Impedance Spectroscopy (EIS).

3. Results and discussion

Electrochemical cells were designed to separate the measurements of cathodic disbonding process from the influence of the impedance of an artificial holiday (Fig. 1). Experiments were done in 3.5% NaCl, KCl and CaCl₂ solutions at room temperature with different coating thicknesses (354, 483 and 1014 μm). Artificial holidays diameters were selected as 3, 6 and 9 mm. Immersion time was 28 days and during the immersion, cathodic potential of -1.5 V (vs. SCE) was applied, but the EIS measurements were done in open circuit potential (OCP).

4. Conclusions

Investigations showed above parameters under over protection conditions were efficacious in cathodic disbonding coating process, but with no logical correlations between each parameter and any disbonded area individually (Figs. 2-4). Model was introduced based on the phase shifts obtained from EIS curves using the break point frequencies and the parameters mentioned above. This model can predict the disbonded areas for electrolytes with a 1:1 cation/anion relationship.

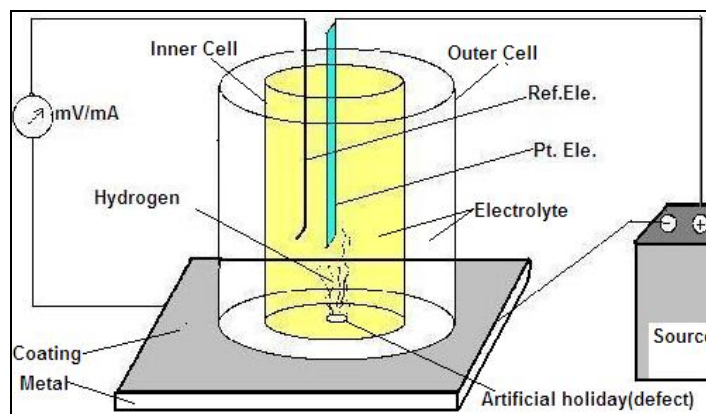


Fig. 1. Electrochemical cells

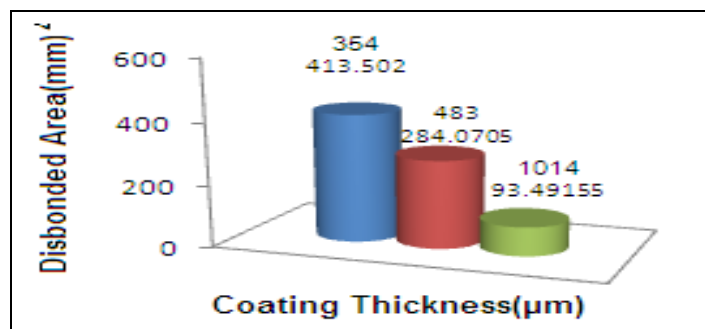


Fig. 2. Effect of Coating Thickness

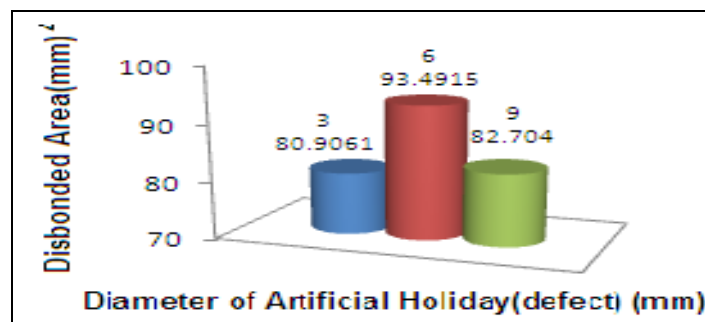


Fig. 3. Effect of Artificial Holiday (Defect)

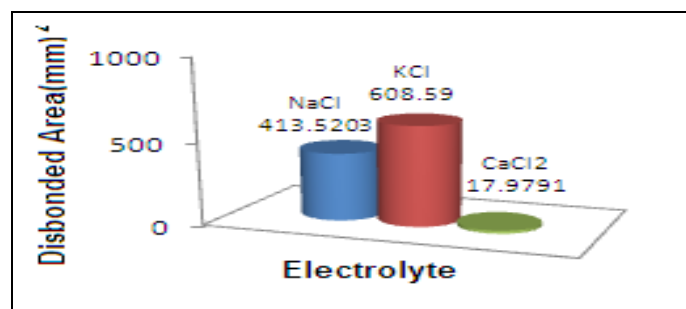


Fig. 4. Effect of Electrolyte

References

- [1] C. Li, B. Cao, Y. Wu, J. Univ. Sci. Technol. B 14 (2007) 414.
- [2] R. N. Parkins, Corrosion'2000, NACE, Houston, paper No. 363, 2000.
- [3] National Energy Board, Report of Public Inquiry Concerning Stress Corrosion Cracking on Canadian Oil and Gas Pipelines, report No. MH-2-95, 1996.
- [4] C. F. Dong, A. Q. Fu, X. G. Li, Y. F. Cheng, Electrochimica Acta 54 (2008) 628.
- [5] J. T. Zhang, J. M. Hu, J. Q. Zhang, C. N. Cao. Prog. Org. Coat. 49 (2004) 293.
- [6] J. L. Luo, C. J. Lin, Q. Yang, S. W. Guan, Prog. Org. Coat. 31 (1997) 289.
- [7] Standard test methods for cathodic disbondment of pipeline coatings, G8-96, ASTM, Philadelphia, PA, USA (2006).
- [8] H. Leidheiser, Jr., W. Wang, L. Igetoft, Prog. Org. Coat. 11 (1983) 19.
- [9] C. Le Pen, C. Lacabanne, N. Pebere, Prog. Org. Coat. 39 (2000) 167.

**Electrochemical study on supercapacitor properties of Poly ortho aminophenol conducting polymer**

M.G. Mahjani*, M. Jafarian A. Ehsani,

Department of Chemistry, Faculty of science, K. N. Toosi University of Technology, Tehran, Iran

(Email: a_ehsani@dena.kntu.ac.ir)

Keywords: Supercapacitor, conducting polymer, impedance spectroscopy**1. Introduction**

The most common electrical energy storage devices are capacitors and batteries. Materials employed to assemble supercapacitor are mainly focused on carbon (including active carbon, carbon aero-gel, and carbon nanotube), metal oxides (including RuO₂, MnO₂, and IrO₂) and electrically conducting polymers (ECPs, including polyaniline, polypyrrole, and polythiophene). The charge storage of carbon is mainly produced from electrical double-layer capacitance mechanism, and the maximum available specific capacitance (Cs) of carbon has reached up to 320 F g⁻¹ [1]. The charge storage of RuO₂ is mainly produced from the pseudocapacitance mechanism, and the available Cs of RuO₂ has reached up to 1170 F g⁻¹ [2]. But RuO₂ is currently too expensive to be commercialized. ECPs have an advantage over noble metal oxides on their low cost, and have an advantage over carbon materials on large pseudocapacitance. The reversible faradic reactions of ECPs accompanied by doping/dedoping of dopants produce high pseudocapacitance. Due to these outstanding properties, ECPs have been intensively studied for supercapacitor application in recent years [3,4].

2. Methods

Poly ortho aminophenol(POAP) fiber with different size on graphite working electrode were prepared by cyclic voltammetry (CV) and normal pulse voltammetry (NPV) techniques in solution of HClO₄, HCl, HNO₃, H₂SO₄ and 0.01M monomer. The electrochemical properties of POAP film investigated by impedance spectroscopy in frequency range of 100KHz to 5mHz in different dc offset potential and 5mv alternating potential. Fractal dimension of the film are obtained in different electrolyte from constant phase element (CPE), or fractal capacitors.

3. Results and discussion

The theoretical maximum specific capacitance (Cs) of POAP/G supercapacitor is estimated to be 2.3×10³ Fg⁻¹. Taking the diffusion of counter-anions and the conductivity of POAP into consideration, only a small part of POAP has contribution to capacitance. Practically, the maximum Cs value measured by CV, EIS, and galvanostatic charge/discharge methods in presentwork for different size of fibers. Firstly, the diffusion of counter-anions in POAP is confirmed to be the rate determining step during the redox. This process degrades the charge/discharge capability of POAP. The porosity of POAP (from fractal dimension) film is a benefit for sufficient contact between the counter-anions and the POAP. Based on these factors, the experimental values are much less than the theoretical one. In order to improve the performance of supercapacitors, the homogeneous POAP nanofibers with large surface area (low diameter and coarse surface) should be applied to modify the substrate.

References

- [1] M.J. Bleda-Martinez, J.A. Macia-Agullo, D. Lozano-Castello, E. Morallon, D. Cazorla-Amoros, A. Linares-Solano, Carbon 43 (2005) 2677.
- [2] I.H. Kim, J.H. Kim, Y.H. Lee, K.B. Kim, J. Electrochem. Soc. 152 (2005) A2170.
- [3] M. Mastragostino, C. Arbizzani, F. Soavi, J. Power Sources 97–98 (2001) 812–815.
- [4] M. Mastragostino, C. Arbizzani, F. Soavi, Solid State Ionics 148 (2002) 493–498.





Improvement of the electrosynthesis and properties of Poly (o-aminophenol) using a SDS Micellar Aqueous Medium

M. Jafarian*, M.G. Mahjani, A. Naeemy, A. Ehsani

Department of Chemistry, Faculty of Science, K.N. Toosi University of Technology, P.O. Box 15875-4416, Tehran, Iran

(Email: jafarian@kntu.ac.ir)

1. Introduction

During the last years, conjugated polymers and oligomers, obtained by electrooxidation of the corresponding monomers, have been the subject of a number of studies devoted to the optimization of the electropolymerization conditions and characterization of the resulting polymers [1]. The investigation and use these materials in, or using electrochemistry evidently well-established and a large number of different application of this system have already been presented. In biosensor production, polymer coating have become of increasing interest in the modification electrode surfaces [2]. Although polymer films exhibit excellent selectivity properties, their use is still a matter of concern because of their relative high detection limit and the low response current. To increase the response current, ferrocene, a satisfactory electron transfer mediator for the amperometric hydrogen peroxide sensor, has been used in the biosensor based on non-conducting polymer films of phenol and its derivatives and an increasing response current of hydrogen peroxide can be observed [3]. Here, we describe in detail the advantages of a novel method of electrochemical preparation of POAP, based on the ability of SDS to form micelle in aqueous media. We demonstrate that the electropolymerization process carried out in the presence of SDS at an oxidation current higher than in an Acidic medium yields better organized POAP films.

2. Methods

The working electrode (graphite) had been polished with No. 2500 Sic emery paper to mirror bright and rinsed with distilled water prior to use. Electrochemical studies were performed in a conventional three electrode cell powered by an EG&G potentiostat/galvanostat run by a computer through M270 commercial software. The potentials were measured against an Ag/AgCl saturated reference electrode with a large 316 stainless steel plate forming the counter electrode. The modified electrodes were prepared by cycling the potential of the working electrode in the range of -250–950 mV vs. Ag/AgCl electrode in synthesis solution. All measurements were carried out at 298 ± 2 K.

3. Results and discussion

In this work, we investigated the preparation of poly (oaminophenol) on the surface of a graphite electrode in the absence and presence of SDS. Fig. 1A shows the 1th and 50th multisweep cyclic voltammograms during electropolymerization in the absence of SDS. As seen in the figure, OAP is oxidized irreversibly at 700mV without corresponding cathodic processes in the reverse scan. During the next cycles, one redox peak (related to oxidation products) appeared at lower potential, and its current did not increase considerably with potential cycling. This occurs because the soluble products produced on the surface of the electrode do not allow the monomer to reach the electrode and produce more monocation radical. Therefore, a longer potential cycling time is needed for transformation of this soluble 3APZ to POAP, which appears at a potential less positive than that of 3APZ [4]. By adding 5mM anionic surfactant of SDS to the monomer solution, the monomer oxidation potential was shifted to less positive potentials (by almost 75mV, see Fig. 1B) and its oxidation current increased. Moreover, the rate of polymerization increased considerably and the redox peaks due to POAP grew simultaneously with 3APZ growth. Furthermore, under successive potential cycling, their peak currents increased and their growth continued. These results show that, in the presence of SDS, the monomer can easily reach the electrode surface and produce more monocation radical. Moreover, a pair of shoulders was observed around 400mV that can be attributed to the presence of SDS in the film. In order to study the effect of varying concentrations of SDS on

POAP growth, the rate of polymerization is not much larger than that observed without SDS. increasing polymer growth rate and current peak shows that the best ability in electrocatalytic oxidation and application in organic and bioorganic sensor.

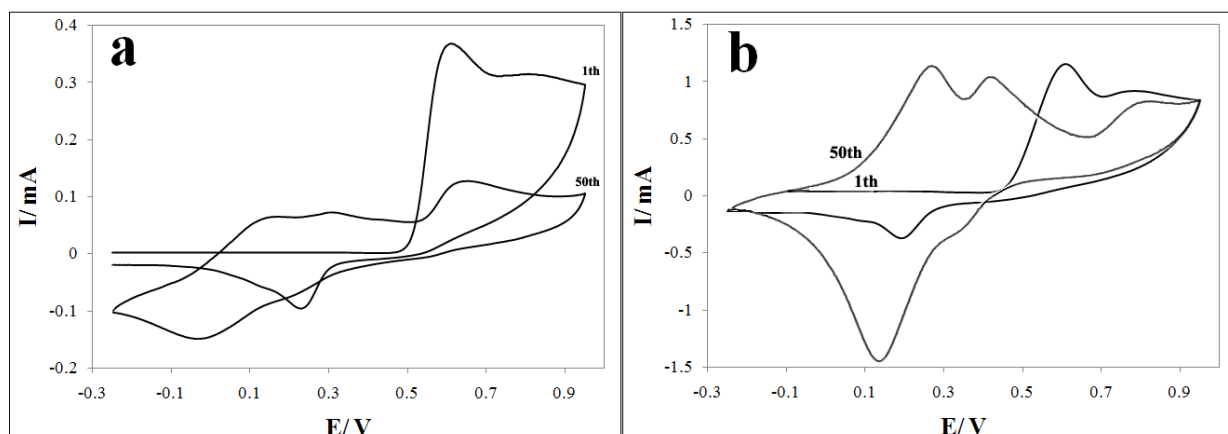


Fig. 1. Electropolymerization of POAP in a 5mM OAP monomer /0.1M HClO₄ solution on the surface of the graphite electrode. (a) in the absence, (b) in the presence of 5mM SDS, at scan rate of 100 mvs⁻¹.surface electrode diameter: 4mm

4. Conclusions

In this paper SDS–POAP/CE was prepared by the electropolymerization of o-aminophenol on a graphite electrode in the presence of SDS. Adding SDS to the monomer solution leads to some modifications in the o-aminophenol polymerization on the electrode including an increase of the polymer growth rate.

Keywords: Poly (O-Aminophenol), SDS, Cyclic Voltammetry, micellar aqueous solution

References

- [1] G. Tourillon, in: T.A. Skotheim (Ed.), Handbook of Conducting Polymers, Marcel Dekker, New York, 1986.
- [2] Z.N. Zhang, H.Y. Liu, J.Q. Deng, Anal. Chem. 68 (1996) 1632–1638.
- [3] Y. Nakabayashi, H. Yoshikawa, Anal. Sci. 16 (2000) 609–613.
- [4] E.M. Genies, M. Lapkowski, C. Tsintavis, New J. Chem. 12 (181) (1988) 18.



Electrochemical impedance spectroscopy study on intercalation and anomalous diffusion of aluminum ions into graphite in basic molten salt (AlCl₃-NaCl-KCl)

M.G. Mahjani, M. Jafarian A. Ehsani,

Department of Chemistry, Faculty of science, K. N. Toosi University of Technology, Tehran, Iran

(Email address: a_ehsani@kntu.ac.ir)

Keywords: impedance, anomalous diffusion, molten salts

1. Introduction

Electrochemical impedance spectroscopy (EIS) is one of the most universal and powerful electroanalytical techniques for fine characterization of kinetic and transport process occurring in thin coated and ion insertion electrodes. Boundary conditions have a strong influence on the control of diffusion processes in electrochemical systems. For these systems, with mobile ions, a diffusion flux implies a Warburg like impedance; this impedance is an $\omega^{1/2}$ function

$$Z(i\omega) \propto (i\omega)^{-1/2} \quad (1)$$

However, in many cases impedance measurements of diffusive processes give rise to power laws in frequency which deviate more or less from the exact 1/2 exponent law[1]

$$Z(i\omega) \propto (i\omega)^{-\beta/2} \quad (0 < \beta < 2) \quad (2)$$

Where ω is the angular frequency of the external electric field. The Warburg-like impedance can be calculated from the Fick diffusion equation for processes with a vanishing relaxation time [1], or from a generalized diffusion equation for processes with a non-vanishing relaxation time [2]. The selective nature of borders and the diffusion length are very important to determine the Warburg impedance from Fick's equation or from a generalized diffusion equation. Usually, the solutions of these problems are limited only to semiinfinite boundary conditions. With vanishing and non vanishing relaxation time processes[1,2], and, moreover, for finite length diffusion conditions, reflective boundary [3] and transmissive boundary conditions, the latter two only for vanishing relaxation time processes. However, the boundary conditions for real electrochemical systems are not total transmissive nor reflective condition; the borders of real systems show a partial transmissive or reflectivenature.

The aim of this paper is to calculate, in the framework of extended irreversible thermodynamics (EIT) [4], a warburg-like impedance for electrochemical molten (AlCl₃-NaCl-KCl) system with generalized boundary conditions for processes with non – vanishing relaxation time in graphite electrode.

2. Methods

Materials used in this work were analytical grade of Merckorigin. AlCl₃ was redistilled while NaCl and KCl were dried at 300 °C prior to use. Fused electrolyte with the composition of 66–20–14 wt.% (AlCl₃–NaCl–KCl) which is equivalent to 48.2–33.4–18.4 mol% had the melting point starting at around 115 °C and terminating nearly at 120 °C as measured in this laboratory. The molten electrolyte was a one phase clear liquid at 140 °C where electrochemical studies were performed. Handling of the materials and the procedures concerning the preparation of the fused electrolyte were much the same as reported elsewhere. The experiments were carried out at 140 °C in a conventional three-electrode cell with a hand polished graphite rod with the surface area of 0.22 cm² forming the working electrode. Its potential was monitored against an aluminum (99.999% purity) reference electrode placed inside the melt. A large graphite rod was used as the counter electrode.

3. Results and discussion

The complex plane plots exhibit fast electron-transfer and two relaxation processes characterized by distributed time constant. At high frequency, the distorted capacitive loop is related to the charge transfer resistance for one step reduction of AlCl₄⁻ in parallel with double-layer capacitance. At low frequency semi infinite and finite warburg are observed which are characteristics of insertion and blocking of Al ions. The processes give rise to change in the active area of the substrate surface. In the diffusion with totally absorbing boundary (Fig.1) the concentration of the AlCl₄⁻ at the boundary remains at the equilibrium level

$$C = 0 \quad (x = L) \quad (3)$$

These standard conditions refer to a random walker absorbed (Eq. (3)) upon encountering a wall at $(x = L)$.

With applying this boundary condition it followed that

$$Q = 3R_w \omega_d^\gamma Z(s)^{-1} = R_w (\omega_d / s)^{\gamma/2} \tanh[(s / \omega_d)^{\gamma/2}] \quad (4)$$

$$Z(s)^{-1} = \frac{1}{R_w} + \frac{1}{Qs^{-\gamma}} \quad (5)$$

Where now $Q = 3R_w \omega_d^\gamma$. Eq. (5) is the parallel combination of a resistance and a CPE. Giving at low frequency a depressed arc in the complex plot.

4. Conclusions

The electrochemical study in molten basic $\text{AlCl}_3\text{-NaCl-KCl}$ show that control diffusion process for AlCl_4^- anions. EIS Studies Show anomalous diffusion with totally blocking and totally absorbing boundary condition for AlCl_4^- anions in graphite working electrode.

The main criterion to identify the anomalous diffusion behavior of AlCl_4^- anions is the slope of the high frequency line (γ) .

References

- [1] J.R. Macdonald (Ed.), Impedance Spectroscopy, Wiley, NewYork, 1987.
- [2] J.R. Ramos-Barrado, P. Galan-Montenegro, C. Criado, J. Chem. Phys. 105 (1996)2813
- [3] C. Ho, I.D. Raistrick, R.A. Huggins, J. Electrochem. Soc. 127(1980)343
- [4] D. Jou, J. Casa-Vazquez, G. Lebon, Extended Irreversible Thermodynamics, Springer, Berlin. 1996

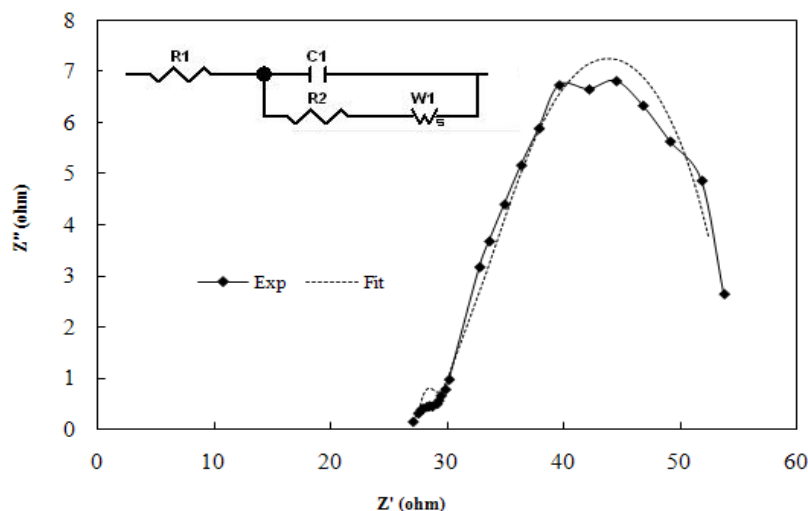


Fig. 1. Nyquist plot and equivalent circuit for diffusion of AlCl_4^- anions with totally absorbing boundary condition in dc offset potential, -1.22V, ($R_1=27.53\text{ohm}$, $C_1=5.72 \times 10^{-6}\text{F}$, $R_2=1.12\text{ohm}$, $W_1\text{-}R=26.42\text{ohm}$, $n=0.37$, $W_1\text{-}T=0.76$)

**Estimation of CMC of sodium dodecyl sulfate in different electrolyte solutions using conductimetry**F. Farshchi¹ Tabrizi, S. Naderi Mighan¹, H. Abedini², M. Bagherzadeh¹, N. Miri³

1-Department of Chemical Engineering, University of Sistan & Baluchestan, Zahedan, Iran

2- Iran Polymer and Petrochemical Institute, P.O. Box: 14965-115, Tehran, Iran

3- Department of Chemistry, University of Sistan & Baluchestan, Zahedan, Iran

(Email: farshchi@eng.usb.ac.ir)

1. Introduction

Micellization phenomena are important industrially as well as biologically and are very interesting chemically, because of their application in pharmacy, cosmetic products and for different tasks related to environmental protection [1].

One of the most significant parameters working with micellar phases is the surfactant critical micelle concentration (CMC) i.e. the concentration above which micelles start to form. Knowledge of this quantity is crucial for both scientific and practical understanding of how surfactants behave and is a topic of major interest due to its unusual physicochemical properties as a result of surfactant aggregation [2]. Many factors such as addition of electrolytes, buffer pH, temperature, addition of organic modifiers, ionic strength of the aqueous solution, presence of additives, etc., make this value different from that determined in pure water [3].

In the case of ionic surfactants, the influence of added electrolytes on their micellization characteristics is attributed entirely to the counter ion effect [4]. A detailed study done on the micellization behavior of SDS with lots of electrolytes like (NaBu, NaAc, NaCl, etc.) [5] and organic compounds like alcohols [6,7] at 25°C; however, literature shows a lack of data for electrolytes such as Na₂CO₃ and KPS (K₂S₂O₈) at 25°C that are widely used in the emulsion polymerization. It is worth noting the absence of Na₂CO₃ in the emulsion polymerization of butadiene causes one cannot reach a conversion more than 10% or 20%. Similarly, KPS used as an initiator in the emulsion polymerization. These materials are, therefore, so crucial for the emulsion polymerization and of course would change the CMC, but there is not enough information about their effects on the CMC in literature.

The aim of this study is to determine the influence of the concentration of Na₂CO₃ and KPS at 25°C on the physical and chemical properties of aqueous solution of sodium dodecyl sulfate (SDS), and declare the empirical relationship between the electrolytes concentration and the CMC.

2. Methods

The salts Na₂CO₃ (Application, 99.5+ %) and KPS (Merck, 99+ %) were used. Distilled water was also used to prepare the solutions. SDS (Merck, 99+ %) was used as received without further purification.

For conductometric measurements, a Radiometer CDM210 conductometer with a Radiometer conductivity cell was used. Conductivity cell was calibrated measuring by triplicate the conductivity of KCl solutions at different concentrations. Experiments were carried out by adding different amounts of surfactant solution to a determinate volume of electrolyte and measuring the conductivity. The range of concentrations measured for each surfactant solution varies in order to obtain enough points before and after the change of slope in the conductivity–surfactant concentration plots.

3. Results and discussion

When the conductivity of solutions with increasing concentration of surfactant is measured, the specific conductivity–surfactant concentration plots show two straight lines with different slope. The first one corresponds to the concentration range below the CMC, when only monomers of surfactant exist in solution. At higher concentrations of surfactant, micelles start to form and a change of slope appears because the conductivity increases in a different manner. The intersection of these two straight lines is taken as the CMC value of the surfactant (fig1). [3].

The values of the CMC obtained in this work for SDS with different concentration of electrolytes at 25°C are presented in table 1. As reported in literature, the CMC value clearly decreases as the concentration of electrolyte increases. This is due to the effect of the electrolyte in micelle formation, that neutralizes the charge at the micelle surface, reduces the thickness of the ionic atmosphere around the surfactant ionic heads and, therefore, the electrostatic repulsions between them, helping in this way the micellization process [2].

Table 1. CMC determined at different electrolyte

concentration at 25°C

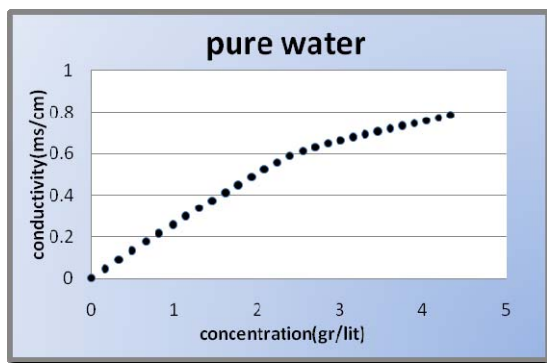


Fig. 1. Conductivity measurements of SDS solution in pure water at 25°C

Electrolyte	Electrolyte concentration(gr/lit)	CMC(gr/lit)
Na ₂ CO ₃	0.5	1.6657
	0.6	1.6477
	0.75	1.4995
	0.95	1.3919
	1.00	1.2987
	3.00	1.1934
	5.00	0.6811
KPS	0.4	1.8433
	0.6	1.6508
	0.8	1.4337
	1.00	1.4148

For each electrolyte studied we have plotted the dependence of CMC of SDS on the electrolyte concentration. The empirical curves at 25°C were fitted by the following equation:

$$y = A \ln(x) + B \quad (1)$$

$$\text{Na}_2\text{CO}_3: A = -0.34, B = 1.412 \quad \text{KPS} : A = -0.706, B = 1.4463$$

Where y is the CMC and x is the electrolyte concentration and this concentration expressed in gr.lit⁻¹. Equation (1) enables us to calculate the values of CMC for a given electrolyte concentration at 25°C

4. Conclusions

In this work, the CMC of one of the most employed surfactant (SDS) that is widely used in emulsion polymerizations at different KPS and Na₂CO₃ concentrations which are the crucial materials in emulsion polymerizations have been determined. Then an empirical relationship was declared. This relationship provides an easy way for researchers to estimate the CMC of a system, at a given electrolyte concentration.

The values of the CMC of SDS have been shown to depend on the kind and concentration of the electrolyte and a reduction in the CMC was observed with increasing in the electrolytes concentrations.

References

- [1] E. Dutkiewicz, A. Jakubowska. Colloid Polym Sci 280 (2002) 1009.
- [2] K. Behara, S. Pandey. Colloid Interf. Sci. 316 (2007) 803.
- [3] E. Fuguet, C. Rafols, M. Roses, E. Bosch. Analytica Chimica Acta 548(2005) 95..
- [4] I.M. Umlong, K. Ismail. Colloids and Surfaces A: Physicochem. Eng. Aspects 299 (2007) 8.
- [5] I.M. Umlong, K. Ismail. J. Surface Sci Technol., 22, (2006), 101.
- [6] C. Bravo, J. Ramon Leis, M. Elena Pena. J. Phys. Chem., 96, (1992), 1957
- [7] H. Gharibi, B.M. Razavizadeh, A.A. Rafati. Colloids and Surfaces A: Physicochemical and Engineering Aspects 136 (1998) 123.

**Effect of organic compounds on the electrochemical behavior of stainless steel in acid solution**

S. M. A. Hosseini, M. Salari

Department of Chemistry, Faculty of Science, Shahid Bahonar University of Kerman, 22 Bahman, Kerman 76175, Iran

(Email: s.m.a.hosseini@mail.uk.ac.ir)

Keywords: Corrosion, Stainless steel, Polarization behavior, Temkin isotherm**1. Introduction**

The inhibition characteristics of some inhibitors in acid corrosion have been reported earlier [1-3]. Organic and inorganic compounds and their derivatives were used successfully as inhibitors for different types of steels and were studied extensively through the last century. Recently, interest is still growing for exploiting other inhibitors for the corrosion of stainless steels [4-7]. This work deals with the study of the inhibition properties of two organic compounds synthesized in our laboratories: ethyl-3-(2-aminoanilino)-2-butenate (A) and ethyl-3-[(2-aminoethyl) amino]-2-butenate (B) as inhibitors for the AISI 316 in 0.5 M H₂SO₄ at 20 to 50 °C using weight loss and potentiostatic polarization techniques.

2. Methods

The electrodes used were machined from stainless steel sheets and were polished with emery papers 800-2500 grade for fine polishing. They were washed thoroughly with doubly distilled water then ultrasonically degreased with acetone. The new organic compounds were synthesized in our laboratory and then their purity was controlled by IR spectrophotometric analysis. For potentiodynamic polarization measurements, the cell was a conventional three electrode Pyrex glass vessel converter with Pt wire as counter electrode, saturated calomel electrode (SCE) as reference electrode and the stainless steel sheet as working electrode. The surface area of each working electrode was 1 cm². The potentiodynamic current potential curves were recorded by changing the electrode potential automatically from -700 mV to +1300 mV with scan rate of 1 mV s⁻¹. Experiments were performed on a BHP-206X Electrochemical Analysis System.

3. Results and discussion

It is observed that the addition of either compound induces a decrease in both anodic and cathodic current, the anodic decrease being more significant. The corrosion potential (E_{corr}) was observed to shift towards more noble potentials with increasing additive concentration, indicating the inhibitors to be of anodic character and formation of a surface film. The values of IE increases with increasing the inhibitor concentration whereas decreases in the following order: compound A > compound B.

The inhibiting effect of these compounds can be attributed to their parallel adsorption at the metal solution interface. The parallel adsorption is owing to the presence of one or more active center for adsorption. The difference in the inhibition efficiencies of the two compounds lie in their structure. The effect of temperature indicates that the temperature increases the values of E_{corr} , shift in the negative direction and the values of I_{corr} increase. This proves that the inhibition occurs through the adsorption of the inhibitor on the surface. The activation energy is higher in the presence of inhibitor than their absence. This type of inhibitor retards the corrosion process at ordinary temperature [8]. Whereas the inhibition is considerably decreased at elevated temperature. The lower values of E_a are possibly good evidence for the physical adsorption mechanism of inhibitors on metal surface. The low and negative values of ΔG_{ads} indicate the spontaneous adsorption of inhibitor on the surface of AISI 316. The negative values of ΔG_{ads} also suggest the strong interaction of the inhibitor molecules onto the alloy surface. The low value of ΔG_{ads} shows that in the presence of acid media physical adsorption of inhibitors may occur. The overall results are in agreement with the values of IE.

Conclusion:

- 1 Organic compounds have proved to be efficient inhibitors for corrosion of AISI 316 in 0.5 M H₂SO₄ solution. These inhibitors act as mixed type inhibitors and the IE was found to increase by increasing the inhibitor concentration.
- 2 The IE obtained from the polarization measurements show good agreement with those obtained from weigh loss experiments.



- 3 The inhibition of stainless steels in 0.5 M H₂SO₄ solution at different temperatures was found to obey the Temkin adsorption isotherm.
- 4 The thermodynamic values obtained from this study E_a , ΔG , ΔH_{ads} and ΔS indicate that the presence of the inhibitors increases the activation energy and the negative values of ΔG indicate the spontaneous adsorption of the inhibitor on the surface of AISI 316.

References

- [1] C. Carboni, P. Peyre, G. Beranger, C. Lemaitre, J. Mater. Sci, 37 (2002) 3715.
- [2] N. Subramanyan, K. Ramkrishnaiha, S.V. Iyer, V. Kapali, Corros.Sci, 18 (1978) 1083.
- [3] G. Trabanelli, Corrosion 47 (1991) 410.
- [4] S.M.A.Hosseini, A. Azimi, Materials and Corrosion, 59 (2008) 41.
- [5] S. M. A. Hosseini, M. Quanbari , M Salari, Indian Journal of Technology, 14 (2007) 376.
- [6] S.M.A.Hosseini, S.Tajbakhsh, Z.Phys.Chem, 221 (2007).
- [7] M.Abdallah, Corros.Sci.44 (2002) 717.
- [8] E.Kamis, F.Bellucci, R.M.Latanision , E.S.H.El- Ashry, Corrosion, 47 (1991) 677.



Solvent effects on protonation and complexation of glutamic acids with molybdenum(VI) in different aqueous solutions of methanol

M. Imanzadeh ^a, A. Shamel ^a, F. Gharib ^b

^aChemistry Department, I. Azad University, Ardabil Branch, Iran ^bChemistry Department, Shahid Beheshti University, Tehran, Evin, Iran.

(Email: imanzade.m@gmail.com)

Keywords: Solvent effect- Solvent polarity- Protonation Constant- Complexation Constant.

1. Introduction

Chemists are usually interested to understand solvent effects on overall solution capabilities that depend on all possible intermolecular interactions between solute and solvent molecules. The initial reports dealing with the influence of solvent in a reaction with solute molecules have been documented since nineteenth century. Solvent effects on transition metal complexes are reviewed and more attention has been paid to binary solvent mixtures in this field. Solute-solvent interactions are much more complex in mixed solvent systems than in pure solvent due to the possibility of preferential solvation by any of the solvent present in the mixtures. Moreover, the solvent-solvent interactions produced in solvent mixtures can affect the solute-solvent interactions and therefore they can also affect preferential solvations.

Purpose

The study of protonation and solvation processes of amino acids in various organic media is important to elucidate their connection between the chemical ability and biological activity.

2. Methods

The formation constants of the species formed in the systems $H^+ + Mo(VI) +$ glutamic acid and glutamic acids have been determined in different aqueous solutions of methanol (0-40 % v/v) at 25 °C, using a combination of spectrophotometric and potentiometric techniques. For each experiment two solutions of $Mo(VI) + glu$ have been prepared with the same concentration, but the ionic strength of the first was maintained with sodium perchlorate and that of the second with sodium hydroxide, both with the same mole fraction of methanol. In all solutions the total concentration of the amino acid and the metal ion were kept constant, $[MoO_4^{2-}] + [amino\ acid] = 2.0 \times 10^{-3} \text{ mol dm}^{-3}$. The first solution was then titrated with the second one. The pH was measured after addition of a few drops of the titrant, and this procedure extended up to the required pH, 5.8. The absorbance of the first solution was then measured when equilibrium was achieved. The procedure was repeated with different solutions of $Mo(VI)$ and the amino acid with varying the mole fraction of $Mo(VI)$ in the range 0-1 in constant of the total concentration of $Mo(VI)$ and each ligand in different aqueous solutions of methanol (0-40 % v/v).

3. Results and discussion

Complexation of molybdenum(VI). we determined the absorbances of solutions of $Mo(VI)$ and the amino acid with total concentration $2.0 \times 10^{-3} \text{ mol dm}^{-3}$ in the UV range (260 – 280 nm) at constant pH 5.8. The observed absorbances were corrected for unreacted $Mo(VI)$ from eq 1 and are plotted in Figure 1.

$$A_c = A_{obs} - \epsilon_{Mo}[Mo(VI)] \quad (1)$$

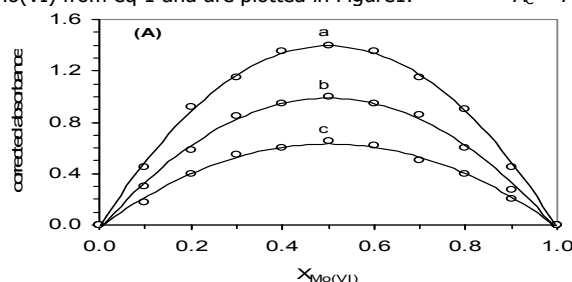


Fig. 1. Corrected absorbances of $MoO_3(glu)^2$ versus mole fraction of $Mo(VI)$ in various wave-lengths, (a) 260 nm, (b) 270 nm, (c) 280 nm.

Protonation Constant. The three protonation constants of amino acid in water-methanol mixed solvents have different behaviors. The protonation constant of the amino, K_3 , and the side chain carboxylic acid, K_2 , groups of the amino acids decreased as the solvent became enriched in the organic component, but the protonation constant of the other carboxylic acid group, K_1 , increased as methanol increased in the mixtures. The correlation between $\log K_3$ and $\log K_2$ with the reciprocal of the dielectric constant of methanol-water mixtures are linear, with correlation coefficients more than 0.99. However, there is no change in the number of charges involved in the protonation equilibria of the zwitterionic form of the amino acid, K_1 .



The solvent polarity has been introduced by Kamlet, Abboud, and Taft (KAT).¹⁻² The multiparametric equation, eq 2, has been proposed for use in so-called Linear Solvation Energy Relationship.

$$\log K = A_0 + a\alpha + b\beta + p\pi^* \quad (2)$$

Where A_0 represents the regression value, π^* is the index of the solvent dipolarity/polarizability, The α coefficient represents the solvent hydrogen-bond donor (HBD) acidity, The β coefficient is a measure of a solvent hydrogen-bond acceptor (HBA) basicity. In eq 1 the regression coefficients a , b and p measure the relative susceptibilities of the solvent-dependent of $\log K$ to the indicated solvent parameters. We used the Gauss-Newton non-linear least-squares method in the computer program to refine the $\log K$ by minimizing the error squares sum from eq 3. Single-parameter correlations of $\log K_1$, $\log K_2$ and $\log K_3$ in terms of individually with α , β or π^* did not give a good results in all cases. As a typical example, the single-parameter correlations of $\log K_1$ are shown by eq 4.

$$S = \sum (pK_{\text{exp}} - pK_{\text{cal}})^2 \quad (3)$$

$$\log K_1 (\text{glu}) = 11.23 - 7.85\alpha \quad (4a) \quad \log K_1 (\text{glu}) = -1.64 + 7.85\beta \quad (4b)$$

$$\log K_1 (\text{glu}) = 5.36 - 3.04\pi^* \quad (4c) \quad (n = 8, r^2 \cong 0.90-0.92 \text{ from eq 3})$$

So, we thought it interesting to correlate $\log K$ versus a multi-parametric equation involving α , β and π^* . However, the result presented from eq 2, multi-parametric equation, indicates significant improvement with regard to the single-parameter models.

$$\log K_1 (\text{glu}) = 0.95 + 1.26\alpha + 3.87\beta - 2.01\pi^* \quad (5a) \quad \log K_2 (\text{glu}) = 0.83 + 0.34\alpha + 0.51\beta + 2.54\pi^* \quad (5b)$$

$$\log K_3 (\text{glu}) = 4.85 + 0.65\alpha + 1.52\beta + 3.07\pi^* \quad (5c)$$

($n = 8$, $r^2 = 0.93, 0.9997, 0.9993, 0.94, 0.9988$ and 0.9998 , respectively)

The calculated values of solvatochromic parameters used for different aqueous mixtures of methanol are listed in Table 1.

Table 1. Kamlet and Taft's Solvatochromic Parameters and the Dielectric Constants of Different Methanol-Water Solvent

Mixtures.	methanol %	α (a)	β (a)	π^* (a)	ϵ_r (a)
	0.0	1.17	0.47	1.09	78.36
	10	1.15	0.49	1.04	73.79
	20	1.13	0.51	0.99	69.22
	30	1.11	0.53	0.94	64.65
	40	1.09	0.55	0.89	60.08

Complexation Constant. In this stage we again used the Gauss-Newton non-linear least-squares method in the computer program to refine the $\log K_5$ by minimizing the error squares sum from eq 2. Single-parameter correlations of $\log K_5$ in terms of individually with α , β or π^* did not give a good result. The result presented in eq 5, multi-parametric equation, indicates significant improvement with regard to the single-parameter models.

$$\log K_5 (\text{glu}) = 20.68 + 1.23\alpha + 3.46\beta - 5.70\pi^* \quad (6a) \quad (n = 8, r^2 = 0.9999 \text{ and } 0.9998, \text{ respectively})$$

The coefficients of π^* , α and β in eq 5 are in the order of $\pi^* > \beta > \alpha$.

Table 2. The Percentage Contribution of Kamlet and Taft's Parameters on the Effect of Different Media on Protonation and Complexation.

species	α	β	π^*
$\log K_1 (\text{glu})$	17.6	54.2	28.2
$\log K_2 (\text{glu})$	10.0	15.0	75.0
$\log K_3 (\text{glu})$	12.4	29.0	58.6
$\log K_5 (\text{glu})$	11.8	33.3	54.9

References:

- [1] Taft, R. W.; Abboud, J. L. M.; Kamlet, M. J. Linear Solvation Energy Relationships. 28. An Analysis of Swain's Solvent "Acidity" and "Basicity" Scales. *J. Org. Chem.* 1984, 49, 2001-2005.
- [2] Kamlet, M. J.; Abboud, J. L. M.; Abraham, M. H.; Taft, R. W. Linear Solvation Energy Relationships. 23 A Comprehensive Collection of the Solvatochromic Parameters, π^* , α , and β , and Some Methods for Simplifying the Generalized Solvatochromic Equation. *J. Org. Chem.* **1983**, 48, 2877-2887.
- [3] Gharib, F.; Zare, K.; Taghavanesh, A.; Monajjemi, M. Ionic Strength Dependence of Formation Constants, Complexation of Mo(VI) with Aspartic Acid. *J. Chem. Eng. Data* **2001**, 46, 1140-1144.



Miscellaneous





Density, dynamic viscosity, and derived properties of binary mixtures of 1,4 dioxane with 3-methyl 1-butanol at 298.15, 303.15 and 308.15 K

A.A .Rostami, A Omrani, M.Mokhtari*

Department of Physical chemistry, University of Mazandaran ,Babolsar, Iran

(Email:mokhtari_6@yahoo.com)

Keywords: Density, 3-methyl 1-butanol, Viscosity, Binary mixture ,Viscosity deviations

1. Introduction

In the chemical industry, information about the viscosity and density of liquid mixtures and their dependence with composition and temperature is very important in different applications. The thermodynamic and transport properties of liquids have been used to understand the molecular interactions between the components of the mixture . Also the nature and type of interactions in binary solvent systems are essential to understanding their behavior in different analytical applications for fetched, process engineering design applications. 1,4dioxane is reported to be valuable in polymer manufacture and as a solvent for natural resins [1-4]. 1,4dioxane is an aprotic solvent which has two lone pairs of electrons on each of these two oxygen atoms. Alcohols are the most well-known solvents used to study the hydrophobic effects [5]. In this paper, we show experimental dynamic viscosity ,density and refractive index of $\{x_1$ 3-methyl 1-butanol $+(1-x_1)$ 1,4dioxane $\}$ at $T=298.15, 303.15$ and 308.15 K.

2. Methods

Materials. High-purity 1,4 dioxane with 3-methyl 1-butanol used in this experiment were purchased from Fluka. They are used without further purification.

Apparatus and Procedure. Densities were measured using a digital vibrating glass tube densimeter (DA-500E, Japan.). The viscosity (η) of the pure components and its mixtures were also determined from the kinematic viscosities (ν) measured using a Abbelohde viscometer with automatic measuring unit (Schott-Grate, AVS 400, Germany). The uncertainty of the time measurement in the viscosimeter is ± 0.01 s.

3. Results and discussion

The measured densities (ρ) and excess molar volume (V^E) for binary system of 1,4 dioxane + 3-methyl 1-butanol at 298.15, 303.15, and 308.15 K at atmospheric pressure are given in Table 1.

The ρ values have been used to calculate the excess molar volumes (V^E) using the following equation:

$$V^E = (x_1 M_1 + x_2 M_2) / \rho_{\text{mix}} - (x_1 M_1) / \rho_1 - (x_2 M_2) / \rho_2$$

Where, x_1 , x_2 , M_1 , M_2 , and ρ_1 , ρ_2 are the mole fractions, molecular weights and densities of pure components 1 and 2, respectively, and ρ_{mix} is the density of the binary mixture. Figure 1 shows that excess molar volumes are negative for mixtures of 1,4 dioxane + 3-methyl 1-butanol at 298.15, 303.15 and 308.15K.

V^E values of the binary mixtures generally originate from chemical, physical, and structural characteristics of the liquid components. Physical effects (dispersion forces) contribute to positive deviations in V^E , whereas chemical and structural effects contribute to the negative V^E . In the present systems, positive V^E arises due to breaking of H-bonds in the self associated alkanol.

Table1. Mole fractions (x_1), densities (ρ) and excess molar volumes of 1,4 dioxane + 3-methyl 1-butanol at 298.15, 303.15 and 308.15K.

X_1	298.15 K		303.15 K		308.15 K	
	ρ (g · cm ⁻³)	V^E (cm ³ .mol ⁻¹)	ρ (g · cm ⁻³)	V^E (cm ³ .mol ⁻¹)	ρ (g · cm ⁻³)	V^E (cm ³ .mol ⁻¹)
0	1.0279	0	1.0223	0	1.0166	0
0.1000	0.9989	0.11385	0.9932	0.14281	0.9878	0.14180
0.2067	0.9696	0.24443	0.9642	0.26701	0.9590	0.27111
0.3006	0.9456	0.32210	0.9406	0.32611	0.9356	0.33305
0.4011	0.9217	0.35300	0.9169	0.35802	0.9120	0.37414
0.5011	0.8994	0.35300	0.8947	0.35721	0.8901	0.37312
0.6090	0.8769	0.29826	0.8724	0.30267	0.8679	0.32704
0.7009	0.8588	0.23923	0.8544	0.24527	0.8501	0.26213
0.8003	0.8403	0.13843	0.8360	0.14654	0.8318	0.17367
0.908	0.8211	0.03940	0.8169	0.04858	0.8129	0.06800
1	0.8050	0	0.8010	0	0.7973	0

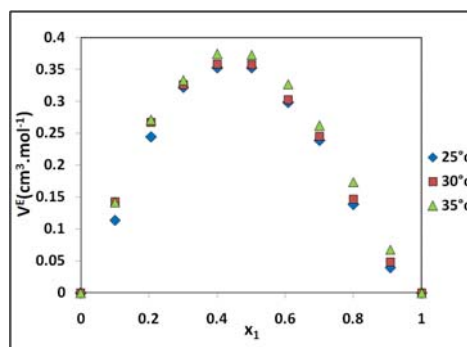


Fig. 1. Excess molar volume, V^E , for 3-methyl 1-butanol (1) + 1,4 dioxane (2) at : ♦, 298.15 K; ■, 303.15 K; ▲, 308.15 K

4. Conclusions

The physical property data for the binary mixtures of 1,4 dioxane with the studied 3-methyl 1-butanol will be useful in process engineering research, because ultimately the properties of the products derived depend upon the interactions of such liquid molecules. It is observed that the curves obtained for V^E are positive over the entire mole fraction range.

References

- [1] R. Besbes, N. Ouerfelli, H. Latrous . Journal of Molecular Liquids. 145 (2009) 1–4.
- [2] A. M. Awwad, H. M. Alsayouri, M. A. Abu-Daibes, K. A. Jbara . J. Chem. Thermodynamics. 40 (2008) 592–598.
- [3] C. Reichardt. Solvents and solvent effects in organic chemistry, 3rd ed., Wiley-VCH, Weinheim, 2003.
- [4] P. C Sadek. The HPLC solvent guide, 2nd ed., Wiley-Interscience, New York, 2002.
- [5] M. I. Aralaguppi, J. G. Baragi J. Chem. Thermodynamics. 38 (2006) 434–442.

**Application of diffusion equation in experimental neutron diffusion parameters**N.Mohammadtabar^a, R.Benvidi^b^a Iran university of Science and Technology^bNuclear Science &Technology Institute, AEOI, POBOX 11365-3486 Tehran, IRAN

(Email: tabar66@hotmail.com)

Keywords: Maxwell-Boltzman, neutron, neutron source, diffusion equation, diffusion length**1. Introduction**

Diffusion equation is a simplified version of Maxwell-Boltzmann transport equation in diffusing media. Solution of diffusion equation is an easier way of looking for neutron behavior rather than what is implied by transport equation. These equations are commonly used by chemical-physics practitioners in the field. One of the applications of diffusion equation is to measure diffusion length of neutron from an extraneous neutron source (Such Am-Be) in water. Comparison of experimental results with theoretical ones shows a good consistency and implies that diffusion Equation is quite applicable for such cases.

2. Method**Theory**

For the purpose of this experimental one needs to know neutron flux distribution, the basic tool. A neutron source with strength Q (neut./s) in an infinite medium, such as water, generates a neutron distribution as [1]

$$\phi = \frac{Q}{4\pi r D} e^{-r/L} \quad (1)$$

In which

ϕ (cm⁻².s⁻¹): neutron flux, Q (s⁻¹): neutron source intensity, r (cm): distance from the source, D (cm): diffusion coefficient, L (cm): diffusion length

In solving original diffusion equation one has assumed neutron source is a point source at least measuring points are far from source so that such an assumption is valid.

Experiment

It is instructive to see how one can find diffusion length from equation 1. In order to achieve this, one has to find neutron flux distribution by experiment. It is a refined practice to find flux using indium foils. By putting several foils at several distances, and following standard practices of neutron activation analysis [2], one can easily measure reactive flux at each.

3. Results and discussion

By employing relation [1] and using other fixed data, one can derive L easily. Table 1 shows derived value of L at each distance from the source using experimental values. Average value of L is around 3.5 cm which is not very different with 2.8 cm as its theoretical value. Diffusion length for neutron in water is a measure of distance travelled from the thermalization point up to the point of capture in medium. It is instructive to know that many processes in chemical-physics involving diffusion are similar to what is happening for neutron in a diffusion medium as they are shown down below as a thermal neutron.



Distance (cm)	1.7	2.5	4	6	7	8.5	10	11	14	16	18
Thermal neutron flow $\frac{n}{cm^2.s}$	10151	27099	36928	35493	34264	27341	22480	18892	10607	6400	4304
Diffusion length(cm)							2.2	2.4	2.9	3.0	3.2
Distance(cm)	18.5	20.5	21.5	22.5	24	27	28	29	31	32.5	34
Thermal neutron flow	3845	2654	2511	1813	1492	891	660	659	266	174	53
Distance(cm)	3.3	3.5	3.6	3.6	3.8	4.0	4.0	4.2	4.0	4.0	3.6

References

- [1] Introduction Nuclear engineering, John R .Lamarsh, Addison Wesley., 1975
 [2] Experimental reactor physics, A.Edward Profio, John Wiley, 1975

**A study of the interaction of calf thymus DNA with Co(III)-salen complex**Z. Mashhadi khoshkhoo^{a*}, M. R. Housaindokht^{a,b}, R. Jalal^{a,b}, H. Eshtiagh Hoseini^{a,b}, H. Mirtababaei^a, M. Mirzaei^a^aDepartment of Chemistry, Ferdowsi University of Mashhad, Mashhad, Iran.^bResearch and Technology Center of Biomolecules, Faculty of Science, Ferdowsi University of Mashhad, Mashhad, Iran.

(Email: Zahra.khoshkhoo@gmail.com)

Keywords: Cobalt-salen, DNA-binding, Fluorescence quenching, Binding constant.**1. Introduction**

A large percentage of chemotherapeutic anticancer drugs are compounds that interact with DNA directly or prevent the proper relaxation of DNA (through the inhibition of topoisomerases). To understand the molecular basis of drug–DNA interactions in details, various physicochemical and biochemical techniques are employed to determine the mechanism of interaction between DNA and drug agents such as spectrophotometric, circular dichroism, spectrofluorometric, melting temperature, isothermal titration calorimetry (ITC) and viscosimetric techniques. Together, these assays are powerful tools to determine the mechanism of previously discovered molecules, and will be crucial to the discovery of the next generation of DNA-binding anticancer drugs [1].

Various types of metallo-salens have been developed over the period of last two decades and their DNA binding and damaging properties have been studied in details for example [SalenAl^{III}] complex, Fe (Salen)Cl, Ni(II) or Mn(III), Cr(III), Cu(II) Salen complexes [2-5].

In this study, The interaction of schiff-base complex of novel Co^{III} complex, [Co(Hsalen)(CH₃OH)(CH₃O)]⁺CH₃COO⁻, where H₂salen denotes C₂₀H₂₆N₄O₄ with calf thymus DNA (CT-DNA) has been investigated in vitro by physicochemical methods such as fluorescence spectrometry and ultra-violet (UV) spectrometry techniques to obtain the intrinsic binding constant (*K_b*) value and to found that this complex can bind to DNA or not?

2. Methods

The cobalt complex was presented by department of chemistry of Ferdowsi University. Experiments were carried out in buffer Tris-HCl, pH 7. Solutions were prepared with distilled deionized water.

Calf thymus DNA was extracted from calf thymus. The stock solution of DNA obtained, was prepared by dissolving DNA in 10 mM Tris-HCl buffer at pH 7.5. The solution gave a ratio of ≥ 1.8 at A_{260}/A_{280} , indicating that the DNA was sufficiently free from protein. The concentration of DNA was determined by monitoring the UV absorbance at 260 nm using $\epsilon_{260} = 6667 \text{ cm}^{-1}$. The stock solution was stored at -20°C.

Absorbance spectra were recorded using a Shimadzu UV-2550 double beam spectrophotometer. The absorbance measurements were performed by keeping the concentration of the complex constant (20 μM) while varying the DNA concentrations from 0.5 μM to 75 μM . The absorbance at 223, 241 and 259 nm was recorded after each addition of DNA.

Fluorescence measurements were made using Shimadzu-RF-1501 spectrofluorophotometer. The concentration of the cobalt complex was fixed (5 μM) while varying concentration of the CT-DNA (4 μM to 123 μM). The cobalt (III) complex in the presence of DNA was excited at 315 nm and the fluorescence spectra were recorded between 350 and 550 nm. The Stern-Volmer quenching constant (*K_{C_{DNA}}*) was calculated with the help of the Stern-Volmer equation.

3. Results and discussion**3.1. Electronic spectra**

The UV absorption spectra of Co-salen with and without the addition of calf thymus DNA are shown in Fig.1. An increase in the intensity (hyperchromism) with a red shift were observed with the addition of (0.5 μM to 75 μM) DNA. If the salen-co interact with DNA, leading to spectral changes. Absorption titrations were carried out by keeping the concentration of the salen-co constant while adding a solution of the CT-DNA in increasing amounts in both cuvettes until the saturations in hyperchromism were observed. The saturation in hyperchromism is quantitatively shown by plotting the A/A_0 vs [DNA], where *A*₀ and *A* are the absorption intensities of the Co-complex in the absence and presence of increased concentrations of DNA, respectively (Fig. 2).

The intrinsic binding constant *K_b* was determined for cobalt complex according to Eq. 1 [6].

$$[\text{DNA}] / (\epsilon_b - \epsilon_f) = [\text{DNA}] / (\epsilon_b - \epsilon_f) + 1/K_b (\epsilon_b - \epsilon_f) \quad (1)$$

where [DNA] is the concentration of DNA in base pairs, $\epsilon_a = A_{obsd}/[\text{compound}]$, ϵ_f = the extinction coefficient for the free compound and ϵ_b = the extinction coefficient for the compound in the fully bound form, respectively.

A plot of $[DNA]/(\epsilon_a - \epsilon_f)$ vs. [DNA] gives K_b as the ratio of the slope to intercept.

The binding constant, K_b , for the cobalt-complex has been estimated to be $0.5 \pm 0.25 \times 10^6 \text{ M}^{-1}$ by the half-reciprocal plot method (Fig. 3).

3.2. Emission spectra

The addition of CT-DNA to Salen-Co solution resulted in a fluorescence quenching. K_{DNA} quenching of CT-DNA molecule was calculated as being $0.9 \times 10^3 \text{ M}^{-1}$ according to Eq. 2.

$$F_0/F = 1 + K_{\text{DNA}} [\text{DNA}] \quad (2)$$

Where F_0 and F refer to the fluorescence intensities in both the absence and presence of CT-DNA, K_{DNA} is the Stern-Volmer quenching constant and [DNA] is the concentration of CT-DNA in mol L^{-1} .

A plot of $(F_0/F) - 1$ vs. [DNA] indicated the K_{DNA} values that it was estimated from this linear plot (Fig. 4).

4. Conclusions

In this study, we unravel the DNA interaction of Co-salen complex. The binding behavior of complex with DNA was characterized by absorption titration and fluorescence. The DNA-binding constant in connection with other experimental observations show that Co-salen can bind to CT-DNA avidly and this complex may be effect the biological activity of CT-DNA.

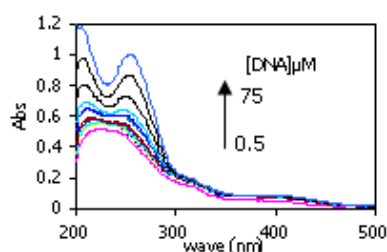


Fig 1: The UV absorption spectra of Co-salen 20 μM with and without the addition of calf thymus DNA from 0.5-75 μM

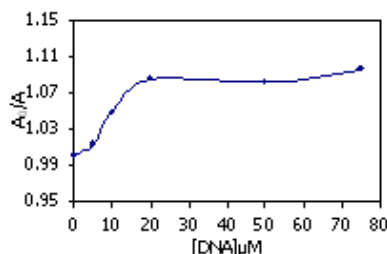


Fig 2: Abs titration of the Co-complex 20 μM in the absence and presence of increased concentrations of calf thymus DNA from 0.5-75 μM

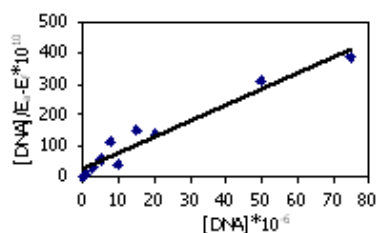


Fig 3: Half-reciprocal plot for binding of Co-complex 20 μM with CT-DNA from 0.5-75 μM

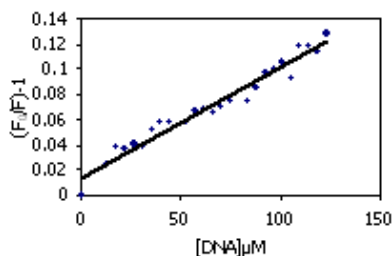


Fig 4: Stern-volmer plot for binding of Co-complex 5 μM with calf thymus DNA from 4-123 μM

References

- [1] R. Palchaudhuri, and P.J. Hergenrother, *Curr Opin Biotechnol* 18 (2007) 497.
- [2] V.G. Vaidyanathan, T. Weyhermuller, B. Unni Nair, and J. Subramanian, *J. Inorg. Biochem.* 99 (2005) 2248.
- [3] A. Rajendran, C. J. Magesh, and P.T. Perumal, *BBA* 1780 (2008) 282.
- [4] A. Silvestri, G. Barone, G. Ruisi, M. Teresa Lo Giudice, and S. Tumminello, *J. Inorg. Biochem.* 98 (2004) 589.
- [5] S.S. Mandal, U. Varshney and S. Bhattacharya, *Bioconjugate Chem.* 8 (1997) 798.
- [6] A.M. Pyle, J. P. Rehmann, R. Meshoyrer, C.V. Kumar, N.J. Turro, and J.K. Barton, *J. Am. Chem. Soc.* 111 (1989) 3051.

Improved IMS Performance using an Inversed Mode of Operation for the Shutter Grid

M. Tabrizchi*, E. Jazan

Department of Chemistry, Isfahan University of Technology, Isfahan 84156-83111, Iran

(Email: m-tabriz@cc.iut.ac.ir)

Keywords: Ion mobility spectrometry, Resolution, Resolving power

1. Introduction

In ion mobility spectrometry (IMS), is a powerful tool for the study of molecular conformations, the separation of mass isomers, and the analysis of complex mixtures [1,2]. IMS is similar to TOF mass spectrometry, except that it operates under atmospheric pressure. More specifically, the sample is ionized and then the ions move in an inert gas under a constant electric field. Although ions are continuously generated, the ion beam is chopped by a shutter grid to create an ion packet. To generate an ion pulse, the grid potential is removed for a short period of time by a pulse generator. The penetrating ion pulse moves in the drift region, where ions are separated according to their individual velocities, which depend on their size. A full description of the method is given in several books and review articles [1-4].

As for other separation techniques, the ability of IMS instrument to resolve two closely spaced peaks is of considerable interest. Many attempts have been made to enhance the resolution of IMS. In this work, we describe a completely different approach and a novel solution to enhance the resolution of IMS. The method simply uses an inverse pulse applied to the shutter grid to create a dip in the ion beam rather than creating an ion packet.

2. Methods

The ion mobility spectrometer used in this study was constructed in our laboratory. A continuous corona discharge ionization source was used with a point-to-plane geometry. A Bradbury-Nielsen type gate [6] was mounted between the ionization region and the drift tube. The gate consisted of two sets of parallel wires mounted on a ceramic frame in a plane perpendicular to the moving direction of ions. When an adequate potential was applied to the wires, the electric field created between the wires could stop penetration of ions; hence, the gate was closed. Conversely, removing the potential opened the gate. In the normal operation, the gate was mostly closed, and it was open only for a short period of time. Figure 1a shows the shape of the applied pulse to the gate for normal operation, as well as the peak shape resulting from such a pulse. In this case, the shutter grid allows a swarm of ions to diffuse into the drift region, forming an ion packet. However, if the applied electric pulse is inversed, as shown in Fig.1b, the shutter grid is always open except for a short time. Unlike the case of normal operation, this situation creates a dip in the ion beam.

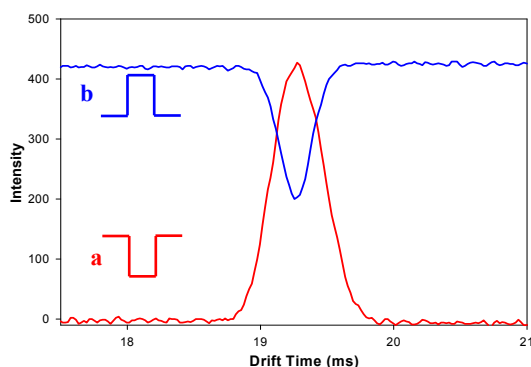


Fig. 1. The ion mobility signal for acetophenone recorded in **a)** Normal operation and **b)** Inverse operation. The applied pulse to the shutter grid is shown for each case

3. Results and discussion

As seen in Fig. 1, the depth and width of the dip are reduced in comparison with the peak. The resolution, based on a single-peak definition ($t/\Delta t$), is increased from 44 to 72, i.e., 63%. The improvement of resolution could be partially due to the lower intensity of the inverse peak. In order to more accurately investigate the change in resolution, the lower intensity of the inverse peak was compensated for by widening the pulse width to obtain the same intensity as the normal one. The dip was then inverted and plotted, along with the peak, in Fig. 2. Both signals were normalized to unity to adjust for the small differences in their intensity. Clearly, the inverse peak is narrower than the normal peak. In this case, the resolving power shows an increase of about 37%. The experiment was repeated for several compounds. In all cases, the resolving power was enhanced considerably. For the cases of the reactant ion (RI) and the increase was as high as 60%. Figure 2 demonstrate that by inverting the shutter grid pulse, it is possible to gain resolution without decreasing the intensity.

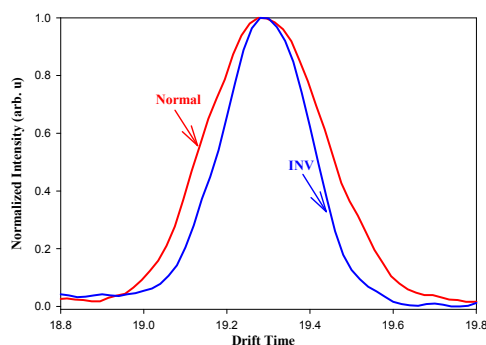


Fig. 2. Increase in resolution due to application of an inversed pulse to the shutter grid for acetophenone.

4. Conclusions

This invention shows that applying an inversed pulse to the shutter grid enhances the separation power of IMS. This is a simple but very effective way of increasing resolution. This method may be applied to other similar pulsed techniques such as time-of-flight mass spectrometry.

References

- [1] Eiceman, G.A. Karpas, Z. Ion Mobility Spectrometry, 2nd ed., CRC Press: Boca Raton, 2005.
- [2] Laiko V.V. J. Am. Soc. Mass Spectrom. 17 (2006) 500.
- [3] Eiceman G.A. Crit. Rev. Anal. Chem. 22 (1991) 17.
- [4] Louis R.H.St. Hill H.H. Crit. Rev. Anal. Chem. 21 (1990) 321.
- [5] Reategui J.A. Spangler G.E. Mangum J.L., US Patent 4,950,893 Aug. 21,1990.
- [6] Bradbury N.E. Nielsen R.A. Phys. Rev. 49 (1936) 388.



Solvatochromic probe absorbance behavior in mixture of 2-hydroxy ethylammonium formate with methanol, ethylene glycol and glycerol

Hadi Salari, Ali Reza Harifi-Mood, Mohammad Reza Gholami

Department of Chemistry, Sharif University of Technology, Azadi Ave, Tehran, Iran

(Email: salari@mehr.sharif.ir)

Keywords: Ionic liquids, Solvatochromic parameters, 2-Hydroxy ethylammonium formate, Solute-solvent interactions;

1. Introduction

During the last decade ionic liquids (ILs) have gathered widespread interest and curiosity as potential environmentally friendly solvents from both the scientific and engineering community^{1,2}. To increase the efficiency of a process (e.g., separation, extraction, synthesis, etc.), one would like to "tune" a solvent or solvent mixture by addition of cosolvents³. In continuing our studies on ILs, in present work, the four solvatochromic parameters (i.e., E_T^N , normalized solvent polarity parameter; n^* , dipolarity/polarizability; β , hydrogen-bond acceptor basicity; α , hydrogen-bond donor acidity) have been determined for binary mixtures of methanol, ethylene glycol and glycerol with 2-hydroxy ethyl ammonium formate at 25°C over the whole range of mole fractions.

2. Method

The ionic liquid (2-hydroxy ethylammonium formate) was prepared by adding drop wise of formic acid to 2-amino ethanol. The IL was characterized as described in literature⁴. An ethanolic solution of the indicators were prepared and stored in a dark glass vial at 4°C. An appropriate aliquot of the solvatochromic probe primary solution was transferred into 1 cm quartz cuvette, and its solution was evaporated by vacuum. The mixture of IL with molecular solvents (methanol, ethylene glycol, glycerol) at different compositions was gravimetrically prepared (± 0.1 mg) for each binary solvent mixture separately and was transferred into the quartz cuvette. The solution was vigorously stirred with a magnetic stirrer, so that a steady-state solution was prepared. Final probe concentrations were $0.5-1 \times 10^{-4}$ mol dm⁻³. UV-Vis absorption spectra of the solutions were recorded.

3. Results and discussion

When small quantities of the IL are added to methanol, the E_T^N parameter increases sharply which is then smoothly enhanced to the value of pure IL. The response patterns show that the influence of the IL is strong at the lowest IL concentration in all mixtures. These results can be related to the preferential solvation of the solutes by the IL through cation. Addition of IL to methanol causes a smooth variation with a S type curve in n^* parameter. These variations in ethylene glycol-IL mixtures are insignificant. It is demonstrated that α values exhibit positive deviation from the ideal behavior in methanol and ethylene glycol-IL mixtures. In addition, a negative deviation in glycerol-IL mixtures is observed. The α parameter trend in glycerol-IL system shows a maximum negative deviation at $X_{IL}=0.3$. There is no distinct difference between the β parameters and α parameters trend. Similar to the HBD trend, when IL is added to methanol or ethylene glycol, the β value increases smoothly. However, by addition of IL to glycerol hydrogen bond acceptor (HBA) basicity decreases sharply to zero at $X_{IL}=0.3$. The solvatochromic parameters (SP) in a binary solvent mixture at a constant temperature can be expressed as in eq (1)

$$SP_m = x_1 SP_1^0 + x_2 SP_2^0 + x_1 x_2 \sum_{j=0}^k A_j (x_1 - x_2)^j \quad (1)$$

where SP_m , SP_1^0 and SP_2^0 are solvatochromic parameters determined in the mixed and pure solvents 1 and 2, respectively. A cross-validation method has been applied to predict any of the parameters. This method is a practical and reliable way to test the predictive significance when little data are available. In Figure 1, the predicted values of SP (E_T^N , n^* , α and β) obtained by the cross-validation method for various binary solvent mixtures have been plotted versus the corresponding experimental. The model shows a good correlation between predicted and experimentally measured values, also no proportional and systematic errors were observed. Therefore, the CNIBS/R-K model is a reasonable one with high confidence for prediction of the solvatochromic parameters in binary solvent mixtures of IL with methanol, ethylene glycol and glycerol.

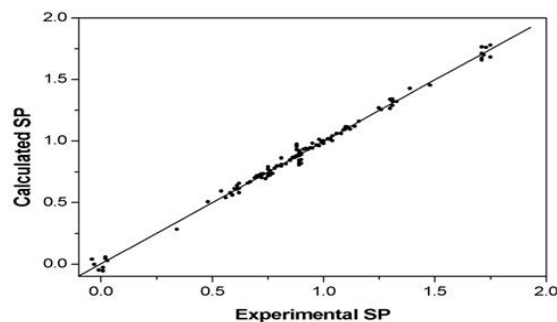


Fig. 1. Predicted values of solvatochromic parameters.

4. Conclusions

The solvatochromic parameters have been determined in binary mixtures of 2-hydroxy ethylammonium formate as an IL with methanol, ethylene glycol and glycerol. This investigation reveals the effect of OH groups in molecular solvents and its influence on solvent-solvent interactions. All studied system show basically similar E_{HBD} response patterns. E_{HBD} increases abruptly to the value of pure IL by increasing IL mole fraction. Slower trend in glycerol-IL mixtures is attributed to increasing dipolarity/polarizability and synchronously decreasing HBD acidity of the media when the IL is added to the glycerol. The n^* , α and the β values show no distinct deviation from the ideal additive behavior. However, positive deviation in methanol-IL system confirms that the mixtures of these solvents are better HBD and HBA than the neat solvents. On the other hand, intermolecular hydrogen bonds cause that HBD and HBA are abruptly decreased in mixture of glycerol and IL so that the β value is zero at many mole fractions of mixtures.

It was proved that the combined nearly ideal binary solvent/Redlich-Kister(CNIBS/R-K) equation can be used with confidence to achieve a correlation between the variation of the solvatochromic parameters and solvent composition, and this equation is able to predict the solvatochromic parameters.

References

- [1] Welton, T. Chem. Rev. 1999, 99, 2071
- [2] Wasserscheid, P.; Keim, W. Angew. Chem., Int. Ed. 2000, 39, 3772.
- [3] Sheldon, R. J. Chem. Soc., Chem. Commun. 2001, 2399.
- [4] Bicak, N. J. Mol. Liq. 2005, 116, 15.

The van der waals interaction between torus-shaped and spherical nanoparticles

M. Moradi, M. Ebrahimzadeh, M. Noormohammadi

Department of Physics, University of Shiraz , Fars, Iran

(Email: Moradi@susc.ac.ir)

Keywords: Van der waals interaction; Colloidal nanoparticle, Torus shape,

1. Introduction

Many practical applications in colloid science come down to the problem of controlling the force between colloidal nanoparticles. For this reason calculating the force between nanoparticles in colloid and any systems containing nanoparticles are important. We are interested in calculating the van der waals interaction, because these interaction have shown their tendency to form persistent aggregates. The concept of a general attractive interaction between neutral atoms was first proposed by Lewis Waals in 1873 to study the interactions of nonideal gases and liquids. Thus, de Boer [1] and Hamaker [2] assumed the intermolecular forces to be strictly pair wise additive. In colloid science and in the systems containing nanoparticles, various shape of particles are exist. Many calculation are done to obtain the van der waals forces between nanoparticles and we discuss them later. As we know, the nanoparticles are large in comparing with the atoms. In general, there exist both repulsive and attractive forces between the atoms, but in our calculation, to obtain the force between nanoparticles, we need to enter only long range attractive forces as discussed in pervious articles [3-5]. We use the van der waals interaction for attractive potential energy and the interaction between atoms is $U_{vdw} = -C/r^6$, where C is the coefficient in the atom-atom pair potential and r is the distance between the two atoms. The interaction energy between two particles may be calculated approximately by summation (or integration) of the interaction energies for all molecular pairs. The van der Waals interaction energy have been derived for particles of various shapes, such as plates, spheres and cylinders [4-6]. The purpose of the present paper is to derive the interaction energy between two torus-shaped and spherical nanoparticles. Torus-shaped particles can serve as a model for biocolloids such as biconcave human red blood cells. The interaction between biconcave red blood cells and spherical lipid nanoparities can be approximated by the interaction between torus-shaped and spherical nanoparticles [7]. Here we start with the van der Waals interaction between parallel ring and disk, then calculate the interaction energy between torus-shaped and spherical nanoparticles.

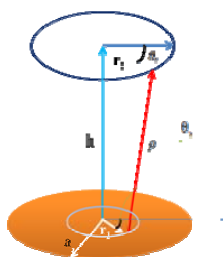


Fig.1. Schematic diagram of parallel ring and disk

2. Methods

The interaction energy between parallel ring and disk

We assume the disk and ring are parallel together with radii a and r_2 , respectively, separated by a distance h and the disk is divided to a large number of rings with the radius of r_1 (Fig.1). All rings are contained the same substance where N_1 is the surface number density of disk and N_2 is the line density of atoms on rings. The distance ρ between a molecule in the above ring and one in the bottom ring within disk is given by:

$$\rho = \sqrt{(r_1 \sin \theta_1 - r_2 \sin \theta_2)^2 + (r_1 \cos \theta_1 - r_2 \cos \theta_2)^2 + h^2} \quad (2)$$

$$\rho = \sqrt{r_1^2 + r_2^2 - 2 r_1 r_2 \cos(\theta_1 - \theta_2) + h^2} \quad (3)$$

Where θ_1 and θ_2 are defined in Fig.1. The van der waals interaction energy between the disk and ring, is written as:

$$u(r_2, a, h) = \int_{\theta_1=0}^a \int_{\theta_2=0}^{2\pi} \frac{CN_1 N_2 r_1 r_2 d\theta_2 d\theta_1 dr_1}{(r_1^2 + r_2^2 - 2r_1 r_2 \cos(\theta_1 - \theta_2) + h^2)^3} \Rightarrow u(r_2, a, h) = -\frac{1}{2h^4 y} \left(CN_1 N_2 r_2^2 \pi^2 (-3r_2^2(a^4 + h^4) + a^6 - r_2^6 + (h^4 - 3r_2^4)(a^2 - h^2) + \text{csign}(r_2^2 + h^2)y) \right) \quad (4)$$

where $y = [a^2 + (a + r_2)^2]^{3/2} [a^2 + (a - r_2)^2]^{3/2}$, Eq.(4) is the van der waals interaction between parallel ring and disk.

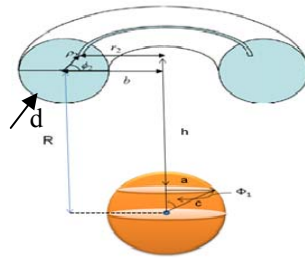


Fig. 2. Schematic diagram of the sphere and torus

The interaction energy between torus-shaped and spherical nanoparticles

In previous section, we obtain the interaction energy between ring and disk containing a large number of atoms. As it is shown in Fig. 2. Each torus, can be divided into a large number of rings and each sphere can be divided into a large number of disk. Therefore we consider the torus-shaped and spherical nanoparticles, where their center separation is assumed to be R . (Fig. 2). The interaction energy, $U(R, c, d)$, between the torus and sphere can be calculated by integrating over Eq. (4). Here we replace the surface density N_1 and the line density N_2 by the volume density ρ . The main point in this step is choosing the limit of integrals properly. Thus

$$U(R, c, d) = CN^2 \int_{\phi_1=0}^{\pi} \int_{\phi_2=0}^{2\pi} \int_{\rho_2=0}^d u(r_2, h, a) c \cos \phi_1 \rho_2 d\rho_2 d\phi_2 d\phi_1 \quad (5)$$

In this integral r_2 , h and a are defined as

$$r_2 = b - \rho_2 \cos \phi_2 \quad (6)$$

$$h = R + \rho_2 \sin \phi_2 - c \cos \phi_1 \quad (7)$$

$$a = c \sin \phi_1. \quad (8)$$

The angles ϕ_1 and ϕ_2 are shown in the figure. This integral can be evaluated numerically.

3. Conclusions

We derived an expression for the van der waals interaction energy between torus-shaped and spherical colloidal particles, Eq. (5) using the interaction between two parallel ring and disk. If we choose the required parameters in the equation properly we could calculate the integral. Fortunately this integral can be evaluated for various size of particles.

References

- [1] J. Israelachvili, Intermolecular & Surface Forces, Academic Press, London 1991.
- [2] H. C. Hamaker, Physica 4 (1937) 1058.
- [3] E.M. Lifshitz, Soviet Phys. JETP 2 (1956) 73
- [4] Langbein, Theory of van der Waals Attraction, Springer, Berlin, 1974.
- [5] L. Mahanty and B. W. Ninham, Dispersion Forces Academic Press, London 1976.
- [6] J. Lyklema, Fundamentals of Interface and Colloid Science, vol. IV, Elsevier Academic Press, London, Chapter 3, 2005.
- [7] Hiroyuki Ohshima, Atsushi Hyono, Journal of Colloid and Interface Science 332 (2009) 251–253

Development a dual-mode non-thermal plasma (NTP) ionization source for gas phase reactions study using ambient mass spectrometry

M. Almassian^{a*}, R. Zhang^b

^a Nuclear Science and Technology Research Center, Tehran, Iran

^b Key Laboratory for Nanosciences, Beijing, China

(Email: mohralmasi@gmail.com)

Keywords : Non-Thermal Plasma, plasma catalysis, Dielectric Barrier Discharge, Mass Spectrometry.

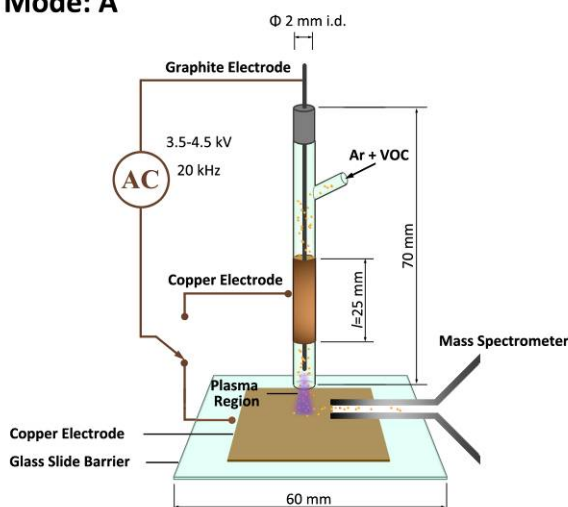
1. Introduction

Non-thermal plasma (NTP) has a long history and has been applied in various areas such as, surface modification [1], pollution control [2], polymers and nanomaterials [3], fuel-cell technology [4], biology and medicine [5]. Extensive research activities aimed at a better understanding of the physical and chemical processes inside a NTP. The development of the NTP devices is an interesting research subject for innovating new methods in order to understand plasma characterizations. The NTP can be produced by the different electrical discharge methods.

2. Methods

we have developed a new NTP device based on dielectric barrier discharge (DBD) [6], which is applicable in two modes. Figure 1 shows the schematic of the applied NTP in the two modes. Argon gas is used as plasma producer, and sample carrier gas. The presented NTP is coupled with a LTQ mass spectrometer, as detector, in ambient conditions. Using the current NTP device, coupled to the mass spectrometer, the gas phase reactions for the toluene, ethyl benzene, ethyl acetate, butyl acetate, methyl isobutyl ketone, pyridine and acetic acid, as representatives of the various classes of the volatile organic compounds (VOCs), were studied.

Mode: A



Mode: B

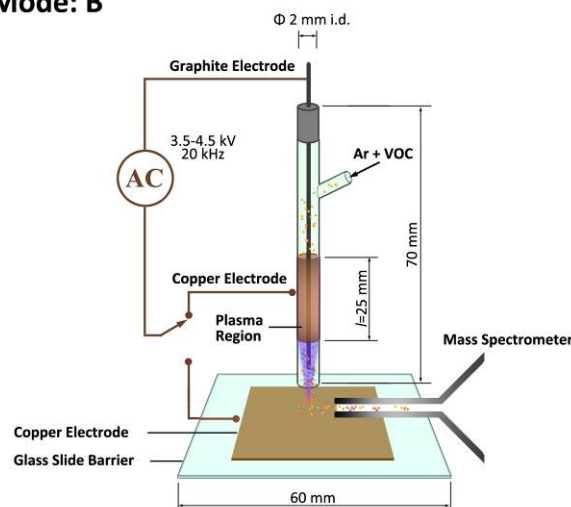


Fig. 1. Schematic of dual-mode NTPMS, and the plasma region position in Mode A and Mode B.



3. Results and discussion

Toluene and ethyl benzene were dihydrogenated on the surface of dielectric barrier. Moreover, most of the resulting mass spectrum has shown the (58+14n) ion series which produced by the radical chain reactions in Mode B. The effect of different parameters, like the plasma gas flow rate, the electrode length, the electrode material and the solvent effect on the spectrum were investigated. Based on the resulting spectrum we found that, inside the NTP, there are several reactions in competition which the final products depend on it. An assumed mechanism for the production of the ion series is proposed.

4. Conclusions

Due to the plasma catalysis concept, many reactions can facilitate the chain reactions in the NTP. Dihydrogenation of the aromatic molecules can progress easily, on the dielectric barrier surface as a surface catalyzed reaction. The developed plasma source can be used to investigate about the catalytic effect of plasma on gas phase reactions and surface catalyzed reactions in the NTP. Based on the results of the current study, application of NTP for polymerization and plasma catalysis of exothermic and endothermic reactions are interesting subjects for future research.

References :

- [1] A. Fridman, Plasma Chemistry 1st ed. Cambridge University Press; New York, 2008.
- [2] J. V. Durme, J. Dewulf, C. Leys, H. V. Langenhove, Applied Catalysis B: Environmental 78 (2008) 324.
- [3] T. Nozaki, K. Okazaki, Plasma Process. Polym. 5 (2008) 300.
- [4] Istadi, N. A. S. Amin, Fuel 85 (2006) 577.
- [5] M. G. Kong, G. Kroesen, G. Morfill, T. Nosenko, T. Shimizu, J. v. Dijk, J. L. Zimmermann, New Journal of Physics 11 (2009) 115012.
- [6] U. Kogelschatz, Plasma Chem. Plasma Process. 23 (2003) 1.



Study on a zinc-manganese fischer-tropsch synthesis catalyst prepared from $[\text{Zn}(\text{H}_2\text{O})_6]_2[\text{Mn}(\text{NCS})_6]/\text{Al}_2\text{O}_3$ precursor

M. Behzad Khoshgouei*, A. R. Rezvani and A. R. Salehi Rad

Chemistry Department, University of Sistan & Baluchestan, Zahedan, Iran, P. O. Box 98135-674

(Email:m.behzad63@gmail.com)

Keywords: Fischer-Tropsch synthesis, precursor, catalyst, complex

1. Introduction

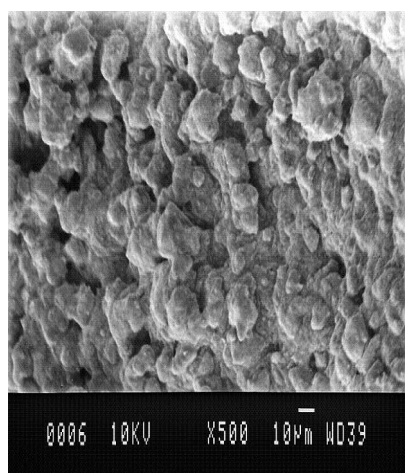
Fischer-Tropsch synthesis (FTS) is one of the attractive methods for the production of hydrocarbons. Also, the conventional sources for the production of synthesis gas (i.e., syngas) are the steam reforming of natural gas and naphtha [1]. Research and development of a high performance catalyst is one of the key technologies for FTS [2]. Generally, catalyst for the FTS consist of metals such as manganese, nickel, cobalt, iron and ruthenium impregnated on supports ranging from metal oxides to zeolites [3,4].

2. Methods

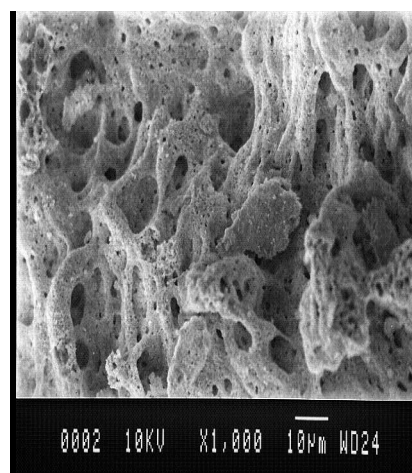
In this study, catalyst has prepared from precursor of $[\text{Zn}(\text{H}_2\text{O})_6]_2[\text{Mn}(\text{NCS})_6]$ supported on the alumina. $[\text{Zn}(\text{H}_2\text{O})_6]_2[\text{Mn}(\text{NCS})_6]/\text{Al}_2\text{O}_3$ was calcined at 773 K for 5 h. $[\text{Zn}(\text{H}_2\text{O})_6]_2[\text{Mn}(\text{NCS})_6]$ complex has been characterized by elemental analysis, XRD, FT-IR, UV-vis spectroscopy. Characterization of both precursor and calcined catalyst were carried out using FT-TR, XRD, SEM, BET specific surface area and thermal analysis methods (TGA and DSC). The activity and selectivity of prepared catalyst has been studied under atmospheric pressure in a range of reactor temperatures using synthesis gas with different H_2/CO molar feed ratios.

3. Results and discussion

The FT-IR spectrum of the $[\text{Zn}(\text{H}_2\text{O})_6]_2[\text{Mn}(\text{NCS})_6]$ complex shows two sets of vibrations due to the aqua and isothiocyanate ligands. In the FT-IR spectrum, the C=S stretching mode of free SCN^- is shifted to higher frequency in the corresponding complex which is consistent with nitrogen bonding to the manganese. The phase analysis of precursor and calcined catalyst were done by XRD technique. The XRD patterns of both precursor and calcined catalyst showed crystalline phases. Characterization of both precursor and calcined catalyst was also carried out using scanning electron microscopy (SEM). All the electron micrographs were obtained from powder specimens of these materials. SEM observations (Fig. 1) have shown differences in morphology of both precursor and calcined catalyst.



(a)



(b)

Fig. 1. SEM micrographs of the $[\text{Zn}(\text{H}_2\text{O})_6]_2[\text{Mn}(\text{NCS})_6]/\text{Al}_2\text{O}_3$ precursor (a) and the calcined catalyst (b)



The BET specific surface area measurements for both precursor and calcined catalyst were carried out and calcined catalyst showed a higher surface area than its precursor. This is in agreement with SEM results, which showed that the agglomerate size of the calcined catalyst is less than its precursor and therefore, leads to an increase in the BET specific surface area of the calcined sample.

The calcined catalyst was also characterized by FT-IR and due to thermal decomposition of isothiocyanate ligands, no vibration bands for C=S and C≡N stretching are seen. In order to consider the stability of prepared catalyst using a novel method, it was tested for 72 h at 450 °C using synthesis gas with molar ratio of H₂/CO=4/1. The obtained results indicate that this catalyst was highly stable and had retained its activity and selectivity for 72 h.

4. Conclusions

We have prepared alumina-supported Zinc-Manganese catalyst from [Zn(H₂O)₆]₂[Mn(NCS)₆]/Al₂O₃ precursor for the Fischer-Tropsch synthesis. This preparation procedure is a novel suitable method to produce higher active catalysts for the Fischer-Tropsch synthesis. During the calcination operation, the morphological features of calcined catalyst are quite different with the [Zn(H₂O)₆]₂[Mn(NCS)₆]/Al₂O₃. The Zinc-Manganese catalyst was studied for the conversion of synthesis gas to light olefins. The catalyst exhibited appreciable hydrogenation of CO activity. This catalyst was also highly stable and had retained its activity and selectivity for 72 h. The reaction conditions were found to be 450 °C with molar feed ratio of H₂/CO=4/1 (GHSV=5400 h⁻¹).

References

- [1] J.R. Rostrup-Nielsen, Catal. Rev. 46 (2004) 247.
- [2] Y. Yang, H. Xiang, R. Zhang, B. Zhong, Y. Li, Catal. Today 106 (2005) 170.
- [3] A.A. Adesina, Appl. Catal. A 138 (1996) 345.
- [4] L. Bruce, J.F. Mathews, Appl. Catal. 4 (1982) 353.

**CO hydrogenation to light olefins over K-Mn/Al₂O₃ catalyst**

A. R. Rezvani*, M. Behzad Khoshgouei, A. R. Salehi Rad

Chemistry Department, University of Sistan & Baluchestan, Zahedan, Iran, P. O. Box 98135-674

(Email:rezvani2001ir@yahoo.ca)

Keywords: precursor, K₄[Mn(NCS)₆] complex, CO hydrogenation, catalyst**1. Introduction**

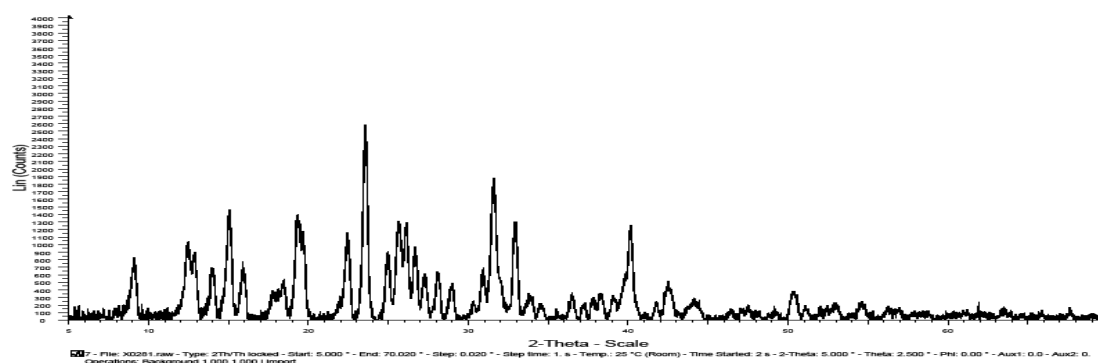
In the Fischer-Tropsch synthesis process, the conversion of syngas (CO+H₂) over a catalyst is one of the most pivotal steps. Consequently, choosing a suitable catalyst is very important [1,2]. Generally, catalyst for the FTS consist of metals such as manganese, nickel, cobalt, iron and ruthenium impregnated on supports ranging from metal oxides to zeolites [3,4].

2. Methods

K-Mn/Al₂O₃ catalyst was prepared by a novel method and studied for the conversion of synthesis gas to light olefins by Fischer-Tropsch synthesis. The catalyst was prepared from K₄[Mn(NCS)₆]/Al₂O₃ precursor. K₄[Mn(NCS)₆] was supported on the alumina and calcined at 500 °C. K₄[Mn(NCS)₆] complex was characterized by elemental analysis, FT-IR, UV-vis and XRD spectroscopy and cyclic voltammetry. The electrochemistry of this complex was investigated in DMF by cyclic voltammetry and differential pulse polarography. Characterization of both precursor and calcined catalyst were carried out using FT-IR, X-ray diffraction, thermal analysis method such as TGA and DSC, scanning electron microscopy (SEM) and BET specific surface area. The activity of prepared catalyst was studied in a fixed bed micro reactor in a range of reactor temperatures using synthesis gas with different H₂/CO molar feed ratios and different operating pressure condition.

3. Results and discussion

The elemental analysis of the K₄[Mn(NCS)₆] complex is entirely consistent with its formulation as is the following spectroscopic characterization. In the FT-IR spectrum, the C=S stretching mode of free SCN⁻ at 749 cm⁻¹ is shifted to 875 cm⁻¹ which in the corresponding complex of K₄[Mn(NCS)₆] which is consistent with nitrogen bonding to the manganese. The C≡N stretching mode of free SCN⁻ was shifted to lower frequency in the corresponding complex. The XRD pattern for the K₄[Mn(NCS)₆] complex is shown in Fig.1.

**Fig. 1.** Powder X-ray diffraction pattern for the K₄[Mn(NCS)₆] complex

The phase analysis of precursor and calcined catalyst were done by XRD technique. The XRD patterns of both precursor and calcined catalyst showed crystalline phases. The morphological features of calcined catalyst are quite different with the precursor and show that the agglomerate size is greatly reduced in compared to the precursor sample described above. Characterization of K₄[Mn(NCS)₆]/Al₂O₃ precursor using TGA, generally have shown a three-stage decomposition. The first weight loss peak low-temperatures is associated to the removal of the physically adsorbed water from the precursor; the second weight loss is due to the decomposition of Mn-N and C=S bonds and the third weight loss peak at high-temperatures may be attributed to the decomposition of C≡N bond. The DSC pattern of the catalyst precursor, exhibited a peak at low-



temperatures attributed to the removal of the physical adsorbed water and two endothermic peaks at mid-temperatures that are due to the various endothermic transition. The peaks at mid-temperatures may be attributed to the decomposition of Mn–N, C=S and C≡N bonds which were accompanied by different weight losses with changes only in rate of weight loss. The calcined catalyst was also characterized by FT-IR and due to thermal decomposition of isothiocyanate ligands, no vibration bands for C=S and C≡N stretching are seen. In order to study the stability of prepared catalyst, it was tested for 72 h at 450 °C using synthesis gas with molar ratio of CO/H₂=0.25.

4. Conclusions

We have reported a novel method to preparation of K-Mn/Al₂O₃ catalyst for the Fischer-Tropsch synthesis. The prepared catalyst was studied for conversion of synthesis gas to ethylene and propylene at 450 °C with molar feed ratio of CO/H₂=0.25. This catalyst showed high activity for the hydrogenation of carbon monoxide. Combining the results of the FT-IR spectra, TGA/DSC curves, classical identification method, and XRD patterns for K₄[Mn(NCS)₆] complex, precursor, and calcined catalyst showed that the complex decomposed to form an oxide of Mn as the solid product and a mixture of sulfur dioxide, carbon dioxide and nitrogen oxides as gaseous products.

References

- [1] G.P. Van der Laan, A.A.C.M. Beenackers, *Catal. Rev. Sci. Eng.* 41 (1999) 255.
- [2] S. Li, G.D. Meitzner, E. Iglesia, *J. Phys. Chem. B* 105 (2001) 5743.
- [3] A.A. Adesina, *Appl. Catal. A* 138 (1996) 345.
- [4] L. Bruce, J.F. Mathews, *Appl. Catal.* 4 (1982) 353.

**Magnetic field effect in thermodynamic studies on binding of amlodipine to HSA:****A spectroscopic approach**Z. Rouhbakhsh Zaeri^a *, M. R. Housaindokht^{a,b}, J. Chamani^c, M. Bahrololoom^a^aDepartment of chemistry, Faculty of Sciences, Ferdowsi University of Mashhad, Mashhad, Iran^bThe Research Institute of Biotechnology, Ferdowsi University of Mashhad, Mashhad, Iran^cDepartment of Biology, Faculty of science, Islamic Azad university-Mashhad Branch, Mashhad, Iran

(Email: zeinabrouhbakhsh@yahoo.com)

Keywords: Human serum albumin, Amlodipine, Magnetic field, UV Spectroscopy, Fluorescence quenching.**1. Introduction**

Human serum albumin (HSA) is the most abundant carrier protein of the blood with a high affinity for a wide range of metabolites and drugs [1]. Amlodipine besylate (Norvasc) a calcium channel blocker with highly potent vasodilating activity, used for the treatment of hypertension, angina pectoris and cerebrovascular disease. It may be used alone or in combination with other antihypertensive agents [2].

The influence of static magnetic fields (SMFs) on biological systems has been a topic of considerable interest for many years. The increasing production of electric (EMFs) and magnetic fields (MFs) due to the expanding use of electronic devices in normal life is encouraging studies on the effects of EMFs and MFs on living organisms, with a view to better protecting human health against their probable unfavorable effects [3].

In this work, the binding parameter of amlodipine with HSA in presence and absence of magnetic field was investigated by means of ultraviolet (UV) absorption and fluorescence spectroscopy.

2. Methods

Human serum albumin (HSA) was purchased from Sigma Chemical Company, and amlodipine was obtained from Tehran-drug Company (Iran), were used without further purification. The samples were dissolved in phosphate buffer solution (0.05 mol L⁻¹, pH 7.4). All solution was used with doubly distilled water.

The UV absorbance spectra of the HSA-drug with varied concentrations of amlodipine were recorded on Shimadzu, UV-2550 spectrophotometer, from 200 to 300 nm.

Fluorescence measurements were carried out in an F-2500 FL Varian fluorescence spectrophotometer, equipped with xenon pulse lamp, with a 1.0 cm quartz cell. The excitation wavelength was 280 nm, and the emission spectra were read at 300 – 500 nm.

A solution of 0.05 % (w/v) HSA was titrated by successive 8.8×10^{-5} M stock solution of amlodipine.

In order to understand the effect of magnetic field, all experiments were also done on the samples that 10 minute exposed in the magnetic field (52 mT).

All the experiments were repeated at least three times. All measurements were performed at room temperature.

3. Results and discussion

In the interaction between HSA and amlodipine, the absorbance of HSA increased with increasing concentration of amlodipine, and a slight blue shift was observed for the maximum peak position. These uv spectroscopy results indicate that interaction occurred between amlodipine and HSA [4].

The Scatchard and Hill equations was employed to analyze the data obtained, for determining of the binding capacity, g, binding constant, K, and Hill constant, n_H .

The results showed that g, n_H , and K in the presence and absence of magnetic field have different values (Table 1).

The fluorescence quenching spectra of HSA at various concentrations of amlodipine showed that HSA had a strong fluorescence emission band at 340 nm and the fluorescence intensity of HSA decreased regularly.

For describing the fluorescence quenching induced by amlodipine using the well-known Stern-Volmer equation:

$$F_0/F = 1 + K_{sv} [Q] = 1 + k_q \tau_0 [Q]$$

Where F_0 and F are the fluorescence intensities in the absence and presence of quencher (amlodipine), respectively, K_{sv} is the Stern-Volmer quenching constant, k_q is the biomolecular quenching constant, τ_0 is the average lifetime of the biomolecular in absence of quencher and its value is 10^{-8} s ($\tau_0 = 10^{-8}$ s) and $[Q]$ is the concentration of quencher [5].

The Stern-Volmer quenching constant, K_{sv} , can be obtained as the slope of the Stern-Volmer plot (Fig. 1): $K_{sv} = 7.5 \times 10^4$ and 3.5×10^4 mol⁻¹ L for HAS in free and exposed samples, respectively.

4. Conclusions

The interaction of amlodipine with HSA was investigated in presence and absence of magnetic field, using spectroscopy techniques. The results showed that the binding parameters were different in free and exposed conditions, but the real mechanism was not clear.

Acknowledgment

This work was supported by Iran National Science Foundation (INSF).

References

- [1] T.K. Maiti, K.S. Ghosh, A. Samanta, S. Dasgupta, J. Photochem. Photobiol. A: Chem. 194 (2008) 297.
- [2] D. Ghosh, A. Das, P.S. Selvan, K.V. Gowda, U. Mandal, A. Bose, S. Agarwal, U. Bhaumik, T. Kumar Pal, J. Chromatogr. B 873 (2008) 77.
- [3] L. Dini, L. Abbro, Micron 36 (2005) 195.
- [4] H. Cheng, H. Liu, Y. Zhang, G. Zou, J. Lumines 129 (2009) 1196.
- [5] T. Lemma, J. Pawliszyn, J. Pharm. Biomed. Ana. 50 (2009) 570.

Table 1. Binding parameters for amlodipine-HSA complex in presence and absence of magnetic field.

	g	n_H	K	R^2
Free	18	1.6907	1.049×10^5	0.9939
52 mT	12	2.0867	1.435×10^5	0.9984

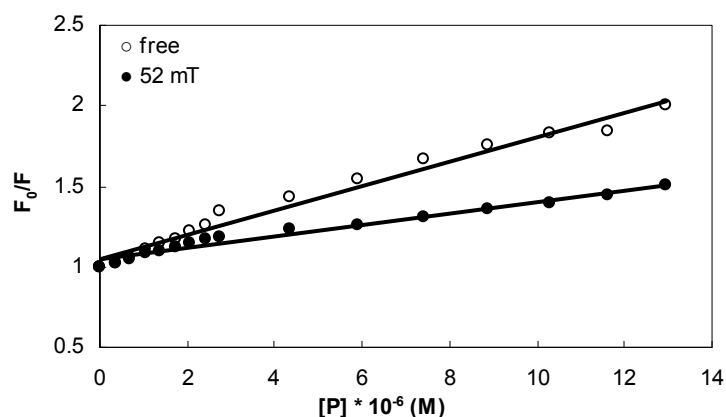


Fig. 1. Stern-Volmer plots for the amlodipine-HSA system in free and exposed system.

**Estimation of gibbs free energy of formation of haloalkanes by qspr modeling**R. Behjatmanesh Ardakani^a, F. Mollaie Poli^{b,*}^a Department of Chemistry, Payame Noor University of Ardakan ,Yazd, Iran^b Department of Chemistry, Payame Noor University of Sirjan, Kerman ,Iran

(Email: f.mollaie@yahoo.com)

Keywords: QSPR, Gibbs Free Energy of Formation, MLR.**1. Introduction**

The Gibbs free energy of formation (ΔG_f°) is a fundamentally important physicochemical property of organic compounds, which plays an important role in all kinds of chemical and biochemical reactions. Prediction of physicochemical properties of materials from their molecular structures has been one of the wishes of scientists and engineers for a long time. One of the useful methods applied for this purpose is that of quantitative structure-property relationship (QSPR) [1]. QSPR is defined as a mathematical model which predicts the physical, mechanical, or chemical properties of materials from their chemical structures. The main goal of QSPR studies is to find a relationship between the structure of a compound expressed in terms of numeric characteristics associated with its chemical structure (which are called molecular descriptors) and the properties of interest. Once a correlation between structure and desired property is found, any number of compounds, including those not yet prepared or even not synthesized, can be readily screened on a computer in order to select structures with the desired properties. In this work, a QSPR study is performed to develop an accurate model for the prediction of Gibbs free energy of formation for 55 Haloalkanes. For this purpose, multivariate linear regression (MLR) is applied to establish quantitative linear relationship between Gibbs free energy of formation and molecular descriptors.

2. Methods

Data set: The experimental standard ΔG_f° values (in kJ mol^{-1}) at 298 K of 55 Haloalkanes were taken from the Chemical Properties Handbook [2]. ΔG_f° has a minimum value of $-678.30 \text{ kJ mol}^{-1}$, a maximum value of -5.1 kJ mol^{-1} , and a mean value of $-178.962 \text{ kJ mol}^{-1}$. The data set was randomly split into a training set of 39 compounds and a test set of 16 compounds for the MLR model.

Calculation of molecular descriptors: In this step, molecular structures of all 55 components were drawn into HyperChem software and optimized using the MM+ molecular mechanics force field. A more precise optimization is done with semi-empirical pm3 method in hyperChem 7.0 software and Thereafter, by Dragon software, constitutional and topological descriptors were calculated using these optimized molecular structures. In addition quantum chemical descriptors were calculated by the ab initio b3lyp/6-311G(d) using GAUSSIAN 98 software. 50 descriptors including the dipole moment, partial atom, total energies, HOMO and LUMO energies, Gap(HOMO-LUMO) , Polarizability, number of various types of atoms and bonds, molecular weight , hardness, electronegativity electrophilicity, Wiener index, Balaban index, minimum and maximum partial charges, etc, have been characterized.

After the calculation of the molecular descriptors, those that stayed constant for all molecules were eliminated and pairs of variables with a correlation coefficient greater than 0.90 were classified as intercorrelated, and one of them in each correlated pair was deleted.

Building a model by mlr analysis

After the descriptor was selected, multiple linear regressions were employed to develop the linear model of the property of interest, which takes the form:

$$Y = b_0 + b_1 X_1 + b_2 X_2 + \dots + b_n X_n$$

In this equation, Y is the property, that is, the dependent variable, X_1 to X_n represent the specific descriptor, while b_1 to b_n represent the coefficient of those descriptor; b_0 is the intercept of this equation.

Model validation: The goodness-of-fit of the resulted QSPR models were judged using statistical parameters such as correlation coefficient (R), Squared correlation coefficient (R^2) , Adjusted $R^2(R^2_{Adj})$, standard error of regression (S.E), and variance ratio (F) at specified degrees of freedom. The generated QSPR equations were also validated by leave-one-out cross - validation correlation coefficient(Q^2). The predictive ability of a QSPR model should be tested on an external set of data that has not been taken into account during the process of developing the model. In particular, to assess the predictive power of QSPR models the correlation coefficient between the predicted and observed property of compounds from an external test (r^2), the correlation coefficients for regressions through the origin (predicted versus observed activities, or observed versus predicted activities, i.e., r_o^2 or $r_o'^2$ respectively), and the slope of the regression lines through the origin (k and k', respectively) were

calculated [3]. Considered a QSPR model to be predictive, if all of the following conditions are satisfied: (i) $Q^2 > 0.5$, (ii) $r^2 > 0.6$, (iii) r_0^2 or $r_0'^2$ is close to r^2 . such that $[(r^2 - r_0^2)/r^2]$ or $[(r^2 - r_0'^2)/r^2] < 0.1$ and (iv) $0.85 \leq k \leq 1.15$.

Moreover, the multi-collinearity among variables was identified using variance inflation factor (VIF). If VIF was greater than 10, it was not considered as a model [4]. The stepwise regression and cross-validation were performed respectively using the statistical software SPSS and MATLAB software.

3. Results and discussion

The result was the following two-variable equation:

$$\Delta G_f^\circ = 184.912 - 177.402 \text{ nF} + 788.620 \text{ HOMO}$$

In this equation, HOMO is the highest-energy orbital with one or two electrons and nF is the number of Fluorine atoms. The two inputs variables in the QSPR model are measured in different units of measurements and the respective coefficients are of different orders of magnitude. In order to examine the importance of each descriptor and answer the question which of the independent variables have a greater effect on the dependent variable in the multiple regression analysis, the standardized regression coefficients were also calculated. This calculation is performed by applying the multiple regression methodology on the standardized values of the independent and dependent variables, i.e. on the values that are obtained after subtracting the mean and dividing by the standard deviation for each variable [5]. The standardized regression coefficients, then, represent the change in a dependent variable that results from a change of one standard deviation in an independent variable. The standardized regression coefficients are presented in the following QSAR model:

$$\Delta G_f^\circ = -0.890 \text{ nF} + 0.122 \text{ HOMO}$$

It is clear that the standardized regression coefficients for all input descriptors are of the same scale. The statistical parameters are shown in Table 1. The plot of predicted versus experimental ΔG_f° for the training and the test set shown in Figures 1 and 2 suggest that the Haloalkanes follow a straight line.

Table 1: Statistical parameters

R	R ²	R ² _{Adj}	S.E	F	Q ²	r ²	r ₀ ²	r ₀ ' ²	r ² - r ₀ ² / r ²	k	k'	vif
0.995	0.989	0.989	21.44	1666	0.987	0.976	0.9711	0.973	0.005	1.02	0.961	3.34

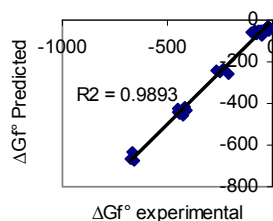


Fig. 1. Predicted versus experimental values of ΔG_f° for training set by MLR

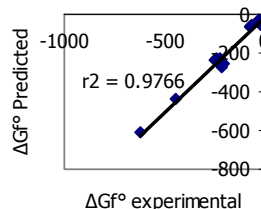


Fig. 2. Predicted versus experimental values of ΔG_f° for test set by MLR

4. Conclusions

The results show close agreement between Predicted values and experimental ones, which demonstrates the reliability of the QSPR model.

References

- [1] Karelson, M. Lobanov, V. Estonia, Chem. Rev. 96 (1996) 1027.
- [2] Dean, LANGE'S HANDBOOK OF CHEMISTRY, Fifteenth Edition, McGRAW-HILL, INC. 1999.
- [3] Golbraikh, A. Tropsha, A. USAJMG. 20 (2002) 269.
- [4] Myers, Classical and Modern Regression with Applications, PWS/KENT, Boston, 1990.
- [5] R. Todeschini, V. Consonni, Handbook of Molecular Descriptors, VCH, Weinheim, 2000.



Micellization of pantanediyl-1,5-bis(hydroxyethylmethylhexadecylammonium bromide) (GSP²) cationic gemini surfactants.

R. Zarganian, A.K. Bordbar, R.Amiri, A.R.Khosropour, I.Mohammadpour Baltork.

Department of Chemistry, University of Isfahan, Isfahan ,Iran

(Email: bordbar@chem.ui.ac.ir , r.zarganian20@gmail.com)

Keyword: gemini surfactant, critical micellar concentration, aggregation number, conductometry, fluorescence.

1. Introduction

In recent years a new class of amphiphilic molecules were found that got attention of many academical and industrial research groups. Gemini surfactant as a member of this class has a appealing properties [1]. Their structures compose of two hydrophilic heads and two hydrophobic tails, and a spacer which is connected two heads or two tails. Hydrophobic tails and spacer could be short or tall, rigid or flexible. Symmetry in structure around spacer does not need [1-4]. Property of this structure is changed with molecular structure. Long non-polar tails causes increase in surface activity, but it decreases their aqueous solubility [5-8]. Gemini surfactants could synthesis in different structures such as more than two heads or two tails, and in order to kind of head divided into three groups, anionic, cationic, and non-ionic [9-13].

In the present study at first, pantanediyl 1, 5 bis (hydroxyl ethyl methyl hexadecyl ammonium bromide) as a novel gemini-surfactant was syntheses, purified and characterized. Then the micellar properties of this gemini-surfactant were comprehensively investigated at various experimental conditions such as temperature and ionic strength using conductometry and fluorescence techniques. Determining the thermodynamic parameters of micellization using mass action model, provides a good form for molecular understanding of micellar process[1-13].

2 Methods

2.1. Materials

n-Hexadecylbromide, 1,5dibromoalkane, and 2(methylamino) ethanol were purchased from the sigma Chemical Company.

2.2. Synthesis

Hydroxy ethyl methyl hexadecyl- amine was obtained by refluxing hexadecyl bromide with 2 (methylamino) ethanol in dry ethanol at 80 °C for 25 h. pantanediyl-1,5 -bis hydroxyethylmethylhexadecylammonium bromide was synthesized by refluxing 2.2 mole of hydroxyl ethyl methyl hexadecyl amine in dry acetone with 1.0 mole of 1, 5 dibromo alkane for 70–96h[14].

3. Results and discussion

3.1 conductometry results

Change in conductivity of surface active aqueous solutions at critical micelle concentration (CMC) point equals to different order ionization of surface active substance before and after CMC point. Before CMC, monomers of surface active act like strong electrolyte and we do not have any micelle. After CMC, micelles became somewhat ionized. Micelle ions with another charge attach to long hydrocarbon tails and lead to decrease in conductivity value. α consider as ionization order, therefore; β consider as neutron charge molar fraction of micelle $\beta=1-\alpha$. CMC values were determined in various temperatures (20,25,30,35,45 °C) and It appears to be the value CMC increases as temperature increase. Figure 1a, shows cmc value at various temperatures found by conductance.

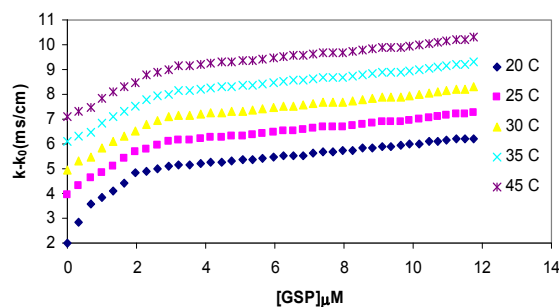


Fig. 1. a. cmc atvarious temperatures found by conductance.

3.2. Fluorescence results

The process of fluorescence quenching provides decrease in fluorescence quantum yield of fluorophore by various molecular interactions. For instance excited state reactions, energy transfer, molecular rearrangement, formation of a non-fluorescent ground state complex (static quenching) and collisional encounter between the fluorophore and quencher (dynamic quenching).

4. Conclusions

The critical micellar concentration of the Gemini surfactant S5 was increased in that temperature increase. In addition ΔG , ΔH and ΔS micellization were determined. Negative values of enthalpy ΔH_{mic} indicate an exothermic nature of the micellization process. Besides salt effect studies show that the values of CMC decrease on increasing the concentration of salt; therefore, their aggregation numbers would be decrease.

References

- [1]. Shukla, D. Tyagi, A Review, J. Oleo Sci. (2006) 381.
- [2]. L.Ting, G. JianBin, , J. Chin. Sci. Bulletin. 52 (2007) 2618.
- [3]. B. Sekhon. Resonance. 4 (2004) 42-49.
- [4]. S. Hait, S. Moulik, A review, Curr. Sci. 82 (2002) 1101.
- [5]. B. Nayak, S. Patel, ARKIVOC, Oxford press Eds. (2006) 22.
- [6]. Z. Chen, G. Liu, Anal.Biochem. 384 (2008) 1-6.
- [7]. U. Laska, A. Wilk, Journal of Surfactants Deterg. 9 (2006) 115.
- [8]. C. Akbari, N. Gill, Electrophoresis. 26 (2005) 415.
- [9]. T. Chakraborty, S. Ghosh, Journal of Colloid Polymer Sci. 285 (2007) 1665.
- [10] W. Brüse, H. Schier, Journal of Surfactants Deterg. 7(2004) 181.
- [11]. O. Rist, A. Rike, Molecules. 6 (2001) 979.
- [12]. S. Manne, T. Schaffer, Langmuir.13 (1997) 6382.
- [13]. K. Holmberg, Wielly interscience Eds., Second Edition (2003).
- [14] J. Briggs, R.B. Dorshow, C.A. Bunton, D.F. Nicoli, J. Chem. Phys. 76 (1982) 775.
- [15] J.H. Fendler, in: J.H. Fendler (Ed.), Wiley–Interscience, New York (1982) Chap. 6.
- [16] F.M. Menger, J.S. Keiper, Angew. Chem. Int. Ed. 39 (2000) 1906.

**QSPR study on logCMC of anionic surfactants using multiple linear regression (MLR) method**R. Behjatmanesh-Ardakani^a, S. M. Mirhoseini-Abram Abadi^b, F. Ghaderiyeh-Mahmood Abadi^{a*}^a Department of Chemistry, Payame-Noor University of Ardakan, Iran^b Department of Statistics, Yazd University, Iran

* (Email: ghaderiah@yahoo.com)

Keywords: QSPR, LogCMC, MLR, PLS.**1. Introduction**

A surfactant is a substance that, when present at low concentration in a system, has the property of adsorbing onto the surfaces or interfaces of the system and of altering to a marked degree the surface or interfacial free energies of those surfaces (or interfaces). The concentration at which Micelle formation occurs is called the critical micelle concentration (CMC) [1].

One of the most successful approaches for the prediction of chemical properties, starting solely with molecular structural information, is modeling of quantitative structure–activity/property relationships (QSAR/QSPR). Multiple linear regression (MLR), principal component regression (PCR), partial least squares (PLS) regression and artificial neural networks (ANN) are the most commonly used modeling methods in QSPR [2].

2. Methods

The training set of 31 compounds, with LogCMC values in the range of -0.333- -3.635, was used to adjust the parameters of the model. The structures of the compounds were preoptimized by the semiempirical method PM3. The closed-shell ground state geometries of the all species were optimized fully at the RHF/6-31G(d) level of theory by the Gaussian 98W software. In order to calculate solvation energies, a continuum model of solvation, the conductor-like polarizable continuum model (CPCM) has been used at the recommended radii in water.

In the present work, the best variables among electronic and topological descriptors were selected using PLS and MLR and then a MLR model was developed to predict the LogCMC of these surfactants.

3. Results and discussion

In the MLR method the following assumptions concerning the residuals are made: (1) for each molecular descriptor x_k , the residuals e_i are from a population that is normally distributed with mean zero. (2) the e_i are independent. (3) they all have the same variance. Based on figure 1, it is reasonable to conclude that the residuals have normal distribution. Figure 6 shows the plot of the standardized predicted values LogCMC against standardized residuals. The points in this plot are randomly scattered about the horizontal line; instead, they suggest the residuals variance is constant.

The best equation obtained for the anionic surfactants is:

$$\text{LogCMC} = 3.978 - 0.031\mu(g) - 0.344\text{NAO}_{\min}(g) - 0.069B \quad (1)$$

where $\mu(g)$, NAO_{\min} , B , are the total dipole moment in gas phase, the min natural atomic orbital taken from the results of natural population analysis (NAO_{\min}) in gas phase and the bond number (B), respectively

Relationships have been found between the total dipole moment and solvation properties of surfactants, therefore in order to calculate the total dipole moment, a CPCM has been used at the recommended radii in water.

$$\text{LogCMC} = 1.956 - 0.0290\mu(aq) + 0.426q_c^+(aq) - 0.0700B \quad (2)$$

The statistical results (R^2 , R^2_{Adj} , F , MS_{E} , PRESS and $D. W.$) are summarized in table 1.

4. Conclusions

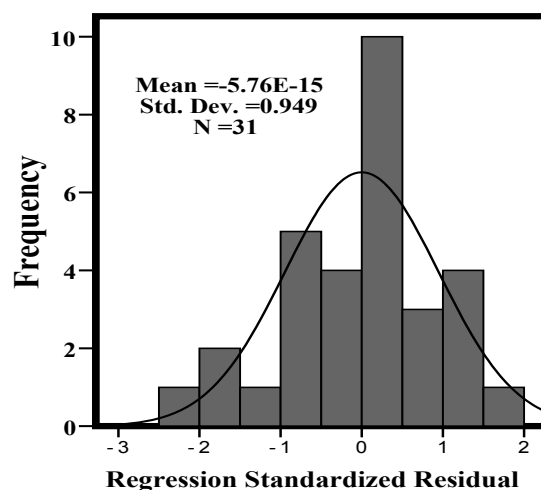


Fig. 1. Frequency against standardized residuals

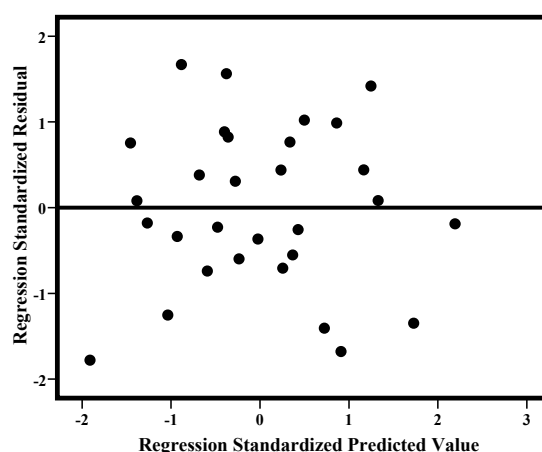


Fig. 2. standardized predicted values LogCMC against standardized residuals

Table 1. Statistical parameters obtained by applying the MLR method to the training set

Eq	R ²	R ² _{Adj}	F	MS _E	PRESS	D.W.	R ² _{L00}	R ² _{LFO}
1	0.989	0.987	778.274	0.007	0.247	2.445	98.44	97
2	0.981	0.978	439.568	0.009	0.338	2.52	97.26	97

According to the descriptors appearing in the proposed models for the CMC we found that the surfactant micellization is mostly related to features which involve size and charge of the hydrophobic tail. In conclusion, good quantity QSPR models for the CMC in this work can be used for prediction of similar anionic surfactants as well as analyzing structural features leading to desired CMCs based on the descriptors used in these models.

References

- [1] B. Jonsson, B. Lindman, K. Holmberg, B. Kronberg, Surfactants and polymers in aqueous solution, John Wiley & Sons, 1999.
- [2] G. Brereton, Chemometrics Data Analysis for the Laboratory and Chemical Plant, John Wiley & Sons, 2003.
- [3] X. Li, G. Zhang, J. Dong, X. Zhou, X. Yan, M. Luo, J. Mol. Struct: (TheoChem). 710 (2004) 119.

**Kinetic investigation of photocatalytic degradation of azo dye by Ag/AgBr modified TiO₂ loaded on zeolite**

M. Padervand, M. Tasviri and M. R. Gholami

Department of Chemistry, Sharif University of Technology, Azadi Ave., Tehran, Iran

(Email: M_padervand@yahoo.com)

Keywords: Zeolite, TiO₂, Sol-gel method, Photocatalytic degradation, Acid Blue 92**1. Introduction**

Zeolites (crystalline aluminosilicates) with uniform nanoscaled pore size and extensive surface area have been applied in the design of operative photocatalytic systems [1-3]. One advantage of zeolites as photocatalyst supports is that the cages and channels in crystalline zeolites can encapsulate molecules in well-defined and unique spatial arrangement, and be used as constrained systems for preparation of active species of catalysts with controlled particle size and shape. Another advantage is that the transfer process of charges is fostered and the charge recombination is delayed, because of the existence of Lewis acid/base sites in zeolite structure [3].

2. Methods**2.1 Reagents**

Clinoptilolite was used as natural zeolite source during this study. Tetraisopropylorthotitanate, Cetyl methyl ammonium bromide and all other chemicals that were used throughout this study purchased from Merck chemical Co. Azo dye (AB92) supplied by the Iran color research center.

2.2 Preparation of photocatalyst

Photocatalysts involving TiO₂ loaded on zeolite were prepared by Sol-gel and deposition method. The precursor solution contains Tetraisopropylorthotitanate, ethanol and nitric acid. The nitric acid was used as catalyst to control the hydrolysis process.

2.3 Evaluation of photocatalytic activity

The photocatalytic activity of the catalysts was evaluated by the photodecolorization of AB92 solution. The photocatalytic experiment was performed in a reactor which was surrounded by a circulating water jacket to maintain constant temperature. The absorption of dye was determined by UV spectrophotometer (GBC cintra40) at $\lambda=574\text{nm}$ and the efficiency of degradation of AB92 was calculated from the equation (1)

$$X = \frac{(C_0 - C)}{C_0} \times 100 \quad (1)$$

In which C_0 and C are the initial concentration and the concentration after degradation respectively.

3. Results and discussion**3.1 XRD and EDX analysis FTIR analysis, SEM analysis and BET analysis****3.2 Photocatalytic comparison of prepared catalysts**

The results of the optimum efficiency of each catalyst are represented in Figure 10. It is obvious that the photocatalytic activity of Ag/AgBr/TiO₂/zeolite is better than other catalysts.

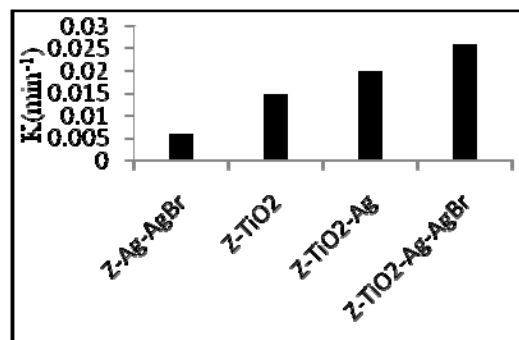


Fig. 10. Comparison of photocatalytic activity of prepared catalysts under the UV light

References

- [1] Noorjahan M, Kumari V.D, Subrahanyam M, Boule P. preparation and photocatalytic activity of PANI/TiO₂ composite film. *Rare Metals* 2007;26:1-7.
- [2] Yahiro H, Miyamoto T, Watanabe N, Yamaura H. Preparation and properties of a news composite photocatalystbased on nanosized titanium dioxide. *Chemical paper* 2008;63:249-54.
- [3] Patterson H.H, Gomez R.S, Lu H, Yson R.L. Nanoclusters of silver doped in zeolites as photocatalyst. *Catal today* 2007;120:168-73.



The effect of surfactants on asphaltene precipitation onset in presence of nano- tetra phenyl porphyrin

M. NikAzar^a, M. A. Safarpour^b, S. Toufani^{b,*}, A. Heidari^c

^a Department of Chemical Engineering, Amirkabir University of Technology, Hafez st., Tehran, Iran

^b Department of Chemistry, Iran University of Science and Technology, Narmak, Tehran, Iran

^c Department of chemistry, Ferdowsi University of Mashhad, Mashhad, Iran

*(Email: toufani@chem.iust.ac.ir)

Keywords: Asphaltene, Nanoparticles, Surfactant, Emulsion stability

1. Introduction

As a definition we can say asphaltenes are a fraction of the crude oil that is soluble in benzene or toluene but insoluble in liquid normal alkanes (e.g. n-pentane or n-heptane). They are polar components and their chemical structure consists of a large number of aromatic rings and aliphatic chains that combine in various ways forming "molecules" with a wide range of molecular weight. Apart from C and H they contain large amounts of hetero atoms (O, S, N and metals) as well [1]. Structurally, resins, are similar to typical surface-active molecules which form micelles around asphaltenes and make them dissolved in crude oil [2]. Regarding resin characteristics, we can use specific surfactants to play role instead of it.

Asphaltene molecules tend to aggregate and create larger particles [1]. As asphaltene troubles we can mention its deposition in wells, pipelines and production equipment that can significantly increase the costs of production operations. The minimization of asphaltene deposition is therefore of great interest [3].

The formation of stable emulsions in the production and refining of crude oil is a challenge which has defied broad and generic resolution for several decades. Rational and systematic approaches to demulsification have been slow to develop due to a lack of fundamental understanding of the molecular origins of emulsion stabilization and the full range of factors which govern emulsion stability [4]. In presence of water, small inorganic particles strongly enhance water-crude oil emulsion stability when interactions with asphaltenes promote particle adsorption at the oil-water interface. Decreased particle sizes, and increased particle concentrations enhanced water-in-oil emulsion stability [2]. Simultaneous emulsification of particles and surfactant led to synergistic stabilization at intermediate concentrations of surfactant; emulsions completely stable to both creaming and coalescence exist at low overall emulsifier concentration [5].

Porphyrins are a group of organic compounds of which many occur in nature. They are heterocyclic macrocycles characterised by the presence of four modified pyrrole subunits interconnected at their α carbon atoms via methine bridges [6].

In this work we investigated the effect of addition of nanoparticle (nano-TPP) and surfactants (LABs, TTAB, ethoxylated alcohol) on asphaltene emulsion stability.

2. Methods

Asphaltene was separated from an Iranian crude oil according to IP143/01. 0.001g of asphaltene was solved in toluene (MERK, extra pure), then n-heptane (MERK, 99%) was added gradually. The asphaltene precipitation onset was determined by Surface Tension (ST) measurement (KSV Sigma 700 tensiometer).

In next step, another solution with the same characteristics was made. 800ppm surfactant LABs (from conventional sources), which was neutralized, was added to solution before n-heptane addition. In a separated experiment, TTAB (MERK , > 96%) and ethoxylated alcohol (2, 3, 4, 5.5 and 7 mole ethoxylated) were used as mentioned for LABs.

A hydrophobic nanoporphyrin was synthesized. 0.0001g Tetra Phenyl Porphyrin (TPP) was solved in 5 mL DMSO, and a stabilizer like TEG was applied then 5mL deionized water was added while applying ultrasonic within 20 minutes. UV-Vis spectrum of synthesized nanoporphyrin is shown in figure 2. These nanoparticles act like nanoasphaltene. Nanoasphaltenes can stabilize the emulsion [7]. We did synthesis the nano- TPP without water with the aid of ethanol and microwave.

After nanoparticle addition to each of the solutions surface tension measurements were done once again.

3. Results and discussion

LABs and ethoxylated alcohols have good ability to stabilize asphaltene. The negatively charged asphaltenes tend to be dispersed by cationic amphiphiles, whereas the positively charged asphaltenes tend to be dispersed by anionic amphiphiles [8]. Fig. 3 shows asphaltene onset without additive.

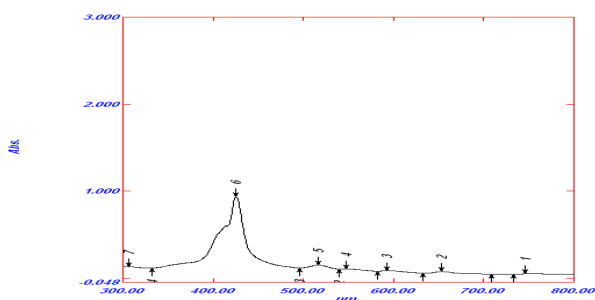


Fig. 1. UV-vis spectrum of nanoporphyrin

Nanoporphyrin has very good interaction with asphaltene molecules in both TTAB, LABs and ethoxylated alcohol solutions. Fig.3 demonstrates asphaltene onset in presence of LABs. In fig.2 the onset point is observed at 73% v/v n-heptane but in fig.3 the onset is improved to over 80% v/v n-heptane. Presence of nanoporphyrin stabilized the asphaltene emulsion as well. The onset point delay was remarkable.

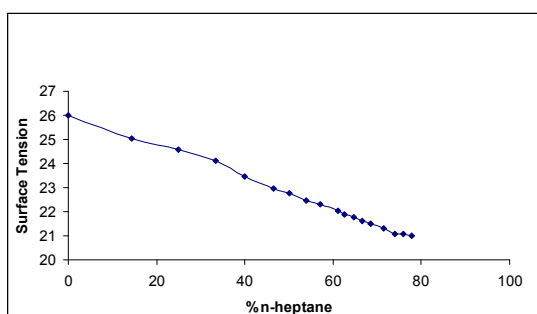


Fig.3 – asphaltene onset without additive

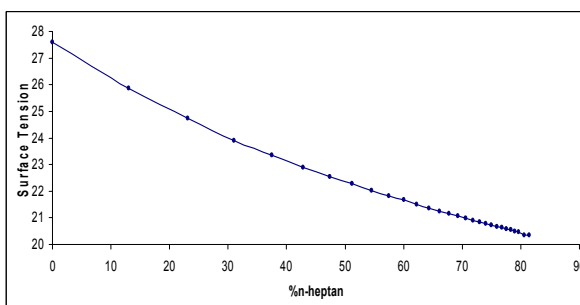


Fig.4 – asphaltene onset in presence of LABs

4. Conclusion

Asphaltene can be stabilized by various surfactants depended on its surface charge. As it was studied, nano- TPP can effect on asphaltene onset in proper way. Nano complexes of porphyrin may be effective.

References

- [1] N.I. Papadimitriou , G.E. Romanos, G.Ch. Charalambopoulou, M.E. Kainourgiakis, F.K. Katsaros, A.K. Stubos , " Experimental investigation of asphaltene deposition mechanism during oil flow in core samples", *Journal of Petroleum Science and Engineering* 57 (2007) 281–293 .
- [2] Andrew P. Sullivan , Peter K. Kilpatrick, " The Effects of Inorganic Solid Particles on Water and Crude Oil Emulsion Stability" , *Ind. Eng. Chem. Res.* 41(2002),3389-3404
- [3] E. Rogel, O. Leo'n, G. Torres, J. Espidel, " Aggregation of asphaltenes in organic solvents using surface tension measurements" , *Fuel* 79 (2000) 1389–1394 .
- [4] Joseph D. McLean , Peter K. Kilpatrick, " Effects of Asphaltene Solvency on Stability of Water-in-Crude-Oil Emulsions" , *journal of colloid and interface science* 189(1997), 242–253 .
- [5] BINKS Bernard P. , DESFORGES Alexandre , DUFF Daniel G. " Synergistic stabilization of emulsions by a mixture of surface-active nanoparticles and surfactant" , *Langmuir* 23(2007), 1098-1106 .
- [6] <http://en.wikipedia.org/wiki/Porphyrin>
- [7] Trond Erik Havre, Johan Sjöblom, "emulsion stabilization by means of combine surfactant multilayer (D-phase) and asphaltene particles", *colloids and surfaces A : Physicochem. Eng. Aspects* 228(2003)131-142 .
- [8] Jiqian Wang, Chuan Li, Longli Zhang, Guohe Que, and Zhaomin Li, The Properties of Asphaltenes and Their Interaction with Amphiphiles, *Energy & Fuels* 23(2009), 3625–3631 .

Investigating the charge distribution in the semiconductor compound ZnTe

Salehi, H^a ; Mirzaei, R^b

^aDepartment of Physics, Shahid Chamran University, Ahvaz, Iran

^bIslamic Azad University Science and Research Branch, Ahvaz, Iran

(Email: roohmir85@yahoo.com)

Keywords: ZnTe, Zinc blende structure, Wurtzite, Charge density

1. Introduction

ZnTe is a direct transition compound semiconductor whose bandgap is 2.26 eV. ZnTe constitutes a family of (IIB–VIA) compounds[1]. This compound is crystallized in the cubic zincblende structure with lattice constant $a=6.1030\text{\AA}$ and wurtzite structure with lattice constants $a=4.320\text{\AA}$ and $c=7.100\text{\AA}$ [2,3]. This compound is used in semiconductor devices, lasers diodes, macro wave generators, solar cells as the substrate layer and green LED materials[4].

On the theoretical side, many authors have studied this semiconductor to explore the electronic properties using various computational methods[1,5,6]. In this work, we study charge distribution in ZnTe using the plane wave sets with pseudopotential in framework of density functional theory(DFT).

2. Methods

The calculations have been performed using plane wave sets with pseudopotential in framework of (DFT) with various generalized gradient approximations (GGA) and local density approximations (LDA), using PWscf package. In this study, for making pseudopotential elements Zn and Te, we select the norm conserving pseudopotential method. The Monkhorst-Pack k -point meshes of $3\times 3\times 3$ for the zinc blende structure and $6\times 6\times 3$ for the wurtzite structure were employed[7].

3. Results and discussions

In fact, electronic charge density is the charge density that shows the electronic charge distribution around atoms. amount of charge distribution around the atoms indicates type bondings between the atoms. High electron density between two atoms indicates a strong bonding and lower electron density shows the weaker bonding between the atoms. electronic density plot shows the density in different positions and indicates where the more electron density points are and so are the less.

Figures 1 and 2 shows the electronic charge density plot in the (110) plane of ZnTe for zinc blende and wurtzite structures. the figures indicate the highest electron charge density on Tellurium atoms precisely, due to the high electronegativity Te in this compound. lower electron charge density in Zn atoms shows that the Zn atoms have lost the electron.

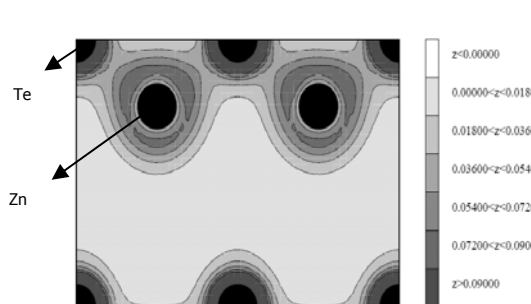


Fig.1. Electronic charge density plot in the plane of ZB structure

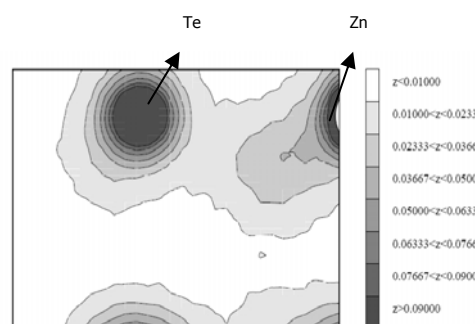


Fig.2. Electronic charge density plot in the plane (110) of WZ structure

There is a strong covalent bonding between the Te and Zn atoms due to Zn^{+2} cations and Te^{-2} anions in this compound. the calculated charge distribution shows a polar covalent feature in bonding Zn-Te. It can be seen that the Te ions is larger than Zn, and there is a charge transfer from Zn to Te. This is because of higher electronegativity of Te than Zn. If the electronic charge density is drawn considering spin coupling, it does not change the obtained results. It can be concluded that the spin does not effect on charge density in this compound. This is highly excellent agreed with experimental results.

4. Conclusions



According to the electronic charge density plot in the (110) plane of ZnTe, the electronic charge density on Te atoms is higher than Zn atoms, this is due to the higher electronegativity of Te than Zn. The lower electronic charge density around Zn atoms shows that the Zn atoms have lost the electron. high electronic charge density between Te and Zn atoms indicates a covalent bonding between Te and Zn atoms. This is highly excellent agreed with available experimental results.

References

- [1] R .Khenata,b. A. Bouhemadou, M. Sahnoun, A. H. Reshak,H. Baltache , M. Rabah,Computational Materials Science .38 (2006) 29–38.
- [2] J.E.Jaffe, R. Pandey , M.J. Seel. Phys. Rev. B 47 (1993) 6299.
- [3] S.Z.Karazhanov, P. Ravindran, U. Grossner, A. Kjekshus , B. G. Svensson,J. Appl. Phys. (2006) 3709
- [4] Wikipedia, the free encyclopedia.mht.
- [5] R.Gangadharan , V. Jayalakshmi , J. Kalaiselvi , S.Mohan ,R. Murugan, B. Palanivel, Journal of Alloys and Compounds 359 (2003) 22–26.
- [6] J.L.Alves, K.Watari , A.C.Ferraz, Brazilian journal of physics, Vol . 24, no.1. March(1994).
- [7] H.J.Monkhorst , J. D. Pack. Phys. Rev. B 13 (1976) 5188.



Solution properties of alkanediyl- α,ω -bis (hydroxy ethyl methyl hexadecyl ammonium bromide) as a Gemini cationic surfactant in aqueous media

M. Tamannaie, R. Amiri, A.K. Bordbar, A.R. Khosropour and I. Mohammad pour.

Address: Laboratory of Biophysical Chemistry, University of Isfahan, Isfahan, 81746-73441, I.R. Iran.

(Email: bordbar@chem.ui.ac.ir, m.tamannaie@chem.ui.ac.ir)

Keywords: Micellization, Conductometry, Gemini surfactant

1. Introduction

Physicochemical properties of surfactant molecules are primarily decided by the structure of the molecule under consideration [1]. Surfactants with two hydrophilic and two hydrophobic groups in the molecule, called „gemini” surfactants (or „dimerism”), have evoked considerable interest since it became evident that this surfactant appear to be superior to the corresponding conventional monomeric surfactants. In the present study, the micellar properties of Alkanediyl- α,ω -bis (hydroxy ethyl methyl hexadecyl ammonium bromide) have been comprehensively investigated using conductometric technique.

2. Methods

2.1. Synthesis of gemini surfactants

This gemini surfactants was synthesized by refluxing 2.2 mol of hydroxyethylmethylhexadecylamine in dry acetone with 1.0 mol of dibromoalkane for 70 to 96 h.

The crude white solid thus obtained was washed with a hexane/ethyl acetate mixture and recrystallized from acetone/ methanol mixture for at least three to four times till the purity of the compound was confirmed through TLC. Products were further characterized through FTIR, ¹HNMR, and elemental analysis [3].

2.2. Conductometric measurements

The CMC values of the gemini surfactant were determined using a conductometer (JENWAY, Model 4510) at different temperature.

3. Results and discussion

The CMC values and thermodynamic parameters calculated from the conductivity were shown in the table 1. The variation of conductivity versus molarities of surfactant at different temperatures is shown in figure 1. The curve has an abrupt fall drawing a reverse sigmoid, the center of which is regarded as the point giving CMC, based on the definition by Philips. During the temperature transition stage, conductance increases sharply with increasing temperature, due to larger dissolution of the surfactant until the CMC. Then after CMC, the conductance increases slowly due to the increase in ionic mobility with increasing temperature [5].

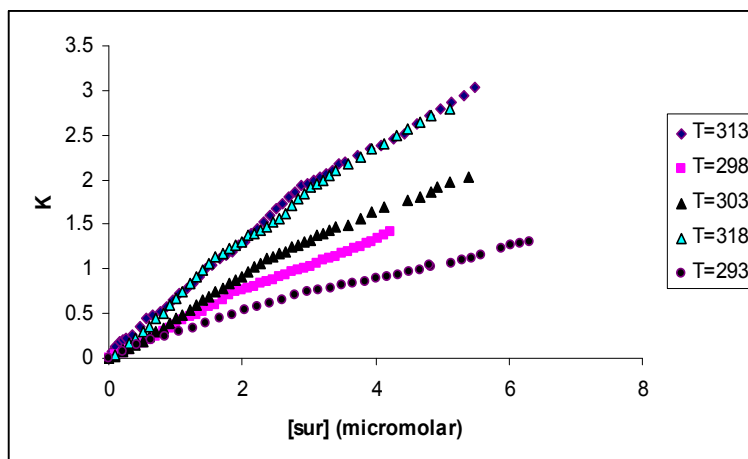


Fig. 1. The variation of specific conductometer vs. concentration of Gemini surfactant in aqueous solutions at different temperatures.

**Table 1.** The data of CMC and thermodynamic parameters of micellization at various temperatures.

T (°C)	CMC	-ΔG (KJ)	ΔH (KJ)	ΔS (J/K)	
20	2.30	73.3	72.8	498.0	0.234
30	2.52	75.0	67.8	471.0	0.203
35	2.49	72.0	69.0	457.0	0.337
40	2.91	72.0	70.4	455.0	0.347
45	2.59	73.6	73.2	462.0	0.354

The above analysis demonstrates can be extracted from conductometric experiment. The results represents the decreasing of entropy change and increasing of α with increasing of temperature. It has been found that increase in the enthalpy change with increase in temperature.

4. Conclusions

In summary, we have shown that conductometric measurements can be used to turn existing thermodynamic models into predictive tools for enthalpy determinations. Although; we have illustrated this for a simple and a self associating Gemini surfactant, there are many more potential applications for other systems. The results represent the endothermic nature of micellization process that corresponds to predominant role of hydrophobic interaction. That is also characterizing as entropy driven process. The release of bound counter ions has been increased due to increasing of temperature that can be related to less stability of micelle and increasing of internal motions.

References

- [1] Th. evenot.C , Grassl.B, Bastiat. G, Binana.W. Physicochem. Eng. Aspects 252 (2005) 105
- [2] M. Fujiwara ,T. Okano, T.-H. Nakashima ,A.A. Nakamura ,G. Sugihara. Colloid polim sci 275 (1997)474
- [3] Vikas Sharma a, Mahendra Borse a, V.K. Aswal b Journal of Colloid and Interface Science 277 (2004) 450
- [4] J. M. Koper, B. Minkenberg, J. Phys. Chem. B 113 (2009) 15597
- [5] J. Zhao, S.D. Christian, B.M. Fung, J. Phys. Chem. B 102 (1998) 7613.



A novel view of the nano-spectroscopic investigation of human serum albumin upon interaction with paclitaxel and estradiol

N. Amani ^{1*}, M.R. Saberi ², J. Chamani ¹

1. Department of Biology, Faculty of Science, Islamic Azad University-Mashhad Branch, Mashhad, Iran

2. Medical Chemistry Division, School of Pharmacy, University Complex, Mashhad, Iran

1. Introduction

Human serum albumin (HSA) is the most abundant protein in blood plasma which exhibits an exceptional ability to reversibly bind a wide range of exogenous and endogenous compounds [1]. It is also important for maintaining normal osmolarity in plasma. HSA consists of 585 amino acids with 17 tyrosyl residues and one tryptophan located in position 214. Paclitaxel is an anticancer and estradiol employ in treatment of breast cancer, hypogonadism and prevention of osteoporosis. Multiple studies on HSA structure and its interaction with different ligand exist in literature. Ghuman and co-workers have shown that the distribution, free concentration and the metabolism of various drugs can be significantly altered as a result of binding to HSA. Thus interaction with plasma proteins, especially HSA, is an important factor to consider in drug development.

Keywords: Human serum albumin; Fluorescence quenching; Paclitaxel; Estradiol

2. Methods

HSA, paclitaxel and estradiol was obtained from sigma company.

A Hitachi F2500 fluorometer was utilized to measure the fluorescence emission spectra. 0.3mg/ml HSA was dissolved in 50 mM phosphate buffer pH=7.4.

3. Results and discussion

Protein fluorescence is quenched by a ligand when the distance between the ligand and the fluorophore in protein is smaller than 7 nm. The fluorescence was strongly quenched, whereas maximum wavelength of tryptophan fluorescence of HSA shifted to shorter wavelength that show an increased hydrophobicity of the region surrounding the fluorophore sites.

The binding constant values, K and the number of binding sites, n were determined from the fluorescence intensity changes [2]. $n_1, K_{sv1}, n_2, K_{sv2}$ were noticed to be 0.9, $1.26 \times 10^{-2} \text{ LM}^{-1}$, 0.8, $7.7 \times 10^{-3} \text{ LM}^{-1}$ for paclitaxel and 0.9, $9.97 \times 10^{-2} \text{ LM}^{-1}$, 0.9, $6.48 \times 10^{-2} \text{ LM}^{-1}$ for estradiol respectively [3]. The fluorescence of HSA is quenched more intensively by paclitaxel than by estradiol. Participation of tyrosine and tryptophan groups in drug-serum albumin complexes is assessed using different excitation wavelengths. Comparison of fluorescence quenching of protein excited at 280 nm and 295 nm allows to estimate the participation of tryptophan and tyrosine group in the complex [4].

In Figure 1 the quenching curves representing 280 nm and 295 nm excitation wavelength do not overlap. This phenomenon shows that in the interaction of paclitaxel with HSA both the tryptophanyl and tyrosyl group take part.

Moreover, the quenching curves of HSA excited at 280 nm and 295 nm the presence of estradiol in Figure 2 overlap below the molar ratio 0.02 and do not overlap above it. It seems that when there are fewer than 0.02 the molar ratio only tryptophanyl residues take part in the interaction, whereas above this molar ratio tryptophanyl and tyrosyl residues participate in that.

4. Conclusions

The type of interactions of drugs to the transporting protein has been studied. The quenching of relative fluorescence of HSA by paclitaxel and estradiol, two drugs recommended for the treatment of cancer particularly brain cancer and hypogonadism, has been analyzed. It was found that both estradiol and paclitaxel have two sets of binding sites in HSA. Estradiol and paclitaxel quenched the fluorescence of HSA through static and dynamic quenching mechanism. On the basis of binding and quenching constants determined from Stern-Volmer equation it has been stated that an affinity to HSA is higher for estradiol than for paclitaxel. The interaction of paclitaxel with HSA both the tryptophanyl and tyrosyl group take part, whereas in the interaction of estradiol with HSA at first only tryptophanyl residues take part in the interaction but later tryptophanyl and tyrosyl residues participate in that.

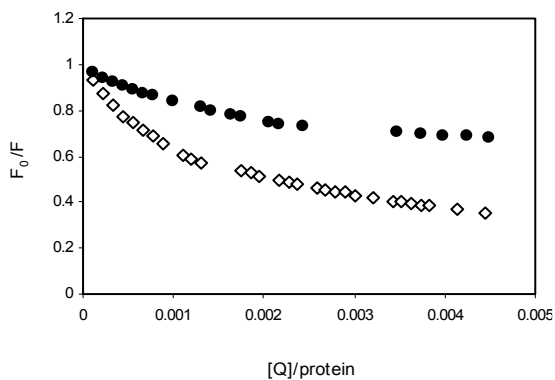


Fig. 1. Quenching curves of HSA in the presence of paclitaxel: $\diamond \lambda_{\text{ex}}=280 \text{ nm}$, $\bullet \lambda_{\text{ex}}=295 \text{ nm}$

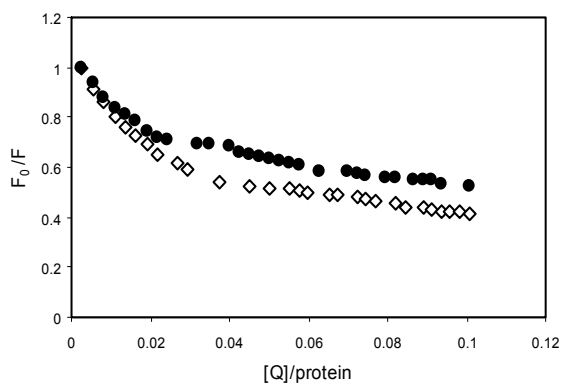


Fig. 2. Quenching curves of HSA in the presence of estradiol: $\diamond \lambda_{\text{ex}}=280 \text{ nm}$, $\bullet \lambda_{\text{ex}}=295 \text{ nm}$

References

- [1] Y. Tang, Q. Zhou, J. Xiang, J. Liao, C. Yu, H. Zhang, L. Li, Y. Yang, G. Xu, J. Colloids and Interface Science, **61** (2008) 75-80.
- [2] F. Cui, Y. Yan, Q. Zhang, J. Du, X. Yao, G. Qu, Y. Lu, J. Carbohydrate Research, (2009) In press.
- [3] C. Dong, S.M. Song, X.L. Hou, Y.B. Wu, S.M. Shuang, C. Yang, Y. Inoue, J. Luminescence, **129** (2009) 169-175.
- [4] A. Sulkowskov, M. Maciazek-Jurczyk, B. Bojko, J. Rownicka, I. Zubik-Skupien, E. Temba, D. Pentak, W.W. Sulkowski, J. Molecular Structure, **881** (2008) 97-106.



Electrolyte effect on interfacial properties and the phase transition from Microstructures to Nanostructures in Ionic/Ionic Surfactants Mixture

B. Sohrabi*, S. Fazeli, M. Moallemi

Department of Physical Chemistry, Iran University of Science and Technology, P.O. Box 16765-163, Tehran, Iran.

(Email: Sohrabi_b@iust.ac.ir, Sohrabi_b@yahoo.com)

Keywords: Catanionic mixtures; Anionic-rich; Cationic-rich; Surface tension; Surface excess concentration; Conductometry.

1. Introduction

Vesicles are double-chain surfactant aggregates that can be used as simplified models of biological membranes, drug delivery systems, and so on.¹ When electrolyte is added to a system of charged catanionic vesicles, the maximum of the interaction potential can be decreased and hence the rate of specific aggregation can be increased; aggregation increases with decreasing electrostatic repulsion. The range of the electrostatic interaction is also decreased with increasing electrolyte concentration as given by the Debye length.² we used molecular thermodynamic theory to examine mixed ionic and nonionic surfactant systems by using this theory; we could explain the experimentally observed behavior in terms of the free energy contributions to mixed micelle formation. Then, we investigated the mixed micelle and adsorption properties of binary surfactant systems containing the cationic and nonionic surfactants in presence of various concentrations of sodium bromide.

In this paper, we determined the adsorption properties of binary surfactant systems containing the cationic surfactant cetyltrimethylammonium bromide (CTAB) and the anionic surfactant sodium dodecyl sulfate (SDS) in electrolyte solution and used from the presented new model by our group for determining the properties of mixed vesicles in presence salt.

2. Methods

CTAB (Merck, 99%), SDS (Merck, 99%), Sodium bromide (Merck, 98%) and D2O (99.95%) were obtained from Merck. All samples were equilibrated at 25°C in a thermostated bath. Aqueous solutions of individual surfactants were prepared using doubly distilled and deionized water.

Surface tension measurements were carried out at 298.15 K by the ring method. In all cases, more than three successive measurements were carried out, and the standard deviation did not exceed $\pm 0.1 \text{ mN.m}^{-1}$.

Conductivity measurements of surfactant solution were made using a conductometer model Jenway 4510. The accuracy of the measurements was $\pm 0.5\% \pm 2$ digits.

The NMR self-diffusion studies were performed at 298.15 K on a Bruker 500 NMR spectrometer using an LED pulse program.³ The peaks corresponding to the N-methyl proton and the methylene groups bonded to oxygen in CTAB and SDS respectively were selected, and the surfactant self diffusion coefficients were obtained from the decreases in the heights of these peaks with increasing pulse gradient strength. The viscosities of the mixed surfactant solutions were measured by using semimicro Cannon Ubbelohde capillary viscometers immersed in a water bath of temperature 25°C. The densities of the mixed surfactant solutions were measured using a 25 mL pycnometer at 25°C.³ In all experiments, the temperature was controlled to within $\pm 0.1^\circ\text{C}$ by circulating thermostated water through the jacketed glass cell in 25°C.

3. Results and discussion

To account for the electrostatic interactions between the oppositely charged surfactant head groups in the vesicle, we calculate the electrostatic free energy contribution, g_{elec} for vesicles in catanionic mixtures using a capacitor model. Also, we determine the transform free energy for vesicles in catanionic mixtures. Figure 1 shows the variations of electrostatic and transform free energy in CTAB concentration for transition from vesicle to mixed micelle in cationic-rich in $C_{NaBr}=0.001 \text{ M}$. According to this figure, electrostatic and transform energies decrease when vesicle transform into mixed micelle. The addition of CTAB decreases the mixed micelle electrostatic free energy due to growth of mixed micelles, while transform free energy is almost constant because this energy relates to hydrophobic hydrocarbon chain. Transform energy is a favorable energy for the formation of vesicles and mixed micelles. The studies show that the composition in a catanionic vesicle is partly controlled by electrostatic free energy, which, in turn depends on the ionic strength of the solution. Also, our experimental observations have shown variations in vesicle size and surface potential with concentration of added salt.

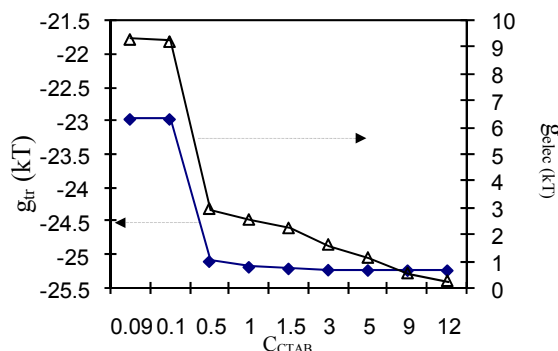


Fig.1. The variations of electrostatic and transform free energy in CTAB concentration for transition from vesicle to mixed micelle $C_{NaBr}=0.001$ M.

The investigations shows that β^M decreases with increasing ionic strength; this can be attributed to increased shielding of the repulsion between head groups in solutions of higher ionic strength. The average value of β^{σ} is more negative than β^M , which is calculated by regular solution theory, indicating stronger synergism in the mixed monolayer than in the mixed micelle.

4. Conclusions

The studies show that in the presence of solvents that remain mainly in the bulk phase of micellar solution and with a dielectric constant lower than water, the changes in the magnitude of the Gibbs free energy contribution associated with the transfer of dodecyl chains from bulk phase into the micelle of interior are the main factor controlling the value of ΔG_{mic}^0 as well as its variations upon changing the vol. percent of EG. On the other hand, the adsorption data in the air-liquid interface showed that the adsorption of surfactant becomes less spontaneous at higher content of EG.

References

- (1) Kaler, E.; Herrington, K. L.; Murthy, A. K.; Zasadzinski, J. A.; Chiruvolu, S. J. Phys. Chem. **1992**, 96, 6698.
- (2) Israelachvili, J. N. Intermolecular and Surface Forces; Academic Press: London, **1992**.
- (3) B.Sohrabi, H. Gharibi, S. Javadian, M. Hashemianzadeh, J. Phys. Chem. B. **2007**, 111, 10069.

A Non-Radioactive Electron Capture Detector for GC

*M. Tabrizchi^a, H. Bahrami^a

^aDepartment of Chemistry, Isfahan University of Technology, Isfahan, Iran

(Email: m-tabriz@cc.iut.ac.ir)

Keywords : Electron Capture Detector, Gas Chromatography, Electron Source, Discharge

1. Introduction

For many years, there has been a strong desire to develop gas chromatographic detectors that detect only specific elements. Among the different types of detectors used for a gas chromatograph, electron capture detectors (ECD) are useful for the detection of electron attaching compounds, such as halogens and nitro-compounds. ECD is the only detector that detects CFCs and chlorine-containing pesticides at trace levels ¹.

Conventional ECDs usually use a radioactive ionization source in form of ⁶³Ni foil ². Usually working with such materials is not very safe and there is always a risk of radioactive contamination. Thus regular leak test and special safety regulations are required. Therefore licensing and waste disposal are required which limits the acceptance of GCs equipped with such detectors in the market place. Another problem which is associated with the use of a radioactive isotope is that in case of depositing unwanted materials, the interior of detection cell cannot be washed easily because it requires a special procedure. Several other electron sources have been suggested as alternatives for the radioactive ⁶³Ni. In this work we explain the use of a novel electron source based on corona discharge in nitrogen as an alternative to radioactive ⁶³Ni in electron capture detector.

2. Methods

In this work negative corona discharge was used as the electron source. Corona discharge is a relatively low-power electrical discharge that takes place at atmospheric pressure. It is generated by applying a high voltage to a sharp metal point that can create a stream of electrons, ionize the carrier gas molecules, and provide a high concentration of ions. When the needle is negative and the buffer gas is nitrogen, the needle produces a huge number of electrons such that the discharge current grows as high as 200 μ A. However, the presence of any electron attaching substance suppresses the discharge and quenches the production of electrons. In this work the source is specially designed such that the sample will not interfere with the discharge. Thus electrons are continuously produced regardless of the presence of electron attaching substances. This objective was achieved by use of a curtain plate, with a small hole, in front of the needle electrode. A shield gas (pure nitrogen) was flowing to prevent penetration of the GC effluent into the corona region. The design is shown in Fig.1.

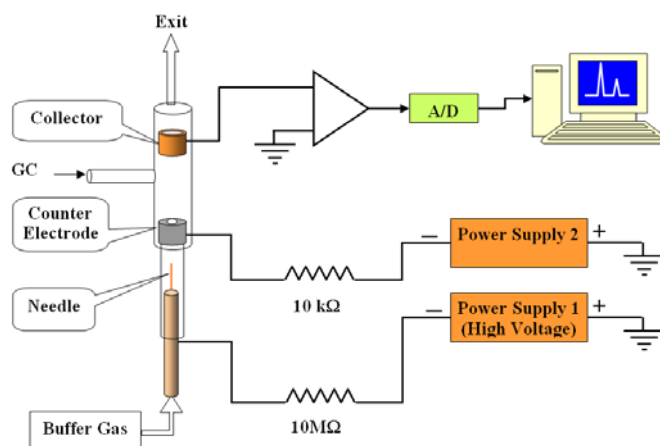


Fig.1. Schematic diagram of the new electron capture detector.

3. Results and discussion

In this design the electron source is separated from the ionization region so that the sample which may exist in the GC effluent can not enter the electron source. Since the electron source is located in a separate space, any contact of the sample gas with the interior space of the electron source is prevented by a flow of nitrogen gas through the electron source. This

guaranties stable and continues production of electrons regardless of the constituents in the second chamber. Electrons, however enters the second chamber where negative ions are formed by electron attachment to neutral molecules.

All the experimental conditions including; the shield gas flow rate, the corona discharge current, the voltage between the curtain plate and collector and temperature were optimized to see the best stability and signal/noise ratio. The detector was successfully coupled to an existing commercial GC (Accuspec model compact II). As test compounds, chloroform and dichloromethane were injected to the GC and the response of the detector was recorded. Fig. 2 shows the response of the detector to a mixture of chloroform (100 ng) and dichloromethane (100 ng). The O₂ peak is due to diffusion of air into the mixture during the preparation of the sample.

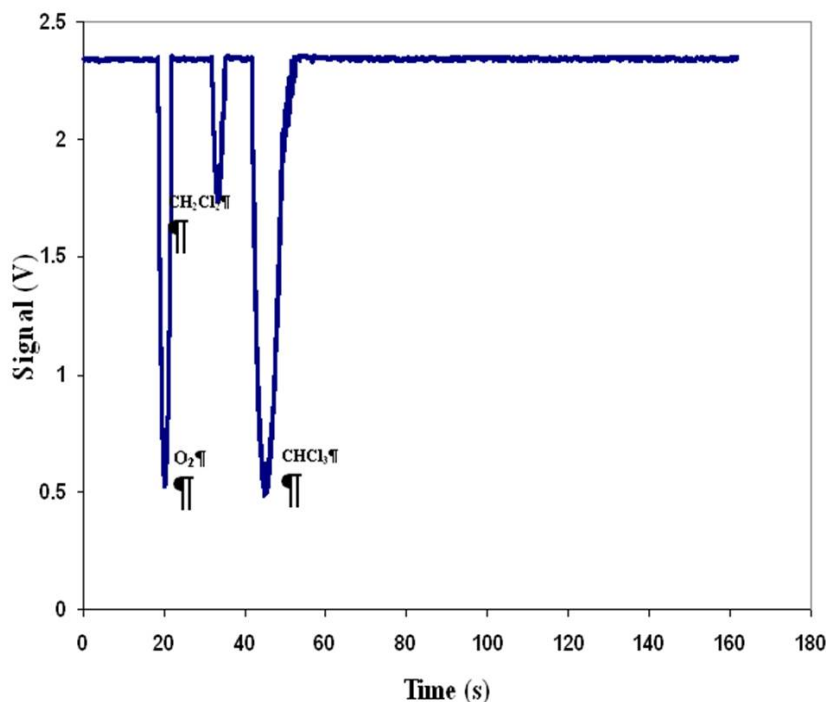


Fig.2. A chromatogram of 100 ng chloroform and 100 ng dichloromethane recorded with the new ECD detector.

4. Conclusions

In this work a non-radioactive electron capture detector was constructed. The detector has a stable electron current which is not affected by the effluent coming from the GC column. It is simple, cheap and safe to be used in the commercial GC's. The detection limit is about 33 pg for chloroform, which is comparable to that reported for ECD's in the literature³. This work was patented both in Iran (45135) and United States (US20090242783).

References

- [1] Skoog, D.A., Holler, F.J., and Nieman, T.A., Principles of Instrumental Analysis, Saunders College Publishing, fifth edition, July 1997.
- [2] Patterson, P.L. and Creek, W., U.S. Patent, No. 4063156, 1977.
- [3] Olansandan, T. A., and Hidetsuru M., Talanta 50 (1999) 851.



The study of structural properties, aromatic stabilization energy and NBO analysis of indole and related analogs via quantum mechanics calculations

A. Bodaghi^{a,*}, S. Jameh-Bozorgchi^{a,b}, J. Hosseini^a, H. Shirani^{a,b}, R. Moradi- Bighashi^c

^aDepartment of Chemistry, Islamic Azad University, Toyserkan Branch, Toyserkan, Iran

^bDepartment of Chemistry, Islamic Azad University, Arak Branch, Arak, Iran

^cYoung researchers Club, Islamic Azad University, Toyserkan Branch, Toyserkan, Iran

*(Email: albodaghi@yahoo.com)

Keywords: Ab Initio, Indole, ASE, NBO, NICS

1. Introduction

Benzo-fused 5-membered heterocyclic compounds are interesting subject for study, because these are very effective reagents in organic syntheses. Indole fragments are featured wide variety of pharmacologically and biologically active compound [1]. Aromaticity of benzo and dibenzo-fused Pyrrole, Furan and Thiophene derivatives has been examined via their NICS values calculated at HF and DFT theory levels [2,3]. few concepts are as frequently used as aromaticity in the current chemical literature. nucleus-independent chemical shifts (NICS), has become the most widely used aromaticity probe due to its simplicity and efficiency. The natural bond orbital (NBO) analysis of donor - acceptor interaction shows the resonance energy $\pi \rightarrow \pi^*$ delocalization. The aromatic stabilization energy (ASE) reveals higher stability of compound. In this research, ASE, NBO and NICS calculations were carried out for compounds 1-3 with using GAUSSIAN 03 package of programs [4-6].

2. Methods

Ab initio calculations were performed using HF/6-311+G** levels of theory with the GAUSSIAN 03 package of programs [5] implemented on a Pentium – pc computer with a 550 MHz processor. Firstly, the considered models were allowed to fully relax during the geometrical optimization by the HF exchange – functional method. Secondly, the NBO and GIAO calculations were carried out on the three geometrically optimized compounds by HF method and the above mentioned standard basis set.

3. Results and discussion

The results of calculations show that ASE of compounds 1 to 2 and 3 in the gas phase are: 60.86, 51.37 and 50.43 Kcal/mol, respectively (table 1). Also, the ASE values of compounds 1-3 in the DMSO solvent are: 61.07, 50.42 and 49.65, respectively. The optimized geometries at HF/6-311+G(d,p) level of theory were used for calculation of NICS values, the results have summarized in table 2. Furthermore, the NBO results revealed that sum of the resonance energy for $\pi \rightarrow \pi^*$ delocalization of compounds 1-3 in the gas phase are: 273.08, 307.47, 302.75 Kcal/mol, respectively and in the DMSO solvent are as follow: 286.22, 306.91, 306.63 Kcal/mol (table 3).

Table 1. The ASE (Kcal/mol)Calculated by HF/ 6-311+G (d,P)

Indole		Phosphindole		Arsindole	
DMSO	GAS	DMSO	GAS	DMSO	GAS
61.071124	60.857586	50.416990	51.367778	49.649683	50.427783

**Table 2.** The NICS value (ppm) calculated by GIAO-HF/ 6-311+G (d,P)

	Indole		Phosphindole		Arsindole	
	6-membered	5-membered	6-membered	5-membered	6-membered	5-membered
	ring	ring	ring	ring	ring	ring
NICS(0)	-10.6575	-12.5498	-9.3160	-1.6706	-8.9874	-0.8691
NICS(0.5)	-11.8840	-12.2785	-10.8843	-3.1057	-10.8389	-2.0256
NICS(1)	-11.4288	-9.9084	-10.9849	-3.7648	-11.0891	-2.7360
NICS(1.5)	-8.4261	-6.7072	-8.1502	-3.0984	-8.2662	-2.4763

Table 3. The sum of NBO (Kcal/mol) Calculated by NBO- HF/ 6-311+G (d,P)

Indole		Phosphindole		Arsindole	
DMSO	GAS	DMSO	GAS	DMSO	GAS
286.22	273.08	306.91	307.47	300.63	302.75

4. Conclusions

The quantum chemical calculations show that the order of stability of compounds 1-3 both in the gas phase and DMSO solvent is : 1>2>3, also indole in the DMSO solvent is more stable than gas phase, but Phosphindole and Arsindole are more stable in the gas phase than solution. The findings revealed that negative values of NICS for Indole is greater on 5-membered ring but for related analogs is greater on 6-membered ring. The NBO analysis based on the optimized ground state geometric using the resonance energy associated with $n \rightarrow n^*$ delocalization increasd from compound 1 to 3 and 2, in the gas phase and the DMSO solvent (The order of this parameter is: 2 > 3 > 1).

Acknowledgment

This research was supported by the Islamic Azad University , Toyserkan, Toyserkan, Iran.

References

- [1] R. j Sundberg,. The Chemistry of Indole; Academic Press; New York, (1996).
- [2] M. Zora, I. Ozaka, Journal of Molecular Structure: THEOCHEM, 638, (2003), 57-162.
- [3] N. Sundarganes, H. Umamaheswari, B. Dominic Joshua, M. Ramalingam, Journal of Molecular Structure: THEOCHEM, 85, (2008), 84-93.
- [4] Z. Chan, C. S. Wannere, C. corminboeuf, R. Puchta, and P. V. R. Schlyere, Chem. Rew, 105 (2005), 3842-3888.
- [5] M. j. Frisch et al. GAUSSIAN 03, Revision C. 01, Gaussian Inc., Wallingford. CT, (2004).
- [6] N. H. Martin, J. E. Rowe, E. L. Pittman, Journal of Molecular Graphics and Modeling, 27 (2009), 853-859.



Author Index

A

Abareshi, M. 501
Abbas Rafati, A. 457
Abbasinia, M. 215
Abbasnejad, S. 143
Abbaspour, M. 187
Abdollahi, R. 339, 363, 365, 367, 369
Abdossamadi, N. 561
Abedi, M. 783
Abedini Khorrami, S. 463
Abedini, E. 97
Abedini, H. 801
Aboulhasanlo, G. 41, 507
Abroshan, H. 713, 727
Abyar, F. 287
Adib, B. 771
Afshari, Z. 395
Aghabozorgi, F. 525
Aghaie, H. 75, 777
Aghazadeh, M. 283
Aghdaei, E. 383
Ahmadi, S. J. 631
Ahmadian, N. 617
Ajloo, D. 701
Akbari-Borhani, H. 471
Akbari Golroudbari, S. 37
Akbarzadeh, H. 713, 727
Akhavan, M. 747
Akhbari shada, M.H. 583
Akvan, F. 793
Alata, I. 317
Alavi, S.
5, 39, 697, 709, 725, 733, 741
Alipour, M. 235
Alizadeh, E. 713, 749
Alizadeh, M. M. 757
Alizadeh, N. 729
Alkorta, I. 529

Almassian, M. 821
Amani, N. 843
Amini, A. 93
Amiri, M. 261, 761
Amiri, R. 831, 841
Amirseifadini, F. 709, 725, 741
Amjad Iranagh, S. 413
Anjomshoa, E. 233
Arab Chamjangali, M. 739
Arabbagheri, A. 707
Arabieh, M. 545
Asad Samani, K. 625
AsadAbadi, S. 437
Ashoori, M. 241
Ashouri, M. 737
Ashrafi, F. 31, 69, 93, 141, 687
Ashrafizaadeh, M. 697, 733
Asli, N. 543
Assaran Darban, R. 305
Azami, S.M. 229
Azimi, S. 621
Azizi Toopkanlu, H. 151
Azizian, S. 395, 399, 415

B

Babaei, J. 417
Babaei, S. 25, 137
Babashpour, S. 121
Bagheri, A. 403, 405
Bagheri, N. 231
Bagheri, S. 555
Bagherzadeh, M. 801
Bahadori, A. 9, 73, 607
Bahrami, H. 847
Bahramifar, N. 31, 69, 93, 141
Bahrololoom, M. 827
Bahrpaima, Kh. 89

Bakhshandeha, A. 181
Balilehvand, S. 699, 715
Banaei, A. 513
Barati, A. 79
Bavafa, S. A. 247, 249, 251
Bayat, M. 661
Bayat, Z. 555, 561, 569, 677
Bazzi, S. 649
Behboudnia, M. 453
Behjatmanesh-Ardakani, R.
173, 247, 251, 597, 599,
829, 833
Behjatmanesh-Ardekani, R.
185
Behnejad, H. 181
Behzad Khoshgouei, M.
823, 825
Benvidi, R. 811
Bezaatpour, A. 27, 81
Bodaghi, A. 577, 849
Bordbar, A.K. 831, 841
Bozorgmehr, M.R. 327, 329
Bresme, F. 743
Broquier, M. 317

C

Chahkandi, B. 647
Chakraborty, Sh. 317
Chamani, J.
33, 291, 299, 305, 327, 329, 331,
333, 827, 843
Choobdari, E. 133

D

Dabbagh, H.A. 527, 587, 615
Dadashbeygi, M. 371



Dadfar, M. 49
 Dadfar, O. 749
 Dahmardeh, S. 543,553
 Daneshdoost, V. 605,
 627,665
 Daneshfar, A. 465,479,487
 Dardab, M. 589
 Darvishpour, M. 601,765,767
 Darvishzad, T. 281
 Darzi, M. 289
 Davari, M. D. 619, 673
 Davari, N. 669
 Davoodi, S. 67
 Dedonder, C. 317
 Dehestani, H 267
 Dehestani, M. 265,
 269,323,679
 Deilam, M. 155
 Deyhimi, F 35,133,783
 Dezhampanah, H. 281,283
 Diarmand, H. 171

E

Ebadi, M. 223
 Ebady, A. 597,599
 Ebrahimi, A.
 277,293,383,385,389,639,64
 9,675, 691
 Ebrahimian Pirbazari, A. 17
 Ebrahimzadeh, M. 819
 Ehsani, A. 785, 795, 797,799
 Elhami, R. 81
 Emadian, M. 677
 Emamia, M. 541
 Entezari, M. H. 503
 Esfandiari, H. 657
 Eshtiagh Hoseini, H. 813
 Eskandari, K. 263
 Eslami, H. 705, 467,717
 Esmaeili, B. A. 195, 197

Esmaili, E. 359
 Esmaili-Taramsari, M.
 509,613

F

Fakhari, F. 31
 Fakhraee, S. 655
 Fakoor, M. 555
 Fallah, H. 719
 Fani, S.L. 5
 Farajtabar, A. 15,55,65
 Faramarzi, E. 87
 Farjamnia, A. 633
 Farmanzadeh, D. 259
 Farrokhnia, M. 205
 Farrokhpour, H.
 159,287,303,527
 Farshchi Tabrizi, F. 801
 Farzi, N. 77
 Fathi, F. 287,311
 Fazeli, S. 845
 Fekri, M. H. 601,765,767
 Felegari, Z. 427
 Foroutan, M. 455,
 461,471,489, 493, 511

G

Galavy, M. 397, 419, 421,
 423
 Ganji, M. D. 477
 Geimachy, G. 83
 Ghaderiyeh-Mahmood Abadi,
 F. 173,833
 Ghaempanah, A.595
 Ghahghayi, Z. 639, 675
 Ghalami –Choobar, B. 769
 Ghalehaghbababaei, Sh. 701
 Ghanadzadeh, A.
 89,143,283,309
 Ghanadzadeh, H. 89,143

Ghanbari, F. 393
 Ghannadi-Maragheh, M. 545
 Gharahbeigi, M. M. 161
 Gharangian, S. 449
 Gharib, F.
 15,21,55,65,71,121,127,353,
 759,805
 Gharibi, M. 637
 Ghasemi, M. A. 571, 671
 Ghasemi, Sh. 355
 Ghasempour, H. 639, 675
 Ghattee, M.H.
 19,139,179,199,273
 Ghayeb, Y. 449
 Ghazanfary, S. 259
 Gheisari, A. 153
 Ghiasi, M. 431
 Gholami, M. R. 355
 Gholami, F. 477
 Gholami, M. R.
 45,355,817,835
 Gholamireza, A. 45
 Ghows, N. 503
 Giahi, M. 393,777
 Gohar, M.J. 611
 Goharshadi, E. K.
 151,187,501
 Gorji, A. 723
 Goudarzi, A. 447,481
 Gyan,H. 683

H

Ha, Ch-Sik 447,481
 Habibi Khorassani, S. M.
 277, 293,383,385, 389,639,
 675, 691
 Habibi Khorassani, M. 649
 Habibi, M. H. 297,321
 Habibi-Yangjeh, A. 343,
 453,469, 475,491,509,613
 Hadidi, R. 493



Hagealirezahi, M. 643
 Haghani, A. 277
 Haghdad, S. 451
 Hajian, A. 415
 Hajmalek, M. 21
 Hakimelahi, R. 75
 Hamadanian, M. 217, 245, 253, 521, 525, 533, 535, 537, 559, 575
 Hamed-Akbari Tousi, S. 291
 Hamoule, T. 409, 433
 Hamoule, T. 401
 Hamzehloo, M. 183
 Harifi-Mood, A. R. 817
 Hasanifard, C. 365
 Hasanzadeh, M. 567
 Hashemi, F. 653, 667
 Hashemi, H. 137
 Hashemi, S. 149, 373
 Hashemian, S. 373
 Hashemianzadeh, S. M. 609, 699, 715
 Hashemianzadeh, S. Majid 457
 Hassan Dad, M. 373
 Heiatian, E. 9
 Heidari, A. 513, 837
 Heidari, F. 163, 165
 Heidari, N. 773
 Heidary, N. 775
 Heydari, M. 79, 267
 Heydarpour Serajeh Lou, E. 345, 387
 Hooshyar, H. 681, 683
 Hooshyara, H. 583
 Hoshyar, H. 435
 Hosseini, J. 577, 849
 Hosseini, M. G. 789
 Hosseini, S. 119, 191
 Hosseini, S. M. 57, 123, 125
 Hosseini, S.M.A. 261, 505, 757, 761, 803,

Hosseini, Se. 77
 Hosseinnejad, T. 631
 Hosseinpour, R. 535
 Housaindokht, M. R. 299, 813, 827

I

Ighaei, M. 49
 Ilbeigi, V. 301
 Iloukhani, H. 61, 63, 109, 129
 Imanzadeh, M. 805
 Izadi, F. 13
 Izadi, Z. 303
 Izadyar, M. 359

J

Jabbari, M. 15, 55, 353
 Jabbaria, M. 541
 Jafari, A.H. 505
 Jafari, Sh. 399
 Jafarian, M. 779, 785, 795, 797, 799
 Jafari-Zare, F. 343
 Jahanbin Sardroodi, J. 17
 Jahanbin Sardroodi, J.r. 685
 jahanbin, J. 49
 Jahromi, R. 273
 Jalajerdi, R. 443
 Jalal, R. 813
 jalali, E. 595
 Jaleh, B. 399
 Jalili, A. H. 171
 Jalili, S. 257, 473, 499, 703, 719, 721, 723, 729, 735, 747
 Jamalizadeh, E. 261, 505
 Jameh-Bozorgi, S. 113
 Jameh-Bozorgi, S. 23, 551, 577, 579, 595, 601, 605, 627, 629, 657, 665, 849

Jamialahmadi, M. 321
 Jamshidi, N. 141
 Jamshidi, Z. 221
 Javadian, S. 539, 623
 Javanmardi, J. 25
 Jazan, E. 341, 815
 Jebali, F. 91
 Jouvét, Ch. 317

K

Kabiri, M. 329
 Kaboli, Z. 355
 Kalantar, Z. 175, 177, 195, 197, 225, 227, 739
 Kalantary-fotooh, F. 559
 Kamalvand, M. 167, 169
 kanaani, a. 319
 Karami, L. 735
 Karamiyar, A. 617
 Karimi Jafari, M. H. 241
 Karimi, A. 487
 Karimi, H. 517
 Karimi, N. 29
 Karimian, R. 625
 Karimi-Jafari, M. H. 241, 545, 631, 633, 737
 Karimpour, N. 397, 419, 421, 423, 429
 Kavian, H. 465, 479
 Kazeman, I. 567
 Kazemian, M. A. 691
 Keshavarz, M. H. 571, 671
 Keshavarzi, E. 163, 165, 167, 169, 189, 449
 Khalili ghaydar, H. R. 113
 Khanahmadzadeh, S. 435, 681
 Khanlarzadeh, K. 129
 Khanpour, M. 193
 Kharazian, B. 257



Khatam, I. 47
 Khezri, B. 583
 Khezrir , B. 435
 Khodabandeh, M. H. 673
 Khodadadi- Moghaddam, M. 469
 Khorrami, M. 225,227
 Khoshbakht, M. 83
 Khoshnevisan, B. 559
 Khosropour, A.R. 831,841
 Kia, R. 255
 Kiani, F. 71,73,607
 Kiani, M. 185
 Kordi Peykani, M. 581
 Koutchakzadeh, Gh. 425
 Kowsari, M. H. 697,733

L

Laleh, S. 297
 Lesani, M. 263
 Loghavi, M. 709,725,741

M

Madadi Mahani, N. 381
 Madani, Gh. 339
 Maftoon-Azad, L. 145
 Maghari, A. 153,157,171,183,191,239,241,633
 Maghsoodlou, M. T. 277, 293, 383,385, 389, 639,675,691
 Mahanpoor, K. 407, 411,439
 Mahjani , M.G. 485,779, 785,795,797,799
 Mahmoodi Asl , S. 567
 Mahmoodinia, M. 243
 Mahmoudzadeh, S. 53
 Majles Ara, M. H. 479
 Makiabadi, B. 549, 641,643

Malekhoseani, H. 411, 439
 Maleki, A. 703
 Maleki, V. M. 239
 Mansoori Kermani, M. 679
 Mashhadi khoshkhoo, Z. 813
 Masoudi, M. 159
 Masoumi, E. 493
 Massahi , Sh. 529,585
 Mazarei, E. 375
 Mehdipour, N. 717
 Mehdizade, S. J. 555, 569,677
 Milani Moghaddam, H. 445, 547,621,653,667
 Miremad, H. 285
 Miremad, S. H. 573
 Mirhoseini-Abran Abadi, S. M. 833
 Miri, N. 801
 Mirtababaei, H. 813
 Mirzaei, A. A 397,419, 421,423,429
 Mirzaei, F. 537
 Mirzaei, M. 813
 Mirzaei, R. 839
 Mirzaie Milani, F. 489
 Moallemi ,M. 845
 Moazzami, M. 121
 Modarress, H. 413
 Moeini, V. 11,155
 Mofidi , J. 793
 Mofidi, F.759
 Moghadam, B. 635
 Moghadari, M. 209
 Moghadasi, J. 125,185,517,705
 Mohajeri, A. 223, 235,243,645, 669,687
 Mohamadimanesh, H. 709
 Mohammad pour, I. 841
 Mohammad-Aghaie, D. 743
 Mohammadi, M. 383,625

Mohammadi, S. Z. 651
 Mohammadimanesh, H. 5, 39,725,741
 Mohammadpour Baltork, I. 831
 Mohammadtabar, N. 811
 Mohammadzadeh Bahar, H. 463
 Mohammadzadeh Jahani, P. 207,543,553
 Mokhtari, H. 161
 Mokhtari, M.809
 Mokhtarpour, M. 773,775
 Mollaie Poli, F. 829
 Mondanizadeh, M. 593
 Moosavi, F. 199,273
 Moosavi, M. 99
 Moradi- Bighashi, R. 849
 Moradi, A. 485, 787
 Moradi, M. 149,161,819
 Moradi, Sh. 463
 Mortezaheb, H. 459,483
 Mortezaheb, H. R. 515
 Moshari, M. 455
 Mossazade Rostamkolahi, A. 135
 Mostafa, B. 107
 Motahari, A. 527
 Motalebipour, M. 637
 Motedayen Aval, G. 447
 Motiee, M. 117
 Mousavi, M.213
 Mousavi, S.A. 713
 Mousavipour, S. H. 375, 377
 Mousazadeh, M. H. 87
 Mozaffari, F. 705
 Mulder, M. F. 295
 Müller-Plathe, F. 467

**N**

Nabavizadeh, S. M. 95
 Naderi Mighan , S. 801
 Naderi, H. 483,515
 Naeemy, A. 797
 Naghavi, F. 307
 Nahali, M. 187
 Najafi, B.
 5,39,697,703,709,725,733,74
 1
 Najafi, M. 563
 Najafi, V. 53
 Najafic, A. R. 541
 Najafpour, J. 557,581
 Najjar, R. 789
 Namayandeh Jorabchi, M.
 187
 Namazian, M. 215
 Namdari, F. 101
 Namdari, H. R.
 Nami, F. 35
 Nasiri, Sh. 293
 Nasiri, T. 769
 Nasirian, Sh. 445
 Nasr Isfahani, V. 219
 Nasrifar, Kh. 7
 Nasrollahzadeh, Z. 357
 Nasseh, S. 217
 Nayeb Hosseini, M. R.
 347,351
 Nazarpour, E. 563,619
 Nejatpoor, M. 677
 Nekoei, A. R. 285,325, 573
 Nemati Kande, E. 131
 Nemat-Talab , H. 577
 Neshati , J. 771,793
 Niazi Hesar Sefeedi, N.
 407,411,439
 Niazi, A. 9,53,117
 NikAzar, M. 837
 Nikmaram, F. R. 581

Nikoofard, H.
 175,177,195,197,225,227,73
 9
 Nilchi, A. 41,507
 Niroomand Hosseini, F. 95
 Nojini, Z. B. 457,609
 Noorani, N. 211
 Noorbala, M. R. 215
 Noorinezhad, M. 539,623
 Noorizadeh, S. 531, 589, 591,
 593
 Noormohammadi, M. 819
 Nori-shargh, D. 73
 Norouzi ,Sa. 561
 Norouzi Bakhsh, M. 347,351
 Norouzi, So. 561
 Nowroozi, A. 207,543,553

O

Oftadeh, M.
 203,209,217,219,237,245,25
 3
 Ohanessian, G. 673
 Omidi, S. 539, 623
 Omidyan, R. 287, 317
 Omrani, A 781, 787,809
 Osouledini, N. 105
 Padervand, M. 835

P

Pakiari, A. H. 205,213,231
 Papari, M. M. 57,125,185,517
 Parsa, H. 591
 Parsafar, G. A.
 101,103,193,713,727
 Parsafar, Gh. A. 707
 Parsi, E. 51
 Peyrovi , M. H. 401,409,433
 Pirhadi, F. 377
 Poorakbar-Esfahani, E. 43

Poorsargol, M. 207,543,553
 Porgham Daryasar, M. 557
 Pourgonabadi, S. 33
 Pournaghdy, M. 777

Q

Qanei nasab, S. 569

R

Rabiei, R. 709,725,741
 Rad, H. 337,361
 Radhoosh, M. 253
 Rafati, A. A. 403,405,427,
 497,609
 Rafatpanah, S. 605,627,665
 Rafi Dargahi , M. 349
 Rafi Dargahi, A. 349
 Rafiei, Sh. 381
 Rahemi, H. 211
 Rahimi Galugahi, M. 731
 Rahimi, H. 155
 Rahmani, S. 791
 Rahmani, Z. 323
 Rahmati Far, M. 85
 Rakhshi, M. 61,63,109
 Ramazani, Sh. 379
 Rashidi, F. 153
 Rashvand avae, M. 779
 Rasouli Garmarodi, S. 41,507
 Rassoli, N. 3
 Rastegar, M. 515
 Rastgar, M. 483
 Rasti , E. 615
 Rasti, S. 237
 Rastkar Ebrahimzadeh, Al.
 685
 Razavi, R. 761
 Razavi, S. 699,715
 Razavizadeh, S. A. 59



Reisi-Vanani, A. I 521

Reissi, M. 3

Reshadi, P. 7, 137

Rezaei Sameti, M.

61, 63, 109, 565, 659, 661, 663

Rezaei-Behbahan, G. 43

Rezayee, T. 175, 177

Rezazadeh, R. 451, 495

Rezazadeh, M. A. 495

Rezvani, A. R. 823, 825

Riazi, M. H. 513

Roohi, H. 233, 249, 549, 635,

641, 643, 689

Rostami, A.A.

71, 135, 607, 781, 787, 809

Rostamian, R. 497

Rostamiyan, R. 89

Rouhbakhsh Zaeri, Z. 827

S

Sabaghian, M. 299

Saber, M.R.

33, 291, 299, 331, 333, 843

Sabour, B. 409, 433

Sabourb, B. 401

Sabouri, M. 739

Saboury, A. A. 43, 313

Sabri, M. 491

Sabzi, F. 123, 137

Sabzyan, H. 603, 693

Sadeghi, R.

45, 51, 107, 115, 433, 681, 683, 6

95

Sadeghi, S. 153, 157

Saed, B. 603

Safarpour, M. A. 275, 837

Safdari, F. 103

Sahraei, R. 447, 479, 465,

487, 481

Saidi, S. 245

Saien, J. 437

Sakeni Alvanag, S. 773

Sakeni, S. 775

Salabat, A. 79, 85

Salabat, S. 519

Salari, A. A. 557

Salari, H. 817

Salari, M. 757, 803

Salehi Rad, A. R. 823, 825

Salehi, H. 839

Salehi, R. 689

Saleh-Moghadam, M. 305

Salehzadeh, S. 661

Salemi, S. 285, 319

Samiee, S. 457

Samiey, B. 349

Samimi, R. 749

sam-salari, S. 293

Sanatgar-Delshad, E. 469

Sardashti, A. 771

Sarfi, S. 487

Sarzehi, S. 327

Sayahi, H. 459, 483

Saydi, H. 519

Scheiner, S. 585

Sedaghat, F. 163

Seif, F. 571, 671

Seifi, S. 127

Sengers, J. V. 181

Setamdideh, D. 683

Setareh, M. 471

Seyed Hosseini, B. 647

Seyed Sadjad, M.A. 75

Seyed Sadjadi, S. A. 513,

791

Shabani shayeh, J. 779

Shadman, M. 731, 745, 751

Shafiee, A. 47

shaghaghi, H. 295, 311

Shahabi, S. 115

Shahamirian, M. 645

Shahebrahimi, Y. 695

Shahidi, M. 505

Shakerzadeh, E. 531

Shamel, A. 83, 121, 127, 805

Shamlouei, H.R. 271,

611, 625

Sharafi, Z. 255

Shariati, F. 653

Shariati, F. 667

Sharif, M. 575

Sharifi, A. 785

Sharifi, S. 9, 71, 73, 117, 607

Sharifzadeh, Z. 269

Sharyari, S. 397

Shayesteh, A. 315

Shekaari, H. 27, 81, 91

Shekarsaraee, S. 143, 309

Shekoohi, Kh. 19

Sherafati, R. 567

Shibaninia, M. 207

Shiralinasab, S. 755

Shirani, H.

23, 551, 577, 579, 849

Shirvani-arani, S. 631

Shojaei Baghini, S. 265

Shokri, N. 465

Siami, A. 11

Sohrabi, B. 845

Sohrabi, N. 3, 755

Sokhanvaran, V. 711

Sokhanvary, E. 111

Soleymani, R. 629

Solimannejad, M. 529, 585

Soltanabadi, A. 711

Soltani, N. 763

Soltanpour, A. 27

Soufi, A. 411, 439

T

Tabrizchi, M.

97, 287, 289, 301, 303, 341, 815,

847

Tafazzoli, M. 295, 311



Taffazoli, M 431
Taghavi Nasrabadi, A.
461,511
Taghizadeh, A. 189
Taghizadeh, M. T. 337,
339,345, 357, 361, 363, 365,
367, 369, 371,387
Taghvaei, V. 453
Taheri, S. 431
Taherpour, A. 443
Tajdini, N. 119
Tamannaee, M. 841
Tarkashvand, A. 417
Tasviri, M. 835
Tavakolizadeh, L. 203
Tavangar, Z. 693
Tavasolli, M. 69
Tayarani, M. 653,667
Tayyari, S. F.
297,307,319,321,325
Teimouri, A. 763
Teimourib, A. 541
tiani Moghadam, S. 85
Toosi, M. R. 401,477
Toufani, S. 837

V

Vahdani, S. 677
Vahedian- Movahed, H.
305,331,333
Vahedpour, M. 729
Vahid, S. 397, 419,421, 423
Vahidi Ferdowsi, A. 721
Vakili, M. 285,319,325,573
Vali pour, A. 533
Vaziri, R. 473,499
Yaghoobie notash, M. 685

Y

Yasar, B. 117

Yazdanbakhsh, M. 321
Yazdi, Z. H. 275
Yazdizade, N. 781
Yeganegi, s.
135,711,731,745,751
Yousefi, F. 517

Z

Zafarani-Moattar, M.T.
13,29,67,131
Zahedi, M. 563,545,619, 673
Zakarianejad, M. 383,385,
389
Zamani, M. 527, 585,651
Zamani, Z. 271
Zanoozi, M. 569
Zardari, P. 789
Zare, H. R. 755
Zare, K. 21,673,681
Zare, M. 139
Zarei, H. A. 37,111
Zarei, V. 401, 409,477
Zarganian, R. 831
Zariny, H. 263
Zebarjad, S. M. 501
Zhang, R. 821
Ziaie, F. 745,751
Zolfaghar, N. 665
Zolfaghari, A. 459,483
Zolfaghari, A. R. 515
Zolghadr, A.R. 179
Zolghadri, S. 313

شرکت مبنا طیف

در سال ۱۳۸۴ با بهره مندی از تجارب چندین ساله موسسین آن در زمینه آنالیز دستگاهی به منظور انجام فعالیت های تخصصی بر روی دستگاههای اسپکتروسکوپی تاسیس گردید. این شرکت در ابتدا با نام بیناب تجهیز ، فقط بروری مارک **VARIAN** فعالیت می نمود اما در سال ۱۳۸۷ به منظور توسعه فعالیت خود، تغییر ساختار داده و با نام مبنا طیف ولی با همان کادر قبلی فروش و سرویس در خدمت کاربران محترم می باشد. شرکت مبنا طیف در حال حاضر ارائه کننده محصولات زیر است:

۱. سیستم های اپتیکال از کمپانی **VARIAN** استرالیا

۲. کروماتوگرافی گازی از کمپانی **DANI** ایتالیا

۳. دستگاههای تست فیزیکی پلیمرها از کمپانی **AMSE** ایتالیا

۴. دستگاههای تست پروسسی پلیمرها از کمپانی **MN Lab Tech** تایلند



Spectrophotometer



Gas Chromatograph



Atomic Absorption



Mabna
Teyf



Behan
Chemical



Binab
Danesh



Behan
Danesh

تهران بلوار آفریقا جنب بلوار گلشهر ساختمان ۱۹۱ واحد ۶۰۳

info@mabnateyf.com

۲۲۰۲۴۳۲۷-۸ ، ۲۲۲۰۳۶۷۲۳-۴

وارش شیمی بهار

نماینده انحصاری کمپانی Anton Paar در ایران

Anton Paar Exclusive Agent in Iran



Laboratory
Online Equipments

ویسکومتر SVM 3000

جهت اندازه گیری پنج پارامتر مهم ویسکوزیته دینامیک ، دانسیته ، ویسکوزیته ، سینماتیک ، اندیس ویسکوزیته (VI) و دما

دانسیتمتر و غلظت سنج آزمایشگاهی

دستگاهی با دقت و صحت بالا جهت اندازه گیری دانسیته ، غلظت ، وزن مخصوص مایعات نظیر مواد نفتی ، نفت خام و انواع روغنها



Anton Paar

Technology in Motion

نشانی: تهران - خیابان دکتر بهشتی - خیابان اندیشه

کوچه اندیشه اول - پلاک ۳۷ - واحد ۱۴

تلفن: ۸۸۴۱۴۰۲۳ - ۸۸۴۱۳۸۱۳ - ۸۸۴۷۲۵۹۵ - ۸۸۴۷۲۵۸۰ فکس: ۸۸۴۱۴۰۵۸

www.vareshchimie.com

Address: Unit 14 - No. 37 - 1st Andisheh alley

Andisheh St - Dr Beheshti Ave - Tehran - IRAN

Tel: +98 21 88414023 - 88413813 - 88472595 - 88472580 Fax: +98 21 88414058

info@vareshchimie.com